EPDIC 9

Proceedings of the
Ninth European Powder Diffraction Conference

held
September 2–5, 2004
in
Prague, Czech Republic

VOLUME I

Editors

Radomir Kužel[1], Eric J. Mittemeijer[2]
and Udo Welzel[2]

[1] Faculty of Mathematics and Physics, Charles University, Prague, Czech Republic
[2] Max Planck Institute for Metals Research, Stuttgart, Germany

Supplement No. 23 of Zeitschrift für Kristallographie
Oldenbourg Verlag

The supplement issue is not included in the subscription price. It is offered to subscribers of the Journal "Zeitschrift für Kristallographie" at a special price of € 240.–
Subscribers of the Journal are not obliged to buy this issue, and are asked to return it to the sender within three weeks.

Printing: Druckhaus "Thomas Müntzer" GmbH, Bad Langensalza

Z. Kristallogr. Suppl. 23 (2006)
ISSN 0930-486-X

EPDIC 9

Ninth European Powder Diffraction Conference

Prague, Czech Republic, September 2–5, 2004

Conference location: Czech Technical University, Prague, Czech Republic

Conference chairman: Radomir Kužel

Organising committee:

I. Cisarova	S. Danis
N. Ganev	R. Gyepes
J. Hasek	D. Havlicek
J. Hybler	L. Kopecky
R. Kralova	R. Novak
P. Rezacova	I. Kuta Smatanova
Z. Sourek	A. Zupcanova

Programme committee:

Y. Andreev	UK
R. Cerny	Switzerland
R. Cernik	UK
J. Fiala	Czech Republic
H. Fuess	Germany
C. Giacovazzo	Italy
H. Goebel	Germany
J.M. Grochowski	Poland
B. Koppelhuber	Austria
S. Ivanov	Russia
V. Kavecansky	Slovakia
J. Kulda	France
M. Kunz	Switzerland
V. Langer	Sweden
E.J. Mittemeijer	Germany
H.F. Poulsen	Denmark
J. Rius	Spain
P. Scardi	Italy
S. Skrzypek	Poland
T. Ungár	Hungary

The EPDIC 9 proceedings have been sponsored by:

- PANalytical
- BRUKER AXS
- Unisantis
- International Centre for Diffraction Data, ICDD
- International Union of Crystallography
- HUBER Diffraktionstechnik GmbH & Co. KG
- Oxford Cryosystems
- X-Ray Optical Systems, Inc.
- STOE & Cie GmbH
- GE Inspection Technologies
- Inel
- Osmic Inc.
- GBC Scientific Equipment Pty Ltd
- Zentiva, a.s. Praha
- Anton Paar
- Röntgenlabor Dr. Ermrich

Preface

Condensation of Scientific Knowledge on Powder Diffraction

Progress of science demands communication. Whereas oral exchanges and letters were the dominant tools for transmitting knowledge from scientist to scientist in "old times", modern technological developments and, above all, the explosive growth of the number of scientists (the number of now living scientists is larger than the cumulative number of scientists who have passed away since the emergence of mankind) have made possible and necessitated global, consequently impersonal, communication means: predominantly papers in hard copy and/or electronic journals.

The enormous amount of scientific results made public in one way or the other can no longer be overlooked by a single person, even if he/she is supported by the best human or electronic "search engines": the sheer number of publications dealing with powder diffraction, to confine us to this field of science, impedes absorbing them. Hence, progress of science is served very much by the writing and publication of critical reviews and books, which ideally should provide the condensed form of the recent advances in a field of science as powder diffraction.

Primary scientific results on powder diffraction can be found in the four typical journals: Journal of Applied Crystallography, Acta Crystallographica A, Powder Diffraction and Zeitschrift für Kristallographie, and, of course, the proceedings of the EPDICs and the Denver conferences. However, many powder diffractionists, in particular the many of them who (also) are materials scientists, which includes the authors of this Preface, publish only a fraction of their scientific output on powder diffraction in the above mentioned journals: one should not be amazed to find important papers devoted to (the development of) powder diffraction in journals like Journal of Applied Physics, Philosophical Magazine, Advanced Engineering Materials, Journal of Alloys and Compounds, Journal of Solid State Chemistry and the like. This serves to illustrate that simple strategies for acquiring information at frontline level, as restricting oneself to the consultation of the typical journals mentioned, are terribly inadequate. Hence, again, we need and are dependent on high quality reviews and books.

Thus we decided, in order to serve you, to look for books and reviews on powder diffraction published since, say, 2000 and to list these with a few comments below. We cannot and do not claim to have been complete. Further, we do not present all that we found: we applied, admittedly personally biased, quality criteria.

Books

V.K. Pecharsky and P.Y. Zavalij, ***Fundamentals of Powder Diffraction and Structural Characterization of Materials****, 2003, Kluwer Academic Publishers, Boston Dordrecht London.*

This *text*book focuses on the basics of structure determination by powder diffraction. The analysis of the crystal imperfection is flagrantly absent, although this is not evident from the title of the book.

W.I.F. David, K. Shankland, L.B. McCusker and Ch. Baerlocher (Eds.), ***Structure Determination from Powder Diffraction Data****, 2002, Oxford University Press, Oxford.*

The book provides a high quality summary of the current knowledge on the (ab initio) determination of the crystal structure of a substance by powder diffraction. It has a strong crystallographic orientation. In a way this book succeeds and complements the well known book edited by R.A. Young on **The Rietveld Method** published in 1993 by the same publisher.

E.J. Mittemeijer and P. Scardi (Eds.), ***Diffraction Analysis of the Microstructure of Materials****, 2004, Springer-Verlag, Berlin Heidelberg New York.*

This is the one of the few books published ever presenting an authoritative overview of the analysis of crystal imperfection (crystallite size, microstrain, dislocation density, stacking and growth faults, (residual) macrostress etc.), through the interpretation of diffraction-line broadening and diffraction-line shift. The book supplies the readers sufficient information to apply the methods themselves.

Reviews

Crystal structure determination

K.D.M. Harris and E.Y. Cheung, ***How to determine structures when single crystals cannot be grown: opportunities for structure determination of molecular materials using powder diffraction data,*** *Chemical Society Reviews, 33(2004), 526-538.*

The paper focuses on the determination of the crystal structure of molecular solids by powder diffraction methods. The first author has published three other reviews with significant overlap with the review mentioned here: see Crystal Growth & Design, 3(2003), 887-895; Current Opinion in Solid State & Materials Science, 6(2002), 125-130; Angewandte Chemie-International Edition 40(2001), 1626-1651.

R.B. Von Dreele, ***Protein crystal structure analysis from high-resolution X-ray powder-diffraction data,*** *Macromolecular Crystallography, Part C, Methods in Enzymology, 368(2003), 254-267.*

V.V. Chernyshev, ***Structure determination from powder diffraction,*** *Russian Chemical Bulletin, 50(2001), 2273-2292.*

Additional references to review papers on structure determination and refinement can be found on the web page maintained by A. LeBail;
see '*http://www.cristal.org/iniref/revpap.html*'.

Line-profile analysis

P. Scardi, M. Leoni and R. Delhez, ***Line broadening analysis using integral breadth methods: a critical review,*** *Journal of Applied Crystallography, 37(2004), 381-390.*

This review (again) demonstrates that integral-breadth methods can be very useful to acquire a general understanding of origins of line broadening. More rigorous (Fourier and synthesis) methods (not dealt with in this review) allow a more detailed interpretation.

P. Klimanek, V. Klemm, M. Motylenko and A. Romanov, ***Substructure analysis in heavily deformed materials by diffraction methods,*** *Advanced Engineering Materials, 6(2004), 861-871.*

This paper of restricted review character has been dedicated to methods for the analysis of the radial (2θ scans) and azimuthal (ω scans) broadening of diffraction-line profiles.

Texture

H.R. Wenk and P. Van Houtte, ***Texture and anisotropy,*** *Reports on Progress in Physics, 67(2004), 1367-1428.*

This substantial review also pays attention to the application of (powder) diffraction methods for the determination of the orientation distribution function. Conventional techniques (pole figure determination) and new developments applying synchrotron radiation and neutrons at non-ambient conditions have been dealt with. The first author has published another review of more limited scope, with the same title, that largely overlaps with the review mentioned here: see Reviews in Mineralogy & Geochemistry, 51(2002), 291-329.

Stress

K. Tanaka, Y. Akiniwa and M. Hayashi, ***Neutron diffraction measurements of residual stresses in engineering materials and components,*** *Materials Science Research International, 8(2002), 165-174.*

This is a review of limited scope that provides a short sketch of the standard diffraction analysis of residual stress and that is particularly interesting because of the applications shown of neutron diffraction analysis to practical cases in the field of materials science and engineering.

K. Tanaka and Y. Akiniwa, ***Diffraction measurements of residual macrostress and microstress using X-rays, synchrotron and neutrons,*** *JSME International Journal Series A-Solid Mechanics and Materials Engineering, 47(2004), 252-263.*

Also this review of these authors has a modest range (see immediately above). It has been taken up here because it highlights the work performed in this area in Japan, which research is otherwise not easily accessible.

U. Welzel, J. Ligot, P. Lamparter, A.C. Vermeulen and E.J. Mittemeijer, ***Stress analysis of polycrystalline thin films and surface regions by X-ray diffraction,*** *Journal of Applied Crystallography, 38(2005), 1-29.*

This review provides the first comprehensive and practical treatment of all possible cases of diffraction-stress analysis for specimens exhibiting either macroscopical elastical isotropy (in the presence of single crystal elastic anisotropy) or macroscopical elastical anisotropy. An overview of models for elastic grain interaction allowing calculation of so-called X-ray elastic constants and X-ray stress factors has been included.

Non-ambient conditions

M.C. Moron, ***Dynamic neutron and synchrotron X-ray powder diffraction methods in the study of chemical processes,*** *Journal of Materials Chemistry, 10(2000), 2617-2626.*

Constraints and (future) possibilities of in-situ neutron and (synchrotron) X-ray powder diffraction methods have been indicated.

R.C. Peterson and H.X. Yang, ***High-temperature devices and environmental cells designed for X-ray and neutron diffraction experiments,*** *High-Temperature and High-Pressure Crystal Chemistry Reviews in Mineralogy & Geochemistry, 41(2000), 425-443.*

W. Paszkowicz, ***High-pressure powder X-ray diffraction at the turn of the century,*** *Nuclear Instruments & Methods in Physics Research, section B, 198(2002), 142-182.*

Experimental, operational aspects of powder diffraction at high pressures have been presented with a view to the possibilities of synchrotron radiation offered by experiments at (11) synchrotron storage rings all over the world.

The writing of a review or book is, for a scientist, a rather undervalued enterprise, because in such publications original results are not presented: naturally, the author is largely concerned with the condensed, elaborated and put-in-context presentation of results obtained by *other scientists* (to facilitate understanding of this depreciation in an extreme way: Nobel prizes are not given for such works). This attitude should change. Firstly, scientists are invariably strongly tributary to such books and reviews, even if they do not refer to these works in their publications … Secondly, the best reviews and books are written by superb scientists active as original researchers themselves. We should give them the honour they deserve.

R. Kužel

Prague

E. J. Mittemeijer
U. Welzel

Stuttgart
October 2005

Editorial Notes

For the first time, the Proceedings of an EPDIC Conference (EPDIC9) have now been published as Supplement No. 23 to the journal 'Zeitschrift für Kristallographie'; the Proceedings of EPDICS 1-8 had been published in the journal 'Materials Science Forum'. The change of the publisher guarantees the timely on-line accessibility of the Proceedings for *anyone* on the word-wide-web (keep an eye on the web pages **www.zkristallogr.de**). The Editors sincerely hope that this free on-line accessibility in combination with the traditional publication of the Proceedings in the form of printed volumes will strengthen the importance of these Proceedings as a medium for the publication of cutting-edge developments and compact state-of-the-art overviews in the field of powder diffraction.

The number of papers in these Proceedings is 98. The total number of papers published in the Proceedings of the preceding EPDIC conferences ranges from 88 to about 190.

The subdivision of the papers over the sections has been largely maintained as for preceding EPDIC proceedings. With reference to the Proceedings of EPDIC8, Section I.3 (Analysis of Microstructure and Macrostress) has now been subdivided in the subsections I.3.1 (Residual Stresses) and I.3.2 (Line Broadening Analysis). A new Section 'III. Software Development' has been introduced, recognizing that a relatively large number of corresponding contributions (six papers) had been submitted. Section III (Neutron Powder Diffraction) has been deleted and the papers on neutron powder diffraction have been distributed over other appropriate sections. Minor adjustments, to adapt the subsections to the submitted papers, have also been performed in the Materials section (IV).

Reviewing the nine editions of the EPDIC Proceedings, the ratios of the numbers of papers on developments in the methods and techniques of powder diffraction and those on applications of powder diffraction methods to specific classes of materials are found to be 1.0, 0.7, 0.5, 1.0, 0.9, 0.5, 0.7, 0.7 and, for the current proceedings, 0.8.

As for the EPDIC8 Proceedings, a strict refereeing procedure was adopted for the Proceedings of EPDIC9. Each contribution was considered by at least two referees. The referees were, to a large extent, participants of EPDIC9. A few (in this sense) external referees were contacted as well.

A paper to be published in proceedings of a conference has to fulfil at least some basic requirements: (i) new findings and/or insight should be presented, (ii) the theory suggested and/or analysis employed has to be correct (iii) the paper should be readable. Roughly ten percent of the submitted papers did not satisfy the above mentioned basic requirements and were rejected. The refereeing procedure did lead to improvements of both the scientific quality and the readability of the papers after revisions. In this way it is hoped that the EPDIC Proceedings escape the fate of much of the so-called 'grey literature'. We thank all referees

for their efforts and time spent on the manuscripts. We also thank the EPDIC9 secretary Ivana Kuta Smatanova for final technical corrections necessary for most of the papers. We did not correct the English used, apart from minor corrections in a few papers.

We sincerely hope that these Proceedings will be a useful collection of papers outlining the newest developments in the field of Powder Diffraction.

R. Kužel

Prague

E. J. Mittemeijer
U. Welzel

Stuttgart
October 2005

European Powder Diffraction Conference Award

Sponsored by PANalytical

The EPDIC award honours outstanding scientific achievements by young scientists in the areas covered within the European Powder Diffraction Conference (EPDIC) Programme. The award winner will be invited to present a plenary talk at the next European Powder Diffraction Conference. The award has a value of 1000 Euro.

The EPDIC Scientific Programme Committee, which is responsible for the nomination of the award, invites everyone to submit short proposals containing descriptions of scientific contributions to be assessed, together with the name of suitable candidates. These proposals should be addressed to the Chairman of the EPDIC Scientific Programme Committee.

Table of Contents

III. SOFTWARE DEVELOPMENT

VOLUME II

IV. MATERIALS

IV.1 Thin Layers

IV.2 Nanocrystalline Materials

IV.3 Metals and Alloys

IV.4.2 *Determination of Crystal Structure*

IV.4.3 *Determination of Magnetic Structure, Magnetic Materials*

IV.4.4 *Microstructure, Phase Analysis*

IV.5 Organic Materials

I. METHOD DEVELOPMENT AND APPLICATION

I.1 Determination of Crystal Structure

Z. Kristallogr. Suppl. **23** (2006) 3-8

Protein polycrystallography

R. B. Von Dreele[1*], P. L. Lee[2], and Y. Zhang[2]

[1]IPNS/APS, Argonne National Laboratory, Argonne, Il 60439 USA
[2]APS, Argonne National Laboratory, Argonne, IL 60439 USA
[*]Contact author; e-mail: vondreele@anl.gov

Keywords: powder diffraction, proteins, crystallization, radiation damage

Abstract. The application of powder diffraction to polycrystalline proteins has seen a number of significant advances. Faster data collection techniques have reduced the sample size requirement to less than 1mg and allowed acquisition of high quality data in <30 s permitting *in situ* exploration of protein crystallization, reactions and radiation damage effects. Recent developments include the formation of heavy atom derivatives that possibly provide a route to protein structure solution.

Fast Data Collection

Our initial experiments in protein powder diffraction [1-3] were all performed with double crystal monochromatized 0.7-1.2 Å synchrotron x-ray radiation and employed a single crystal analyzer detector. Thus, the data scans were all single point step scans each requiring several hours to complete; only a few seconds were used to accumulate the scattered intensity at each point. The instrumental contribution to the diffraction line width was ~0.005° 2Θ; the sample broadening corresponding to ~1 μm crystallites is similar so that the observed line widths are ~0.01° 2Θ. The samples were relatively large to enhance the scattered intensity; they were typically 8mm in length and 1.5 mm in diameter. Each one was a slurry of polycrystalline protein in saturated solvent packed to maximum density (~ 50 %) in a sealed glass capillary. This required 10-15 mg of protein for each experiment. Repeated measurements on freshly prepared samples gave virtually identical powder diffraction patterns; refinement of lattice parameters from these data gave results that were commensurate with the precision (1 part in > 50,000). Slight modification of the preparation conditions (pH, salt content, etc.) induced anisotropic changes in lattice parameters of 0.2-0.3 %, far in excess of the measurement precision. A radiation damage experiment showed that the source intensity (line X3B1 at NSLS) allowed exposures of 12 h for HEW lysozyme before significant degradation became apparent. Use of shorter wavelengths allowed even longer exposures.

We attempted similar experiments at line 1-BM at APS. These did not succeed because of higher radiation damage from the greater source intensity. Consequently, a new method of data collection was developed. Line 1-BM is equipped with paired bent mirrors and a double crystal monochromator that allow both longitudinal and sagittal focusing of the incident beam. The focus positions were placed at the surface of a MAR345 image plate detector positioned 700-900 mm beyond the sample position. The image plate was displaced vertically

to provide greater 2Θ range than otherwise available and a small angle beam stop was positioned to remove the direct beam (figure1). This diffraction geometry is in essence that of a low angle Guinier camera giving a high-resolution diffraction pattern on the image plate (figure 2). Typical exposure is 30 s and multiple exposures can be summed to further improve counting statistics.

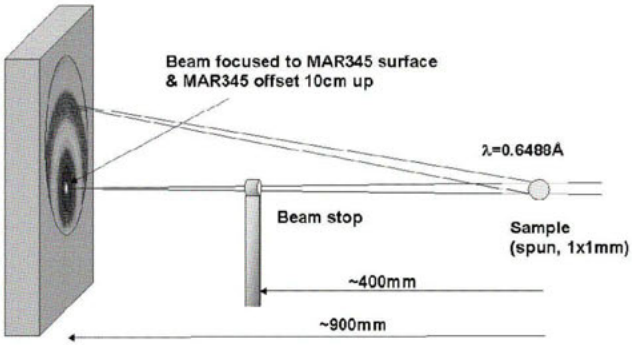

Figure 1. Use of MAR345 image plate for protein powder diffraction at beam line 1-BM at APS.

In these experiments the focusing in the vertical plane is better than that in the horizontal plane. Thus, we perform integration of a "pie" section covering 60-90° azimuthal angle of the image centered about the vertical and extending to a d-spacing of ~2.5 Å. Considering the reduction in data acquisition time and sample size as well as improved counting statistics, the resulting powder diffraction data (figure 3) from a ~1 mg sample shows 10^4-10^6 improvement in experimental quality over that from a single point detector.

This approach completely removes the problem of radiation damage in these materials and allows *in situ* tracking of processes on minutes-to-hours time scales. Preliminary experiments using samples held in 50-200 μm nylon loops suggest that further reductions in sample size by an order of magnitude or more are possible. However, the instrumental peak broadening is ~5X wider due to the 300 μm point spread on the image plate and ~200 μm sagittal focus image size; when combined with the sample broadening this gives diffraction peaks which are ~0.035° 2Θ wide. One can anticipate that improvements in beam optics and detector technology will result in significant reduction in peak widths.

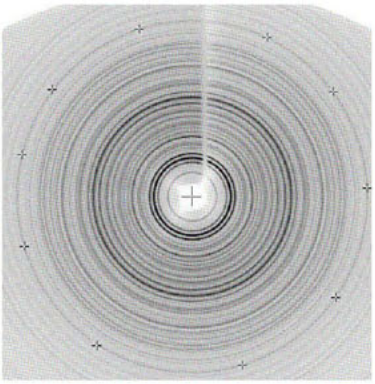

Figure 2. Powder diffraction pattern of hen egg white (HEW) lysozyme obtained at the 1-BM line at APS with 0.619A radiation in a 40s exposure on a MAR345 image plate. Crosses mark ring used to determine image center (+).

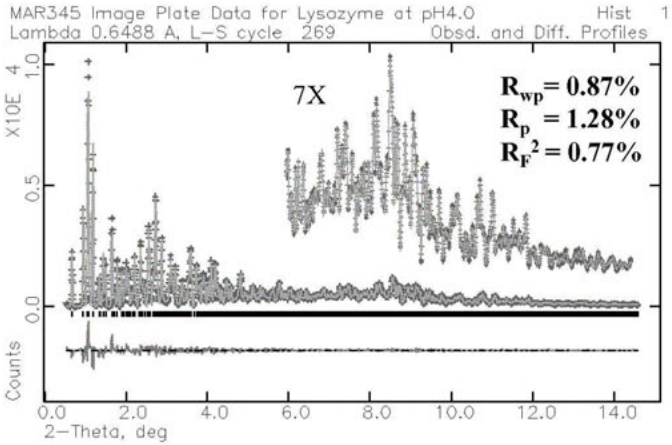

Figure 3. Powder diffraction pattern and resulting fit from Rietveld refinement of HEW Lysozyme. The background contribution has been subtracted for clarity.

In situ Crystallization and Radiation Damage Studies

The fast data collection techniques afforded the opportunity for investigating *in situ* the crystallization of hen egg white (HEW) lysozyme and its decay due to radiation damage. Figure 4 shows the result of a sequence of exposures each for 30s spaced 300 s apart for HEW lysozyme. The individual reflections display different behavior for those with l≠0; apparently the c-axis shows an initial decrease followed by a substantial increase in line with the change

in the a- and b-axes. This is in contrast to some single crystal radiation damage measurements that generally show a monotonic increase in the lattice parameters [4, 5]. Work is in progress to determine, if possible, the origin of these changes from powder diffraction.

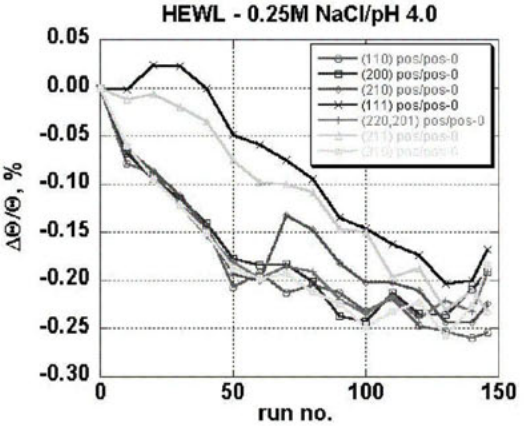

Figure 4. Bragg peak positions for HEW lysozyme as a function of beam exposure.

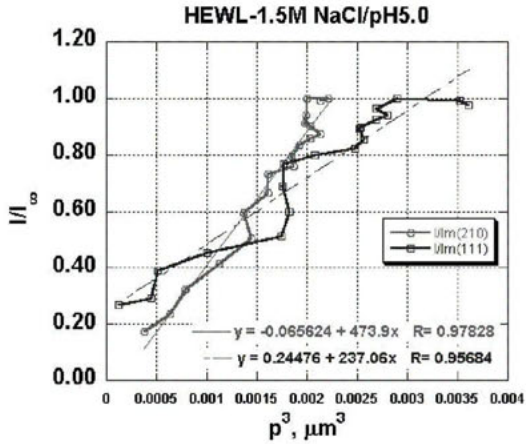

Figure 5. Crystal growth of HEW lysozyme; plot of reflection intensity and cube of particle size for the (210) and (111) reflections.

We also investigated the nucleation and growth of HEW lysozyme crystals from liquid-liquid two-phase mixtures formed under high protein and NaCl concentrations [6]. In this experiment a time series of 30 s exposures separated by 300 s showed a transformation from an amorphous phase to polycrystalline tetragonal HEW lysozyme in ca. 1.5 h. Single peak fits gave reflection intensities, peak widths and positions during the crystallization. The peak widths show a sharpening as the crystallization proceeds; this is attributed solely to crystal

growth as the derived particle size scales cubically with the peak intensity (figure 5). In addition, there was evidence that the radiation inhibited crystal nucleation as some samples did not show any crystallization over several hours exposure while neighboring regions of the same sample not exposed to radiation were completely crystallized. The reflection position changes during crystal growth also displayed some evidence of a "surface tension" effect with the peaks first shifting to higher angles and then reversing as the crystallites grew. Further study is in progress of these effects.

Xenon gas heavy atom derivative of HEW lysozyme

An initial experiment to insert Xe atoms into HEW lysozyme used 8 bar pressure onto material precipitated from pH4 1.0M NaCl buffer. The resulting powder pattern was subjected to a Rietveld refinement of nonatomic parameters (scale, lattice, background and profile) using a fixed HEW lysozyme model refined from a previous native powder pattern from the same buffer composition following procedures reported previously [3]. The set of structure factors extracted during this refinement were used

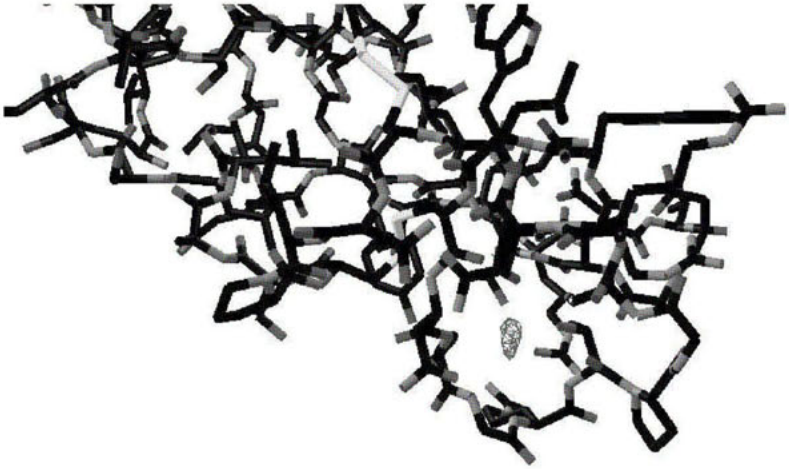

Figure 6. Model of HEW lysozyme and a 4σ difference map showing possible heavy atom location arising from exposure to 8bar Xe gas.

to create a difference density (figure 6) that showed the largest peak (>4σ) located in a pocket formed by residues 50, 51, 60 & 66-69. This site is empty in a ΔF map generated from structure factors extracted via Rietveld refinement from the powder pattern obtained from native material. Subsequent refinement of the atom fraction Xe showed only ~40% occupancy. This site is different from that found in a single crystal study of higher pH material where the Xe was found in a hydrophobic site in the HEW lysozyme active site groove [7]. Work is in progress to further explore formation of Xe heavy atom derivatives.

Conclusions

Fast data collection techniques using 2D imaging give greatly improved protein powder diffraction patterns and enable *in situ* studies of crystal growth, radiation damage and heavy atom binding to a known protein structure. It is likely that further developments will improve resolution and data collection speed.

References

1. R.B. Von Dreele, 1999, *Jour. Appl. Crystallogr.* **32,** 1084-1089.
2. R.B. Von Dreele, P.W. Stephens, R.H. Blessing and G.W. Smith, 2000, *Acta Crystallogr.* **D56,** 1549-1553.
3. R.B. Von Dreele, 2001, *Acta Crystallogr.***D57**, 1836-1942.
4. Blake, C.C.F. & Phillips, D.C., 1962, *Biological Effects of Ionizing Radiation at The Molecular Level*, pp. 183-191. Vienna: IAEA.
5. Ravelli, R.B.G., Theveneau, P., McSweeny, S., & Chafrey, M., 2002, *J. Synch. Rad.* **9**, 355-360.
6. Muschol, M. & Rosenberger, F., 1997, *J. Chem. Phys.* **107**, 1953-1962.
7. Prange, T., Schiltz, L., Colloc'h, N., Longhi, S., Bourguet, W., & Fourme, R. 1998, *Proteins: Str. Funct. and Gen.* **30**, 61-73.

Acknowledgements. Use of the Advanced Photon Source was supported by the U.S. Department of Energy, Basic Energy Sciences, Office of Science, under Contract No. W-31-109-Eng-38.

Z. Kristallogr. Suppl. **23** (2006) 9-14

Using the parallel tempering algorithm to overcome complex problems in structure determination of inorganic materials with laboratory X-rays

T. Bataille[1,*], N. Mahé[1], E. Le Fur[1,2], J.-Y. Pivan[1,2], D. Louër[1]

[1]Laboratoire de Chimie du Solide et Inorganique Moléculaire (UMR 6511 CNRS), Institut de Chimie, Université de Rennes I, Avenue du Général Leclerc, 35042 Rennes, France
[2]Ecole Nationale Supérieure de Chimie, Campus de Beaulieu, Rennes, France
[*]Contact author; e-mail: thierry.bataille@univ-rennes1.fr.

Keywords: powder diffraction, parallel tempering algorithm, direct methods, laboratory X-rays, inorganic compounds

Abstract. The crystal structures of two inorganic compounds, $Na_2[VO(HPO_4)]_2(C_2O_4).2H_2O$ and $YK(C_4O_4)_2$, have been solved *ab initio* from laboratory X-ray powder diffraction data using the parallel tempering algorithm. It is assumed that one reason of the failure of the direct methods in structure determination is the noticeable diffraction line overlap displayed by the powder patterns. Then, we discuss the influence of line broadening on the efficiency of the direct methods and the parallel tempering algorithm to solve back the crystal structure of γ-$Zn_2P_2O_7$ from powder diffraction patterns simulated for several crystallite sizes.

Introduction

Ab initio structure determination from powder laboratory X-ray diffraction data remains a challenge in many cases. One of the major problems is the lack of accurate structure factor amplitudes, due to the projection of the three-dimensional reciprocal lattice onto the one-dimensional 2θ space. This feature is dramatically exacerbated by diffraction line broadening observed when using laboratory X-rays instead of synchrotron X-rays and in case of samples with a microstructure, i.e. small diffracting domains and/or structural imperfections. If the degree of diffraction line overlap is severe, the extraction of integrated intensities cannot provide enough Bragg reflections to solve the crystal structure. Few years ago, direct space approaches, such as Monte-Carlo simulated annealing (MC-SA) method [1] or genetic algorithm [2, 3], were successfully applied to solve *ab initio* the crystal structure and molecular packing of organic molecules. These methods become undoubtedly efficient with the fast development of computer technology, provided that (i) powder data are accurately collected

(with negligible preferred orientation), (ii) diffraction line profiles are correctly modelled, (iii) Bragg peaks have been properly indexed and (iv) the chemical formula and molecular diagram are known. However, the application of direct space methods for solving crystal structures of inorganic and mineral compounds remains often tricky. Indeed, data collection using rotating capillaries is often unreliable, at least when conventional X-ray sources are used due the X-ray absorption of heavy atoms, and the crystal structures of these compounds generally result from the assembly of isolated atoms rather than large molecules. Procedures to circumvent these problems have been elaborated, e.g. the introduction of a partial model obtained from the direct methods into a MC-SA algorithm, using coordination polyhedra [4] or the potential energy minimisation combined with the MC-SA optimisation [5]. Recently, the parallel tempering algorithm [6] has been used in the program FOX [7]. The software also proposes the introduction of coordination polyhedra and molecules in the starting model, as well as a variation of a preferred orientation parameter.

In the present study, we describe the successful application of the parallel tempering approach to solve the crystal structure of two inorganic materials, namely $Na_2[VO(HPO_4)]_2(C_2O_4).2H_2O$ and $YK(C_4O_4)_2$, for which the structure determination failed when using the direct methods. Additionally, we discuss the influence of line broadening on the efficiency of the direct methods and the parallel tempering algorithm to solve back the crystal structure of γ-$Zn_2P_2O_7$ [8] from powder diffraction patterns simulated for several crystallite sizes.

Collection of high-resolution powder X-ray diffraction data

High quality powder data were obtained with a Siemens D500 diffractometer, with the Bragg-Brentano optics, using monochromatic Cu$K\alpha_1$ radiation (λ = 1.5406 Å) selected with an incident beam curved-crystal germanium monochromator. The patterns of $Na_2[VO(HPO_4)]_2(C_2O_4).2H_2O/YK(C_4O_4)_2$ were scanned at room temperature, over the angular range 10-120/10-150° (2θ), with step lengths of 0.02/0.03° (2θ) and counting times of 71/66 s $step^{-1}$. Powder pattern indexing was performed with the program DICVOL04 [9]. Structure determination was carried out using the direct methods program EXPO [10] including a whole-pattern decomposition iterative algorithm [11], and with the parallel tempering algorithm available in the global optimization program FOX [7]. Structure refinement was achieved with the program FULLPROF [12] available in the software package WINPLOTR [13]. The Rietveld refinement was carried out with a pseudo-Voigt function to describe the individual line profiles. The background was modelled with a linear interpolation between refined intensity points. The program DIAMOND (version 2.1e), supplied by Crystal Impact, was used for structure drawing.

Ab initio structure determination

$Na_2[VO(HPO_4)]_2(C_2O_4).2H_2O$

The title compound was hydrothermally prepared in powder form in the course of the investigation of open-framework mixed vanado-phosphato-oxalate materials. The first twenty lines of the pattern were indexed on the basis of a monoclinic solution and the complete review and least-squares refinement of the thirty-two diffraction lines led to the unit cell dimensions a = 6.349(1) Å, b = 17.144(3) Å, c = 6.557(1) Å, β = 106.59(2)°, V = 684.0 $Å^3$

[refined zero-shift 0.011° (2θ), M_{20} = 48, F_{32} = 79(0.007,56)]. The extinction conditions were consistent with space group $P2_1/m$. The direct methods were firstly used in order to locate the heaviest atoms, V, P and Na. Since the expected O atoms were not found from subsequent difference Fourier syntheses, the heavy atoms could not be properly attributed to the electron density positions on the alone basis of peaks height. Then, the absence of significant preferred orientation allowed starting the structure solution using the parallel tempering algorithm available in FOX. The initial model consisted in one PO_4 tetrahedron, one rigid C_2O_4 group, two Na atoms and two water O atoms. The V atom was assumed to be at the centre of an octahedron, according to common results reported in the literature. A reasonable model was found after 4.4 million moves (110 minutes), with a PC equipped with two AMD Athlon 1.7GHz processors. At the end, one sodium atom needed to be replaced by one water molecule, while the other water molecule was removed from the structure model. The final Rietveld refinement led to satisfactory R values. Figure 1a shows the best agreement obtained between observed and calculated patterns. Results of the refinement are given in table 1.

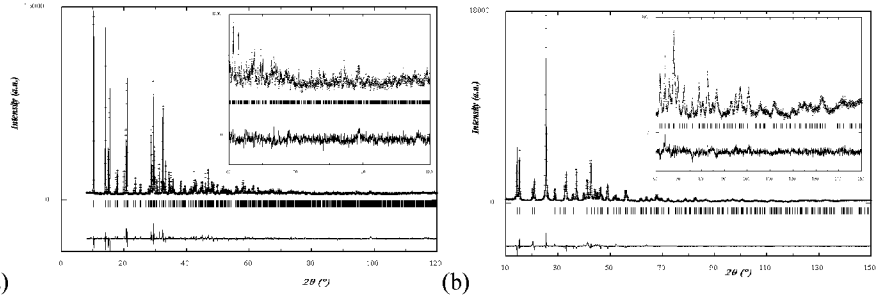

Figure 1. Final Rietveld plots for (a) $Na_2[VO(HPO_4)]_2(C_2O_4).2H_2O$ and (b) $YK(C_4O_4)_2$. The experimental data are represented by crosses, while the calculated pattern is shown by the solid line. The lower trace corresponds to the difference curve between observed and calculated patterns. The Bragg reflections are shown by the vertical bars.

Table 1. Details of the Rietveld refinements for $Na_2[VO(HPO_4)]_2(C_2O_4).2H_2O$ and $YK(C_4O_4)_2$.

Compound	$Na_2[VO(HPO_4)]_2(C_2O_4).2H_2O$	$YK(C_4O_4)_2$
Z	4	2
No. of atoms	13	4
No. of reflections	1110	269
No. of structural parameters	51	11
No. of profile parameters	25	22
R_F	0.071	0.035
R_B	0.092	0.071
R_p	0.052	0.077
R_{wp}	0.067	0.098
R_{exp}	0.038	0.053

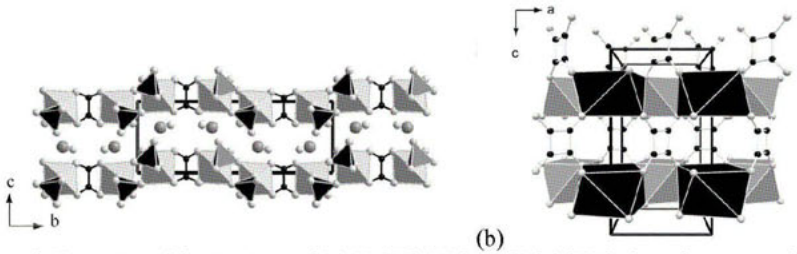

Figure 2. Projection of the structures of (a) $Na_2[VO(HPO_4)]_2(C_2O_4).2H_2O$ along the a *axis and (b) $YK(C_4O_4)_2$ along the* b *axis (medium grey polyhedron: VO_6 / YO_8, black polyhedron: PO_4 / KO_8, black sphere: C, pale grey sphere: O, medium grey sphere: Na).*

The structure (figure 2a) consists of anionic layers of oxalato-phosphate of vanadium between which are located Na^+ and water molecules. One layer is made of double-chains of corner-sharing PO_4 and VO_6 polyhedra, connected by the oxalate groups.

$YK(C_4O_4)_2$

The squarate compound was obtained at 240 °C during the thermal decomposition of the precursor $[Y(H_2O)_6]K(C_4O_4)_2(H_2C_4O_4)$ [14]. As for a majority of decomposition products, its powder pattern exhibits a significant diffraction line broadening, i.e. five times larger than the instrumental resolution function of the Siemens D500 diffractometer. The first 20 lines were indexed with DICVOL04 on the basis of a tetragonal symmetry, with unit cell dimensions a = 6.2011(5) Å, c = 11.639(1) Å, V = 447.6 Å^3 [refined zero-shift 0.007° (2θ), M_{20} = 57, F_{20} = 71(0.006,44)]. Due to the high crystal symmetry and the small volume, a few number of Bragg positions were available in the whole pattern. In addition to the broadened lines, the amount of reflections only allowed to find the extinction condition of reflections $0kl$, $l = 2n + 1$. Thus, eleven space groups were retained in this symmetry. Structure determinations using the direct methods and difference Fourier calculations were attempted for each selected space group, leading to unreliable models. Consequently, a structure solution was carried out in the triclinic space group $P1$ with the program FOX, in order to avoid symmetry errors. The starting model consisted of two Y and two K atoms and four squarate groups. The solution was found after 6.3 million trials (10 hours, AMD Athlon XP 3000+ processor). From the positions of atoms of the same species displayed by the program, symmetry elements were retrieved leading to the correct space group $P4/mcc$. The final Rietveld refinement led to satisfactory R factors and a chemically plausible structure model. Figure 1b shows the best agreement obtained between observed and calculated patterns. Results of the refinement are given in Table 1. The pillared structure, displayed in figure 2b, consists of layers of Y and K atoms connected by pendant squarate groups. A layer is built from alternating edge-sharing yttrium and potassium antiprisms.

Influence of diffraction line overlap on structure determination

The diffraction line overlap, observed in the powder diffraction patterns of the two compounds, is generally the major restraint in structure determination using the direct methods. On the contrary, it is expected that the direct space approach should be less sensitive to this feature. In order to verify this assumption, powder diffraction patterns were simulated for

nanocrystalline powders. The structure model of the inorganic decomposition product γ-$Zn_2P_2O_7$, whose structure was determined *ab initio* from powder diffraction data [8] [S. G. *Pbcm*, a = 4.9504(5) Å, b = 13.335(2) Å, c = 16.482(3) Å, V = 1088.1(2) Å^3], was used to generate calculated patterns [15]. Samples were assumed to be strain-free, with isotropic and monodisperse crystallites. Various crystallite diameters D were selected in the range 80-1200 Å. The apparent sizes ε_β (= 3D/4) were transformed into integral breadths β^* (= ε_β^{-1}) and, then, expressed in 2θ units $\beta_{2\theta}$ (= $\lambda\beta^*/\cos\theta$) for selected diffraction lines within the angular range 9-80° (2θ). To avoid unnecessary truncation errors with Lorentzian profiles [16], a Gaussian function was preferred to describe individual reflections. The angular dependence of FWHM was modelled with the usual quadratic function in tanθ from the FWHM values of the Gaussian reflections calculated from the relation FWHM = $0.9394\beta_{2\theta}$ [17].
Using the simulated patterns, the crystal structure of γ-$Zn_2P_2O_7$ was solved back using the programs EXPO and FOX. The efficiency of the direct methods was estimated by the number of correct electron peak positions found. Using the parallel tempering algorithm, it was pointed out that both the calculation time per trial and the number of trials increased when crystallite diameter decreased. A penalty factor E [= $(N_t/D)^{½}$], combining the number of trials N_t required to find the structure model and the crystallite diameter D (in Å), was then calculated. This result deserves the following comments:

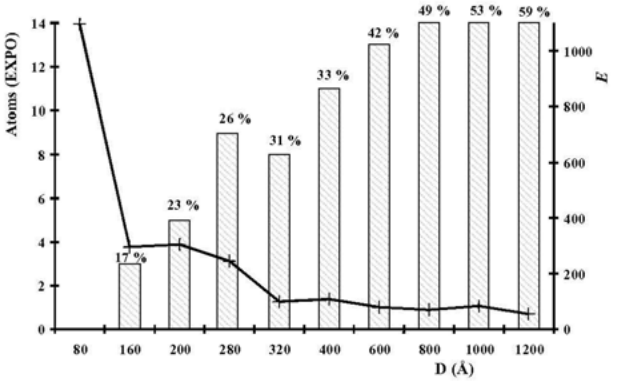

Figure 3. Comparison of the efficiency of direct methods and parallel tempering algorithm applied to powder patterns simulated for various spherical crystallite diameters D (Å) from the crystal structure of γ-$Zn_2P_2O_7$. The number of atoms (on 14 independent atoms) found by EXPO is shown by the histogram, together with the percentage of statistically independent reflections (%)[10 and refs therein], the penalty factor E related to the direct space method is represented by the solid line.

- D ≥ 400 Å: the crystal structure could be solved easily by the two approaches. The direct methods required a few minutes only, while the parallel tempering needed a few hours.
- 160 Å ≤ D ≤ 320 Å: the structure was also solved by the two approaches. While the parallel tempering algorithm was moderately affected by line broadening, the direct methods provided only half atoms. Subsequent different Fourier calculations were thus time-consuming.
- D = 80 Å: the extraction of integrated intensities was not possible, due to the excessive diffraction line broadening. The structure model was found by FOX after longer time.

Concluding remarks

This study demonstrates the efficiency of a direct space approach to solve the crystal structure of inorganic compounds when the direct methods fail, especially in the case of noticeable diffraction line overlap. However, it is also shown, through the structure determination of γ-$Zn_2P_2O_7$, that some atoms are usually found using the direct methods. Then, it is useful to consider this partial model for structure completion using a global optimisation approach.

References

1. Newsam, J. M., Deem, M. W. & Freeman, C. M., 1992, *Accuracy in Powder Diffraction II. NIST Special Publ. No.* **846**, 80.
2. Kariuki, B. M., Serrano-Gonzalez, H., Johnston, R. L. & Harris, K. D. M., 1997, *Chem. Phys. Lett.*, **280**, 189.
3. Shankland, K., David, W. I. F. & Csoka, T., 1997, *Z. Kristallogr.*, **212**, 550.
4. Altomare, A., Cuocci, C., Giacovazzo, C., Grazia, A., Moliterni, G. & Rizzi, R., 2004, *Mater. Sci. Forum*, **443-444**, 23.
5. Putz, H., Schön, J. C. & Jansen, M., 1999, *J. Appl. Crystallogr.*, **32**, 864.
6. Falcioni, M. & Deem, M. W., 1999, *J. Chem. Phys.*, **110**, 1754.
7. Favre-Nicolin, V. & Cerny, R., 2002, *J. Appl. Crystallogr.*, **35**, 734.
8. Bataille, T., Bénard-Rocherullé, P. & Louër, D., 1998, *J. Solid State Chem.*, **140**, 62.
9. Boultif, A. & Louër, D., 2004, *J. Appl. Crystallogr.*, **37**, 724.
10. Altomare, A., Burla, M. C., Camalli, M., Carrozzini, B., Cascarano, G. L., Giacovazzo, C., Guagliardi, A., Moliterni, A. G. G., Polidori, G. & Rizzi, R., 1999, *J. Appl. Crystallogr.*, **32**, 339.
11. Le Bail, A., Duroy, H. & Fourquet, J. L., 1988, *Mater. Res. Bull.*, **23**, 447.
12. Rodriguez-Carvajal, J., 1990, in *Abstracts of the Powder Diffraction Meeting*, edited by J. Galy & D. Louër (Toulouse, France), p. 127.
13. Roisnel, T. & Rodriguez-Carvajal, J., 2001, *Mater. Sci. Forum*, **378-381**, 118.
14. Mahé, N. & Bataille, T., 2004, *Inorg. Chem.*, **43**, 8379.
15. Bataille, T. Audebrand, N., Boultif, A. & Louër, D., 2004, *Z. Kristallogr.*, **219**, 881.
16. Toraya, H., 1985, *J. Appl. Crystallogr.*, **18**, 351.
17. Langford, J. I., 1978, *J. Appl. Crystallogr.*, **11**, 10.

Acknowledgements. The authors are grateful to Dr N. Audebrand and J.-F. Colin for helpful discussions. G. Marsolier and S. Lanoë are indebted for their technical assistance in X-ray powder data collection.

Z. Kristallogr. Suppl. **23** (2006) 15-20

Molecular crystal structures from powder X-ray diffraction techniques

Eugene Y. Cheung and Kenneth D.M. Harris*

School of Chemistry, Cardiff University, Main Building, Park Place, Cardiff CF10 3AT, United Kingdom
*Contact author; e-mail: HarrisKDM@cardiff.ac.uk

Keywords: powder diffraction, structure solution, genetic algorithms

Abstract. This paper presents an overview of the genetic algorithm technique for structure solution from powder diffraction data, and gives a number of examples that illustrate the application of this technique to solve crystal structures of different types of molecular solids, including oligopeptides and multi-component co-crystals.

Introduction

In recent years, most reported crystal structure determination of organic molecular solids from powder diffraction data [1–4] has used the direct-space strategy for structure solution, although a number of successful structure determinations of such materials using traditional approaches for structure solution have also been reported [5].

The direct-space strategy [1] follows a close analogy to global optimization procedures, which find applications in many areas of science. Trial structures are generated in direct space, independently of the experimental powder diffraction data, and the suitability of each trial structure is assessed by directly comparing the powder diffraction pattern calculated for the trial structure and the experimental powder diffraction pattern. This comparison is quantified using an appropriate figure-of-merit. Our implementations of the direct-space strategy have used the weighted powder profile R-factor R_{wp} (i.e. the R-factor normally used in Rietveld refinement), which considers the entire digitized intensity profile point-by-point, rather than the integrated intensities of individual diffraction maxima. Each trial structure is defined by a set (Γ) of structural variables, which represent the position, orientation and intramolecular geometry of each molecule in the asymmetric unit. The position is defined by the coordinates $\{x, y, z\}$ of the centre of mass or a selected atom, and the orientation is defined by the rotation angles $\{\theta, \phi, \psi\}$ around a set of orthogonal axes. In general, the bond lengths and bond angles are fixed (either using standard values for the type of molecule under study or using the known geometry of a similar molecule), and the intramolecular geometry is specified by a set of variable torsion angles $\{\tau_1, \tau_2, ..., \tau_n\}$ that define the molecular conformation. Thus, in general, there are 6+n variables, $\Gamma = \{x, y, z, \theta, \phi, \psi, \tau_1, \tau_2, ..., \tau_n\}$, for each molecule in the asymmetric unit.

The aim of the direct-space strategy is to locate the trial crystal structure that corresponds to the lowest R-factor, and is equivalent to exploring a hypersurface R(Γ) to find the global minimum. In principle, any technique for global optimization may be used to find the global minimum on the R(Γ) hypersurface, and most work in this field has employed Monte Carlo/simulated annealing or genetic algorithm techniques. Our most recent work has focused on the genetic algorithm. This paper gives an overview of the genetic algorithm (GA) technique for structure solution from powder diffraction data, and highlights recent applications of the technique to solve the structures of molecular crystals.

The Genetic Algorithm Technique for Structure Solution

The GA technique carries out global optimization by analogy with the processes of evolution that occur in biological systems. Thus, the technique investigates the evolution of a population through successive generations, and involves familiar evolutionary operations such as mating, mutation and natural selection. Our GA technique [6–8] for structure solution from powder diffraction data has been implemented in the program EAGER [9]. The technique investigates the evolution of a population of trial crystal structures, with each member of the population defined by a set of variables Γ, as discussed above. As each member of the population is uniquely characterized by the values of these variables, the set Γ defines its "genetic code". The initial population comprises N_p randomly generated structures. The population is then allowed to evolve through subsequent generations by applying the evolutionary operations of mating, mutation and natural selection. Through these operations, a given generation (population P_j) is converted to the next generation (population P_{j+1}). The number N_p of structures in the population is constant for all generations, and N_m mating operations and N_x mutation operations are performed during the evolution from population P_j to population P_{j+1}. The quality ("fitness") of each structure in the population depends on its value of R-factor (lower R-factor represents higher fitness).

In the mating procedure, a given number (N_m) of pairs of structures ("parents") are selected from the population. The probability of selecting a given structure as a parent is proportional to its fitness. For each pair of parents, two new structures ("offspring") are generated by distributing parts of the genetic codes of the two parents among the two offspring. It is important to note that the mating operation generates new structures by redistributing the existing genetic information in different ways, but does not create any new values of the individual genetic variables. New values of the genetic variables are instead introduced into the population by the mutation procedure, in which a given number (N_x) of structures are selected at random from the population and random changes are made to parts of their genetic code to create mutant structures. These changes may either be small random displacements from the existing values (dynamic mutation) of the genetic variables or replacement of the existing values by new random values (static mutation). The original structures from which the mutants are derived are still retained within the population. In the natural selection procedure, only the structures of highest fitness (lowest R-factor) are allowed to pass from one generation to the next generation in the GA calculation. After the population has evolved for a sufficiently large number of generations, the structure with lowest R-factor should be close to the correct structure.

An important feature of the GA technique (in contrast to other global optimization methods such as standard Monte Carlo/simulated annealing techniques) is that it involves the simultaneous sampling of many different regions of the R(Γ) hypersurface, and furthermore, information about these different regions of the R(Γ) hypersurface is passed actively between different members of the population by the mating procedure. Thus, the GA technique represents a parallel, rather than a sequential, search of the hypersurface, and as such it can readily benefit from the use of parallel computing strategies. We note that other evolutionary algorithms such as differential evolution are also amenable to parallelization [10]. In addition to the basic GA strategy described above, other features implemented within our GA program EAGER include an implementation of Lamarckian evolution [8] (in which each new structure generated in the GA calculation is subjected to local minimization of R_{wp} with respect to the variables in Γ), a parallel GA [11] (involving the evolution of several sub-populations with occasional migration of trial structures between the sub-populations), and an algorithm for rapid evaluation of R_{wp} within the context of direct-space structure solution [12].

Examples of Structure Determination from Powder Diffraction Data Employing the GA Technique for Structure Solution

The complexity of direct-space structure solution calculations is dictated primarily by the dimensionality of the hypersurface explored (i.e. the total number of structural variables in the set Γ). The greatest challenges occur when the number of structural variables is large, and arises when there is considerable molecular flexibility (i.e. the number of variable torsion angles is large) and/or when there are several independent molecules in the asymmetric unit. In all examples presented below, the powder diffraction data were recorded on a laboratory powder X-ray diffractometer, and R_{wp} was used as the basis of the figure-of-merit in the GA calculation. The next two subsections focus on multi-component co-crystal structures and conformationally flexible molecules respectively.

Multi-Component Co-Crystals

The structure of the 1:1 co-crystal containing benzoic acid ($C_6H_5CO_2H$; BA) and pentafluorobenzoic acid ($C_6F_5CO_2H$; PFBA) has been determined [13] from powder X-ray diffraction data using our parallel GA technique for structure solution. High-resolution solid state ^{13}C NMR of the co-crystal indicates that the asymmetric unit contains two molecules of BA and two molecules of PFBA. In space group *Cc*, the values of *x* and *z* for one molecule can be fixed arbitrarily, and thus a total of 26 structural variables are required in the GA calculation (each of the four independent molecules in the asymmetric unit has one variable torsion angle). The structure was solved within 170 generations for four sub-populations each containing 50 trial structures. The structure (figure 1a) comprises stacks of alternating BA and PFBA molecules, with two crystallographically independent types of stack. There is hydrogen bonding between the carboxylic acid groups of molecules in the two types of stack. All interactions of this type involve a BA molecule in one stack and a PFBA molecule in the other stack. The two independent BA molecules and the two independent PFBA molecules differ appreciably in conformation (i.e. the torsion angle between the carboxylic acid and aryl units). The fact that this torsion angle is larger for one molecule of each type can be explained by the need to avoid repulsive F•••O interactions in the structure.

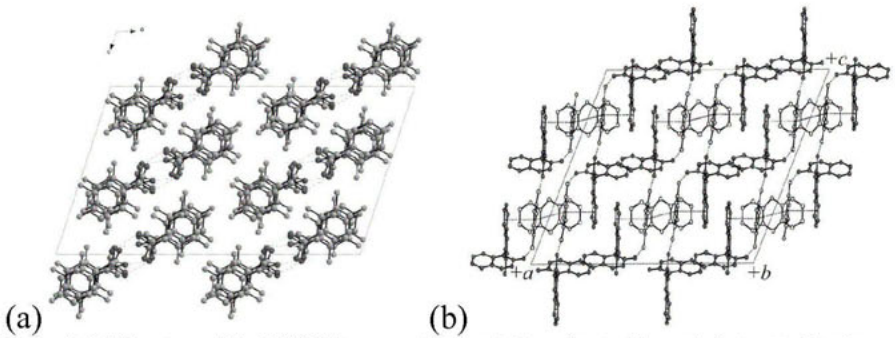

Figure 1. (a) Structure of the BA/PFBA co-crystal viewed along the stacking axis. Inter-stack hydrogen bonding involving the carboxylic acid groups is clearly evident. (b) Crystal structure of the BN/BQ/AN co-crystal. Dotted lines indicate the π-stacking interactions and hydrogen bonded chains.

Many molecular co-crystals cannot be prepared by conventional solution phase crystallization, but can instead be prepared by grinding together the "pure" solid phases of the constituent molecules. Materials prepared in this manner are virtually always microcrystalline powders, and are therefore not amenable to structural characterization by single crystal X-ray diffraction. We have demonstrated [14] the use of powder X-ray diffraction to determine the structure of a co-crystal material prepared by the solid state grinding route. The material contains three molecular components – racemic bis-β-naphthol (BN), benzoquinone (BQ) and anthracene (AN). Structure solution was carried out using our parallel GA method in space group *C*2/*c*. The contents of the asymmetric unit (confirmed on the basis of high-resolution solid state ^{13}C NMR data) comprise one BN molecule, one BQ molecule and half of an AN molecule (which resides on a two-fold axis), and the structure solution calculation involved a total of 17 structural variables. The structure was solved within 50 generations for two sub-populations each containing 100 trial structures. The structure (Figure 1b) is based on three different interaction motifs: edge-to-face interactions between BQ (edge) and AN (face) molecules, face-to-face interactions between BQ and BN molecules, and chains of O–H•••O hydrogen bonds involving BN and BQ molecules. Structural characterization of co-crystal materials prepared by grinding procedures has previously been limited by the fact that the preparation procedure intrinsically produces polycrystalline powders, but it is clear that structure determination from powder diffraction data has a crucial role to play in the structural characterization of new co-crystal phases produced in this way.

Flexible Molecules: Structural Rationalization of Oligopeptides

An understanding of the molecular conformations and intermolecular interactions in crystalline oligopeptides can provide important insights into the structural properties of polypeptide sequences in proteins [15]. However, these materials often cannot be prepared as single crystals appropriate for single crystal X-ray diffraction studies, and the use of powder diffraction data may represent the only viable route for structure determination [16]. We discuss two examples of oligopeptide structures (Piv–^{L}Pro–Gly–NHMe and Piv–^{L}Pro–γ-Abu–NHMe)

determined from powder X-ray diffraction data using our GA technique for structure solution. The interest in both materials concerns their potential to form β-turn conformations [17]. In the GA structure solution calculation [18] for Piv–^{L}Pro–Gly–NHMe, the genetic code comprised 9 variables (in space group $P1$, the position $\{x, y, z\}$ of the molecule is fixed arbitrarily). The structure was solved within 50 generations for a population size of 100 trial structures. Figure 2a shows the final refined structure of Piv–^{L}Pro–Gly–NHMe, in which the molecule adopts a Type II β-turn conformation stabilized by an intramolecular 4→1 hydrogen bond between the C=O group of the Piv residue and the methylamide N–H group (N•••O, 2.99 Å; N•••O–C, 140.6°).

The second material Piv–^{L}Pro–γ-Abu–NHMe differs from Piv–^{L}Pro–Gly–NHMe by the introduction of two additional CH_2 units within the peptide chain. In the GA structure solution calculation [19], the genetic code comprised 13 variables. The structure was solved within 20 generations for a population size of 100 trial structures. In the crystal structure, Piv–^{L}Pro–γ-Abu–NHMe adopts a folded conformation (Figure 2b), with a short C–H•••O interaction [H•••O, 2.51 Å; C•••O, 3.59 Å; C–H•••O, 172.4°; hydrogen atom position normalized according to standard geometries from neutron diffraction] between one of the α-methylene hydrogen atoms of the γ-Abu residue and the C=O group of the Piv residue. This C–H•••O interaction defines an intramolecular cyclic 10-atom motif, similar to that observed in the classical β-turn (which involves an intramolecular N–H•••O hydrogen bond).

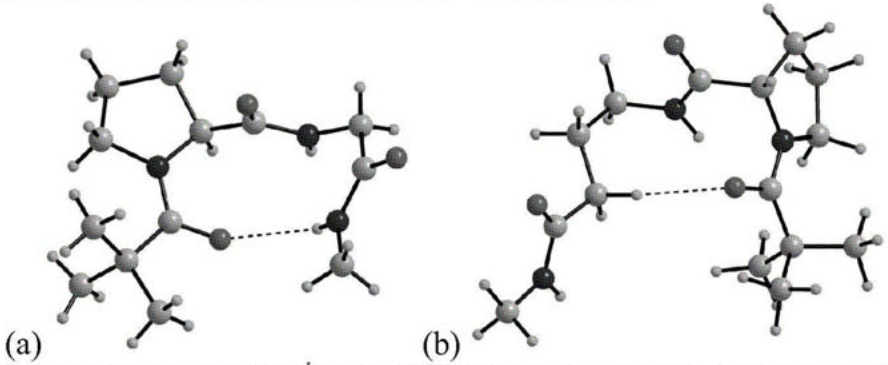

Figure 2. (a) Conformation of Piv–^{L}Pro–Gly–NHMe in the crystal structure, showing the formation of a type II β-turn. (b) Conformation of Piv–^{L}Pro–γ-Abu–NHMe in the crystal structure, showing the formation of an intramolecular C–H•••O=C interaction.

References

1. Harris, K.D.M., Tremayne, M., Lightfoot, P., Bruce, P.G., 1994, *J. Am. Chem. Soc.*, **116**, 3543.
2. Harris, K.D.M., Tremayne, M., 1996, *Chem. Mater.*, **8**, 2554.
3. Harris, K.D.M., Tremayne, M., Kariuki, B.M., 2001, *Angew. Chemie, Int. Ed.*, **113**, 1674.

4. David, W.I.F., Shankland, K., McCusker, L.B., Baerlocher, C. (Editors), 2002, *Structure Determination from Powder Diffraction Data* (Oxford University Press/International Union of Crystallography).
5. Brunelli, M., Wright, J.P., Vaughan, G.R.M., Mora, A.J., Fitch, A.N., 2003, *Angew. Chemie, Int. Ed.*, **42**, 2029.
6. Kariuki, B.M., Serrano-González, H., Johnston, R.L., Harris, K.D.M., 1997, *Chem. Phys. Lett.*, **280,** 189.
7. Harris, K.D.M., Johnston, R.L., Kariuki, B.M., 1998, *Acta Crystallogr.*, **A54**, 632.
8. Turner, G.W., Tedesco, E., Harris, K.D.M., Johnston, R.L., Kariuki, B.M., 2000, *Chem. Phys. Lett.*, **321**, 183.
9. Habershon, S., Turner, G.W., Kariuki, B.M., Cheung, E.Y., Hanson, A.J., Tedesco, E., Albesa-Jové, D., Chao, M.H., Lanning, O.J., Johnston, R.L., Harris, K.D.M., 2003, *EAGER, Computer Program for Structure Solution from Powder Diffraction Data* (Cardiff University and University of Birmingham).
10. Seaton, C.C., Tremayne, M., 2002, *Chem. Commun.* 880.
11. Habershon, S., Harris, K.D.M., Johnston, R.L., 2003, *J. Comp. Chem.*, **24**, 1766.
12. Habershon, S., Cheung, E.Y., Harris, K.D.M., Johnston, R.L., 2004, *Chem. Phys. Lett.*, **390**, 394.
13. Albesa-Jové, D., Kariuki, B.M., Kitchin, S.J., Grice, L., Cheung, E.Y., Harris, K.D.M., 2004, *ChemPhysChem*, **5**, 414.
14. Cheung, E.Y., Kitchin, S.J., Harris, K.D.M., Imai, Y., Tajima, N., Kuroda, R., 2003, *J. Am. Chem. Soc.*, **125**, 14658.
15. Fischer, G., 2000, *Chem. Soc. Rev.*, **29**, 119.
16. Seebach, D., Matthews, J.L., Meden, A., Baerlocher, C., McCusker, L.B., 1997, *Helv. Chim. Acta*, **80**, 173.
17. Seebach, D., Brenner, M., Rueping, M., Schweizer, B., Jaun, B., 2001, *Chem. Commun.*, 207.
18. Tedesco, E., Harris, K.D.M., Johnston, R.L., Turner, G.W., Raja, K.M.P., Balaram, P., 2001, *Chem. Commun.*, 1460.
19. Cheung, E.Y., McCabe, E.E., Harris, K.D.M., Johnston, R.L., Tedesco, E., Raja, K.M.P., Balaram, P., 2002, *Angew. Chemie, Int. Ed.*, **41**, 494.

Acknowledgements. We are grateful to EPSRC, Cardiff University, University of Birmingham, Purdue Pharma, Ciba Specialty Chemicals, Wyeth, Proctor and Gamble, Accelrys and Astra-Zeneca for supporting our research in the field covered by this article. The contributions of other research group members and collaborators mentioned in the references are also gratefully acknowledged.

Z. Kristallogr. Suppl. **23** (2006) 21-26

On the uncertainty of lattice parameters refined from neutron diffraction data

B. Peplinski[1,*], D. M. Többens[2], W. Kockelmann[3], R. M. Ibberson[3]

[1]Federal Institute for Materials Research and Testing (BAM), Richard-Willstätter-Str. 11, 12489 Berlin, Federal Republic of Germany
[2]Hahn-Meitner-Institute (HMI), SF2, Glienicker Str. 100, 14109 Berlin, Germany
[3]ISIS Facility, Rutherford Appleton Laboratory (RAL), Chilton, Didcot, OX11 0QX, UK
*Contact author; e-mail: burkhard.peplinski@bam.de

Keywords: uncertainty, lattice parameter refinement, neutron diffraction, Rietveld method

Abstract. Factors crucial to the reliable estimation and minimization of the uncertainty of measurement of lattice parameters refined from neutron diffraction data are analysed. Estimates of the uncertainty of measurement are derived from diffraction data of a reference material collected at one constant wavelength and two time-of-flight neutron diffractometers.

Introduction

Lattice parameter refinements from neutron diffraction (ND) data may be preferred to those from diffraction data collected with conventional X-rays or synchrotron radiation, for example if investigations on coarse-grained powders, with volumes of up to several cubic centimetres, are meant to be representative for the *whole* specimen. For these kind of analyses ND takes advantage of the high penetration of neutrons for most elements (isotopes), allowing them to simultaneously probe the whole volume of a thick specimen with nearly no attenuation. Furthermore, with ND the observed intensities of Bragg reflections are averaged over a larger number of crystallite *orientations* than the high-resolution modes of the conventional X-ray or synchrotron radiation techniques usually allow. This is a consequence of the large equatorial and axial divergence normally employed in constant wavelength ND beam optics and of the wide wavelength spectrum and the large acceptance angles of the detector banks used in time-of-flight (ToF) ND.
If a lattice parameter refinement is carried out by the Rietveld method or a related technique, then usually the only available measures of the uncertainty of the refined lattice parameters are the estimated standard deviations (e.s.d.s) calculated by the full pattern fitting program. However, e.s.d.s are measures of precision rather than of accuracy and these two terms must not be confused. For a sound estimation of the measurement uncertainty of lattice parameters that are refined from ND diffraction data more information is needed than just the e.s.d.s that are provided by the Rietveld refinement of the diffraction pattern of the sample.

General considerations

The uncertainty of measurement of refined lattice parameters has three aspects common to all types of ND instruments. These are 'wavelength calibration', 'neutron-optical aberrations & line profile modelling' and 'serial correlation' which will be discussed individually.

Wavelength calibration

Bragg's law involves a 100% correlation between the d-values (and therefore the lattice parameters) of a crystallographic phase and the wavelength of the diffracted radiation. Thus for any assumed value of the wavelength λ another set of lattice parameters results, whereas the agreement indices and the e.s.d.s *remain the same*. Since for *all* neutron diffractometers the wavelength is not known *per se,* as would be the case with characteristic X-ray radiation, even under the idealising assumption of the complete absence of any systematic errors from the model and from the observed data, the lattice parameters are completely *indeterminate.* Therefore, a determination of accurate lattice parameters by constant wavelength ND or ToF ND *necessarily* includes calibration procedures with reference materials (CRM) that have lattice parameters certified *for a given temperature* by *independent* analytical techniques. The propagation of the error which is associated with the calibration *has to* be accounted for in the estimation of the *combined standard uncertainty* (for definitions of metrological terms see [1] or derived publications; see also equations (2) and (3)) of the lattice parameters of the sample! If the ND analysis of the actual sample as well as the calibration procedure are carried out by the Rietveld method, then the estimation of the combined standard uncertainty of the refined lattice parameters can be *based* on the e.s.d.s of these *two* Rietveld analyses.

Neutron optical aberrations & line profiles

Bragg's law implies that the position of the diffraction lines and the wavelength are numbers, whereas in practise they are single-numbered *characteristics of intensity distributions*. Extracting from the *observed* diffraction pattern an *unbiased*, i.e. hypothetical diffraction pattern, which has been corrected for all aberrations is *the* precondition for the determination of accurate line positions $2\theta_{corrected}$ from which unbiased d-values and lattice parameters can be calculated. Within the framework of the 'fundamental parameter approach' (FPA) accurate mathematical modelling of the observed diffraction line profiles is achieved by convoluting the individual contributions. In constant wavelength ND the diffraction pattern $I(2\theta)_{observed}$ is described by a convolution of the wavelength distribution Λ, the instrument function, and sample-related contributions. In ToF-ND $I(2\theta)_{observed}$ and Λ are replaced by $I(d)_{observed}$ and by the time structure of the neutrons leaving the moderator, respectively.

Serial correlation

e.s.d.s calculated by many Rietveld programs are not reliable measures of the '*probable errors*', because, in many cases, they are systematically too small due to 'serial correlation' (for Cooper's criticism on the reliability of e.s.d.s in the Rietveld method see [2]). Therefore, uncorrected e.s.d.s are not only no measure of accuracy, but can also be an *unreliable* measure of the precision of refined lattice parameters. E.s.d.s are calculated under the assumption that the values in the *difference* curve are independent observations. However, adjacent individual points in the difference curve are not independent but correlated by the profile function used. The extent of this correlation depends on the size of the 2θ sampling steps used for

data collection and evaluation. A formula for estimating the corrections that should be applied to the e.s.d.s has been given by Berar and Lennan [3] who established that e.s.d.s calculated by Rietveld programs *without* consideration of serial correlations are often too small by a factor of approximately two. Multiplying the uncorrected e.s.d. by a correction factor gives the $\text{e.s.d.}_{\text{corrected}}$, i.e. an estimate of the standard deviation that also includes serial correlation.

Types of ND instruments

Further aspects of the uncertainty of measurement have to be analysed *separately* for each of the following three types of ND instruments:

A. High-resolution scanning powder diffractometers for monochromatic neutrons, equipped with *parallel* collimators placed in front of the detectors and restricting the *equatorial* divergence of the diffracted beam (prototype: D1A and D2B at the ILL)
B. High-resolution powder ToF-ND instruments
C. Powder diffractometers for monochromatic neutrons in Debye-Scherrer-geometry with one (or several) position-sensitive detector(s) providing resolution in the equatorial plane

Design characteristics of ND instruments of type A

Diffractometers of type A often use large monochromators of quite complex design which produce an incident beam with a large axial convergence. Soller collimators are usually not used with this type of diffractometer. The intensity distribution in the incident monochromized neutron beam is not necessarily homogeneous along the goniometer axis. The existence of a wavelength spread in the incident beam as shown by [4] means in practise that in Bragg's law the wavelength λ is to be replaced by its effective value $\lambda_{\text{eff.}}$.
The large axial convergence/divergence in the incident beam of this type of diffractometer causes distortions of the diffraction line profiles and line shifts ([5] and literature given therein). Within the framework of the 'fundamental parameter approach' these axial effects can be accounted for by the 'axial divergence correction function' $f_{axial\ divergence,\ approx.}(2\theta)$ which depends on axial divergence, geometry and dimensions of the instrument and the sample as well as on the width and shape of the reflections which are influenced by the real structure of the specimen. In general this function can be determined only approximately due to correlations between some of the parameters. The contributions to the 'axial divergence correction function' are convoluted with each other. This means that they are *not* additive.
For a diffractometer of type A the equatorial cross section of the incident beam can be chosen so large that it exceeds the diameter of even large sample containers by far. The most essential design element of this type of diffractometer are tight Soller-like collimators in front of each detector, that limit the *equatorial* divergence typically to about 5' or 10', making the detector angular-sensitive, rather than position-sensitive. The sampling volume of each detector again exceeds the diameter of even large sample containers by far. This very large sampling volume provided by the intersection of the wide incident beam with the wide detected diffracted beams make this type of instrument *insensitive* to small and even moderate sample displacements in the *equatorial* plane. This means that any eccentricity of the sample in the order of a few tens of a mm or even a mm will cause no line shifts in the dif-

fraction patterns. This is an inherent advantage of this type of instruments as it eliminates one of the main factors detrimental to high accuracy of lattice parameter refinements. The only remaining systematic error of 2θ-position is the residual shift of the zero point, which has to be refined *together* with the wavelength.

Contribution of the calibration procedure to the uncertainty of refined lattice parameters (ND instruments of type A)

The following three, yet contradicting optimization criteria for carrying out an accurate 'wavelength calibration' with a calibrant are a dilemma for which constant wavelength neutron diffractometers do not provide a solution:

a) It would be necessary to use for the Rietveld refinement a range of the diffraction angle as wide as possible, including explicitly the low angle region, as only this allows for the highest accuracy in the 'wavelength calibration'. The largest possible range of diffraction angles results in the largest changes of the sine-function which - according to Bragg 's law - is a necessary pre-condition for the simultaneous refinement of the two strongly correlated parameters 'wavelength' and 'zero point'.
b) It would be necessary to use for the Rietveld refinement only the angular region around 180° (2θ), as there the conversion error reaches its minimum.
c) It would be necessary to use for the Rietveld refinement only the angular region about 90°, as there the influence of the axial aberrations (and of the residual errors in the mathematical model describing the axial divergence error correction) on the angular positions of the diffraction lines reaches its minimum.

This dilemma also contributes to the situation (see preceding section), that the 'wavelength calibration' not necessarily yields the true physical values of these two strongly correlated parameters, but just their effective values. These effective values might depend on the choice of the low- (LAL) and high angle limit (HAL) used for the refinements.

The effects mentioned so far lead to the following rewriting of Bragg's law:

$$d_{hkl} = \frac{\lambda_{eff.}}{2\sin\left\{\theta_{obs.} + EPS_{1,eff.} + f_{axial\ divergence,\ approx.}(2\theta)\right\}} \tag{1}$$

with λ_{eff} = effective value of λ; $\theta_{obs.}$ = observed halved diffraction angle; $EPS_{1,eff.}$ = effective value of the zero point correction for the detector bank. Estimating the *combined* standard uncertainty u of the wavelength calibration three uncorrelated contributions have to be taken into account:

$$\left(u(\lambda_{eff.})/\lambda_{eff.}\right)^2_{combined} \approx \left(u(\lambda_{eff.})/\lambda_{eff.}\right)^2_{calibrant,\ Rietveld,\ corrected\ for\ serial\ correlation} + \left(u(a_{CRM})/a_{CRM}\right)^2_{certificate} + \left(u(a_{CRM})/a_{CRM}\right)^2_{T-calibration} \tag{2}$$

The first term on the right-hand side of equation (2) contains the contribution from the Rietveld refinement for the calibrant. Data for this term can be extracted from Table 2. They

show that this term is the moderately dominating one if silicon powder is used as a calibrant. The second term on the right-hand side is the uncertainty of the lattice parameter of the CRM (a_{CRM}) that is stated in the certificate. The third term accounts for the uncertainty of the lattice parameter that is associated with the temperature of the calibration ($T_{calibration}$).

Uncertainty of refined lattice parameters (instruments of type A)

It is good practice not to release the zero point during the refinement of the data of the sample, but to keep it fixed at the value from the 'wavelength calibration'. Thus inaccuracies of the refined lattice parameter(s) are avoided and their e.s.d.s are minimized.
The combined relative standard uncertainty u of a lattice parameter a_i of a phase refined from a diffraction pattern collected at the temperature T_{sample} can be estimated by equation (3).

$$\begin{aligned}\left(u\left(a_i\right)/a_i\right)^n_{combined} \approx & \left(u\left(a_i\right)/a_i\right)^n_{sample,\,Rietveld,\,corrected\ for\ serial\ correlation} \\ & + \left(u\left(a_i\right)/a_i\right)^n_{sample,\,axial\ divergence\ error\ correction} \\ & + \left(u\left(a_i\right)/a_i\right)^n_{T-sample} + \left(u\left(\lambda_{eff.}\right)/\lambda_{eff.}\right)^n_{calibration,\,combined}\end{aligned} \tag{3}$$

with n = 2 or 1 if there is no correlation at all or maximum correlation, respectively.
In those cases where the second and third term on the right-hand side are negligible the use of n=1 will be especially appropriate, as the remaining two contributions are strongly correlated (same instrument, Rietveld program, line profile model). The symbols in equation (3) have the same meanings as in equation (2).
The metrological connection between equations (2) and (3) is maintained *only* if the following conditions are fulfilled:

a) *identical* apparative conditions (settings of the monochromator and detector; factually analysed sample height) are used for the sample and for the calibrant (CRM);
b) *identical* mathematical models of axial divergence are applied in the Rietveld evaluation of the diffraction patterns of the sample and of the calibrant (CRM).

ND instruments of type B (ToF)

ToF diffraction patterns are displayed as I(d) and Bragg's law reads in this representation as

$$d_{hkl} = \frac{h}{m}\,\frac{1}{2\left(L_o + L_1\right)\sin\theta}\,t \tag{4}$$

with h = Planck constant, m = neutron mass, L_o = the moderator-to-sample distance, L_1 = the sample-to-detector distance, $L = L_o + L_1$ the total flight path and t = the total time-of-flight.
For each channel of the position-sensitive detector bank the product $L \cdot \sin\theta$ has to be calibrated. Sample displacement leads to changes in the flight path, $\Delta(L_o+L_1)$, and to angular shifts $\Delta\theta$, which can result in considerable shifts of the diffraction lines in a ToF diffraction pattern [6]. But from the differentiated version of equation (4) it is clear that using very large flight paths and only the backscattering region, the influence of moderate sample displacement on the observed d-values can be diminished to practically zero.

Results from three ND instruments

Diffraction data of NIST SRM640c (silicon powder) were collected at a constant wavelength and at two ToF neutron diffractometers. Details of data collection and evaluation are given in Table 1. The uncorrected estimated standard deviations and the corrected estimated standard deviations, multiplied by the coverage factor k=2, resulting from these lattice parameter refinements are summarized in Table 2. The latter are *not* yet the expanded uncertainties $U_{95\%}$ of the complete lattice parameter refinements as they do *not* include the *additional* uncertainty associated with the calibration.

Table 1. Conditions applied for the collection and evaluation of the diffraction data.

instrument	E9 (HMI)	ROTAX (ISIS)	HRPD (ISIS)
detector bank(s)	64 ^{3}He multidetector	backscattering (# 3)	backscattering (# 1)
range of d-values / Å	0.9 – 6.0	0.4 – 3.0	0.5 – 2.1
data accumulation / h	7	8	10
profile function, program	FPA [5], Fullprof.2K	double-exponential-pseudo-Voigt, GSAS	

Table 2. Estimated relative measurement uncertainties $u(a_o)/a_o$ of the lattice parameter of silicon as derived from Rietveld refinements.

instrument	E9 (HMI)	ROTAX (ISIS)	HRPD (ISIS)
$e.s.d._{uncorrected}\,(a_o)/a_o$	$5.5 \cdot 10^{-6}$	$6.8 \cdot 10^{-6}$	$1.4 \cdot 10^{-6}$
$2 \cdot e.s.d._{corrected}\,(a_o)/a_o$	$1.8 \cdot 10^{-5}$	$2.7 \cdot 10^{-5}$	$5.6 \cdot 10^{-6}$

Conclusion

To accurately refine lattice parameters from neutron diffraction data the conditions used for data collection and data evaluation should be carefully chosen. The lattice parameter of a well-crystallized cubic material can be refined with an expanded relative uncertainty of $U_{95\%}(a)/a \approx 5 \cdot 10^{-5}$ using a high-resolution multi-collimator/multi-detector diffractometer for monochromatic neutrons or a high-resolution ToF-ND instrument. With a dedicated ToF-ND instrument a value of $U_{95\%}(a)_i/a_i \approx 1 \cdot 10^{-5}$ is feasible.

References

1. BIPM, IEC, IFCC, ISO, IUPAC, IUPAP, OIML, 1993, *Guide to the expression of uncertainty in measurement (GUM).*
2. Sakata M., Cooper M.J., 1979, *J. Appl. Cryst.*, **12**, 554.
3. Berar J.F., Lennan P., 1991, *J. Appl. Cryst.*, **24**, 1.
4. Holden T.M., 1996, *Mater. Res. Soc. Symp. Proc.*, **376**, 385.
5. Többens D.M., Z. Krist., *this Proceedings of EPDIC-9, Prague*, 2004, accepted.
6. Wang X.-L., Wang Y.D., Richardson J.W., 2002, *J. Appl. Cryst.*, **35**, 533.

Acknowledgements. One of the authors (B.P.) would like to thank Prof. G. Will, University of Bonn, as well as Dr. S. Noack and Dr. W. Hässelbarth, both BAM, for helpful discussions.

I.2 Qualitative and Quantitative Phase Analysis

Z. Kristallogr. Suppl. **23** (2006) 29-34

Application of the Rietveld method to the severely superimposed diffraction patterns of technical products containing a large number of solid solution phases

B. Peplinski*, P. Köcher, G. Kley

Federal Institute for Materials Research and Testing (BAM)
Richard-Willstätter-Str. 11, D-12489 Berlin, Federal Republic of Germany
*Contact author; e-mail: burkhard.peplinski@bam.de

Keywords: phosphorus recovery, Rietveld method, sewage sludge ash

Abstract. The Rietveld method was used to reliably interpret severely superimposed diffraction patterns of a sewage sludge ash before and after being turned into an ecologically desirable, high-quality fertilizer by a newly-developed method of thermochemical treatment. The thermochemical treatment causes severe changes in the phase composition of the ash, which can be described as a mixture of a large number of solid solution phases.

Introduction

Many countries require a) the removal of phosphorus from wastewater before discharging it into the ambient environment and b) the development of technologies for the reuse of the recovered phosphorus [1]. By doing so, local rivers and lakes are protected from eutrophication (phosphorus pollution), and the world's limited resources of mineral phosphorus can be used more economically. Although phosphorus recovery from sewage sludge is already practised on a larger scale, the economically and ecologically *sensible* reuse of millions of tons p.a. of recovered phosphates is still being debated. The principal obstacle for the reuse of sewage sludge ashes as phosphate fertilizer in agriculture is their high content of ecologically harmful heavy metals, such as Zn, Cu, Pb, Cd, Hg, which exceeds the legal limits considerably. A new technology [2] is being developed at the BAM that reduces the content of ecologically harmful heavy metals in sewage sludge ashes to a value, orders of magnitude below today's legal limits. Sewage sludge ashes treated with *this* technology *can* be used as ecologically desirable, high-quality fertilizers. In addition, this treatment increases the bioavailability of the phosphorus content from a low original value of 65 to 100%; cost effectiveness is an essential advantage of the technology. The new technology has been developed on chemical intuition and decades of experience. The chemical and phase composition of *sewage sludge* ashes are different from those of ashes from coal burning power stations. The temperature-time regime of sewage sludge incineration typically includes only 5 s in the

hottest zone at a temperature of about 850 °C. Therefore, sewage sludge ashes are *non-equilibrium* mixtures of a large number of interdispersed crystallographic phases. The element distribution and phase composition of five *untreated* sewage sludge ashes were recently investigated thoroughly by a variety of analytical techniques including X-ray powder diffraction (XRD), although the latter was not used to its full potential [3]. The phase transformation processes accompanying the thermochemical treatment [2] of sewage sludge ashes have not been investigated until now.

Samples

The phase composition of four products (P0-P3) was analysed. P0 is a sewage sludge ash from a large municipal wastewater treatment plant where $FeCl_2$ was the precipitation agent. P1-P3 were obtained after small-scale thermochemical treatment was carried out on P0 according to [2]. For each of these three products slightly different process parameters were employed. For each thermochemical treatment, 100 g of the ash, P0, were hand-pressed into a brick-shaped moulding 10 x 5 x 2 cm^3 in size, put on a sintered corundum tray, soaked with 100 g of a $MgCl_2$ solution (400 g $MgCl_2$/kg) and inserted into a large muffle furnace. The latter was heated up to 1050°C, kept at this temperature for 2 h, and then cooled to room temperature. The product, P1, is a homogenized blend of five batches produced under identical conditions, yielding a final product of about 600 g.

The effectiveness of this treatment in reducing the content of ecologically harmful *heavy metals* is demonstrated by the results of element analyses carried out using X-ray fluorescence spectrometry (XRF) (table 1). The mass fractions of the *main* elements in these ashes are given in table 2. The thermochemical treatment of the ash leads to an increase in its MgO content and also causes an increase in the bioavailability of the total phosphate content of this ash. This is documented by the data in table 3. These analyses were carried out by [4] using the 'standard citric acid test for the bioavailability of phosphate fertilizers' [5] in

Table 1. Mass fractions of ecologically harmful heavy metals in a sewage sludge ash before (P0) and after (P1-P3) thermochemical treatments according to XRF analyses.

ash	mass fraction / (mg/kg)					
	Zn	Cu	Pb	Sn	Cd	Hg
P0	2680	1560	191	88	3	0.33
P1	27	165	< 2	13	< 0.3	< 0.01
P2	28	42	< 3	17	< 0.3	< 0.01
P3	420	220	< 3	66	< 0.3	< 0.01

Table 2. Mass fractions of the main elements in the ashes P0-P3 according to XRF.

ash	mass fraction / %											
	Na	Mg	Al	Si	P	S	K	Ca	Ti	Mn	Fe	Cl
P0	2.3	1.3	5.5	11.1	6.8	1.2	1.1	10.3	0.4	0.15	15.8	< 0.01
P1	2.1	8.9	4.8	10.7	6.5	< 0.002	0.3	10.0	0.4	0.15	13.7	0.01
P2	2.4	8.0	4.6	9.5	5.8	< 0.04	0.3	10.6	0.4	0.15	13.9	1.10
P3	3.5	7.6	4.2	9.1	5.5	0.08	1.0	10.7	0.4	0.15	13.7	< 0.1

Table 3. Mass fraction of the total P_2O_5 content, $w(P_2O_5)$, and percentage of the bioavailable P_2O_5 of the total P_2O_5 contained in P0 and in P1 (data from [4]).

ash	starting material	additive	$w(P_2O_5)$ / %	bioavailable P_2O_5 / %
P0	100% P0	none	15.5	65
P1	50% P0	50% $MgCl_2$ solution	14.9	93

conjunction with the inductively coupled plasma optical emission spectrometry (ICP) for the quantification of phosphorus.
All samples analysed by XRD were pulverized and homogenized in a vibratory disc mill using a tungsten carbide grinding set. Specimens analysed by XRD had a size of either Ø 38 mm x 2 mm or 38 mm x 22 mm x 2 mm and were prepared by front-loading.

Data collection and data treatment

XRD measurements were performed on a Bruker-AXS D-5000 diffractometer (∅ = 401 mm) working in Bragg-Brentano geometry using an 1.0° aperture slit, a 0.1 mm receiving slit, a sample spinner (0 or 15 rpm), a curved graphite monochromator in the diffracted beam and a scintillation counter. Data were collected in the 2Θ-range from 5° to 120° in steps of 0.02° using from 10 to 30 seconds per step. Samples were measured with two types of radiation: Cu $K\alpha_{1,2}$ (40 kV, 40 mA) and Co $K\alpha_{1,2}$ (40 kV, 30 mA). The corresponding diffraction patterns were identical if represented as 'multiple-wavelengths plots', that is as 'intensity versus *d-value* curves'.
Whole powder pattern analyses were carried out using the Rietveld program package BGMN [6-7] which employs the fundamental parameter approach (see also [8] and references therein). The Rietveld analysis of these complicated phase mixtures was assisted by Rietveld refinements of the diffraction patterns of tailor-made model ash samples with *simplified* chemical and phase compositions and of single-phase model samples. The latter were either BAM candidate reference materials (hematite; cordierite) or mineralogical samples kindly given to us by the Institute of Mineralogy, Natural History Museum, Central Institute of the Humboldt University Berlin and by the Mineralogical collection of the Friedrich Schiller University Jena.

Results and discussion

The sewage sludge ash investigated in this work contains, in its *original* state, i.e. *before* the thermochemical treatment, – according to the XRD results – both glassy and well crystallized fractions. The latter can be described as a mixture of four main components (1-4) and eight minor components (5-12), which belong to the solid solution series: 1 = whitlockite (see table 4), 2 = quartz, 3 = hematite (α-Fe_2O_3), 4 = a non-equilibrium (pseudo)cubic phase from the multi-dimensional solid solution series of spinel-like maghemite (γ-$Fe(III)_2O_3$), 5 = anorthic feldspar, 6 = olivine, 7 = talc ($Mg_3Si_4O_{10}(OH)_2$), 8 = mica, 9 = rutile (TiO_2), 10 = anhydrite ($CaSO_4$), 11 = monoclinic γ-$(Mg,Fe,Zn,Ca)_3(PO4)_2$, 12 = is possibly an orthorhombic solid solution phase of the carnegieite low type ($NaAlSiO_4$).
The diffraction patterns and their Rietveld analysis (Figure 1) revealed that the thermochemi-

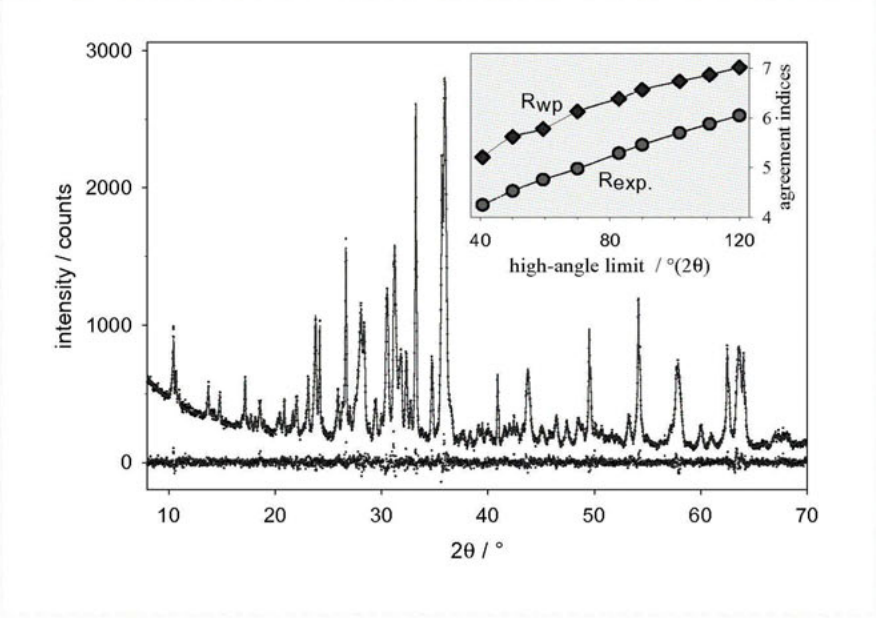

Figure 1. Observed (dotted line) and calculated (solid line) diffraction pattern, difference curve and agreement indices (small box) for the thermochemically treated ash P1 (phase composition: ten crystallographic phases, all of which belong to solid solution series).

cal treatment changes the phase composition of this sewage sludge ash markedly. The large amount of glassy phase present in the original, i.e. untreated ash P0 has completely disappeared in the thermochemically treated ashes, P1-P3. Clear evidence of this is the drastic change in the background of the diffraction patterns determinated by the Rietveld method (Figure 2). Many of the crystalline phases also underwent phase transformations. This is equally true for the phosphate and for the non-phosphate phases. Table 5 summarizes the results of the Rietveld analysis for the qualitative and semi-quantitative phase analysis of the samples, P1-P3. In P1-P3 up to three phosphate phases (whitlockite, stanfieldite and chlorapatite) are detected, whereas in P0 only one major phosphate phase (whitlockite) is observed. The total of the phosphate phases is roughly the same in the three products, P1-P3. The same is true for the mass fraction of stanfieldite. On the contrary, the mass fraction of chlorapatite varies over a wide range, apparently at the expense of whitlockite. The detection of 8 wt.-% chlorapatite in P2 agrees with the exceptionally high mass fraction of chlorine detected in this particular sample by XRF (table 2).

The reliability of the results of the qualitative and semi-quantitative phase analysis of these samples is illustrated by the excellent agreement indices achieved in Rietveld analyses of the diffraction patterns using high-angle limits (HAL) from 40 up to 120 °(2θ) (Figure 1 gives the actual values of the agreement indices for sample P1, which are also representative of those of the other samples analysed). The results of the semi-quantitative phase analyses are not influenced by systematic variations of the high-angle limit. Such a stability of the results

further contributes to the confidence in the correctness of the phase *identification* on which the semi-quantitative analysis is based. Table 4 gives some additional information on the crystallographic phases detected in these thermochemically treated ashes.

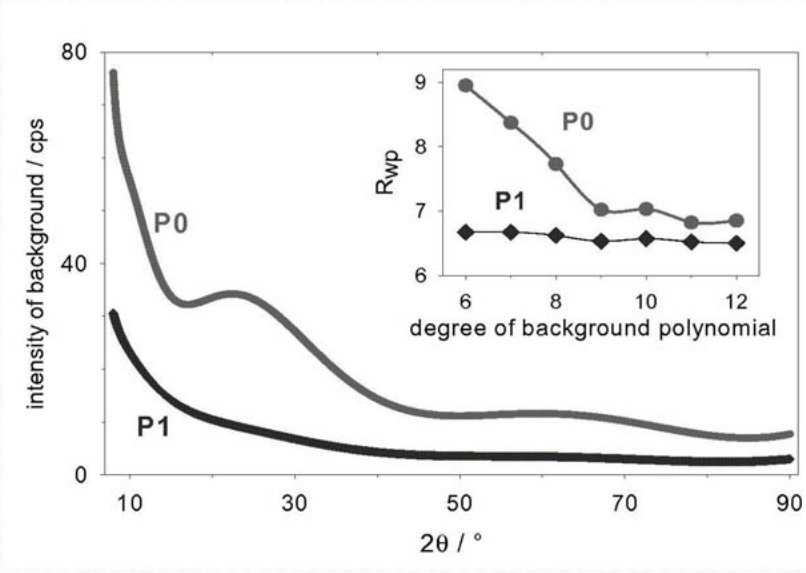

Figure 2. Background intensity in the diffraction patterns of P0 and of P1 as determined by Rietveld analyses using background polynomials of the 10th degree.
(small box: Agreement index R_{wp} achieved in Rietveld analyses of the ashes P0 and P1 in dependence on the degree of the background polynomial used in these calculations; LAL = 8°, HAL = 90°).

Table 4. List of crystallographic phases detected in the thermochemically treated sewage sludge ashes, P1-P3 (N_{os} = number of occupied sites in the asymmetric unit).

No.	abbr.	full name	chemical formula (simplified)	crystal system	N_{os}
1	whit	whitlockite	$(Ca,Mg,Fe)_{10}(PO_4)_6(PO_3OH)$	trigonal/rhomboh.	18
2	stan	stanfieldite	$Ca_{3-x}(Mg,Fe)_{3+x}(PO_4)_4$	monoclinic	40
3	clap	chlorapatite	$Ca_5(PO_4)_3Cl$	monoclinic	21
4	byto	bytownite	$(Ca,Na)(Al,Si)_4O_8$	triclinic	52
5	hema	hematite	Fe_2O_3	trigonal/rhomboh.	2
6	hyps	hypersthene	$(Mg,Fe,Ca)_1Si_1O_3$	orthorhombic	10
7	indi	indialite	$(Mg,Fe)_2Al_4Si_5O_{18}$	hexagonal	5
8	quar	quartz	SiO_2 ; $(Si,Al,Mg)O_2$	trigonal/rhomboh.	2
9	oliv	olivine	$(Mg, Fe^{2+})_2SiO_4$	orthorhombic	6
10	spin	spinel	$(Al,Fe)_2\ Mg_1O_4$	cubic	3

Table 5. Results of qualitative and semi-quantitative phase analyses of the thermochemically treated sewage sludge ashes P1 (three samples), P2 and P3 for abbreviations, see table 4; data from Rietveld analyses with LAL = 8° and HAL = 70°. For agreement indices, see the inset in the upper right corner of Figure 1, which gives the actual values for P1 that are representative of the other samples as well.

ash & sample number		weight fraction / %									
		phosphates			non-phosphates						
		1.	2.	3.	4.	5.	6.	7.	8.	9.	10.
		whit	stan	clap	byto	hema	hyps	indi	quar	oliv	spin
P1	1.	15.0	13.2	5.2	11.7	8.7	19.4	3.0	3.7	2.1	18.1
	2.	14.7	12.5	5.3	12.1	8.7	19.1	3.0	3.5	2.5	18.7
	3.	14.5	12.4	5.2	12.2	8.8	19.6	3.1	4.0	2.4	17.7
P2	1.	2.4	11.1	18.5	0	13.7	21.0	19.6	2.0	1.2	10.5
P3	1.	24.0	9.5	0	8.6	5.3	9.5	0	5.9	8.9	28.5

Conclusion

The phase composition of a sewage sludge ash and several related products was determined qualitatively and semi-quantitatively using XRD. These technical products have an extremely demanding phase composition and severely superimposed diffraction patterns. The reliability of phase identification was confirmed by the excellent agreement indices yielded by the Rietveld method, which used the fundamental parameter approach. The outcome of this investigation serves as a basis for the deeper understanding of the phase formation processes associated with the application of the new technology and stimulates its further development.

References

1. http://www.nhm.ac.nk/mineralogy/phos/ (Natural History Museum, London)
2. Köcher, P., Kley, G., Brenneis, R., '*Method for the separation of ecologically harmful heavy metals from sewage sludge ashes*', German patent 102 43 840.4; accepted 30.01.2004
3. Schirmer, Th., 1998, '*Mineralogical investigation of sewage sludge ashes and of bricks produced with additions of sewage sludge ashes*', Aachen, Shaker, (Ph.D. thesis TU Clausthal-Zellerfeld 03.07.1998)
4. Schnug, E., Fleckenstein, J., 2003, *Federal Agricultural Research Centre (FAL), section Plant Nutrition and Soil Science, Braunschweig, laboratory report* 29. January 2003.
5. Bassler, R. (Hrsg.), 1995, *Die Untersuchung v. Düngemitteln, 4. Auflage*, Darmstadt.
6. copyright by Bergmann J.; distributed by GE Inspection Technologies, Ahrensburg, Germany
7. http://www.bgmn.de.
8. Cheary, R.W., Coelho, A.A., 1992, J. Appl. Cryst., **25**, 109.

Z. Kristallogr. Suppl. **23** (2006) 35-40

Application of X-ray diffraction in forensic science

Marek Kotrlý

Institute of Criminalistics Prague, Strojnicka 27, P.Box 62/KUP, 170 82 Prague 7, Czech Republic
Contact author; e-mail: kotrly.kup@email.cz

Keywords: forensic science, powder diffraction, phase analysis

Abstract. XRD analysis is not an extremely popular technique within forensic science community. It has been used in this field for many years, but only in a few specialized laboratories around the world. Its popularity as an analytical technique in this area has been fluctuating over last thirty years.
Standard methodology of XRD was modified and optimized for small amounts of samples. As a results it is possible to work with 10^{-6} g of a sample. Currently, XRD analysis is employed in soil analyses, analyses of explosives and post blast residues, pigment and paints analyses, goods identification, analyses of unknown substances, plastics and polymers, alloys and metals, identification of degraded bones and drug analyses.

Introduction

XRD analysis is not an extremely popular technique within forensic science community [1]. It has been used in this field for many years, but only in a few specialized laboratories around the world (e.g. FBI (USA), BKA (Germany), FSS (England), NFI (Netherlands), central laboratories in Poland, Ukraine and Russia, laboratories in Japan and Australia). Its popularity as an analytical technique in this area has been fluctuating over last thirty years. This could be ascribed to the transition from photographic to diffractometric methods, and from manual interpretation to identification via electronic databases, which has been relatively slow over the past three decades.
XRD analysis started to be employed at the Institute of Criminalistics Prague (ICP) in the 60s of the past century for identifying short-circuit products on copper conductors. In the 90s there was a lab with two goniometers in classic Bragg-Brentano reflexion geometry and with another radiation source, which is utilized for Guinier and Gandolfi cameras with a classic film. Film carriers from these chambers are subsequently digitalized and evaluated as records from both goniometers. ICDD database and client databases are used for evaluation.

Methodology

In forensic field is necessary to work with small amounts of samples. Goniometer was modified for monocrystal Si cuvette in orientation parallel with plane 432. As the second step primary geometry of goniometer (position and size of slits, Soller slits and monochromators) was tested, step size factor and exposition time for gaining optimal pulse statistic for distinction of poor diffractions. For processing low-quality records PC programs ZDS and Bede ZDS for Search/Match are used. Diffraction peak position is determined by the third and fourth derivatives. Searching for up to ten phases in the mixture with the high differentiate process algorithm is possible [2].
As a result it is possible to work with 10^{-6} g of a sample.

The importance of XRD and phase analysis in forensic science lies namely in:

- the possibility of analysis of quite small-volume samples [3]
- the method is relatively non-destructive (the sample can be used for further analyses even after possible powdering) it follows from the mentioned fact that probative value of the material is preserved
- the method allows exact identification of phases in a mixture (unlike other instrumental chemical methods)
- in majority of cases it is possible to determine quantity (or semiquantity) of substance in a mixture
- the method is conclusive for potential court proceedings

Currently, XRD analysis is employed at ICP in 7 main areas:

Soil analyses
In complex analyses and soil comparisons the method is indispensable for determination of clay fraction. Other available analytical methods (EDS/WDS, XRF, FTIR, etc.) are not capable of performing exact determination of phases, namely alumosilicates. Our own calibration sets are used for semiquantitative XRD analysis (figure 1).

Explosives and post blast residues
With determination of explosives and post-blast residues, direct determination of inorganic and organic phases of explosives and post-blast residues (following the sampling of the post-blast scene and possible separations and concentrations of the material) is used. XRD methods are used also for evaluation of the effect of separation and concentration methods of post-blast residues during their testing. The post-blast scene is usually very difficult to analyse, since there are particles of all kinds of materials destroyed by the explosion, in which there are relics of post-blast residues dispersed all over, often below the detection limits. That is why different concentration and separation procedures capable of reducing the content of contaminants are used. During tests of effect of these methods, phase XRD analysis with semiquantitative evaluation proved the most convenient.

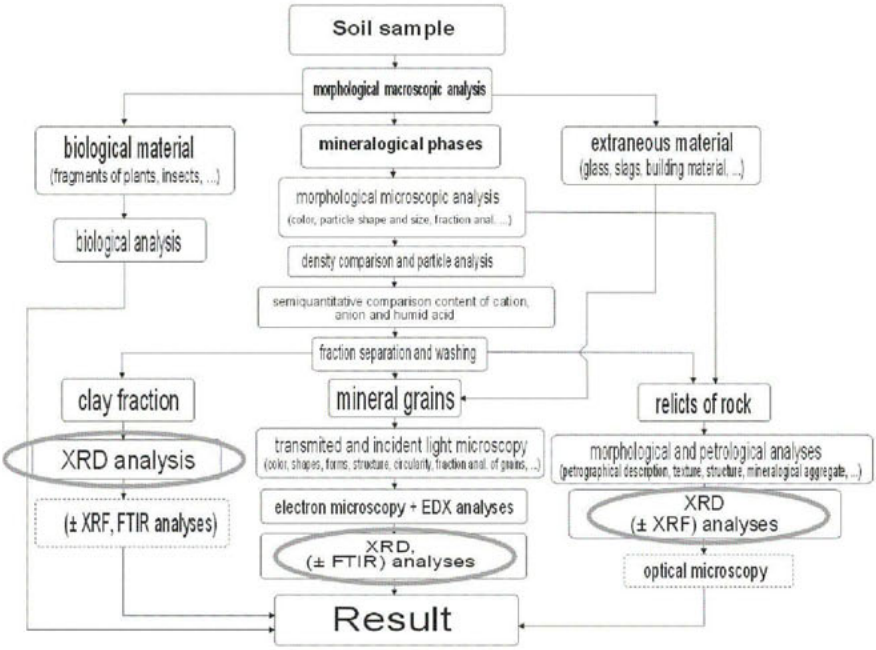

Figure 1. Block diagram of forensic soil analysis

Pigments and paints analyses

Pigments and paints analyses XRD methods are used in complex expert examination during determination of phases of artworks (paintings, sculptures etc.), car paints (analyses of abrasions and fragments after traffic accidents), analysis and comparison of lacquer systems of tools and instruments, lacquer systems used in building industry and some analyses of printing colours and paints (figure 2).

Examination of pigments of artworks is requested for solving the following issues:

- partial examination to determine the age of the painting (on the basis of used pigments, canvas type etc.)
- confirmation of originality of adjustments of the paintings, or affiliation of the painting and the frame (e.g. confirmation that the pictures were in original frames prior to the theft)
- distinguishing the original from forgery (the most complex expert examinations, in which an expert from the National Gallery participates) [4]

One of the revolutionary types of pigments is so called "effect", plate-like, or colour-variable pigments. These pigments are based on small metallic or dielectric particles covered by one or more layers of oxides and fixed in a transparent layer. Depending on the angle of incident light, the proportions between reflected and absorbed beams are changing, total reflections and interference occur. The result is a completely different colour perception from different angles (e.g. dark green - orange). Forensic identification and comparison of colour variable pigments (the size of the particles - X - X00 micrometers and thickness of the wrapping layers in X - X00 nm) present complex process, which includes methods like light microscopy in transmitted light and polarization, reflected light and polarization, electron microscopy, EDS and XRD analyses, FTIR etc [5].

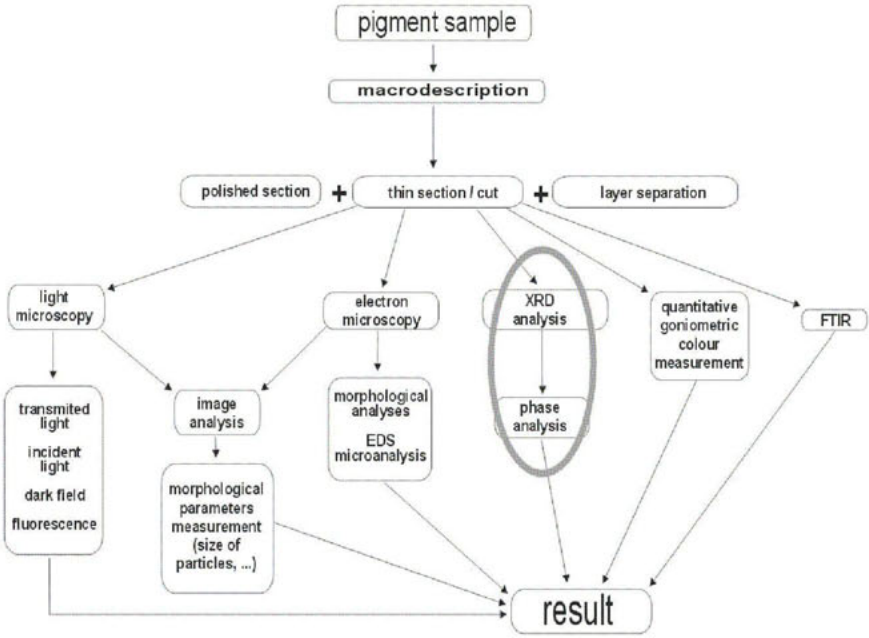

Figure 2. Block diagram of complex forensic identification and comparison of colour variable pigments.

Goods identification

Identification of type and origin of goods customs and financial frauds, counterfeiting of original branded products, money laundering. XRD methods belong to the complex of methods used for determination of the exact type of goods or material (e.g. materials for semiconductor components, fertilizers and pesticides, special heat-resistant materials, precious stones, etc.)

Unknown substances analyses

Identification of unknown substances, potential poisons and contaminants - these analyses are requested for complex analyses of materials that can harm the environment or are subject to special treatment (industrial accidents and leakage of dangerous substances (figure 3), attempts to dispose of these substances on ordinary waste dumps, threatening and extortionate letters currently frequent packets with unknown white powder etc.). For these types of analyses it is necessary to use special user databases comprising standards of poisons and substances, which are not included in common commercial databases.

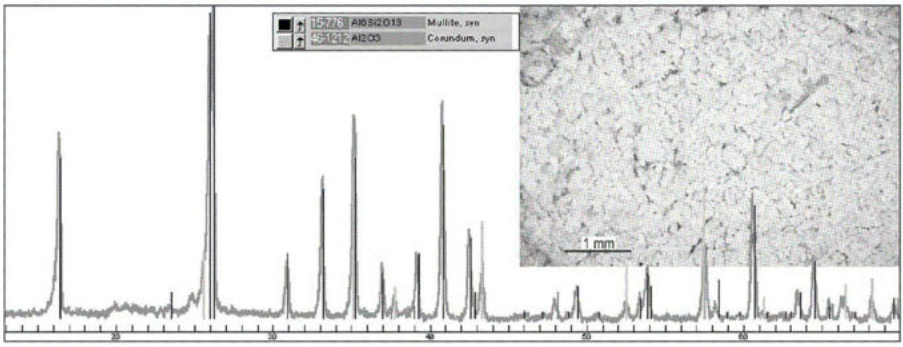

Figure 3. Identification of white powder from the threatening letter (from the "anthrax" period), picture from optical microscope.

Degraded bones

Confirmation of degraded skeletal discovery, burnt, fragments damaged or unusual to such extent that anthropologists require confirmation of composition. In this sphere, it is used for confirmation of phases, present in bone construction (figure 4).

Drugs

Quantitative drug analyses - with the aid of powder diffraction it is possible to reach higher precision of quantitative analysis of some narcotic mixtures than with instrumental methods of organic analysis (FTIR, GC). XRD analysis is in many cases faster and sample preparation is simpler. Internal standard is used for quantitative analysis.

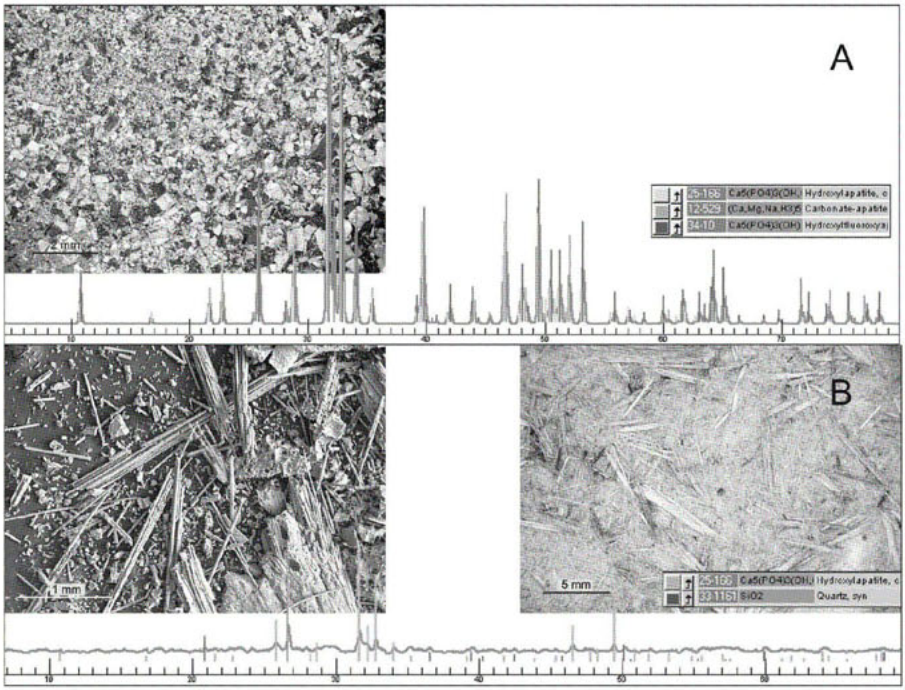

Figure 4. Comparison of two spectra of bones: A is recent, relevant relic of bone after a fire; B is relic from fossil bone (picture from optical microscope and SEM-BSE).

Further development of XRD methods in forensic science will be perhaps brought by capillary optics and its application in micro diffraction, which even today allows execution of non-destructive analysis from point sized under 100 micrometers.

References

1. Thatcher, P.J. & Briner, G.P., 1986, *Powder Diffraction,* **1**, pp.320-324.
2. Ondrus, P., 2003, *Materials Structure*, **10**, No 1a, pp. 22-24.
3. Rendle, D.F., 2003, *The Rigaku Journal*, **19**/No.2 & **20**/No.1, pp. 11-22.
4. Kotrly, M. & Turkova, I., 2003, *Forensic Science International*, **136**, supl. 1, p. 357.
5. Kotrly, M., 2003, *Forensic Science International*, **136**, supl. 1, pp. 356-357.

Acknowledgements. XRD methods at Institute of Criminalistics Prague was supported by grant-aided projects of the Czech Republic Ministry of Interior MVCR RN 19961997008, MVCR RN 19982000005.

I.3 Analysis of Microstructure and Macrostress

I.3.1 *Residual Stresses*

Z. Kristallogr. Suppl. **23** (2006) 43-48

Diffraction stress analysis of grain interaction in polycrystalline materials

U. Welzel*, S. Fréour, A. Kumar, E. J. Mittemeijer

Max Planck Institute for Metals Research, Heisenbergstr. 3, 70569 Stuttgart, Germany
* Contact author; e-mail: u.welzel@mf.mpg.de

Keywords: grain interaction, stress analysis, surface anisotropy, grain-shape texture

Abstract. This work summarises recent developments of so-called direction-dependent elastic grain-interaction models. The notion 'direction-dependent' grain-interaction signifies that different grain-interaction constraints prevail along different directions in a specimen. Practical examples of direction-dependent grain interaction are the occurrence of surface anisotropy in thin films (and, possibly, surface regions of bulk polycrystals) and the occurrence of a grain-shape (morphological) texture.

Introduction

Elastic grain-interaction models describe the distribution of stresses and strains over the differently oriented grains of a mechanically stressed polycrystal. These models allow the calculation of mechanical and diffraction (X-ray) elastic constants (diffraction (X-ray) stress factors for the case of mechanically elastically anisotropic samples), relating lattice strains to mechanical stresses, from single-crystal elastic data [1,2]. Usually, the grain-interaction models proposed by Voigt, Reuss, Neerfeld-Hill or Eshelby-Kröner are employed [1]. These models devised for bulk polycrystals with an isotropic microstructure imply that (in the absence of crystallographic texture) a polycrystal as a whole is macroscopically elastically isotropic. They have therefore been termed 'isotropic grain-interaction models' [2]. However, polycrystals cannot generally be considered as being macroscopically elastically isotropic. Two cases of direction-dependent (anisotropic) grain interaction can be distinguished: the case of *surface anisotropy* and the case of a *grain-shape texture*.

Surface anisotropy / reduced dimensionality: In a (columnar) thin film (or the surface layer of a bulk polycrystal), each crystallite is surrounded by neighbouring crystallites in only two dimensions. Thus, the grain-interaction perpendicular to the surface can be different from the grain interaction parallel to the surface: direction-dependent grain interaction occurs [3-7]. It appears obvious that deviations from an isotropic 'microstructure', as due to the reduced dimensionality of a thin film, may generally have an impact on the grain interaction.

Grain-shape texture: Following this line of reasoning, it can be anticipated that a polycrystal composed of non-spherical grains with their principal axes being aligned more or less preferentially along certain directions in the specimen (i.e., a *grain-shape or morphological texture* occurs) exhibits macroscopically elastically anisotropic behaviour too, i.e. also in this case

anisotropic grain-interaction occurs [9]. This work summarises recent developments of anisotropic grain-interaction models, presents a comparison and an experimental example.

Theoretical background

Surface anisotropy / reduced dimensionality [3-7]

In the following, an at least transversely elastically isotropic polycrystal is considered. Grain-interaction assumptions taking into account that in (columnar) thin films and surface layers of bulk polycrystals, neighbouring grains surround a grain in only two dimensions can, for example, be formulated as follows (cf. also [8]): (i) in the plane of the film, the strains are equal for all crystallites and (ii) the stresses perpendicular to the layer are identical for all crystallites. These grain-interaction assumptions fix certain stress and strain tensor components to corresponding mechanical average values (mechanical averages are indicated by brackets < >):

$$\boldsymbol{\varepsilon}^S = \begin{pmatrix} \langle \varepsilon_{11}^S \rangle & \langle \varepsilon_{12}^S \rangle & \Diamond \\ \langle \varepsilon_{12}^S \rangle & \langle \varepsilon_{22}^S \rangle & \Diamond \\ \Diamond & \Diamond & \Diamond \end{pmatrix}, \quad \boldsymbol{\sigma}^S = \begin{pmatrix} \Diamond & \Diamond & \langle \sigma_{13}^S \rangle \\ \Diamond & \Diamond & \langle \sigma_{23}^S \rangle \\ \langle \sigma_{13}^S \rangle & \langle \sigma_{23}^S \rangle & \langle \sigma_{33}^S \rangle \end{pmatrix} \qquad (1), (2)$$

The superscript S indicates that a tensor is expressed in the specimen frame of reference S. The tensor components marked by $\Diamond$ are not explicitly specified for every crystallite, but these components can be calculated from Hooke's law for every crystallite, $\varepsilon_{ij}^S = s_{ijkl}^S \sigma_{kl}^S$. The s_{ijkl}^S are the single crystal elastic compliances. Hooke's law represents a system of nine equations for eighteen unknowns, but as the strain $\boldsymbol{\varepsilon}$ and stress $\boldsymbol{\sigma}$ tensors are symmetric (i.e. $\varepsilon_{ij} = \varepsilon_{ji}$ and $\sigma_{ij} = \sigma_{ji}$), Hooke's law is a short notation for six independent equations for twelve independent unknowns. If six components of the twelve unknowns are known, as a consequence, the other components can be calculated by solving Hooke's law.

Extreme grain-interaction assumptions (e.g. the stresses perpendicular to the layer are identical for *all* crystallites) are adopted in the above described Vook-Witt (VW) model. In terms of the bulk models it could be said that Voigt behaviour ('equality of strains') is attributed to the in-plane directions, whereas Reuss behaviour ('equality of stresses') is attributed to the direction perpendicular to the film surface. Thus, the Vook-Witt model will generally be incompatible with the true elastic behaviour of a polycrystal. To overcome this problem, the inverse Vook-Witt model (iVW), required for the construction of an effective grain-interaction model, has been proposed [2,5,6]. The grain-interaction assumptions for the inverse Vook-Witt model are as follows: (i) the in-plane stress is equal for all crystallites and (ii) the strain perpendicular to the film surface is equal for all crystallites:

$$\boldsymbol{\varepsilon}^S = \begin{pmatrix} \Diamond & \Diamond & \langle \varepsilon_{13}^S \rangle \\ \Diamond & \Diamond & \langle \varepsilon_{23}^S \rangle \\ \langle \varepsilon_{13}^S \rangle & \langle \varepsilon_{23}^S \rangle & \langle \varepsilon_{33}^S \rangle \end{pmatrix}, \quad \boldsymbol{\sigma}^S = \begin{pmatrix} \langle \sigma_{11}^S \rangle & \langle \sigma_{12}^S \rangle & \Diamond \\ \langle \sigma_{12}^S \rangle & \langle \sigma_{22}^S \rangle & \Diamond \\ \Diamond & \Diamond & \Diamond \end{pmatrix}. \qquad (3),(4)$$

The tensor components marked by ◊ are not explicitly specified for every crystallite, but these components can be calculated, as described above for the VW model.
The above formulated grain-interaction assumptions allow the calculation of the mechanical elastic constants and the diffraction stress factors.
The need for introducing the iVW model can be understood as follows: The number of grain-interaction models of extreme types of grain-interaction assumptions is two for bulk materials (Reuss and Voigt). However, four types of extreme grain-interaction models then can be formulated for (columnar) thin films, as two principal directions, each with two extreme grain-interactions, occur. These extreme grain-interaction models are the Reuss, the Voigt, the VW and the iVW models. In a so-called effective grain-interaction model, the mechanical and diffraction elastic constants (or diffraction stress factors) are calculated as arithmetic weighted averages of the elastic constants obtained from a set of extreme grain-interaction models. A well known example for an effective grain-interaction model is the Neerfeld-Hill model (= 'average' of 'Reuss' and 'Voigt', in case of isotropic grain interaction). Here, a weighted average of the Reuss, Voigt, VW and iVW models is proposed for cases of anisotropic grain interaction. The background of any averaging of (extreme) grain-interaction models to describe physical reality could be described as follows: A real sample is conceived to be constituted from separate volume fractions of crystallites, each of which obeys a certain type of grain-interaction (for details, see Refs. [5,6]). Note that such grain-interaction models may also be relevant in the context of layered structures and one-dimensional structures (e.g. in Al interconnects or damascene Cu lines), i.e. generally in the context of reduced dimensionality.

Grain-shape (morphological) texture [9]
In order to calculate the elastic constants of a polycrystal from single-crystal elastic data in the Eshelby-Kröner (EK) model, the crystallites surrounding an individual grain (inclusion) in a polycrystal are conceived as an elastically homogenous matrix with the elastic properties of the entire polycrystal. Traditionally, a spherical shape of the inclusions is considered [1]. A grain-shape (morphological) texture can be incorporated in the EK model by considering ellipsoidal inclusions with their principal axes aligned along common directions in the specimen frame of reference. The shape of the crystallites can be described by a shape parameter η, which is defined as the ratio of the principal axis of the ellipsoid in the z-direction (a_3) of the specimen frame of reference and the principal axes of the ellipsoid in the x-direction (a_1) and the y-direction (a_2) in the specimen frame of reference, respectively: $\eta = a_3 / a_1 = a_3 / a_2$. Thus, the considered ellipsoids exhibit rotational symmetry with respect to a common axis (here taken as the surface normal of the specimen).

Diffraction stress analysis and diffraction analysis of elastic grain interaction
The unknown stress tensor components $\langle \sigma_{ij}^S \rangle$ can be obtained as fit parameters in a (least-squares) minimisation of the difference χ^2,

$$\chi^2 = \sum_i \omega_i^2 \left(\varepsilon_i^{calc} \left(\langle \sigma^S \rangle, hkl, \varphi, \psi \right) - \varepsilon_i^{meas} \left(hkl, \varphi, \psi \right) \right)^2 \qquad (5)$$

where the ε_i^{meas} represent the measured lattice strains. The index *i* stands for all lattice strains determined from measurements (for all different ψ, φ and/or *hkl* analysed). The ω_i are

weighing factors which can be used to reflect the statistical relevance of the measured strains $\varepsilon_i^{meas}(hkl,\varphi,\psi)$ in the result of the minimisation and could correspond to the inverse of the squares of the standard deviations of the measured strains. For the case of macroscopically elastically anisotropic specimens considered here, the diffraction strains, ε_i^{calc}, have to be calculated from

$$\varepsilon_i^{calc}\left(\left\langle\sigma^S\right\rangle,hkl,\varphi,\psi\right)=F_{mn}(\psi,\varphi,hkl)\left\langle\sigma_{mn}^S\right\rangle, \qquad (6)$$

where the $F_{mn}(\psi,\varphi,hkl)$ are the so-called diffraction (X-ray) stress factors [1,2]. The following variant of the above-described method has been proposed [5,6]: In addition to the unknown stress tensor components, parameters related to the grain interaction can be refined in the fitting procedure. If the elastic grain interaction in the specimen can be parameterised by parameters f_i, which are not known a priori, they can be used as fitting parameters in addition to the unknown stress tensor components. Such additional fitting parameters could, for example, be the weighing factors for the individual models in an effective grain-interaction model. This fitting is possible as the grain-interaction parameters have a distinct influence on the diffraction stress factors. Non-linear $\sin^2\psi$-plots are characteristic for the occurrence of anisotropic grain interaction. It is essential to use measured data recorded from various reflections *simultaneously* in the fitting, in order to obtain unique fit results.

Results and discussion

Mechanical elastic constants [3-7,9]

Components of the mechanical stiffness tensor calculated employing various grain-interaction models have been gathered in table 1. The stiffness tensor corresponds to transverse elastic isotropy and thus consists of five independent components (it holds that $\mathbf{C}_{22}^S=\mathbf{C}_{11}^S$, $\mathbf{C}_{23}^S=\mathbf{C}_{13}^S$, $\mathbf{C}_{55}^S=\mathbf{C}_{44}^S$ and $\mathbf{C}_{66}^S=\frac{1}{2}\left(\mathbf{C}_{11}^S-\mathbf{C}_{12}^S\right)$) for cases of anisotropic grain interaction. For the traditional EK model ($\eta=1$), an isotropic mechanical stiffness tensor is obtained, i.e. only two independent components occur ($\mathbf{C}_{11}^S$, $\mathbf{C}_{12}^S$). It can be concluded that the effect of the grain interaction on the mechanical elastic constants is relatively weak.

Table 1. Independent components of the mechanical stiffness tensor of copper in Voigt notation (single-crystal elastic stiffnesses taken from [10]; unit = GPa).

Cu	$\mathbf{C}_{11}^S$	$\mathbf{C}_{33}^S$	$\mathbf{C}_{44}^S$	$\mathbf{C}_{12}^S$	$\mathbf{C}_{13}^S$
VW	202.39	198.88	47.16	102.65	106.16
EK ($\eta=0.1$)	202.16	199.43	47.41	103.15	105.89
EK ($\eta=1$)	201.30	201.30	48.17	104.95	104.95
EK ($\eta=10$)	200.84	202.15	48.49	105.84	104.52
iVW	200.80	204.08	49.56	106.84	103.56

Diffraction stress factors [3-7,9]

The effect of the type of grain interaction on the diffraction (X-ray) stress factors will be demonstrated using plots of lattice strain $\varepsilon(hkl,\varphi,\psi)$ versus $\sin^2\psi$ (so-called $\sin^2\psi$-plots) assuming that the polycrystal considered is subjected to a planar, rotationally symmetric state of stress ($\left\langle\sigma_{11}^S\right\rangle=\left\langle\sigma_{22}^S\right\rangle=\sigma_{//}$). $\sin^2\psi$-plots calculated employing the different grain-interaction

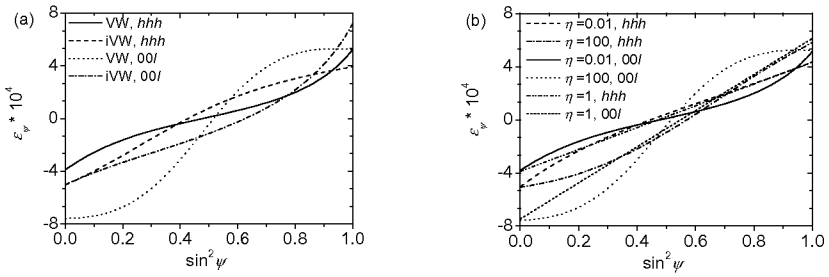

Figure 1. $\sin^2\psi$-plots for the hhh and 00l reflections of a crystallographically untextured copper polycrystal subjected to a plane-rotationally symmetric state of stress (100MPa) according to the (a) Vook-Witt (VW) and inverse Vook-Witt (iVW) models and (b) Eshelby-Kröner model involving different ellipsoidal crystallite morphologies (single-crystal elastic stiffnesses taken from [10]).

models are shown in figure 1. The macroscopic elastic anisotropy (transverse isotropy) is reflected by the occurrence of non-linear $\sin^2\psi$-plots. Only for the traditional EK model (η =1; spherical grain morphology), linear $\sin^2\psi$-plots occur, as in this case, the polycrystal presents macroscopic isotropy. It can be concluded from figure 1 that the effect of the grain interaction on the diffraction stress factors generally is much more pronounced than the effect on mechanical elastic constants.

Comparison of the direction-dependent grain-interaction models [11]

Similarities in the results obtained for both the mechanical elastic constants (cf. table 1) and the diffraction stress factors (cf. figure 1) from the different models occur. It has been found both on the basis of numerical calculations, analytical simplifications of certain tensors involved in the EK model and plausibility considerations, that the grain-interaction assumptions in the EK model are similar to those of the VW model if disc-like grain morphology is considered, whereas the grain-interaction assumptions in the EK model are similar to those of the iVW model if needle-like grain morphology is considered. These findings imply that for certain (hypothetical) cases, the effect of surface anisotropy on elastic properties of polycrystals cannot be distinguished from the effect of a grain-shape texture.

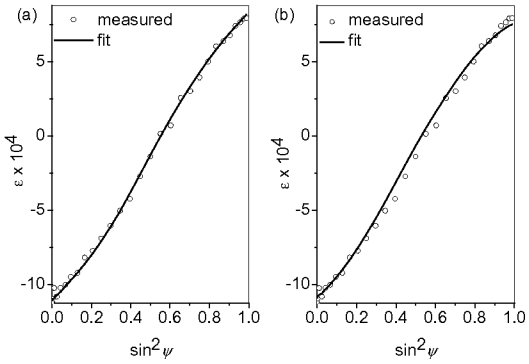

Figure 2. $\sin^2\psi$-plots for the 200 reflections of a copper thin film fitted employing grain-interaction models accounting for surface anisotropy (a, $\sigma_{//}$ =130MPa) and grain-shape texture (b, $\sigma_{//}$ =138MPa) (for details, see [12]).

An experimental example

Six reflections of a sputter-deposited copper layer of thickness 500nm have been fitted simultaneously employing the

above explained strategy for stress analysis (see figure 2, showing exemplary $\sin^2\psi$-plots for the 200 reflections; [12]). A better fit to the experimental data has been obtained for the case of surface anisotropy. These findings are in line with the results of microstructural investigations. The specimen has a columnar microstructure with an average grain-aspect ratio close to one. Thus, surface anisotropy occurs.

Summary

(i) The traditional grain-interaction models due to Voigt, Reuss, Neerfeld-Hill and Eshelby-Kröner are inappropriate for the stress analysis of specimens exhibiting direction-dependent grain interaction.
(ii) Thin films are generally mechanically elastically anisotropic also in the absence of crystallographic texture, due to the occurrence of *surface anisotropy*. The elastic grain interaction of such polycrystals can be modelled employing an effective grain-interaction model combining the extreme Reuss, Voigt, Vook-Witt and inverse Vook-Witt models.
(iii) Polycrystals with a *grain-shape (morphological) texture* are mechanically elastically anisotropic also in the absence of crystallographic texture. Their elastic grain interaction can be modelled employing an extension of the traditional Eshelby-Kröner model.
(iv) For extreme grain-shape textures (discs and needles, parallel and perpendicular to the surface, respectively), the grain interaction in the Eshelby-Kröner model exhibits similarities with the grain interaction in the Vook-Witt and inverse Vook-Witt models, respectively.
(v) (X-ray) Diffraction is a sensitive tool to investigate elastic grain interaction. Grain-interaction parameters can be refined together with the unknown stress tensor components.

References

1. Welzel, U., Ligot, J., Lamparter, P., Vermeulen, A. C. & Mittemeijer, E. J., 2005, *J. Appl. Cryst.* **38**, 1.
2. Welzel, U. & Mittemeijer, E. J., 2003, *J. Appl. Phys.* **93**, 9001.
3. van Leeuwen, M., Kamminga, J.-D. & Mittemeijer, E. J., 1999, *J. Appl. Phys.* **86**, 1904.
4. Leoni, M., Welzel, U., Lamparter, P., Mittemeijer, E.J.& Kamminga, J.-D., 2001, *Phil. Mag. A* **81**, 597.
5. Welzel, U., Leoni, M. & Mittemeijer, E. J., 2003, *Phil. Mag.*, **83**, 603.
6. Welzel, U., Leoni, M. & Mittemeijer, E.J., 2004, in: *Diffraction analysis of the microstructure of materials*, edited by Mittemeijer, E.J. & Scardi, P. (Springer, Berlin), pp. 363-390.
7. Welzel, U. & Fréour, S. in preparation.
8. Vook, R.W. & Witt, F., 1965, *J. Appl. Phys.* **36**, 2169.
9. Koch, N., Welzel, U., Wern, H. & Mittemeijer, E. J., 2004, *Phil. Mag.* **84**, 3547.
10. Meyers, M. A. & Chawla, K. K., 1984, *Mechanical metallurgy, principles and applications* (Englewood Cliffs, New Jersey: Prentice-Hall), p. 57.
11. Welzel, U., Fréour, S. & Mittemeijer, E.J., 2005, *Phil. Mag.* **85**, 2391.
12. Kumar, A., Welzel, U. & Mittemeijer, E.J., submitted.

Z. Kristallogr. Suppl. **23** (2006) 49-54

Accurate absolute peak positions for multiple {*hkl*} residual stress analysis by means of misalignment corrections

Arnold C. Vermeulen

PANalytical, Lelyweg 1, 7602 EA Almelo, The Netherlands
e-mail: arnold.vermeulen@PANalytical.com

Keywords: residual stress, accurate positions, alignment errors, misalignment corrections

Abstract. For reliable triaxial or multiple {*hkl*} residual stress analysis results it is essential that the peak positions are accurate in an absolute sense. In this paper a set of analytical formulas describing the effects of peaks shifts due to remaining alignment errors is tested on a stress-free reference specimen. With the misalignment parameters obtained software corrections can be applied on measured peak position in stress measurements employing combined tilting (χ-tilt and ω-offset).

Introduction

Managing alignment errors is the key to success in obtaining reliable XRD stress data. For the classical $\sin^2\psi$ residual stress analysis using relative peak positions, only two alignment errors are relevant: *specimen displacement* and *incident beam misalignment* [1,2,3]. For advanced residual stress analysis methods using absolute peak positions, other alignment errors become relevant too [3]: *zero beam shift*, *chi axis misalignment* and *omega axis misalignment*. Therefore, for triaxial stress analysis and multiple {*hkl*} stress analysis all alignment errors must be taken into consideration. When employing focusing optics all of the alignment errors must be determined and corrected for. The corrections can be done by tuning the hardware (for large errors) [1] and/or by software (for the remaining errors) [2,3].
The issue of alignment errors in the field of single crystal diffraction with respect to crystal centring [4], where data of reflection-antireflection pairs of the same {*hkl*} reflection can be analysed, and/or with respect to angular misalignments (non-parallel or non-perpendicular orientation) of the rotation axes [5] is also discussed. For these cases it is generally assumed that the rotation axes and the incident beam intersect each other perfectly. However in a powder diffractometer, spatial displacements of the rotation axes and the incident beam (i.e. the above-mentioned misalignments) may occur and these are together with the displacement of the specimen surface the main potential sources of error in residual stress analysis.
The complete procedure to obtain accurate absolute peak positions when applying combined tilting (applying both χ-tilt and ω-offset) involves measuring peak positions of a calibration/reference powder specimen over the full 2θ and the full χ and (ω-θ) ranges. The peak

shifts with respect to the theoretical peak positions are analysed with a multivariate linear least squares (multiple linear regression) fitting procedure. Such a procedure was used earlier by Convert & Miege (1991) [1] to analyse specimen displacement and incident beam misalignment on a single reflection. Applying this on *multiple* reflections enables the possibility to analyse *all* alignment errors and to include other sources of peak shift, like: error in stress-free lattice parameters, thermal expansion, error in wavelength, transparency, et cetera. The relevance of these errors will be discussed. The fit parameters obtained – describing the remaining alignment errors – are used for a software correction of the measured peak positions.

Theory

If the alignment errors of an instrument are known they can be used to obtain accurate absolute peak positions by correcting the measured peak positions according to:

$$2\theta_{corr} = 2\theta_{meas} - \Delta 2\theta_{ze} - \Delta 2\theta_{sp,\chi} - \Delta 2\theta_{eq} - \Delta 2\theta_{ax} - \Delta 2\theta_{\chi,\omega} - \Delta 2\theta_{\omega,2\theta}, \qquad (1)$$

where $2\theta_{corr}$ is the corrected angle, $2\theta_{meas}$ is the measured angle and $\Delta 2\theta_{xx}$ are the alignment errors of the instrument. A full set of misalignment formulas has been presented earlier by Vermeulen (2000) [3] for the omega-stress and chi-stress modes. Here an overview of a generalised modular set of formulas for the combined tilts mode (i.e. employing both ω- and χ-tilting) is presented in table 1. The same formulas will be the basis for a fitting procedure to determine the misalignments on a series of measurements on a stress-free reference specimen.

Two additional errors, the transparency error (see also [6]) and the reference error, both of which may play an additional role in either the determination of or the corrections for the

Table 1. Generalised set of peak shift formulas for zero beam shift ($\Delta 2\theta_{ze}$), specimen displacement w.r.t. chi axis ($\Delta 2\theta_{sp,\chi}$), incident beam misalignments (equatorial $\Delta 2\theta_{eq}$ and axial $\Delta 2\theta_{ax}$), and axis misalignments (chi w.r.t. omega axis $\Delta 2\theta_{\chi,\omega}$ and omega w.r.t. 2theta axis $\Delta 2\theta_{\omega,2\theta}$) for combined tilts mode, which includes both omega-stress mode (χ=0) and chi-stress mode (ω=θ). With goniometer radius R.

Error	Function	Combined tilts mode	
$\Delta 2\theta_{ze}$ (°)	$2\theta_{ze}$	$2\theta_{ze}$	(2)
$\Delta 2\theta_{sp,\chi}$ (°)	$h_{sp,\chi} f_{sp}$	$h_{sp,\chi} \frac{180}{\pi} \frac{2}{R} \frac{\sin\theta}{\sin\omega\cos\chi} \cos\theta$	(3)
$\Delta 2\theta_{eq}$ (°)	$h_{eq} f_{eq}$	$h_{eq} \frac{180}{\pi} \frac{2}{R} \frac{\sin(\omega-\theta)}{\sin\omega} \cos\theta$	(4)
$\Delta 2\theta_{ax}$ (°)	$h_{ax} f_{ax}$	$h_{ax} \frac{180}{\pi} \frac{2}{R} \frac{\sin\theta\sin\chi}{\sin\omega\cos\chi} \cos\theta$	(5)
$\Delta 2\theta_{\chi,\omega}$ (°)	$h_{\chi,\omega} f_{\chi,\omega}$	$h_{\chi,\omega} \frac{180}{\pi} \frac{2}{R} \frac{\sin\theta}{\sin\omega} \cos\theta$	(6)
$\Delta 2\theta_{\omega,2\theta}$ (°)	$h_{\omega,2\theta} f_{\omega,2\theta}$	$h_{\omega,2\theta} \frac{180}{\pi} \frac{2}{R} \cos\theta$	(7)

Table 2. Additional set of formulas to correct peak positions for an isotropic error in the reference ($\Delta 2\theta_{ref}$) and for transparency ($\Delta 2\theta_{tr}$). With cubic lattice parameter a, wavelength λ, linear expansion coefficient α, temperature T and linear absorption coefficient μ.

Error	Function	Combined tilts mode	
$\Delta 2\theta_{ref}(°)$	$\varepsilon_{ref} f_{ref}$	$\varepsilon_{ref} \frac{180}{\pi} 2\tan\theta$	(8)
		$\varepsilon_{ref}=\Delta a/a_o$, $\varepsilon_{ref}=\Delta\lambda/\lambda$, or $\varepsilon_{ref}=\alpha\Delta T$	
$\Delta 2\theta_{tr}(°)$	$\mu^{-1} f_{tr}$	$\mu^{-1} \frac{-180}{\pi} \frac{2 f_{tau}}{R} \frac{\sin\theta\cos\theta}{\sin\omega\cos\chi}$	(9a)
		$f_{tau} = \frac{\sin^2\theta - \sin^2(\omega-\theta)}{2\sin\theta\cos(\omega-\theta)}\cos\chi$	(9b)

alignment errors, are presented as examples in table 2. For the reference error only the isotropic term is included as occurs for cubic materials. In principle anisotropic terms can be added for use with non-cubic reference materials.

Procedure

The misalignment analysis is applied here in a generalised form using a multivariate linear least squares (multiple linear regression) fitting procedure (see also [1]):

$$2\theta_{meas,j} - 2\theta_{ref,j} = 2\theta_{ze} + h_{sp,\chi} f_{sp,j} + h_{eq} f_{eq,j} + h_{ax} f_{ax,j} + h_{\chi,\omega} f_{\chi,\omega,j} + h_{\omega,2\theta} f_{\omega,2\theta,j}, \quad (10)$$

where $2\theta_{ze}$ is a constant and $f_{sp}, f_{eq}, f_{ax}, f_{\chi,\omega}$ and $f_{\omega,2\theta}$ are goniometric functions describing the peak shift due to specimen displacement, equatorial beam misalignment, axial beam misalignment, chi axis misalignment and omega axis misalignment, respectively. Table 1 gives an overview of the above functions and the linear misalignment parameters, $h_{sp,\chi}$, h_{eq}, h_{ax}, $h_{\chi,\omega}$, and $h_{\omega,2\theta}$.

In order to obtain a meaningful set of misalignment parameters, attention must be paid to their specific dependencies on the angles θ, ω and χ. Hence in the measured set of data the following angle ranges must be included:

- Positive and negative χ-tilt angles to separate h_{ax} and $h_{sp,\chi}$.
- Positive and negative ω-offset angles to separate h_{eq} and $h_{sp,\chi}$.
- A large χ range to separate $h_{sp,\chi}$ and $h_{\chi,\omega}$.
- A large ω range and 2θ range to separate $h_{\chi,\omega}$ and $h_{\omega,2\theta}$.
- A large 2θ range to separate $h_{\omega,2\theta}$ and $\Delta 2\theta_{ze}$.

Experimental

The experiments were performed on a PANalytical X'Pert PRO MRD system with a horizontal goniometer and an XYZ-stage mounted on a half-circle Eulerian cradle. The pre-aligned fast interchangeable PreFIX optics modules for point focus geometry were used.

All measurements were performed on a stress-free Au powder specimen. We measured the (111), (200), (220), (311), (331), (420), (422) and (511)/(333) reflections with positive and

negative tilts over the full measurable range (up to $\sin^2\psi_{max}$= 0.1 … 0.8 for omega-stress and $\sin^2\psi_{max}$= 0.9 for chi-stress). In one additional series of measurements combined tilts were applied (omega-stress series combined with χ=30°). Finally in a series of measurements an artificial specimen displacement of +200 µm was introduced with the z-movement of the XYZ-stage. In all series the tilts were applied with $\sin^2\psi$ steps of 0.1.

Results

The multiple linear regression analysis based on equation (10) is firstly applied to a large data set consisting of a series of χ-tilt measurements and a series of ω-offset measurements to obtain a full description of the alignment condition of the used diffractometer system. An additional parameter for the reference error (see equation (8) in table 2) is added to equation (10) in order to refine the strain-free lattice parameter of the Au reference powder (PDF 04-0784: a_o=4.07860 Å). A correction for transparency (see table 2) was omitted since it would

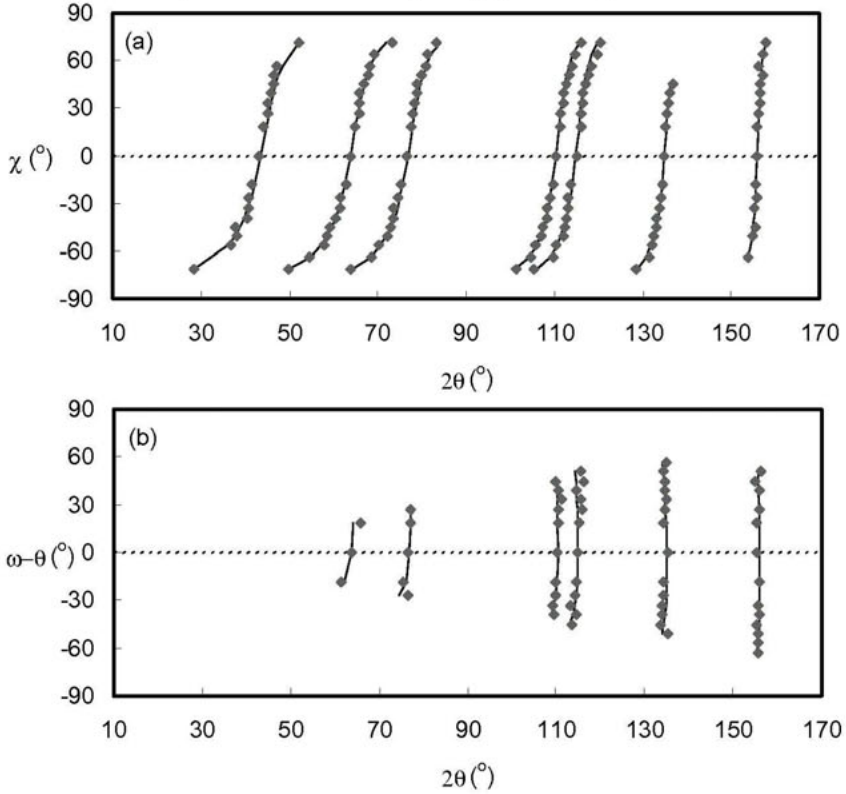

Figure 1. Graphical results of a simultaneous fit on (a) a series of χ-tilt measurements and (b) a series of ω-offset measurements. The relative 2θ peak displacements are magnified with a factor of 100 for more clarity. See table 3 for the numerical results.

Table 3. Results of multiple linear regression analysis with equation (10).

Parameter	Data set		
	Analysed	Example 1: Combined tilts	Example 2: Displaced specimen
$\Delta 2\theta_{ze}$ (°)	0.026 (4)	0.026	0.026
$h_{sp,\chi}$ (μm)	-45 (3)	-45	149 (1)
h_{eq} (μm)	-50 (9)	-50	-50
h_{ax} (μm)	121 (2)	121	121
$h_{\chi,\omega}$ (μm)	-51 (12)	-51	-51
$h_{\omega,2\theta}$ (μm)	0	0	0
a_{Au} (Å)	4.07834 (2)	4.07830 (1)	4.07827 (1)
$\sigma(2\theta)_{meas}$ (°2θ)	0.0372	0.0256	0.0817
$\sigma(2\theta)_{fit}$ (°2θ)	0.0055	0.0098	0.0075

have no significant effect. It was assumed that the ω axis and 2θ axis coincide ($h_{\omega,2\theta}$=0).
In the analysis the data points whose individual deviation was too large were successively removed from the analysed set starting with the data point with the largest deviation until the remaining data points fit within a range of –4 and +4 times their average standard deviation. The removed data points had typically, originated from reflections showing a distorted profile shape due to too large defocusing effects (i.e. too close to the theoretical value for $\sin^2\psi_{max}$).
The results are shown in table 3. Figures 1a and 1b show the graphical results. Note the significant reduction in standard deviation before and after applying the software correction in the last two rows of table 3.

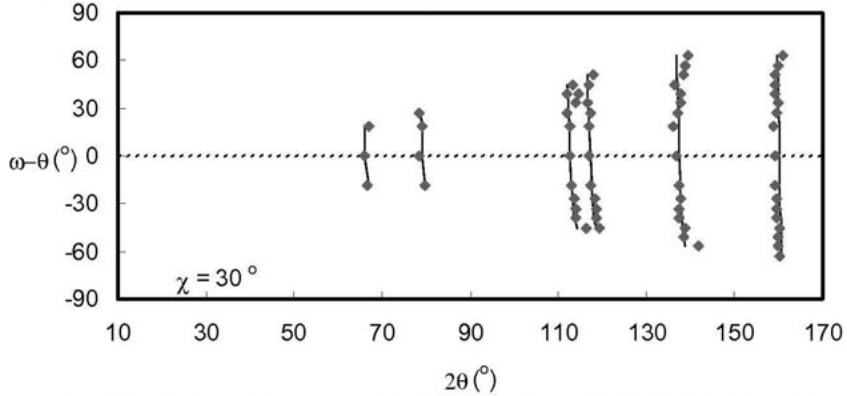

Figure 2. Graphical results of a fit on a series of combined tilt measurements (ω-offset combined with fixed χ=30°) using the analysed parameters (see figure 1) as fixed fit parameters. The only free fit parameter is the reference error (i.e. lattice parameter). The relative 2θ peak displacements are magnified with a factor of 100 for more clarity. Note that the largest changes with respect to figure 1b occur at low 2θ angles and high ω-offsets. See table 3 for the numerical results.

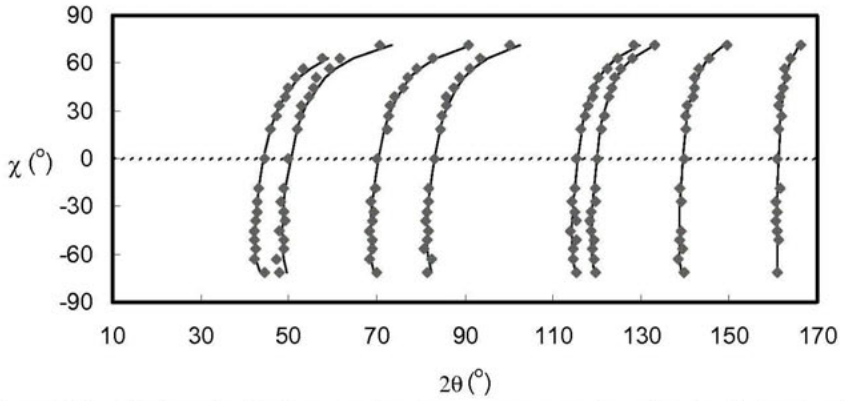

Figure 3. Graphical results of a fit on a series of measurements on the artificially displaced specimen (Δz=+200μm) using the analysed parameters (see figure 1) as fixed fit parameters. The only free fit parameters are the specimen displacement (Δh_{sp}=+194μm) and the reference error (i.e. lattice parameter). The relative 2θ peak displacements are magnified with a factor of 100 for more clarity. See table 3 for the numerical results.

In a second step the parameters obtained from the first analysed set were applied on two example sets of data both with an unique collection of data points measured on the same specimen but under different conditions. In the first example a set with combined tilts is tested against the set of parameters of the analysed set (see table 3 and figure 2). In the second example a set originating from a deliberately displaced specimen (+200 μm) is tested against the analysed parameters with the displacement parameter as additional free fit parameter (see table 3 and figure 3).

Conclusions

With the method presented in this paper a full set of alignment errors are quantified, which is relevant for measurements over the full 2θ range and when applying χ-tilt or ω-offset or combined tilting. The method can be used as part of an iterative procedure to improve the alignment of the hardware. Alternatively the results can be used for a software correction procedure in order to obtain reliable absolute peak positions. This will make it possible to perform accurate triaxial or multiple {*hkl*} residual stress analysis.

References

1. Convert, F. & Miege, B., 1992, *J. Appl. Cryst*, **25**, 384.
2. Vermeulen, A.C. & Houtman, E., 2000, *Mat. Science Forum*, **347-349**, 17.
3. Vermeulen, A.C., 2000, in *Proc. ICRS-6 conf.*, Oxford, UK, pp. 283-290.
4. King, H.E. & Finger, L.W., 1979, *J. Appl. Cryst*, **12**, 374.
5. Dera, P. & Katrusiak, A., 1999, *J. Appl. Cryst*, **32**, 193.
6. Vermeulen, A.C., 2001, *Mat. Science Forum*, **378-381**, 166.

Z. Kristallogr. Suppl. **23** (2006) 55-60

Diffraction stress analysis of strongly fibre-textured gold layers

A. Kumar, U. Welzel*, E.J. Mittemeijer

Max Planck Institute for Metals Research, Heisenbergstr. 3, 70569, Stuttgart, Germany
*Contact author; e-mail: u.welzel@mf.mpg.de

Keywords: residual stress analysis, crystallite group method, crystallographic texture

Abstract. For diffraction stress analysis of specimens exhibiting a crystallographic fibre-texture being simultaneously strong and sharp, the crystallite group method (CGM) can be employed. However, adoption of the CGM for diffraction stress analysis involves approximations which can lead to considerable errors in the derived stress values. Erroneous stress results can also arise from the simultaneous use in a single stress analysis of lattice-strain data obtained from multiple *hkl* reflections, which requires the measurement of absolute peak positions, whereas the measurement of only peak shifts suffices if the analysis is based on only one *hkl* reflection. The different sources of errors have been discussed and an experimental example has been presented for the case of instrumental aberrations.

Introduction and theoretical background

X-ray diffraction is frequently employed for the analysis of the mechanical stresses in polycrystalline specimens. The simplest analysis procedure is the so-called $\sin^2\psi$-method employing diffraction (X-ray) elastic constants. Measured lattice strains for a specific reflection at a certain angle φ are plotted with respect to $\sin^2\psi$, where ψ is the angle between the sample surface normal and the diffraction vector and φ denotes the rotation of the sample around the sample surface normal. The components of the mechanical stress tensor can be determined from the slopes of straight lines (or parameters of the ellipses for the cases of presence of shear stresses) occurring in such plots. The applicability of this approach is limited to crystallographically untextured specimens presenting isotropic grain interaction [1].

The most general approach is based on the use of the so-called diffraction (X-ray) stress factors and generally involves the use of the crystallographic orientation distribution function (ODF) and the adoption of an appropriate grain-interaction model [1,2]. This method is cumbersome (involving numerical calculus and the use of the orientation distribution function) and, although straightforward, rarely used in practice. For specimens exhibiting crystallographic texture being simultaneously strong and sharp, the crystallite group method (CGM) is a simple alternative for diffraction stress analysis [1,3].

The case of a single crystal-like texture is considered first: all crystallites with the same crystallographic orientation form a crystallite group. Usually, the Miller indices of the crystallographic planes oriented parallel to the sample surface, $\{mnr\}$, and the indices of the S_1 axis

of the specimen frame of reference in the crystal frame of reference, <*uvw*>, are used for defining the orientation of a particular crystallite group [3].

The strain tensor of a crystallite group in the specimen frame of reference (indicated with the superscript *S*) ε_{ij}^{S} is related to the stress tensor σ_{kl}^{S} by Hooke's law employing single-crystal elastic compliances transformed to the specimen reference frame s_{ijkl}^{S}:

$$\varepsilon_{ij}^{S} = s_{ijkl}\sigma_{kl}^{S} \tag{1}$$

In equation (1), ε_{ij}^{S} and σ_{kl}^{S} have to be considered as averages over all (spatially distributed) crystallites in the specimen belonging to the crystallite group under consideration. Equation (1) holds also for the lattice strain measured by diffraction, provided that for the strain measurement, only crystallites of the crystallite group under consideration contribute to a diffraction line. Thus, the measured lattice strain for a given *hkl* reflection is the strain along the direction of the diffraction vector $\vec{m}$, identified by the angles φ and ψ:

$$\varepsilon_{\varphi\psi}^{hkl} = \varepsilon^{\vec{m}} = m_i^S \varepsilon_{ij}^S m_j^S = m_i^S s_{ijkl}^S \sigma_{kl}^S m_j^S \tag{2}$$

Next, the case of a fibre texture is considered: an ideal orientation in this case is defined like in the single-crystal case, but the orientations of crystallites are assumed to be randomly distributed with respect to the surface normal of the specimen. Thus, for the fibre textured case, specifying only the Miller indices of the crystallographic planes oriented parallel to the sample surface, {*mnr*}, suffices for identifying an ideal orientation. Equation (2) can also be employed for the fibre-textured case (subject to certain conditions; see below) if a plane, rotationally symmetric state of stress occurs ($\sigma_{12}^S = \sigma_{13}^S = \sigma_{23}^S = \sigma_{33}^S = 0$, $\sigma_{11}^S = \sigma_{22}^S$) because only in this case, no averaging is required over the diffracting crystallites at $\psi = 0$. Analytical simplifications of equation (2) can be derived and examples have been summarised in table 1.

Table 1. Simplified $\sin^2\psi$ *-laws and the corresponding strain-free directions (indicated by* ψ^**) for two different fibre textures of cubic materials. The* s_{ij} *are the components of the single-crystal compliance tensor in Voigt notation.* $s_0 = s_{11} - s_{12} - \frac{1}{2}s_{44}$.

fibre texture	simplified $\sin^2\psi$ -law	strain-free direction
{111}	$\varepsilon_\psi = (2s_{12} + \frac{2}{3}s_0 + \frac{1}{2}s_{44}\sin^2\psi)\sigma_{\parallel}$ (3)	$\sin^2\psi^* = \left(-2s_{12} - \frac{2}{3}s_0\right)/\frac{1}{2}s_{44}$ (4)
{100}	$\varepsilon_\psi = (2s_{12} + (\frac{1}{2}s_{44} + s_0)\sin^2\psi)\sigma_{\parallel}$ (5)	$\sin^2\psi^* = -2s_{12}/\left(\frac{1}{2}s_{44} + s_0\right)$ (6)

Applicability of the crystallite group method; case of fibre-texture

Principal problems. The application of the CGM involves simplifying assumptions with respect to the elastic grain interaction and the approximation of the texture in terms of ideal orientations. It has been demonstrated by Welzel & Mittemeijer [4] that considerable errors can arise if:

(i) the grain interaction in the specimen is not of the Reuss type
(exceptions are, for example, the cases of {111} and {100} fibre textures of cubic materials, for which the use of the CGM implies no assumptions with respect to the elastic grain interaction);

(ii) the texture is not sufficiently strong;

(iii) the texture consists of more than one crystallite group.

It has also been demonstrated that it is generally not straightforwardly possible to estimate the errors involved in employing the CGM for diffraction stress analysis and in many cases, such errors are unnoticed in the literature.

Experimental aspects. The measurement of the lattice strain of a (fibre-texture) crystallite group using a particular *hkl* reflection is not possible for all tilt angles ψ. As the diffraction vector has to be oriented perpendicular to the *hkl* planes to obtain diffracted intensity, an *hkl* reflection can only be found for certain tilt angles ψ, which depend upon the crystal structure of the material and the orientation of the crystallite group under investigation with respect to the specimen frame of reference. On the one hand, it is thus possible to measure the lattice strains for different crystallite groups in a specimen separately, provided that enough *hkl* and ψ combinations can be indicated that are unique for only one of the crystallite groups of the specimen. On the other hand, this is a limitation as the number of lattice strain measurements is restricted to a number of particular *hkl* reflections and orientations. As an example, for the case of a {111} fibre texture of a cubic material the use of (only) the 311 reflection would allow measurements at only three tilt angles (29.50^0, 58.52^0, 79.98^0). Generally, the simultaneous use of multiple reflections in a stress analysis will thus be required in order to have a sufficient number of lattice strains for various $\sin^2\psi$ in order to perform a reliable stress determination. However, for combining different reflections in the stress analysis, the measurement of absolute lattice strains is necessary, whereas the measurement of relative lattice strains suffices if only one *hkl* reflection is employed. Thus, the CGM based on the use of multiple reflections is more prone to errors than methods relying on the use of only one particular *hkl* reflection. Against this background, special emphasis will be put on the simultaneous use of multiple reflections in view of instrumental aberrations in the following.

Analysis of fibre-textured gold layers

Experimental

Au layers of three thicknesses (200 nm, 500 nm and 2 μm) were sputter-deposited onto thermally oxidized silicon <510> wafers using a planar direct-current magnetron (power: 100W) in an ultra-high vacuum chamber using Ar as a sputter gas. The X-ray diffraction measurements were carried out using a Philips X'Pert MRD Pro diffractometer equipped with an Eulerian cradle (four-circle goniometer). Cu Kα radiation emerging from the point focus of a sealed X-ray tube operated at 45 kV and 40 mA was converted to a parallel beam by an X-

ray lens. The diffracted beam was passed through a parallel plate collimator (acceptance angle 0.27^0) and a flat graphite analyzer before being detected by a proportional counter. The use of parallel beam geometry (based on an X-ray lens), makes it possible to measure diffraction patterns without any significant instrumental aberrations (apart from 2θ offset) with respect to the peak shape and peak position even at very large tilt angles [5].

Results and discussion

Texture. The crystallographic texture was analysed on the basis of θ/2θ-scans and {111} pole figures. The θ/2θ -scan of the Au specimen of thickness 200 nm is shown in figure 1. The arrows mark the expected position of diffraction lines of Au. Obviously, the 111 and 222 reflections appear. This suggests that: (i) the specimen is strongly {111} textured and (ii) only a very small fraction (about 0.2%) of 311 texture component exists. These findings have been confirmed by inspection of the {111} pole figures and they hold also for the Au layers of thicknesses 500 nm and 2 μm. The pole figures also demonstrate that fibre symmetry occurs. The texture is not only very strong but also very sharp: The pole width is only about 7° (full width at half maximum; similar pole widths have also been found for the other two specimens).

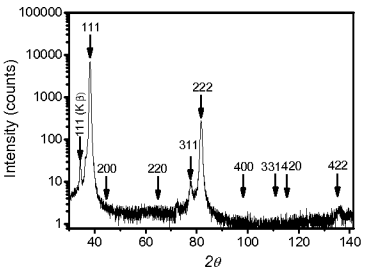

Figure 1. θ/2θ - scan of the Au specimen of thickness 200 nm. The arrows mark the expected positions of diffractions lines of Au.

Based on these findings it can be concluded that a stress analysis of these specimens employing the CGM should be straightforwardly possible, as these specimens fulfil all criteria concerning the applicability of the CGM.

Stress analysis. Diffraction lines have been recorded at all intensity poles of six reflections of the {111} crystallite group and the peak maximum positions θ_ψ^{hkl} corresponding to the $K\alpha_1$ component have been determined by fitting asymmetric (split) Pearson VII functions considering a $K\alpha_1$-$K\alpha_2$ doublet with an intensity ratio of 0.5.

In a first attempt, the following analysis strategy has been adopted. The lattice strains can be calculated from the measured peak positions as:

$$\left(\varepsilon_\psi^{hkl}\right)_{meas} = \left(\frac{\lambda}{2\sin\theta_\psi^{hkl}} - \frac{a_0}{\sqrt{(h^2+k^2+l^2)}}\right) \Bigg/ \left(\frac{a_0}{\sqrt{(h^2+k^2+l^2)}}\right), \qquad (7)$$

where λ is the wavelength of Cu $K\alpha_1$ radiation and a_0 is the strain-free, reference lattice parameter. a_0 should be considered as unknown, because in a thin film the lattice parameter can generally deviate from the corresponding bulk value. Thus, by fitting ε_ψ (equation (3); see table 1) to $\left(\varepsilon_\psi^{hkl}\right)_{meas}$ (equation (7)), it is possible to determine the unknowns $\sigma_\parallel$ and a_0.

The result of such an analysis has been presented in figure 2 for the Au specimen of thickness 200 nm. Obviously, the result is very unsatisfactory, as a large scatter of the data points with respect to the fitted straight line occurs. Similar results have also been obtained for the

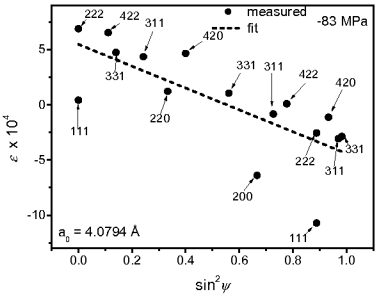

Figure 2. CGM $\sin^2\psi$ *-plot using the stress* $\sigma_{||}$ *and the strain-free lattice parameter as fit parameters (layer thickness 200 nm).*

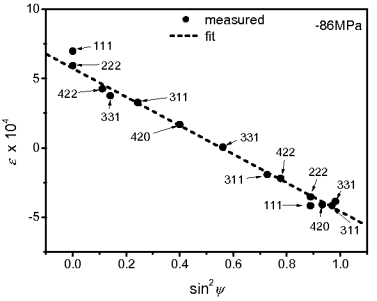

Figure 3. CGM $\sin^2\psi$ *-plot using the strain-free lattice spacings (separately determined for each reflection) and only the stress* $\sigma_{||}$ *as fit parameter (layer thickness 200 nm).*

specimens of thicknesses 500 nm and 2 µm.

To achieve a more consistent analysis, the following modified approach has been adopted. Plots of the lattice spacing d_ψ^{hkl} versus $\sin^2\psi$ have first been constructed for each reflection (*hkl*) separately. The strain-free lattice spacing d_0^{hkl} can be extracted from such plots by interpolating at $\sin^2\psi^*$ (cf. equation (4) in table 1; note that this is only possible if at least two poles occur for the considered reflection).

Then, the lattice stain $\left(\varepsilon_\psi^{hkl}\right)_{meas}$ can be calculated as $\left(\varepsilon_\psi^{hkl}\right)_{meas} = \left(d_\psi^{hkl} - d_0^{hkl}\right) / d_0^{hkl}$. The result of such an analysis has been presented in figure 3 for the Au specimen of thickness 200 nm. Obviously, a very satisfactory agreement of the fitted line and the measured data points occurs. However, in this approach, the strain-free lattice *spacings* d_0^{hkl} for the different reflections have been taken as independent parameters. The corresponding lattice *parameters* have been plotted versus the diffraction angle in figure 4 (open circles). Obviously,

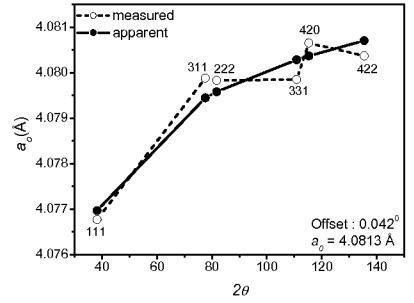

Figure 4. Open circles: Variation of the (apparent) strain-free lattice parameter as a function of the diffraction angle (layer thickness 200nm); Filled circles: effect of 2θ *offset.*

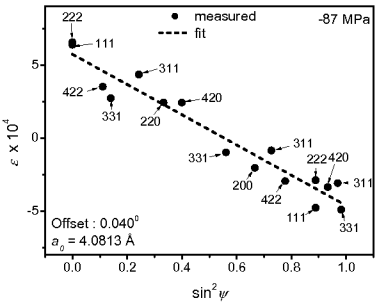

Figure 5. CGM $\sin^2\psi$ *-plot using the stress* $\sigma_{||}$*, the lattice constant and the offset as fit parameters (layer thickness 200 nm).*

the values of d_0^{hkl} obtained for the different reflections (and as used in Figure 3) are incompatible, as they do not correspond to the same lattice parameter. The systematic variation of the lattice constant as a function of the diffraction angle suggests the effect of an instrumen tal aberration. In the parallel beam geometry employed in this work, the only significant instrumental aberration can stem from an offset of the scale of the diffraction angle $\Delta 2\theta$. The effect of an instrumental offset on the "apparent" lattice parameter, i.e., the lattice parameter that will be determined in a diffractometer with this instrumental aberration, has also been shown in figure 4 (line with filled circles). It follows that the observed variation of the measured lattice parameter is largely due to an instrumental offset. This instrumental aberration can be taken into account in equation (7) by replacing θ_ψ^{hkl} by $\theta_\psi^{hkl} - \frac{1}{2}(\Delta 2\theta)$. Then, by fitting ε_ψ (equation (3)) to $\left(\varepsilon_\psi^{hkl}\right)_{meas}$ (equation (7)), it is possible to determine the unknowns $\sigma_{||}$, a_0 and $\Delta 2\theta$. The result of such an analysis has been presented in figure 5 for the Au specimen of thickness 200 nm. A satisfactory agreement of the measured data points and the fit has been achieved employing this modified approach. The results obtained for the three specimens of different thickness have been summarised in table 2. Comparing figures 3 and 5, it becomes obvious that the fit quality is less good in figure 5. The remaining scatter is due to the effect of stacking faults. The treatment of stacking faults in the analysis proposed in this work will be reported elsewhere [6].

Table 2.Results of the stress analysis employing the CGM using the stress $\sigma_{||}$, the lattice constant a_0 and the instrumental offset $\Delta 2\theta$ as fit parameters.

layer thickness [nm]	$\sigma_{||}$ [MPa]	a_0 [Å]	$\Delta 2\theta$ [°]
200	-87(7)	4.0813(2)	0.040(2)
500	-65(6)	4.0811(2)	0.034(2)
2000	74(7)	4.0811(2)	0.032(2)

Conclusion

The crystallite group method is an easily applicable approach to the stress analysis of strongly fibre-textured specimens but intrinsic errors are often left unnoticed. Strength, sharpness and type of texture have to be evaluated before an appropriate analysis can be chosen. If multiple reflections are simultaneously used in a diffraction stress analysis, the determination of absolute peak positions deserves special attention. As an example, instrumental errors can be accounted for by the introduction of additional fitting parameters.

References

1. Welzel, U., Ligot, J., Lamparter, P., Vermeulen, A.C. & Mittemeijer, E.J., 2005, *J. Appl. Cryst.*, **38,** 1.
2. Welzel, U. & Mittemeijer, E.J., 2003, *J. Appl. Phys.*, **93**, 9001.
3. Hauk, V., 1997, *Structural and residual stress analysis by nondestructive methods* (Amsterdam: Elsevier).
4. Welzel, U. & Mittemeijer, E.J., 2004, *Mat. Sci. For.*, **443 - 444**, 131.
5. Leoni, M., Welzel, U. & Scardi, P., 2004, *J.Res.Natl.Inst.Stand. Technol.*, **109**, 27.
6. Kumar, A., Welzel, U. & Mittemeijer, E.J., in preparation.

Z. Kristallogr. Suppl. **23** (2006) 61-66

Residual stress measurement of gold artefacts by Debye ring analysis

P. Zanola[1], D. Benedetti[1], E. Bontempi[1], V. Villa[2], G. Baronio[2], M. Tosti[3], R. Roberti[2], L. E. Depero[1,*]

[1]INSTM and Laboratorio di Chimica per le Tecnologie, Università di Brescia, via Branze 38, 25123 Brescia, Italy
[2]Dipartimento di Ingegneria Meccanica, Università di Brescia, via Branze 38, 25123 Brescia, Italy
[3]SPIN Srl S. Casciano V.P. (Fi), Italy
Contact author; e-mail: laura.depero@ing.unibs.it

Keywords: jewellery, gold, residual stress, microstructure, XRD[2]

Abstract. In the case of precious and rare art manufacts, usually bearing complex geometry, the conventional X-ray Diffraction technique can be very difficult or even impossible to be applied. On the contrary by means of microbeam small area can be analysed and the microstructure of differently treated surfaces can be investigated.
Recently, two-dimensional (2D) detectors have been developed for laboratory X-ray diffractometers. Thus, nowadays it is possible to collect high quality diffraction data of a significant part of the diffraction cones during the exposure time and the structure and microstructure of small surface area can be assessed. Moreover, by the analysis of the diffraction cones distortion, the residual and/or applied stresses can be measured.
In the present work the structure, microstructure, and residual stress present in representative gold artefacts are discussed mainly on the basis of bidimensional X-ray microdiffraction (μXRD[2]) and microfluorescence (μXRF). A gold ring has been analysed before and after deformation and the distribution of residual stress measured along the circumference has been compared with the stress analysis results from FEM simulation.

Introduction

The use of electrodeposited precious metals in the electronic industry for the production of highly reliable parts has resulted in an increasing interest in the properties of such deposits. The strong correlation among physical, chemical, metallurgical, and electronic properties of metals has led to the development of a large number of new characterization techniques, to well understand the properties of these coatings.
The study of the material in the case of jewellery applications should be as well accurate and elaborate to satisfy the highly refined expectations of the final customer, justified by the high level product typology. Indeed, a lot of research has been done in these years on several technology and applications of gold [1]. Then jewellery industry or other precious metals

manufactures should be among the most interested sectors in non-destructive testing techniques.
The techniques based on X-ray probe have a significant impact on the characterization of metals mainly because of their simplicity, reliability, quantitative and non-destructive nature. In particular, X-ray diffraction (XRD) has played a leading role, as a fundamental tool for structural and microstructural analysis.
In recent years advanced techniques have been developed, in combination with the availability of intense collimated beams from synchrotron sources. This has make X-rays a versatile and powerful tool for the study of surfaces, monolayers or defect with high spatial resolution (few μm). These improvements allowed the development of new laboratory instruments [2].
In this work we present advanced X-ray techniques for the structural characterisation; in particular micro bi-dimensional X-ray Diffraction (μXRD^2) and micro X-ray Fluorescence (μXRF). These techniques have been applied to the characterization of old, rare, precious metal artefacts with the purpose of investigating micro areas and map the structure, microstructure and the residual stress state. For the residual stress evaluation, a new advanced method based on the study of the Debye ring deformation has been used [3]. Preliminary results on the comparison between calculated stress and experimental residual stress are also reported.

Experimental

Different types of commercial gold products (earrings, chains and rings) have been studied.
Micro-X Ray Fluorescence measures were obtained by means of a Unisantis μXRF system using an acquisition time of 60 seconds for all the samples.
Two-dimensional X-ray micro-diffraction experiments were performed by means of a D-Max Rapid Rigaku system equipped with an Image Plate detector. The incident beam was collimated by a collimator with a diameter of 300 μm. The sample was mounted at 0 or 45° with respect to the vertical axis and the Ω angle was fixed at 19°. The time collection was 30 minutes for each pattern. In this work, the recently proposed approach to calculate residual stress based on the Debye rings deformation has been applied [3, 4].
The simulation of the stress state of a compressed gold ring were performed using a COSMOSWORKS 2003 [5] FEM application (linear field) integrated by a SOLIDWORKS 2003 modelling system. The analysed ring was bound and compressed with a vertical compressive force of 300 N.

Results and Discussion

A number of different gold artefacts have been used in the present investigation to discuss the potentialities of the XRD^2 technique in the control of jewellery items.
In figure 1 the analysed surfaces of an hand-made earring are pointed out.
The first analysed surface (figure 1a) is close to the solder area. This region can be particularly critical for the mechanical stresses that are expected as a consequence of local overheating and un controlled heat-cooling cycle. The XRD^2 pattern shows the presence of large crystallites that may indicate anomalous grain growth during the soldering.

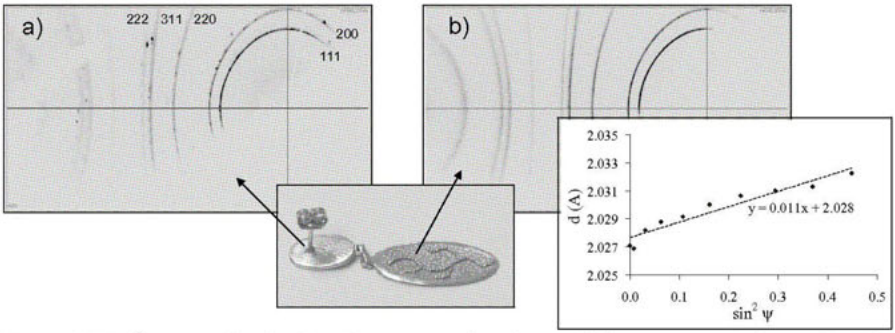

Figure 1: XRD² images of an hand-made earring analysed in two different points: a) close to the solder area and b) in the punch area. For the first analysed surface shows the presence of large crystallites that may indicate anomalous grain growth during the soldering. For the second area, residual strain are calculated with the DRAST method [3].

In the punch area of the same earring more homogeneous intensities along the Debye rings of the gold phase have been detected; from their deformation a residual stress state is also expected to be present.

Because of the key role of residual stress in the mechanical performance of gold artefacts, the local strains in the investigated area were carefully evaluated by means of the DRAST (Debye Ring Analysis for STress measurements) method [3]. This method is based on the fact that the presence of a residual stress determines a Debye ring distortion. Each point of the image plate (2ϑ, β) is related to (ϕ, ψ) values which define the direction of diffraction vector in the sample system. Thus, each point of the Debye ring corresponds to a ϕ, ψ values. If the elastic model can be applied and the elastic modulus is known, from the d-$\sin^2\psi$ regression the value of the residual stress can be calculated. Thus, the quantitative analysis of the deformation of the Debye ring of the 200 reflection was performed. Using a d_0 equal to that found for $\psi = 0$ ($2\theta = 44.59°$) and the Young modulus E = 80 GPa the calculated residual stress is 250 MPa. The measured tensile stress can effectively be the consequence of the cold work manufacturing process.

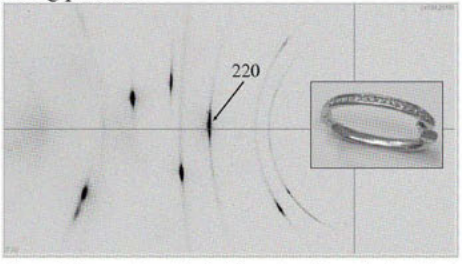

Figure 2. XRD² image collected for another kind of earring (see the inset) shows that, in addition to a residual stress state (about 690 MPa), a strong [110] preferred orientation is present. The maximum of the 220 reflection at ψ=0 is indicated by an arrow.

In figure 2 the XRD² image collected for another kind of earring shows that, in addition to a residual stress state (about 690 MPa), a preferred orientation is present. Infact in this case the

intensity along the Debye rings of the 220 reflection has a pronounced maximum at $\psi = 0$ as a result of a quite strong [110] preferred orientation. The observed preferred orientation is consistent with the cold rolling process to obtain the semi prished bar that is then bent to obtain the final elliptical shape of the earring; the residual stress state is the consequence of the cold working operations.

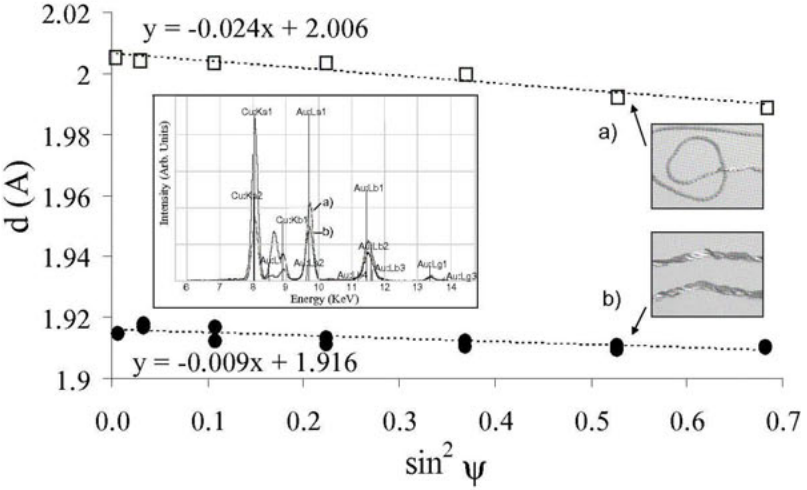

Figure 3. d-sin$^2\psi$ plots calculated for the corresponding XRD^2 patterns collected from the surface of two necklaces with a different gold percentages. The gold content, roughly calculated from the 200 position, corresponds to 18 (sample a) and 12 carats (sample b), as confirmed by XRF analysis (shown in the inset).

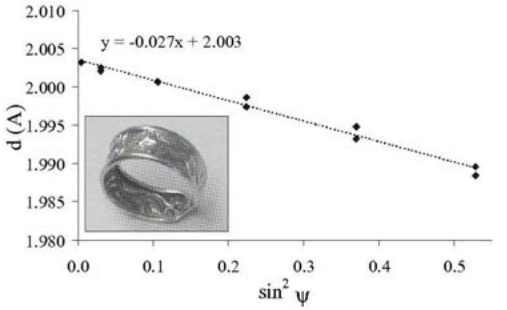

Figure 4. Application of the DRAST method [3] to calculate residual stress for a gold ring (shown in the inset). This kind of measurement is not possible with conventional XRD diffraction experiments.

In figure 3 the d-sin$^2\psi$ plots calculated for the corresponding XRD^2 patterns collected from the surface of two necklaces with a different gold percentages are shown. From the figure it is evident the difference on the average positions of the 200 reflection. Considering the 200

peak position of pure gold and copper, 0.2039 nm and 0.1808 nm respectively, and a linear interpolation, the alloys of the two necklaces appear to have roughly 45 at. and 80 at. of gold. These gold content corresponding to 12 and 18 carats is quite overestimated, as confirmed by XRF analysis (see Figure 3). Indeed, one should consider that other metals are present in the alloys and a tarature must be performed to obtain quantitative data.

In both the analysed points a compressive stress is present (about 260 e 670 MPa respectively). The analysis of a gold ring, that is as well as the above reported measurements not possible with conventional XRD diffraction experiments, allows to ascertain a compressive stress state (about 750 MPa) in the artefact shown in Figure 4.

To assess the reliability of the DRAST method in the measurement of residual stresses of gold artefacts, the following experiment was carried out on a simple gold ring (i.e. a wedding ring) with the initial diameter of 21.67 mm. The residual stress has been first measured on the as received ring in correspondence of the flat area shown in Figure 5; a value of about –970±20 MPa has been found as the mean of 8 measures at every 45° in the radial direction along the circumference.

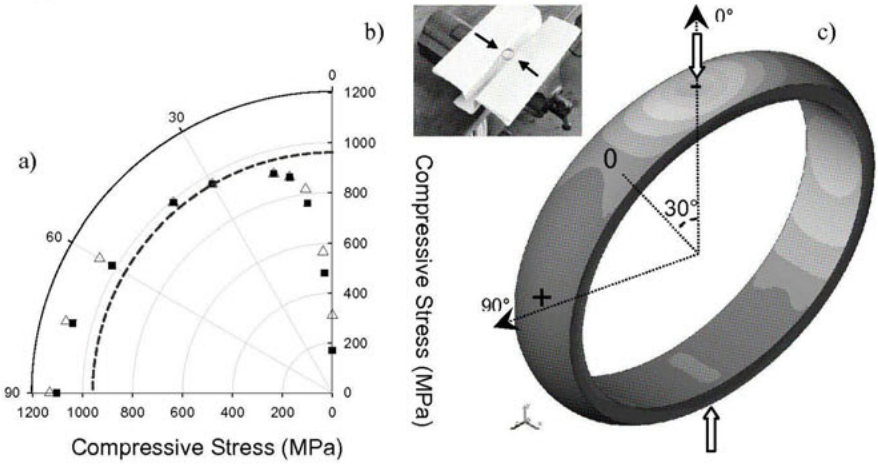

Figure 5. The residual stress has been calculated before and after the deformations (Figure 5a) for a simple gold ring, with the initial diameter of 21.67 mm. It is interesting to note that the residual stress (shown in Figure 5b) behaviour follows that of the applied stress and modelled by means of COSMOSWORKS 2003 (Figure 5c).

The ring has then been first plastically deformed (see Figure 5b) by displacement controlled compression along a diameter, obtaining minimum and maximum diameter values in the unloaded ring of 21.00 and 22.32 mm respectively; a second additive deformation yielded 20.20 and 23.08 mm final diameter values. The residual stress obtained by the DRAST method by means of several measurements throughout a quarter of circumference (because of the symmetry of the experiment) are shown in Figure 5a, where the compression direction corresponds to the 0° direction. At 90°, where tensile stresses are applied during the deformation of the ring, compressive residual stresses are further increased up to 1100 MPa, while at 0°, where compressive stresses are applied, the residual stress resulting from the

deforming operation superimpose to the initial one with a net resulting value of near 300 MPa. The residual stresses yielded by the compressive deformation of the ring have therefore a 0 value in correspondence of the 30° direction, where the initial residual stress state remains unchanged; this corresponds to the 0 stress value obtained by linear elastic FE simulation (see Figure 5c), by means of COSMOSWORKS 2003 [5], of the deformation of the ring (an elasto-plastic simulation could not be carried out since no information is available about yield strength and flow properties of the gold alloy of the ring). The additional deformation of the ring results only in a moderate change of the residual stress state obtained after the first compressive deformation; this result is consistent with the fact that each region of the circumference (except the one at 30°) is bent during the ring deformation, and after the initial plastic yielding of the outer and inner diameters, plastic deformation continues to spread out though the radial section with only a moderate increase of the maximum applied stress.

Conclusion

In this paper different applications of the XRD^2 technique have been shown taking into account typical jewellery artefacts like earrings, necklaces, and rings. By the analysis of the 2 dimensional X-ray pattern the microstructure of the items can be investigated and quantitatively described; the obtained results mast be considered preliminary, but show the potentialities of the method provided that the x-ray diffraction results can be coupled with detailed information about the manufacturing history and the material properties.
As shown by the different experiments reported in the paper, local preferred orientation, crystallite size, and residual stress can be estimated.
The reliability of the DRAST method in the measurement of residual stresses has been assessed by a specific test on a ring, whose residual stress state has been measured in the as received conditions and after a two step plastic deformation by a displacement controlled compression of the ring itself along a diameter. The residual stress distributions obtained by the proposed method are all consistent with the manufacturing and deformation conditions for both the as received ring, with homogeneous residual stress as expected from the symmetry of the ring, and the deformed state where additional residual stresses are in accordance with the stresses induced by the plastic deformation operation, as inferred by a simple FE simulation of the elastic deformation of the ring.

References:

1. http://www.gold.org/discover/sci_indu/GBull
2. E Bontempi, M. Gelfi, L E Depero, 2003, in "*Research Advances in Chemistry of Materials*", R.M. Mohan (Ed.) Global Research Network, 21- 41.
3. M. Gelfi, E. Bontempi, R. Roberti and L. E. Depero, 2004, *Acta Materialia* **52**, 583-589.
4. M. Gelfi, E. Bontempi, R. Roberti, L. Armelao and L. E. Depero, 2004, *Thin Solid Films* **450**, 143-147.
5. http://www.solidworks.com/pages/products/cosmos/cosmosworks.html

Z. Kristallogr. Suppl. **23** (2006) 67-72

X-ray residual stress measurement in titanium nitride thin films

M. Dopita[1*], D. Rafaja[2]

[1]Charles University, Faculty of Mathematics and Physics, Ke Karlovu 3, 121 16 Praha 2, Czech Republic
[2]Institute of Physical Metallurgy, TU Bergakademie Freiberg, Gustav-Zeuner-Str. 5, D-09599 Freiberg, Germany
[*]Contact author, e-mail: dopita@mag.mff.cuni.cz

Keywords: X-ray diffraction, thin films, residual stress

Abstract. This contribution compares and discusses three different approaches commonly used for determination of the residual stresses from X-ray diffraction data – the $\sin^2\psi$, $f(\psi)$ and the Direct Solution method. For the calculation of the X-ray elastic constants (XECs), three grain interaction models were compared – Reuss, Voigt and Neerfeld-Hill. The best reliability of the results was achieved using the $f(\psi)$ method because of its highest statistical relevance. The elastic grain interaction of the thin films was most accurately described by the Reuss model.

Introduction

Thin polycrystalline films play a very important role in many technical applications. In particular, TiN thin films are extensively used as coatings for drills and cutting tools because of their ultra-high hardness and high corrosion and wear resistance. Crucial parameters influencing strongly the mechanical properties of the thin films are the residual stress and the degree of the mechanical anisotropy, which is caused by the anisotropy of the elastic constants and related to the interaction between neighbouring crystallites. In this study, we investigated the microstructure of CVD thin TiN films on sintered tungsten carbides in terms of the stress-free lattice parameters, residual stresses and mechanical interaction between neighbouring crystallites (i.e. elastic grain interaction). A precise knowledge of the stress-free lattice parameter, together with the information on the overall chemical composition, specifies whether foreign atoms are accommodated in the host crystal structure or not. Three approaches were used for data analysis: the $\sin^2\psi$ method [1], the $f(\psi)$ method [2] (a modification of this method is known as the crystallite group method [3]) and the Direct Solution method [4].

Experimental details

Thin films of titanium nitride were deposited using CVD on cemented carbide substrates at approximately 900°C. Two samples are discussed in this study, which were deposited on

substrates with slightly different Co and (Ta, Nb) C contents in the tungsten carbide. Thickness of the thin films was roughly 4 μm. The substrate material was mechanically precleaned and chemically cleaned before deposition.

The X-ray diffraction measurements were performed with CuKα radiation on a Seifert PTS 3000 diffractometer equipped with an Eulerian cradle (ψ- diffractometer). Such diffractometer allows the sample to be tilted about the angle ψ from the coplanar geometry. This setup requires an X-ray tube with a point focus. Because of a rapid decrease of the diffracted intensity with increasing diffraction angle 2θ (due to the small thickness and high surface roughness of the thin films), only first few reflections were recorded. The step size was 0.05° in 2θ, the counting time 40 s per step. Specimens were tilt between -25° and 25° from the symmetrical position; the increments of the tilting angle were chosen to obtain equidistant steps in $\sin^2\psi$ For higher ψ, diffracted intensity was too low (due to the collimation of the primary beam, small thickness and high surface roughness of the thin films) to get useful diffraction data. For each sample, pole figures were measured to get information on the preferred orientation of crystallites.

For an accurate calculation of the residual stress, the lattice strain has to be measured with the relative accuracy of 10^{-4} or better. Therefore, the effect of the instrumental aberrations on the peak positions must be corrected. For the ψ-diffractometer, the main sources of the instrumental aberrations are the shift of the zero position of the diffractometer and the sample displacement like for conventional diffractometers, and the shift of the incident beam from the ψ axis (irradiated area is displaced from the ψ axis). For all aberrations mentioned above, particular analytical expressions exist. However, the combination of these errors results in too many instrumental parameters, which cannot be refined together with the parameters of the microstructure model (see below). For this reason, the instrumental aberrations were determined using silicon standard. To keep the position of the sample possibly unchanged, the samples were measured once without standard and once with the silicon powder brought on the sample surface. Each calibration measurement was done in the same 2θ and ψ range as investigated samples were measured. The shift of the diffraction lines of silicon was described by a general quadratic function:

$$\Delta 2\theta = b_1\theta^2\psi^2 + b_2\theta^2\psi + b_3\theta\psi^2 + b_4\theta^2 + b_5\psi^2 + b_6\theta\psi + b_7\theta + b_8\psi + b_9, \qquad (1)$$

The coefficients of the correction function, b_i, were refined using the least-squares method.

Residual stress analysis using X-ray diffraction

The analysis of the residual stresses using the X-ray diffraction methods is based on the measurement of the interplanar spacing in different macroscopic directions. This yields information on the elastic lattice deformation that must be recalculated into the residual stress using suitable diffraction elastic constants. Assuming a rotationally symmetrical biaxial state of the residual stress (quasi-isotropic specimen, no shear stress), which is usually satisfied in the case of thin films, the dependence of the elastic lattice deformation ε_ψ^{hkl} on the inclination from the perpendicular direction ψ can be expressed in the form of the so-called $\sin^2\psi$ formula [1]:

$$\varepsilon_\psi^{hkl} = \frac{d_\psi^{hkl} - d_0}{d_0} = \frac{a_\psi^{hkl} - a_0}{a_0} = \left(2s_1^{hkl} + \frac{1}{2}s_2^{hkl}\sin^2\psi\right)\sigma_{\parallel}, \qquad (2)$$

In (2), the symbols *hkl* are the Miller indices of the crystallographic planes. s_i^{hkl} are the X-ray elastic constants (XECs) that are, in general, dependent on the crystallographic direction.
In our study, the XECs were calculated from the single-crystalline elastic constants [5] using alternatively Voigt [6], Reuss [7] and Neerfeld-Hill [8, 9] models. The Voigt model supposes the same strain tensor in all crystallites independent of their orientation. The Reuss model assumes the same stress tensor in all crystallites. In a material composed from elastically anisotropic crystallites, the lattice strain within the Reuss model depends consequently on the crystallographic direction. The Neerfeld-Hill model [8, 9] yields the XECs as an average of the elastic constants obtained from the Voigt and Reuss models.

Experimental results

1) The $\sin^2\psi$ method

An example of the dependence of the lattice parameters a_ψ^{hkl} on $\sin^2\psi$ is shown in figure 1. a_ψ^{hkl} were calculated from the corrected line positions using the Bragg equation and the relationship between the d-spacing and the lattice parameter. The mechanical anisotropy of the thin film is apparent from different offsets and different slopes of the a_ψ^{hkl} vs. $\sin^2\psi$ plots for different crystallographic planes. The residual stress $\sigma_{||}$ can be calculated from (2), if the XECs are known for the respective crystallographic direction *{hkl}*. The stress-free lattice parameter, a_0, is obtained from the a_ψ^{hkl} vs. $\sin^2\psi$ plot at $\sin^2\psi_0 = -4\, s_1^{hkl} / s_2^{hkl}$.

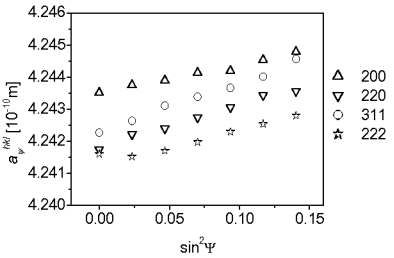

Figure 1. The $\sin^2\psi$ plot for reflections hkl measured in the sample B.

2) The $f(\psi)$ method

The $f(\psi)$ method involves the XECs directly into the construction of the dependence of the measured lattice parameters on the macroscopic direction. The lattice parameters are plotted as a function of $f(\psi) = 2s_1^{hkl} + \frac{1}{2} s_2^{hkl} \sin^2\psi$. All crystallographic directions are taken into account during the calculation of the residual stress and the stress-free lattice parameter, which improves the reliability of results. Still, an appropriate grain interaction model must be used for calculation of the XECs. The residual stress is calculated from the slope of the a_ψ^{hkl} vs. $f(\psi)$ plot; the stress-free lattice parameter is to be found at $f(\psi) = 0$. An example illustrating the effect of the mechanical anisotropy is shown in figure 2. The Voigt model is apparently not suitable for fitting the experimental data as it cannot explain the observed anisotropy of the lattice deformation (the dependence of the lattice deformation on the crystallographic direction).

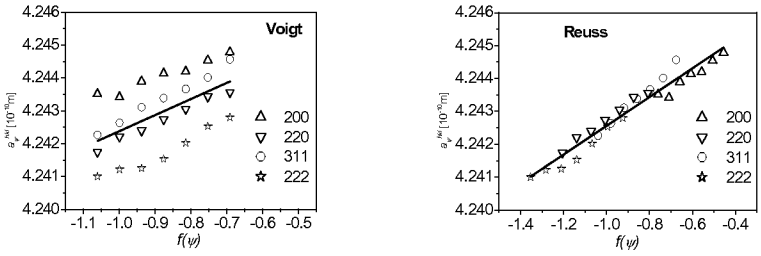

Figure 2. The a_{ψ}^{hkl} vs. $f(\psi)$ plot for Voigt and Reuss crystallite interaction models. Data were taken on the sample A.

3) Direct Solution method

The last method in this comparison uses mechanical (averaged) elastic constants s_i^{mech} for the calculation of the dependence of the elastic lattice deformation on the macroscopic direction ψ (for detailed description of the method, see [4]):

$$\varepsilon_{\psi}^{hkl} = \frac{a_{\psi}^{hkl} - a_0}{a_0} = \left\{ 2s_1^{mech} + 2K_2\left(\Gamma - \frac{1}{5}\right) + \left[\frac{1}{2}s_2^{mech} - 3K_2\left(\Gamma - \frac{1}{5}\right)\right]\sin^2\psi \right\}\sigma_{\parallel} \qquad (3)$$

The mechanical elastic constants can easily be calculated from the Young's modulus E and from the Poisson ratio ν: $s_1^{mech} = -\nu / E$, $\frac{1}{2}\, s_2^{mech} = (1+\nu)/E$. To be able to compare the different grain interaction models, s_1^{mech} and s_2^{mech} were calculated from the XECs, see [4]. $\Gamma(hkl) = (h^2k^2+h^2l^2+k^2l^2) / (h^2+k^2+l^2)^2$ is the well-known cubic orientation factor. K_2 is a parameter that quantifies the effect of the anisotropy of the single-crystalline elastic constants on the crystallographic anisotropy of the observed lattice strain in a polycrystalline sample. It can either be calculated from the respective grain interaction model or refined by using the least-squares method [4]. A combination of both approaches was applied in our work. K_2 was taken from [4] and fixed in the first step of the refinement; only a_0, and $\sigma_{\parallel}$ were refined. In the second step of the fitting procedure, the parameter K_2 was refined additionally. The effect of the starting grain interaction model on the refined data is illustrated in figure 3.

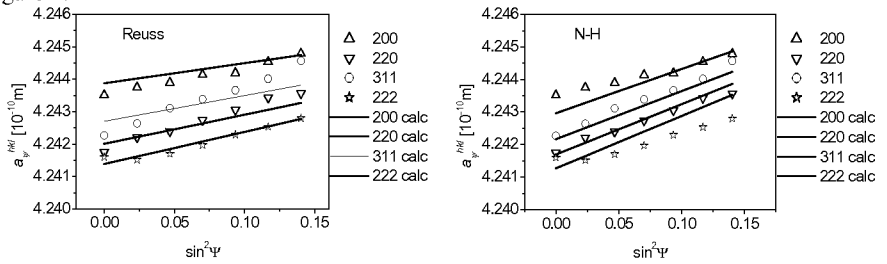

Figure 3. Measured (symbols) and fitted (lines) data for measured reflections and Reuss and Neerfeld-Hill (N-H) interaction models using Direct Solution method. The data were taken for the sample B.

Table 1 summarises the residual stresses and the stress-free lattice parameters for the samples A and B as obtained using the $\sin^2\psi$ and $f(\psi)$ methods. Table 2 summarises the residual

stresses, stress-free lattice parameters and the degree of anisotropy of the lattice deformation for both samples as calculated using the Direct Solution method.

Table 1. Residual stress and stress-free lattice parameter for both samples obtained using the $\sin^2\psi$ and $f(\psi)$ methods. Standard deviations in estimation of individual stress free lattice parameter are of order of 10^{-4}-10^{-3} Å, those for residual stresses of 0.1 GPa.

sample	A						B					
model	Reuss		Voigt		N-H		Reuss		Voigt		N-H	
	σ [GPa]	a_0 [Å]	σ [GPa]	a_0 [Å]	σ [GPa]	a_0 [Å]	σ [GPa]	a_0 [Å]	σ [GPa]	a_0 [Å]	σ [GPa]	a_0 [Å]
						$\sin^2\psi$						
200	0.96	4.2487	0.71	4.2491	0.98	4.2489	1.06	4.2478	0.87	4.2477	0.96	4.2480
220	0.79	4.2480	0.86	4.2478	0.84	4.2479	1.09	4.2470	1.12	4.2468	1.13	4.2479
311	0.77	4.2475	0.75	4.2475	0.76	4.2475	1.16	4.2473	1.21	4.2470	1.35	4.2477
222	0.95	4.2463	1.00	4.2458	1.02	4.2461	0.99	4.2460	0.96	4.2453	0.88	4.2460
<hkl>	0.87	4.2476	0.83	4.2475	0.90	4.2476	1.08	4.2470	1.04	4.2467	1.08	4.2474
e.s.d.	0.10	0.0009	0.13	0.0014	0.12	0.0012	0.07	0.0008	0.15	0.0010	0.21	0.0009
						$f(\psi)$						
	1.01	4.2486	0.94	4.2484	0.95	4.2498	1.00	4.2470	0.92	4.2458	0.97	4.2470

Table 2. Residual stress, stress-free lattice parameter and the degree of the mechanical anisotropy for both samples obtained using the Direct Solution method.

sample	A			B		
model	K_2 [TPa^{-1}]	a_0 [Å]	σ [GPa]	K_2 [TPa^{-1}]	a_0 [Å]	σ [GPa]
Reuss	-0.76(8)	4.2487(6)	0.97(6)	-0.79(9)	4.2472(4)	0.96(7)
Voigt	0	4.2483(11)	0.91(13)	0	4.2463(12)	0.85(15)
N-H	-0.48(11)	4.2497(9)	0.95(9)	-0.51(10)	4.2470(8)	0.92(11)

The microstructure parameters obtained from the $\sin^2\psi$-method (a_0 and σ) vary for individual reflections. The amount of this variation (e.s.d. in table 1) indicates the suitability or unsuitability of the respective grain interaction model. Although the same XECs were used for the $\sin^2\psi$ and the $f(\psi)$ methods, the arithmetic means of the residual stresses and the stress-free lattice parameters obtained from the $\sin^2\psi$ method (<hkl> in table 1) were not identical with the parameters obtained from the $f(\psi)$ method. The reason is different averaging of the refined parameters in both approaches. The microstructure parameters calculated using the direct solution method match with those obtained from the $f(\psi)$ method within the experimental accuracy. This is consistent with the result that the starting K_2-value was only insignificantly changed during the refinement.

It is evident that the linear fits in figures 2 and 3 do not approximate the experimental data exactly. The departure of the experimental data from the solid lines correlates with the variation of the microstructure parameters calculated for different crystallographic directions from the $\sin^2\psi$ method. The differences between the experimental data and the linear fit shows furthermore that none of the grain interaction models can doubtless be applied to the thin films under study. The reasons could be a different interaction between crystallites in samples with tensile (our samples) and compressive residual stresses [4] and/or different origin of the residual stress. In our samples, the residual stress results from a combination of the

different thermal expansion of the substrate and the thin film with the diffusion of carbon into the thin films during the CVD deposition process. The penetration of carbon into the thin films was indicated by the observed increase of the stress-free lattice parameters comparing with the intrinsic value of 4.2418 Å [10], and confirmed by wavelength-dispersive X-ray analysis (WDX). The presence of tensile residual stress of (1.0 ± 0.1) GPa in our samples can cause a development of local cracks or voids in the thin films, which can modify the interaction between adjacent crystallites and change the observed anisotropy of the lattice parameters with respect to the applied grain interaction model.

Summary

In the CVD TiN thin films deposited on cemented carbides, a strong anisotropy of the measured lattice parameters – dependence of the lattice parameter on the crystallographic direction – was observed. The difference between the lattice parameters measured on the lattice planes *{h00}* and the stress-free lattice parameter is significantly smaller than the departure of the lattice parameters obtained from the interplanar spacing of the lattice planes *{hhh}* from the stress-free lattice parameter. Such anisotropy is related to the *{111}* easy deformation direction as known for TiN and similar compounds [11,12]. Tensile residual stress of (1.0 ± 0.1) GPa was found in both samples. To compare the three approaches discussed above, we can summarise that we achieved the best reliability of the microstructure parameters using the grain interaction model, which yields anisotropic lattice strain in a polycrystalline sample, in conjunction with a method of the residual stress calculation, which uses whole set of measured data. For our samples, the most reliable results were obtained using the Reuss model and $f(\psi)$ or the Direct Solution methods.

References

1. Noyan I.C., Cohen J.B., 1987, *Residual Stress*, (Berlin: Springer Verlag).
2. Perry A.J., Valvoda V. and Rafaja D., 1992, *Thin Solid Films,* **214**, 169.
3. Kuzel R., Cerny R., Valvoda V., Blomberg M., Merisalo M., 1994, *Thin Solid Films* **247**, 64.
4. Kamminga J.-D., De Keijser T.H., Mittemeijer E.J. and Delhez R., 2000, *J. Appl. Cryst.,* **33**, 1059.
5. Kim J.O., Achenbach J.D., Mirkarimi P.B., Shinn M., Barnett S.A., 1992, *J. Appl. Phys.,* **72**, 1805.
6. Voigt W., 1910, *Lehrbuch der Kristallphysik,* (Berlin, Leipzig: Teubner).
7. Reuss A., 1929, *Z. Angew. Math. Mech*, **9**, 49.
8. H. Neerfeld, 1942, *Mitt. K.-Wilh.-Inst. Eisenforschg.*, **24**, 61.
9. Hill R., 1952, *Proc. Phys. Soc. London*, **65**, 349.
10. Pluger J., Fink J., Weber W. and Bohnen K.-P., 1984, *Phys. Rev. B,* **30**, 1155.
11. Rafaja D., 2004, *Adv. Eng. Mater.,* **6,** 577.
12. Rafaja D., Havela L., Kužel R., Wastin F., Colineau E. and Gouder T., 2005, *J. Alloys Comp.,* **386**, 87.

Acknowledgements. This work is a part of the research plan MSM 0021620834 financed by the Ministry of Education of the Czech Republic.

I.3.2 *Line Broadening Analysis*

Z. Kristallogr. Suppl. **23** (2006) 75-80

Dislocation line broadening

R. Kužel

Department of Electronic Structures, Faculty of Mathematics and Physics, Charles University, 121 16 Praha 2, Ke Karlovu 5, Czech Republic,
*Contact author; kuzel@karlov.mff.cuni.cz

Keywords: line profile analysis, dislocations, microstrain

Abstract. The influence of dislocations on X-ray diffraction line profile broadening is briefly discussed. The broadening can be described by several parameters. For instance, the line width is proportional to the Burgers vector of dislocations, to the square-root of dislocation density and to the so-called orientation (contrast) factor. The orientation factor determines the *hkl* dependence of broadening and it is a function of elastic characteristics of the material investigated and orientation of the diffraction vector with respect to the Burgers vector and dislocation line. Since completely random dislocation distribution of dislocations is impossible, another parameter connected to the dislocation correlation (cut-off radius) must be included in the description. The theory of dislocation-induced line broadening has been developed many years ago, but it still needs development allowing its practical application to line profile analysis. General problems of present line profile analysis on samples with dislocations are mentioned.

Introduction

The most complete kinematical theory of X-ray diffraction by real crystals has been formulated by M. A. Krivoglaz [1 – 2]. It allows classification of the lattice defects according to their influence on the diffraction pattern. Theoretical analysis of the scattering consisting of the Bragg peak and the diffuse lines can be performed for different lattice defects and their displacement field. It shows that diffraction effects are determined by the behaviour of displacement field with the distance from the defect. The defects with rapidly decreasing field lead to the reduction of integrated intensity (static Debye-Waller factor), shift of the Bragg peaks and appearance of diffuse scattering – these are the so-called defects of the first-kind. The defects with slowly decreasing ($1/r$) displacements destroy the Bragg term and only concentrated diffuse scattering can be observed as the broadened quasiline – the lattice defects of the second kind. Point defects, their clusters, precipitates and small dislocation loops belong to the former while dislocations to the latter type. The type of displacement field plays the most decisive role for the classification of the defects. This is based on the physical nature of the defects and it has been derived for their random distribution.
However, the situation is more complicated in practice. The effects can look differently due to correlation which can screen and reduce the displacement field of the defects in some cases and enhance it under other conditions. Then the defects which belong to the first kind by their physical nature can sometimes look like the 2nd type defects, e.g. because of their

high concentration. An interesting case of precipitates and dislocation loops has been investigated [2]. Under certain conditions, special doublets of the Bragg and diffuse scattering can be observed simultaneously.
In many cases, the relations for line shift and broadening are given by the product of several functions – function of the diffraction vector, function of the defect strength and the so-called orientation factor. This factor determines the *hkl*-dependence of the diffraction parameter. It is determined by the elastic characteristics of the material and by the orientation of the defects with respect to the diffraction vector and crystallographic axes.

Dislocation-induced line broadening

Dislocations and 2nd kind stresses are the main reasons for the so-called strain broadening. The problem was treated by Williamson and Smallman in 1956 [3], but only for a single dislocation. Krivoglaz and Ryaboshapka [4] assumed statistically random distribution of dislocations and derived relations for integral breadth and Fourier coefficients. Integral breadth is proportional to the square-root of dislocation density and the so-called orientation factor determining the *hkl*-dependence. Wilkens has shown that a completely random distribution of dislocations is unrealistic [5] and introduced the so-called restrictedly random distribution characterized by the dislocation density ρ and cut-off radius R_c (the radius of the region within which the distribution is random). This parameter can be taken as a measure of correlation in dislocation distribution. Krivoglaz, Martynenko and Ryaboshapka [6] generalized their original model by including pair correlation functions and came to similar results. Further extension was done by Ungar, Groma et al. [7] who introduced more parameters and included the case of dislocation polarization. Calculations for dislocation dipoles, dislocation loops and dislocation walls were also performed mostly by Krivoglaz, Ryaboshapka and Barabash [review in 8 and 9, 10]. In recent years, the most frequently used formalism for description of dislocation-induced line broadening is that of Wilkens. However, similar but not identical Krivoglaz description [6] for not too strong correlation in dislocation arrangement can be used as well. It was applied first in [11].
Integral breadth (in 1/d) can be approximated as follows

$$\beta_h = b\sqrt{\rho}\sqrt{\chi}\sqrt{\frac{\ln P}{2}}A\frac{\sin\theta}{\lambda}, \qquad (1)$$

where ρ is the mean dislocation density, b is the magnitude of the Burgers vector, the P factor is related to the correlation in dislocation arrangement and factor A is close to unity. For dislocation density determination the knowledge of the orientation factor χ (often called as contrast factor and denoted by C) is necessary. The correlation factor P must be estimated for example from the profile shape or better from Fourier coefficients.

Orientation (contrast) factor

The orientation factor depends on the indices h, k, l and determines the anisotropy of line broadening. Formulae for the orientation factors for the most common dislocations in cubic materials were published by Krivoglaz [1]. General relations for calculation of the orientation factors were derived in papers [12, 13] based on the formalism for description disloca-

tion displacement field by Teodosiu and Steeds. In order to calculate the factor, some model – dislocation types must be considered.
Then the factor can be calculated according to the following relation

$$\chi^{hkl} = \sum_{K,L}^{6} \mathrm{E}_{KL} < \mathrm{G}_{KL} >, \tag{2}$$

where E is the elastic and G the geometric part. The *elastic part* is determined by the displacement field of a single dislocation of the given type in the material studied and depends on its elastic characteristics (constants).

$$E_{ijkl} = \frac{1}{\pi} \int_{0}^{2\pi} D_{ij} D_{kl} d\varphi, \qquad D_{ij} = \frac{2\pi r}{b} \frac{\partial u_i}{\partial r_j}, \tag{3}$$

where u is the displacement at r and φ, the polar coordinates of the dislocation. The *geometric part* is given by the relations

$$G_{ijkl} = A_{ij} A_{kl} \qquad A_{ij} = \gamma_i \gamma_j, \tag{4}$$

where γ_i are directional cosines between the i axis of coordinate system connected with the slip plane and the diffraction vector.
As each type gives characteristic anisotropy of line broadening, in some cases it is possible to estimate dominating dislocation types from such anisotropy. Crystal symmetry must be taken into account and corresponding averaging over all symmetrically equivalent directions must be performed for the calculations of orientation factors. The calculations must be numerical in general case of elastic anisotropy. In case of preferred orientation of lattice defects in the sample, appropriate weights must be taken in the averaging. If more slip systems are active (and dislocations with different Burgers vector) it is better to include the Burgers vector in the orientation factor. Useful simple relations for orientation factors of polycrystalline cubic and hexagonal materials without preferred grain and defect orientation were derived by Ungar et al [14 - 16]. For cubic materials it is

$$\langle \chi_{hkl} \rangle = \langle \chi_{h00} \rangle (1 + qH) = \langle \chi_{h00} \rangle \left[1 + q \frac{h^2k^2 + h^2l^2 + k^2l^2}{\left(h^2 + k^2 + l^2\right)^2} \right]. \tag{5}$$

If the elastic constants of the material are known, two parameters $\langle \chi_{h00} \rangle$ a q can be expressed as as functions of elastic constants and then easily calculated for different dislocation types [15]. For hexagonal materials the following relation has been derived [16]

$$\langle \chi_{hkl} \rangle = \alpha + \frac{[\beta(h^2 + k^2 + i^2) + \gamma l^2] l^2}{[h^2 + k^2 + i^2 + (3/2)(a/c)^2 l^2]^2}, \tag{6}$$

where $i = h - k$, α, β and γ are constants depending on the elastic constants of the crystal and the type of dislocations and on c/a ratio of two lattice parameters of hexagonal system.
Calculations of the orientation factors for non-random defect distribution in thin films were published by Armstrong et al [17, 18]. Recently, the program ANIZC has been made available. This can calculate orientation factors for cubic, hexagonal and trigonal crystals [19].

Dislocation-correlation factor

The correlation factor can be expressed as

$$P = r_c \sqrt{B_{hkl}} \approx \sqrt{\pi \rho R_c}\ , \tag{7}$$

where

$$B_{hkl(i)} = 2\pi \sum_{i=1}^{N} b_i^2 \rho_i \chi_{hkl(i)} \left(\frac{\sin^2 \theta_{hkl}}{\lambda^2} \right) \tag{8}$$

for the case of N dislocation slip systems. The quantity R_c is the cut-off radius and r_c is its value modified by the second orientation factor ξ_c [6]. In general, the calculation of P is more complicated. It depends itself on the dislocation density and the value r_c is unknown. Its value can be estimated from the profile shape. We can take rough estimation as follows: for P = 3 is the shape between Cauchy and quadratic Cauchy (C2) functions, P = 5 corresponds to C2, for higher P it is close to the Gauss function. Hence, with the increasing correlation in dislocation arrangements the profile tails are extended. For the estimation also the dependence of ratio FWHM/β vs. P can be used. However, the profile shape is sensitive to P only for small P values. On the other hand, the linear dependence β vs. sin θ is justified strictly speaking only for $P > 3$ [6, 2].

For precise evaluation, the Fourier analysis, must be applied

$$\ln A_{hkl}(L) = -B_{hkl} L^2 \ln \frac{r_c}{L}\ . \tag{9}$$

It follows that the plot ln A(L)/L^2 vs. ln L should be linear (at least in the region of validity of the used approximations). The slope of the plot then gives B_{hkl} and the ln L intercept the value ln r_c, i.e. also the correlation factor P. Similar expression has been obtained by Wilkens [5]. His formalism is used for the description of dislocation line broadening in two programs using the method of total powder pattern fitting (or multiple profile fitting) – program by Leoni and Scardi [20], and Ribarik and Ungár [21, 22]. Usually the *hkl* dependence of r_c is neglected. Fourier coefficients can be expressed as follows

$$A^D_{\{hkl\}} = \exp\left[-\frac{\pi}{2} b^2 \langle \chi \rangle_{hkl} \rho L^2 d^{*2}_{\{hkl\}} f(L/R_e) \right], \tag{10}$$

where d^* is the interplanar spacing of the planes *hkl* and function f is given by the relation

$$f(\eta) = -\ln \eta + (7/4 - \ln 2) + 512/90\pi\eta + (2/\pi)(1 - 1/4\eta^2) \int_0^{\eta} \arcsin V / V dV -$$

$$-(1/\pi)(769/180\eta + 41\eta/90 + 2\eta^3/90)(1-\eta^2)^{1/2} - \tag{12}$$

$$-(1/\pi)(11/12\eta^2 + 7/2 + \eta^2/3)\arcsin\eta + \eta^2/6,$$

for $\eta \le 1$ and $f(\eta) = 512/90\pi\eta - [11/24 + (1/4)\ln 2\eta](1/\eta^2)$, for $\eta \ge 1$ (13)

where η can be expressed as follows

$$\eta = (1/2)\exp(-1/4)(L/R_e) \tag{14}$$

The above function can be expressed in a simplified form [23] and it is discussed in the contribution of N. Armstrong in these proceedings. The validity of the leading terms of expression (11) has been demonstrated for different types of dislocations [24].
In principle, it is possible to include higher order terms into the relation (11), i.e. the terms proportional to $(Ld^*)^4\ \rho^2$ [2, 5, 7]. However, more detailed analysis of these terms has not been done (except partially [7]). The terms are more significant in case of higher correlation of dislocations and presence of dislocation dipoles and their weight is more pronounced for higher diffraction angles and in central part of the diffraction profile.
Quite detailed analysis of inhomogeneous distribution of dislocations is possible from careful measurements of profile tails and evaluation of moments [25].

Some conclusions

In spite of the fact that the line profile analysis of dislocation-induced line broadening has been improved in last years, there are still problems more significant than in crystallite size description. This is especially high correlation between dislocation density and dislocation-correlation factor. The latter is related to the shape of the profile but careful measurement with high statistics of counts is necessary for its determination. The correlation is inherent in the description and cannot be completely overcome by different optimization algorithms. While for nearly random distribution of dislocations the methods work well, for highly-correlated or strongly inhomogenous distribution of dislocations appropriate description which could be easily applied in the profile analysis is missing. Most of work was concentrated on the development of Wilkens approach – the model of restrictedly random distribution of dislocation. The potential of alternative Krivoglaz approach based on the pair-correlation functions in the description of dislocation arrangements may still have not been used enough.
Nearly no studies have been devoted to relations and/or separation between the broadening caused by the 2nd kind stresses and by dislocations. The only attempt was published in [26]. However, the presence of such stresses can significantly influence the results in some cases.
Another problem can arise from sample statistics. Line profiles may not be representative enough if only few grains are in the diffraction condition. This can happen for large grains in sample, especially in high-resolution setup. Special case often found for example in annealed samples which were originally heavily deformed is bimodal grain size distribution when some of the grains grow quickly while other particles remain small. This can be seen on very long profile tails which could be ascribed to higher correlation in dislocation arrangement (small cut-off radius).
Finally, in-plane or in-depth inhomogeneity of the sample can influence the line profile analysis significantly and should be taken into account.
It can be concluded that combination of diffraction line profile analysis with additional X-ray and other techniques is always desirable.

References

1. M. A. Krivoglaz, 1969, *Theory of X-ray and Thermal Neutron Scattering by Real Crystals* (New York: Plenum Press).

2. M. A. Krivoglaz, 1996, *X-ray and Neutron Diffraction in Nonideal Crystals* (Berlin: Springer-Verlag).
3. G. K. Williamson and R.E. Smallman, 1956, *Philos.Mag.* **1**, 34-46.
4. M. A. Krivoglaz and K. P. Ryaboshapka, 1963, *Phys.Met.Metallogr.* **15**, 18-31.
5. M. Wilkens, 1970, *Phys.Stat.Sol. A*, **2**, 359-370.
6. M. A. Krivoglaz, O.V. Martynenko and K. P. Ryaboshapka, 1983, *Fiz. Met. Metalloved,* **55**, 5-17.
7. T. Ungár, I. Groma and M. Wilkens, 1989, *J.Appl.Cryst.*, **22**, 26.
8. R. I. Barabash, 1999, in *Defect and Microstructure Analysis by Diffraction.* Ed. by R. L. Snyder, J. Fiala and H. J. Bunge, (Oxford University Press), pp. 127-140.
9. R. I. Barabash, P. Klimanek, 2001, in *Advances in Structure Analysis*, edited by R. Kužel, J. Hašek (Prague: Czech and Slovak Crystallographic Assoc.) pp. 438 – 448.
10. R. I. Barabash, P. Klimanek, 1999, *J. Appl. Cryst.* **32**, 1050-1059.
11. R. Kužel and P. Klimanek, 1989, *J. Appl.Cryst.*, **22**, 299-307..
12. P. Klimanek and R. Kužel, 1988, *J.Appl.Cryst.*, **21**, 59-66.
13. P. Klimanek and R. Kužel, 1988, *J.Appl.Cryst.*, **21**, 363-68.
14. T. Ungár and G. Tichý, 1999, *Phys. Stat. Sol.*, **17**, 42-43.
15. T. Ungár, I. Dragomir, A. Révész and A. Borbély, 1999, *J. Appl. Cryst.*, **32**, 992-1002.
16. I. Dragomir, T. Ungár, 2002, *J. Appl. Cryst.*, **35**, 556-564.
17. R. Cheary, E. Dooryhee, P. Lynch, N. Armstrong, S. Dligatch, 2000, *J. Appl. Cryst.* **33**, 1271-1283.
18. N. Armstrong, P. Lynch, 2004, in *Diffraction Analysis of the Microstructure of Materials*, edited by E. J. Mittemeijer, P. Scardi, (Berlin: Springer), pp.249 -286.
19. P. Scardi, M. Leoni, 2002, *Acta Cryst. A*, **58**, 190-200.
20. A. Borbély, J. Dragomir-Cernatescu, G. Ribárik, T. Ungár, 2003, *J. Appl. Cryst.*, **36**, 160 – 162.
21. G. Ribárik, T. Ungár and J. Gubicza, 2001, *J. Appl. Cryst.*, **34**, 669-676.
22. T. Ungár, J. Gubicza, G. Ribárik and A. Borbély, 2001, *J. Appl. Cryst.*, **34**, 298-310.
23. J. G. M. van Berkum, 1994, PhD thesis, Delft University of Technology. The Netherlands.
24. J. D. Kamminga, R. Delhez, 2000, *J. Appl. Cryst.*, **33**, 1122-1127.
25. I. Groma, A. Borbély, 2004, in *Diffraction Analysis of the Microstructure of Materials,* edited by E. J. Mittemeijer, P. Scardi, (Berlin: Springer) pp.287 - 307.
26. D. Breuer, P. Klimanek, W. Pantleon, 2000, *J. Appl. Cryst.* **33**, 1284-1294.

Acknowledgement. This work is a part of the research program MSM 0021620834 financed by the Ministry of Education of the Czech Republic.

Z. Kristallogr. Suppl. **23** (2006) 81-86

Considerations concerning Wilkens' theory of dislocation line-broadening

N. Armstrong[1,*], M. Leoni[2], P. Scardi[2]

[1]Department of Applied Physics, University of Technology Sydney, PO Box 123, Broadway, NSW 2007, Australia.
[2]Dipartimento di Ingegneria dei Materiali e Tecnologie Industriali, Università di Trento, 38050 Trento, Italy.
[*]Contact author; e-mail: Nicholas.Armstrong@uts.edu.au

Keywords: line profile analysis, dislocations, Wilkens' model, Fourier coefficients, powder diffraction

Abstract. When applying Wilkens' dislocation line broadening theory, the dependence on each individual slip system need to be considered, since the Fourier coefficients result from a convolution product over all active slip-systems. Corresponding diffraction profiles are qualitatively and quantitatively different from those obtained by considering, as in most literature approaches, average coefficients. Simulations show the impact of the different models in the case of screw and edge dislocations contained in cerium oxide.

Introduction

X-ray Line Profile Analysis (LPA) is currently evolving towards a direct interpretation of line broadening in terms of microstructural properties. This development is particularly timely as advances in materials science and nanotechnology require reliable, robust and complementary analysis techniques. Interpreting line-profile broadening in terms of microstructural properties of materials (dislocations, stacking faults/twins, crystallite shape and size distributions, etc.) has resulted in LPA complementing other experimental techniques such as transmission electron microscopy (see [1] for state-of-art methods).
The ability to numerically evaluate the dislocation contrast factors for elastically anisotropic materials [2-5] has enabled the microstrain broadening component of recorded X-ray line profiles to be interpreted in terms of the type, spatial arrangement and density of dislocations [6-8]. This development has also been accompanied by an increased application and critical assessment of dislocation-based models [9-12]. In particular the Wilkens' model [13-15] has received considerable attention. This model defines analytical expressions for the dislocation Fourier coefficients in terms of two free parameters: the total average dislocation density, ρ; and an effective outer cut-off radius of the strain field, R_e.
The physical basis for the analytical Fourier coefficients defined by Wilkens [13-15] is the so-called *restrictedly random distribution* of dislocations, an *ad hoc* model developed to overcome the logarithmic divergence in the Krivoglaz theory [16,17]. Despite the simplified

hypotheses, Wilkens' work provides a basic model that allows for the characterisation of dislocation broadened line profiles. Furthermore, Krivoglaz [17] pointed out that the introduction of the R_e parameter can account for correlation functions and distortion screening. More recently, Groma [10] has developed a general theory concerning the dislocation correlation functions, and takes into consideration both weak and strong dislocation-dislocation correlations. This generalised theory is directly applicable to inhomogeneous dislocation distributions that are experimentally observed. The theory was applied to account for the asymmetry of line-profiles from dislocations dipoles and dislocation walls [18].
The influence of ρ and R_e on Fourier coefficients and line profiles is examined in the context of two models: the first (referred to as *simplified* model) assumes that the analytical Fourier coefficients defined by Wilkens [13-15] are the average coefficients from *all* active slip-systems in a polycrystalline specimen. The second *full* model considers the analytical Fourier coefficients for each individual slip-system. A convolution product over all active slip-systems defines the resultant Fourier coefficients for a given *hkl*.
This paper questions these analytical expressions for the dislocation Fourier coefficients and in particular the physical significance of R_e. When used to simulate Fourier coefficients and whole diffraction patterns for selected materials, the two models produce qualitatively and quantitatively different results.

Theoretical background to Wilkens' model

Restrictedly random distribution model
The restrictedly random distribution model assumes that a large cylindrical crystallite of radius R_0 and cross-sectional area F_0 is divided into p^2 sub-areas, where straight dislocations for a single slip-system are randomly positioned parallel or antiparallel to each other, and parallel to the cylinder axis (see [14] Sec. III, p.1199). The dislocation density, ρ, for the restrictedly random distribution is given by $\rho = N_0 / F_0$, where N_0 is the total number of dislocations in the total cross-sectional area F_0, and N_p is the number of dislocations in the sub-area F_p. Moreover, the radius of the sub-area, R_p is approximately equal to the outer cut-off radius, R_e, of the dislocations system (see [15] Sec. 2.1, p. 360). This defines the physical basis on which the analytical Fourier coefficients are derived.

Simplied Wilkens' model
The application of the Wilkens' theory for analysing dislocation-broadened line-profiles involves modelling the Fourier coefficients as [7,8]

$$A(L, d^*_{hkl}) = \exp[-\tfrac{\pi}{2} b^2 d^{*2}_{hkl} L^2 \rho \langle C_{hkl} \rangle f^*(L / R_e)] \qquad (1)$$

where b is the magnitude of Burgers vector; d^*_{hkl} is the magnitude of the diffraction vector; and L is the Fourier length. In this model both ρ and R_e are free parameters that can be determined from the experimental data. The average contrast factor $\langle C_{hkl} \rangle$ accounts for the elastic anisotropy of the medium and for the geometrical (or orientational) anisotropy arising from the presence of dislocations in the material.
The f^* function in (1) plays an important role in quantifying the Fourier coefficients for all L. This function phenomenologically describes the dislocation-dislocation correlations that appear in the higher-order Fourier coefficients: in the region of small L the coefficients de-

crease with a negative curvature and, as L increases, they pass through a point of inflexion and decrease to zero with a positive curvature. The full definition is given in [14] (A.7 &.A.8, p. 1213).

Full Wilkens' model

The second formulation, called *full Wilkens model,* includes the slip-system and *hkl* dependencies into the Fourier coefficients as:

$$A\left(L,d^*_{hkl}\right)=\prod_{j=1}^{N} A_j\left(L,d^*_{hkl}\right)=\exp\left[-\frac{\pi}{2}b^2\ d^{*2}_{hkl}\ L^2\ \frac{\rho}{N}\sum_{j=1}^{N} C^j_{hkl} f^*\left(\eta_j\right)\right] \tag{2}$$

where $A_j(L,d^*_{hkl})$ is the Fourier transform for the j-th slip-system and $\frac{1}{N}\sum_{j=1}^{N} C^j_{hkl} f^*(\eta_j)$ defines the slip-dependency of the contrast factors C^j_{hkl}. The averaging of the product $C^j_{hkl} f^*(\eta_j)$ is in direct contrast to the averaging of C^j_{hkl} only (i.e., $\frac{1}{N}\sum_{j=1}^{N} C^j_{hkl}$) used in the simplified model (and in most literature). In (2) it is implicitly assumed that ρ is the sum of the dislocations densities ρ_j assumed equal on all slip systems. The η_j in (2) are given by

$$\eta_j = L\frac{\sigma_j}{2R_e}\exp[\ K(\mu_j)-\alpha] \tag{3}$$

where $\sigma_j = |\sin\psi_j|$, ψ_j is the angle between scattering and dislocation line vectors (respectively $\vec{g}$ and $\vec{l}_j$), μ_j is the inner product of $\vec{g}$ and Burgers vector $\vec{b}_j$, whereas the $K(\mu_j)$ function is defined in [14] (Appedix 3, p. 1219). Here we define the η-coefficients as

$$\eta-coefficients=\frac{\sigma_j}{2}\exp[K(\mu_j)-\alpha] \tag{4}$$

which modulate the Fourier correlation length, L, with respects to R_e, while defining the geometrical orientation of the slip-system. Figure 1 shows the η-coefficients for cerium oxide (CeO_2) containing screw and edge dislocations. In the figure, we notice that η-coefficients=1 corresponds to (1). On averaging the η-coefficients over all slip-systems, we observe that $<\eta$-coefficients$> \propto d^*_{hkl}$.

Further averaging over the *hkl* results in $<<\eta$-coefficients$>>\sim 1$, since the areas above and below unity are approximate equal. Of course this may not be the case for materials with different lattice parameter and it depends on the extension of the Ewald sphere.

Some observations about R_e

The Fourier coefficients are on the whole phenomenologically correct, in that they decrease monotonically to zero for increasing L. In fact, to prevent the divergence of the coefficients, Wilkens [14] introduces $K(\mu)$ into f^* such that:

$$f(m/R_e)-K(\mu)\rightarrow f^*(m/R_e-K(\mu))=f(m/R'_e) \tag{5}$$

with $R'_e=R_e e^{-K(\mu)}$. It is worth noting that Wilkens redefinition of the outer cut-off radius results in a "watering down" of the physical meaning of R_e. Similarly, Groma [19] introduced R''_e as an *effective* cut-off radius, defined as $R''_e=e^2R_e\approx 7.39R_e$ [20].

Kamminga & Delhez [11,12] simulated numerically a restrictedly random distribution of dislocations and showed that $R_e = 0.58D$, where D is the dimension of the sub-areas. It is also

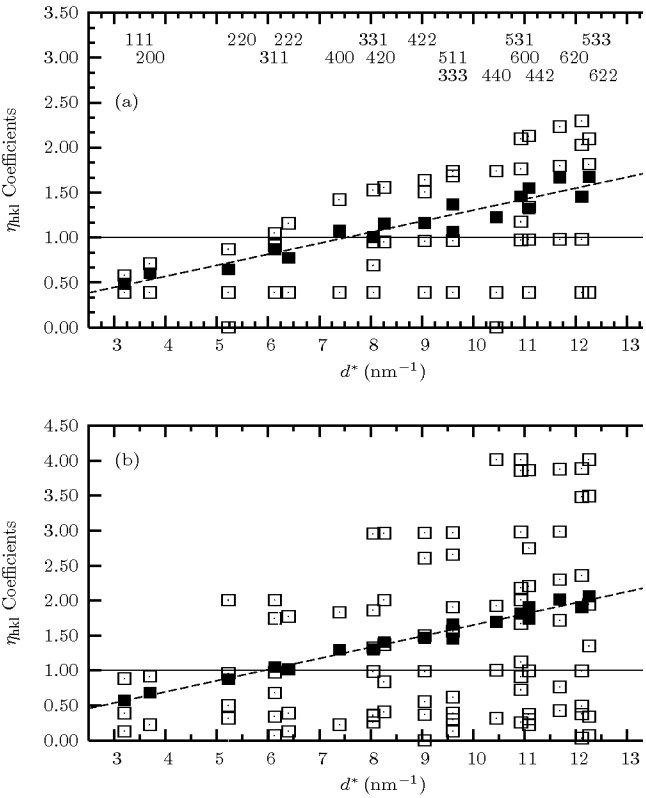

Figure 1. η-coefficients as a function of the diffraction vector for cerium oxide containing screw (a) and edge (b) dislocations. Values for specific slip systems (□) and average over slip systems (■).

interesting to observe that if $R_p \approx R_e$ where $\pi R_p^2 = D^2$, we have $R_e = 0.56D$. This result suggests that a suitable R_e can be defined in terms of the dimensions of the sub-areas.The above results, confirmed by the work of Lynch [21] on strained gold thin films, who pointed out that R_e should be considered as a length parameter, rather than a physical parameter.

Underlying assumptions of the Simplified & Full models

The *hkl* dependence in the simplified model (1) only appears in $\langle C_{hkl} \rangle$ and d^*_{hkl}, whereas the two free parameters, ρ and R_e, are independent of *hkl*. Moreover, (1) defines the "average" Fourier coefficients for a given *hkl*, for all active slip-systems in the powder specimen. In comparison, (2) takes into account the slip-dependency of the Fourier coefficients and is essentially a convolution product of the Fourier coefficients from all active slip-system where the geometrical orientation of the slip-plane is also considered.

The above considerations clearly point out the differences between the models, and firmly place the Full model on a better physical basis.

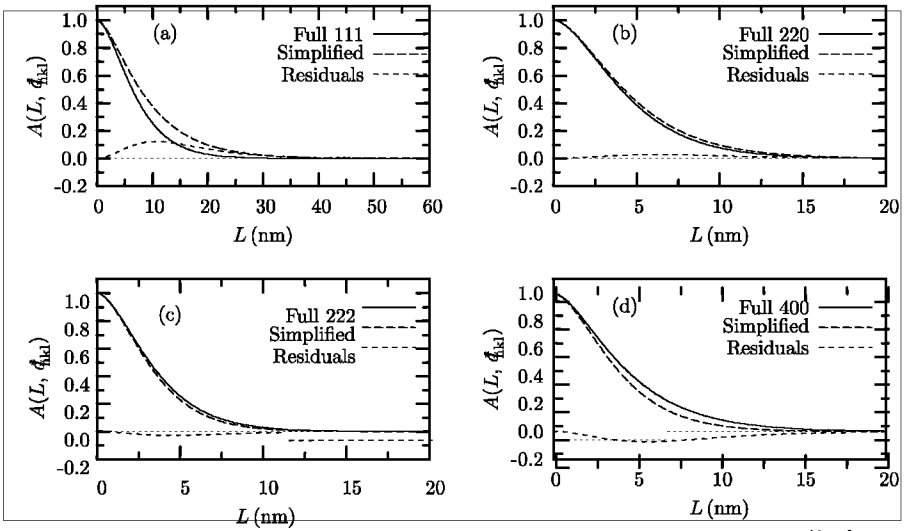

Figure 2. Simulated Fourier coefficients for ceria containing screw dislocations ($\rho = 2.0\times10^{16}$ m^{-2} R_e=10.0 nm). (111) (a), (220) (b), (222) (c) and (400) (d) reflections according to full (line) and simplified (dash) models. Difference (residual) is reported below (short dash)

Figure 2 shows the Fourier coefficients for both the Simplified and Full models assuming screw dislocations with $\rho = 2.0 \times 10^{16}$ m^{-2} and $R_e = 10.0$ nm. The Wilkens parameter $M = R_e\sqrt{\rho} \approx 1.4$ is in the range of applicability for the theory [14,15]. The contrast factors were calculated using the approach outlined in [1] (Chapter 10) for a {111}<110> slip-system (i.e. N=12). The Fourier coefficients illustrate the difference between the models as d^*_{hkl} increases, in accordance with the trend observed for the <η-coefficients>. The two models are approximately equal only for <η-coefficients> ≈ 1 (i.e., (220) and (222)).

Concluding remarks

In this paper we have discussed the theoretical basis for the Wilkens' model and two variants have been proposed: the *Simplified* model, does not take account for the dependency of the Fourier coefficients on the slip-system; the *Full* model does account for this dependency. This is highlighted in the definition of the η-coefficients, (3). Consequently, the results for the full and simplified models will agree only when the average η-coefficients are approximately equal to unity.

Besides the differences between simplified and full models discussed so far, a basic problem of models derived from Krivoglaz-Wilkens theories is the ambiguity in the definition of R_e. As discussed in the present work, this ambiguity is partly due to the "watering down" resulting from Wilkens hypotheses necessary to guarantee the convergence of the Fourier coefficients. As a consequence, values of ρ and R_e should only be correct to an order of magnitude

and R_e, in particular, should be regarded just as a length parameter, rather than a true measure of the outer cut-off radius.
It can therefore be concluded that research efforts in this area should be addressed to the development of models that can: (*i*) provide expressions for the Fourier coefficients valid for any L; (*ii*) account for higher order dislocation interaction terms; and (*iii*) correctly define physical parameters of the dislocation ensemble.

References

1. Mittemeijer, E.J., & Scardi, P., (editors), 2004, *Diffraction Analysis of the Microstructure of Materials*, (Berlin: Springer).
2. Wilkens, M. , 1987, *Phys. Stat. Sol.*, **104**, K1-K6.
3. Klimanek, P. & Kužel, R., 1988, *J. Appl. Cryst.*, **21**, 59-66.
4. Ungár, T., Dragomir, I., Revesz, A., Borbely, A., 1999, *J. Appl. Cryst.*, **32**, 992-1002.
5. Armstrong, N, & Lynch, P., 2004, in *Diffraction Analysis of the Microstructure of Materials*, edited by E.J. Mittemeijer & P. Scardi (Berlin: Springer), pp. 249-307.
6. Scardi, P., Leoni, M., Dong, Y.H., 2000, *Eur. Phys. J.* **B18**, 23-30
7. Ribarik, G., Ungar, T. & Gubicza, J., 2001, *J. Appl. Cryst.*, **34**, 669-676.
8. Scardi, P., Leoni, M., 2002, *Acta Cryst.* **A57**, 604-613.
9. Levine, L.E. & Thomson, R., 1997, *Acta. Cryst.*, **A53**, 590-602.
10. Groma, I, 1998, *Phys. Rev. B* , **57**, 7535-7542.
11. Kamminga, J.-D. & Delhez, R., 2000, *J. Appl. Cryst.* **33**, -1122-1127.
12. Kamminga, J.-D. & Delhez, R., 2001, *Mat. Sci. Forum*, **378-381**, 142-147.
13. Wilkens, M., 1970, in *Fundamental aspects of dislocation theory*, edited by J. A. Simmons, R. de Witt & R. Bullough (NBS Spec. Publ. 317), pp.1191-1193.
14. Wilkens, M., 1970, in *Fundamental aspects of dislocation theory*, edited by J. A. Simmons, R. de Witt & R. Bullough (NBS Spec. Publ. 317), pp.1195-1221.
15. Wilkens, M., 1970, *Phys. Stat. Sol.* **A2**, 359-370.
16. Krivoglaz, A. & Ryaboshapka, K.P., 1963, *Fiz. metal. metalloved.*, **15**, 18-31.
17. Krivoglaz, A., Martynenko, O.V. & Ryaboshapka, K.P., 1983, *Phys. Met. Metall.*, **55**, 1-12.
18. Groma, I. & Monnet, G., 2002, *J. Appl. Cryst.*, **35**, 589-593.
19. Groma, I., Ungar, T. & Wilkens, M., 1988, *J. Appl. Cryst.*, **21**, 47-53.
20. Ungar, T., Gubicza, J., Ribarik, G. & Borbely, A., 2001, *J. Appl. Cryst.*, **34**, 298-310.
21. Lynch, P., 2003, PhD thesis, Department of Applied Physics, University of Technology, Sydney, Australia.

Z. Kristallogr. Suppl. **23** (2006) 87-92

Momentum method applied to evaluation of size and strain in ball-milled iron

A. Borbély*, A. Révész and I. Groma

Eötvös Roland University, Department of General Physics, Budapest, H-1518, POB. 32
*Contact author; e-mail: borbely@ludens.elte.hu

Keywords: diffraction, line profile analysis, crystallite size, dislocation density

Abstract. The momentum method for the evaluation of size and strain parameters from X-ray peaks is applied to the case of a ball-milled iron powder. The Warren-Averbach analysis and the anisotropy of the peak widths revealed by the Williamson-Hall plot indicate that broadening is caused by lattice strain and anisotropic crystallite size. The separation of the two components was performed based on the momentum method developed for the case of size and dislocation induced strain broadening. The evaluations show that the crystallite sizes in the 211 and 100 directions are smaller than in the 110 direction. The coherent domains are rather small ranging from 5 to 10 nm and contain of about one dislocation. No indication for the presence of stacking faults was found.

Introduction

Determination of meaningful and reliable crystallite size and strain parameters from XRD peaks is a challenging task for nowadays evaluation techniques. With this respect microstructurally based models are welcome since they predict the asymptotic shape of XRD peaks, which can be directly compared with experiment. This is especially true in case of nanomaterials when due to the small crystallite size a nearly Lorentzian type peak shape is expected. If the crystallites contain lattice defects, then the resulting profile is the convolution of the size profile characterizing the shape of the crystallites and the average structure factor characteristic for the lattice defect [1]. It is known, that in case of an infinite crystal containing dislocations the tails of the peak-profile decay as $|q|^{-3}$, where q is the deviation from the reciprocal lattice point. According to the general theory of dislocation induced XRD peak broadening [2, 3] only this asymptotic behaviour can be anticipated, the shape of the whole profile being unknown. The only exception from this is the special case of restrictedly random distribution of dislocations, a model developed by Wilkens [4], who was able to calculate the entire peak shape. It is however, questionable if this special dislocation distribution is valid in any practical situation. If not, it is safer to consider only the asymptotic behaviour of the measured profile. This doesn't mean however, that the Wilkens model and its incorporation in multiprofile fitting programs [5-8] to replace physically less justified peak-functions, is not applicable. We only want to stress that in such cases a microstructural justification of the selected

evaluation method should be given. If the selected method cannot be justified, then only the general model is reliable.
For the evaluation of size and strain parameters we have selected a momentum method. Theoretically calculated functions of the asymptotic behaviour of different order momentums are fitted to the experimental data and the size and strain parameters are obtained from the parameters of the fitted functions [3, 9]. The advantages of the momentum method are related to the fact that during integration, statistical errors in the measurement may cancel out, and to the possibility to visually check that their form satisfies the theoretical predictions. Based on this visual check one can readily realize if the assumed source of broadening is present in the measurement or not, excluding by this the blind use of sophisticated software for cases where it is not applicable. The method is exemplified on X-ray peak measurements done on ball-milled and heat-treated iron powder samples.

Experimental technique and results

High purity iron powder with initial particle size of approximately 45 μm was ball milled in a Pulverisette-P7 (Fritsch) planetary ball-mill with a hardened steel ball. To avoid oxidation, the powder samples were sealed in the steel container under vacuum. Ball-milling was carried out for a duration of 1 month. Some part of the ball-milled powder was annealed in a calorimeter by heating it up to 570°C at a rate of 2K/min.
X-ray line profile experiments were carried out on a special high resolution double crystal diffractometer with negligible instrumental line broadening [10]. As X-ray source the line focus of a sealed Co tube operated at 40 kV and 25 mA was used. The primary X-ray beam was monochromatized by a symmetrically cut plane Ge monochromator using the (440) reflection. The monochromator was tuned for the $CoK\alpha_1$ line, so that the $CoK\alpha_2$ component was completely suppressed. The beam reflected from the monochromator passed through a thin slit of about 0.2x4 mm. The line profiles were recorded by a linear position-sensitive X-ray detector of OED-50 type Braun, Munich.
Figure 1 shows 110 Bragg peaks recorded from the iron powder in the ball-milled and annealed conditions. It is evident that annealing at 570°C produces a tremendous sharpening of the peak. Similar effects were observed in the case of the 200, 211 and 220 reflections, too. In order to set up a strategy for the evaluation of microstructural parameters of the ball milled and annealed samples it is always worth to study the behaviour of the peaks widths, for example in a Williamson-Hall (W-H) plot [11]. In this plot various parameters can be used to characterize broadening. The most often used ones are the integral width and the width at half maximum. However, the width at a given relative height from the peak maximum can also be chosen and as shown by [12] all such widths have similar qualitative behaviour. Figure 2a shows the widths at a relative intensity of 0.1 as a function of the diffraction vector. It can be observed that the widths measured on the ball-milled sample show anisotropic broadening, while those corresponding to the annealed sample are nearly constant. Broadening is more pronounced for the 200 and 211 peaks, while the 110 and 220 reflections are less broadened. It is known that for bcc crystals this broadening sequence can be produced by stacking faults [13], however existing literature results [14-16] and present evaluations indicate the presence of microstrains, which should be first taken into account. Microstrain was attributed to dislocations, and to check this a presentation of the data in a

modified W-H plot [17] was done. This is shown in figure 2b, where the peak widths are plotted as a function of $K\sqrt{C}$, where K is the scattering vector and C is the contrast factor.

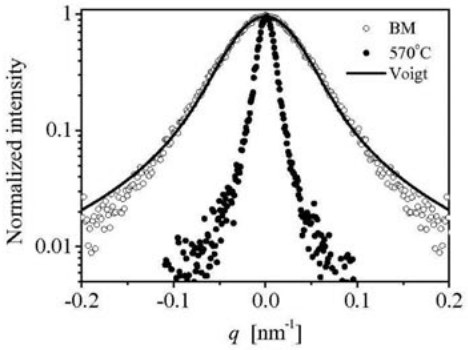

Figure 1. 110 *Bragg peaks recorded from the ball-milled (BM, open symbols) and annealed iron powder (full symbols). The solid curve is a Voigt function fitted to the ball-milled data.*

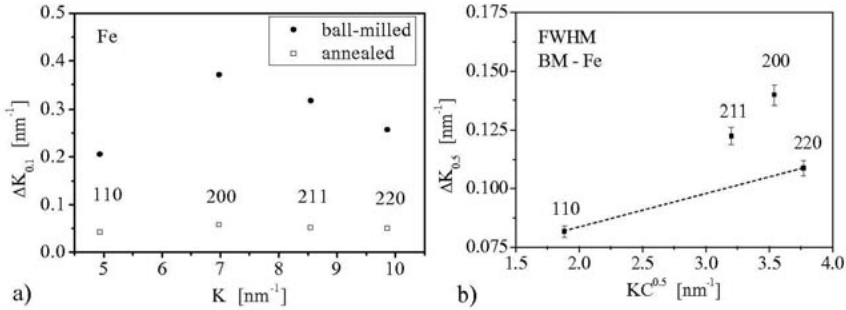

Figure 2. a) Williamson-Hall plot of peak-widths (ΔK) at 0.1 from maximum measured on ball-milled and annealed samples b) Modified W-H plot of widths at half maximum of the same reflections as in a).

The contrast factors were calculated with the program ANIZC [18] taking into account the second order elastic constants of Fe (the use of the program is free and can be found at http://metal.elte.hu/anizc). The results for the diffraction vectors used in the present investigation are given in table 1.

Table 1. Average contrast factors of screw and edge dislocations calculated with the program ANIZC.

g	110	200	211	**g**	110	200	211
$\mathbf{C_s}$	0.1040	0.3055	0.1040	$\mathbf{C_{e\,(110)}}$	0.1780	0.2647	0.1781

In the calculation of the average contrast factor it was assumed that edge dislocations belong to the ½[111](110) slip system. Identical C values are obtained, however, for the

½[111](211) system, too, with one exception for the 200 diffraction vector, the value of which is 0.2185. Since the contrast factors of 110, 211 and 220 reflections are identical they should lie on a monotonously increasing curve if the assumption of isotropic size of the *modified* Williamson-Hall plot applies. According to figure 2b this is not the case. The 211 and the 200 reflections lie above the line connecting the points corresponding to the 110 and 220 reflections. This means that there is an additional broadening, which can be attributed to smaller crystallite sizes in the respective directions compared to the 110 direction.

To evaluate the apparent crystallite size (ε_F) and the dislocation density (ρ) we have adopted the momentum method. According to the theory explained in [9,19] the second and fourth order restricted momentums have the following form:

$$M_2(q) = \frac{1}{\pi^2 \varepsilon_F} q - \frac{1}{4\pi^2} \frac{L}{K^2 \varepsilon_F^2} + \frac{1}{2\pi^2} \Lambda \rho \ln\left(\frac{q}{q_0}\right), \tag{1}$$

$$\frac{M_4(q)}{q^2} = \frac{1}{3\pi^2 \varepsilon_F} q + \frac{\Lambda \rho}{4\pi^2} + \frac{3\Lambda\rho}{(2\pi)^4 \varepsilon_F} \frac{\ln(q/q_2)}{q}, \tag{2}$$

where K is the Scherrer constant, L is the taper parameter and Λ, q_0 as well as q_2 are also constants [9]. It can be seen, that if there is only size broadening, then the second and fourth order momentums show a linear behaviour at large q values ($\rho = 0$). In case of dislocation induced broadening the second order momentum has a logarithmic behaviour, while the fourth order momentum tends to a constant value ($\varepsilon_F = \infty$). In case of combined broadening the linear terms are still the leading ones, but the dislocation density in equation (1) and the cross term in equation (2) can have quite large contributions of about 50%. The nonlinear fit of equation (2) to the fourth order momentum is presented in figure 3. It is clear that the theoretically derived functions fit well the experimental points for approximately half of the data (of about 250 points, not all shown in the figure). We mention that the fitting parameters are not very sensitive to the fitting interval, however a minimum of about 100 data points *at the end of the curves* should always be considered. It can be observed that

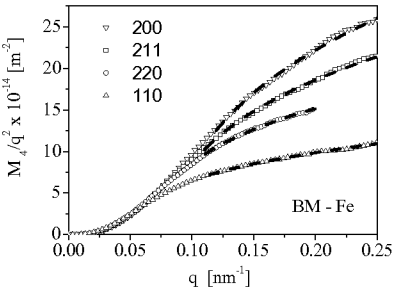

Figure 3. Fourth order momentum of the peaks measured on the ball-milled samples.

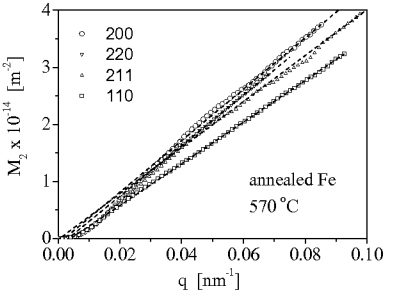

Figure 4. Second order momentum of the peaks measured on the annealed samples

the 220 peak was not measured in a sufficiently large interval, as the other peaks. This renders the evaluation of the 220 peak rather difficult and fitting function (2) at the end of the curve yields in a too large value of the apparent crystallite size (of about 24 nm). For this reason the 220 momentum was excluded from the evaluation of microstructural parameters. All the other peaks were evaluated in the same reciprocal space interval ranging from about 0.13 to 0.25 nm^{-1}. During evaluations the second and fourth order momentums were fitted simultaneously for different values of the background. That fit was accepted, which gave the smallest difference (generally smaller than 10%) between the size parameters. The average results are presented in table 2. Important to note that minimum difference condition imposed in the size parameters of the two momentums resulted in dislocation density values, which were also equal within an experimental error of 20%.

Table 2. Apparent crystallite size and average dislocation-dislocation spacing obtained from the second and fourth order momentums of the peaks measured on the ball-milled (BM) and annealed (A) iron powder. For comparison the same quantities obtained from the conventional and modified W-A procedures [17] *(applied to 110 and 220 reflections) are also given (W-A).*

g (BM)	110	200	211	W-A	**g** (A)	110	200	211	W-A
ε_F [nm]	11	4.3	3.3	9	ε_F [nm]	28	22	25	36
$1/\sqrt{\rho}$ [nm]	4.5	5.5	4.0	8	$1/\sqrt{\rho}$ [nm]	51	136	240	48

Figure 4 shows the second order momentums of the peaks measured on the annealed samples. As estimated from the modified W-H plot, the defect concentration is very small in these samples and the asymptotic behaviour of the momentums is definitely linear, in accordance with equation (1). The intercepts of the fitted lines are negative leading to a positive value of the *taper* parameter [1]. The error of the intercept was however large and could not be used for the evaluation of the crystallite shape. This explains the large scatter of dislocation densities also, which were obtained from fourth order momentum. Table 2 gives the crystallite sizes obtained from a conventional Warren-Averbach (W-A) procedure [20], too. These are equal within an error of 25% with the sizes obtained from the momentum method.

Discussion and conclusions

The apparent crystallite sizes given in table 2 confirm the qualitative conclusions of the modified W-H plot (figure 2b). The coherent domains in the ball-milled iron are smaller in the 211 and 200 directions than in 110. This indicates the existence of a size anisotropy, which contradicts the stacking fault assumption ($\varepsilon_{211} > \varepsilon_{200}$). During annealing at 570°C of the ball-milled powder the grains recrystallize and have nearly the same size in all investigated directions. Very instructive is the comparison of crystallite sizes obtained from the momentum method and the conventional W-A procedure. In case of ball- milled samples the apparent sizes differ by about 20%, while for the annealed samples the difference is larger, of about 25%. The agreement between the two methods can be considered satisfactory, taking into account their different approaches the momentum method is a single peak method, while the W-A is a multi-peak one. In fact the same quantity, the area weighed crystallite size is determined, once from the asymptotic behaviour of the momentums and once from the zero

extrapolated values of the Fourier-coefficients. So, the agreement should be not very surprising. It is important to note the consistency of the results for dislocation densities obtained from the investigated peaks, which are equal within an error of 20%. This is not the case of the annealed samples, when the strain is small and the dislocation densities are determined with a large error. Based on these and the good agreement between theoretically calculated momentums with experimental data the following conclusions can be drawn:

- the momentum method enabled a coherent explanation of broadening observed on the ball-milled iron as an alternative to the faulting theory, which alone could not be accepted due to the large microstrain obtained from both the momentum and W-A analysis.
- the powder contains dislocations and there is of about one dislocation per crystallite. This indicates that the Wilkens model of restrictedly random distribution of dislocations might be applicable to nano-powders, since the basic assumption of the model, a sample made up of scattering regions of equal size containing the same number of dislocations is fulfilled.
- if the X-ray peaks are measured in a sufficiently large interval, then generally there is no need to fit the experimental profiles by peak-functions, which asymptotic behaviour is different from theoretical predictions (see for example the Voigt function shown in figure 1).

References

1. Wilson, A. J. C., 1962, *Proc. Phys. Soc.*, **80**, 286-294.
2. Groma, I., Ungár, T., & Wilkens, M., 1988, *J. Appl. Cryst.*, **21**, 47-53.
3. Groma, I., 1998, *Phys. Rev. B*, **57**, 7535-7542.
4. Wilkens, M., 1970, *Fundamental Aspects of Dislocation Theory*, National Bureau of Standards (US) Special Publication No. 317, Vol. II, edited by J. A. Simmons, R. de Wit & R. Bullough, pp. 1195-1221. Washington, DC: N.B.S.
5. Ungár, T., Gubicza, J., Ribárik, G. & Borbély, A. 2001, *J. Appl. Cryst.* **34**, 298-310.
6. Wu, E., Gray, E. Mac A. & Kisi, E. H., 1998, *J. Appl. Cryst.*, **31**, 356-362.
7. Lutterotti, L. & Gialanella, S., 1998, *Acta Mater.*, **46**, 101-110.
8. Scardi, P. & Leoni, M., 2004, in *Diffraction Analysis of the Microstructure of Materials*, edited by E.J. Mittemeijer & P. Scardi (Berlin: Springer), pp. 51-91.
9. Borbély, A. & Groma, I., 2001, *Appl. Phys. Lett.*, **79**, 1772-1774.
10. Wilkens, M. & Eckert, H., 1964, *Z. Naturforschung*, **19a**, 459.
11. Williamson, G.K. & Hall, W.H., 1953, *Acta Metall.*, **1**, 22.
12. Borbély, A., Guiglionda, G. & Driver, J.H., 2002, *Z. für Metallkunde*, **93**, 689-693.
13. Warren, B.E., *X-ray diffraction*, 1969, Addison-Wesley, New-York, p. 311.
14. Révész, A., Ungár, T., Borbély, A. & Lendvai, J., 1996, *Nanost. Mat.*, **7**, 779-788.
15. Tian, H.H. & Atzmon, M., 1999, *Acta mater.*, **47**, 1255-1261.
16. Vives, S., Gaffet, E. & Meunier, C., 2004, *Mat. Sci. Engng.*, **A366**, 229-238.
17. Ungár, T. & Borbély, A., 1996, *Appl. Phys. Lett.*, **69**, 3173-3175.
18. Borbély, A., Dragomir-Cernatescu J., Ribárik, G., & Ungár. T., 2003, *J. Appl. Cryst.*, **36**, 160-162.
19. Borbély, A. to be published.
20. Warren, B.E. & Averbach, B.L., 1950, *J. Appl. Phys.* **21**, 595; ibid. 1952, **23**, 497.

Acknowledgements. The authors gratefully acknowledge the financial support of the Hungarian Scientific Research Found (OTKA) under the contract No. T-034999 and T-043519. BA is a grantee of the János Bolyai Scholarship.

Z. Kristallogr. Suppl. **23** (2006) 93-98

Microstructure of severely deformed metals from X-ray line profile analysis

J. Gubicza[1], N. H. Nam[1], K. Máthis[2] and V. V. Stolyarov[3]

[1]Department of Solid State Physics, Eötvös University, Budapest, Hungary
[2]Department of Metal Physics, Charles University, Prague, Czech Republic
[3]Institute of Physics of Advanced Materials, Ufa State Aviation Technical University, Ufa, Russia
*Contact author; e-mail: gubicza@ludens.elte.hu

Keywords: severely deformed metals, line profile analysis, crystallite size, dislocation structure

Abstract. Two essentially different materials, cubic $Ti_{49.8}Ni_{50.2}$ shape memory alloy and hexagonal AZ91 Mg alloy, were deformed by equal channel angular pressing (ECAP). The microstructure developed as a result of severe plastic deformation was studied by X-ray line profile analysis. The correlation between the microstructure and the mechanical behavior was also investigated. Below 100 °C the tensile strength of the Mg alloy increased as a consequence of the increase of the dislocation density owing to ECAP. Above 200 °C the strength decreased and the ductility increased as a result of the breakage of the $Al_{12}Mg_{17}$ precipitates due to ECAP. The analysis of the dislocation contrast factors of $Ti_{49.8}Ni_{50.2}$ revealed that <100>{110} dislocations with <111> line vector formed during ECAP.

Introduction

Severe plastic deformation is an effective tool for producing bulk ultrafine grained (submicron grain sized or nanostructured) metals [1]. One of the most common severe plastic deformation methods is equal channel angular pressing (ECAP) – a technique that results in a homogeneous sub-micron grain structure of the workpiece [1]. The ultrafine-grained materials produced by ECAP have unique mechanical properties, e.g. very high strength at room temperature and good ductility at high temperature [1]. For understanding the mechanical behaviour of materials produced by ECAP it is necessary to characterize their microstructure. X-ray diffraction line profile analysis is a widely used method for studying the microstructure of nanocrystalline materials [2,3]. The standard methods of line profile analysis based on the full widths at half maximum, the integral breadths and the Fourier coefficients of the profiles provide the apparent crystallite size and the mean square strain. In severely deformed materials where the lattice distortions are primarily caused by dislocations the mean square strain can be expressed in terms of the characteristic parameters of the dislocation structure [4]. In these formulas the anisotropic strain broadening of the line profiles is taken into account by the contrast factors of dislocations [5]. Since the values of the dislocation

contrast factors depend on the dislocation slip systems present in the crystal, the evaluation of X-ray line profiles for the contrast factors permits the determination of the dislocation structure [6]. In the last few years, a fast development in computing made it possible to work out procedures for determining the parameters of the microstructure by fitting the whole diffraction profiles [7-9]. In the recently elaborated multiple whole profile (MWP) fitting method, the measured intensity profiles, or their Fourier transforms are fitted by theoretical functions calculated on the basis of a model of the microstructure [9]. This procedure makes it possible to determine both the crystallite size distribution and the dislocation structure in ultrafine grained materials.

In this paper two examples are shown for the effectiveness of X-ray line profile analysis in the study of microstructure of ultrafine grained materials produced by ECAP: a cubic $Ti_{49.8}Ni_{50.2}$ shape memory alloy and a hexagonal AZ91 Mg alloy. The correlation between the microstructure and the mechanical properties is also investigated.

Experimental details

The $Ti_{49.8}Ni_{50.2}$ specimen in rod form was annealed at 800 °C for 1 hour and then it was quenched in water to homogenize the structure and to eliminate the thermomechanical prehistory [10]. The mean grain size of this initial state was 80 μm. The sample was subsequently deformed in an ECAP die at 450 °C. The diameter of the die channels was 16 mm and the angle of the intersecting channels was 110° [10]. The ECAP deformation was repeated up to 8 passes following route B_C [1].

The main alloying elements in the Mg-based AZ91 alloy are Al (9.1 wt.%) and Zn (0.88 wt.%). The total concentration of other impurities (Mn, Si, Fe, Cu, Ni and Be) is less than 0.2 wt.%. The shape of the specimen was a rectangular parallepipid with 9 mm in length and cross section of 4 x 10 mm^2. The initial state of the specimen was created by solution heat treatment at 413 °C for 18 hours. The sample was deformed by 8 ECAP passes at 270 °C using a 90° die following route C [1].

The microstructure of the ECAP treated specimens was investigated by X-ray line profile analysis. The X-ray diffraction profiles were measured on the cross-section perpendicular to the axis of ECAP treatment. The X-ray diffraction experiments were performed using a high-resolution diffractometer (Nonius FR591) with rotating Cu anode (λ = 0.15406 nm) and a Ge monochromator. The instrumental broadening ($\Delta 2\Theta$ = 0.006°) was negligible compared to the measured peak broadening ($\Delta 2\Theta$ = 0.1-0.3°) therefore instrumental correction was not performed. The profiles were recorded by a linear position sensitive gas-flow detector (OED 50 Braun, Münich). The peak profiles were evaluated by the MWP fitting procedure described in detail in reference [9]. In this method, the Fourier coefficients of the experimental profiles are fitted by the theoretical Fourier transforms calculated on the basis of a model of the microstructure. In this model, the crystallites have a spherical shape and a log-normal size distribution, and the lattice strains are assumed to be caused by dislocations. The procedure has five or six fitting parameters for cubic or hexagonal crystals, respectively: (i) the median and the variance, m and σ, of the log-normal size distribution function, (ii) the density and the arrangement parameter of dislocations, ρ and M, and (iii) the q (cubic crystals) or q_1 and q_2 (hexagonal crystals) parameters in the contrast factors of dislocations. The arithmetic, the area- and the volume-weighted mean crystallite sizes can be calculated from

m and σ using formulas given in reference [7]. In this paper only the volume-weighted mean crystallite size, $\langle x \rangle_{vol}$ is presented. The q or q_1 and q_2 parameters describe the dislocation slip systems present in the specimen.

Results and discussion

ECAP treated $Ti_{49.8}Ni_{50.2}$

The $Ti_{49.8}Ni_{50.2}$ specimen has B2 cubic structure. The X-ray line profile analysis was carried out only on the fundamental reflections as the superlattice peaks were very weak. The measured (open circles) and the fitted (solid line) Fourier transforms for five fundamental reflections of $Ti_{49.8}Ni_{50.2}$ deformed by 8 ECAP passes are shown in figure 1. The volume-weighted mean crystallite size and the dislocation density obtained from the fitting are 72±8 nm and $16\pm2\cdot10^{14}$ m^{-2}, respectively. This means that ultrafine grained microstructure is formed from the initial material as a result of ECAP. It has been shown recently by high resolution transmission electron microscopy that <100>{110} dislocations with <111> line vector were formed in $Ti_{50}Ni_{50}$ during high pressure torsion [11]. The q parameter value of these dislocations in $Ti_{49.8}Ni_{50.2}$ was determined by detailed numerical calculations using the equations from [12] and the elastic constants from [13]. This yielded the q value of 2.19 which is in good agreement with the experimental value of q parameter (2.1±0.1) determined by line profile analysis for ECAP treated $Ti_{49.8}Ni_{50.2}$ specimen. This indicates that the dislocations formed during ECAP are <100>{110} dislocations with <111> line vector, similarly as in the case of high pressure torsion. Mechanical tests show that ECAP results in the increase of the yield stress (YS) from 600 to 1140 MPa and the ultimate tensile strength (UTS) from 940 to 1240 MPa while the elongation to failure is reduced from 40 to 25% at room temperature [14]. These changes can be attributed to the large increase of the dislocation density owing to ECAP.

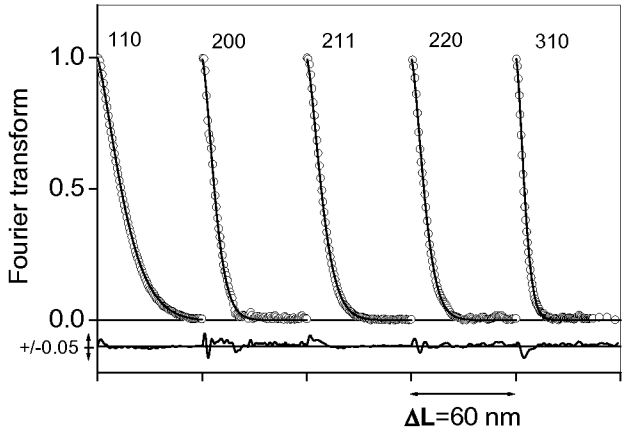

Figure 1. The measured (open circles) and the fitted (solid line) Fourier transforms for $Ti_{49.8}Ni_{50.2}$ deformed by 8 ECAP passes.The difference is also shown in the bottom part of the figure.

AZ91 Mg alloy deformed by ECAP

X-ray diffraction phase analysis shows that the initial state of AZ91 Mg alloy is a supersaturated solid solution. During high temperature ECAP $Al_{12}Mg_{17}$ precipitates are formed. Scanning electron microscopy (SEM) investigations reveal that these precipitates have rod-like shape which breaks into smaller parts owing to severe shear deformation during ECAP [15]. X-ray line profile analysis of the reflections of the Mg alloys shows that ECAP results in the reduction of the crystallite size from 253±38 nm to 97±10 nm and the increase of the dislocation density from $0.4\pm0.1\cdot10^{14}$ m^{-2} to $2\pm0.2\cdot10^{14}$ m^{-2}. The value of the arrangement parameter of dislocations, M, obtained from the fitting decreases from 2.5 to 1.6 during ECAP indicating the increase of the dipole character of the dislocation structure.

The q_1 and q_2 parameters of the contrast factors depend on the character of dislocations and therefore enable the determination of the prevailing dislocation slip systems in the sample. The q_1 and q_2 values for the eleven possible slip systems in Mg according to Kuzel and Klimanek [5] have been calculated and listed in table 2 in reference [16]. The eleven dislocation slip systems can be classified into three groups based on their Burgers vectors: b_1=1/3<-2110> (<a> type), b_2=<0001> (<c> type) and b_3=1/3<-2113> (<c+a> type). A computer program was elaborated to determine the Burgers vector population from the experimental values of q_1 and q_2 [17]. There are 4, 2 and 5 slip systems in the <a>, <c> and <c+a> Burgers vector groups, respectively. The program selects some slip systems from each group and averages their calculated q_1 and q_2 values with equal weights. The relative fractions of the Burgers vectors were calculated by making the measured and the weighted averaged theoretical values of q_1 and q_2 equal. If the weights have positive values the program stores them as one of the possible solutions. After examining all possible solutions, ranges of the three weights are obtained as the final solution. It was found that in the initial state the relative fractions of the <a>, <c> and <c+a> Burgers vectors are 68-86%, 0-15 % and 0-14 %, respectively. The abundance of <a>-type dislocations besides the <c>- and <c+a>-type dislocations can be explained by the smallest formation energy of <a>-type dislocations. After high temperature ECAP the relative fractions of the <a>, <c> and <c+a> Burgers vectors are changed to 54-58%, 0-2 % and 38-42 %, respectively. It should be noted that for the ECAP treated specimen a weak texture was established in which hexagonal basal planes were parallel to the longitudinal axis of the billet. The effect of this texture on the microstructural parameters determined by X-ray line profile analysis can be neglected as a good agreement was found between the shape of peak profiles obtained from the longitudinal and cross sections.

The mechanical behavior of the ECAP treated Mg alloy was studied by tensile test at room temperature, 100, 200 and 300 °C. The tensile measurements took 15-30 min depending on the temperature. After failure of the samples the microstructure was investigated by X-ray line profile analysis at room temperature. The volume-weighted mean crystallite size and the dislocation density are plotted as a function of temperature of deformation in figure 2. It can be seen that the dislocation density decreases while the crystallite size increases after 100 °C with increasing temperature because of the recovery of the microstructure. Below 100 °C the UTS is higher for the ECAP treated specimen than that for the initial state by about 30%. This can be explained by the higher dislocation density developed during ECAP deformation. At the same time above 200 °C the UTS for the ECAP sample is half of that for the initial state. Moreover, the elongation to failure is 3 and 6 times higher for the ECAP specimen than for the initial state at 200 and 300 °C, respectively. This increase of the ductility

can be attributed to the breakage of the rod-like $Al_{12}Mg_{17}$ precipitates during ECAP which facilitates the dislocation motion necessary for the recovery of the microstructure. The relative fractions of Burgers-vectors obtained on the tensile deformed ECAP samples are plotted as a function of deformation temperature in figure 3. The increase of the relative fraction of <c+a> dislocations can be observed at high temperature (300 °C).

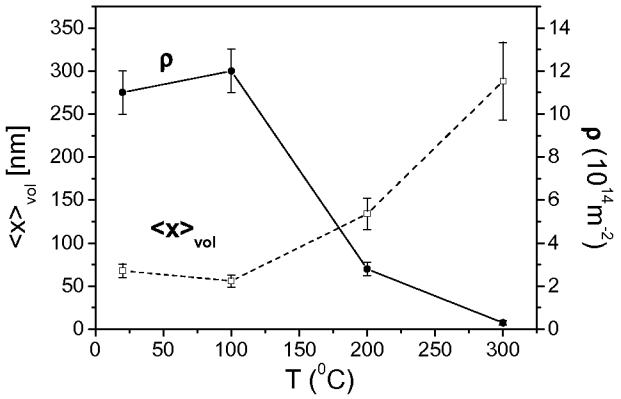

Figure 2. The dislocation density, ρ, and the volume-weighted mean crystallite size, $\langle x \rangle_{vol}$ as a function of temperature of tensile test performed on the ECAP treated Mg alloy. The microstructural data were determined after the failure of the samples.

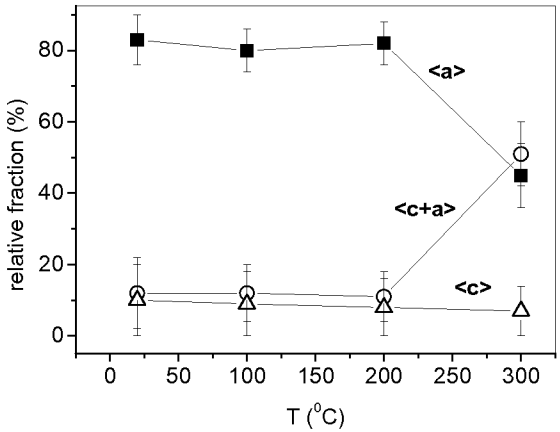

Figure 3. The relative fractions of <a>, <c> and <c+a> dislocations as a function of temperature of tensile test performed on the ECAP treated Mg alloy.

Conclusions

The analysis of the anisotropic strain broadening of the diffraction peaks of $Ti_{49.8}Ni_{50.2}$ suggests that <100>{110} dislocations with <111> line vector are formed during ECAP. The ECAP deformation of AZ91 Mg alloy results in the increase of the dislocation density which causes the increase of the tensile strength below 100 °C. During ECAP the $Al_{12}Mg_{17}$ precipitates in AZ91 Mg alloy breaks into smaller parts. This facilitates the recovery of the microstructure under tensile load above 200 °C which results in the decrease of strength and the increase of ductility compared to the initial state. The analysis of the contrast factors shows the abundance of of <a>-type (1/3<-2110>) dislocations. During deformation of AZ91 alloy at 300 °C the relative fraction of <c+a> (1/3<-2113>) dislocations increases.

References

1. Stolyarov, V.V., Zhu, Y.T., Alexandrov, I.V., Lowe, T.C. & Valiev, R.Z., 2003, *Mater. Sci. Eng. A,* **343**, 43.
2. Rafaja, D., Klemm, V., Schreiber, G., Knapp, M. & Kuzel, R., 2004, *J. Appl. Cryst.,* **37**, 613.
3. Armstrong, N. & Kalceff, W., 2004, *J. Res. Natl. Stand. Technol.*, **109**, 155.
4. Wilkens, M., 1970, *Phys. Stat. Sol. (a)*, **2**, 359.
5. Kuzel jr., R. & Klimanek, P., 1989, *J. Appl. Cryst.,* **22**, 299.
6. Kamminga, J.-D. & Delhez, R., 2001, *Mater. Sci. Eng. A,* **309-310**, 55.
7. Langford, J.I., Louër, D. & Scardi, P., 2000, *J. Appl. Cryst.*, **33**, 964.
8. Scardi, P. & Leoni, M., 2002, *Acta Cryst. A*, **58**, 190.
9. Ungár, T., Gubicza, J., Ribárik, G. & Borbély, A., 2001, *J. Appl. Cryst.* **34**, 298.
10. Pushin, V.G., Stolyarov, V.V., Valiev, R.Z., Kourov, N.I., Kuranova, N.N., Prokofjev, E.A. & Yurchenko, L.I., 2002, *Annales de Chimie - Science des Materialux*, **27**, 77.
11. Rentenberger, C., Waitz, T., & Karnthaler, H.P., 2004, *Scripta Mater.*, **51**, 789.
12. Ungár, T., Dragomir, I., Révész, Á. & A. Borbély, 1999, *J. Appl. Cryst.,* **32**, 992.
13. Ren, X., Miura, N., Zhang, J., Otsuka, K., Tanaka, K., Koiwa, M., Suzuki, T., Chumlyakov, Yu.I. & Asai, M., 2001, *Mater. Sci. Eng. A,* **312**, 196.
14. Stolyarov, V., Prokofiev, E., Prokoshkin, S., Dobatkin, S., Trubitsyna, I., Khmelevskaya, I., Pushin, V., Zhu Y.T. & Valiev, R.Z., *Acta Mater.,* in preparation.
15. Máthis, K., Gubicza, J., & Nam, N.H, *J. All. Comp.* 2005, **394**, 194.
16. Dragomir, I.C. & Ungár, T., *J. Appl. Cryst.* 2002, **35**, 556.
17. Máthis, K., Nyilas, K., Axt, A., Dragomir, I., Ungár, T. & Lukáč, P., 2004, *Acta Mater.*, **52**, 2889.

Acknowledgements. This research was supported by Hungarian National Scientific Research Fund (OTKA) under contract numbers T-042714, T-043247 and F-047057.

Z. Kristallogr. Suppl. **23** (2006) 99-104

Burgers Vector Populations in hot rolled titanium determined by X-ray Peak Profile Analysis

I. C. Dragomir[1*], G. A. Castello-Branco[2, 3], G. Ribarik[4], H. Garmestani[1], T. Ungar[4] and R. L. Snyder[1]

[1]School of Materials Science and Engineering, Georgia Institute of Technology, Atlanta, Georgia 30332-0245, USA
[2]Materials Science and Engineering, University of Florida P.O. Box 116400, Gainesville, Florida 32611-6400, USA
[3]Centro Federal de Educacao Tecnologica, CSF-RJ, Rio de Janeiro, RJ, Brazil, 22710
[4]Department of General Physics, Eötvös University Budapest, H-1518, P.O.B 32, Budapest, Hungary
[*]Contact author, e-mail: iuliana.cernatescu@mse.gatech.edu

Keywords: titanium, X-ray Peak Profile Analysis, dislocations, Burgers Vector Population

Abstract. Commercially pure alpha-titanium was deformed by hot rolling at 268° C for reduction levels of 40%, 60% and 80%. The dislocations densities and types in terms of Burgers Vector Populations at different deformation rates were established using X-ray Peak Profile Analysis. The dislocation model of anisotropic broadening of peak profiles was used to determination the Burgers vector distribution, and their evolution as the deformation proceeds to higher degrees in alpha-titanium samples presented here. It was found that the <a> dislocation type dominate at all deformation levels investigated in this study. The population of the <c+a> dislocation type is significant after 40% reduction and it becomes marginal for higher deformation rates. The <c> type dislocation population was found to be marginal at all deformation levels.

Introduction

Due to their outstanding properties titanium and titanium alloys are very attractive in a large variety of applications: aerospace, biomedical, and commercial applications [1, 2]. In order to improve and to control the mechanical proprieties of titanium it is important for understanding and explaining the formation of certain microstructure during deformation. On the other hand to explain and understand the deformation process information such as dislocation density, dislocation type and slip system activation are critical. Alpha-titanium has a hexagonal close-packed structure. Unlike the cubic crystals where usually one major type of slip system is activated during deformation in the hexagonal crystals, there are several fun-

damentally different slip systems types that are contributing simultaneously to the deformation [3-5]. The determination of the dislocations slip systems type by using conventional techniques such as TEM is rather difficult when the dislocation density reaches values as high as $10^{10}/cm^2$. On the other hand throughout the sample preparation process necessary for the TEM experiments the original microstructure may change. Other alternatives on investigating the microstructure are X-ray and neutron diffraction techniques. Recent works have shown that by using the method of X-ray Peak Profile Analysis information about the dislocation densities and dislocation type can be extracted from the X-ray pattern [6-10].
In the present study commercially pure alpha-titanium was deformed by rolling at 268° C for the following reduction rates: 40%, 60% and 80%. X-ray Peak Profile Analysis technique was employed to determine the changes in dislocation density and dislocation types with deformation.

Experimental procedures

Titanium specimens were rolled at 268° C to a reduction of 40%, 60% and 80%. A Lindberg/Blue model BF51800 electrical furnace was used to heat the samples. In order to obtain a homogeneous deformation a step-size of 5%, for reduction was applied. After each pass of 5% the sample was immediately returned to the furnace for reheating and again deformed to an additional reduction of 5%. The procedure was repeated until the desired reduction level was achieved. After the final step the samples were cooled in air. In order to remove the formed oxide layer before the X-ray diffraction experiments each sample was chemically etched.
The diffraction profiles necessary for the X-ray Peak Profile Analysis were measured using an Alpha-1 PANalytical Diffractometer set up in Bragg-Brentano geometry. Symmetrical incident beam Johansson monochromator allowed only the Kα1 component of Cu radiation to be used. In order to reduce the instrumental broadening effect 1/4° divergent slit, 1/2° anti-scattering slit and 0.02 rad soller slits was used on the incident beam peath. On diffracted beam side a 5.0 mm anti-scattering slit and a 0.02 rad. soller slit was used. A mask of 5mm was used to adjust the size of the probing X-ray spot. The profile data acquisition was done using a solid-state position-sensitive ultra-fast detector (X'Celerator, PANalytical). For each sample the following reflections were measured: 0002, $10\bar{1}1$, $10\bar{1}2$, $11\bar{2}0$, $10\bar{1}0$, $10\bar{1}3$ and 0004. The instrumental broadening was measured using NIST SRM (660a). As the measured profile is a convolution of the physical with the instrumental profile the Stokes-correction based on the Fourier transforms of the profiles was used to determine the physical line profiles [11]. Background and instrumental profile correction were done with the MKDAT program described elsewhere [10].

Burgers Vector Population

The X-ray peaks are broadened due to the small crystallite size and to the crystal lattice imperfections in materials. It has been shown by Wilkens that in a dislocated crystal the distortion Fourier coefficients of the physical profiles can be written in terms of dislocation density and strain anisotropy. The latest can be taken in account by introducing the contrast factors of dislocation [12, 13]:

$$A_L^D = \exp\,[-\ 2\pi^2 L^2 g^2\,(\rho\,\overline{Cb^2}\,/4\pi)\,f(\eta)], \qquad (1)$$

where g is the absolute value of the diffraction vector, L is the Fourier variable, ρ is the dislocation density, $\overline{Cb^2}$ is the average contrast factor of the dislocations present in the sample multiplied by the square of the dislocations Burgers vector and $f(\eta)$ is the Wilkens function [12]. In the case of hexagonal crystals the average contrast factor of dislocation can be written as follows [9]:

$$\overline{C}_{hk.l} = \overline{C}_{hk.0}\,[1 + q_1 x + q_2 x^2], \qquad (2)$$

where $x = (2/3)(l/ga)^2$, q_1 and q_2 are parameters which depend on the elastic properties of the material, $\overline{C}_{hk.0}$ is the average contrast factor corresponding to the *hk.0* type reflections, a is the lattice constant in the basal plane, g is the diffraction vector and l is the last index of the *hk.l* reflection for which the $\overline{C}_{hk.l}$ is evaluated. Since the contrast factor is a measurable parameter and it depends on the relative orientation of the diffraction vector and the line- and Burgers vectors of the dislocations, the X-ray peak profiles of the specimen can provide information about the dislocation types in the specimen. By inserting equation (2) in (1) it can be seen that only two parameters related to the contrast factor can be determined experimentally: q_1 and q_2. The measured values of q factors, $q_1^{(m)}$ and $q_2^{(m)}$, can be written in terms of numerically calculated average contrast factors of i number of slip systems considered in the evaluation:

$$q_1^{(m)} = \frac{1}{P}\sum_i h_i \overline{C}_{hk.0}^{(i)} b_i^2 q_1^{(i)}\ ,\ q_2^{(m)} = \frac{1}{P}\sum_i h_i \overline{C}_{hk.0}^{(i)} b_i^2 q_2^{(i)} \ \text{ and } \sum_i h_i = 1, \qquad (3)$$

where h_i is the fraction of dislocations which slips in the i-th slips system, $\overline{C_{hk.0}^{(i)}}$ is the theoretical value of the average contrast factor corresponding to the i-th slips system for the *hk.0* reflection, $q_1^{(i)}$ and $q_2^{(i)}$ are the q-factors of the i-th slip system, $P = \sum_i h_i \overline{C}_{hk.0}^{(i)} b_i^2 = \overline{b^2 C_{hk.0}}^{(m)}$ and $0 \le h_i \le 1$.

According to Honeycomb [14] and Klimanek & Kuzel [15] in a hexagonal crystal there are eleven possible slip systems. By taking this into account, the possibility of measuring q_1 and q_2 offers three independent equations and eleven unknowns [9]. This means that equations (3) can give an exact solution only by making certain assumptions about the activated dislocation slip systems. In the present work it is assumed that a particular Burgers vector type has random (or uniform) distribution in the different slip systems. In this case h_i terms in equations (3) become the fractions of dislocations with the three fundamental Burgers vectors types defined in the hexagonal systems: $\boldsymbol{b}_1$=1/3<$\overline{2}$110>, $\boldsymbol{b}_2$=<0001>, and

$\boldsymbol{b}_3$=1/3<$\bar{2}$ 113>. At the same time $\overline{C_{hk.0}^{(i)}}$, $q_1^{(i)}$ and $q_2^{(i)}$ become an averaged over the slip systems, each corresponding to the same Burgers vector type. The set of values for h_i obtained from equations (3) by using the above-mentioned assumption is called Burgers Vector Population [9]. In order to solve equations (3) the numerically calculated values of $\overline{C}_{hk.0}$, q_1 and q_2 for all slip systems are required. The theoretical values of $\overline{C}_{hk.0}$, q_1 and q_2 for titanium in the case of the most common slip systems were calculated and published previously in reference [9].

Results and Discussion

In the present work the Multiple Whole-Profile (MWP) fitting procedure was used to evaluate the q parameters in equation (2) and the dislocation densities from the X-ray diffraction pattern. In this procedure the Fourier coefficients of the measured physical profiles are fitted all at once by the product of the theoretical functions for size and strain caused by distortion in the crystal. In this evaluation process it is assumed that the peak broadening is caused by the smallness of the crystallites and by strain due to the dislocations. Details of the MWP method can be found in reference [10]. The usage of the average contrast factor of dislocations in the X-ray Peak Profile Analysis assumes that within a slip system type every slipping direction has the same probability. This assumption is not anymore valid when the specimen exhibits strong crystallographic texture. Due to the rolling deformation process the titanium samples studied here show a pronounced texture. In order to overcome this difficulty a random polycrystalline specimen was emulated for each sample by mixing the strongest diffraction peaks from the three different faces of the orthogonal sample to form a full diffraction pattern [16, 17]. These mixed patterns were then used in the MWP evaluation. The results for the dislocation densities and the arrangement parameter, M, are listed in table 1. for the titanium specimens deformed at 40%, 60% and 80% reduction levels. M is defined by Wilkens as the dislocation arrangement parameter [12]. The value of M gives the strength of the dipole character of dislocations: the higher the value of M, the weaker the dipole character and the screening of the displacement fields of dislocations [13]. The values of M in table 1. show that the dislocations in the titanium samples studied here are quasi-homogeneous distributed and exhibits a week dipole character. It can be observed from table 1. that the increment of ρ is small in accordance with a dynamic recovery effect, where dislocation annihilation that may occur due to the high deformation temperature. The solutions of the equations (3) for Burgers Vector Population are illustrated in figure 1. The results show that: I) in the specimen deformed at 40% reduction the <c+a> and <a> types of dislocation are dominating the dislocation population present in the sample; II) at higher deformation levels the population of <a> type dislocations increases and the presence of <c+a> dislocations decrease; III) at all deformation levels the fraction of <c> dislocations type is marginal. The results are in good agreement with the well known fact that dislocations with $\boldsymbol{b}$=<0001> Burgers vector are sessile, thus their presence is practically unchanged in the deformation range studied here [18]. The activity of <c+a> dislocations plays an important role in dynamic recovery. Screw dislocations of <c+a> type can move to the next slip planes by double cross slip followed by dislocation annihilation, which leads to a decrease of <c+a> dislocations at higher strains.

The results presented here are in good correlation with previous TEM studies, where the <a> dislocation types are most frequently observed in deformed titanium and <*c*+*a*> and <*c*> types are also reported [18, 19].

Table 1. Dislocation densities and arrangement parameter, M, obtained from MWP evaluation for different rolling reductions.

Rolling Reduction [%]	40% reduction	60% reduction	80% reduction
M	2.9	1.7	1.1
$\rho[1/cm^2]$	$5x10^{10} \pm 5$ %	$8x10^{10} \pm 10$ %	$10^{11} \pm 7$ %

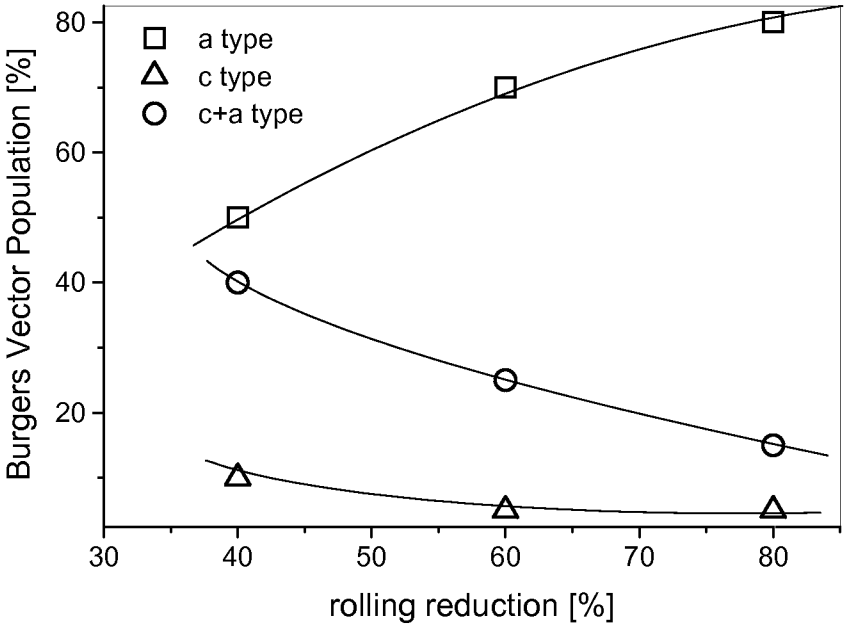

Figure 1. The h_i fractions (see the text) of the three fundamental Burgers vector types, <a>, <c> and <c+a>, as a function of rolling reduction percentage. Note that in the figure the solutions to equations (3), the h_i fractions, were transformed in percentages.

Conclusions

By using Peak Profile Analysis methods the evolution of dislocation density and the Burgers Vector Population has been evaluated as a function of rolling reduction in hot rolled titanium. It was found that the <a> types of dislocations are dominating the whole deformation range studied here. The percentage of <c+a> dislocation type is present significantly at 40% reduction level, but decreases as the deformation proceeds to higher values. The fraction of <c> dislocation type is minimal during the whole deformation process. It was also established that the dislocation density slightly increases as the reduction degree increases.

References

1. Gorynin, I. V., 1999, *Mater. Sci. & Eng., A*: **263(2)**, 112.
2. Teoh, S. H., Thampuran, R., Seah, K. H. W. & Goh, J. C. H., 1997, J. *Mater. Sci. Lett.* **16(8)**, 639.
3. Kim, J. H., Semiatin, S. L. & Lee, Ch. S., 2003, *Acta Mater.*, **51(18)**, 5613.
4. Stefansson, N., Semiatin, S. L., 2003, *Metall. Mater. Trans. A*, **34(3)**, 691.
5. Yadav, S. & Ramesh, K. T., 1997, *Mater. Sci. Eng. A*, **246**, 265.
6. Scardi P. & Leoni M., 2004, in *Diffraction Analysis of the Microstructure of Materials*, edited by E.J. Mittemeijer & P. Scardi (Berlin: Springer), pp 51-91.
7. Scardi P. & Leoni M., 2002, *Acta cryst. A*, **58**, 190.
8. Ungár, T., Dragomir, I., Révész, Á. & Borbély, A.,1999, *J. Appl. Cryst.* **32,** 992.
9. Dragomir IC. & Ungár T., 2002, *J. Appl. Cryst.* **35**, 556.
10. Ribárik G, Ungár T & Gubicza J., 2001, *J. Appl. Cryst.*, **34**, 669.
11. Stokes A. R. & Wilson A. J. C., 1944, *Proc. Phys. Soc. London*, **56**, 174.
12. Wilkens, M., 1970, *Phys. stat. sol.* (a), **2**, 359.
13. Wilkens, M.: Fundamental Aspects of Dislocation Theory, National Bureau of Standards (US) Special Publication No. 317, Vol. II, edited by J. A. Simmons, R. de Wit & R. Bullough, 1970, Washington, DC: N.B.S.
14. Honeycombe, R. W. K., 1984, *The Plastic Deformation of Metals*, (Edward Arnold Publ. Ltd., London).
15. Klimanek, P. & Kuzel Jr., R., 1988, *J. Appl. Cryst.* **21**, 59.
16. Gubicza J., Dragomir I. C., Ribárik G., Baik S. C., Zhu Y. T., Valiev R. Z. & Ungár T., 2003, *Zeitschrift für Metallkunde*, **94**, 1185.
17. Glavicic M. G., Salem A. A. & Semiatin S. L., 2004, *Acta Mater.*, **52(3)**, 674.
18. Jones I.P. & Hutchinson W.B., 1982, *Acta Metall.*, **29**, 951.
19. Song S. G. & Gray I.I.I. G.T., 1995, *Acta Metall.*, **43**, 2339

Acknowledgements. We gratefully acknowledge the support of PANalytical Inc.

Z. Kristallogr. Suppl. **23** (2006) 105-110

Spatial fluctuations of the microstructure during deformation of Cu single crystals

M. Kerber[1], E. Schafler[1,3,*], P. Hanak[2], G. Ribàrik[2], S. Bernstorff[4], T. Ungàr[2], M. Zehetbauer[1]

[1]Institute of Materials Physics, University Vienna, A-1090 Vienna, Austria
[2]Department of General Physics, Eötvös University Budapest, H-1518 POB., Hungary;
[3]Institute for Materials Science, Austrian Academy of Science, A-8700 Leoben, Austria
[4]Sincrotrone ELETTRA, Basovizza, I-34012 Trieste, Italy
[*]Contact author; e-mail: schafler@ap.univie.ac.at

Keywords: line profile analysis, single crystal deformation, dislocation structure

Abstract. Using X-ray Bragg Peak profile analysis (XPA) together with the very high intensity of synchrotron radiation, it was possible to study the evolution of several microstructural quantities, such as the density of dislocations ρ and their arrangement M with high lateral resolution during deformation.
Observing copper single crystals during compression a discontinuous behaviour of the dislocation density was observed in spatial scans. This can be interpreted as a consequence of the propagation of deformation waves in contrast to the homogeneous deformation observed in polycrystals. This effect has been recently documented by strain measurements of metal single crystals, which exhibit distinctive single slip behaviour in the initial stages of deformation. The results are discussed in terms of the formation of a network of deformation cells, continuously interacting with newly produced mobile dislocations.

Introduction

Historically the rigorous investigation of single crystal deformation was the basis for the description of work hardening in terms of stages. Stage I or 'easy glide' depends very strongly on the orientation of the crystal since only one single slip is active, a condition not always met. Stage II is characterized by the highest and constant rate of strain hardening and is described to be independent of the deformation temperature. Stage III exhibits a decreasing hardening coefficient and is very sensitive to the temperature and the rate of deformation [1-3]. These stages have also been identified in polycrystals. An additional Stage IV was discovered by Stüwe and Kovács [4], who have shown that at large deformations the decrease of the work hardening rate drops to zero and can stay constant up to a value larger than four of equivalent true strain. Later on Stage V exhibits another drop of hardening.
For the explanation of the macroscopic plastic flow constitutive dislocation models are considered [5, 6]. One of the basic assumptions of these models is that the material and its behaviour is identical for all (micro) volumes, therefore averaging over the elementary proc-

esses of plastic deformation is appropriate. However, there are numerous experimental indications that the plastic flow is inhomogeneous and localized in certain regions of the material. Based on the results of an advanced strain measurement technique Zuef and co-workers suggest moving deformation fronts as the mechanism of single crystal deformation and explain it by a self-exited wave model [5,6].
Moreover it is known that the inhomogeneous distribution of the generated dislocations in the material leads to the formation of a deformation cell structure. This cell structure governs the strength behaviour on the microscopic level [7] and is the subject of numerous investigations. Additionally this microstructure is the precursor of the subgrain structure and can lead even to a nanocrystalline structure if deformed by the methods of severe plastic deformation (SPD) [8]. It is thus essential for the further progress of the understanding of the deformation process to find the relation between the heterogeneity of the flow behaviour and the microstructure.
This work tackles this task via in-situ X-ray Bragg Profile Analysis using synchrotron radiation yielding microstructural parameters with a high time and lateral resolution: At low deformations the spatial distribution of the deformation induced dislocations show strong fluctuations which seems to get stationary at higher deformation.

Experimental

In the present case, {100} oriented cylindrical Cu single crystals were deformed by using a compact compression test machine (30 kN) with a mass of about 10 kg, which was placed on a robust 5-axis Eulerian-cradle goniometer such that the specimen surface illuminated by the X-ray beam was in the eucentric point of the goniometer. The irradiated area on the specimen was continuously monitored by a far-working-distance microscope (Questar QM 100).
A x-z table enabled to correct the macroscopic transverse contraction as well as the scanning procedure on the crystal with an initial step-width of $\Delta z = 0.1$ mm, decreasing to $\Delta z = 0.09$ mm for $\varepsilon = 0.16$ ($\varepsilon = \ln(d_0/d)$ due to the effective height reduction. This ensured that the identical scan path on the sample was measured for each deformation degree. During the lateral scans the deformation was stopped (loaded static measurement).
The X-ray diffraction experiments were carried out at the SAXS beamline of the ELETTRA synchrotron in Trieste using 8 keV photons which were provided by a 57-pole permanent magnet wiggler and a pair of asymmetrically cut Si(111) double-crystal monochromator with an intrinsic resolution of $\delta\lambda/\lambda = 5\text{x}10^{-4}$ [9]. After the monochromator the beam was focused by a toroidal mirror (focus size <1.2 x 0.6 mm^2). The flux density in the focal point was $7\text{x}10^{12}$ photons mm^{-2} s^{-1} at 200 mA beam current. A four-edge movable slit system at about 600 mm upstream from the focal position of the beam made it possible to reduce the beam size down to 30x40 μm^2. A second set of adjustable slit at about 200 mm upstream from the focal position was applied to reduce parasitic slit scattering induced by the first set of slits. The 40 μm spot size on the specimen and the wavelength dispersion and focusing divergence of the X-ray beam correspond to an angular resolution of about 0.005 Deg. (in 2θ). The (400) peak profiles of the single crystal (see more details below) were measured in reflection by a 50 mm gas filled linear position sensitive detector (OED-50 Braun, Munich). The linear resolution of the detector is about 80 mm, which means that the physically relevant angular resolution of the instrument is better than 0.01 Deg. (in 2θ) at a specimen to detector distance

of 450 mm. This is about 5 times smaller than the FWHM of the (400) peak profile measured from the undeformed virgin crystal. The number of counts in the maxima was between $3x10^4$ and 10^6. Due to the low noise of the detector the peak to background ratio was 10^5 for the small deformations decreasing with increasing deformation to about 10^3. Previous work where the microstructure of deformed Cu was investigated by means of XPA, at the same synchrotron source, with similar experimental conditions [10, 11] showed that no instrumental correction of the line profiles measured is necessary for the present evaluation.

Evaluation procedure

The broadening of the diffraction profiles is assumed to be caused by two effects: finite size of the scattering volume and strain fields caused by dislocations. For the latter the dislocation model of lattice distortions as given by Wilkens [12] is applied. The resulting formula for the Fourier coefficients is [13]:

$$A(L) = A^S(L)\, A^D(L) = A^S(L) \exp[- 2\pi^2 L^2 g^2 \frac{\rho \overline{C} b^2}{4\pi} f(\eta)], \qquad (1)$$

The superscripts S and D indicate size and distortion broadening, L is the Fourier variable, g is the absolute value of the diffraction vector, ρ is the dislocation density, $\overline{C}$ is the average dislocation contrast factor, b is the absolute value of the Burgers vector and $f(\eta)$ is a function derived explicitly by Wilkens [12] ($\eta \sim L/R_e$, with R_e the effective outer cut-off radius of dislocations). The contrast factor depends on the elastic constants and on the relative orientation of the Burgers-, line- and diffraction vector, and has been evaluated numerically for a large number of elastic constants in cubic crystals in [14]. In the present case there exists one type of slip system and therefore, only C on the right hand side of equation (1) was averaged according to [14] over all possible combinations of line and Burgers vectors and for equal population of edge and screw dislocations despite the fact, that this is not necessarily the case here. The Wilkens model assumes that the dislocations are randomly distributed in the region defined by R_e. All this may be an oversimplification but was convenient for the present analysis: The single profiles were evaluated by a modified Multiple Whole Profile fitting procedure [15]. The fitting of size broadening was disabled due to the virgin single crystal deformed and the contrast parameter was fixed to the numerical estimate, since only single profiles were fitted. Thus only the dislocation density and R_e were free parameters. No unphysical solutions for the fitting parameters occurred.

Results and Discussion

The lateral distributions of the dislocation density at 40 identical positions on the Cu single crystal for each deformation degree, as determined by evaluation of the measured X-ray line profiles, are shown in figure 1. As can be seen the dislocation density fluctuates over the whole scan path independent of the deformation degree ε. These fluctuations are well above the error of the method being about $1x10^{13}m^{-2}$: The relative magnitude of the variations is about 30-40 % for all scans.

An analysis of the same experiment with respect to a high resolution concerning the deformation degree showed a wavy behaviour of the dislocation density with increasing deforma-

tion [10]. It seems that the fluctuations of the dislocation density with deformation degree have a correspondence to those in space observed here.

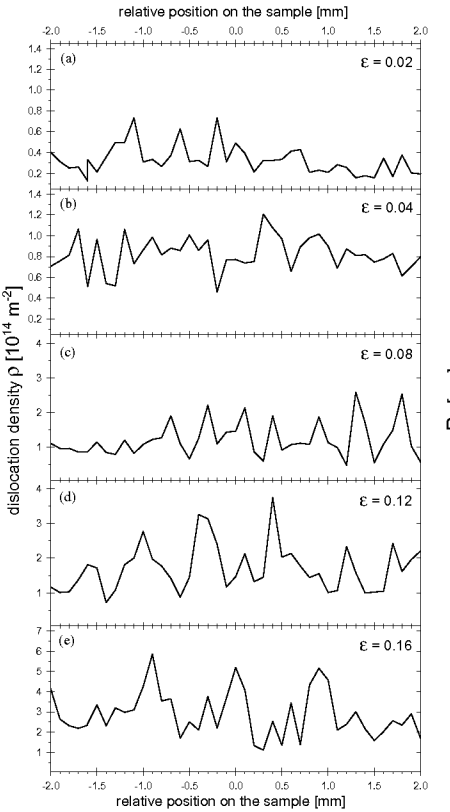

Figure 1. The lateral scans for different deformations ε: The dislocation density. Note the different scale of the y-axis!

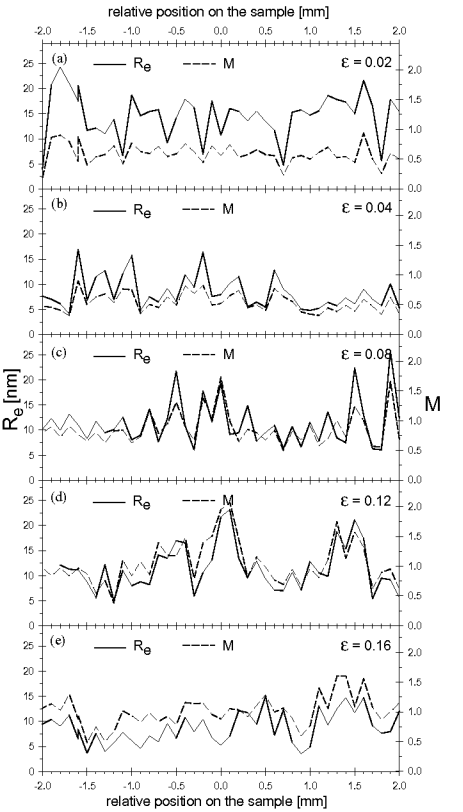

Figure 2. The lateral scans for different deformations ε: The outer cut-off radius and the dislocation arrangement parameter M.

(The relative position on the sample (x-axis) is the normalized initial stepwidth at ε = 0.02.)

This would be in agreement with the observation of Zuev's et al. [5,6] who found propagating strain fronts in metallic single crystals instead of a homogeneous distribution of strain. Although not markedly visible in figure 1, another feature appears to happen: up to a deformation of $\varepsilon = 0.08$ (figure 1(a)–(c)) the fluctuations of ρ are definitely not stationary. But for deformations $\varepsilon \geq 0.08$ (figure 1(c)–(e)) the variation pattern seems to stabilize (especially if one looks at the most pronounced maxima and minima). Please note the different scales of the dislocation density in figure 1(a)-(e). This result can be interpreted in such a way that the dislocations are still mobile after they formed dislocation dipoles, but that they get sessile when the dipoles pile up to dislocation dipole walls.

Figure 3(a) shows the plot of the average values of the dislocation density for each scan versus the deformation. A moderate growing of the dislocation density at small ε ($\rho < 10^{14}m^{-2}$) is followed by a strong increase up to $3.8x10^{14}m^{-2}$ from $\varepsilon = 0.12$ to $\varepsilon = 0.16$. The dislocation arrangement parameter M shown in figure 3(b) exhibits a non-monotonic behaviour. At smallest deformation M decreases slightly, indicating an increased screening of the strain fields by dipole formation. With further deformation M increases as a consequence of a strain intensive dipole arrangement within the cell walls at an increasing number of the latter. For the highest deformation the arrangement parameter M decreases, which can be interpreted as the beginning of the transformation of the cell wall structure to a tilt wall character [11]. In this structure the screening of the dislocation strain field is increased, which allows the dislocation density to increase strongly. It has been shown that this transformation takes place at the same time as the transition of deformation stage III to stage IV, for the case of polycrystals [11] as well as for single crystals [10].

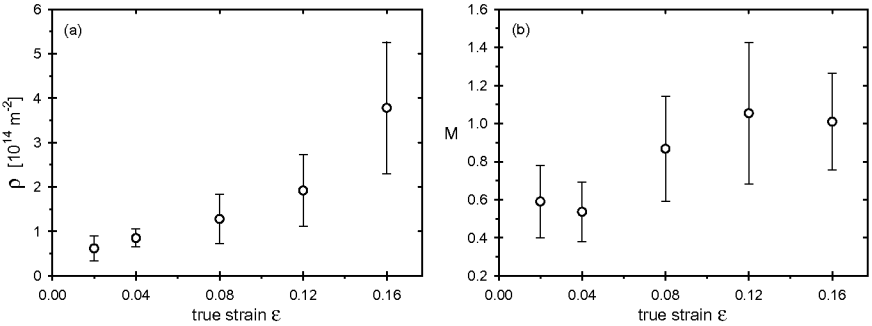

Figure 3. The averaged values from the scans for (a) the dislocation density and (b) the dislocation arrangement parameter M as a function of ε. The error bars indicate the standard deviation.

The lateral distribution of the outer cut-off radius R_e of the dislocation-strain-field and of the dislocation-arrangement-parameter $M = R_e(\rho)^{0.5}$ is shown in figure 2. The plots of both quantities are over all parallel to each other but antiparallel when compared to the graph of the dislocation density. This agrees with the interpretation of R_e as an indicator for the screening of the strain field. At $\varepsilon = 0.16$ the concurrent behaviour of M and R_e starts to disappear: At locations with similar values of R_e the values of the dislocation density differ noticeable as a result of the changing dislocation arrangement. This supports the conclusion of a beginning cell wall transformation when reaching stage IV of deformation.

The results are in agreement with numerous investigations from Transmission Electron Microscopy (TEM) of dislocation microstructure developing during early plastic deformation (see, e.g. [4]). However, neither has it been possible up to now to measure the microstructural evolution during deformation nor to obtain quantitative information on the dislocation density and particularly the strain field of dislocation arrangements as a function of (deformation) time and lateral position.

Summary

The investigation of the spatial distribution of the deformation induced dislocations showed a strongly fluctuating behaviour which seems to get stationary at higher deformation of $\varepsilon = 0.12$ when dislocation dipoles become sessile by forming a cell structure. This agrees with the fact, that the evolution of the strain field screening shows the typical behaviour of the initial formation of a cell wall structure, which later transforms to a less strain-intensive one.

References

1. Diehl J, Mader S, Seeger A., 1955, *Z Metallkde* **46**, 650.
2. Lücke K, Lange H., 1953, *Z Metallkde* **44**, 183.
3. Blewitt TH, Coltman RR, Redman JK., 1955, *Dislocations and mechanical properties of crystals* (New York: Wiley).
4. Kocks, U.F., Mecking, H., 2003, *Progr. Mat.Sci.* **48**, 171.
5. Zuef, L.B., Danilov, V.I., 1999, *Phil. Mag. A* **79**, (1999) 43.
6. Zuef, L.B., V.I. Danilov, V.I., Barannikova, S.A., I.Y. Zykov, I.Y., 2000, *Appl. Phys. A* **71**, 91.
7. Argon, A.S., in *Physical Metallurgy*, 1996 ed. P. Haasen, R.W. Cahn, North Holland, Vol. 3, ch.22, p. 1957
8. Mingler, B., Karnthaler, H.P., Zehetbauer, M., Valiev, R.Z., 2001, *Mater. Sci. Eng. A* **319-321**, 242
9. Amenitsch, H., Bernstorff, S., Kriechbaum, M., Lombardo, D., Mio, H., Rappolt M. and Laggner, P., 1997, *J. Appl. Cryst.* **30**, 872.
10. Schafler, E., Simon, K., Hanak, P., Tichy, G., Bernstorff, S., Ungar, T., Zehetbauer, M., 2005, *Acta. Mater.* **53**, 315.
11. Zehetbauer, M., Kral, R., Schafler, E., Bernstorff, S., Amenitsch, H., Ungar, T., 1999, *Acta. Mater.* **47**, 1053.
12. Wilkens M., 1979, in *Fundamental Aspects of Dislocation Theory*, ed. J. A. Simmons, R. de Wit, R. Bullough, Vol. II. Nat. Bur. Stand. (US) Spec. Publ. No. 317, Washington, DC. USA, p. 1195.
13. Warren, B.E., 1959, *Progr. Metal Phys.* **8**, 147.
14. T. Ungár, Dragomir, I., Revesz, A., Borbely, A., 1999, *J. Appl. Cryst.* **32**, 992.
15. Ribárik, G, Ungár, T. and Gubicza, J., 2001, *J. Appl. Cryst.* **34**, 669.

Acknowledgements. The Austrian (FWF) and the Hungarian (OTKA) Science Funds are acknowledged for support under projects P-17095-N02 (A) and T-046990 & T-043247 (H).

Z. Kristallogr. Suppl. **23** (2006) 111-116

Analysis of polydisperse ball-milled fluorite powders using a full pattern technique

M. Leoni[1,*], G. De Giudici[2], R. Biddau[2], M. D'Incau[1], P. Scardi[1]

[1]University of Trento, Department of Materials Engineering and Industrial Technologies, 38050 via Mesiano 77, Trento, Italy
[2]University of Cagliari, Department of Earth Sciences, 09100 via Trentino 51, Cagliari, Italy
[*]Contact author; e-mail: Matteo.Leoni@unitn.it

Keywords: Whole Powder Pattern Modelling, ball-milling, size distribution, powder dissolution

Abstract. X-ray Powder Diffraction is particularly suited to the analysis of nanocrystalline materials. Both structural and microstructural information can nowadays be obtained simultaneously by full pattern processing techniques.
Among those, Whole Powder Pattern Modelling (WPPM) outperform most traditional Line Profile Analysis (LPA) techniques by giving a direct interpretation of the diffraction pattern in terms of physical microstructural models.
In the present work we illustrate a recent evolution of the WPPM approach, allowing the refinement of a general domain-size distribution not related to any *a priori* fixed analytical profile or size distribution shape. Besides the description of the new algorithm, we show the results of the analysis of ball-milled synthetic fluorite powders.
The new WPPM procedure provides a detailed information on the evolution of the grinding process with time: the decrease and change of shape of the grain size distribution with the milling time is accompanied by a steady increase in defect content. The increase in defects is shown to be a major responsible for the higher reactivity and therefore for the high dissolution rates of ball-milled fluorite powders.

Introduction

The dissolution/precipitation of mineral species is a central issue in the chemistry of Earth surface and therefore a key to a better environmental protection: acid mine drainage, chemical weathering and biomineralisation, just to cite some examples [1-4], are controlled by those reactions. Several factors affect the dissolution reactions of a mineral species. Among those, surface reactivity and defect content are known to play a key role. As shown in [5], for instance, surface reactivity (and therefore dissolution rate) is enhanced by the presence of

surface heterogeneities (at the atomic level) and surface outcrops of (linear or planar) lattice defects. The extent of the exposed surface, thus the size of the mineral particles, is also a controlling factor in a dissolution reaction: as could be figured-out, the smaller the particles, the higher the specific area, the higher the reactivity (see e.g. [1,2,6,7]). It can be inferred that a highly defective, nanometer-sized material would exhibit an unusually high reactivity and a tendency to dissolution/restructuring with respect to a perfect and coarse-grained counterpart. To prove this experimentally on a test material, techniques are needed for particles comminution, for creating lattice defect and for the quantitative evaluation of both of the previous. High energy ball-milling has already been proven as a valid tool for the production of highly defective metallic and ceramic nanopowders [8,9], whereas Whole Powder Pattern Modelling (WPPM) [10,11] can provide a quantitative microstructural insight of the milled powders. Among the possible test materials, fluorite (CaF_2) was chosen because it couples a simple chemistry with a highly symmetric structure and because independent dissolution studies are available in the literature [12].
In this work, the relationships between domain size distribution, defect content and dissolution rate of fluorite are analysed and interpreted.

Experimental

Synthetic fluorite powder samples (Carlo Erba Analyticals RPE, purity 99%, batch 433587) were milled in a Fritsch "Pulverisette 4" planetary mill for increasing times (1 to 128 h, following a geometric progression) at a rotation speed of the main disk Ω = 200rpm and a disk/planet speed ratio ω = -1. In particular, about 2.10±0.01 g of fluorite, 4 % wt. of ethanol and 12 balls (powder/balls ratio r = 1/40) were milled together in two counter-rotating vials (46ml nominal volume) sealed in air.
An Environmental Scanning Electron Microscope (ESEM, Philips XL30) was used for the morphological analysis of the powders: a partial pressure of 0.6 torr was selected, allowing observation of the powders at 20kV without any need for metallization.
Room-temperature dissolution (22° C) was studied in custom polyethylene batch reactors under vigorous and constant stirring: 0.1 g of fluorite and 1 liter of deionised water at pH = 2.0 were used for each run. The acid solution was prepared by adding hydrochloric acid to MilliQ deionised water (resistivity 18 $M\Omega\ cm^{-1}$). The solutions were periodically sampled and analyzed for dissolved calcium by Inductively Coupled Plasma Optical Emission Spectroscopy (ICP-OES, ARL 3520).
Diffraction data were collected at λ = 0.100336 nm on station 2.3 at the Daresbury Laboratory Synchrotron Radiation Source (SRS) in flat-plate geometry: both the patterns of fluorite and of the SRM 660a line-profile standard [13] were collected under the same experimental conditions. The non-destructive microstructural analysis was conducted following the WPPM approach implemented in the PM2K program [14].

Results

ESEM analysis of milled powders
From the ESEM micrographs (an example is provided in figure 1), it is clear how ball milling has a marked influence on the fluorite powder morphology. The starting material is com-

posed of well separated micrometer-sized cubical particles (figure 1a): those particles tend to aggregate during milling, leading initially to a marked multimodal distribution (small and large particles coexists) and subsequently, after about 4 h of milling, to the disappearance of the cubical features (flat faces and sharp edges, figure 1b). The observed agglomeration is possibly due to the electrostatic particle-particle attraction on the micrometer scale.

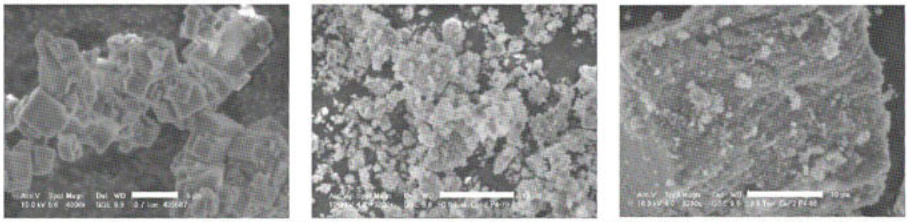

Figure 1. ESEM morphology of the fluorite samples: (a) as received (scale bar 5μm), (b) milled 8 h (scale bar 10μm), (c) milled 128 h (scale bar 10μm).

Milling for more than 32 h causes those coarse aggregates to apparently recrystallise, as they show regular shapes and extended flat facets. However, small particles and debris produced by the severe deformation of the coarse recrystallised aggregates, are still present (figure 1c).

Dissolution of the powders

Figure 2 shows the trend of calcium concentration in solution measured by ICP-OES as a function of time.

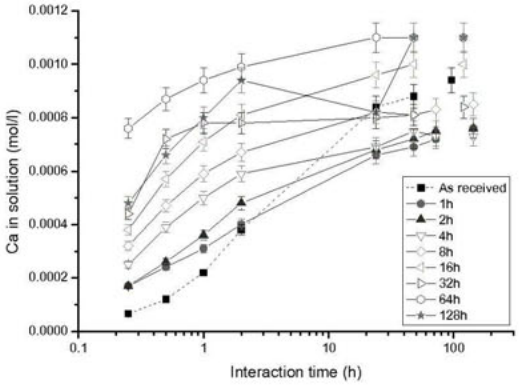

Figure 2. Calcium in solution (mol/l) as a function of interaction time.

For a given dissolution time, the quantity of dissolved calcium has a significant dependence on milling time. The maximum difference among the specimens is by a factor 5, and is observed after 15 min of interaction. Such a difference decreases with experimental time and, after two days, is about a factor 2. This is due to a progressive increase in the concentration of the reaction products in the interacting solution [15], that implies a progressive approach

to a near-equilibrium condition [3]. Dissolution rates can be obtained by dividing the measured calcium concentration by the time elapsed from the beginning of the experiment. The calculated values reflect the same differences observed for calcium concentration. Indeed, dissolution rates ranges from 1.13×10^{-7} to 8.4×10^{-7} mol l^{-1} s^{-1} after 15 min, and between 3.9×10^{-9} and 6.4×10^{-9} mol l^{-1} s^{-1} after 48 hours. As optical inspection and some ESEM images (not shown in this paper) clearly indicate, the fluorite grains suspended in the solution tend to aggregate changing thus the total mineral surface exposed to the interaction with the solution. As a consequence, dissolution rates normalised by mineral surface area are expected to give slightly erroneous results as they would be calculated with an intrinsically low accuracy.

Microstructural analysis using WPPM and the general size-distribution approach

A diffraction pattern can be imagined as the sum of a background and a set of diffraction peaks, each of them modelled independently on the basis of a physical description both of the instrument (in terms of optical components and diffraction geometry) and of the material under study (in terms of crystalline structure and microstructure). Folded instrumental and material contributions lead to the observed peak shape, whereas crystalline structure is mainly related to the (relative) integrated intensity of the peaks. Line broadening sources (i.e. certain microstructures) leave a (more ore less) distinctive fingerprint on peak profiles: by synthesising a pattern based on a physical modelling of the expected microstructure and refining the physical parameters describing the model, this fingerprint can be detected and valuable microstructural information obtained on the material under study. This is the principle on which Whole Powder Pattern Modelling [10-12] is based. Each profile is built from its Fourier Transform (FT): the FT contribution to a profile, related to a vast set of defects, can be found in the literature (see e.g. [10-12] and references therein). In the present study:

- instrumental contribution: profiles measured on the SRM 660a line profile standard are symmetrical and are therefore modelled using pseudo-Voigt functions as proposed in [10,11]. This is one of the less-biased approaches to the determination of the instrumental contribution to the profile breadth and shape;
- defects contribution: dislocations and stacking faults can be thought as the major sources of line-profile broadening in fluorite. Suitable models can be found in the cited literature. In the proposed case, faulting effects are faint and fall below the detection limit of the technique.
- finite domain-size contribution: particles (see ESEM data above) are more or less cubical and a complex size distribution is present. However, coherently diffracting domains do not necessarily have a cubical shape. As cubical and spherical shapes lead in this case to close results, the less biased spherical shape is chosen. For the domain-size distribution, the approach proposed in [12] will be used and a finite size-distribution histogram will be refined for each specimen.

Results of the modelling are shown in figure 3: in particular, figure 3a shows raw data, modelled pattern and residual (difference between them) for the powder milled 128 h, whereas figures 3b-d shows the trend of dislocation density (ρ_{disl}), average domain size $\langle D \rangle$ and variance of the corresponding distribution ($\langle D^2 \rangle - \langle D \rangle^2$) for all specimens as a function of milling time (log scale). Additionally, table 1 summarises the microstructural WPPM results for the whole set of milled samples.

Correlations can be found between the data of figure 2 and those of figure 3: in particular the increased activity of the powders corresponds to an increased quantity of defects and a decreased domain size. However, in [15] it was shown that domain size has a significant effect on the (apparent) solubility constant of milled fluorite only when it is very small (<*D*> <5 nm). As this is valid also for this study, the observed increase in surface reactivity is mainly due to the increase in dislocation density (cf. figures 3b and 3c). This seems to be supported also by the increase in the strain energy U_{strain} reported in table 1 and calculated for the dislocation density obtained through WPPM (cf. also [15]. Calculation involved the following constants for fluorite: shear modulus μ = 33.77 GPa, Poisson ratio ν = 0.26, density ρ = 3.18 g/cm^3, molecular weight MW = 78.03 g/mol).

Table 1. Average domain size (<D>), dislocation density (ρ_{disl}), effective outer cut-off radius (R_e), edge character (f) and strain energy U_{strain} (dependent on R_e and ρ_{disl}) obtained from WPPM results.

Milling time (h)	1	2	4	8	16	32	64	128
<*D*> (nm)	87(27)	24(2)	28(1)	20(1)	16.9(8)	19(2)	17.3(8)	12.9(1)
ρ_{disl} (10^{15} m^{-2})	2.1(3)	3.8(3)	4.6(6)	5.8(2)	7.0(20)	7.7(31)	9.6(16)	11.9(20)
R_e (nm)	3(1)	4.3(1)	7.5(1)	6.4(1)	4.6(1)	7.2(1)	6.6(1)	3.4(1)
f	0.47(3)	0.65(2)	0.9(1)	0.7(1)	0.96(6)	0.87(2)	0.67(9)	0.67(2)
U_{strain} (J/mol)	25	65	117	128	136	190	215	170

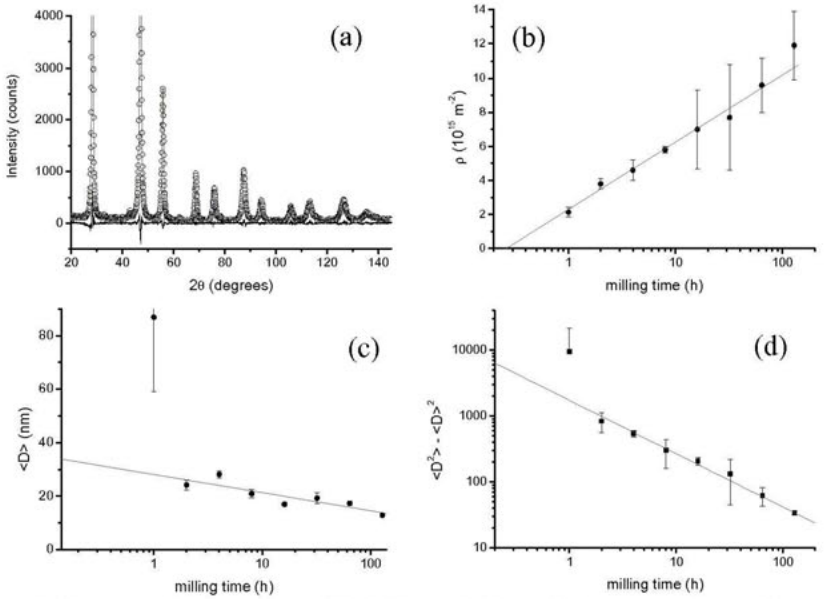

Figure 3. (a) Pattern of the powder milled for 128h. In (b)-(d), trend of dislocation density (ρ), mean domain size (<D>) and variance of domain size distribution (<D^2>-<D>^{2}) as a function of milling time (log scale), respectively. A linear fit of the data is proposed as guide for the eye.

Concluding remarks

The mechanical action of ball milling enhances the reactivity of fluorite powders: the major causes are to be sought in the milling process itself that increases the energy of the material both by reducing the size of the particles (storage of surface energy) and by increasing their defect content (storage of elastic energy). The evolution of the relative weight of the two effects can be studied by analysing the corresponding diffraction patterns using Whole Powder Pattern Modelling.

References

1. Labrenz M., Druschel G.K., Thomsen-Ebert T., Gilbert B., Welch S.A., Kemner K.M., Logan G.A., Summons R.E., De Stasio G., Bond P.L., Lai. B, Kelly S.D. & Banfield J.F, 2000, *Science*, **290**, 1744-1747.
2. Lower S.K., Hochella M.F & Beveridge T.J., 2001, *Science*, **292**, 1360-1363.
3. Lasaga, A.C., 1998, *Kinetic theory in Earth sciences* (Princeton: University Press).
4. Banfield J.F. & Zhang H., 2001, in *Nanoparticles and the environment, Reviews in Mineralogy and Geochemistry 44 MSA*, edited by J.F. Banfield & A. Natrovsky.
5. Schott J., Brantley S., Crerar D., Guy M. & Willaime C., 1989, *Geochimica et Cosmochimica Acta*, **53**, 373-382.
6. Hannon J.B., Tersoff J. & Tromp R.M., 2002, *Science*, **295**, 299-301.
7. Campbell C.T., Parker S.C. & Starr D.E., 2002, *Science*, **298**, 811-814.
8. Kano J. & Saito F., 1998, *Powder Technology*, **98**, 166-170.
9. Salimon A.I., Korsunsky A.M. & Ivanov A.N., 1999, *Mat. Sci. Eng.* **A271**, 196-205.
10. Scardi P. & Leoni M., 2002, *Acta Cryst.*, **A58**, 190-200.
11. Scardi P. & Leoni M., 2004, in *Diffraction Analysis of the Microstructure of Materials*, edited by E.J. Mittemeijer & P. Scardi (Berlin: Springer), pp. 125-145.
12. Leoni M. & Scardi P., 2004, *J. Appl. Cryst.*, **37**, 629-634.
13. Cline J. P., Deslattes R. D., Staudenmann J.-L., Kessler E. G., Hudson L. T., Henins A. & Cheary R. W., 2000, Certificate SRM660a, NIST, Gaithersburg, MD, USA.
14. Leoni M., Confente T. & Scardi P., this volume.
15. De Giudici G., Biddau R., D'Incau M., Leoni M. & Scardi P., 2005, *Geochimica et Cosmochimica Acta*, 69 [16], 4073-4083.

Acknowledgements. This work was supported by the basic research funds of the Italian Ministry of University and Research, PRIN 2003-2004 project "Mechanisms of surface interactions in mineral phases: kinetics of dissolution, of crystal growth and their modelling". The Council for the Central Laboratory of the Research Councils and the European Union under the TMR project are acknowledged for synchrotron beam time provision. Dr Steve Thompson is deeply acknowledged for the precious experimental support on SRS station 2.3.

Z. Kristallogr. Suppl. **23** (2006) 117-122

Anisotropic microstrain broadening due to compositional inhomogeneities and its parametrisation

A. Leineweber*, E. J. Mittemeijer

Max Planck Institute for Metals Research, Heisenbergstraße 3, D-70569 Stuttgart, Germany
*Contact author; e-mail: a.leineweber@mf.mpg.de

Keywords: line broadening, microstrain, iron nitrides, composition variations

Abstract. The anisotropic and asymmetric microstrain-like line broadening of hexagonal ε-FeN_y (y = 0.407) was analysed. It is ascribed to composition fluctuations (local deviations of y) leading to lattice-parameter fluctuations as origin of the line broadening because the extent of the observed anisotropy agrees with values predicted from the concentration dependence of the lattice parameters of ε-FeN_y. Different approaches to parametrise the anisotropy of line broadening caused by composition fluctuation for different crystal systems and their advantages and disadvantages are discussed.

Introduction

Diffraction-line broadening due to the presence of microstrains is considerably simplified if the strain (regarded here as a deviation of the lattice parameters from a *reference* set of lattice parameters) is constant in each coherently diffracting crystallite [1]. In that case the diffraction angle of the reflection *hkl* from a crystallite is shifted to the value $2\theta_{hkl} = 2\theta_{0,hkl} + \Delta 2\theta_{hkl}$ with

$$\Delta 2\theta_{hkl} = -2e_{hkl} \tan \theta_{0,hkl} \qquad (1)$$

where $2\theta_{0,hkl}$ is the diffraction angle pertaining to the d-spacing $d_{0,hkl}$ calculated from the reference lattice parameters and e_{hkl} is the strain in the crystallite along the direction of the diffraction vector with $e_{hkl} = (d_{hkl} - d_{0,hkl})/d_{0,hkl} << 1$. The microstrain contribution to the overall diffraction-line profile (called f, to be convoluted with the other contributions like instrumental broadening, size, stacking faults, etc.) is then the superposition of all subprofiles from all crystallites according to the probability density function (*pdf*) $p_{e_{hkl}}(e_{hkl})$.

The analysis given here supposes that e_{hkl} is solely a function of a single, scalar variable y (for the detailed treatment, see Ref. [2]) which can vary from crystallite to crystallite and which is related with a *reference* value y_0 (for example, but not necessarily, the arithmetic average) pertaining to the unstrained crystal by $y = y_0 + \xi$. Then the strain of a crystal is

$$e_{hkl}(\xi) = \left(d_{hkl}(\xi) - d_{0,hkl}\right)/d_{0,hkl} \approx \left(d_{0,hkl}^{-2} - d_{hkl}^{-2}(\xi)\right)/\left(2d_{0,hkl}^{-2}\right), \qquad (2)$$

with

$$d_{hkl}^{-2}(\xi)=\mathbf{a}^*\cdot\mathbf{a}^*(\xi)h^2+\mathbf{b}^*\cdot\mathbf{b}^*(\xi)k^2+\mathbf{c}^*\cdot\mathbf{c}^*(\xi)l^2+2\mathbf{b}^*\cdot\mathbf{c}^*(\xi)kl+2\mathbf{a}^*\cdot\mathbf{c}^*(\xi)hl+2\mathbf{a}^*\cdot\mathbf{b}^*(\xi)hk$$
$$=\alpha_{200}(\xi)h^2+\alpha_{020}(\xi)k^2+\alpha_{002}(\xi)l^2+\alpha_{011}(\xi)kl+\alpha_{101}(\xi)hl+\alpha_{110}(\xi)hk$$
$$=\sum_{H+K+L=2}\alpha_{HKL}(\xi)\,h^H k^K l^L\,. \qquad (3)$$

If for each value of ξ the unit cell parameters obey the crystal system's symmetry restrictions as for the *reference* state (which is expected, if ξ, y quantify composition, temperature, etc., and no phase transition occurs over the relevant range of ξ) the functions $\alpha_{HKL}(\xi)$ have to obey these restrictions as well [2]. A first order Taylor-series expansion of $\alpha_{HKL}(\xi)$ gives together with Eq. (2):

$$e_{hkl}(\xi)=-\frac{1}{2}d_{0,hkl}^2\left(\sum_{H+K+L=2}\left(\frac{d\alpha_{HKL}(\xi)}{d\xi}\right)_{\xi=0}h^H k^K l^L\right)\xi\,. \qquad (4)$$

Thus the shape of the line profile contribution $f(\Delta 2\theta_{hkl})$ is given by the *pdf* $p_\xi(\xi)$:

$$p_{e_{hkl}}(e_{hkl})\,de_{hkl}=p_\xi(\xi)d\xi \qquad (5)$$

with

$$de_{hkl}=\left|-\frac{1}{2}d_{0,hkl}^2\sum_{H+K+L=2}\left(\frac{d\alpha_{HKL}(\xi)}{d\xi}\right)_{\xi=0}h^H k^K l^L\right|d\xi\,. \qquad (6)$$

If $p_\xi(\xi)$ is asymmetric, the shapes of $p_{e_{hkl}}(e_{hkl})$ and thus of $f(\Delta 2\theta_{hkl})$ are reflected with respect to $e_{hkl}=0$ when e_{hkl} changes its sign. Otherwise, the shape of $f(\Delta 2\theta_{hkl})$ is the same for each reflection *hkl*, and only changes its width with the direction of the diffraction vector, where the width (integral breadth, FWHM, (variance)$^{1/2}$) is related with the corresponding width of the *pdf* $p_\xi(\xi)$, $\delta\xi$ by

$$\delta(\Delta 2\theta_{hkl})=2\tan\theta_{0,hkl}\times\delta(e_{hkl})$$
$$\delta(\Delta 2\theta_{hkl})=\tan\theta_{0,hkl}\,d_{0,hkl}^2\left|\sum_{H+K+L=2}\left(\frac{d\alpha_{HKL}(\xi)}{d\xi}\right)_{\xi=0}h^H k^K l^L\right|\times\delta\xi\,. \qquad (7)$$

If the derivatives $(d\alpha_{HKL}/d\xi)_{\xi=0}$ are unknown, one may substitute $(d\alpha_{HKL}/d\xi)_{\xi=0}\times\delta\xi = D_{HKL}$, leading to

$$\delta(\Delta 2\theta_{hkl})=\tan\theta_{0,hkl}\,d_{0,hkl}^2\left|\sum_{H+K+L=2}D_{HKL}h^H k^K l^L\right|, \qquad (8)$$

and use D_{HKL} as fitting parameters.

The microstrain-like diffraction-line broadening exhibited by a hexagonal ε-FeN$_y$ powder sample with average y of 0.433 was investigated. The composition fluctuationes are largely symmetrical and Gaussian and characteristed by (variance(y))$^{1/2}$ = (variance(ξ))$^{1/2}$= 0.008 [2]. The present paper reports the analysis of a new model case for anisotropic diffraction-line broadening due to composition variations where an *asymmetric* composition distribution is observed leading to *asymmetric* microstrain-like broadening. Furthermore, the handiness of different choices of fitting parameters to describe the anisotropy is discussed.

Experimental and data evaluation methods

X-ray diffraction measurements

An ε-$FeN_{0.407}$ ($Fe_3N_{1.22}$, *average* composition from chemical analysis) powder as used in Ref. [3,4] and a LaB_6 powder (NIST standard reference material 660a) were separately suspended in iso-propanol and sedimented on a (510) cut Si crystal plate (wafer) using a supporting brass ring during evaporation of the liquid. By this method laterally homogeneous thin powder layers were obtained. Diffraction analysis of these two specimens was performed employing a powder diffractometer Philips X'Pert MPD equipped with a graphite monochromator in the diffracted beam, applying CoKα radiation and the same measurement conditions for both specimens. The diffraction patterns were recorded in the range $40° < 2\theta < 110°$.

Diffraction-profile fitting

Rietveld-like refinements without atomic structure model (Pawley fits) were performed using the program TOPAS [5]. The instrumental profile was determined on the basis of the LaB_6 data employing the fundamental parameters approach and allowing for additional refinement of certain profile components [6]. Fixing the parameters of the instrumental profile, the diffraction data of ε-$FeN_{0.407}$ were fitted considering only the subcell pertaining to the hcp type arrangement of Fe atoms to generate the reflection positions. Anisotropic physical diffraction-line broadening was allowed for by convoluting the instrumental profile with pseudo-Voigt functions:

$$f_{hkl}(\Delta 2\theta_{hkl}) = \frac{(1-\eta)}{B_{0,hkl}}\sqrt{\frac{\ln 16}{\pi}}\exp\left(-\frac{\ln 16(\Delta 2\theta_{hkl})^2}{B_{hkl}^2}\right) + \frac{2\eta}{\pi B_{0,hkl}\left(4(\Delta 2\theta_{hkl})^2/B_{hkl}^2+1\right)} \qquad (9)$$

with η being a pseudo-Voigt mixing parameter, and $B_{0,hkl}$ being the full width at half maximum (which is taken here as the measure for the reflection width $\delta(\Delta 2\theta_{hkl})$) expressed using Eq. (8), taking $D_{200} = D_{020} = D_{110}$, $D_{101}=D_{011} = 0$ in accordance with the hexagonal crystal system that holds for ε-$FeN_{0.407}$ (space group $P312$ [3]),

$$B_{0,hkl} = d_{0,hkl}^2 \tan\theta_{0,hkl}\left|D_{200}\left(h^2+hk+k^2\right)+D_{002}l^2\right| \qquad (10)$$

In order to allow for reflection asymmetry a 'split pseudo Voigt' description with B_{hkl} in Eq. (10) as $B_{hkl} = B_{0,hkl}(1+as)$ for $\Delta 2\theta_{hkl} < 0$ and $B_{hkl} = B_{0,hkl}(1-as)$ for $\Delta 2\theta_{hkl} > 0$, and $-1 < as < 1$. For symmetrical pseudo-Voigt functions $as = 0$ holds.

Results and Discussion

X-ray diffraction measurements

Comparing the reflections of ε-$FeN_{0.407}$ with the instrumental profile function indicates the presence of considerable anisotropic microstrain broadening similar to that observed for $FeN_{0.433}$ [2]. Allowance for symmetric microstrain broadening according to Eqs (9-10) leads to reasonable fits to the diffraction data. However, the fits are significantly improved if allowance is made for asymmetry in Eq. (9). Then the final results are $D_{200} = 7.53(9)\times10^{-4}$ Å^{-2}, $D_{002} = 1.51(3)\times10^{-4}$ Å^{-2}, $\eta = 0.017(5)$ and $as = 0.66(3)$ (see Figure 1). According to Eqs (7-8) the fitting parameters can be associated with the composition dependence of the lattice para-

meters and the full width at half maximum of the *pdf* of composition, B_ξ, i.e. $D_{HKL} = (d\alpha_{HKL}/d\xi)_{\xi=0} \times B_\xi$. From $3^{1/2}a$ = 4.4652 Å + 0.6851 Åy and c = 4.2433 Å + 0.3903 Åy as lattice parameters of (slowly cooled) ε-FeN$_y$ [4] one obtains quite similar values for B_ξ from both D_{200} and D_{002}, B_ξ = 0.0147(2) and B_ξ = 0.0165(4).

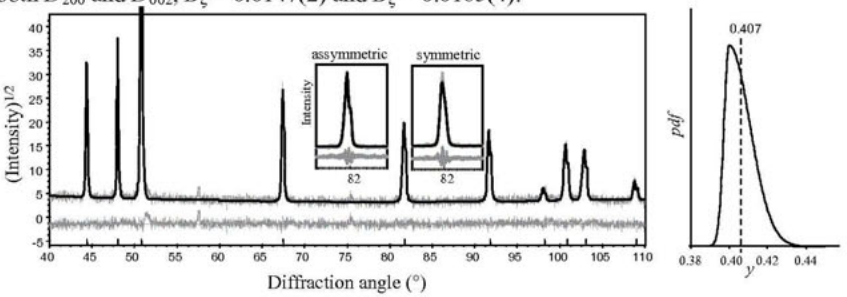

Figure 1 Left: Fit to the powder diffraction data of hexagonal ε-FeN$_{0.407}$ considering an asymmetric and anisotropic diffraction-line broadening according to Eq. (10-11). The insets show direct comparisons between consideration and non-consideration of asymmetry of p(ξ). The reflections at 57° and 76° are superstructure reflections due to the N ordering not considered here. The probability density function for the composition y (right) as calculated from the line broadening has its maximum at y = 0.400, which is different from the average y = 0.407 due to the asymmetry of the distribution.

The asymmetry of the probability density function is as = –0.66(3) (i.e. the negative value of that for the line broadening) due to $(d\alpha_{HKL}/d\xi) < 0$ (see Eqs (1) and (4)). Since the *pdf* is asymmetric, its *maximum* and *average* do not conincide. The maximum position is obtained as y_0 = 0.400 from the asymmetry and B_ξ assuming $\eta = 0$.

Parametrisation opportunities

The formulation of the anisotropy of $f(\Delta 2\theta_{hkl})$ or of $p_{e_{hkl}}(e_{hkl})$ can straightforwardly be incorporated in Rietveld-like refinements, as shown above. Considering in the following the width $\delta(e_{hkl})$,

$$\delta(e_{hkl}) = 1/2 \times d_{0,hkl}^2 \left| \sum_{H+K+L=2} D_{HKL} h^H k^K l^L \right|, \qquad (11)$$

and neglecting possible effects of asymmetry (see below Eq. (6)), one may check whether the six fitting parameters D_{HKL} (for the most general triclinic case) are really the best choice for refinement and for their possible afterwards interpretation. First of all, the parameters describing the direction dependence of the microstrain have a dimension (length^{-2}), and their magnitude depends on the numerical values of the lattice parameters. If one would consider the superstructure unit cell due to N ordering, $a' = 3^{1/2}a_{hcp}$, $c' = c_{hcp}$ for FeN$_{0.407}$, the magnitude of the fitting parameters would change. This can be overcome [2] by factoring out α_{HKL} in Eqs (7-8) i.e. $d\alpha_{HKL} = \alpha_{HKL} d\ln\alpha_{HKL}$, leading to

$$D_{HKL} = (d\alpha_{HKL}/d\xi)_{\xi=0}\, \delta\xi = \alpha_{HKL} (d \ln \alpha_{HKL}/d\xi)_{\xi=0} = \alpha_{HKL}\gamma_{HKL} \qquad (12)$$

or

$$\delta(e_{hkl}) = \frac{1}{2} d_{0,hkl}^2 \left| \sum_{H+K+L=2} \alpha_{HKL} \gamma_{HKL} h^H k^K l^L \right| . \quad (13)$$

γ_{HKL} are dimensionless quantities with the same symmetry restrictions as for D_{HKL}, and do not change in the above-mentioned case of lattice basis transformation. Isotropic line broadening occurs if all γ_{HKL} are equal. Problems arise, however, when any α_{HKL} with HKL = 110, 101 and 011 is accidentally zero, which can occur for rhombohedral, monoclinic or triclinic lattices if any of the free lattice angles is 'accidentally' 90° (see Eq. (3)). In that case Eq. (12) must not be applied, and γ_{HKL} would approach infinity. This can be easily seen for the monoclinic case ($\gamma_{011} = \gamma_{110} = \alpha_{011} = \alpha_{110} = 0$ due to symmetry):

$$\delta(e_{hkl}) = \frac{1}{2} d_{0,hkl}^2 \left| \alpha_{200} \gamma_{200} h^2 + \alpha_{020} \gamma_{020} k^2 + \alpha_{002} \gamma_{002} l^2 + \alpha_{101} \gamma_{101} hl \right| . \quad (14)$$

This formulation fails for $\beta = 90°$, because then $\alpha_{101} = 2a^*c^*\cos\beta^* = 0$. By this any symmetry-allowed information from D_{101} is lost (cf. Eq. (12)).

Another alternative to Eq. (11) avoiding the described complication of Eq. (12-13) is to formulate strain and diffraction vector with respect to a cartesian basis, e.g. $\mathbf{e}_1 = \mathbf{a}/a$, $\mathbf{e}_2 = \mathbf{e}_3 \times \mathbf{e}_1$, $\mathbf{e}_3 = \mathbf{c}^*/c^*$. Then, for the triclinic case the diffraction vector becomes

$$\mathbf{g} = (g_1 \quad g_2 \quad g_3)^T = \left(\frac{h}{a} \quad -\frac{h\cos\gamma}{a\sin\gamma} + \frac{k}{b\sin\gamma} \quad ha^*\cos\beta^* + kb^*\cos\alpha^* + lc^* \right)^T , \quad (15)$$

and $|\mathbf{g}| = g = 1/d_{0,hkl}$.

The strain along the diffraction vector is

$$e_{hkl} = d_{0,hkl}^2 g_j e_{ij} g_i . \quad (16)$$

Applying simple rules of error propagation and taking into account that the strain varies only with ξ one obtains from Eqs (15-16)

$$\delta(e_{hkl}) = d_{0,hkl}^2 \left| \frac{d}{d\xi} \left[g_1^2 e_{11} + 2g_1 g_2 e_{12} + 2g_1 g_3 e_{13} + g_2^2 e_{22} + 2g_2 g_3 e_{23} + g_3^2 e_{33} \right]_{\xi=0} \times \delta\xi \right| , \quad (17)$$

and, after substitution, $p_{ij} = (de_{ij}/d\xi)_{\xi=0} \times \delta\xi$, it follows

$$\delta(e_{hkl}) = d_{0,hkl}^2 \left| g_1^2 p_{11} + 2g_1 g_2 p_{12} + 2g_1 g_3 p_{13} + g_2^2 p_{22} + 2g_2 g_3 p_{23} + g_3^2 p_{33} \right| . \quad (18)$$

By inserting g_1, g_2 and g_3 and considering the symmetry restrictions for the crystal system, it is possible to determine the symmetry rules for p_{ij} which are basically those of symmetrical second rank crystal physical property tensors [7] relating a scalar with a second rank tensor (e.g. anisotropic thermal expansion) or a vector with a vector (e.g. anisotropic diffusion coefficient) giving in particular $p_{11} = p_{22}$; $p_{12} = p_{13} = p_{23} = 0$ for the hexagonal case dealt with in the previous sections. Furthermore, for all crystal systems the case of isotropic line broadening is given by $p_{11} = p_{22} = p_{33} = p$ and $p_{12} = p_{13} = p_{23} = 0$ leading to

$$\delta(e_{hkl}) = d_{0,hkl}^2 \left| g_1^2 + g_2^2 + g_3^2 \right| p = p . \quad (19)$$

Hence the case of isotropic line broadening is as readily detected from analysis of the fitted p_{ij} parameters as from γ_{HKL} parameters, but the problem described above for the formulation according to Eq. (13) does not occur for Eq. (18). This can be shown for the monoclinic case, leading by insertion of g_1, g_2 and g_3 into Eq. (18) and with the symmetry restriction of $p_{12} = p_{23} = 0$ to

$$\delta(e_{hkl}) = d_{0,hkl}^2 \left| \begin{array}{l} \dfrac{h^2}{a^2}\left(p_{11} - \dfrac{2\cos\beta}{\sin\beta} p_{13} + \dfrac{\cos^2\beta}{\sin^2\beta} p_{33} \right) \\ + \dfrac{hl}{ac}\left(\dfrac{2}{\sin\beta} p_{13} - \dfrac{2\cos\beta}{\sin^2\beta} p_{33} \right) + \dfrac{k^2}{b^2} p_{22} + \dfrac{l^2}{c^2 \sin^2\beta} p_{33} \end{array} \right| . \quad (20)$$

It follows that the case where the monoclinic angle approaches $\beta = 90°$ can unproblematically be dealt with:

$$\delta(e_{hkl}) = d_{0,hkl}^2 \left| \frac{h^2}{a^2} p_{11} + 2\frac{hl}{ac} p_{13} + \frac{k^2}{b^2} p_{22} + \frac{l^2}{c^2} p_{33} \right| . \quad (21)$$

Conclusion

The anisotropic powder-diffraction line broadening due to small fluctuations of composition around a reference composition in priciple can be straightforwardly analysed in the course of a Rietveld-like analysis provided that the probability density function for the composition is sufficiently simple, e.g. a split pseudo-Voigt function as employed here. The symmetry restrictions for such an anisotropy can be derived [2]. In the present case the significantly *asymmetric* line broadening of a hexagonal iron nitride sample of the average composition $FeN_{0.407}$ was successfully analysed. It was furthermore shown that a Cartesian description of the anisotropic compositional strain is advantegous for the definition of the parameters describing the anisotropy, because in that case isotropic microstrain broadening can straightforwardly be detected and analysed for all possible types of symmetry.

References

1. Stokes, A.R. & Wilson, A.J.C., 1944, *Proc. Phys. Soc. London*, **56**, 174.
2. Leineweber, A. & Mittemeijer, E.J., 2004, *J. Appl. Crystallogr.* **37**, 123.
3. Leineweber, A., Jacobs, H., Hüning, F., Lueken, H. & Kockelmann, W., 2001, *J. Alloys Compd.*, **316**, 21.
4. Liapina, T., Leineweber, A., Mittemeijer, E.J. & Kockelmann, W., 2004, *Acta Mater.*, **52**, 173.
5. *Topas, General Profile and Structure Analysis Software for Powder Diffraction Data*, V2.0 (Bruker AXS GmbH, Karlsruhe, Germany).
6. Cheary, R.W. & Coelho, A., 1992, *J. Appl. Crystallogr.*, **25**, 109.
7. Nye, J.F., 1976, *Physical Properties of Crystals* (Clarendon Press, Oxford).

Z. Kristallogr. Suppl. **23** (2006) 123-128

X-ray diffraction from epitaxial thin films: an analytical expression of the line profiles accounting for microstructure

A. Boulle*, R. Guinebretière, A. Dauger

Science des Procédés Céramiques et de Traitements de Surface – CNRS UMR 6638, ENSCI, 47 à 73 avenue Albert Thomas 87065 Limoges Cedex
*Contact author; e-mail: a_boulle@ensci.fr

Keywords: X-ray diffraction, thin films, microstructure, roughness, thickness fluctuations

Abstract. An analytical interference function describing the X-ray diffraction line profile of epitaxial thin films is derived. This interference function describes the intensity distribution in a direction perpendicular to the film surface and accounts for the combined effects of different type of defects: interface and surface roughness and their state of correlation, cumulative and non cumulative lattice disorder. The derived interference function is analytical which allows easy implementation and can hence be used for routine analysis of the microstructure of thin films.

Introduction

During the three past decades X-ray diffraction (XRD) has become essential for the non-destructive characterization of epitaxial thin film structures. There are two theories that describe the scattering from thin crystals. The rigorous dynamical theory [1] applies mainly to perfect, or nearly perfect crystals. Takagi [2] and Taupin [3] extended this theory to the case of non-ideal crystals containing a slowly varying strain profile. The numerical or iterative resolution (within the lamellar approximation) [4, 5] of the Takagi-Taupin equations enables one to recover depth-resolved information concerning strain and/or composition in the films. Real structure effects, *e.g.* random lattice spacing fluctuations, remain very difficult to incorporate into dynamical theory [6]. Besides, the more approximate kinematical scattering theory has attracted much attention as it more easily deals with structural defects commonly encountered in real crystals.

The description of the intensity distribution diffracted by a thin crystal of thickness t actually goes back to Laue [7] who first derived the interference function known as the Laue function: $\sin^2 Q(t/2)/\sin^2 Q(d/2)$, where Q is the length of the scattering vector and d the interplanar spacing of the diffracting planes. In practice however, this relation doesn't apply to most samples as the presence of defects strongly alters the shape of the intensity distribution, principally by suppressing the interference fringes. Several authors modified this expression in order to account for the effect of defects: thickness fluctuations [8, 9],

roughness [10] and lattice disorder [9,11]. The combined effects of different defects are in general handled using a numerical integration of the expression of the intensity distribution.
In this communication we derive a generalized interference function able to describe analytically the XRD profile of a single epitaxial thin film with a microstructure made of different type of defects: film thickness fluctuations, roughness, cumulative and non-cumulative random lattice spacing fluctuations. We emphasize that the concepts used in the present paper are not new when considered separately (see for instance refs [8-11]). However, to our knowledge we present here the first derivation of an analytical expression where all these defects are taken into account simultaneously. Each of these defects affect the XRD profiles in a distinct fashion which enables one to recover these parameters by a direct quantitative comparison of the generalized interference function with experimental data. This task is greatly simplified by the analytical character of the proposed function which allows a straightforward implementation in any existing computing program (or even any spreadsheet software) and makes it attractive for routine use. However, when more complicated structures are considered (multilayers for instance) then the intensity distribution taking into account microstructural defects still has to be numerically evaluated (this can be for instance performed using the freely available program SUPREX [9]).
The paper is organized as follows. In the first section we focus on the effects of a non-ideal morphology (thickness fluctuation and roughness). In the second section, we consider the effect of additional lattice spacing fluctuations.

Effects of a non-ideal morphology

Framework and assumptions

The derivation is carried out within the framework of kinematical scattering theory. Within this theory, the amplitude diffracted along a rod perpendicular to the film surface is given by [12]:

$$E(q_z) \approx F_h \iiint dx\,dy\,dz \cdot \Omega(x,y,z) \exp(-iq_z z) \qquad (1)$$

where F_h is the structure factor of the reflection with vector **h**. $\Omega(x,y,z)$ is the shape factor of the crystal (equal to 1 when the position vector $\mathbf{r} = (x,y,z)^T$ points within the crystal, and 0 outside), q_z is the z component of the reduced scattering vector $\mathbf{q} = \mathbf{Q} - \mathbf{h}$ (**Q** being the scattering vector and the z axis being chosen parallel to the outwards film surface normal).
In the following, we consider a film made of flat crystallites for which the shape factor can be written $\Omega(x,y,z) = \Omega(x,y).\Omega(z)$, and $\Omega(z) = 1$ if $z \in [z_L, z_U]$, otherwise $\Omega(z) = 0$ (with z_U and z_L being the coordinates of the upper and lower surface of the film, respectively). In the case of a perfectly flat film the intensity computed with the aid of equation (1) is $|F_h|^2 \sin^2(q_z t/2) / (q_z/2)$. If the film is not perfectly flat, z_U and z_L are functions of the in-plane coordinates (x,y). We assume in-plane statistical homogeneity so that $z_U(x,y)$ and $z_L(x,y)$ can be described by random variables of the in-plane coordinates such as $z_{U,L}(x,y) = \langle z_{U,L} \rangle + \Delta z_{U,L}(x,y)$. These variables are connected through the film thickness $t = z_U - z_L$ (which is also a random variable) and are therefore not independent. The subsequent averaging procedure is greatly simplified if one is able to identify independent random variables [13]. It can hence be noticed that the roughness of the substrate (σ_L) is in general induced by the different preparation steps undergone by the substrate (cutting, polishing,…), whereas thickness

fluctuations (σ_t) are solely dependent on the deposition process. A convenient choice of independent random variables is therefore z_L and $t = z_U - z_L$.

Different parts of the film scatter coherently

We first consider the case where different parts of the sample (with different z_L and t) illuminated by the X-ray beam scatter coherently. The intensity is given by $I = \langle E \rangle \langle E \rangle^*$, and we therefore average the scattered amplitude over all possible values of t and z_L. In performing this average we assume that all random variables can be described by continuous probability density functions (PDFs), *i.e.* the film thickness is much greater that the smallest height variation, that is to say one interplanar spacing. In the case of very thin films discrete PDFs must be used [8,13]. Additionally we shall arbitrarily assume Gaussian PDFs. Obviously, different PDFs will yield different diffraction profile shapes. For instance the effect of the crystal lattice termination has been deeply studied in the field of crystal truncation rod scattering on semi-infinite crystals [14-16] and, though to a lesser extent, in thin film XRD [8, 17]. In fact, it turns out that equation (1) can be solved analytically for several interesting cases. For brevity we focus on the Gaussian PDF, solutions for other distributions will be given in a forthcoming paper. With these assumptions the intensity can be written

$$I(q_z) = |F_h|^2 \exp\left(-q_z^2 \sigma_L^2\right) / q_z^2 \times \left\{ 1 + \exp\left[-q_z^2 \left(\sigma_L^2 + \sigma_U^2 - 2r\sigma_L\sigma_U\right)\right] - 2\exp\left[-\frac{1}{2} q_z^2 \left(\sigma_L^2 + \sigma_U^2 - 2r\sigma_L\sigma_U\right)\right] \cos\left(q_z \langle t \rangle\right) \right\} \quad (2)$$

The interface correlation coefficient ($r = \langle \Delta z_L \, \Delta z_U \rangle / (\langle \Delta z_L^2 \rangle \langle \Delta z_U^2 \rangle)^{1/2}$) describes how the substrate/film and the film/air interfaces are correlated; $r = \pm 1$ for completely correlated (+1) and anti-correlated (-1) interfaces, and $r = 0$ for uncorrelated interfaces.

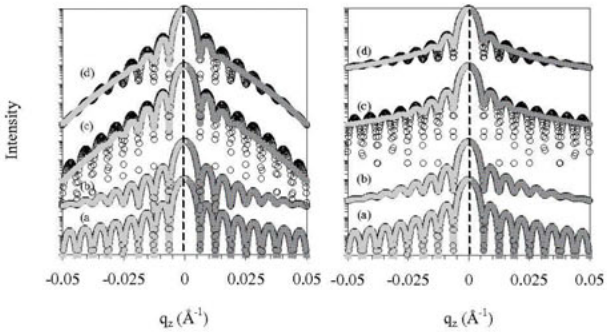

Figure 1. (left) and figure 2 (right): influence of σ_L, σ_U and r on the diffraction profile of a 100 nm-thick film calculated with equation (2) (left) and (3) (right). (a) $\sigma_L = \sigma_U = 0$; (b) $\sigma_L = 0$, $\sigma_U = 5$ nm; (c) $\sigma_L = \sigma_U = 5$ nm; (d) $\sigma_L = 5$ nm, $\sigma_U = 10$ nm. Circles: r = 1; light grey line on left side of dashed line: r = 0; dark grey line on right side: r = -1.

Figure 1 represents diffraction profiles calculated for a 100 nm-thick film, with interplanar spacing d = 5 Å, for different values of the σ's and r. Inspection of equation (2) and figure 1 reveals that σ_L affects the decay of the intensity when moving away from the Bragg position $q_z = 0$ (*i.e.* the intensity decreases faster that $1 / q_z^2$), whereas σ_t ($= \sigma_L^2 + \sigma_U^2 - 2r\sigma_L\sigma_U$) affects

the damping of the thickness fringes. The effect of the interface correlation coefficient is most easily understood by examination of figure 1(c) for which $\sigma_L = \sigma_U$. For $r = 1$ (circles) we have $\sigma_t = 0$, and the only effect is an accentuated decay of the diffracted intensity. For $r = 0$ (light grey line) $\sigma_t = \sqrt{2}\,\sigma_L$, the intensity decreases at the same rate as for $r = 0$ but in addition the oscillations are damped. Finally for $r = -1$ (dark grey line) $\sigma_t = 2\sigma_L$, the damping is more pronounced. It appears that σ_L and σ_t affect the XRD profile in a very distinct fashion, these parameters can hence be determined by fitting equation (2) to an experimental profile. Moreover, if the surface roughness σ_U is known from a complementary experiment (*e.g.* atomic force microscopy) then the interface correlation coefficient can also be determined.

Different parts of the film scatter incoherently

We now investigate the case where different parts of the sample with different z_U and t scatter incoherently, which happens for instance when the film exhibits a mosaic structure. In such a case, the quantity being averaged is the intensity, *i.e.* we have to compute $\langle EE^* \rangle$. With the same assumptions as above this average can be calculated analytically:

$$I(q_z) = \frac{|F_h|^2}{q_z^2}\left\{2 - 2\exp\left[-\frac{1}{2}q_z^2\left(\sigma_L^2 + \sigma_U^2 - 2r\sigma_L\sigma_U\right)\right]\cos\left(q_z\langle t\rangle\right)\right\} \quad (3)$$

Inspection of equation (3) reveals that the sensitivity to interface roughness (*i.e.* the term $\exp(-q_z^2\sigma_L^2)$) is lost. This is easily understood: since different parts of the sample scatter incoherently, all information concerning the beam path difference is therefore lost in the diffracted intensity, *i.e.* the total intensity is the sum of the intensities scattered by different parts of the sample with different thickness. Figure 2 shows calculated profiles with the same parameters as for figure 1. Figure 2 indeed shows that the only effect altering the line shape is a damping of the fringes, the rate of decay is unaffected. This effect particularly visible in figure 2(c): for $r = 1$ and $\sigma_U = \sigma_L$, $\sigma_t = 0$ and the profile is a Laue function, whereas for decreasing r the fringes are damped. In addition we observe an excess intensity in the profile tails in figure 2 as compared to figure 1 (this is most easily evidenced in the profiles (b)). This additional intensity correspond to the diffuse scattering $\mathrm{cov}(E,E^*)$, since $\langle E.E^* \rangle = \langle E \rangle.\langle E^* \rangle + \mathrm{cov}(E,E^*)$. It should be noticed that the same parameters (roughness and thickness fluctuations) can be evaluated by X-ray reflectivity. However, contrarily to X-ray reflectivity, XRD (when performed at non grazing incidence) is not a surface-sensitive technique. Therefore the roughness values probed by X-ray reflectivity are in general in the range of a few angstroms [12], whereas the values probed by XRD are about one order magnitude larger (as in the present case), or even larger. In that respect these two techniques are complementary. The applicability of the equations derived have been tested using diffraction profiles recorded from thin films of ZrO_2 doped with 10 mol% Y_2O_3 epitaxially grown on sapphire with thickness ranging between 40 and 70 nm [18,19]. The results derived from a least-squares fitting procedure (not shown here) are identical to those obtained using numerical integration of equation (1).

Effects of lattice disorder

The effect of lattice disorder is in general more complicated to handle because this effect is strongly dependent (in terms of magnitude and direction) on the nature of the defect

involved. In the presence of lattice disorder the position vector **r** in equation (1) should be replaced with **r**+**u**(**r**), where **u**(**r**) is a displacement vector and is a function of the position vector. In the general case there is no analytical solution, in particular when **u**(**r**) is a non linear function of **r**, then equation (1) must be numerically evaluated. Analogously when the film contains randomly distributed strain ($\varepsilon_{ij} = du_i/dx_j$, i,j = 1,2,3) then the diffracted intensity can be described as the convolution of a profile due to strain effects and a profile due to size effects [20]. In some cases however an analytical solution can be obtained. In particular in case of randomly distributed displacements, the overall intensity is reduced by the so-called Debye-Waller factor $\exp(-h^2\sigma_u^2)$, where σ_u is the standard deviation of the displacement PDF (assumed to be Gaussian). Finally, when the lattice planes are randomly distorted, but the displacements u_z accumulate from one plane to another [9,11], this effect can be accounted for by substituting the reduced scattering vector in equation (2),with [13] $q_z - ih^2\sigma_u^{(c)2}/2d$ where $\sigma_u^{(c)}$ is the standard deviation of the displacement PDF (assumed to be Gaussian), the superscript (c) stands for cumulative.

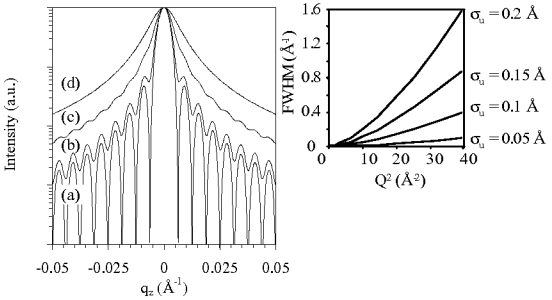

Figure 3. Influence of cumulative lattice disorder on the diffraction profile of a 100 nm-thick film. (a) to (d): $\sigma_u^{(c)}$ = 0 ; 0.1 ; 0.15 and 0.2 Å. Inset: evolution of the full width at half maximum (FWHM) with the squared scattering vector

The influence of the latter effect on the diffraction profiles is depicted in figure 3. This type of disorder broadens the main peak as well as the thickness fringes. In contrast to morphological effects, it is dependent on the order of reflection (since it is function of Q_z, and not q_z). This type of disorder mainly has a phenomenological interest in that it produces peak and fringes broadening similarly to what is encountered with several type of defects. However, it is unlikely that the actual state of disorder in thin films can be described in such a simple way. Therefore the values of $\sigma_u^{(c)}$ cannot be straightforwardly interpreted on a quantitative level (in terms of defects densities for instance). If such interpretations have to be performed, other approaches should be used (see for instance ref. [12]).

Conclusions

We have derived a generalized interference function that takes into account the effects of interface roughness, surface roughness, interface correlations and cumulative and non cumulative lattice disorder. This interference function is completely analytical and can be written, in the case where different parts of the film scatter coherently:

$$I(q_z)=|F_h|^2 \exp\left(-h^2\sigma_u^2-q_z^2\sigma_L^2\right)\Big/\left[q_z^2+\left(\frac{h^2\sigma_u^{(c)2}}{2d}\right)^2\right]$$
$$\times\left\{1+\exp\left[-q_z^2\sigma_t^2-h^2\sigma_u^{(c)2}\frac{\langle t\rangle}{d}\right]-2\exp\left[-\frac{1}{2}\left(q_z^2\sigma_t^2+h^2\sigma_u^{(c)2}\frac{\langle t\rangle}{d}\right)\right]\cos\left(q_z\langle t\rangle\right)\right\}$$

and $\sigma_t^2 = \sigma_L^2 + \sigma_U^2 - 2r\,\sigma_L\sigma_U$. When different parts of the film scatter incoherently a similar equation is straightforwardly obtained from equation (1) as previously detailed.

References

1. Authier, A., 2001, *Dynamical theory of X-ray diffraction, IUCr monograph on crystallography* 11. (Oxford University Press).
2. Takagi, S., 1962, *Acta Cryst.*, **15**, 1311, 1969, *J. Phys. Soc. Jap.*, **26**, 5, 1239.
3. Taupin, D., 1964, *Bull. Soc. Franç. Minér. Crist.*, **87**, 469.
4. Bartels, W. J., Hornstra, J., W. Lobeek, D. J., 1986, *Acta Cryst. A*, **42**, 539.
5. Halliwell, M. A. G., Lyons, M. H., Hill, M. J., 1984, *J. Cryst. Growth*, **68**, 523.
6. Pavlov, K. M., Punegov, V. I., 2000, *Acta Cryst. A*, **56**, 227.
7. Friedrich, W., Knipping, P., Laue, M., 1913, *Annalen der Physik*, **14**, 971.
8. Miceli, P. F., Palmstrøm, C. J., Moyers, K. W., 1992, *Appl. Phys. Lett.*, **61**, 17, 2060.
9. Fullerton, E. F., Schuller, I. K., Vanderstraeten, H., Bruynseraede, Y., 1992, *Phys. Rev. B*, **45**, 16, 9292.
10. Gibaud, A., Cowley, R. A., McMorrow, D. F., Ward, R. C. C., Wells, M. R., 1993, *Phys. Rev. B*, **48**, 19, 14463.
11. Zolotoyabko, E., 1998, *J. Appl. Cryst.*, **31**, 241.
12. Holý, V., Pietsch, U., Baumbach, T., 1999, *High resolution X-–ray scattering from multilayers and thin films, Springer tracts in Modern Physics* 149 (Berlin: Springer), p63.
13. Boulle, A., Guinebretière, R., Dauger, A., 2004, *J. Phys. IV* (France) **118**, 183.
14. Andrews, S. R., Cowley, R. A., 1985, *J. Phys. C*, **18**, 6427.
15. Robinson, I. K., 1986, *Phys. Rev. B*, **33**, 6, 3830.
16. Harada, J., 1992, *Acta Cryst. A*, **48**, 764.
17. Ern, C., Donner, W., Dosch, H., Adams, B., Nowikow, D., 2000, *Phys. Rev. Lett.*, **85**, 9, 1926.
18. Boulle, A., Pradier, L., Masson, O., Guinebretière, R., Dauger, A., 2002, *Appl. Surf. Sci.*, **188**, 80.
19. Boulle, A., Masson, O., Guinebretière, R., Dauger, A., 2003, *Thin Sol.Films*, **434**, 1.
20. Warren, B. E., X-ray diffraction, 1969 (New-York: Addison-Wesley) p268.

Z. Kristallogr. Suppl. **23** (2006) 129-134

Microstructure of post-deformed ECAP-Ti investigated by Multiple X-Ray Line Profile Analysis

E. Schafler[1,3,*], K. Nyilas[2], S. Bernstorff[4], L. Zeipper[1,5], M. Zehetbauer[1], T. Ungàr[2]

[1]Institute of Materials Physics, University Vienna, A-1090 Vienna, Austria
[2]Department of General Physics, Eötvös University Budapest, H-1518 POB., Hungary;
[3]Institute for Materials Science, Austrian Academy of Science, A-8700 Leoben, Austria
[4]Sincrotrone ELETTRA, Basovizza, I-34012 Trieste, Italy
[5]ARC Seibersdorf research GmbH, A-2444Seibersdorf, Austria
[*]Contact author; e-mail: schafler@ap.univie.ac.at

Keywords: line profile analysis, severe plastic deformation, dislocation structure

Abstract. 99.5% pure α-Ti was deformed by equal channel angular pressing (ECAP) at 450°C for 8 passes in route B_C. Samples which were manufactured out of the bulk have been deformed by compression up to 80% true strain and analysed by Multi reflection X-ray Line Profile Analysis (MXPA). It turned out that from the 11 slip systems possible in hexagonal Ti only those with Burgers vector b_1 = 1/3 < 110> (<a> type) and b_3 = 1/3 < 113> (<c+a> type) have been activated during compression. After the ECAP deformation area weighted mean of the coherently scattering domain size has a relatively small value of about 40 nm. During the additional compression it stays fairly constant, whereas the size distribution function broadens slightly. After the ECAP process the dislocation density is considerably high at $2x10^{15}$ m^{-2} and increases up to 5 times with growing post-deformation.

Introduction

With severe plastic deformation (SPD) it is possible to produce nanostructured bulk materials with special magnetic, electronic and mechanical properties. In particular the much higher ductility as compared to 'conventional' produced (gas phase, electrodeposition) nanomaterials is of great importance for most technical applications regarding e.g. the fatigue properties. The physical background of the formation of the nanostructure is not yet fully understood. Especially the enhanced ductility during post-deformation of SPD materials is of technological interest. The aim of this work is to investigate the post-deformation of Ti by using MXPA. With this method the structural size and its distribution in ultra-fine grained materials as well as other microstructural parameters like dislocation density, their arrangement and long range internal stresses can be determined [2, 3], making it possible to

characterize the microstructural development with respect to the deformation and recovery mechanisms.

Experimental

Commercially pure (CP) Titanium grade 2 mill-annealed samples with a diameter of 40 mm have been produced by equal channel angular pressing (ECAP) at 450°C-400°C for 8 passes by route B_C (90° rotation after each pass). For further deformation experiments cylindrical samples of 5 mm in height and 3 mm in diameter have been machined from the material. After compression deformation at room temperature to strains of $\varepsilon = 0.21$, $\varepsilon = 0.4$ and $\varepsilon = 0.82$ ($\varepsilon = \ln(h_0/h)$, h_o is the initial height and h the final height of the sample), all samples have been cut by spark erosion perpendicular to the compression axis at half height. Afterwards, the surface has been polished and etched. MXPA has been applied to these samples using synchrotron radiation of 1.54Å wavelength at the SAXS-beamline at the Sincrotrone ELETTRA Trieste, Italy. With the high intensity and brilliance of the beam it was possible to record up to 11 reflections simultaneously by using four position sensitive detectors. Only by using synchrotron radiation could problems like low reflectivity of such high deformation states as well as increased background scattering due to the high impurity content be solved. The following reflections have been recorded and evaluated by with the Multiple Whole Profile fitting procedure (MWP [4]): {011}, {102}, {103}, {200}, {112}, {021}, {203}, {121}, {114}.

Evaluation procedure

The broadening of the diffraction profiles is assumed to originate from two effects: crystallite smallness and strain fields caused by dislocations. Using well-established functions the size profile is evaluated under the assumption that the crystallites (or coherently scattering domains) are spherical and that their size is distributed as a lognormal distribution [5]. For the strain broadening the dislocation model of lattice distortions [6] is applied. The resulting formula for the Fourier coefficients is in the present case given by [7, 8]:

$$A(L) = A^S(L)\, A^D(L) = A^S(L) \exp[-2\pi^2 L^2 g^2 \frac{\rho \overline{Cb^2}}{4\pi} f(\eta)], \qquad (1)$$

The superscripts S and D indicate size and distortion broadening, L is the Fourier variable, g is the absolute value of the diffraction vector, ρ is the dislocation density, C is the dislocation contrast factor, b is the absolute value of the Burgers vector and $f(\eta)$ ($\eta \propto L/R_e$, with R_e the effective outer cut-off radius of dislocations) is a function derived explicitly by Wilkens [6].
In the case of hexagonal crystals there exist three major slip systems: basal, prismatic and pyramidal. Each of them consists of several sub-slip-systems, with fundamentally different Burgers vectors [2, 9]. It is thus necessary to average over the contrast as well as over the burgers vectors. If the dislocations are randomly populated among the different sub-slip-systems this averaging can be expressed in formula (1) by using:

$$\overline{Cb^2} = \sum_{i=1}^{N} f_i \overline{C}^{(i)} b_i^2 \,, \qquad (2)$$

where N is the number of activated slip systems, $\overline{C}^{(i)}$ is the average dislocation contrast factor corresponding to the i-th slip system and f_i are the fractions of the particular sub-slip systems by which they contribute to the broadening of a specific reflection. The average contrast factors for a single sub-slip-system in hexagonal crystals are [8]:

$$\overline{C} = \overline{C}_{hk0}\,[1 + q_1 x + q_2 x^2\,]. \qquad (3)$$

Here $x = (2l^2)/(3a^2g^2)$, q_1 and q_2 are parameters depending on the elastic constants and on the dislocation slip systems active in the crystal [8], a is the lattice parameter in the hexagonal basal plane, l is the third independent index of the reflection. The q_1 and q_2 parameters and the values of C_{hk0} have been evaluated numerically for a large number of hexagonal crystals in [8]. The experimental values for q_1 and q_2, denoted as $q_1^{(m)}$ and $q_2^{(m)}$ are provided by the computer program package MWP (multiple whole profile fitting program) [4], in which the MXPA is implemented. Equations (1-3) show that the X-ray measurements provide only two independent parameters which are related to the Burgers vector distribution: $q_1^{(m)}$ and $q_2^{(m)}$. This means that there is no possibility to determine the activities of each individual sub-slip-system separately. However, by making some physically based assumptions or by using auxiliary information on slip, the relative fractions of the three basic Burgers vector types can be obtained. There are in principle three independent equations offered by the measurements, which could either be solved for the 3 Burgers vector types by averaging or if the active sub-slip-systems are explicitly known. For details see Ref. [8], section 3.1. The three Burgers vector types are: $b_1 = 1/3\langle 110\rangle$ (<a> type), $b_2 = \langle 0001\rangle$ (<c> type) and $b_3 = 1/3\langle 113\rangle$ (<c+a> type).

Máthis et al. have developed a computer program [10] to determine the Burgers vector populations as follows: A formal solution to the three afore mentioned equations under the assumption that the sub-slip-systems are equally populated within the three Burgers vector types, is always possible. A sub-slip-system is only activated if the corresponding Schmid factor is large enough. In a general case it is quite plausible that not all sub-slip-systems will be activated. Taking this into account a numerical procedure has been worked out where the number of sub-slip-systems in the calculation is reduced systematically in such a way that all possible combinations in the combinatorial sense are taken into account. This numerical procedure provides a matrix of solutions for the possible fractions h_i. This matrix of solutions is evaluated for the three Burgers vector types, <a>, <c> and <c+a> respectively. Once the active slip systems are determined, the effective dislocation contrast factors can be calculated. From these values equation (2) can be evaluated and the average dislocation density can be determined. For more details see [8].

Results and Discussion

The evaluation of the profiles for the different deformation states yielded the experimental q-parameters presented in table 1. These values represent the basis of the further evaluation of the fractions h_i for the three different Burgers vector types with the procedure described in the last paragraph of the previous section. The analysis of the solution matrix of the fractions

h_i in the case of the investigated specimens yields the results also shown in table 1. A general feature for all sample states is that the fraction $h_i^{<c>}$ is more or less zero.

Table 1. The experimental q-parameters and the resulting fractions h_i of the three Burgers vector types.

	as processed	**ε = 0.21**	**ε = 0.4**	**ε = 0.82**
$q_1^{(m)}$	-0.549	-1.287	-0.403	-1.173
$q_2^{(m)}$	0.462	0.348	0.410	0.117
<a>	0.4	0.55	0.5	0.75
<c+a>	0.6	0.45	0.5	0.25
<c>	0	0	0	0

This means that only two Burgers vector types govern the deformation process: <a> and <c+a>. Right after the equal channel angular pressing process the <c+a> Burgers vectors slightly dominate. As is known from literature, the most common slip modes have an <a>-Burgers vector over the entire temperature range [11]. The <c+a>-type slip is the second frequent mentioned one in the literature [12] and its frequency increases with temperature [11]. Thus the high fraction of <c+a>-type after the ECAP process is plausible as the extrusion temperature was between 400°C and 450°C. The post-deformation was performed at room temperature; hence the activated slip should be predominantly of <a>-type. That the fraction $h_i^{<a>}$ of <a>-type increases to 0.75 after an additional cold compression of ε = 0.82 underlines this interpretation. The non-monotonic evolution of the fractions can be explained by inhomogeneity effects of the deformation, however, a clear trend in accordance with basic findings in the literature is apparent.

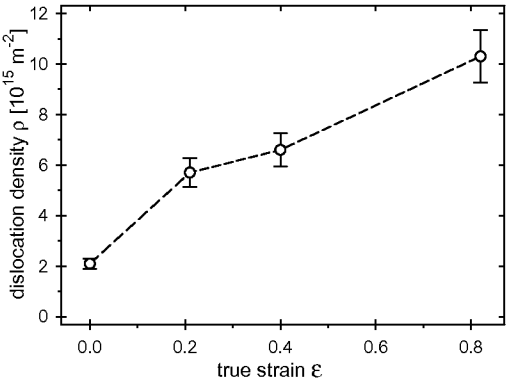

Figure 1. Evolution of the dislocation density as a function of post-deformation after ECAP.

With these results for the fractions the dislocation density can be calculated. In figure 1 the evolution of the dislocation density ρ with increasing compression deformation after the ECAP processing is shown. The dislocation density after 8 passes ECAP amounts to $2 \times 10^{15} m^{-2}$. This value is not in good agreement with a previous determination [13], since there the Burgers vector fractions h_i have been assumed to be 1/3 due to the lack of a proper evaluation procedure like the one used here. The further strong increase of the dislocation

density to values of about $1x10^{16}m^{-2}$ with the additional compression deformation to $\varepsilon = 0.82$ is plausible as it has been done at room temperature and is comparable to results from Zhu et al. [14]. This number of the deformation induced dislocations could also be confirmed by results from residual electrical resistivity measurements [15].

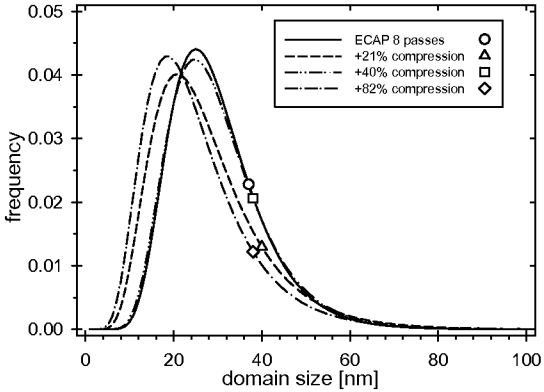

Figure 2. Distribution of the scattering domain size for the different deformation states. The symbols indicate the area-weighted mean value.

The other important parameters determined by the MXPA are the coherently scattering domain size and its distribution. Figure 2 shows the obtained lognormal size distributions for the as processed state and the states of subsequent compression deformation. The single symbols on the lines representing the distribution are the values of the specific area weighted mean of the domain diameter as defined in [4]. It stays more or less constant at about 40 nm. The shape of the distribution does also not change strongly, if at all it broadens a little. According to the classical definition the coherently scattering domains are the regions of the crystal lattice over which the X-ray diffraction is coherent or, in other words, undistorted lattice regions bounded by any structural defect [16]. According to this definition all misorientations bigger than about 1°- 2° will border the domains. Investigations of the microstructure by Scanning Electron Microscopy showed a substructure inside 800 nm big grains [13]. The size of this sub-boundary structure fits well to the coherently scattering domain size obtained here. One may conclude that this sub-boundaries incorporate the dislocations produced by the additional compression deformation, which leads to a misorientation increase of the subgrains.

Summary

Post-deformed ECAP-Ti has been investigated by Multi reflection X-ray Line Profile Analysis using up to 11 reflection for the evaluation. The application of an advanced procedure for the determination of the dislocation contrast conditions yielded the following results and interpretations: (i) Straight after the ECAP processing the prevailing Burgers vectors are of <a> and <c+a>-type, where the <c+a>-fraction dominates. Practically no <c>

type seems to be present in all sample states investigated. With proceeding cold deformation by compression the <a>-fraction increases and later dominates the overall population. This is in good accordance with basic findings of the plasticity of Ti reported in literature. (ii) the resulting dislocation density amounts to $2x10^{15}$ m^{-2} right after the ECAP process and increases up to $1x10^{16}$ m^{-2} after a compression up to $\varepsilon = 0.82$. (iii) the size and distribution of the coherently scattering domains, which represent the smallest unit of the microstructure, do not change significantly with the subsequent deformation after the ECAP process. It is assumed that the defects produced during the post-deformation process are incorporated into the sub-boundary structure enclosing the coherently scattering domains, which leads to a further increase of the misorientation between the subgrains.

References

1. Valiev, R.Z.; Islamgaliev, R.K.; Alexandrov I.V., 2000, *Progr. Mater. Sci.* **45**, 103.
2. Ungár, T., Gubicza, Ribárik, G., Borbély, A., 2001, *J. Appl. Cryst.* **34**, 298.
3. Schafler, E., Zehetbauer, M., Ungar; T., 2001, *Mater.Sci.Eng. A* **319-321**, 220.
4. Ribárik. G, Ungár T. and Gubicza, J., 2001, *J. Appl. Cryst.* **34**, 669.
5. Krill, C. E.; Birringer, R., 1998, *Phil. Mag. A* **77**, 621.
6. Wilkens, M.1970, in *Fundamental Aspects of Dislocation Theory*, ed. J. A. Simmons, R. de Wit, R. Bullough, Vol. II. Nat. Bur. Stand. (US) Spec. Publ. No. 317, Washington, DC. USA, p. 1195.
7. Warren BE. 1959, *Progr. Metal Phys.* **8**, 147.
8. Dragomir, I.C., Ungár, T., 2002, *J. Appl. Cryst.* **35**, 556.
9. Kuzel jr., R., Klimanek, P., 1989, *J. Appl. Cryst.* **22**, 299.
10. Máthis, K., Nyilas, K., Axt, A., Dragomir-Cernatescu, I., Ungár, T., Lukác,P., 2004, *ActaMater.* **52**, 2889.
11. Conrad, H., 1981, *Progr. Mater. Sci.* **26**, 123.
12. Paton, E.; Williams, J. C. and Rauscher, G. P., 1973, *Titanium, Science and Technology* (New York: Plenum Press) p.1049.
13. Schafler, E.; Zeipper, L.; Zehetbauer, M. J., 2004, Proc. 2nd Int. Conf. on Nanomaterials by Severe Plastic Deformation: Fundamentals – Processing – Applications, Vienna, Dec. 2002, J. Wiley VCH Weinheim, p.426.
14. Zhu, Y.T., Huang, J.Y., Gubicza, J., Ungár, T., Wang, Y.M., Ma, E., Valiev, R.Z., 2003, *J.Mater.Res.* **18(8)**, 1908.
15. Zeipper, L., 2004, Thesis, University Vienna.
16. Warren; B. E., 1990, *X-ray diffraction* (New York: Dover Publ.)

Acknowledgements. The Austrian (FWF) and the Hungarian (OTKA) Science Funds are acknowledged for the financial support under projects P-17095-N02 (A) and T-046990 & T-043247 (H).

Z. Kristallogr. Suppl. **23** (2006) 135-140

The Dislocation-Structure and Crystallite-Size in Forsterite (Olivine) Deformed at 1400 °C by 11 GPa

Krisztián Nyilas[1], Hélène Couvy[2, 3], Patrick Cordier[3] and Tamás Ungár[1,*]

[1]Department of General Physics, Eötvös University Budapest, Hungary
[2]Bayerisches Geoinstitut, Universität Bayreuth, Germany
[3]Laboratoire de Structure et Propriétés de l'Etat Solide, ESA CNRS 8008, Université des Sciences et Technologies de Lille, Villeneuve d'Ascq, France
[*]Contact author; e-mail: ungar@ludens.elte.hu

Keywords: dislocation structure, high-pressure, high-temperature, forsterite

Abstract. Synthetic forsterite samples were shear-deformed at 11 GPa, 1400°C in the multianvil apparatus. The deformation microstructures have been characterised by x-ray diffraction peak broadening and strain anisotropy analysis. The evolution of strain and stress are characterised as a function of the time duration of the high-pressure, high-temperature experiments.

Introduction

Olivine is by far the most abundant mineral of the upper mantle. It is also considered to be the weakest phase and hence to control the rheology of the upper mantle. For this reason, it has been clear for a long time that modelling the nature of convection in the outer 400 km of the Earth's mantle requires a good knowledge of the plastic properties of olivine. Many studies have been conducted to investigate the deformation mechanisms and flow laws of olivine single crystals [1] and polycrystals [2,3]. In order to determine the microstructure we use X-ray line profile analysis. Dislocations are characterised by a long-range strain field causing a peak broadening around the fundamental Bragg reflections. Conventional peak profile analysis methods of Williamson & Hall [4] and Warren & Averbach [5] have been upgraded by taking into account the contrast effect of dislocations on peak broadening [6]. The contrast factor, C, is a function of the hkl indices of the reflection, the Burgers- and line vectors of the dislocations, b and l, and the elastic constants of the crystal in a similar way as in TEM. C is thus characteristic for a given slip system. The anisotropic contrast effect of dislocations has been used to model the strain anisotropy observed on x-ray diffraction profiles of cubic and hexagonal crystals [7]. Here the technique has been extended to orthorhombic crystals [8]. This technique has the advantage over TEM that it provides information on a large number

of dislocations that are more statistically relevant and it can be applied to high dislocation densities, e.g. $10^{18}m^{-2}$. Besides the modified Williamson-Hall and Warren-Averbach methods whole profile fitting procedures [9] have been developed and used here for the determination of the experimental values of dislocation contrast factors.

Experimental technique

Shear deformation in the multianvil apparatus

High-pressure experiments have been performed at the Bayerisches Geoinstitut in a 1200 tonne, MA-8 type, multianvil apparatus. After hot-pressing, the dense specimens exhibit a fairly uniform grain size of 10-15μm. The forsterite sample is sandwiched between two hard alumina pistons cut at 45°. The sample is thus deformed in a shear configuration.

X-ray diffraction peak broadening analysis

Monochromatic CuKα radiation from a fine focus rotating anode (Nonius FR 521), operated at 40kV, 70mA was used. The footprint of the beam on the specimen was 0.1x0.8mm. The diffraction profiles were registered by a linear position sensitive gas filled detector (OED 50. Braun, Munich) at a distance of 140mm from the specimen.

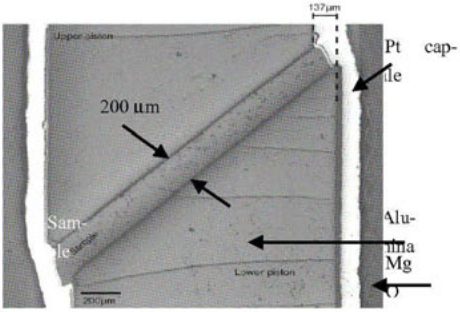

Figure 1. Enlargement of the sample capsule. The sample itself is the narrow slanted strip (in crossection) in the diagonal of the graph. In the diffraction experimens the "sample" was aligned parallel to the line direction of the X-ray beam.

The linear resolution of the detector is about 80μm. The specimen was mounted on a two axis standard crystallographic goniometer-head with additional x-y translations in the horizontal plane in order to move the specimen within the X-ray beam with high precision. The specimens were cut as in Figure 1. Consequently, the forsterite is surrounded by alumina and contains some Pt. The sample was rotated to have the beam parallel to the forsterite layer, and the diffraction vector was perpendicular to the surface. Three windows have been found in the entire diffraction angle range where only the reflections of forsterite are present. In these three windows the profiles of five reflections have been investigated: (021), (101), (002), (130), (220). As can be seen on figure 2.

Evaluation of strain anisotropy

Strain anisotropy in X-ray line-profile analysis means that neither the full-width at half maximum (FWHM) nor the integral breadths nor the Fourier coefficients in the Warren-Averbach plot are monotonous functions of the diffraction vector or its square, g or g^2. It can be rationalised by the dislocation contrast factors, C, which, on the other hand provide useful further information on the dislocation structure of the specimen [9, 6]. If all possible slip systems are randomly populated or if the specimen is more or less texture free the contrast factors corresponding to the same *hkl* indices can be averaged over the permutations of the indices [7].

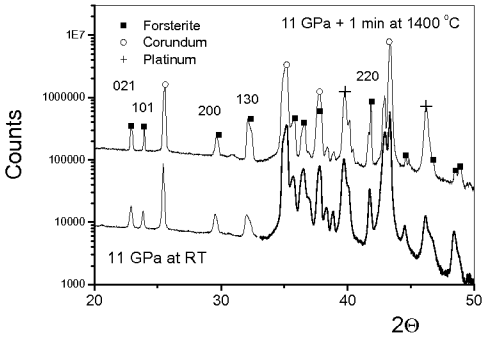

Figure 2. Mesured powder patterns of two typical specimens obtained by the high-resolution microdiffraction arrangement.

The specimens are compact bulk polycrystalline materials in which the deformation proceeds mainly by shear under the present experimental circumstances. The Taylor requirement of compatibility of the deformation of polycrystalline samples means that in each grain or crystallite at least five slip systems must operate. Obviously the five slip systems in the different grains will be very different bunches of slip systmes varying from grain to grain since the crystallites are of different crystallographic orientations. Under these conditions the average dislocation contrast factors are the only physically realistic choice. For cubic and hexagonal crystals the numerical parameters in the average contrast factor formula are well understood [7]. For orthorhombic crystals the average contrast factors are:

$$\overline{C} = \alpha + \beta[(h^4 + a_1 k^4 + a_2 l^4 + a_3 h^2 k^2 + a_4 h^2 l^2 + a_5 l^2 k^2)/(h^2/a^2 + k^2/b^2 + l^2/c^2)^2] \,, \qquad (1)$$

where *a*, *b* and *c* are the lattice constants, h, k and l are the Miller indices and a_i, i=1-5 are numerical constants depending on the dislocation type and the elastic constants of the crystal. α and β are auxiliary constants, which influence only the absolute value of $\overline{C}$, but do not influence the hkl dependence of it. The average contrast factors for orthorhombic crystals are calculated numerically by using the general formula for contrast factors [10, 7]. The physical interpretation of the a_i constants in terms of different dislocation types and/or elastic constants is, however, not yet available. In the present case, the a_i numerical constants are de-

termined by fitting the FWHM of the five measured profiles according to the modified Williamson-Hall equation. From the a_i values, obtained here, relative values of the contrast factors, $\overline{C}^*$ were calculated. A large number of experiments [9] has shown that the approximate mean of the average contrast factors is: $<\overline{C}> \cong 0.4$. The mean of the $\overline{C}^*$ values were adjusted accordingly. With these calculated and adjusted $\overline{C}$ values the dislocation densities are calculated by using the multiple whole profile (MWP) fitting procedure that applies physically well established profile functions for the size and strain profiles, respectively [5]. The convolutional MWP method automatically avoids ill- conditioning in various deconvolution methods [11].

Results

Typical peak profiles of the 101 reflections as a function of the duration of the specimens at the deformation temperatures are shown in figure 3. It can be seen that the "null test" specimen reveals the largest broadening in accordance with the fact that it was compressed at room temperature but not heated.

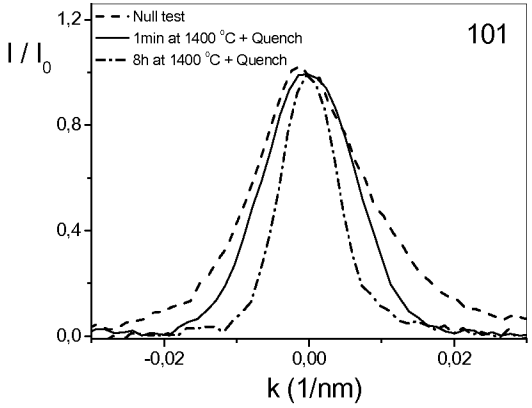

Figure 3. Typical profiles of the 101 Bragg peaks in three different specimens. The decrease of peak width with annealing time can be observed.

The peak broadening decreases with holding time at high temperature. The FWHM of the five investigated reflections are shown in the classical Williamson-Hall plot in figure 4 as a function of K ($K = 2\ sin\theta/\lambda$, where θ is the diffraction angle and λ the wavelength of the X-rays). The strongly non-monotonous behaviour of the FWHM values indicate a pronounced strain anisotropy. Using the average dislocation contrast factors, the *modified* Williamson-Hall plot can be constructed as shown for four different specimens in figure 5. It can be seen that, within experimental error, the strong strain anisotropy is well rationalized by the dislocation model of strain. The very different slopes of the straight lines fitted to the data points indicate large differences in the lattice strains in the different specimens, the larger slope

indicates more strain. The dislocation structure can only be characterised by at least two parameters, the density and the arrangement of dislocations, ρ and M, where $M = R_e\rho^{1/2}$ and R_e is the effective outer cut-off radius of dislocations. The slope alone in the *modified* Williamson-Hall plot can certainly not provide the two parameters, ρ and M. The entire profile is not only broadened but its shape is also influenced by the dislocation structure. Therefore, the breadth and the profile shape in a whole profile analysis enable to determine the two parameters, ρ and M, simultaneously, cf. [9].

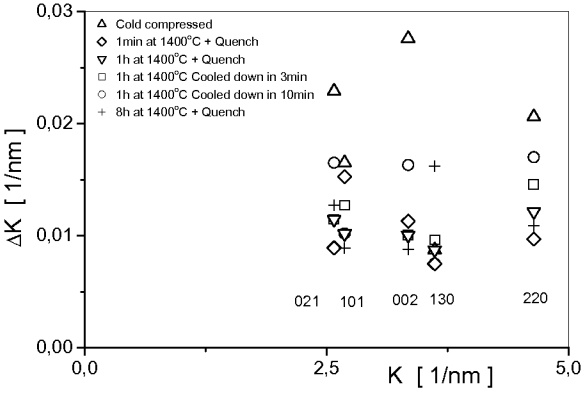

Figure 4. Classical Williamson-Hall plot corresponding to the five investigated forsterite reflections in the different specimens.

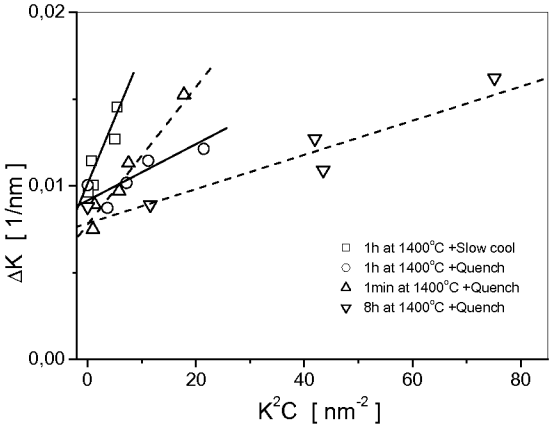

Figure 5. Modified Williamson-Hall plots corresponding to the five investigated forsterite reflections (For the sake of clarity only 4 typical specimens are shown).

The MWP fitting method [9] provides the crystallite size parameters in terms of the median and the variance, *m* and σ, of the log-normal size distribution function. From *m* and σ the area average mean crystallite diameter, $\langle x \rangle_{area}$, can be calculated as: $\langle x \rangle_{area} = m \exp(2.5\sigma^2)$. The size parameters and the dislocation densities in the different specimens are listed in Table 1. The dislocation densities found with this method are in good agreement with the densities measured by TEM investigations [12].

Table 1. The median, m and the variance, σ of the crystallite size distribution function, the area average mean crystallite diameter, $\langle x \rangle_{area}$, and the average dislocation density, ρ, in the different specimens.

Specimen	m [nm]	σ	$\langle x \rangle_{area}$ [nm]	ρ [10^{14} m^{-2}]
cold compression	55 (5)	0.38 (0.05)	80 (5)	16 (4)
1 minute at 1400 °C and quenched	161 (10)	0.01 (0.01)	160 (10)	2.2 (0.5)
1 hour at 1400 °C and cooled down in 3 min	94 (10)	0.19 (0.05)	105 (10)	2.2 (0.5)
1 hour at 1400 °C and cooled down in 10 min	63 (5)	0.36 (0.05)	90 (5)	2.8 (0.5)
1 hour at 1400 °C and quenched	118 (10)	0.06 (0.02)	120 (10)	0.04 (0.03)
8 hours at 1400 °C and quenched	122 (10)	0.12 (0.05)	130 (10)	0.09 (0.03)

Due to high temperature deformation the crystallite size increases, and the dislocation density decreases as compared to cold compression. During slow cooling under pressure the deformation process proceeds while cooling, producing intermediate large dislocation densities. Quenching freeses the state in which the material was at high temperatures, producing the smallest dislocation densities.

References

1. Bai, Q. & Kohlstedt, D.L. 1992, *Tectonophysics*, **206**, 1-29.
2. Hirth, G. & Kohlstedt, D.L. 1995, *J. Geophys. Res.*, **100**, 1981-2001.
3. Mei, S. & Kohlstedt, D.L. 2000, *J. Geophys. Res. Solid Earth*, **105**, 21457-21469
4. Williamson, G.K. & Hall, W.H. 1953, *Acta Metall.*, **1**, 22-31.
5. Warren, B.E. & Avenbach, B.L. 1950, *J. Appl. Phys.*, **21**, 595-610.
6. Ungár, T. & Borbély, A. 1996, *Appl. Phys. Lett.*, **69**, 3173-3175.
7. Ungár, T. & Tichy, G., 1999, *Phys. Stat. Sol. A*, **147**, 425-434
8. Cordier, P, Ungár T., Zsoldos, L. and Tichy, G., 2004, *Nature*, **428**, 837.
9. Ribárik, G., Ungár, T., Gubicza, J. 2001, *J. Appl. Cryst.*, **34**, 669-676.
10. Wilkens, M. 1970, *Phys. Stat. Sol. A*, **2**, 359-370.
11. Armstrong, N., Kalceff, W. 1998, *J. Appl. Cryst.*, **31**, 453-460.
12. Couvy, H., Frost, D., Heidelbach, F., Nyilas, K., Ungár T., Mackwell S., Cordier, P. 2004, *European Journal of Mineralogy*, **16**, 877-889.

Acknowledgements. The authors are grateful to the Hungarian National Science Foundation, OTKA T-046990.

Z. Kristallogr. Suppl. **23** (2006) 141-146

Diffuse X-ray scattering from GaN/SiC (0001) thin films

S. Daniš* and V. Holý

Department of Electronic Structures, Faculty of Mathematics and Physics, Charles University, 121 16 Prague 2, Czech Republic
*Contact author; e-mail: danis@mag.mff.cuni.cz

Keywords: thin films, diffuse x-ray scattering, dislocation density, gallium nitride

Abstract. A statistical theory of x-ray scattering from dislocations oriented perpendicular to the surface in semiconductor thin films is presented. We apply this theory to the description of diffuse x-ray scattering from both screw and edge threading dislocations in GaN thin films grown on SiC substrate. Our theory predicts a non-Gaussian shape of scattered intensity maxima in x-ray diffraction. The screw and edge dislocation densities are obtained from simulations of the experimental data.

Introduction

Epitaxial layers of Group III nitrides contain a large amount of structural defects compared to other III-V compounds such as GaAs. In hexagonal GaN (0001) layers, the dominant defects are dislocations with dislocation lines perpendicular to the surface (threading dislocations) with the Burgers vectors $\mathbf{b}_e$ = 1\3<11-20> (edge dislocations), $\mathbf{b}_s$ = <0001> (screw dislocations), and $\mathbf{b}_m$ = 1/3<11-23> (mixed dislocations) [1-3]. The density of the threading dislocations can reach 10^{11} cm^{-2} and dense arrays of misfit dislocations are also present at the substrate-layer interface [4-6]. Using the ultrahigh vacuum ballistic electron emission spectroscopy Ding et al. [7] were able to characterize even individual threading dislocations in GaN. In addition to other techniques for the structural characterization of nitride layers x-ray diffraction and reflectivity measurements have been reported in several investigations [2,8-12].

Scattering theory

Using the statistical kinematical scattering theory according to Krivoglaz [18], the scattered intensity from samples containing dislocations can be expressed as

$$I(\mathbf{q}) = A\int_V \mathrm{d}^3\mathbf{r}\int_V \mathrm{d}^3\mathbf{r}'\, \mathrm{e}^{-\mathrm{i}\mathbf{q}(\mathbf{r}-\mathbf{r}')}\, \mathrm{e}^{-T(\mathbf{r}_\parallel-\mathbf{r}_\parallel';z,z')}, \qquad (1)$$

where the constant A contains the polarizability of the material and the intensity of the primary beam. $\mathbf{q}$ is the scattering vector whose origin lies in the reciprocal lattice point $\mathbf{h}$, V is the sample volume. $\mathbf{r}_{\|}$, z are the components of the position vector $\mathbf{r}$ parallel and perpendicular to the surface, respectively, and

$$T(\mathbf{r}_{\|}-\mathbf{r}_{\|}') = \sum_{\alpha} \rho_{\alpha} \int_S \mathrm{d}^2\mathbf{r}_{\|}'' \Phi(\mathbf{r},\mathbf{r}',\mathbf{r}_{\|}''), \tag{2}$$

$$\Phi(\mathbf{r},\mathbf{r}',\mathbf{r}_{\|}'') = 1 - \mathrm{e}^{-\mathrm{i}\mathbf{h}.(\mathbf{u}_{\alpha}(\mathbf{r}_{\|}-\mathbf{r}_{\|}'')-\mathbf{u}_{\alpha}(\mathbf{r}_{\|}'-\mathbf{r}_{\|}''))}. \tag{3}$$

Here the index α denotes the dislocation type, ρ_{α} is the density of the dislocations of type α (in cm^{-2}), and $\mathbf{u}_{\alpha}(\mathbf{r}_{\|},z)$ is the displacement field at the point $\mathbf{r} \equiv (\mathbf{r}_{\|},z)$ due to the dislocation of type α crossing the sample surface in the origin $\mathbf{r}=0$. The integral in Eq. (2) runs over the irradiated sample surface S. The explicit formulas for the displacement vector of edge and screw straight dislocations perpendicular to the sample surface including the influence of the surface can be found in Ref [14]. In deriving Eq. (2) we have assumed that the positions of the dislocations are statistically *not correlated*.

Symmetrical diffraction, screw dislocations

The integral expression in Eq. (2) can be evaluated for screw dislocations and a symmetric diffraction. In this case, both the diffraction vector $\mathbf{h}$ and the Burgers vector $\mathbf{b}_s$ of the screw dislocations are perpendicular to the sample surface. Since the scattering depends on dot product $\mathbf{h}.\mathbf{u}$, only the vertical component $\mathbf{u}_z$ of the displacement field of a screw dislocation plays a role [14].

$$u_z(\mathbf{r}) = \frac{b_s}{2\pi} \arctan\frac{y}{x}. \tag{4}$$

This component is not affected by the surface relaxation of internal stresses. Then, the function T is (Eq.(2))

$$T(x_t) = \rho_s \int_0^{R_c} r\mathrm{d}r \int_0^{2\pi} \mathrm{d}\varphi \left\{ 1 - \exp\left[-i\beta_s \left(\arctan\frac{r\sin\varphi}{r\cos\varphi + x_t} - \varphi \right) \right] \right\}, \tag{5}$$

where ρ_s is the density of screw dislocations, $x_t \equiv |\mathbf{r}_{\|}-\mathbf{r}_{\|}'|$ and $\beta_s = \mathbf{h}.\mathbf{b}_s/(2\pi)$. The cut-off radius R_c ensures the convergence of this integral and it can be chosen as $R_c = 1/\sqrt{\rho_s}$ [13]. For symmetrical reflections in GaN (0001) is β_s an integer and integrals in Eq.(4) can be evaluated analytically.

Experimental Setup

Reciprocal space maps were measured by using high-resolution x-ray diffractometer X'Pert MRD (PANAnalytical). We used a Goebel mirror and 4-bounce symmetrical Bartels Ge220 monochromator in the incident beam and 3-bounce monochromator in the diffracted beam. CuKα_1 radiation was used for all measurements. The GaN/SiC (0001) sample was prepared

by metalloorganic vapor deposition epitaxy (MOVPE). The thickness of GaN layer was 200nm.

Symmetrical diffraction - experiment

Fig.1 shows a q_x-scan for the reflection 002. The solid line corresponds to a calculated intensity distribution for a screw threading dislocation density $\rho_s=6.9\cdot10^9$ cm^{-2}.

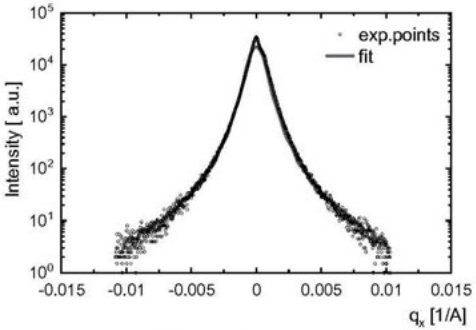

Figure 1. q_x scan measured for GaN/SiC thin film, symmetrical 002 reflection. Circles correspond to experimental data, straight line denotes fitting according to Eq.(1), concentration of screw threading dislocation was estimated to $\rho = 6.9\cdot10^9$ cm^{-2}.

Comparison of measured reciprocal space maps with calculated ones is shown in Figure 2. One can see that observed intensity distribution includes another contribution - from edge threading dislocation (if surface relaxation is neglected this contribution is equal to zero, **h.u**=0).

Asymmetric diffraction, screw dislocations

The displacement field **u(r)** is defined by expressions (see [14]):

$$u_x(\mathbf{r})=\frac{b_s}{2\pi}\frac{y}{R-z} \quad u_y(\mathbf{r})=-\frac{b_s}{2\pi}\frac{x}{R-z} \quad u_z(\mathbf{r})=\frac{b_s}{2\pi}\arctan\frac{y}{x}, \qquad (6)$$

where $R^2=x^2+y^2+z^2$, b_s is the length of the Burgers vector. The correlation function $T(|\mathbf{r}_{||}-\mathbf{r}_{||}'|;z,z')$ is defined by equation (2).

Asymmetric diffraction, edge dislocations

The displacement field **u(r)** is defined by expressions (surface relaxation is neglected):

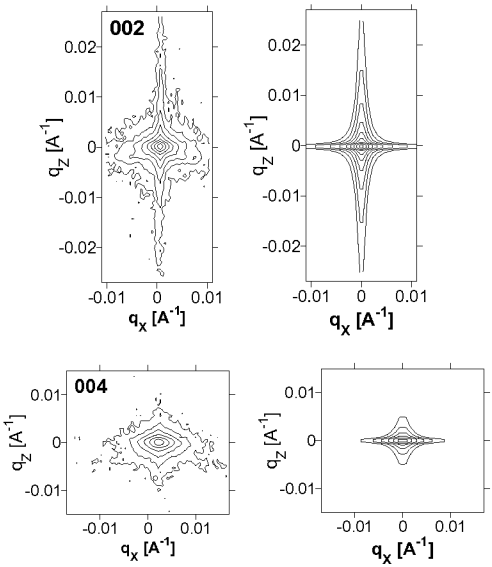

Figure 2. Reciprocal space maps of 002 diffraction measured (left up) and simulated (right up). At the bottom, the measured map (left) of 004 diffraction as well as simulated one (right) of GaN thin layer are shown. Contour lines denote calculated reciprocal space maps for $\rho = 6.9 \cdot 10^9$ cm^{-2}. *Maps are shown on logarithmic scale, step between iso-contour lines correspond to* $10^{0.5}$.

$$u_x(\mathrm{r}) = \frac{b_e}{2\pi}\left[\arctan\frac{y}{x} + \frac{xy}{2(1-\nu)(x^2+y^2)}\right]$$

$$u_y(\mathbf{r}) = -\frac{b_e}{2\pi}\left[\frac{1-2\nu}{4(1-\nu)}\ln(x^2+y^2) + \frac{x^2-y^2}{4(1-\nu)(x^2+y^2)}\right] \qquad (7)$$

$$u_z(\mathbf{r}) = 0\,,$$

where ν is Poisson ratio and b_e is the length of the Burgers vector of edge dislocation. In GaN, there are three symmetrical orientation of the Burgers vector $\mathbf{b}_e$. When computing the correlation function $T_e(|\mathbf{r}_{||}\text{-}\mathbf{r}_{||}\text{'}|;z,z\text{'})$ an averaging over different orientation of $\mathbf{b}_e$ is necessary. After this averaging the correlation function is defined by following formula:

$$T_e(\mathbf{r}_{||} - \mathbf{r}_{||}';z,z') = \rho_e \int \mathrm{d}^2\mathbf{r}_{||}\left(1 - J_0\left(\sqrt{A^2+B^2}\right)\right), \qquad (8)$$

where J_0 is the Bessel function and A and B are the coefficients defined by $\mathbf{u}(\mathbf{r})$. The correlation function is then given by sum of contributions from screw and edge threading dislocations,

$$T(\mathbf{r}_{\|}-\mathbf{r}_{\|}';z,z') = T_S(\mathbf{r}_{\|}-\mathbf{r}_{\|}';z,z') + T_e(\mathbf{r}_{\|}-\mathbf{r}_{\|}';z,z')\,. \tag{9}$$

The density of screw threading dislocation was determined from symmetrical diffraction 002. Figure 3 shows a q_x-scan of GaN thin layer for asymmetrical diffraction 114. The density of edge threading dislocations was determined from the fit, $\rho_e=2.5\cdot10^{12}$ cm^{-2}. Figure 4 shows measured (lef) and calculated (right) reciprocal space maps for the asymmetrical diffraction 114. We can see that the agreement between measured and calculated maps is as not good as for symmetrical reflections. This can be caused by the sample bowing (R~1m) or by neglectig the surface relaxation for displacement field for edge threading dislocations.

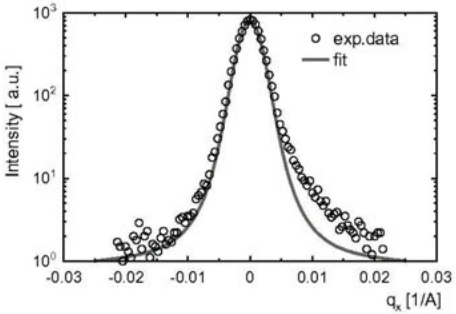

Figure 3. q_x scan of GaN/SiC thin film. Open circles mean measured data, straight line denotes the calculated intensity distribution for a screw dislocation density $\rho_s = 6.9\cdot10^9$ cm^{-2} and an edge threading dislocations density $\rho_e = 2.5\cdot10^{12}$ cm^{-2}.

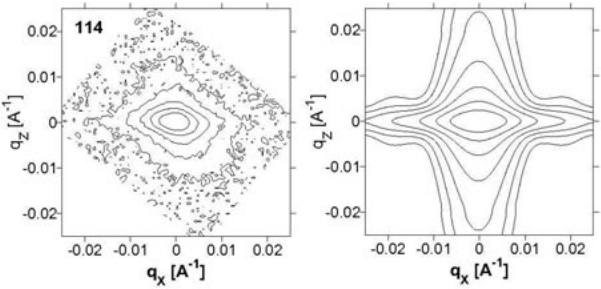

Figure 4. Measured (left) and calculated (right) reciprocal space maps of 114 diffraction. Screwand edge threading dislocation densities were determined from q_x scan ($\rho_s = 6.9\cdot10^9$ cm^{-2}, $\rho_e = 2.5\cdot10^{12}$ cm^{-2}), see Fig. 3. Maps are shown on logarithmic scale, step between iso-contour lines correspond to $10^{0.5}$.

Concluding remarks

The statistical theory of x-ray scattering from crystals with randomly distributed dislocations has been used for the description of diffuse x-ray scattering from screw and edge threading dislocations in GaN/SiC layer. The theoretical calculations are based on the deformation field of individual dislocations taking the surface relaxation of the internal stresses fully into account. In contrast to conventional approaches published previously [2, 13, 15], our exact theory predicts a non-Gaussian shape of the scattered intensity maxima. This fits much better to the experimental data and allows for a more precise determination both of the type as well as of the densities of dislocations.

References

1. For a recent review see e.g. S.C. Jain, M. Willander, J. Narayan, and R.V. Overstraeten, 2000, *J. Appl. Phys.* **87**, 965 and references therein.
2. T. Metzger, R. Hoepler, E. Born, O. Ambacher, M. Stutzmann, R. Stoemmer, M. Schuster, H. Goebel, S. Christiansen, M. Albrecht and H. P. Strunk, 1998, *Phil. Mag. A* **77**, 1013.
3. O. Ambacher, 1998, *J.Phys.D: Appl.Phys.* **31**, 2653.
4. S. D. Lester, F. A. Ponce, M. G. Crawford, and D. A.Steigerwald, 1995, *Appl. Phys. Lett.* **66**, 1249.
5. J. S. Speck and S. J. Rosner, 1999, *Physica* (Amsterdam) **273B/274B**, 24.
6. S. Kaiser, H. Preis, W. Gebhardt, O. Ambacher, H. Angerer, M. Stutzmann, A. Rosenauer, D. Gerthsen, 1998, *Jpn. J. Appl. Phys.* **37**, 84.
7. H.-J. Im, Y. Ding, J. P. Pelz, B. Heying, and J. S. Speck, 1998, *Phys.Rev. Lett.* **87**, 106802.
8. A. Krost, J. Blasing, M. Luneburger, H. Protzmann, and M. Heuken, 1999, *Appl. Phys. Lett.* **75**, 689.
9. B. Heying, X. H. Wu, S. Keller, Y. Li, D. Kappolnek, B. P. Keller, S. P. Denbaars, and J. S. Speck, 1996, *Appl. Phys. Lett.* **68**, 643.
10. H. Heinke, V. Kirchner, S. Einfeldt, and D. Hommel, 2000, *Appl. Phys. Lett.* **77**, 2145.
11. M. A. Tagliente, L. De Caro, L. Tapfer, P. Waltereit, O. Brandt, and K.-H. Ploog, 2002, *J. Appl. Phys.* **92**, 70.
12. Z. Zhong, O. Ambacher, A. Link, V. Holý, J. Stangl, R. T. Lechner, T. Roch, and G. Bauer, 2002, *Appl. Phys. Lett.* **80**, 3521.
13. M. A. Krivoglaz, 1996, *X-Ray and Neutron Diffraction in Nonideal Crystals*, (Springer Berlin, Heidelberg, New York).
14. S. J. Shaibani and P. M. Hazzledine, 1981, *Phil. Mag. A* **44**, 657.
15. P. Gay, P. B. Hirsch and A. Kelly, *Acta Metall.*, 1953, **1**, 315.

Acknowledgements. This work is a part of the research plan MSM 0021620834 financed by the Ministry of Education of the Czech Republic. The partial financial support by the Grant Agency of Czech Republic (project No. 202/04/P258) is gratefully appreciated. GaN/SiC sample was kindly provided by O. Ambacher (TU Ilmenau, Germany)."

Z. Kristallogr. Suppl. **23** (2006) 147-154

Test of applicability of some powder diffraction tools to nanocrystals

Z. Kaszkur[1,*]

[1]Institute of Physical Chemistry PAS, Kasprzaka 44/52, Warszawa 01-224, Poland.
[*]Contact author; e-mail: zbig@ichf.edu.pl

Keywords: nanocrystals, Bragg law, Warren-Averbach method, atomistic simulation, Williamson-Hall, full profile analysis

Abstract. The paper is focused on showing systematic difficulties involved in structure analysis of nanocrystals using diffraction, caused by two factors characteristic for nanocrystals: disobeying of the Bragg law and dependence of lattice constant from the crystallite size. Although the effect on estimations via Scherrer equation may be considered negligible the Warren-Averbach analysis can be seriously affected as well as the results of a full profile analysis.

Introduction

The worldwide policy oriented on nanotechnology and nanomaterials results in growing number of publications using diffraction methods to discuss structural features of nanocrystals. There are however two fundamental problems that may modify interpretation of the results of this research but are not commonly acknowledged. One of them is the phenomenon that small nanocrystals no longer obey the Bragg law precisely and shift of the diffraction peaks position grows the smaller the nanocrystal.
The second phenomenon gains experimental evidence and for some class of materials is already established, but its consequences are not realised. It is the observation that the lattice constant of small nanocrystals depends on their size. This effect was theoretically suggested by Pauling and found many literature observations e.g. for transition and alkali metals. For other nanoparticles the length of bonds can be expected to increasingly depend on the state of their surface. Both effects are usually not considered as a factor affecting interpretation of various powder diffraction techniques.
The objective of this work is to test some of these diffraction techniques using diffraction patterns calculated for energy relaxed nanocrystals and their size distributions. The calculated patterns based on realistic atomistic models, with all atom positions known, offer unique possibility to test analytical methods which in the case of nanocrystals are always approximate. The models used were closed shell palladium cubooctahedra and their log-normal volume distributions relaxed with Sutton & Chen n-body potentials.

Nanocrystallinity -structural features

The principal properties of nanocrystals relevant to diffraction and discussed here concern two phenomena. One of them is the observation that nanoclusters of different size are characterised by different average lattice constant determined from the position of several diffraction maxima. The other is that those different diffraction maxima do not point to one consistent lattice constant when the Bragg law is applied. This shows that the Bragg law in the case of nanocrystals becomes only approximate. Both phenomena can be used for experimental characterization of nanoclusters and deserve close examination. They are presented below on examples of patterns of palladium nanoclusters modelled with use of the n-body Sutton-Chen potentials[1]. The patterns were computed via the Debye formula. The models used were a lognormal volume distribution of regular Pd cubooctahedra, bimodal lognormal distribution and some single closed shell cubooctahedra. The relaxation leads to contraction of the outer layer of the clusters and formation of a stress free strain. This effect was tested on a single-crystal models with several faces exposed and found to agree with experiment [2]. For nanocrystalline Pd particles the magnitude of contraction was tested experimentally measuring peak shift on oxygen chemisorption [3,4].

Peak position dependence on cluster size

Diffraction peak position while decreasing the crystallite size can be affected in a number of ways. One effect is due to increasing width of the diffraction profiles and, as the profile theoretically is multiplied by atomic factor function steeply decreasing with scattering angle, the peak maximum is shifted towards lower angles, the more, the smaller the crystallite. The second factor affecting peak position may be attributed to cluster surface relaxation with increased role of the surface atoms when decreasing the crystallite size. The third and sometimes not realised factor is the change of peak position with crystallite size related only to a limited length Fourier series, thus observed for crystallites being small fragment of ideal periodic lattice (non relaxed).

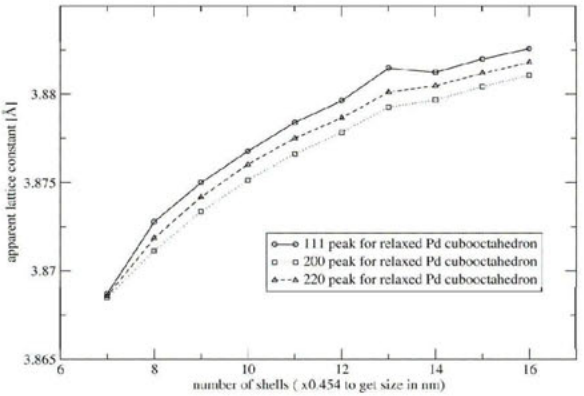

Figure 1. Lattice constant of relaxed, closed shell Pd cubooctahedra as measured from reflections of a calculated pattern. The bulk lattice constant used a=3.89 Å.

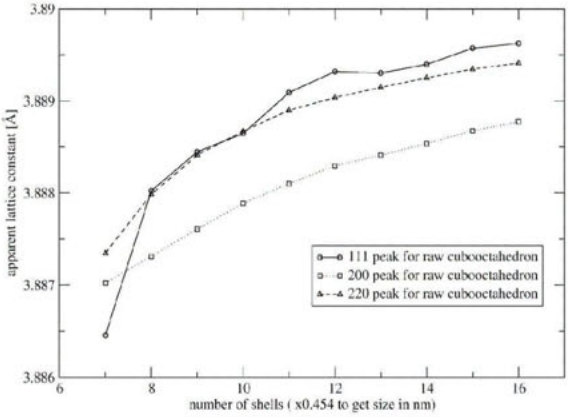

Figure 2. Lattice constant of raw, closed shell Pd cubooctahedra as measured from reflections of a calculated pattern. The bulk lattice constant used a=3.89 Å.

To avoid the first, easiest to account factor, the peak positions further analysed were determined by fitting analytical profile (Pearson VII) to the pattern intensity divided by square of atomic factor function and multiplied by square sine of the scattering angle. This choice of analysed function follows analysis of Warren [5]. Figure 1 shows the lattice constant of Pd nanocrystals relaxed with Sutton-Chen potentials as determined from 111, 200 and 220 reflections. To show that the lattice constant *a* as obtained from the Bragg law and diffraction peak position for nanocrystals does not correspond to the real interatomic distances, figure 2 displays *a* versus cluster size for three first fcc reflections. The analysed patterns were calculated for raw models i.e. the cubooctahedra were fragments of ideal fcc lattice with the same interatomic distances.

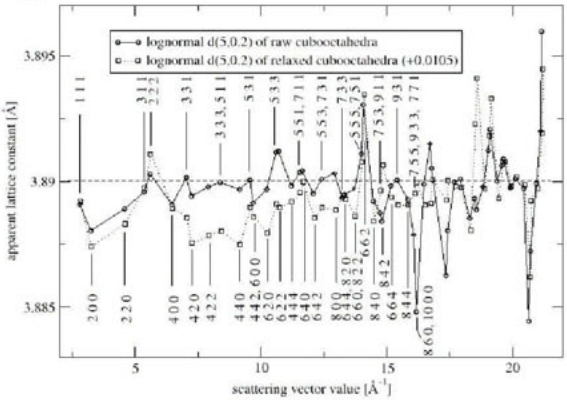

Figure 3. Lattice constant for size distribution of raw and relaxed, closed shell Pd cubooctahedra as measured from reflections of a calculated pattern. The dotted horizontal line marks the value of lattice constant accepted for the potential. Note the shift of diagram for the relaxed model by 0.0105Å.

Disobeying of the Bragg law

The Bragg law applied to diffraction maxima corresponding to different Miller indices results for nanocrystals in different lattice constant and the spread of its value increase the smaller the crystallite. The example of this spread gives figure 3 for the calculated pattern from a lognormal volume distribution of relaxed cubooctahedra, centred on 5nm with dispersion 0.2. The Miller indices of the peaks corresponding to the data points are given for the lower angle part. The diagram shows more subtle variation than that caused by high pressure in nanocrystalline diamond and explained in [6] by a core-shell non energy-relaxed model. The observed variation of the apparent lattice constant (ALP) is difficult to explain structurally. It is evident that the ALP versus k vector length for the relaxed model is shifted down from that for the raw model by 0.0105Å and the values are even less in the range 7-14$Å^{-1}$. The general impression that the odd Miller indices peaks (including multiplicities) give slightly greater ALP than the even ones is confirmed only statistically.

Effect of nanocrystalinity on the results of powder diffraction analysis.

Effect on the Scherrer method

For nanocrystals like for polycrystals the peak width may be affected by the cluster order and increasing disorder may lead to underestimation of the cluster size down to 1.5 nm for amorphous clusters [3]. For well ordered nanocrystallites however the dependence of peak position on cluster size may cause additional peak broadening when a cluster size distribution is considered. Trying to estimate its magnitude we can assume small clusters for which the peak shift effect is considerable. For 3nm Pd crystallites assuming as the least favourable scenario, that some clusters are relaxed and some, for some reason have saturated surface bonds (e.g. via oxygen chemisorption) the additional broadening of 111 peak that should be observed causes 7% error in size estimation (comp. figure 1 and 2). This effect may be noticeable in comparative study but usually has no practical importance.

Effect on the Warren-Averbach analysis of size and strain

The theory behind the Warren-Averbach method of size and strain broadening separation [5] does not account for the dependence of the lattice constant on the cluster size. Of great importance is also fact that the true interatomic spacing for nanocrystals is not determined by the peak position. This results in strain distribution that may have semi-Gaussian shape but it centroid is shifted from zero because the strain related atom shifts are considered relative to wrong, determined from the peak position, lattice spacing [7]. The detailed analysis of the errors involved is given elsewhere [7].

These principal difficulties of the W-A method may be illustrated by a simple test. Having precise model at our disposal we can calculate ab initio both: column length distribution and strain distribution. From these data by the inverse Fourier Transform we can calculate the peak shape and compare it with the originally calculated via the Debye formula pattern. Such test for a single nanocrystal (uniform model) shows a perfect fit [7]. If however the size distribution is considered, both compared peaks disagree and the misfit is mainly due to the fact that the peak broadening originating from the spread of lattice constant is in W-A theory attributed to strain because it contribution changes with scattering angle proportionally to

tg(θ) [7]. This results in wrong strain term that differs substantially from the one calculated ab initio from the model.

For noticable lattice parameter differences the strain determination is heavily affected and its analysis via W-A method is impossible. A relatively narrow mono-modal size distribution on the other hand, could be well determined in W-A analysis [7] that is illustrated in figure 4.

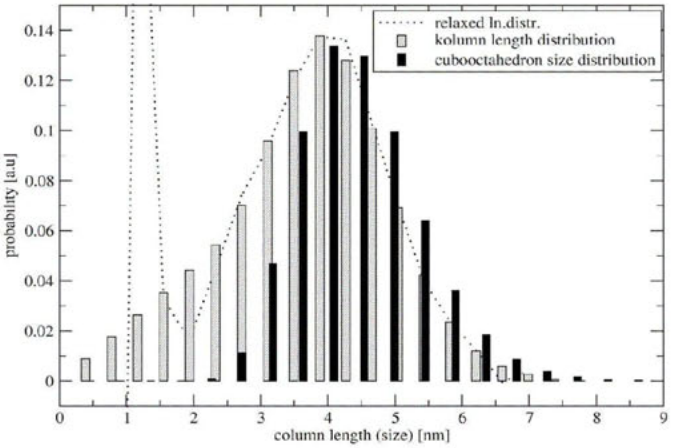

Figure 4. The model size and column length distribution compared to the distribution recovered via the experimental-like peak shape analysis for monomodal Pd size distribution.

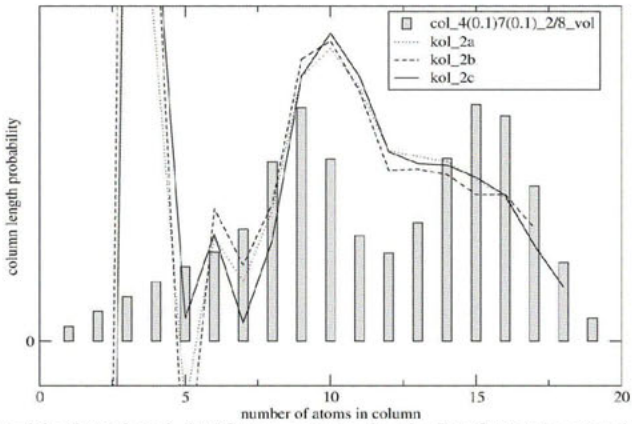

Figure 5. The model column length distribution compared to the distribution recovered via the experimental-like peak shape analysis and various methods of background estimation for bimodal Pd size distribution.

The well visible error for small column length arises from a substantial difficulty of background estimation in the case of nanocrystalline pattern resulting in so called Hook effect.
A similar experimental-like determination of a column length distribution from the calculated pattern for a bimodal size distribution (figure 5) results already in significant errors and these errors are inherent to the method [7]. Substantial errors are expected also in the case of a broad cluster size distributions. They origin from rewriting of the size Fourier coefficient terms and the simple Bertaut interpretation [8] cannot be simply used.

Effect on the Williamson-Hall plot analysis

A simple form of the Williamson-Hall plot drawn for the presented in figure 4 size distribution for relaxed and raw cubooctahedra is shown in figure 6. Analysis of the FWHM of the peaks shows clearly an appearance of a stress free strain term for the relaxed cubooctahedra. The integral peak width analysis suggests zero dislocation density in agreement with the model. The obtained from the analysis average crystallite size is slightly in error. The original lognormal distribution was centred at 5nm with dispersion 0.2. The estimated from the model surface weighted size was 4.62 nm and the volume weighted size 4.71 nm.

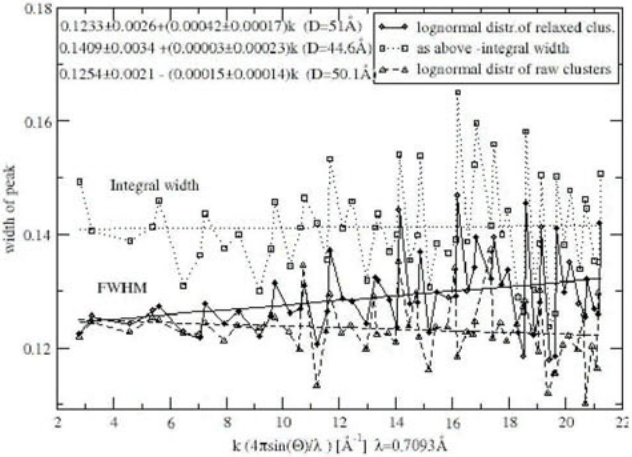

Figure 6. Williamson-Hall plot for the calculated diffraction pattern of the size distribution of relaxed cubooctahedra.

The determined peak width error is difficult to estimate but is considerably smaller than the observed scatter of points. This suggests systematic effects that may include strain and stress anisotropy but are not limited to these factors.

Effect on the full profile analysis

Principal features of nanocrystals that may severely affect results of any full profile fit include :(i) disobeying of the Bragg law, (ii) appearance of asymmetry and broadening related to spread of lattice constant, (iii) appearance of non crystallographic forms (icosahedra, dodecahedra), (iiii) non applicability of the Debye-Waller description of temperature effect. The first factor (i) causes a least square minimisation routine to wander in a parameter space at a distance from the maximum convergence area making it sensitive to local non-physical

minima. The second (ii), may be responsible for a difficult to express analytically peak shape.

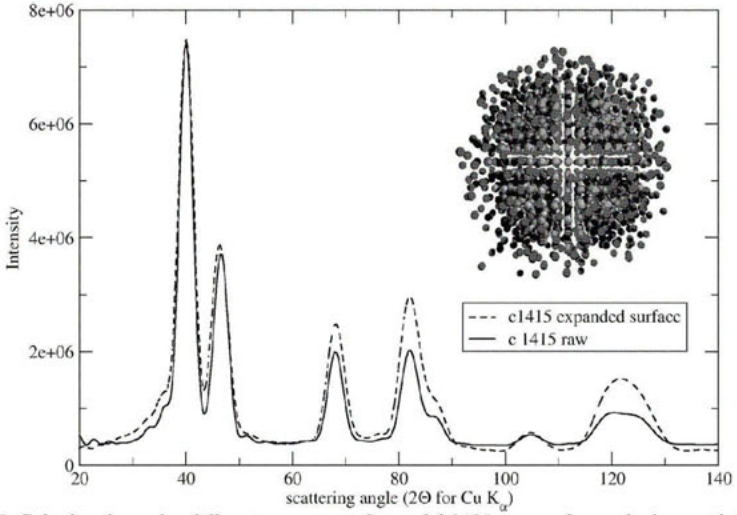

Figure 7. Calculated powder diffraction pattern of a model 1415 atom cubooctahedron with its surface expanded imitating formation of a surface compound.

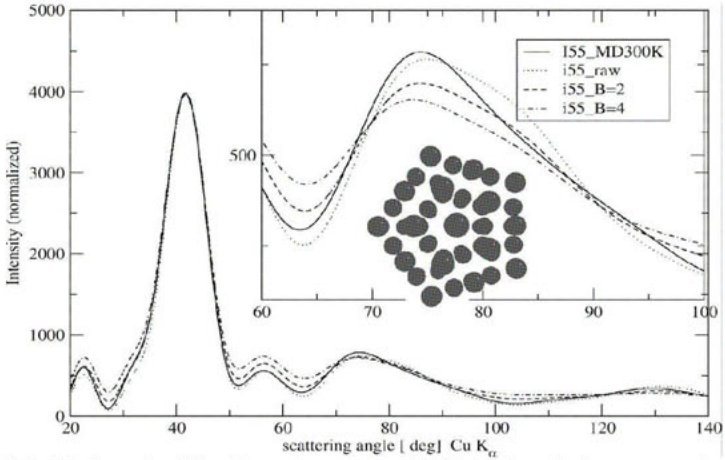

Figure 8. Calculated powder diffraction pattern of a model 55 atom icosahedron averaged over MD run at 300K compared to raw 55 atom icosahedron pattern with different Debye-Waller factors applied.

The factors (iii) and (iiii) reflect fundamental problems of various least square routines attempting to fit an experimental pattern to sum of patterns of various more or less arbitrary models. Such procedures are however sensitive to the initial choice of possible models and any choice limits the natural richness of the nano-world occurring due to large surface inter-

acting with varying environment. As an example figure 7 presents diffraction pattern of the Pd cluster model with surface roughened like in formation of a surface non ordered compound. It may be e.g. similar to the effect of formation of subsurface oxide with only strong scatterers – Pd atoms shown. The characteristic asymmetric broadening observed would be difficult to describe otherwise.

To illustrate that the Debye-Waller description of the temperature effect may be insufficient for nanocrystals as composed in large part of surface atoms oscillating thermally differently than the bulk atoms, figure 8 displays calculated powder diffraction pattern of 55 atom icosahedron that was averaged over molecular dynamics run at temperature 300K. This pattern is compared to that of ideal icosahedron with different temperature factors included via the Debye-Waller scheme. The maximum at 70-90 deg. evidently can not be fitted to ideal icosahedron model.

The above mentioned phenomena causing difficulty in correct description of the diffraction pattern may wrongly direct convergence of any least square procedure employed in a full profile analysis.

References

1. Sutton, A.P., Chen, J., 1990, *Philos. Mag. Lett.*, **61**, 139.
2. Kaszkur, Z., Mierzwa, B., 1998, *Philos.Mag. A.*, **77**, 781.
3. Kaszkur, Z., 2000, *J.Appl.Cryst.*, **33**, 87.
4. Kaszkur, Z., 2000, *J.Appl.Cryst.*, **33**, 1262.
5. Warren, B.E., 1969, *X-Ray Diffraction*, (Reading, Massachusetts: Addison-Wesley), pp. 251-275.
6. Pałosz, B., Grzanka, E., Gierlotka, S., Stel'makh, S., Pielaszek, R., Bismayer, U.,Neuefeind, J., Weber, H.-P., Proffen, T.H., Von Dreele, R., Pałosz, W., 2002, Z.Kristallogr., **217**, 497.
7. Kaszkur, Z., Mierzwa, B., Pielaszek, J., 2005, *J.Appl.Cryst.*, accepted.
8. Bertaut, E.F., 1950, *Acta Cryst.*, **3**, 14.

Acknowledgements. The work was financially supported by the State Committee for Scientific Research grant no.4 T09A 180 24.

Z. Kristallogr. Suppl. **23** (2006) 155-160

Influence of coherent connection of crystalline blocks on the diffraction pattern of nanostructured materials

S.V. Cherepanova*, S.V. Tsybulya

Boreskov Institute of Catalysis, Lavrentieva 5, Novosibirsk, 630090 Russia
*Contact author; e-mail: svch@catalysis.nsk.su

Keywords: powder diffraction, nanostructured materials, diffuse scattering, 1D disordered crystal model, X-ray diffraction patterns simulation

Abstract. The diffraction effects such as anisotropic broadening of diffraction peaks, their splitting to the relatively broad and narrow components, their shifts and/or the appearance of new ones can result from a coherent connection of nanoblocks. These effects can be mistakenly ascribed to size or strain anisotropy, bimodal size distribution, change in lattice constants and/or the presence of additional phases correspondingly. Developed software [1,2] provides correct interpretation of the peculiarities of the X-ray diffraction patterns of materials containing planar defects arising from coherent connection of nanoblocks, that is illustrated by several examples. For 1D nanostructured materials, the type and the concentration of the planar defects can be determined on the basis of fitting of the whole pattern. If the microstructure is modulated in more than one direction, only single diffraction peaks can be analysed using the model of 1D disordered crystal.

Introduction

Materials, which are composed of nanoblocks coherently attached to each other, represent a broad class of nanostructured solids. Usually they refer to 1D nanostructures, but 2D and 3D are also possible in some cases.

The former materials are composed of plate-like blocks of nanosized thickness. In this case blocks are always coherently connected. Among 1D nanostructures one can distinguish three types of systems consisting of blocks which have *i*) the same structure and composition, *ii*) the same composition but different structure, *iii*) different composition. Earlier [1,2] we analysed peculiarities of diffraction patterns of 1D nanostructures which are coherent systems with the blocks of the same composition but different in structure. In this paper, we present some results of the investigation of the α-Fe_2O_3 sample built up of the plate-like blocks of the same structure and composition. Blocks are separated by antiphase boundaries.

In its turn, 2D and 3D nanostructures don't imply coherent connection of blocks in common case. Studies of γ-Al_2O_3 and η-Al_2O_3 samples revealed that they consist of nanoblocks coherently attached to each other in several directions. The proposed mechanism of

formation of such nanostructures is vacancy ordering along crystallographic planes in non-stoichiometric oxides.
Coherent connection of the blocks, as well as other types of planar defects inherent to nanomaterials, cause the diffuse scattering in the vicinity of Bragg maxima (that is usually described as broadening of the peaks, their shifts and splitting) and/or in background region (appearance of diffuse peaks or halo). Analysis of the diffraction effects was carried out with the use of developed software [1,2], which makes it possible to simulate X-ray diffraction pattern including diffuse scattering. Since calculations are performed on the base of 1D disordered crystal model, the method is well suitable for the investigation of materials with different types of planar defects lying in one direction. For such materials good correspondence between simulated and experimental diffraction patterns can be achieved. Nanostructured materials with microstructures modulated in more than one direction can be also studied with the method, but mainly qualitatively. The 1D disordered crystal model doesn't take into consideration the planar defects lying in several directions simultaneously. Only one system of planar defects can be examined in one calculation. Nevertheless the main diffraction peculiarities can be revealed by successive analysis of influence of all possible defects.
The HREM data for all samples under study were published earlier [3-5].

Influence of antiphase boundaries

In the oxide systems planar defects such as antiphase boundaries shifting cation layers and keeping anion ones *can cause anisotropic broadening of diffraction lines*. We observed such a diffraction effect on the diffraction patterns of synthetic α-Fe_2O_3 prepared by thermal decomposition of goethite at 400 °C during 4 hours with following calcination up to 1100 °C. Figure 1 shows dependence of FWHM on 2Θ for α-Fe_2O_3 sample calcinated at 500 °C. The diffraction peaks can be sorted into two groups: relatively broad and narrow peaks. One can see that 012 diffraction peak is broader than 036 one. So the diffraction phenomenon couldn't be explained by size or strain effects.
HREM reveals the presence of planar defects along (001) plane [3]. In the paper [3] these defects were regarded as random shifts of plate-like blocks. We argue the presence of antiphase boundaries, which are caused by $(001)\frac{a}{3}<120>$ shift, which keep oxide sublattice. It is evident from comparison between diffraction patterns simulated for perfect crystal of corundum type structure (figure 2a) and crystal containing antiphase boundaries along (001) planes (figure 2b), that such defects don't influence on diffraction lines for which $|h-k|$ is divisible by 3. At the same time, other diffraction lines become broader in the presence of antiphase boundaries. Since planar defects are situated in one direction, good correspondence between simulated and diffraction patterns has been achieved at definite concentration of antiphase boundaries (figure 2b, 2d)

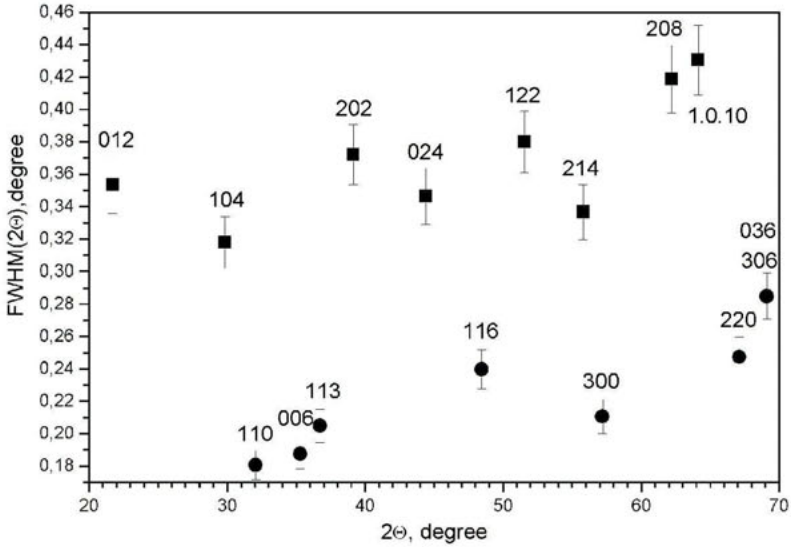

Figure 1. FWHM of diffraction peaks of α-Fe_2O_3. Relatively broad peaks (squares); relatively narrow peaks (circles).

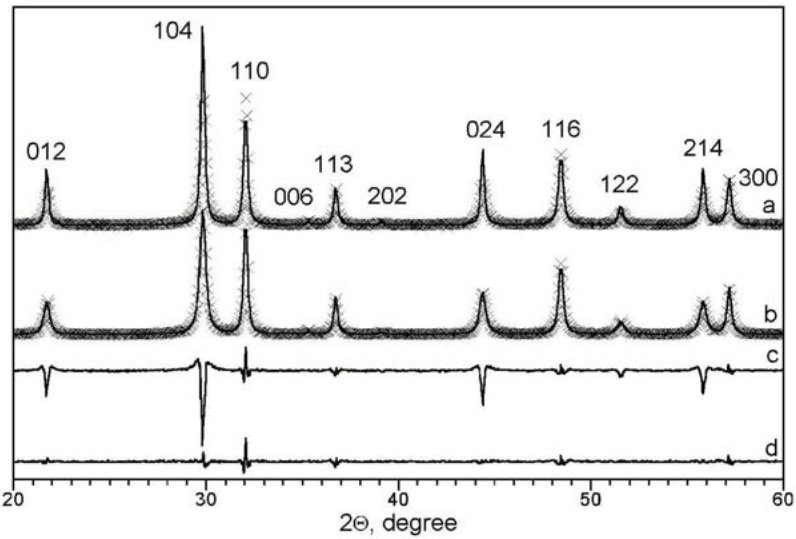

Figure 2. a) experimental data (cross) and diffraction pattern simulated for perfect crystal of corundum type structure (line); b) experimental data (cross) and diffraction pattern simulated for crystal containing 3% of antiphase boundaries (line); c) difference curve for a; d) difference curve for b.

Planar defects introducing additional anisotropy in crystal

In the previous case planar defects don't introduce additional anisotropy in crystal, because they are in a [001] direction which is singled out in hexagonal crystal. If planar defects are situated in one of the several equivalent crystallographic directions they can induce *splitting of diffraction lines on relatively broad and narrow components.* For example, planar defects situated in one of the four <111> directions in cubic crystal causes broadening of six peak components from eight whereas two components are kept without changes. One can see such 111 peak splitting on the X-ray diffraction pattern of η-Al_2O_3 prepared by thermal dehydration of bayerite (figure 3). This diffraction effect could be ascribed to bimodal particle size distribution, but 222 peak is not split.

HREM reveals that sample of η-Al_2O_3 consists of plate-like parallelogram blocks coherently attached to each other [4]. Each block is cut by two {110} planes and by one {111} plane, which is developed. Our program doesn't allow taking into account planar defects in three directions simultaneously. But we have the possibility to analyse the influence of planar defects in each direction step by step. For example, our simulations show, that antiphase boundaries along the {111} planes, which are caused by shift on the vector of half dislocation $\{111\}\frac{a}{4}<110>$, lead to splitting of the 111 peak, but don't influence the 222 peak. Diffraction pattern calculated in the range of 111 peak for the model containing 20 % of antiphase boundaries is given in comparison with the experimental one on the figure 3b.

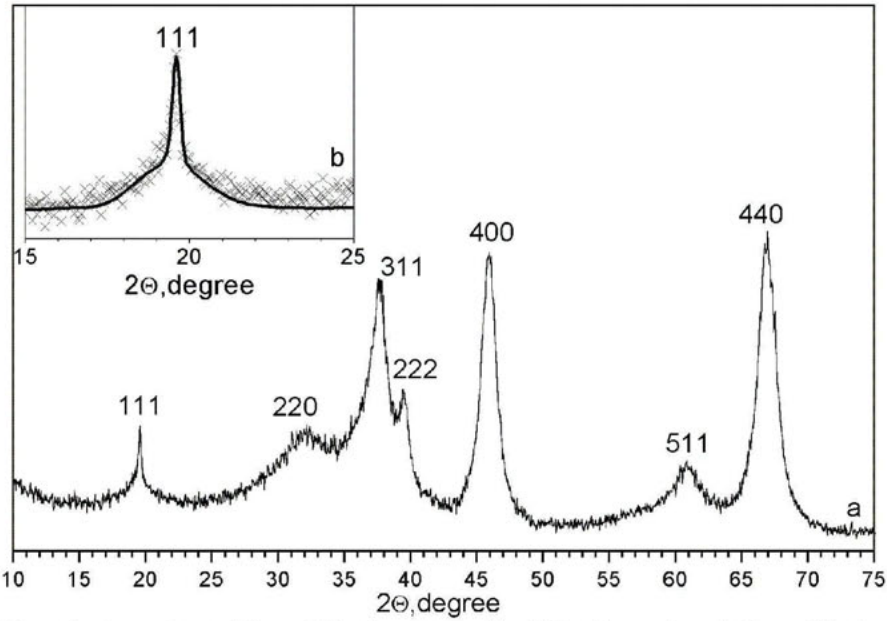

Figure 3. a) experimental X-ray diffraction pattern of η-Al_2O_3; b) experimental X-ray diffraction pattern in the range of 111 peak (cross) and simulated one (line).

High concentration of planar defects randomly distributed in particle

High concentration of planar defects randomly distributed in particle can cause *appearance of asymmetric hk peaks due to diffuse scattering concentration in the positions of present or absent hk0 reflections*. Such peaks appear as a result of loss of periodicity in one direction. Turbostratic carbon, which structure is characterised by random shifts of graphite layers, can be considered as structure with high concentration (100%) of planar defects. Simulation of X-ray scattering shows that only *00l* peaks and asymmetric diffuse *hk* ones present on the XRD pattern of turbostratic structure [1, 2].

In some cases, appearance of *hk* peaks near diffraction lines can cause the *apparent shift of these lines*. In particular, this is observed on the γ-Al_2O_3 diffraction patterns where 311 peak is shifted to smaller angles. The shift is about 0.3°. The γ-Al_2O_3 sample prepared by thermal dehydration of boehmite is characterised by a high concentration of planar defects [5]. HREM reveals that sample of γ-Al_2O_3 consists of plate-like blocks of hexagonal prism shape predominately. Each block is cut by two {111} planes, one {100} and {110} planes. Blocks are also coherently attached to each other. We systematically analysed the influence of planar defects situated along {100}, {110} and {111} planes in spinel type structure on the position of 311 peak. Simulations show that a high concentration of planar defects, which are

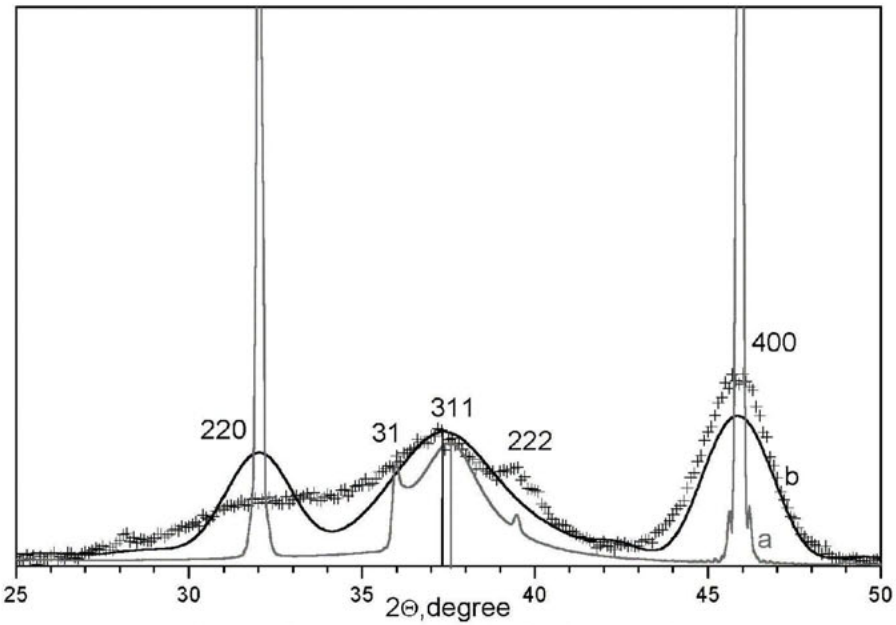

Figure 4. Experimental X-ray diffraction pattern of γ-Al_2O_3 (cross); X-ray diffraction patterns simulated for spinel-type structure model containing 20 % of planar defects (line): a) particle size D_{CSD}=50 nm; b) D_{CSD}=10 nm.

caused by a shift on the vector of half dislocation $\{100\}\frac{a}{2}<100>$, leads to the appearance of 31 peak in the 310 position whereas reduced 311 peak are still present on the simulated diffraction pattern (figure 4a). The 31 peak is noticeable on the diffraction pattern simulated for particle size of 50 nm. When sizes of particles are small enough, 31 and 311 peaks became unresolved, which leads to an apparent shift of the 311 peak towards smaller angles, whereas positions of other peaks are kept without changes (figure 4b).

Conclusions

We discussed very briefly the problem of interpretation of diffraction patterns of nanostructured materials with coherent connections of crystalline blocks. Diffraction patterns of such nanostructured materials could not be calculated on the basis of the model of 3D periodic crystallite of definite shape and size, since diffuse scattering is considerable in addition to Bragg diffraction. These effects practically aren't analysed in the literature, while experiments give many examples of coherent connection of crystalline blocks not only in 1D nanostructures, but also in 2D and 3D ones.

References

1. Tsybulya, S.V., Cherepanova, S.V. & Kryukova G.N., 2004, in *Diffraction Analysis of the Microstructure of Materials*, edited by E.J. Mittemeijer & P. Scardi (Berlin: Springer), pp. 93-124.
2. Cherepanova, S.V. & Tsybulya, S.V., 2004, in Proceedings of EPDIC 8, edited by Y.Andersson, E.J.Mittemeijer & U.Welzel (Switzerland: TTP Ltd), pp.87-90.
3. Kryukova, G.N., Tsybulya ,S.V., Solovyeva, L.P, Sadykov, V.A. & Andrianova M.P., 1991, *Mater. Sci. Engineering* A, **149**, 121.
4. Kul'ko, E.V., Ivanova, A.S., Litvak, G.S., Kryukova, G.N. & Tsybulya, S.V., 2004, *Kinetics and Catalysis*, **45**.
5. Kryukova, G.N., Klenov, D.O., Ivanova, A.S. & Tsybulya, S.V., 2000, *J. European Ceramic Society*, **20**, 1187.

Acknowledgements. This study was supported by the Russian Foundation of Basic Research, grants No. 04-03-32346 and No. 05-02-16070.

I.4 Texture

Z. Kristallogr. Suppl. **23** (2006) 163-168

Automated Crystal Orientation Measurement by backscatter Kikuchi diffraction

Robert A. Schwarzer

Dept. of Physics, Clausthal University of Technology, D-38678 Clausthal-Z., Germany
*Contact author; e-mail: Schwarzer@tu-clausthal.de

Keywords: Automated Crystal Orientation Measurements, EBSD

Abstract
A short introduction to automated individual grain orientation measurement on bulk surfaces by evaluating backscatter Kikuchi patterns in the SEM is given.

Introduction

*A*utomated *C*rystal *O*rientation *M*easurement (*ACOM*) by *B*ackscatter *K*ikuchi *D*iffraction (*BKD*) in the SEM, also named "*Automated EBSD*", has become an invaluable tool of materials science and geology during the last decade [1]. Automated EBSD is now widely accepted since it enables crystallography of small grains in the surface of bulk specimens to be studied in the SEM in a much easier and efficient way than was previously possible by the acquisition of electron spot and channeling patterns in transmission or reflection electron diffraction. ACOM is performed in the SEM by digitally scanning the beam spot across the specimen, acquiring and transferring one backscatter Kikuchi pattern after the other to the computer, indexing it and calculating the crystal orientation of the grain under the beam spot. Spatial resolution is in the range of <0.05 μm, accuracy of orientation measurement is limited to about 0.5°, and speed is between 30.000 and 200.000 orientations per hour, depending on the hardware. If intragranular structure is of no concern, it is sufficient to acquire the orientation of each grain only once, and iterative mesh refinement [2] has proven very effective by concentrating measurement along grain boundaries. Mesh refinement is inadequate if the microstructure contains twinned grains or if a broad grain size distribution is present.
The principal objectives of ACOM are a quantitative description of the microstructure of selected areas on *bulk surfaces* in a short time on a grain-specific level by the determination of quantitative, statistically significant data sets of crystal orientations, misorientations, the CSL character of grain boundaries (Σ), local crystal texture (pole figures, ODF, MODF, OCF) and derived entities, phase discrimination [3] when possible phases in a sample are supposed, and phase identification [4] when only the element composition but not the crystal lattice of the material under the beam is known. As a further characteristics, the *crystallographic direction* of the grain boundary normal **n** can be determined by measuring the spatial inclination of the

grain boundary plane, e.g. by serial sectioning. A survey over this technique and many typical applications are described in a recent book [5] that summarizes the contributions to a dedicated meeting in St. Louis (MO) in 2000.
The grain orientations are commonly depicted in pseudo-colors on the scanning grid to form *C*rystal *O*rientation *M*aps (*COM*) [6] which represent "images" of the microstructure with the advantage of providing quantitative orientation contrast. In a similar way, misorientations across grain boundaries, Σ values of grain boundaries, or other microstructural characteristics and derived entities are visualized by staining the grains in the micrograph with specific colors. All grain boundaries exceeding some tenth of a degree are identified. Stereological as well as orientation data, as sensitive indicators of the production process, are readily available. ACOM thus enables a major progress in the quantitative characterization of microstructure. Orientation contrast in conventional microscopy, on the other hand, relies on various mechanisms of contrast formation which are related to lattice orientation gradients, but in rather complex ways. BKD is steadily replacing bulk X-ray techniques in the analysis of crystal texture, due to the wide availability of SEM and commercial EBSD systems and the wealth of microstructural information on a mesoscale that is not so easily obtained with any other technique. The importance of knowing crystal texture is due to the fact that most natural and man-made materials consist of polycrystalline solids and important material properties depend on the orientation as well as the misorientation distributions of the grains constituting the polycrystal.

Details of the technique

High energy electrons are strongly forward scattered when impinging on a bulk surface. Therefore, the specimen surface has to be steeply inclined in the SEM at typically 20° to 30° to the beam, in order to produce a BKD of sufficient intensity. This high specimen tilt has several unfavorable consequences on digital beam scanning methods:

1. The diffraction geometry, in particular the position of the pattern center (which marks one of the reference directions of the orientation frame) and the distance from beam spot to screen ("camera length"), changes from one scanning step to the next.
2. The beam spot runs out of focus when scanning down the tilted specimen line after line.
3. Short working distances on which the microscope lenses have been optimized for obtaining a high resolution and high beam currents cannot be used, if large specimens have to be accommodated in the chamber.
4. The beam spot on the specimen as well as the crystal orientation maps and conventional SEM images, when taken at the same steep specimen tilt, are heavily foreshortened. Spatial resolution in x- and y-direction differ by about a factor of 3.
5. The rectangular scan field is distorted to a trapezoid on the inclined specimen surface, if the x-direction of the scan and the tilt axis of the specimen are not precisely aligned. When dynamic focusing is engaged at low magnification, scan field rotation, as well, has to be controlled by the software to correct for image rotation of the magnetic objective lens of the SEM as a function of the focus setting.
6. Standard secondary electron and backscatter electron detectors for image acquisition are not well suited since the signal height is modulated with the distance between the beam spot and the detector.
7. A steep specimen tilt is incompatible with most quantitative EDS programs which is an obstacle to simultaneous element analysis and crystal orientation measurement.

The software of an advanced EBSD system must account for the first difficulties. In addition to driving the digital beam scan, software has to control, as a function of the beam spot position at all magnifications and working distances, the automated "on-the-fly" calibration of both the position of the pattern center and the beam spot-to-screen distance, as well as dynamic focusing of the probe-forming lens [7]. Otherwise errors in calculated grain orientations may exceed several degrees or indexing may even fail, in particular at low magnifications. For that purpose, the SEM has to be operated under full ACOM software control (figure 1) which comprises the setting of the final-lens current, control of camera operation and synchronization of pattern acquisition, reading the actual microscope magnification and accelerating voltage, and - unless the pattern background is not modeled - control of the digital signal processor and modes of SEM operation to switch between imaging and spot mode for the automated acquisition of flat images. A simple test on the accuracy of automated system calibration can be made by measuring across a large field on a single crystal and checking the uniformity of orientation data.

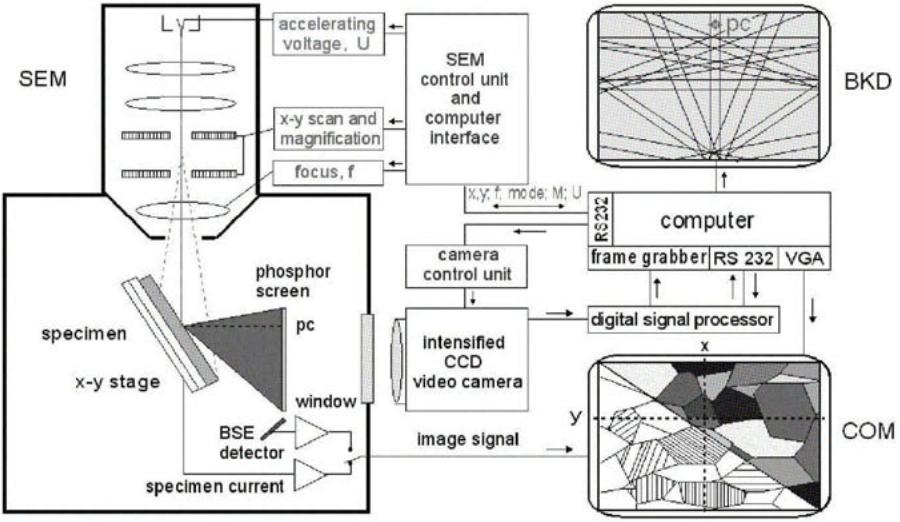

Figure 1. Schematic set-up of an advanced EBSD system. The SEM is under full control of the ACOM software to enable dynamic focusing, system calibration and background correction "on the fly".

The geometry of a Kikuchi pattern is unique for the crystal structure and the crystal lattice orientation of the grain under the beam, and the crispness of the pattern, called "*P*attern *Q*uality" (PQ), is an indication of the perfection of the diffracting crystal volume. It is sufficient for indexing to know the *positions and widths* of some bands in the pattern. The geometrical features of a pattern are extracted by automated pattern recognition. In a first step, the intense background is modelled and stripped off. A Radon transformation of the Kikuchi pattern, followed by a profile analysis of the Radon peaks by constraints and verification by an artificial neural network (ANN), yield the positions and widths of the dominant bands in the pattern [8]. This approach is more flexible and faster than the extraction of band positions

by the usual cross-correlation process with butterfly-shaped filter masks applied on Hough transformed patterns [9, 10], whereas line filtering, gradient or contour tracing methods, as common tools in binary pattern recognition, are not well suited since Kikuchi bands form characteristic broad stripes of intensity rather than thin lines, and their edges ("Kikuchi lines") are often fragmented, diffuse and noisy. Pattern Quality is obtained straightforward from the magnitudes of high Fourier frequencies of a 1D FFT in band normal direction across the centers of the Radon peaks [8]. The calculated values of Pattern Quality are not much affected by pixel noise, because the Radon transformation corresponds to an integration of band edge intensities along the particular band, and hence noise along this direction is fairly well averaged off. In addition, the 1D Fourier coefficients of Radon peaks describe the averaged shape of every evaluated band edge only in the direction *perpendicular* to the particular band rather than over *all polar* directions in the diffraction pattern, if a 2D FFT of the raw diffraction pattern is evaluated. The Pattern Quality can be used to discriminate between deformed and recovered or recrystallized grains in a microstructure. Pattern quality maps of coarse grain metals clearly display grain boundaries and surface scratches, and often show features which look like a dislocation network. A diffuse pattern, however, may also result from a foreign surface layer such as carbon of excessive thickness (which may have been deposited by intention to avoid specimen charging), a contamination layer due to poor vacuum conditions, a deformation layer from inadequate sample preparation, or an insufficiently focused beam spot.

Typically the positions of the 5 to 10 smallest and most intense bands of a pattern are passed to the indexing routine. Consideration of the first 3 to 4 families of {hkl} planes is usually sufficient for uniquely indexing a backscatter Kikuchi pattern since it covers a large angular range of about 100° in reciprocal space. Reference directions in the specimen space (e.g. specimen normal and transverse directions in the specimen surface) are finally indexed, and the crystallographic orientation of the grain is described either in (hkl)[uvw] notation, by three Euler angles, (φ_1, Φ, φ_2), or by the rotation matrix, $\mathbf{g}$, which transform the specimen coordinate system under consideration into the crystal-fixed coordinate system. A simulated Kikuchi pattern to this solution is finally displayed on the monitor for comparison. Details of the indexing routine can be found in [11].

Figure 2 shows the crystal orientation maps (COM), the pattern quality map and the grain boundary map of a hot-rolled titanium sheet metal. In the COM the (gray) shades indicate a continuous bending of the orientations within the grains which is correlated with a reduced pattern quality due to a locally increased dislocation density. Twins are clearly revealed. It is worth noting that the maps are only graphical representations of the microstructure to ease imagination. They are backed by the complete information about the grain orientations in every measured point such providing means of a quantitative description of the microstructure on a grain-specific scale.

Conclusion

Crystal lattice orientation measurement grain by grain yields information on the microstructure that is not obtained by any other technique. In particular the study of correlations between spatial and orientation parameters is enabled. A new field of microstructural characterization named *Orientation Stereology* [12] has developed that merges conventional quantitative materialography with texture analysis. ACOM databases provide ideal input sets to Fi-

nite Element simulations. At each point of the scan grid, the x-y coordinates are recorded that stand for the position (nodal mesh point), along with three Euler angles describing the local grain orientation, and the pattern quality describing the local lattice strain.

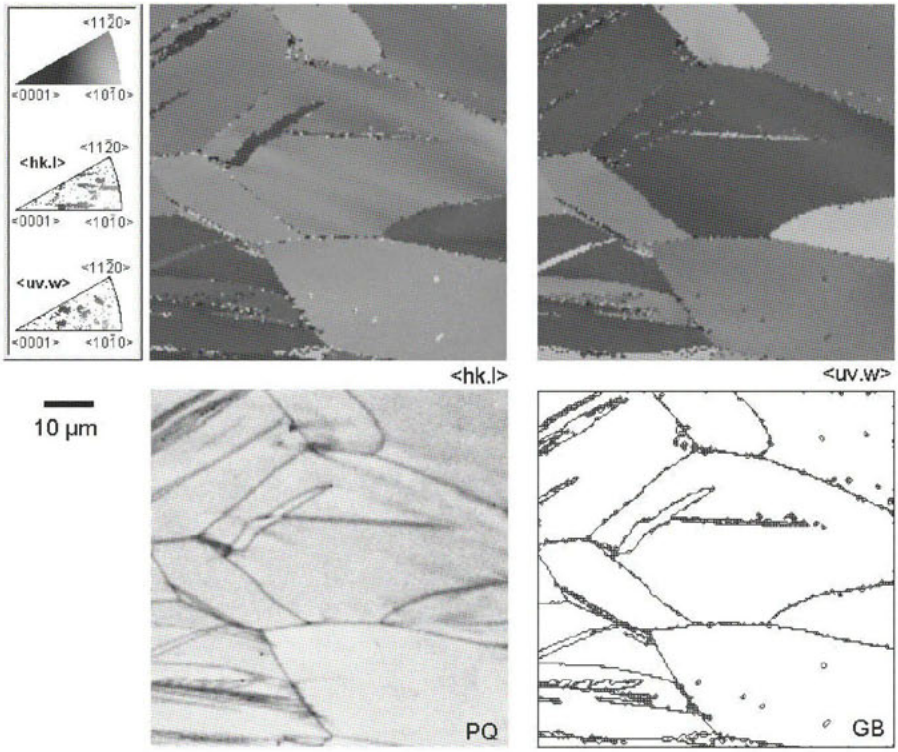

Figure 2. ACOM measurement on a hot-rolled titanium sheet. Crystal Orientation Maps (COM) of the specimen normal direction <hk.l> and the transverse direction <uv.w>, the Pattern Quality Map (PQ), and the grain boundary map (GB) have been constructed from the set of individual grain orientation data. The inverse pole figures for the <hk.l> and <uv.w> direction are on the left hand side along with the color code triangle.

References

1. R. A. Schwarzer, 2003, *The Physics of Metals and Metallography* **96**, Suppl. 1. 104-115.
2. R. A. Schwarzer, 1999, *Microscopy and Microanalysis* **5**, Suppl. 2, 242-243.

3. R. A. Schwarzer, 2002, *Analytical and Bioanalytical Chemistry (ABC)* **374**, 699-702.
4. R. P. Goehner and J. R. Michael, 1996, *J. Res. Natl. Inst. Stand. Technol.* **101**, 301-308.
5. A. J. Schwartz, M. Kumar and B. L. Adams (eds.), 2000, *Electron Backscatter Diffraction in Materials Science*. Kluwer Academic / Plenum Press.
6. D. Gerth and R. A. Schwarzer, 1993, *Textures and Microstructures* **21**, 177-193.
7. R. A. Schwarzer, 1997, *Micron* **28**, 249-265.
8. R. A. Schwarzer and J. Sukkau, 2003, *Adv. Engin. Materials* **5**, 601-606.
9. N. C. Krieger Lassen, 1994, *Automated Determination of Crystal Orientations from Electron Backscattering Patterns*. PhD Thesis, Danemarks Tekniske Universitet, Lyngby.
10. B. L. Adams, S. I. Wright and K. Kunze, 1993, *Metallurgical Transactions* **24A**, 819-831.
11. S. Zaefferer and R. A. Schwarzer, 1994, *Z. Metallkunde* **85**, 585-591.
12. H. J. Bunge and R. A. Schwarzer, 2001, *Adv. Engin. Materials* ***3***, 25-39.

Z. Kristallogr. Suppl. **23** (2006) 169-174

A simple technique for correcting diffraction intensities for the effects of preferred orientation in calcite samples

S. Battaglia[1,*], L. Leoni[2]

[1]Institute of Geosciences and Earth Resources 56124 PISA Italy –Via G.Moruzzi, 1
[2] Department of Earth Science 56126 PISA Italy – Via S.Maria 53
[*]Contact author; e-mail: battaglia@igg.cnr.it

Keywords: diffraction, preferred orientation

Abstract. A new instrumental technique has been developed to enable minimising preferred orientation effects in powder diffraction intensity measurements on minerals with easy cleavage fracture. The method calls for using a conventional diffractometer with a modified sample-holder, by which it is possible to rotate the powder sample by a few degrees around the diffractometer horizontal axis to make diffraction measurements free of preferred orientation effects.

Introduction

X-ray powder diffraction is a non-destructive technique for characterising crystalline materials. The method has been widely adopted for qualitative phase identification and quantitative phase analysis where precise and reproducible intensity measurements are required. Successful application of quantitative methods requires careful, proper sample preparation in order to obtain a specimen that presents a very large number of randomly oriented, uniformly sized crystallites to the x-ray beam. (see the excellent and concise article by Bish and Reynolds in Bish and Post [1] for a summary of most of what you need to know for all-purpose XRD sample preparation). Unfortunately, absolute random particle orientation can only exist if the shape of the particles is spherical. In real samples, random grain morphologies are rarely the norm. Instead, almost all materials exhibit some degree of preferred orientation, and the measured diffraction intensities will therefore be incorrect [2]. Such errors can be neglected in procedures for routine identification of common phases, but in the event the data is to be used for quantitative phase analyses, correction of the intensities is necessary in order to account for the influence of the preferred orientations. Crystal morphology causes preferred particle orientations in polycrystalline specimens, especially crystal fragments whose shapes are influenced primarily by cleavage (Taylor and Norrish, 1966 [2]; Zevin and Viaene, 1990 [3]; Cline and Snyder, 1983 [4]). Many methods have been proposed to overcome this thorny problem, some via theoretical mathematical approaches [5] others by using specific apparatus, such as the Schulz back reflection technique [6,7], and still others by randomising the samples [8]. However, no method has yet to resolve the problem using a simple and rapid technique with a standard diffractometer. Moreover, methods calling for prolonged comminution cannot be considered valid alternatives. In fact, several authors have shown that

prolonged grinding causes many materials and minerals to undergo radical changes in their physical and chemical characteristics [9]. We have also tested cryoscopy grinding in order improve results in terms of preferred orientations, but this type of comminution involves adding many further variables, such as the duration of grinding and, especially, the temperature-time relation during the cycle of warming to maximum temperature and cooling to ambient temperature. We have therefore abandoned such testing and have come to the conclusion that only a suitable combination of various methods can overcome this problem (fine powders, simple techniques to achieve random orientation in sample mounts, etc.). It is in this perspective that the present paper describes a method which enables minimising, via a simple method, preferred orientation effects in diffraction intensity measurements on minerals with easy cleavage fracture by using a conventional diffractometer with a modified sample-holder.

Materials and Apparatus

In order to check the effectiveness of the proposed method in reducing the effects of preferred orientation, we carried out a series of tests on calcite and quartz samples. The easy cleavage of the calcite phase can cause preferred orientation in powder diffraction specimens when the powder is compacted during X-ray test sample preparation. On the other hand, quartz has a minimal relative degree of preferred orientation, so it can be used for comparisons between a mineral with hard effect (calcite) and a free mineral (quartz) by orientation. In the tests conducted no technique for randomising the sample particle orientation was used to supplement the proposed methodology. The quartz and calcite powders were respectively prepared by ring-mill grinding quartz crystals and pure marble with polygonal textures, a grain size of 0.06-0.4 mm (mean value, 0.25 mm), no accessory minerals and very frequent mechanical twins, followed by sieving, with collection of particles passing through a 325 mesh. The intensity measurements were performed with a Philips diffractometer using: CuK_α (Ni-filtered) radiation at 40 kV and 20mA, a PW3710 microprocessor operated by Microsoft-DOS PC, 1° divergence and scatter slits, 0.1 mm receiving slit and a scintillation counter. The selected peaks 104, 113 and 116 for calcite, index referred to hexagonal axes, and 101 for quartz, were scanned by the $\theta/2\theta$ method with a step of 0.005°, measuring for 2 seconds per step. Precise determinations of the net area (°counts), FWHM (°2Theta) and Integral Breadth were made by PC APD 3.6 software for automated powder diffraction analysis. The 104 reflection correspond to the rhombohedral cleavage of calcite and therefore exhibits considerable orientation effects; on the contrary the 113 and 116 lines do not show the same relevant effects.

Experimental trials

In a conventional X-ray diffractometer system with Bragg-Brentano parafocusing geometry, Bragg reflection occurs mostly from particles whose crystallographic planes are approximately parallel to the sample-holder's external surface. For this reason, a homogeneous, randomly oriented powder must be used. By modifying the sample-holder as illustrated in Figure 1, we rotated it by a few degrees around the diffractometer's horizontal axis, as shown in Figure 2. In this type of arrangement, the geometry of the apparatus is such that the focusing condition is not reached for every angular position, with consequent broadening of the Bragg reflection and decrease in intensity. Thus, the contribution to Bragg reflection originates from planes of crystals inside the samples that are not parallel to the sample's external surface.

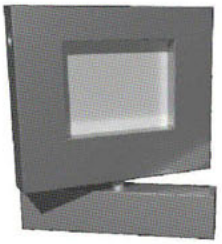

Figure 1. Modified sample-holder.

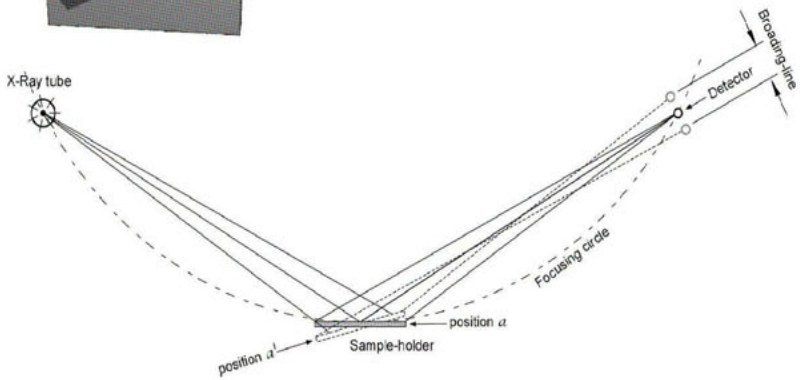

Figure 2. Schematic representation of the geometry of the apparatus: position a represents the normal focus condition, while in position a' the geometry of the apparatus has been modified (together with the focusing conditions).

Results and Discussion

The intensity measurements were made at various positions, rotating the sample holder in a counter-clockwise direction. Five independent calcite and quartz samples were prepared for testing (the powder was packed into the sample-holder each time).

A good reproducibility of the intensities for the 104 peak of calcite, samples, was obtained by rotating the sample-holder until the ratio between full width at half maximum (°2Theta) (FWHM) and the Integral Breadth of each intensity measurement approximated unity (for the definitions of FWHM and Integral Breadth see "X-ray diffraction procedures", chapter 5, p. 298-300 [10]), suggesting that under these defocusing experimental conditions, which involve only moderate variations of peak intensity and peak profile, most of the orientation effects were eliminated. Tables 1 and 2 summarise the results obtained from the tests conducted, while Figure 3 shows the respective plots. The various angular positions of the sample holder during the X-ray measurements are indicated in column 1 as *a, b, c,* etc., starting at the "*a*" position, where the plane of the powder was tangent to the focusing circle, up to the endpoint when the ratio **FWHM / Integral breadth** approached unity (see last column in Tables 1 and 2). The angular positions *b, c, d,*.. were not at the same positions in each of the five tests of the calcite and quartz samples examined; only the *a* position remained constant. Figure 3 reports the regression lines obtained for the calcite and quartz phases by plotting the net-area values versus the FWHM / Integral breadth ratios. Only the first 3 samples are included for the sake of clarity, though the trend is the same for all the samples. In Figure 3, the plots for calcite (left) and quartz (right) show different trends: while the calcite lines converge in a area centring about an approximate value of 800 Net area (°counts) and a FWHM/Integral breadth ratio of 1.00 (corresponding to a calcite diffraction intensity free of

preferred orientation effects), the quartz lines are parallel, revealing "no immediate convergence". The standard deviation is about 19% for the initial calcite measurements and 2.2% for the final ones, while for the quartz the corresponding values are 2.85 and 2.75 %. The decrease in intensity, contrary to the increasing ratio for the quartz samples, is attributable to defocusing of the line: all the regression lines shown the same slope. On the contrary, the calcite samples' regression lines show a slope varying from sample to sample, with lower slopes for the samples exhibiting more orientation effects (calcite 3, see Table 1 and Figure 3). This corresponds to a more rapid intensity decrease on the "x" axis for the same increase in the ratio on the "y" axis than in the other regression lines. Lastly, Table 3 shows the measured area intensities of the 104 Bragg lines, together with the intensities of the 113 and 116 lines. The experimental line intensities measured on three calcite samples, labelled calcite 1a …calcite 3a (Table 3), were also corrected, as described, for preferred orientation effects, and compared with the corresponding calculated intensities for CuK_α radiation (see Table2 in Battaglia et al. [11] i.e., 217.67, 44.29 and 51.37 respectively. These calculated values have been, divided by 2000 to facilitate comparison with Graf [12] and Runnells [13]). The ratio values (I/I_1) reported in Table 3 have been obtained by taking the calculated and observed intensity of line 104 to be 100. The comparisons in the last three columns of Table 3 show that the I/I_1 ratio of the corrected intensities (final position) are in better agreement with the calculated ratio than the ratio of the experimental initial position intensities. The proposed method therefore appears to effectively correct the diffraction intensity for preferred orientation effects. A slight misalignment of the powder sample-holder (about 0.5-1° from the focusing condition), until the *FWHM/Integral Breadth* approximates unity, is sufficient to induce a significant decrease in the contribution of the preferred orientated grains to peak intensity. It is, of course, up to the individual analyst to decide whether alternative techniques should also be utilised at the same time.

Table 1. Data obtained from X-ray diffraction intensity measurements carried out on five calcite samples. Column one shows the various sample-holder positions assumed during the tests, starting from the normal position, a, to finish at the sample-holder position at which the ratio FWHM/Integral breadth approximates unity (last column). ***σ%****= Standard deviation % of the Net area (°counts) measurements.*

Sample holder position	Net area (°counts)	FWHM (°2Theta)	Integral breadth (°2Theta)	FWHM/Integral breadth	
a	**1288**	0.187	0.220	0.850	
b	1111	0.265	0.290	0.913	
c	1067	0.481	0.502	0.957	**Calcite 1**
d	803	0.422	0.435	0.971	
e	**788**	0.487	0.480	1.014	
a	**1430**	0.199	0.228	0.874	
b	1207	0.200	0.238	0.842	
c	1049	0.363	0.383	0.948	**Calcite 2**
d	855	0.517	0.527	0.981	
e	**795**	0.568	0.563	1.009	
a	**1828**	0.188	0.221	0.851	
b	1755	0.196	0.227	0.863	**Calcite 3**
c	1643	0.251	0.267	0.940	
d	**789**	0.651	0.631	1.032	
a	**1892**	0.191	0.228	0.839	**Calcite 4**
e	**805**	0.555	0.554	1.002	
a	**1190**	0.200	0.230	0.873	**Calcite 5**
e	**835**	0.502	0.484	1.036	
σ%	Initial position	18.63			
σ%	Final position	2.17			

Table 2. Data (as in Table 1) but for quartz samples. ***σ%*** *= Standard deviation % of the Net area (°counts) measurements.*

Sample holder position	Net area (°counts)	FWHM (°2Theta)	Integral breadth (°2Theta)	FWHM/Integral breadth	
a	**3487**	0.179	0.209	0.855	
b	3245	0.205	0.233	0.878	
c	3084	0.187	0.211	0.886	
d	2984	0.222	0.243	0.913	**Quartz 1**
e	2874	0.242	0.263	0.919	
f	2514	0.326	0.339	0.961	
g	2432	0.429	0.415	1.034	
a	**3218**	0.204	0.239	0.855	
b	2738	0.228	0.259	0.881	**Quartz 2**
c	2753	0.371	0.387	0.960	
d	2494	0.367	0.378	0.970	
a	**3417**	0.173	0.195	0.887	
b	3244	0.217	0.234	0.927	**Quartz 3**
c	2312	0.380	0.367	1.035	
a	**3350**	0.182	0.206	0.883	**Quartz 4**
d	2460	0.412	0.376	1.095	
a	**3280**	0.207	0.165	0.873	**Quartz 5**
d	2440	0.432	0.431	1.002	
σ%	Initial position	2.85			
σ%	Final position	2.75			

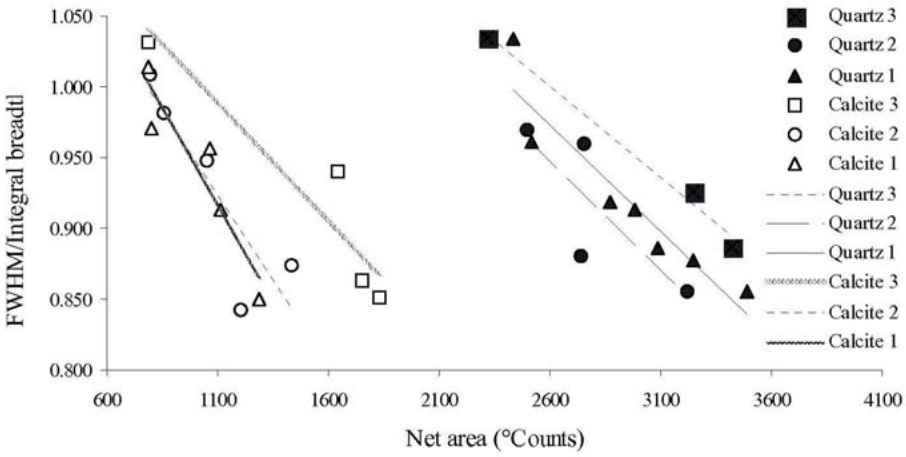

Figure 3. Plot of Net area (°Counts) vs. the ratio FWHM/Integral breadth for calcite and quartz samples.

Table 3. Observed and calculated integrated intensities of three Bragg lines 104, 113, 116.

	Calcite 1a			**Calcite 2a**			**Calcite 3a**		
Net area (°counts)	Bragg lines			Bragg lines			Bragg lines		
	104	113	116	104	113	116	104	113	116
Initial sample holder position	1794	190	177	1890	179	165	1264	185	188
Final sample holder position	845	167	161	852	169	155	824	170	164
$I/I_{1\ calculated}$	100	20,3	23,6	100	20,3	23,6	100	20,3	23,6
$I/I_{1\ experimental}$ (Final position)		**19,8**	**19,1**		**19,8**	**18,2**		**20,6**	**20,0**
$I/I_{1 experimental}$ (Initial position)		**10,6**	**9,9**		**9,5**	**8,7**		**14,6**	**14,9**

References

1. Bish D. L. & Reynolds R. C. Jr. 1989. in Modern Powder Diffraction (D. L. Bish & J.E. Post, editors) *Reviews in Mineralogy*, Volume **20**, Mineralogical Society of America, USA.

2. Taylor R.M. & Norrish K. 1966. *Clay Minerals* **6**, 127-142.

3. Zevin L., and Viaene W., 1990. *Clay Minerals* **25**, 401-418.

4. Cline J.P. and Snyder R.L., 1983. *Adv. X-Ray Anal*, **26**, 111-117.

5. Valvoda V. 1986. *Powder Diffraction,* Vol.**1** N° 2.

6. Bonarski J. T., Wròbel M. and Pawlik K. 2000. *Materials Science and Technology* vol.**16**, 657-662.

7. Valvoda V. 1987. *J. Appl. Cryst.* **20**, 453-456.

8. Zhang G., Germaine J.T., Martin R. T. and Whittle A. J. (2003) *Clays and Clay Minerals* vol **51**, N°2, 218-225.

9. Battaglia S., Franzini M., and Leoni L. 1990. *Powder Diffraction* **5**,101-103.

10. Klug H. P. and Alexander L. E. 1974. : *X-ray Diffraction Procedures for Polycrystalline and Amorphous Materials* (Wiley, New York).

11. Battaglia S.,Franzini M., and Leoni L. 1978. *Atti Soc. Tosc. Sci. Nat., Mem.*, serie A,**85** 147-159.

12. Graf D. L. 1961. *Am. Mineralogist* **46** 1283-1316.

13. Runnells D. D. 1970. *Jour. Sed. Petrology* **40**, 1158-1166.

Z. Kristallogr. Suppl. **23** (2006) 175-180

Influence of extinction phenomenon on determination of the orientation distribution function

G. Gómez-Gasga[1], T. Kryshtab[2,*], J. Palacios-Gómez[2], A. de Ita de la Torre[1]

[1]Universidad Autónoma Metropolitana, Av. San Pablo 180, 02200 México D.F.
[2]Instituto Politécnico Nacional-ESFM, Av. IPN, Ed. 9 U.P.A.L.M., 07738, México D.F.
[*]Contact author; e-mail: tkrysh@esfm.ipn.mx

Keywords: x-ray diffraction, texture, extinction, pole figure, orientation distribution function

Abstract. The influence of the extinction phenomenon on the directly measured pole figures (PF) and calculated orientation distribution function (ODF) is demonstrated for the case of aluminium samples after cold rolling to different reductions and thermal annealing. Pole figures for low index reflections 111, 200, 220 and for high index reflection 222, 400, 420 were measured. An aluminium powder standard sample was also measured. The ODFs were calculated from these PFs data for low and high index reflections separately. The ODF obtained from low index PFs shows systematically lower values of grains orientation density than those obtained from high index PFs. Such inequality of obtained ODFs is attributed to the stronger effect of primary and secondary extinction on the diffraction of low index reflections. The obtained ODFs are also not qualitatively similar. This indicates extinction anisotropy due to the primary extinction coming from recrystallized non equiaxial crystallites.

Introduction

Texture analysis deals with the orientation distribution of the grains in polycrystalline materials. The common X-ray technique for texture evaluation provides quantitative texture data in conventionally accepted formats, i.e. PFs or ODF. These measurements provide information on the volume fractions of the sample having particular orientations and it is referred to as macrotexture [1]. Macrotexture ODFs cannot be measured directly, but they need to be calculated from PFs data obtained for different directions. The PFs, obtained from the measurements of integrated intensity of diffracted X-rays, should be measured first. Each step of the texture analysis has specific sources of mathematical and experimental errors. The progress achieved in the mathematical aspects of texture analysis [2] is often in contrast to the lesser accuracy of experimental input data. One source of systematic physical errors in PF measurements is the phenomenon of extinction that cannot be avoided and must be taken into account [3-5]. Two types of extinction can be distinguished. The first one occurs in large

diffracting crystallites (about 10^{-4} - 10^{-5} cm), where the incident beam intensity can be significantly reduced by the dynamical scattering processes (primary extinction). The second type of extinction takes place when the crystallites are sufficiently similarly oriented so, that either the incident or diffracted beam for one crystallite is diminished by the diffraction from another crystallite (secondary extinction). Adequate extinction corrections and acceptable algorithms of isotropic approximation for integrated intensities of real crystals have been introduced into the kinematic theory [6-8]. The general problem of extinction anisotropy was considered in the theoretical publications [9,10].

In the case of textured materials, for example in annealed samples, when the primary and secondary extinctions are present simultaneously, the integrated intensity of the diffracted beam is affected both by the orientated distribution of grains and by the phenomenon of extinction, which reduces the pole densities (PD) in PF and leads to an incorrect interpretation. Textured materials are anisotropic media and extinction can be anisotropic.

In the present work we demonstrate the influence of extinction phenomenon on PFs measured for low and high index reflections and on the ODFs calculated from these PFs.

General terms for the extinction correction

The necessity for corrections of the integrated intensities for reflections affected by extinction has been recognized. When both types of extinction occur in the mosaic sample, the coefficient of the integrated reflectivity R_m for the symmetrical Bragg reflection and nonpolarized radiation can be represented from the kinematical integrated reflectivity R_{kin} as [7,8]:

$$R_{kin} = Q_{kin} C_1 / 2\mu \ \text{(a)} \ \Rightarrow \ R_m = Q_{kin} C_1 \varepsilon / 2\left(\mu + g\varepsilon C_2 / C_1^2\right) \text{(b)}, \qquad (1)$$

where Q_{kin} is the kinematical integrated reflectivity per unit volume, μ is the linear absorption coefficient, $C_n = \left[1 + \cos^{2n}(2\theta)\right]/2$ is the polarization factor, θ is the diffraction angle, ε and g are the coefficients of the primary and secondary extinction, respectively.

The conventional term for the primary extinction coefficient is $\varepsilon = tanh(pq)/pq$, where p is the number of reflecting planes and q is the wave amplitude reflected from a single plane of atoms [11]. Within the framework of the dynamic diffraction theory [12], the phenomenon of the primary extinction can be expressed in the terms of the domain thickness l in the direction of the diffraction and the extinction length Λ for this reflection as $\varepsilon = tanh(l/\Lambda)/(l/\Lambda)$ [3]. The primary extinction effect can be determined by the ratio l/Λ. For the symmetric Bragg reflection the extinction length can be presented as [12, 3]:

$$\Lambda = \sin\theta v_c / \left|C_{dyn}\right| r_0 \lambda F_H = (1/2d)\left(v_c / \left|C_{dyn}\right| r_0 F_H\right) = (1/2d)\left(const / \left|C_{dyn}\right| F_H\right), \qquad (2)$$

where λ is the radiation wavelength, F_H is the structure factor, v_c is the unit cell volume, r_0 is the classical radius of the electron, and $C_{dyn} = \left(1 + \left|\cos 2\theta\right|\right)/2$ is the polarization factor.

The secondary extinction coefficient g is defined by the angular deviation of the normal of the diffracting planes of domains from the average direction over the crystal and for a given direction <*hkl*> it does not depend on radiation wavelength and order of reflection.

The PD in the textured sample is defined as $P = I^T/I^P$, where I^T and I^P are the integrated intensities from the textured and powder standard samples, respectively. The correct value of the pole density P_{cor} can be determined from the use of the ratio of equations (1b) and (1a) [3]:

$$P_{cor} = P\left(\mu + g\varepsilon Q_{kon} C_2 / C_1^2\right) / \varepsilon\mu \,. \qquad (3)$$

Thereby, if the phenomenon of extinction is present, the correct value of the PD will be larger than the PD measured directly.

Experimental results and discussion

Aluminium samples after cold rolling to different reductions and thermal annealing were used for investigation. An aluminium powder standard sample was also measured at fixed geometrical conditions. The PFs for low index reflections 111, 200, 220 and for high index reflection 222, 400, 420 were measured by use of an Euler Cradle with a Bruker X-ray diffractometer. Point focus non-polarized Cu and Co radiations were used. The corrections for defocusing and normalisation of PF were carried out. The duration of measurements for weak second order reflections was several times longer than the duration for low index reflections. The calculations of ODFs were made from PFs obtained for low and high index reflections separately. For ODF calculation the popLA software was used.

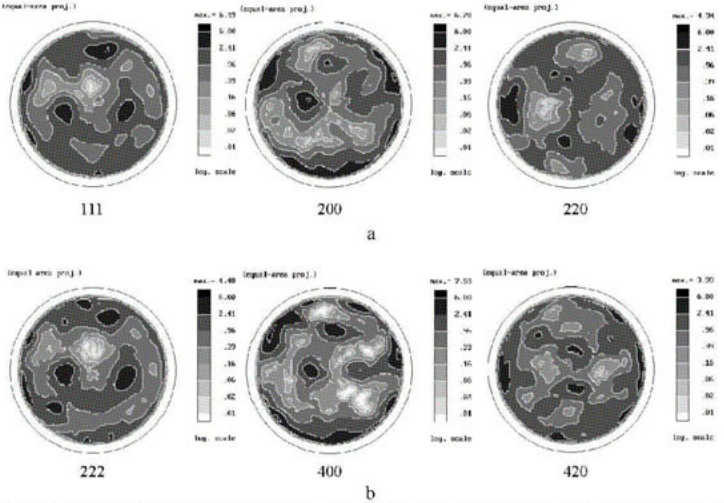

Figure 1. The direct pole figures measured: for low index reflections 111, 200, 220 (a) and high index reflections 222, 400, 420 (b).

In figure 1, the direct PFs obtained for an aluminium sample (rolled to 35% reduction, annealed 10 min at 300 °C) with Cu K_α radiation are shown. As can be seen from the comparison of the PFs for the same direction, they are similar, but not in the whole circle. For the <111> direction we see that PF obtained for second order reflection 222 has more details, but the maximum of PD is 4.48 and less than the PD maximum (6.49) in the PF obtained for 111 reflection. At the first brush, it is possible to make the conclusions that extinction phenomenon is not present and even that the measurements are made incorrectly. If the extinction phenomenon is absent and grains distribution is uniform in the depth, these PFs must coincide. X-ray technique gives average result over a volume fraction below the surface. The penetration depth for 222 reflection is twice as large than for 111 reflection and in the case of

heterogeneous distribution of grains and grain size we can expect that the maxima will be different. The presence of more details in the PF obtained for 222 reflection just indicates this heterogeneity. The extinction phenomenon comes out clearly at the measurements of PFs for 200 and 400 reflections. The PD maximum for PF obtained for 200 reflection is less and equals to 6.70 and for PF obtained for 400 reflection is 7.53, as expected.

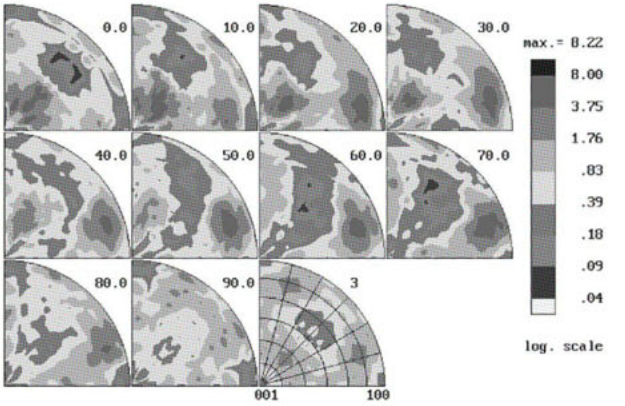

Figure 2. The ODF calculated from PFs obtained for low index reflections 111, 200, 220.

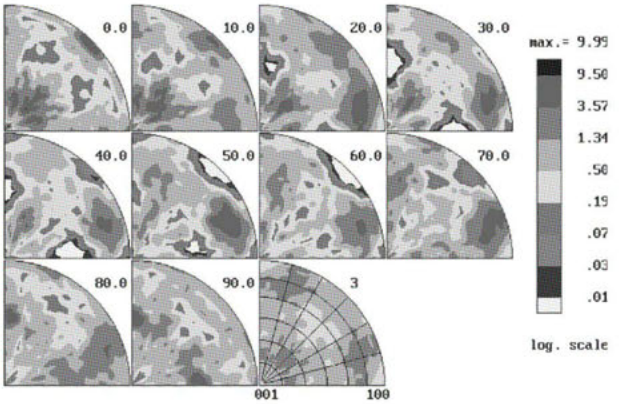

Figure 3. The ODF calculated from PFs obtained for high index reflections 222, 400, 420.

The calculated ODFs from low and from high index reflections are shown in figures 2 and 3, respectively. The ODF calculated from PFs obtained for low index reflections and ODF calculated from PFs obtained for high index reflection even qualitatively are not similar. Although the PD maxima in PFs for the second order 222 and 420 reflections were slightly less than for the first order reflections, the maximum of ODF obtained from PFs for high index reflection is about 20% higher than that one obtained for low index reflections.

The effect of the extinction phenomenon on PFs measured is demonstrated by investigation of an aluminium sample rolled to 70% reduction and annealed for 10 min at 360 °C. Nonpo-

larized Co K_α -, and Cu K_α - radiations were used. The influence of the primary and secondary extinction on PDs for different reflections and radiation wavelengths can be evaluated in the terms of the extinction length Λ and an addition to the absorption coefficient μ by comparing the ratio between the values of μ and $Q_{kin}C_2/C_1^2$ (see equation (3)). Calculated parameters for evaluation of the primary and secondary extinction are presented in Table 1.

Table 1. Calculated values of the absorption coefficient μ, the extinction length Λ_{kkl} and the extra term $Q_{kin}C_2/C_1^2$ for Co K_α-, and Cu K_α- radiations.

Radiation	μ (cm^{-1})	Λ_{111} (μm)	Λ_{222} (μm)	$Q_{kin}C_2/C_1^2{}_{111}$ (cm^{-1})	$Q_{kin}C_2/C_1^2{}_{222}$ (cm^{-1})
Co K_α	198.09	1.69	7.35	19.47	9.94
Cu K_α	131.44	1.63	8.09	13.24	6.35

For the first order reflections the difference in extinction length Λ for both radiations is very small and the effect of the primary extinction for these radiations must be almost the same. Extinction lengths for the second order reflections are larger than those for the first order ones by a few times, but the value of Λ for Co K_α - radiation is smaller than the one for Cu K_α - radiation. Therefore, the sensitivity to primary extinction of 222 reflections decreases noticeably, but the effect of the primary extinction is stronger for Co K_α - radiation.

The comparison of the ratio between the values of $Q_{kin}C_2/C_1^2$ and μ for evaluation of the influence of the secondary extinction shows that the ratio is approximately the same for different wavelengths and for the first and second order reflections is about 0.1 and 0.05, respectively. The sensitivity to the secondary extinction for different wavelengths is the same and for the second order reflections is less than the first ones. So, PFs measured for low index reflection with Co K_α -, and Cu K_α - radiations are affected by the phenomenon of the primary and secondary extinction stronger that those for high index reflections.

The direct PFs obtained for an aluminium sample (rolled to 70% reduction, annealed for 10 min at 360 °C) with Co K_α- and Cu K_α- radiations are shown in figure 4.

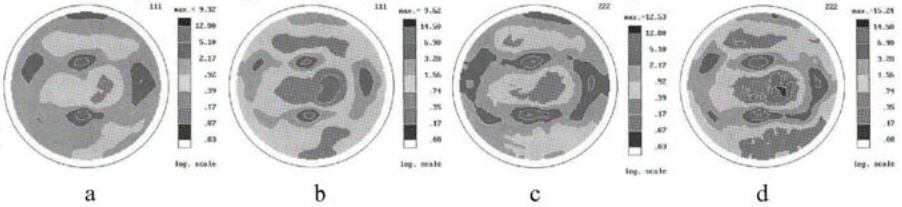

a b c d

Figure 4. The direct pole figures measured for111 reflections with Co K_α- (a) and Cu K_α-(b) radiations and for 222 reflections with Co K_α-(c) and Cu K_α-(d) radiations, respectively.

The PFs for 111 reflection obtained with Co K_α -, and Cu K_α - radiations are similar and have approximately the same values of PD maxima as 9.32 and 9.62, respectively. The PFs for 222 reflections obtained with both radiations also similar, but have more details and the values of PD maxima increased noticeably. In this case the value of PD maximum for Cu K_α - radiation is 15.24 and larger than for Co K_α - radiation (12.53) due to less influence of the primary extinction, as was expected from the preliminary evaluations. PFs obtained from low as well as from high index reflections are also affected by the secondary extinction, but the high index reflections are less affected than low index reflections. More details are present in

the PFs for 222 reflection obtained with both radiations, indicating heterogeneous distribution of grains and grain size in the depth and/or less influence of the extinction phenomenon. Extinction is also found to be anisotropic due to the primary and secondary extinction coming from anisotropic inelastic deformation properties and non equiaxial recrystallization [3]. From the obtained results it is possible to conclude that ODFs calculated from low index PFs are affected by the extinction phenomenon. The qualitative difference between calculated ODFs testifies to anisotropic extinction. The corrections of pole figures due to the extinction phenomenon will give new changes in the ODF and the values of pole densities will increase more noticeably as observed in figure 3.

Conclusions

We have demonstrated the influence of the extinction phenomenon on the directly measured PFs and calculated ODFs. The ODF obtained from low index PFs shows lower values of grains orientation density than those obtained from high index PFs. The reason of such inequality of obtained ODFs is a stronger effect of primary and secondary extinction on the diffraction of low index reflections. Obtained ODFs are not qualitatively similar one to another, which indicates the extinction anisotropy. To calculate the ODF completely free from the extinction effect, it is necessary to use the corrected PFs, which must be obtained at the first step of measurements. At the moment this task is beyond the scope of the present work.

References

1. Randle, V. & Engler, O., 2000, *Introduction to Texture Analysis Macrotexture, Microtexture and Orientation Mapping* (Amsterdam: Gordon and Beach Science Publisher).
2. Bunge, H.-J., 1996, *Textures and Microstructures*; **25**, 71.
3. Kryshtab, T., Palacios-Gómez, J., Mazin, M. & Gómez-Gasga, G., 2004, *Acta Materialia,* **52/10**, 3027.
4. Mücklich, A. & Klimanek, P., 1994, *Mater. Science Forum*, **157-162**, 275.
5. Yamakov, V. & Tomov, I. J., 1999, *Appl Cryst*; **32**, 300.
6. Chandrasekhar, S., 1960, *Adv. Phys*; **9**, 363.
7. Zachariasen, W.H., 1963, *Acta Cryst.*, **16**, 1139.
8. Zachariasen, W.H., 1967, *Acta Cryst.*, **23**, 558.
9. Popa, N.C. 1987, *Acta Cryst. A*, **43**, 304.
10. Tamazyan, R.A. 1993, *Sov. Crystallography*; **38(6)**, 730.
11. James, RW., 1965, *The Optical Principles of the Diffraction of X-Rays* (3rd ed. London: G.Bell).
12. Pinsker Z.G., 1978, *Dynamical Scattering of X-Rays in Crystals* (New York: Springer-Verlag Berlin Heidelberg).

Acknowledgements. Authors would like to thank the CONACyT of Mexico for financial support of this work by the projects 32088-E, 29304-U and 44475-F.

II. INSTRUMENTAL

Z. Kristallogr. Suppl. **23** (2006) 183-188

First test measurements at the new structure powder diffractometer (SPODI) at the FRM-II

R. Gilles[1*], M. Hoelzel[1,2], M. Schlapp[1,2], F. Elf[3], B. Krimmer[1], H. Boysen[4], H. Fuess[2]

[1]Technische Universität München, ZWE FRM-II, Lichtenbergstr. 1, 85747 Garching, Germany.
[2]Technische Universität Darmstadt, FB Material- und Geowissenschaften, Petersenstr. 23, 64287 Darmstadt, Germany.
[3]Mineralogisch-Petrologisches Institut und Museum der Universität Bonn, Poppelsdorfer Schloss, 53115 Bonn, Germany.
[4]Ludwig-Maximilians-Universität, Depart. für Geo- und Umweltwissenschaften, Theresienstr. 41, 80333 München, Germany
[*]Contact author: ralph.gilles@frm2.tum.de

Keywords: neutron diffraction, structure powder diffractometer, instrumentation

Abstract. In framework of a cooperation between the Technische Universität Darmstadt and the Ludwig-Maximilians-Universität München, funded by German government (BMBF), the new Structure Powder Diffractometer (SPODI) has been built at the neutron source FRM-II in Garching near München (see figure 1). The instrument operates in the angle-dispersive mode with a pre-selected wavelength. This contribution gives an overview of the status and the innovations of new components included in the concept [1-2]. Particular highlights of the set-up are, for example, the sophisticated supermirror neutron guides (trumpet shape) for thermal neutrons, the high take-off angle of 155° realized with 17 individual modules of an unconventional orientation (551) of the germanium monochromator (each module consists of 37 wafers !), the 300 mm high collimators with tapered sidewalls to enlarge the effective detection area, the position sensitive detector providing 2D array detection with multifarious evaluation procedures and the space optimized shielding with different special materials (to improve the signal to background ratio) etc. The realization of this layout aims at higher intensity, improved resolution and better profile shapes. Monte Carlo simulations of the complete instrument including the sample were carried out to match all components.

Introduction

The design and status of the new Structure POwder DIffractometer (SPODI) is reviewed. To solve complicated structures reliably by powder diffraction not only high resolution and

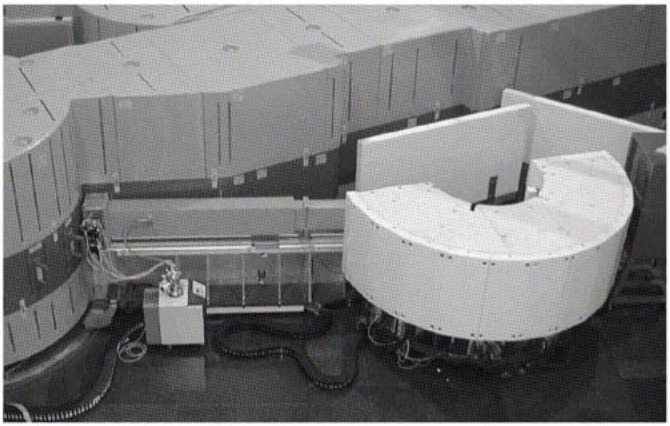

Figure 1. Set-up of the Structure POwder DIffractometer SPODI at the FRM-II.

intensity are essential, but, in addition, require "good" peak profiles that can be described as perfectly as possible. For strongly overlapping reflections, uncertainties in the exact shape can lead to an incorrect distribution of the intensities. Moreover, such knowledge virtually increases the resolution of the instrument far beyond that given by the widths of the peaks. Similar arguments hold for a good peak to background ratio which can be achieved not only by a low background, but also by narrow tails of the peaks. Finally, such "good" peak shapes should be maintained up to large scattering angles 2θ. Based on these considerations, computer simulations have been used to optimize both the single components and their interaction along the instrument. The resulting concept together with test measurements of individual components at other neutron sources have been described in references [1-4]. The high flux at the sample position with neutrons of very low vertical divergence (because of the 5m distance to the monochromator) allows the unique possibility to integrate a small-angle scattering apparatus in the whole system.

Results and Discussion

Currently, the alignment of the individual monochromator modules is conducted in order to optimize the focusing of the beam at the sample position (figure 2). After a preliminary adjustment of the focusing monochromator the beam was directed to the sample position with a mounted corundum sample. As one of the first patterns figure 3 shows the diffractogram of a measurement without sample collimator and preliminary adjustment of the detector electronics. Fitting by the Rietveld method results in the identification of the expected peaks with broad FWHM's. This pattern includes no correction of the umbrella effect [5] as the intensity was simply summed up in vertical direction, i.e. without using the position sensitivity. Within the limited beam time of 8 hours, the reduced reactor power of 1.5 MW and the preliminary alignment of components a maximum of 26000 counts in peak intensity was reached. Analyzing a single peak, the (116) reflection, with different integration of heights along the detector displays the shifts of the determined peak position ($\Delta 2\theta$ up to 0.11°) and

the increasing asymmetry in the peak profiles for larger detector heights (figure 4). The fitting parameter η which describes the Lorentzian contribution in the Voigt function (the value $\eta = 0$ stands for a pure Gaussian function and $\eta = 1$ for a Lorentzian function, respectively) resulted in values $\eta \leq 0.1$ for the different detector heights indicating a nearly perfect Gaussian profile.

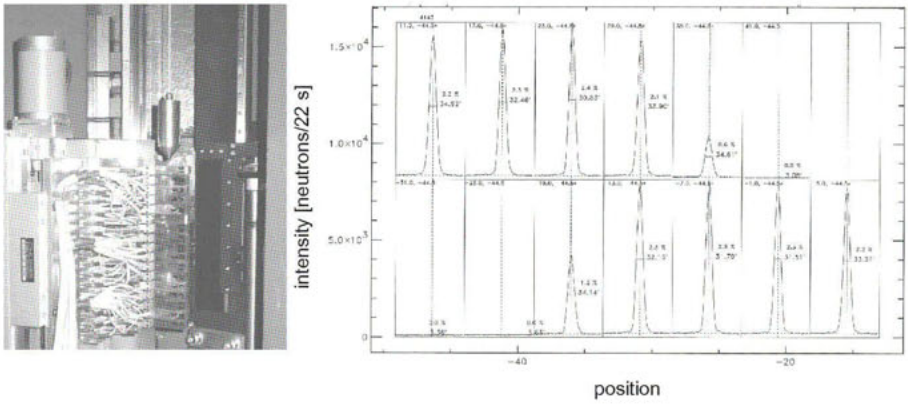

Figure 2. Left: Photograph of the germanium monochromator (551) installed in the monochromator drum. Each of 17 modules (below the plumb) can be aligned by the three motors to vary the focusing on the sample position. Right: On each single monochromator module at different positions (lengthwise the crystal) rocking curves were measured to determine the mosaicities in horizontal direction.

This effect of peak shift and peak asymmetry increases dramatically with decreasing scattering angle towards $2\theta = 0°$ or with increasing scattering angle towards $2\theta = 180°$. The peak profiles are not constant over the whole range of 2θ. This turns out clearly by remembering the Debye-Scherrer diffraction geometry: The powder sample is centered at the intersection point of primary beam and cylinder axis, which are perpendicular. The sample position is the starting point of the Debye-Scherrer cones. The cone axes coincide with the primary beam and are perpendicular to the cylinder axis. The Debye-Scherrer rings, or ring sections, respectively, are intersection lines of the cylindrical detector and these cones (figure 5). Unrolling the cylinder to a plane and taking into account the dimensions of the SPODI detector yields figure 6. The two-dimensional detector matrix has to be transformed to a one-dimensional diffractogram for further processing by Rietveld programs. Figure 7a shows a section of the detector matrix in the range of about 149° to 157° in 2θ. The curvature of the Debye-Scherrer lines can be clearly seen. Because the detector electronics is not yet adjusted in an optimal way, the upper area above the detector height of 0 cm is not an exact mirror image of the lower area below 0 cm.

The simplest method to transform the detector matrix is to perform a vertical summation of counting rates along the columns. The deficiencies have already been discussed in context of figure 4. Applying this method to the matrix of figure 7a yields in the dotted line of figure 7b. The situation is quite severe because of the high scattering angles.

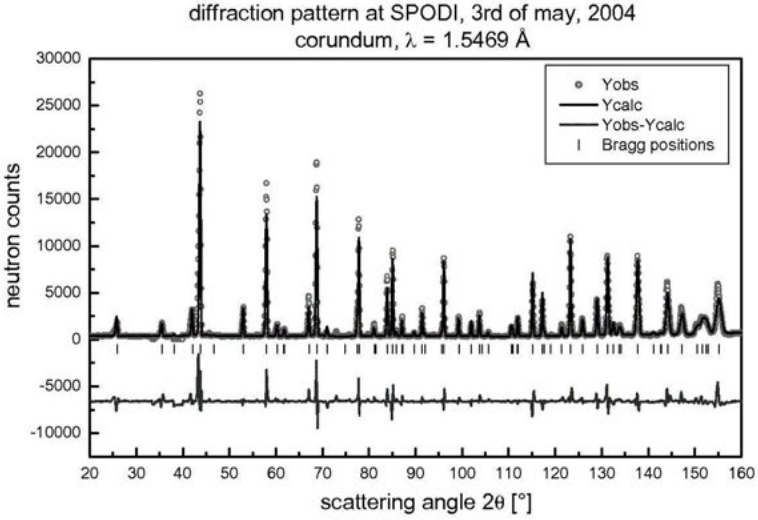

Figure 3. First diffraction pattern of corundum measured at SPODI with full detector height of 300 mm.

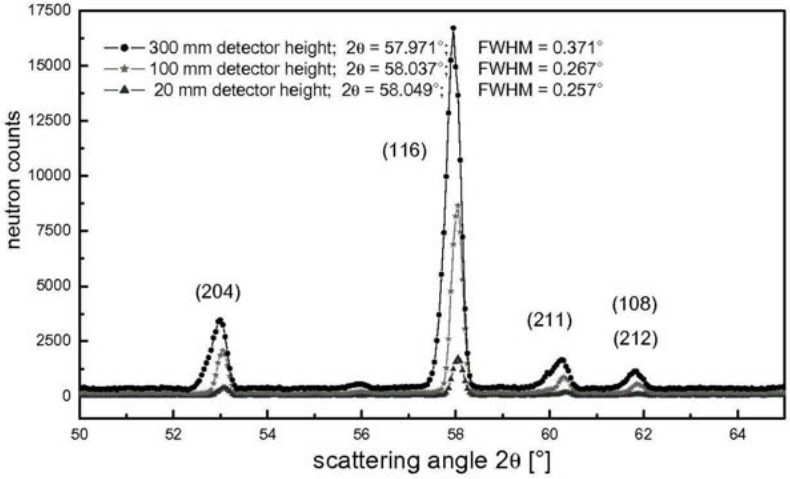

Figure 4. Part of corundum diffraction pattern with evaluation for different detector heights displaying the shift of peak position and asymmetry of the profiles.

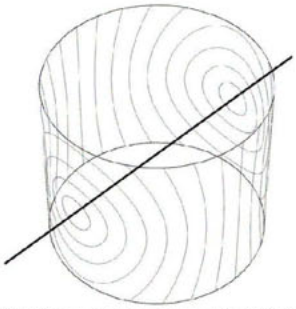

Figure 5. Principle of powder diffraction patterns on a cylindrical detector. The primary beam (thick line) penetrates the cylinder at scattering angles $2\theta = 0°$ and $2\theta = 180°$. Neighboring lines have a difference of $10°$ in 2θ.

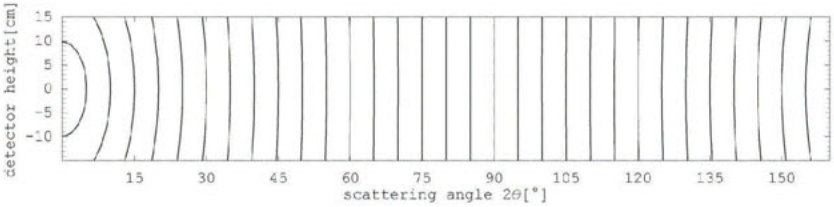

Figure 6. Theoretical Debye-Scherrer lines at the SPODI detector with $\Delta 2\theta = 5°$.

One way to avoid peak shifts and peak asymmetries and to conserve all information inherent in the diffraction experiment is to integrate along Debye-Scherrer lines. The detector matrix can be considered as a rectangular grid, whereas the theoretical Debye-Scherrer lines form a curvilinear grid. Therefore it is necessary to calculate the intensities at the points of the Debye-Scherrer grid from the surrounding matrix grid points. This is performed by bilinear (horizontal and vertical) interpolation dependent on the distance. Finally the intensities have to be normalized in relation to the arc length of the lines recorded by the detector. The result of this computer time consuming procedure is shown as solid line in figure 7b. In comparison to the first method there are significant less peak position shifts and asymmetries of the peak profile shape and, more important, the FWHM is reduced and the resolution is enhanced.

Conclusion and Outlook

First measurements at the new structure powder diffractometer SPODI have already shown the great potentials of the instrument. It was the first time at FRM-II that a monochromatic beam has been directed to a sample to obtain a diffraction pattern. The preliminary alignment of the monochromator revealed a high intensity at the sample position at a reduced reactor power of 1.5 MW and confirmed the McStas simulations for the choice of tilting angle and focusing geometry [3]. The quasi two-dimensional detector allows enhancements of the resolution and more accurately determinations of peak positions as shown by the corundum measurement which was evaluated by simple vertical summation and position sensitive

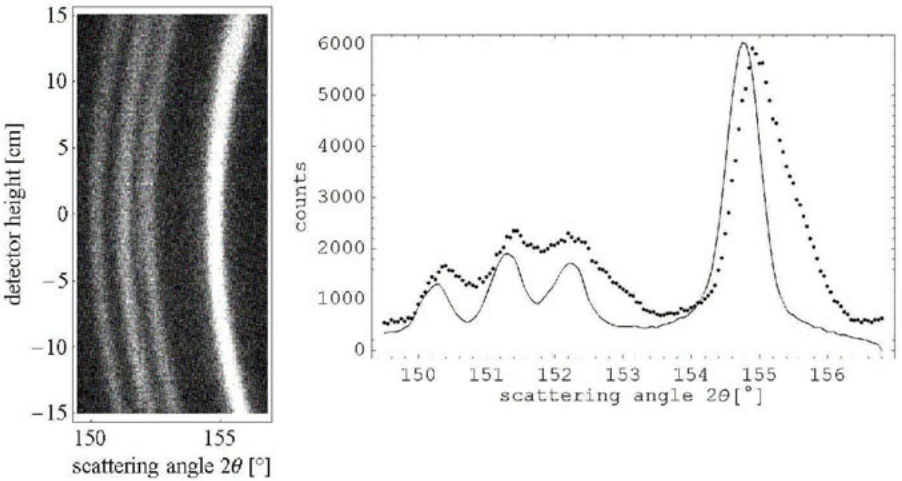

Figure 7a (left). Detail of the detector matrix after the exposure of the detector system with neutrons scattered by a corundum sample. Figure 7b (right). Comparison of transformation methods: vertical summation (dotted) and summation along Debye-Scherrer rings (solid) of measurement in figure 7.

summation along Debye-Scherrer rings. Experiments with the full reactor power of 20 MW will allow beam time of about 45 minutes for a pattern as shown in figure 3. The next steps in the near future will be the detector calibration of each tube with preamplifier (determination of efficiency), optimization of the transmission values of the 80 detector collimators and the different sample collimators, characterization of the instrument resolution function for different wavelengths or take-off angles of the monochromator and flux measurements of the various focusing geometries. In parallel it is planned to install the SANS option with an image plate detector to extend the wide angle part to the small angle region.

References

1. Gilles R., Artus G., Saroun J., Boysen H., Fuess H., *Physica B*, **276 – 278**, (2000), 87.
2. Gilles R., Krimmer B, Saroun J., Boysen H., Fuess H., *Materials Science Forum*, **378-381** (2001), 282.
3. Gilles R., Krimmer B., Boysen H., H. Fuess, *Applied Physics A*, **74** [Suppl.] (2002), 148.
4. Hoelzel M., Gilles R., Schlapp M., Boysen H., Fuess H., *Physica B*, **35** (1-3S) (2004), E 671.
5. van Laar B., Yelon W.B., *J. Appl. Cryst.*, **17**, 1984, 47.

Acknowledgement. The support of this work by the German BMBF under grant FKZ03-FU5FRM is gratefully acknowledged.

Z. Kristallogr. Suppl. **23** (2006) 189-194

EXED – the new Extreme Environment Diffractometer at the Hahn-Meitner-Institut Berlin

J. Peters[1,*], K. Lieutenant[2], D. Clemens[1] and F. Mezei[1,3]

[1]Hahn-Meitner-Institut Berlin, Glienicker Str. 100, 14109 Berlin, Germany
[2]Institut Laue-Langevin, BP 156, Grenoble Cédex 9, France
[3]LANSCE, Los Alamos National Laboratory, Los Alamos, NM 87545, USA
[*]Contact author; e-mail: peters@hmi.de

Keywords: powder diffraction, time-of-flight monochromator, high magnetic field, extreme environments

Abstract. The Extreme Environment Diffractometer EXED, which is currently under construction at the Hahn-Meitner-Institut (HMI) Berlin and shall become operational in 2006, is presented here. The general ideas of the design are given and a special attention is addressed to resolution excellence including first simulation results.

Introduction

The EXED instrument is a very high resolution time-of-flight powder diffractometer, which has been optimised for diffraction in extreme environments. A special focus is on high magnetic fields and thus the instrument will be equipped with a dedicated 25 T cryomagnet. The instrument is being built at the steady state reactor BERII of the HMI, but its sophisticated chopper system allows the application of the time-of-flight (TOF) principle and, compared to a common crystal monochromator instrument, EXED offers a number of advantages on a continuous source: a) it can provide higher resolution, comparable to what is now achieved at synchrotron radiation sources; b) it makes small d-spacing readily accessible; c) it is more efficient in terms of neutron intensity for conventionally high resolution neutron diffraction work and d) it facilitates the use of extreme sample environment equipment by providing a full coverage of the relevant Q domain at very limited angular access in scattering angles. The physical reason for these advantages is that at high scattering angles good resolution can be achieved without collimators.

Instrument description

A schematic view of the EXED instrument is given in figure 1. It uses the TOF technique at a continuous neutron source originally proposed by Buras [1] in the 1960's, which was further developed and tested in HMI-Budapest Neutron Scattering Centre collaboration [2] in the 1990's.

The main advantages of the TOF methods are that a) high resolution can be achieved in backscattering geometry without the need to use collimators (i.e. at an enhanced detector solid angle and incoming beam divergence) and b) the full relevant Q-range can be covered by limited angular access allowed by extreme sample environment equipments.
The chopper system allows a very flexible use of the instrument: As the repetition rate is not defined by the source, bands of arbitrary width of d-spacing can be achieved in the forward as well as the backward scattering direction. In addition, a slewing of the chopper phases permits a continuous variation of the wavelength band. In the backward direction it can be combined with a very high resolution. The EXED beam line is unique in the sense that it has access to both the cold and the thermal moderator and takes advantage of a large wavelength band ranging from 0.7 - 20 Å with local maxima at 1.4 and 3.8 Å.

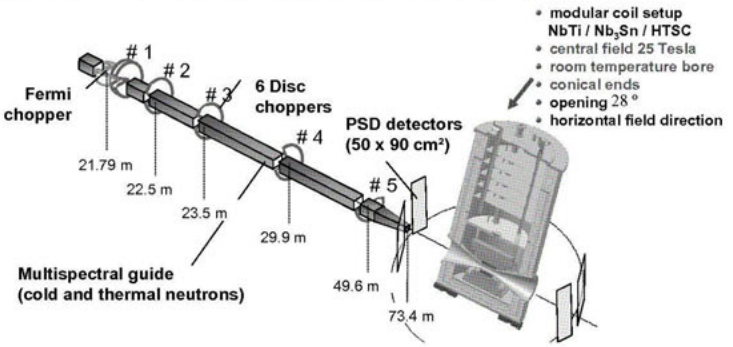

Figure 1. Schematic view of the EXED instrument. The grey tubes correspond to a ballistic neutron guide (straight guide and the compressor [3,4]). The neutron pulses are produced alternatively by a Fermi chopper or by a counter rotating double disk chopper (# 1). The other disk choppers (# 2-4) are frame overlap choppers and a wavelength band chopper (# 5). The position sensitive gas detectors can be moved around the sample and the magnet.

As the magnet has an angular aperture of maximum ± 14°, it can be used in a symmetric as well as in asymmetric neutron beam configuration, which leads to a maximum scattering angle of 28° at one side of the neutron beam (see figures 2a,b).
In the day-one configuration, the instrument will essentially have two purposes: High resolution diffraction and neutron diffraction in highest magnetic fields.

High resolution (powder or single crystal) diffraction
It will be the task of the Fermi chopper to create pulses in the highest resolution domain. The curved Fermi chopper package will allow time resolutions of $\Delta t \approx 6$ µs. In the backward direction (150 – 178°) a total resolution of 0.07 % > $\Delta d/d$ > 0.027 % can thus be achieved at $d \approx 1$ Å with a secondary flight path of 6 m and pin hole collimation (see figure 2a). With a secondary flight path of 2 m, a total resolution of 0.13 % > $\Delta d/d$ > 0.03 % is obtained in backward direction at the same d-spacing (see figure 2b). A typical resolution function in backscattering configuration is shown in figure 3a for both secondary flight paths. Using the converging exit of the guide, a flux of about 4 x 10^5 n/cm²/s has been calculated at the sample (2 x 2 cm²) by Monte Carlo simulations [5] of the instrument, taking a wavelength range of 0.7 Å < λ < 1.8 Å and a repetition rate of 60 Hz.

The detector banks are planned to be equipped with tubes with a diameter of 1 cm and an effective length of 90 cm, which are filled with ^{3}He gas. They shall be position sensitive with a resolution of 1 cm and will cover an effective surface of 50 x 90 cm² (W x H). It will be possible to move them around the sample position or to translate them. In the 2 m position, the two detector banks will cover a 28° scattering angle range, while in the 6 m position only 10° are covered. In the latter configuration, a movable vacuum tank between the sample and the detectors will be used to reduce air scattering.

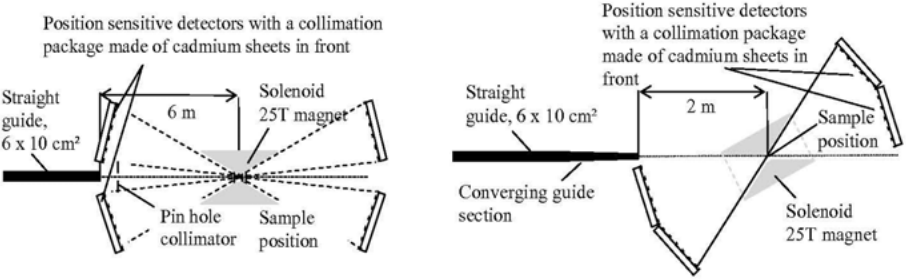

Figure 2. a) Schematic layout of the symmetrical scattering configuration, which can achieve highest resolutions with a secondary flight path of 6 m and a pin hole collimator. b) Schematic layout of the asymmetrical scattering configuration, which can achieve high resolutions with a secondary flight path of 2 - 6 m.

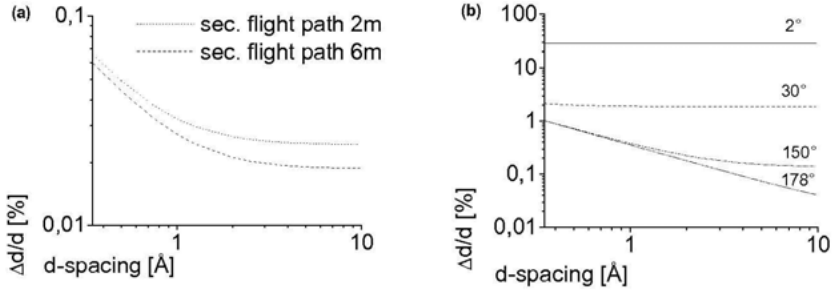

Figure 3. a) Resolution function in backscattering configuration with Fermi chopper for the angle of 2θ = 176° and a horizontal divergence of the incoming beam of 0.15° at 6 m and 0.2° at 2m. b) Resolution function for the case of the double disc chopper used to produce pulses (full line at 2°, dashed line at 30°, dotted line at 150°, dashed-dotted line at 178°). The horizontal divergence of the incoming beam is 0.25°. The secondary flight path is 2 m, sample size 2x2 cm², beam cross section 6x10 cm², ΔL = 1 cm.

Different collimation modules can be applied to further optimise the resolution: the final removable converging guide section significantly increases the flux on the sample. Or, alternatively, a pin hole collimator (see figure 2a) permits the fine tuning of the horizontal and vertical divergences. The *d*-spacings and momentum transfers *Q* accessible with the various detector bank configurations are listed in table 1. The instrument is designed for both narrow-bandwidth and broad-bandwidth operations, the latter achieved by repetition-rate reduction and/or chopper slewing.

Table 1. Various detector bank configurations. For the two first columns the symmetrical arrangement of the detector is supposed with the corresponding angular coverage of 14° on each side of the neutron beam axis, the two last columns correspond to an asymmetrical arrangement with an angular coverage of 28° on one side of the neutron beam axis.

Bank	(171 ± 7)°	(9 ± 7)°	(164 ± 14)°	(16 ± 14)°
d-spacing	(0.35 – 10.1) Å	(2.52 – 571) Å	(0.35 – 10.4) Å	(1.35 – 573) Å
Q	(0.62 – 17.9) $Å^{-1}$	(0.011 – 2.49) $Å^{-1}$	(0.6 – 17.9) $Å^{-1}$	(0.011 – 4.64) $Å^{-1}$

Higher intensity diffraction

For applications that need higher intensity the pulses are created by the double disc chopper with a typical time resolution of $\Delta t \approx 100$ µs, which results in an average total resolution of $\Delta d/d \approx 0.36$ % at $d = 1$ Å in backscattering configuration (see figure 3b). The corresponding flux at the sample is estimated by Monte Carlo simulations to be 3 x 10^6 n/cm²/s with a repetition rate of 60 Hz and a wavelength band range of $0.7 < \lambda < 1.8$ Å. In the backscattering geometry the effect of magnetic fields can be studied on the overall (chemical) crystal structure. Magnetic Bragg peaks need to be studied in the forward scattering direction (B approximately perpendicular to Q).

The multispectral extraction system

Both cold and thermal neutrons are delivered by a supermirror beam extraction system [6] placed behind the moderators. The guide has various coatings on all sides ($1.5 < m < 2.4$). This new extraction concept is based on a ballistic guide [3,4]: by enhancing the guide cross section by a factor of two in both dimensions, the number of reflections is reduced by about four and thus, an enhanced beam can be delivered over large distances (≈ 80 m). A 17 m long kink section, made of 4 parts that are each offset by 0.1° with respect to the initial beam direction, removes high-energy neutrons ($\lambda < 0.7$ Å). It is important to remember that the choppers become transparent for lower λ values. Apart from the kink section, the guide is essentially straight (60 m) and has a cross section of 60 x 100 mm² (W x H). The guide has four 30 mm gaps that accommodate the single disc choppers (# 2 – 5) and approximately a 300 mm gap for both the double disc chopper (# 1) and the Fermi chopper. At the end of the guide, a 7.5 m long converging exit [7] allows a good focussing on the sample. As an alternative the converging section can be completely removed. This last option allows for a longer secondary flight path of 6 m and small divergences.

The chopper system

The guide system and five disc chopper housings share a common vacuum, only the Fermi chopper, with two different slit packages, has a separate housing and a separate vacuum. The curved Fermi chopper slit package can achieve the highest time resolution with a pulse length of 6 µs FWHM at wavelengths between 0.7 and 5.6 Å. The resolution can be adjusted to the requirements of the specific experiment by extending the pulse length to up to 4000 µs with the help of alternate choppers (lower resolution straight Fermi chopper and the first double disc chopper with variable slit width). The intermediate single disc choppers # 2, 3 and 4 remove higher orders and the last single disc chopper defines the wavelength band (see figure 4).

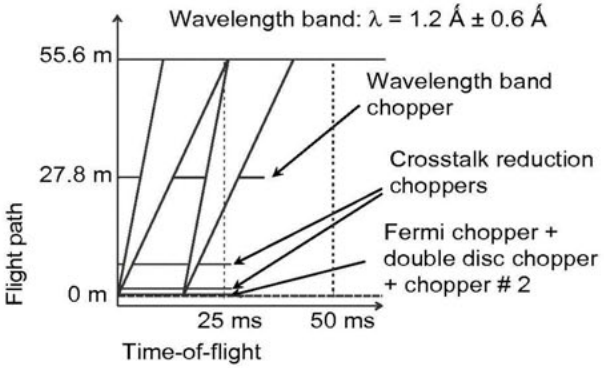

Figure 4. Time-of-flight diagram for the EXED diffractometer using the Fermi chopper to produce the pulses. The double disc chopper runs simultaneously to avoid that two consecutive pulses of the Fermi chopper are transmitted at highest repetition rate. In this example, a wavelength band of $\Delta\lambda$ = 1.2 Å is obtained at a repetition rate of 60 Hz.

Furthermore, the wavelength band can be varied continuously by a so-called slewing of the chopper phases. In fact, the chopper phase can be calculated through

$$\phi[^\circ] = f[Hz]\frac{L[m]\lambda_0[A]}{3.956}\frac{360}{1000}, \qquad (1)$$

where ϕ is the chopper phase, f the chopper frequency, L the distance between the aforesaid chopper and the first chopper and λ_0 the averaged wavelength.
The double discs have two windows – one of the same width as the cross section of the guide and the second one three times that wide. The angular arrangement of the windows on a given pair of discs allows us to select a single pair of windows of identical width, one on each disc, that transmit neutrons by choosing an appropriate relative phase of the two choppers.

Sample environments and further possible extensions

The most important feature is the high field steady state magnet which can create a magnetic field of up to 25 T (later on possibly 40 T). Depending on the range of scattering angle required, the magnet can either be used in a symmetric or an asymmetric neutron beam configuration (see figure 2) or it can be removed from the experiment to allow for usual diffraction work. Additionally to the magnet or separately, further sample environment elements like cryostats creating low or high temperatures ranging from 1.5 – 700 K and pressure cells of up to 20 kbar can be employed. In a medium-term perspective possible extensions are a small angle scattering (SANS) option with a collimator length of up to 6 m and an inelastic neutron scattering option combined with high magnetic fields.

Simulation results

First Monte Carlo simulations using the VITESS package [5] show typical powder pattern diagrams for an Al sample and confirm the theoretically calculated resolution in backscattering direction of $\Delta d/d \approx 3 \times 10^{-4}$ (see figure 5) for the wavelength range of 0.7 Å < λ < 1.8 Å and at scattering angles 156° < 2θ < 179°.

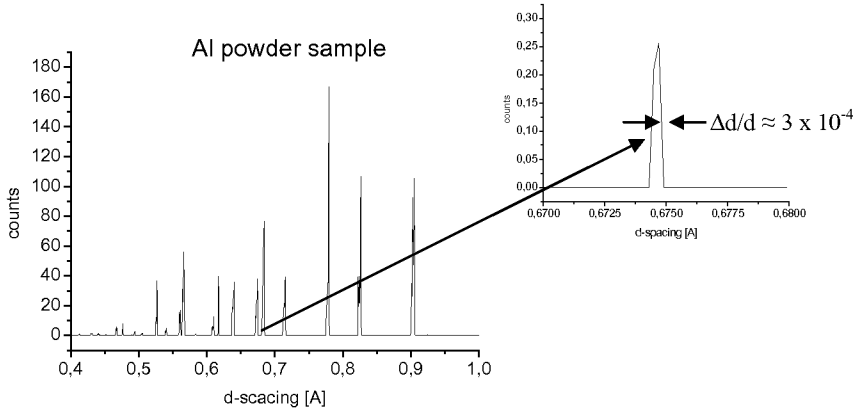

Figure 5. Powder pattern MC simulation results for 0.7 Å < λ < 1.8 Å and 156° < 2θ < 179° as a function of the d-spacing. At 2θ ≈ 176° and λ = 1.34 Å (right hand side figure), nearly the highest total resolution of δd/d ~ 3×10⁻⁴ is obtained.

Concluding remarks

The EXED instrument will be an all-purpose powder and single crystal diffractometer with a main emphasis on extreme environment conditions, primarily very high magnetic fields. It can satisfy high resolution as well as higher flux requirements. The proposed wavelength range is suited to cover crystal and magnetic structure needs. The instrument shall become operational in 2006 and will then be integrated into the BENSC user service instruments of the HMI Berlin.

References

1. Buras, B., 1963, *Nukleonika*, **8**, 259.
2. Stride, J.A. et al., 2000, *Nucl. Instr. Meth. Phys.Res. A*, **451**, 480.
3. Mezei, F., 1997, *J. Neutron Res*, **6**, 3.
4. Mezei, F., Russina, M. & Schorr, S., 2000, *Physica B,* **276 – 278**, 128.
5. VITESS website: www.hmi.de/projects/ess/vitess.
6. Mezei, F., Russina, M., Patent submitted in Berlin, 23.01.2002
7. Lieutenant, K. et al., *Proc. SPIE 49th Ann. Meeting (Int. Soc. f. Opt. Eng.)*, 2004, 5536, 134.

Z. Kristallogr. Suppl. **23** (2006) 195-198

R2D2: a new neutron powder diffractometer at NFL

A. Wannberg[1], M. Grönros[1], A. Mellergård[1], L-E. Karlsson[1], R. G. Delaplane[1,*], B. Lebech[2]

[1]Studsvik Neutron Research Laboratory, Uppsala University, SE-61182 Nyköping, Sweden
[2]Risø National Laboratory, Materials Research Department, DK-4000 Roskilde, Denmark
[*]Contact author, e-mail: Robert.Delaplane@studsvik.uu.se

Keywords: powder diffraction, neutron instrument, axial divergence

Abstract. The neutron powder diffractometer R2D2 (formerly named TAS3) has been transferred from the Risø National Laboratory and installed at the Studsvik Neutron Research Laboratory (NFL). Using a vertically focusing Ge(511) monochromator with a take-off angle of 90°, the incident neutron beam wavelength is 1.551 Å. The instrument has a bank of twenty ^{3}He detectors mounted on air cushions for positioning. Projects making use of this instrument include complex metal hydrides, magnetic materials, complex metal oxides and nano-structured materials.

Introduction

The neutron powder diffractometer R2D2 (formerly named TAS3) has been transferred from the Risø National Laboratory and installed at the Studsvik Neutron Research Laboratory (NFL). The reason for the transfer is the untimely permanent shut down of Risø's research reactor DR3 in 2000. Since there is a long tradition of the application of neutron diffraction to structural studies within the user community of NFL, the newly commissioned R2D2 instrument will provide an excellent complement to the existing facilities.

Description of the instrument

The technical specification for R2D2 is given in table 1, which is similar to the corresponding previous set-up of TAS3 at Risø. TAS3 had been designed and constructed as a multipurpose instrument with three different detector configurations [1]. The new instrument R2D2 has been installed with only the multi-detector arm, suitable for studies of powder samples. The same vertically focusing Ge(511) monochromator is used with a fixed take-off angle of 90°, giving an incident neutron beam wavelength of 1.551 Å. The bank of twenty ^{3}He detectors is mounted behind twenty 10' Soller collimators and the entire collimator-detector bank with shielding moves on air cushions. A complete powder diffraction pattern is obtained with a 5° scan. R2D2 has been designed with the optional setting of a Soller collimator (10') for

Table 1. Technical specification

Type of instrument	Two-axis diffractometer
Beam tube	H9 thermal, tangential
Monochromator	Vertically focusing Ge(511) / $2\Theta_M$=90°
Max beam size	10 x 50 mm^2 (sample position)
Neutron flux	5 x 10^6 n cm^{-2} s^{-1} (sample position)
Incident wavelength	1.551 Å
Angular range	4° < 2Θ < 140°
Collimation	α_1: 60' α_2: 10' Soller (optional, see figure 1) α_3: 10' Soller
Detectors	20 ^{3}He detectors, 5° separation 20 x 100 mm^2
Data acquisition and instrument Control	PC LabVIEW™

the secondary collimation (α_2) giving an improved resolution function. The resolution curves with and without secondary collimation are shown in figure 1.

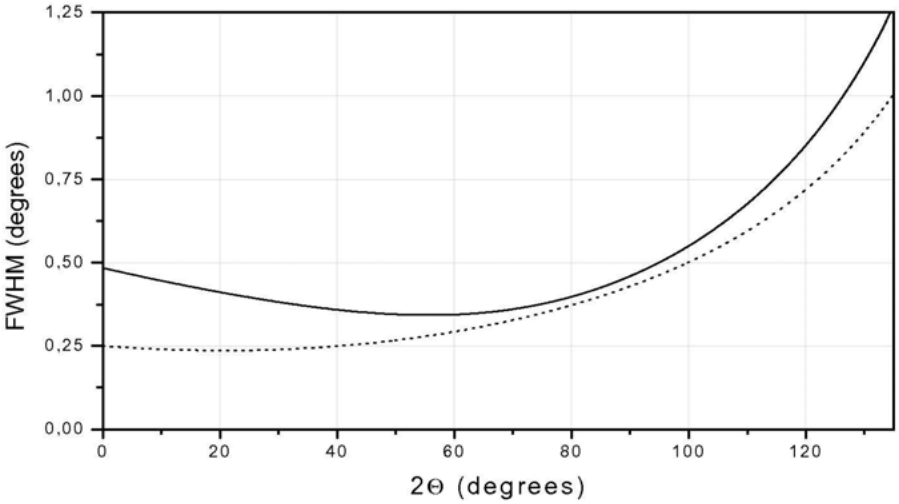

Figure 1. Resolution curves for the two different set-ups; no α_2 Soller collimator (solid curve) and 10' α_2 Soller collimator (dotted curve).

The data acquisition and instrument control software has been completely rewritten for PC LabVIEW™ providing a flexible instrumentation platform with a modern user interface. Instrument calibration parameters are determined using a least-squares fitting program that uses data from all peaks in a wide-angle scan (including the anti-parallel setting) of a standard reference material (e.g. Si, NIST 640c). Since the instrument is considerably affected by axial divergence, the formalism in [2,3] has been adopted. For the purpose of instrument calibration, a simplified version of the profile function has been implemented where only the approximate peak shifts (proportional to cot Θ) are used and not the full asymmetric shape. The output from data reduction can be obtained in formats suitable either for GSAS [4] or FullProf [5]. An example of a refinement of alumina (Al_2O_3, NIST 676) is shown in figure 2. The Gaussian part of the resolution function could be minimised using standard least-squares to yield U=0.385,V=-0.375 and W=0.201. In a refinement of data with the secondary collimation inserted, we obtained U=0.1924, V=-0.0709 and W=0.0625.

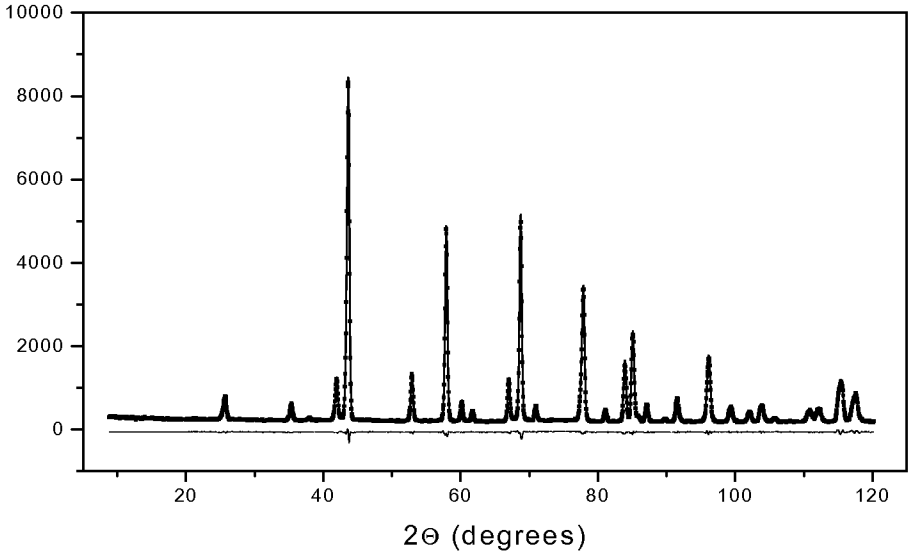

Figure 2. Rietveld refinement of the Al_2O_3 standard; observed (dots), calculated (solid curve).

In most of the collected data analysed so far, best fits for the asymmetry parameters in the Cox-Finger-Jephcoat (CFJ) approach [3] were obtained with S/L≈0.054 and D/L≈0.085, in which 2S is the sample height, 2D is the detector height and L is the sample to detector distance.

These values are close to the nominal ones as obtained with 2S = 5 cm, 2D = 10 cm and L = 60 cm. It was found that the CFJ profile function is the preferred description to account for the axial divergence, as compared to the standard low-angle corrections.

Applications

Projects currently making use of this instrument include diffraction studies of complex metal oxides such as perovskites, complex metal hydrides, magnetic- and nano-structured materials. Effective use of R2D2 has been demonstrated together with *in situ* experiments performed on SLAD (Studsvik Liquids and Amorphous materials Diffractometer) [6], a high intensity, low resolution instrument. A sample undergoing changes in structure as a function of temperature or pressure can be rapidly monitored on SLAD and then transferred to R2D2 when a new phase has developed and higher resolution is needed.

References

1. http://www.fys.risoe.dk/fys/ron/neutrons/facilities/tas/tas3/tas3desc.htm.
2. B. van Laar and W.B. Yelon, 1984, *J. Appl. Cryst.*, **17**, 47-54.
3. L. W. Finger, D. E. Cox and A. P. Jephcoat, 1994, *J. Appl. Cryst.*, **27**, 892-900
4. A.C. Larson and R.B. von Dreele, "*General Structure Analysis System (GSAS)*", Los Alamos National Laboratory Report LAUR, 1994, 86-748.
5. J. Rodriguez-Carvajal, "*FULLPROF: A Program for Rietveld Refinement and Pattern Matching Analysis*", Abstracts of the Satellite Meeting on Powder Diffraction of the XV Congress of the IUCr, Toulouse, France, 1990, p. 127.
6. A. Wannberg, A. Mellergård, P Zetterström, R.G. Delaplane, M. Grönros, L-E. Karlsson, R.L. McGreevy, 1999, *J. Neutron Res.*, **8**, 133-154.

Acknowledgements. We thank the Risø staff members for assistance in the preparation for transportation of the instrument and for valuable discussions during the course of installation. Financial assistance from the Göran Gustafson Foundation for transportation expenses is acknowledged. Financial support for instrument installation from Professor Gunnar Svensson (Stockholm University) within the framework of a Swedish Research Council project on studies of transition metal oxides is also acknowledged.

Z. Kristallogr. Suppl. **23** (2006) 199-204

Bent perfect crystal monochromator at the monochromatic focusing condition

Y. N. Choi[1], S. A. Kim[1], S. K. Kim[1], S. B. Kim[1], C. H. Lee[1], P. Mikula[2,*], M. Vrána[2]

[1]HANARO Center, KAERI, Yuseong, Daejeon 305-600, Korea
[2]Nuclear Physics Institute and Research Centre Řež, Ltd., 25068 Řež, Czech Republic.
[*]Contact author; e-mail: mikula@ujf.cas.cz

Keywords: powder diffraction, monochromatic focusing, bent crystal monochromator

Abstract. In conventional diffractometry with a mosaic monochromator due to a nonnegligible λ–θ correlation of the monochromatic beam impinging the sample, the resolution considerably differs in the parallel (+,-) and anti-parallel (+,+) setting. However, a bent perfect crystal (BPC) monochromator at monochromatic focusing condition can provide equal resolution properties at both parallel and anti-parallel setting and gives a chance to use both sides of the scattering plane. Three diffraction geometries with the BPC monochromators were tested and the received data of *FWHM* of the line profiles and the corresponding $\Delta d/d$ prove the possibility of simultaneous measurements in both settings.

Introduction

Conventional neutron diffractometers employing mosaic monochromators are used only in the parallel (+,-) measurement setting, because the resolution of the anti-parallel (+,+) setting is much worse [1]. However, if we could use both settings with the equivalent resolution, the measurement efficiency could be twice of that related to the traditional mode. A strong difference in the resolution properties in the parallel and antiparallel settings is brought about by a nonnegligible λ–θ correlation of the monochromatized beam impinging the sample in the scattering plane. In order to overcome this problem the momentum distribution of the monochromatized neutrons should be symmetric with respect to the axis of the beam impinging the sample. Three monochromator arrangements which could provide a rather highly collimated monochromatic neutron beam with a negligible λ–θ correlation and a reasonable $\Delta\lambda$ (keeping the luminosity and the instrument resolution on a feasible level) have been already tested. These are:

1. *Fully asymmetric diffraction (FAD) geometry of the Si-BPC monochromator* [2]. The FAD geometry of the monochromator is in fact a limiting case of the Fankuchen geometry [3] that implicates some limitations on the crystal (monochromatized beam is passing the crystal slab along its longest edge and exits it from the end face). At present, due to a low attenuation, Si-crystal is the best candidate for this purpose.

2. *Dispersive double-crystal setting* [4]. A strongly dispersive double-crystal arrangement of two mosaic or bent perfect crystals or combination of them is another set up having a negligible θ–λ correlation of the monochromatic neutrons in the scattering plane and can provide a sufficient neutron current at the sample position [4].
3. *Multiple reflection 'Umweganregung' monochromator*. This monochromator is based on a multiple reflection process realized in one crystal which can be observed when more than one set of planes are simultaneously operative for a given wavelength [5-8]. It has been already demonstrated [8] that strong multiple reflection effects observed in elastically deformed crystals can be used for ultra-high monochromatization and diffraction studies.
This paper deals with another setup of the BPC monochromator adjusted for the monochromatic focusing. Contrary to the above mentioned monochromator geometries where a narrow phase-space element is parallel to the beam axis, in this case the phase-space element is aligned perpendicularly to the beam axis.

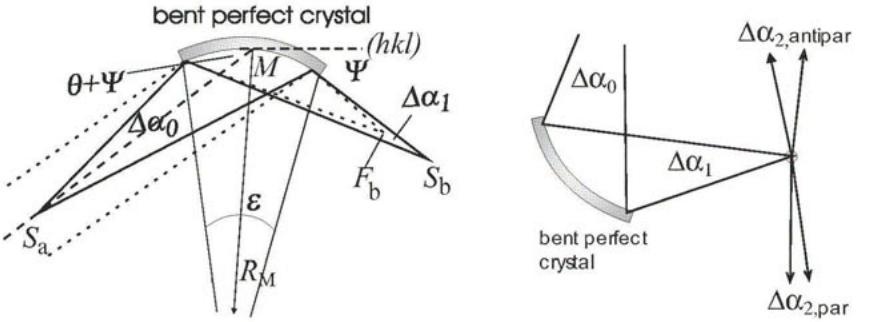

Figure 1. Real space representation of diffraction by BPC-crystal monochromator - (a) and schematic sketch of a powder diffractometer in parallel and antiparallel settings – (b).

General Formalism

Mosaic monochromators have been used for several decades and the geometrical optics of diffractometers (or spectrometers) employing Soller collimating systems are at present well understood. Caglioti's treatment [9] relates to the case of diffraction on powdered samples the *FWHM* of the diffraction line profiles depends on the monochromator take-off angle ($2\theta_M$), the scattering angle ($2\theta_S$), collimator angles (α_i) and the mosaic spread of the monochromator (β). In the simplest case of $\alpha_1 = \alpha_2 = \alpha_3 = \beta \equiv \alpha$ we arrive at [1]

$$FWHM = \alpha\,[(11\text{-}12a_{SM}+12a_{SM}^2)/6]^{1/2}, \qquad (1)$$

where $a_{SM} = (d\lambda/d\theta)_{monochr} / (d\lambda/d\theta)_{sample} = -\tan\theta_S / \tan\theta_M$ is the dispersion parameter. In the (+,-) setting, the related Bragg angles have the opposite signs and the dispersion parameter a is positive, while in the antiparallel (+,+) setting Bragg angles have the same signs and a is negative. As can be seen from (1), the square of the *FWHM* is a parabola of variable a_{SM} with a minimum at $a_{SM} = 1/2$. Furthermore, $FWHM_{antipar}$ is always larger than $FWHM_{par}$.
The BPC monochromator has tunable reflectivity and resolution properties [10]. Characteristics of diffracted beams and line profiles related to the investigated samples strongly depend

on bending radius, diffraction geometry (symmetric or asymmetric), crystal thickness and monochromator-sample distance. In addition to focusing in real space one of the prominent characteristics of a BPC monochromator is that one can easily manipulate the λ–θ correlation of the monochromatized beam impinging the sample. This property often allows to exploit focusing in momentum space [10].

For imaging in the scattering plane by a thin cylindrically bent perfect crystal the general lens formula ($f_a/a + f_b/b = 1$) can be used, where $f_{a,b} = (R_M \sin(\theta_M \pm \psi))/2$ is the focal length dependent on the angle ψ of the asymmetry cut (see figure 1). In practice, the monochromator-sample distance L_{MS} is fixed and should coincide with the image distance b ($b = L_{MSb}$) of a point source S_a being at a distance $a = L_{SaM}$ before the monochromator. In case of the parallel incident beam L_{MS} should coincide with f_b. For given θ_M and the bending radius R_M for any point of the sample, we arrive at the relation

$$a(R_M) = f_M/(1 - f_M/b) \tag{2}$$

where $f_M = R_M \cdot \sin(\theta_M \pm \psi)/2$ is the focal length. Then, the sample is reached by a $\Delta\alpha_1$–convergent bunch of strongly θ–λ correlated rays according to [10]

$$\Delta\lambda/\lambda = \Delta\alpha_1 (1 - L_{MS}/2f_M)\cot\theta_M . \tag{3}$$

The angular convergencies (or divergencies) $\Delta\alpha_0$ and $\Delta\alpha_1$ of the rays in the bunch before and behind the monochromator, respectively, are related as

$$\Delta\alpha_1 = 2\varepsilon(R_M) - \Delta\alpha_0 \tag{4}$$

where $\varepsilon(R_M) = (W/R_M)\sin(\theta_M \pm \psi)$ is the total change of the angle of incidence over illuminated crystal length (W is the width of the incident beam). A typical application of real space focusing is to focus the beam from e.g. a thermal neutron guide with a large cross-section on a small sample, thus transforming the area is into a solid angle.

In powder diffractometry, an angular analysis of the beam diffracted by the sample is performed. The beam diffracted by the sample of the divergence $\Delta\alpha_2$ (each ray of the beam incident on the sample is diffracted with the same probability) is also correlated according to

$$\Delta\alpha_2 = \Delta\alpha_1 [2a_{SM}(1 - L_{MS}/2f_M) - 1] \tag{5}$$

$$\Delta\lambda/\lambda = \Delta\alpha_2 \cot\theta_M (1 - L_{MS}/2f_M)/[2a_{SM}(1 - L_{MS}/2f_M) - 1]. \tag{6}$$

Setting $\Delta\alpha_2 = 0$ in (5), we arrive at the optimum condition for R_M,

$$R_{M,opt} = 2L_{MS}/[\sin(\theta_M \pm \psi)(2 - 1/a_{SM})], \tag{7}$$

which results in a (quasi-)parallel diffracted beam. A small divergence of the diffracted beam is independent of $\Delta\alpha_1$ and is brought about by focusing uncertainties $\Delta\alpha_{2t}$ and $\Delta\alpha_{2w}$ as a result of a nonnegligible thickness of the monochromator t_M (responsible for a nonnegligible effective mosaicity) and a finite width of the sample w [10] as

$$\Delta\alpha_{2t} = 2(t_M/R_M)a_{SM}/\tan(\theta_M \pm \psi), \quad \Delta\alpha_{2w} = w(2a_{SM} - 1)/L_{MS} . \tag{8}$$

Of course, the condition (7) is much easier fulfilled in the parallel diffraction geometry which requires a larger bending radius. Inspection of (7) reveals that contrary to the geomery with a mosaic monochromator in this case the beam (quasi-)parallelity can be achieved even for a large range of a_{SM}. However, if $\Delta\alpha_{2,par} = 0$ at the (+,-) setting, at the (+,+)

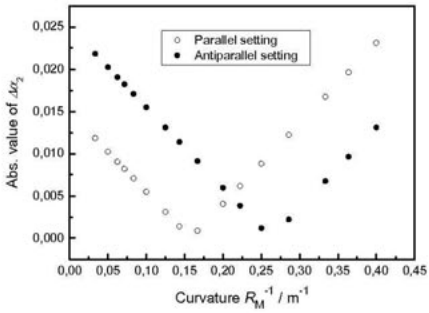

Figure 2. Example of the behaviour of the scattered beam divergence versus crystal curvature for $\Delta\alpha_1$=5x10^{-3} rad, L_{MS}=2m, a_{SM}=2 and θ_M=25°.

setting $\Delta\alpha_{2,antipar} = 4\Delta\alpha_1 \cdot a_{SM} \cdot (1-L_{MS}/2f_M)$. For smaller values of the radius R_M ($R_M<R_{M,opt}$), the value of $|\Delta\alpha_{2,par}|$ increases while the value of $|\Delta\alpha_{2,antipar}|$ decreases approaching a minimum (see figure 2). However, at $R_{MF}=L_{MS}/\sin(\theta_M \pm \psi)$ there is an intersection of both parabolas where the divergences of the scattered beam for both diffraction settings are equal ($|\Delta\alpha_{2,par}| = |\Delta\alpha_{2,antipar}|$) and simultaneously $\Delta\lambda/\lambda = 0$. It means that all neutrons within the $\Delta\alpha_1$ divergence have the same wavelength. This effect is known as *monochromatic focusing*.

Experimental Results and Discussion

The test experiment has been carried out at the beam port ST1 of the HANARO reactor in KAERI. The experimental set-up and three diffraction geometries of the BPC monochromator are shown in figure 3 (SDG means symmetric diffraction geometry and ADG/compression or ADG/expansion mean the asymmetric diffraction geometry with the output beam compression or beam expansion, respectively). The take-off angle $2\theta_M$= 45°, the monochromator-sample distance L_{MS}=3 m and sample-detector distance L_{SD}=0.6 m were fixed and brought about some limitations. Since the distance L_{SD} was rather short, the *FWHM* of the diffraction line profiles of the used polycrystalline sample (Cu-rod) were strongly affected by its width (Φ=4.5 mm) and the spatial resolution of the 2d-PSD (200 mm (W) x 200 mm (H)) of 2 mm. Only these two parameters contribute to the resolution by an uncertainty of about 28 min of arc. As shown in figure 3, three typical diffraction geometries were chosen to investigate the dependence of the *FWHM* of the line profiles and the ($\Delta d/d$)-resolution on the bending radius R_M. For the SDG-experiment, a Si(220) slab of the dimensions of 200x30x3 mm^3 was used as the monochromator crystal. For the ADG/compression and ADG/expansion experiments, Si(211) slab (t_M=3.8 mm) with 311 planes at Ψ=10° and a special cut of Si-slab (t_M=3.8 mm)

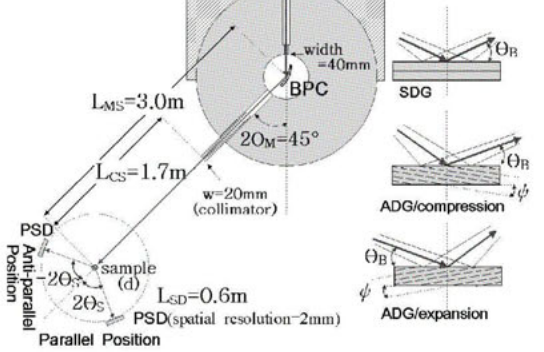

Figure 3. Experimental set-up and diffraction geometries used in the test at ST1 beam port of the HANARO reactor.

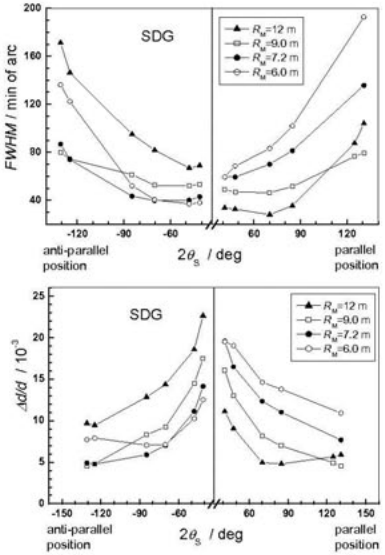

Figure 4. Results of FWHM and Δd/d resolution for Si(220)-slab (λ=0.147 nm) for SDG condition (θ_M=22.5°).

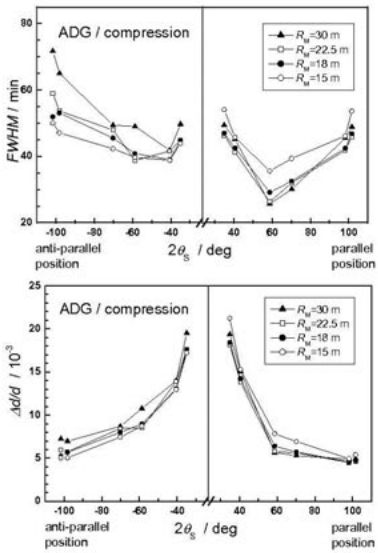

Figure 5. Results of FWHM and Δd/d resolution for Si(311)-slab (λ=0.125 nm) for ADG/compression condition ($\theta_M - \Psi$=12.5°.

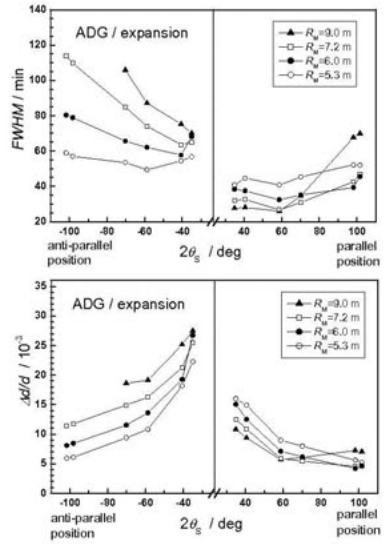

Figure 6. Results of FWHM and Δd/d resolution for Si(311)-slab (λ=0.125 nm) for ADG/expansion condition ($\theta_M + \Psi$=42.5°).

with the planes (311) at Ψ=20°, respectively, were used. The calculated values of the bending radii R_{MF} corresponding to the individual geometries are 7.84 m, 13.9 m and 4.46 m, respectively.

Figures 4-6 display the related experimental results and demonstrate that when R_M approaches R_{MF}, the resolution becomes equivalent in both diffraction geometries. However, these results cannot be considered from the point of view of the real resolution properties of the BPC monochromator (see (8)). Inspection of figures 4-6 reveals that the best achieved resolution in all cases approaches the value given by the spatial resolution of the detector and the width of the sample. It can also be seen from figures 4-6, that monochromatic focusing condition can be easier achieved in the diffraction geometry with the SDG and (mainly) ADG/compression geometry because of larger values of R_{MF} which fact also allows employing thicker monochroma-

tor crystal slabs. The reflectivity power of the BPC elements is well known [10] and the phase space element given just by $\Delta\alpha_1$ and $\Delta\lambda$ could be easily predicted. It should also be mentioned that in the range of scattering angles $2\theta_S$, where condition (7) is not fulfilled, the divergence $\Delta\alpha_2$ depends on the divergence $\Delta\alpha_1$ of the beam incident on the sample (see eq. (5)) and at the *monochromatic focusing* condition $\Delta\alpha_2=\Delta\alpha_1$. Then, the angular resolution of the scattering device can be controlled by a proper adjustment of $\Delta\alpha_1$ by a collimator. For finding the optimum parameters (crystal cut, thickness and bending radius) Monte Carlo simulations would be desirable [11].

Conclusion

By employment of the BPC monochromator at the *monochromatic focusing* condition the possibility of equal and quite flat resolution property of powder diffraction in both the parallel and the antiparallel settings has been demonstrated. Thus, it permits to extend the range of scattering angles considerably. It can be efficiently used e.g. in strain/stress measurements when two strain components can be measured simultaneously. Another application of such focusing monochromator could be for inelastic scattering experiments on a triple axis spectrometer [12] where a BPC-analyzer at the *monochromatic focusing* condition can be used.

References

1. Bacon, G.E., *Neutron Diffraction*, (Clarendon Press, Oxford, 1975) pp.101-111.
2. Mikula, P., Lukáš, P., Michalec, R., 1987, *J. Appl. Cryst.* **20,** 428.
3. Fankuchen, I., 1937, Nature, **139,** 193.
4. Mikula, P., Vrána, M., Choi, Y.N., Kim, S.A., Oh, H.S., Sung, K.H., Lee, C.H., *Mater. Sc. Forum*, 2002, **404-407,** 299.
5. Renninger, M., 1960, *Zeitschrift für Kristallographie,* **113,** 99.
6. Moon, R.M., Shull, C.G., 1964, *Acta Cryst.* **17,** 805.
7. Kuich, G., Rauch, H., 1967, *Nukleonik,* **3,** 139.
8. Mikula, P., Kulda, J., Vrána, M., Michalec, R.T., Vávra, J., *Nucl. Instrum. Methods,* 1982, **197,** 563.
9. Caglioti, G., *Thermal Neutron Scattering*, (editted by B.T.M. Willis, 1970, Clarendon Press, Oxford, pp. 14-33.
10. Wagner, V., Mikula, P., Lukáš, P., 1994, *Nucl. Instrum. Methods A*, **338,** 53.
11. Kulda, J., Šaroun, J., 1996 *Nucl. Instrum. Methods A,* **379,** 155.
12. Šaroun, J., Kulda, J., 1997, *Physica B*, **234-236,** 1102.

Acknowledgements. We are grateful to Mr. B.H. Choi, Mr. Y.H. Choi, Mr. K.P. Hong, Dr. M.K. Moon and Dr. V.T. Em for the experiment preparations and to Ms. H.S. Oh for the data processing. This work was supported by the Korean Ministry of Science and Technology through the National Nuclear R&D Programme and the Scientist Visiting Program and in the Czech Republic by the projects GA-CR (No. 202/03/0891), COST – OC P7.003, AV0Z10480505 and MSM2672244501.

Z. Kristallogr. Suppl. **23** (2006) 205-210

Multiple-reflection neutron bent-perfect-crystal (BPC) monochromator

P. Mikula[1,*], M. Vrána[1], V. Wagner[2]

[1]Nuclear Physics Institute and Research Centre Řež, Ltd., 25068 Řež, Czech Republic
[2]Physikalisch-Technische Bundesanstalt, Bundesallee 100, 38116 Braunschweig, Germany
[*]Contact author; e-mail:mikula@ujf.cas.cz

Keywords: neutron diffraction, monochromator, multiple reflections

Abstract. A high-resolution monochromator performance based on a multiple reflection effect realized in cylindrically BPC element has been recently tested with the aim of its possible employment in instruments for powder diffractometry. It has been found that the diffractometer employing such monochromator provides a very high resolution (*FWHM* of the instrumental $\Delta d/d$ - profile can be less than 8×10^{-4}) in the vicinity of usually used $2\theta_S \approx 90^\circ$ and a good luminosity. Due to the unique resolution, the diffractometer equipped with such a monochromator can be used for fine substructure studies of polycrystalline materials.

Introduction

It is known that the effects of multiple Bragg reflections (often referred as to simultaneous reflections) in X-ray or neutron diffraction can be observed when a crystal lattice is oriented in such a way that more than one set of planes are simultaneously operative for a given wavelength. Using a terminology of reciprocal lattice space, these effects occur when a second reciprocal lattice point (or more) is brought onto the Ewald sphere. Multiple diffraction effects can result in a so called *Aufhellung* (reducing the intensity of a strong primary reflection) or *Umweganregung* (increasing the intensity of a weak primary reflection or simulation of forbidden primary reflection). For X-rays, the umweg-diffraction peaks were first observed by Renninger [1]. In the simplest case of the umweg-effect a particular weak or forbidden primary reflection is strengthened by a successive cooperation of the two allowed reflections, secondary and tertiary, which are defined by the scattering vectors $\boldsymbol{g}_1$, $\boldsymbol{g}_2$ and $\boldsymbol{g}_3$, respectively. Scattering vectors $\boldsymbol{g}_2$ and $\boldsymbol{g}_3$ are in relation to $\boldsymbol{g}_1$ as $\boldsymbol{g}_1 = \boldsymbol{g}_2 + \boldsymbol{g}_3$. It follows from

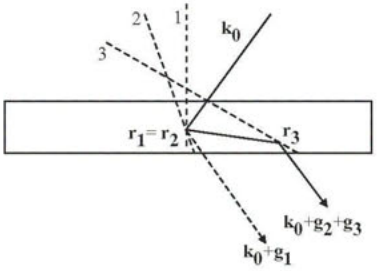

Figure 1. Schematic diagram of a two-step multiple Bragg reflection simulating a weak or forbidden reflection. The numbers 1,2 and 3 represent the primary, secondary and tertiary reflection planes, respectively.

the crystal symmetry that when a secondary reflection fulfils the Bragg condition simultaneously with the primary one, there exists automatically the tertiary reflection defined by $\boldsymbol{g}_3 = \boldsymbol{g}_1 - \boldsymbol{g}_2$. Since Renninger's first observation of the umweg-peaks many theoretical and experimental investigations of the generally n-beam cases have been published (see e.g. [2], where many related references can be found).
However, the flux of thermal neutrons is usually not sufficient for the observation of such small dynamical effects in perfect single crystals. Therefore, in the case of neutron diffraction, the multiple reflection effects have been reported only in a few papers dealing with mosaic or deformed single crystals. Similarly to the neutron investigations of "Aufhellung" and "Umweganregung" effects in mosaic crystals [3,4], we have found that multiple reflection effects resulting in *Umweganregung* can be also observed in elastically deformed perfect crystals [5,6]. In related experiments we have demonstrated that the *Umweganregung* intensity of the monochromatic beam amplified by ultrasonic vibrations or by cylindrical bending can be more than one order magnitude higher than the intensity related to the allowed reflection of a perfect nondeformed crystal. Furthermore, as it was already experimentally proved due to the fact that the second and third system of reflection planes are mutually in the dispersive setting, the doubly reflected beam has a narrow band-width $\Delta\lambda/\lambda$ in the range from 10^{-4} to 10^{-3} and divergence of the orders of minutes of arc. It was pointed out that the umweg-effect can possibly be used for a high-resolution monochromatization [6]. The purpose of the experiment presented in this paper was identifying strong umweg-effects with the outlook of a possible exploitation for high-resolution monochromatization when using three different cuts of cylindrically bent perfect silicon crystal slabs set for symmetric transmission geometry.

General remarks

For investigation of multiple reflection effects usually two methods are used:
a. Method of azimuthal rotation of the crystal lattice around the scattering vector of the primary reflection for a fixed wavelength.
b. Method of θ–$2\theta_D$ scan in the white beam for a fixed azimuthal angle.
The former method was used in our earlier experiments [5, 6]. In the present case we preferred the latter method of θ–$2\theta_D$ scan when setting the cylindrically bent perfect Si-crystal slabs in the polychromatic neutron beam in the diffraction geometry for symmetric transmission. This method permitted us to determine strong umweg-effects at different wavelengths. In comparison to mosaic crystals, just the choice of a suitable geometry and elastic deformation may substantially lower the relative contribution of higher orders which would be very important in cases when an umweg-monochromator would be envisaged for a practical employment. It is known that the integrated reflectivity of a deformed crystal is a function of the scalar product $(\boldsymbol{g}\cdot\boldsymbol{u})$ [7] which may be zero for both forbidden and its higher order reflections, i.e. $(\boldsymbol{g}_1\cdot\boldsymbol{u})=0$ and the corresponding integrated reflectivity is independent of the deformation represented by the displacement of atoms $\boldsymbol{u}$. This is also valid in our case of cylindrical bending and symmetric transmission geometry. On the other hand, $(\boldsymbol{g}_2\cdot\boldsymbol{u}) = -(\boldsymbol{g}_3\cdot\boldsymbol{u})$ need not to be zero and the deformation can bring about a large increase of the umweg-effect keeping the integrated reflectivity related to the higher order reflections

constant. Furthermore, contrary to dynamical diffraction on perfect crystals, the quasiclassical approach can be applied for interpretation of the umweg-effects [8]. As schematically displayed on figure 1, according to this approach, the multiple diffraction process simulating the primary reflection in the point r_1 can be assumed as a series of successive secondary and tertiary beam reflections taking place in two different points r_2 and r_3 (which generally have different deformations), respectively. We suppose that the mutual separation of of these two points is larger than the extinction length. Then, on the basis of this kinematical assumption, the so-called n-beam case which is well known in the dynamical diffraction by perfect crystals can be considered as simultaneous action of several independent pairs of secondary and tertiary reflections.

Calculation

From the geometry displayed in figure 2 it is possible to derive the following relations

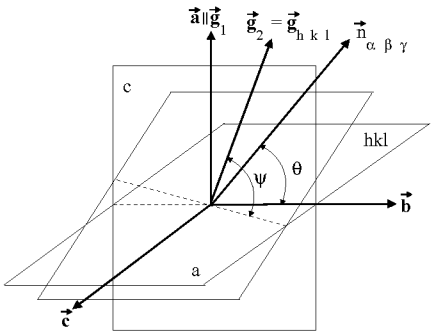

Figure 2. Coordinate system for description of the secondary reflection occuring with the basic primary reflection.

$$\begin{aligned} \boldsymbol{n}_{\alpha\beta\gamma} \cdot \boldsymbol{g}_1 &= |\boldsymbol{g}_1| \sin\theta \\ \boldsymbol{n}_{\alpha\beta\gamma} \cdot \boldsymbol{g}_{hkl} &= |\boldsymbol{g}_{hkl}| \sin\psi \\ \boldsymbol{n}_{\alpha\beta\gamma} \cdot \boldsymbol{b} &= |\boldsymbol{b}| \cos\theta, \end{aligned} \qquad (1)$$

where $|\boldsymbol{n}_{\alpha\beta\gamma}| = 1$ from the definition and

$$\sin\psi = (d_1/d_{hkl}) \sin\theta \qquad (2)$$

is given from the Bragg condition (d is the lattice spacing).

Then, for crystal slabs used in our experiment we could derive the relations providing Bragg angles θ of the primary reflection where secondary reflection represented by the Miller indices h,k,l can participate at the *Umweganregung* (or *Aufhellung*) as

1. For the crystal slab with the largest surface parallel to (1̲10) and the longest edge parallel to [111]

$$\tan\theta = (3/2)^{1/2}(-h+k) / [(h^2+k^2+l^2)/m - h-k-l]. \qquad (3)$$

2. For the crystal slab with the largest surface parallel to (11̲2) and the longest edge parallel to [111]

$$\tan\theta = (1/2)^{1/2}(-h-k+2l) / [(h^2+k^2+l^2)/m - h-k-l]. \qquad (4)$$

3. For the crystal slab with the largest surface parallel to (1̲10) and the longest edge parallel to [001]

$$\tan\theta = (1/2)^{1/2}(-h+k) / [(h^2+k^2+l^2)/\mathrm{m} - l]. \qquad (5)$$

The parameter m in the relations (3)-(5) means the order of the primary reflection.

Using the formulae (3)-(5), one can easily identify secondary and tertiary reflections participating in *Umweganregung* with respect to a chosen primary reflection. However, when setting the crystal in the polychromatic incident beam, similarly to a single reflection case,

the presence of higher (or lower) orders can be found. For example, if in our case we are interesting in *Umweganregung* with respect to a forbidden primary Si(222) reflection, in many cases one can also find *Umweganregung* effect with respect to the primary reflections Si(111), Si(333), Si(444) etc., simultaneously. In practice, all undesirable higher (or lower) order contributions can be eliminated by a neutron wavelength selector. Sometimes, the wavelength distribution of neutrons passing through the neutron guide can be favourable, when undesirable higher order contributions are automatically eliminated, because their corresponding shorter wavelength neutrons are not present in the spectrum. Therefore, in our case we omitted all umweg-contributions corresponding to the neutron wavelengths smaller than 0.08 nm. Furthermore, one should consider that the reflection probability related to individual secondary and tertiary reflections is rather small for shorter neutron wavelengths [8]. Contrary to the mosaic crystals, in our case of cylindrically bent perfect crystals for a detailed estimation of the individual umweg-contributions the value of the scalar product $|\boldsymbol{g}_{2,3}\cdot\boldsymbol{u}|/(|\boldsymbol{u}|\cdot|\boldsymbol{g}_{2,3}|)$ plays also an important role.

Search for strong umweg-effects

The experimental search of the umweg-effects appearing at different wavelengths was done on the POLDI diffractometer installed at the end of the thermal neutron guide in GKSS Geesthacht. Having at a disposal three cylindrically bent Si-crystal slabs of different cut, after setting them for symmetric transmission, we carried out θ–$2\theta_D$ scans in the θ–range from 7° to 60° (for one azimuthal position) with the largest surface of the crystal perpendicular to the scattering plane. Then, the elastic deformation brought about by bending could have a strong effect on reflections participating in *Umweganregung*. In order to achieve large scattering angles $2\theta_D \leq 120°$ in the course of the search for umweg-effects, the Si-slabs were situated in the white beam at the sample position. Therefore, the cross-section of the incident white beam was limited by a diaphragm of 3 x 3 mm^2 situated in the guide tube of about 3 m before the bent crystal. Figures 3-5 display parts of the individual scans where the umweg-effects were strongly excited. For the sake of comparison, the scan with a flat nonbent crystal as well as the background are also introduced in figure 3. It should be pointed out that the individual crystal slabs were of different thicknesses. This parameter is also very important for an estimate of the reflectivity power of the umweg-monochromator. Roughly, it can be said that the intensity of the umweg-effect is linearly proportional to the crystal thickness. Then, of course, the divergence $\Delta\theta$ of the diffracted beam and the $\Delta\lambda$ spread increases correspondingly. As it has been already pointed out before [6] a practical use of multiple reflection monochromator requires an optimization procedure for the curvature with respect to the individual umweg-effect.

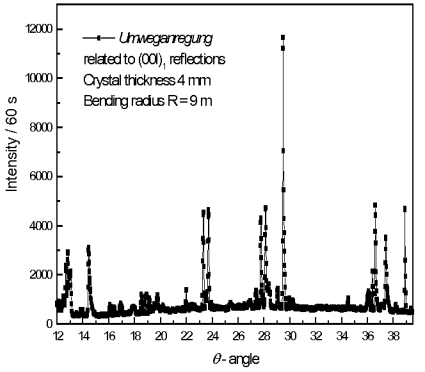

Figure 3. θ–$2\theta_D$ scan with the crystal slab (the largest face parallel to (110)) set for $(00l)_1$ reflections in the symmetric transmission geometry.

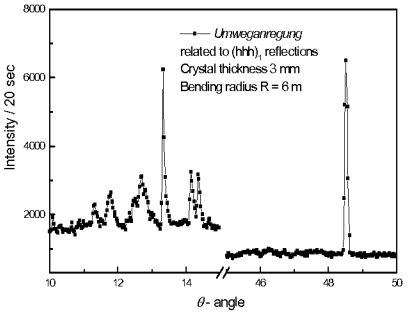

Figure 4. θ–$2\theta_D$ scan with the crystal slab (the largest face parallel to (112)) set for $(hhh)_1$ reflections.

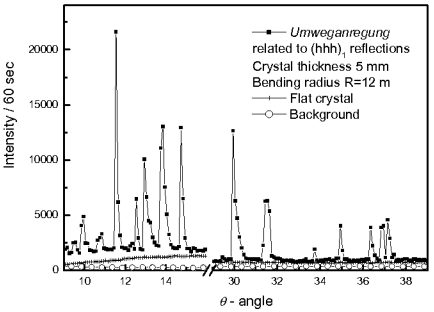

Figure 5. θ–$2\theta_D$ scan with the crystal slab (the largest face parallel to (110)) set for $(hhh)_1$ reflections.

Experimental test of the umweg- monochromator

For the present experimental studies we chose the effect observed at θ_M= 29.956° which is related to the simulation of the forbidden 222 reflection by a co-operative action of 153/1-3-1 and -31-1/513 (secondary/tertiary) reflections at λ=0.156 nm (see figure 5). It has been already proved in the experiment with a single crystal sample depending on the crystal curvature the monochromatic beam from the umweg-monochromator is highly parallel within the divergence of about (1-5)x10^{-4} rad and has excellent $\Delta\lambda/\lambda$ resolution [6]. In the present case the monochromatic beam obtained by this multiple reflection monochromator was used in powder diffraction test carried out with a solid α-Fe polycrystalline standard sample (Φ= 2 mm). Figure 6 displays several diffraction profiles that clearly prove the applicability of the umweg-monochromator for high-resolution diffraction studies. *FWHM* of the diffraction profiles are however, determined by the spatial resolution of the used PSD (1.5 mm) and the width of the sample of 2 mm. Therefore, it can be considered as an upper limit. Then, this performance we used for investigation of Fe-reflections in an induction hardened S45C steel rod (Φ=20 mm) having different phase composition at different distances from the rod axis. The gauge volume was determined by 2 mm wide slits in the incident as well as diffracted beam. Figure 7 displays the diffraction profile obtained at the distance 8 mm from the axis. Similarly, figure 8 displays the diffraction profile obtained at the distance 6 mm from the axis. Thanks to the used high-resolution monochromatic beam, after a fitting procedure we could reliably determined contributions of the individual phases.

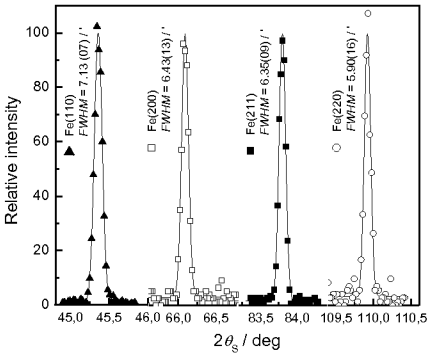

Figure 6. Examples of the α-Fe profiles taken with the umweg-monochromator.

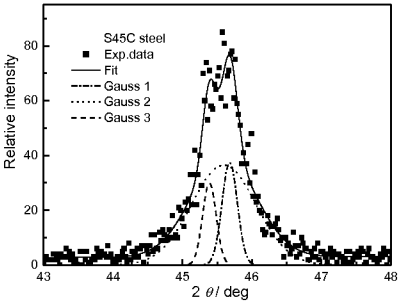

Figure 7. Induction-hardened S45C steel diffraction profile taken at 2 mm under the surface with the fitted profiles related to the perlitic, ferritic and martensitic phases.

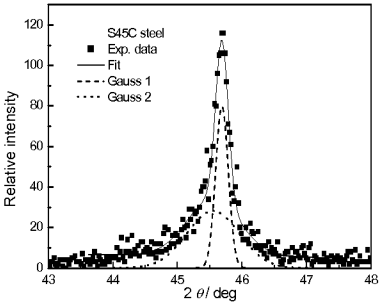

Figure 8. Induction-hardened S45C steel diffraction profile taken at 4 mm under the surface with the fitted profiles related to the ferritic and martensitic phases.

Conclusion

Diffractometers employing umweg-monochromator can provide very high resolution at low take-off angles. The resolution can be comparable to that of back-scattering instruments. They can be efficiently used namely at high-flux neutron sources. For finding the optimum parameters of the umweg-monochromator (crystal cut, thickness and bending radius) and the performance of the scattering device Monte Carlo simulations would be desirable [9].

References

1. Renninger, M., 1960, *Zeitschrift für Kristallographie,* **113**, 99.
2. Chang, S.H., *Multiple Diffraction of X-rays in Crystals* (Springer Verlag, 1984; Moscow "Mir", 1987).
3. Moon, R.M., Shull, C.G., 1964, *Acta Cryst.* **17,** 805.
4. Kuich, G, Rauch, H., 1967, *Nukleonik* **3,** 139.
5. Mikula, P., Michalec, R.T., Vrána, M., Vávra, J., 1979, *Acta Cryst.* A **35,** 962.
6. Mikula, P., Kulda, J., Vrána, M., Michalec, R.T., Vávra, J., 1982, *Nucl. Instrum. Methods* **197,** 563.
7. Takagi, S., 1962, 1962, *Acta Cryst.* **15,** 1311.
8. Kulda, J., Mikula, P., 1985, *Phys. Stat. Sol. (a),* **92,** 95.
9. Šaroun, J., Kulda, J., 1997, *Physica B* **234-236**, 1102.

Acknowledgements. We are grateful to dr. K. Inoue from the Faculty of Science and Technology, Ryukoku University for a kind providing the induction-hardened S45C steel sample and GKSS Geesthacht where the experiments were carried out. This work was in the Czech Republic supported by the research projects GA-CR (No. 202/03/0891), COST – OC P7.003, AV0Z10480505 and MSM2672244501.

Z. Kristallogr. Suppl. **23** (2006) 211-216

Wavelength calibration in conventional SANS setup with a mechanical velocity selector

L. Almásy*, A. Len, M. Markó, E. Rétfalvi

KFKI Research Institute for Solid State Physics and Optics,
POB 49, Budapest – 1525, Hungary
*Contact author; e-mail: almasy@sunserv.kfki.hu

Keywords: small-angle neutron scattering, velocity selector, wavelength calibration, silver behenate

Abstract. In the conventional setup of a small-angle neutron scattering instrument a nearly monochromatic neutron beam is formed by means of a mechanical velocity selector. We studied the influence of the wavelength distribution in the incident beam on the wavelength of the neutrons reaching the sample. The assumption that the wavelength spectrum behind the selector equals to the product of the incident spectrum of the thermalized neutrons and the transmission window of the selector predicts satisfactorily the wavelength measured at sample position. An approximate relation is given between the effective wavelength and the selector rotation speed. The described method of wavelength calibration can improve the precision of size determination in SANS experiment.

Introduction

In the conventional setup of a small-angle neutron scattering instrument the neutron beam is monochromatized by means of a mechanical velocity selector. The main factors that determine the wavelength of the neutrons reaching the sample are the wavelength distribution in the incident beam, the transmission characteristics of the selector and those of the mirror-coated neutron guides. The knowledge of the right wavelength is essential for obtaining size parameters with precision as high as one percent. A possible source of error in wavelength calibration can be the assumption that the wavelength is inversely proportional to the selector rotation speed.

In the present work, we derived an approximate analytical formula that gives the wavelength of the neutrons reaching the sample in function of the selector speed, and compared it with the experimentally determined effective wavelength. The latter was measured using a silver behenate powder sample.

The neutron spectrum transmitted by the selector

The transmission function of a velocity selector is determined by its geometrical parameters, it has usually a triangular shape, and the position of its center, $\lambda^{selector}$, is related to the speed of rotation:

$$\lambda^{selector} = C / \omega , \qquad (1)$$

where C is a constant, and ω is the selector rotation speed. Due to its simplicity, equation (1) is used widely for the calculation of the neutron wavelength from the selector rotation speed. The constant C is determined by the geometry of the selector and the tilt angle between the selector axis and the neutron beam; it can be determined experimentally by measuring the wavelength at certain selector speed, or calculated from the specifications of the selector.
In a real experiment the neutrons that reach the sample have some unknown wavelength distribution, which can often be well approximated by a Gaussian distribution, centered at λ^{eff} . The effective wavelength however does not necessarily coincide with $\lambda^{selector}$. For the SANS instrument at NIST, the observed difference between the calculated wavelength and the measured one was attributed to the slope of the incident spectrum [1]. Calibrating the selector with wavelength resolution 10% FWHM at ILL, a relation $\lambda^{eff} = A + B / \omega$ has been obtained [2]. The small offset parameter A led to a deviation from equation (1) less than 1% over the investigated λ-range. Authors of a recent paper [3] noted that the non-flat incident spectrum deforms the transmitted spectrum, and therefore the actual wavelength should be measured rather than calculated.

It is well-known that the wavelength distribution of the neutrons in the beam behind the selector can be written as the product of the selector transmission function and the wavelength distribution in the incident beam [4, 5]. In λ-space, the distribution $\Phi^{transmitted}(\lambda, \omega)$ of the neutrons transmitted by the selector is:

$$\Phi^{transmitted}(\lambda, \omega) = \phi_{selector}(\lambda, \omega)\ \Phi^{incident}(\lambda) \quad , \qquad (2)$$

where $\phi_{selector}(\lambda, \omega)$ is the selector transmission function at speed ω (ω is omitted in the further formulas) , and $\Phi^{incident}(\lambda)$ is the neutron wavelength distribution in the incident beam. For simplicity, we do not consider the angular distribution of neutrons in the different parts of the beam.
The scattered neutrons are registered by detectors with wavelength-dependent efficiency. For a given detector, an 'effective' neutron spectrum can be introduced: $\Phi^{incident\_effective}(\lambda) = \Phi^{incident}(\lambda) \cdot \eta(\lambda)$, where $\eta(\lambda)$ is the detector efficiency. All measurements described below were performed with the same detector, so for simplicity we keep the notation $\Phi^{incident}(\lambda)$ for the efficiency-weighted neutron spectrum.

If the incident spectrum is not flat (for example Maxwell-like distribution), then, according to equation (2), the peak of the wavelength distribution $\Phi^{transmitted}(\lambda)$ does not coincide with the position of the center of the selector transmission function $\phi_{selector}(\lambda)$, and so the effective wavelength of neutrons reaching the sample is shifted with respect to $\lambda^{selector}$.
The wavelength shift can be calculated in linear approximation, using Gaussian selector transmission function $\phi_{selector}(\lambda) = \exp\left(-(\lambda-\lambda^{selector})^2/2\sigma^2\right)$ and approximating the shape of the incident spectrum within the selector transmission window by a constant slope:

$$\Phi_{lin}^{incident}(\lambda) = m\ \lambda + b\ , \tag{3}$$

where m is the slope of the spectrum: $m = d\Phi^{incident} / \left. d\lambda \right|_{\lambda^{selector}}$. From equations (2) and (3) the shift in the position of the peak of $\Phi^{transmitted}(\lambda)$ can be calculated:

$$\lambda^{eff} - \lambda^{selector} = D\left(\sqrt{1+\left(\frac{\sigma}{D}\right)^2} - 1\right), \tag{4}$$

where $D = \Phi^{incident}(\lambda^{selector}) / 2m$. Here $\lambda^{selector}$ is the nominal wavelength given by equation (1), in which the constant C must be determined at the position of the maximum of the spectrum. The such calculated effective wavelength λ^{eff} corresponds to the position of the maximum of $\Phi^{transmitted}(\lambda)$; this is the quantity useful in the analysis of the experimental scattering curves, if the non-symmetric shape of $\Phi^{transmitted}(\lambda)$ is not taken into account.

Experimental

The effective wavelength at different selector speeds was determined using a silver behenate powder sample. Silver behenate gives a strong reflection at $q = 0.1076$ Å^{-1} [6], which can be conveniently measured by a position sensitive detector within a wide range of wavelengths and sample-detector distances, making it suitable for wavelength and resolution calibrations of SANS instruments [6-8].
The experiments have been performed on the SANS instrument operating at a cold neutron beamline at the Budapest Research Reactor [9], equipped with a multidisk type velocity selector [10, 11]. The rotation speed can be varied between 700 and 7000 rot/min, transmitting neutrons with wavelengths between 3.8 and 38 Å at zero tilt angle between the selector axis and the direction of the neutron beam. The tilt angle can be adjusted within ±4°. In the present experiment the angle was set at -3.6°, in order to provide a large wavelength spread of 0.45 relative FWHM. The selector speed was varied from 1750 to 5500 rot/min, cor-

responding to a nominal wavelength window from 2.2 to 7.0 Å. The scattered neutrons were registered by a 64 × 64 cm BF_3-filled position sensitive detector with 1 cm pixel size.
The radii of the Debye-Scherrer rings from the silver behenate powder were obtained by fitting the two-dimensional scattering patterns by a corresponding two-dimensional function, in which the radial cross-section of the peak had a Gaussian form. The effective wavelength λ^{eff} was calculated at each rotation speed from the position of the first Bragg peak.
The form of the intensity spectrum was determined by measuring the scattering from a 1 mm thick light water sample at the same rotation speeds; the count rate on the detector is shown in figure 1. The change of the apparent forward scattering of water with the wavelength has been taken into account by applying the Jacrot factor [12]. No corrections were made for the wavelength dependence of the detector efficiency. For the elastically scattered neutrons it is taken into account by using the notion of the efficiency-weighted neutron spectrum. However, the energy gain of a certain part neutrons scattered by water could not be taken into account in this way. Use of another scatterer, or the attenuated beam could be more advantageous for the measurement of the beam intensity.

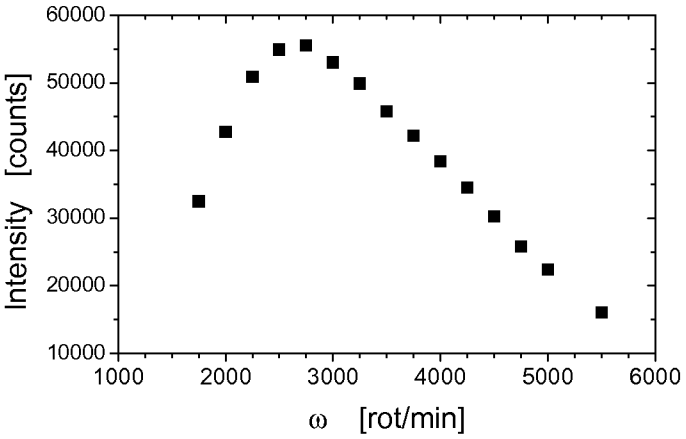

Figure 1. The scattering intensity from a water sample at different selector speeds.

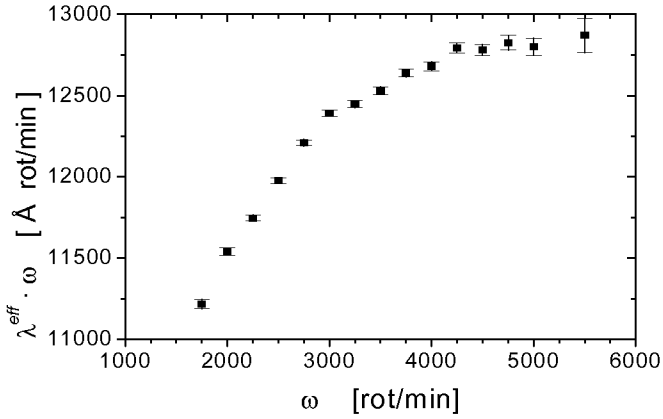

Figure 2. Product of the measured wavelength and the selector rotation speed.

Results and discussion

In figure 2 the product of the measured effective wavelength λ^{eff} and the rotation speed is shown in function of the selector rotation speed. The deviation of $\lambda^{eff} \cdot \omega$ from a constant value indicates that the measured wavelength is not inversely proportional to the selector speed. Comparing this curve with the form of the spectrum measured using a water sample (figure 1), the correlation between the spectrum and the wavelength shift is well seen. The relative wavelength shift, $(\lambda^{eff} - \lambda^{selector}) / \lambda^{selector}$, can be read out from figure 2. In the present experiment, with a broad selector transmission window, it reached values up to 10%. Such uncertainty in the wavelength is much larger than the desired precision of the size determination in SANS experiments.

In figure 3 the experimental wavelength shift is compared to the shift calculated using equation (4). In spite of the various approximations used, there is a rather good agreement between the measured and the calculated wavelength shift. The difference between the two curves is larger at small wavelengths; this can probably be attributed to the higher curvature of the spectrum in this region.

The wavelength resolution in this experiment was rather moderate. A narrower wavelength spread improves the approximation used in equation (3), as the linearity of the shape of the incident spectrum is better within a narrow transmission window. Instead of using the unknown $\Phi^{incident}(\lambda)$, we used the transmitted spectrum smeared by the selector. With a narrow wavelength spread, the difference between $\Phi^{incident}(\lambda)$ and the intensity distribution measured behind the selector would be smaller. Therefore, the removing of the selector

for the determination of the incident spectrum can be avoided, and measurements in the time of flight mode are not necessary.
The described procedure can serve as a convenient and efficient method of wavelength calibration, and can improve the accuracy in SANS experiments.

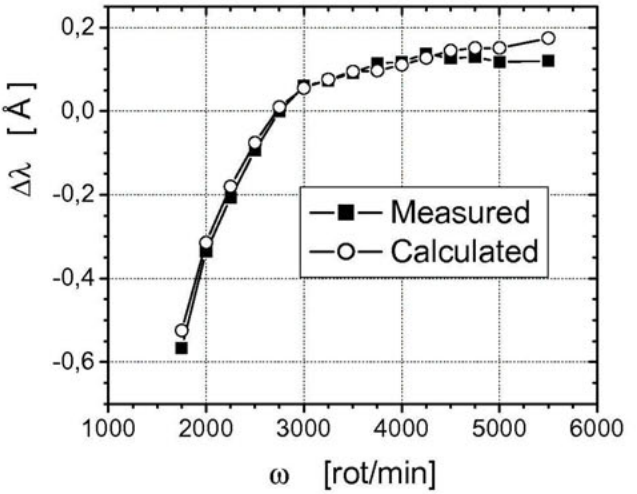

Figure 3. The measured wavelength shift $\Delta\lambda = \lambda^{eff} - \lambda^{selector}$ *and the shift calculated using equation (4).*

References

1. Glinka, C.J., Rowe, J.M., LaRock, J.G., 1986, *J. Appl. Cryst.*, **19**, 427.
2. Lindner, P., 1998, ILL Technical Report LI 11 T.
3. Strunz, P., Mortensen, K., Janssen, S., 2004, *Physica B,* **350**, e783.
4. Von Höhne, P., 1961, *Annalen der Phys.,* **7**, 50.
5. Friedrich, H., Wagner, V. & Wille, P., 1989, *Physica B*, **156-157**, 547.
6. Gilles, R., Keiderling, U. & Wiedenmann, A., 1998, *J. Appl. Cryst.*, **31**, 957.
7. Keiderling, U., Gilles, R. & Wiedenmann, A., 1999, *J. Appl. Cryst.*, **32**, 456.
8. Gilles, R., Keiderling, U., Strunz, P., Wiedenmann, A., Fuess, H., 2000, *Materials Science Forum*, **321-324,** 264.
9. Rosta, L., 2002, *Appl. Phys. A*, **74**[Suppl.], S52.
10. Rosta, L., 1989, *Physica B,* **156-157**, 615.
11. Rosta, L., 1991, *Physica B,* **171**, 562.
12. Jacrot, B., 1976, *Rep. Progr. Phys.*, **39**, 911.

Z. Kristallogr. Suppl. **23** (2006) 217-222

Neutron RTOF diffractometer FSD for residual stress investigation

A. M. Balagurov[1], G. D. Bokuchava[1], E. S. Kuzmin[1], A. V. Tamonov[1,*], V. V. Zhuk[1]

[1]Frank Laboratory of Neutron Physics, JINR, Dubna, Russia
[*]Contact author; e-mail: tamonov@nf.jinr.ru

Keywords: residual stress; RTOF method; neutron diffraction, pulsed reactor, Fourier method

Abstract. In this paper we present the construction a new neutron Fourier diffractometer FSD and the details of the diffractometer's design. FSD is a specialized neutron diffractometer which is dedicated exclusively for residual stress studies the IBR-2 pulsed reactor in FLNP JINR. The principle of a Fourier stress diffractometer is based on an application of the reverse time-of-flight (RTOF) method – a kind of correlation technique – at long pulsed neutron sources. The FSD design satisfies the requirements of high luminosity, high resolution, a specific sample environment, a wide range of d_{hkl}, and fixed scattering angle $2\theta = \pm 90°$.

Introduction

Experiments for mechanical internal stress studies start to occupy noticeable positions in research programs of leading neutron centers. To conduct such experiments, specialized neutron diffractometers are being created. The experience of application of neutron diffraction to study residual stresses with the HRFD diffractometer in Dubna [1] arouses vast interest on the side of science and Russian industry. Therefore, the new project for construction of a neutron diffractometer (Fourier stress diffractometer) dedicated exclusively for residual stress studies recently started at beam №11A of IBR-2 pulsed reactor in FLNP JINR. All experimental facilities of IBR-2 are open to the general scientific community. The User Guide for neutron experimental facilities at FLNP and Guide for sample environment experimental equipment on the IBR-2 spectrometers is available on request.
The work is conducted by joint efforts of collaborators from FLNP (JINR), PNPI (Gatchina), IfZP (Dresden), GKSS (Geesthacht) and ISSP (Budapest).

RTOF-method

A neutron TOF diffractometer for residual stress studies at IBR-2 pulsed reactor should satisfies the requirements of high luminosity, high resolution, a specific sample environment, a wide range of d_{hkl} and fixed scattering geometry.

The IBR-2 pulsed reactor in Dubna is a long pulse neutron source. So the resolution for the conventional TOF-experiments is poor due to the large width of the initial reactor pulse of 230 μs. After thermalization the pulse width grows up to 320 μs [2]. The Fourier technique is the best way from a practical viewpoint to decrease neutron pulse duration and accordingly to improve the resolution of the TOF diffractometer to $\Delta d/d$ as small as $5 \cdot 10^{-4}$ at the expense of an intensity loss by factor of 4 only [3]. Here the so called reverse time-of-flight (RTOF) method – a kind of correlation technique – is of advantage. It's verified by the experience of application of neutron diffraction to study residual stresses with the HRFD diffractometer.
The RTOF-method assumes the application of a fast Fourier chopper for the neutron beam intensity modulation and measuring of high-resolution correlation spectra. In the RTOF-method data acquisition is conducted at the continuous changing of Fourier chopper rotation frequency from zero to some maximal frequency ω_m. The time component of the resolution function is defined by the resolution function of the Fourier chopper, which depends on its frequency distribution function $g(\omega)$:

$$\Delta t_0 / t \approx \int_o^{\Omega} g(\omega) \cos(\omega t) d\omega \qquad (1)$$

where $\Omega = N\omega_m$ – maximal modulation frequency of neutron beam intensity, N – number of slits of Fourier chopper. With a reasonable choice of ω_m the effective neutron pulse width Δt_0 equals Ω^{-1} and for N = 1024, ω_m = 100 Hz (FSD parameters) gives a value ~ 10 μs. This means that for a total flight path (from Fourier chopper to detector) of ~ 6.5m and scattering angle of $2\theta = 90°$ the time component of the resolution function equals $\Delta t_0/t \approx 2 \times 10^{-3}$ at d = 2Å.

Fourier stress diffractometer

FSD – Fourier stress diffractometer is a specialized neutron RTOF diffractometer dedicated exclusively for residual stress studies. Such type of diffractometers is used at PNPI (Gatchina, Russia, diffractometer mini-SFINKS [4]), GKSS (Geesthacht, Germany, diffractometer FSS [5]) and FLNP JINR (Dubna, Russia, diffractometer HRFD [1]).
The FSD diffractometer is situated on beam 11a of the IBR-2 pulsed reactor in FLNP JINR with a water moderator which generates thermal neutron pulses with a frequency of 5 Hz (figure 1).
The main functional units of the FSD diffractometer are:

- a long curved mirror neutron guide for background suppression;
- a fast Fourier chopper;
- a straight mirror neutron guide to form the thermal neutron beam on the sample;
- a detector system;
- sample environment;
- data acquisition system, including specialised RTOF analysers.

FSD main parameters is shown in table 1.

Table 1. FSD main parameters.

Curved neutron guide	mirror, Ni-covered
length	19 m
Straight neutron guide	mirror, Ni-covered
length	5.01 m
Moderator - sample distance	28.14 m
Chopper - sample distance	5.55 m
Thermal neutron pulse width:	
low-resolution mode	320 μs
high-resolution mode	9.8 μs
High resolution detectors:	
BackScattering	^{6}Li, time focusing
ASTRA	ZnS, combined electronic & time focusing
Low-resolution detectors	^{3}He tubes
Wavelength interval	0.9 ÷ 8 Å
Flux at sample position:	
without Fourier chopper	1.8×10^{6} n/cm^{2}/sec
with Fourier chopper	3.7×10^{5} n/cm^{2}/sec

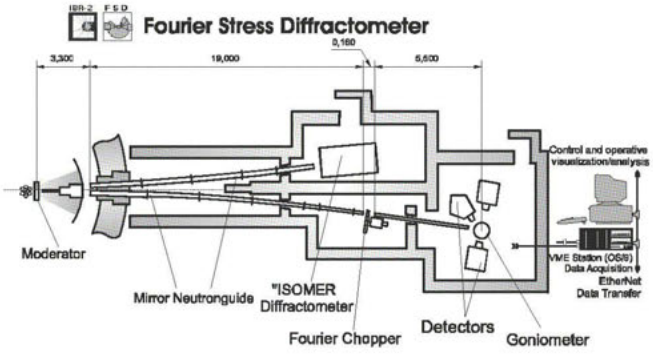

Figure 1. Layout of Fourier stress diffractometer on beam 11a of the IBR-2 pulsed reactor in FLNP JINR (Dubna, Russia).

Main functional units

Detector system

The detector system of Fourier stress diffractometer should have the largest feasible solid angle of observation to obtain data of high statistical accuracy for small gauge volume within acceptable experiment duration. Simultaneously, the geometrical component of the diffractometer resolution function should not noticeably exceed the time component. The method of geometrical time focusing [6] used so far in neutron TOF diffractometry has one essential limitation. The linear dimensions of a geometrically focused detector expand drastically with an increase of the solid angle. Therefore, the principle of the combined electronic-geometry focusing was proposed in [7].

The FSD detector system includes two ASTRA detectors at average scattering angles $2\theta=\pm 90°$ and an additional backscattering BS detector ($2\theta \approx -141°$) composed of sixteen ^{6}Li scintillation elements (figure 2). Each ASTRA detector consists of 7 elements with ZnS plates as a scintillator. At the first stage of FSD construction MultiCon detectors were used. Now the second generation of ZnS detectors - ASTRA are installed at FSD. A peculiarity of the ASTRA detector is the combined use of electronic and time focusing of a scattered neutron beam that allow realizing fundamentally new design of a detector system with large solid angles (0.286 steradians for each ASTRA detector). All 7 elements of detector are electronically focused using appropriate channel width for each detector analyser. Thus the electronic time focusing gives the same scale d_{hkl} for all detector elements. At the same time the scintillator surface of each detector element is arranged according to the neutron time focusing conditions, which gives high-resolution value for each individual detector element. Such a set-up essentially increases luminosity of the FSD diffractometer (by factor of 10 in comparing with the actual prototype of HRFD diffractometer) at saving high-resolution on interplanar spacing. At the present time two 1st elements of ASTRA detectors are assembled and installed on FSD and two 2nd elements are assembled. Main parameters of detectors are shown in table 2.

Table 2. Main parameters of FSD detectors.

Detector / Parameter	BS	ASTRA Left (1st element)	ASTRA Right (1st element)
Scattering angle 2θ, °	140.864	106.5	106.5
d_{hkl}-range, Å	0.51 – 5.39	0.638 – 7.39	0.638 – 7.39
$\Delta d/d$ (d=2 Å)			
Total resolution	2.281×10^{-3}	4.775×10^{-3}	4.995×10^{-3}
-Time resolution	1.458×10^{-3}	1.595×10^{-3}	1.535×10^{-3}
-Geometrical part	1.754×10^{-3}	3.180×10^{-3}	3.460×10^{-3}

Experiments

Recent experiments have shown that the FSD parameters confirm the suitability of the diffractometer for residual stress studies with required accuracy. An example of diffraction spectra from the α-Fe standard sample measured on FSD in high-resolution mode by ASTRA detector is shown at figure 3.

Sample environment

Sample environment system includes the linear scanner, 5-axis goniometer "HUBER" for a measurement of the full residual strain tensor (figure 4), the loading machine "TIRA-test" for in-situ experiments and definitions of materials elastic properties, a mirror furnace for an investigation of materials at high temperatures (up to 1000 °C) (figure 5). All of these devices can be used simultaneously that allows expanding experiment's opportunities and for example allows defining the dependence of material elastic properties on temperature etc.

At present the gauge volume within the sample is defined by two boron carbide slits with variable size installed on incident and scattered neutron beams. In future this slit system will be replaced by radial collimators.

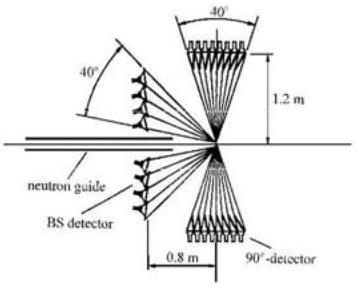

Figure 2. The detector system of FSD diffractometer.

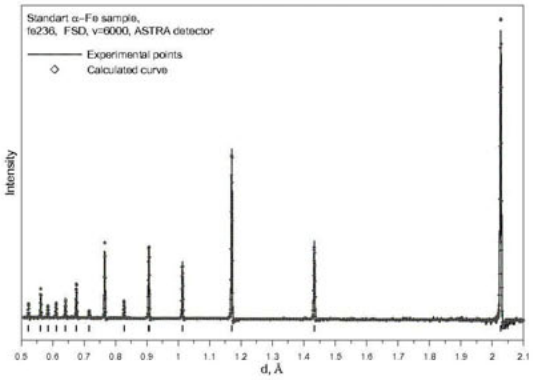

Figure 3. Example of spectra.

Figure 4. 5-axis goniometer "HUBER".

Figure 5. Mirror furnace.

Fourier chopper

Fourier – chopper is manufactured from high-strength Al based alloy and consists from two parts: stator and rotor. The stator is fixed at the platform. The rotor is a 540 mm disk which is connected to motor axis. The rotor has got 1024 equal radial slits which are filled with Gd_2O_3. The slits width is 0.7 mm. The stator has got the same slits. When the rotor rotates with speed 6000 rpm then maximal beam modulation frequency 100 kHz is reached.

Software and hardware

A VME based accumulation, control and supervising system has been maintained at FSD. The general advantages for the new software complex are:

- direct diffractometer management by the VME computer in the experimental hall;
- remote supervising (and later control) possibilities via the local area network;
- modern window-styled graphical user interface;
- spectra visualization during measurement;

- ease of extending the complex to handle new experimental equipment;
- ease of making changes in the experimental procedure (program).

Conclusion

- FSD parameters confirm the suitability of the diffractometer for residual stress studies with required accuracy of 20 - 30 MPa (for steel).
- The RTOF-method is the best choice for long pulsed neutron sources, which allows high resolution in interplanar spacing ($\Delta d/d \approx 1\times10^{-3}$) to be achieved, while maintaining high flux at the instrument.
- The main advantage of the RTOF-method is the possibility of simultaneously measuring many reflections, which allows the determination of residual strains along various (hkl) directions in a crystal and correspondingly crystallographic anisotropy of strains can be determined.
- The FSD resolution function has rather simple dependence on interplanar spacing d, which allows one to easily estimate microstrain averaged on all (hkl) directions from analysis of width of several diffraction peaks.

References

1. Aksenov V. L., Balagurov A. M., Simkin V. G., Bulkin A. P., Kudrjashev V. A., Trounov V. A., Antson O., Hiismaki P., 1997, *J. Neutron Res.* **5**, 181.
2. Anan'ev V. D. et al, 1985, *Neutron scattering in the 'Nineties'*, Conf. Proc., (Vienna, IAEA), p.429.
3. Hiismaki, P., Poyry, H., Tiitta, A., 1988, *J. Appl. Cryst.* **21**, 349.
4. Trounov V. A., 1995, *"M.SFINKS" Diffractometer at Gatchina Reactor.* Proceeding of the Meeting ICANS-XIII and ESS-PM4 (Villigen, PSI, Switzerland), **1**, pp. 247-260.
5. Priesmeyer H., Schroder J., Kudryashev V. A., Keuter J. M. et al., 1994, *Neutron Research*, 2, 129.
6. Carpenter J. M., 1967, *Nucl. Instr. and Meth.* **47**, 179.
7. Kudryashev V. A., Trounov V. A., Mouratov V. G., 1997, *Physica B* **234–236**, 1138.
8. Bokuchava G. D., Aksenov V. L.,Balagurov A. M., Zhuravlev V. V., Kuzmin E. S., Bulkin A. P., Kudryashev V. A., Trounov V. A., 2002, *Applied Physics A: Materials Science & Processing* **74**, S86-S88.

Acknowledgements.
This work was supported in the framework of an agreement between BMBF (Germany) and JINR. And so it was supported by RFBR grant № 04-02-97249.
The authors are indebted to Prof. V. L. Aksenov, Prof. J. Schreiber, Dr. V. G. Simkin, Dr. V.V. Sumin, N. R. Shamsutdinov for support in design and construction of FSD and support in neutron experiments.

III. SOFTWARE DEVELOPMENT

Z. Kristallogr. Suppl. **23** (2006) 225-230

Indexing with the successive dichotomy method, DICVOL04

D. Louër[1,*], A. Boultif[2]

[1]Laboratoire de Chimie du Solide et Inorganique Moléculaire (UMR 6511 CNRS), Institut de Chimie, Université de Rennes, Avenue du Général Leclerc, 35042 Rennes, France
[2]Département de Cristallographie, Institut de Physique, Université Mentouri, 25000 Constantine, Algeria
[*]Contact author, e-mail: Daniel.Louer@free.fr.

Keywords: powder diffraction, pattern indexing, dichotomy method, computer program, DICVOL

Abstract. A new version of the program based on the dichotomy principle for powder pattern indexing is reported. The new facilities of the program DICVOL04 include a tolerance for spurious diffraction lines, a refinement of the zero-point shift together with that of cell parameters, an *a priori* search for a zero-point offset in the input data, a reviewing of all available powder data from the indexing solution found from, generally, the first twenty lines. New strategies have been introduced to limit the risk to miss a solution. The program efficiency is shown with many tests. Additionally, the robustness of the program with respect to the minimum of lines required for finding solutions is presented and examples of two-phases patterns are used to test the performance of the program.

Introduction

Indexing of powder diffraction patterns with the successive dichotomy method was introduced in 1972 [1]. The algorithm, working in the direct parameter space and taking into consideration errors on peak measurement, was presented as an exhaustive approach to the indexing problem. Initially applied to powder diffraction data of materials with a crystal symmetry down to orthorhombic, the method was later extended to lower symmetry cases [2,3]. The dichotomy method has been used successfully in many structural studies, including more than fifty *ab initio* structure determinations carried out, from laboratory monochromatic X-rays [4], in the group *Cristallographie des Poudres et Réactivité des Solides* of the University of Rennes. Although DICVOL91 [3] is a powerful indexing program, some needs were accumulated over more than ten years of usage. Consequently, a new version of the computer program has been written, in which new important facilities have been implemented [5]. These new features are reviewed here. The performance of the program DICVOL04 is illustrated with representative applications, including powder data with spurious diffraction lines. Additionally, the program behaviour for limit cases is investigated, such

as indexing of patterns of mixed phases and, also, the minimum number of lines from which the correct solution is found in a series of patterns.

The dichotomy method

Powder pattern indexing is based on the basic quadratic equation obtained by squaring the diffraction vectors **d***, i.e. $Q_{hkl} = f(a,b,c,\alpha,\beta,\gamma,h,k,l)$ (= d^{*2}) where a, b, c, α, β, γ are the cell parameters and hkl the Miller indices of the observed diffraction lines. In the dichotomy method the parameter space is scanned by dividing cell edges and angles into equal intervals (i.e. 4 Å and 5° for linear and angular parameters, respectively), so that the entire space is divided into volume domains. (Some constraints and a specific strategy are introduced for the triclinic case, for details see refs 3 and 5.) For each volume domain a pattern is calculated, not as usual through discrete Q_{hkl}, but in terms of ranges $[Q_-(hkl),Q_+(hkl)]$. A domain can contain a solution if for every observed line Q_i the following inequality is verified:

$$Q_-(hkl) - \Delta Q_i < Q_i < Q_+(hkl) + \Delta Q_i, \qquad (1)$$

where ΔQ_i is the absolute error on the observed Q_i. If so, each domain edge is divided, according to the dichotomy principle, to give volume sub-domains analysed as before. The dichotomy process is applied at six levels. Each crystal lattice is explored separately, starting from the cubic side of the symmetry sequence. The strategy of the dichotomy algorithm consists of searching the smallest cell volume(s) according to the universal crystallographic convention, i.e. 'the smallest repeat unit for which its delineating vectors are parallel, or coincide with, important symmetry directions in the lattice'. The figure of merit (FoM) M_N [6] is used to check the validity of the solution(s) and, also, as a filter to discard (mathematical) solution(s) with too low FoM.

DICVOL04, new features

The new features of the program DICVOL04 are as follows.

Zero-point shift

An analysis of the zero-angle offset in the input data can be performed. Generally, powder data for indexing must be collected with accuracy, after minimising the magnitude of usual instrumental aberrations (see ref. 7). It is well known that the figures of merit used to check the validity of solutions decrease dramatically with zero-point and random errors [7]. In DICVOL04, if the zero-point shift is small, a least-squares refinement of its position can be performed together with the refinement of the cell parameters, as soon as a solution is found. Although the zero-point offset is not the alone aberration, particularly with data collected with the capillary mode, the extra degree of freedom in the least-squares refinement is beneficial to the figures of merit (FoM). This is illustrated in table 1 with powder data of pharmaceutical materials collected with the Debye-Scherrer optics, using monochromatic X-rays.

Table 1. Effect of zero-point shift refinement (Z-s) on figures of merit: M, F (M/F) and M', F' (M'/F'), calculated with and without zero-point refinement, respectively.

Compound	$M'_{20}/F'_{20}(<\Delta(2\theta)>,N_{cal})$	Z-s (°2θ)	$M_{20}/F_{20}(<\Delta(2\theta)>,N_{cal})$
Piracetam I (M)	146/293(0.0021,33)	-0.007	158/314(0.0019,33)
Piracetam II (Tr)	47/84(0.0079,30)	0.032	69/134(0.0052,29)
Piracetam III (M)	24/48(0.0109,37)	0.033	26/50(0.0109,37)
Theophylline (O)	55/92(0.0062,35)	-0.029	97/191(0.0030,35)
Sulfaguanidine (M)	34/86(0.0063,37)	-0.020	49/118(0.0046,37)

For significant zero-point shifts, an option is proposed to analyse input data prior to embarking in the indexing stage. The procedure is based on the reflection-pair method [8]. It should be noted that the procedure may fail if the zero-point offset is too large. The method is not unambiguous. Indeed, if the selected lines in a pair are not harmonic reflections, then the reflection-pair method is not applied properly. Consequently, the sign of the zero-point shift can be opposite of that of the true shift. Some facilities have been incorporated in DICVOL04 to manage this situation. The powder data of $BaCd(PO_3)_4$ [9], with an absolute error of 0.03° (2θ), can be used to illustrate such a case. Even with a small shift of 0.02° (2θ) in the observed data, from a systematic analysis of possible reflection pairs, DICVOL04 finds two zero-point shifts with opposite signs, i.e. -0.058° et 0.024°. The program uses these two estimations successively. With the first zero-point shift (-0.058°) a wrong solution is suggested [a = 16.516(6), b = 9.201(3), c = 14.458(5) Å, β = 115.09(3)°, M_{20} = 12], while with the second shift (0.024°) the correct solution is found [a = 14.958(5), b = 9.203(3), c = 7.230(3) Å, β = 90.84(4)°, M_{20} = 20].

This last facility is particularly of interest for powder data collected at non ambient temperature with the parafocusing Bragg-Brentano optics. A representative example is pattern indexing of the thermal-decomposition-product neodymium oxide nitrate, whose indexing solution (M_{15} = 88) was only obtained after an *a priori* search for a zero-point offset (-0.144° 2θ) [10].

Cell analysis

A current problem with pattern indexing is related to the multiple solutions that can be generated within the input errors. The problem can be more serious with lower (monoclinic and triclinic) symmetry. The concept of reduced cell for a normalised description of crystal lattices [11,12] is used in DICVOL04 to identify equivalent solutions. Since the reduced cell is unique, its calculation for low symmetry cell can also be useful for the detection of higher symmetry. The reduced form of a unit cell is also valuable in phase identification by means of crystallographic data bases. Moreover, it must be noted that lattice-metric-singularity cases can easily be detected by the separate scan of each crystal lattice up to the input maximum cell volume (default 2500 $Å^3$). A typical example is the hexagonal pattern, which can be indexed with an orthorhombic unit cell having a volume half that of the hexagonal cell [7].

Spurious diffraction lines
A tolerance for unindexed diffraction lines has been incorporated in DICVOL04. In the context of the dichotomy algorithm, unindexed lines can be due to the presence of an impurity in the sample and to peak position error(s) not correctly estimated. Spurious diffraction lines can be dealt with by allowing for a user-defined number of unindexed reflections. The unindexed line tolerance must be used with prudence, since it increases the risk to miss the correct solution. In order to improve the analysis of examples at a high impurity tolerance level, an option selected in the input file by a negative number of spurious lines (e.g. -15) is available. Then, the program runs successively, starting from an impurity tolerance level 0, then 1, 2, .., until the input limit (e.g. 15). The CPU time is obviously increased, but the impurity tolerance levels are scanned according to an optimum strategy.

Powder data reviewing
A reviewing of all available data (e.g. 50) is carried out as soon as a solution has been suggested from, generally, the first 20 lines. It is a useful check of solution(s) likelihood, since unindexed lines among the input data are displayed. It is also useful for the inspection of absent reflections if there is an interest in the derivation of possible space groups.

Program tests

DICVOL04 has been tested with many powder diffraction data, most of them have been discussed in detail by Boultif and Louër [5]. These tests include the successful indexing of the 71 powder diffraction data in Section 20 of the NBS Monograph 25 [9], all 29 triclinic patterns reported in the whole Monograph 25, some powder data of drugs collected with the Debye-Scherrer geometry, using a monochromatic radiation (for additional examples see table 1), as well as powder data reported as 'difficult' cases [13,14].

Number of lines required for indexing

It is admitted that the first twenty diffraction lines are generally sufficient for indexing powder diffraction patterns. Clearly, this empirical number ($N_c = 20$) must be increased for unit cells having a short axis. For curiosity and, also, for testing the robustness and stability of DICVOL04, all 71 patterns in Section 20 of the NBS Monograph No. 25 [9] were used for assessing the minimum number of lines N_{min} from which the correct solution is found. The mean numbers of lines $<N_{min}>$, averaged over all patterns in a lattice class, are as follows:
- *Cubic lattices* (9 patterns): $<N_{min}> = 5$, greatest value 7 for the powder data of $Bi_{12}GeO_{20}$ and that of the isomorphous phase $Bi_{12}TiO_{20}$.
- *Tetragonal lattices* (11 patterns): $<N_{min}> = 7$, greatest values 13 for $NaBa_2(NbO_3)_5$ [lattice constant ratio $a/c = 2.4$] and 12 for $KSr_2(NbO_3)_5$ [$a/c = 3.2$].
- *Hexagonal lattices* (17 patterns): $<N_{min}> = 6$, greatest value 11 for $NaGe_2(PO_4)_3$ [$c/a = 2.7$].
- *Orthorhombic lattices* (16 patterns): $<N_{min}> = 7$, greatest value 14 for $Li_2Ti_3O_7$ [$b/c = 3.2$, $b/a = 1.9$].
- *Monoclinic lattices* (18 patterns): $<N_{min}> = 10$, greatest value 18 for Eu_2O_3 [$a/b = 3.9$, $c/b = 2.4$] and $Zr(HPO_4)_2.H_2O$ (p.114) [$b/c = 2.8$, $b/a = 2.7$].

It is interesting to note that, as expected, the highest values of N_{min} are obtained for powder data characterised by a unit cell having a short axis, as shown by the lattice constant ratios. This case can be further illustrated by the pattern of zinc hydroxide nitrate $ZnOHNO_3.H_2O$ (a = 17.95 Å, b = 3.260 Å, c = 14.272 Å, β = 114.91°) [15]. The first fourteen lines have a zero k index. To obtain the correct solution N_{min} = 19 is required, as a consequence of the short axis (ratio a/b = 5.5). All these examples confirm that the use of 20 lines for pattern indexing is, generally, a good compromise for single phase patterns, though it should preferably be increased if a dominant zone is expected.

Two-phases patterns

Although powder pattern indexing is one of the most demanding applications of the powder method, namely data quality must be high and impurity lines must be avoided, it is of interest to investigate the behaviour of DICVOL04 with respect to mixed patterns, e.g. two-phases patterns. Logically, the number of lines N used for the indexing stage must be, at least, roughly doubled. Only the pattern with higher density of lines, among the N lines selected for indexing, is indexed by DICVOL04. The list of unindexed lines can subsequently be used for a separate run of DICVOL04 to index the pattern of the second phase. A few examples have been tested and, surprisingly, the results are not bad. The powder data were taken in the NBS Monograph No. 25 (Sections 20, 2 for $Na_4P_4O_{12}.4H_2O$ and 21 for α-$ZnMoO_4$). The results are summarized in table 2.

Table 2. Two-phases patterns indexed with DICVOL04. N is the number of lines used for indexing the pattern of the phase with a dominant number of diffraction lines, N_{imp} is the unindexed line tolerance among the N lines, N_{imp} <0 denotes a successive analysis from an impurity tolerance level 0 up to N_{imp}. Lattices are defined as follows: tetragonal (T), hexagonal (H), orthorhombic (O), monoclinic (M) and triclinic (Tr).

Mixed phases (Symmetry)	N	N_{imp}	No. of solutions	CPU time (min)
$MgSiO_3$ (M) + $Fe(NbO_3)_2$ (O)	50	+20	10	129
$BaTi_2O_5$ (M) + $BaTiO_3$ (H)	50	-20	7	2203
Ta_2WO_8 (O) + $SrZr_4(PO_4)_6$ (H)	36	-16	1	0.1
$SrAl_2O_4$(M) + $KSr_2(NbO_3)_5$ (T)	40	-16	1	32
$Zn_3(VO_4)_2$ (O) + YbF_3 (O)	50	-20	2	2
$CsH_5(PO_4)_2$ (M) + $CrWO_4$ (M)	50	-12	1	35
$Na_4P_4O_{12}.4H_2O$ (Tr) + $ZrTiO_4$ (O)	40	-6	1	10
$SrZr_4(PO_4)_6$ (H) + $KSr_2(NbO_3)_5$ (T)	50	-25	1	0.8
α-$ZnMoO_4$ (Tr) + $CsH_5(PO_4)_2$ (M)	40	-14	1	166

Concluding remarks

The new version of the program DICVOL04, based on the dichotomy principle, has been considerably improved with respect to the previous versions. Several useful facilities have been implemented. It must be noted that the program should not be used as a black box. The user must know all facilities offered by the program, as well as the strategy driving the search of solutions. The usual recommendation about the quality of the powder data to be used is still valid. Clearly, the new facilities, e.g. zero-point shift analysis and the impurity line tolerance, should not be taken as a justification for neglecting the quality of the adjustment of the powder diffractometer used for data collection. Finally, the performance of the new program has been proved with many applications. The success rate of DICVOL04 has been found high, even for the data used in the studies of limit cases, i.e. the number of lines required for correctly indexed the patterns and the mixed patterns. All these results are clearly informative in the context of *ab initio* structure determination.

References

1. Louër, D. & Louër, M., 1972, *J. Appl. Crystallogr.*, **5**, 271-275.
2. Louër, D. & Vargas, R., 1981, *J. Appl. Crystallogr.*, **15**, 542-545.
3. Boultif, A. & Louër, D., 1991, *J. Appl. Crystallogr.*, **24**, 987-993.
4. Louër, D. & Langford, J. I., 1988, *J. Appl. Crystallogr.*, **21**, 430-437.
5. Boultif, A. & Louër, D., 2004, *J. Appl. Crystallogr.*, **37**, 724-731.
6. Wolff, P. M. de, 1968, *J. Appl. Crystallogr.*, **1**, 108-113.
7. Louër, D., 1992, in *Accuracy in Powder Diffraction II*, NIST Special Publication No. 846, edited by E. Prince & J. K. Stalick (Gaithersburg, MA: US Department of Commerce), pp. 92-104.
8. Dong, C., Wu, F. & Chen, H., 1999, *J. Appl. Crystallogr.*, **32**, 850-853.
9. Morris M. C., McMurdie, H. F., Evans, E. H., Paretzkin, B., Parker, H.S., Pyrros, N. P. & Hubbard, C. R., 1984, in *Monograph No. 25*, Sect. 20, National Bureau of Standards (Washington: U. S. Department of Commerce).
10. Bataille, T., Audebrand, N., Boultif, A. & Louër, D., 2004, Z. *Kristallogr.*, **219**, 881-891.
11. Azároff, L. & Burger, M. J., 1958, *The Powder Method* (New York: McGraw-Hill).
12. Mighell, A. D., 2001, *J. Res. Natl. Inst. Stand. Technol.*, **106**, 983-995.
13. Neumann, M. A., 2003, *J. Appl. Crystallogr.*, **36**, 356-365.
14. Coelho, A. A., 2003, *J. Appl. Crystallogr.*, **36**, 86-95.
15. Eriksson, L., Louër, D. & Werner, P.-E., 1989, *J. Solid State Chem.*, **81**, 9-20.

Z. Kristallogr. Suppl. **23** (2006) 231-236

Powder3D: An easy to use program for data reduction and graphical presentation of large numbers of powder diffraction patterns

B. Hinrichsen, R. E. Dinnebier* and M. Jansen

Max Planck Institute for Solid State Research, Heisenbergstraße 1, 70569 Stuttgart, Germany
*Contact author; e-mail: r.dinnebier@fkf.mpg.de

Keywords: powder diffraction, data reduction, software

Abstract. The presented software facilitates data reduction of multiple powder diffraction patterns. Many operations are automated for the application to huge sets of patterns collected during diffraction experiments in dependence of time, temperature, pressure and composition. The features include basic data reduction procedures, such as background reduction, K-α stripping, smoothing and Le Bail fitting. Many file formats are supported to provide interoperability with GSAS, Fullprof and Crysfire (amongst others). The software is freely available for non-profit use at http://www.fkf.mpg.de/xray/.

Introduction

One of the major advantages of powder diffraction compared to other analysing techniques is to (indirectly) measure changes of the entire crystal structure as a function of time, pressure, temperature, chemical composition, magnetic field etc.
Once online image plate readers and high resolution CCD cameras become available, they shall force changes in methods of data analysis and presentation. Typical readout times are now on the order of seconds. Soon, milliseconds will become standard, producing huge amounts of data which need to be processed efficiently. The new software solution presented here aims to provide a tool for just this purpose. The maximum number of imported powder patterns which can be processed simultaneously is only dependent on the speed and memory of the computer used.

Methods

Series of powder patterns can be imported from well known freeware programmes such as Fit2D [1], which allow data conversion from two dimensional image plate/CCD data to one dimensional powder patterns in a batch process. At the present time the implemented functionalities in Powder3D include data reduction for WPPF and Rietveld refinement as

well as powerful graphical tools for the display and print out of 2D and 3D powder diffraction data (see figures showing the phase transformations and decomposition of $Rb_2C_2O_4$[5]). The software design and functionality has been optimised to allow a substantial amount of automation, if desired by the user. All actions can be either applied to a single data set, multiple data sets or the entire series of powder patterns. Additional individual powder patterns can be loaded and if necessary a wavelength conversion can be applied to allow for better comparison between data measured at different sources.
An assistant for whole pattern decomposition using Fullprof [2] has been implemented.
The software has been entirely written in the IDL programming language using object-oriented code. The compiled code can be run using the IDL Virtual Machine™ that is freely available for various platforms. So far Powder3D has been tested on the Windows® operating system only.

Background reduction

A robust algorithm based on an adaptive low-pass filter [3] is incorporated for background reduction. The user sets the 2Θ-window and the number of iterations. One improvement on Brückner's algorithm is its iterative application on the already background corrected diffractogram. This circumvents the otherwise inherent intensity loss. Background points that describe the background via linear interpolation are then calculated. Background points can be added and removed manually. These are exported in GSAS or Fullprof friendly formats. Once satisfactory settings have been found the reduction can be applied to any set of patterns.

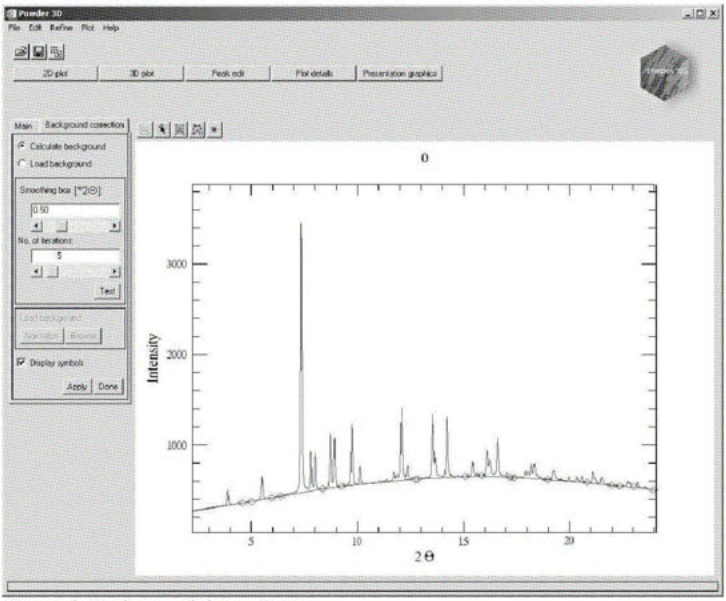

Figure 1. Background determination.

Smoothing

Full width at half maximum (FWHM) optimised smoothing [4] is implemented. The variation of the FWHM over 2Θ is defined via an interactive diagram fitting the Caglioti formula [6].The user can assign number of iterations, polynomial order and FWHM factor. A preview of the smoothed and difference curve are displayed. As with the background reduction this function can be applied automatically to any defined set of patterns.

$K\alpha_2$ stripping

For laboratory data sets, $K\alpha_2$ stripping [7] is provided with the possibility to retain either α_1 or α_2 patterns.

Peak hunt and peak profile refinement

Greater user interaction is required for these functions therefore they do not lend themselves to automation. A peak search function using the second derivative of the profile intensity is implemented. Borders for the peak search can be set. Another interactive Caglioti diagram defines the convolution range and therefore the sensitivity of the peak search. Located peaks can be saved in the Crysfire [8] format for indexing. In case of non-uniform peak widths, several peak hunts with varying parameters can be combined. It is possible to delete and add peaks manually. Once peaks have been found, these can be fitted using a pseudo-Voigt function corrected for axial divergence [9]. The refined peak positions can again be exported for indexing.

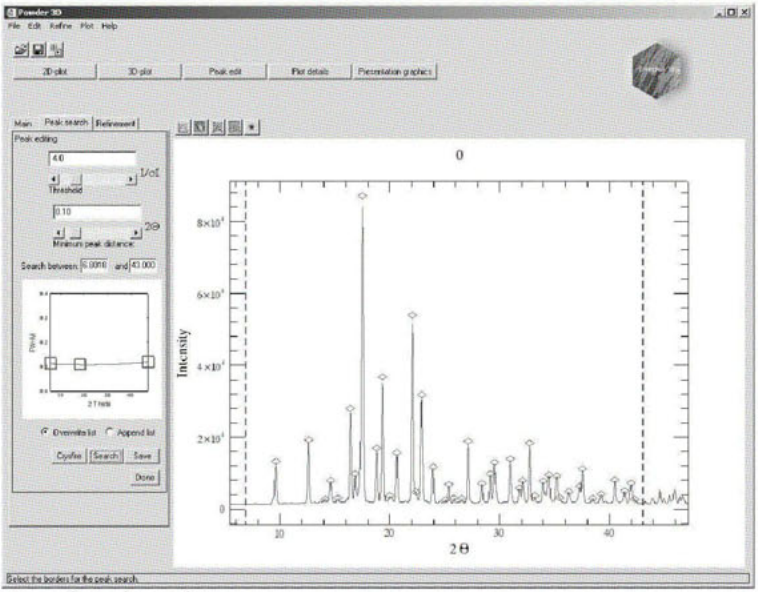

Figure 2. Peak searching.

Whole pattern decomposition

Fullprof input files are generated for profile matching [10], Crysfire summary files can be read and profile factors from peak refinements can be imported. Fullprof PCR-files can also be read. Combined with basic error checking mechanisms this provides a simple mechanism to create input files for Le Bail refinements. Le Bail type fits of multiple phases using phase ranges as defined by the user can thus be performed semi-automatically in dependence on the pattern number. After a series of successful Fullprof runs, arbitrary parameters of the output files can be numerically and/or graphically displayed in dependence on the pattern number.

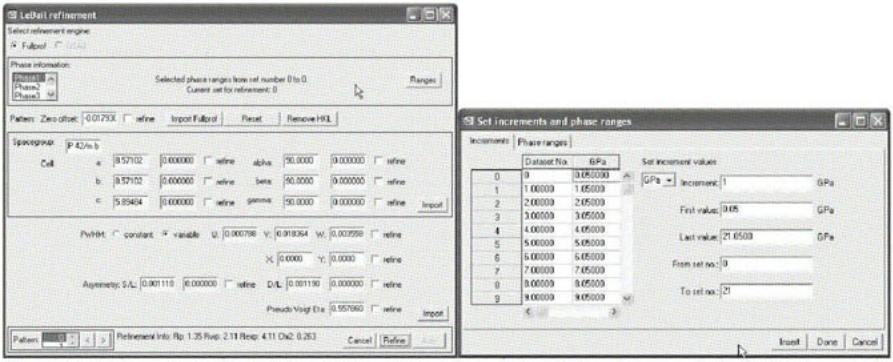

Figure 3. Window for Le Bail fitting (left) and the increment and phase range window (right).

Graphics

Powerful graphics capabilities are supplied for viewing single and multiple powder patterns. Up to six colour coded single patterns can be viewed simultaneously. Automatic scaling aids the comparison of patterns with differing intensities. Interactive zooming and ergonomic pattern navigation have been realized. An AVI film of sequential single patterns and of a user definable length can be exported. Multiple patterns can be displayed in three dimensions as lines, as a shaded surface or as a simulated Guinier film plot. Orientation, position, scale, titles, colour and lighting of the line and shaded plots are user definable. The extremely versatile iTools^{TM} software is included, allowing the creation of complex publication quality graphics (see figure 6). All graphics windows can be copied, printed or exported with a user-defined resolution.

Supported file formats

Data in the form of XY formatted sequential files can be imported as described above. Files can be exported as standard Fullprof or GSAS data files. A file containing the complete data array can be exported for use in alternative visualization programmes. Data files can also be saved in an internal binary format.

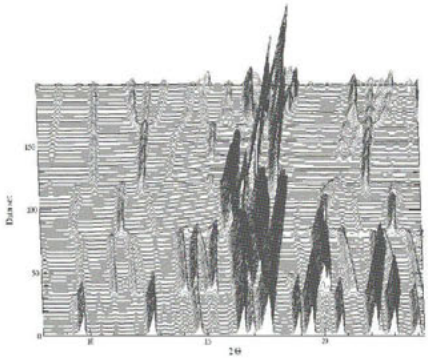

Figure 4. A 3D line plot of $Rb_2C_2O_4$ and its decomposition products in dependence of temperature.

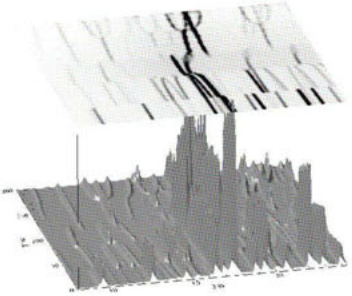

Figure 6. An example of a plot produced by iTools™.

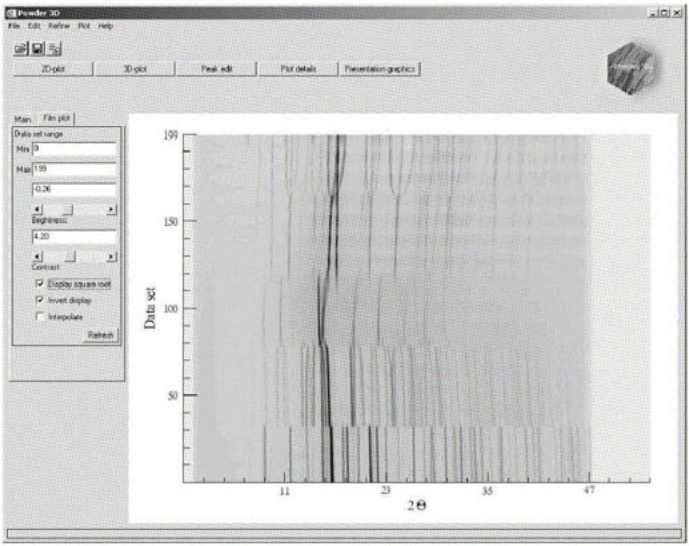

Figure 5. $Rb_2C_2O_4$ data displayed as a simulated Guinier film plot.

Summary

A software package tailored for the data reduction and presentation of powder diffraction patterns has been presented. The functionality has been tested on a variety of data sets containing up to 500 powder patterns.

References

1. Hammersley, A. P., Svensson, S. O., Hanfland, M., Fitch, A. N., and Hausermann, D. (1996) Two-Dimensional Detector Software: From Real Detector to Idealised Image or TwoTheta Scan. *High Pressure Research*, **14**, 235-248
2. Rodríguez-Carvajal, J. (2001) Recent Developments of the program FULLPROF. *Commission on Powder Diffraction Newsletter*, **26,** 12-19.
3. Brückner, S. (2000) Estimation of the background in powder diffraction patterns through a robust smoothing procedure. *J. Appl. Cryst.*, **33**, 977-979.
4. Dinnebier, R. E. (2003) FWHM optimised polynomial smoothing filters: A practical approach. *Powder Diffraction*, **18(3)**, 199-204.
5. Dinnebier, R. E.; Vensky, S.; Jansen, M.; Hanson, J. (2005) Crystal Structures of and Topological Aspects on the High Temperature Phases and the Decomposition Products of the Alkali Oxalates $M_2[C_2O_4]$, M=(K,Rb,Cs). *Chemistry, a European Journal.*, **11(4)**, 1119-1129.
6. Caglioti, G.; Paoletti, A.; Ricci, F. P. (1958) Choice of collimators for a crystal spectrometer for neutron diffraction. *Nucl. Instr.*, **3**, 223-228.
7. Ladell, J.; Zagofsky, A.; Pearlman, S. (1975) Cu $K\alpha_2$ elimination algorithm. *J. Appl. Cryst.*, **8**, 499-506.
8. Shirley, R. (2002) The Crysfire 2002 System for Automatic Powder Indexing: User's Manual.
9. Finger, L. W. (1998) *PROFVAL*: functions to calculate powder-pattern peak profiles with axial-divergence asymmetry. *J. Appl. Cryst.*, **31**, 111.
10. Le Bail, A.; Duroy, H.; Fourquet, J. L. (1988) *Ab-initio* structure determination of $LiSbWO_6$ by X-ray powder diffraction. *Mat. Res. Bull.*, **23**, 447-452.
11. iTools is a trademark of Research Systems Inc., Boulder, CO, USA
12. Windows is a registered trademark of Microsoft Corporation, Redmond, WA, USA

Acknowledgements. The authors would like to thank J. Hanson (BNL, USA) for his help during *in situ* powder diffraction experiments and helpful discussions. Financial support by the Fonds der chemischen Industrie (FCI) is gratefully acknowledged.

Z. Kristallogr. Suppl. **23** (2006) 237-242

BRASS, the Bremen Rietveld analysis and structure suite

J. Birkenstock, R.X. Fischer*, T. Messner

[1]Universität Bremen, FB5-Kristallographie, D-28359 Bremen
*Contact author, e-mail: rfischer@uni-bremen.de

Keywords: Rietveld refinement program, *BRASS*, *STRUPLO*

Abstract. *BRASS* consists of a suite of programs for the refinement, presentation, and evaluation of crystal structures. Latest extensions are the implementation of a grid search analysis, the introduction of an extended version of the modified pseudo-Voigt profile function, the handling of peak broadening due to anisotropic strain, and beam-overflow intensity corrections for circular sample surfaces. The user is guided through the Rietveld run by consecutive steps from the powder pattern display to the refinement procedure and the display of the results. Quantitative phase analyses can be performed on up to 15 crystalline phases. The crystal structure drawing module *STRUPLO* provides various options for calculating and listing distances and angles, and to calculate the void space not occupied by atoms.

Introduction

The Rietveld method was introduced by Rietveld [1,2] for the least squares refinement of profile and crystal structure parameters based on step intensities. The program was originally written in ALGOL [3] and became readily available for the diffraction community when FORTRAN versions of the program [4,5] were distributed. Meanwhile, many Rietveld programs as public domain or commercial software offer a wide range of options for the refinement and characterization of crystal structures. *BRASS*, the *Bremen Rietveld Analysis and Structure Suite* represents an integrated program package with modules for profile analyses, crystal structure refinements, quantitative phase analyses, powder pattern display, Fourier calculations, and crystal structure drawings. All program modules are embedded in a complex user interface with a sophisticated file handling, designed to guide the user through the Rietveld analysis procedure. A predecessor of the program package was introduced in [6] which contained a distance least squares module not yet implemented in the current version of *BRASS*. This feature will be considered again in future releases.
BRASS can be downloaded from the *BRASS* homepage (http://www.brass.uni-bremen.de/) of the Central Laboratory for Crystallography and Applied Material Sciences (ZEKAM) at the university of Bremen. After download, an installer will guide through the installation procedure. *BRASS* is continuously supported by a team of scientists at the university of Bremen. However, any contribution which can be easily implemented in this program package will be welcome.

User interface

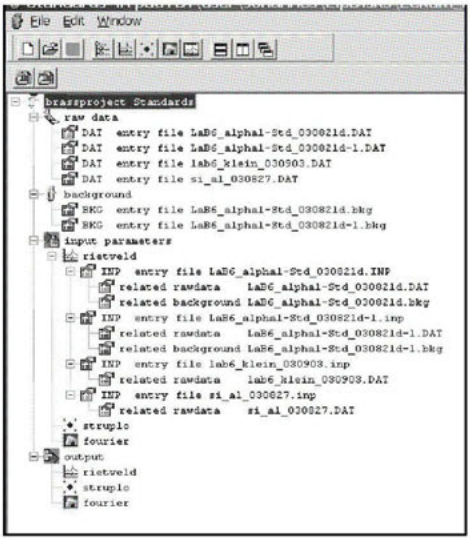

Figure 1. Screen copy of user interface with project manager.

The user interface written in DELPHI controls all actions and data handling. It executes the program modules, records and displays the results, and guides the user through the Rietveld analysis. On starting a new project, the program *project manager* creates a directory structure and assigns data files to the project in an easy registration process. All registered files are displayed in an *Explorer*-like tree view as shown in figure 1. A double click on the respective entry in the project tree executes the corresponding module. E.g., a double click on an INP file entry automatically opens the Rietveld window, a double click on a BST file entry invokes the STRUPLO window. However, all modules can be accessed directly via the buttons in the project managing bar, providing short links to the project manager, Rietveld program, structure drawing program STRUPLO, Fourier calculations and graphics, and to the powder pattern display. An online display shows the progress in each step of the refinement. The full history of the results in each of the refinement cycles is stored which permits an analysis of the individual shifts and convergence behavior of the variable parameters. Great care is bestowed on recording intermediate steps after successful refinement cycles using the file handling bar (figure 2) which offers options for saving and restoring preliminary or intermediate refinement results.

Figure 2. File handling bar.

Raw data handling and powder pattern display

Intensity data are read in formatted as dat files (used in many Wiles and Young derivative programs) or as xrdml or udf files from PANalytical instruments. More formats will be added soon. The graphics display of the powder pattern offers the usual options for the display of observed and calculated intensities with difference plot as well as zoom and scrolling modes. Line modes and colours can be changed in a separate panel. Intensities, 2θ, and d-values are displayed for the current cursor positions. Background is displayed as calculated from the background function or it can be entered by hand linearly interpolated between adjacent set points.

Rietveld kernel

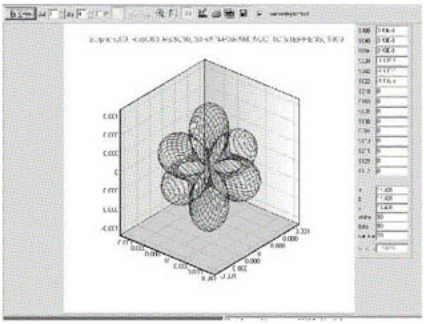

Figure 3. Three-dimensional representation of strain parameters.

The program kernel used in *BRASS* can be considered a derivative of the FORTRAN program written by Wiles and Young [5], and extensively modified by Hill and Howard [7], and Fischer et al. [6,8] who programmed the PC-Rietveld plus package distributed by the X-ray equipment supplier Philips Analytical (Almelo) which is now PANalytical. The well established code has been modified again and extended extensively. Probably the most important extension is the handling of peak profiles broadened due to anisotropic strain [9], as also used e.g. in GSAS [10] and FULLPROF [11]. In BRASS a similar, extended variant is used as described very detailed in the GSAS user manual. The algorithm is incorporated into the pseudo-Voigt function given in [12]. Accordingly, the strain effect is considered in terms of the Gaussian and Lorentzian peak widths as expressed in equations (1) and (2) (for details see [9,12]). A graphics tool has been programmed to visualize the anisotropic strain in three-dimensional space as shown in figure 3. This tool will be integrated soon into the BRASS package.

$$FW_G(2\theta)=\sqrt{\left(U_G+(1-\eta)^2\cdot\left(\sum_{H,K,L}S_{HKL}\cdot h^H\cdot k^K\cdot l^L\right)\cdot d^4\right)\cdot\tan^2\theta+V_G\cdot\tan\theta+W_G+\frac{P_G}{\cos^2\theta}} \quad (1)$$

$$FW_L(2\theta)=\left(U_L+\eta\cdot\sqrt{\sum_{H,K,L}S_{HKL}\cdot h^H\cdot k^K\cdot l^L}\cdot d^2\right)\cdot\tan\theta+W_L+\frac{P_L+PA_L\cdot\cos\phi}{\cos\theta} \quad (2)$$

with

$$\begin{aligned}\sum_{H,K,L}S_{HKL}\cdot h^H\cdot k^K\cdot l^L = {} & S_{400}\cdot h^4+S_{040}\cdot k^4+S_{004}\cdot l^4+3\cdot\left(S_{220}\cdot h^2\cdot k^2+S_{202}\cdot h^2\cdot l^2+S_{022}\cdot k^2\cdot l^2\right)\\ & +2\cdot\left(S_{310}\cdot h^3\cdot k+S_{130}\cdot h\cdot k^3+S_{301}\cdot h^3\cdot l+S_{103}\cdot h\cdot l^3+S_{031}\cdot k^3\cdot l+S_{013}\cdot k\cdot l^3\right)\\ & +4\cdot\left(S_{211}\cdot h^2\cdot k\cdot l+S_{121}\cdot h\cdot k^2\cdot l+S_{112}\cdot h\cdot k\cdot l^2\right)\end{aligned} \quad (3)$$

and the variable parameters U_G, V_G, W_G, U_L and W_L (designated for instrumental contributions) and η, S_{HKL} (= S_{400}, S_{040}, …, S_{112}), P_G, P_L and PA_L (for sample effects).
Intensity loss due to beam overflow at low angles is accounted for according to the procedures given in [13] for rectangular sample holders and in [14] for circular sample surfaces. The program handles data from Bragg-Brentano diffractometers as well as from transmission instruments with flat and cylindrical samples. Transmission factors for cylindrical samples are calculated after [15]. Alternatively to electron density calculations by Fourier and difference Fourier methods, the user can perform a grid search as introduced in [16]. The posi-

tional parameters of a dummy atom are shifted on a grid in the asymmetric unit of the unit cell. At each position the occupancy factor of the dummy atom is refined and occupancies and residuals are then plotted in *xy*-layers of the unit cell. Standardless quantitative phase analyses for up to fifteen crystalline phases yield their weight and molar fractions and the overall chemical composition of the crystalline part of the sample. In a separate frame of the user interface, all dependent parameters are listed with their assignments to the refinable root parameters as shown in figure 4. A report is generated listing the chronological sequence of all actions invoked by the controls of the file handling bar (figure 2). This report can be edited and appended by own text. Online graphics show the refinement progress represented by the sequence of residuals and the status of convergence after each cycle.

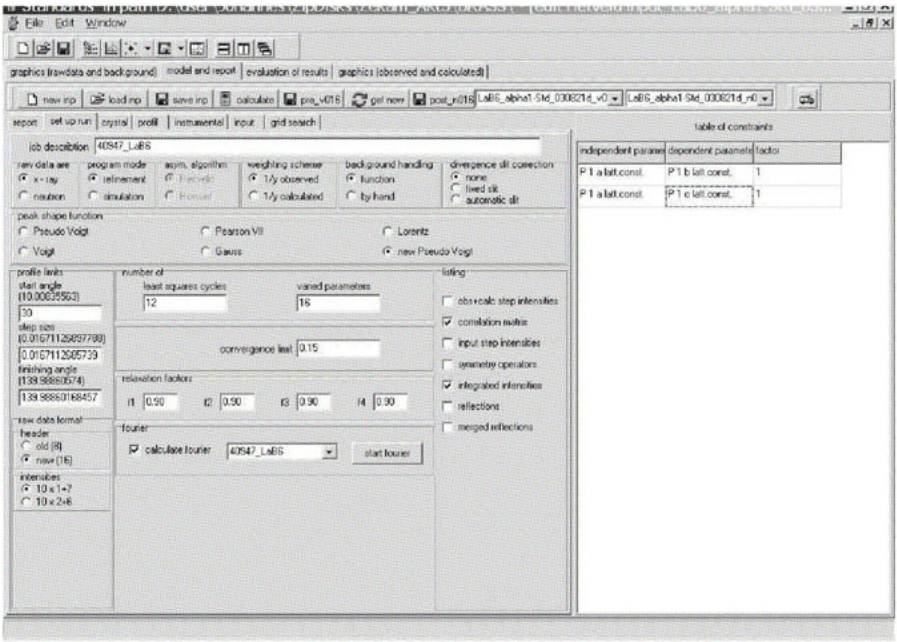

Figure 4. User interface with the "set up run" dialog of the Rietveld module and the list of dependent parameters.

Fourier calculations, electron density, and grid search maps

The numerical part of the FOURIER program is based on Allan Zalkin's FORDAP Fourier program [Lawrence Berkeley Laboratory, Berkeley, CA] in its version modified by James A. Ibers [Northwestern University, Evanston, IL]. Peaks and troughs in the electron density maps are interpolated and sorted according to their electron density (pseudo nuclear density for neutron diffraction data) values. The results can be graphically displayed in layers of the unit cell as contour maps or in a three-dimensional representation. The same graphics routine is used for the representation of the grid search maps.

Crystal structure drawings and crystal chemical calculations

STRUPLO, initially programmed in FORTRAN by Fischer [17] is completely rewritten in Delphi with extensive modifications. The program uses the routine from reference [18] for the derivation of the symmetry operators from the Hermann-Mauguin space group symbol translated to Delphi. Crystal structures can be displayed in ball and stick representation and as polyhedral models as shown in figure 5.

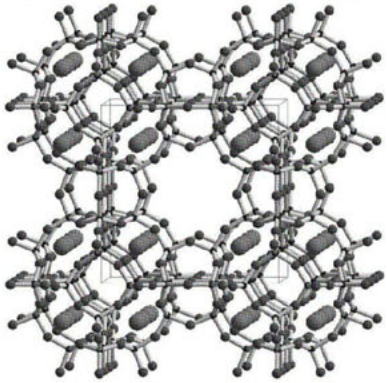

a) Ball and stick model

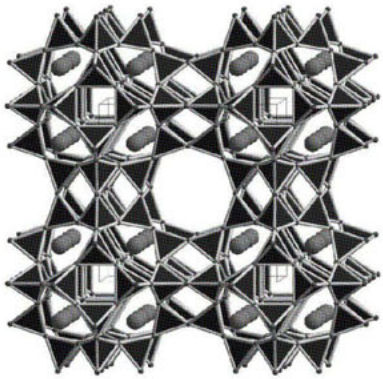

b) Framework of AlO_4 and SiO_4 tetrahedra

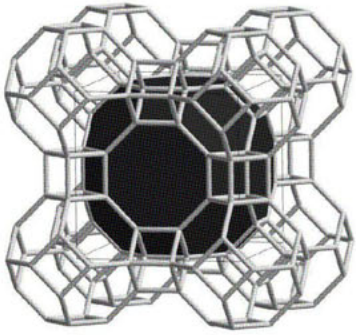

c) Framework with central $4^{12}6^8 8^6$ unit (α-cage, grc unit) drawn nontransparently

d) Framework with $4^6 6^8$ units (grc units, sodalite cages, blue)and 4^6 units(red) drawn semi transparently.

Figure 5. The crystal structure of zeolite A in various representations.

All individual structural units like bonds, atoms, and polyhedra can be identified or deleted by mouse click on the respective object. They can be restored at any time from the list of deleted items. Distances and angles are listed for all atoms in the asymmetric unit. In addition, they can be calculated online for selected atoms. The void space, i.e., the empty space

not occupied by atoms, is calculated according to the procedure described in [19]. This is especially useful to determine diffusion paths, e.g., in porous materials like zeolites.

References

1. Rietveld, H.M., 1967, *Acta Crystallogr.* **22**, 151-152.
2. Rietveld, H.M., 1969, *J. Appl. Crystallogr.* **2**, 65.
3. Rietveld, H.M., 1967, *Reactor Centrum Nederland, Research Report 1967.*
4. Hewat, A.W., 1973, *Atomic Energy Research Establishment, Harwell* 1973.
5. Wiles, D.B. & Young, R.A., 1981, J. Appl. Crystallogr. **14**, 149-151.
6. Fischer, R.X., Messner, T. & Kassner, D., 2000, in *Berichte aus Arbeitskreisen der DGK Nr. 9, VII. Workshop powder diffraction: Structure determination and refinement from powder diffraction data*, edited by E. Dinnebier (Deutsche Gesellschaft für Kristallographie), pp. 201-208.
7. Hill, R.J. & Howard, C.J, 1986, *Australian Atomic Energy Commission Research Establishment, Research Report M112.*
8. Fischer, R.X., Lengauer, C., Tillmanns, E., Ensink, R.J., Reiss, C.A. & Fantner, E.J., 1993, *Materials Science Forum* **133-136**, 287-292.
9. Stephens, P.W., 1999, *J. Appl. Crystallogr.* **32**, 281-289.
10. Larson, A.C. & Von Dreele, R.B., 2000, *General Structure Analysis System (GSAS), Los Alamos National Laboratory LAUR* 86-748.
11. J. Rodriguez-Carvajal, FULLPROF 2000, ILL
12. Thompson, P., Cox, D.E. & Hastings, J.B., 1987, *J. Appl. Crystallogr.* **20**, 79-83.
13. Fischer, R.X., 1996, *Powder Diffraction* **11**, 17-21.
14. Krüger, H. & Fischer, R.X., 2004, *J. Appl. Crystallogr.* **37**, 472-476.
15. Birkenstock, J., 2004, *Abstracts to the IX. EPDiC (Prague 2004)* in: *Materials Structure in Chem., Biol., Phys. And Techn.*, **11**, no. 1a, 229-230.
16. Baur, W.H. & Fischer, R.X., 1986, in *Advances in X-ray analysis*, Vol. 29, edited by C.S. Barrett, J.B. Cohen, J. Faber, R. Jenkins, D.E. Leyden, J.C. Russ & P.K. Predecki. (Plenum Publishing Corporation), pp. 131-141.
17. Fischer, R.X., 1985, *J. Appl. Crystallogr.* **18**, 258-262.
18. Burzlaff, H. & Hountas, A., 1982, *J. Appl. Crystallogr.* **15**, 464-467.
19. Küppers, H. & Liebau, F., 2004, *Proceedings of the DGK-Tagung* 2004, Oldenbourg Verlag, München, 120.

Acknowledgements. We are indebted to PANalytical (Almelo, the Netherlands) for granting permission to use some program codes for the *BRASS* freeware program. We thank Michael Wendschuh and Christoph Vogt (Bremen) for their valuable comments on the program and the extensive testing of the beta versions.

Z. Kristallogr. Suppl. **23** (2006) 243-248

FAULTS, a new program for refinement of powder diffraction patterns from layered structures

M. Casas-Cabanas[1,2], J. Rodríguez-Carvajal[2,*], M.R. Palacín[1]

[1]Institut de Ciència de Materials de Barcelona (CSIC), Campus UAB E-08193 Bellaterra, Catalonia, Spain
[2]Laboratoire Léon Brillouin (CEA-CNRS), CEA/Saclay, 91191 Gif-sur-Yvette Cedex, France
[*]Contact author; e-mail: juan@llb.saclay.cea.fr

Keywords: FAULTS, powder diffraction, layered structures, refinement

Abstract. A new program for refinement of layered structures is herein presented. FAULTS is based in the DIFFaX program, developed by Treacy et al. [1], which simulates selected area electron diffraction and powder (X-ray and neutrons) diffraction patterns by means of a recursion algorithm that calculates the incoherent sum of diffracted intensities of layered structures of any crystal system containing planar defects. In order to deal with the limitations of a simple simulation, refinement of all the parameters involved in the calculation of the diffracted intensities has been implemented in FAULTS.

Introduction

Layered systems include a large number of mineral families and synthetic compounds of great technological importance with applications as electroactive materials, superconductors, catalysts, lubricants, sensors and magnetic storage materials, among others. Their structural features, including those associated to certain defects, are directly related to their physical-chemical properties. Indeed the microstructural characterization of these materials is of essential importance and requires the determination of parameters specific to different types of defects, such as their amount and exact location.

So far, a widely used tool to interpret the diffraction data of one-dimensionally disordered systems is the DIFFaX program [1], which allows the simulation of powder X-ray and neutron diffraction patterns. As approximate, or merely qualitative, results may not be sufficient for a thorough microstructural characterization, a computerized comparison of the DIFFaX calculated intensities with experimental data would be of great help. A modification of the DIFFaX code including this possibility has been recently reported [2]. Independently, we have also developed an alternative code for the same purpose but following a quite different data treatment. The resulting code is the FAULTS program which can be used for the refinement of layered structures containing coherent planar faults.

Program specifications

As DIFFaX, FAULTS is a Fortran program but written in the new standard Fortran 95. The program FAULTS conserves the kernel of DIFFaX, which has been transformed into a Fortran 95 module, and adds other modules from the Crystallographic Fortran Modules Library (CrysFML) [3]. It can be used to refine XRD and NPD patterns of crystal systems with any type of coherent planar defect, such as twins and stacking faults.

The refinable parameters are read by FAULTS from a free format input data file, similar to that of DIFFaX, where the structure is described in terms of layers of atoms which interconnect via stacking operations that occur with a certain probability. Each value used to describe the structure is associated to a refinement code that allows the introduction of restrictions. The high and low limits of free parameters as well as the nature of the boundary conditions are provided by the user.

The experimental XRD or NPD patterns can be read from many different formats and background treatment can be achieved by linear interpolation or by polynomial fitting.

Another major feature of FAULTS is the implementation of a more adequate isotropic size broadening treatment which takes into account the Gaussian (HG) and Lorentzian (HL) contributions to the FWHM in addition to the consideration of a finite number of layers per crystallite already present in DIFFaX. The profile calculated by DIFFaX is convoluted with a Voigt function taking into account the size and instrumental effects. The FWHM of the Gaussian (H_G) and Lorentzian (H_L) components of the size/instrumental peak profile have an angular dependence given by equations (1) and (2):

$$H_G^2 = U\tan^2\theta + V\tan\theta + W + \frac{4\ln 2\lambda^2}{\pi D_g^2\cos^2\theta} \quad (1)$$

$$H_L = X\tan\theta + \frac{2\lambda}{\pi\ D_l\cos\theta} \quad (2)$$

Were U, V, W, X, D_g and D_l are refinable parameters. Of course it is better to know a priori the parameters constituting the instrumental resolution function (IRF) and fix them. This treatment allows a successful description of the separate contributions to line broadening of instrumental features, finite crystallite size and planar defects.

The refinement can be carried out using local optimisation algorithms, like Nelder-Mead simplex [4], or global ones, as Simulated Annealing [5] or Multilevel Clustering [6, 7], all of them implemented in CrysFML [3].

The quality of the agreement between observed and calculated profiles is given by a set of indices such as the conventional R_P and R_{WP} values, or χ^2, that are calculated at the end of each refinement cycle.

Example: Stacking faults in nickel hydroxide

Nickel hydroxide is used as the positive electrode material in Ni/Cd, Ni/H_2 or Ni/MH batteries. It presents a brucite type structure consisting in NiO_2 slabs made of edge-sharing octahedra. It is well known that the best electrochemical activities are obtained with small particle size materials [8]. It is also believed that the presence of structural defects enhances the elec-

trochemical performances of nickel hydroxide. DIFFaX simulations have been reported for this material with the hypothesis of the existence of stacking faults in the structure [9,10] in order to explain the abnormal broadening of the (10*l*) and (20*l*) diffraction lines ($l \neq 0$).
A stacking fault may be defined as a breaking in the normal stacking sequence of a structure. In the ideal structure of $Ni(OH)_2$, free of stacking faults, the oxygen atoms are placed alternatively in the A and B positions of a triangular lattice, whereas the nickel ions are in the centre of the oxygen octahedra, in C positions. Considering only the oxygen sheets, the perfect structure may thus be written as ABABAB. In the presence of a stacking fault, the oxygen atoms of the next sheet shift to position C instead of position A. If the following sheet of oxygen atoms is located just above those as two positions below, ABCBCB configuration, a growth type stacking fault is obtained. In contrast, if the following sheet of oxygen atoms is located just above those as three positions below, ABCACA configuration, the result is a deformation type stacking fault [11].
Considering both types of stacking faults, the oxygen sequence can be described with four different layer types, each one containing two sheets of oxygen atoms: AB, CA, CB and BC, as described in figure 1.

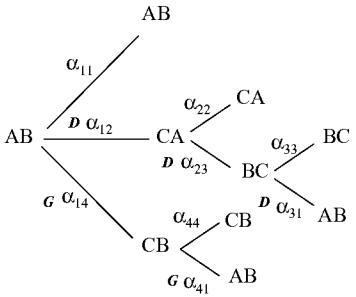

Figure 1.Possible layer transitions for a nickel hydroxide containing stacking faults, where α_{ij} is the probability transition from layer i to layer j and D and G indicate deformation and growth type faults respectively.

Analysis of simulated data

A simulated XRD pattern for $Ni(OH)_2$ has been used to analyse and test out the program. Most of the initial values of the refinement have been chosen far enough from the correct ones not to bias the result. All the refined parameters using the Nelder-Mead simplex optimisation algorithm are detailed in table 1 and a visual comparison between the calculated and the simulated powder patterns and their difference is shown in figure 2.
In the first stage of the refinement the R_p value was 133.26% and at the end of the refinement diminished down to 1.09%. All the refined parameters are very close to those used in the simulation except those involved in the IRF, but the obtained values of *U, V*, and *W* lead to a Caglioti curve practically identical to the one obtained with the values of these parameters used in the simulation.

FAULTS refinement of the XRD pattern of a $Ni(OH)_2$ sample

The refinement of an experimental pattern corresponding to a $Ni(OH)_2$ sample has been carried out using the FAULTS program assuming the existence of stacking faults.

The $Ni(OH)_2$ sample was synthesized by addition of 1M nickel sulphate solution to 2N NaOH solution at 70°C. The mean particle diameter is around 139Å as determined by TEM.

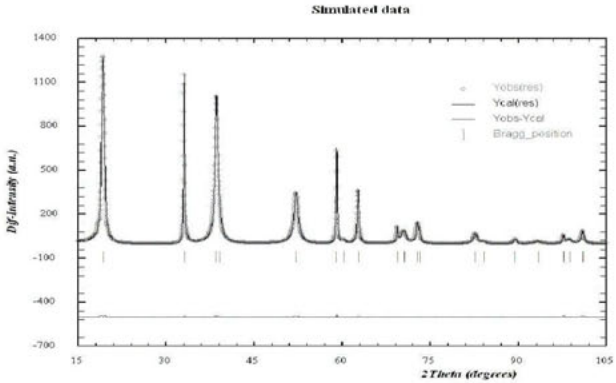

***Figure 2**. Simulated ("observed") versus calculated patterns. The simulated pattern is the dotted curve and calculated pattern, using the FAULTS refinement, is the continuous curve; the diagram underneath shows the difference between them.*

***Table 1**. Description, initial and refined value for all parameters used in the analysis of simulated data.*

parameter	Description	Simulation	Initial	Refined
U	instrumental resolution function (IRF) parameter	0.0036	0.001	0.0013
V	IRF parameter	-0.0036	-0.001	-0.001
W	IRF parameter	0.0023	0.001	0.0012
X	Lorentzian contribution to FWHM parameter	0.0306	0.01	0.0122
Dl	Lorentzian contribution to FWHM parameter	339.7	500	328.4
a, b	cell parameters	3.1293	3.3293	3.1286
c	cell parameter	4.6038	4.7038	4.6046
Xo	atomic position along c axis for atom2	0.2202	0.3202	0.2201
Biso Ni	Temperature factor atom1	1.0620	0.1	1.0696
Biso O	Temperature factor atom2	0.75961	0.1	0.7319
Num_layers	number of layers per crystallite	35.0	80.0	35.0
α11	stacking probability layer 1-1	0.80	0.75	0.80
α12	stacking probability layer 1-2	0.05	0.10	0.05
α22	stacking probability layer 2-2	0.95	0.90	0.95
α23	stacking probability layer 2-3	0.05	0.10	0.05
α31	stacking probability layer 3-1	0.05	0.10	0.05
α33	stacking probability layer 3-3	0.95	0.9	0.95

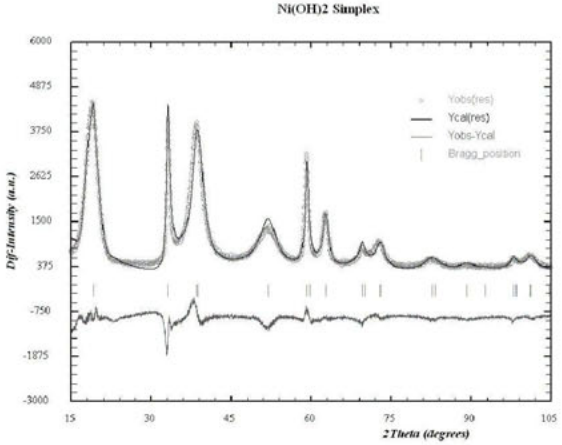

Figure 3. Comparison of observed and calculated patterns corresponding to nickel hydroxide. The observed pattern is the dotted curve and the calculated pattern, using the Nelder-Mead simplex optimisation algorithm, is the continuous curve; the diagram underneath shows the difference between them.

***Table 2**. Refined values for all parameters used in the analysis of an experimental XRD pattern corresponding to nickel hydroxide.*

Parameter	Refined value (Simplex)	Refined value (Simulated Annealing)
x	0.0242	0.0131
Dg	1079.8	1091.7
Dl	91.8	85.1
a, b	3.1241	3.1251
c	4.6454	4.6525
Biso Ni	0.6518	0.6398
Biso O	0.1574	0.8995
z O	0.2266	0.2290
Num_layers	7.4	7.4
α11	0.60	0.61
α12	0.15	0.21
α14	0.25	0.18
α22	0.80	0.78
α23	0.20	0.22
α31	0.20	0.22
α33	0.80	0.78
α41	0.25	0.23
α44	0.75	0.77

The X-ray diffraction pattern was obtained with a Siemens D-500 diffractometer with Cu-Kα radiation and a step size of 0.03º (2θ). In order to avoid preferential orientation effects, the sample was side loaded in the sample holder.
The results of the refinement, performed with both Nelder-Mead simplex and Simulated Annealing optimisation algorithms, both leading to very similar results, are reported in table 2. The *U, V*, and *W* parameters from the instrumental resolution function were not refined as they were obtained from a LaB_6 standard. The obtained R_p values are 6.83% in the case of the Nelder-Mead simplex calculation and 7.12% for the Simulated Annealing. A comparison between the calculated, the observed and difference powder patterns is shown in figure 3.
The results indicate the presence of 20-25% growth faults. An important part of the anisotropic broadening comes from the size effect (refined number of layers ≈7.4). The accuracy of the results is further confirmed by the values obtained for the in-plane particle size, which are in agreement with the TEM observations.

Concluding remarks

An extension of the DIFFaX program, FAULTS, has been developed in order to refine XRD and NPD patterns of defective layered materials. The FAULTS program provides a useful tool in microstructural refinement and has already been tested in nickel hydroxide electroactive materials. A copy of the program is available from the authors upon request.

References

1. M.M. Treacy, J.M. Newsam, M.W. Deem, 1991, *Proc. R. Soc. London Ser. A*, **433**, 499-520.
2. M. Leoni, A.F. Gualtieri, N. Roveri, 2004, *J. Appl. Cryst.*, **37** , 166-173.
3. J. Rodriguez-Carvajal and J. González-Platas, 2003, IUCr *CompCom Newsletter*, **1,** 50-58 (available at http://www.iucr.org/iucr-top/comm/ccom/newsletters/).
4. J.A. Nelder, R. Mead, 1965, *The computer journal*, **7,** 308-313.
5. S. Kirkpatrick, C. D. Gelatt, Jr., M. P. Vecchi, 1983, *Science*, **220,** 671-680.
6. Boender, C.G.E., A.H.G. Rinnooy Kan, G.T. Timmer, L. Stougie, 1982, *Mathematical Programming,* **22**, 125-140.
7. Csendes, T., 1988, *Acta Cybernetica*, **8,** 361-370.
8. McBreen, J., 1990, *Modern aspects of electrochemistry,* **21**, (Plenum Press).
9. C. Delmas, C. Tessier. 1997, *J. Mater. Chem.*, **7**(8), 1439.
10. C. Tessier, P.H. Haumesser, P. Bernard, C. Delmas. 1999, *J. Electrochem. Soc.,* **146**(6), 2059-2067.
11. M.T.Sebastian, P. Krishna, 1994, *Random, non-random and Periodic Faulting in Crystals*, (Gordon and Breach Science Publishers).

Acknowledgements. We are grateful to the Ministerio de Ciencia y Tecnologia (MAT 2000-0128-P4-03), the CSIC (I3P program) and the Departament d'Universitats, Recerca i Societat de la Informació de la Generalitat de Catalunya for financial support.

Z. Kristallogr. Suppl. **23** (2006) 249-254

PM2K: a flexible program implementing Whole Powder Pattern Modelling

M. Leoni[1,*], T. Confente[1], P. Scardi[1]

[1]University of Trento, Department of Materials Engineering and Industrial Technologies, 38050 via Mesiano 77, Trento, Italy
[*]Contact author; e-mail: Matteo.Leoni@unitn.it

Keywords: Whole Powder Pattern Modelling, convolutive approach, line profile analysis.

Abstract. Whole Powder Pattern Modelling (WPPM) has been recently proposed as a self-consistent low-bias technique for the microstructural investigation of nanocrystalline materials. Through WPPM, a set of physical parameters actually describing the Fourier transform of diffraction line profiles, can be easily extracted from the diffraction data.
In order to cope with the need for a higher flexibility (to test, compare and use new line broadening models) and with the request for additional features, the existing code implementing WPPM has been redesigned and improved.
The result is a general tool for nonlinear least squares minimisation, highly problem-independent and user-customisable through the use of macros or by a custom software development kit. A set of libraries have been written in the form of plug-ins, actually implementing WPPM and the microstructural models proposed in the literature. The work shows software architecture and examples of application of the program to real cases of study.

Introduction

The applications of nanostructured and nanosized materials are increasing and evolving very quickly. Nanostructured materials, in fact, show often striking properties if compared to their coarse-grained counterpart [1]. This alone is sufficient to justify the need (especially in industry) for fast and reliable techniques for qualitative and quantitative characterisation of nanocrystalline materials.
Most of the available analysis techniques are bare adaptations of methodologies currently employed for the study of coarse-grained materials. Among them, Transmission Electron Microscopy (TEM) is perhaps the most straightforward, as it gives direct and visual information on the microstructure up to the atomic resolution. On the other hand, X-ray diffraction is the most appealing as it can provide both structural and microstructural information faster, with a better statistics and without the need for difficult sample preparation.
Several techniques exists for the analysis of diffractograms, most of them relying on post-processing of profile-shape data extracted from the pattern through profile fitting with an arbitrary bell-shaped function. Their meaning is however mostly *qualitative* as recently pointed out (cf. e.g.[2]). For quantitative analysis, full pattern techniques are preferable as

they directly extract microstructural information from the measured data. Among those, Whole Powder Pattern Modelling (WPPM) [3] has been shown to outperform traditional techniques, providing results in agreement with those attainable by TEM. In WPPM, a synthetic pattern, generated from a physical modelling of the materials microstructure, is best fitted to the data: models linking the microstructure to the Fourier transform of the line profiles are readily available in the literature (see e.g. [3-6]).
A free and flexible nonlinear least squares fitting software package, named PM2K, is shown here: WPPM, as well as other methods of analysis based on least squares fitting (the Rietveld method, for instance) can be built as plug-ins on top of it. Several of the models available in the literature for the microstructural analysis can coexist and can be simultaneously refined.

Architecture

PM2K has been designed with modularity and expansibility in mind. Wherever possible, the software has been written to be problem-independent and easy to expand without rewriting or recompiling the whole source code. Three main entities can be identified in the program:

- kernel
- plug-ins
- user interface

General Multi-user/Multitask Nonlinear Least Squares Minimisation Kernel
The core of the software package is a custom Nonlinear Least SQuares (NLSQ) routine based on an adaptation of the Levenberg-Marquardt algorithm [7]. The routine is completely model-independent, it works on *n*-dimensional datasets and it can run multiple minimisation in parallel (on separate minimisation threads). A simple interface is provided for the users to write custom functions to be minimised. Each minimisation thread is associated with a username/password and some session data (init files, output files, running context): the owner can freely connect and disconnect from the running kernel to check the status of the minimisation threads running in the background. Faster execution, easier portability and small code has been obtained by writing the kernel as stand-alone application driven through a TCP/IP port. A 3-tier architecture [8] was chosen for the kernel (figure 1) and three independent logical units are therefore present in it: a unit requesting services (client-tier), a unit providing services (application-server-tier) and another unit handling the data (data-server-tier). More precisely, the client-tier receives and processes all requests for calculation and application control, therefore interfacing the external world with the running application. The calculation routine is implemented entirely in the server-tier and is therefore completely isolated from the user: its scope is to provide the various clients a set of services. The data-server tier will provide the application server the data to process. Any change in the interface with the external world or the data won't therefore affect the calculation code. As all calculation can be run remotely (as a TCP connection can be done between computers connected through the Internet), the system is designed to work through input files: indication concerning I/O data files, parameters and models are passed to the kernel in a user command file. A symbolic expression parser processes the command file, identifying the internal and external (user) commands, the parameters (and their status) and the symbolic links between them.

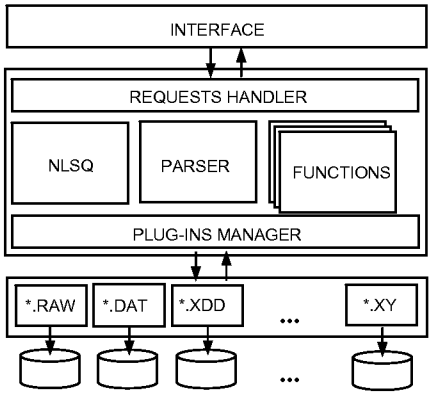

Figure 1. three-tier architecture adopted for the kernel of PM2K.

Plug-ins

The routines providing the function to be minimised and all additional functions to be used in the input file (in this case those implementing the line-profile broadening models) are compiled independently as dynamic loading libraries and linked to the kernel at runtime. A plug-ins development kit (any C++ compiler required to compile the provided demo plug-in) is available to the users that can therefore easily implement their own models into the kernel.

Bundled plug-ins are sufficient for a microstructural analysis of nanocrystalline materials using the WPPM approach: a library provides the function for recognising base entities like phases, peaks, patterns, Fourier convolution, whereas most of the available models for line-profile broadening provided in the literature are implemented as additional plug-ins. For example it is possible to account for:

- Instrumental broadening: Rietveld-Caglioti formula (pseudo-Voigt fit of profiles collected on a suitable line-profile standard), FPA (Fundamental Parameters Approach, in development)
- Size broadening:
    - histogram model for size distribution (sphere, cube, tetrahedron, octahedron, ellipsoid, hexagonal prism, cylinder, harmonics)
    - analytical model for size distribution (delta, lognormal, gamma, generalised gamma, York distributions of sphere, cube, tetrahedron, octahedron, ellipsoid, hexagonal prism, cylinder, harmonics)
- Strain broadening:
    - dislocations (fcc,bcc,hcp) using the simplified and full Wilkens models
    - dislocations (all symmetries) using harmonics invariant or Green function
    - Houska-like models (Houska, Adler-Houska, modified Houska)
- Effective broadening (size/strain contribution are mixed)
    - Harmonics model
- Faulting:
    - recursion equations (Warren) for fcc, bcc and hcp
    - correlation probability

  - correlation matrices
  - recursive approach (convergence towards DIFFaX+)
- Antiphase Boundaries in ordered phases (Wilson-Zsoldos models using both finite and infinitesimal differences)
- Grain Surface Relaxation (original model coping with size-independent relaxation-zone width and a modified model with size-dependent relaxation)
- Possible easily implemented additional broadening models
  - full micromechanical model
  - grain-dependent lattice parameter variation
  - broadening due to stoichiometry fluctuations

Information on most of those models can be found in the cited references.
The handling of data files is also done through plug-ins: handling of the most common data formats is already provided in the default I/O plug in, but extra types can be easily added (particularly useful when dealing with synchrotron data files whose format is seldom standard). A least-recently-used caching mechanism is provided on most calculation routines for increased performance.

Interface

In order to send minimisation jobs to and to manage the running threads in the kernel, a lightweight graphical user interface is provided (figure 2). It does not pretend to be a scientific plotting package, as several of them (both commercial and non commercial) are readily available. It is designed to allow an easy editing of the input file (syntax highlighting is provided) and easy communication with local or remote kernels.
A minimal plotting facility is provided as to allow the user to follow the ongoing minimisation.

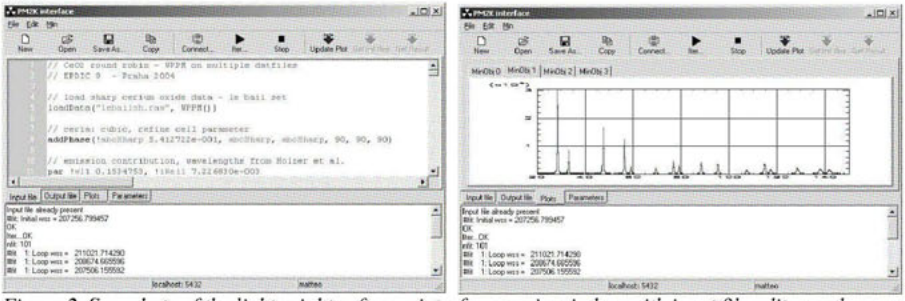

Figure 2. Snapshots of the lightweight software interface: main window with input file editor and graphical display of the ongoing minimisation are shown.

Input/output files

I/O files are free-format and case-sensitive: symbolic names can be associated to parameters and symbolic links can be made between them. Comments can be inserted in the files for better understanding: the kernel will update the minimised parameters and provide estimated standard deviations and statistical indicators directly embedded in the input file. Details on the functionality of the single commands can be found in the documentation provided with each plug-in. An example input file is shown in figure 3.

```
//Fluorite, W=200, w=-1, milled 128h
loadData("CaF2 128h.raw", WPPM(0 , 0 -1.402767e-002   ))
enableFileFit()

// emission profile, 2 components
addWavelength(!wl00 0.15405981, !iRel00 1.0)
addWavelength(!wl01 0.15444565, !iRel01 0.475)

addPhase(abc 5.466148e-001, abc, abc,!albega 90*deg2rad, albega, albega)

// Cagliotì curve, instrumental function
par !CU 0.00216, !CV  -2.88483E-4, !CW  0.00232
par !Ca 0.78497, !Cb  -0.01026,
addCS(CagliotiUVWabc(CU, CV, CW, Ca, Cb, 0))

// size broadening
addCS(ArbitraryDis("sphere","128h.dis"))

// strain broadening (dislocations)
par rho 1.195593e-002    min 1e-3,Re 3.366895e+000    min 0.1 max 15
par mixp 6.781664e-001    min 0 max 1, burgers :=abc*sqrt(2.0)/2.0;
addCS(Wilkens(rho, Re, 0.104228, 0.388633, 0.126335, 0.060745,  mixp, burgers))

addPeak( 1,  1,  1 , 0 1.921538e+001)
addPeak( 2,  0,  0 , 0 8.682141e-002)
addPeak( 2,  2,  0 , 0 5.303777e+001)
addPeak( 3,  1,  1 , 0 2.168472e+001)
addPeak( 2,  2,  2 , 0 2.057162e-001)
addPeak( 4,  0,  0 , 0 1.012830e+001)
addPeak( 3,  3,  1 , 0 1.043699e+001)
addPeak( 4,  2,  0 , 0 7.422948e-001)
addPeak( 4,  2,  2 , 0 2.068071e+001)
addPeak( 3,  3,  3 , 0 1.139791e+000)
addPeak( 5,  1,  1 , 0 7.322273e+000)
addPeak( 4,  4,  0 , 0 6.372131e+000)
addPeak( 5,  3,  1 , 0 9.266431e+000)
addPeak( 4,  4,  2 , 0 7.190306e-001)
addPeak( 6,  0,  0 , 0 2.574079e-001)
addPeak( 6,  2,  0 , 0 9.465344e+000)
addPeak( 5,  3,  3 , 0 3.507835e+000)
addPeak( 6,  2,  2 , 0 6.143811e-001)

// impurity (Fe)
addPhase(Feabc 2.951808e-001, Feabc, Feabc, albega, albega, albega)
addCS(CagliotiUVWabc(CU, CV, CW, Ca, Cb, 0))
addCS(SizeDistribution("sphere","lognormal",muFe 4.399712e+000,sigmaFe 6.522219e+000))
addPeak( 1,  1,  0 , 0 6.138348e-001)
addPeak( 2,  0,  0 , 0 4.262200e-001)
addPeak( 2,  1,  1 , 0 4.658796e-001)
addPeak( 2,  2,  0 , 0 2.108752e-013)
addPeak( 3,  1,  0 , 0 1.727325e-001)
mul(LPFactor(0, 26.57))
add(ChebyshevBkg(0 9.656695e+000,0 1.550488e-001,0 -4.631108e-005,0 5.436695e-009))
```

Figure 3. Example of input file syntax.

Testing

The program has been thoroughly tested on several datasets (against previously published data). The case of a fluorite powder is shown here: the powder has been ball-milled for 128h in a planetary mill at a speed of the main disk Ω = 200rpm and with a planet-to-disk speed ratio ω = -1 (sample from a set presented in [9]). Due to the severe mechanical work, the powder becomes nanocrystalline and full of defects (dislocations and faults, mainly). The pattern, collected on a Rigaku PMG/VH diffractometer using Cu radiation (produced at 40kV, 30 mA) was refined using PM2K and the input file shown in figure 3 (see also [9] for details). The raw data and the result of the modelling are shown in figure 4a. The corresponding domain size distribution, modelled according to [4] is presented in figure 4b (histogram). Besides size broadening, a dislocation density ρ = 11.9(20) 10^{15} m^{-2} was obtained. Iron (bcc), present as impurity (coming from the vial and ball used for the milling), was modelled together with the fluorite powder and contributed to a Goodness of Fit (GoF) value of 1.23 (R_{wp} = 7.48671%, R_{exp} = 6.08649%).

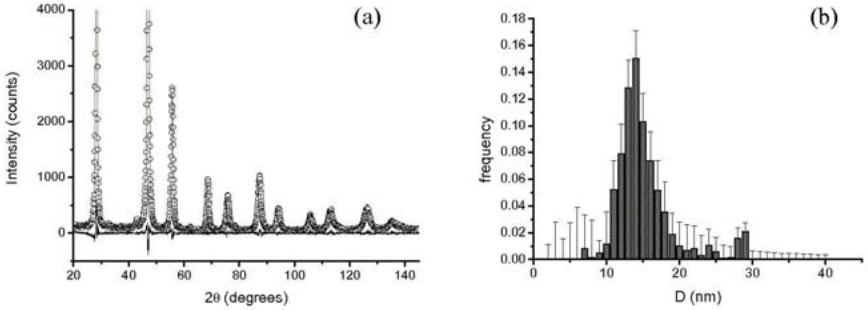

Figure 4. WPPM results for the fluorite powder: a) raw data (circles), model (line) and residual (difference between the previous two). In b) the corresponding refined domain size distribution is shown.

Concluding remarks

A flexible general least squares minimisation software is presented. A set of plug-ins has been designed for it, fully implementing Whole Powder Pattern Modelling (WPPM): through them, microstructural information can be extracted from diffraction data. Most of the available models of line profile broadening, based on a convolutive Fourier approach, have been or can be easily implemented as plug-ins for the software to extend its range of applicability. The program has been thoroughly tested on various nanocrystalline metals and ceramics.

References

1. Gleiter, H., 2000, *Acta Mater.* **48**, 1-29.
2. Scardi P., Leoni M. & Delhez R., 2004, *J. Appl. Cryst.* **37**, 381-390.
3. Scardi P. & Leoni M., 2002, *Acta Cryst.* **A58**, 190-200.
4. Leoni M. & Scardi P., 2004, *J. Appl. Cryst.* **37**, 629-634.
5. Scardi P. & Leoni M., 2004, in *Diffraction Analysis of the Microstructure of Materials*, edited by E.J. Mittemeijer & P. Scardi (Berlin: Springer), pp. 51-91.
6. Leoni M. & Scardi P., 2004, in *Diffraction Analysis of the Microstructure of Materials*, edited by E.J. Mittemeijer & P. Scardi (Berlin: Springer), pp. 413-454.
7. Levenberg, K., 1944, *Quart. Appl. Math.* **2**, 164-168.
8. Eckerson, W. W., 1995, *Open Information Systems* **10** [1], 3-20.
9. Leoni M., De Giudici, G., Biddau R., D'Incau M., Scardi P. This volume.

Acknowledgements. Dr Maurizio Marchese (University of Trento - Department of Information and Communication Technology) is deeply acknowledged for the precious hints and software engineering support during the development of PM2K.

Z. Kristallogr. Suppl. **23** (2006) 255-260

Calculating the peak shape of axially focussing powder diffractometers

D. M. Többens

Hahn-Meitner-Institut, Berlin, Germany
Contact author; e-mail: Daniel.Toebbens@gmx.de

Keywords: peak asymmetry, instrumentation, computer programme

Abstract. The use of axially focussing monochromators causes a partially ordered distribution of rays with particular high inclination angles with respect to the macroscopic diffraction plane. This has a strong influence on the axial asymmetry function. The various effects and their interaction are discussed. A programme for the calculation of the resulting peak shape from instrumental parameters is presented.

Introduction

The accurate description of the shape of individual peaks is essential for high quality Rietveld refinements. Systematic errors of the peak shape reduce the precision of the refinement and can result in parameters refined to systematically wrong values. Pure numerical Monte-Carlo simulations of instruments and their peak shapes show good results. However, they still take too long to be used in routine Rietveld refinement, where relevant parameters, i.e. sample height, can vary from one measurement to the next. In neutron powder diffraction, axially focussing monochromators have become widely used. The geometry of these instruments (see figure 1) results in peak shapes for which a description by currently available non-MC models is not satisfying. The peak shape is mainly determined by the instrumental axial asymmetry function (AAF), which will be discussed in the following.

Asymmetry for a single ray

In powder diffraction each ray diffracted at the sample does not result in an individual diffracted ray but in a Debye cone with an opening angle 2θ and the cone axis coinciding with the incident ray. The projection of this cone on the detector in combination with the width of the detector aperture not being zero is the main source of axial asymmetry. This effect has been discussed in detail in many publications (i.e. [1,2]). Thus here it will be treated only in brief and detailed discussion will only cover those aspects which are specific for axially focussing monochromators.

To derive the equations for the intersection of a Debye cone with a cylindrical detector only simple geometry is needed. In the geometry discussed here (see figure 1) the macroscopic diffraction plane (MDP) of the instrument is the common plane of the centres of sample,

monochromator and source and the middle line of the detector opening. The axis of the detector cylinder coincides with the axis of the sample cylinder; both are normal to the MDP. The origin of the Debye cone is the point where the respective incident ray hits the sample and is defined by its height z above the MDP. The cone axis is parallel to the respective incident ray and is defined by its vertical tilt angle β with respect to the MDP. Here the sign of β has been chosen in such a way that it is positive if the incident ray moves in positive z -direction. The intersection is a function of z, β, the opening angle 2θ of the Debye cone, the radius R of the detector cylinder and the height h above the MDP at the detector. These parameters correspond with the azimuth angle φ, which would bring the diffracted ray out of the MDP into its actual position, by

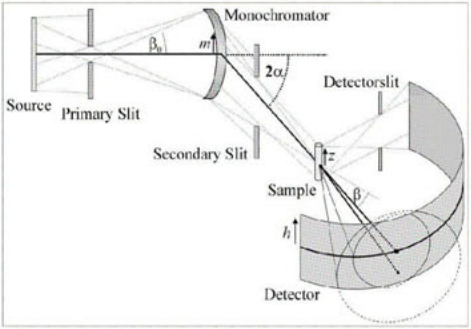

Figure 1. *Geometry and ray paths for a powder diffractometer with axially focussing monochromator. The macroscopic diffraction plane is indicated by thick lines. See text for symbols.*

$$\sin\varphi = \left(\frac{h-z}{\sqrt{(h-z)^2 + R^2}} - \sin\beta\cos 2\theta \right) \cdot \frac{1}{\cos\beta \sin 2\theta} \quad . \tag{1}$$

The observed diffraction angle $2\theta_{obs}$ results from a projection parallel to the cylinder axis into the MDP; note that this is different for detectors with axial position sensitivity (i.e. [3]). It is expressed by

$$\cot 2\theta_{obs} = \cot 2\theta \frac{\cos\beta}{\cos\varphi} - \sin\beta \tan\varphi \tag{2}$$

which can be transformed to a function of $\varphi(2\theta_{obs})$:

$$\sin\varphi = \frac{1}{A^2 + B^2} \left(BC \pm A\sqrt{A^2 + B^2 - C^2} \right) \tag{3}$$

with $A = \cot 2\theta_{obs}$, $B = \sin\beta$, $C = \cos\beta \cdot \cot 2\theta$. The two solutions indicated by $\pm$ result from the fact, that a given value of $2\theta_{obs}$ generally corresponds to two different values of φ (in parabolic approximation the upper and the lower arm of the $\varphi(2\theta_{obs})$-parabola). The intensity resulting from those two solutions has to be summed up, if both are inside the observed φ-range.

Since the intensity of a ray diffracted from a powder sample is distributed evenly on the Debye cone, the intensity distribution in $2\theta_{obs}$ for a given value of 2θ therefore is derived from the first derivation of $\varphi(2\theta_{obs})$. The resulting AAF is

$$I(2\theta_{obs}) = \frac{1}{\sin^2 2\theta_{obs}} \cdot \frac{1}{\cos\varphi} \cdot \frac{1}{A^2 + B^2} \cdot \left(\frac{2ABC}{A^2 + B^2} \pm \left[\frac{A^2 - B^2}{A^2 + B^2} \cdot \sqrt{A^2 + B^2 - C^2} - \frac{A^2}{\sqrt{A^2 + B^2 - C^2}} \right] \right) \quad . \tag{4}$$

Numerical calculation of this is easy. Since in this geometry there is no good approximation valid for the full range of 2θ the accurate expression should be used. The addend dominating

the shape of the aberration function is the last one, since β is normally small. If $A^2+B^2=C^2$ it causes a singularity in (4) at

$$2\theta_{obs,sing} = \operatorname{acot}\sqrt{1-\cos^2\beta\cdot(1-\cot^2 2\theta)} \quad . \tag{5}$$

This singularity corresponds with those rays of the Debye cone which are parallel to the

$$\varphi_{sing} = \operatorname{asin}(\tan\beta\cdot\tan 2\theta) \quad . \tag{6}$$

macroscopic diffraction plane and thus with the first derivation of $2\theta_{obs}(\varphi)$ being zero. The respective value of φ results from (3) as

This singularity, if inside of the φ range which the detector covers, marks one limit in $2\theta_{obs}$ of the axial aberration function. It must be emphasised, that due to the influence of β the $2\theta_{obs}$-value of the singularity moves significantly, in contrast to the parallel beam case [1], where $\beta = 0°$. The limited height H of the detector determines the observed φ-range; only those parts of the Debye cone for which $|h| \le H/2$ holds will be detected. The corresponding limits in φ and $2\theta_{obs}$ can be calculated from equation (1) and (2), respectively.

Effects of focussing

In a geometry with an ideally focussing monochromator all rays hit the sample at the same point, at $z = 0$. The height of the sample, otherwise an important factor for the asymmetry function, is thus effectively zero. β on the other hand is a smooth distribution which is determined solely by the height of the monochromator and its distance from the sample. This situation is similar to the parallel beam model [1] in which $\beta = 0$ and z is a smooth distribution. However, the shape of the resulting AAF and its dependency on the Bragg angle are different. This is most easily demonstrated at $2\theta \rightarrow 90°$, in which case the Debye cone becomes a flat disc and (2) becomes $2\theta_{obs}\text{-}2\theta \approx \beta\cdot\varphi$ approximately, assuming $|\beta|$ is small; first derivation results in an approximation of the intensity $I \propto \beta^{-1}$. The resulting AAF for an individual ray is box shaped with limits for which

$$2\theta_{obs,limit} - 2\theta \propto \beta\cdot(\pm 0.5\cdot H - z)/R$$

holds. $|\beta|$ thus influences the final intensity distribution twofold: it results in a linear increase of the first derivative and thus of the intensity from each individual

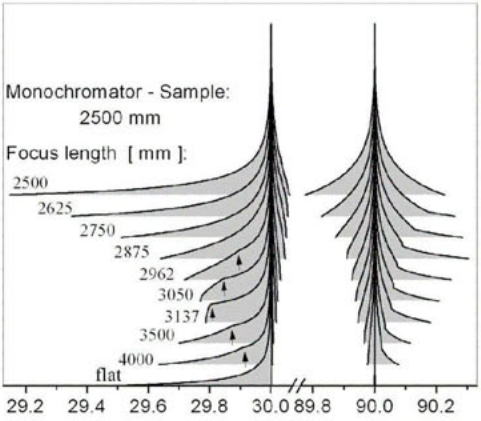

Figure 2. *AAF of an ideally focussing monochromator for various values of the focus length L. Calculations are done with monochromator-sample distance S = 2500mm, monochromator height 300 mm, sample height 40 mm, detector height 72 mm and detector radius R = 550 mm. The estimated optimum for the focus length would be L ≈ S + R = 3050 mm; at 2θ=30° the optimum of L is slightly higher. At L>2885mm rays from the outer parts of the monochromator miss the sample due to values of |z| > 20 mm.*

ray. Also the number of rays contributing to the intensity at a given distance $2\theta_{obs}$-2θ from the ideal position 2θ decreases linearly with increasing $|\beta|$ due to the movement of the limits $2\theta_{obs,limit}$. As a result the final intensity distribution at $2\theta \approx 90°$ is proportional to $1/(2\theta_{obs}-2\theta)^2$, resulting in a peak broadening of approximately Lorentzian character, which vanishes for the parallel beam case where $\beta = 0$.

If the focus length L of the monochromator is moved away from the monochromator-sample distance S the relation between β and z for each ray is

$$\tan(-\beta) = \frac{m}{L} = \frac{z}{L-S} \tag{7}$$

where m is the height at the monochromator. Of practical importance is the case $L > S$, where the focus lies behind the sample. In this case positive values of z correspond to negative values of β (and *vice versa*), resulting in a tendency of asymmetry effects to cancel each other. The asymmetry is at a minimum when the observed diffraction angles at the upper and lower border of the detector are the same:

$$2\theta_{obs}(h = -H/2) = 2\theta_{obs}(h = +H/2) \quad . \tag{8}$$

Because of the 2θ-dependence of equation (1) there is no single optimum instrument setting for all diffraction angles. Therefore a discussion of the extreme conditions is useful (see figure 2). For $2\theta \rightarrow 90°$ the Debye cones become flat; the asymmetry vanishes for $\beta = 0$, which, if valid for all rays, means a parallel beam. However, this goes against the very idea of increasing the intensity by use of a focussing monochromator. For low diffraction angles from equation (1) and (8) follows $z_{opt} \approx -R \cdot \sin\beta$, assuming $R \gg z$ and $|\beta|$ small. With this from equation (7) follows $L_{opt} \approx S + R$ as the optimum focus length, which puts the focus point at the position of the detector. In order to maximise the observed intensity the sample should be as high as the beam at the sample position S, which is easily calculated from (7). The sample height resulting from this calculation is surprisingly large, i.e. for the E9 diffractometer [4] with S = 250 cm, R = 100 cm and total monochromator height M = 30 cm the total length of the sample should be $2z_{max}$ = 9 cm.

Non-ideal effects

In praxis, various deviations from the ideal geometry discussed above result in variations of the axial asymmetry function:

1) Ideal focussing can be reached only if the rays in the primary beam are in perfect order, i.e. a parallel beam or a point source. However, a realistic source has an axial extension. Since this instrument geometry does not use collimators in the axial direction the relation between vertical tilt and height of the rays is no longer unambiguous in this case. In contrast to angular divergencies axial ones result in asymmetric broadening of the reflections due to their influence on z and β. If the intensity distribution from the source is non-uniform it also has to be considered.

2) Vertical slits limiting the height of the flight path at one or several positions also will influence the peak shape. One has to distinguish slits between source and sample from those between sample and detector. The first type will block rays from the sample and thus remove them from the calculation completely, thus changing the β, z-distribution. The latter will only block a part of the respective Debye cone. This results in changes of the borders of the AAF

in so far, as for some rays one or both of the borders are not determined by height and radius of the detector but by the intersecting slit.

3) Focusing monochromators are typically made from a row of individually flat single crystals which are tilted to provide focussing. Thus rays which are diffracted at different heights of the monochromator are nonetheless diffracted at identical diffraction vectors. This changes the relation between β and z. This effect is most clear for an parallel primary beam: with ideal focussing all rays hit the sample at the very center with $z = 0$. The AAF would result from a smooth distribution in β. With a monochromator made from a limited number of flat single crystals all parallel incident rays diffracted from one crystal plate have the same value of β, but z becomes a continuous distribution. Since changes in β shift the AAF the resulting overall function is of "comb-like" shape.

4) The real monochromator diffraction angle $2\theta_M$ for a given ray generally deviates from the macroscopic monochromator diffraction angle 2α defined as $2\theta_M$ for zero values of β_0 and β. The relation results from simple geometry as

$$\cos 2\theta_M = \cos\beta_0 \cdot \cos\beta \cdot \cos 2\alpha + \sin\beta_0 \cdot \sin\beta \quad . \tag{9}$$

These individual Bragg diffraction angles result in wavelength differences for the individual rays (naturally this holds for a white primary beam only). Respective shifts arise due to the corresponding changes in the Bragg diffraction angles 2θ at the sample, influencing the peak shape especially at high 2θ angles. A related effect is, that in order for 2α to be constant for different combinations of β_0 and β the diffraction vectors of the monochromator have to have slightly different horizontal orientations. However, this is negligible, since normally the horizontal mosaicity of the monochromator crystals is high compared to these variations. The vertical mosaicity, however, is normally quite small.

The programme Quasimodo

In order to study the effects resulting in the peak shape of this instrument geometry and in order to calculate a profile for use in Rietveld refinement the programme QUASIMODO has been written. It calculates the axial asymmetry function by means of a combination of ray tracing and analytical approach. The ray source is modelled as a linear source of limited height with isotropic emission. The number of rays calculated is controlled by the increments in height and tilt angle. Each calculated ray is described by its initial height above the MDP and by its initial angle β_0 with respect to it; no weighting of the intensity is done. From the height m at the monochromator and the distance L of an ideal focus point an ideally diffracted ray is assigned and the corresponding monochromator diffraction vector is calculated as the bisector. In the case of disordered incident rays a suitable - linear for the vertical tilt angle, parabolic for the horizontal tilt angle - function of the height of the diffraction position at the monochromator is fitted to the individual values and used in the following. If the monochromator consists of individual flat plates, the tilt angle value at the center of the respective plate is used for all rays. After the calculation of the focus, reorientations of the monochromator can be calculated. For those rays hitting the monochromator the reflected ray is calculated according to the Laue equation based on the orientation of the diffraction vector of the respective monochromator crystal. The height of the ray is compared to the respective apertures of monochromator, sample and slits and rays are removed from the calculation accordingly. For each ray hitting the sample an axial asymmetry function for a Bragg reflec-

tion with a given value of 2θ is calculated according to the functions (1)-(6), (9) given above. No approximations are used in this calculations. Shifts due to deviations in the wavelength as discussed above are applied after that. The AAF of all rays are added up to give the final AAF. This final AAF is numerically convoluted with a Gaussian function in order to include the horizontal broadening. This also avoids the problem of artificial spikes [5]. The calculated profiles can be fitted to experimental peaks using individual values for position, intensity and background and for the peak width of the convoluted Gaussian either individual values or the Caglioti function. The programme allows refinement of various instrumental parameters, of the Caglioti parameters and of contributions from a second wavelength. The output contains the calculated values for the ray distribution and various peak parameters like shift of the peak maximum and broadening. The calculated peak shapes are *inter alia* given in the format used by the Rietveld programme FULLPROF for learned profile shapes. The programme is written in Fortran77; the source code is available from the author.

Experimental test

Experimental tests of the model have been done with data measured on E9 [4] using various setting of the primary axial divergence, focussing length of the monochromator, wavelength and the heights of sample and detector opening. A detailed discussion would be to long for this article and would be of small informative value in any case; it will thus be restricted to some general remarks: In all cases the quality of the resulting fit was superior to those from previously available models, i.e. $\chi^2 = 1.45$ for points with Bragg contribution from a sample of NIST silicon measured with a wavelength of $\lambda = 1.798$ Å compared to $\chi^2 = 3.42$ for a refinement of the same data using an optimised parallel beam model [1]. Refinement of individual parameters of the model resulted in physically meaningful values close to the real ones. This is also the case for the refined peak width of the Gaussians folded with the AAF in order to model the broadening resulting from horizontal divergencies. The refined resolution function concurs with the Caglioti function [6] to ±1' for the divergencies of the instrument collimators and the mosaic spread of the monochromator. The general conclusions with respect to peak shape and peak shift drawn in a previous paper [7] are still valid. However, compared to this previous simpler model the introduction of a proper treatment of detector slits and of the variations of actual diffraction angles at the monochromator due to β_0 and β has been introduced. This resulted in both lower residuals for the fits to experimental data and in parameters of the model refining to values even closer to the physical ones.

References

1. Finger, L. W., Cox, D. E. & Jephcoat, A. P., 1994, *J. Appl. Cryst.* **27**, 892.
2. Cheary, R. W. & Coelho, A. A., 1998, *J. Appl. Cryst.* **31**, 851.
3. Gilles, R., et al., 2004, *Z. Krist. - Proceedings of EPDIC 9*, submitted.
4. Többens, D. M., et al., 2001, *Mater. Sci. Forum.* **378-381**, 288.
5. Cheary, R. W. & Coelho, A. A., 1998, *J. Appl. Cryst.* **31**, 869.
6. Caglioti, G., Paoletti, A. & Ricci, F. P., 1958, *Nucl. Inst.* **3**, 223.
7. Többens, D. M. & Tovar, M., 2002, *Appl. Phys. A* **74**, 136.

Author Index

Volume I: pp. 1–260
Volume II: pp. 261–618

EPDIC 9

Proceedings of the
Ninth European Powder Diffraction Conference

held
September 2–5, 2004
in
Prague, Czech Republic

VOLUME II

Editors

Radomir Kužel[1], Eric J. Mittemeijer[2]
and Udo Welzel[2]

[1] Faculty of Mathematics and Physics, Charles University, Prague, Czech Republic
[2] Max Planck Institute for Metals Research, Stuttgart, Germany

Supplement No. 23 of Zeitschrift für Kristallographie
Oldenbourg Verlag

The supplement issue is not included in the subscription price. It is offered to subscribers of the Journal "Zeitschrift für Kristallographie" at a special price of € 240.–
Subscribers of the Journal are not obliged to buy this issue, and are asked to return it to the sender within three weeks.

Printing: Druckhaus "Thomas Müntzer" GmbH, Bad Langensalza

Z. Kristallogr. Suppl. 23 (2006)
ISSN 0930-486-X

EPDIC 9

Ninth European Powder Diffraction Conference

Prague, Czech Republic, September 2–5, 2004

Conference location: Czech Technical University, Prague, Czech Republic

Conference chairman: Radomir Kužel

Organising committee:

I. Cisarova	S. Danis
N. Ganev	R. Gyepes
J. Hasek	D. Havlicek
J. Hybler	L. Kopecky
R. Kralova	R. Novak
P. Rezacova	I. Kuta Smatanova
Z. Sourek	A. Zupcanova

Programme committee:

Y. Andreev	UK
R. Cerny	Switzerland
R. Cernik	UK
J. Fiala	Czech Republic
H. Fuess	Germany
C. Giacovazzo	Italy
H. Goebel	Germany
J.M. Grochowski	Poland
B. Koppelhuber	Austria
S. Ivanov	Russia
V. Kavecansky	Slovakia
J. Kulda	France
M. Kunz	Switzerland
V. Langer	Sweden
E.J. Mittemeijer	Germany
H.F. Poulsen	Denmark
J. Rius	Spain
P. Scardi	Italy
S. Skrzypek	Poland
T. Ungár	Hungary

The EPDIC 9 proceedings have been sponsored by:

- PANalytical
- BRUKER AXS
- Unisantis
- International Centre for Diffraction Data, ICDD
- International Union of Crystallography
- HUBER Diffraktionstechnik GmbH & Co. KG
- Oxford Cryosystems
- X-Ray Optical Systems, Inc.
- STOE & Cie GmbH
- GE Inspection Technologies
- Inel
- Osmic Inc.
- GBC Scientific Equipment Pty Ltd
- Zentiva, a.s. Praha
- Anton Paar
- Röntgenlabor Dr. Ermrich

Preface

Condensation of Scientific Knowledge on Powder Diffraction

Progress of science demands communication. Whereas oral exchanges and letters were the dominant tools for transmitting knowledge from scientist to scientist in "old times", modern technological developments and, above all, the explosive growth of the number of scientists (the number of now living scientists is larger than the cumulative number of scientists who have passed away since the emergence of mankind) have made possible and necessitated global, consequently impersonal, communication means: predominantly papers in hard copy and/or electronic journals.

The enormous amount of scientific results made public in one way or the other can no longer be overlooked by a single person, even if he/she is supported by the best human or electronic "search engines": the sheer number of publications dealing with powder diffraction, to confine us to this field of science, impedes absorbing them. Hence, progress of science is served very much by the writing and publication of critical reviews and books, which ideally should provide the condensed form of the recent advances in a field of science as powder diffraction.

Primary scientific results on powder diffraction can be found in the four typical journals: Journal of Applied Crystallography, Acta Crystallographica A, Powder Diffraction and Zeitschrift für Kristallographie, and, of course, the proceedings of the EPDICs and the Denver conferences. However, many powder diffractionists, in particular the many of them who (also) are materials scientists, which includes the authors of this Preface, publish only a fraction of their scientific output on powder diffraction in the above mentioned journals: one should not be amazed to find important papers devoted to (the development of) powder diffraction in journals like Journal of Applied Physics, Philosophical Magazine, Advanced Engineering Materials, Journal of Alloys and Compounds, Journal of Solid State Chemistry and the like. This serves to illustrate that simple strategies for acquiring information at frontline level, as restricting oneself to the consultation of the typical journals mentioned, are terribly inadequate. Hence, again, we need and are dependent on high quality reviews and books.

Thus we decided, in order to serve you, to look for books and reviews on powder diffraction published since, say, 2000 and to list these with a few comments below. We cannot and do not claim to have been complete. Further, we do not present all that we found: we applied, admittedly personally biased, quality criteria.

Books

V.K. Pecharsky and P.Y. Zavalij, ***Fundamentals of Powder Diffraction and Structural Characterization of Materials****, 2003, Kluwer Academic Publishers, Boston Dordrecht London.*

This *text*book focuses on the basics of structure determination by powder diffraction. The analysis of the crystal imperfection is flagrantly absent, although this is not evident from the title of the book.

W.I.F. David, K. Shankland, L.B. McCusker and Ch. Baerlocher (Eds.), ***Structure Determination from Powder Diffraction Data****, 2002, Oxford University Press, Oxford.*

The book provides a high quality summary of the current knowledge on the (ab initio) determination of the crystal structure of a substance by powder diffraction. It has a strong crystallographic orientation. In a way this book succeeds and complements the well known book edited by R.A. Young on **The Rietveld Method** published in 1993 by the same publisher.

E.J. Mittemeijer and P. Scardi (Eds.), ***Diffraction Analysis of the Microstructure of Materials****, 2004, Springer-Verlag, Berlin Heidelberg New York.*

This is the one of the few books published ever presenting an authoritative overview of the analysis of crystal imperfection (crystallite size, microstrain, dislocation density, stacking and growth faults, (residual) macrostress etc.), through the interpretation of diffraction-line broadening and diffraction-line shift. The book supplies the readers sufficient information to apply the methods themselves.

Reviews

Crystal structure determination

K.D.M. Harris and E.Y. Cheung, ***How to determine structures when single crystals cannot be grown: opportunities for structure determination of molecular materials using powder diffraction data,*** *Chemical Society Reviews, 33(2004), 526-538.*

The paper focuses on the determination of the crystal structure of molecular solids by powder diffraction methods. The first author has published three other reviews with significant overlap with the review mentioned here: see Crystal Growth & Design, 3(2003), 887-895; Current Opinion in Solid State & Materials Science, 6(2002), 125-130; Angewandte Chemie-International Edition 40(2001), 1626-1651.

R.B. Von Dreele, ***Protein crystal structure analysis from high-resolution X-ray powder-diffraction data,*** *Macromolecular Crystallography, Part C, Methods in Enzymology, 368(2003), 254-267.*

V.V. Chernyshev, ***Structure determination from powder diffraction,*** *Russian Chemical Bulletin, 50(2001), 2273-2292.*

Additional references to review papers on structure determination and refinement can be found on the web page maintained by A. LeBail;
see '*http://www.cristal.org/iniref/revpap.html*'.

Line-profile analysis

P. Scardi, M. Leoni and R. Delhez, ***Line broadening analysis using integral breadth methods: a critical review,*** *Journal of Applied Crystallography, 37(2004), 381-390.*

This review (again) demonstrates that integral-breadth methods can be very useful to acquire a general understanding of origins of line broadening. More rigorous (Fourier and synthesis) methods (not dealt with in this review) allow a more detailed interpretation.

P. Klimanek, V. Klemm, M. Motylenko and A. Romanov, ***Substructure analysis in heavily deformed materials by diffraction methods,*** *Advanced Engineering Materials, 6(2004), 861-871.*

This paper of restricted review character has been dedicated to methods for the analysis of the radial (2θ scans) and azimuthal (ω scans) broadening of diffraction-line profiles.

Texture

H.R. Wenk and P. Van Houtte, ***Texture and anisotropy,*** *Reports on Progress in Physics, 67(2004), 1367-1428.*

This substantial review also pays attention to the application of (powder) diffraction methods for the determination of the orientation distribution function. Conventional techniques (pole figure determination) and new developments applying synchrotron radiation and neutrons at non-ambient conditions have been dealt with. The first author has published another review of more limited scope, with the same title, that largely overlaps with the review mentioned here: see Reviews in Mineralogy & Geochemistry, 51(2002), 291-329.

Stress

K. Tanaka, Y. Akiniwa and M. Hayashi, ***Neutron diffraction measurements of residual stresses in engineering materials and components,*** *Materials Science Research International, 8(2002), 165-174.*

This is a review of limited scope that provides a short sketch of the standard diffraction analysis of residual stress and that is particularly interesting because of the applications shown of neutron diffraction analysis to practical cases in the field of materials science and engineering.

K. Tanaka and Y. Akiniwa, ***Diffraction measurements of residual macrostress and microstress using X-rays, synchrotron and neutrons,*** *JSME International Journal Series A-Solid Mechanics and Materials Engineering, 47(2004), 252-263.*

Also this review of these authors has a modest range (see immediately above). It has been taken up here because it highlights the work performed in this area in Japan, which research is otherwise not easily accessible.

U. Welzel, J. Ligot, P. Lamparter, A.C. Vermeulen and E.J. Mittemeijer, ***Stress analysis of polycrystalline thin films and surface regions by X-ray diffraction,*** *Journal of Applied Crystallography, 38(2005), 1-29.*

This review provides the first comprehensive and practical treatment of all possible cases of diffraction-stress analysis for specimens exhibiting either macroscopical elastical isotropy (in the presence of single crystal elastic anisotropy) or macroscopical elastical anisotropy. An overview of models for elastic grain interaction allowing calculation of so-called X-ray elastic constants and X-ray stress factors has been included.

Non-ambient conditions

M.C. Moron, ***Dynamic neutron and synchrotron X-ray powder diffraction methods in the study of chemical processes,*** *Journal of Materials Chemistry, 10(2000), 2617-2626.*

Constraints and (future) possibilities of in-situ neutron and (synchrotron) X-ray powder diffraction methods have been indicated.

R.C. Peterson and H.X. Yang, ***High-temperature devices and environmental cells designed for X-ray and neutron diffraction experiments,*** *High-Temperature and High-Pressure Crystal Chemistry Reviews in Mineralogy & Geochemistry, 41(2000), 425-443.*

W. Paszkowicz, ***High-pressure powder X-ray diffraction at the turn of the century,*** *Nuclear Instruments & Methods in Physics Research, section B, 198(2002), 142-182.*

Experimental, operational aspects of powder diffraction at high pressures have been presented with a view to the possibilities of synchrotron radiation offered by experiments at (11) synchrotron storage rings all over the world.

The writing of a review or book is, for a scientist, a rather undervalued enterprise, because in such publications original results are not presented: naturally, the author is largely concerned with the condensed, elaborated and put-in-context presentation of results obtained by *other scientists* (to facilitate understanding of this depreciation in an extreme way: Nobel prizes are not given for such works). This attitude should change. Firstly, scientists are invariably strongly tributary to such books and reviews, even if they do not refer to these works in their publications … Secondly, the best reviews and books are written by superb scientists active as original researchers themselves. We should give them the honour they deserve.

R. Kužel

Prague

E. J. Mittemeijer
U. Welzel

Stuttgart
October 2005

Editorial Notes

For the first time, the Proceedings of an EPDIC Conference (EPDIC9) have now been published as Supplement No. 23 to the journal 'Zeitschrift für Kristallographie'; the Proceedings of EPDICS 1-8 had been published in the journal 'Materials Science Forum'. The change of the publisher guarantees the timely on-line accessibility of the Proceedings for *anyone* on the word-wide-web (keep an eye on the web pages **www.zkristallogr.de**). The Editors sincerely hope that this free on-line accessibility in combination with the traditional publication of the Proceedings in the form of printed volumes will strengthen the importance of these Proceedings as a medium for the publication of cutting-edge developments and compact state-of-the-art overviews in the field of powder diffraction.

The number of papers in these Proceedings is 98. The total number of papers published in the Proceedings of the preceding EPDIC conferences ranges from 88 to about 190.

The subdivision of the papers over the sections has been largely maintained as for preceding EPDIC proceedings. With reference to the Proceedings of EPDIC8, Section I.3 (Analysis of Microstructure and Macrostress) has now been subdivided in the subsections I.3.1 (Residual Stresses) and I.3.2 (Line Broadening Analysis). A new Section 'III. Software Development' has been introduced, recognizing that a relatively large number of corresponding contributions (six papers) had been submitted. Section III (Neutron Powder Diffraction) has been deleted and the papers on neutron powder diffraction have been distributed over other appropriate sections. Minor adjustments, to adapt the subsections to the submitted papers, have also been performed in the Materials section (IV).

Reviewing the nine editions of the EPDIC Proceedings, the ratios of the numbers of papers on developments in the methods and techniques of powder diffraction and those on applications of powder diffraction methods to specific classes of materials are found to be 1.0, 0.7, 0.5, 1.0, 0.9, 0.5, 0.7, 0.7 and, for the current proceedings, 0.8.

As for the EPDIC8 Proceedings, a strict refereeing procedure was adopted for the Proceedings of EPDIC9. Each contribution was considered by at least two referees. The referees were, to a large extent, participants of EPDIC9. A few (in this sense) external referees were contacted as well.

A paper to be published in proceedings of a conference has to fulfil at least some basic requirements: (i) new findings and/or insight should be presented, (ii) the theory suggested and/or analysis employed has to be correct (iii) the paper should be readable. Roughly ten percent of the submitted papers did not satisfy the above mentioned basic requirements and were rejected. The refereeing procedure did lead to improvements of both the scientific quality and the readability of the papers after revisions. In this way it is hoped that the EPDIC Proceedings escape the fate of much of the so-called 'grey literature'. We thank all referees

for their efforts and time spent on the manuscripts. We also thank the EPDIC9 secretary Ivana Kuta Smatanova for final technical corrections necessary for most of the papers. We did not correct the English used, apart from minor corrections in a few papers.

We sincerely hope that these Proceedings will be a useful collection of papers outlining the newest developments in the field of Powder Diffraction.

R. Kužel

Prague

E. J. Mittemeijer
U. Welzel

Stuttgart
October 2005

European Powder Diffraction Conference Award

Sponsored by PANalytical

The EPDIC award honours outstanding scientific achievements by young scientists in the areas covered within the European Powder Diffraction Conference (EPDIC) Programme. The award winner will be invited to present a plenary talk at the next European Powder Diffraction Conference. The award has a value of 1000 Euro.

The EPDIC Scientific Programme Committee, which is responsible for the nomination of the award, invites everyone to submit short proposals containing descriptions of scientific contributions to be assessed, together with the name of suitable candidates. These proposals should be addressed to the Chairman of the EPDIC Scientific Programme Committee.

Table of Contents

III. SOFTWARE DEVELOPMENT

VOLUME II

IV. MATERIALS

IV.1 Thin Layers

IV.2 Nanocrystalline Materials

IV.3 Metals and Alloys

IV.4.2 *Determination of Crystal Structure*

IV.4.3 *Determination of Magnetic Structure, Magnetic Materials*

IV.4.4 *Microstructure, Phase Analysis*

IV.5 Organic Materials

IV. MATERIALS

IV.1 Thin Layers

Z. Kristallogr. Suppl. **23** (2006) 263-268

X-ray scattering from interface dislocations in highly mismatched oxide epitaxial films

R. Guinebretière*, A. Boulle, O. Masson, A. Dauger

Science des Procédés Céramiques et de Traitements de Surface, CNRS, UMR 6638. ENSCI, 47 Av. A. Thomas 87065 Limoges, France.
*Contact author; e-mail: r_guinebretiere@ensci.fr

Keywords: X-ray diffraction, misfit dislocations, reciprocal space mapping, epitaxial layer

Abstract. Relaxation mechanisms in a highly mismatched epitaxial oxide thin film have been studied. Zirconia islands have been epitaxially grown on magnesia single crystal. We have shown by reciprocal space mapping that the 20% misfit between zirconia and magnesia was relaxed through both interdiffusion and the formation of misfit dislocations. The analysis of transverse scans performed through symmetrical reflections strongly suggests the existence of a square network of misfit dislocations.

Introduction

It is well known that the physical properties of thin layers are often greatly influenced by the microstructure of the films. Among microstructural parameters the state of strain of the film is probably the most important. During the last decade a large amount of work has been devoted to the determination of strain and strain gradients in epitaxial thin films. Nevertheless, most of the studies were devoted to semiconductor or metallic thin films. The main specificity of oxide materials is that they exhibit high defect densities as compared to semiconductor materials. In particular strain relaxation in epitaxial oxide films can be driven by many different mechanisms simultaneously such as misfit dislocations [1], islanding [2], film buckling [3], rotational disorder [3], domains formation [4], phase transition [5] and also chemical-dependent processes like interfacial diffusion inducing the formation of solid solutions.

One of the key points on the way to the understanding of the properties of devices made of oxide thin films is certainly the quantitative determination of the strain relaxation mechanisms. Among the different experimental approaches to this problem X-ray diffraction (XRD) is probably the most efficient. As shown by several authors [6], reciprocal space mapping (RSM) allows to study the microstructure of thin films on a highly quantitative level. In this paper RSM is used to separate different relaxation mechanisms in order to determine the respective influence of strain-related mechanisms (i.e. interfacial dislocations) and chemistry-related relaxation mechanism (i.e. interfacial diffusion) in epitaxial oxide thin

films. Transverse scans exhibiting symmetrical secondary maxima will be analyzed in relation to the presence of an interfacial dislocations network.
Previous TEM studies on ZrO_2 thin films grown on MgO allowed us to evidence a simple cube on cube epitaxy [7, 8]. However, this system is highly mismatched (~20%) important relaxation mechanism such as misfit dislocations are hence expected. Moreover, due to the well known solid solution phase in the zirconia-rich region of the zirconia – magnesia phase diagram [9], interfacial diffusion between magnesia and zirconia is also expected to play an important role.

Experimental

Reciprocal space maps have been recorded on a modified double crystal diffractometer [7, 10] using the $CuK\alpha_1$ radiation of a rotating anode generator operating at 10 kW. A four-reflection monochromator made of two channel-cut Ge(220) crystals provides a highly monochromatic ($\Delta\lambda/\lambda = 1.4\times10^{-4}$) and parallel beam ($\Delta\theta$ = 12 arcsec). X-rays scattered by the sample are collected on a curved position-sensitive detector (PSD) covering 120°. The two dimensional intensity distributions were recorded through one set of measurements. The incidence angle ω varies step by step and for each ω value the 2θ intensity distribution is directly recorded by the PSD. In spite of the large broadening of the reciprocal lattice points (RLP), the measurements were performed in only few hours. The samples were elaborated through a specific sol-gel process already described elsewhere [7]. Pure zirconia thin films have been deposited onto (001) cut magnesia substrates by sol-gel dip-coating. The synthesis of a stable sol has been carried out in the Zr n-propoxide / acetylacetone / ethanol [11]. The chosen concentration of the Zr precursor and the dip-coating parameters led to 30nm-thick polycrystalline films after heating at 600°C. Subsequent thermal treatment at 1500°C during one hour induces the formation of zirconia islands epitaxially grown on the magnesia substrate [7, 8].

Results

Epitaxial relationships and magnesia –zirconia interdiffusion
Epitaxial relationships between zirconia islands and magnesia substrate where determined through reciprocal space mapping and ϕ-scan experiments. A RSM performed near the (002) magnesia RLP shown in figure 1a. The position of the (002) zirconia RLP with respect to the (002) MgO RLP clearly indicate that the (002) zirconia and magnesia planes are parallel. The in plane orientation was determined using the (204) zirconia asymmetric reflection. The corresponding ϕ-scan is given figure 1b. The zero value of the ϕ angle was previously fixed at the point corresponding to the intensity maximum of the (204) substrate reflection. The epitaxial relationships can thus be written as $(001)_{ZrO2}$ // $(001)_{MgO}$ and $[100]_{ZrO2}$ // $[100]_{MgO}$.
Under atmospheric pressure, zirconia exhibits three different polymorphs [9]. At room temperature the stable phase is monoclinic (space group: $P2_1/c$), between 1170 and 2350°C the tetragonal phase (space group: $P4_2/nmc$) is stable and from 2350°C to the fusion point at 2700°C zirconia exhibits cubic symmetry (space group: Fm3m). Several orthorhombic phases have been observed under pressure [9]. High temperature or high pressure stable phases can be observed under normal conditions in at least two different cases. Firstly, the

introduction of cationic dopants induces the stabilization of tetragonal, cubic or sometimes orthorhombic zirconia [12]. Secondly, it is well known that the decreasing of the crystal size in the nanometric range induces the formation of metastable zirconia grain under tetragonal or cubic phase [13]. The description of the transitions mechanisms between those different phases is still under debate [14].

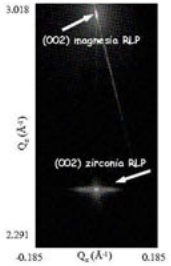

Fig1a

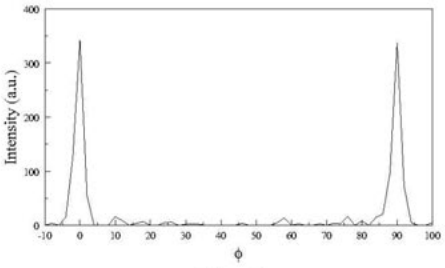

Fig. 1b

Figure 1. (a) Reciprocal space map near the (002) magnesia node. (b)ϕ-scan measurement made on the (204) asymmetric zirconia reflection.

The first step to separate compositional and strain effects is to determine the actual phase of the zirconia crystals constituting the epitaxial islands. Preliminary measurements allowed us to exclude the monoclinic form. Thus, we consider that zirconia has an orthogonal lattice. The mean values of the zirconia cell parameters where determined using the positions of symmetric and asymmetric reflections. Considering that the c lattice parameter is taken along the normal to the interface, a, b and c parameters where determined. The values obtained were very close each others and finally they can be considered, within an uncertainty of few thousandths of angstrom, equal to a = b = c= 5.096 Å.

Figure 2 shows the map of the asymmetrical (-204) reflection. Considering cubic materials, two extreme situations, schematically presented in figure 3, can be encountered. In the case of a coherent interface, the continuity of the lattice through the interface induce an alignment along Q_z of asymmetric RLPs of both the substrate and the layer (see figure 3a). On the contrary, a semi-coherent interface induces an alignment of the RLPs along the diffraction vector Q (see figure 3b). Figure 2 clearly shows that this latter situation applies in our case, the zirconia film is fully relaxed. Several measurements performed at different azimuths of the sample, led to the same conclusions.

Taking into account this result we are now able to determine the mean chemical composition of the zirconia islands. Indeed, since the layer is not homogeneously strained, the value of the cell parameter can be directly related to the amount of magnesia introduced in the zirconia film. The relationship between the dopant ratio and the cell parameter of cubic zirconia has been investigated by many authors. Ten years ago, Yashima et al. [15] have proposed a review of experimental values published in the literature. Taking into account of 16 different dopants and extrapolating the data to pure zirconia, those authors found that the cell parameter at room temperature of the virtual pure unstressed cubic zirconia is equal to 5.1063 Å. Concerning magnesia doped zirconia they proposed the following relationship where x is a molar ratio: a (Å) = 5.1063-0.184 x_{MgO}. More recently E. H. Kisi and C. J. Howard [16]

proposed another equation : a (Å) = 5.122-0.3140 x_{MgO}. Following those two equations we have found a dopant amount respectively equal to 5.6 % and 8.3 %. One may conclude that the magnesia contents between 5 and 10%.

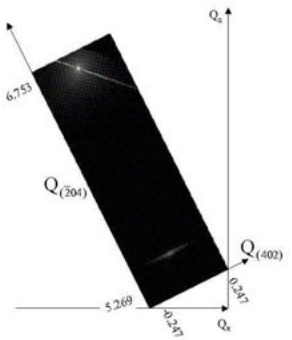

Figure 2. Reciprocal space map of the asymmetric(-204) zirconia reflection.

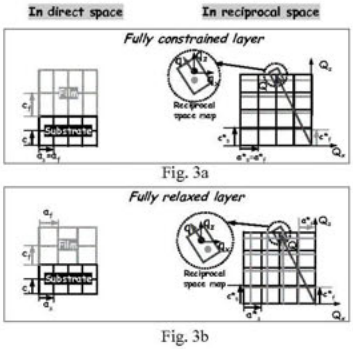

Figure 3. Schematic draw of the influence of the relaxation on the relative position of the substrate and film reciprocal nodes.

Microstructural characteristics and relaxation mechanism

RSMs of the (002) and (004) zirconia reflections were recorded for three azimuth angles along the [100], [110] and [010] directions. Sections of those maps along the normal to the interface and in the interface plane were performed in order to characterize the out-of-plane and the in-plane microstructure.

Out-of-plane characterization

In general, the broadening of the RLP in the Q_z direction is mainly related to the size of the coherent domains and to microstrains along the normal to the interface. We have shown that it is possible to extract quantitative values of size and strains in oxide thin films by simulation of the diffraction profiles with specific models based on the kinematical diffraction theory [6, 17]. Nevertheless, such procedure requires a good knowledge of the defaults inducing the broadening. In this paper we have used a more simple method based on the simulation of the diffraction profiles with Voigt functions [18]. The separation of the size and microstrain effects was performed using a modified Williamson-Hall [18, 19] procedure. We have already shown [20] that this method gives reliable results and is well suited for thin films containing a high density of defects. According to those plots the mean crystal size along the normal to the interface is t = 100 nm and the root mean squared strain is equal to 0.18%.

In plane microstructure

The transverses scans of the (002) and (004) RLPs measured along [100] are given in figure 4. First of all, one can see that the two profiles are identical when plotted as a function of the reduced scattering angle. Such a behavior indicates that the broadening is essentially related to rotational disorder. The size of the coherent diffracting domains is close to the micrometer scale. The second feature of the profiles is that they exhibit two symmetrical secondary maxima. The observation of such peaks can be related to the existence of a preferential value of the tilt angle of the (00l) planes. On the basis of numerical simulations, Kaganer et

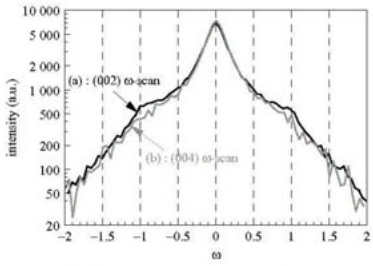

Figure 4. Superposition of the transverse scans across the (002) and (004) zirconia RLPs.

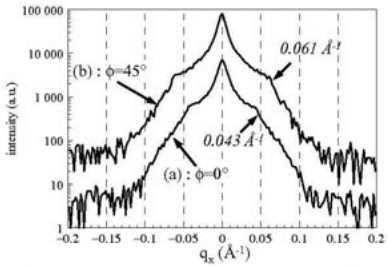

Figure 5. transverse scans across the (002) zirconia RLPs recorded at different azimuths.

al. have attributed such satellites to an inclined edge component of the Burgers vector of misfit dislocations [21]. The additional or missing half planes are hence inclined with respect to the (00l) planes and consequently inclined with respect to the interface.

The influence of such misfit dislocations on the transverse scan profile must be dependent on the azimuth angle. We show in figure 5 two transverse scans of the (002) zirconia RLP recorded along the [100] and [110] azimuth. The position of the satellites are respectively at (-0.043 $Å^{-1}$; 0.043 $Å^{-1}$) and (-0.061 $Å^{-1}$; 0.061 $Å^{-1}$). One can notice that the ratio of the two values is equal to $\sqrt{2}$. A square network of misfit dislocations inclined with respect to the interface can be inferred from those results.

Discussion

We have determined in this work that the zirconia islands are made of magnesia doped cubic zirconia and are fully relaxed. The amount of magnesia has been estimated between 5 and 10 molar percent. One can notice that this large uncertainty is mainly due to the lack of accurate data concerning the dependence of the cell parameter of cubic zirconia as function of the magnesia amount. Taking into account the temperature of the thermal treatment, we can conclude that the islanding process took place in a tetragonal – cubic two-phased part of the zirconia – magnesia phase diagram [9]. The stabilization of the cubic phase during cooling down is probably related to the appearance of strains. We have previously concluded that the islands are free of homogeneous strain. We have also shown that the zirconia islands contain microstrains. The presence of heterogeneous strain is known to affect the relative stability of the polymorphs [23]. Such an effect in the case of ZrO_2 remains to be confirmed.

The transverses scans across the RLP associated to symmetrical reflections suggested the presence of a square network of misfit dislocations. Moreover, these dislocations are inclined with respect to the interface. The slip systems in the fluorite structure are <110>{111}, <110>{110} and <110>{100}. With the constrain that the dislocation line should be parallel to the in-plane <100> direction, the most probable system was found to be <110>{110}.

Conclusions

Relaxation mechanisms involving in zirconia epilayer deposited onto magnesia single crystal have been studied. A semi-coherent interface between the zirconia islands and the substrate has been evidenced using reciprocal space mapping. We have shown that interdiffusional

processes are inducing the formation of zirconia – magnesia solid solution resulting in the stabilization under the cubic form of the magnesia doped zirconia crystals.
Reciprocal space mapping showed that relaxation probably takes places by the introduction of interfacial dislocations. A square dislocation network was inferred from the analysis of transverse scans of the zirconia symmetrical RLPs.

References

1. Mathews, J. W. & Blakeslee, A. E., 1974, *J. Cryst. Growth*, **27,** 118.
2. Srolovitz., D. J., 1989, *Acta Metall.*, **37,** 621.
3. Chambers S. A. 2000, *Surf. Sci. Rep.*, **39**, 105.
4. Narayan, J. B. & Larson, C., 2003, *J. Appl. Phys.*, **93,** 278.
5. Guinebretière, R., Bachelet, R., Boulle, A., Masson, O., Lecomte, A. & Dauger, A., 2004, *Mater. Sci. Eng. B.*, **109,** 42.
6. Fewster, P.F., 1997, *Crit. Rev. Sol. State Mater. Sci.*, **22**, 69. Boulle, A., Masson, O., Guinebretière, R. & Dauger, A., 2004, In *Diffraction analysis of the microstruture of materials,* edited by E.J.Mittemaijer & P.Sardi (Berlin : Springer) pp. 505-526.
7. Guinebretière, R., Dauger, A., Masson, O. & Soulestin, B., 1999, *Phil. Mag. A*, **79,** 1517.
8. Guinebretière, R., Soulestin, B & Dauger, A., 1998, *Thin Sol. Films*, **319,** 197.
9. Kisi, E., 1998; *Zirconia engineering ceramics*. (Zürich, Switzerland :Trans Tech Publications Ltd).
10. Boulle, A., Masson, O., Guinebretière, R., Lecomte, A. & Dauger, A., 2002, *J. Appl. Cryst.*, **35,** 606.
11. Guinebretière, R., Dauger, A., Lecomte, A. & Vesteghem, H., 1992, *J. Non-cryst. Solids*, **147,** 542.
12. Li, P., Chen, I.W. & Penner-Hahn J.E. 1994, *J. Am. Ceram. Soc.*, **77,** 118. Li, P., Chen, I.W. & Penner-Hahn J.E. 1994, *J. Am. Ceram. Soc.*, **77,**1281. Li, P., Chen, I.W. & Penner-Hahn J.E. 1994, *J. Am. Ceram. Soc.*, **77,** 1289.
13. Garvie, R.C., 1965, *J. Phys. Chem.*, **69,** 1238. Baldinozzi, G, Simeone, D., Gosset, D. & Dutheil, M, 2003, *Phys. Rev. Lett.*, **90** 216103.
14. Smirnov, M., Mirgorodsky, A. & Guinebretière, R., 2003, *Phys. Rev. B*, **68,** 104106.
15. Yashima, M., Ishizawa, N. & Yoshimura M., 1992, *J. Am. Ceram. Soc.*, **75,**1550.
16. Kisi, E. H. & Howard C.J, 1998, In *Zirconia engineering ceramics*, edited by H. Kisi (Zürich, Switzerland :Trans Tech Publications Ltd), pp1-36.
17. Boulle, A., Pradier, L., Masson, O., Guinebretière, R. & Dauger A., 2002, *Appl. Surf. Sci.*, **188**, 80. Boulle, A., Masson, O., Guinebretière, R. & Dauger A, 2003, *Thin Sol. Film*, **434**, 1.
18. Langford J. I., 1992 in *NIST Proc. of "Accuracy in powder diffraction II.* Pp. 110
19. Williamson, G. K. & Hall W. H., 1953, *Acta Met.*, **1,** 22.
20. Boulle, A., Legrand, C., Guinebretière, R., Mercurio, J. P. & Dauger, A., 2001, *Thin Sol. Film*, **391,** 42.
21. Kaganer, V.M., Kölher, R., Schmidbauer, M., Opitz, R. & Jenichen, B., 1997, *Phys. Rev. B* **55,** 1793.
22. Balzar, D., Ramakrishnan, P. A. , Spagnol, P., Mani, S., Hermann, A. M. & Matin, M. A., *Jpn. J. Appl. Phys.* **41**, 6628.

Z. Kristallogr. Suppl. **23** (2006) 269-274

Influence of magnetron sputtering conditions on the parameters of TiN coatings on steel substrates

R. Mirchev[1], V. Antonov[1], I. Iordanova[1,*], P. J. Kelly[2]

[1]Department of Solid State Physics and Microelectronics, Faculty of Physics, University of Sofia, 5 blvd. James Bouchier, 1164 Sofia, Bulgaria
[2]Centre for Advanced Materials and Surface Engineering, University of Salford, Salford, M5 4WT, United Kingdom
[*]Contact author; e-mail: ivanka@phys.uni-sofia.bg

Keywords: TiN coatings, magnetron sputtering, crystallographic texture, residual stresses

Abstract. The influence of the discharge current during reactive closed-field unbalanced magnetron sputtering on some important parameters of TiN coatings on steel substrates is analyzed. X-ray experiments are performed in two modes namely symmetric Bragg-Brentano (B-B) and grazing incidence asymmetric Bragg diffraction (GIABD).

Introduction

Titanium nitride (TiN) is wear- and corrosion-resistant material over a large temperature interval. When applied on different steel components, TiN coatings show good adhesion to the substrate, which makes the material suitable for different surface applications. TiN coatings can be deposited by several techniques, including ion-beam sputtering methods. In these techniques the target of the depositing material is sputtered by ions from a plasma initiated in an inert gas (usually Ar) atmosphere and the sputtered atoms condense as a film on the coated substrate. TiN coatings are often applied by reactive sputtering in which case the target is made of Ti, and besides Ar, a certain amount of N_2 is introduced into the chamber. Recently, closed-field unbalanced magnetron sputtering (CFUBMS) [1, 2] has been used for the production of dense and hard coatings, the properties of which are being extensively investigated. Despite the significant discrepancies between different authors analysing the relationship between technological parameters, structure formation and properties of TiN films and coatings, some facts can be considered as already established, such as that the formation of compressive residual stresses increases hardness [3-6]. However, the researchers are not so unanimous about the mechanisms of formation and the influence of crystallographic texture and its parameters on properties of TiN coatings applied by magnetron sputtering and in particular by reactive CFUBMS. This is mainly due to the complexity of the coating formation process and its dependence on a number of parameters, each of which has a particular influence on the properties. This paper investigates the dependence on the dis-

charge current of phase composition, crystallographic texture, physical broadening of X-ray peaks and residual stresses in TiN coatings applied by reactive CFUMS.

Description of the specimens and the experimental techniques

TiN coatings of about 4μm thickness were deposited by reactive CFUBMS at the Centre for Advanced Materials and Surface Engineering, University of Salford, UK. The 38x38 mm substrates were cut from rolled EM2 high-speed steel sheet and were ion etched prior to coating. Coating runs were carried out at DC discharge currents of 4, 6 and 8A (corresponding to target powers of 1.40, 2.16 and 2.96 kW, respectively). All other deposition conditions were held constant for each run. The coating runs were performed in a mixture of high purity Ar and N_2 at a pressure of 2.5×10^{-3} mbar.

X-ray analyses were realized with Cu Kα radiation and a plane graphite monochromator in front of the scintillation detector applying symmetric Bragg-Brentano (B-B) and grazing incidence asymmetric Bragg diffraction (GIABD) [7]. For the B-B method the usual θ-2θ scans were performed, while for GIABD the incident angle (α) was fixed and only 2θ rotation occurred [7]. The B-B patterns correspond to {hkl} parallel to the surface while those registered in GIABD correspond to {hkl} declined to the surface at an angle $\psi = \theta - \alpha$. The diffraction peaks were least square fitted by pseudo-Voight analytical functions. The analyses were performed along two surface directions. The one referred to as $\varphi = 0^0$ coincides with the rolling direction (RD) of the substrate and the other defined as $\varphi = 90^0$ is perpendicular to it and thus coinciding with the transverse direction (TD). During analysis the samples were fixed so that the analyzed φ-direction was parallel to the goniometer's vertical axis.

Experimental Results and Discussion

The patterns for the three samples registered via GIABD at $\alpha = 2^0$ (Figure1a) are qualitatively similar and typical for polycrystalline materials containing mainly TiN peaks and a few very low intensity broad TiO peaks. Similar patterns have been registered at $\alpha = 10^0$, i.e. for higher penetration depths, and because of their similarity only the pattern for the coating applied at a discharge current of 8 A is presented in figure 1b. Besides TiN peaks, the $\alpha=10^0$ patterns also have some additional Fe peaks from the substrate and a few very low intensity peaks that can be revealed only at higher magnifications and correspond to a negligible amount of Ti which has obviously been deposited prior to TiN formation on the substrate.

In figure 2 the intensity distribution of X-ray diffraction peaks corresponding to {420} planes declined at different ψ angles to the surface is presented. Maximum intensities of the peaks normalised to those of a powder standard are used for the plots. For each α (i.e. Ψ) angle, {420} profiles have been registered along the $\varphi = 0^0$ and $\varphi = 90^0$ surface directions. It is obvious that for each coating the curves corresponding to the two directions are different, which indicates a non-uniform distribution of crystallographic directions in the surface. In all cases, the texture peaks are better defined at $\varphi = 90^0$, while in the perpendicular $\varphi = 0^0$ direction, they are broader and have lower intensities. According to the crystallographic relations in cubic lattices the more intensive peak at $\Psi \approx 40^0$ may be attributed to {111} planes parallel to the surface, while the lower intensity peak at $\Psi \approx 20^0$ to {110}+{100} planes being

parallel to the surface. Crystallographic texture has also been analysed using Harris coefficients for the {111}, {200}, {220}, {311} and {420} diffraction peaks for the investigated coatings, in comparison to the TiN powder standard in B-B geometry.

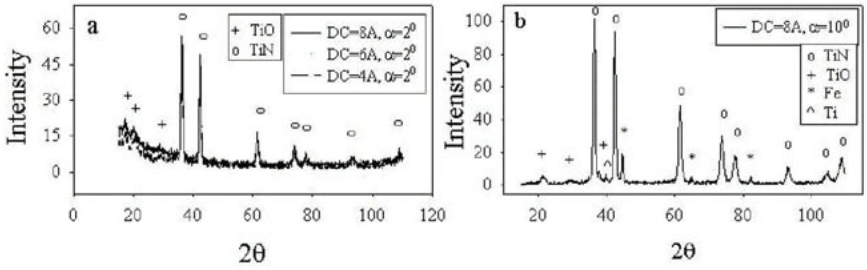

Figure 1. X – ray diffraction patterns registered in GIABD: a) for the three coatings at $\alpha = 2^0$ incident angle; b) for the coating applied at DC = 8 A and $\alpha = 10^0$ incident angle.

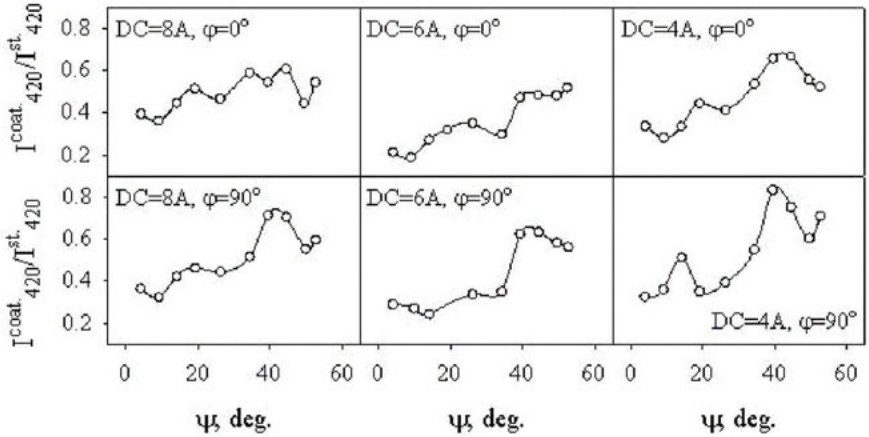

Figure 2. Normalised maximum intensity of the registered in GIABD mode peaks corresponding to {420} planes versus ψ angle which they make with the surface.

By this method it has been confirmed that the predominating texture component corresponds to {111} planes parallel to the coating surface and from the Harris coefficient values it follows that the share of crystallites with such orientation varies from 45 % to 35 % when the discharge current increased from 4 A to 8 A. Simultaneously the share of crystallites with {110} planes parallel to the surface increases from 20 % to 30 %, while for all the coatings the share of micro-volumes with {100} parallel to the surface is constant at about 15 %. Thus, it follows that the crystallographic direction distribution both normal to the surface and in the coating surface is non uniform, which can cause normal and plane anisotropy. The

results show that in all coatings the integral physical broadening, β_{111}, in the main texture component is mainly due to the lattice micro-strain while for the {100} component none of the models (concerning micro-strain caused by randomly distributed dislocations or related to non uniform dislocation distribution accompanied by a domain sub-structure formation) is suitable for the explanation of the observed broadening. However, for all cases the relation $\beta_{111} > \beta_{200}$ between the {111} and {100} texture components is fulfilled (figure 3a), which according to [8] corresponds to compact TiN coatings. This result agrees with the structure zone model [2], according to which dense (zone 2) structures in CFUMS coatings are formed at homologous temperatures as low as $T_s/T_m \sim 0.13$. The plots in Fig.3 demonstrate the non-uniformity of the substructure parameters of the micro-volumes with different orientations due to their anisotropic behaviour during the formation of the coatings, and are in agreement with Refs. [8-11]. Lower β values, corresponding to higher discharge currents, are probably due to different thermal conditions experienced during coating formation at the different deposition conditions. SEM surface observations showed a tendency of the microstructure to coarsen with increasing discharge current, which explains the observed decrease of β due to the higher temperatures reached at higher discharge currents. Lattice parameters for TiN have been estimated from the centroids of the {111} and {100} peaks registered in B-B mode. For all coatings the $a_{111}^{TiN} > a_{200}^{TiN}$ relation is fulfilled, which according to [9] corresponds to compact and stoichiometric structures.

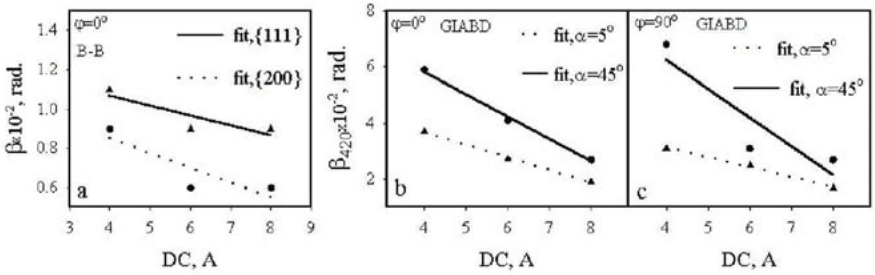

Figure 3. β_{111} and β_{200} (a) and β_{420} (b, c) versus DC.

Coating formation on steel substrates with rather different parameters from those of TiN occurs in complicated complex conditions, involving permanent bombardment with energetic atoms and ions, chemical reaction on the surface and non-isothermal temperature conditions. Increasing discharge current leads to a denser plasma, higher flux and energies of the sputtered Ti atoms and higher substrate ion current densities, i.e. to bombardment of the coatings by higher currents of more energetic particles. Thus, one of the consequences of increasing discharge current may be formation of denser coatings. The unit cell volume was evaluated by the computer program Powder, applying the least square fit of the centroids of all the TiN peaks registered in GIABD at $\alpha = 2^0$. The obtained results show a tendency of the unit cell volume to decrease with increasing discharge current which may be due to the formation of higher compressive residual stresses and denser packing in the coatings.

The $\sin^2\psi$ analysis performed along the $\varphi = 0^0$ and $\varphi = 90^0$ directions of the {420} peaks via GIABD showed a good $d_{\{420\}} = f(\sin^2\psi)$ linearity for all coatings. The negative slopes of the

plots in figure 4a point to the existence of compressive residual stress in both surface directions. They have been evaluated as follows [12]:

$$\sigma_{\varphi} = (E_{420}/1+\nu_{420}).(1/d_0).(\partial d_{420}/\partial \sin^2\psi) \quad (1)$$

where, d_0 and $\partial d/\partial \sin^2\psi$ are the intercept and gradient in the $\sin^2\psi$ plots; E_{420}, ν_{420} are the Young's modulus and Poisson's ratio evaluated from s_{ij} compliances following the Reuss formalism.

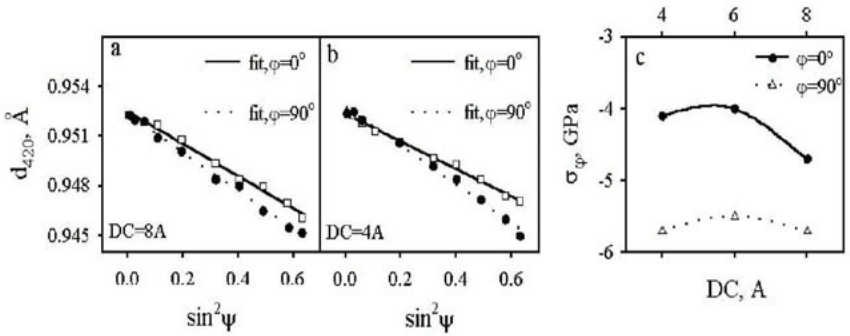

Figure 4. Linear $\sin^2\psi$ plots (a,b) and residual macro-stress values as a function of DC (c)

The obtained $E_{<210>}$ = 434 GPa and $\nu_{<210>}$ = 0.19 values are in a good agreement with the data used by other authors. The evaluated absolute errors of residual stress values in all cases were less than the size of the symbols in the plots of figure 4c. Thus, it is obvious that the compressive macro-stresses are anisotropic in the surface showing weaker dependence on discharge current and having higher absolute values in the $\varphi = 90^0$ direction along which the texture maximums are more pronounced. The maximum compressive stresses in both φ-directions are formed in the coating deposited at DC = 8 A, while in that deposited at DC = 6 A, they are minimum, being comparable, but a bit less than those in the coating deposited at DC = 4 A. This deviation from the expected tendency of increasing compressive residual stresses with increasing discharge current for the coating applied at DC = 6 A confirms that the structure formation process during magnetron sputtering is rather complex. Similar deviations for the coating applied at DC = 6 A in respect to the other two coatings were observed during the preliminary wear-resistance and Vickers micro – hardness tests. We hope that the reasons for these and some other deviations concerning the coating deposited at DC = 6 A will be revealed in our further investigations in the subject.

Summary

The investigated TiN coatings deposited by reactive CFUBMS on rolled M2 steel substrates are polycrystalline, compact and stoichiometric. Crystallographic texture is characterized by a non-uniform distribution of crystallographic directions normal and in-plane to the coating

surfaces. From 35 % to 45 % of the micro-volumes (depending on the discharge current) are oriented with the {111} plane parallel to the surface. Higher discharge currents cause increases in deposition temperature and thus lead to texture scattering and some relaxation processes accompanied with a decrease in the breadth of the diffraction peaks. Due to the anisotropy of the TiN lattice, and to crystallographic texture, different micro-volumes undergo non uniform deformation during their formation and concurrent bombardment by high energy particles. The restrictions for deformation applied by the substrate and compact surrounding matrix are probably the reasons for the formation of residual compressive macrostresses parallel to the surface. Their anisotropy in the two investigated lateral directions is in agreement with the revealed non-uniform distribution of crystallographic directions in the coatings surface.

References

1. P. J. Kelly, R. D. Arnell, W. Ahmed, A. Afzal, 1997, *Materials &Design*, **17,** No4, 215.
2. P. J. Kelly, R. D. Arnell, 2000, *Vacuum*, **56**, 159.
3. Y. Pauleau, 1992, in *Advanced Techniques of Surf.Eng.*, vol.1, edited by W.Gissler and A.Jehn, (Klwer Academic Publishers), pp. 135-179.
4. V.Valvoda, A. J. Perry, L. Hultman, J. Musil, S. Kadlec, 1991, *Surf. Coat. Technol.*, **49,** 181.
5. V.Valvoda, R. Cerny, R. Kuzel Jr., L. Dobiasova, J. Musil, V. Poulek, J. Vyskocil, 1989, *Thin Solid films*, **170**, 201.
6. J. Chevalier, J. P. Chobert, J. Spitz, 1981, *Thin Solid Films*, **80**, 263.
7. T. C. Huang, 1990, *Advances in X-ray Analysis*, **33**, 91.
8. R. Kuzel, Jr., R. Cerny, V. Valvoda, M. Blomberg, M. Merisalo, S. Kadlec, 1995, *Thin Solid Films*, **268**, 72.
9. V. Valvoda, 1995, *J.of Alloy and Compounds*, **219**, 83.
10. D. Rafaja, V.Valvoda, R. Kuzel, A. J. Perry, J. R. Treglio, 1996, *Thin Solid Films*, **86-87**, 302.
11. R. D. Arnell, J. S. Colligon, K. F. Minnenbaev, V. E. Yurasova, 1996, **47**, 425.
12. P. S.Prevey, 1986 in *Metals Handbook v.10,* edited by ASM (Metals park, Ohio 44073), pp. 380-392.

Acknowledgements. The financial support by Marie Curie Foundation is highly appreciated. We are also thankful to Mrs. R. Zouq for the application of TiN coatings by reactive CFUBMS and to the Scientific fund of Sofia University for the partial financial support for the performed X-ray experiments.

Z. Kristallogr. Suppl. **23** (2006) 275-280

Structural and microstructural characterisation of ZrN coatings for decorative applications

P. Zanola[1], E. Bontempi[1], M. Gelfi[2], M. Tosti[3], R. Roberti[2], L. E. Depero[1,*]

[1]INSTM and Laboratorio di Chimica per le Tecnologie, Università di Brescia, via Branze 38, 25123 Brescia, Italy;
[2]INSTM and Dipartimento di Ingegneria Meccanica, Università di Brescia, via Branze 38, 25123 Brescia, Italy
[3]SPIN Srl, S. Casciano V.P. (Fi), Italy.
[*]Contact author; e-mail: laura.depero@ing.unibs.it

Keywords: coating, residual stress, XRD[2]

Abstract. The residual stress plays a primary role in the performances of the protective coatings and thus in the lifetime of coated components. Indeed, the residual stress may even result in the detachment of the coating, and favour the corrosion of both the coating and the substrate. In this paper we studied ZrN coatings for decorative purposes. The correlations among substrate phase, surface morphology and residual stress is discussed. The DRAST method was applied to evaluate residual stress based on the analysis of 2D diffraction images.

Introduction

Zirconium nitride belongs to the fourth-column transition metal mononitrides, that includes titanium and hafnium nitrides. These compounds have the NaCl-type of structure and they are characterized by high melting point, high Young's modulus, chemical inertness and hardness. They are conductors and have metallic reflectance. Thanks to these properties, titanium nitride (TiN) and zirconium nitride (ZrN) have extensively been studied for industrial applications. Because of their good wear resistance they are applied as hard coating thin films to improve the lifetime of mechanical components, such as cutting tools and dies [1]. In electronics industry they are used as electrical contacts and diffusion barriers [2,3]. Nowadays ZrN is utilized as a constituent of multi-component and multi-layer nitride coatings, which are known to perform better than the traditional TiN coatings in tribological applications [4]. Because of their gold-like colour [5], TiN and ZrN are also used instead of gold coatings [6-8], that have poor mechanical properties.
The increasing interest on these coatings is also related to their possible use to overcome allergy problems caused by nickel. Indeed, severe normatives today regulate the application

of this metal in items that are supposed to be in contact with skin. Thus the usage of coatings on decorative items not only improves their mechanical properties, but also protect from secondary undesirable effects of substrate metals.
In this paper we studied ZrN coatings applied to decorative components. The aim of this work is to understand the relationship among phase composition of both layer and substrate, surface morphology and residual stress. In the discussion, the potentials of a new advanced method for the residual stress measurement based on the analysis of the Debye rings deformation are shown.

Experimental

The sample list is reported in table 1. The bulk material is brass and two samples families characterized by Ni (5 μm) or Cu (8 μm)-bronze (5 μm) substrates were considered. A sublayer of Pd (or Pd-In) (0.2-0.4 μm) has been deposited on the substrate. The sublayers were electroplated with a current density ranging from 0.5 to 4 A/dm^2. The ZrN layers were deposited in a Propower 1100 D5 high vacuum coating equipment. In particular, the ZrN was deposited using cathodic arc evaporation for 20 minutes. Carbon was introduced in the PVD chamber in order to tune the coating colour. The substrate bias was 90-100 V and during deposition the temperature of the substrate, measured by a thermocouple, was kept constant at 210 °C. Two thickness of ZrN were deposited, namely 0.3 and 0.6 μm.

Table 1. Analysed samples. The thickness of the layers are in micron and indicated in the bracket. The crystalline phases were identified by WAXRD. The JC-PDF card number is indicated in the bracket.

Sample	Substrate	Sublayer	Coating	Crystalline phases (JC-PDF card number) [9]
Ni1a	Ni (5)	Pd (0.2)	ZrN (0.3)	Zhanghengite (021231) + $GA-Brass (50133) (brass1), Ni (040850), Pd (461043), ZrN (741217)
Ni1b	Ni (5)	Pd (0.2)	ZrN (0.6)	brass1, Ni, Pd, ZrN
Ni2a	Ni (5)	Pd (0.4)	ZrN (0.3)	brass1, Ni, Pd, ZrN
Ni2b	Ni (5)	Pd (0.4)	ZrN (0.6)	brass1, Ni, Pd, ZrN
Ni3a	Ni (5)	Pd/In (0.2)	ZrN (0.3)	brass1, Ni, Pd/In, In/Ni/Zr alloy (351202), ZrN
Ni3b	Ni (5)	Pd/In (0.2)	ZrN (0.6)	brass1, Ni, Pd/In, In/Ni/Zr alloy, ZrN
Ni4a	Ni (5)	Pd/In (0.4)	ZrN (0.3)	brass1, Ni, Pd/In, In/Ni/Zr alloy, ZrN
Ni4b	Ni (5)	Pd/In (0.4)	ZrN (0.6)	brass1, Ni, Pd/In, In/Ni/Zr alloy, ZrN
Cu1a	Cu (8)-bronze (4)	Pd (0.2)	ZrN (0.3)	Zhanghengite (021231) + brass (710397) (brass2), Cu (040836), bronze (011240), Pd (461043), ZrN
Cu1b	Cu (8)-bronze (4)	Pd (0.2)	ZrN (0.6)	brass2, Cu, bronze, Pd, ZrN
Cu2a	Cu (8)-bronze (4)	Pd (0.4)	ZrN (0.3)	brass1, Cu, bronze, Pd, ZrN
Cu2b	Cu (8)-bronze (4)	Pd (0.4)	ZrN (0.6)	brass1, Cu, bronze, Pd, ZrN
Cu3a	Cu (8)-bronze (4)	Pd/In (0.2)	ZrN (0.3)	brass1, Cu, bronze, ZrN
Cu3b	Cu (8)-bronze (4)	Pd/In (0.2)	ZrN (0.6)	brass1, Cu, bronze, ZrN
Cu4a	Cu (8)-bronze (4)	Pd/In (0.4)	ZrN (0.3)	brass1, Cu, bronze, Pd, ZrN
Cu4b	Cu (8)-bronze (4)	Pd/In (0.4)	ZrN (0.6)	brass1, Cu, bronze, Pd, ZrN

Metallographic analysis was carried out by means of an optic microscope Reichert-Jung MeF3. Glancing Incidence angle X-Ray Diffraction (GIXRD) and wide angle X-ray diffraction (WAXRD) data were collected by a Bruker "D8 Advance" diffractometer equipped with a Göbel mirror. The beam was collimated by slits and a scintillator detector was used.
Two-dimensional X-ray micro-diffraction experiments were performed by means of a D-Max Rapid Rigaku system equipped with an Image Plate detector. The incident beam was collimated by a collimator with a diameter of 300 μm. The sample was mounted at 45° with respect to the vertical axis and the Ω angle was fixed at 21°. The time collection was 40 minutes for each pattern. In this work, the recently proposed approach to calculate residual stress based on the Debye rings deformation has been applied [10].

Results and discussion

Wide Angle X-Ray Diffraction (WAXRD), Glancing Incidence angle X-Ray Diffraction (GIXRD), and two-dimensional X-Ray Diffraction (XRD^2) experiments were performed on all the samples. In Table 1 the crystalline phases are reported. All the diffraction peaks have been identified. The nominal composition of the coatings has been confirmed.

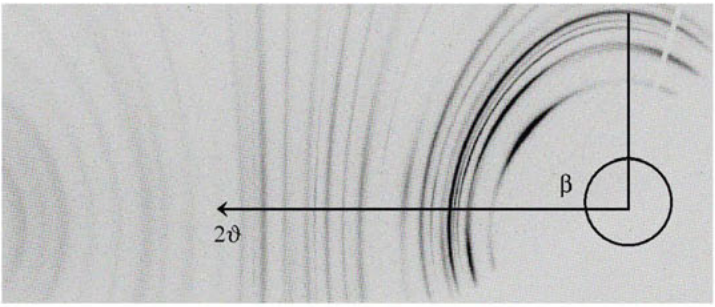

Figure 1. Two-dimensional micro-diffraction image of sample Ni3b. Below, on the right side of the pattern, no signal is revealed because of the sample shadow.

As an example, in Figure 1 the XRD^2 image of sample Ni3b is shown. All the samples present a strong [111] preferred orientation of the ZrN phase. From the two dimensional spectra the preferred orientation seems similar for all the samples. The average size of the crystallite for ZrN phase have been evaluated by the Sherrer equation and is in between 10-15 nm. However, peak broadening due to microstrains is not considered [11]. Thus the crystallite average size may be significantly larger then these values.
Because of the key role of residual stress in the performance of the protective coating (mechanical behaviour, adhesion and corrosion resistance), the strains were carefully evaluated by means of the DRAST (Debye Ring Analysis for STress measurements) method [10]. This method is based on the fact that the presence of residual stress determines Debye ring distortions. Each point of the image plate ($2\vartheta,\beta$) is related to (ϕ,ψ) values which define the direction of diffraction vector in the sample space [10]. Thus, each point of the Debye ring corresponds to a $d_{\phi,\psi}$ value. If the elastic model can be applied and the elastic modulus is known,

the value of the residual stress can be calculated from the d-sin$^2\psi$ plot. Even if a preferred orientation is present, in this case the analysis of the residual stresses can be performed.
For the (111) planes of the ZrN phase, a good linear fit for the d-sin$^2\psi$ regression was found for all the samples (R^2>0.99). Assuming $\sigma_1=\sigma_2$, $\sigma_3=0$ and the elastic modulus of ZrN E(111)=267 GPa [12], for all the coatings the calculated residual stresses are compressive and vary between 7-9 GPa.

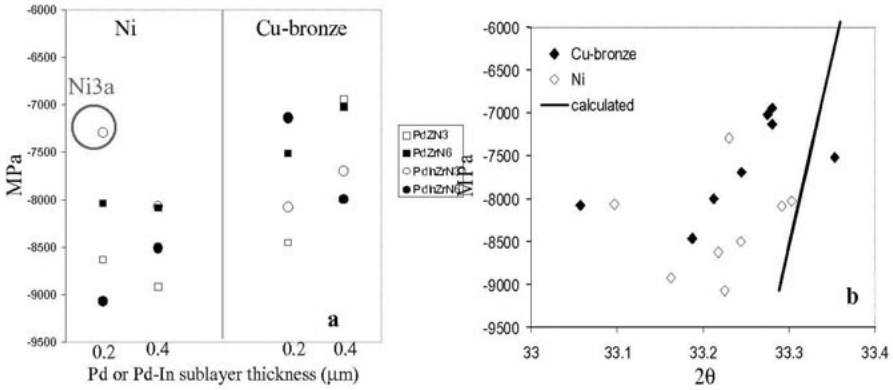

Figure 2. (a) Stress values of the two sample families (Ni and Cu-bronze) plotted against the thickness of the sublayer, Pd (squares) or Pd-In (circles). Residual stresses of the two samples families plotted against 2θ position of 111 reflection evaluated from the θ-2θ experiment. The unfilled and filled samples refer to 0.3 and 0.6 μm ZrN thickness respectively (b).

The stress values are reported in Figure 2a. For corresponding coatings, those on Ni substrate have higher stress values with respect to those on Cu-bronze, except sample Ni3a. However, in this case the metallographic analysis shows a high density of crackings and the detachment of the coating; that can justify the low value of the stress. This result may be due to the difference in the linear thermal expansion coefficients of these phases. Moreover, it should be noted the significant difference in the sublayer thickness, namely 5 μm and 12 μm for Ni and Cu-bronze respectively.
In Figure 2b the residual stresses calculated for the two families of coatings, with Ni and Cu-bronze, are plotted against the 2θ peak position derived from θ-2θ experiments, thus corresponding to the d_{111} distance of the planes parallel to the surface. The calculated 2θ values as a function of the stress are shown by the line in the same Figure.
To separate the chemical from the mechanical contribution to the peak shift, the displacement of the ZrN 111 reflection were calculated by subtracting from the experimental 2θ values, obtained with θ-2θ experiments, those calculated on the basis of the stress measures evaluated by DRAST method and considering a Poisson ratio of 0.2 [13]. In Figure 3 the obtained Δ2θ for Ni and Cu-bronze substrate are shown.

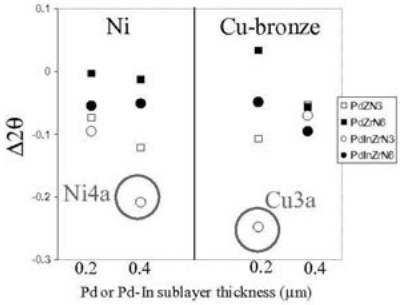

Figure 3. Shift of the 111 reflection after the subtraction of the residual stress contribution.

On the basis of these results the following observations can be done. The samples with Pd-In sublayer present larger shifts compared with the corresponding samples with a Pd sublayer. The samples with the higher thickness of the ZrN layer have lower shifts (filled circles and squares). Samples Ni4a and Cu3a present the largest shift. The correlation between the Pd and Pd-In sublayer and the peak shift suggests that these layers diffuse into the ZrN coating thus changing the cell parameters of the ZrN phase. This seems to be confirmed by the fact that thicker ZrN coatings have lower $\Delta 2\theta$. However, in particular for samples Ni4a and Cu3a, the effect of C in the shift of the 111 reflection of ZrN cannot be excluded. Indeed, the ZrC phase is isostructural to ZrN and the peak position of the 111 reflection in this case is at 2θ=33.21°. On the basis of the metallographic analysis, the Ni samples always show a morphology with cracking and swelling, as shown in figure 4 (a) and (b). In particular for sample Ni3a, Figure 4b, swelling effects are evident and it is the consequence of the detachment of the superficial coating from the substrate. As discussed before, this may justify the low stress value.

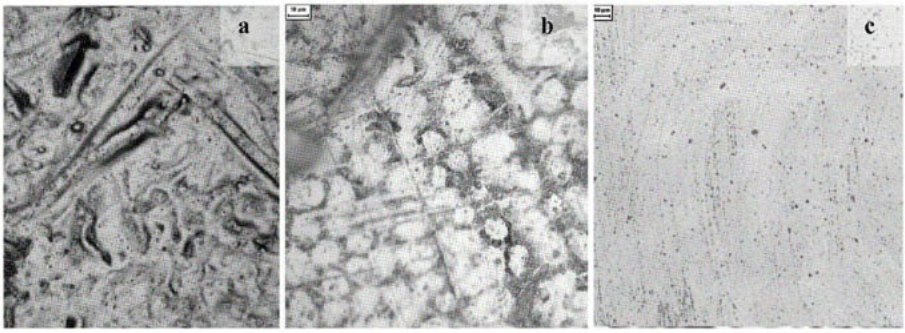

Figure 4. Optic microscopy image of sample Ni4b (a), Ni3a (b) and Cu1a (c);

Contrarily, the Cu-bronze samples exhibit a good external morphology. The resultant coatings are well deposited, with good adhesion to the substrate and no cracking or swelling are visible, as shown in Figure 4c.

Conclusions

The analysis of ZrN coatings on different substrate allows to study the morphology, microstructure and structure of the coatings.
The residual stress analysis of the ZrN coatings was performed by the evaluation of the 2D diffraction pattern. The contribution of the residual stress to the d_{111} distance parallel to the surface was separated from the structural changes, probably due to compositional effects, tentatively ascribed to the diffusion of the Pd (or Pd-In) sublayer and/or the presence of C in the phase.
The main conclusions are the following:

- The residual stress on Ni sublayer are generally larger compared to those found on the coating on Cu-bronze sublayer. This may be due to the difference in the thermal expansion of these phases or due to the significant difference in the substrates thickness.
- The changes of the 2θ position of the 111 reflection, as found by θ-2θ experiments, after the correction for the residual stress, suggest a diffusion of the Pd (Pd-In) sublayer in the ZrN coating. In the case of Pd-In sublayer the changes are larger with respect to the ZrN coating on Pd sublayers.
- C is present in the ZrN phase and modifies the lattice parameters. Indeed, generally, the 111 reflection is at lower 2θ angle.
- ZrN coating on Cu-bronze substrates show a better morphology with respect to the Ni ones. This result is very interesting for decorative industry application.

References

1. J. Vetter, R. Rochotzki, 1990, *Thin Solid Films, **192(2)*** 253-261.
2. S. Kanamori, 1986, *Thin Solid Films* **136.** 195.
3. K. Hinode, Y. Homma, M. Horiuchi, T. Takahashi, 1997, *J. Vac. Sci. Technol. A* **15 (4)** 2017.
4. O. Knotek, F. Loftler, G. Kramer, 1992, *Surface and Coatings Tech.* **54/55** 241.

A. Schlegel, P. Wachter, J. J. Nickl and H. Lingg, 1977, *J. Phys. C,*. **10**, 4889.

5. U. Beck, G. Reiners, I. Urban, H. A. Jehn, U. Kopacz, H. Sahack, 1993, *Surf. Coat. Technol.* **61**, 215
6. P. C. Johnson, H. Randhawa, 1997, *Surf. Coat. Technol.* **33,** 53;
7. M. Nose, T. Nagae, M. Yokota, S. Saji, M. Zhou, M. Nakada, 1999, *Surf. Coat. Technol.* **116-119**, 296.
8. JC-PDF dtabase, International Centre for Diffraction Data, 2003.
9. M. Gelfi, E. Bontempi, R. Roberti, L. E. Depero, 2004, *Acta Mater.*, **52**, 583-589.
10. H. J. Ramos and N. B. Valmoria, 2004, *Vacuum* **73**, 549-554.
11. Gelfi, M.; Bontempi, E.; Rigato, V.; Patelli, A.; Guizzi, A.; Roberti, R.; Tosti, M.; Depero, L. E., *Computational and Experimental Methods* (2003), 7 (Surface Treatment VI), 317-331.
12. Perry A. J, *Thin Solid Films* 1990, **193/194**, 463.

Z. Kristallogr. Suppl. **23** (2006) 281-286

Chalcogenide films on glass substrate as attenuators of X-ray radiation

S. R. Lukić*, D. M. Petrović, G. R. Štrbac, D. D. Štrbac

Department of Physics, Faculty of Sciences, Trg Dositeja Obradovića 4,
21000 Novi Sad, Serbia and Montenegro
*Contact author; e-mail: svetdrag@im.ns.ac.yu

Keywords: chalcogenides, thin films, X-ray radiation, linear attenuation coefficient

Abstract. The paper describes a study carried out with the aim of establishing the effect of copper on some characteristics of chalcogenides in the Cu-As-Se system. We present the results of investigating the possibility of X-ray attenuation in standard glasses K-8, by coating them with thin chalcogenide films from the $Cu_xAs_{50}Se_{50-x}$ (x = 5, 10 and 15 at%) amorphous system. Dependence of protection level on the thin film thickness and values of linear attenuation coefficient were determined. The influence of chalcogenide glass composition on relevant parameters was also investigated.

Introduction

Amorphous chalcogenides are the materials involving sulphides, selenides or tellurrides of the elements of the fourth and fifth groups of the Periodic Table, whereas the majority of other elements can also enter the combination. Multicomponent chalcogenide glasses are widely applicable in the field of semiconductor techniques. The great interest in these materials is due to the simple technology of their preparation in bulk forms and thin films; chemical and radiation durability; relatively good thermal and mechanical properties; low optical losses; their transparency and photosensitivity in IR and VIS spectral regions, as well as the possibility of widely varying properties with their composition. That determines the possibilities for their practical application for pulse generation of acoustic and optical radiation. Thin films deposited from chalcogenide glasses are applicable in opto- and microelectronics for different purposes – electrical switches, data recording, protective, passivity and optical coatings [1-5].

Many investigations showed that interesting behaviours could be obtained by introducing transition metals into the matrix of chalcogenide glasses. The great variations of important glass characteristics are achieved by introducing Cu, Ag or Cd atoms into chalcogenide systems. It has been found that the presence of Cu in amorphous arsenic-selenides leads to the increase of density, microhardness, softening temperature, and to a decrease of the activation energy of electrical conductivity. In addition to the known good mechanical, thermal, magnetic or variable electrical properties, investigations were also oriented to elucidate the changes in optical features of glasses with the introduction of copper into its matrix [6].

It is well known that X-rays include the vawelengts that have potential adverse effects on human health. With the energies around 1.2 keV, they are not extremely harmful radiation, which means that lower intensities in short periods, which are used in medical diagnostic tests, or special X-ray examinations, based on different absorption in healty and unhealthy tissues and bones, make acceptable doses in most cases.
Standard transparent glasses do not exhibit high absorption, i.e. significant attenuation of scattered waves. This was a reason for the beginning of investigations of the synthesis of new glass systems that would be suitable in respect of their transsparency, stability and other characteristics for reducing the negative effects of X-rays.
This paper presents the results of an investigation of the possibility of X-ray attenuation in standard glasses K-8 coated with thin chalcogenide films. These investigations are of great importance for X- ray radiation and its negative influence in diagnostic centers in cities and urban areas.

Experimental

Thin-film samples were prepared by thermal evaporation in vacuum of powdered previously synthesized complex glasses.
The investigated glasses of $Cu_xAs_{50}Se_{50-x}$ type, with various concentration of Cu (5, 10 and 15 at %), were synthesized from high-purity elemental components by fast cooling from the melt. The process was carried out in semiautomatic horizontal tube furnaces Carbolite, Model CTF 12/65, with a temperature controller Eurotherm 91-3, according to the empirically defined cascade regime (figure 1). Cooling at a rate of 800 ^{0}C/min resulted in amorphous samples. Such regime of the synthesis with a cascade increase of temperature made it possible to reduce the pressure due to the vapours of interacting arsenic with selenium and copper. This prevented the ampoule from destruction during the synthesis. To facilitate sample homogenisation, the melt was kept at the highest temperature for a prolonged time (17-20 hours) [7].
As the result of successful syntheses the corresponding amorphous materials in the form of oval rods with no visible fissures or defects, were obtained in appropriate yields. Amorphous character of samples was checked by X-ray diffraction and polarization microscopy.
In order to obtain films from the synthesized glasses that are homogeneous and exhibit high optical characteristics, their preparation was conducted using a specially constructed evaporator. Its use enabled to carry out discrete evaporation at opti-

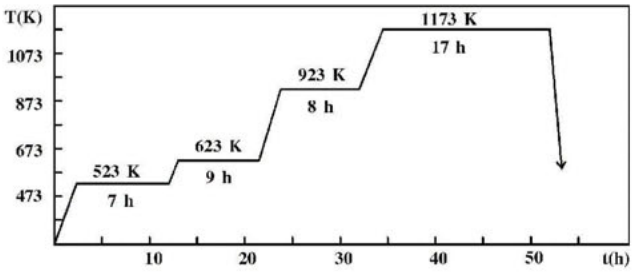

Figure 1. Diagram of the process of obtaining glasses $Cu_xAs_{50}Se_{50-x}$.

mally high temperatures (430 - 600 °C), whereas the composition of the prepared films, within tolerable limits, was close to the molten glasses.
Condensation was carried out on the substrates made of the standard glass K-8 of the known index of refraction, kept at room temperature ("cold" substrates). Film thickness in the course of evaporation was controlled by optical method on the basis of the interference of reflected laser beam. It was 1.24, 0.86 and 0.97 μm, for the films with 5, 10 and 15 at % Cu, respectively. Substrate thickness was 0.133 cm.

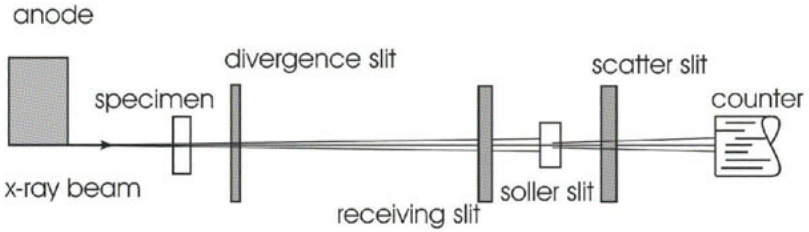

Figure 2. System for measuring the level of X-ray attenuation.

The X-ray diffraction measurements were performed on a conventional PW 1373-PW 1065/50 (Philips) diffractometer equipped with copper target X-ray tubes and non-monochromatised radiation.
To simulate continual X-ray spectrum in a wide range of radiation use was made of the 15 kV voltage, which enabled generation of the continual X-ray spectrum of the wavelength higher than 0.082 nm.
Measurements of the absorption level of the continual X-ray spectrum were carried out with the system sketched in figure 2.
Considering that linear absorption coefficient is a function of wavelength it is clear that used system enabled the determination of an average linear absorption coefficient.

Results and discussion

Tables 1 and 2 show the results obtained for investigated samples in accordance with the standard dependence:

$$I = I_o \cdot \exp(-\mu d) \qquad (1)$$

where I_0 is the initial X-ray beam intensity, I is the intensity after the absorption, μ is the linear absorption coefficient and d is the sample thickness.

Table 1. Results of measurement for air and standard glass: exposure time, corresponding numerical value of X-ray beam intensity and calculated values of linear absorption coefficient.

sample	for 10 s	for 20 s	for 40 s
air (initial X-ray intensity) (I_0)	121077	244999	494657
glass K-8 (I) (d=0.133cm)	4592	9024	18241
μ (cm^{-1})	24.602	24.822	24.824

Although it seems that the values of linear absorption coefficients for the chalcogenide coats could be obtained by the simple modification of equation (1) if the beam path in the glass and the beam path in the sample layer are considered separately, such approach can not be made. It is known that in layered structures, especially in layered structures prepared from multi component chalcogenide glasses such as investigated samples, the intermediate layer is formed, whose characteristic are different from both glass substrate and deposited layer [8]. Considering that there is adhesive interaction between molecules of the sample layer and the glass substrate the only result that can be calculated from the experimental data is the linear absorption coefficient for layered system glass + coating.

Table 2. Results of measurement for air and glasses with coats.

sample		air	$Cu_5As_{50}Se_{45}$	$Cu_{10}As_{50}Se_{40}$	$Cu_{15}As_{50}Se_{35}$
t=10 s	I	1052747	13031	12276	9600
	μ (cm^{-1})	/	32.99	33.45	35.29
t=20 s	I	2104877	28114	25087	18566
	μ (cm^{-1})	/	32.42	33.28	35.54
t=40 s	I	4200346	57443	50823	39727
	μ (cm^{-1})	/	32.24	33.17	35.02
t=100 s	I	10525221	140064	121414	103469
	μ (cm^{-1})	/	32.45	33.53	34.73
t=200 s	I	21041876	270292	248256	195831
	μ (cm^{-1})	/	32.71	33.36	35.14
t=400s	I	42083752	561117	484698	379568
	μ (cm^{-1})	/	32.43	33.54	35.38

Linear dependence of the number of measured pulses on exposure is naturally expected, and it only illustrates the correctness of measurement in the given experimental system. On the other hand, the increased slope in the series from the standard glass proper to the sample with the film having maximal content of selenium (i.e. the minimal content of copper) indicates a significant effect of the coating. In view of the relation (1) it is evident that beside the absorption coefficient the exponent contains also sample thickness as a variable quantity of the same rank, so that in calculating the value of the linear absorption coefficient it is necessary to take also into account the value of this quantity.

In table 3 are presented the investigated samples with total thickness of the glassy system, mean value of the thickness of chalcogenide coat and averaged values of linear absorption coefficient for all the measurements performed. It can be seen that the chalcogenide coat increases significantly the value of the glassy system absorption .

Table 3. Thickness of the glassy system and mean values the linear absorption coefficient.

Sample	d [cm]	Δd [cm]	μ_{sr}[cm^{-1}]
glass K-8	0.133	0	24.75
glass K-8 + $Cu_5As_{50}Se_{45}$	0.133124	0.000124	32.54
glass K-8 + $Cu_{10}As_{50}Se_{40}$	0.133086	0.000086	33.39
glass K-8 + $Cu_{15}As_{50}Se_{35}$	0.133097	0.000097	35.18

The introduction of copper into the matrix of the As-Se glass results in

the appearance of a large number of structural units. The method of high-temperature X-ray diffraction enabled identification of 10 forms of structural elements in the glasses with significant copper content [9]. Our previous studies of physical properties of these glasses [6, 10-12] indicated that the compound Cu_3AsSe_4 has a key role in the structural properties, has the main role in bonding and improving the structural network of amorphous systems and its characteristics determine the structural changes at higher temperatures.

On the basis of different techniques such as DDTA, DSC analysis, vibration spectra in far-infrared region and especially high temperature X-ray diffraction, it was possible to identify the occurence of Cu_3AsSe_4 structural unit as well as a number of accompanying structural entities whose nature depends on the composition of the system.

The existence of this unit was directly proven in $Cu_x(AsSe)_{100-x}$ system [13], $Cu_x(As_2Se_3)_{100-x}$ system [14] and in materials of type, which has been investigated, in present paper [15]. Figure 3 shows the course of increasing crystallinity of Cu_3AsSe_4 and Cu_2Se on the basis of the change of the diffraction maximum registered in the X-ray spectrum of the glassy $Cu_{10}As_{50}Se_{40}$ in the vicinity value of Bragg's angle of $2\theta = 28^0$ (for CuK_α radiation).

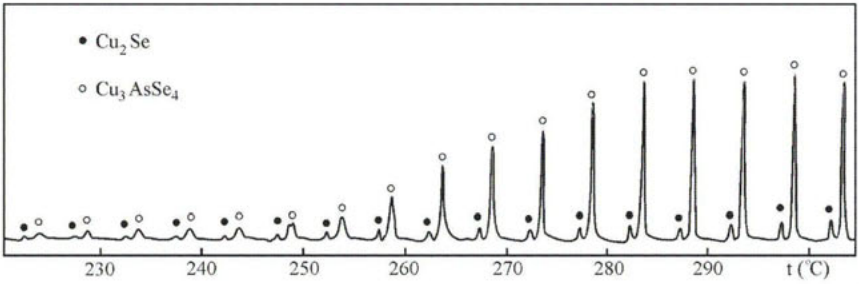

Figure 3. Temperature dependence of the intensity of diffraction maximum in the vicinity of $2\theta = 28^0$.

The data suggest the possibility that the compound Cu_3AsSe_4 is most probably formed in the processes of spontaneous cooling of the amorphous AsSe matrix. Structural unit Cu_3AsSe_4 is of sphalerite type analogue to modifications of copper (I) thiosulphate which crystallizes so that their structure could be considered as a modification of ZnS in which 1/4 Zn is replaced with Cu and 3/4 Zn with As [16].

Dependence of protection level on thin film thickness and values of linear attenuation coefficient were determined, as well as the influence of glass composition on relevant parameters. It has been determined that chalcogenide coats significantly increase the absorption power of the investigated system, i.e. the linear absorption coefficients increased in the interval from 30.6% to 42.6%. In the investigated coats, copper content has a great influence on the absorption coefficient increase.

Conclusion

The introduction of copper into the matrix of the As-Se glass results in the appearance of a large number of structural units.

The results obtained in the study of the possibility of attenuation of continual X-ray radiation by standard K-8 glasses coated with thin chalcogenide films showed that a significant effect was achieved already with the coats of the order of magnitude of one micrometer. It was found that the coat of the type $Cu_xAs_{50}Se_{50-x}$ increases the linear absorption coefficient of continual X-ray radiation up to 42.6 %. The increasing trend follows the increase in the atomic ratio of copper in the structural network of amorphous film.

References

1. Seddon, B., 1995, *J. Non-Cryst. Solids*, **184**, 44.
2. Elliott, S.R., 1986, *J. Non-Cryst. Solids*, **81**, 71.
3. Ewen, P.J.S. & Owen, A.E., 1992, *High Performance Glasses* (Eds. M.Cable and J.M.Parker, Blackie, London).
4. Madan, A. & Shaw, M.P., 1988, *The Physics and Applications of Amorphous Semiconductors* (Academic Press, Inc., Boston - San Diego).
5. Lukić, S.R., 1998, Sol. State Phenom., **61/62**, 97.
6. Lukić, S.R., Petrović, D.M. & Petrović, A.F., 1998, *J. Non-Cryst. Solids,* **241**, 74.
7. Lukić, S.R., Cvejić, Ž.N., Petrović, D.M. & Skuban, F, 2003, *J. Non-Cryst. Solids*, **326/327**, 83.
8. Derjagin, B. & Smilga, V., 1967, *J. Appl. Phys*. **38**, 4609.
9. Lukić, S.R. & Petrović, D.M., 1999, *J. Optoelectron. Adv. Mater*., **1(4)**, 43.
10. Lukić, S.R., Petrović, D.M., Petrović, A.F. & Rosola, I.J., 1994, *J. Mater. Sci. Letters,* **13**, 1769.
11. Lukić, S.R., Petrović, D.M., Turyanitsa, I.I. & Dobosh, M.V., 1998, *J. Therm. Analysi,s* **52**, 553.
12. Lukić, S. R., Petrović, D. M., Petrović, A. F. & Popović, Ž. N., 2000, *Mat. Sci. Forum*, **321/324**, 525.
13. Lukić, S.R., Petrović, D.M., Petrović, A. F., Skuban, S. J., Rosola, I.J. & Turyanitsa, I.I., 1992/93, *Rev. Researcs, Fac. Sci., Novi Sad, Phys. Series,* **22/23**, 31.
14. Lukić, S.R., Petrović, A. F. & Petrović, D. M., 2000, *Proc. of the First Balkan Conf. on Glass Science And Technology*, Volos, Greece, 134.
15. Lukić, S.R., Petrović, D.M., Rosola, I.J. & Turyanitsa, I.I., 1991, *Book of Abstr. of XII Yugoslav Symposium on the Physics of Condensed Matter*, Skopje, Yugoslavia, 34.
16. Hurlbut C.S. & Klein C., *Manual of Mineralogy*, 1977, (John Wiley & Sons, Inc., New York).

Acknowledgements. This work was partly financed by the Ministry for Science and Environmental Protection of the Republic of Serbia, within the project "Amorphous and Nanostructural Chalcogenides and Ceramics", No. 1812.

Z. Kristallogr. Suppl. **23** (2006) 287-292

Effect of annealing conditions on structural transformation of ZnS thin film

T. Kryshtab[1,*], J. Palacios Gómez[1], M. Mazin[2]

[1]Instituto Politécnico Nacional-ESFM, Av. IPN, Ed. 9 U.P.A.L.M., 07738, Mexico D.F.
[2]Institute of Semiconductor Physics NASU, Pr. Nauky, 45, Kyiv, 03028, Ukraine
[*]Contact author, e-mail: tkrysh@esfm.ipn.mx

Keywords: crystal structure, annealing, thin film, phase transition

Abstract. Thin films of ZnS and ZnS doped with Cu and Al, i.e. ZnS:Cu, ZnS:[Cu, Al] with the thickness up to 1 μm were deposited by electron-beam evaporation (EBE) from three ZnS, ZnS:Cu and ZnS:[Cu, Al] targets onto ceramic $BaTiO_3$ and glass substrates heated up to 150-200 °C. The films were annealed at the atmospheric pressure in S_2-rich ambient atmosphere at 600-1000 °C. The ZnS films were doped with Cu and Cl using the thermal treatment in a mixture of ZnS with the compounds of Cu and Cl. The ZnS:Cu and ZnS:[Cu, Cl] films were Ga co-doped by annealing in the S_2-rich ambient atmosphere with additional vapors of Ga. The duration of each annealing was one hour. X-ray diffraction (XRD) technique and atomic force microscopy (AFM) were used for the investigation. Thin films deposited from different targets have only zincblende crystal structure. The annealing of ZnS, ZnS:Cu films at 1000 °C in S_2-rich atmosphere both with and without Ga co-doping does not result in the change of crystal structure. The diffusion of Cu and Cl into ZnS lattice at the annealing leads to phase transition from zincblende to wurtzite structure at 800 °C, change of texture and increase of grain size. The phase transition temperature depends on the presence, type and ratio of doping elements. It was shown that Ga and Cl act as activators of recrystallization processes at the annealing.

Introduction

The necessity of full-color displays fabrication results in the further development and investigation of an efficient emitting material. Historically, the best blue-emitting thin-film material is SrS:Cu, but alternative thin-film phosphors are also possible. ZnS is known as a highly efficient phosphor material and with Cu doping it can be used as blue-emitting active layer. ZnS:Cu has a deeper dark blue emission than SrS:Cu. However, by the reasons of the fast degradation and relatively low brightness of ZnS:Cu alternating-current thin film electroluminescent (TFEL) devices, these films are still not adequate for practical purposes. The microstructure of the films (grain and subgrain size, texture), concentration of dopant and the effect of Cu incorporation into the lattice of ZnS influence the operating parameters and degradation stability of TFEL devices. The substitution of Zn in oxidation state +2 by Cu in oxidation state +1 in ZnS lattice results in the presence of either interstitial cation or anion vacancy

unless monovalent counter anion such as Cl^- or trivalent cation such as Al^{3+} or Ga^{3+} is also present. Hence, the solubility of Cu in ZnS lattice may be very dependent on counter ion concentration. It was also reported that an effective powder electroluminescent material must contain both zincblende (3C) and wurtzite (2H) phases [1,2]. For example, for the best electroluminescent properties of ZnS:Tm, Li powder the optimal ratio between wurtzite and zincblende phases was 0.76 : 0.24 [2]. The normal phase transition temperature from 3C to 2H is accepted to be 1020 ^{0}C with the 2H being stable at the higher temperature [3], but both phases can be present at ambient temperature. It is known that the zincblende type structure predominates when the bonding is predominantly covalent whereas the more ionic systems favour the wurtzite form [4]. It has been reported that quite low concentrations of impurities affects the transition temperature between the two forms in the case of AgI [5]. The fabrication technology of thin film active layers, which depends on the deposition technique, post deposition film annealing and substrate materials, is of paramount importance for the development of new ZnS:Cu based TFEL devices.
In the present work the effect of an original non-vacuum annealing [6] of ZnS thin films deposited by EBE according to the annealing conditions and type of substrate on film's crystal structure and surface morphology was investigated.

Experimental details

The ZnS films were deposited by EBE onto ceramic $BaTiO_3$ and glass substrates. Three types of the targets ZnS, ZnS:Cu and ZnS:[Cu, Al] were used. The Cu concentration in the ZnS:Cu target varied from 0.2 to 0.5 at. % and the Al concentration in the ZnS:[Cu, Al] was 0.1 at. %. The substrate was heated up to 150-200 °C. The film thickness varied from 0.6 to 1 μm.
The ZnS and ZnS:Cu films were annealed after deposition at the atmospheric pressure by the use of an original method [6]. The annealing was carried out in a S_2-rich ambient atmosphere prepared by decomposition of sulfur containing compound such as ZnS powder. Thin films were annealed at different conditions. 1) The ZnS and ZnS:Cu films were annealed in a ZnS powder at 600-800 °C; 2) The ZnS and ZnS:Cu films were annealed in a S_2-rich atmosphere with additional vapors of Ga at 800-1000 °C; 3) The ZnS films were annealed in the mixture of a ZnS powder with the compounds of Cu and Cl at 600-800 °C for doping the films with Cu, Cl by a thermodiffusion method. The ratio of Cu and Cl concentrations in the mixture was varied, the Cl concentration was equal to 2 at. % in all mixtures and Cu concentration was varied from 0.03 to 0.3 at %; 4) The ZnS films were also annealed by two steps: a) in the mixture of a ZnS powder with the compounds of Cu and Cl at 650 °C, b) in the S_2-rich atmosphere with additional vapors of Ga at 800-950 °C. Each annealing was carried out during one hour. The crystal structure of the films was investigated using a Siemens D500 X-ray diffractometer operating in ϑ-2ϑ standard symmetric geometry (Co K_α radiation) and by use of D8 Advance Bruker X-ray diffractometer with Eulerian cradle (Co K_α radiation). Surface morphology of the films was investigated by AFM (Park Scientific).

Results and discussion

The XRD patterns show that ceramic $BaTiO_3$ substrate has the usual polycrystalline structure and the glass one is amorphous with a thin SnO_2 polycrystalline contact layer. Before EBE, the poly-

crystalline ZnS, ZnS:Cu and ZnS:[Cu,Al] in the target had the wurtzite crystal structure. After EBE, the remaining part of the material in the target had the zincblende crystal structure without reference to doping elements. The XRD patterns of the ZnS, ZnS:Cu and ZnS:[Cu, Al] films deposited onto glass and ceramic substrates from three different targets revealed only zincblende crystal structure with the preferred orientation of grains in the <111> direction. Typical XRD patterns of ZnS/glass and ZnS/ceramic structures are shown in figure 1a and 1b, respectively. Since, the position of 111 diffraction line for zincblende structure almost coincides with 002 diffraction line for wurtzite structure and films were strongly preferred orientated, we investigated the crystal structure of the films by use of X-ray texture goniometer with Eulerian cradle for measuring the XRD patterns from the films at different orientations by inclination and rotation of the samples. Any other diffraction lines that coincide with wurtzite structure were not observed.

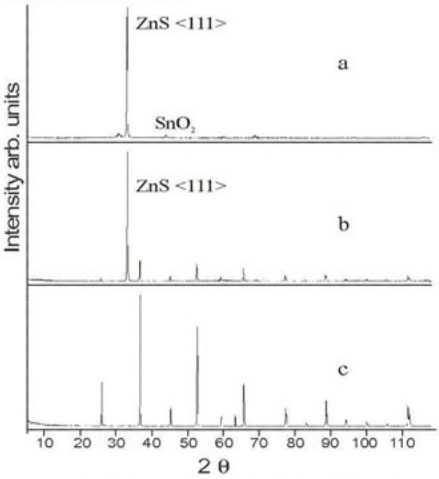

Figure 1. XRD patterns of ZnS/glass (a) and ZnS/ceramic (b) structures and ceramic substrate (c).

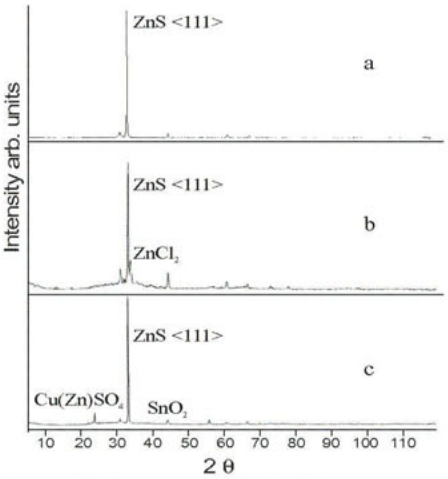

Figure 2. XRD patterns of the ZnS/glass structures after annealing at 600 °C in a ZnS powder (a); in the mixture of ZnS with compounds of Cu and Cl; C_{Cl} = 2 % and: C_{Cu} = 0.03 % (b); C_{Cu} = 0.3 % (c).

The annealing of ZnS film deposited onto a glass substrate in a ZnS powder at 600 °C did not result in structural changes (figure 2a). The film annealing in the mixture of a ZnS powder with the compounds of Cu and Cl at 600 °C (the Cl concentration (C_{Cl}) was 2 at. % and the Cu concentrations (C_{Cu}) were 0.03 at. % and 0.3 at. %, respectively) did not lead to a phase transition and change in the grains preferred orientation. A small peak of $ZnCl_2$ compound (figure 2b) and very small peaks of Cu(Zn) SO_4 (figure 2c) were observed after the annealing in the mixture with the Cu concentrations C_{Cu} = 0.03 % and C_{Cu} = 0.3 %, respectively. Another small additional peaks relate to a thin SnO_2 polycrystalline contact layer.

After the annealing of ZnS and ZnS:Cu films deposited onto ceramic substrate in S_2-rich atmosphere with and without vapors of Ga at 1000 °C we did not observe any changes in the crystal structure, though the annealing temperature is very close to the ZnS phase transition temperature of 1020 °C. A strong phase transition was observed after the annealing of ZnS film in

the mixture of a ZnS powder with the compounds of Cu and Cl (C_{Cu} = 0.2 % and C_{Cl} = 2 %) at 800 °C (figure 3a). After two steps of annealing the phase transition for ZnS:[Cu, Cl, Ga] films was also observed. The first annealing was carried out with the same concentrations of Cu and Cl in the mixture at 650 °C. The changes in crystal structure and texture were not observed after this annealing. The fraction of grains, which were transformed, depends on the temperature of the second annealing in the S_2-rich atmosphere with vapors of Ga. After the second annealing at 800 °C a small peak of the ZnS hexagonal phase from {100} planes was detected (figure 3b). The film annealed at the higher temperature of 950 °C has the hexagonal structure with preferred orientation in <100> direction almost in whole volume (figure 3c). A small fraction of Cu (Zn)SO_4 was also formed. In the case of ceramic substrate the additional peaks relate to $BaTiO_3$ polycrystalline substrate.

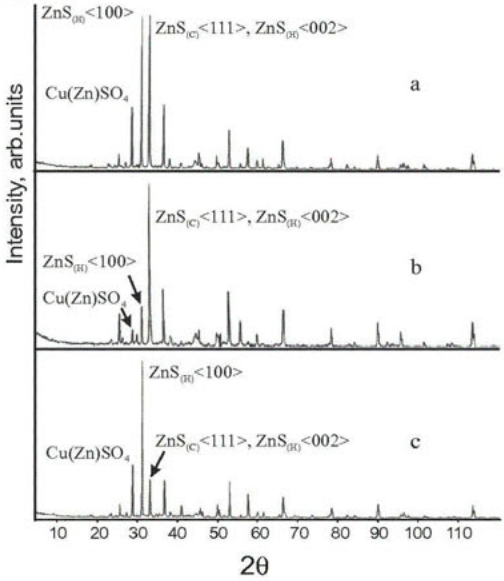

Figure 3. XRD patterns of ZnS/ceramic structures after annealing: in the ZnS with compounds of Cu and Cl mixture; C_{Cl} = 2 %, C_{Cu} = 0.2 % at 800 °C (a); two steps of annealing with the second one in the S_2-rich atmosphere with additional vapors of Ga at 800 °C (b); and 950 °C (c).

The investigations of the surface morphology of ZnS, ZnS:Cu and ZnS:[Cu, Al] thin films by AFM showed that the ZnS:Cu films with thickness of some tenths of micron deposited on a glass substrate had the smaller grain size of 80 nm and more homogeneous grain size distribution than the films deposited on $BaTiO_3$ substrate with the grain size of 210 nm. The films with thickness about 1 μm had complicated surface morphology regardless of substrate. The grain were not close-cut separated, had sub-grain structure and grain sizes varied. The influence of the doping elements in ZnS in a target and annealing conditions on the surface morphology for ZnS/glass films is illustrated in figure 4. The smallest grain size was observed for as-deposited ZnS film (figure 4a). For the film deposited from the ZnS:[Cu, Al] target the enlargement of grain size takes place (figure 4b). So, Cu and Al dopants from the target

affect the grain growth process. After the annealing of ZnS film in a S_2-rich atmosphere at 600 °C some increase of grain size is observed (120-180 nm). The effect of annealing in the mixture of ZnS with the compounds of Cu and Cl at 600 °C on the recrystallization process depends on the Cu and Cl concentrations in the mixture. The grain size increases up to 400 nm after the annealing in mixture with C_{Cu} = 0.03 % (figure 4c) and up to 800-1000 nm with C_{Cu} = 0.3 % (figure 4d). The grains become unruffled and grain boundaries become clear-cut.

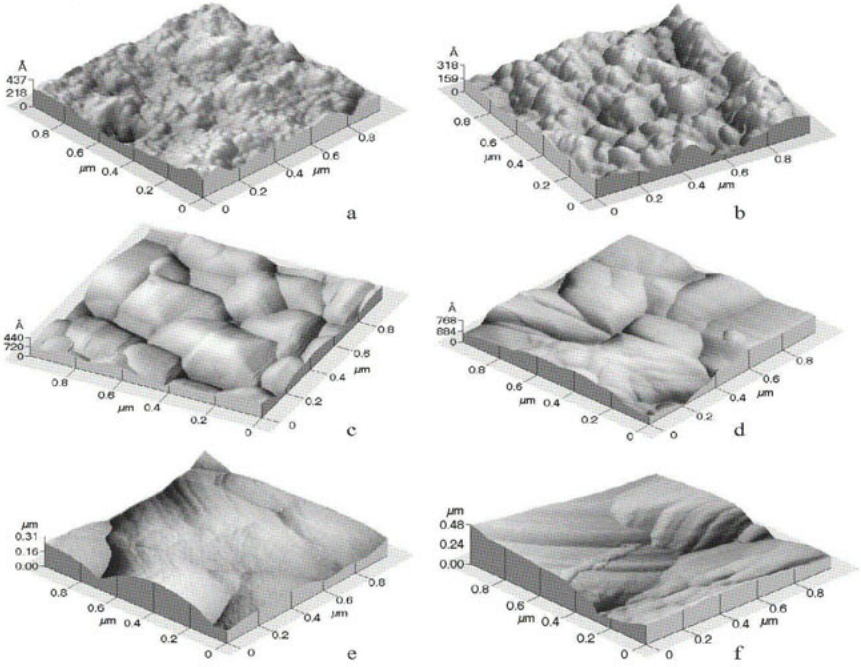

Figure 4. AFM images of the surface morphology of the films: ZnS/glass (a); ZnS:[Cu, A]l/glass (b); ZnS/glass annealed at 600 °C in the ZnS with compounds of Cu and Cl mixture with C_{Cl} = 2 % and: C_{Cu} = 0.03 % (c); C_{Cu} = 0.3 % (d); ZnS-Cu, Cl, Ga/ceramic after two steps of annealing with the second annealing in the S_2-rich atmosphere with additional vapors of Ga at 800 °C (e) and 950 °C (f).

After the annealing of the ZnS and ZnS:Cu films grown on $BaTiO_3$ substrate in a S_2-rich atmosphere at 950 °C the film's surface morphology differed slightly. The separated small grains with sub-grains were observed. Annealing of the ZnS film in the S_2-rich atmosphere with Ga vapors at 950 °C did not lead to substantial difference of surface morphology as compared with the annealing in a S_2-rich atmosphere. After Ga co-doping of the ZnS:Cu film via annealing in S_2-rich atmosphere with Ga vapors at 950 °C the grains enlarge (~800 nm) and become clear-cut. The grain surface becomes smooth and sub-grains are not observed. At such annealing Ga acts with Cu as activator of recrystallization processes. The surface of the ZnS:[Cu, Cl] film after the annealing in the mixture of ZnS with the compounds of Cu and Cl at 800 °C consists of large and small grains. After two steps of annealing for the ZnS:[Cu, Cl, Ga] films the major changes of surface morphology such as clear-cut smooth grains with largest

grain size (≥ 1 μm) are observed (Fig. 4e and 4f). At two steps of annealing the diffused atoms of Ga with atoms of Cu and Cl induce strong grain growth processes.

According to the obtained results about the influence of annealing conditions on structural transformations in ZnS film it is possible to assume that co-doping of ZnS:Cu film by different atoms of Ga or Cl leads to different results. At the annealing process Ga acts only as activator of collecting and secondary recrystallization processes and facilitates the formation of coarse-grain with high crystalline perfection, but without any phase transition up to 1000 °C. Co-doping by Cl atoms leads not only to facilitation of recrystallization process, but also to reduction of the phase transition temperature. Apparently, this difference can be explained on the basis of the conception of co-dopant incorporation into the lattice of ZnS compound. The incorporation of counter trivalent cation of Ga^{3+} in Zn sublattice for stabilization of Cu^{+} dopant in the same sublattice does not reduce the covalent bindings. The incorporation of counter anion of Cl^{-} in S sublattice with cation of Cu^{+} in Zn sublattice changes the bindings in the lattice to more ionic. The amount of Cu and Cl atoms diffused into ZnS lattice during the annealing in the mixture at 650 °C is the same, but part of them can be gathered at the dislocations, sub-grain and grains boundaries. The distribution of these atoms in both sublattices depends on the temperature of the second annealing. The additional annealing at 950 °C results in more homogeneous distribution of Cu and Cl in sublattices and, hereby, increases the amount of Cu-Cl binding, which influences the phase transition temperature. The film annealed at such conditions has the hexagonal structure almost in whole volume.

Conclusions

The ZnS, ZnS:Cu and ZnS:[Cu, Al] thin films deposited by EBE from different targets of ZnS with and without doping elements have only zincblende crystal structure regardless of doping elements and type of substrate. The non-vacuum annealing of these films in S_2-rich atmosphere both with and without Ga vapors at 1000 °C does not lead to the change in crystal structure. The doping of ZnS films with Cu and Cl by thermodiffusion results in decrease of the phase transition temperature. For ZnS:Cu, Cl film the fractional phase transition takes place at the temperature of 800 °C. The assumption that amount of Cu-Cl binding in ZnS lattice affects the phase transition temperature is proposed. It is clarified that Ga and Cl act as activators of recrystallization process.

References

1. Ballentyne, D.W.G., 1960, *J. Electrochem. Soc.*, **107,** 807.
2. Boudghene Stambouli, A., Hamzaoui, S. & Bouderbala, M., 1996, *Thin Solid Films,* **283**, 204.
3. Brady. G.S., 1971, *Materials Handbook* (New York: McGraw Hill Book Company).
4. Arterton, A., Brightwell, J.W., Mason, S., Ray, B. & Viney, I.V.F., 1992, *Journal of Crystal Growth*, **117**, 1008.
5. Minagawa, T., 1980, *J. Phys. Soc. Japan*, **49**, 285.
6. Khomchenko, V.S., Rodionov, V.E. & Tzyrkunov, Yu.A., 1998, *Proceedings of 7th Inter. Symposium "Advanced Display Technologies"*, Minsk, Byelorussia, 218.

Z. Kristallogr. Suppl. **23** (2006) 293-298

Electrocrystallization of Pt layers onto Au substrates; an X-ray diffraction study

I. Yu. Molina[1*], L. M. Plyasova[1], S. V. Cherepanova[1], E. R. Savinova[1], G. A. Tsirlina[2]

[1]Boreskov Institute of Catalysis, Pr. Lavrentieva 5, Novosibirsk 630090, Russia
[2] Moscow State University, Vorob'evy Gory 1, Moscow 119992, Russia
[*]Contact author; e-mail: molina@catalysis.nsk.su

Keywords: nano-particles, structure, electrolytic deposits, deposition potential

Abstract. An X-ray diffraction study of the structural features of Pt electrodeposited on Au substrates was performed. The influence of the deposition potential, electrochemical ageing and model catalytic reactions on the structural characteristics of deposits has been analysed. It has been shown that under the conditions employed highly defective electrolytic deposits are formed composed of nm-sized particles (10-30 nm). Electrochemical ageing and model electrochemical reactions lead to the relaxation of the defect structure of electrodeposited Pt, which is expressed in an increase of lattice parameter and particle size and decrease in the values of strains and density of randomly distributed dislocations. The data obtained showed that the deposition potential is a key parameter determining structural characteristics of Pt electrolytic deposits, and allowed to reveal the minimum of intergrowth degree of Pt nano-particles.

Introduction

Noble metals electrodeposited on various supports have been used in electrochemistry since the times of Kolrausch [1]. Metal electrodeposits are of considerable interest in electrocatalysis, electrosynthesis and for sensor applications. Usually electrolytic deposits are composed of nano-sized grains interconnected through grain boundaries, have high specific surface area and posses high defectiveness. It has been noticed [2,3] that adsorption and catalytic properties of electrodeposited metals of the Pt Group depend on the deposition potential. However, so far this phenomenon has not been studied systematically. The attempts of X-ray diffraction study of the nature of this dependency were based on two approaches: (1) to study thick deposits (the amount of deposited metal is ~ 5-15 mg/cm^2), in this case the reflections from the support are not observed, and (2) to separate the deposit from the support and to study it independently. Unfortunately, thick deposits are highly inhomogeneous and fragile, which complicates the interpretation of experimental results. Moreover, separation of the deposit from a support is a damaging procedure, which results in a loss of valuable information concerning the structure and texture of the deposits. In this work we have studied structural features of Pt electrodeposited on Au supports with thickness less than 1 μm without separa-

tion from the supports. The effect of the deposition potential, electrochemical ageing (potential cycling up to receiving stationary voltammetric characteristics) and model catalytic reactions (CO and methanol oxidation) on the structural features of deposits has been evaluated.

Experimental

The samples for investigation were prepared via electrodeposition onto Au foil from H_2PtCl_6 solutions at constant potential in the range from 25 to 550 mV. The amount of electrodeposited Pt was 0.5-1 mg/cm^2 and the estimated thickness varied from 0.20 to 0.80 μm. The X-ray diffraction patterns were obtained using URD-63 (Freiberger Praezisionsmechanik) and D-8 (Bruker) diffractometers with CuKα-radiation with a scanning method within the angle interval 2θ = 30-90° with 0.02° 2θ step and the exposition time of 10-20 s. The averaged lattice parameters were calculated with least-squares method using a program system "Polikristall" [4]. To determine the instrumental broadening an α-Al_2O_3 standard (SRM 676 from NIST) was used. Preliminary examination of the samples on the presence of stacking faults did not reveal them in perceptible quantities, therefore all calculations were carried out in assumption that only crystallite size and strains contribute to the line broadening. Low peak intensities on high angels and as a result low accuracy of estimated breadths did not allow us to separate the crystallite size and strains using two (or more) orders of a reflection in any direction. Therefore a single-line Voigt analysis method was used to calculate the crystallite size and strains [5]. In this method all profiles are described by Voigt functions which are convolutions of Cauchy and Gaussian functions. From the full width at half maximum and the integral breadth of a Voigt profile one can obtain the integral breadths of the constituting Cauchy and Gaussian profiles. It is assumed that Cauchy component of the profile is due to crystallite size and the Gaussian component of the profile is due to strains. Density of randomly distributed dislocations in the grain was calculated from crystallite size and strains according to [6-8]. For several samples particle size distribution in <111> direction has been calculated [9]. The calculations were performed with use of a program developed in our laboratory. In this program Warren-Averbach method [10] is employed. The program deals with no experimental peaks but with their approximation with Pseudo-Voigt function, that makes it possible to use large enough region for calculation of Fourier coefficients. This, in its turn, allows us to avoid so-called Hook effect, which appears from truncation.

Results

Let us consider the initial samples of Pt electrodeposited on Au foil at different deposition potentials. Selected X-ray diffraction patterns are presented in figure 1. One can observe narrow reflections from the Au substrate, with crystallite size more than 100 nm and quite broad reflections from the electrodeposited Pt. Table 1 represents the values of Pt crystallite size in <111> direction. The dependence of crystallite size on the deposition potential is shown in figure 2. The crystallite size is in the range 12-17 nm and decreases with the deposition potential, while an increase of strains is observed (table 1). The similar situation as for the strains is observed for dislocation density (see figure 3).

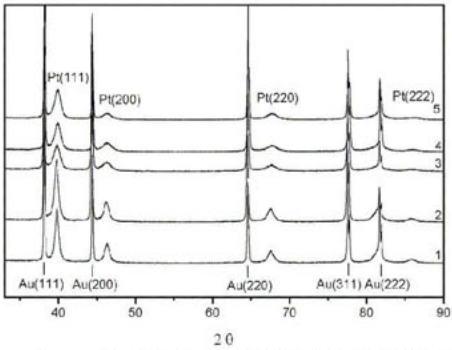

Figure 1. X-ray diffraction patterns of initial Pt/Au: (1)-Pt/Au(25), (2)-Pt/Au(100), (3)-Pt/Au(300), (4)-Pt/Au(400), (5)-Pt/Au(500). Figures in brackets denote the deposition potential in mV.

Table 1. Crystallite size, strains, density of randomly distributed dislocations, lattice parameter before and after electrochemical ageing and reaction. Figures in brackets – the particle size calculated from particle size distribution. The accuracy of D calculation is 5 % from the calculated value.

Sample (E_d, mV)	D (111), nm	Δd/d (111)	$\rho*10^{-11}$ (111) (cm^{-2})	a, Å
	Initial samples, after ageing, after reaction			
Pt/Au (25)	17	0.003(2)	2.39(1)	3.919(4)
	20	0.003(2)	2.03(9)	3.917(6)
	23 (22)	0.003(2)	1.77(8)	3.925(2)
Pt/Au (50)	16	0.002(8)	2.15(6)	3.919(1)
	19	0.003(4)	2.30(7)	3.918(2)
	28 (27)	0.002(9)	1.30(1)	3.922(3)
Pt/Au (100)	16	0.003(5)	2.74(6)	3.921(1)
	18	0.003(5)	2.49(6)	3.916(7)
	20 (18)	0.004(1)	2.51(1)	3.921(3)
Pt/Au (200)	14	0.006(6)	5.79(3)	3.915(2)
	17	0.005(1)	3.80(3)	3.919(2)
	20 (16)	0.005(9)	3.71(5)	3.922(5)
Pt/Au (300)	13	0.008(8)	8.43(1)	3.917(7)
	15	0.005(2)	4.38(1)	3.913(5)
	14 (13)	0.004(9)	4.47(5)	3.922(1)
Pt/Au (400)	13	0.007(6)	7.63(1)	3.913(1)
	15	0.005(2)	4.47(1)	3.915(4)
	18 (15)	0.006(1)	4.14(9)	3.920(3)
Pt/Au (500)	13	0.008(8)	8.24(3)	3.910(4)
	14	0.004(6)	4.12(4)	3.916(5)
	19 (15)	0.006(6)	4.38(6)	3.918(3)
Pt/Au (550)	13	0.007(8)	7.53(1)	3.913(1)
	16	0.004(7)	3.73(4)	3.913(1)

The differences in the crystallite size for samples obtained at 25-100 mV and 200-550 mV are noticeable but not very large, while the values of the strains and dislocation density differ two or more times. Lattice parameter of the electrodeposited Pt is decreased in comparison with the value for bulk metal (a = 3.923 Å) [11] and a systematic decrease with deposition potential is observed (see table1). The decrease of lattice parameter for electrodeposited Pt has been noted earlier [2] and probably is the common property of electrodeposited metals [12]. The main reason for the lattice compression could be a composite nature of the deposits, which consist of multiple nm size crystals originating from repeated secondary nucleation events. Secondary Pt crystal growing in the neighborhood of each other may exert mutual strain. It should be noted that the most abrupt changes of structural parameters occur in the deposition potential range 100-200 mV.

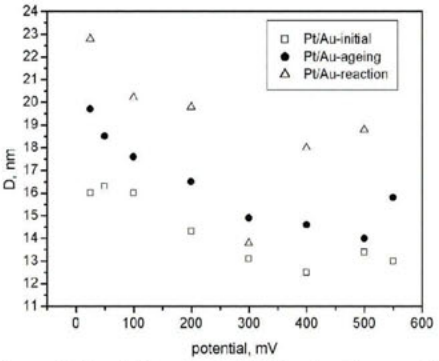

Figure 2. Crystallite size in <111> direction vs. deposition potential.

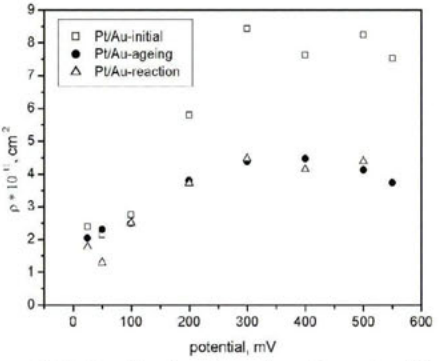

Figure 3. Dislocation density vs. deposition potential.

Let us consider the changes of the parameters under electrochemical ageing and electrocatalytic reactions. The conditions employed lead to an increase of the crystallite size for all samples (figure 2, table1). Values of strains and dislocation density remain practically invariable for samples obtained at small deposition potentials (up to 100 mV), at that time for samples obtained at low overvoltage an abrupt decrease in the values of strains and dislocation density is observed (figure 3, table 1). Pt lattice parameter increases for all samples and approaches the value for bulk metal. It is evident that electrochemical ageing and electrocatalytic reactions lead to the relaxation of the defect structure of electrodeposited Pt and the most abrupt changes are observed for more defective samples obtained at deposition potentials more than 100 mV. The values of strains and dislocation density remain rather high for these samples even after ageing and reactions.

Samples after electrochemical reactions were better crystallised and it was possible to measure the (222) reflection integral breadths with enough accuracy to calculate particle size distribution. Selected graphs are presented in figure 4, the values of average crystallite size, obtained from particle size distribution, are listed in table 1 in brackets. Calculations show that particle size distributions are bimodal with significant part of small size particles (less than 10-12 nm). There is good correspondence between average crystallite size obtained from single-line Voigt analysis and particle size distribution. From particle size distribution

(which represents the mass portion w_i of particles with size D_i) we could calculate theoretical specific surface area by the formula $S_{cal}=\sum w_i S_i/m_i$, where S_i is the surface area of particle with size D_i and m_i is the mass of particle with size D_i.

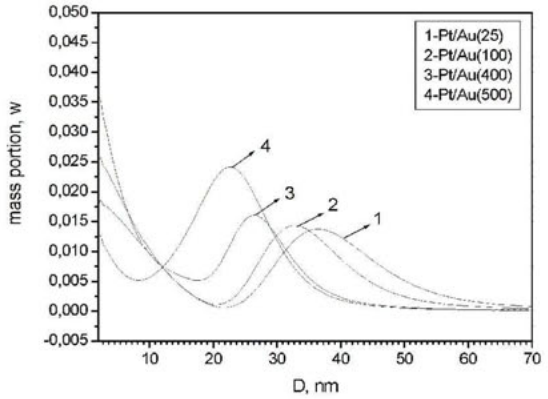

Figure 4. Particle size distribution for selected Pt/Au samples after electrochemical reactions. Particle size distribution is normalized on 1.

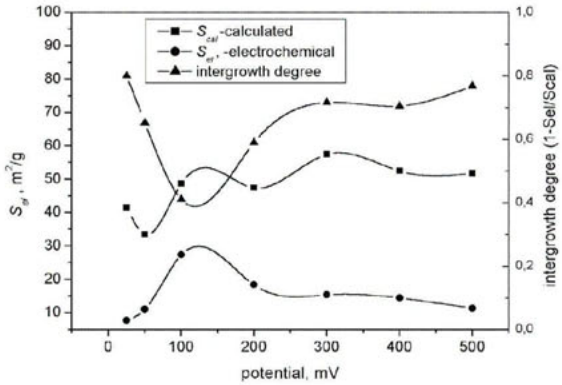

Figure 5. Specific surface areas (electrochemical and calculated) and intergrowth degree vs. deposition potential.

Comparison of the values of S_{el} (measured with electrochemical method) and S_{cal} (calculated in assumption of spherical particles) has shown that in the potential range 100-200 mV the intergrowth degree of Pt particles (that characterizes the part of the Pt surface available for adsorption) is minimum (figure 5). This could explain an anomalous increase of specific surface area of Pt films in this potential range.

Summary

By means of X-ray powder diffraction the samples of Pt electrodeposited on Au substrates have been investigated. The influence of deposition potential, electrochemical ageing and model electrochemical reactions on the structural features of deposits has been evaluated. It was shown that:
Electrodeposited Pt belongs to nano-crystalline materials (average particle size is 10-30 nm), the structure of nano-particles is highly distorted which is expressed in rather high values of strains, dislocation densities and decrease of lattice parameters.
Structural parameters of electrodeposited Pt depend at a great extent on the deposition potential: an increase of deposition potential leads to an increase of defectiveness of deposits.
Electrochemical ageing and model electrochemical reactions lead to the relaxation of the defect structure, the most abrupt changes occur for more defective samples obtained at 200-550 mV.
The data obtained allowed to reveal the minimum of intergrowth degree of Pt nano-particles.
The obtained results could be used for production of electrodeposited materials with optimum defectiveness.

References

1. Kolraush, F., 1897, *Ann. Phys. Chem.* **60**, 315.
2. Gamburg, Yu.D., Petukhova, R.P., Podlovchenko, B.I. & Polukarov, Yu.M., 1974, *Russian Journal of Electrochemistry*, **10**, 751 (in Russian).
3. Petrii, O.A., Tsirlina, G.A., Pron'kin, S.N., et.al., 1999, *Russian Journal of Electrochemistry*, **35**, 8 (in Russian).
4. Tsybulya, S.V., Cherepanova, S.V. & Solovieva, L.P., 1996, *J. Struct. Chemistry*, **37**, 332 (in Russian).
5. Langford, J.I., Delhez, R., Keijser, Th.H. & Mittemeijer, E.J., 1988, *Aust. J. Phys.* **41**, 173.
6. Williamson, G.K. & Smallman, R.E., 1956, *Phil. Mag.* **1**, 34.
7. Smallman, R.E. & Westmacott, K.H., 1957, *Phil. Mag.* **2**, 669.
8. Valiev, R.Z. & Aleksandrov, I.V., 2000, "Nanostructural materials obtained by severe plastic deformation", *M.Logos*, 272.
9. Bertaut, E., 1950, *Acta Crystallogr.* **3**, 14.
10. Warren, B.E. & Averbach, B.L., 1950, *J.Appl. Phys.* **21**, 595.
11. PCPDFWin, Ver 1.30, JCPDS ICDD, Swarthmore, PA, USA, 1997, N 04-0802.
12. Gamburg, Yu.D., 1999, *Russian Journal of Electrochemistry*, **35**, 1020 (in Russian).

Acknowledgements. The work was supported by the Russian Foundation for Basic Research (projects N 01-03-33132, N 03-03-06348).

Z. Kristallogr. Suppl. **23** (2006) 299-304

Residual stress mapping in the zirconia electrolyte layer of a high-temperature solid oxide fuel cell

Werner Fischer* and Günther Blass

Research Centre Jülich GmbH, Institute for Processes and Materials in Energy Systems, 52425 Jülich, Germany
*Contact author; email: w.fischer@fz-juelich.de

Keywords: powder diffraction, residual stress mapping, solid oxide fuel cell, yttria-stabilized zirconia

Abstract. X-ray residual stress evaluation has been employed to measure stress distributions in the electrolyte layer of a single anode-supported planar solid oxide fuel cell at several manufacturing steps. The mainly thermal residual stress in the about 10 µm thick electrolyte layer is about -560 MPa at room temperature and constant across the whole cell plate. Chemical reduction of the anode leads to a slight reduction of the compressive stress to -520 MPa, still ensuring that the electrolyte layer remains under compression up to operation temperature of about 800°C.

Introduction

Several designs of solid oxide fuel cells (SOFC) are under development worldwide. In the Research Centre Jülich the anode-supported planar concept with a very thin electrolyte layer and a resulting low operation temperature has been developed reaching an electrical power of 10 kW this year. A single cell of this SOFC design is a sandwich consisting of the substrate carrying four additional layers. One of these layers, the electrolyte layer, separates the anode space from the cathode space. It is made of ion-conducting 8 mol.-% yttria-stabilized zirconia (8YSZ), has a thickness of about 10 µm and has to be gas-tight. This gas-tightness under service conditions and during thermal cycling is crucial for cell operation. Tensile stress which might lead to fracture of the electrolyte layer during manufacturing or during operation has to be avoided.
In this study X-ray stress evaluation [1-4] has been utilized to map the residual stress distribution in the electrolyte layer of a single cell plate at four steps of its synthesis. Deformation (warp) of cell plates during manufacturing indicated that reasonable stress seems to occur, which should be quantified with respect to sign, magnitude, and distribution across the cell.

Experimental details

An overview of materials and technologies used for manufacturing of a cell plate is given in figure 1. This study is focussed on manufacturing steps of the electrolyte layer only (centre

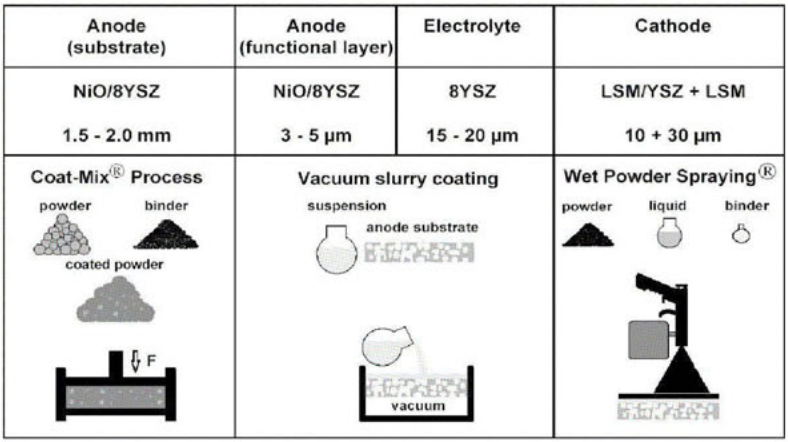

Figure 1. Materials and technologies used for manufacturing a single cell plate of a solid oxide fuel cell [5].

of figure 1). Thermal processing of the cell mainly determines the stress field in the electrolyte layer. Residual stress is a result of the mismatch between the thermal expansion coefficients of adjacent layers and by the volume change during reduction of the anode. At sintering temperature all thermal stresses disappear, but it increases during cooling and later changes during thermal cycling between room temperature and operation temperature of about 800°C. To avoid cracking of the dense electrolyte layer it has to remain at least up to this temperature under compression. But on the other side the compressive stress should not exceed the fracture strength of YSZ under compression of about 1 GPa [6]. In order to get more insight into the stress state of the electrolyte layer, we investigated this stress distribution at several manufacturing steps:

1. as-deposited (stress-free, check of the experimental set-up),
2. after sintering at 1400°C/5h/air,
3. after a 'flattening' procedure (1360°C/1h/air/mechanical load 1kg) needed to remove the warp of the cell plate occurring during sintering,
4. after reduction of NiO to Ni in the substrate at 900°C/10h/Ar+4%H_2.

Figure 2 shows schematically these different manufacturing steps of a planar cell.

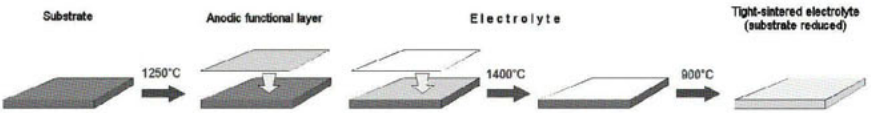

Figure 2. Processing steps influencing the residual stress state of a single cell plate.

Standard $\sin^2\psi$ method in ψ-geometry has been employed for X-ray measurement of lattice strain in YSZ at room temperature. To achieve a local resolution of about 1 mm^2 for strain measurement a polycapillary half-lens was mounted in the incident beam path. The parallel beam behind the half-lens was collimated to 0.6x1 mm^2. All measurements were made at the same cell. The dimensions of that cell were 55x55x2 mm^3. The lattice strain in the electrolyte layer has been measured across a centred 50x50 mm^2 area divided into 10x10 equidistant points. Strain has been determined assuming a plane unidirectional strain field. X-ray elastic constants of Eigenmann et al. [7] were used for converting strain to stress.

Further experimental details and methods applied for data evaluation are compiled in table 1.

Table 1. Experimental detail and data evaluation.

Diffractometer	Philips XPert MRD 3050/65 with Eulerian cradle and motorized sample stage
Radiation	Cu-K, 40 kV/50 mA
Primary optics	K_β filter, polycapillary semi-lens, cross slit collimator 0.6x1 mm^2
Reflection, 2θ range	Reflection (620), 140° – 146.5°, $\Delta 2\theta$ = 0.05°, 10s/step
Method	ψ tilt, $\sin^2\psi \leq 0.5$, equidistant in $\sin^2\psi$
Corrections	Absorption, linear background, Lorentz polarization, Rachinger $K_{\alpha 2}$ subtraction
Peak position	Centre of gravity, parabola fit, manual
Elastic constants	$E_{(620)}$ = 215 GPa, $\upsilon_{(620)}$ = 0.29
X-ray elastic constants	s_1 = -1.35/TPa, 1/2 s_2 = 6.0/TPa

Results and discussion

The stress distributions are presented graphically in figure 3. For visualisation of the stress values grey shading is used in such a way that the stress spread over the grey key equals to 200 MPa in all graphics. This ensures the comparability of fluctuations for different manufacturing steps. Dark grey corresponds to a low stress value; light grey indicates a high stress value. Additionally, the mean stress and the standard deviation are given for each map.
Figure 3a (electrolyte layer as-deposited) may act as a check of the experimental set-up including data evaluation. The electrolyte layer before sintering should not have any residual stress, of course, since it is an agglomerate of sedimented and tried YSZ powder particles. This figure may serve as indicator for the precision of the strain measurement.

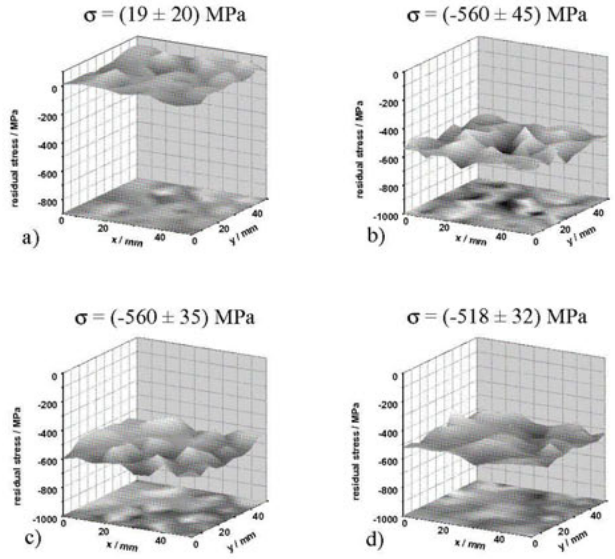

Figure 3. Residual stress distributions in the electrolyte layer at several manufacturing steps, a) as-deposited, b) as-sintered, c) sintered and flattened, and d) sintered, flattened and anode finally reduced.

Figure 3b (electrolyte layer after sintering at 1400°C for 5h at air) shows that at room temperature the electrolyte layer comes under a strong compressive residual stress of about 560 MPa. This stress is constant across the whole cell. Its fluctuation including experimental uncertainty is 45 MPa. During sintering a slight warp of the cell plate occurs. Since cell plates will be stacked later in a SOFC stack this warp is not acceptable. Therefore it is removed by heating the cell under load of 1 kg at 1360°C for 1 h at air. This flattening procedure could imply the danger of crack formation. Figure 3c shows the stress distribution in the electrolyte layer after flattening. The overall stress level at room temperature remains unchanged at 560 MPa compression. The stress level and its homogeneity do not differ from that before flattening, suggesting that at 1360°C the system anode/electrolyte can compensate a mismatch via a quasi-plastical behaviour. The stress fluctuation becomes somewhat smaller (35 MPa), indicating also defect annealing.

During operation the anode of the cell has to be reduced to obtain an electrically conducting anode formed by the porous sinter body of YSZ and nickel. The chemical reduction of NiO to Ni at 900°C for 10 h in an Ar+4%H_2 significantly changes the volume and the physical properties of the anode. Consequently, the residual stress in the electrolyte layer is altered. Figure 3d shows the stress distribution after anode reduction. The level of the compressive stress goes down to 520 MPa, but it is still constant across the whole cell. The stress fluctuation is further reduced to about 30 MPa.

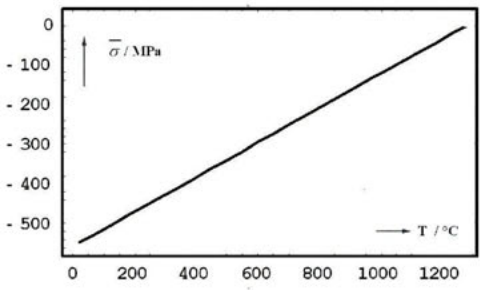

Figure 4. Thermo-elastically modelled stress in the electrolyte layer vs. temperature after chemical reduction of the anode material [8].

The essential question is whether or not this compressive stress at room temperature is sufficient to hold the electrolyte at operation temperature of about 800°C under compression? Malzbender et al. [8] provided thermo-elastical calculations for modelling the stress in the electrolyte layer in dependence of temperature. The result of this simulation is summarized in figure 4. The calculated residual stress level at room temperature agrees well with our results for the reduced cell plate. This figure shows further that about 520 MPa are sufficient to ensure a remaining compressive stress in the electrolyte layer at operation temperature, so that a malfunction of a cell due to crack formation should not occur.

Conclusions

X-ray residual stress mapping permits the experimental determination of 2D stress distributions with a lateral resolution of about 1 mm using standard X-ray diffraction equipment, when a polycapillary half-lens is applied in the incident beam path. The stress state of the 10 µm thin electrolyte layer in a single planar solid oxide fuel cell is mainly determined by the thick supporting anode substrate. Sign and magnitude of the residual stress depend of the difference in the thermal expansion coefficients of both materials. The flattening procedure applied to the cell plate for removing the slight warp introduced during sintering of the electrolyte layer decreases the stress fluctuation. It does not change the absolute stress level. Chemical reduction of NiO to Ni in the porous anode substrate necessary for cell operation lowers the absolute stress level in the electrolyte layer for about 10%. The electrolyte layer remains even at operation temperature under compressive stress. Results of thermo-elastical modelling confirm the X-ray stress data with respect to sign and magnitude quite well.

References

1. Eigenmann, B. & Macherauch, E., 1995, *Mat.-wiss. u. Werkstofftech.*, **26**, 148-160.
2. Eigenmann, B. & Macherauch, E., 1995, *Mat.-wiss. u. Werkstofftech.*, **26**, 199-216.
3. Eigenmann, B. & Macherauch, E., 1996, *Mat.-wiss. u. Werkstofftech.*, **27**, 426-437.
4. Eigenmann, B. & Macherauch, E., 1996, *Mat.-wiss. u. Werkstofftech.*, **27**, 491-501.
5. Menzler, N.H., Blass, G., Giesen, S. & Buchkremer, H.P., 2002, *Mat.-wiss. u. Werkstofftech.*, **33**, 367-371.
6. Kato, T., Wang, N.S., Negishi, A., Momma, A., Kasuga, Y. & Nozaki, A., 1999, in: *Proc. 3rd Int. Fuel Cell Conf.* (Nagoya/Japan), p. 461
7. Eigenmann, B., Scholtes, B. & Macherauch, E., 1989, *Mat.-wiss. u. Werkstofftech.*, **20**, 314-325.
8. Malzbender, J., Wakui, T., Steinbrech, R.W. & Singheiser, L., 2004, *Proc. 6th Europ. SOFC Forum* (Lucerne/Switzerland), p. 329

Z. Kristallogr. Suppl. **23** (2006) 305-310

Ultrashort period Cu/Si and Ni/C multilayers for X-ray mirrors

M. Jergel[1*], M. Ožvold[1,2], R. Senderák[1], Š. Luby[1], E. Majková[1]

[1]Institute of Physics, Slovak Academy of Sciences, Dúbravská cesta 9, 845 11 Bratislava 45, Slovak Republic
[2]Department of Material Engineering, Faculty of Materials Science and Technology, Slovak University of Technology. J.Bottu 24, 917 24 Trnava, Slovak Republic
[*]Contact author; e-mail: fyzijerm@savba.sk

Keywords: X-ray reflectivity, interface diffuse scattering, X-ray mirror, multilayer

Abstract. Ultrashort period Cu/Si and Ni/C multilayers for X-ray interference mirrors were prepared by UHV e-beam deposition onto a heated substrate. An optimum deposition temperature of 80°C was found. The multilayer quality was probed by specular X-ray reflectivity and interface diffuse scattering at $CuK_{\alpha 1}$ wavelength. An asymmetry between the A/B and B/A interfaces was detected. Thermal stability tests revealed that Cu/Si multilayers are applicable only below 100 °C while the Ni/C ones collapse at 350 °C. Ni/C multilayers are superior also in terms of shorter correlation lengths with implications for the imaging contrast.

Introduction

Interference multilayer mirrors have become an indispensable part of instrumentation in astronomy, lithography, plasma diagnostics, at synchrotron storage rings and in other fields. Compositionally sharp and geometrically smooth interfaces are required for high reflectivity. Interfaces may further degrade under heavy thermal loads at operation. In addition to optical criteria, thermodynamic ones are thus also important for the material pair choice.
Cu/Si and Ni/C multilayers with ultrashort periods are applicable for hard X-rays and the latter ones also for soft X-ray microscopy. Long-term room-temperature (RT) stability and narrow interfaces have been reported for dc sputtered Cu/Si multilayers [1]. Sputtered Ni/C mirrors were found to be stable up to 300 °C [2, 3]. The interface width proved to be larger here due to the island growth of Ni. Ni/C mirrors have been prepared mainly by sputtering [4-7] or by pulsed laser deposition (PLD) [8-10]. The UHV electron beam evaporation was tried only in a few cases [11, 12]. To suppress the interface roughness, an in situ ion-beam etching of Ni layers was applied.
In our work, we report on ultrashort period Cu/Si and Ni/C multilayers deposited by UHV electron beam evaporation with in situ substrate heating and on their thermal stability. An increased surface diffusion length of adatoms is expected to heal the interface roughness as a simpler and cheaper alternative to the ion beam etching.

Experimental

The samples were deposited in a UMS 500 Balzers apparatus in a vacuum of 10^{-7} Pa onto silicon wafers with a native oxide layer. Typically, 10-15 periods of 1.5-3.2 nm were deposited starting with Si (Ni) and the same layer was used as a cover layer. Deposition temperatures up to 160 °C were tested. A vacuum furnace annealing (10^{-4} Pa) was applied.
The multilayer stack was analyzed by the specular X-ray reflectivity (XRR) and X-ray diffuse scattering at grazing incidence (GIXDS). The measurements were performed on a high-resolution diffractometer equipped with a GaAs double crystal monochromator located in the primary beam and providing $CuK_{\alpha 1}$ radiation at the output. A maximum counting rate of $10^5 s^{-1}$ was within the linear response of a NaI(Tl) scintillation detector. The internal layer structure was examined on a Bragg-Brentano powder diffractometer equipped with a focusing graphite monochromator in the diffracted beam.

Results and discussion

Examples of the XRR and GIXDS simulations for a Cu/Si multilayer are shown in figure 1 with the simulation parameters gathered in table 1. The specular XRR was evaluated by the optical recursive approach [13] supposing error function interface profiles. The GIXDS was calculated within the distorted-wave Born approximation (DWBA) [14]. Amorphous and polycrystalline layers with typically randomly rough interfaces were found. Therefore we adopted a statistical interface description. A lateral correlation function as suggested in [15] was considered for all interfaces. It provided the real (geometrical) interface roughness, σ, the lateral correlation length, ξ, and the Hurst parameter, H, which is connected with the fractal interface dimension as D=3–H. An exponential decay of the vertical correlation (conformality) of the interface profiles with the interface distance was supposed, being controlled by a single vertical correlation length L_{vert}. This phenomenological model was convenient in the interval of the roughness frequencies covered by our GIXDS measurements.
Layer thicknesses, t, and interface widths, σ_{eff}, were first extracted from the XRR fit, being mutually independent parameters. For Ni/C multilayer, also layer densities, ρ, had to be set as free parameters (table 2) to adjust the XRR fit around the critical angle. All these parameters were further fixed in the GIXDS simulations to obtain σ, ξ, L_{vert} values which do not affect the XRR in the first order DWBA. Several sample and detector scans were taken and fitted for a given sample to avoid a GIXDS fit ambiguity as much as possible. Finally, H value, influencing only a small region around the specular reflection, was refined separately.
The as-deposited Cu/Si multilayers were amorphous. An optimized deposition temperature of 80 °C provided a minimum interface width, σ_{eff}, and intermixing quantified by σ_{eff}-σ. An asymmetry between Cu/Si and Si/Cu interfaces shows that Cu layers grow rougher. The interface widths are rather independent of the multilayer period down to 2 nm and increase below that value. Here, Cu layer discontinuities may occur which affects both types of interfaces. The vertical correlation length is comparable with the total multilayer thickness giving rise to a pronounced resonant diffuse scattering around the Bragg peaks.
A quickly saturating reflectivity drop by ≈ 25 % on the 1st Bragg peak was observed at RT within 2 weeks after deposition of Cu/Si multilayers. A strong mixing and interdiffusion brought about a severe suppression of the Bragg peaks on the 100 °C/1h annealing and multi-

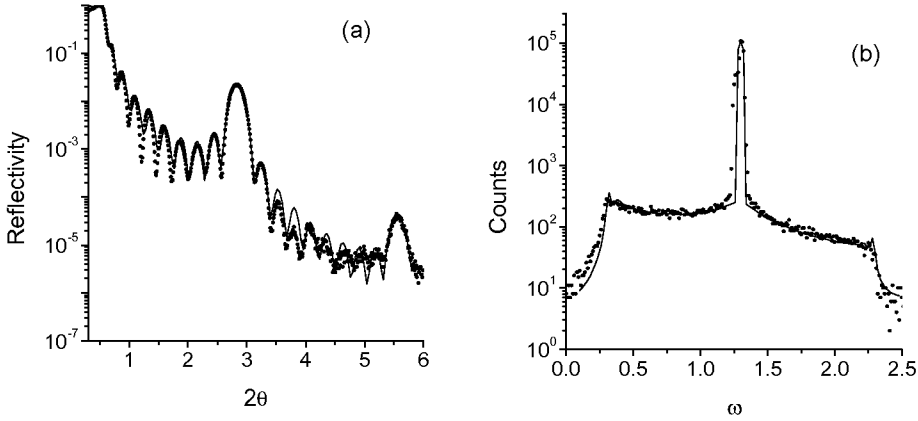

Figure 1. The specular XRR (a) and GIXDS (b) curves for a Cu/Si multilayer deposited at 80 °C with the simulation parameters indicated in table 1. The latter curve was measured by a sample scan with the detector fixed at the 1st Bragg maximum, ω being the angle of incidence (dots – measured points, line – simulation).

Table 1. The XRR and GIXDS simulation parameters of Cu/Si multilayers. t, Λ, σ_{eff}, σ, ξ, L_{verb}, H stand for the layer thickness, multilayer period, interface width, interface roughness, lateral and vertical correlation lengths, and Hurst parameter, respectively. Bulk densities were used for the simulations.For Λ<2 nm, the GISAX around the 1st Bragg maximum was too low above the background to be reliably simulated.

deposition temperature	RT	80°C	80°C
t_{Cu} (nm)	1.22	1.27	0.65
t_{Si} (nm)	2.25	1.9	0.98
Λ (nm)	3.47	3.17	1.63
$\sigma_{effSi\text{-}on\text{-}Cu}$ (nm)	0.7	0.5	0.7
$\sigma_{effCu\text{-}on\text{-}Si}$ (nm)	0.6	0.45	0.6
$\sigma_{Si\text{-}on\text{-}Cu}$ (nm)	0.4	0.3	---
$\sigma_{Cu\text{-}on\text{-}Si}$ (nm)	0.35	0.25	---
ξ (nm)	10	10	---
L_{vert} (nm)	30	30	---
H	0.2	0.3	---

layer collapsed on the 200 °C/1h one.Here, an onset of η‘ (Cu,Si) tetragonal phase formation (JCPD-ICDD data set file no. 23-0224) was observed, presumably in the intermixed regions. Fast grain-boundary diffusion of Si into Cu then accelerated the multilayer degradation.

The interface quality is more sensitive to the deposition temperature in Ni/C multilayers where a well resolved Bragg peak in the XRR curve was observed only close to 80 °C (figure 2). A comparison of the simulation parameters (table 2) with the Cu/Si multilayer of a simi-

lar period grown at 80 °C (table 1) shows rougher and more intermixed metalloid-on-metal interfaces. Their larger roughness is induced by Ni growth while the intermixing is due to diffusion of C into Ni at the deposition. The interface width reaches the value 1 nm for the multilayer period below 3 nm suggesting agglomeration effects in Ni. This observation compares well with a percolation threshold around 2 nm found in sputtered samples [16] at which Ni forms coalescent layers. The interface correlation lengths are much shorter in Ni/C multilayers (cf. table 1 and 2) while fractal behaviour (H<1) is observed in all cases. Such a behaviour was reported for Ni/C multilayers previously from AFM [7].

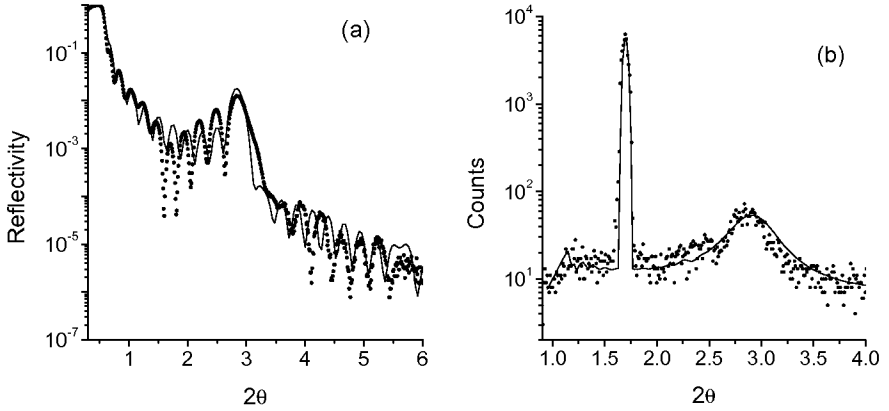

Figure 2. The specular XRR (a) and GIXDS (b) curves for a Ni/C multilayer deposited at 80 °C with the simulation parameters indicated in table 2. The latter curve was measured by a detector scan with the detector fixed at the 1st Bragg maximum (dots – measured points, line – simulation).

A step-like vacuum annealing from 100 °C up to 350 °C with 50 °C steps and a duration of 4 hours at each step was applied to the sample presented in figure 2. After each annealing, the sample was cooled down in vacuum and measured at RT. A gradual increase of the σ_{eff}-σ difference (table 2) indicates proceeding interdiffusion. A decrease of the Ni layer densities in the advanced stages of the annealing shows that the dominant diffuser is carbon. A multilayer breakdown occurs on the 350 °C annealing. There is a systematic decrease of the C layer densities correlated with an increase of the multilayer period starting at 150 °C (figure 3). A similar period increase was reported in sputtered Ni/C multilayers [5,17] and was explained by a transformation of the amorphous into the graphitic-like structure. We could observe the graphitization by the XRD mainly in the advanced stages due to the weak scattering power and small scattering volume of carbon. Crystalline grain growth in very thin layers governs also interface morphology and is reflected in an increase of the lateral correlation length and decay of the interface conformality. The graphitization affects only slightly the interface widths before the carbon diffusion into nickel develops at higher temperatures. Carbide crystallization is dominant after the multilayer collapses. Thermal stability studies of sputtered and PLD Ni/C mirrors gave similar results [2, 3, 9].

Table 2. The XRR and GIXDS simulation parameters of a Ni/C multilayer deposited at 80 °C. ρ is the layer density. 4 hour annealings at each temperature were successively applied to the same sample. The GISAX was not measured in the temperature region where the XRR did not change qualitatively.

annealing temperature	as-dep.	100 °C	150 °C	200 °C	250 °C	300 °C
t_{Ni} (nm)	1.26	1.26	1.28	1.32	1.33	1.34
t_C (nm)	1.89	1.89	1.92	1.98	1.99	2.01
Λ (nm)	3.15	3.15	3.2	3.3	3.32	3.35
ρ_{Ni} (g/cm^3)	8.9	8.9	8.9	8.5	8.5	8.0
ρ_C (g/cm^3)	2.2	2.2	2.1	2.0	2.0	1.8
$\sigma_{effC\text{-}on\text{-}Ni}$ (nm)	0.65	0.65	0.7	0.75	1.1	1.6
$\sigma_{effNi\text{-}on\text{-}C}$ (nm)	0.45	0.45	0.5	0.55	0.7	1.2
$\sigma_{C\text{-}on\text{-}Ni}$ (nm)	0.35	---	---	---	0.5	0.8
$\sigma_{Ni\text{-}on\text{-}C}$ (nm)	0.25	---	---	---	0.3	0.4
ξ (nm)	5	---	---	---	8	10
L_{vert} (nm)	10	---	----	---	3	`1
H	0.25	---	---	---	0.18	0.25

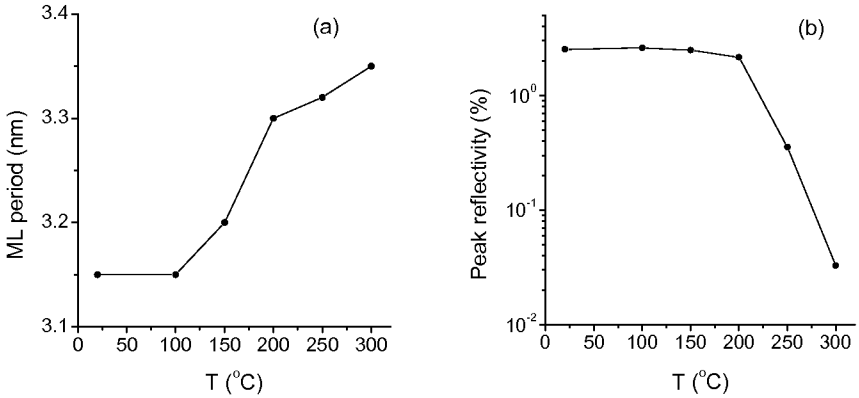

Figure 3. Temperature evolution of the multilayer period and peak reflectivity on the 1st Bragg maximum of a Ni/C multilayer annealed as indicated in table 2.

Conclusions

UHV electron-beam evaporation onto a heated substrate proved to be a promising method to prepare ultrashort period Cu/Si and Ni/C multilayers. Their quality in terms of interface width and roughness as well as thermal stability are fully comparable with those of the mirrors of larger periods deposited by other techniques (e.g. [2,3,5,9]). A deposition temperature of 80°C provided the best resolved and most intense Bragg peaks in the XRR curve for both types of multilayers. The build-up of the interface roughness is minimized at this deposition temperature while the intermixing between the constituents is not developed yet. As-

deposited Ni/C multilayers exhibit a larger roughness and intermixing at the metalloid-on-metal interfaces and are more prone to form discontinuous layers at extremely short periods which are better accessible in Cu/Si mirrors. On the other hand, Ni/C multilayers exhibit the breakdown at a temperature by 250°C higher than Cu/Si ones which are applicable only at operation temperatures below 100°C. Ni/C multilayers are superior to Cu/Si ones also in terms of smaller correlation lengths resulting in less intense resonant diffuse scattering around the Bragg peaks. This feature has positive implications for specular imaging contrast.

References

1. Windt, D.L., 1999, *Appl. Phys. Letters*, **74**, 2890.
2. Lodha, G.S., Pandita, S., Gupta, A., Nandedkar, N.V.: & Yamashita, K., 1996, *J. Electr. Spec. & Related Phenomena*, **80**, 453.
3. Nakajima, K., Aoki, S., Sudo, S. & Fujiwara, S., 1992, *Jap. J. Appl. Phys.*, **31**, 2864.
4. Friedrich, J., Diel, I., Kunz, C., Di Fonzo, S., Müller, B.R. & Jark, W., 1997, *Appl. Optics*, **36**, 6329.
5. Dupuis, V., Ravet, M.F., Tete, C., Piecuch, M., Lepetre, Y., Rivoira, R. & Ziegler, E.:, 1990, *J. Appl. Phys.*, **58**, 5146.
6. Borchers, C. & Michaelsen C., 2002, *Phil. Mag. A*, **82**, 1195.
7. Ulmeanu, M., Serghei, A., Mihailescu, I.N., Budau, P. & Enachescu, M., 2000, *Appl. Surf. Sci.*, **165**, 109.
8. Kovalenko, N.V., Mytnichenko, S.V. & Chernov, V.A., 2003, *JETP Letters* **77**, 80.
9. Chernov, V.A., Chkalo, E.D., Kovalenko, N.V. & Mytnichenko, S.V., 2000, *Nucl. Instr.& Methods A*, **448**, 276.
10. Dietsch, R., Holz, T., Weissbach, T. & Scholz, R., 2002, *Appl. Surf. Sci.* **197**, 169.
11. Pershin, Y.P., Zubarev,Y.N., Kondratenko, V.V., Poltseva, O.V., Ponomarenko, A.G., Servryukova, V.A. & Verhoeven, J.:, 2002, *Metallofizika i Noveishie Tekhnologii*, **24**, 795.
12. Puik, E.I., Van der Wiel, M.J., Zeulenmaker, H. & Verhoeven, J., 1991, *Appl. Surf. Sci.*, **47**, 251.
13. Underwood, J.H. & Barbee, T.W., 1981, *AIP Conf. Proc.*, **75**, 170.
14. Holý, V. & Baumbach, T., 1994, *Phys. Rev. B*, **49**, 10668.
15. Sinha, S.K., Sirota, E.B., Garoff, S. & Stanley, H.B., 1988, *Phys. Rev. B*, **38**, 2297.
16. Borchers, C., Ricardo, P. & Michaelsen, C., 2000, *Phil. Mag. A*, **80**, 1669.
17. Djavanbakht, T., Carrier, V., Andre, J.M., Barchewitz, R. & Troussel, P., 2000, *J. de Physique IV*, **10**, 281.

Acknowledgements. This work was partly supported by the Slovak governmental project no. 2003-SO 51/03R0600/01, Slovak grant agencies APVT, project no. APVT-51-021702, and VEGA, project no. 2/3149/23, and COST P7 Action. V. Holý is acknowledged for providing the DWBA software.

IV.2 Nanocrystalline Materials

Z. Kristallogr. Suppl. **23** (2006) 313-318

Microstructure of nanocrystalline materials studied by powder diffraction

T. Ungár

Department of General Physics, Eötvös University Budapest,
H-1518, POB 32, Budapest Hungary
Contact author; e-mail: ungar@ludens.elte.hu

Keywords: powder diffraction, nanocrystalline materials, particle size, micro strain, dislocations, contact stresses

Abstract. Powder diffraction is a powerful complementary tool for studying different physical and chemical aspects of the microstructure in nanocrystalline materials. It tells about the crystal structure, crystallinity, crystallite size and size-distribution and about macro-, meso- and micro strains in and between particles. Several different methods are available which provide either qualitative or quantitative information about these properties. Transmission and scanning electron microscopy, though very local, can be of great help in the interpretation of the fundamentally average information provided by X-ray powder diffraction.

Introduction

Crystalline materials can be classified, in a broader sense, as nanocrystalline if the average grain size is much smaller than a micron. It can be either in the form of a loose powder or a polycrystalline bulk material. Since "nanocrystalline materials" is one of the major buzzwords in the present decade, a variety of procedures to produce them have been elaborated varying from single atom or cluster condensation [1], through different chemical reactions [2] down to crystallisation from the bulk amorphous phase [3] or fragmentation by ball milling and different techniques of severe plastic deformation [4]. Latter are, in particular, the methods of equal channel angular pressing (ECAP) [5], high pressure torsion (HPT) [6] or corrugated cold rolling (CCR) [7]. Depending on the way the material was produced the grain size and size distribution and the strain or stress state, frozen into the crystallites, are varying over vide scales. The average crystallite size in inert-gas condensed metals like copper can vary between 5 to 20 nm together with dislocation densities at the order of magnitude of several times 10^{15} m^{-2} [8]. Nanocrystalline foils produced by electrodeposition can contain extremely high densities of stacking faults [9]. Stacking faults can become one of the major type of lattice defects in materials with very high stacking fault energy, e.g. in aluminium [9, 10], in which under conventional circumstances stacking faults can not be observed. Powder specimens produced by the chemical precursor method can be as small as 5 to 10 nm without even a single dislocation [11]. Hexagonal materials like titanium can be produced by the ECAP method to have an average grain size of about 50 nm and dislocation densities as high

as 10^{16} m^{-2} [12]. The strength of this material can exceed the strength of its conventional grain size counterpart by one order of magnitude [13].
Depending on the purpose for what the material has been prepared and the procedure by which it has been produced the microstructure can be very different. Due to constantly improving laboratory diffractometers [14] and high intensities and high angular resolution at powder diffraction beam lines at synchrotrons [15], powder diffraction has become one of the most powerful tools to determine the microstructure of nanocrystalline materials.
According to the kinematical theory of powder diffraction if the crystallites are free from lattice defects and the average crystallite size is larger than a few microns, however, not much larger than about 10 microns, the physical line profiles of the diffraction peaks are delta functions [16]. In the measured powder patterns these delta functions are convoluted with the instrumental functions of the diffractometer. To the best knowledge of the present EPDIC community such a powder pattern is realised by the measurement of a good LaB_6 standard specimen, e.g. the LaB_6 standard specimen. If the crystallites become smaller than about a micron or the lattice becomes distorted by any kind of lattice defects the physical line profiles will no longer remain delta functions. The deviations from the ideal delta function type can be very different. The diffraction peaks can be: (i) shifted, (ii) broadened, (iii) asymmetric, (iv) the broadening can be anisotropic with *hkl* and (v) any of these effects can be combined. In recent years it has been shown that the physical origin of strain anisotropy is the extremely anisotropic strain field of dislocations [17-24]. The effect of dislocation on the broadening of different *hkl* reflections, especially in polycrystalline materials, can be summarized in a fairly simple form of average dislocation contrast factors [24]. The fundamental parameters in determining the contrast factors can be determined by whole profile fitting numerical procedures. The physical interpretation of these parameters can reveal several details about the dislocation structure in nanocrystalline materials. The same whole profile fitting procedures provide size distribution density functions of the coherently diffracting domains [25-27]. The interpretation of size-distribution either in terms of crystallite size-distribution or in terms of other physical units in the material is the virtue of the experimentator. An important X-ray optical effect related to nanocrystalline particles smaller than about 5 nm has recently been discovered by Rafaja and coworkers [28]. It has been shown that if the coherently scattering domains are smaller than about 5 nm and the specimen has a strong texture, or if the adjacent domains have only very small orientation differences, the first few reflections can show considerably smaller broadening than what would correspond to the domain size according to the kinematical theory [28].

Crystallite size and size-distribution, the correlation between TEM and X-ray diffraction

Krill and Birringer have investigated the size-distribution of nanocrystalline palladium by both, TEM and X-ray line profile analysis [29]. The specimen was prepared by inert-gas condensation and cold compaction. The size Fourier coefficients were determined by the Warren-Averbach method [30] applied to the (111) and (222) reflections. Authors have shown that if the shape of the crystallites can be assumed to be more-or-less uniform, the area- and the volume-weighted mean crystallite sizes, $\langle x \rangle_{area}$ and $\langle x \rangle_{volume}$, can be determined from the linear intercept, L_0, and the area under the size Fourier coefficients, respec-

tively. These two mean sizes of crystallites can be used for the determination of a crystallite size-distribution function. By assuming further, that the size-distribution is log-normal, authors determined the median and the variance, m and σ, of the size-distribution function [29]. The particle size-distribution density was also determined by using dark field TEM micrographs of the same specimens. The good correlation between the TEM and X-ray data can be seen in figure 4 of reference [29].

Almost strain free ceria specimens were produced in the laboratory of Louër [25]. The high resolution TEM micrograph in figure 3 of reference [25] shows nanocrystalline particles in the range between 2 and 7 nm. The size distribution function was also determined by the Rietveld type whole-powder-pattern fitting, using pseudo-Voigt and Pearson VII profile functions and assuming Gaussian or log-normal size distribution functions. The TEM data have substantiated the log-normal size-distribution function as it can be seen in figure 4 of reference [25].

The size distribution of ball milled Si_3N_4 particles has been determined by TEM and X-rays [31]. The TEM micrograph in figure 6 of reference [31] shows well separated spherical crystallites. The size distribution density functions obtained from TEM and the whole profile fitting procedure of X-ray diffraction profiles (Multiple-Whole-Profile [MWP] fitting method, where the size and strain profile functions are physically sound theoretical functions [32]) are shown in figure 5 of reference [31]. A good correlation between the TEM and X-ray data can be observed.

Shape anisotropy in nanocrystalline ZnO was investigated by high resolution TEM and analysing the Williamson-Hall plots [33] of diffraction patterns [34]. An excellent particle model has been derived for ZnO as shown in figure 4 of reference [34]. Shape anisotropy in general has been investigated for different crystallite shapes in [35,36]. A relatively good correlation between TEM and X-ray size-distribution has been claimed in ball milled Cu and Ni and two of their alloys in [37].

The grain size in a large number of metals and alloys have been investigated concomitantly by TEM and X-rays [29,37-45]. When comparing all the available data it turns out that the TEM size is usually larger than the X-ray size. Often it is claimed that the X-ray size is related to small misorientations between adjacent subgrains [46]. It can be shown, however, that subgrains are not necessarily misoriented. Still, the size of subgrains is in strong correlation with the size provided by X-rays [47]. In most cases investigated here strain has also been determined. In spite that in very specific cases there is an apparent correlation between crystallite size and strain, see for example figure 5 of reference [41], the different metals or materials (cf. [48]) reveal very different correlations between size and strain. Plotting the average crystallite size versus strain a power-law correlation with the powers ranging between 1 and 3 can readily be observed. This behaviour indicates that strain and size are two different and independent physical parameters characterising the microstructure and any correlation between the two is only relevant for a specific material prepared by a specific method and the correlation cannot be generalized.

Strain from powder diffraction

Strain, as a feature of microstructure, is so diverse and complex that its treatment within such a short overview as the present one is out of question. The most what can be done here is that a list of keywords, far from being complete, is provided with a few references. First of all strain has two major categories: (i) homogeneous and (ii) inhomogeneous strain. On top of that, even these two different kinds of strain can interchange into each other if the volume in which they are considered are increased or decreased. For example, strain within a dislocation dipole can be homogeneous, however, far from the dipole it is inhomogeneous. Or, the strains caused by second order stresses in a polycrystal is homogeneous within a grain, however, it is inhomogeneous in the whole specimen. The sources of strain show also great variety. Lattice defects are the trivial sources: point defects like vacancies or interstitials, precipitates or inclusions, dislocations, grain boundaries, chemical fluctuations, open surfaces or contact surfaces in powders. The effects which they cause can be very different, not only depending on their species, but also on their amount and, especially on their distribution. Probably there is no unified or general way by which strain can be characterised, since any number deduced from an analysis provides just a rather specified one-sided aspect of the particular strain which prevails in the specimen. Especially, when the microstrain is given as a percentage number derived as the value of the root-mean-strain corresponding to a particular L value of the Fourier variable, its physical meaning cannot be related to any other parameter observed by other methods. There are serious attempts to extract strain in terms of dislocation densities and arrangements from X-ray diffraction patterns [32,36,49-55]. However, especially in nanocrystalline materials dislocations, in the classical sense, are not always the real source of strain, cf. [56]. The further elaboration of strain in nanocrystalline materials in terms of powder diffraction will be done elsewhere.

References

1. Gleiter, H., 1989, *Progr. Mater. Sci.*, **33**, 223-315.
2. Guillou, N., Auffrédic, J. P. and Louër, D., 1995, *Powder Diffr.*, **10**, 236-240.
3. Révész, Á., Heunen, G., Varga, L.K., Suriñach, S. and Baró, M.D., 2004, *J. Alloys & Compounds*, **368**, 164-168.
4. Valiev, R.Z., Ishlamgaliev R.K. and Alexandrov I.V., *Progr. Mater. Sci.*, 2000, **45**, 103.
5. Segal, V.M., 1995, *Mater. Sci. Eng.* **A197**, 157–164.
6. Zehetbauer, M.J., Stüwe, H.P., Vorhauer, A., Schafler, E. and Kohout, J., 2003, Adv. Eng. Mater., **5**, 330-337.
7. Huang, J. Y., Zhu, Y. T., Jiang H. and Lowe, T. C., 2001, *Acta mater.*, **49**, 1497–1505.
8. Ungár, T., Ott, S., Sanders, P., Borbély, A. and Weertman, J. R., 1998, *Acta Mater.* **46**, 3693-3699.
9. Jia, D., Ramesh, K.T., Ma, E., Lu L. and Lu, K., 2001, *Scripta mater.*, **45**, 613.

10. Liao, X. Z., Zhou F., and Lavernia, E. J., Srinivasan, S. G., Baskes, M. I., He, D. W. and Zhu, Y. T., 2003, *Appl. Phys. Let.*, **83,** 632-634.
11. Audebrand, N., Guillou, N., Auffrédic J. P. and Louër, D., 1996, *Thermochim. Acta*, **286**, 83-87.
12. Zhu Y.T., Huang, J.Y. Gubicza J., Ungár, T. Wang Y.M., Ma, E. and Valiev, R.Z., 2003, *J. Mater. Res.*, **18**, 1908.
13. Stolyarov, V.V., Zhu, Y.T., Alexandrov, I.V., Lowe, T.C. and Valiev, R.Z., 2000, *Mater. Sci. Eng.*, **A299**, 59.
14. Vermeulen A.C.and Houtman, E., 2000, *Mater. Sci. Forum*, **347-349**, 17-22.
15. Fitch, A. N., 1996, *Mater. Sci. Forum*, **228–231**, 219.
16. Warren, B.E., 1969/1990, *X-ray Diffraction*, Dover Publ., New York.
17. Krivoglaz, M. A., 1996, in *X-ray and Neutron Diffraction in Nonideal Crystals*, Springer-Verlag, Berlin Heidelberg New York.
18. Wilkens, M., 1970, *phys. stat. sol.* (a) **2**, 359-370.
19. Wilkens, M., 1970, in *Fundamental Aspects of Dislocation Theory*, ed. J. A. Simmons, R. de Wit, R. Bullough, Vol. II. Nat. Bur. Stand. (US) Spec. Publ. No. 317, Washington, DC. USA, p. 1195-1221.
20. Klimanek, P. and Kuzel Jr., R. J., 1988, *Appl. Cryst.* **21**, 59-66.
21. Kuzel Jr., R. & Klimanek, P. J., 1988, *Appl. Cryst.*, **21**, 363-368.
22. Ungár, T. and Borbély, A., 1996, *Appl. Phys. Lett.*, **69**, 3173-3175.
23. Ungár, T., Dragomir, I., Révész, Á., and Borbély, A., 1999, *J. Appl. Cryst.* **32**, 992-1002.
24. Ungár, T. and Tichy, G., 1999, *phys. stat. sol.* (a) **171**, 425-434.
25. Langford, J.I., Louër, D. and Scardi, P., 2000, *J. Appl. Cryst.*, **33**, 964-974.
26. Scardi, P. and Leoni, M., 2002, *Acta Cryst.*, **A58** 190-200.
27. Ungár, T., Gubicza, J., Ribárik, G. and Borbély, A., 2001, *J. Appl. Cryst.*, **34**, 298-310.
28. Rafaja, D., Klemm, V., Schreiber, G., Knapp, M. and Kuzel, R., 2004, *J. Appl. Cryst.*, **37**, 613-620.
29. Krill, C. E. and Birringer, R., 1998, *Phil. Mag.*, **A77**, 621-640.
30. Warren, B. E. and Averbach, B. L., 1950, *J. Appl. Phys.* **21**, 595-595.
31. Gubicza, J., Szépvölgyi, J., Mohai, I., Ribárik, G. and Ungár, T., 2000. *Mat. Sci. Eng.*, **A280**, 263-269.
32. Ribárik, G., Ungár, T. and Gubicza, J., 2001, *J. Appl. Cryst.*, **34**, 669-676.
33. Williamson, G. K. and Hall, W. H., 1953, *Acta metall.*, **1**, 22-31.
34. Louër, D., Auffredic, J.P., Langford, J.I., Ciosmak, D. and Niepce, J.C., 1983, *J.Appl.Cryst.*, **16**, 183-191.
35. Vargas, R., Louër, D. and Langford, J. I., 1983, *J. Appl. Cryst.*, **16**, 512-518.

36. Scardi, P. and Leoni, M., 2001, *Acta Cryst.*, **A57**, 604-613.
37. Guerrero-Paz, J. and Jaramillo-Vigueras, D., 1999, *NanoStructured Materials*, **11**, 1195–1204.
38. Valiev, R. Z., Kozlov, E. V., Ivanov, Yu. F., Lian, J., Nazarov, A. A. and Baudelet, B., 1994, *Acta metall. mater.*, **42**, 2467-2476.
39. Terwilliger, Ch. D. and Chiang, Y. M., 1995, *Acta Met. Mater.*, **43**, 319-328.
40. Sanders, P.G., Fougere, G.E., Thompson, L.J., Eastman, J.A. and Weertman, J.R., 1997, *Nanostruct. Mater.*, **8**, 243.
41. Tian, H.H. and Atzmon, M., 1999, *Acta mater.*, **47**, 1255-1261
42. Gubicza, J., Dragomir, I. C., Ribárik, G., Zhu, Y. T., Valiev, R. Z. and Ungár, T., 2003, *Mater. Sci. Forum*, **414-415**, 229-234.
43. Zhu, Y.T., Huang, J.Y., Gubicza, J., Ungár, T., Wang, Y.M., Ma, E. and Valiev, R.Z., 2003, *J. Mater. Res.*, **18**, 1908-1917.
44. Gubicza, J. Nam, N.H. Balogh, L. Hellmig, R.J. Stolyarov, V.V. Estrin, Y. and T. Ungár, 2004, *J. Alloys Comp.*, **378**, 248–252.
45. Sanders, P.G., Fougere, G.E., Thompson, L.J., Eastman, J.A. and Weertman, J.R., 1997, *Nanostruct. Mater.*, **8**, 243.
46. Bolmaro, R.E., Brokmeier, H.G., Signorelli, J.W.,Fourty, A. and Bertinetti, M.A., in *Diffraction Analysis of the Microstructure of Materials*, edited by E.J. Mittemeijer & P. Scardi (Berlin: Springer), pp. 391-410.
47. Tichy, G., Ungár, T., Gubicza, J. and Hellmig, R., 2004, in preparation.
48. Ungár, T., Martinetto, P., Ribárik, G., Dooryhee, E., Walter, Ph. and Anne, M., 2002, *J. Appl. Phys.*, **91**, 2455-2465.
49. Islamgaliev, R.K., Chmelik, F. and Kuzel, R., 1997, *Mater. Sci. Eng.*, **A237** 43-51.
50. Ungár, T., Leoni, M. and Scardi, P., 1999, *J. Appl. Cryst.*, **32**, 290-295.
51. Ungár, T., Gubicza, J., Ribárik G. and Borbély, A., 2001, *J. Appl. Cryst.*, **34**, 298–310.
52. Scardi, P. and Leoni, M., 2002, *Acta Cryst.*, **A58**, 190-200.
53. Borbély, A. and Groma, I., 2001, *Appl. Phys. Letters*, **79**, 1772-1774.
54. Ribárik, G., Gubicza, J. and Ungár, T., 2004, *Mater.Sci.Eng.*, A, in the press.
55. Kužel, R., Matej, Z., Cherkaska, V., Pešicka, J., Cizek, J., Procházka, I. and Islamgaliev, R.K., 2004, *J. Alloys Comp.*, in the press.
56. Palosz, B., Grzanka, E., Gierlotka, S., Stel'makh, S., Pielaszek, R., Bismayer, U., Neuefeind, J., Weber, H.-P., Proffen, Th., Von Dreele, R. and Palosz, W., 2002, *Z. Kristallographie*, **217**, 497-509.

Acknowledgements. The author is grateful to the Hungarian National Scirnce Foundation, OTKA T-043247 and T-046990.

Z. Kristallogr. Suppl. **23** (2006) 319-324

Preparation and characterization of isometric gold nanoparticles with pre-calculated size

M. Šlouf[1], R. Kužel[2], Z. Matěj[2]

[1]Institute of Macromolecular Chemistry, Academy of Sciences of the Czech Republic, Heyrovskeho nam. 2, 162 06 Praha 6, Czech Republic
[2]Department of Electronic Structures, Faculty of Mathematics and Physics, Charles University, 121 16 Praha 2, Ke Karlovu 5, Czech Republic
*Contact author; kuzel@karlov.mff.cuni.cz

Keywords: line profile analysis, nano materials, transmission electron microscopy

Abstract. Four colloidal solutions containing gold nanoparticles of various sizes (around 5, 10, 30 and 80 nm) were prepared. Our preparation technique enables preparation of particles with pre-calculated size, i. e. the size of the particles can be chosen (within the range of 4 - 100 nm) and the experiment adjusted to obtain particles of the desired size. They were studied by transmission electron microscopy, UV/vis spectroscopy and X-ray diffraction. The particle sizes obtained by the three methods were in quite a good agreement. TEM and X-ray diffraction revealed also a presence of twins.

Introduction

Nanoparticles of precious metals like gold, silver, platinum have been intensively studied in last years. They found applications as surfaces in chemical analysis, as carriers of molecules, as markers in transmission electron microscopy (TEM) etc. Metal nanoparticles can compose more or less stable colloid solutions. Their size can be controlled by appropriately selected process of preparation. In this work, the gold particles were prepared and characterized in solution by UV/vis spectroscopy and in solid state by TEM and powder diffraction.

Experiment

Preparation of Au nanoparticles

Preparation of colloidal Au nanoparticles was described as early as at the end of 19th century. We used a combination of the techniques already described [1]. They were slightly modified so that we were able to obtain particles with arbitrary size. Our new technique is based on several-step reduction of $H[AuCl_4]$ water solution by combination of $Na[BH_4]$ and NH_2OH solutions. The whole preparation procedure is as follows: (i) choice of an average particle size d_{theor} (ii) calculation of solution concentrations, (iii) performing $H[AuCl_4]$ reduc-

tion according to previous step and (iv) experimental determination of real average particle size d_{exp}. Usually it is found $d_{exp} < d_{theor}$, but the discrepancy is less than 20 %. In this study, we intended to prepare four different sets of particles.

UV/vis spectra
Colloidal solutions of gold nanoparticles appear red in colour. The exact hue of the solution depends, among other things, on the size of the particles and can be measured by means of UV/vis spectroscopy. UV/vis spectra of gold nanoparticles in water were measured in the range of wavelength λ = 300 - 900 nm with step 2 nm.

Transmission electron microscopy (TEM)
Approx. 2 ml of Au colloidal solution was transferred to microscopic grid covered with carbon film and left to evaporate. Dry Au particles were examined in microscope JEM 200CX (Jeol, Japan). All TEM microphotographs were taken at acceleration voltage 100 kV, recorded on a photographic film and digitized with pc-controlled digital camera DXM1200 (Nikon, Japan). Image analysis of TEM micrographs was performed with program LUCIA (LIM, Czech Republic).

X-ray diffraction (XRD)
Films of colloidal Au particles were collected onto the surface of a microscopic glass and measured with a Philips X'Pert PRO diffractometer. A laboratory X-ray tube and the Goebel mirror producing a quasi parallel beam of Cu Kα doublet radiation and a parallel slit collimator with a flat monochromator in the diffracted beam were used. In this parallel beam geometry 2θ scans with an angle of incidence $\gamma = 2°$ and a counting time 30-50 s (different for various samples) were performed for each sample. A large step $\Delta 2\theta = 0.1°$ was selected because of large profile broadening. The NIST LaB_6a standard powder on pure glass substrate was measured for correction of instrumental effects. Diffraction line broadening was analysed by the modified Williamson-Hall (WH) plots [e.g. 2, 3] and the whole profile modelling (WPPM) approach with the program PM2000 [4, 5].

Results

Particle size & shape
In this study we intended to prepare four different sets of particles, denoted as Au1, Au2, Au3 and Au4, with average sizes 4.5, 11.7, 35.0 and 105.8 nm, respectively. The average sizes and shapes of the particles were determined by image analysis of TEM micrographs (figures 1 - 4). The particles were more-or-less isometric, approximately spherical in shape. The crystal planes were observable as well, especially for larger particles (figure 3). The agreement between theoretically calculated and experimentally determined sizes was quite good (table 1).

Agreement between UV/vis and TEM
UV/vis spectra of the Au colloidal solution exhibit one local absorption maximum, denoted as λ_{max} in the following text. The maximum occurs due to surface plasmon absorption. According to theory, λ_{max} should shift slowly towards higher λ with increasing size of the parti-

cles. In our study the size of the particles d_{exp} was determined by TEM and corresponding shift of λ_{max} was clearly observed (figure 5). Moreover, it was found that λ_{max} is a linear

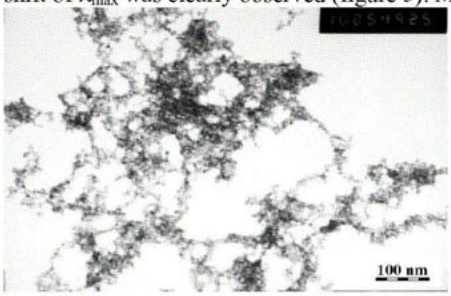

Figure 1. TEM microphotograph of colloid Au1.

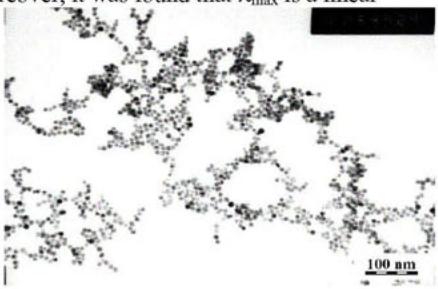

Figure 2. TEM microphotograph of colloid Au2.

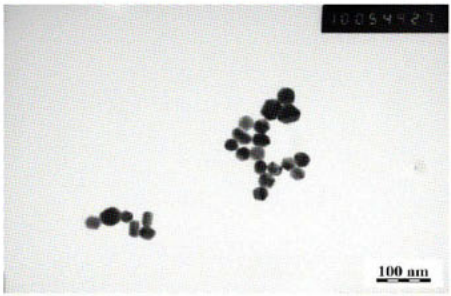

Figure 3. TEM microphotograph of colloid Au3.

Figure 4. TEM microphotograph of colloid Au4.

function of d_{exp} in the whole range (figure 6), which is in agreement with our previous studies.

X-ray powder diffraction line profile analysis

Rather surprising feature of studied samples is a strong anisotropy of line broadening and a sharp slope of the WH plot (figure 7). Anisotropy of line broadening cannot be justified by the size broadening effect of any isometric shape of particles. It can be explained, if dislocations [e.g. 3, 6-8] and stacking faults [e.g. 9, 10] are taken into considerations. Then the modified Williamson-Hall plot (x-axis multiplied by the contrast factor accounting for the broadening anisotropy – calculated by the ANIZC program [8]) is quite smooth (figure 8). The same is true for the whole powder pattern modelling method. The WPPM fits are significantly improved if dislocations, deformation and twin faults are included in the microstructure refinement (figure 9). Without this option a good fit cannot be achieved. Anisotropic line broadening of nanoparticles produced by a solution route has been also observed e.g. in [11].

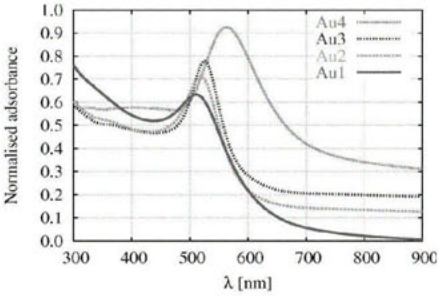

Figure 5. UV/vis spectra of colloidal solutions of Au1, Au2, Au3 and Au4.

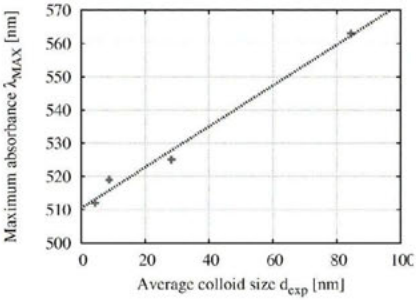

Figure 6. Maximum absorption of colloidal solution λ_{max} as a function of experimentally determined size of colloidal particles d_{exp}.

Because of low intensity scattered by a small amount of gold in thin film samples and the low resolution of the employed experimental geometry the counting statistics ($R_{expected}$ = 4.80% for Au-2, 9 parameters) is not completely sufficient for determination of all microstructural parameters simply running the WPPM. However, diffraction patterns were simulated for many sets of microstructure parameters. The lognormal grain size distribution was used, but it was assumed that its asymmetry is not too high (basing on the TEM investigations). Resulting R-factors (R_{wp} = 5.97%, GOF = R_{wp}/ $R_{expected}$ = 1.24 for Au-2) and also shape of simulated peaks and their agreement with measured data were studied and confidence limits of refined parameters (many times greater than errors estimated from LSQ-fitting) were determined (table 1). The errors of the grain size mean values are comparable with the widths of the grain size distributions. These values are significantly affected by the grain size distribution shape, which cannot be uniquely determined from our measured X-ray data.

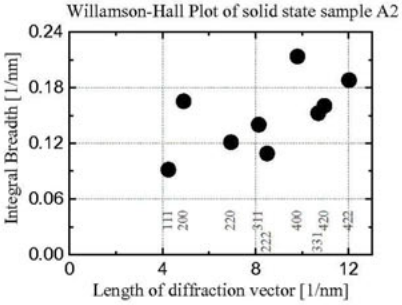

Figure 7. Williamson-Hall plot for A2.

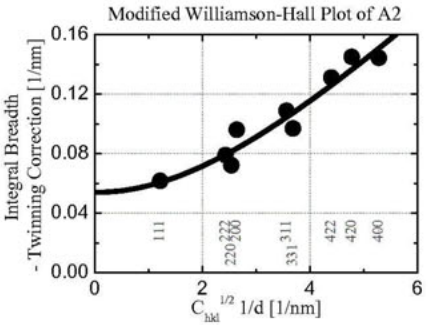

Figure 8. Modified Williamson-Hall plot for A2. Line broadening caused by twinning was subtracted from measured integral breadths.

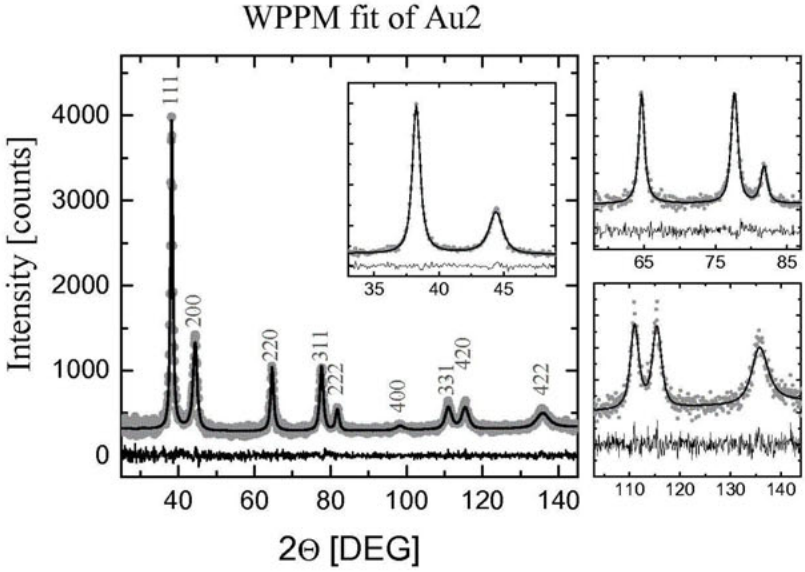

Figure 9. Whole profile modelling of diffraction pattern of sample Au2 by using the program PM2000 [4, 5].

X-ray results are in a reasonable agreement with the observations by other methods for samples Au2-4. Finally, very good fits of diffraction patterns were obtained but physical interpretation of the parameters - twin faults and especially high dislocation densities of the order of 10^{15} m^{-2} (strains) should be further critically discussed and investigated. However, presence of twins is also indicated on TEM pictures (figure 3, different contrast inside a single particle).

Conclusions

- A new method for preparation of colloidal isometric Au nanoparticles in solution was introduced. Size of the particles can be selected in advance within the range from 4.5 to 120 nm.
- With increasing size of the particles the size distribution slightly broadens.
- The particles were characterized in solution by means of UV/vis spectroscopy and in the solid state by TEM and XRD. As to particle size, a good agreement between the three techniques was found.

Au nanoparticles with well-defined size can be employed in many fields. Our final goal is to use them as calibration particles for dynamic light scattering experiments.

Table 1. Agreement among theoretically calculated values of average diameter of the particles d_{theor}, experimentally determined average diameter d_{exp} and maximum of the absorption λ_{abs}.

	d_{theor} (nm)	d_{exp} (nm)	λ_{abs} (nm)	d_{diff} (nm)	β_{twin}
Au1	4.5	4.3	512	10 ± 6	0.08 ± 0.03
Au2	11.1	8.8	519	15 ± 5	0.07 ± 0.02
Au3	33.4	28.3	525	31 ± 5	0.05 ± 0.01
Au4	101.5	84.5	563	92 ± 20	0.012 ± 0.005

References

1. J. Turkevich, P. C. Stevenson, J. Hillier, 1951, *Disc. Faraday Soc.*, **11**, 55-75.
2. T. Ungár, I. Dragomir, Á. Révész, A. Borbély, 1999, *J. App. Cry*st., 32, 992-1002.
3. G. Ribárik, T. Ungár and J. Gubicza, 2001, *J. Appl. Cryst.*, **34**, 669-676.
4. P. Scardi, M. Leoni, 2002, *Acta Cryst. A*, **58,** 190-200.
5. P. Scardi, M. Leoni, Y. H. Dong, 2000, *Eur. Phys. J. B*, **18,** 23-30.
6. M. A. Krivoglaz, 1996, *X-ray and Neutron Diffraction in Nonideal Crystals* (Berlin: Springer-Verlag).
7. R. Kužel and P. Klimanek, 1989, *J. Appl.Cryst.,* **22**, 299-307.
8. A. Borbély, J. Dragomir-Cernatescu, G. Ribárik, T. Ungár, 2003, *J. Appl. Cryst.*, **36**, 160-162.
9. B. E. Warren, 1969, *X-ray diffraction* (Addison-Wesley).
10. P. Scardi, M. Leoni, R. Delhez, 2004, *J. Appl. Cryst.*, **37**, 381-390.
11. T. Ungár, I. Dragomir-Cernatescu, D. Louer, N. Audebrand, 2001, *J. Phys. Chem. Sol.* **62** , 1935-1941.

Acknowledgement. This work was supported through grant GACR 106/04/1118 awarded by the Grant Agency of the Czech Republic. This work is also a part of the research plan MSM 0021620834 financed by the Ministry of Education of the Czech Republic.

Z. Kristallogr. Suppl. **23** (2006) 325-330

Bulk characterization of multiwall carbon nanotubes

Jette Oddershede[1] and Kenny Ståhl[1,*]

[1]Department of Chemistry, Technical University of Denmark, Building 207, DK-2800 Lyngby, Denmark
[*]Contact author; e-mail: kenny@kemi.dtu.dk

Keywords: carbon nanotubes, Debye equation, structure simulations

Abstract. The bulk structural properties of multiwall carbon nanotube samples can be estimated by comparing experimental X-ray powder diffractograms with simulations obtained using the Debye equation. Results typically indicate that the samples contain tubes with dimensions distributed within the following bounds: lengths of 5-15 nm, diameters of 15-25 nm, and walls 10-20 layers thick with a spacing between adjacent layers of 3.35-3.60 Å. The apparent short tube lengths obtained can be explained by the observed bending of the tubes. Furthermore it is possible to obtain information about impurities.

Introduction

Multiwall carbon nanotubes (MWCNTs) consist of several layers of rolled graphene sheets. Since this new type of material was discovered some 15 years ago [1] it has been studied extensively and the suggested applications have been numerous. Many of the studies have focused on the structure of the tubes because of the intimate structure/function relationship. Studies applying TEM and ED [2,3] are very illustrative, but both these structural probes suffer from the fact that they are local. The bulk properties of the sample depend on the average structure, which can only be determined in combination with a global probe. Powder diffraction is the obvious choice for studying the bulk structure of MWCNTs as the tubes are periodic in nature and give rise to distinct diffraction peaks. In addition, powder diffraction will detect crystalline impurities. Many different models have been suggested to explain the diffraction pattern arising from the MWCNTs. The simplest of these are of the disordered graphite type where structural parameters such as the interlayer spacing, the crystallite size and the ordering within a single graphene layer are refined [4-6]. Recently a more sophisticated approach taking into account the actual structure of the tubes has been suggested [7-9]. The basis for this approach is the Debye equation (1) stating that the diffracted intensity from a collection of scatterers can be calculated as a sum over all the interatomic distances r_{ij} [10].

$$I(Q) = \sum_{i,j} f_i(Q) f_j(Q) \frac{\sin(Qr_{ij})}{Qr_{ij}}. \qquad (1)$$

Here $Q = 4\pi \sin\theta / \lambda$ is the scattering vector. The method thus requires the calculation of all atomic positions for a given MWCNT structure followed by the application of equation (1) to obtain the diffractogram. The structural parameters of the MWCNTs can then be systematically varied and the simulated diffractograms compared to the experimental ones in order to obtain a qualified estimate of the bulk structure. Studies of the effects of varying different structural parameters have been carried out previously [7,8], but in a very wide Q-range (0-24 $Å^{-1}$). For these comparative studies a standard crystallographic Q-range (0-7 $Å^{-1}$) is sufficient, and using a longer wavelength will in general give higher angular resolution. The present work has by means of the Debye equation studied the effects of varying: I) the chiral angle, II) the rolling characteristics, III) the structure perpendicular to the tube, and IV) the bending of the tubes in comparison to experimental X-ray diffraction data from bulk MWCNT samples.

Simulations

The MWCNT diffractograms closely resemble that of graphite. Peaks of the *hk*0 (within a layer) and 00*l* (between layers) type dominate due to the limited correlation between different graphene sheets (turbostratic disorder) [3,5,11]. The graphite 100 (2.95 $Å^{-1}$) and 110 (5.11 $Å^{-1}$) peaks are found in a more saw-toothed version due to the turbostratic stacking [12,13] and/or the curvature of the graphene sheets [3]. The peaks corresponding to the interlayer spacing, 002 (1.85 $Å^{-1}$), 004 (3.70 $Å^{-1}$), etc. are shifted to slightly lower Q-values, reflecting the fact that the spacing between the multiple walls of the tubes is slightly larger (3.40 Å) than the interlayer spacing in graphite (3.35 Å).

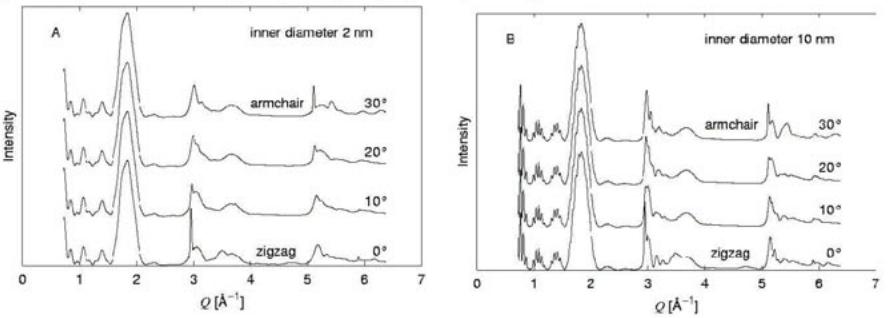

Figure 1. Variation of the chiral angle for different diameters.

I) Chiral angle. From figure 1A it is clear that the value of the chiral angle (the angle between the interatomic vector and the cylinder axis of the tube) greatly affects the appearance of the diffractogram when the diameter of the tube is small. Figure 1B shows that the effect is less pronounced for tubes with larger diameter (the tube length and wall thickness is the same for both diffractograms), but nevertheless it is still present contrary to the conclusions of Koloczek et al.: "*...for wider carbon nanotubes no conclusion about chirality can be drawn from analysis of their diffraction patterns.*" [8]. The reason for this conclusion is probably that the analyses were performed over the full Q-range of their simulated diffractograms (0-24 $Å^{-1}$), while the differences are better seen in the details of a more limited Q-range. Based on the observations concerning the chiral angle and the appearance of the ex-

perimental diffractograms given in figure 6 it was chosen to consistently use a chiral angle of 15° in the following.

II) Rolling characteristics. The question of whether the MWCNTs are structured as concentric cylinders or as scrolls (figure 2B) has been addressed a number of times [5,12-16] with very different approaches and results, without reaching a definite conclusion. It was previously noted [8] that concentric cylinders with a very constant d-spacing between adjacent cylinders give rise to a splitting of the interlayer diffraction peaks (figure 2A). However, it can easily be shown that these splittings average out if a continuous distribution of different tube diameters (a very realistic model of a true bulk sample) is applied. In figure 2A this average can be compared to the diffractogram simulated for a single scroll type MWCNT with a diameter corresponding to the mean of the distribution used for the concentric average. As there is hardly any difference between the concentric average and the scroll, the conclusion must be that it is not possible to distinguish between averaged concentric cylinders and scrolls from a standard diffraction experiment. Since the latter simulations are much faster to perform, only simulations for scroll type MWCNTs are presented in the following.

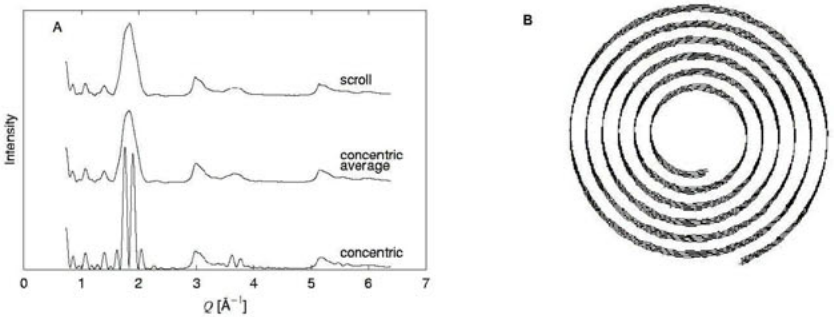

Figure 2. Concentric or scroll type tubes?

III) Structure perpendicular to the tube. Variations in the length and diameter of the MWCNTs affect only the *hk*0 peaks, and these effects have already been extensively described [8]. Instead focus was brought into the effects causing a broadening of the 00*l* interlayer peaks. These have previously been characterized as size (arising from the wall thickness) and strain (due to a distribution of d-spacings) broadening effects [3, 5, 11, 13].

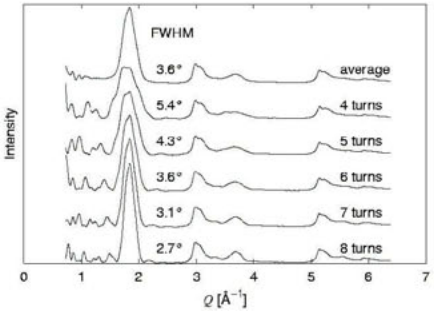

Figure 3. Effects of varying the wall thickness of the tubes.

It is obvious that a finite number of layers will lead to a broadening of the 00*l* peaks. In addition the simulations in figure 3 show that a true sample contains a distribution of different wall thicknesses, as the ripples at low Q-values disappear when an average is performed. From an inspection of the experimental diffractograms in figure 6 it is easily seen that a strain broadening of the 00*l* peaks is present, since the 004 peak is much wider as compared to the 002 peak than what would be expected if only size broadening was considered. Furthermore the experimentally observed broadening is asymmetric whereas size broadening is purely symmetric. The asymmetry can be modelled by letting the d-spacing vary between 3.35 Å and 3.60 Å with a higher probability of the smaller spacings.

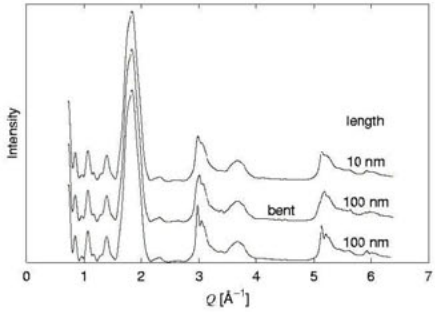

Figure 4. Effects of bending the tubes.

IV) Bending of the tubes. Figure 4 illustrates how the diffractogram from a tube with a length of 100 nm resembles that of a tube with a length of only 10 nm if the longer tube is bent with a 160 nm radius of curvature (compare with figure 5A). Defects in the tubes (figure 5) will have the same effect on the diffractogram; to make the tubes appear shorter than they actually are.

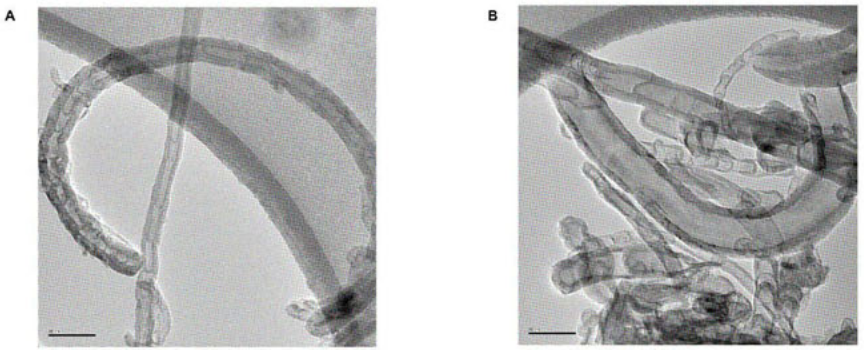

Figure 5. TEM images corresponding to the experimental diffractograms in figure 6 (scale bar 50 nm). A purchased as: Outer diameter 15 ± 5 nm, length 1-5 μm, and purity ~ 95 %. B purchased as: Outer diameter 30 ± 10 nm, length 1-5 μm, and purity > 95%..

Discussion

The simulated diffractogram in figure 6A is for a scroll type MWCNT with a chiral angle of 15°, an isotropic temperature factor coefficient of 2 Å^2 to describe the thermal motions, 10-14 turns, a length of 7.5 nm, an inner diameter of 12 nm (outer diameter 18-21 nm), and a distribution of d-spacings between 3.35 Å and 3.60 Å. The background is modelled by a 6th order Chebyshev polynomial. The fit between experiment and simulations is excellent except for the low Q side of the 002 peak (perhaps even larger d-spacings than 3.60 Å are present in the sample) and the high Q side of the 100 peak (possibly arising because the stacking of graphene layers is not completely turbostratic giving rise to a low intensity graphite 101 peak at 3.1 Å^{-1}). The simulated diffractogram in figure 6B is for a MWCNT with 16-20 turns, an outer diameter of 22-25 nm and a length of 10 nm.

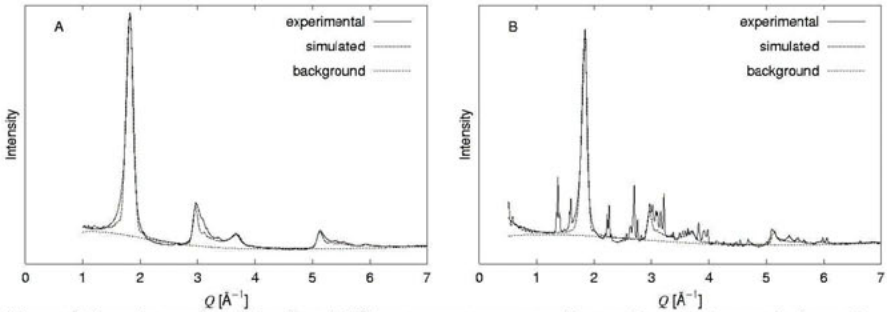

Figure 6. Experimental and simulated diffractograms corresponding to the TEM images in figure 5. The experimental diffractograms were recorded in transmission mode with a HUBER G670 Guinier camera (λ = 1.087 Å) at beam line I711 (MAXLAB, Lund, Sweden) on tablets pressed from 50 mg of commercial MWCNT samples.

The experimental diffractogram of figure 6B is recorded on a sample with contaminations from carbides of Fe, Co and/or Ni since these metals were used as catalysts in the fabrication of the MWCNTs. From the corresponding TEM image (figure 5B) it is obvious that this sample contains more impurities than the one shown in figure 5A, but how much more and which type of impurities it is not possible to tell from the TEM images. The increased amount of impurities is also evident from the experimental diffractograms in figure 6, but as opposed to the TEM technique X-ray diffraction offers the opportunity to identify the impurities.

The fact that even though TEM images demonstrate that the tubes are of the order 1 µm long, the simulations only indicate lengths in the order of 10 nm has been noted previously [9]. In the light of the simulations of bent MWCNTs in figure 4 and the TEM images in figure 5, the most probable explanation to this discrepancy is the bent shapes of the tubes. Previous TEM studies [12] have suggested that a high concentration of defects in the tubes could be another reason for coherence lengths in the order of only 10 nm.

Conclusions

Comparing experimental and simulated powder diffractograms, even in the standard Q-range 0-7 $Å^{-1}$, is an excellent way to determine bulk structural parameters for MWCNTs. It is possible to detect and identify impurities and to determine the average chiral angle, while concentric or scroll type tubes cannot be distinguished. Good estimates of the tube dimensions, i.e. length, diameter, wall thickness and interlayer spacing, and more importantly the distribution of these can be obtained from the comparisons. The simulations have made it evident that all of the structural parameters in the bulk samples should be determined as distributions rather than as single values.

One considerable problem still remains: the effects of the different parameters on the appearance of the diffractograms correlate strongly. A way to solve this correlation problem and more unambiguously quantify the experimental bulk tube dimensions is to conduct PCA (Principal Component Analysis) on diffractograms simulated for MWCNTs with different structural characteristics and extract basis functions corresponding to each parameter. It should then be possible to describe the experimental diffractograms as linear combinations of the basis functions, and to simply read the structural characteristics of the bulk samples from the coefficients. This development is in progress.

References

1. Iijima, S., 1991, *Nature*, **354**, 56.
2. Amelinckx, S., Lucas, A. & Lambin, P., 1999, *Rep. Prog. Phys.*, **62**, 1471.
3. Lambin, Ph., Loiseau, A., Culot, C. & Biró, L.P., 2002, *Carbon*, **40**, 1635.
4. Shi, H., Reimers, J.N. & Dahn, J.R., 1993, *J. Appl. Cryst.*, **26**, 827.
5. Reznik, D., Olk, C.H., Neumann, D.A. & Copley, J.R.D., 1995, *Phys. Rev. B*, **52**, 116.
6. Pasqualini, E., 1997, *Phys. Rev. B*, **56**, 7751.
7. Kołoczek, J., Kwon, Y.-K. & Burian, A., 2001, *J. Alloys Comp.*, **328**, 222.
8. Kołoczek, J. & Burian, A., 2004, *J. Alloys Comp.*, **382**, 123.
9. Kołoczek, J., Burian, A., Dore, J.C. & Hannon, A.C., 2004, *Diamond Rel. Mat.*, **13**, 1218.
10. Debye, P., 1915, *Ann. Phys.*, **46**, 809.
11. Burian, A, Dore, J.C., Fischer, H.E., Sloan, J. & Szczygielska, A., 1999, *Proceedings of SPIE*, **3725**, 107.
12. Zhou, O., Fleming, R.M., Murphy, D.W., Chen, C.H., Haddon, R.C., Ramirez, A.P. & Glarum, S.H., 1994, *Science*, **263**, 1744.
13. Maniwa, Y., Fujiwara, R., Kira, H., Tou, H., Nishibori, E., Takata, M., Sakata, M., Fujiwara, A., Zhao, X., Iijima, S. & Ando, Y., 2001, *Phys. Rev. B*, **64**, 073105.
14. Bandow, S., 1997, *Jpn. J. Appl. Phys.*, **36**, 1403.
15. Cumings, J. & Zettl, A., 2000, *Science*, **289**, 602.
16. Xu, G., Feng, Z., Popovic, Z, Lin, J. & Vittal, J.J., 2001, *Adv. Mater.*, **13**, 264.

Z. Kristallogr. Suppl. **23** (2006) 331-336

Neutron diffraction studies of the atomic vibrations of bulk and surface atoms of nanocrystalline SiC

S. Stel'makh[1,*], E. Grzanka[1], Y. Zhao[2], W. Palosz[3], B. Palosz[1]

[1]Institute of High Pressure Physics UNIPRESS, ul. Sokolowska 29/37, 01-142 Warsaw, Poland
[2]Los Alamos Neutron Science Center, Los Alamos, NM 87545, USA
[3]BAE Systems, NASA, Marshall Space Flight Center, SD46, Huntsville, AL 35812, USA
[*]Contact author; e-mail: svrit@unipress.waw.pl

Keywords: powder diffraction, neutron diffraction, atomic vibrations

Abstract. Thermal atomic motions of nanocrystalline SiC were characterized by two temperature atomic factors B_{core} and B_{shell}. With the use of wide angle neutron diffraction data it was shown that at the diffraction vector of above 15 $Å^{-1}$ the Wilson plot gives directly the temperature factor of the grain interior (B_{core}). At lower Q values the slope of the plot provides information on the relative amplitudes of vibrations of the core and shell atoms.

Introduction

It is widely recognized that a nanocrystal has non-uniform structure where atoms located at the surface differ from those in the grain interior with respect to their surrounding and, thus, have different properties. A diffraction experiment can determine the static (average) equilibrium arrangement of the atoms and elastic properties of materials. This work is dedicated to examination of thermal atomic motions in nanocrystals based on the analysis of Bragg type scattering. Theoretical calculations show that vibrational density of states of the inner atoms of nanograins is similar to those in the bulk [1 - 3] and, since the atoms at the surface have fewer neighbors, they vibrate with amplitudes larger than those in the bulk. A diffraction experiment provides information on all atoms forming the material and their properties. The "only" problem is in finding methods of elaboration of the diffraction experiments (of nanocrystalline material) which would discern between different properties of the core and shell atoms. In this work we discuss whether in a diffraction experiment we can distinguish between and evaluate thermal vibrations of inner and surface atoms of nanocrystals of SiC. We focus on application of the Wilson method of determination of the atomic temperature factors with the use of wide angle neutron diffraction. Recently we used X-ray diffraction to examine thermal atomic motions in 8 nm nanocrystalline SiC for loose powders and dense sintered materials [4]. We showed that some qualitative information concerning overall

temperature factors and Debye temperatures can be withdrawn from those data. We found that the key problem in determination of the temperature factors is separation of Thermal Diffuse Scattering (TDS) from Bragg scattering. Here we show that neutron diffraction is much better suited for such studies. (*Note*: alternative to examination of thermal atomic motions with application of Bragg scattering and Wilson method is PDF analysis [5]. It requires high quality data to obtain G(r) functions for which quantitative analysis of shapes of individual peaks can be done. Our data are not good enough to do such analysis.)

Experimental

SiC powders with the average grain size of 8, 15, and 23 nm obtained from silane by laser-driven synthesis [6] were examined. Before the measurements, powders were annealed in vacuum for 3 h at 400°C. Based on the analysis of the core-shell structure of these powders with application of the concept of the apparent lattice parameter (*alp*) [7,8], we evaluated the thickness of the surface shell and found it to be between 0.5 and 1 nm. That corresponds to a content of the surface atoms between 50% in the smallest and 20% in the largest grains. Neutron diffraction measurements were done using the HIPD diffractometer at LANSCE in the Los Alamos National Laboratory (Q_{max} = 28 Å^{-1}).

Data analysis

Determination of the overall thermal parameter B_T using the Wilson plot

It is a common practice to describe isotropic thermal vibrations using an overall temperature parameter B_T [9, 10]. This parameter is a quantity proportional to the mean square of the atomic displacement $\langle u^2 \rangle$: $B_T = 8\pi^2 \langle u^2 \rangle$. In a diffraction experiment, due to thermal vibrations, a decrease in Bragg intensities with an increase in the diffraction vector Q is observed:

$$I = I_o e^{-2M}, \tag{1}$$

where: $2M = 2B_T(\sin^2\Theta/\lambda^2)$, ($Q = 4\pi \sin\Theta/\lambda$). Simultaneously with a decrease (attenuation) in Bragg intensities, there is an incoherent scattering (TDS) which increases with an increase in the diffraction vector:

$$TDS = N(1 - e^{-2M}). \tag{2}$$

The B_T values can be determined experimentally from a dependence of the relative intensity of Bragg reflections on the scattering vector Q using the formula (3) given by Wilson [9]:

$$\ln (I_{exp} / I_{calc}) = 2 \ln K - 2B_T(\sin^2\Theta/\lambda^2), \tag{3}$$

where K is the scaling factor associated with the structure factor $|F_o(hkl)|$; the logarithm of the relative Bragg intensities plotted against $(\sin^2\Theta/\lambda^2)$ yields a straight line with the slope of $2B_T$.

Application of the Wilson plot to nanocrystals; a need for determination of TDS

For microcrystalline materials individual Bragg reflections are relatively narrow and separated from each other. To obtain net Bragg intensities it is sufficient to determine the diffuse background scattering by joining the minima of intensity between the peaks. For X-ray measurements, this background includes the instrument background, Compton scattering, fluorescence and other effects, and TDS (equation (2)). In a routine procedure of determination of B_T with use of the Wilson method TDS does not need to be accounted for. However, it has to be examined very carefully for nanocrystalline materials for which a large part of diffuse scattering belongs to Bragg intensities. This is caused by very strong broadening, thus overlap of the reflections due to the size effect, internal strains, disorder, etc. After all corrections for diffuse background are done, the remaining intensity is Bragg scattering and TDS. The distinction between Bragg and TDS scatterings has to be done very accurately and, in practice, *the analysis of attenuation of Bragg intensities for nanocrystalline materials has to be done simultaneously with the analysis of TDS.*

Comparison of application of X-ray and neutron scattering

In general, X-ray and neutron diffraction measurements provide the same information about the structure of materials, so they are equally appropriate for the analysis of the atomic thermal motions. However, determination of TDS from neutron scattering data is more straightforward than a similar analysis of X-ray data. For our purpose, the biggest advantage of neutron diffraction is that the scattering amplitude is constant in the whole range of the diffraction vector and, therefore, the shape of TDS is much better defined than for X-rays.

Theoretical calculations of the effect of thermal vibrations on the diffraction patterns of nano-crystals

The presence of thermal vibrations leads to a scatter of atoms about their perfect lattice positions. The effect of these atomic motions on the diffraction pattern can be simulated by calculating scattering on crystal lattices where atoms are located not in their perfect lattice positions but occupy positions about equilibrium with probability proportional to the time they spend at a certain distance from the equilibrium position during thermal motions [4]. We did theoretical calculations of the diffraction patterns of the models of SiC nanocrystals assuming that the motions of individual atoms are not correlated and that they are harmonic and isotropic. The probability of finding an atom in a given position about its equilibrium position is described by a Gaussian function with a maximum at a given lattice site.

Strategy of analysis of thermal vibrations in nano-crystals

In a conventional study of thermal atomic motions done using the Wilson procedure one searches for a unique value of the overall temperature factor B_T. Such approximation obviously cannot be used for nanocrystals which have two kinds of atoms (the grain interior and the surface) with different properties. It was suggested that the temperature parameter B can be approximated by a linear combination of the temperature atomic factors of the core and surface atoms [10]:

$$B = pB_{core} + (1 - p)B_{shell}, \quad (4)$$

where p is the fraction of the atoms in the grain core.

Calculation of theoretical TDS scattering for nanocrystals

TDS is incoherent with contributions from the atoms, proportional to their vibration amplitudes (equation (2)) and their abundance. Assuming only uncorrelated atomic motions, contributions to TDS from different atoms are additive. The Wilson plot is used to determine overall temperature factors, equivalent with the assumption that individual atoms are undistinguishable; thermal vibrations are referred to an average atom with an average amplitude. Accordingly, TDS which represents incoherent scattering of the average atom can be calculated with equation (2). For a nanocrystal with a core-shell structure one has to discern between two kinds of such "average" atoms (of the core and shell), and equation (2) should be replaced with (5):

$$TDS_{total} = pTDS_{core} + (1 - p)TDS_{shell}. \quad (5)$$

For given diffraction data this function has to be normalized before it is substracted from the total scattering (yielding net Bragg intensity). On a normalized neutron pattern, S(Q), TDS always reaches unity at very large Q values (c.f. figure 2).

Results

Effect of different vibrations in the core and shell atoms on the Wilson plot

We examined a series of models of SiC nanocrystals assuming different temperature factors for the core and shell atoms and different thicknesses of the surface shell. For these models we calculated theoretical diffraction patterns and Wilson plots. TDS was calculated using equation (5). Figure 1 shows the results of elaboration of two theoretical diffraction patterns with different vibrations and equal number of the atoms in the grain core and the surface shell. Each experimental point represents an average value over several reflections occurring near a given $\sin\Theta/\lambda$. For $Q > 15$ Å^{-1} the plot is linear with a well defined slope corresponding to B_{core} = 0.24 and 0.14 Å^2 for models (i) and (ii), respectively. These are exactly the B_{core} values used in our models. That shows that for core atoms (small vibration amplitude) the Wilson plot yields reliable B values. For $Q < 15$ Å^{-1} the plot shows a complex shape: the slope can be defined only for the smallest Q values and corresponds to B equal to 0.40 for model (i) and 0.72 Å^2 for model (ii). Using equation (4) and taking B_{core} and B_{shell} of the models (i) and (ii) we get exactly the same B values. This shows that the Wilson plot can indeed be used to evaluate the atomic vibrations in the grain core and shell.

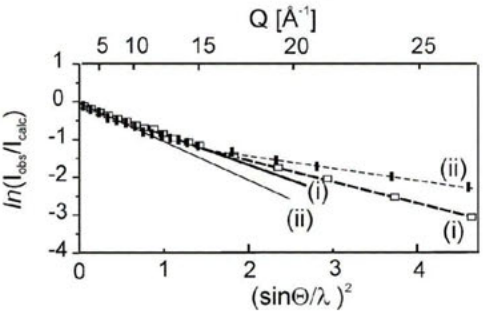

Figure 1. Theoretical Wilson plots obtained for diffraction patterns of 8 nm SiC nanocrystal with 1.0 nm thick surface shell calculated for two models of thermal vibrations with equal number of atoms in the grain core and shell:
(i) B_{core}=0.24 Å^2, B_{shell} = 0.55 Å^2 ; (ii) B_{core}=0.14 Å^2, B_{shell} = 1.30 Å^2.

Experimental determination of the temperature factors B_{core} and B_{shell} for SiC powders

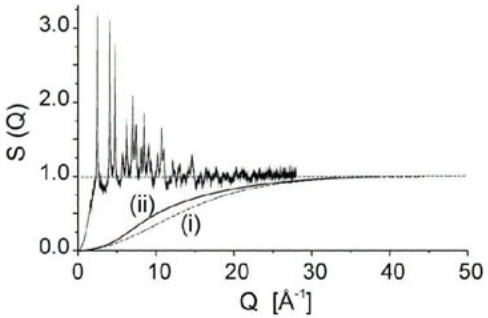

Figure 2. Experimental neutron diffraction pattern of 8 nm SiC nanocrystalline powder. TDS intensities were calculated for equal numbers of core and surface atoms and different vibrations: (i) B_{core} = 0.165 Å^2, B_{shell} = 0.50 Å^2; (ii) B_{core} = 0.165 Å^2, B_{shell} = 0.85 Å^2.

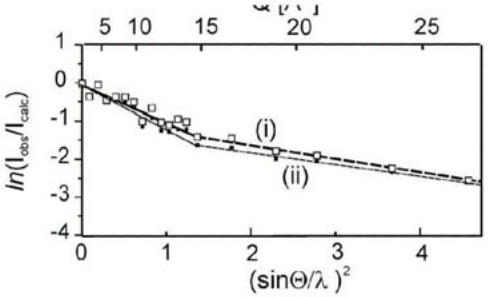

Figure 3. Experimental Wilson plots calculated for 8 nm SiC nanocrystalline powder after substraction of TDS intensities corresponding to vibration models (i) and (ii) (c.f. figure 2).

To make a Wilson plot one needs to assume a certain shape of TDS_{total} scattering. That requires information on the relative number of core and surface atoms and amplitudes of their vibrations, i.e. information which we never know at the start of the work. As a first approximation we assume that the atoms in the grain core vibrate as in the bulk material, corresponding to the average value of B_{core} = 0.165 Å^2 [4]. Next we assume that the atoms in the surface shell vibrate with an amplitude about two times larger than in the grain core; this yields B_{shell} between 0.5 and 0.9 Å^2. Figure 2 shows the experimental neutron diffraction pattern of our 8 nm SiC nanocrystalline powder and two different TDS intensities calculated from equation (5). The shape of the experimental Wilson plots in figure 3 is similar to the theoretical plots presented in figure 1. Taking TDS calculated for B_{shell} values of 0.5 and 0.85 Å^2 we get the slopes for large Q corresponding to B_{core} = 0.16 and 0.175 Å^2. This shows that the selection of TDS has little effect on the B_{core} value determined by the Wilson method. For low Q we get slopes corresponding to B values of 0.5 and 0.7 Å^2. By using equation (4) and assuming B_{core} = 0.165 Å^2 and equal number of core and surface shell atoms (p = 0.5) we get B_{shell} = 0.84 and 1.22 Å^2. We can tell that the real value of B_{shell} is between these two values. They correspond to vibration amplitudes between 0.21 and 0.25 Å, about two times larger than the average vibration amplitude of the inner grain atoms; B_{core} = 0.165 Å^2 corresponds to the vibration amplitude of about 0.09 Å (amplitude $\cong 2\langle u^2\rangle^{1/2}$). Figure 4 shows the Wilson plots obtained for 15 and 23 nm SiC powders, where TDS was taken assuming B_{core} = 0.165 and B_{shell} = 0.85 Å^2. The B_{core} values calculated for large Q for 15 and 23 nm samples are the same as for 8 nm sample. The B values calculated for small Q values are 0.41 and 0.34 Å^2, i.e. smaller than for 8 nm powder, which is consistent with a decrease in the content of the surface atoms with an increase in the grain size. The B_{shell} values calculated from equation (4) for those two samples are 0.9 and 0.95 Å^2, in good agreement with the value obtained for 8 nm sample (between 0.84 and 1.22 Å^2).

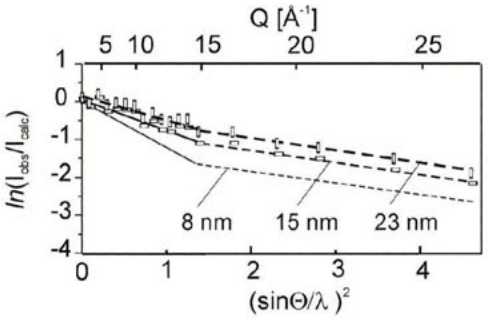

Figure 4. Experimental Wilson plots calculated for 15 and 23 nm SiC nanocrystalline powder after substracting TDS intensities; 33% and 22%, respectively, of the atoms are in the surface shell. The plot of the 8 nm powder is also shown.

Summary

Analysis of the atomic temperature factors of nanocrystals requires simultaneous evaluation of Thermal Diffuse Scattering. The Wilson method can be applied for evaluation of thermal motions of the core and surface-related atoms in nanocrystals. Application of wide angle neutron scattering enables a direct evaluation of thermal vibrations in the core of nanocrystals. For SiC nanocrystals, the thermal factor B_{shell} for the surface atoms is 4 to 5 times larger than B_{core}; this corresponds to 2 - 2.5 times larger amplitude of vibrations of the atoms at the surface relative to thermal vibration of the atoms in the interior of the grains. Although here we interpret the Wilson plots as if they reflected thermal vibrations only, one has to remember that the B_T parameter determined by the method may include also a contribution from the static lattice distortions. The contribution of the static disorder can be evaluated using a similar procedure but investigating the temperature dependence of the temperature factors. That study is currently under way.

References

1. R. Meyer, L.J. Levis, S. Prakash & P. Entel, 2003, *Phys.Rev. B*, **68**, 104303.
2. A. Kara & T.S. Rahman, 1998, *Phys.Rev.Lett.*, **81**, 1453.
3. J.Trampenau, K.Bauszus, W.Petry & U. Herr, 1995, *Nanostructured Mater.*, **6**, 551.
4. S. Stel'makh et.al., 2004, *J. Alloys Compounds* **382**, 138.
5. Th. Proffen, S.J.L. Billinge, T. Egami & D. Louca, 2003, *Z.Kristallogr.*, **218**, 132.
6. F. Huisken. B. Kohn. R. Alexandrescu, S. Cojocaru, A. Crunteanu, C. Reynaud & G. Ledoux, 1999, *J. Nanopart. Res.* **1**, 293.
7. B. Palosz et al., 2002, *Z. Kristallogr.*, **217**, 497.
8. B. Palosz et al., 2002, *Acta Phys. Pol. A*, **102**, 57.
9. M.F.C. Ladd & R.A. Palmer, 1994, *Structure Determination by X-Ray Crystallography* (Plenum Press, New York).
10. J. Harada & K. Ohshima, 1981, *Surf. Sci.*, **106**, 51.

Acknowledgements. Support of this work by the Office of Biological and Physical Sciences of NASA and the US Department of Energy/LANL-LANSCE (project #2002060) is gratefully acknowledged. The SiC powders were provided by SPAM/LFP, Laboratory "Edifices Nanometriques" from Matter Science Division, DSM, CEA, Saclay, Program "Polonium", Nr 4956.I/2003.

Z. Kristallogr. Suppl. **23** (2006) 337-342

Phase transition in nanocrystalline ZnO

E. Grzanka[1,*], S. Gierlotka[1], S. Stelmakh[1], B. Palosz[1], T. Strachowski[1], A. Swiderska-Sroda[1], G. Kalisz[1], W. Lojkowski[1], F. Porsch[2]

[1]Institute of High Pressure Physics, Sokolowska 29/37, 01142 Warsaw, Poland
[2] HASYLAB at DESY, Notkestr. 85, D-22603 Hamburg, Germany
[*]Contact author; Ewa Grzanka, e-mail: elesk@unipress.waw.pl

Keywords: nanocrystals, high pressure, phase transition, ZnO

Abstract. The size effect on the high pressure phase transition of ZnO nanocrystals with grains from 18 up to 30 nm has been investigated. The phase transition from B4 (hexagonal wurtzite structure) to B1 (cubic rocksalt structure) was induced by high pressure and measured by energy-dispersive in situ synchrotron radiation powder diffraction in a diamond anvil cell under pressures up to 40 GPa at room temperature. It was found that the transition pressure of the B4 to B1 transformation in nanocrystalline ZnO is much higher than that in microcrystalline ZnO.

Introduction

Zinc oxide powders are widely used in a variety of applications such as varistors, opto- and acusto-electronics, pigments and components for cosmetic industries, sunscreens, rubber, etc. Zinc oxide is also a well known luminescent material and a good candidate for ionizing radiation detection. Currently, there is a new promising area of luminescent research, i.e. luminescence of nanocrystals. Nanocrystals often show novel physical and chemical properties, different than those of the corresponding bulk material. The basic observations of the greater luminescence intensity for smaller nanocrystals were reported in [1]. Due to a potential application of nanocrystalline ZnO in luminescent devices, it is essential to examine structural stability of this material, what is the subject of this work.

Experimental

ZnO is prepared by many methods such as gas condensation, aerosol spray pyrolysis, hydrolysis in polyoil media, thermal oxidation of metallic Zn, sol-gel process, precipitation, solid-state microwave decomposition and hydrothermal technique. We used the hydrothermal method to synthesize nanocrystalline zinc oxide by decomposition of zinc chloride (0.1M) in an aqueous solution, alkalized by KOH to the pH value of 12 or with addition of urea (its weight ratio to zinc chloride ranging from 1:2 to 1:5) [2]. A microwave digestion system (model Uni Clever Plazmatronika) was used to conduct the reactions. The maximum temperature and pressure that can be achieved in the microwave system were

300 °C and 12 MPa, respectively. The synthesis was done in a teflon container at pressures up to 4 MPa.

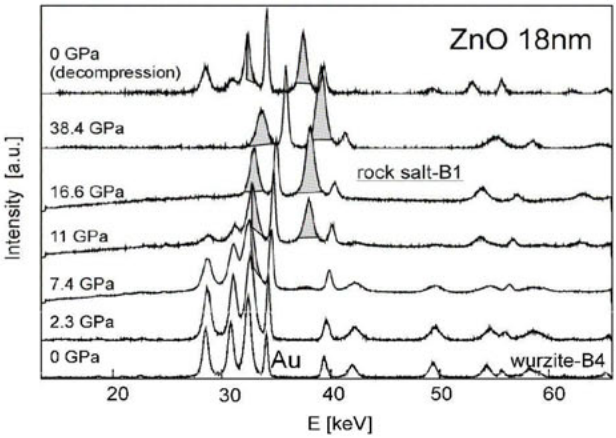

Figure 1. In situ high pressure diffraction patterns collected for18 nm ZnO at room temperature under increasing pressure and after decompression.

To evaluate grain size, nanocrystalline ZnO were measured with D5000 SIEMENS powder diffractometer, using CuKα_1 radiation, instrumental broadening was 0.08°. Two approaches were applied to calculate the grain size. At first, grain sizes were determined with Scherrer formula and the correction for instrumental broadening was applied. At second, analysis of size-strain was applied in terms of Williamson-Hall plot. It was calculated that nanocrystalline ZnO has average grain sizes 18 ± 2 nm , 22 ± 2 nm, and 30 ± 3 nm and strain is equal $0.5*10^{-4}$. The grain sizes calculated with above methods were comparable in the range of errors. The above three nanocrystalline zinc oxide powders and a few μm sample as a reference, were examined using a diamond anvil cell at pressures up to 40 GPa at the F3 beamline at HASYLAB (for simplicity, in the next part of this article and on the pictures, the grain sizes will be given without error bars). The diffraction data were collected *in situ* in the energy dispersive geometry using gold as the pressure marker. The experiments were performed under (i), hydrostatic conditions with mineral oil as the pressure medium, and (ii), under so-called isostatic pressure conditions (without a pressure medium). X-ray powder diffraction patterns were recorded at room temperature under initially increasing and then decreasing pressure.

Results

The diffraction patterns obtained for 18 nm grain size ZnO powder are shown in figure 1. The rock-salt B1 phase (figure 1 - grey color) coexists with wurtzite B4 phase from 7.4 GPa up to 11 GPa. High pressure B1 phase is stable up to 40 GPa and, after decompression, coexists with the B4 phase. It has been reported in the literature that the transition pressure of

12 nm grain size ZnO is 15.1 GPa, i.e. 50% larger than that for microcrystalline powder (9.5 GPa): the phase transition of microcrystalline ZnO from B4 (wurtzite) to B1 (rock salt) begins around 9 GPa and ends approximately at 11 GPa [3,4].
We examined similarly the B4 to B1 transition for 18, 22, and 30 nm ZnO. Elaboration of the experimental data is presented in figures 2 to 5. Figure 2 shows a plot of the intensity ratio of the I_{200} (B1) to I_{100} (B4) peaks for 18 and 30 nm powders as a function of pressure; similar plots were presented for micro- and 12 nm ZnO in ref. [3]. The increase in the transition pressure with a decrease in the grain size observed in figure 2 agrees with previous data [3].

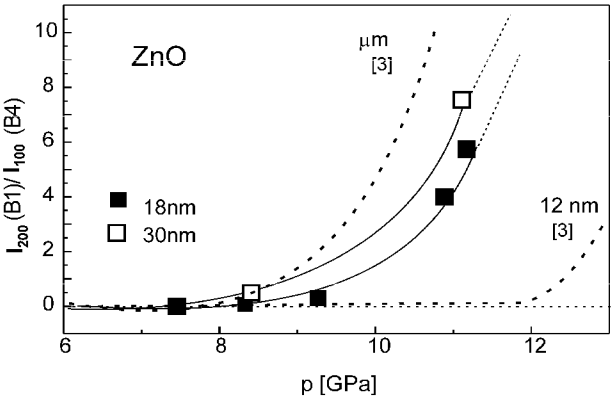

Figure 2 Changes of the intensity ratio of the Bragg reflections (200)(rock salt B1) to (100)(wurtzite B4 phase) with an increase in pressure for ZnO powder of 18 and 30 nm grains.

In figure 3 we show an estimate of the transition pressure from changes of FWHM of 101 (B4) (=111 B1) reflection assuming that the transition pressure corresponds to the minimum at which the reflection broadening occurs: approximately 10.8 GPa for 30 nm and 12 GPa for 18 nm powder. Figure 4 presents changes in the intensity ratio (I_{100} : I_{002}) of B4 Bragg reflections which show very different shapes for micro- and nanocrystalline powders. This is an indication of a difference in the mechanisms of the B4 to B1 transition between nano- and micron-size grains. We suggest that a very strong increase in the ratio I_{100} : I_{002} for large grains results from a simultaneous growth of a number of domains of B1 phase at low pressures in the starting B4 phase, what leads to very strong internal stresses. A single nano-grain tends to remain as a single phase structure and therefore the intensity ratio I_{100} : I_{002} (B4) varies only a little. An increase in the external stress applied to the ZnO powders above the transition pressure does not lead to an increase in strains observed in large grains, but to a strong increase in micro-strain in nanograins, figure. 5. Above 12 GPa one observes a strong increase in micro-strains in 18 nm ZnO, but a smaller increase in 30 nm powder. In µm-size samples no increase in micro-strain up to 40 GPa pressure is observed. Similar behaviour was found for these materials under isostatic pressure conditions. We suggest that the increase in strains in nanograins is related to a very large surface area of the grains (inter-

grain interfaces) which obviously have different elastic properties from the bulk (interior of the grains) [5].

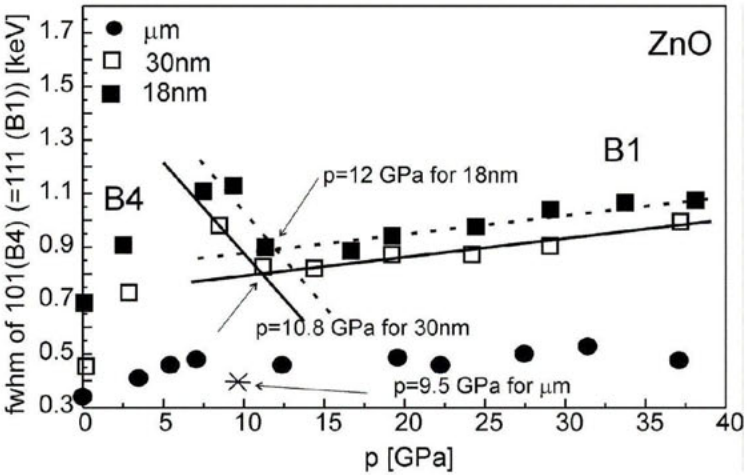

Figure 3. Change of broadening of Bragg reflections ((101) wurtzite B4 phase = (111) rock salt B1) with pressure under increasing hydrostatic pressure conditions.

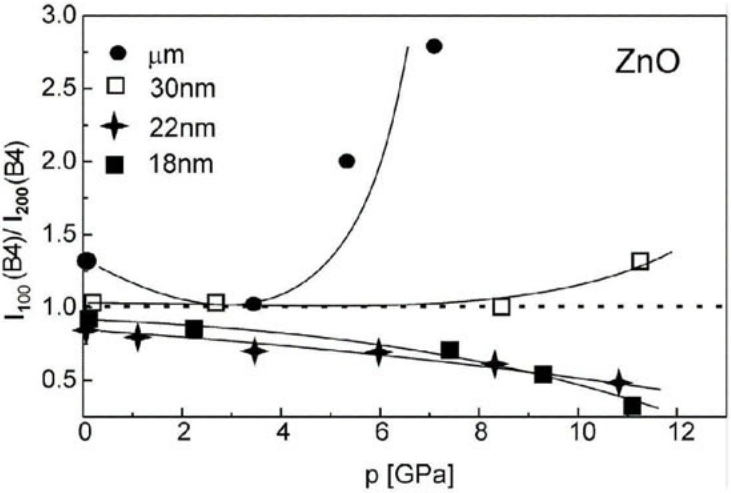

Figure 4. Changes of the intensity ratio of Bragg reflections (100) - B1 phase to (002) -B4 phase below the transition pressure for micro and nanocrystalline ZnO.

Summary and conclusions

The high-pressure behaviour of nanocrystalline ZnO with grain sizes of 18, 22, 30 nm, and a few microns was investigated by in situ synchrotron X-ray radiation powder diffraction using the diamond anvil cell under the pressures of up to 40 GPa. It was found that the transition pressure for nanocrystalline ZnO is much higher than in microcrystalline samples. The transition pressure at room temperature increases from 9.5 GPa for microcrystalline sample up to 12 GPa for 18 nm ZnO, what is in good agreement with literature data [3]. We associate these differences in the transition pressures with differences in the atomic structure of nano- and micro-crystalline grains. We attribute this effect to the structure of the grain surface. In a micrometer size powders the surface atoms constitute only a small fraction of the material and their effect on the overall properties of the material can be ignored. The situation is different in small, nano-size particles where, due to their size, a considerable fraction of the atoms form the surface of the grain. Assuming that the surface shell has the thickness of 1 nm, a 10 nm diameter grain contains 25 % of its atoms in the surface layer, while a 4 nm grain has 60 % of such atoms. That shows that, in very small objects, the number of surface-related atoms can exceed the number of the „bulk" atoms. A presence of such large fraction of the atoms and different surroundings of the atoms in the surface and bulk regions is one of the sources of unique properties of these materials. Based on the studies on phase transitions in a variety of nanocrystalline materials, ZnO [3], CdSe, CdS, Si [6-8] it was concluded that changes in the transition pressure in nanocrystals are caused primarily by surface energy differences between the phases.

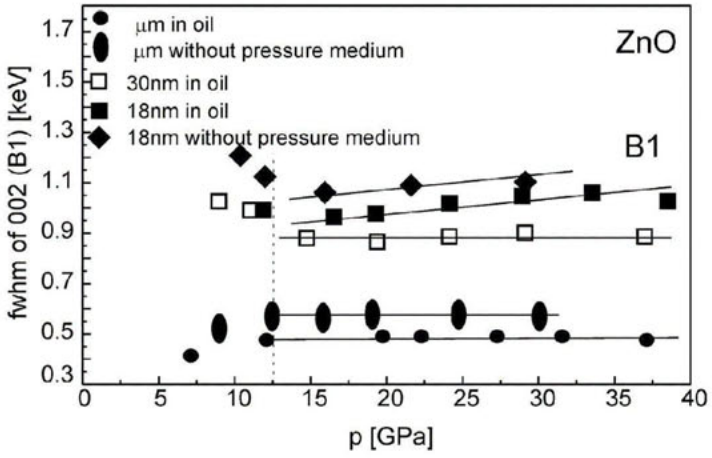

Figure 5 Change in broadening of the Bragg reflection (002) for rock salt B1 phase above the transition pressure for micro and nanocrystalline ZnO.

References

1. G.A.Kachurin, I.E.Tyschenko, K.S.Zhuralev, N.A.Pazdnikow, V.A.Volodin, A.K.Gutakovsky, A.F.Leier, W.Skorupa, R.A.Yankow, 1997, *Nuclear Instruments and Methods in Pysics Research B*, **122**, 571.
2. T.Strachowski, E.Grzanka, B.Palosz, A.Presz, L.Slusarski, W.Lojkowski, 2003, *Solid State Phenomena*, **94**, 189.
3. J.Z.Jang, J.S.Olsen, L.Gerward, D.Frost, D.Rubie, J.Peyronneau , 2001, *Europhys. Lett*., **50**, 48.
4. F.Decremps, J.Zhang, C.Lieberman, 2000, *Europhys. Lett*., **51** (3), 268.
5. B. Palosz, S. Stel'makh, E. Grzanka, S. Gierlotka, R. Pielaszek, U. Bismayer, S. Werner, and W. Palosz, 2004, *J. Phys.: Condens. Matter* **16**, S353.
6. S.H.Tolbert and A.P.Alivisatos, 1994, *Science*, **265**, 373.
7. S.H.Tolbert and A.P.Alivisatos, 1995, *J.Chem. Phys*, **102**, 4642.
8. S.H.Tolbert, A.B.Herhold, L.E.Brus, A.P.Alivisatos, 1996, *Phys.Rev.Lett*, **76,** 2205.

Acknowledgements. This work was supported by the Polish Committee for Scientific Research – grant PBZ/KBN-095/T08/2003, the Polish –German Project POL-00/009, DESY-HASYLAB Project II-02-025 and in part by the EC Grant "Support for Centers of Excellence" No. ICA1-CT-2000-70005 and also G1MA-CT-2002-04055.

IV.3 Metals and Alloys

Z. Kristallogr. Suppl. **23** (2006) 345-350

Study of martensitic transformation in fatigued stainless steel by neutron diffraction stress analysis

Yu. V. Taran[1,*], M. R. Daymond[2], E. C. Oliver[2], J. Schreiber[3]

[1]FLNP, Joint Institute for Nuclear Research, 141980 Dubna, Moscow region, Russia
[2]ISIS, Rutherford Appleton Laboratory, Chilton, Oxon OX11 0QX, UK
[3]EADQ, Fraunhofer Institute for Nondestructive Testing, D-01326 Dresden, Germany
[*]Contact author; e-mail: taran@nf.jinr.ru

Keywords: powder diffraction, neutron, fatigue, stress, stainless steel

Abstract. The elastoplastic properties of a stainless steel AISI 321with austenitic matrix and martensitic inclusions induced during cyclic tensile-compressive fatigue loading were studied using neutron diffraction. Nonlinear behaviour of the martensite elastic strain response in the plastic region was observed, while the austenite response remained practically linear. A clear trend of increasing elastic modulus with fatigue level was noted in the austenite of the low-cycle fatigued samples; the residual strains in austenite and the deviatoric components of residual microstresses in both phases were determined as a function of fatigue. The axial and transverse elastic constants of austenite and martensite in the high-cycle fatigued samples are distinctly different. In search of the reason of the last effect we have carried out on-line low-cycle plastic deformation transformation of one of the high-cycle fatigued samples.

Introduction

Austenitic stainless steels (ASS) are widely used in engineering applications. A major concern in a number of applications, including nuclear power plants, is fatigue damage of ASS components. The assessment of the actual fatigue damage and thus the remaining fatigue lifetime of materials is a task of great practical relevance. During fatigue loading microstructural changes occur in ASS which affect both the mechanical and physical properties of the steel. In particular, in some ASS a metastable austenitic *fcc* structure is converted into the ferromagnetic α'-martensite tetragonal distorted lattice. The extent of distortion strongly depends on the carbon content. For low carbon steels the tetragonal structure does not deviate much from the *bcc* lattice of α-Fe.

Many investigations have shown the influence of the martensitic transformation on the fatigue properties of ASS (see, e.g., [1]). Whereas the mechanical properties of austenitic steel are well known [2], a transforming or partly transformed material is much more difficult to characterise due to the interaction between two phases. For instance, any elastic mismatch and plastic misfit between the martensite and austenite, as well as the larger specific volume

of martensite, are likely to cause considerable stresses throughout the sample. Knowledge of the residual stress state of the phases and their relation to the fatigue process is very important, in order to develop a proper understanding of how the individual phases interact to produce the bulk mechanical response of the material.
Comprehensive stress measurements in a multiphase material with neutron diffraction can be performed on dedicated time-of-flight diffractometers at neutron pulsed sources equipped with modern strain scanners and ad hos stress rigs which can operate in quasistatic and low-cycle modes, on demand. One such stress diffractometer was the ENGIN instrument [3] at the ISIS neutron pulsed facility. Now the new ENGIN-X instrument [4] has replaced the earlier one. We have used both instruments in our investigations.
This paper describes in detail a study of a low carbon metastable austenitic stainless steel of type AISI 321 with varying martensite volume fractions produced by plastic deformation during cycle fatigue, reported in brief in [5-7].

Experimental details

Two sets of samples were prepared from the steel AISI 321. The first set (annealed at 1070 °C and quenched in air) was cycled under stress control with amplitude of 330 MPa at a frequency of 5 Hz (high-cycle fatigued (HCF) samples). The second set (1050 °C/water) was cycled under strain control with amplitude of 1% at 0.5 Hz (low-cycle fatigued (LCF) samples).
Both sets of the samples were measured [5, 6] using the *in situ* stress rig under tensile stress control on the ENGIN instrument at the ISIS pulsed neutron facility. The stress rig loading axis is horizontal at 45° to the incident neutron beam, thus providing simultaneous measurements of strains parallel (axial) and perpendicular (transverse) to the applied stress. A neutron gauge volume is formed inside the central part of the sample in a form of a rectangular parallelepiped, located at 45° to the sample axis, by using two multislit radial collimators in front of the ± 90° detectors and a primary slit in front of the sample, respectively.
One of the HCF-samples was subjected to HCF-LCF- plastic deformation transformation [7] on the ENGIN-X instrument. The experiment was performed using the stress rig by rotation in two modes: 1) a low-cycle mode at a frequency of 0.1 Hz under stress control to increase the fatigue level of the sample, and 2) a quasistatic mode to make neutron diffraction measurements of the applied stress-elastic strain responses of austenite and martensite phases in the state achieved. The method proposed was the first of its kind, providing on-line non-destructive characterization of the cyclic deformation behaviour of stainless steel.
The lattice parameters of the austenitic and martensitic phases were determined by the Rietveld refinement in a d-spacing interval from 0.04 to 0.23 nm in which 38 austenite and 32 martensite reflections are observed. The direct result from data processing is the dependence of the phase lattice parameter a_{ii} on the applied stress σ_L for directions 'ii' equal to '11' or '33', corresponding to the axial or transverse direction, respectively. From the linear fit of the elastic part of the phase curves $a_{ii}(\sigma_L)$ one obtains the zero stress intercepts I_{11} and I_{33}. To calculate the applied stress-elastic strain responses of individual phases, the phase residual strain and subsequently the phase residual stress, the stress-free phase lattice parameter a_0 has to be known. Usually in order to determine this parameter a sample is made with the same structure and chemical composition, but free from internal stresses. However, in our

case such samples were not available. A rough, and typically sufficient, approximation for calculating elastic strains $\varepsilon_{ii}=(a_{ii}-I_{ii})/I_{ii}$ is to use the intercepts I_{ii} instead of parameter a_0.

Results and Discussion

HCF-results. An example of the applied stress-elastic strain responses of austenite and martensite is shown for the sample no. 13 in figure 1. While the axial martensite strain deviates from linearity quite significantly in the bulk plastic regime, the deviation in the austenite response was very small compared to that expected based on simple load sharing arguments.

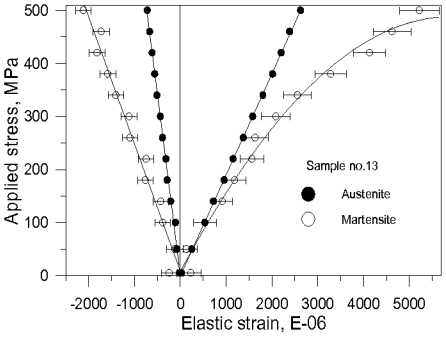

Figure 1. Phase applied stress-elastic strain responses for the HCF-sample no. 13.

In HCF-samples the elastic constants of austenite and martensite were found to be strongly different (table 1). Moreover, the ratio of axial and transverse elastic constants E_{ax}/E_{tr} for martensite is almost twice that observed in austenite (0.28 - 0.30). The mechanism for this unusual behaviour is unclear, but may be linked to the shape of the martensite precipitates. The neutron elastic constants are almost independent of the fatigue level while the bulk value of the Young's modulus E_{bulk} measured by a gauge extensometer during the neutron experiment decreases with increasing fatigue.

Table 1. The HCF-samples: mechanical and neutron data.

Sample	12		13	
Cycles	$3\cdot10^4$		$6\cdot10^4$	
Level of fatigue [%]	30		60	
Mart. fraction [Vol.%]	4		5	
E_{bulk} [GPa]	181(9)		124(5)	
Phase	austenite	martensite	austenite	martensite
E_{ax} [GPa]	190(1)	159(15)	190(1)	151(30)
E_{tr} [GPa]	705(14)	331(33)	684(14)	248(13)
E_{ax}/E_{tr}	0.270(6)	0.48(9)	0.278(6)	0.61(12)

LCF-results. The examples of the dependences of the phase lattice parameters on the applied stress σ_L and the applied stress-elastic strain responses of austenite and martensite for the axial and transverse directions are shown for the sample B in figures 2 and 3, respectively.
In LCF-samples the elastic constants of austenite and martensite were found out to be close (table 2). Note that the austenite elastic constants increase slowly with fatigue level, for the fatigue level ≥ 10%. According to a principle of superposition, the Young's modulus E_s of the two phase system should approximately follow the equation $E_s=(1-F_{mar})E_{ax,aus}+F_{mar}E_{ax,mar}$ where F_{mar} is the volume fraction of the martensite (table 2). The results of this calculation are plotted in figure 4, and give a roughly linear dependence of the summed modulus as a function of fatigue level. However, the bulk material Young's modulus reported in table 2 are too scattered to either support or rule out this increase out. We can therefore only say that

our data demonstrates an increase in the austenite modulus as a function of fatigue, with only weak evidence that the sample modulus as a whole increases with fatigue level.

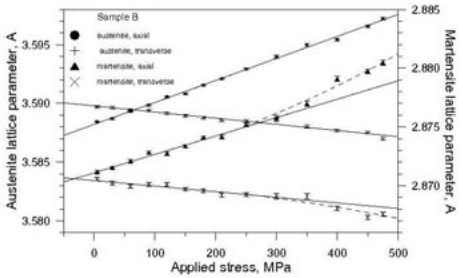

Figure 2. Phase lattice parameters vs the applied stress for the LCF-sample B.

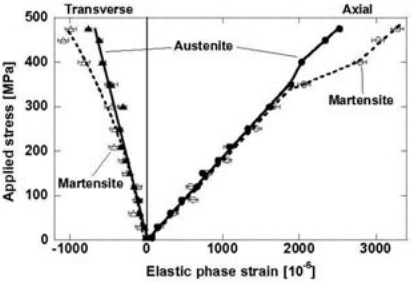

Figure 3. Phase applied stress - elastic strain responses for the LCF-sample B.

Table 2. The LCF-samples: mechanical and neutron data.

Sample	A	B	C	D	E	F	G	H
Cycles	1161	1053	789	521	251	115	51	0
Fatigue [%]	100	90.7	68.0	44.9	21.6	9.9	4.4	0
F_{mar} [vol.%]	24.7(7)	25.4(3)	20.0(4)	14.9(3)	6.0(2)	2.2(2)	0.65(15)	0
E_{bulk} [GPa]	-	-	194(3)	180(3)	182(2)	178(2)	180(3)	186(2)
				Austenite				
E_{ax} [GPa]	-	190(2)	192(2)	185(2)	176(2)	170(2)	175(2)	170(3)
E_{tr} [GPa]	-	681(27)	681(31)	661(23)	623(15)	610(16)	635(14)	918(86)
E_{ax}/E_{tr}	-	0.282(11)	0.282(13)	0.280(10)	0.282(7)	0.278(8)	0.275(6)	0.185(18)
				Martensite				
E_{ax} [GPa]	-	182(7)	197(12)	199(14)	166(17)	183(50)	-	-
E_{tr} [GPa]	-	561(72)	900(256)	411(54)	703(250)	655(515)	-	-
E_{ax}/E_{tr}	-	0.325(44)	0.219(66)	0.485(72)	0.236(87)	0.28(23)	-	-

As is seen in figure 2 the axial and transverse lattice parameters for each phase do not intersect at zero applied stress. This is most likely due to the presence of residual deviatoric stresses from processing and fatigue history. This origin of the effect is reinforced by the fact that the cross over stress σ_L^* for axial and transverse lattice parameters is of opposite sign for the austenite and martensite phases. It is possible to show that if the elastic properties of both phases are similar the phase intersection σ_L^* is linked by formula $\sigma_L^* = -(\tau_{11}^R - \tau_{33}^R)$ with the deviatoric components τ_{11}^R and τ_{33}^R of the phase residual stress tensor $\sigma_{ij}^R = \delta_{ij}\tau_H^R + \tau_{ij}^R$ where $\tau_H^R = \mathrm{Tr}(\sigma_{pq}^R)/3$ is the hydrostatic stress and the trace $\mathrm{Tr}(\tau_{pq}^R) = 0$. Assuming the transverse symmetry of the sample we have $\tau_{33}^R = -\tau_{11}^R/2$. Thus, we can calculate the deviatoric phase residual stresses from the experimental values of the phase intersections (figure 5). The austenite shows a compressive deviatoric stress in the axial direction, while the martensite shows a balancing tensile deviatoric stress. The austenite deviatoric compressive stress increases with fatigue, however the tensile deviatoric stress in

the martensite decreases in magnitude, corresponding to the increasing volume fraction of martensite. The transverse component is opposite in sign and half of the axial component.

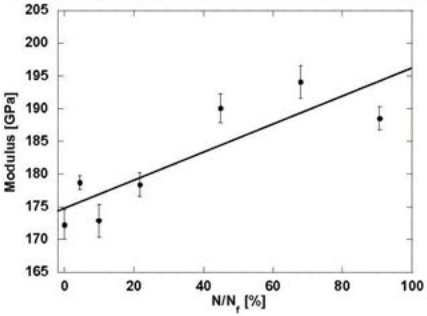

Figure 4. The Young's modulus from a principle of superposition vs the fatigue level.

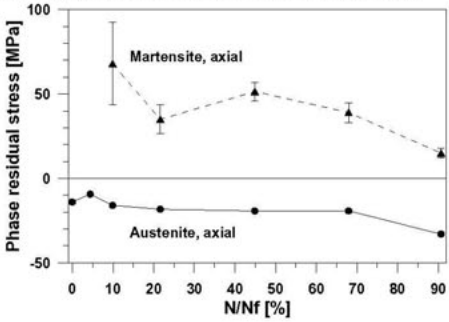

Figure 5. Phase deviatoric residual stresses in the axial direction vs the fatigue level.

As is seen in figure 3 the axial martensite response deviates from linearity quite significantly in the plastic regime, yet only weak deviations are seen in the axial austenite and transverse martensite responses. Converting the results presented in figure 3 in the total phase stresses in the axial direction by help of Hooke's law and using a volume averaging rule for the macrostress $\sigma_{11,M} = (1\text{-}F_{mar})\sigma_{11,aus} + F_{mar}\sigma_{11,mar}$ we have calculated the dependence of the macrostress on the applied stress. The dependence is illustrated in figure 6 for the sample B where the applied stress is deducted from the macrostresses as well as from the total phase stresses. Thus the applied stress induces additional microstresses in the austenite which are comparable in magnitude to those introduced due to fatigue, while more appreciable microstresses are induced in the martensite during the tensile loading than those from fatigue. These microstresses correspond to the nonlinear behaviour of the martensite elastic strain response that we have observed during testing of HCF- and LCF-samples.

HCF-LCF-transformation. In search of the reason of the high value of the Poisson's ratio of the martensite in HCF-samples we have carried out on-line low-cycle plastic deformation transformation of one of them (sample no. 13) beginning from the state obtained at the finish of HCF-testing and continuing at increasing fatigue levels close to the point of fracture for LCF-testing. The applied stress-elastic strain responses of the austenitic and martensitic phases of the sample after 1000 cycles (the martensite fraction of 19 vol. %) is shown in figure 7. Linear fit of the data presented on figure 7 in the stress interval of 0-300 MPa has given the following elastic constants of the phases: a) austenite: E_{ax} = 228(2) GPa, E_{tr} = 873(24) GPa, E_{ax}/E_{tr} = 0.261(7); b) martensite: E_{ax} = 121(11) GPa, E_{tr} = 312(10) GPa, E_{ax}/E_{tr} = 0.388(12). Results obtained are close to results of HCF-testing: it is observed that there is a major difference of the elastic constants of austenite and martensite as well as a relatively high value of the ratio of axial and transverse elastic constants in martensite. Thus, the HCF-LCF-transformation exerted a weak influence on the mechanical properties of the sample. However, a significant transformation of the martensite morphology has apparently taken place that was manifested in the occurrence of new effects during the tensile testing of the transformed sample no. 13: 1) the austenite axial elastic strain response deviates from linearity upon yielding, indicating the sharing of applied load with the martensite phase and the generation of compressive and tensile internal stresses in austenite and martensite respec-

tively; 2) the martensite transverse elastic strain response deviates from linearity indicating the generation of compressive internal stresses in the transverse direction.

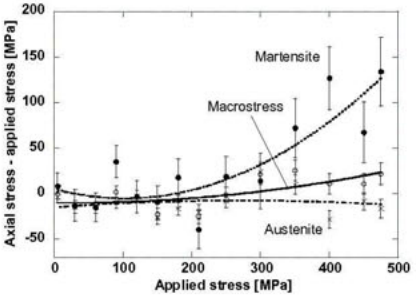

Figure 6. Differences of both the phase stresses and the macrostress from the applied stress vs the applied stress for sample B.

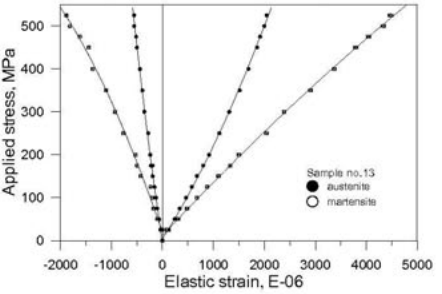

Figure 7. Applied stress - elastic strain responses of austenite and martensite for the transformed sample no. 13.

Conclusion

The application of the time-of-flight neutron diffraction on the ENGIN and ENGIN-X instruments at the ISIS pulsed neutron source to separate the individual responses of phases in multiphase materials is demonstrated on the example of samples from stainless steel AISI 321 cycled by uniaxial tensile-compressive loading under stress and strain control at frequencies of 0.5 and 5 Hz, respectively. Nonlinear behaviour of the martensite elastic response in the plastic region is observed for all samples, while the austenite elastic response practically remains linear throughout the measured stress range. The axial and transverse elastic constants of austenite and martensite are distinctly different in the high cycle fatigued samples, especially in the transverse direction; the ratio of axial and transverse elastic constants for martensite is much greater than observed in austenite phase. The on-line low cycling plastic deformation transformation of one of the high cycling fatigued samples has confirmed this result.

References

1. Bokuchava, G.D., Luzin, V.V., Schreiber, J., Taran, Yu.V., 1999, *Textures and Microstructures*, **33**, 279.
2. Daymond, M.R., Bourke, M.A., Dreele, R.B., et al., 1997, *J.App.Phys.*, **82**, 1554.
3. Johnson, M.W., Edwards, L., Withers, P.J., 1997, *Physica B*, **234-236**, 1141.
4. Daymond, M.R., Edwards, L., 2004, *Neutron News*, **15**, 24.
5. Taran, Yu.V., Daymond, M.R., Schreiber, J., Wright, J.S., 2000, in *The ISIS Facility Annual Report* (RAL-TR-2000-050, Chilton), ENGIN report of RB 11007.
6. Taran, Yu.V., Daymond, M.R., Eifler, D., Schreiber, J., 2001, in *The ISIS Facility Annual Report* (RAL-TR-2001-050, Chilton), ENGIN report of RB 12023.
7. Taran, Yu.V., Daymond, M.R., Oliver, E.C., Schreiber, J., 2004, in *The ISIS Facility Annual Report* (RAL-TR-2004-050, Chilton), ENGIN-X report of RB 14590.

Z. Kristallogr. Suppl. **23** (2006) 351-356

The evaluation of the kinetics of ordering processes in $Ni_{1+\delta}Sn$ (δ = 0.35, 0.50) by X-ray powder diffraction

A. Leineweber*, E.J. Mittemeijer

Max Planck Institute for Metals Research, Heisenbergstraße 3, 70569 Stuttgart, Germany
*Contact author; e-mail: a.leineweber@mf.mpg.de

Keywords: phase transformations, order-disorder transformation, Ni-Sn alloys, intermetallic phases, kinetics of phase transformations

Abstract. Annealing-time resolved X-ray powder diffraction data were evaluated to trace the kinetics of various ordering processes in $Ni_{1+\delta}Sn$ alloys (δ = 0.35, 0.50). Activation energies between 165 and 210 kJ/mol were observed. The relation between the magnitude of the activation energies and the corresponding processes is discussed.

Introduction

The binary system Ni-Sn represents a series of non-stoichiometric phases $Ni_{1+\delta}Sn$ with Ni_2In/NiAs type structures: a NiAs type sub-structure is formed by Ni(1)Sn (Sn taking the place of As) with additional *interstitial* Ni(2) atoms occupying – with an occupancy of δ – the centres of the trigonal-bipyramids formed by five Sn atoms. In the hexagonal high-temperature (HT) phase, with about $0.27 \leq \delta \leq 0.65$, these Ni(2) atoms show no long-range order. Occupational ordering of Ni(2) is exhibited, however, by the three different but structurally similar orthorhombic low-temperature phases (LT, LT', LT" [1-5], Figure 1), where the commensurate LT phase (Figure 2) occurring near the composition $Ni_{1.50}Sn$ can be regarded as a lock-in phase of the incommensurate LT' and LT" phases which exist at lower and higher Ni contents, respectively. All three phases can be regarded as modulated structures with respect to the same average structure (Figure 2). The order-disorder phase-transition temperature is strongly composition dependent, e.g. the disordered HT-$Ni_{1.50}Sn$ transforms to the ordered LT phase below 782 K, whereas for $Ni_{1.35}Sn$ the LT' phase forms below 686 K. The equilibrium phase transitions occur discontinuously, i.e. by a first order transition [2]. States of (dis)order can be retained at ambient temperatures by quenching the alloys in water.

Annealing followed by quenching experiments indicate that significant disordering can already be present in the low-temperature phase just below the order-disorder temperature. This is exhibited by a decrease in the integral intensities of the superstructure reflections accompanied by changes in the orthorhombic lattice parameters which become closer to the values of the high-temperature phase [4]. This can be expressed in terms of a decrease of the

orthorhombic distortion, $3^{-1/2}a_{orth}/b_{orth}-1$ (being 0 for the hexagonal HT phase, compare Figure 2), and an increase of the *effective c/a ratio*, of $(c/a)_{eff} = c_{orth}/(a_{orth}b_{orth}/3^{1/2})^{1/2}$, which is to be compared with the value of the HT phase, c_{HT}/a_{HT}.
The present paper reports X-ray powder diffraction investigations on non-equilibrium states of $Ni_{1+\delta}Sn$ obtained by various heat-treatment procedures, providing insight into the mechanism of the different observed processes.

Experimental

Preparation and heat treatment
HT-$Ni_{1.50}Sn$ and HT-$Ni_{1.35}Sn$ powders of good crystallinity, as indicated by narrow X-ray diffraction lines, were produced from the corresponding, massive solid alloys (preparation described in Ref. [3]), by powdering in a mortar (particle size: 5-40 μm). To realise strain relief, the powder was encapsulated in a quartz tube and annealed at 1023 K for 15 min followed by water quenching. A part of the HT-$Ni_{1.35}Sn$ batch was subsequently annealed for 4 d at 683 K, i.e. just below the equilibrium transition temperature LT'→HT (see Figure 1).
The thus obtained three different powder batches,
HT-$Ni_{1.50}Sn$ quenched from T_1 = 1023 K,
HT-$Ni_{1.35}Sn$ quenched from T_1 = 1023 K, and
LT'-$Ni_{1.35}Sn$ quenched from T_1 = 683 K
were subsequently sealed in quartz capillaries and annealed at various temperatures T_2 < 600 K for certain periods of time (in oil or salt baths) and subsequently quenched.

X-ray diffraction measurements
For studying the structural changes occurring upon annealing X-ray powder diffraction was performed without and with (for lattice-parameter determination) internal Ge standard with CuKα1 radiation (1.54056 Å) on

- a Philips X'Pert MPD diffractometer (thin powder layers on Si wafers cut parallel to the (510) plane measured in reflection),
- a Huber G670 Guinier camera with integrated imaging plate system (thin powder layers on mylar foil measured in transmission), and on
- an Enraf-Nonius FR552 Guinier camera equipped with imaging plates which were read out on a Fujifilm BAS5000 imaging plate scanner (samples on adhesive tapes, measured in transmission).

Data evaluation of X-ray diffraction measurements
The X-ray powder diffraction patterns were evaluated (software: [7,8]) in terms of

- the hexagonal or orthorhombic lattice parameters from the reflection positions after correction of the 2θ scale using the Ge standard reflections;
- the physical diffraction-line broadening determined on the basis of beforehand determined instrumental profile and fitting, in a convolution procedure, the parameters of a pseudo-Voigt function representing the physical line broadening.

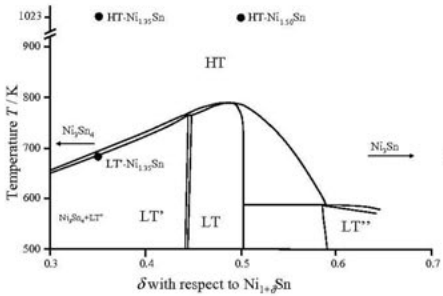

Figure 1. Tentative phase diagram Ni-Sn in the $Ni_{1+\delta}Sn$ range considering recent work [4-6]. The black points indicate temperatures at which the three powder samples used in this study were equilibrated prior quenching.

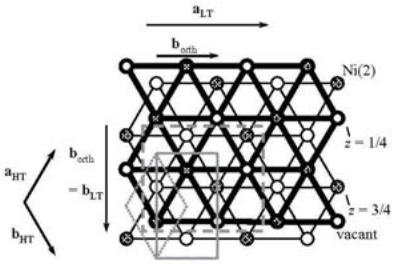

Figure 2. Projection of the hcp-type arrangement of the trigonal-bipyramidal sites in $Ni_{1+\delta}Sn$ indicating the Ni(2) distribution in ideal LT-$Ni_{1.50}Sn$. Its unit cell as well as those of the HT phase and of the orthorhombic average structure are indicated.

Results and Discussion

Ordering of HT-$Ni_{1.50}Sn$ quenched from 1023 K

The ordering of $Ni_{1.50}Sn$ upon annealing below 680 K (leading to LT) occurs in a two-stage fashion [6]:

Stage I. Formation of the long-range ordered state, as evidenced by the appearance of broad superstructure reflections at the end of this stage, indicating the presence of small and faulted domains. In spite of the appearance of the superstructure reflections, during this *stage I* the pattern represented by the fundamental reflections seems to 'remain hexagonal', only the lattice parameters change such that the axial ratio c_{HT}/a_{HT} increases approaching the *effective c/a* of the orthorhombic low-temperature phase (Figure 3).

Stage II. Coarsening of the domains, as indicated by sharpening of the initially broad superstructure reflections. Simultaneously, the fundamental reflections split in accordance with the orthorhombic distortion observed for the final LT phase. It must be stressed, that from the stage on where an analysis of the superstructure reflections becomes feasible, their integrated intensities remain constant.

Kinetic data of *stage I* have been reported on the basis of in-situ and ex-situ X-ray powder diffraction tracing the annealing time-dependent *c/a ratio* for different annealing temperatures [6]. Data from ex-situ experiments are presented in Figure 3, for T_2 = 490 K, 510 K, 530 K ([6], respectively) and 490 K (new).

The kinetics of *stage II* was investigated by tracing the line broadening of four different superstructure reflections, employing 'virginal' HT-$Ni_{1.50}Sn$ annealed at T_2 = 553 K, 568 K, 583 K and 598 K. The Scherrer-type line broadening of the four reflections was analysed in terms of the averaged 'effective' domain size (Figure 4; the effective domain sizes obtained for the different superstructure reflections vary as observed previously for other ordered alloys with small domains [9]). Significant microstrain broadening contribution to the line

broadening of the superstructure reflections was excluded by comparison with the widths of the fundamental reflections.

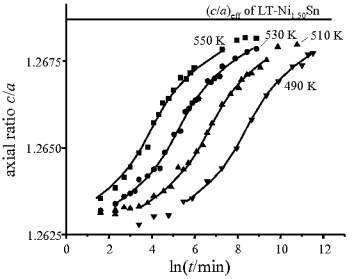

Figure 3. Annealing-time dependent increase of c/a upon annealing HT-$Ni_{1.50}Sn$ at various temperatures T_2, data updated with respect to [1]. The solid curves represent fits according to Eq. (2).

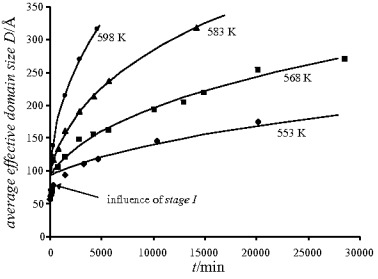

Figure 4. Coarsening of small-domain LT-$Ni_{1.50}Sn$ produced by annealing HT-$Ni_{1.50}Sn$ (stage 2 of order formation). The solid curves represent fits according to Eq. (2).

Ordering of HT-$Ni_{1.35}Sn$ quenched from 1023 K

The analogue of *stage I* of ordering of HT-$Ni_{1.50}Sn$ was investigated for HT-$Ni_{1.35}Sn$ quenched from 1023 K. A similar behaviour as for HT-$Ni_{1.50}Sn$ was observed for HT-$Ni_{1.35}Sn$ upon annealing at T_2 = 458 K, 473 K, 493 K, and 513 K (*cf.* Figure 5).

Stage II was not investigated for $Ni_{1.35}Sn$ because for this composition the superstructure reflections were too weak to evaluate and trace the line-widths systematically.

Increase of long-range order in LT'-$Ni_{1.35}Sn$ quenched from 683 K

For LT'-$Ni_{1.35}Sn$ the degree of long-range order decreases strongly with increasing temperature from 473 K und 673 K [4]. Nevertheless, even for samples equilibrated just below the order-disorder transition temperature, the satellite reflections are sharp, indicating large, and largely unfaulted ordered domains. An orthorhombic distortion is evident from the clearly split fundamental reflections. Such a state is present for the LT'-$Ni_{1.35}Sn$ batch quenched from 683 K.

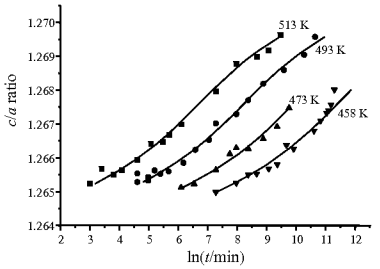

Figure 5. c/a increase during stage I of ordering occurring upon annealing HT-$Ni_{1.35}Sn$ quenched from T_1 = 1023 K. The solid curves represent fits according to Eq. (2).

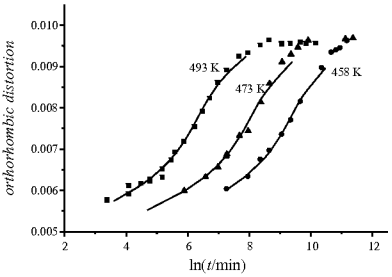

Figure 6. Increase of the 'orthorhombic distortion' due to an increase of long-range order in LT'-$Ni_{1.35}Sn$ quenched from T_1 = 683 K. The solid curves represent fits according to Eq. (2).

Upon annealing at T_2 = 458 K, 473 K, 493 K, 503 K, 513 K and 533 K the *(integral) intensities* of the satellite reflections increase and at the same time the *orthorhombic distortion* and *effective c/a ratio* increase. The latter three quantities are found to be related with each other in a linear fashion, independently of T_2, indicating that each of these parameters supplies in principle the same kinetic information. The most accurately determinable variable is the orthorhombic distortion, which was, therefore, used to trace the progress of ordering. Upon prolonged annealing the orthorhombic distortion approaches asymptotically a slightly T_2-dependent equilibrium value (Figure 6).

Determination of activation energies

Various ways exist to obtain kinetic information from annealing time and temperature dependent data. If

-for each annealing temperature T_2 the reaction path is the same (the reaction is 'isokinetic'),

-the end-state of the process is T_2-independent, and

-an Arrhenius-type behaviour for the 'reaction rate' $v = \mathrm{d}p/\mathrm{d}t$ is assumed ($v(p) = v_0(p) \cdot \exp[-Q/RT_2)]$) where p denotes the property characterising the progress of the considered process, the 'equivalence time method' can be employed [10,11] to determine the (p independent) activation energy Q without further assumptions concerning $v_0(p)$. The basic equation for this method is

$$t(p,T_2) = \tau(p) \cdot \exp(Q/RT_2) \qquad (1)$$

where $t(p,T_2)$ is the annealing time needed to change the system from a specific starting point (e.g. p_{start}) to p at the (constant) annealing temperature T_2. τ is the fictitious time needed for the same at infinite T_2, i.e. $\tau(p) = \int_{p_{start}}^{p} [\mathrm{d}p'/v_0(p')]$.

If $p(t,T_2)$ is plotted vs. $\ln(t)$, parallel curves shifted with respect to each other along the $\ln(t)$ scale are obtained. If their shape can be approximated e.g. by polynoms,

$$\ln\tau(p) + Q/RT_2 = \ln(t) = b_3 p^3 + b_2 p^2 + b_1 p + b_0(T_2) \qquad (2)$$

with T_2-independent fitting parameters b_1, b_2 and b_3, and T_2-dependent $b_0(T_2) = \beta_0 + Q/RT_2$ (β_0 being T_2 independent), one can determine the activation energy Q in an Arrhenius-type fashion by plotting $b_0(T_2)$ vs. T_2.

Here, p was taken as the *c/a* ratio for the *stage I* ordering process for HT-$Ni_{1.50}Sn$ and HT-$Ni_{1.35}Sn$, which yielded activation energies of 165(4) kJ/mol and 166(3) kJ/mol. Taking, furthermore, for p the *orthorhombic distortion* for annealing of LT'-$Ni_{1.35}Sn$ quenched from 683 K, an activation energy of 160(2) kJ/mol is obtained.

The kinetics of the domain coarsening in *stage II* of the ordering of HT-$Ni_{1.50}Sn$ could in principle also be analysed in terms of Eq. (2). However, for coarsening a widely accepted rate law is known,

$$D^n(t) - D_0^n = B(T_2)\,t \qquad (3)$$

with which the experimental parameters could well be fitted to experimental data. D is the average 'effective' domain size from four superstructure reflections, D_0 the effective domain size at t = 0 fitted to 90 Å, n an exponent fitted to n = 2.9 and a rate constant $B(T_2)$ satisfying an Arrhenius equation $B(T_2) = B_0\exp(-Q/RT_2)$. An activation energy of 212 kJ/mol was obtained, where the D < 100 Å data were excluded for fitting.

The result of D_0 = 90 Å might be considered as peculiar surprising because the starting material shows no superstructure reflections at all. However, the apparent anomaly may be understood because for short annealing times and low annealing temperature the time needed to complete *stage I* may not be neglected, as has been done for the analysis performed here according to Eq. (3).
The three activation energy values determined for the *stage I* of order formation in HT-$Ni_{1.50}Sn$ and HT-$Ni_{1.35}Sn$ as well as for the increase of long-range order in LT'-$Ni_{1.35}Sn$ are about equal: 160-165 kJ/mol. The rate-determining step of these processes is apparently the same and could be related with the atomic mobility of the ordering Ni(2). A considerably higher activation energy of about 210 kJ/mol is obtained for domain coarsening. However, also here the mobility of Ni(2) should be rate-determining when the domain-orientation is changed upon coarsening (three differently orthorhombic domain orientations are possible with respect to the original hexagonal lattice). This suggests a domain interface control of the coarsening, i.e. that the specific domain interface structure inhibits Ni(2) mobility.

Conclusion

- The equivalence-time method was successfully employed to determine three different activation energies pertaining to three different ordering processes in $Ni_{1+\delta}Sn$ from annealing-time and annealing-temperature dependent X-ray powder diffraction data only assuming an Arrhenius-type behaviour of reaction rate. For a fourth process the application of a specific rate law was possible (domain coarsening).
- The higher activation energy found for domain coarsening compared to the other three processes suggests a special role of the domain interfaces in the coarsening kinetics.

References

1. Brand, P., 1967, *Z. Anorg. Allg. Chem.*, **353**, 270.
2. Fjellvåg, H. & Kjekshus, A., 1986, *Acta Chem. Scand.*, **A40**, 23.
3. Leineweber, A., Ellner, M., & Mittemeijer, E.J., 2001, *J. Solid State Chem.*, **159**, 191.
4. Leineweber, A., 2004, *J. Solid State Chem.*, **177**, 1197.
5. Leineweber, A. & Mittemeijer, E.J., 2002, E.J., *Z. Anorg. Allg. Chem.*, **628**, 2147.
6. Leineweber, A., Mittemeijer, E.J., Knapp, M. & Baehtz, C., 2004, *Mater. Sci. Forum*, **443-444**, 247.
7. *Topas, General Profile and Structure Analysis Software for Powder Diffraction* Data, V2.0, Bruker AXS GmbH, Karlsruhe, Germany.
8. Toby, B. H., 2000, *CMPR - package of programmes* (National Institute of Standards, USA; http://www.ncnr.nist.gov/xtal).
9. Wilson, A.J.C., 1962, X-ray Optics, 2nd ed. (Methuen, London, U.K.).
10. Mittemeijer, E. J., 1992, *J. Mater. Sci.*, **27**, 3977.
11. Burke, J., 1965, *The Kinetics of Phase Transformations in Metals* (Pergamon Press, Oxford, UK).

Z. Kristallogr. Suppl. **23** (2006) 357-362

In situ neutron diffraction study of the low cycle fatigue of the α–γ duplex stainless steel

P. Lukáš[1], O. Muránsky[1], J. Polák[2] and P. Jenčuš[1]

[1]Nuclear Physics Institute, 250 68 Řež, Czech Republic
[2]Institute of Physics of Materials, Žižkova 22, 616 62 Brno, Czech Republic
*Contact author: P. Lukáš; e-mail: lukas@ujf.cas.cz

Keywords: neutron diffraction, fatigue, duplex steel, residual stress

Abstract. The mechanism of the low cycle fatigue in α-γ duplex stainless steel was examined by the neutron diffraction technique performed in situ upon mechanical exposure consisting of the tension-compression cycles with the strain amplitude of 0.8 %. Deformation response of both constituent components, i.e. ferrite and austenite, was studied in situ during the individual applied cycle in detail. Furthermore, the evolution of the residual strains in both phases after tensile and compressive unloading was monitored during cycling. Information on the evolution of lattice strains and microstrains has been obtained from the diffraction profiles collected during the fatigue experiment. The results show different deformation behavior and hardening of austenite and ferrite. The evolution of internal stresses and residual stresses detected in both phases during individual cycles is strongly affected by initial stresses present in both phases. These thermal stresses are introduced into the individual phases of the duplex steel during cooling from high (homogenization) temperature due to different thermal expansion coefficients of the constituent phases.

Introduction

The first generation of duplex stainless steels were developed more than 70 years ago in Sweden for use in the sulfite paper industry [1]. Duplex alloys were originally developed to overcome corrosion problems caused by chloride-bearing cooling water and other aggressive chemical process fluids. Nowadays, the duplex steels are established in a wide range of products from pipes and paper machines through heat exchangers and pressure vessels to chemical tankers. The high strength of the duplex steels enables both weight and cost savings when using them as corrosion resistant material. The application of duplex steels to the structures subjected to the external stress has increased the demand for full understanding of the fatigue processes in these materials.

Both corrosion resistance and excellent mechanical properties of duplex stainless steels can be explained by their chemical composition based on high contents of Cr and Mo and balanced microstructure of approximately equivalent volume fractions of ferrite and austenite. Duplex steels combine some of properties of each constituent phase - they are resistant to

stress corrosion cracking although less than the ferritic steels; their toughness is higher than that of the ferritic steels but lower in comparison with the austenitic steels. The two-phase microstructure provides higher resistance to pitting and stress corrosion cracking in comparison with conventional stainless steels. Moreover, additions of nitrogen can promote hardening by interstitial solid solution mechanism, which raises the yield strength and ultimate strength values without loss of toughness [2].

The neutron diffraction method presents a well established method to investigate the load sharing between the ferritic and austenic grains. Information provided by this method is related to a large sample volume because of high penetration ability of thermal neutrons. This technique allows determination of the strain tensor in each phase separately and has been successfully used for studying load sharing between phases and the study of the effects of macro- and microstresses on mechanical properties of different kinds of materials [6-8]. In two-phase materials, like duplex stainless steels, microstresses between the two phases are always present due to differences in physical and mechanical properties between the two phases.
In the present study, the in-situ neutron diffraction was carried out to analyze the initial residual stress of both phases and to evaluate the evolution of micro- and macrostresses during both static and cyclic loading. The diffraction response of austenitic and ferritic phases to hardening/softening process during the cyclic straining was investigated.

Experimental

The experimental material is a commercial duplex stainless steel SAF 2507 provided by Sandvik AB (Sandviken, Sweden) in a form of a rod of diameter 30 mm. The specimens for tension/compression low cycle tests were machined to the diameter of 5 mm and the gauge length of 14 mm. The chemical composition of the SAF 2507 steel is given in table 1. The heat treatment consisted of annealing at the temperature of 1050 °C for 1 hour and, subsequently, water-cooling was applied. The microstructure consisting of austenitic grains surrounded by ferritic matrix is shown in figure 1. The phase composition was determined by the image analysis, the austenite volume fraction of 34% has been found.

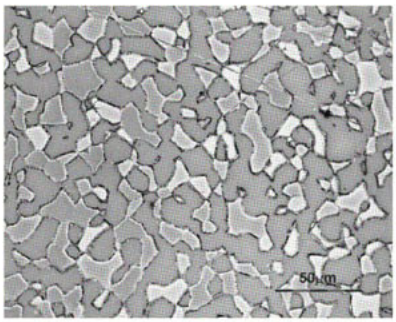

Figure1. The microstructure of SAF2507 steel.

Table 1. Chemical composition of SAF 2507 steel (in wt. %).

C	Cr	Mo	Ni	N
0.02	25	3.8	7	0.27

The diffraction experiment was performed at the NPI Řež by using the dedicated stress/strain diffractometer TKSN-400 equipped with tension-compression testing machine which enables loading up to 20 kN. Both diffractometer and deformation rig are fully PC controlled by SCP program enabling very flexible measuring schemes. The neutron diffraction spectra are collected during temporarily stopovers of the testing machine, in the regime of constant stress or strain or during unloading. The linear position sensitive detector enables fast acquisition of the diffraction spectra in a relatively narrow 2θ band ($2\theta \cong 8^{\circ}$) with high instrumental resolution of $\Delta d/d \approx 2\text{x}10^{-3}$. This dedicated facility [3,4] is mostly used for *in situ* investigations of the deformation processes in different kinds of materials [4-8]. In the present experiment, the detector window was set to $2\theta \sim 68^{\circ}$ to cover both ferrite (110) and austenite (111) reflection (2θ = 69.15° and 67.42°, respectively). Only axial lattice strain component was measured in this experiment.

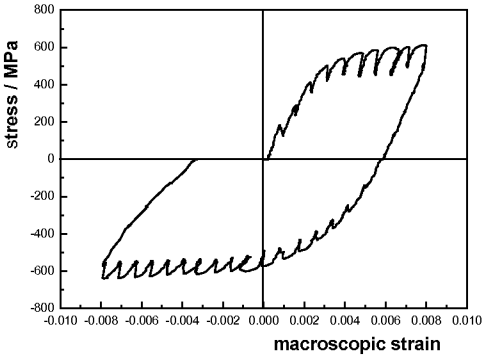

Figure 2. The incremental mechanical test of the individual tensile/compressive cycle. The diffraction spectra were measured during temporary stops of the deformation machine.

Results

Two types of experiments were performed. One specimen was used for detailed examination of the stress-strain response and internal stress measurement *in situ* during tensile-compressive load cycle with the strain amplitude of 0.8 %. In this case, the diffraction spectra were recorded after each strain step of 0.08 %. The corresponding σ–ε curve (hysteresis loop) is shown in figure 2. The lattice strains of austenitic and ferritic phase evaluated from the diffraction spectra were measured during temporary stops of the deformation machine and are summarized in figure 3. The elastic lattice strain is a measure of the relaxed applied stresses in both phases. Note an interesting effect - the tensile residual strain is detected in ferrite both after compressive and tensile half-cycle while the austenite remains compressed upon the same conditions. The similar behavior of residual strains was observed in both phases when 70 tensile/compressive cycles of the same strain amplitude of 0.8 % were applied to the other specimen. The diffraction spectra were measured for 2 hours in the initial state and in the stress-free state after tensile and compressive unloading. The stress-time history of this fatigue experiment can be seen in figure 4. In general, the evaluation of angular shifts of individual diffraction profiles can be

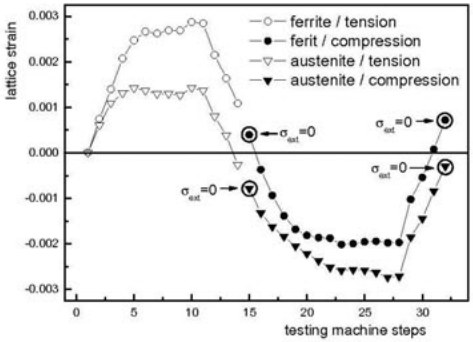

Figure 3. Time evolution of lattice strains evolving in ferrite and austenite in situ upon one cycle. One step of the testing machine represents the strain step of 0.08%. Note the residual lattice strains at stress-free state after tensile and compressive loading.

used for determining of the changes of the internal strains and stresses [6, 7] in both phases during the cycling. The evolution of diffraction peak width provides information on microstresses [9]. These measurements yield information on the changes of the lattice parameter due to residual lattice strains. However, due to different thermal expansion coefficients of the austenitic and ferritic phase significant thermal stresses are generated in both phases in the initial state due to cooling from the homogenization temperature. In the present paper, the thermal stresses are not reported absolutely and the lattice strains in ferrite and austenite are artificially reset to zero in the initial state. The measured changes in lattice strains are thus related to the initial state of the duplex steel only. This dependence is reported in figure 5. Appreciable changes of the internal residual strains in both phases take place after the first cycle, in subsequent cycling the changes are small. Since elastoplastic cyclic loading of materials results in complete relaxation of the mean stress to zero, the true residual elastic strains and thus residual stresses in each phase after unloading from tension and compression in saturated state (around 70 cycles) are algebraically equal but have opposite signs [10]. Using this argument the true residual strains in each phase were calculated and using elastic moduli of appropriate phases and the residual stresses in both phases were evaluated. They are shown in figure 6. By using of this rescaling the initial tensile stress in austenite and the initial compressive stress in ferrite are in agreement with the higher thermal expansion of the austenite (around 1.65×10^{-5} K^{-1}) than of the ferrite (1.1×10^{-5} K^{-1}). In austenite, the first half-cycle in compression and following unloa-

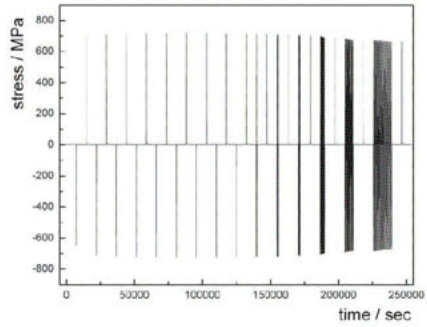

Figure 4. Stress evolution during the cycling process.

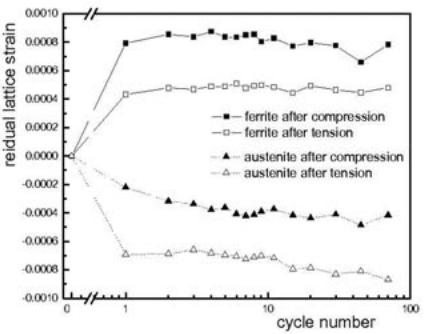

Figure 5. Evolution of changes of the lattice strains as a function of number of cycles.

ding reduces the tensile stress to a small negative value and following half-cycle in tension produces again larger tensile residual stress. The mean residual stress in each cycle decreases and the residual stresses after unloading become very soon symmetrical. Similarly in ferrite, the initial compressive residual stress is reduced.
The elastic stresses, which arise due to different thermal expansion coefficient are opposite in both phases but plastic deformation due to this stresses is negligible. Cyclic deformation results in appreciable increase in the dislocation density and formation of the characteristic structure [11, 12]. This results in the broadening of the diffraction profiles both in ferrite and in austenite. The profile width is plotted vs. number of loading cycles in figure 7. In agreement with the cyclic hardening curve of the material [10, 11] the initial increase is high and shows tendency to saturation. The hardening effect is clearly observable from the mechanical record of the stress needed to reach maximum and minimum strain in a cycle (figure 4). Increase of the external stress amplitude during the first three cycles is apparent whereas slight softening starts above 10^{th} cycle. The cycling softening can be explained due to localization of plastic deformation in persistent slip bands [12].

Conclusions

The investigation of low-cycle fatigue of dual phase stainless steel by using neutron diffraction method has brought interesting novel information on behavior of individual phases in the natural composite structure of duplex steel. The internal elastic stresses can be evaluated from the changes of the position of diffraction profiles and compared with the macroscopic stress-strain response and its evolution in cyclic straining. Initial stresses induced by cooling from high temperature due to different thermal expansion of both phases relax rapidly with cyclic straining. The residual elastic stresses in ferrite and in austenite after unloading from tension and compression and their evolution in cyclic loading was documented. Both phases show cyclic hardening, which results in the broadening of the diffraction profiles.
Because the only axial components of the residual lattice strains of both phases were measured in the present experiment, these strain components could not be necessarily balanced to demonstrate the total stress equilibrium. The knowledge of the stress free value of the austenite and ferrite lattice parameter, as well as the measurement of the radial strain components

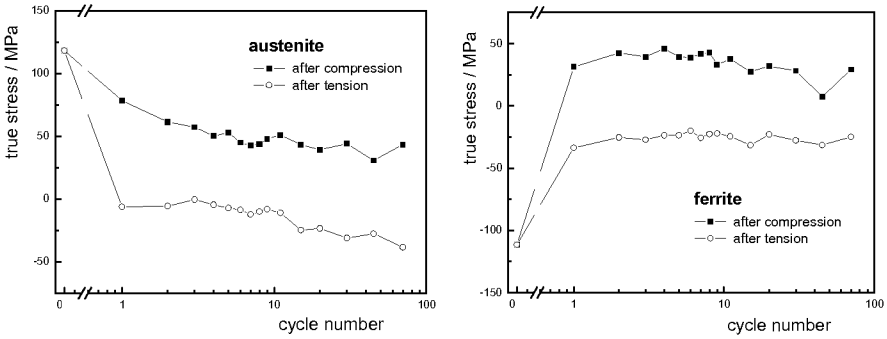

Figure 6. Estimate of true residual stresses evolving in both phases upon cycling (see text).

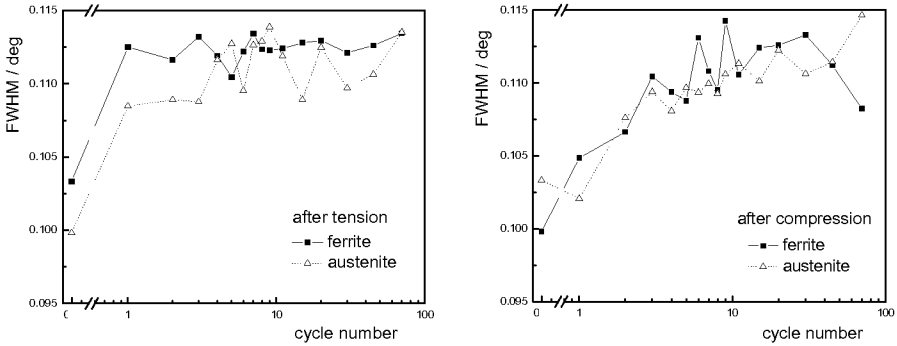

Figure 7. Evolution of the profile width as a measure of the microstresses.

would be of a great importance in creating of a more complex scheme of deformation and fatigue behavior of the duplex steels. This will be a subject of our further experimental studies.

References

1. www.lapump.com/html/duplex_stainless.html
2. www.azom.com
3. P.Mikula, M.Vrána, P.Lukáš, V. Wagner, 2002, *in Recent Advances in Experimental Mechanics,* ed. E.E.Gdoutos, (Dordrecht: Kluwer Academic Publishers), p.457-466.
4. www.ujf.cas.cz
5. P. Lukáš, P. Šittner, D. Neov, V. Novák, M. Vrána, P. Mikula, 2000, *Physica B,* **276/278**, 845-846.
6. Tomota, Y., Lukáš, P., Harjo, S., Park, J.H., Tsutchida, N., Neov, D., 2003, *Acta Mat.,* **51**, 819-830.
7. S. Harjo, Y. Tomota, P. Lukáš, D. Neov, M. Vrána, P. Mikula, M. Ono, 2001, *Acta Mat.* **49** (13), 2471-2479.
8. P. Lukáš, Y. Tomota, S. Harjo, D. Neov, P. Strunz, P. Mikula, 2001, *J. Neutr. Res.,* **9**, 415-421.
9. P. Strunz, P. Lukáš, D. Neov, 2001, *J. Neutr. Res.*, **9**, 99-106.
10. J. Polák, J., T. Kruml and S. Degallaix, 1993, *Scripta Metall.,* **29**, 1553-1558.
11. S. Degallaix, A. Seddouki, G. Degallaix, T. Kruml and J. Polák, 1995, *Fatigue Fract. Engng. Mater. Struct.,* **18**, 65-77.
12. Kruml, J. Polák, K. Obrtlík, S. Degallaix, 1997, *Acta Mater.*, **45**, 5145 - 5151.

Acknowledgements. The authors are grateful to the Grant Agency of the Academy of Sciences of the Czech Republic (contracts A1048107/01 and A2041201) and Grant Agency of the Czech Republic (contract 202/03/0891) for their support.

Z. Kristallogr. Suppl. **23** (2006) 363-368

SANS investigation of precipitate microstructure in nickel-base superalloys Waspaloy and DT750

P. Strunz[1,2,*], J. Zrník[3], T. Seliga[4], H. J. Penkalla[4]

[1]Nuclear Physics Institute, 25068 Řež near Prague, Czech Republic
[2]Laboratory for Neutron Scattering, ETHZ & PSI, CH-5232 Villigen PSI, Switzerland
[3]Technical University of Košice, Dept. of Materials Science, Park Komenského 11, 04001 Košice, Slovakia
[4]Research Center Jülich, Institute for Materials and Processes in Energy Systems, D-52425 Jülich, Germany
[*]Contact author; e-mail: strunz@ujf.cas.cz

Keywords: superalloys, precipitation, small-angle neutron scattering

Abstract. Microstructure of Waspaloy and DT750 Ni-base superalloys was investigated after the heat treatment as well as after long thermal exposure by Small-Angle Neutron Scattering (SANS). The SANS results clearly showed that there are large differences even between samples of the DT750 superalloy produced using different facilities. The modified heat treatment used for DT750 suppressed the formation of secondary precipitates. A strong influence of the thermal exposure on the superalloy microstructure was observed which can have an impact on the mechanical properties.

Introduction

The nickel-base superalloys are multicomponent alloy systems which are used at severe working conditions (rotors, discs or blades in turbines). The structure stability and creep resistance of superalloys is dependent on morphology and volume fraction of precipitates, predominantly γ', which strengthen the γ-phase matrix [1]. Various techniques (TEM, SEM, X-ray, neutron diffraction) are necessary in order to characterize the superalloy microstructure, especially its γ'-precipitate morphology.
Waspaloy (WASPALOY is a trademark of the United Technology Corporation) is a nickel-base polycrystalline superalloy [2], strengthened by γ' precipitates with bimodal size distribution, having excellent high-temperature strength and good resistance to corrosion, notably to oxidation. It is used for aerospace and gas turbine engine components at service temperatures up to 700°C for critical rotating applications (compressor and rotor discs, shafts, rings). Although this and similar superalloys were extensively studied by various macroscopic and microscopic techniques (see e.g. [3] and references therein), still deeper understanding of the processes taking place at the precipitate level during long-term thermal exposure is necessary

in order to optimize the microstructure and thus to improve the high temperature microstructural stability. Moreover, the need to develop new superalloys enabling still higher operational temperatures accelerates the necessity of microstructural investigations, also by non-traditional techniques. The SANS method [4] can contribute substantially to the morphology investigation of γ' precipitates in nickel base superalloys [5], frequently even in-situ [6-8].
The present SANS experiment was aimed to provide bulk information on the γ'-precipitate morphology in long-term thermally exposed Waspaloy and in the superalloy denoted DT750, which is derived from Waspaloy by the modification of the composition and heat treatment.

Experimental

Waspaloy (composition in wt%: Fe 0.57, Cr 19.22, Nb 0.01, Ti 3.13, Al 1.22, C 0.033, Co 19.35, Mo 4.52, Ni balance) was solution annealed at 1080 °C for 4h with subsequent cooling to 850 °C with a rate of 4K/min, then air cooled (AC) to room temperature (RT), followed by two-step precipitation heat treatment at 850 °C for 4h and at 760 °C for 16 h (steps separated by AC to RT). The microstructure of Waspaloy after heat treatment is shown in figure 1.
In order to avoid freckle formation, the composition of Waspaloy was modified (in wt%: Fe 0.61, Cr 19.3, Nb 1.46, Ti 1.61, Al 1.45, C 0.027, Co 19.3, Mo 4.45, Ni bal.) and the experimental alloy was denoted DT750. The heat treatment of this alloy was simplified: DT750 has been solution treated at 1080 °C for 4 h, cooled with cooling rate of 4K/min directly (i.e. without cooling to RT) to the precipitation temperature of 800 °C and aged for 16h.
The microstructure of these two superalloys obtained using the above described treatments was investigated by SANS. At the same time, the morphological changes (precipitate size and their volume fraction) resulting from the long thermal exposure of the alloys were examined in dependence on the temperature and time of exposure (see table 1 for the overview).
The presented SANS measurement was carried out at SANS-II facility of SINQ user lab at Paul-Scherrer Institut Villigen, Switzerland [9]. Platelet samples of about 2 mm thickness and 14 mm diameter were measured at room temperature. The scattering data were collected at several experimental geometries (the sample-to-detector distance varied from 1 m to 6 m, and the neutron wavelength λ from 4.55 Å to 19.6 Å). The covered scattering vector $\boldsymbol{Q}$ range was 1×10^{-3} Å^{-1} – 0.35 Å^{-1} (i.e. 1×10^{-2} nm^{-1} < Q < 3.5 nm^{-1}), where the magnitude $Q = |\boldsymbol{Q}| = |\mathbf{k}-\mathbf{k}_0|$, $\mathbf{k}_0$ and $\mathbf{k}$ being the wavevectors of incident and scattered neutron, respectively, and $|\mathbf{k}| = |\mathbf{k}_0| = 2\pi/\lambda$. The measured raw data were corrected for background scattering and calibrated to the absolute scale. The magnitude of the resulting differential macroscopic cross section is proportional to the square scattering contrast of the γ' precipitates and their volume fraction. However, the exact determination of scattering contrast is practically not possible (because of the chemical-composition uncertainty of γ and γ' phases), hindering thus a direct determination of the volume fraction. Therefore, this quantity has to be derived indirectly from the modelling of the microstructure and scattering curves.

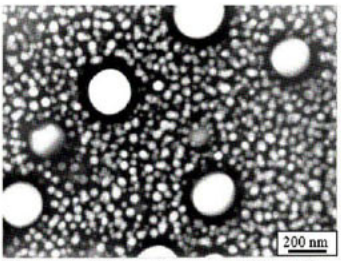

Figure 1. Microstructure of Waspaloy after the standard heat treatment.

Evaluation and results

The full measured scattering profiles collected at RT for the different thermally exposed samples are presented in figures 2 and 3 for the standard Waspaloy and DT750, respectively. The diagrams show the scattering cross section $d\Sigma/d\Omega$ vs. scattering vector magnitude Q.
SANS data were processed using the NOC program [7]. The procedure is based on the numerical simulation of a scattering profile using a three-dimensional (3D) microstructural model of a particle system. The modelled scattering curve thus also contains the interparticle-interference effect. The calculated profile is then fitted to the experimental curve in order to find the optimum microstructural parameters (i.e. γ'-precipitate size, their volume fraction, eventually center-to-center distance) which fit best the experimental data. In the used model, the form of γ' precipitate was approximated - in agreement with the indication obtained by electron microscopy (see figure 1) - by the spherical shape. Size distribution was simulated by a log-normal curve. Selected fitted curves are displayed in figures 2 and 3 as well by lines through the symbols which represent the measured data.

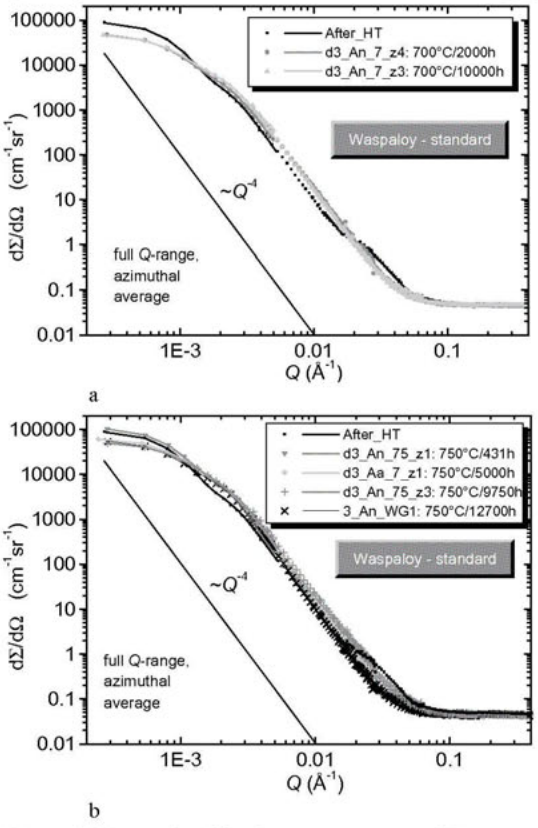

Figure 2. Measured and fitted scattering curves of Waspaloy: (a) thermally exposed at 700°C, (b) at 750°C.

Figures 2a and 2b show the measured scattering curves for the standard Waspaloy in the full Q-range. There is an extra scattering observable in the pattern (above $Q = 0.002$ Å^{-1}), which is superimposed on the scattering background originating from large-scale inhomogeneities as carbides or nitrides (this scattering background changes with the slope proportional to Q^{-4} at larger Q values). The increased scattered intensity at around $Q = 0.03$ Å^{-1} indicates secondary precipitation (i.e. relatively small precipitates) in the heat treated alloy without any additional thermal exposure (figure 2a). These secondary precipitates - precipitated most probably on cooling from the hold temperature during the heat treatment - have the mean (volume weighted) size equal to 150 Å, the center-to-center distance of 210 Å and their volume fraction is around 15 %. The diagrams do not provide an indication of the presence of secondary precipitates in

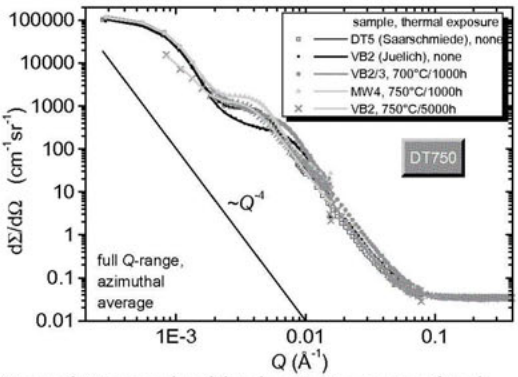

Figure 3. Measured and fitted scattering curves of modified Waspaloy (DT750).

the samples exposed both at 700 or 750 °C in the standard Waspaloy.
Figure 3 displays the detailed measured and evaluated scattering curves for modified (DT750) alloy at low Q-values. There is no scattering exceeding the Q^{-4} scattering background as well as constant incoherent background detectable in the modified heat treated alloy (see figure 3) at large Q-values (i.e. for $Q > 0.02$ Å^{-1}). It means that there is no indication of the secondary precipitation for this modified alloy at all.

Increase of the scattering in the low-Q region (i.e. in the range $0.002 < Q < 0.01$ Å^{-1}) can be interpreted as an interparticle-interference maximum originating from the relatively dense (20-35%) population of γ' precipitates. The microstructural models corresponding to the optimum fits are displayed in figure 4.

Discussion

The bulk parameters of primary precipitates resulting from the evaluation (mean size, distance and volume fraction of γ' precipitates) are stated in table 1. When comparing the standard Waspaloy with its modification DT750, one can recognize much coarser precipitates in standard Waspaloy (220 nm) than in DT750 (102, respectively 62 nm). The volume fraction of primary precipitates is also larger in DT750 after heat treatment; however, a large part of γ' volume fraction (15%) is occupied by the secondary precipitates (not reported in the table 1) in the standard Waspaloy.
It can be noticed that a large difference exists between the alloys prepared at different places (Saarschmiede, Juelich): the heat treatments are nominally identical but can vary in details (e.g. cooling rates from solution temperature and from the γ'-stabilisation step to RT).
Thermal exposure has then an additional effect on the growth of γ' precipitates. The evolution of microstructure with thermal exposure is slightly different in both alloys.

Standard WASPALOY

Even at the shortest thermal exposures, the secondary precipitates disappear on expense of the growth of primary precipitates. The precipitates grow first without significant change of the center-to-center distance (see sample d3_An_7_z4, i.e. 700 °C/2000h in table 1). Only after this initial period, the distance between the precipitates starts to increase. The volume fraction slightly decreases at the longer exposure times or higher temperature, which could be an indication of dissolution of the smallest precipitates from their size distribution after long-term exposure.

Table 1. Results of the SANS-data evaluation for all thermal exposures of both superalloys. Volume-weighted values of the mean size are reported.

Alloy	Sample name	heat treatment at	thermal exposure	mean size (Å)	mean distance (Å)	volume fraction
Waspaloy	After_HT		none	2200	3180	0.10
	d3_An_7_z4		700°C/2000h	2730	3210	0.25
	d3_An_7_z3		700°C/10000h	2870	3403	0.27
	d3_An_75_z1		750°C/431h	2820	3420	0.25
	d3_Aa_7_z1		750°C/5000h	2950	3580	0.22
	d3_An_75_z3		750°C/9750h	2920	3830	0.20
DT750	DT5	Saarschmiede	none	1020	1310	0.21
	VB2	Juelich	none	620	740	0.21
	VB2/3	Juelich	700°C/1000h	750	800	0.35
	MW4	Juelich	750°C/1000h	1190	1400	0.27
	VB2	Juelich	750°C/5000h	1200	1520	0.20

DT750

The sample VB2/3, i.e. the sample with the shortest examined exposure (700 °C/1000h) exhibits significant increase of the volume fraction of γ' precipitates with respect to the non-exposed one. This effect occurs without a significant change of the distance of the precipitates. The temperature of exposure 700 °C is most probably sufficient enough to allow the diffusion of elements and growth of precipitates. On the other side, this temperature is low enough not to cause dissolution of the smaller precipitates in the size distribution. Exposures at higher temperatures (750 °C/1000h or 5000h) results similarly as in the case of standard Waspaloy in coarsening of precipitates and gradual decrease of the volume fraction.

It can be seen that DT750 contains finer primary precipitates also after thermal exposure than Waspaloy (cf. samples d3_Aa_7_z1 and VB2, both exposed at 750 °C for 5000h).

Conclusions

The experiment had clearly revealed the secondary precipitation in the standard Waspaloy after the heat treatment. These precipitates, however, are already not present in thermally exposed specimens (at least not with a significant volume fraction). As the secondary precipitation is not observed in DT750 (which was not cooled to room temperature between the

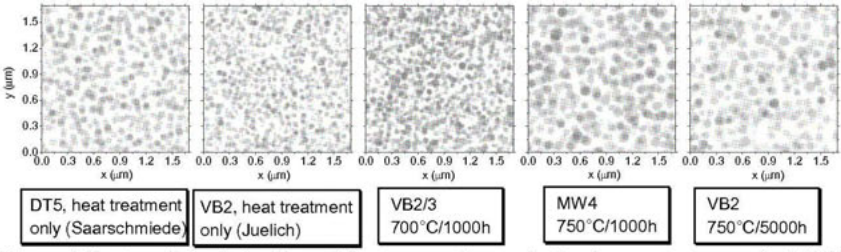

Figure 4. Sections through the 3D models corresponding to the fitted scattering curves for DT750.

individual steps of the heat treatment), the creation of the secondary precipitates in the standard Waspaloy occurs most probably on the cooling either from 850 °C or from 760 °C to RT during the heat treatment.

The SANS results clearly showed that there are large differences even between samples of the modified superalloy DT750 heat treated at different facilities (Saarschmiede, Juelich). It means that the microstructure of DT750 strongly depends on the details of the heat treatment (e.g. cooling rate).

A strong influence of the thermal exposure on the microstructure of both superalloys was observed which can have an impact on the mechanical properties. When comparing both investigated superalloys, the modified alloy (DT750) exhibits finer dispersion of γ' precipitates, both after heat treatment and after additional long-term thermal exposure.

References

1. Durand-Charre, M., 1997, *The microstructure of superalloys* (Amsterdam, The Netherlands: Gordon and Breach Science Publishers).
2. http://www.specialmetals.com/documents/Waspaloy.pdf
3. Mannan, S., Patel, S. & deBarbadillo, J., at http://www.specialmetals.com/documents/Long%20Term%20Thermal%20Stability%20of%20INCONEL%20Alloys%20718,%20706,%20725,%20783,%20909%20and%20Waspaloy%20at%20593C%20and%20704C.pdf
4. Kostorz, G., 1979, in *Neutron Scattering (Treatise on materials science and technology)*, edited by G. Kostorz (NY: Academic Press), 227-289.
5. Zrník, J., Strunz, P., Horňák, P., Vrchovinský, V. & Wiedenmann, A., 2002, *Applied Physics A*, **74**, 1155-1157.
6. Strunz, P., Mukherji, D., Gilles, R., Rösler, J. & Wiedenmann, A., 2003, *Materials Science Forum*, **426-432**, 821-826.
7. Strunz P., Gilles R., Mukherji D. & Wiedenmann A., 2003, *J.Appl.Cryst.*, **36**, 854-859.
8. Mukherji, D., Strunz, P., Del Genovese, D., Gilles, R., Rösler, J. & Wiedenmann, A., 2003, *Metall. Trans. A*, **34**, 2781-2792.
9. Strunz, P., Mortensen, K. & Janssen, S., 2004, *Physica B*, **350**, e783-e785.

Acknowledgements. The support from SINQ (PSI Villigen, CH) enabling to carry out the SANS experiment is gratefully acknowledged. P. Strunz acknowledges the support through the projects GA-CR 202/03/0891, MSM 2672244501 and IRP AV0Z10480505.

Z. Kristallogr. Suppl. 23 (2006) 369-374

Diffraction analysis of iron materials after surface machining

M. Čerňanský[1,*], N. Ganev[2], J. Barcal[3], J. Drahokoupil[1,2], K. Kolařík[2]

[1]Institute of Physics, Academy of Sciences of the Czech Republic, Na Slovance 2, 182 21 Praha 8, Czech Republic
[2]Faculty of Nuclear Sciences and Physical Engineering, Trojanova 13, 120 00 Praha 2, Czech Republic
[3] Faculty of Mechanical Engineering, Technická 4, 166 07 Praha 6, Czech Republic
[*]Contact author; e-mail: cernan@fzu.cz

Keywords: iron materials, surface treatment, size-strain, residual stress, phase analysis

Abstract. The aim of the paper is to present the possibilities of X-ray diffraction analysis for characterisation of surface layers after machining by using electro discharge machining (EDM) and electro chemical cutting (ECM), in comparison with "classical" grinding of steels. Residual macroscopic stress, crystallite size, microstress and phase composition were found for the mentioned methods of surface treatment. Anomalous diffraction profiles were observed especially after the method EDM. It can be caused by the bimodal distribution of crystallite size.

Introduction

The sign and magnitude of residual stresses and generally all diffraction characteristics of treated surfaces always depend on the type of material and on the parameters of applied technology of their machining. The character of stresses on the workpiece surface and beneath it affects its functionality. Compressive stresses increase fatigue limit and improve wear resistance, whereas tensile stresses decrease fatigue strength and make destruction of frictional surfaces easy. Profiles of diffraction lines contain important information about the real structure of polycrystalline materials. Small crystallite size and lattice strains (or microstresses) are reasons of broadening of diffraction profiles.

Samples under investigation

The research is being carried out on two sets of steel specimens:

- a tool steel (Czech grade 19 436 – 2.0 % C, 12.0 % Cr, 0.4 % Mn) – typical material for dies, casting moulds, shearing and cutting tools. The samples were prepared from material in as-received (NK) and quenched (K) state. Quenching was performed in the oil bath of temperature 220 – 250 °C after heating at 940 – 970 °C.

- a low-alloy steel (Czech grade 14 220 – 0.15 % C, 1.0 % Cr, 1.4 % Mn) – standard for studying the effect of heat and structure phenomena on the shaped surfaces, material was in as-received state.

The squared samples 15 × 15 × 7 mm^3 were prepared by using two methods of unconventional machining and grinding:

- ***Electro-discharge machining*** (fine cut) was realised with an AGIEETRON IMPAKT device using graphite and copper electrodes. Working conditions were automatically optimised on the base of the required roughness of the treated surfaces. The quenched samples are designated EDM K G, EDM K Cu, unquenched as EDM NK G, EDM NK Cu.
- ***Electro chemical grinding*** was performed using a WENAT device with $NaNO_3$ electrolyte and a diamond wheel. The samples are analogically labelled ECM K in the quenched and ECM NK in the as-received state.
- ***Ground samples*** were prepared with cooling on a horizontal surface grinding machine *BPH 20* with an *A99 25K9V* grinding wheel and the feed $v = 35\ m \cdot s^{-1}$.

X-ray diffraction methods used

- A 2θ/θ – diffractometer Siemens with CrKα radiation was used to measure diffraction patterns for phase and profile analysis.
- Line profiles were fitted by the Pearson-VII function. Only three diffraction lines can be obtained from steel (ferrite) with Cr-radiation. Furthermore a significant anisotropy of elastic constants is present in iron. Consequently, methods which use more reflections for the separation of particle size and microstrain broadenings are questionable in this case. Our application of Williamson-Hall plot confirms it. Therefore, single line methods were used, especially the Voigt single line method [1] and the single line Fourier analysis method [2].
- Macroscopic stress analysis was performed in the longitudinal (σ_L) and transversal (σ_T) direction by means of an ω-goniometer SIEMENS with CrKα radiation. Calculation of average residual stresses within the penetration depth of applied radiation (2 – 6 μm) was based on the shift of the centroid of ferrite {211} diffraction line [3] and X-ray elastic constants $½s_2 = 5.76 \cdot 10^{-6}\ MPa^{-1}$, $-s_1 = 1.25 \cdot 10^{-6}\ MPa^{-1}$.

Results

Phase analysis

Besides the ferritic (α-Fe) and austenitic (γ-Fe) phases a minority fraction of Cr_7C_3 (PDF No 11-550, 5-720, 6-0683) was observed in the surface layers of 19436 samples (figures 1, 2). The ratio of the two Fe crystallographic phases was estimated using the method designed by J. Fiala that does not require standards [4]. Owing to the high content of Cr and C in 19436 samples, the fraction of retained austenite is large. Quenching in oil is mild and it led to stabilization of the austenite [5]. The content of martensite could therefore be neglected as the approximating of {211} line with Pearson-VII function vindicated it.

The treating by EDM leads to an additional increase of the austenite in 19436 samples. The more pronounced increase in the case of graphite electrode than in the case of Cu electrode (figure 2) could be explained by the higher heat loading when a graphite electrode is used.

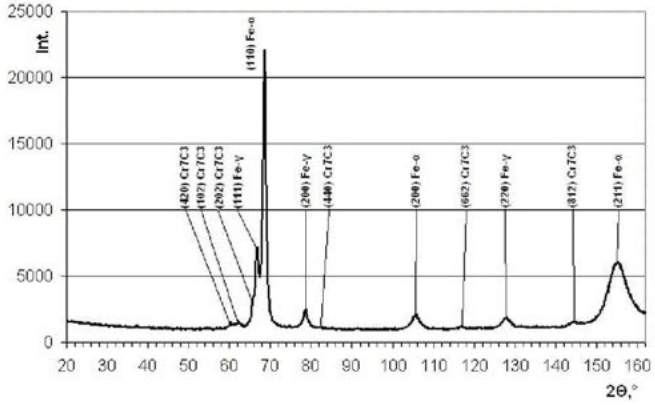

Figure 1. Diffraction pattern of the ground sample 19436 K.

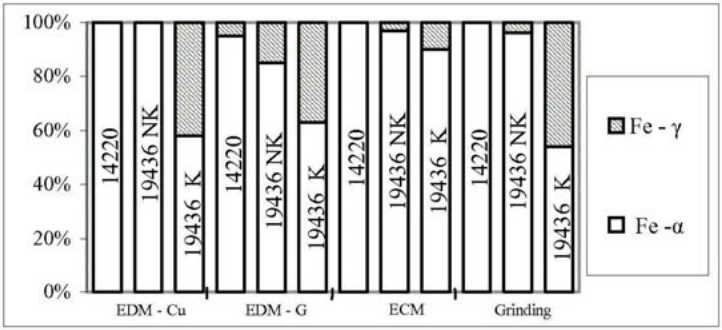

Figure 2. Comparative plot of the phase content in the surface layers of cut samples.

Microstresses and Crystallite Size

Both, the Voigt single line method and the single line Fourier analysis method give qualitatively the same results. Only numerical values are rather different. The results of the more popular method of Voigt function are in figures 3, 4.

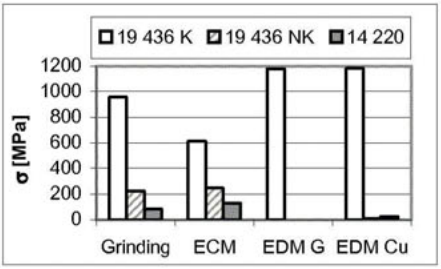

Figure 3. Microstress in the samples.

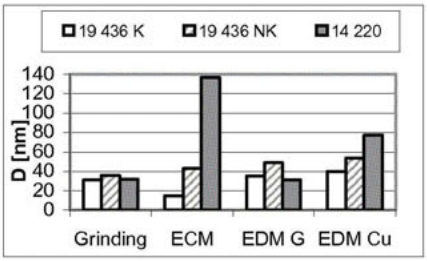

Figure 4. Crystallite size in the samples.

The shape factors of the 211 lines are smaller than the shape factor of the Cauchy line in the case of the samples 14220 NK and 19436 NK. This anomaly can be explained by the bimodal distribution of profile-broadening effects (e.g. of crystallite sizes) [6]. The dependence of the shape factor of the 211 line versus $sin^2\ \psi$ is in figure 5 (ψ is the angle between the normal of diffracting planes and the normal of specimen surface).

The Fourier coefficients of the 110 line of the sample 19436 NK EDM G (with probably bimodal distribution of particle size) are indicated in figure 6 by squares. The Fourier coefficients in the case of the unimodal distribution of particle size can be approximated by the exponential function – circles in figure 6.

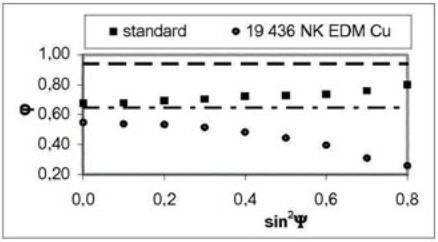

Figure 5. The shape factor of the line 211

Cauchyian limit,

Gaussian limit.

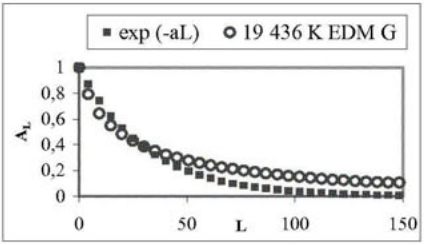

Figure 6. Plot of the Fourier coefficients.

Macroscopic residual stress analysis

The "classical" $\sin^2\psi$ method was used for evaluation of macroscopic residual stresses in surface layers of the investigated samples (see table 1). The tilt angle ψ was varied from 0 ° ($sin^2\psi = 0$) to 63.14 ° ($sin^2\psi = 0.8$). The obtained plots of diffraction angle θ^{211}, versus $sin^2\psi$ were linear with correlation coefficients $R > 0.85$ that gave reasons for assumption of two-dimensional state of residual stresses. The widths W in the last column of the table 1 represent the integral breadth of the diffracted doublet Cr $K\alpha_1$, $K\alpha_2$.

Table 1. Average residual stresses σ_T, σ_L of the ferrite phase and integral width W of α-Fe {211} CrKα diffraction line.

Machining	Steel	σ_T, MPa	σ_L, MPa	W, °2θ
EDM Cu	14220	58 ± 5	82 ± 6	1.89
	19436 NK	-71 ± 9	-75 ± 10	1.87
	19436 K	215 ± 10	269 ± 12	5.55
EDM G	14220	350 ±12	312 ± 10	2.45
	19436 NK	304 ± 14	314 ± 18	2.16
	19436 K	242 ± 10	295 ± 16	5.50
ECM	14220	-261 ± 11	-313 ± 5	2.00
	19436 NK	-316 ± 19	-503 ± 16	2.85
	19436 K	-1073 ± 35	-1419 ± 62	5.13
Grinding	14220	-391 ± 13	-12 ± 22	2.81
	19436 NK	-303 ± 8	-78 ± 12	2.97
	19436 K	-451 ± 11	-44 ± 15	5.14

The inaccuracy represents the standard deviation of calculated values of residual stresses.

Conclusions

i. Biaxial state of residual macroscopic stresses found on the electro discharge cut surfaces is nearly isotropic, i.e. $\sigma_L \approx \sigma_T$.

ii. Considerably higher tensile stresses in the surface layers of the samples cut with a graphite electrode correspond to a higher heat loading in this case of machining conditions.

iii. Only compressive residual macroscopic stresses were obtained on the electro chemically treated surfaces. It is a result of the predominant mechanical interaction of the diamond wheel with the treated material. The state of residual stresses is slightly anisotropic and $\sigma_L > \sigma_T$ (table 1).

iv. The ground samples have an appreciably anisotropic state of compressive residual stresses where $\sigma_L \gg \sigma_T$.

v. The quenched samples from the 19436 steel treated by electro discharge machining have larger microstresses than the samples treated by electro chemical

machining and by grinding. On the contrary, the as-received samples from the same material and the samples of the steel 14220 treated by electro discharge machining have microstresses approximately equal to zero.

vi. When the Cu electrode was used the electro discharge treatment leads to narrower diffraction lines than in the case of the graphite electrode. The particle size in the case of the graphite electrode is smaller than after electro discharge machining with Cu electrode.

vii. The treatments electro discharge machining and grinding lead to the similar diffraction broadening, but its reasons are different.

viii. The anomaly of the shape factor and the course of the Fourier coefficients (caused probably by the bimodal distribution of particle size) are relatively good observed in the case of the as received samples 19436 and the samples of the steel 14220 treated by electro discharge machining.

References

1. De Keijser, Th.H., Langford, J.I., Mittemeijer, E.J. & Vogels, B.P.,1982, *J. Appl. Cryst.* **15**, 308.
2. Nandi, R.K., Kuo, H.K., Schlosberg, W., Wissler, G., Cohen, J.B. & Crist Jr, B.,1984, *J. Appl. Cryst.* **17**, 22.
3. Kraus I. & Ganev N., 1999, in: *Industrial Applications of X-Ray Diffraction,* edited by F.H. Chung & D. K. Smith (New York: Marcel Dekker), pp. 793-811.
4. Fiala J.,1967, *Kovove Mater.* **5**, 559.
5. Schumann, H., 1983, *Metallographie* (Leipzig: VEB Deutscher Verlag für Grundstoffindustrie, 11th ed.), p. 369.
6. Young, R.A. & Sakthivel, A.,1988, *J. Appl. Cryst.* **21**, 416.

Acknowledgements. *The research was supported by the Grant Agency of the Czech Republic (Grant No 106/03/1039) and by the Research Project AV0Z10100520 granted by the Academy of Sciences of the Czech Republic.*

Z. Kristallogr. Suppl. **23** (2006) 375-380

Non-destructive phase analysis and residual stresses measurement using grazing angle X-ray diffraction geometry

S. J. Skrzypek[1*], J. Jeleńkowski[2], T. Borowski[2], W. Ratuszek[1] and T. Wierzchoń[2]

[1]Faculty of Metallurgy and Materials Science, University of Science and Technology - AGH, Al. Mickiewicza 30, 30-059 Kraków, Poland
[2]Faculty of Materials Science, University of Technology, 02-507 Warszawa, ul. Wołoska 141, Poland
[*]Contact author; skrzypek@uci.agh.edu.pl

Keywords: high nickel alloy, surface layers, grazing incidence angle X-ray diffraction geometry, phase composition, residual macrostresses

Abstract. Strain induced martensite was formed in a surface layer of N26MT2Nb high nickel austenitic steel during machining. Properties of obtained surface layers influence on efficiency of the following coating deposition process.
Application of classical X-ray diffraction $sin^2\psi$ methods and classical Bragg-Brentanno diffraction geometry in these kinds of examinations make some problems in term of X-ray real depth of penetration. Therefore application of X-ray diffraction methods, which are based on grazing incidence angle X-ray diffraction geometry make possible to get real value of residual macrostresses and additionally could be suitable in estimation of their gradient-like distribution. The methods based on this geometry to X-ray diffraction phase and residual stresses analysis enabled to get their distribution versus thickness under surface in non-destructive way. This methodology was applied to surface layer characterisation of high-nickel austenitic alloy after different type of machining.

Introduction

A heat-treated N26MT2Nb austenitic steel with microstructure containing aged martensite attains high unit strength (R_m/ρ) and high toughness (K_{Ic}) [1]. When this steel is austenitic (nuclear power engineering, space technology) or austenitic-martensitic (constructional elements, tools), especially when it is not hardened, it exhibits defects analogues to 18-8 austenitic steel [2]. Its advantage in comparison to some classical austenitic steels is good intercrystalline corrosion resistance, especially when microstructure of this alloy appears like duplex steel or when this steel has a mixed nanocrystalline and/or microcrystalline microstructure. Many advantages of this steel are connected with mechanical instability of austenite that

means its flexibility to martensite transformation during plastic strain (TRIP effect) and its ability to internal work hardening and ageing. Mechanical properties of this steel can be changed over a wide range [1,3] and a nitriding process can improve them when a diffusion layer form nitrogen austenite without chromium-nitride compounds. Formation of such layers involves low temperature of nitriding what considerably elongates process time. There are important reasons that electro-spark nitriding of N26MT2Nb steel with a formed strain induced martensite layer can reduce temperature and time of the process [4].
The aim of this research was to examine phase composition and residual macroscopic stresses in the surface layers of N26MT2Nb austenitic alloy in which, thanks to plastic strain – by abrasive paper grinding and shot peening – the formed strain induced martensite can be obtained and assessment of useful layers to electro-spark nitriding can be established. Temperature and time of nitriding process were adjusted to the temperature of stability of strain-induced martensite.
An additional goal of research was to reveal new properties of surface layers by an application of X-ray diffraction methods based on grazing incidence angle X-ray scattering geometry (GID) [6,7]. The benefits of application of GID geometry in quantitative phase analysis and macroscopic residual stresses measurement in surface layers of high nickel austenitic alloy are presented.

Investigated alloy

An austenitic alloy with Ni, Ti, Mo and Nb (see chemical composition in table 1) after high temperature plastic deformation was slowly cooled down. After that the samples were homogenised at temperature of 1100 °C during 2 hours. The microstructure in this state consisted of large grains of 150-200 μm in diameter. In this austenitic state without precipitation, this alloy performs the ability to martensite phase transformation under some plastic deformation. The samples before electro-spark nitriding were subjected to a surface preparation treatment by grinding with abrasive paper no. 120#, polishing and/or burnishing by steam of steel balls with diameter of 3 mm with a speed of 300 m/sec during 5 min. The aim of this surface preparation was mainly to get some degree of strain-induced martensite (α') in the surface layer.

Table 1. Chemical composition of investigated alloy in atomic % .

	Ni	Ti	Al.	Mo	Nb	C	Si	Mn	S	P
N26T2MNb	26.0	2.15	0. 04	1.15	0.11	0.02	0.11	0.17	0.009	0.007

The applied methods to surface layer analysis

A phase content and residual stress gradient-like distribution in the near surface volume can be determined using the standard X-ray diffraction methods (Bragg-Brentano geometry, B-B) with repeating for several wavelengths. However, these methods are not advised for the analysis of heterogeneous states because the penetration depth of X-ray radiation varies significantly during measurement. As a result, the volume for which the measurement is performed is not well defined and the interpretation of the results is complex. Therefore the diffraction methods based on the grazing incidence angle X-ray diffraction geometry were

applied to phase analysis and elastic strain measurement. The based on GID geometry approach to gradient-like phase and residual stress distribution analysis are characterised by a small and constant incidence angle (α) and by different lengths and orientations of scattering vector [6, 7]. Two X-ray diffraction methods were used i.e. $g\text{-}sin^2\psi$ for residual stress measurement [6, 7] and quantitative phase analysis by means of internal reference method [8]. By change of incidence angle α thickness of measured surface layer is different what make possible non-destructive scan versus depth (Z). For investigated alloy this relation was calculated (see results in table 2).

Table 2. Calculated depths of X-ray beam penetration for GID and BB diffraction geometries [7, 8].

Angle α [deg]	1	2	5	9	14	20	BB
Depth Z [μm]	0.9	1.8	3.8-4.1	6-7	8-10	11-14	0-26

Results

The applied X-ray diffraction methods under GID geometry revealed characteristic fine structure of the surface layers, which were neglected so far due to standard methodology limitations. Diffraction patterns were recorded by means of D8 Advance diffractometer (Bruker) using filtered λCoKα wavelength. The line focal spot of Co tube and 0.1 mm slit of incidence beam was used for GID and B-B geometries. On the proportional detector arm a special Soller system (0.15°) was used.

Phase distribution in the surface layer after surface preparation

The ground samples with no.120 abrasive paper contained different amount of α' martensite: from 81 % for a surface layer of ~1 μm thick to 34.5 % for a surface layer of 11-14 μm thick (see figure 1 and table 3). Whereas polished samples contained from 41,2 vol.% to 3 vol.%

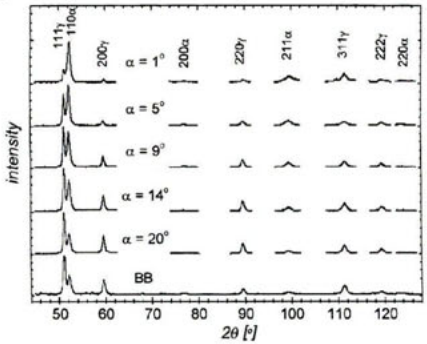

Figure 1. Diffraction patterns for different incidence angles α of grazing angle X-ray diffraction and Bragg-Brentano(BB) geometry of ground samples.

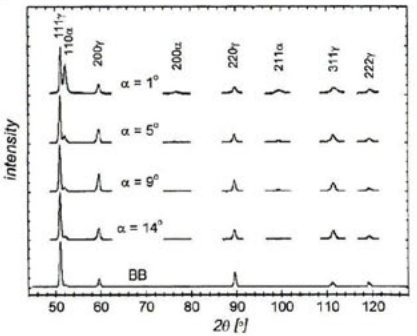

Figure 2. Diffraction patterns obtained by grazing angle incidence X-ray diffraction (for different α angle) and Bragg-Brentano geometry (BB) for polished samples

of α' martensite respectively in the same thickness of surface layers (see figure 2 and table 4). The thin surface layers of the burnished samples contained almost pure α' martensite and the thickness of the surface layer with transformed strained martensite is much larger (see figure 3 and table 5).

Table 3. Quantitative phase composition and residual macrostresses in the surface layers of ground samples.

Layer thickness [μm] and α angle [deg]	Amount of α' and γ phase [vol.%]		Residual stress [MPa]	
	V_γ+-0.6	V_α+-0.6	σ_α	σ_γ
0.85/1	19	81	+932	+495
3.8-4.1/5	38	62	+755	+754
6-7/9	48	52	+648	+477
8-10/14	56	44	+596	+385
11-14/20	65,5	34,5	+731	+379
26/B-B	71.8	28.2		

Table 4. Amount of austenite (γ), strained martensite (α') and level of residual macrostresses in polished samples.

Layer thickness [μm] and α angle [deg]	Amount of α' and γ phase [vol.%]		Residual stress [MPa]	
	V_γ+-0.6	V_α+-0.6	σ_γ	σ_γ
0.85/1	10.5	89.5	+243	-8
3.8-4.1/5	13.8	86.2	-83	-168
6-7/9	20.7	79.3	-126	-283
8-10/14	28.1	71.9	--238	-329
11-14/20	33.6	66.3	-196	-254
0-26/B-B	41.0	59.0		

Discussion

The surface treatment of high nickel alloy consisted in mechanical preparation of the surface to the subsequent nitriding. The mechanical treatment was to create a special microstructure, phase composition and state of residual stresses. Among others, the obtained surface layers contained a different amount of strained martensite α'. The maximum content of strained martensite approached 90 vol % and the content of this phase gradually decreased with the increase of thickness. The measured residual macrostresses differ from large tensile for ground samples (table 3), to large compressive for burnished samples (table5). They were calculated for mechanical elastic constants equal for both phases i.e. E = 207 GPa and ν = 0.29. The both phases were not textured. Therefore elastic constants can be regarded as isotropic. The results obtained by means of grazing incidence angle X-ray-diffraction (see figures 1-3, tables 3-5) refer to several layers (see table 1) and the results present average values for each thickness according to the rules of X-ray diffraction-methodology. The structural characteristics are gradient-like and they can emphasise diffusion of nitrogen atoms during following thermo-chemical treatment.

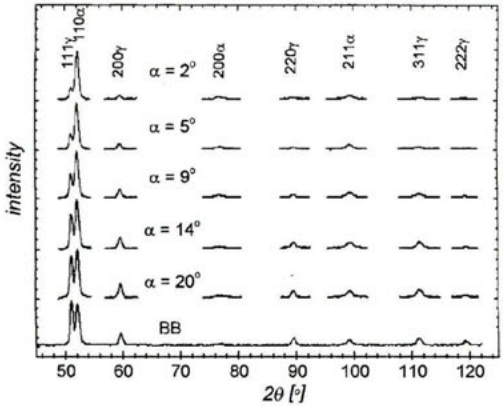

Figure 3. Diffraction patterns for different incident angles α of grazing angle X-ray diffraction and Bragg-Brentano (BB) geometry of burnished samples.

Table 5. Amount of austenite (γ), strained martensite (α') and level of residual macrostresses in burnished samples.

Layer thickness [μm] and α angle [deg]	Amount of α' and γ phase [vol.%]		Residual stress [MPa]	
	V_γ+-0.6	V_α+-0.6	σ_γ	σ_γ
0.85/1	10.5	89.5	-901	-255
3.8-4.1/5	13.8	86.2	-562	-209
6-7/9	20.7	79.3	-7	-365
8-10/14	28.1	71.9	-47	-239
11-14/20	33.6	66.3	-109	-174
0-26/B-B	41.0	59.0		

Concluding remarks

The new methodological approach revealed that the mechanical surface treatment of an austenitic N26MT2Nb alloy is very influential on surface layer properties and on following diffusion processes during the electro-spark nitriding. The described experiments enabled to conclude as following:

1. The grinding, polishing and burnishing produce different surface layers consisting of different amounts of austenite and strained martensite and different level of residual macrostresses. Thickness of these surface layers is different in terms of changed structure and properties in comparison with bulk alloy.

2. The dynamical burnishing of coarse grain N26MT2Nb austenitic alloy produces a larger then 30 μm thick surface layer with gradient like austenite and strained martensite distribution.

3. An application of X-ray diffraction methods based on grazing incidence angle X-ray-diffraction geometry reveals new ability in characterisation of this type of surface layers.

References

1. Jeleńkowski J., 1994, *Materials Science and Technology*, **10**, 1073.
2. Zhiwej Yu., Xiaolei Xu., Liang Wang at all., 2002, *Surface and Coatings Technology* **153**, 125.
3. Uvarov A. I., Vasechkina T. P., 2001, *Phys. Met. Metallov*. **4** .92.
4. Burakowski T., Wierzchoń T.,1995, Inżynieria powierzchni metali. WNT Warszawa.
5. Jeleńkowski J., Kurzydłowski K. J., Rożniatowski K.,2003, *Inżynieria Materiałowa*, **6**, 505.
6. Skrzypek S.J. and Baczmanski A., 2001, *Adv. X-ray Anal.*, **44**, 134.
7. Skrzypek, S.J., Baczmański A., Ratuszek W. and Kusior E. J ,2001,.*J. Appl. Cryst.*, **34**, 427.
8. Cullity B.D., Stock S.R., 2001, *Elements of X-Ray Diffraction*, 3-rd edition, Prentice Hall Upper Saddle River, NJ 07458.

Acknowledgements. Authors wish to acknowledge Mr Artur Zakrzewski's contribution in research project which was supported by Polish Committee for Scientific Research - KBN under grant nr 4 T08C 018 25.

Z. Kristallogr. Suppl. 23 (2006) 381-386

Thermal stability of the microstructure of severely deformed copper

L. Balogh[1,*], J. Gubicza[2], R. J. Hellmig[3], Y. Estrin[3], and T. Ungár[1]

[1]Department of General Physics, Eötvös University, Budapest, Hungary
[2]Department of Solid State Physics, Eötvös University, Budapest, Hungary
[3]Institute for Materials Engineering and Technology, Clausthal University of Technology, Clausthal, Germany
[*]Contact author; e-mail: balevi@metal.elte.hu

Keywords: copper, equal channel angular pressing, X-ray diffraction, dislocation, bimodal structure

Abstract. Copper specimens were deformed by equal channel angular pressing (ECAP) up to 8 passes. The microstructure was studied by X-ray line profile analysis. The crystallite size is reduced to a few tens of nanometers even after the first ECAP pass and it does not change significantly during further deformation. At the same time, the dislocation density increases gradually up to 4 ECAP passes. The thermal stability of the microstructure is examined by differential scanning calorimetry (DSC). The temperature of the DSC peak decreases whereas the stored energy increases with increasing strain. At the beginning of the heat release a bimodal grain structure develops indicated by a special double-peak shape of the diffraction line profiles.

Introduction

Bulk ultrafine grained metals can be produced by severe plastic deformation (SPD) [1,2]. If the conditions (e.g. temperature, dimensions of the sample) of SPD methods are selected properly, the manufactured specimens meet the following requirements [2]: i) high angle grain boundaries dominate in the ultrafine grained structure, ii) the microstructure is uniform within the whole volume of the specimen and iii) the materials have no cracks or mechanical damage. One of the most common SPD methods is equal channel angular pressing (ECAP). This method provides ultrafine grained metal billets with homogeneous microstructure. A billet can be deformed repeatedly using this method as the shape of the specimen does not change during ECAP deformation.

The microstructure of the ultrafine grained materials can be effectively studied by X-ray diffraction peak profile analysis. The broadening of a profile is caused by size and strain effects simultaneously. In deformed metals the lattice distortions are mainly caused by dislocations, so the strain broadening can be expressed in terms of the parameters of the dislocation structure [3,4]. The anisotropic strain broadening is taken into account by the contrast

factors of the dislocations [4,5]. The dislocation structure can be determined by the evaluation of the X-ray profiles for the contrast factors because their values depend on the dislocation slip systems present in the crystal. Developments in computing enable procedures to be elaborated for determining the characteristic parameters of the microstructure by fitting the whole diffraction profiles [6-9]. In the present work the Multiple Whole Profile (MWP) fitting method is used in which the measured intensity profiles are fitted by theoretical functions calculated on the basis of the model of microstructure [8,9]. This procedure enables the determination of both the crystallite size distribution and the dislocation structure in ultrafine grained materials.
In this paper the microstructure of severely deformed copper is studied as a function of strain up to $\varepsilon=9.2$. The high strain values are achieved by the ECAP technique. The thermal stability of the ultrafine grained microstructure is also investigated. The characteristic parameters of the crystallite size distribution and the dislocation structure are determined by X-ray line profile analysis.

Experimental

Technical purity copper specimens (99.99%) were annealed at 450 ^{0}C for 2 hours prior to ECA pressing to obtain a defined initial state. They were subsequently deformed by 1, 2, 4 or 8 ECAP passes using a 90° die following route C (the billet after each pass is rotated by 180° around its longitudinal axis). Each pass corresponds to an equivalent strain of $\varepsilon=1.15$. This means that the samples were deformed for strain values of 1.15, 2.3, 4.6 and 9.2. An additional specimen has been deformed for $\varepsilon=0.7$ by compression using an MTS™ hydraulic machine. Thermal stability of the ultrafine grained microstructure was investigated by differencial scanning calorimetry (DSC) using a Perkin-Elmer™ DSC2 calorimeter.
The microstructures of the deformed and the heat-treated specimens were investigated by X-ray peak profile analysis. The X-ray diffraction profiles were measured on the cross section of the billets. The measurements were performed by a double crystal diffractometer (Nonius™ FR591) with negligible instrumental broadening using CuKα_1 radiation ($\lambda=0.15406$ nm). The intensity profiles were recorded by a linear position sensitive gas-flow detector (OED™ 50 Braun, Munich). The measured data were evaluated by the MWP fitting method. The procedure is described in detail in references [8,9]. The measured intensity profiles are fitted by theoretical line profiles and from the procedure the following parameters of the microstructure are obtained: (i) the median m and the variance σ of the log-normal size distribution function, (ii) the density ρ and the arrangement parameter M of dislocations, (iii) the q parameter, which characterizes the contrast factors of dislocations and describes the type of dislocations (edge or screw). The arithmetic, area- and volume-weighted mean crystallite sizes can be calculated from m and σ using formulas given in reference [6]. In this paper only the area-weighted mean crystallite size, $\langle x \rangle_{area}$ is presented. The magnitude of M gives the strength of the dipole character of dislocations: a higher M value corresponds to a weaker dipole character and weaker screening of the displacement fields of dislocations.

Results and discussion

The microstructure of copper as a function of strain

The area-weighted mean crystallite size has a value of 62±7 nm even after a single ECAP pass. The crystallite size does not change significantly by further ECAP deformation. At the same time the dislocation density increases from 8×10^{14} m^{-2} to 28×10^{14} m^{-2} when the number of ECAP passes increases from 1 to 4. The dislocation density does not change significantly with further deformation. The experimental value of the q parameter is 2.0±0.1 for all samples. The q parameter values for copper corresponding to pure screw and edge dislocations in the <110>{111} slip system were determined by detailed numerical calculations using the equations from [10] and the elastic constants from [11]. This yielded the q values of 2.4 or 1.7 for pure screw or edge dislocations, respectively. The experimental value of q for ECA pressed Cu agrees well with the arithmetic average of the values calculated for pure edge and screw dislocations, which suggests that the character of dislocations is half edge – half screw. The M parameter decreases with increasing strain up to 4 ECAP passes. Its value is 2.2 at $\varepsilon = 0.7$ and 1.1 at $\varepsilon = 4.6$. For higher strains M remains almost constant. The decrease of the value of M indicates that with increasing strain the dipole character of the dislocation structure becomes stronger. It was established that after 4 ECAP passes there are no further changes in the microstructure.

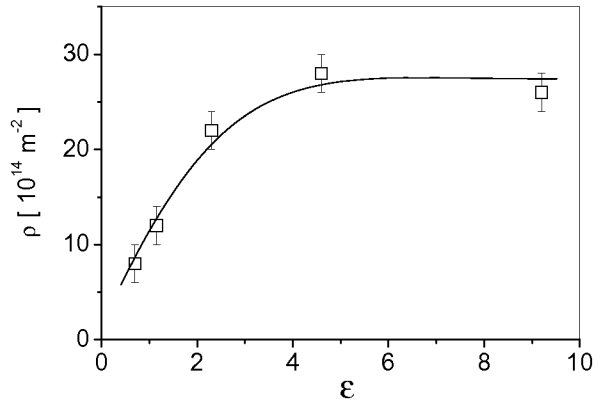

Figure 1. The dislocation density (ρ) as a function of strain.

Thermal stability of the microstructure

The deformed copper specimens were subjected to DSC scans from 300 K to 1000 K at a heating rate of 40 K/min. For each sample a broad exothermic peak was observed on the DSC curve which corresponds to the release of the stored strain energy during the recovery of the microstructure. The maximum of the peak and the evolved heat as a function of strain are shown in figures 2 and 3, respectively. The maximum of the exothermic peak in the DSC curve shifted to lower temperature values and the heat released during the heat-treatment increased with increasing of deformation up to ε=2.3. These changes can be explained by the

rise of the density and the stronger dipole character of dislocations with increasing strain. The dislocation density vs. strain (figure 1) and the stored energy vs. strain (figure 1) relations are similar, because the dislocations are the main source of strains in SPD materials. The slight difference in the strains of saturation for the two quantities can be explained by the reduction of the strain energy with the stronger dipole character of dislocation arrangement.

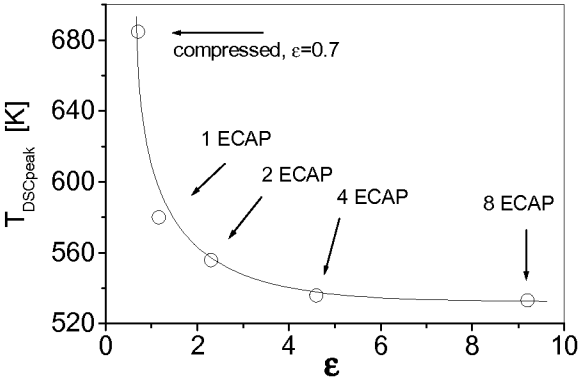

Figure 2. The temperature of the exothermic DSC peak as a function of strain.

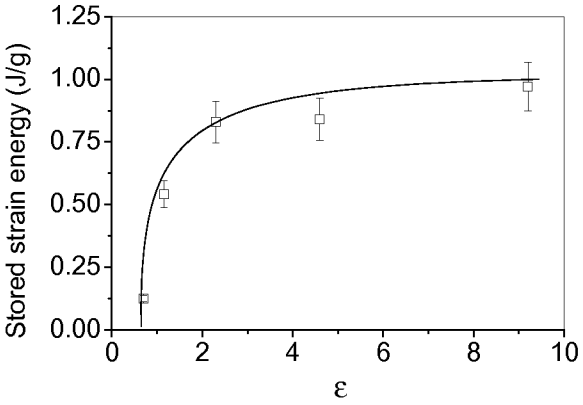

Figure 3. The stored energy released during the recovery of the microstructure as a function of strain. This energy was determined as the area of the exothermic peak in the DSC scan.

The recovery of the microstructure was studied for ε=0.7, after 1 ECAP and 8 ECAP passes. The specimens were heated at 40 K/min and when the desired temperature was reached, they were quenched at 200 K/min. The temperatures were chosen before the DSC peak, at the top

of the peak and one after the peak. Figure 4 shows the evolution of the area-weighted mean crystallite size and the dislocation density as a function of temperature in the case of the 8 ECAP specimen. The other two samples show almost identical behaviour, only the values of the temperatures and of dislocation densities being different.

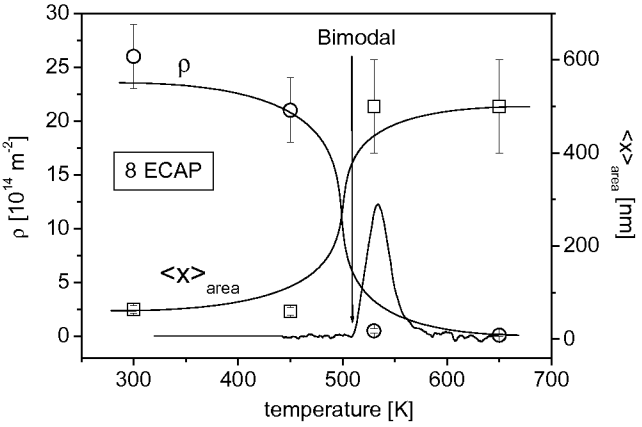

Figure 4. The area-weighted mean crystallite size and the dislocation density as a function of temperature for the sample deformed by 8 ECAP passes.

At a temperature corresponding to the beginning of the DSC peaks, none of the peaks could be fitted by a single theoretical profile and each peak seems to be the sum of a narrow and a broad peak. This special shape of the diffraction peaks has been observed previously by Kuzel et al. [12] for a copper sample deformed by torsion under 6 GPa pressure and annealed at 250 °C for 100 minutes. Figure 5 shows the 311 peak for the specimen quenched from 500K (dashed line), from which it can be seen that indeed the diffraction profile does consist of two peaks. It was found that the broad peak can be well approximated by the profile measured before the heat-treatment, which indicates that the broad subprofile corresponds to the non-recovered volumes of the material. The profile for the non annealed specimen (the dotted line in figure 5) matches perfectly the tail part of the peak recorded after annealing (the dashed line in figure 5) after dividing the intensity by an appropriate factor. The difference between the two profiles (the solid line in figure 5) gives a sharp peak which corresponds to the recovered volume of the material.

Conclusions

The microstructure of severely deformed copper specimens was investigated by X-ray peak profile analysis. It was found that the crystallite size is reduced to about 60 nm even at ε=0.7 and further refinement can not be achieved by increasing strain. At the same time the dislocation density increases and the dipole character of dislocations becomes stronger with increasing strain up to ε=4.6. These changes in the dislocation structure result in the decrease

of the temperature of recovery and an increase in the stored energy released during annealing. The recovery starts inhomogeneously forming bimodal microstructure in the sample.

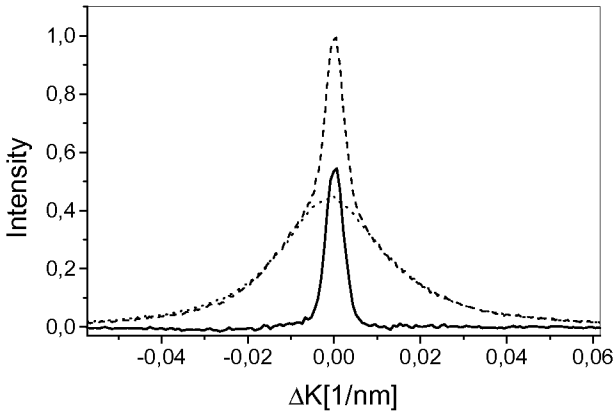

Figure 5. The difference between the 311 peak for copper deformed by 8 ECAP passes and quenched from 500 K (dashed line) and that of the non-annealed sample (dotted line) gives a sharp peak (solid line).

References

1. Baik, S.C., Estrin, Y., Kim, H.S., Jeong H.T. & Hellmig, R.J., 2002, *Mater. Sci. Forum* **408**, 697.
2. Stolyarov, V.V., Zhu, Y.T., Alexandrov, I.V., Lowe T.C. & Valiev, R.Z., 2003, *Materials Science and Engineering* A **343**, 43.
3. Krivoglaz, M.A., 1996, *Theory of X-ray and Thermal Neutron Scattering by Real Crystals*, Plenum Press, New York
4. Wilkens, M., *Phys. Stat. Sol.,* 1970, (a) **2,** 359
5. Kuzel, R. & Klimanek, P., 1988, *J. Appl. Cryst.* **21,** 363
6. Langford, J.I., Louer, D. & Scardi, P., 2000, *J. Appl. Cryst.* **33,** 964
7. Scardi, P. & Leoni, M., 2002, *Acta Cryst.* A **58,** 190
8. Ungár, T., Gubicza, J., Ribárik, G. & Borbély, A., 2001, *J. Appl. Cryst.* **34**, 298.
9. Ribárik, G., Ungár, T. & Gubicza, J., 2001, *J. Appl. Cryst.* **34,** 669.
10. Ungár, T., Dragomir I., Révész, Á. & Borbély, 1999, *A., J. Appl. Cryst.* **32**, 992
11. Hearmon, R.F.S., 1966, *Landolt-Börnstein* **1**, 1
12. Kuzel, R., Holy, V., Cernansky, M., Kubena, J., Simek, D. & Kub, J., 2004, *Diffraction analysis of the microstructure of materials*, edited by E. J. Mittemeijer & P. Scardi (Berlin: Springer) pp. 229-245.

Acknowledgements: This research was supported by the Hungarian National Scientific Research Fund (OTKA) under contract numbers T-046990, T-043247 and F-047057.

Z. Kristallogr. Suppl. **23** (2006) 387-392

Archaeometric study of Dutch Tin-Lead spoon fragments from Amsterdam: 1500 - 1775 AD. A neutron diffraction study

D. Visser [1,*], W. Kockelmann [2], P. Hallebeek [3], J. Veerkamp [4], W. Krook [4]

[1]NWO-Physics, ISIS Facility, Rutherford Appleton Laboratory, Chilton, Didcot OX11 0QX, UK
[2]ISIS Facility, Rutherford Appleton Laboratory, Chilton, Didcot OX11 0QX, UK
[3]Netherlands Institute for Cultural Heritage (ICN), Department of Conservation Science, Gabriël Metsustraat 8, 1071 EA Amsterdam, The Netherlands
[4]Archaeology Amsterdam, Noordermarkt 45, 1015 NA Amsterdam, The Netherlands
[*]Contact author; e-mail: d.visser@rl.ac.uk

Keywords: archaeometry, Rietveld phase analysis, neutron diffraction, texture analysis

Abstract. A feasibility study using neutron scattering has been applied to antique Dutch tin-lead spoon fragments obtained from excavations within the town boundaries of Amsterdam dating to the period 1500-1775 AD. Detailed quantitative information on the tin-lead compositions has been obtained, which suggests different production methods. The microstructure of the spoon fragments has been studied using neutron diffraction pole figure scanning. This contribution demonstrates the suitability of time-of-flight neutron diffraction for the study of strongly curved (antique) metallic objects.

Introduction

Over the last few decades more than 600 complete tin lead spoons and numerous incomplete parts have been excavated within the town boundaries of Amsterdam. The earliest types of these spoons date back to 1350 AD, while the latest are from ca 1775 AD. Amsterdam has been an important centre for the production of tin-lead spoons during this era. Normally the soft material of a tin-lead spoon deteriorates quickly over time so relative few antique examples have been saved for prosperity. The finds in Amsterdam are exceptional in that they were well preserved in the clay / peat soil, producing a patina, consisting of iron and/or coppersulfides: pyrite (FeS_2), marcenite (FeS_2), chalcosite (CuS_2), chalcopyrite ($CuFeS_2$) and pyrrhotite ($Fe_{1-x}S$) [1], by which the objects have been well conserved.
Initial investigation with X-ray fluorescence on archaeologically dated tin-lead spoons showed a large variation of the Pb content over the period 1350 - 1750 AD. The introduction of regulatory measures and control of the production by the Guild around 1530 shows a

dramatic reduction of the use of lead in the production of the spoons. These measures were taken to reduce the health hazards induced by lead.
The X-ray fluorescence measurements seem to suggest that only a low Pb content, ~ 5 to 10 %, was allowed after the regulation. That after a while the tin-casters ignored the rules is also obvious. [1].
The tin-lead content as measured by X-ray fluorescence analysis, was carried out by scanning the x-ray beam over a small 2 × 2 mm area of the spoon. The patina on this area had to be removed first, before measurements could be taken. Using neutron scattering as an investigative probe, a non-destructive analysis of the objects can be achieved. The tin-lead spoons are transparent to neutron radiation while in the case of X-ray diffraction as well as X-ray fluorescence only the top 10 microns of the object can be accessed. Much larger areas of the objects can be illuminated by neutron beams and therefore one might obtain a better estimation of the element and/or phase ratios of tin and lead in the antique spoons. Rietveld phase analysis of the diffraction data provides insight into the phases present. Pole figures constructed from rotational diffraction data of the spoons and phase analysis in relation to the Pb-Sn phase diagram [2] indicate the processes used in the production of the tin lead spoons.
In this paper we present a study on a set of antique spoon fragments to demonstrate the feasibility of the neutron scattering approach for quantitative phase analysis and eventually aiding to the dating of the antique tin spoons.

Objects

For the feasibility study we use four antique objects: (***a***) a big flattened spoon end with a metallic lustre, (***b***) a large patinated spoon scoop with a gold lustre, (***c***) a small brownish spoon scoop, as well as a spoon handle (***d***), See figure 1. These objects could not be archaeologically dated using producers marks [1]. The dimensions of the spoons are similar to contemporary ones varying from about 5 - 3 cm in length with a thickness between 1 - 1.5 mm.

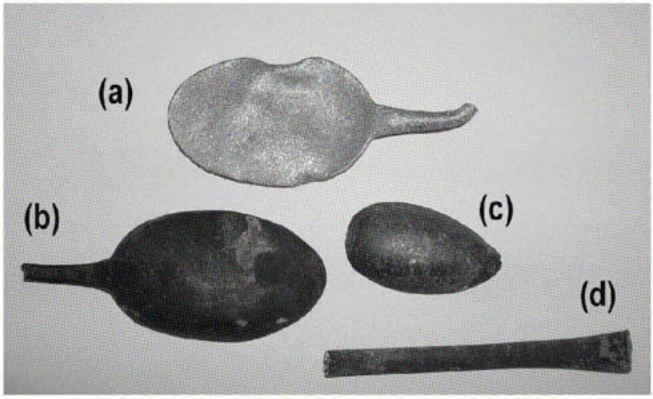

Figure 1. Amsterdam antique spoon fragments.

Neutron Time of Flight (TOF) diffraction

The objects figures were placed on the ROTAX TOF-diffractometer at the ISIS Facility, Rutherford Appleton Laboratory . A neutron beam with a size of 20 x 20 mm was used. The object were hanging in the (beam) centre of a large vacuum vessel using a upside down candle stick arrangement with the object kept in place by a vanadium sachet, with the hollow parts of the spoon scoops facing the incoming beam. The spoon handle was positioned vertically in the beam. Diffraction data were obtained from three diffraction banks. The diffraction profiles of each bank were fitted simultaniously using a multiphase Rietveld refinement in the GSAS code. Surprisingly good fits were obtained by using three phases; Sn: with space group $I4_1/amd$, a = 5.8315 Å and c = 3.1814 Å; Pb: space group F m-3m, a = 4.9493 Å and a Sn-Pb (70-30%) alloy with slightly varying lattice parameters, space group $I4_1/amd$, a ≈ 6.13 Å and c ≈ 3.55 Å [2]. In figure 2 the diffraction profiles and fits of only the back scattering bank 3 are shown. The simultaneous refinement of the separate data of bank 1, 2 and 3 showed that three of the objects: (***a***), (***c***), (***d***) can be described by the three phases outlined above, while the big brown spoon (***b***) is a composite of lead and tin. The results of the refinements are given in table 1. It should be noticed that very small reflections at d-spacings 3.64, 2.09 and 1.25 Å could not be indexed. Only one common overall temperature factor was refined for all phases.

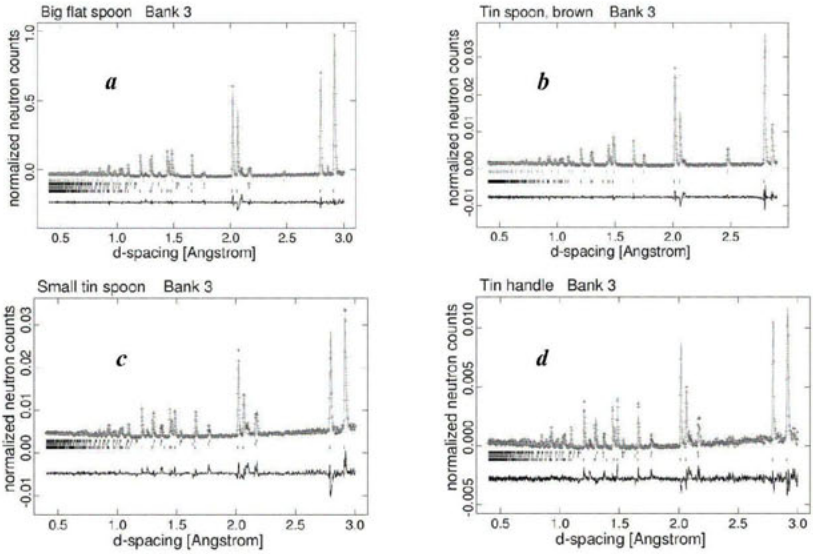

*Figure 2. GSAS refinements of the Amsterdam antique spoons fragments (**a-d**). The observed and calculated profiles relate to the ROTAX bank 3 detector.*

Differences in the observed and calculated profiles are caused by the texture and orientation of the grains of the different components in the object. Because each bank views the object from a different angle, the relative orientation of the crystallites might become the dominant factor for individual reflection intensities. Averaging the diffraction data from a rotational scan of the object helps to alleviate this problem. The effect will be a broadening of the reflection profile of the individual phases being due to variations of zero-points and scattering volumes for different orientations. The Rietveld analysis results of the averaged diffraction patterns are also given in table 1. Figure 3 shows a comparison of fits before and after averaging.

Table 1. Weight fractions (wt%) of tin/lead phases. The values in brackets are obtained from the analysis of the „sum pattern" over 108 sample orientations. The Rietveld esd's are approximately 0.5 wt%. The profile R-value R_{wp} (%) is given for ROTAX bank 3.

	(*a*) flat spoon	(*b*) brown spoon	(*c*) small spoon	(*d*) spoon handle
Sn	91.1 [89.7]	87.8 [88.6]	81.3 [82.7]	83.8 [85.2]
Pb	2.1 [2.1]	12.2 [11.4]	0 [0]	0 [0]
Sn-Pb	8.0 [8.2]	0 [0]	18.7 [17.3]	16.2 [14.9]
R_{wp}	11.3 [8.2]	9.5 [5.0]	13.8 [9.8]	15.22 [12.3]

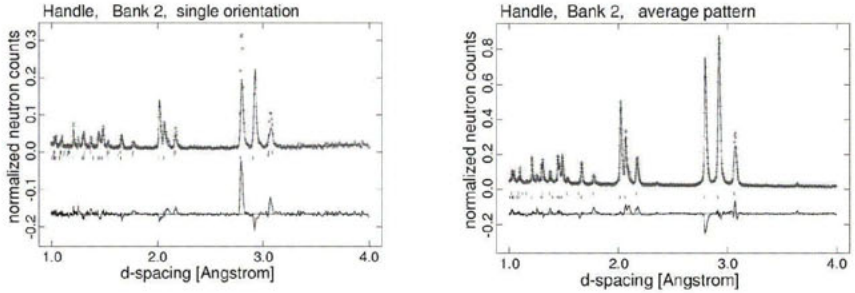

Figure 3. Comparison of bank 2 diffraction patterns for the handle before (left) and after (right) averaging over 108 sample orientations.

Texture of the spoon fragments

The textures of metals and composites, either just as they have crystallized or in their worked form can be described using texture components derived from ideal orientations of the objects components/phases as determined by their ideal structure [3]. The distributions of the components in space can be represented in the form of pole figures. In real objects the poles are smeared out providing information on the density of the preferred orientation direction variation of a particular crystallographic direction in the object.
We obtained pole figures for the four spoon fragments. The objects were mounted on a horizontal phi-axis of a texture goniometer. The scoop was placed perpendicular to the beam direction. The beam size was 10 × 10 mm during these measurements. Diffraction data were collected rotating the object every 10° around the phi axis totalling 350°. The same process was repeated for a further two omega positions of the phi-axis 20° apart. In total 108 data sets were produced which provide incomplete measured pole figures. Using the MAUD software package [4] full pole figures for the (200), (220), (103) reflections were constructed for the majority Sn phase of the objects. See figure 4.

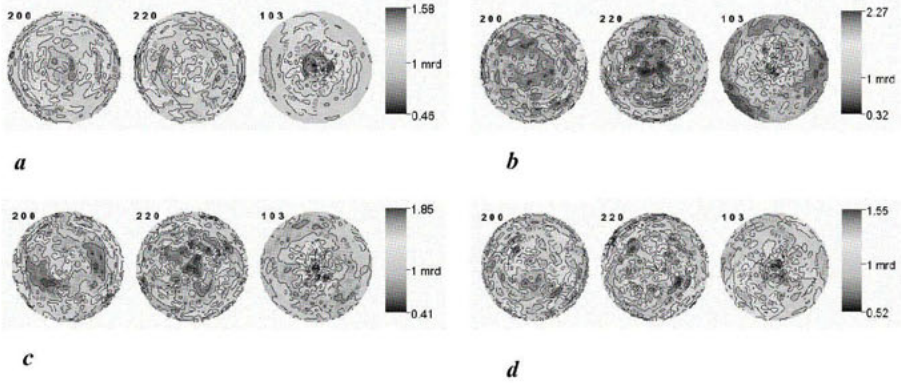

*Figure 4. The pole figures for (200), (220) and (103) reflections of the Amsterdam antique spoon fragments (**a-d**). The initial orientations (phi = 0°) of the objects were as follows: (**a**,**b**) handle vertical to the incoming beam , (**c**) the handle along the incoming beam, (**d**) the handle's initial position was tilted 45° in respect to the incoming beam.*

Discussion, outlook and conclusions

Rietveld phase analysis of the antique spoon objects (***a***), (***c***) and (***d***) shows that the observed diffraction patterns are well accounted for by three phases: a tin and a lead phase and a lead-tin alloy with a composition close to 30-70%. An improved fit can be obtained by introducing two Sn-Pb alloys of equal composition but slightly different lattice parameters. For instance, the best fit to object (***c***) shows Sn-Pb alloy mixtures for which the unit cells are: a = 6.1200 Å and 3.5285 Å and 6.1385 Å and 3.5800 Å. The weight percentages of these phases are 10.4% and 7.4%, respectively. A distribution of slightly different phases of the same

alloy is commonly observed for casted alloys, due to a variation in stoichiometry. This alloy phase cannot form by slow cooling. Spoon fragment (***b***) consists only of a Sn and Pb phase. These phases are most likely not element pure, an aspect ignored in the present study.
The weight fraction of the Sn-Pb phase given in Table 1 presents the summation over the two individual Sn-Pb fractions because the fractions are highly correlated. The second set of values, given in the square brackets, is based on averaged data sets obtained from the individual data sets (108 different orientations) used in the construction of the pole figures. The R values of the profile fits to this data are better, but the profile data do not necessarily represent a perfect 'powderlike' average because of the incomplete orientation coverage, misalignments of the object on the texture goniometer as well as the crystallite size distribution in the object. The results for the weight fraction of the phases from both fits are equal within 3σ. Therefore single refinement weight analysis is an acceptable representation for the phase content.
The pole figures of all objects show that there is not a strong preferred orientation of the crystallites in the objects as expected for a soft matrix like the tin lead spoon. However, some preferred orientation trends can be observed in the spoons. The pole figures indicate that crystallites have a preferred orientation of the [*00l*] direction perpendicular to the spoon scoop (***b***, ***c***) and [00*l*] is aligned parallel to the spoon handle (***d***). In (***a***) one finds that the [*110*] direction perpendicular to the spoon scoop is preferred in contrast to (***b***) and (***c***). The difference between (***a***) and (***b***, ***c***) is probably due to its 'hammered' form.
Encouraged by the results above, we have studied 25 antique spoons from Amsterdam archaeologically dated to the period 1350-1775 AD. Within this group of objects, we found that most spoons have only Pb and Sn phases. Some of them have re-inforced Fe handles. Four spoons dated to the period 1725-1775 AD showed the 'extra' alloyed Sn-Pb phase. This means that a different manufacturing procedure, next to the traditional one, was in use during this period. The Pb/Sn fraction ratio versus time for this group of objects based on the neutron diffraction data strongly supports the statements made in the introduction [1].

References

1. H.A. Ankersmit, P. Hallebeek, J. Veerkamp and W. Krook. Arts 2002. *7th International Conference on Non Destructive Testing* etc., 1-8. Antwerpen 2002.
2. P.R. Sarode, A.R. Chetal. 1974. *Curr. Sci.* **43** 339.
3. E. Jansen, W. Schäfer, A. Kirfel and J. Palacios. 1998. *Materials Science Forum* **278-281** 502 and references therein.
4. L. Lutterotti. *MAUD: Material Analysis Using Diffraction.* http://www.ing.unitr.it/~luttero/maud/index.html.

Z. Kristallogr. Suppl. **23** (2006) 393-398

Characterisation of radiation-induced precipitates in reactor pressure vessel steels

J. Šaroun[1,*], J. Kočík[2], E. Garcia-Matres[3], O. Muraňský[1,4], P. Strunz[1]

[1]Nuclear Physics Institute, ASCR, 25068 Řež near Prague, Czech Republic
[2]Nuclear Research Institute plc., 25068 Husinec-Řež 130, Czech Republic
[3]Hahn-Meitner-Institut, Glienicker Str. 100, 14109 Berlin, Germany
[4]Charles University, Faculty of Mathematics and Physics, Ke Karlovu 3, 121 16 Praha 2, Czech Republic
[*]Contact author; e-mail: saroun@ujf.cas.cz

Keywords: small-angle neutron scattering, precipitates, steels, irradiation embrittlement

Abstract. Integral characteristics of radiation-induced precipitates in reactor pressure vessel steels of different compositions were measured by *Small-Angle Neutron Scattering (SANS)*. While mean radii of these precipitates were similar for all materials (between 1 to 1.5 nm), significant differences were observed in volume fractions, which were much higher for high-Cu steels compared to the low-Cu ones exposed to similar fluence. The ratio of total to nuclear scattering contrasts (*A-ratio*) indicates the presence of high level of atoms with low scattering length (probably Mn) in addition to Cu and Fe. Comparison of measured *A*-ratios with atom-probe microscopy shows that true volume fractions of low-Cu precipitates might be higher than those following from scattering intensity due to their partial magnetisation.

Introduction

Embrittlement of steels exposed to high doses of neutron irradiation essentially reduces the lifetime of reactor pressure vessels (RPV). The degradation of mechanical properties due to the irradiation is closely related to the creation of ultra-fine precipitates resulting from radiation-enhanced diffusion processes in damaged crystal lattice. There are significant differences in the nature of the *radiation-induced precipitates (RIP)* depending on the composition of RPV steels. Measurements by atom probe field ion microscopy (APFIM) and atom probe tomography (APT) show that copper-rich precipitates appear in steels with high levels of Cu after relatively low fluence [1,2]. On the other hand, rather diffuse aggregates of other solute atoms are formed if copper content is low like in the VVER-type RPV steels [3]. These aggregates contain high amount (> 80 at.%) of iron, while the content of solute atoms (typically Mn, Si, P and Ni) depends on the matrix composition. In both cases, the radiation-induced

features have similar mean radius of about 1 nm and lead to similar embrittlement effects manifested as increase in yield strength, hardness or ductile-to-brittle transition temperature. While APT provides valuable data on composition and inner structure of the precipitates, their mean size or volume fraction can be measured efficiently by *Small-Angle Neutron Scattering (SANS)* [2,4-7]. Although the information content of SANS data is too low to describe the complex microstructure of steels in detail, this method has substantial advantage of yielding integral characteristics of the precipitates like volume fraction, mean size or size distribution averaged over macroscopic sample volumes. These statistically representative parameters can be thus directly related to the mechanical parameters characterising embrittlement [5]. Moreover, magnetic interaction of neutrons with heterogeneities in ferromagnetic matrix permits to determine the ratio of total and nuclear scattering cross-sections (so called *A-ratio*) as an additional parameter, which helps to assess chemical compositions of the precipitates. In the presented study, we have employed the SANS method to characterise RIP in VVER-type steels with varying Cu, Ni and P contents and the western-type steel A533B. From magnetic component of SANS, we have evaluated volume fractions and size distributions of the precipitates assuming their non-ferromagnetic character. Observed differences in radiation sensitivity (*i.e.* the dependence of RIP volume fraction on fluence) are discussed with the help of measured *A*-ratios and known chemical composition of the steels.

Experimental

The investigated materials included the base metals of the Cr-Mo-V and Cr-Ni-Mo-V steels (used in VVER 440 and 1000 reactors), the Cr-Ni-Mo-V steel alloyed additionally with Cu and P and the IAEA reference steel A533-B. Steel compositions are listed in Table 1. More details on composition, sample treatment and results of TEM analysis can be found in [8].

Table 1. Composition of materials in wt%.

steel	sample	Si	Mn	P	Cr	Ni	Mo	V	Cu
15Kh2MFA	A0, A13	0.17	0.46	0.014	2.90	0.07	0.66	0.31	0.07
A533-B, Cl.1	C0, C1	0.25	1.40	0.019	0.12	0.84	0.50	0.003	0.14
15Kh2NMFA	D0-D2	0.26	0.59	0.005	2.22	1.27	0.63	0.09	0.03
15Kh2NMFA + Cu	E0,E1	0.17	0.48	0.012	2.06	1.28	0.56	0.10	0.30
15Kh2NMFA + P	F0,F1	0.20	0.34	0.021	2.14	1.27	0.58	0.10	0.08

Specimens A0 … F0 are original unirradiated materials used for reference. The other samples were irradiated at the light-water research reactor LVR-15 in Řež at temperatures 275 - 300°C. The fluxes and fluence for neutron energies $E < 0.5$ MeV are given in Table 2.

Table 2. Irradiation parameters

specimen	A13	C1	D1	D2	E1	F1
flux [10^{16} m^{-2} s^{-1}]	57	57	29.5	34	26	26
fluence [10^{24} m^{-2}]	0.56	0.6	0.29	0.97	0.15	0.18

The SANS measurements were carried out at the BENSC-V4 instrument [9] of the Hahn-Meitner Institute in Berlin for two detector distances of 1.1 m and 4 m and mean neutron

wavelength of 0.6 nm, resulting in the total accessible range of scattering vector magnitudes (0.2 - 3) nm^{-1}. The specimen magnetisation was saturated by horizontal magnetic field of 1.1 T (*i.e.* maximum achievable at the instrument). Measurements with varying field proved that 1.1 T is sufficient for measurements in the high-Q range of our interest.

SANS data analysis

Preliminary raw-data treatment involved corrections on detector efficiency and absolute calibration of scattering cross-sections using water standard. Subsequent evaluation of real-space information from SANS data represents a typical ill-posed inverse problem. Usually, direct deconvolution and Fourier inversion is not possible due to strong resolution smearing, truncation effects and noise. Therefore, indirect Fourier transformation technique [10] is applied, which permits to fit a real-space model with additional physically justified constraints and resolution corrections directly to experimental data. The fitting model has to be simplified so that it shows only main features actually resolved in scattering data and includes information already known from measurements by other methods. In our case, the fitting model was constructed as follows.

An average scattering particle (precipitate) is represented by a non-magnetic homogeneous sphere in ferromagnetic iron matrix. The particle is characterised by fixed magnetic scattering contrast, $\Delta\rho_M = 4.97 \cdot 10^{10}$ cm^{-2}, resulting from saturated magnetisation of ferrite. The nuclear scattering contrast, $\Delta\rho_N$ is a free parameter reflecting average chemical composition of the particle. The size distribution of particles in reference (unirradiated) samples is described by a set of 5 cubic splines on logarithmic scale of radii in the range $R_{max}/R_{min} = 15$. The maximum radius, R_{max} and spline amplitudes representing volume fractions are also free parameters. For irradiated samples, a second population of particles with lognormal size distribution described the radiation-induced precipitates. In addition, background was fitted as a sum of constant incoherent scattering and Porod scattering from large particles, $I(Q) \sim Q^{-4}$, distinguishing nuclear and magnetic components in both terms. In summary, the model scattering function is expressed in radial coordinates as [11]

$$\frac{d\Sigma}{d\Omega}(Q,\alpha) = \sum_p \left[(\Delta\rho_{N,p})^2 + (\Delta\rho_{M,p}\sin\alpha)^2\right] \int_{R\,max}^{R\,min} \varphi_p(R) F^2(QR) V(R) dR + I_B(Q,\alpha) \quad , \qquad (1)$$

where $Q \equiv |\mathbf{Q}|$ is the magnitude of scattering vector, α is the angle between magnetic field and $\mathbf{Q}$, F(x) is the sphere form factor, $V(R)$ is the volume of a sphere with radius R and $\varphi(R)$ is the size distribution of volume fractions. The sum is made over the two populations of particles, *i.e.* the RIP and the precipitates present in non-irradiated state. The background has the form

$$I_B(Q,\alpha) = \Sigma_{inc,N} + \Sigma_{inc,M} \sin^2\alpha + \left(A + B\sin^2\alpha - C\sin^4\alpha\right) Q^{-4} . \qquad (2)$$

The term with $sin^4\alpha$ had to be added to fit our model correctly to the measured Porod scattering. It might arise from interparticle interference (*i.e.* non-trivial structure factor) of large precipitates and/or from imperfect alignment of magnetic domains.

For each material, the reference sample was fitted first. Resulting distribution of medium-sized precipitates was then fixed and used to fit corresponding irradiated samples with the lognormal distribution of RIP added. The procedure was thus equivalent to the subtraction of signals from irradiated and reference samples.

The above-described model was implemented in the program SASProFit [12] developed at NPI Řež. This program permits to fit 2-dimensional data sets (128x128 points) for the both Q-ranges simultaneously. Instrumental smearing is applied correctly to the 2-dimensional data. We thus avoid possible errors, which may arise, if magnetic and nuclear scattering components are separated from data smeared by instrument resolution effects during raw-data treatment.

Results

The size distributions for reference and irradiated samples are shown in figure 1. In all cases, RIP can be recognised as the peak at $R \sim 1.5$ nm. This peak is much higher for the materials containing copper (C, E) than for the low-Cu steels. Except for sample D1, the peak position remains roughly the same and the differences in peak integral should therefore correspond to differences in number density of RIP.

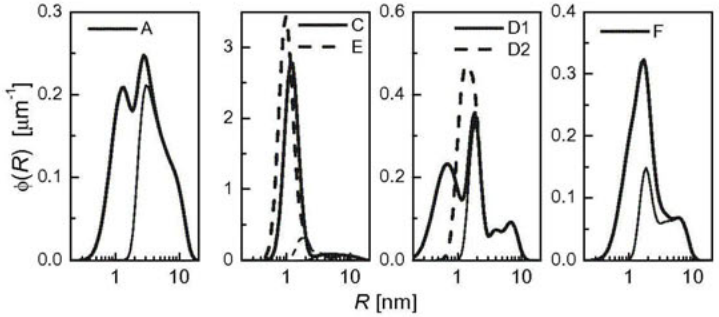

Figure 1. Size distributions of precipitates. Thin lines show corresponding unirradiated states.

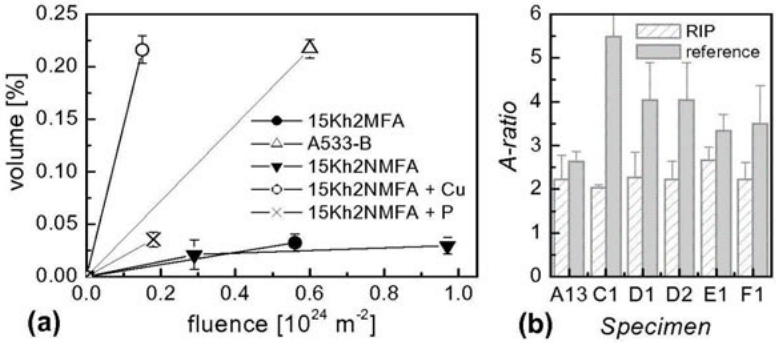

Figure 2. (a) Volume fractions of radiation-induced precipitates (RIP) for steels of different compositions (see Table 1). (b) A-ratios for RIP and medium-sized precipitates present already in reference material.

However, changes in magnetic scattering contrast can also play role (see discussion). Fig.2a showing integrated volume fractions of RIP documents the differences in radiation sensitivity of precipitation between different steels.
Values of A-ratio, $A = 1 + (\Delta\rho_M/\Delta\rho_N)^2$ fitted for the two populations of precipitates are shown in figure 2b. While $\Delta\rho_M$ is the same for all non-magnetic precipitates, $\Delta\rho_N$ depends on their chemical composition. Differences in A-ratios therefore indicate varying chemical composition of the precipitates.

Discussion

Although the A-ratio alone is not sufficient for determination of chemical composition, it can help in considering possible role of different solute atoms in formation of RIP. Nuclei with scattering lengths much lower than Fe like V, Mn, Cr or vacancies increase the contrast for nuclear scattering and lead thus to low values of A-ratio. On the contrary, nuclei with scattering lengths close to iron like Ni or Cu raise the A-ratios.

Unirradiated materials
Unirradiated materials are characterised in our results by the population of precipitates in the range of radii between 2 and 20 nm. Obviously, there are also larger precipitates in the steels, but they are not resolved in the Q-range of our measurements and contribute only by the Porod background. In the given size-range, vanadium-carbides are known to exist in VVER-type steels [3, 8]. Indeed, the low A-ratio observed in sample A is close to the value $A = 2.4$ resulting from the composition of VC particles measured by APFIM in [3] and to other SANS results [6]. For the other steels, *A-ratios* are higher and indicate the presence of precipitates with different composition. Possible candidates from those actually observed in RPV steels in this size range are VN and Mo_2C precipitates [13]. In the A533 steel (C), the vanadium-carbides cannot form and the average A-ratio is thus even higher.

Radiation-induced precipitates
We have observed much higher volume fractions of RIP in high-Cu steels (C, E) than in the low-Cu ones (A, D, F), though they were irradiated to similar fluence (see Fig.2a). This is not surprising, as copper is known to contribute to the formation of RIP with the highest enrichment factor. However, the *A-ratios* were much lower than we could expect for Cu precipitates ($A > 6$ [7, 14]). Probable explanation is in high level of Mn (> 30 at.%) and/or magnetisation of these precipitates. Such high Mn content was actually observed by APT in steels with high Cu and Mn levels [1, 14].
The volume fractions were evaluated under assumption that the precipitates are non-magnetic. While there is persistent controversy concerning the magnetic properties of Cu-rich precipitates [2, 14, 15], this assumption is almost certainly incorrect for RIP in low-Cu steels (samples A,D,F) with high (> 80 at.%) concentration of iron [3]. Consequently, the measured volume fractions can appear lower due to the lower than assumed magnetic contrast. As a possible scenario, let us consider a solute aggregate with composition measured in [3], Fe + 12 at.% Si + 13 at.% Mn and assume 5 % of vacancies in the feature. This composition yields $A = 2.3$ equal to those measured for samples A, D and F provided that the average magnetic moment per Fe atom in the aggregate is by factor 0.7 lower than in the ferrite matrix. True volume fractions would then be higher by factor 4.1 compared to those in figure 2.

Conclusions

SANS method is sufficiently sensitive to resolve differences in radiation-induced precipitation (RIP) for different RPV steels, as well as the differences in microstructure of reference materials under the study. The newly created precipitates have approximately the same radius for all materials. The differences in volume fractions can thus be interpreted as differences in number densities and/or chemical composition. Measured A-ratios are in agreement with APT analyses if we assume high Mn content in Cu-rich precipitates in steels with high Cu level and non-zero magnetisation of Fe-Mn-Si clusters observed in low-Cu steels. The low-Cu steels show much slower growth of RIP volume fraction with fluence. This can be however influenced by lower than assumed scattering contrast.

References

1. Miller, M.K., Russel, K.F., Sokolov, M.A. & Nanstad, R.K., 2003, *J. Nucl. Mater.* **320**, 177-183.
2. Hyde, J.M., Ellis, D., English, C.A. & Williams, T.J., 2001, *Effects of radiation on Materials: 20th International symposium* (Philadelphia: ASTM STP 1405), pp. 262-287.
3. Miller, M.K., Russell, K.F., Kočík, J. & Keilová, E., 2000, *J. Nucl. Mater.* **282**, 83-88.
4. Böhmert, J., Viehrigh, H.-W., Ulbricht A., 2001, *J. Nucl. Mater.* **297**, 251-261.
5. Böhmert, J., Viehrigh, H.-W., Ulbricht A., 2004, *J. Nucl. Mater.* **324**, 71-78.
6. Grosse, M., Böhmert, J., Gilles, R., 1998, *J. Nucl. Mater.* **254**, 143-150.
7. Böhmert, J., Ulbricht A., Kryukov, A., Nikolaev, Y. & Erak, D., *Effects of radiation on Materials: 20th International symposium* (Philadelphia: ASTM STP 1405), pp. 383-397.
8. Kočík, J., Keilová, E., Čížek, J. & Procházka, I., 2002, *J. Nucl. Mater.* **303**, 52-64.
9. Keiderling, U. & Wiedenmann, A., 1995, *Physica* B **213&214**, 895-897.
10. Glatter, O., 1980, *J. Appl. Cryst.* **13**, 7-11.
11. Kostorz, G., 1979, in *Treatise on materials science and technology, Vol.15, Neutron scattering*, edited by G. Kostorz (New York: Academic Press), pp. 229-247.
12. Šaroun, J., http://omega.ujf.cas.cz/~saroun/SAS
13. Miller, M.K., Burke, M.G., 1992, *J. Nucl. Mater.* **195**, 68-82.
14. Miller, M.K., Wirth B.D., Odette G.R., 2003, *Mater. Sci. Eng.* **A533**, 133-139.
15. Asoka-Kumar, P., Wirth, B.D., Sterne, P.A., Howell, R.H., Odette, G.R., 2002, Phil. Mag. Letters 82, 609-615.

Acknowledgements. This work was supported by the Grant Agency of the Czech Republic (projects 106/02/0557 and 202/03/0891) and the MSM project No. 2672244501. Access to the BENSC facility was supported by the EC IHP programme No. HPRI-CT-2001-00138.

Z. Kristallogr. Suppl. **23** (2006) 399-404

Structure analysis of $NiZr_2$ in reciprocal and real space

N. Mattern[1*], J. Sakowski[2], C. Baehtz[3]

[1]Leibniz-Institute for Solid State and Materials Research IFW Dresden
[2]Department of Physics, University Rostock
[3]Department for Material- and Geo -Sciences, Technical University Darmstadt
[*]Contact author; e-mail: n.mattern@ifw-dresden.de

Keywords: metallic glasses, high temperature X-ray diffraction, short-range order, thermal expansion, $Ni_{33}Zr_{67}$

Abstract. The temperature dependence of the geometric structure of amorphous and crystallized $Ni_{33}Zr_{67}$ was investigated by means of in situ synchrotron X-ray diffraction. The crystal structure parameters of the tetragonal $NiZr_2$ phase were determined by the Rietveld refinement of the X-ray diffraction patterns. The lattice parameters a_0, c_0, and therefore the inter-atomic distances increase linearly with temperature. The behavior of the short-range order was analyzed by the corresponding atomic pair correlation functions $G(r)$. The position of the first maximum of $G(r)$ at r_1 decreases with temperature. The analysis of real space data of the crystallized state of $Ni_{33}Zr_{67}$ shows that the measured $G(r)$ function consists of several superimposed, non-resolved inter-atomic distances. The individual distances increase with temperature in agreement with the Rietveld analysis. The position of the first maximum r_1 is additionally influenced by the thermal broadening of the distance distributions leading to the "unphysical" reduction of r_1 with temperature.

Introduction

The short-range order in non-crystalline materials is revealed by the analysis of the atomic pair correlation function $G(r)$. For metallic glasses and metallic elemental liquids the position of the first maximum of $G(r)$ stays constant or even decreases with temperature [1,2]. The aim of this work was to compare the temperature behavior of the short-range order of a binary metallic glass with that of its corresponding crystalline state. The $Ni_{33}Zr_{67}$ alloy was chosen because the amorphous state crystallizes isomorphous into $NiZr_2$, and the alloy is related to the new class of Zr-based bulk metallic glasses [3].

Experimental

Amorphous $Ni_{33}Zr_{67}$ ribbons 3 mm in width and 25 μm in thickness were prepared by means of rapid quenching technique from the melt. X-ray diffraction (XRD) patterns proofed the amorphous state of the as cast material. To analyze the temperature dependence of the crystal

structure part of the ribbons was annealed under vacuum at 400°C for 30 min. The annealed crystalline, and brittle ribbons were powderized and filled into a capillary. Temperature dependent X-ray diffraction patterns were recorded in Debye-Scherrer geometry at the powder diffraction beam-line B2 of HASYLAB. The experimental set-up ($\lambda = 0.6993$ Å) consists of a STOE furnace and an image plate detector (OBI). The exposure time was 5 – 10 min per diagram depending on the DORIS current. To analyze the temperature behavior of the short-range order, *in situ* XRD measurements were conducted at the high-energy beam-line BW5 of HASYLAB (wave length $\lambda = 0.1076$ Å). The experimental setup consists of a high temperature chamber and an image plate detector enabling to record diffraction pattern in transmission geometry within 30s and up to a scattering vector $q = 200$ nm^{-1} ($q = 4\pi\sin\theta/\lambda$) [4]. The amorphous as-quenched sample (stack of 20 ribbons) was stepwise measured and heated up to 400 °C where crystallization took place. Afterwards the sample was cooled down to 20 °C and the temperature dependent XRD measurement was repeated with the crystallized material.

Results and discussion

Figure 1 shows the XRD patterns of the crystallized $Ni_{33}Zr_{67}$ alloy measured from 800 °C to room temperature. The annealed material consists of the tetragonal $NiZr_2$ phase. Up to the highest temperature T = 800 °C, tetragonal $NiZr_2$ is registered only. The crystal structure

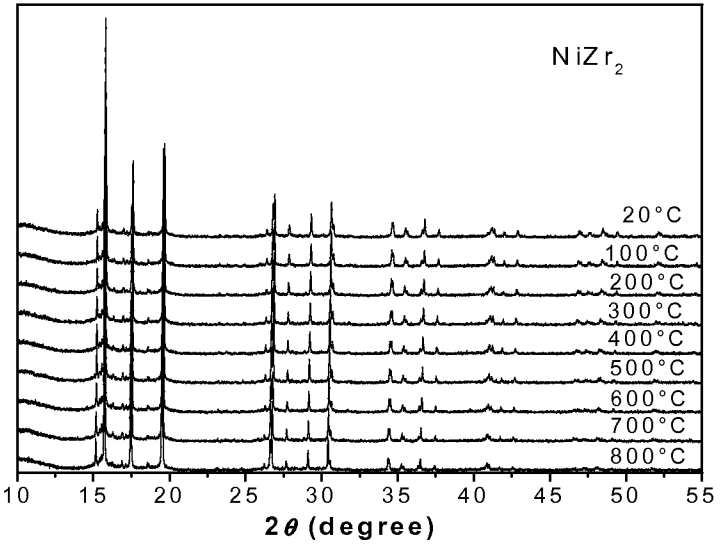

Figure 1. XRD patterns of crystallized $NiZr_2$ at elevated temperatures.

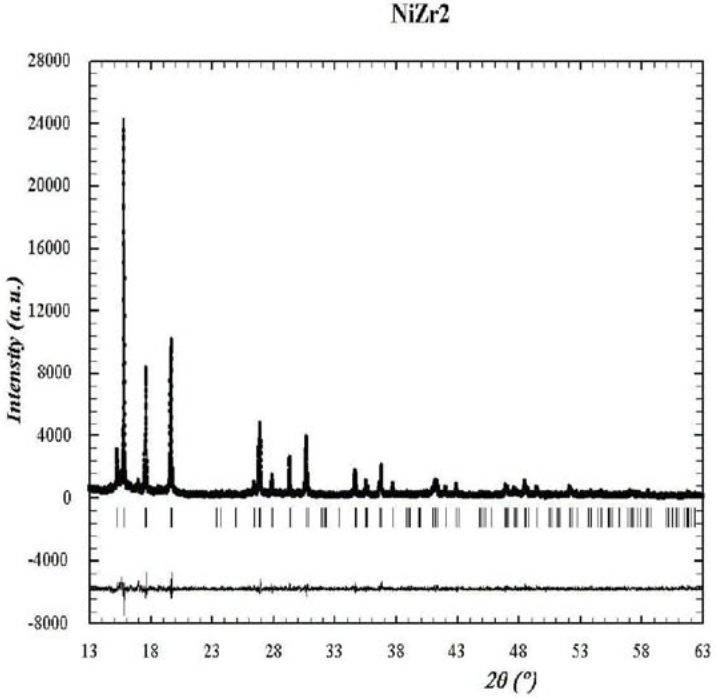

Figure 2. Rietveld plot of tetragonal $NiZr_2$ at room temperature.

parameters were refined using FULLPROF software. Figure 2 shows as an example the Rietveld plot of the room temperature measurement. The calculated crystal structure parameters versus temperature are given in table 1. A linear thermal expansion is observed with the linear expansion coefficients $\alpha_a = 9.5 \times 10^{-6}$ /K, and $\alpha_c = 9.1 \times 10^{-6}$/K respectively. The position of the Zr atom at 8*h* (x, x+1/2, 0) stays constant. A linear increase of all inter-atomic distances with temperature follows from the crystal structure parameters given in table 2.

Table 1. Crystal structure parameters of tetragonal $NiZr_2$ (S.G. 140).

	50°C	100°C	200°C	300°C	400°	500°C	600°C	800°C
a / Å	6.4905	6.4952	6.5030	6.5107	6.5186	6.5256	6.5328	6.5448
c / Å	5.2679	5.2707	5.2752	5.2802	5.2859	5.2917	5.2987	5.3147
x (8*h*)	0.8357	0.8360	0.8359	0.8356	0.8359	0.8359	0.8362	0.8359
B / Å^{-2}	0.07	0.23	0.47	0.63	0.91	1.15	1.37	1.78

The Rietveld method is based on the analysis of the positions and intensities of Bragg reflections. This allows us to determine the long-range average structure of the crystal. The short-range order of any material can be characterized by its atomic pair correlation function, which is well known for amorphous substances [5]. The method of atomic pair correlation functions has recently been applied also to crystalline materials [6]. The reduced atomic pair correlation function $G(r)$ is obtained by the Fourier transform of the structure factor $S(q)$ [5]:

$$G(r) = 4\pi \cdot r(\rho(r) - \rho_0) = \frac{2}{\pi} \cdot \int [S(q) - 1] \cdot q \cdot \sin(q \cdot r) \cdot dq \,, \qquad (1)$$

where $\rho(r)$ is the atomic density pair correlation function, and ρ_0 is the mean atomic density. The structure factor $S(q)$ is calculated from the elastic scattered intensity in absolute units [5]. Large values of q are required for resolution in $G(r)$ and to reduce the termination errors. Figure 3 shows the measured structure factors $S(q)$ of amorphous and crystallized $Ni_{33}Zr_{67}$ at room temperature. At elevated temperatures the heights of the maxima of $S(q)$ become reduced due to the temperature factor both for the amorphous and the crystallized sample. Figure 4 shows the corresponding atomic pair correlation functions $G(r)$. They differ clearly between the amorphous and the crystallized state due to the rearrangement of the atoms during the crystallization. The curves represent the superposition of the three partial atomic pair correlation function [5]. The two submaxima of the first maximum can be attributed to the nearest neighbor distances Ni-Zr, and Zr-Zr. The positions of the maxima are shifted and become broadened with temperature, which is related to the thermal expansion, and to the increase of the mean square displacement of the atoms.

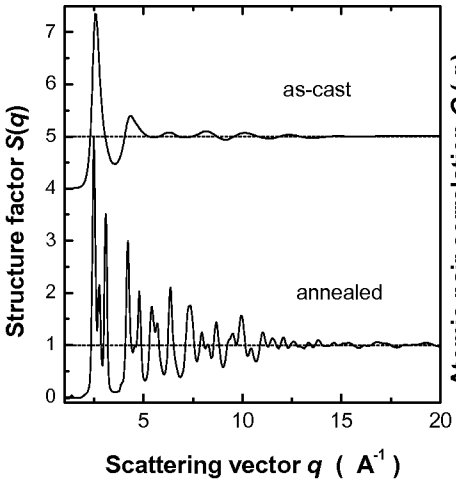

Figure 3. Structure factors S (q) of amorphous and and crystallized $Ni_{33}Zr_{67}$.

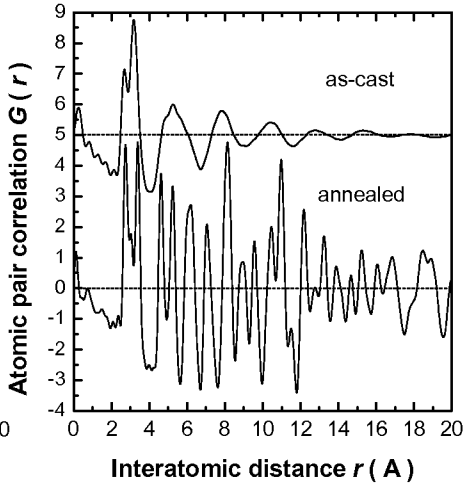

Figure 4. Atomic pair correlation functions of amorphous and crystallized $Ni_{33}Zr_{67}$.

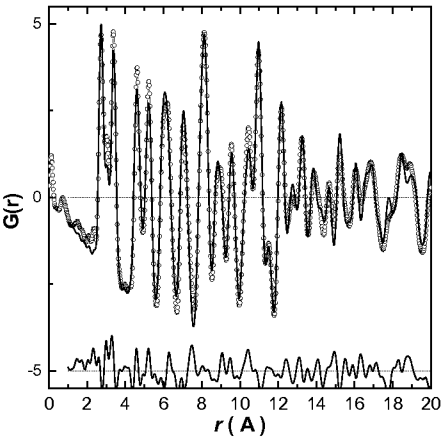

Figure 5. PDFFIT of crystallized NiZr.

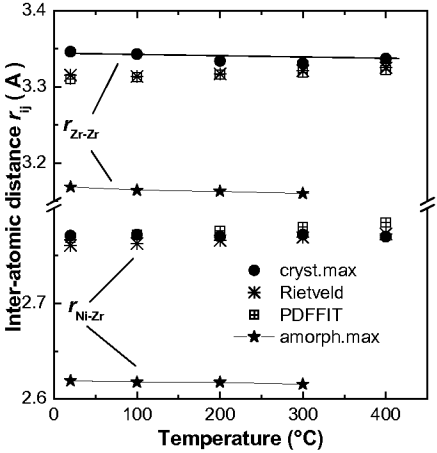

Figure 6. Interatomic distances of $Ni_{33}Zr_{67}$.

The atomic pair correlation functions $G(r)$ of the crystallized material were analyzed by a fit of the crystal structure parameter using PDFFIT [7]. Figure 5 shows one of the resulting plots. From the results of the real space fit procedure the inter-atomic distances can be calculated. Table 2 and figure 6 compare the values of the nearest neighborhood calculated by different methods. The positions of the two components of the first maximum of experimental $G(r)$ decrease slightly with increasing temperature (* amorphous, • crystalline). From the crystal structure of $NiZr_2$ follows that the first coordination sphere consists of 6 different

Table 1. Interatomic distances in of amorphous and crystallized $Ni_{33}Zr_{67}$

		(N_{ij})	rt.	100°C	200°C	300°C	400°C
amorphous	$r^1_{Ni\text{-}Zr}$/Å	(8)	2.619	2.618	2.617	2.615	-
	$r^1_{Zr\text{-}Zr}$/Å	(11)	3.169	3.164	3.163	3.160	-
crystalline	$r^1_{Ni\text{-}Zr}$/Å	(8)	2.771	2.772	2.770	2.772	2.770
	$r^1_{Zr\text{-}Zr}$/Å	(11)	3.346	3.343	3.334	3.321	3.337
crystalline Rietveld	$r^1_{Ni\text{-}Zr}$/Å	(8)	2.761	2.763	2.766	2.769	2.772
	$r^1_{Zr\text{-}Zr}$/Å	(1)	3.011	3.013	3.016	3.023	3.024
		(2)	3.071	3.073	3.076	3.079	3.082
		(4)	3.387	3.389	3.392	3.396	3.400
		(4)	3.432	3.434	3.438	3.443	3.447
	$r^1_{Ni\text{-}Ni}$/Å	(2)	2.639	2.640	2.641	2.642	2.643
crystalline PDFFIT	$r^1_{Ni\text{-}Zr}$/Å	(8)	2.769	2.772	2.776	2.780	2.785
	$r^1_{Zr\text{-}Zr}$/Å	(1)	2.958	2.962	2.951	2.947	2.941
		(2)	3.104	3.105	3.117	3.124	3.133
		(4)	3.370	3.372	3.372	3.372	3.373
		(4)	3.442	3.446	3.450	3.457	3.462
	$r^1_{Ni\text{-}Ni}$/Å	(2)	2.642	2.643	2.649	2.651	2.655

inter-atomic distances: Ni–Ni (N = 2 at 2.64 Å), Ni-Zr (N = 8 at 2.77 Å), Zr-Zr (N = 1 at 3.01 Å), Zr-Zr (N = 2 at 3.10 Å), Zr-Zr (N = 4 at 3.39 Å), and Zr-Zr (N = 4 at 3.43 Å). These individual distances are not resolved in the experimental $G(r)$ curve. The inter-atomic distances can be calculated from the results of the pair correlation function fit as well as from the results of the Rietveld refinement (table 2). There is a general good agreement between both methods within about ± 0.01Å. Reciprocal and real space data analysis shows an increase of the partial inter-atomic distances with temperature. The weighted averages (by coordination number N) of the Zr-Zr distances are shown in figure 6 (✳: Rietveld, ⊞: PDFFIT). The comparison with the behavior of the first maximum positions of the measured atomic pair correlation function $G(r)$ shows differences especially for the temperature dependence. Obviously the values of the maxima position of the experimental $G(r)$ curve give only a rough estimate of the inter-atomic distances. The total pair correlation functions have a complicated shape from the superimposition of different distances unable to fit with simple mathematic functions. With increasing temperature the width of the distance distribution increases due to the enhanced thermal oscillations of the atoms that affects the maxima position additionally.

Conclusions

The short-range order in amorphous and in crystallized $Ni_{33}Zr_{67}$ is quite different. The analysis of the atomic pair correlation function of the crystallized state in real space agrees well with those of the Rietveld refinement in reciprocal space. The atomic pair correlation function $G(r)$ contains contributions of different distances, which cannot be resolved in the experimental data. In the case of complex structures, the maxima positions of $G(r)$ and their temperature dependences are not directly related to the behavior of the individual inter-atomic distances.

References

1. Mattern, N., Eckert, J., Kühn, U., Hermann, H., Sakowski, J., Herms, G. & Neuefeind, J., 2002, Appl. Phys. Lett. **80**, 4525.
2. Schenk, T., Holland-Moritz, T.D., Simonet, V., Bellissent, R. & D.M. Herlach, D.M., 2002 Phys. Rev. Lett. **89**. 075507.
3. Inoue, A. & Takeuchi, A., 2002, Mater. Trans. JIM **43**, 1892.
4. Sakowski, J., & Herms, G., 2000, in: "Hasylab Annual Report", Part 1, 985.
5. Wagner, C.N.J., 1972, in "*Liquid Metals, Chemistry and Physics*", edited by S.Z. Beer (Marcel Dekker Inc., New York), 257.
6. Billinge, S.J.L., 1998, in „*Local Structure from Diffraction*", edited by S.J.L. Billinge & M.F. Thorpe (New York, Plenum)137.
7. Proffen, T., Billinge, S.J.L., 1999, J. Appl.Cryst.**32** , 572.

Acknowledgements. The author N.M. is grateful to R.B. Neder and T. Proffen for supplying us with the PDFFIT program and for valuable discussions.

Z. Kristallogr. Suppl. **23** (2006) 405-410

In situ high temperature XRD studies of the crystallisation of melt-spun $Mg_{77}Ni_{18}Y_5$

A. Teresiak, A. Gebert, M. Savyak, N. Mattern, M. Uhlemann

Leibniz-Institut für Festkörper- und Werkstoffforschung IFW Dresden, P.O. Box 270016, 01171 Dresden, Germany

*Contact author; e-mail: a.teresiak@ifw-dresden.de

Keywords: high temperature XRD, Mg-alloys, metallic glasses, metal-hydrides, hydrogen

Abstract. The thermal behaviour of $Mg_{77}Y_5Ni_{18}$ ribbons in the as-quenched and the hydrogen charged state was studied under hydrogen atmosphere up to 0.5 MPa and under high vacuum conditions. The crystallisation starts at $T_A > 150$ °C and begins at 130 °C after ball-milling. $Mg_2(Ni,Y)$, the metastabile Mg_6Ni and pure Mg were formed. Galvanostatically charged samples with 0.3 wt% < [H] < 0.6 wt% show the same phase formation during heat treatment. The formation of Mg_6Ni is inhibited by increasing hydrogen concentration [H] in the samples. Mg_6Ni is decomposed at $T_A > 250$ °C into Mg and Mg_2Ni. Yttrium phases were observed only at $T_A > 250$ °C. The grains sizes of the thermally formed phases decrease with increasing hydrogen content in the as-quenched samples. The galvanostatic charging with [H] = 1.42 wt% leads to the formation of the fcc complex compound Mg_2NiH_4 at 250 °C under a hydrogen atmosphere of 0.5 MPa besides $Mg_2NiH_{0.2-0.3}$, YH_2, YH_3 and MgH_2. The absorption/desorption process of the Mg_2NiH_4 could be proved. Under desorption conditions (40kPa hydrogen) the compound decomposes into Mg_2Ni and hydrogen at $T_A > 250$ °C. The process is reversible.

Introduction

Magnesium-based compounds are well-known materials for hydrogen storage. Particularly, Mg-Ni-compounds show a high hydrogen capacity. Additives of Y or rare earth elements, as La or Ce can also enhance the hydrogen absorption in such compounds [1]. Various non - equilibrium methods like intensive ball milling or rapid quenching are used to refine the microstructure and to improve the kinetics [2, 3]. The $Mg_{77}Ni_{18}Y_5$ composition was selected because of the capability of hydrogen charging by electrochemical methods at room temperature for Mg-TM-*RE*-glasses (*RE* = rare earth element or Y, TM = transition metal) and the easy glass-formation [4,5]. *In situ* high temperature X-ray diffraction allows the direct observation of the phase formation at elevated temperatures and at different partial pressures. The goal of the present work was the study of the thermal behaviour of $Mg_{77}Ni_{18}Y_5$ ribbons under hydrogen atmosphere up to 0.5MPa and under high vacuum conditions. The influence of electro-chemical hydrogen charging before heating on the phase formation was analysed. Furthermore, the influence of ball-milling of the ribbons on the gas-solid reaction with hydrogen at elevated temperatures was investigated.

Experimental

The master alloy $Mg_{77}Ni_{18}Y_5$ was prepared by induction melting. $Mg_{77}Ni_{18}Y_5$ glassy ribbons were prepared by melt spinning in Argon atmosphere [6]. The chemical composition of the ribbons was determined by inductive coupled plasma optical emission spectroscopy (ICP-OES). The galvanostatic charging with hydrogen was performed at room temperature in 0.1m NaOH + As_2O_3 and a current density *i* of -1mA/cm². The ribbons were crushed in a mortar or ball-milled under Argon atmosphere for 4h and 200rpm by means of a RETSCH PM4000 planetary ball mill and tungsten carbide vials. The hydrogen content [H] was determined using the carrier hot gas extraction technique (LECO 402 hydrogen analyser). XRD was carried out by means of a Θ-Θ PANalytical X'Pert PRO system with CoK_α radiation. The thermal behaviour was observed *in situ* using a high temperature X-ray attachment XRK900 (PAAR) and an X'Celerator semiconductor detector. The X-ray patterns were recorded at 25°C < T_A< 400°C in the 2Θ region 20° - 100° and in a time window of only about 12 minutes. The samples were annealed in high-vacuum and in a hydrogen atmosphere with 60kPa and 0.5MPa to initiate a gas-solid reaction at elevated temperatures. A heating rate of 10 K/min was used in all cases. After the heat treatment XRD patterns were recorded for the determination of the lattice parameters using a PANalytical MPD system with CoK_α radiation and in the 2Θ region 20° - 140°. The microstructure was studied using transmission electron microscopy (TEM, JEOL2000 FX microscope).

Results and discussion

The as-quenched alloys show only diffuse maxima in the X-ray patterns (figure 1). This indicates the presence of amorphous or nanocrystalline microstructures in the samples. A TEM image of this as-quenched state is shown in figure 2. Nanocrystals with an average size of 5 nm (dark dots in the figure) could be found besides the predominantly amorphous matrix. The FWHM of the first amorphous peak is about 6° - 9° for the as-quenched, the

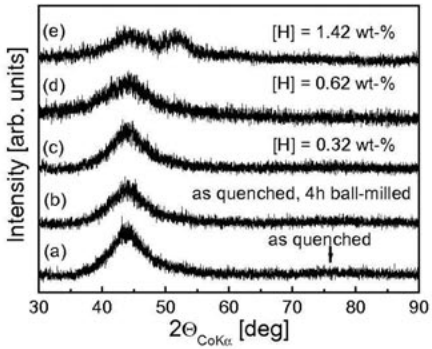

Figure1. X-ray patterns of the as-quenched state (a), the ball-milled sample (b) the electrochemical charged samples (c-d).

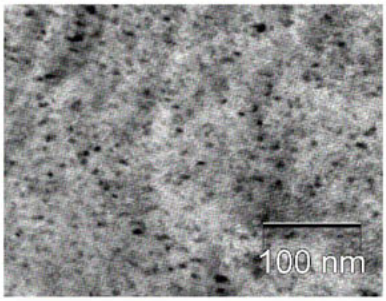

Figure2. TEM image of the as quenched $Mg_{77}Ni_{18}Y_5$ ribbons: The dark dots indicate the nanocrystals

ball-milled and electrochemically charged samples, with a sample-independent peak position. Furthermore, the sample with [H] = 1.42 wt% shows a second peak besides the first one, pointing out the formation of a second phase.

Figure 3 shows the crystallisation behaviour of an as-quenched and additionally ball-milled sample under high vacuum conditions. Ball-milling for 4h was performed to generate fresh surfaces for achieving a gas–solid reaction with the H_2 atmosphere in the high temperature chamber. The first crystallised phase $Mg_2(Ni,Y)$ with Mg_2Ni structure could be observed at an annealing temperature of T_A = 130°C. It is assumed, that the growth of the already existing nanocrystals is accelerated by the additional energy input by the ball – milling process. The metastable cubic Mg_6Ni phase already occurs at T_A = 150°C and additional Mg at T_A = 200°C with very broad peaks. The crystallisation of the as-quenched samples starts at T_A of 150°C < T_A < 200°C as also described by Spassov for similar compositions [2].

Figure 4 shows the estimated volume fractions of the crystallised phases for the unmilled and the ball-milled samples during the heat treatment. The volume fraction V_{c1} of a crystallised phase in a multi-phase mixture is directly proportional to the X-ray intensities of this phase:

$$V_{c1} \sim \frac{I_{c1}}{I_c + I_a} \qquad with\ I_c = I_{c1}+I_{c2}+I_{c3}+...+I_{cn} \qquad (1)$$

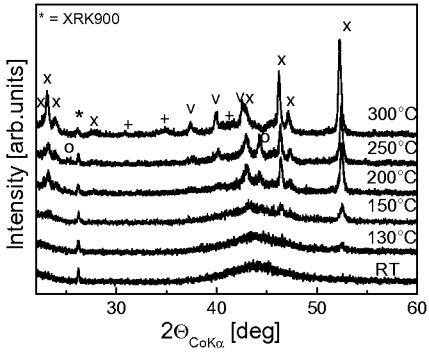

Figure 3. X-ray powder patterns of the 4h ball-milled ribbons up to 250°C and the as-quenched material at 300°C v = Mg, x = $Mg_2(Ni,Y)$, o = Mg_6Ni, + = NiY.

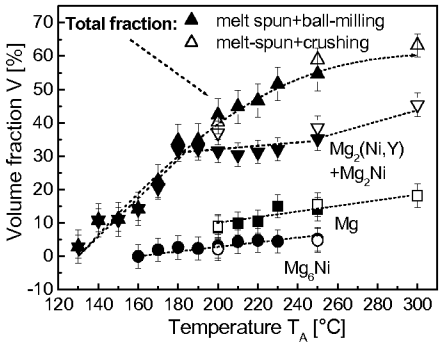

Figure 4. Volume fractions of the crystallised phases after annealing the only crushed material (holed symbols) and the ball-milled ribbons (filled symbols).

The $I_{c1...cn}$ means the sum of integral intensities of first phase to the phase n and the I_a is that of residual amorphous phase [7]. The graph shows a continuous increase of the crystalline fraction with increasing temperature. In spite of the crystallisation of the ball-milled sample at lower temperature, the curves show the same progression up to 300 °C. At T_A > 250°C the metastable Mg_6Ni is decomposed into Mg_2Ni and pure Mg. The Y is dissolved in $Mg_2(Ni,Y)$ up to T_A = 250 °C replacing the Ni partially [8]. Yttrium leaves the $Mg_2(Ni,Y)$ phase at 250°C < T_A < 300 °C and forms the NiY phase with the Ni from the decomposed Mg_6Ni phase. After cooling, the lattice parameters of the remaining $Mg_2(Ni,Y)$ phase with a = 5.242 Å and c = 13.357 Å are also increased compared with the pure Mg_2Ni with a = 5.190 Å and c = 13.220 Å [9]. Obviously, the yttrium leaves the $Mg_2(Ni,Y)$ phase very slowly. The sample

was cooled to room temperature already after 15 min. Furthermore, the complete crystallisation is only achieved after longer time at T_A = 300 °C. The crystallisation process of the ball-milled samples under a 0.5 MPa hydrogen atmosphere proceeds in the analogous manner. A gas-solid reaction could not be achieved. It is assumed, that the detected hydrogen after heat treatment is located in the grain boundaries.

The crystallisation of the galvanostatic charged samples with a hydrogen concentration up to 0.6 wt% starts at 170 °C with the formation of $Mg_2(Ni,Y)$ phase. The phase composition at 230 °C and about 60 kPa hydrogen starting pressure for different electrochemically charged

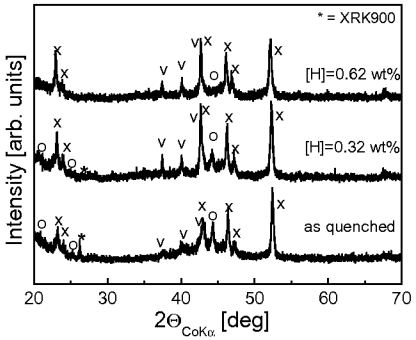

Figure.5. X-ray powder patterns of different charged samples at T_A = 230°C: v = Mg, o = Mg_6Ni, x = $Mg_2(Y,Ni)$.

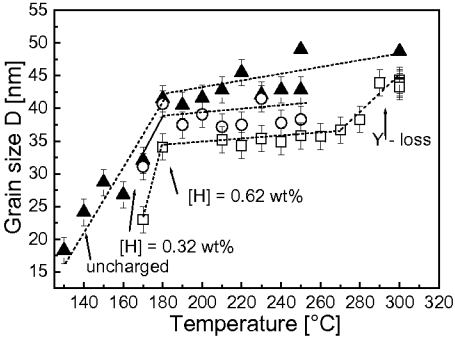

Figure 6. Grain sizes D of the $Mg_2(Ni,Y)$ or $Mg_2NiH_{0.2-0.3}$ phase, respectively, in dependence on temperature and galvanostatic charging.

samples is shown in figure 5. With increasing temperature and hydrogen content obtained by electrochemical charging the formation of Mg_6Ni is inhibited in favour of pure magnesium and Mg_2Ni. Above T_A = 250°C Mg_6Ni is decomposed in all cases. Furthermore, a solid solution Mg_2NiH_x ($0.2 < x < 0.3$) is formed. Figure 6 shows the grain sizes for the $Mg_2(Ni,Y)$ phase. The grain sizes D were estimated from the FWHM of the X-ray reflections. Crystal growth and grain sizes decrease with increasing electrochemical charging. Furthermore, Y seems to inhibit the crystal growth in presence of hydrogen. At T_A > 260 °C a clear increase of the grain size D is observed relating to the Y loss from the $Mg_2(Ni,Y)$ phase.

For samples having a hydrogen concentration of 1.42wt% after galvanostatic charging the crystallisation of $Mg_2(Ni,Y)$ and Mg_6Ni is observed only at T_A = 230 °C. At T_A = 250 °C the complex compound Mg_2NiH_4 is formed (figure 7). Mg_2NiH_4 shows the cubic high temperature modification [10]. At equilibrium conditions this phase is formed only at 300 °C [11]. Already at T_A = 260 °C the tetragonal MgH_2 phase, YH_2 and YH_3 with very broad reflections were found. The Mg_6Ni phase is decomposed at T_A > 260 °C. With increasing T_A the amount of MgH_2 increases. At T_A = 300 °C the crystallisation is complete. Mg_2NiH_4 is stable up to 300 °C under hydrogen atmosphere. The volume fractions of the single phases during heating could not be determined due to the strong overlap of the X-ray reflections and the relatively small intensities. After cooling the lattice constants and the quantitative composition of the phase mixture were determined by using X-ray methods. The deviations were relatively large and were estimated to be 3 wt% for the phase composition and ±0.005Å for the lattice parameters. The presence of approx. 6 wt% YH_3 and approx. 5 wt% YH_2 in the phase mixture show, that Y is released from the $Mg_2(Ni,Y)$ phase at higher temperatures.

The remaining Mg_2Ni with about 57wt% shows increased lattice constants with $a \approx 5.254$ Å and $c \approx 13.423$ Å. This is in agreement with the values of Mg_2NiH_x ($0.24 < x < 0.29$) [12]. The Mg_2NiH_4 phase with about 25 wt% in the sample shows a lattice constant of $a = 6.503$Å in a good agreement with constants given by the literature [10]. The average grain size is about 33-38 nm. The total hydrogen concentration [H] of the phase mixture is about 1.84 ± 0.15wt%. That means, the hydrogen of the chamber atmosphere was included in the phase transformation.

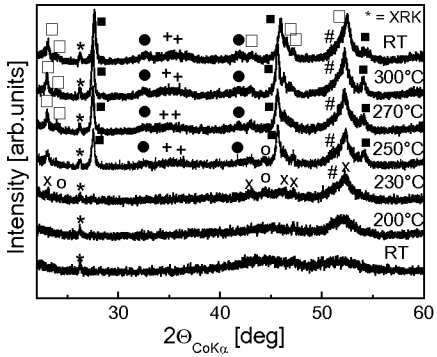

*Figure 7. Crystallisation of $Mg_{77}Ni_{18}Y_5$ after electrochemical charging with [H]= 1.42 wt% ■ = Mg_2NiH_4,, ● = MgH_2,,+= YH_3, YH_2 □ = $Mg_2(Ni,Y)$, **x** =Mg_2NiH_x ($0.24 < x < 0.29$) # =MgO, *= XRK900.*

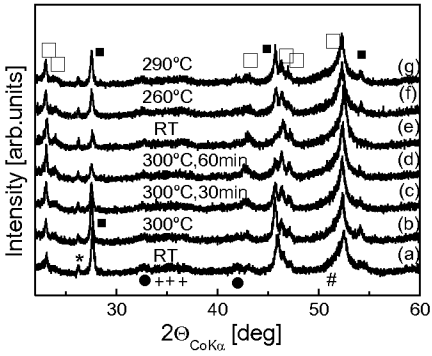

Figure 8. Desorption of Mg_2NiH_4, fcc: at $T_A = 300$°C and 40 kPa H_2 (b-d) repeated absorption: 200 kPa H (f,g).

A second heat treatment was performed under desorption conditions (60 kPa hydrogen). The desorption of hydrogen is characterised by the phase transformation of Mg_2NiH_4 into Mg_2Ni and hydrogen according to $Mg_2NiH_4 \rightleftharpoons Mg_2Ni + 2H_2$ and starts at $T_A > 250$ °C. The volume fraction of Mg_2NiH_4 decreases with increasing temperature in favour of Mg_2Ni and hydrogen. The process of phase transformation is reversible. The Mg_2NiH_4 phase forms again under a hydrogen atmosphere already with 0.2 MPa (figure 8).
The formation of Mg_2NiH_4 was not achieved for the other electrochemically charged samples with 0.3 or 0.6 wt% hydrogen, respectively. Neither the annealing of the charged amorphous samples leads to the formation of the Mg_2NiH_4 phase nor the isothermal heat treatment at T_A = 300 °C with a hydrogen pressure of 0.5 MPa for about 11 hours.

Summary and prospect

The as-quenched $Mg_{77}Ni_{18}Y_5$ ribbons show an amorphous - nanocrystalline microstructure.
The crystallisation of the $Mg_{77}Y_5Ni_{18}$ ribbons in the as quenched and the hydrogen charged state with a hydrogen content up to 1.4wt% could be observed under hydrogen atmosphere up to 0.5 MPa and under high vacuum conditions by *in situ* high temperature XRD.
Under high vacuum, the crystallisation of the glassy $Mg_{77}Ni_{18}Y_5$ starts at T > 150 °C for the only crushed material and at T = 130 °C for 4h ball-milled ribbons caused by the additionally energy input. The phases $Mg_2(Ni,Y)$, the metastabile Mg_6Ni at T_A = 160 °C and pure Mg at

T_A = 200 °C were formed. The integration of yttrium in the Mg_2Ni structure could be confirmed. Above T_A = 250 °C yttrium is released from the $Mg_2(Ni,Y)$ phase and forms YNi. Under 0.5 MPa hydrogen atmosphere the phases were observed in the same succession. Above T_A = 250 °C the stable YH_3 is formed.
The galvanostatic charged samples show a similar crystallisation behaviour as the uncharged ribbons. But, with increasing temperature and hydrogen concentration [H] the formation of Mg_6Ni is inhibited in favour of pure Mg. Mg_6Ni is decomposed at $T_A > 250$ °C in all cases.
Y- phases were detected at temperatures $T_A > 250$ °C as YH_2 or/and YH_3.
The grain sizes of the crystallised phases decrease with increasing [H]. Obviously, Y stabilises the fine-grained microstructure of the main phase up to 250 °C with about 35-40 nm in presence of hydrogen.
The electrochemical charged ribbons with [H] = 1.42 wt% show another thermal behaviour. The crystallisation is retarded because of the longer diffusion paths and starts only at T_A = 230 °C with the formation of Mg_2Ni. At T_A = 250 °C the fcc complex compound Mg_2NiH_4 phase is observed simultaneously with YH_2,YH_3 and MgH_2.
The hydrogen absorption/desorption process of Mg_2NiH_4 could be demonstrated between room temperature and 300 °C.
The conditions of the formation of Mg_2NiH_4 will be investigated in future. Further investigations will deal with the influence of higher current density on the electrochemically charging and the crystallization behaviour.

References

1. Gerard, N., Ono, S., 1992, *Magnesium Alloys and Intermetallic Compounds,* in: *Hydrogen in Intermetallic Compounds II*, ed.: L. Schlapbach, Topics in Applied Physics 67, Springer-Verlag, p.181
2. Spassov, T., Köster, U., 1999, *J. Alloys Comp.* **287**, 243
3. Ruggeri, S., Lenain, C., Roue, L., Liang, G., Huot, J., Schulz R., 2002, *J. Alloys Comp.* **339,** 195
4. Savyak, M., Hirnyj, S., Bauer, H.-D., Uhlemann, M., Eckert, J., Schultz, L., Gebert, A., 2004, *J. Alloys Comp.,* **364** , 229
5. Spassov, T., Lyubenova, L., Köster, U., Baró, M.D., 2004, *Mater. Sci. Eng.*, **A375-377**, 794
6. Gebert, A.; Wolff, U., John, A., Eckert, J., Schultz, L., 2001, *Mater. Sci. Eng.*, **A299**, 125
7. Klug, H.P., Alexander, L.E., 1974, in *X-ray diffraction procedures,* edited by J. Wiley & sons, inc. (New York, London)
8. Spassov, T., Köster, U., 1998, *J. Alloys Comp.*, **379**, 279
9. Soubeyroux, J.L., Fruchart, D., Mikou, A., Pezat, M., Darriet, B.,1980, *J. Less-Common Met.*, **74**, 65-65
10. Garcia, G.N., Abriata, J.P., Sofo, J.O., 1999, *Physical Review, Serie 3.*, **59**, 11746
11. Reilly, J.J., Wiswall, R. H., Inorg. Chem. 7 (1968) 2254
12. Senegas, J., Mikou, A., Pezat, M., Darriet, B., 1984, *J. Sol. State Chem.*, **52**, 1

Acknowledgements. The authors would like to thank Mrs. K. Hennig for sample preparation, Mrs. A. Voß for the realisation of the chemical analysis, Mrs. Ch. Mickel for the TEM investigations and Mrs. B. Opitz for the XRD phase analysis.

Z. Kristallogr. Suppl. **23** (2006) 411-416

Complex intermetallic compounds in the Mg-Ir system solved by powder diffraction

Radovan Černý[1], Guillaume Renaudin[1†], Yaroslav Tokaychuk[1] and Vincent Favre-Nicolin[2]

[1]University of Geneva, 24 quai Ernest-Ansermet, CH-1211 Geneva 4, Switzerland
[2] CEA/Grenoble, 17, rue des Martyrs, F-38054 Grenoble Cedex 9, France
[*]Contact author; e-mail: Radovan.Cerny@cryst.unige.ch

Keywords: intermetallic compound, structure solution, global optimization

Abstract. The crystal structures of two new topologically close-packed intermetallic compounds, MgIr (*Cmca*, 25 atoms) and $Mg_{2-x}Ir_{3+x}$ (x=0.067, *C*2/*m*, 11 atoms) were fully characterized by high resolution synchrotron powder diffraction and global optimization of a structural model in direct space. The simulated annealing algorithm (in parallel tempering mode) and computer program *Fox* were used.

Introduction

In the Mg–Ir phase diagram [1] only the composition interval of 0–25 at.-% Ir is reported. Recently, two groups [2] independently discovered new phase $Mg_{1+x}Ir_{1-x}$ (x = 0-0.054) and could characterize the crystal structure of this compound on the basis of powder and single crystal X-ray diffraction. The iridium-rich part of the binary magnesium-iridium system was later reinvestigated, and a new binary compound with the refined composition of $Mg_{2+x}Ir_{3-x}$ (x = 0.3) with monoclinic $V_2(Co_{0.57}Si_{0.43})_3$ structure type was reported [3] from single crystal X-ray diffraction. Here we report on an independent structural characterization of these two compounds, MgIr and $Mg_{2-x}Ir_{3+x}$, as observed by X-ray powder diffraction.

Experiment and Results

Synthesis

Details of MgIr synthesis are given in [2]. $Mg_{2-x}Ir_{3+x}$ was first observed as a by-product during the synthesis of MgIr. The final sample was prepared by sintering from element powders, with the nominal composition of Mg_2Ir_3. Compressed pellet was sealed in a steel

† Current address: Laboratoire des Matériaux Inorganiques, Université Blaise Pascal de Clermont-Ferrand, 24 avenue des Landais, 63177 Aubière Cedex, France

ampoule with 1 bar of Ar and heated in a furnace at 1070 K for 2 h, then annealed at 870 K during 1 week and quenched in a cold water. No single crystals were obtained. Electron Probe MicroAnalysis (EPMA) has shown the composition of $Mg_{42(6)}Ir_{58(6)}$ and Ir metal as impurity.

Powder diffraction

Synchrotron powder diffraction data of both compounds were obtained at the Swiss-Norwegian Beam Line (SNBL) at the ESRF Grenoble (sample in a 0.2 mm glass capillary, six analyser crystals detector). Details of the data collection are given in table 1.

Structure solution and refinement

The crystal structures of both compounds were solved and refined using the synchrotron powder diffraction data. First 26 (MgIr) and 25 ($Mg_{2-x}Ir_{3+x}$) observed reflections were used for indexing by using the program DICVOL91 [4]. An orthorhombic cell with Figures-of-Merit M = 13.2 and F = 108.0(0.0024, 101) was found for MgIr and monoclinic with Figures-of-Merit M = 14.6 and F = 18.3(0.0091, 150) for $Mg_{2-x}Ir_{3+x}$. The refined values of lattice parameters from a final Rietveld refinement are given in table 1. From the analysis of MgIr powder pattern the extinction symbol *C-c*(*ab*) was concluded corresponding to the space groups *C*2*cb*(41) and *Cmca*(64). The centrosymmetric group *Cmca* was used for the structure solution of MgIr. From the analysis of $Mg_{2-x}Ir_{3+x}$ powder pattern the extinction symbol *C*1-1 was concluded corresponding to the space groups *C*2(5), *Cm*(8) and *C*2/*m*(12). The centrosymmetric group *C*2/*m* was used for the structure solution of $Mg_{2-x}Ir_{3+x}$.

Table 1. Data collection parameters and crystal data of MgIr and $Mg_{2-x}Ir_{3+x}$.

Formula	MgIr	$Mg_{2-x}Ir_{3+x}$, x=0.067(2)
space group	*Cmca*	*C*2/*m*
a [Å]	18.46948(6)	18.5699(2)
b [Å]	16.17450(5)	5.18715(4)
c [Å]	16.82131(5)	8.49233(6)
β [°]		97.2209(5)
V [Å^3]	5025.11(3)	811.54(1)
Wavelength [Å]	0.50012	0.49969
μ [mm^{-1}]	38.8	47.9
Density(calc.) [g cm^{-3}]	10.95	13.02
2θ interval [°]	2.215 - 41.890	1.024 -36.580
χ^2	3.02	1.50
R_{wp} (bgr. corrected)	0.094	0.144
R_B (all reflections)	0.056	0.056

The structures of both compounds were solved by the global optimization of structural models in direct space using the simulated annealing (in parallel tempering mode) and the program *Fox* [5]. As a cost function, the integrated R_w factor [5] and anti-bump function (based on minimal distances Mg-Ir = 2.7 and Mg-Mg = 2.8 Å) weighted 0.55/0.45 were used. As both crystal structures were expected to be closely packed, the expected volume per atom was estimated as 15-20 Å^3. No density measurements were available, and no indication of structural relations with a known structure types were found from the analysis of the cell parameters. First, we have localized iridium atoms using the advantage of *Dynamical Occupancy Correction* [5] in automatic identification of the special crystallographic positions and of merging excess atoms. In next runs localized iridium atoms were kept fixed, and free magnesium atoms were introduced subsequently till all magnesium atoms were localized. For the correct solution the integrated R_w was 0.09 and 0.15 for MgIr and $Mg_{2-x}Ir_{3+x}$, resp.

The crystal structures of both compounds were refined by the Rietveld method using the synchrotron data and the program *FullProf.2k* [6]. Iridium metal was identified as an impurity in both samples. The background was interpolated between fixed points in both refinements. The runs were performed where the occupancies of individual atomic sites were refined. In MgIr all sites refined to a full occupancy and no mixed sites were observed. In $Mg_{2-x}Ir_{3+x}$ one magnesium site (see the discussion) has shown a mixed occupancy with iridium. The refined composition is $Mg_{1.933(2)}Ir_{3.067(2)}$.

In the final run of MgIr structure refinement 76 parameters were refined (main phase: 57 positional and 2 isotropic displacement, 3 cell, 7 pseudo-Voigt profile function and 1 scale parameter; impurity: 1 displacement, 1 cell, 3 pseudo-Voigt profile function and 1 scale parameter). For refined structural parameters see [2], the Rietveld plot is shown in figure 1.

When refining the structure of $Mg_{2-x}Ir_{3+x}$ an anisotropic line broadening was observed with a clear tendency for 0*k*0 reflections being less broadened than the others. The line broadening was modeled with the pseudo-Voigt function available in the *FullProf.2k* program (profile no. 7) describing the broadening of Lorentzian part of the diffraction profile as due to the size effect and that of Gaussian part as due to the strain effect. Gaussian size and Lorentzian strain broadenings were found to be negligible. The anisotropy of size broadening was modeled by a spherical harmonics model according to the formula

$$\beta_{\mathbf{h}} = \frac{\lambda}{\cos\theta} \sum_{lmp} a_{lmp} y_{lmp}(\Theta_{\mathbf{h}}, \Phi_{\mathbf{h}}) \tag{1}$$

where $\beta_{\mathbf{h}}$ is the size contribution to the integral breadth of reflection **h**, and y_{lmp} ($\Theta_{\mathbf{h}}$, $\Phi_{\mathbf{h}}$) are the normalized real spherical harmonics. Modeling up to the fourth order of spherical harmonics (nine coefficients a_{lmp}) appeared to be enough. Apparent crystallite size was maximal in the ***b***-axis direction (4250 Å) and much lower in directions perpendicular to the ***b***-axis (between 670 and 2000 Å). The anisotropy of strain broadening was modeled by the variance of a quartic form M_{hkl} in reciprocal space according to [7]

$$\sigma^2(M_{hkl}) = \sum_{\substack{HKL \\ \{H+K+L=4\}}} S_{HKL} h^H k^K l^L \tag{2}$$

Nine coefficients S_{HKL} were refined due to the monoclinic symmetry. The maximum strain was lower in the ***b***-axis direction (0.00046) and higher in the directions perpendicular to the ***b***-axis (between 0.0007 and 0.00117). For more details on the size-strain analysis used with the *FullProf.2k* program see the program's manual. In the final run of $Mg_{2-x}Ir_{3+x}$ structure refinement 54 parameters were varied (main phase: 26 positional and 2 isotropic displacement, 4 cell, 20 pseudo-Voigt profile function and 1 scale parameter; impurity: 1 scale parameter). For refined structural parameters see table 2, the Rietveld plot is shown in figure 1.

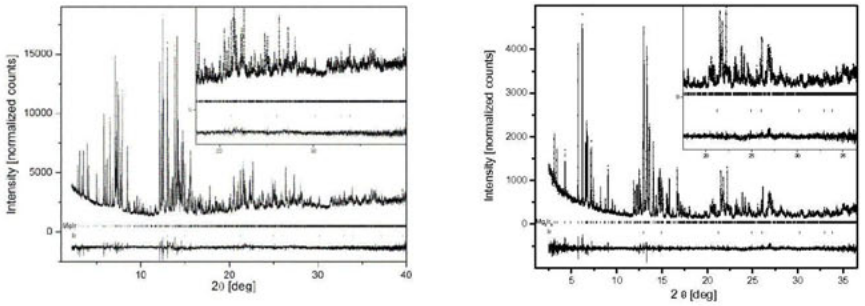

(a) *(b)*

Figure 1. Rietveld plots of MgIr (a) and $Mg_{2-x}Ir_{3+x}$ (b).

Table 2. Atom positional and displacement parameters for $Mg_{2-x}Ir_{3+x}$.

atom	site	*x*	*y*	*z*	B[Å^2]
Ir1	8*j*	0.40951(9)	0.2357(3)	0.2957(2)	0.51(1)
Ir2	8*j*	0.16756(9)	0.2496(4)	0.2271(2)	$=B_{Ir1}$
Ir3	4*i*	0.8702(2)	0	0.0294(3)	$=B_{Ir1}$
Ir4	4*i*	0.1351(2)	0	0.4655(3)	$=B_{Ir1}$
Ir5	4*i*	0.2144(2)	0	0.7408(3)	$=B_{Ir1}$
Ir6	2*c*	0	0	1/2	$=B_{Ir1}$
Mg7	4*i*	0.025(1)	0	0.174(2)	0.6(1)
*M*8	4*i*	0.4228(5)	0	0.007(1)	$=B_{Mg7}$
Mg9	4*i*	0.286(1)	0	0.435(2)	$=B_{Mg7}$
Mg10	4*i*	0.281(1)	0	0.067(2)	$=B_{Mg7}$
Mg11	4*i*	0.562(1)	0	0.382(2)	$=B_{Mg7}$

$M = Mg_{0.833(5)}Ir_{0.167(5)}$

Discussion and Conclusions

Crystal chemistry

Both compounds can be classified as topologically close-packed phases as the coordination of nearly all atoms has a form of Frank-Kasper polyhedra. It is quite difficult to relate the MgIr crystal structure with structures of other known intermetallic compounds. For more discussion see [2].

The structure of $Mg_{2-x}Ir_{3+x}$ is a binary variant of the type $V_2(Co_{0.57}Si_{0.43})_3$. It is the second representative of this type. Interestingly the mixed Co/Si sites in the silicide corresponds to the iridium sites in $Mg_{2-x}Ir_{3+x}$, and vanadium sites to the magnesium sites and mixed site *M*8. All iridium sites in $Mg_{2-x}Ir_{3+x}$ have slightly distorted icosahedral coordination, the magnesium sites and the mixed site *M*8 have slightly distorted coordination by Frank-Kasper polyhedra with CN 14-16. From six magnesium sites in $Mg_{2-x}Ir_{3+x}$ four were observed as mixed between magnesium and iridium in the single crystal study in [3], and the site *M*8 was observed as fully occupied by magnesium. The refined composition is then $Mg_{2.30}Ir_{2.70}$, richer in magnesium than in our study where it is $Mg_{1.933}Ir_{3.067}$, to which corresponds the cell volume larger by 1.5% than the cell volume observed in this work. The homogeneity range of $Mg_{2-x}Ir_{3+x}$ is probably quite large, however, it necessary to notice that the samples from [3] corresponds to 1270 K, and that from this work to 870 K, due to different annealing procedures.

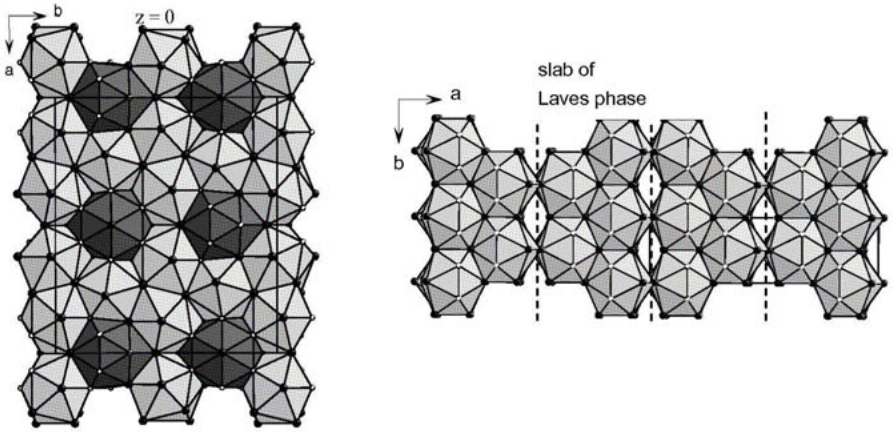

Figure 2. (a) Structural slab of MgIr. (b) Projection of $Mg_{2-x}Ir_{3+x}$ structure along the c-axis showing (100) slabs derived from $MgIr_2$ Laves phase. Polyhedra: Ir-centered icosahedra in light grey, Mg-centered Frank-Kasper polyhedron with CN=16 in dark grey. Ligand atoms: Ir as small white and Mg as larger black spheres.

The structure of $Mg_{2-x}Ir_{3+x}$ can be also viewed (see figure 2) as build from (100) slabs derived from hexagonal Laves phase $MgIr_2$ [8] ($MgZn_2$ type, observed also by us). The slabs are derived by a distortion of iridium-centered Mg_6Ir_6 icosahedra and by interchanging one magnesium and iridium site compared to the Laves phase. The lattice parameters *b* and *c* of $Mg_{2-x}Ir_{3+x}$ that correspond to lattice parameters *a* and *c* of the Laves phase $MgIr_2$, resp., are slightly larger in $Mg_{2-x}Ir_{3+x}$ due to the structural distortion.
Anisotropic line broadening observed in $Mg_{2-x}Ir_{3+x}$ and explained mainly as due to anisotropic size effect can be now understood from stacking of Laves phase-like slabs: In *a*-axis direction the slabs are interrupted by planar faults (see figure 2), *b*-axis direction is without faults, and with shortest periodicity. Consequently the apparent crystallite size is largest in *b*-axis direction and smallest in *a*-axis direction.
The interatomic distances Ir–Ir cover the range of 2.45-2.66 Å in MgIr and of 2.53-2.74 Å in $Mg_{2-x}Ir_{3+x}$, and, to the best of our knowledge, are the shortest ones ever observed. These Ir-Ir contacts are significantly shorter than the sum of the covalent radii for two iridium atoms (2.54 Å), and than the distances in *fcc* iridium (2.72 Å). We can assume significant Ir-Ir bonding in both compounds. These short Ir-Ir distances are also shorter than those usually observed in iridium cluster compounds (2.63-2.73 Å). The Mg-Mg distances are in the range of 2.85-3.73 Å in MgIr and of 2.75-3.42 Å in $Mg_{2-x}Ir_{3+x}$. Most of the Mg-Mg distances are shorter than the average Mg-Mg distance of 3.20 Å in *hcp* magnesium. The shortest distance of 2.75 Å is that between the mixed occupied site *M*8 and Mg10. The Mg-Ir distances are in the range of 2.57-3.51 Å in MgIr and of 2.76-3.17 Å in $Mg_{2-x}Ir_{3+x}$. Considering the course of the interatomic distances, we can assume more or less isotropic and strong bonding within both compounds.

References

1. Binary Alloy Phase Diagrams. (1996). Second Edition, version 1.0, ASM International.
2. Černý, R., Renaudin, G., Favre-Nicolin, V., Hlukhyy, V. and Pöttgen, R. (2004) *Acta Cryst. B* **60**, 272-281.
3. Hlukhyy, V. and Pöttgen, R. (2004) *Solid State Sciences* **6**, 1175-1180.
4. Boultif, A. and Louër, D. (1991). *J. Appl. Cryst.* **24**, 987-993.
5. Favre-Nicolin, V. and Černý, R. (2002) *J. Appl. Cryst.* **35,** 734-743, see also: *http://objcryst.sourceforge.net* and *Z. Kristallographie* (2004) **219** 1-10.
6. Rodríguez-Carvajal, J. (2002). *'Program FullProf.2k, Version 2.20*, Laboratoire Léon Brillouin (CEA–CNRS), France.
7. Stephens, P.W. (1999) *J. Appl. Cryst.* **32**, 281-289.
8. Hlukhyy, V. and Pöttgen, R. (2004) *Z. Naturforsch.* **59b**, 943-946.

Acknowledgements. We thank the staff of the Swiss-Norwegian Beam Line (BM1) at ESRF, Grenoble, for help with the synchrotron powder diffraction experiment, and Michael Schindl (University of Geneva) for help with the EMPA. The work was partly supported by the Swiss National Science Foundation, grant No. 2100-053847.98.

IV.4 Minerals and Inorganics

IV.4.1 *Structural Changes, Non-Ambient Conditions*

Z. Kristallogr. Suppl. **23** (2006) 419-424

Low temperature SR-XRPD study of åkermanite-gehlenite solid solution

M. Merlini[1*], M. Gemmi[1], G. Artioli[1]

[1]Dipartimento di Scienze della Terra "A. Desio", Università degli Studi di Milano, via Botticelli 23, I-20133, Milano, Italy
[*]Contact author; e-mail: marco.merlini@unimi.it

Keywords: melilite, thermal expansion, solid solution, powder diffraction

Abstract. Low temperature thermal expansion coefficients of members of the solid solution gehlenite (ge)-åkermanite (åk) were measured by synchrotron radiation X-Ray powder diffraction. The linear thermal expansion coefficient is maximum for a composition with about 50 % content of åk. In åk-rich compositions an incommensurate modulated structure is present. The ge-åk solid solution shows a non-ideal behaviour, with negative excess volume near the ge end-member.

Introduction

Melilites are a group of minerals which form solid solutions between the end members gehlenite ($Ca_2Al_2SiO_7$, ge) åkermanite ($Ca_2MgSi_2O_7$, åk), soda-melilite ($NaCaAlSi_2O_7$, NaMel) and Fe-bearing end members [1]. The structure is tetragonal (space group $P\text{-}42_1m$) and consists of layers of tetrahedra centered by Mg, Si and Al and connected by Ca polyhedra [2]. The importance of these minerals resides in the fact that almost pure members of the series gehlenite-åkermanite are among the first silicates that condensed from the solar nebula and they are found in chondritic meteorites. Melilites also crystallise in alkaline magmatic rocks, whose origin is restricted to significant geodynamic environments. Therefore a modelling of their thermodynamic parameters is valuable in order to improve the accuracy of phase equilibria calculations, which could have important implications in petrologic studies, for example for the accurate determination of the thermal history of meteorites or the solidification temperature of alkaline rocks... Usually the thermodynamic calculations involving phase equilibria of melilites are performed assuming the ideality of the solid solution [3]. However the double substitution Mg+Si↔Al+Al calls for major investigation on the ideality of the ge-åk solid solution. Another important feature of melilites is the presence of an incommensurate modulated (IC) structure, especially for åk-rich compositions, which transforms into a normal (N) one upon heating [4-6]. The temperature of IC-N phase transition is of 80 °C for pure åkermanite and it is decreased by Al↔(Mg+Si) substitution [7]. In order to detail the crystal-chemistry and the thermodynamic properties of the melilite solid solution, we are investigating the structural features of these minerals as a function of temperature and composition, in particular in the ternary compositional join åk-ge-NaMel. In a

previous work [8] we described the thermal expansion of åkermanite and gehlenite, focusing on the IC-N phase transition. In this paper we report the results of low temperature X-ray powder diffraction study on the åk-ge binary join performed at the beam line ID31 at ESRF, Grenoble, in the temperature range 20-300 K. The thermal expansion and the volume behaviour of the solid solution are discussed.

Experimental

Materials and methods

Melilites in the binary join gehlenite-åkermanite were synthesised from glasses obtained by mixing and melting pure MgO, CaO, Al_2O_3 and SiO_2 in the appropriate stoichiometric ratios at a temperature of 1150 °C. Crystals with sizes up to 250 μm were obtained. The products were characterised by powder and single-crystal X-ray diffraction. The chemical composition was checked with electron microprobe analysis, using an ARL-SEMQ instrument. The operating conditions were 15 kV and 300 nA and the measured elements were calibrated against kaersutite. The compositions obtained in the ge-åk binary join were pure gehlenite, $ge_{92}ak_{08}$, $ge_{65}ak_{35}$, $ge_{46}ak_{54}$, $ge_{25}ak_{75}$ and åkermanite. The low temperature X-ray powder diffraction study was performed at the beamline ID31 at ESRF, Grenoble. The beamline was equipped with a closed circle He cryostat, which allows a minimum temperature of about 5-10 K. We collected X-ray powder pattern in the temperature range of 20-290 K. The wavelength used was 0.4959 Å, calibrated against standard silicon (NIST SRM 640c) and the angular range explored was 3-28 °2θ, corresponding to a d-space interval of 9.5-1.02 Å. The powder pattern were analysed by the full profile Rietveld method using the GSAS software [9]. The refined parameters were the lattice parameters, an overall zero shift correction, two parameters of a pseudo-Voigt function for the peak shape modelling, the atomic coordinates, and two isotropic thermal parameters, one for the cations and the other for the oxygen atoms. The agreement factors R_{Wp} and R_{Bragg} in the different Rietveld refinements are in the range 12-18% and 4-9% respectively.

Results and discussion

The lattice parameters values for the samples investigated at the different temperatures are summarised in table 1. The volumetric thermal expansion, α, is defined as

$$\alpha(T)=(1/V)(\partial V/\partial T)_P. \quad (1)$$

Integration of (1) gives

$$V(T)= V(T_0)\exp\int_{To}^{T}\alpha(T)dT\,. \quad (2)$$

A polynomial expression for α(T) is commonly used for describing its temperature dependence [10]. The experimental data in the range 20-290 K have been fit using only a linear term in T:

$$\alpha(T)=a_0T \quad (3)$$

There is no absolute term in (3), since at 0 K the thermal expansion is null. The a_0 coefficients derived from the fit are plotted against composition in figure 2 and are also reported in table 1. The thermal expansion coefficient shows a maximum for the composition $ge_{46}ak_{54}$.

For åk-rich compositions melilites undergo a phase transition to an IC structure at low temperature and their thermal expansion decreases.

Table 1. Lattice parameters (Å),cell volume (Å^3) and a coefficients of thermal expansion (according to the equation α(T)=aT) for the samples studied.

T (K)	gehlenite			$ge_{92}ak_{08}$			$ge_{46}ak_{54}$		
	a	*c*	vol	*a*	*c*	vol	*a*	*c*	vol
20	7.6801(5)	5.0581(5)	298.35(4)	7.6912(5)	5.0426(5)	298.29(4)	7.7478(5)	5.0298(5)	301.93(4)
50	7.6802(5)	5.0583(5)	298.37(4)	7.6914(5)	5.0430(5)	298.33(4)	7.7483(5)	5.0299(5)	301.98(4)
80	7.6804(5)	5.0588(5)	298.41(4)	7.6916(5)	5.0435(5)	298.38(4)	7.7485(5)	5.0303(5)	302.02(4)
110	7.6807(5)	5.0597(5)	298.49(4)	7.6920(5)	5.0442(5)	298.45(4)	7.7494(5)	5.0310(5)	302.13(4)
150	7.6817(5)	5.0608(5)	298.63(4)	7.6929(5)	5.0457(5)	298.61(4)	7.7505(5)	5.0322(5)	302.29(4)
200	7.6833(5)	5.0632(5)	298.90(4)	7.6944(5)	5.0477(5)	298.84(4)	7.7534(5)	5.0340(5)	302.62(4)
250	7.6850(5)	5.0652(5)	299.15(4)	7.6960(5)	5.0500(5)	299.10(4)	7.7552(5)	5.0360(5)	302.88(4)
290	7.6864(5)	5.0669(5)	299.36(4)	7.6979(5)	5.0520(5)	299.37(4)	7.7574(5)	5.0380(5)	303.17(4)
T (K)	$ge_{25}ak_{75}$			åkermanite					
	a	*c*	vol	*a*	*c*	vol	a (*10^{-8})		
20				7.8258(5)	5.0085(5)	306.74(4)	gehlenite	8.0(1)	
50				7.8260(5)	5.0086(5)	306.76(4)			
80				7.8265(5)	5.0086(5)	306.80(4)	$ge_{92}ak_{08}$	8.54(6)	
100	7.7787(5)	5.0154(5)	303.47(4)						
110				7.8272(5)	5.0087(5)	306.86(4)	$ge_{46}ak_{54}$	9.65(15)	
150	7.7801(5)	5.0159(5)	303.61(4)	7.8285(5)	5.0090(5)	306.98(4)			
200				7.8308(5)	5.0094(5)	307.18(4)	$ge_{25}ak_{75}$	9.6(2)	
220	7.7834(5)	5.0176(5)	303.97(4)						
250				7.8337(5)	5.0098(5)	307.44(4)	åkermanite	7.22(3)	
290	7.7882(5)	5.0206(5)	304.53(4)	7.8364(5)	5.0101(5)	307.67(4)			

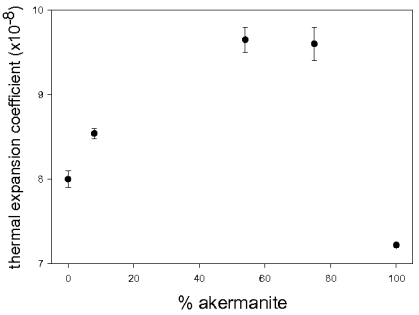

Figure 1. Low temperature thermal expansion coefficient a for melilites, according to the equation α(T)=aT .

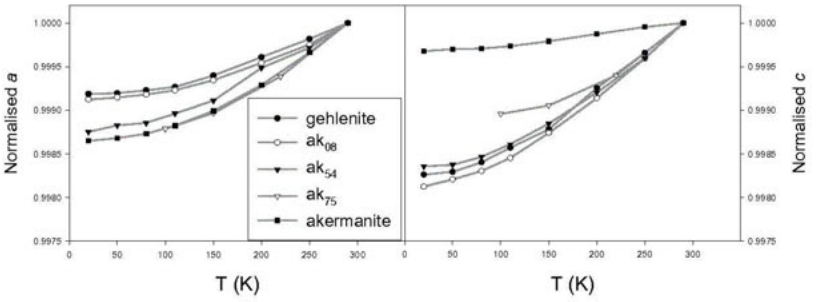

Figure 2. Lattice parameters a and c normalised to the values at 290 K for melilites.

The different thermal behaviour of the IC phase with respect to the normal one is also evidenced by the thermal expansion along the main crystallographic directions (figure 2). In åkermanite and $ge_{25}ak_{75}$ (IC phase) the thermal expansion is greater along *a* than along *c*; on the contrary in ge-rich composition (normal phase) the expansion is greater along *c*. The temperature dependence of the crystallographic ratio *c/a* is hence a good indicator for the presence of the IC or of the normal phase as function of T and composition. In figure 3 the *c/a* ratio (normalised to 290 K) is plotted against temperature. Starting from the lowest temperature and moving towards room temperature, åk-rich melilites show a decrease of the *c/a* ratio, while gehlenite, ak_{08} and ak_{54} behave in the opposite way.

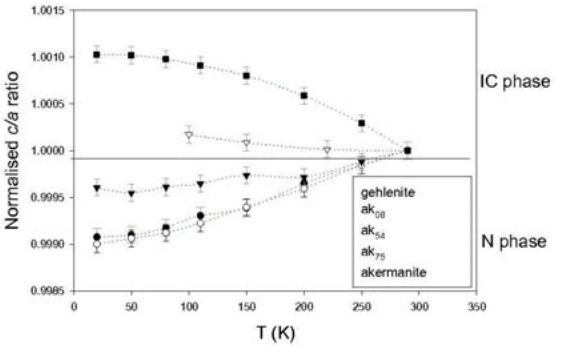

Figure 3. Normalised c/a ratio vs. temperature for melilites

For what it concerns the ideality of the solid solution, we observed a negative excess volume near the gehlenite end-member (figure 4). The volume behaviour in this solid solution re-

sembles the S-shaped volume curve that it is usually observed in silicate binary solid solution, as described in [11]. The negative excess volume near the gehlenite end-member can be explained by the fact that the larger size of Mg cation with respect to Al can be easily accommodated in the quite expansible T1 site as the åkermanite content increase.

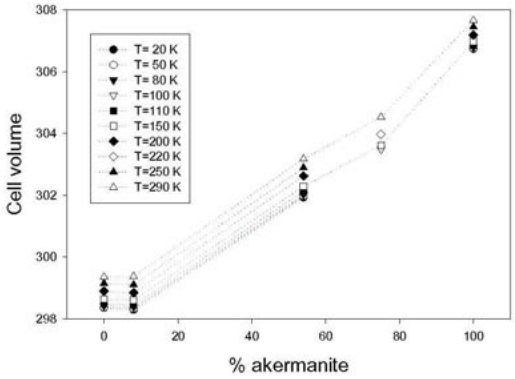

Figure 4. Cell volume vs. composition at different temperatures, from 20 to 290 K.

In order to better understand the low temperature behaviour of the åkermanite-gehlenite solid solution, we also analysed the results of crystal structure refinements. In figure 5 the polyhedral volume of the two non-equivalent tetrahedral T1 and T2 sites normalised to the ones of gehlenite at 20 K are plotted against temperature. The 8-coordinated Ca site is not shown because its volume does not vary significantly with T and composition. It is assumed that the biggest Mg cation [12] goes in T1 site while Si occupies T2 and Al both sites. Our results are in accordance with [13] and reveal an increase of the T1 site volume of 30 % and a decrease of T2 site volume of 10 % with the increase of åk content in melilite. In the temperature range investigated the T-sites thermal expansion is too small to be significantly observed. Preliminary results of high temperature thermal expansion indicate also that the T1 site has a greater thermal expansion than T2 and the thermal expansion of T1 increase with increasing content of Mg in the site.

References

1. Deer,W.A., Howie, R.A., & Zussman, J., 1992, *An introduction to the Rock-Forming Minerals* (Longman)
2. Warren, B.E, 1930, *Z. Kristallogr.* 74, 131-138.
3. Yoneda S. & Grossman L., 1995, *Geoc. Cosmoch. Acta*, **59**(16), 3413-3444.
4. Hemingway, B.S., Evans, H.T.Jr., Nord, G.L.Jr., Haselton, H.T.Jr, Robie, R.A. & McGee, J.J., 1986, *Can. Mineral.*, **24**, 425-434.

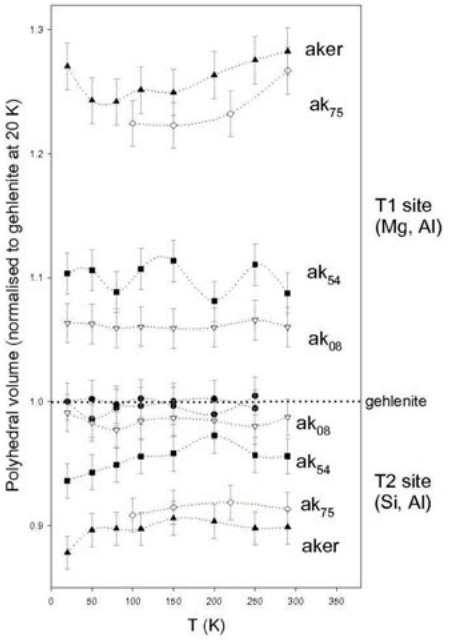

Figure 5. Polyhedral volume of T1 and T2 sites normalised to the ones of gehlenite at 20 K.

5. Seifert, F., Czank, M., Simons, B. & Schmahl, W., 1987, *Phys. Chem. Minerals*, **14**, 26-35.
6. Rothlisberger, F., Seifert, F. & Czank, M., 1990, *Eur. J. Mineral.*, **2**, 585-594.
7. Seifert, F. & Rothlisberger, F., 1993, *Mineral and Petrol.*, **48**, 179-192.
8. Merlini, M., Gemmi, M. & Artioli, G., 2005, *Phys Chem Minerals*, 32(3), 189-196.
9. uLarson, A.C. & Von Dreele, R.B., 1988, *Laur 86-748, Los Alamos National Laboratory, Los Alamos*, NM 87545.
10. Fei, Y., 1995, in *Mineral Physics and Crystallography: a handbook of physical constants,* edited by T.J. Ahrens (AGU Reference Shelf 2).
11. Newton, R.C. & Wood, B., 1980, *Am. Mineral.,* **65**, 733-745
12. Waldbaum, D.R. & Woodhead, J.A., 1975, *Fortschr. Miner.*, **52**, 119-131.
13. Swainson, I.P., Dove, M.T., Schmahl, W. & Putnis, A., 1992., *Phys Chem. Minerals,* **19**, 185-195.

Acknowledgements. We acknowledge Andy Fitch of the ESRF ID31 beamline for the assistance in the data collection. Monica Dapiaggi and Walter Tiano helped in experimental work.

Z. Kristallogr. Suppl. **23** (2006) 425-429

Study of the structural evolution and selectivity of Wyoming montmorillonite in relation with the concentration of Cu^{2+} and Ni^{2+}

W.Oueslati[1], H. Ben Rhaiem*, M.S. Karmous, S. Naaman
A. Ben Haj Amara

Laboratoire de Physique des Matériaux, Faculté des Sciences de Bizerte, Tunisia
*Contact author; e-mail: hafsia.rhaiem@fsb.rnu.tn

Keywords: smectite, heavy metals, selectivity

Abstract. This paper aims at characterizing the structural evolution and the selectivity of a dioctahedral smectite (Wyoming montmorillonite) saturated by heavy metals cations. The quantitative analysis of XRD patterns is achieved using an indirect method based on the comparison of XRD experimental patterns to calculated ones. The study is achieved in two steps: first the Cation Exchange Capacity (CEC) is saturated with one cation Cu^{2+}, Ni^{2+}. There are two heavy metal cations occurring in holdhouse trash. The resulting complexes were respectively labelled Wy-Cu and Wy-Ni. Secondly the clay is placed in presence of bionic solution: Cu-Ni with different concentrations in order to understand the selectivity of the clay for these cations. XRD quantitative analysis showed that for low concentrations the d_{001} spacing corresponds to the Wy-Cu complex, whereas for high concentration the d_{001} spacing can be attribuated to the Wy-Ni complex. This means that at low concentrations, the clay CEC is saturated with low hydration state cation (Cu^{2+}) which is characterized by one water layer. For high concentrations, the clay fixe the cation with high hydration state (Ni^{2+}) characterised by two water layers.

Introduction

Smectite minerals are the most active constituents of soils and are the main component of bentonite rocks. The structural formula of dioctahedral alumino-smectites in the series montmorillonite beidillite is:
$(Al_{2-y}Mg_y)(Si_{4-x}Al_x)O_{10}(OH)_2M_{x+y,}\ nH_2O$ when y>x, smectite is called montmorillonite [1]. Layer stacking are generally influenced by the nature of the interlayer cation, the nature and number of solvation molecules, the di- or tri octahedral character of the mineral, the mean crystallite size and the ordering of interlayer cations over the available hexagonal cavities. The main objective of this work is to characterize the structural evolution and the selectivity of a dioctahedral smectite in presence of solutions with various concentrations and contain-

ing different pairs of divalent cations essentially present in household trash. XRD analysis was used in order to determine the structural characteristics along the C* axis. The interpretation of XRD patterns is based on the comparison between experimental and calculated ***00l*** reflection patterns.

Materials and methods

In order to characterize the selectivity of clay minerals for heavy metal cations, we used a sample reference: the Wyoming montmorillonite which structural formula is:

$$\left(Si_{3,923}Al_{0,077}\right)\left(Al_{1,459}Ti^{4+}_{0,018}Fe^{3+}_{0,039}Fe^{2+}_{0,045}Mg^{2+}_{0,382}\right)O_{10}(OH)_2\left(Ca^{2+}_{0,177}Na^{+}_{0,027}\right)$$

The clay fraction (< 2μm) was prepared according to the classic protocol of extraction given by Tessier & Robert [2]. The crude material was first Na-exchanged and extracted by sedimentation. The resulting complex was designed Wy-Na. Heavy metal complexes were prepared by washing the Wy-Na complex several times with 1N solutions of $CuCl_2$, $NiCl_2$ or $CaCl_2$ in order to synthesize Wy-Cu, Wy-Ni and Wy-Ca complexes respectively. The excess of chloride was eliminated by washing the clay in distilled water and by subsequent dialysis. To study the structural evolution and the selectivity of the montmoriollonite saturated Na we placed Wy-Na complex in presence of mixtures containing (50 % Cu^{2+}, 50 % Ni^{2+}) with various concentrations ($1N \rightarrow 10^{-3}N$). Oriented preparations were prepared by depositing clay suspension onto a glass slide [3]. XRD patterns were recorded on air-dried samples using a D8 advance Bruker installation, by reflection setting, using Cu-Kα radiation. The mineralogical and structural characteristics were determined by comparing the experimental XRD patterns with the theoretical patterns calculated from structural models [4-5-6] and using the matrix expression developed by Drits & Tchoubar [7].

$$I_{00}(2\theta) = L_p Spur\ (Re[\ \phi][W]\left\{[I] + 2\sum_{n}^{M-1}[(M-n)/n][Q]^n\right\})$$

where Re is the real part of the final matrix, Spur, the sum of the diagonal terms of the real matrix; L_p, the Lorentz-polarization factors; M,the number of layers per stack; n, an integer varying between 1 and M-1; [Φ], the structure factor matrix; [I], the unit matrix; [W], the diagonal matrix of the proportions of the different kinds of layers, and [Q], the matrix representing the interference phenomena between adjacent layers. The relationships between the layer fractions (W) and the junction probabilities (P) are given by: $W_1 + W_2 = 1$, $P_{11} + P_{12} = 1$, $W_1P_{12} = W_2P_{21}$ [5]. XRD patterns were calculated using the z-coordinates (Z_n) of Drits [8]. The origin of the atomic coordinates was placed on the plane surface oxygen atoms.

Results and Discussion

Homogeneous samples

XRD patterns produced respectively by Wy-Ni, Wy-Na and Wy-Cu complexes are given in figures 1a, 1b and 1c and showed two 001 reflections respectively at 2θ = 5.85° (d_{001} = 15.08 Å), 2θ = 7.31° (d_{001} = 12.29 Å) and at 2θ = 7.21° (d_{001} = 12.36 Å). We reported in table 1 the d_{00l} values deduced from the ***00l*** reflection positions for these reference complexes. We can

notice a similar basal spacing d_{001} for the Wy-Na and Wy-Cu complexes, it will be difficult to distinguish between the pair (Cu^{2+}, Na^{2+}) using a simple qualitative analysis of XRD patterns. In order to resolve this problem, the complexes were subjected to a thermal traitement "HOFFMAN-KLEMEN effect" [9] or chemical analysis [10]. HOFFMAN-KLEMEN demonstrated that, for this type of minerals, when saturated by cations with small ionic radius and a heating up to 250°C during 24 hours, the cation migrates to the octahedral vacancies and the material loses its hydration properties.

Quantitative analysis

In table 2, we report the structural parameters obtained from the quantitative analysis of XRD patterns.

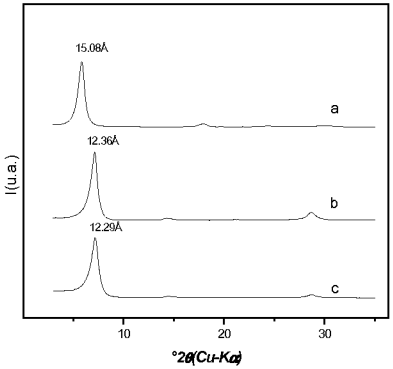

Figure 1. Experimental XRD patterns of reference samples: Wy-Ni (a), Wy-Cu (b) and Wy-Na(c).

sample	Wy-Na	Wy-Cu	Wy-Ni
d_{001}	12,29 Å	12,36 Å	15,08 Å
2θ°	7,31	7,21	5,85
d_{002}	6,12Å	6,18 Å	*
2θ°	14,40	14,40	
d_{003}	4,12 Å	4,13 Å	4,94 Å
2θ°	21,35	21,3	17,94

*Table 1. Basal spacing and reflection position for reference sample. (* weak intensity).*

Table 2 . Structural parameters for the reference sample: n & Z_n number and position of exchangeable cation per half unit cell, M: layer number per particle.

samples	d_{001}(Å)	n	Z_n (Å)	Succession law	M
Wy-Na	12.29	0.33	10.0	W_1 =1 P_{11} =1 P_{12}=0	8
Wy-Cu	12.36	0.17	10.0	W_1 =1 P_{11} =1 P_{12}=0	8
Wy-Ni	15.08	0.17	10.2	W_1=0,92 P_{11}=0.95 W_2=0,08 P_{21}=0.58	7

Structural evolution and selectivity of samples in accordance with the concentration of the solution in the case of Cu^{2+},Ni^{2+} mixture

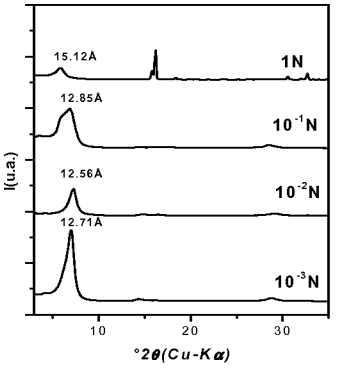

Figure 2. XRD patterns obtained for decreasing normalities (0.5 N to 0.510^{-3}N) for a mixture containing (50% Cu^{2+} 50% Ni^{2+})

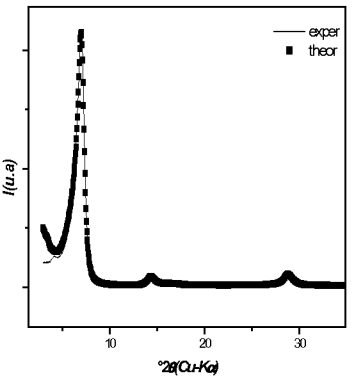

Figure 3. comparison between experimental and calculated XRD pattern for a 10^{-3}N mixture.

The XRD patterns obtained for decreasing normality (0.5 N to 0.5 10^{-3}N) for a mixture containing (50% Cu^{2+} and 50% Ni^{2+}) are reported in figure 2.
When the complex is placed in presence of a 0.5 N mixture, the XRD pattern is characterised by a reflection at $2\theta = 5.89°$ ($d_{001} = 15.12$ Å). When the normality of the mixture varies from 0.5 10^{-1}N to 0.5 10^{-3}N, examination of figure 2 shows the apparition of a basal reflection situated at $2\theta = 6.81°$ ($d_{001} \approx 12$ Å), for low concentration, attributable to a complex Cu^{2+} saturated. We reported in figure 3 the best agreement between experimental and calculated XRD pattern in the case of mixture concentration equal to 10^{-3} N. In table 3, we summarized the main structural parameters deduced from quantitative XRD analysis.
Examination of table shows that for low concentration, the material fixes cations with lower hydration state whereas for high concentration, cation with higher hydration properties is preferentially retained.

Conclusion

This structural study shows that the reference complexes i.e. Wy-Na, Wy-Cu and Wy-Ni are respectively characterised with 12.29 Å, 12.36 Å and 15.08 Å basal spacings. The quantitative analysis showed that the complex Wy-Ni is characterised by a two water layer hydration state whereas the Wy-Na and Wy-Cu are characterised by a one water layer hydration state. The selectivity was carried out for a mixture containing two heavy metal cations (Cu^{2+}, Ni^{2+}) and for concentration varying from 0.5 N to 0.5 10^{-3} N. The results obtained showed that: for low concentration, the d_{001} spacing corresponds to the Wy-Cu complex whereas for

high concentration, the d_{001} spacing can be attribuated to the Wy-Ni complex. This means that at low concentration the clay CEC is saturated with low hydration state cation (i.e.Cu^{2+}), for high concentration, the clay fixes the cation with high hydration state (i.e. Ni^{2+}).

Table 3. structural parameters deduced from XRD quantitative analysis: n & Z_n number and size of exchangeable cation per half unit cell, M: layer number per particle, S1: solution at 10^{-1}N, S2: solution at 10^{-2}N, S3: solution at 10^{-3}N.

Sample	d_{00l}(Å)	n	Z_n(Å)	Succession law	M
Wy-Na+S1	d_{001}=12.85; d_{004} =3.11	0.13 Ni^{2+} 0.04 Cu^{2+}	9.8	W_1=0.77;P_{11}=0.89 W_2=0.23;P_{21} =0.36	6
Wy-Na+S2	d_{001}=12.56; d_{002}=6.16 d_{003}=4.18 ; d_{004} =3.10	0.01 Ni^{2+} 0.16 Cu^{2+}	9.5	W_1=0.93 P_{11}=0.98 W_2=0.07 P_{21}=0.65	8
Wy-Na+S3	d_{001}=12.71 d_{002}=6.01 d_{004} =3.05	0.01 Ni^{2+} 0.16 Cu^{2+}	9.8	W_1=0.85;P_{11}=0.92 W_2=0.15; $_{21}$=0.45	10

References

1. Güven N., 1988, Smectites. In S.W. Bailey, Ed.,Hydrous Phyllosilicates Reviews Mineralogy, Mineralogical Society of America, **16**,pp. 497-559.
2. Robert M & Tessier D., 1974, *Ann. Agron.* **25**, pp. 859-882.
3. Plançon A., 1981, *J.Appl. Cryst.* **14**, pp. 300-304.
4. Pons, C.H., de la Calle, C. and de Vidales, M., 1995, *Clays and Clay minerals* **43**, pp. 246-254.
5. Ben Rhaiem H.,Tessier D. & Ben Haj Amara A., 2000: *Clay Minerals* **35**, pp. 375-381.
6. Ben Haj Amara A., 1997, *Clay Minerals* **32**, pp. 463-470.
7. Drits A.V. & Tchoubar C. (1990) *X-ray diffraction by disordered lamellar structures.* 371pp.Springer Verlag, New-York, Berlin, Heidelberg
8. Drits V.A., 1975, *The structural and crystallochemical features of layer-silicates. in Crystallochemistry of Minerals and Geological Problems* (A.G. Kossovskaya, editor). Nauka, Novosibirsk, Russia, pp. 35-51.
9. Hoffmann U.& Klemen E., 1950, *Zeistschrift für Anorganische und Allegemeine Chemie* **262**, pp. 95-99.
10. Mering J. Glaeser R., 1954, *Bull. Soc. Fr. Minéral. Cristallogr.* **77**, pp. 519-530.

Z. Kristallogr. Suppl. **23** (2006) 431-436

The interlayer structure and thermal behavior of Cu and Ni montmorillonites

M. S. Karmous, H. Ben Rhaiem*, S. Naamen, W. Oueslati and A. Ben Haj Amara.

Laboratoire de Physique des Matériaux, Faculté des Sciences de Bizerte, Tunisia
*Contact author; e-mail: hafsia.rhaiem@fsb.rnu.tn

Keywords: heavy metals, trapping, smectite, temperature

Abstract. The threat of environmental pollution from the release and dispersal of heavy metals accumulated in soil minerals led to extensive research focusing on the fixation of these heavy metals cations on smectites. The main objective of this study is to investigate the intercalation and diffusion of heavy metals cations such as Cu^{2+} and Ni^{2+} into Wyoming montmorillonite. The Cation Exchange Capacity (CEC) of purified Wyoming montmorillonite was saturated with Cu^{2+} or Ni^{2+} cations. The resulting complexes will be designed Wy-Cu and Wy-Ni. The obtained samples were then heated at moderate temperature in order to trap definitively the different cations within the clay structure. The quantitative analysis of XRD patterns using an indirect method allows us to characterise the structural evolution of these samples. The method permits to determine the number and the position of the intercalated cations and water molecules in the interlamellar space. The comparison between experimental and calculated X-ray patterns using structural models showed that for air-dried samples: (1) the Wy-Cu complex is characterised by a basal spacing of 12.4Å. (2) the Wy-Ni air-dry sample is characterised by a basal spacing of 14.8Å. These distances correspond to one and two water layers between the silicate sheets respectively for the Wy-Cu and Wy-Ni complexes. After thermal treatment, quantitative XRD analysis shows that until 250°C, the basal spacing decreases up to 10Å. This decrease is attributed to the loss of interlamellar water. When increasing temperature up to 350°C, a proportion of Cu^{2+} and Ni^{2+} cations diffuses into the octahedral vacancies and this proportion increases when increasing the heating duration.

Introduction

Some searchers carried out their research to study the treatment of the soil contaminated with waste using heat treatment. Farag [1] reported the use of incineration as a method to treat soil contaminated by leckage from waste dumps. Varlakov [2] used heat treatment (between 800 and 1000°C) to decontaminate soil from radioactive and toxic substances; heat treatment caused reduction of the cation exchange. Other studies of the heavy metals adsorption in the clay [3, 4] allowed determination of the Ni^{2+} local structure. It is well known that when dioctahedral smectites saturated with small interlayer cations (e.g. Li^{+}, Cu^{2+} or Zn^{2+}; ionic radius

< 0.97Å) are heated, these cations move into octahedral vacancies [5, 6]. This migration process reduces the apparent negative layer charge and causes a loss of expandability.

Materials and methods

Wyoming montmorillonite was purified and Na exchanged. The obtained clay is characterised by a structural formula [7]:
$(Si_{3.96}\ Al_{0.04})(Al_{1.53}\ Fe^{3+}_{0.18}\ Mg^{2+}_{0.26}\ Ti^{4+}_{0.01})O_{10}(OH)_2(Na^{+}_{0.35})$, xH_2O; the charge deficit is located in the octahedral sheets. Montmorillonite Cu^{2+} and Ni^{2+} complexes were prepared by conventional ion exchange reactions using aqueous solution of appropriate metal chlorides. After the ion exchange, the resulting solids were washed repeatedly with deionised water until a negative $AgNO_3$ test was obtained and deposed on glass slide to obtain an oriented aggregate. The air-dried samples are heated from 50°C up to 400°C with a step of 50°C and maintained for 24 h. The heated samples at a temperature T are designed Wy-Cu-T or Wy-Ni-T. All samples are analysed using a D8-advance diffractometer (CuKα radiation).
The mineralogical and structural characteristics were determined by comparing the experimental X-ray patterns with the theoretical patterns calculated from structural models [8, 9 &10]. The method permits determination of the number and the position of the intercalated water molecules. The atoms coordinates used are given in table 1 (Drits &Tchoubar [10]).

Table1. Positions and numbers of the different cations

Atoms	Number	Z_n (Å)
O_1	2	0
O_2	1	0.20
O_3	2	2.25
O_4	2	4.31
O_5	1	6.26
O_6	2	6.59
OH_1	1	1.98
OH_2	1	4.28
Si	2	0.59
Si	2	6.04
Al	2	3.43
Na	0.35	9.25

The origin of the atomic coordinates was taken at the basal oxygen atoms. The diffracted intensity for a unit-cell along the 00 rod of the reciprocal space was calculated using the matrix formalism [10]:

$$I_{00}(2\theta) = L_p \mathrm{Spur}\left(\mathrm{Re}[\phi][W]\left\{[I] + 2\sum_{n}^{M-1}[(M-n)/M][Q]^n\right\}\right)$$

where $Lp = \psi \frac{1+\cos^2 2\theta}{\sin 2\theta}$ [11, 12], Ψ is the orientation factor of the particles and Re is the real part of the final matrix; Spur is the sum of the diagonal terms of the real matrix; M, the number of layers per stack; n, an integer varying between 1 and M-1; [Φ], the structure factor matrix; [I], the unit matrix; [W], the diagonal matrix of the proportions of the different kinds of layers and [Q], the matrix representing the interference phenomena between adjacent layers.

Results and discussion

Air dried samples

The *001* basal reflections (Fig. 1b. 1c) produced by exhibit basal spacings of 14.76Å and 12.4Å for Wy-Ni-50 Wy-Cu-50 complexes respectively. This difference is due to the hydration state of the interlayer cations.

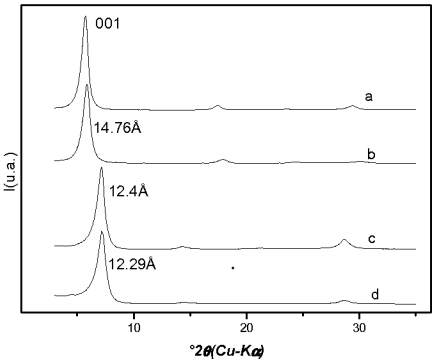

Figure 1. XRD experimental patterns of the Wy-Ca (a) ,Wy-Ni (b) ,Wy-Cu (c) and Wy-Na (d)

The best agreement (Figs. 2a, 2b) is obtained using: one water molecule at Z_n=9.25Å for Wy-Cu-50 and 1.2 water molecule at Z_n=9.25Å for Wy-Ni-50 per half unit-cell. For the two complexes, the interlayer cation (Cu^{2+} and Ni^{2+}) is situated in the middle of the interlamellar space.

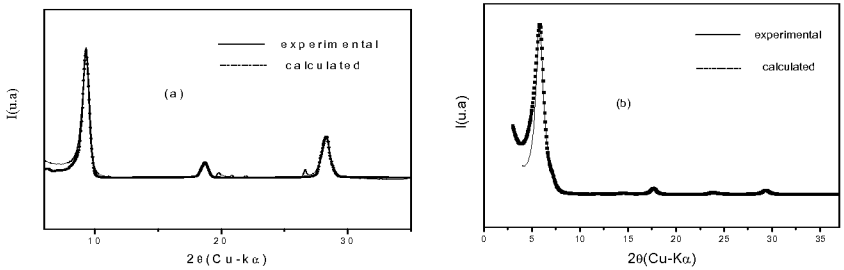

Figure 2. Comparison between experimental and calculated patterns: a) Wy-Cu-50, b) Wy-Ni-50.

Heated samples: Figure 3 shows XRD patterns corresponding to complexes heated at temperatures T between 50° and 350°C: Wy-Cu-T and Wy-Ni-T. Examination of figure 3 shows that the Wy-Cu complex undergoes two structural changes; the first, at 200°C, is characterised by a decrease of the basal spacing from 12.4Å to 9.95Å and corresponds to the sample dehydration; the second occurs at 350°C and corresponds to a decrease of the basal spacing from 9.95Å to 9.54Å, the latter can be attributed to the cation migration into the clay structure. For the Wy-Ni complex, the basal spacing decreases from 14.76Å to 10.27Å at 200°C and from 10.27Å to 9.56Å at 350°C.

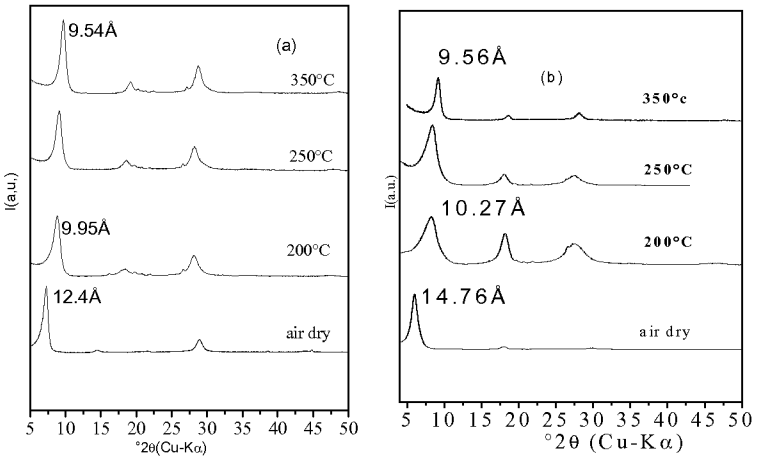

Figure 3. XRD experimental patterns of the Wy-Cu (a) and the Wy-Ni (b) during thermal treatment.

The changes observed at 350°C are not due only to a simple dehydration phenomenon but to a new structural rearrangement. In the following study we will determine the causes of these observed changes. Cations with small ionic radius diffuse into the hexagonal or the octahedral sheets [13, 14 & 15]. We will examine different structural models where the cation is placed: (1) in the middle of the interlamellar space at z_n=9.25Å, (2) in the hexagonal hole at z_n=6.04Å or (3) in the octahedral vacancies at z_n=3.43Å

Wy-Ni-350: The qualitative interpretation of Wy-Ni-350 XRD pattern exhibits three reflections situated at 9.56Å, 4.78Å and 3.18Å. We supposed that the structural change is due to a dehydration phenomenon. The disagreement between the experimental and calculated patterns using this hypothesis is reported in figure 4. In a second step, we supposed that the totality of cations diffuses into the octahedral sheet; we notice that a disagreement between the experimental and theoretical subsists. The best agreement of the heated sample during 72 hours (Fig. 5) is obtained when 40% and 60% of the interlamellar cations are placed repectively in the octahedral vacancies and the middle of the interlayer space. Subsequently, we studied the structural evolution when varying the heat duration.

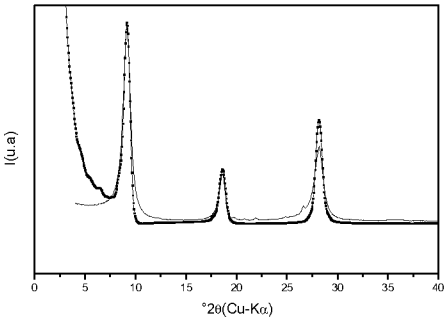

Figure 4: Disagreement between experimental (–) and theoretical (·····) XRD patterns obtained by placing 100% of the CEC in the middle of the inter-lamellar space.

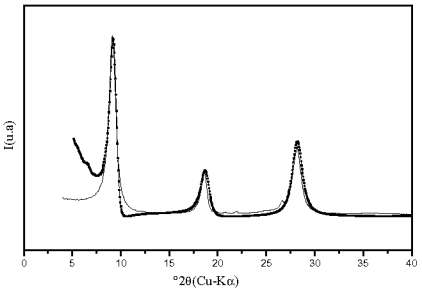

Figure 5. The best agreement between theoretical (·····) and experimental (–) curves is obtained for 40% of Ni^{2+} diffuses into the octahedral vaccancies at Z_n=3.4Å and 60% remains in the middle of the interlamellar space at Z_n=8Å.

Wy-Cu-350: The best agreement between the experimental and calculated intensity ratios (table 2) is obtained when 90% and 10% of Cu^{2+} cations are placed in the octahedral vacancies (Z_n=3.3Å) and interlamellar space (Z_n=9.2Å) respectively.

Table2: Variation of the I_{002}/I_{001} and I_{003}/I_{001} ratios in accordance with the quantity and the position of the Cu^{2+} cations.

Cu_{hex}: Copper cation placed in the hexagonal holes; Cu_{oct}: Copper cation placed in the octahedral cavity and Cu_{int}: Copper cation in the interlamellar space

	Exp Wy-Cu	70%Cu_{hex} 30% Cu_{int}	90%Cu_{hex} 10% Cu_{int}	100%Cu_{hex} 0% Cu_{int}	70%Cu_{oct} 30% Cu_{int}	90%Cu_{oct} 10% Cu_{int}
I_{002}/I_{001}	0.123	0.335	0.269	0.232	0.21	0.119
I_{003}/I_{001}	0.347	0.518	0.487	0.415	0.518	0.339

Conclusion

The present study shows that the complexe Wy-Cu presents one layer hydrate state (d_{001} = 12.4Å) and the Cu cation is located in the middle of interlayer space for temperature ≤ 200°C and its hydration shell diminishes with temperature. For temperature > 200°C, Cu migrates into the octahedral lacunae, where they saturate the charge of the sheet [16]. The complexe Wy-Ni looses its hydration properties at 300 °C and 200 °C, and for higher temperatures, the Ni diffuse into the silicate structure.

References

1. Farag, I., 1993. *Chemical Engineer.*, **538**, 11-16.
2. Varlakov, A., Sobolev, I., Barinov, A., Dimitriev, S., Karlin, S., Flit, V., 1997. In Proceed ings of the 1996 MRS fall Meeting, Moscow, Russia. Materials Research Society, Pitts burgh, PA, pp. 591-594.
3. Ford, R.G., Sparks, D.L., 2000. *Environ. Sci. Technol.* **34**, 2479-2483.
4. Hesterberg, D., Sayer, D.E., Zhou, W., Rbarge, W.P., Plummer, G.M., 1997. *J. Phys.*, IV (France) 7 (C2) 833-834.
5. Hofmann, U., Klemen, R., 1950.. *Anorg.Allg. Chem.* **262**, 95-99.
6. Greene-Kelly. R., 1955. *Min. Mag.* **30**, 604-615.
7. Ben Rhaïem, H. Ben Haj Amara , A. Ben Brahim J. and Pons C.H., 1998, *Materials Science Forum* Vols.278-281, pp.868-872.
8. Plançon, A., 1981, *J. Appl. Cryst.* **14**, 300-304.
9. Pons, C. H, de la calle, C. and de Vidales, M. 1995. *Clays & Clay Miner.* **43**, 246-254.
10. Drits V.A.& Tchoubar C, 1990, *X-ray Diffraction by Disordered Lamellar Structures: Theory and Application to Microdevided Silicates and Carbons.Springer.*Verlag, New York.
11. Reynolds., 1986, *Clays & Clay Miner.* **34,** 359-367.
12. Ben Haj Amara, A., Ben Brahim, J., Plançon, A. and Ben Rhaiem, H., *J. Appl. Cryst.* **31**, 654-662.
13. Ben Haj Amara, A .,1987, *Clay Minerals.* **22**, 305-318.
14. Calvet, R., Prost.,1971, *Clays & Clay Miner.***19,** 175-186.
15. Heller-Kallai, L., Mosser, C., 1995. *Clays & Clay Miner.* **43**, 738-743.
16. Mosser, C., Michot, L J., Villieras, F and Romeo, M. 1997. *Clays & Clay Miner.* **45**, 798-802.

Z. Kristallogr. Suppl. **23** (2006) 437-442

Structural characterisation of high-temperature K-exchanged sodalite

M. Dapiaggi[1*], G. Artioli[1], C. Mazzocchia[2], M. Merlini[1]

[1]Dipartimento di Scienze della Terra "A. Desio", Università degli Studi di Milano, via Botticelli 23, I-20133 Milano, Italy
[2]Dipartimento di Chimica, Materiali e Ingegneria Chimica "G. Natta", Politecnico di Milano, piazza L. Da Vinci 32, I-20133 Milano, Italy
[*]Contact author, email: monica.dapiaggi@unimi.it

Keywords: structure refinement, nuclear waste, high temperature, K-sodalite

Abstract. The exchange reaction of Na-sodalite with KCl was studied by means of high-temperature X-ray powder diffraction, ex-situ and in-situ, up to 800 °C. The powder data were fully refined with the Rietveld method and showed that a substantial amount of K enters the structure in the same crystallographic position of Na, causing some Cl ions to be displaced from their position. The paper shows that sodalite is a potentially good matrix for trapping alkaline metal ions from the electrorefining process of nuclear waste and proposes a method to quickly estimate the amount of K in the structure.

Introduction

The extended use of IFR (Integral Fast Reactor) nuclear plants of the last generation must be accompanied by in-depth studies about waste management and inertisation prior to storage in repository sites, with the aim of reducing the environmental impact of nuclear waste. Electro-refining cells produce, as a by-product, highly soluble alkaline and alkaline-earth chlorides that must be trapped in some inert matrix, temperature and transmutation resistant. Zeolites and framework materials are potentially a good matrix for trapping such ions within their channels.
Sodalite has a framework constituted by the union of SiO_4 and AlO_4 tetrahedra, in which each oxygen is common between two tetrahedra; Al and Si are completely ordered. Sodalite cages are cubo-octahedral, delimited by eight six-membered rings of tetrahedra, parallel to {111}; the rings define channels that intersect to form large cavities [1]. Cavities are occupied by Cl^- ions, tetrahedrally coordinated by Na^+ ions. Sodalite is the Na member, but it can easily host also potassium ions and water molecules, so that it is potentially a good matrix to trap alkaline metals [2-4]. In this paper, the solid solution of Na-sodalite and K-sodalite is the subject of a crystal-chemical study, in order to evaluate the possibility of trapping (and retaining) K ions at the site normally occupied by Na and to check how the substitution affects the other species occupying the cavity. The potassium ions are, in fact, much larger than the sodium ions and this can affect the occupancy of the site in a complex way. Substitutional

solid solutions are seldom ideal along the compositional join, and this is a first attempt to study the variation of the structural features along the join Na-K.

Experimental

Na-sodalite ($Na_8Si_6Al_6O_{24}Cl_2$) was synthesised under hydrothermal conditions from a natural kaolinite ($Al_2Si_2O_5(OH)_4$) in a 4M solution of sodium hydroxide, at 80 °C. Kaolinite is a promising starting material, due to its Si:Al = 1:1 ratio and to its low costs. The so-obtained Na-sodalite was exchanged with K at high temperature via a solid state reaction with excess KCl. Two different procedures were followed: the exchange was performed (i) *ex-situ* at 800 °C in an oven, and (ii) *in-situ* in a hot chamber attached to a Philips X'pert powder diffractometer. In the former, Na-sodalite was mixed with excess KCl (1:10 in weight), pressed in a pellet, in order to help the contact between K ions and sodalite, and then heated at a temperature higher than the melting point of KCl (772 °C), temperature at which sodalite structure is still stable. The pellet was heated at 800 °C for 12 hours overnight and then quenched rapidly. The pellet was then ground in an agate mortar and then washed with deionised water, in order to dissolve the excess KCl. X-ray data collection was performed using a Philips X'pert θ-θ diffractometer, with CuKα wavelength, in the range 5-100 °2θ, step size 0.02 °, counting time 4 s/step. The optics on the incident beam encompass a fixed divergence slit of 1/2 °, while, on the diffracted beam, a receiving slit of 0.1 mm and a crystal analyser were used. The exchange reaction was also monitored *in-situ* in a hot-chamber (AHT PAP1600) installed on the diffractometer, with two different proportions of sodalite : KCl (5:1 and 10:1 in weight). *In-situ* experiments allow to follow the reaction by looking at the diffraction patterns at the different temperatures, making it possible to evaluate the change of the cell parameter as a function of time and temperature. The sample was recorded at room temperature and every 100 °C up to 600 °C and then two more nominal temperatures were examined: 670 and 770 °C. The sample "real" temperature is carefully calibrated [5], and the difference between nominal temperature and real temperature is within 30 °C, so that 770 °C corresponds to 800 °C at the sample, as the controlling thermocouple is not in direct contact with the sample. For each pattern, the cell parameter was refined by means of the Rietveld method, using the program GSAS [6].
The starting sample, i.e. the end-member Na-sodalite, and the exchange products (ex-situ, 5:1 and 10:1 in situ) were refined by means of full-profile Rietveld refinement procedure.

Na-Sodalite has symmetry space group $P\bar{4}3n$, with a cell edge of 8.870 Å. Cl occupies the special position 2a (0,0,0), Si occupies the special position 6d (1/4,0,1/2), Al the other 6d (1/4,1/2,0), Na the position 8e (x,x,x; with x = 0.1777), and the framework oxygen occupies the general position 24i (0.1401, 0.4385, 0.1487) [7].
The refinement procedure was divided into three steps:

1) starting from literature structure [7], only framework atoms were refined; Na and Cl were kept fixed at this early stage.
2) Na atom was deleted and a Fourier difference map was calculated to check for the presence of K and other species in the cavities. The atomic positions found in the Fourier difference map were used in the subsequent refinement; the Fourier difference map shows two peaks at two 8e) positions, with x = 0.17 and x = 0.45, respectively. The first one corresponds to Na position, the second one is different from the positions of the

original structure. As K is a larger ion with respect to Na, it is likely that some of the Cl has to leave its original crystallographic site and to occupy the site where the Fourier difference map found an electron density peak. The two sites for Cl were constrained to keep electroneutrality accordingly to the different multiplicity of the two sites.

3) the structure was then fully refined , by adding some substitution of K ions in the Na site and the new Cl site (Cl2). Na and K were constrained to share the same site coordinates, the same thermal factor, and complementary occupancies. All the atoms in the framework (Si, Al, O) were constrained to have the same thermal factor.

Results and discussion

The cell parameters were evaluated on a diffractometer carefully aligned and calibrated with the aim of minimising the goniometer zero displacement. The in-situ experiment allowed the direct evaluation of the cell parameter with increasing temperature; figure 1 shows the variation of the cell parameter as a function of temperature for the sample with 5:1 proportion of KCl : sodalite. It can be readily appreciated that, up to about 450 °C, the fit of the cell parameters follows nicely the thermal expansion of pure Na-sodalite [8], whereas at higher temperatures, the exchange reaction begins and the cell parameter increase is due to the exchange of the smaller Na ions with the larger K ions. This can be clearly seen in the abrupt change of slope taking place at about 450 °C.

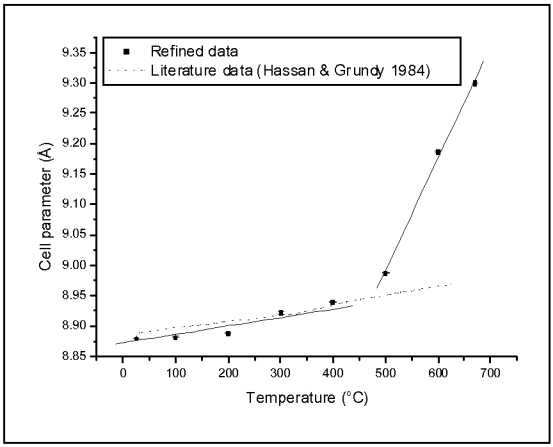

Figure 1. Thermal expansion of K-sodalite in the in-situ experiment (5:1 KCl:sodalite). The dotted line represent the thermal expansion of pure Na-sodalite from the paper by Hassan & Grundy, 1984).

From the diffraction patterns, it is possible to roughly estimate the quantity of reactants still present in the mixture, as the KCl diffraction peaks decrease in intensity with temperature due to the reaction with Na-sodalite, to sublimation, and finally to melting at temperatures higher than 772 °C.

The following step in the study of solid solution Na-K sodalite was the full refinement of the structure, with the refinement strategy described in the experimental section. The results of

the structure refinements are shown in Table 1, together with literature data from Beagley et al. [2], for a direct comparison with the structure of a K-sodalite. Only the refined parameters are shown in the table. Due to the high degree of correlation between site occupancies and thermal parameters, the number of refinable parameters had to be kept to a minimum, and this was achieved by using the constraints described in the experimental section.

Table 1. Structural parameters of the four sodalites refined; for comparison, the same parameters from Beagley et al. [2] are shown. Cl1 and Cl2 represent 2a) and 8e) positions, respectively.

Constraints applied:
U_{iso} (Na)=U_{iso} (K)=U_{iso} (Cl1)=U_{iso} (Cl2)
U_{iso}(Si)=U_{iso} (Al)=U_{iso}(O)

		Na-sodalite ($Na_8Si_6Al_6O_{24}Cl_2$)	In situ (5:1) ($K_{0.4}Na_{4.4}Si_6Al_6O_{24}Cl_2$)	In situ (10:1) ($K_5Na_3Si_6Al_6O_{24}Cl_2$)	Ex-situ ($K_{3.7}Na_{4.3}Si_6Al_6O_{24}Cl_2$)	Beagley, Henderson, Taylor (1984) ($K_{7.6}Na_{0.4}Al_6Si_6O_{24}Cl_2$)
Cell parameter(Å)		8.88535 (4)	8.9825 (9)	9.1450 (4)	9.0939 (6)	9.253 (2)
O (framework)	x	0.137 (1)	0.138 (2)	0.1400 (7)	0.1396 (5)	0.1363 (18)
	y	0.444 (2)	0.451 (2)	0.4609 (8)	0.4572 (5)	0.4786 (12)
	z	0.150 (1)	0.152 (2)	0.1538 (7)	0.1508 (5)	0.1586 (17)
	U_{iso}	0.034 (3)	0.030 (3)	0.019 (2)	0.022 (1)	0.006 (3)
Na	x	0.178 (1)	0.178 (1)	0.1791 (4)	0.1788 (3)	0.1876 (5)
	occ.	1	0.85 (5)	0.44 (3)	0.50 (2)	0.05
	U_{iso}	0.058 (4)	0.062 (7)	0.060 (3)	0.069 (2)	0.022 (2)
K	occ.	0	0.15 (5)	0.56 (3)	0.50 (2)	0.95
Cl1	occ.	0.92 (2)	0.55 (9)	0.48 (3)	0.23 (6)	1
Cl2	x	-	0.439 (9)	0.437 (3)	0.454 (3)	
	occ.	-	0.113 (2)	0.131 (8)	0.192 (2)	
R_{wp}		0.2082	0.1987	0.1441	0.1044	
R_p		0.1459	0.1426	0.1121	0.0744	
R_{Bragg}		0.1081	0.1105	0.0362	0.0266	

In figure 2 it can be clearly seen that the insertion of K ion in the structure causes the displacement of some Cl ions from their cavity. The distance between the two sites is only about 2.8 Å, so that, when a large K ion substitutes a smaller Na, some of the neighbouring large Cl ions are displaced from their original site to the 8e) site found in the Fourier difference map. The distance Cl1-K is about 2.84 Å, and the displacement from this position to the new one allows some of the bond lengths from K to Cl to be larger, as there are three independent distances Cl2-K: 2.68 Å, 3.87 Å, and 4.05 Å. The K occupancies are diagrammed in

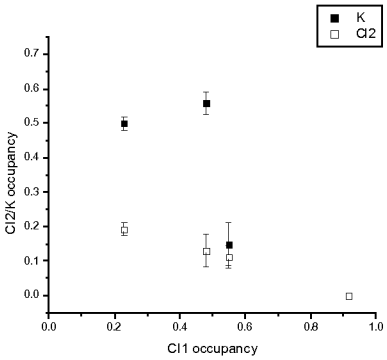

Figure 2. Cl2 and potassium occupancy as a function of Cl1 occupancy. Please note that for Cl1 occupancy = 0.92, the data for K and Cl2 occupancies are superimposed.

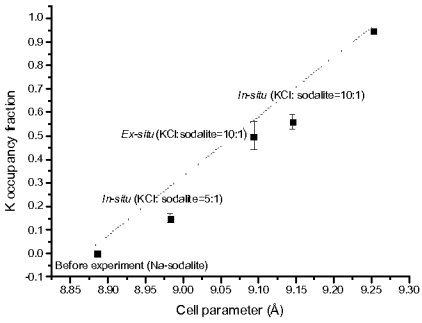

Figure 3. K occupancy as a function of cell parameter in the various experiments. The dotted line represents a linear fit between the Na and the K end member sodalite, from Beagley et al. [2].

figure 3 as a function of the cell parameter, which is also affected by K/Na substitution. The dotted line represents a theoretical linear fit between the Na end member and an almost completely K substituted sodalite ($K_{7.6}Na_{0.4}Al_6Si_6O_{24}Cl_2$, [2]). Our refined K occupancies tend to deviate from ideality: the structural properties of the substitutional solid solutions rarely fulfil the ideal Vegard's rule, and the properties of the intermediate members of solid solutions can hardly be inferred from the linear combination of the properties of the end members. Still, the correlation between the occupancy of the K site and the cell dimensions is pretty good: a linear fit gives an agreement parameter close to one (R = 0.988). A parabolic fit gives a similar agreement (R = 0.9848), but with better diagnostic performances (Table 2). In the table, the K content of the structure is inferred from the cell dimensions in three ways:

1. linear fit from the theoretical values in literature

$$K\% = 100 * (-22.46 + 2.53 * a(\text{Å})) \quad (1)$$

2. linear fit from our refined data

$$K\% = 100 * (-23.02 + 2.59 * a(\text{Å})), \text{ with } R^2=0.979 \quad (2)$$

3. parabolic fit from our refined data

$$K\% = 100 * (186.8 - 43.71 * a(\text{Å}) + 2.55 * a(\text{Å})^2), \text{ with } R^2=0.992 \quad (3)$$

As shown in the table, the worst predictive performances are found for the Na end member, whose K content is always negative instead of zero. This can be due to fitting problems close to the end-member. The remaining K compositions fit quite well with the refined occupancy values, especially for K>40%, for which the fit nr. 2 and 3 give values whose differences from the real value are within a few percent. Anyway, if one wants to rely only on literature data, despite the error due to non-ideality, the cell parameter may still be a quick measure of the degree of completion of the exchange reaction, as the difference calculated-real is below

10% for K>40%. These results were confirmed by some preliminary analyses by atomic absorption spectrometry of the potassium present in sodalite structure.

Table 2. Comparison of the three fitting equations (1), (2), (3), for the experimental data and of their predictive performances. The second column shows the refined K occupancy.

	K occupancy	K calculated Linear, literature	K calculated Linear, refined data	K calculated Parabolic, refined data
Na-sodalite	0	0.2	-0.7	-0.21
In-situ (5:1)	0.15 (6)	0.27	0.25	0.17
Ex-situ	0.50 (2)	0.55	0.53	0.44
In-situ (10:1)	0.56 (3)	0.68	0.67	0.58
Beagley, Henderson, Taylor, 1982	0.95	0.95	0.94	0.93

Conclusions

The sodalite structure proved to be a good matrix for trapping alkaline metal ions from the electrorefining process of nuclear wastes. This preliminary work proved that a substantial amount of K ions can be successfully trapped within a sodalite matrix through a high temperature solid state exchange reaction (above 450 °C) with the corresponding chloride, and provided an empirical correlation between cation occupancy and cell parameters as a mean to quickly estimate the K content of exchanged samples.

References

1. Baerlocher, Ch., Meier, W.M. & Olson, D.H., 2001, *Atlas of Zeolite Framework Types*, 5th edition, Amsterdam: Elsevier.
2. Beagley, B. Henderson, C.M.B. & Taylor, D., 1984, *Mineralogical Magazine*, p. 459-464.
3. Depmeier, W., 1984, *Acta Crystallographica,* B40(3), p. 185-91.
4. Depmeier, W., 1987, *Journal of Inclusion Phenomena*, 5(2), p. 279-82.
5. Dapiaggi, M., Artioli, G. & Petras, L., 2002, *The Rigaku Journal*, 19(1), p. 35-41.
6. Larson, A.C. & Von Dreele, R.B., 2000, General Structure Analysis System (GSAS),Los Alamos National Laboratory Report LAUR 86 –748
7. Löns, J. & Schultz, H., 1967, *Acta Crystallographica*, 23, p. 434-436.
8. Hassan, I. & Grundy, H. D., 1984, *Acta Crystallographica*, B40, 6-13.

Z. Kristallogr. Suppl. **23** (2006) 443-448

A time-resolved X-ray powder diffraction method to trace the decomposition of PdB_y solid solutions

T. G. Berger[1], A. Leineweber[1,*], E. J. Mittemeijer[1], M. Knapp[2]

[1]Max Planck Institute for Metals Research, Heisenbergstr. 3, D-70569 Stuttgart, Germany.
[2]Institute for Materials Science, Darmstadt University of Technology, Petersenstr. 23, D-64287 Darmstadt, Germany.
[*]Contact author; e-mail: a.leineweber@mf.mpg.de

Keywords: palladium-boron alloys, miscibility gap, compositional changes, line broadening

Abstract. A powder diffraction method is presented for reconstructing probability density functions for the composition, $p(y)$, of a PdB_y solid solution material with composition (y)-dependent lattice parameter from the simultaneous analysis of all reflections in the powder diffraction patterns. The method is applied to the decomposition of a solid solution in a miscibility gap: two 'boundary phases' appear which gradually approach but don't attain fully the compositions of the expected equilibrium phases whereas a significant amount of material with intermediate compositions remains.

Introduction

X-ray powder diffraction provides information about the atomic structure (size and symmetry of unit cell, atom positions and displacements) of crystalline materials via the positions (Bragg angles) and intensities of reflections. Analysis of the width and shape of diffraction-line profiles, furthermore, allows extraction of microstructural information, e.g. in terms of microstrain and crystallite size [1]. Analysis of this *physical broadening*, denoted f, is, however, considerably hindered by the instrumental contribution g, with which f is convoluted leading to the real measured profile h. Various convolution and deconvolution methods exist to determine the physical from the measured profile [2]. The present work aims at developing a method to reconstruct complicated *probability density functions* for composition, $p(y)$, of a solid solution material, with composition (y)-dependent lattice parameters, from the simultaneous analysis of *all* reflections in the powder pattern.
The solid solution considered here is the palladium-rich solid solution PdB_y. It exhibits an extraordinarily high interstitial solid solubility up to about $PdB_{\sim 0.25}$ above temperatures of 440°C (y in PdB_y denotes both the atomic ratio and the occupancy by boron atoms of the octahedral sites in the *ccp* palladium host lattice) as well as several low-temperature phases and two-phase fields below temperatures of about 400-450°C [3]. A remarkable and for binary interstitial solid solutions rare feature is the miscibility gap with a critical temperature

of T_{crit} = 410°C which covers at the monotectic temperature of T_{mono} = 312°C a composition range of about $0.03 < y < 0.10$ (figure 1) [4, 5]. Decomposition in this miscibility gap upon annealing can be considered as a redistribution of boron atoms over the octahedral interstices leading to changes in the probability density function for composition $p(y)$ as averaged over the sample, which shows up in a characteristic way in powder diffraction patterns.

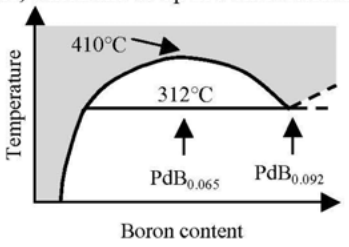

Figure 1. Part of the Pd-B phase diagram with the miscibility gap [3]. The grey shaded area shows the phase field of the solid solution.

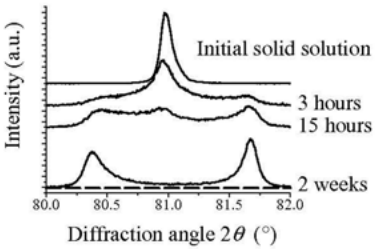

Figure 2. 311-Diffraction peak group ($CuK\alpha_1$ radiation) recorded from a $PdB_{0.064}$ sample annealed for various times at 340°C.

Experimental

Preparation and heat treatment

$PdB_{0.064}$ was prepared by arc melting under argon from weighted amounts of palladium foils and an appropriate amount of boron pieces. $PdB_{0.050}$, previously used in a neutron diffraction study, was prepared similarly from ^{11}B [7]. Both reguli were checked for homogeneity [5-7]. The powder samples (filed from the reguli) were sealed under vacuum in quartz capsules, annealed at 800°C for 5 min and subsequently quenched in water. The annealing was performed to relieve deformation stresses due to the filing procedure. The composition was calculated [6] by

$$a = a_0 + \alpha \cdot y = 3.8920 + 0.6882y \,[\text{Å}] \quad (1)$$

The heat treatments for the decomposition were performed from 3 hours till up to 8 weeks (in sealed quartz tubes encapsulated in a salt bath for up to 4 days, longer annealings in a furnace) at 340°C or 355°C with subsequent water quenching.

X-ray diffraction measurements

X-ray powder diffraction measurements of the initial, stress-relieved solid solution and of the subsequently annealed samples were performed

- *in house* on a Philips X'Pert MPD instrument ($CuK\alpha_1$ radiation in Bragg-Brentano geometry, powder samples were deposited as a thin layer together with internal silicon standard powder on Si wafers cut parallel to the (510) plane) and
- for two selected $PdB_{0.064}$ specimen, one quenched from 800°C to preserve the solid solution and one annealed for 18 days at 340°C to evoke the decomposed state, employing synchrotron radiation with $\lambda = 1.1315$ Å on the B2 beamline [8], HASYLAB, Hamburg (no internal standard, separate LaB_6 standard (SRM 660a) measurements; powder deposited on Kapton foil, measurements performed in transmission geometry).

All reflections were recorded by measuring over 2θ (diffraction-angle) subranges sufficiently large to determine the background at both sides of each reflection (group).

Data evaluation method

The decomposition of the initially homogeneous solid solution into a boron-rich and a boron-poor solid solution phase is clearly revealed by the occurring splitting of the Bragg reflections. For short annealing times (e.g. figure 2), the original solid solution is still present. Even after the longest applied heat-treatment times (8 weeks at 340°C and 2 weeks at 355°C), still considerable diffraction-line broadening remains which is asymmetric for both the high and the low boron components ('boundary phases') such that residual intensity between the pairs of reflections remains. To analyse the time-dependent decomposition as observed in the X-ray diffraction patterns, the reflection profiles were modelled using the program TOPAS [9] as described below.

X-ray data evaluation

For each heat treatment, all individually measured reflections, from PdB_y as well as from the internal standard (*in house* data), were merged into one data set after manually subtracting the background. This complete pattern was modelled in a Rietveld-like fashion, considering a convolution of three line-broadening contributions:

$$h = g \otimes f_1 \otimes f_2 \tag{2}$$

with g and f_1 taken as *Voigt* functions with angle-dependent Gaussian and Lorentzian full width at half maximum values B_L and B_G, respectively. The instrumental profile g was determined from the internal Si standard (*in house* data) or the separately measured LaB_6 standard (*synchrotron* data), respectively, by fitting *LY*, *LX*, *GU*, *GV*, *GW* according to:

g: $\quad B_{g,L} = LY \tan\theta + LX/\cos\theta$; $\qquad B^2_{g,G} = GU \tan^2\theta + GV \tan\theta + GW$. (3)

The structural line broadening f_1 of the two quenched solid solution samples was described semi-empirically by size and anisotropic microstrain broadening, fitting L_1, L_2, S_1, S_2, G_2:

f_1: $\quad B_{f_1,L} = L_1 \tan\theta + L_2/\cos\theta$;

$$B^2_{f_1,G} = \left(S_1 + S_2 \frac{h^2k^2 + k^2l^2 + h^2l^2}{\left(h^2 + k^2 + l^2\right)^2} \right) \tan^2\theta + \left(G_2/\cos\theta\right)^2 . \tag{4}$$

The present description of the microstrain broadening anisotropy was derived from the assumption of an isotropic microstress distribution leading to anisotropic microstrain if the crystals are elastically anisotropic [10] (as is the case for Pd).

The additional line broadening occurring in the diffraction patterns of the annealed specimen, f_2, can be attributed to the occurrence of decomposition-induced compositional variations described by $p(y)$, starting from a delta-shaped distribution for the initial solid solution. For the annealed samples $p(y)$ was approximated by a frequency polygon (figure 3) with composition steps of $\Delta y = 0.001$. Due to the composition dependence of the lattice parameters of the cubic crystal lattice (equation (1)) of PdB_y, $p(y)$ reflects itself directly in each reflection [11]. In Topas [9] this was incorporated in terms of a multiphase refinement of 120 'phases' with composition values y' which are spaced by Δy. Each 'phase' $PdB_{y'}$ has been ascribed a compositional line broadening contribution corresponding to a trapezoid (shaded in grey in figure 3) with a width of $2\alpha\Delta y \tan\theta/a$ (cf. equation (1)), and an area (integral intensity) proportional to $(p(y')+p(y'+\Delta y))/2$.

Penalty functions to achieve stability in refinements of *p(y)*

Refining the $p(y')$ values without any constraints leads to severe correlations between different $p(y')$ [12,13]. These correlations can be reduced to achieve physically realistic 'smooth' $p(y)$ by application of so-called penalty functions (*PF*). These serve as contribution to the overall χ_{pen}^2 (*penalised least squares*), additional to the usual χ^2 from the difference between observed and the calculated profile [14]:

$$\chi_{pen}^2 = \chi^2 + (K \cdot PF)^2 \qquad K: \quad \text{penalty weighting factor [9]} \qquad (5)$$

Commonly [12,13], these penalty functions are modified integrals of the first or second derivatives of $p(y)$, e.g. as used here:

$$PF_1 = \int q_1 \cdot (p'(y))^2 dy \qquad q_1: \quad p^{-1}(y). \qquad (6)$$

$$PF_2 = \int q_2 \cdot (p''(y))^2 dy \qquad q_2: \quad \left(C^2 + (p''(y))^2\right)^{-1}. \qquad (7)$$

A compromise for the weight K of the penalty function contribution to the overall χ^2 must be found to obtain a reasonable $p(y)$: In case of too low weight the correlations are not sufficiently suppressed; in case of a too high weight, physical features in the shape of $p(y)$ may be suppressed ('*oversmoothing*') [13]. In the present case, the application of the penalty function was allowed to increase the χ^2 value by not more than 10% as compared to the value obtained with an unconstrained refinement. For most of the performed refinements, PF_1 produced satisfactory results; PF_2 (with another constant C to be adjusted empirically) was only used for the refinement of the microstrain broadening change (see Results).

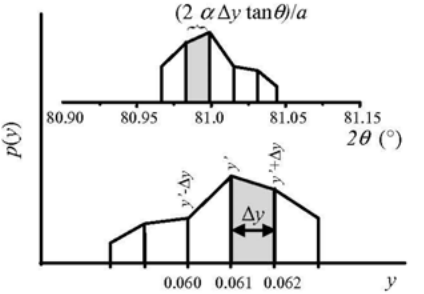

Figure 3. Frequency polygon type description of the probability density function of composition p(y) and the corresponding line-broadening f_2 for the 311-reflection. The grey area shows the contribution associated with composition y=0.061 (with an area proportional to (p(y')+p(y'+Δy)/2)).

Results and Discussion

Results for $p(y)$ obtained with the described method are shown in figures 4a-c for $PdB_{0.064}$ and $PdB_{0.050}$ annealed for various times at 340°C and $PdB_{0.050}$ annealed for various times at 355°C.

Initially, $p(y)$ contains a remaining contribution from the original solid solution. Its phase fraction was determined by subtracting an estimated parabolic 'background $p(y)$' between the two 'boundary phases' (figure 4a). The time-dependence of the molar phase fraction (referring to the formula PdB_y) of the parent solid solution is similar for the three samples, but the $PdB_{0.064}$ sample decomposes much faster than the $PdB_{0.050}$ at the same temperature of 340°C. Further, $PdB_{0.050}$ decomposes faster at 340°C than at 355°C (figure 5). Therefore the driving force for the decomposition has its maximum in the middle of the miscibility gap.

The values of the boundary (product) phase compositions (figure 6) were determined by a parabolic fit to the three locally highest $p(y')$ values in the range of the local maxima pertaining to the high and low boron product phases. For short annealing times the $p(y)$ of the $PdB_{0.050}$ sample, annealed at 355 °C, did not show clear local maxima for the 'boundary phases', therefore the two shortest annealing times were omitted. For long annealing times, differences in the 'boundary phase' composition for the same temperature occur, which are not expected by the phase diagram (cf. figure 6).

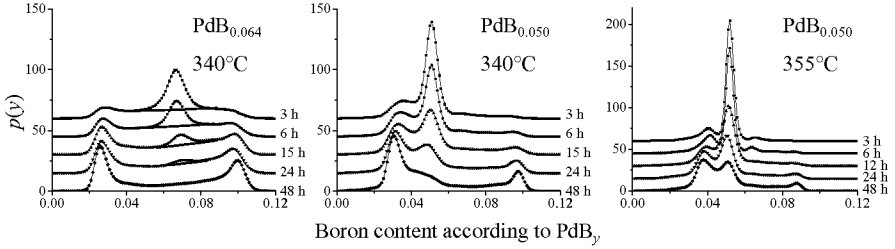

Figure 4a-c. p(y) for different annealing times and different initial compositions. Clearly visible is the faster decomposition for $PdB_{0.064}$ compared to $PdB_{0.050}$ and for 340°C compared to 355°C (estimation of the fraction of initial solid solution has been indicated in 4a).

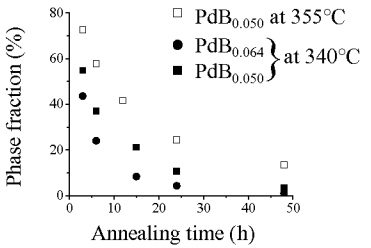

Figure 5. Relative phase fractions of the initial solid solutions vs. annealing time.

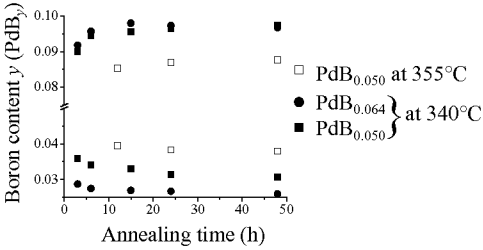

Figure 6. Boundary product phase compositions vs. annealing time. For $PdB_{0.050}$ at 355°C the shorter annealing times could not be analysed (see text).

So far in the analysis the line profile parameters of the microstructural line-broadening, f_1, were kept constant and taken equal to those determined for the initial solid solution. Since the mechanical microstrain broadening is anisotropic (cf. equation (4)), it should be possible to detect a change in f_1 upon decomposition, given sufficient resolution of the data, as it was the case for the *synchrotron* measurements. Unconstrained refinement of S_1 and S_2 (equation (4)) was not possible due to the correlation of the S_1 parameter with the also $\tan\theta$-dependent line broadening due to $p(y)$. Therefore the ratio S_1/S_2 was fixed to the value of the initial solid solution. By stepwise increasing S_1 and S_2 it could be shown that there is indeed an increase of microstrain broadening upon decomposition. The first derivative as used in PF_1 has its highest values at the inflection points of $p(y)$ located at the 'flanks' of $p(y)$, thus the penalty function may suppress subtle width-related effects. Therefore, for the analysis of S_1 and S_2, the penalty function PF_2 was employed which has its highest values at the maxima of $p(y)$. The resulting $p(y)$ are shown in figure 7 for the initial solid solution values of S_1 and S_2 characterising the anisotropic microstrain broadening and for 5 S_1 and 5 S_2; in the last case a distinctly improved fit to the measured diffraction pattern was achieved. It follows that

changes in S_1 and S_2 influence $p(y)$: broader f_1 due to higher values of S_1 and S_2 leads to a 'sharpened' $p(y)$ (figure 7).

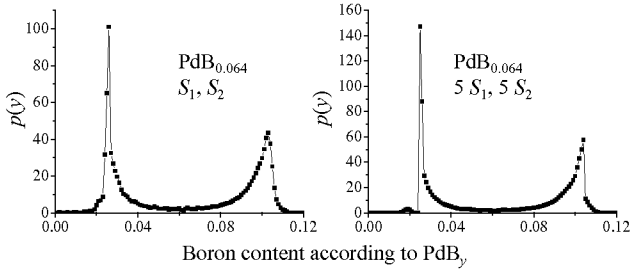

Figure 7. p(y) as determined from synchrotron data adopting microstrain broadening parameters S_1 and S_2 equal to those of the solid solution (left) and 5 times as large (right) (PF_2 applied).

Conclusions

A method has been presented to determine presuppositionlessly composition distributions of decomposing solid solutions from complicated diffraction-line profile shapes in an simultaneous evaluation of all reflections in a powder diffraction pattern. This composition distribution is determined by convolution fitting of a probability density function $p(y)$ with an instrumental broadening contribution g measured by internal standards and a microstrain and size broadening contribution f_1 measured from a parent solid solution sample.

References

1. Delhez, R., de Keijser, Th. H., Mittemeijer, E. J., 1982, Fresenius Z. Anal. Chem. 312 (1), 1.
2. Snyder, R. L. & Fiala, J. & Bunge, H.-J, 1999, *Defect and Microstructure Analysis by Diffraction* (Oxford University Press), chapter 26 -27.
3. Liao, P. K., Spear, K. E., Schlesinger, M. E., 1996, *J. Phase Equilib.* **17**, 340.
4. Alqasmi, R. A., Brodowsky, H., Schaller, H.-J., 1982, *Z. Metallkde.* **73**, 331.
5. Beck, M., Mittemeijer, E. J., 2001, *Z. Metallkde.* **92**, 1271.
6. Beck, M., Ellner, M., Mittemeijer, E. J., 2001, *Acta Mater.* **49**, 985.
7. Berger, T. G., Leineweber, A., Mittemeijer, E. J., Fischer, P., 2004, *Phys. Stat Sol. A* **201**, 1484.
8. Knapp, M., Baehtz, C., Ehrenberg, H., Fuess, H., 2004, *J. Synchrotron Rad.* **11**, 328.
9. TOPAS, *General Profile and Structure Analysis Software for Powder Diffraction Data*, V2.0, Bruker AXS GmbH, Karlsruhe, Germany.
10. Stokes, A. R., Wilson, A. J. C., 1944, *Proc. Phys. Soc.* **56**, 174.
11. Leineweber, A., Mittemeijer, E. J., 2004, *J. Appl. Cryst.* **37**, 123.
12. Good, I. J., Gaskins, R. A., 1971, *Biometrica* **58**, 255.
13. Louboutin, R., Louër, D., 1969, *Acta Cryst.* A **25**, 335.
14. Coelho, A. A., 2000, *J. Appl. Cryst.* **33**, 899.

Z. Kristallogr. Suppl. 23 (2006) 449-454

γ'-Fe_4N formation in decomposing ε-Fe_3N: A powder diffraction study using synchrotron radiation

T. Liapina[1], A. Leineweber[1,*], E. J. Mittemeijer[1], M. Knapp[2], C. Baehtz[2], Z. Q. Liu[3], K. Mitsuishi[3], and K. Furuya[3]

[1]Max Planck Institute for Metals Research, Heisenbergstraße 3, D-70569 Stuttgart, Germany.
[2]Institute for Materials Science, Darmstadt University of Technology, Petersenstr. 23, D-64287 Darmstadt, Germany
[3]National Institute for Materials Science, Tsukuba 305-0003, Japan
*Contact author; e-mail: a.leineweber@mf.mpg.de

Keywords: iron nitrides, interstitial compounds, diffraction-line broadening

Abstract. As-prepared and annealed (up to 3 days at 633 K and 673 K) ε-$Fe_3N_{1.0}$ powders were studied by powder diffraction using synchrotron radiation and transmission electron microscopy. The data reveal the formation of γ'-Fe_4N in few powder particles and enrichment of the remaining ε-phase with N indicating inter-particle N transfer. Structural diffraction-line broadening due to local composition fluctuations was identified in the X-ray line profiles by fitting applying a convolution procedure.

Introduction

The investigation of iron nitrides is largely motivated by their role in metallurgy and also by their possible potential as magnetic recording materials. The most important iron nitride phases are ε-FeN_y (y = 0.22-0.49; Fe: hcp - hexagonal close packed) and γ'-Fe_4N (Fe: ccp - cubic close packed) (Figure 1). In both cases N occupies octahedral interstitial sites. Most studies on these iron nitrides were performed on compound layers generated on the surfaces of massive substrates of iron or steel. The iron nitrides in such layers contain N concentration gradients associated with the inward diffusion of N during nitriding.

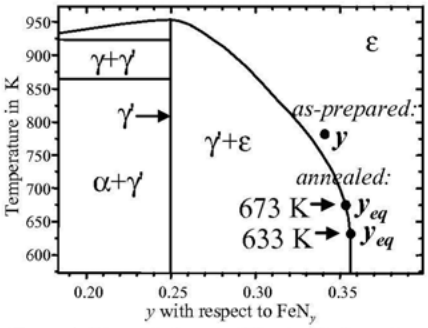

Figure 1. Simplified part of the Fe-N phase diagram.

Homogeneous iron nitrides can be prepared upon nitriding of iron powders or thin foils employing moderate nitriding times. In particular iron nitride powders are well suited for structural analysis by powder diffraction methods which are able to determine quantitatively very small changes in composition [1] and the presence of minute compositional inhomogeneities [2]. Previous experiments on the behaviour of ε-iron nitride powders upon annealing [3,8] showed that at 623 K precipitates of γ'-Fe_4N are formed in ε-$FeN_{0.33}$ powder, which leads to an enrichment of the remaining ε-phase with N (final composition $FeN_{0.36}$), in accordance with the phase diagram (Figure 1) and as also observed for bulk specimens [4-8]. However, understanding of the transformation mechanism (in powders) lacks. The formation of γ'-Fe_4N in ε-FeN_{y_0} can be written as

$$\varepsilon\text{-}FeN_{y_0} \rightarrow \delta\,\gamma'\text{-}FeN_{1/4} + (1-\delta)\,\varepsilon\text{-}FeN_{y_{eq}}, \quad \text{with} \quad \delta = 4(y_{eq} - y_0)/(4y_{eq} - 1), \tag{1}$$

where y_0 indicates the original N content and y_{eq} denotes the concentration corresponding to the phase boundary ε+γ'/ε at the annealing temperature (Figure 1). In this work this transformation was studied in detail by high-resolution powder diffraction employing synchrotron radiation, as well as by transmission electron microscopy (TEM) analysis.

Experimental

ε-Fe_3N (denoted *as-prepared*) was prepared by the treatment of iron powder with a NH_3/H_2 gas mixture in technical nitridation furnaces (Carl Gommann KG, Remscheid (D)) at 780 K followed by slow cooling which took several hours. Chemical analysis of the *as-prepared* powder was performed by carrier gas hot extraction and yielded the composition $Fe_3N_{1.0}$ with < 0.1 mass% C and < 0.2 mass% O. Annealing of this powder was carried out in evacuated quartz tubes at 633 K and 673 K for up to 3 days followed by quenching the quartz tubes in water at room temperature (further denoted as *1d 633K*, *3d 633K*, *1h 673K*, *1d 673K* and *3d 673K*). High resolution powder diffractometry was performed using synchrotron radiation (B2 station, HASYLAB, Hamburg; λ = 1.13985 Å). The powder samples were sedimented on Kapton foil (transmission geometry). Additionally, SRM660a LaB_6 (NIST, USA) was measured as a standard to determine the instrumental resolution. TEM was carried out using a JEM-ARM1000 electron microscope (accelerating voltage: 1 MeV). To this end powder samples were embedded in epoxy resin. The TEM specimen preparation procedure is described elsewhere [9].

Results and discussion

Basic analysis of the TEM and X-ray powder diffraction data

Transmission electron microscopy (Figure 2) reveals that γ'-precipitate grains form only in relatively few powder particles. This contrasts with the lamellar precipitation of γ' inside of ε-grains observed in bulk samples [4-7].

Analysis of X-ray powder diffraction data confirms the formation of γ' upon annealing as well as shows that simultaneously changes occur in the ε-reflections. The shifts of the 110 and 103 (*hkl* values refer to the hcp type substructure of the iron atoms, the superstructure due to N ordering is not considered here) reflections of the ε-iron nitride (Figure 3) are representative for those of the other reflections: (i) in general, an increase of the d-spacings due to

the expected increase of the N content [1] upon annealing; (ii) as evident from the shortest time annealed sample (*1h 673K*), an increase of *c* and a decrease of *a* if a sample is quenched (as for all annealed samples) instead of slowly cooled ([1]; Quenching leads to higher retained disorder of N in the superstructure of the ε-phase as compared to slow cooling; this affects the lattice parameters in the observed fashion).

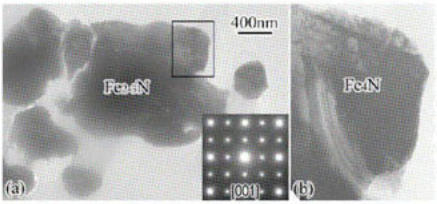

Figure 2. (a) TEM bright field image of some particles in an ε-FeN_y + γ'-Fe_4N sample (ε-FeN_y annealed for 4 days at 657 K). The inset is a diffraction pattern of a γ'-Fe_4N grain ([001] zone) taken at the top right area of the central $Fe_{2.3}N$ (ε-FeN_y) particle.

(b) The γ'-Fe_4N grain outlined in (a).

Quantification of these effects has been achieved by fitting the line profiles preliminarily with split pseudo-Voigt (*spV*) functions

$$f(x) = \frac{(1-\eta)}{B}\sqrt{\frac{\ln 16}{\pi}}\exp\left(-\frac{\ln 16(x)^2}{B^2(1\pm As)^2}\right) + \frac{2\eta}{\pi B(4x^2/(B^2(1\pm As)^2)+1)}, \qquad (2)$$

where $x = 2\theta - 2\theta_0$, B = FWHM (full width at maximum), As and η are peak shape parameters, where η is the mixing parameter and As quantifies the peak asymmetry with "+" for $x < 0$ and "–" for $x > 0$; The fitted peak maxima, $2\theta_0$, of all measured reflections were employed to fit the lattice parameters, a and c, by minimising $\sum_{hkl}(2\theta_{0,\mathrm{obs}} - 2\theta_{0,\mathrm{calc}}(a,c))^2$.

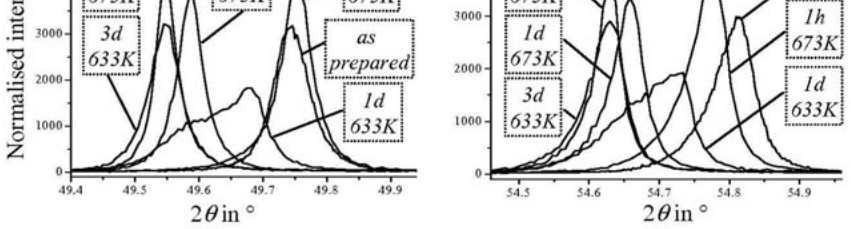

Figure 3. 110 and 103 reflections of ε-FeN_y: as prepared and annealed samples.

The lattice parameters of the ε-iron nitride samples confirm their dependence on the cooling procedure [1], which was slow cooling for the *as-prepared* and quenching for the annealed samples (Figure 4). Furthermore, the observed lattice parameters increase upon prolonged annealing indicating an increase of N content in ε compatible with the appearance of reflections of γ'. The determined lattice parameters of the ε-iron nitrides after annealing indicate that the equilibrium N concentration according to [1, 10] has been reached for the *3d 673K* sample, but not for the others (note that for the lower annealing temperature the equilibrium N concentration and corresponding lattice parameters should be higher [10]).

The FWHM values for the recorded reflections of the ε-phase are shown in figure 5.

It follows that long-time annealing at high temperature (*3d 673K*) leads to relatively narrow (compared to *as-prepared*) ε-iron nitride reflections, which are, however, still significantly broader than those of the standard LaB_6. This remaining, additional (compared to LaB_6) line broadening is strikingly asymmetric and anisotropic: i.e. reflections with diffraction vectors close to *00l* (e.g. 103, 104) show significant "tails" on the low angle side, whereas *hk0* reflections show the reverse. For intermediate states of γ'-precipitation (as for the *1d 633K*) very large and extremely anisotropic line broadening occurs as exhibited by a non-monotonous evolution of the line widths with $2\theta_0$ (Figure 5).

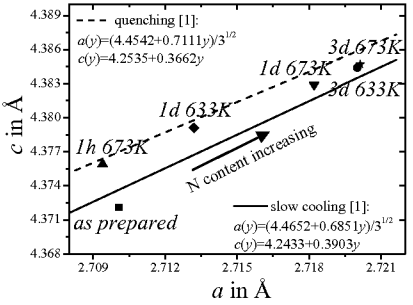

Figure 4. Lattice parameter c vs. lattice parameter a, for as prepared and annealed ε-iron nitrides, together with relations for slowly cooled and quenched samples [1].

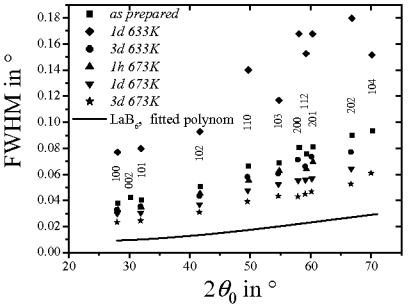

Figure 5. Full width at half maximum (FWHM) of the measured reflections of ε-iron nitrides and LaB_6 (line shown is the third-order polynomial used to fit the omitted individual values.)

Interpretation of line broadening from the ε-phase

According to the observations described above different ε-iron nitrides should have mainly two different sources for structural line broadening (*f', f''*) relative to LaB_6 which is assumed to represent the instrumental broadening, *g*. The *3d 673K* sample exhibits only one structural contribution *f'* of yet unidentified origin, thus having the overall profile $g \otimes f'$, which is apparently typical for all ε-iron nitrides in this range of composition. All other samples exhibit additionally a contribution *f''* due to composition variations with a typical line-width anisotropy [2]. This gives for the overall profile, *h*:

$$h = g \otimes f' \otimes f'' . \tag{3}$$

To extract the *f''* profile for all reflections (Topas [11]), first $g \otimes f'$ was fitted for each *hkl* by *spV* functions (convoluted for technical reasons [11] with a fixed contribution due to a narrow wavelength spectrum) on the basis of the *3d 673K* data. Then, for all other iron nitride data, this (now fixed) $g \otimes f'$ was further convoluted with a *spV* function representing the compositional contribution *f''* with fitted parameters.

The compositional broadening *f''*

If the line broadening given by *f''* is only caused by compositional microstrain broadening, then the *hkl* dependent FWHM values B_{hkl} of *f''* should behave like (which holds for the hexagonal crystal system) [2]:

$$B_{hkl} = d_{hkl}^2 \tan\theta_{0,hkl} \left| D_{200}(h^2 + k^2 + hk) + D_{002} l^2 \right| , \tag{4}$$

with D_{200} and D_{002} as (fitting) parameters, which are related to the FWHM of the compositi-

on distribution function in terms of y and the composition dependence of the lattice parameters according to [2]:

$$D_{200} = \left|\frac{\partial}{\partial y}\frac{4}{3a(y)^2}\right| \cdot FWHM_y \quad \text{and} \quad D_{002} = \left|\frac{\partial}{\partial y}\frac{1}{c(y)^2}\right| \cdot FWHM_y \cdot \tag{5}$$

The observed B_{hkl} values obtained for the line broadening contribution f'' for the different samples are shown in figure 6 together with curves calculated on the basis of the fitted values of D_{200} and D_{002}. For the broad reflections of the *1d 633K* and *as-prepared* samples the B_{hkl} values agree well with equation (4), i.e. the D_{002}/D_{200} ratios agree well with those calculated on the basis of the known concentration dependencies of the lattice parameters. In contrast with the *width* parameter B_{hkl} the peak *shape* parameters should be *hkl*-independent [2]. However, slight diffraction-vector direction dependent variations in As_{hkl} and η_{hkl} occur. This may suggest that the assumptions underlying the separation of the different line-broadening contributions (see above section) are not ideally fulfilled. It should be noted that upon prolonged annealing the B_{hkl} values due to f'' become narrow compared to $(g \otimes f')$, so that the results of the convolution fitting procedure suffer from larger relative errors and poorer fits to equation 4 occur (cf. figure 6).

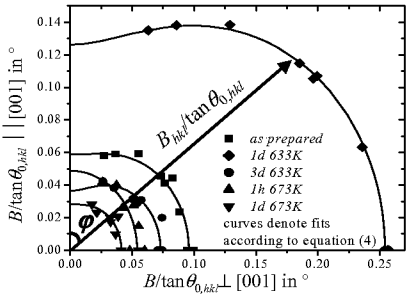

Figure 6. Anisotropy of the microstrain-like compositional broadening observed for the ε-phase of various annealed samples (experimental data corrected for 3d 673K data). φ is the angle between the diffraction vector and the [001] direction.

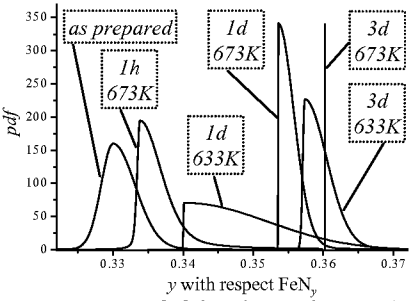

Figure 7. Probability density function (pdf) for composition y of the as-prepared and annealed ε-iron nitrides. (Note that no composition variations were assumed for the 3d 673K sample).

The probability density functions of the composition y [2] for ε in the different samples were obtained from the averaged D_{200} and D_{002} values, the fitted lattice parameters and the relations between lattice parameters and composition [1], as well as the averaged peak *shape* parameters of the f'' contribution to the line broadening (Figure 7). For all samples asymmetric distributions of the composition were obtained. Intermediate states of γ'-precipitation (*1d 633K*) show quite broad composition distributions.

N transfer between powder particles upon γ'-precipitation

The TEM observations together with the X-ray analyses indicate how N is redistributed over the remaining ε-phase in the powder upon annealing when reaction (1) occurs: γ' forms only in a few powder particles leading readily to an increase of N content of the ε-phase in *these* particles. If N redistribution can only occur within an individual powder particle, the N con-

tent would remain constant for the ε-phase particles without γ'-precipitate(s), and considerable concentration differences between the ε-phases of the different particles will result (e.g. for *1d 673K*). However, the experiments showed that upon *prolonged* annealing the concentration differences between particles with and without precipitates were reduced, leading to the virtual absence of concentration variations in the powder after the end of the precipitation (*3d 673K*). This implies N transfer between particles via direct mechanical contact of the (mainly spherical) particles, since N transport via the gas phase can be excluded: loss of N_2 to the atmosphere is well known to be fully irreversible [12]. The small mechanical contact areas between the different particles make this N transport from particle to particle slow.

Conclusions

Annealing of ε-Fe_3N powder at 633 K and 673 K leads to (i) precipitation of γ'-Fe_4N grains in only a few powder particles, in contrast with the occurrence of fine, lamellar precipitates in massive ε-samples; (ii) increase of ε-phase lattice parameters due to increase of N content in the remaining ε-phase.
Analysis of the X-ray diffraction-line profiles indicates that (i) at least two types of structural broadening occur for ε-Fe_3N, i.e. a compositional variation and a not yet identified contribution; (ii) long-time annealing leads to homogenisation of the ε-phase, thereby removing the compositional broadening.

References

1. Liapina, T., Leineweber, A., Mittemeijer, E.J. & Kockelmann, W., 2004, *Acta Mater.*, **52**, 173.
2. Leineweber, A. & Mittemeijer, E.J., 2004, *J. Appl. Crystallogr.* **37**, 123.
3. A. Leineweber, PhD thesis, University of Dortmund (1999).
4. Liapina, T., Leineweber, A. & Mittemeijer, E.J., 2003, *Scr. Mater.* **48**, 1643.
5. Schröter, W., Russev, R., Ibendorf, K., Vatev, E., 1982, *Wiss. Z. d. Techn. Hochsch. Karl-Marx-Stadt*, **24**, 6.
6. Gerardin, D., Morniroli, J., Michel, H., Gantois, M., J., 1981, *Mater. Sci.*, **16**, 159.
7. Jutte, R.H., Kooi, B.J, Somers, M.A.J., Mittemeijer, E.J., 1997, *Oxid Met*, **48**, 87.
8. Malinov, S., Böttger, A.J., Mittemeijer, E.J., Pekelharing, M.I. & Somers, M.A.J., 2001, *Metall. Mater. Trans. A*, **32**, 59.
9. Liu, Z.Q., Leineweber, A., Mittemeijer, E.J., Witsuishi, K., Mitsuishi, K. & Furuya, K. to be published.
10. Mittemeijer, E.J., Somers, M.A.J., 1997, *Surf. Eng.***13**, 483.
11. TOPAS, General Profile and Structure Analysis Software for Powder Diffraction Data, V2.0, Bruker AXS GmbH, Karlsruhe, Germany.
12. Lehrer, E., 1930, *Z. Elektrochem*, **36**, 383.

Z. Kristallogr. Suppl. **23** (2006) 455-459

X – ray powder diffraction study of leucite crystallisation

M. Novotna[1], J. Maixner[2*]

[1]Inst. of Inorganic chemistry AS CR, 250 68 Řež, Czech Republic
[2]Inst. of Chemical Technology in Prague Technická 5, 166 28 Praha 6, Czech Republic
[*]Contact author; e-mail: maixnerj@vscht.cz

Keywords: leucite, crystallisation, phase transformation, powder diffraction

Abstract X-ray powder diffraction analysis was used to study leucite ($KAlSi_2O_6$) crystallisation from amorphous precursors prepared by hydrothermal synthesis. Crystallisation of leucite was monitored at 800 °C, 900 °C and 1000 °C. At these high temperatures the stable form of leucite is a cubic one (high leucite), and a displacement phase transformation to tetragonal form (low leucite) takes place as it cools. The process of leucite transformation was studied using X-ray powder diffractometer D8 equipped with MRI high temperature chamber. It was detected that the transition from high temperature phase into the low leucite occurs below 550 °C.

Introduction

Leucite based ceramic materials are a subject of an extensive scientific interest in recent years, especially in the field of dental prosthesis. Ceramic structures are used to replace missing teeth, tooth structure lost to disease or trauma, and unaesthetic, but otherwise healthy, tooth enamel [1]. The significant attributes of dental ceramics are its aesthetical (it can be coloured to closely resemble teeth it must replace) and chemical (stability toward oral flora and corrosive components of foods and saliva) qualities. The presence of leucite, exhibiting a high thermal expansion coefficient, in a porcelain matrix enables its fusion to metal reinforcement and so achieve high mechanical strength. In addition in last few years [2, 3] it was hypothesized that leucite, thanks to its phase-transition behavior, could potentially toughen leucite-glass (porcelain) systems and so lead to dental materials having high fracture toughness.

The crystal structure of leucite is based on the isometric alumosilicate framework of the ANA topology [4]. The main secondary building units of this framework are fourfold, sixfold and eightfold rings of $(Al, Si)O_4$ tetrahedra. The sixfold rings are arranged axially, forming structural channels parallel to <111>. Such a channel arrangement is typical of feldspathoids and some of zeolites. In comparison with feldspars and other framework structures without channels, they show many possibilities for structural modification, including framework distortion or ionic mobility.

Naturally occurring leucite crystallises in the cubic phase, with space group Ia3d. On cooling below the temperature of about 630 °C, there is a phase transition to a tetragonal form and at

room temperature leucite has a space group I41/a. The conversion of cubic leucite into the tetragonal modification involves deformation of the sixfold rings, i.e. channels distortion, which is accompanied by slight movements of the K^+ ions. The transformation is martensitic, it proceeds by slipping and twinning mechanism, during which the atoms retain their neighbours and move over a distance that is smaller than their original mutual one [5].
Our previous [6] studies have investigated new preparation procedures of homogeneous leucite powders using hydrothermal conditions. As these technologies were found very promising, further research was carried out. The present paper reports an X-ray powder diffraction study of the leucite crystallisation from amorphous precursors prepared by hydrothermal synthesis. It is of special interest to monitor the process of leucite phase transformation from cubic to tetragonal, seeing that this transition is substantial for the toughening mechanism in leucite dental ceramics.

Experimental

Amorphous alumosilicate powders were prepared as a precursor material by hydrothermal synthesis. Starting sols were prepared from fine-ground amorphous silica powder (SiO_2, Polskie Odczynniki Chemiczne Gliwice, PL), sodium hydroxide solution (NaOH, Lachema, CZ) and aluminium powder (Al, Lachema, CZ). These materials were processed hydrothermally at 200 °C for 2h in a Teflon lined stainless steal autoclave. After the hydrothermal treatment, the content of the autoclave was washed with boiling distilled water, vacuum filtered and dried in an oven at 100 °C.

Room temperature X-ray diffraction analysis
Prepared amorphous powders were subsequently heated at 800 °C, 900 °C and 1000 °C for definite time periods. X-ray powder diffraction data were collected at room temperature with an X'Pert PRO powder diffractometer using parafocusing Bragg-Brentano geometry using CuK_α radiation (λ = 1.5418 Å, U = 40 kV, I = 30 mA). Data were scanned over the angular range 5-60 °(2θ) with a step size of 0.02 °(2θ) and a counting time of 0.3 s $step^{-1}$. Data evaluation were performed in the software package HighScore and the degree of crystallised leucite was determined by quantitative analysis using an external standard of pure low tetragonal form of leucite.

High temperature X-ray diffraction analysis
Temperature dependent X-ray powder diffraction (TDXD) was carried out with a Bruker AXS D8 powder diffractometer using CuK_α radiation (λ = 1.5418 Å, U = 40 kV, I = 30 mA). The sample was placed on a Pt/Rh ribbon in a MRI high-temperature oven-camera and VPSlits were used to fix the constant irradiated length (20 mm). Data were scanned over the angular range 25-28 °(2θ) with a step size of 0.02 °(2θ) and a counting time of 1.2 s $step^{-1}$. The heating and cooling process was controlled by Eurotherm 2404. The sample was heated with rate 100 °C/min.
The process involved two heating and cooling cycles, starting with a hydrothermally synthesised amorphous powder. During the first temperature treatment, the crystallisation of high cubic leucite on heating and its transition to low tetragonal form on cooling was monitored. The reversibility of the transformation was studied at the second cycle.

Results and discussion

Room temperature X-ray diffraction analysis

Table 1 gives conditions of the high temperature treatment (heating temperatures and times) and corresponding percentage of leucite formed from amorphous precursor. The percentage of formed leucite sharply rises with increasing temperature. Figure 1 compares XRD traces of samples after six hours of calcination at 800 °C, 900 °C and 1000 °C. On one hand, at 800 °C no traces of crystallisation were observed. On the other hand at 1000 °C completely crystallised product was obtained.

Table 1. Conditions of the high temperature treatment and corresponding percentage of the leucite.

Temperature [°C]	Time	Crystallised Leucite[%]	Temperature [°C]	Time	Crystallised Leucite[%]
800	6 hrs	0	1000	15 min	0
900	2 hrs	2	1000	30 min	13
900	4 hrs	21	1000	2 hrs	71
900	6 hrs	34	1000	6 hrs	100

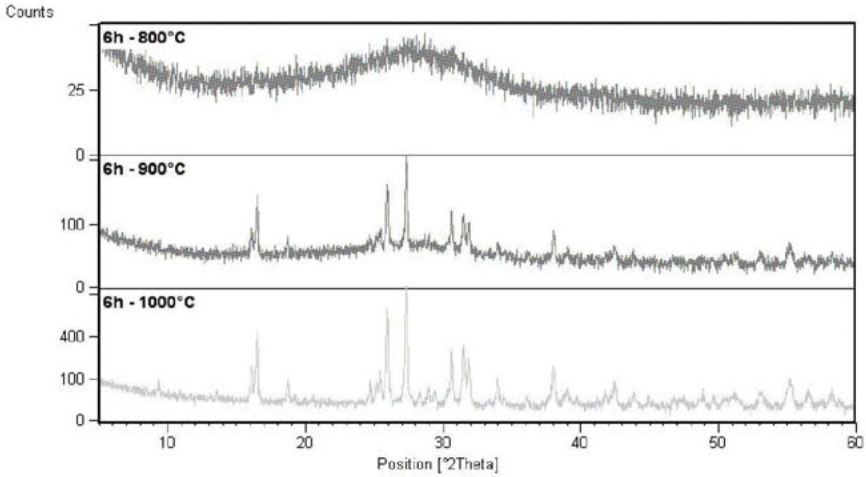

Figure 1. Comparison of samples after 6 hours of calcination at 800°C, 900°C and 1000°C.

High temperature X-ray diffraction analysis

Figure 2 demonstrates first temperature treatment cycle. Starting with hydrothermally synthesised amorphous powder, the first sign of crystallisation was observed at 1100 °C. Significant high temperature leucite phase formation was recorded at 1200 °C, observing the (400) reflection, the strongest line of cubic leucite. During the cooling process the (400) reflection is split into the two tetragonal reflections (004) and (400) at about 550 °C. The transition into the tetragonal form is finished at about 400 °C. At room temperature only the tetragonal form was present.

The course of the second cycle is illustrated at Figure 3. Starting with the material obtained after the first cycle, the formation of the high temperature cubic leucite phase was first observed at about 500 °C and the process was completed at about 600 °C. Reverse transformation proceeded identically with the first cycle upon cooling.

Conclusions

- The optimal temperature for the preparation of leucite is 1000 °C.
- Temperature X-ray analysis demonstrated phase reversibility of the prepared leucite.
- The transformation from the C-leucite into the T- leucite occurs at about 550 °C.

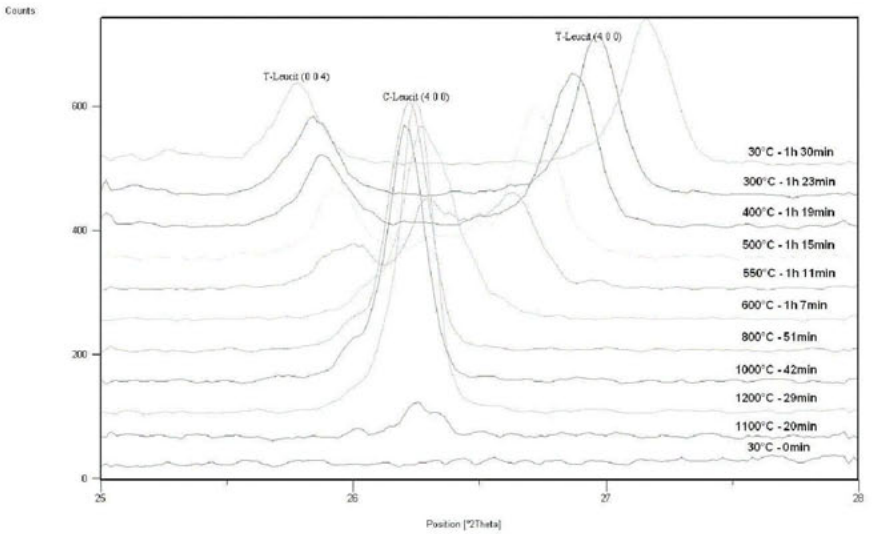

Figure 2. 1st cycle: crystallisation of cubic leucite from starting amorphous precursor material on heating, transition to tetragonal leucite on cooling.

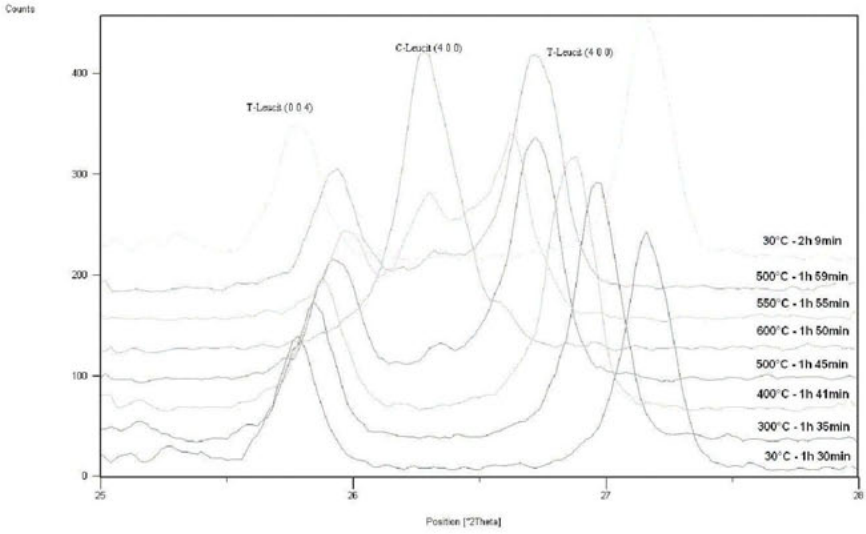

Figure 3. 2nd cycle: Phase transformation to cubic leucite and back to tetragonal leucite.

References

1. Kelly, J.R., 1197, Annu. Rev. Mater. Sci., 27, 443.
2. Rasmussen, S.T., Groh C.L., Brien W.O., 1998, Dent. Mater., 14, 202.
3. R. Morena, P.L. Lockwood, 1986, J. Am. Cer. Soc., 64 C 74
4. Meier, W.M., Olson, D.H., 1992, Atlas of Zeolite Structure Types (Butterworth, London), p. 200.
5. Palmer, D.C., Dove, M.T., Ibberson R.M., Poqwell B.M., 1997, Am. Miner., 82, 16
6. Novotna, M., Satava, V., Kostka, P., Lezal, D., Maixner, J., Klouzkova, A., 2004, Glass Technol., 45, 105.

Acknowledgements
This work was supported by GA CR Grant 104/03/0031.

Z. Kristallogr. Suppl. **23** (2006) 461-466

Neutron diffraction structure study of borosilicate based matrix glasses

M. Fábián[1], E. Sváb[1*], Gy. Mészáros[1], L. Kőszegi[1], L. Temleitner[1], E. Veress [2]

[1]Research Institute for Solid State Physics and Optics, H-1525, Budapest POB 49. Hungary
[2]Babeş-Bolyai University, Faculty of Chemistry, 11 Arany János St., RO-3400 Cluj, Romania
[*]Contact author; e-mail: Dr. E. Sváb, svab@szfki.hu

Keywords: borosilicate glasses, radioactive host media, neutron diffraction, RMC modelling

Abstract. We have performed structure study on a newly synthesized sodium borosilicate matrix glass system with general composition of $65SiO_2*5B_2O_3*25Na_2O$ $*5BaO$ *(mole%)* doped with CeO_2 and ZrO_2 with the aim to model radioactive PuO_2 and also, to increase the hydrolytic and network stability of the glasses. Neutron diffraction experiments have been performed and reverse Monte Carlo modelling was applied to obtain the partial atomic pair correlation functions. We have established that ZrO_2 is an effective glass stabilizer, and the short-range structure of the CeO_2 doped samples preserves the basic network configuration of the matrix glasses, making them suitable for radioactive waste material storage.

Introduction

Borosilicate glasses are of significant current interest as suitable materials for isolating host media for radioactive waste material storage [1-4]. Although the investigation of boron containing matrix glasses is challenging, only a few neutron diffraction studies have been reported in the literature so far [5].

The aim of the present study was to investigate the network glass configuration of a newly synthesized sodium borosilicate glass system doped with CeO_2 and ZrO_2. Matrix glass with the general composition of $65SiO_2*5B_2O_3*25Na_2O$ $*5BaO$ was prepared, where BaO serves as glass stabilizer. Radioactive waste material PuO_2 was modelled by addition of CeO_2 to the host glass. Since *Pu* and *Ce* coordinations are rather similar in complex oxide environments, it can be expected that *Pu* coordination in a glass network is properly simulated by *Ce*. In order to increase both the hydrolytic and network stability of the matrix glass, ZrO_2 was added.

Here we present our neutron diffraction experiments and results obtained by reverse Monte Carlo (RMC) modelling, characterizing the short-range structure of the investigated glass system. Details of sample preparation and sample characteristics are also described.

Experimental

Sample preparation

Host glass compositions were synthesized by melting 50 g quantities of previously homogenized powder mixtures obtained from the properly weighed dry starting components: SiO_2, Na_2CO_3, BaO, H_3BO_3, and ZrO_2 in platinum crucible at 1300-1450 °C in atmospheric conditions. The raw materials used were: SiO_2, Na_2CO_3 and H_3BO_3 as supplied by Reactivul (Bucuresti), BaO and ZrO_2 by Merck (Darmstadt).

The sample series with different ZrO_2 content was prepared with the general composition of $(65\text{-}x)SiO_2*5B_2O_3*25Na_2O*5BaO*xZrO_2$ (mole%) $x=0,1,2,3,4,5$. The melt was quenched by pouring it on a stainless steel plate.

The second sample series was prepared by re-melting 90 wt% of the corresponding host glass with addition of 10 wt%CeO_2 supplied by Fluka (Darmstadt). It was homogenised for several hours at high temperature as described above, and thereafter quenched. The general composition of the five samples is:

$90\ wt\%\{(65\text{-}x)SiO_2*5B_2O_3*25Na_2O*5BaO*xZrO_2\}+10\ wt\%CeO_2$.

Powder samples for neutron diffraction measurements were prepared by powder milling of the quenched glasses in an agate mill.

Neutron diffraction measurements

Neutron diffraction measurements were performed at the 10 MW Budapest research reactor using the 'PSD' [6,7] and 'MTEST' [8] neutron powder diffractometers. Monochromatic wavelength of λ=1.07 Å was used, and the diffraction spectrum was measured in the scattering vector range Q= 0.95-9.8 $Å^{-1}$. The powder specimens of about 3-4 g were filled in cylindrical vanadium sample holder of 8 mm diameter, 50 mm height and 0.07 mm wall thickness. Since the specimens were prepared from natural boron being high neutron absorbent, accurate transmission measurements were performed. Transmission of the samples was between 80 and 82%.

Correction and normalization procedures utilized to obtain the structure factor $S(Q)$ from the measured pattern was described in our previous work [9]. For data treatment to obtain the atomic pair correlation functions, both the traditional direct Fourier transformation technique and reverse Monte Carlo (RMC) simulation [10] were applied.

Sample characterization

Density of the produced samples was measured at 20 °C by a picnometer calibrated at the same temperature. Values between 2.35 and 2.95 gcm^{-3} were found depending on composition. The hydrolytic stability of the specimens was measured by static method [see e.g. 2].

Despite of the great hydrolytic stability of the samples, the first few neutron diffraction experiments revealed their tendency to superficially adsorb H_2O. Atmospheric humidity caused a surface swelling of the air-kept samples, and the hydrolysed layer produced significant incoherent inelastic scattering, hindering the coherent scattering of the specimens (see figure 1/a). In order to dry the samples, heat treatment was applied at 120 °C for 4 hours under vacuum conditions, which proved to be completely sufficient to obtain neutron diffraction pattern adequate for data treatment. For illustration, neutron diffraction patterns of the

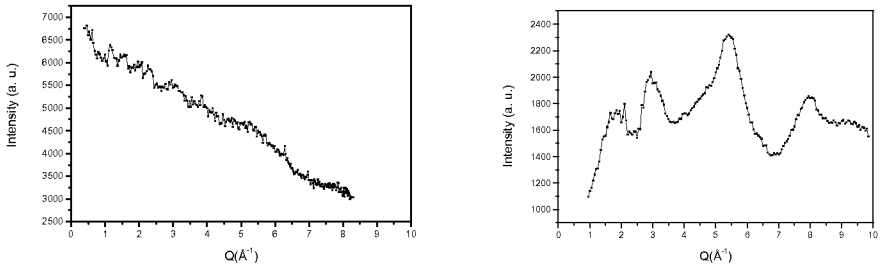

a/ b/

Figure 1. Neutron diffraction pattern of $65SiO_2*5B_2O_3*25Na_2O*5BaO$ (mole %) glass: ***a****/ air-kept state with superficially absorbed H_2O (5 wt%) **b**/ after heat treatment. The sample contains a small amount of crystalline phase.*

$65SiO_2*5B_2O_3*25Na_2O*5BaO$ specimen are shown in figure 1/a,b in air-kept state and after the applied heat treatment.

From the neutron diffraction pattern we have established that BaO is not sufficient to stabilize completely the amorphous structure (see figure 1/b), while ZrO_2 proved to be an effective glass stabilizer. All our ZrO_2 doped host glass samples were in pure amorphous-state, Bragg-peaks were not detected.

Addition of CeO_2 to the host matrix did lead to formation of crystallites, embedded in the glassy network. By increased addition of ZrO_2 content to the matrix, the glass network could be stabilized. The CeO_2 containing specimens proved to be completely amorphous with ZrO_2 amount above 3 mole%.

Data treatment and results

As a first step of data evaluation process the total reduced atomic distribution function, $G(r)$ characterizing the average one-dimensional atomic pair correlations was calculated from $S(Q)$ by sine Fourier transformation [see e.g. 9]:

$$G(r) = \frac{2}{\pi} \int_0^{Q_{max}} Q\left[S(Q) - 1\right] \sin Qr \, dQ \ , \qquad (1)$$

where the integration limit Q_{max} was selected at the highest Q value where $S(Q)=1$ to minimize termination errors. For illustration, figure 2/a,b shows $S(Q)$ and $G(r)$ for the $60SiO_2*5B_2O_3*25Na_2O*5BaO*5ZrO_2$ glass. The information content of $G(r)$ is very limited for this multi-component system being the weighted sum of the partial pair correlation functions. From $G(r)$, anyhow, we can derive some information, namely: the Si-O and B-O first neighbour distributions overlap, resulting in the first peak at r=1.6 Å. The second peak at r=2.6 Å contains mainly the O-O first neighbours, as it is expected from the literature, and due to the sharp form of the peak we can suppose that most of the cation-oxygen first neighbours give contribution at this position. The position of these two peaks, denoting the *1st and 2nd* coordination spheres do not show significant changes as a function of Zr-content or/and Ce-content, meaning that the basic network configuration is preserved. Slight de-

crease of the *1st* peak intensity with increasing *Zr*-content may be observed, meaning the decreased number of first neighbour *Si-O* atomic pairs due to the presence of large Zr and/or Ce ion.

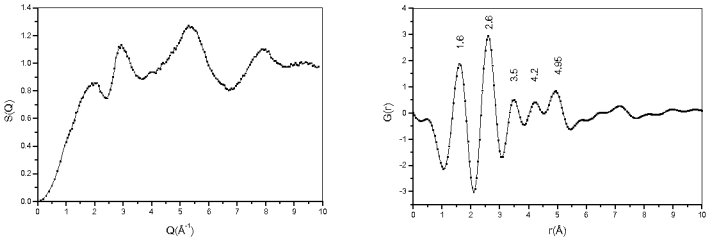

a/ b/

Figure 2. Glass $60SiO_2*5B_2O_3*25Na_2O*5BaO*5ZrO_2$ (mole%): a/ Structure factor S(Q) and b/ total reduced distribution function G(r) calculated by Fourier- transformation.

In order to get deeper insight into the atomic configuration, the reverse Monte Carlo (RMC) simulation technique was applied [10]. Our multicomponent glass system contains $k = 4, 5, 6$ different types of scattering centres, resulting in $k(k+1)/2 = 10, 15, 21$ partial pair correlation functions, $g_{ij}(r)$. Because of the very high number of $g_{ij}(r)$'s, the number of simulated parameters is enormously high, and the obtained results should be handled very carefully. For the RMC starting model a disordered atomic configuration was built up. The calculation consists of minimizing the squared difference between the experimental and calculated structural factors $S(Q)$ by moving atoms randomly. The following definitions and basic relations are used in RMC calculations:

$$S(Q) = \frac{\sum_{i,j}^{k} c_i c_j b_i b_j S_{i,j}(Q)}{\left[\sum_{i,j}^{k} c_i b_j\right]^2} \tag{2}$$

$$S_{i,j}(Q) = 1 + \frac{4\pi\rho}{Q}\int_0^\infty r\left[g_{i,j}(r) - 1\right]\sin Qr\, dr\,, \tag{3}$$

$$g_{i,j}(r) = 1 + \frac{1}{2\pi^2 r\rho}\int_0^\infty Q\left[S_{i,j}(Q) - 1\right]\sin Qr\, dQ\,, \tag{4}$$

where ρ is the number density, c_i, c_j the molar fractions of components and b_i, b_j the coherent neutron scattering amplitudes. $S_{ij}(Q)$ are the partial structure factors whose sine Fourier transforms are $g_{ij}(r)$. For simplicity, we denote the $g_{ij}(r)$ functions as $g(r)$ in the forthcoming description.

The convergence of the RMC calculation was good and the final calculated $S(Q)$ matched very well the experimental structure factors, as it is illustrated in figure 3/a for the $90\%\{60SiO_2*25Na_2O*5BaO*5B_2O_3*5ZrO_2\}+10\%CeO_2$ sample.

We could successfully calculate most of the *g(r')'s*, and the atomic distances of the glass network was calculated. The partial atomic correlation functions *g(r)* are very similar for all samples, therefore here we present the obtained results only for the 90%{*60SiO$_2$*25Na$_2$O* 5BaO*5B$_2$O$_3$*5ZrO$_2$*}+10%*CeO$_2$* glass, representing all investigated samples. The *Si-O and B-O* pair correlation functions contributing to the *1st* coordination shell of *G(r)* are shown in figure 3/b,c. For the first neighbour *Si-O* and *B-O* distances 1.6 Å and 1.5 Å were revealed, respectively. The *O-O, Na-O, Ce-O, Zr-O, Ba-Zr and Na-Zr g(r)'s* contributing to the *2nd* coordination sphere of *G(r)* are collected in figures 3/d-i.
More detailed analyses of the g(r)'s, regarding coordination numbers, bond angles, distributions at the 3rd coordination sphere are in progress.

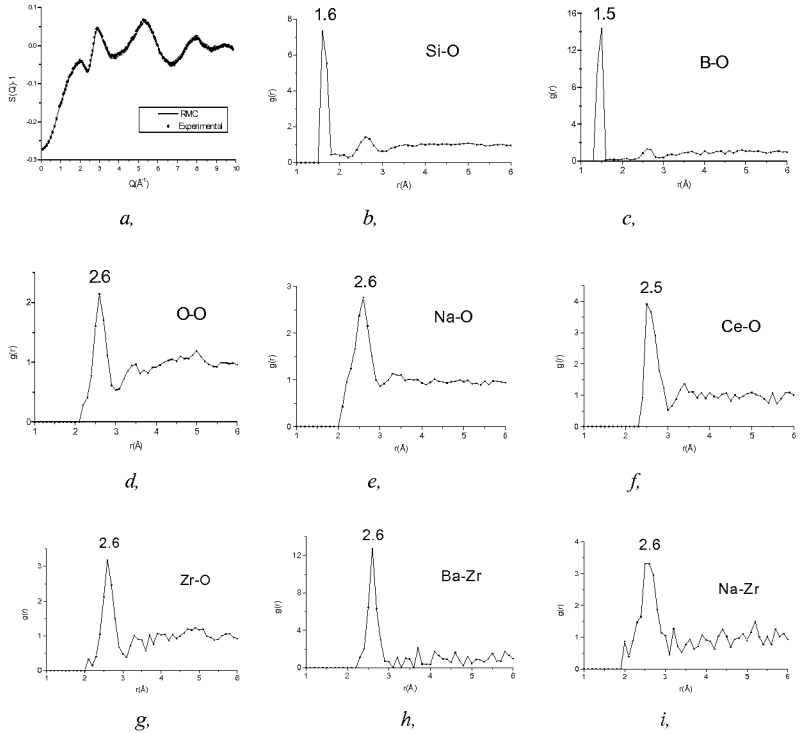

*Figure 3. Glass 90%{60SiO$_2$*5B$_2$O$_3$*25Na$_2$O*5BaO*5ZrO$_2$}+10%CeO$_2$: a/ Structure factor S(Q)-1, experimental (dots) and RMC simulation (solid line); b/Si-O, c/B-O, d /O-O, e/ Na-O, f/Ce-O, g/Zr-O, h/Ba-Zr, i/Na-Zr partial pair correlation functions g(r), as obtained by RMC simulation.*

Conclusions

We have performed neutron diffraction study on a newly synthesized sodium-borosilicate glass added with CeO_2 and ZrO_2, with the aim to model isolating host media for storage of radioactive waste materials. The following main findings have been revealed:
- The air-kept samples did show tendency to superficially adsorb H_2O. Heat treatment at 120 °C for 4 hours under vacuum conditions proved to be completely sufficient to dry the specimens.
- Addition of BaO proved to be not sufficient to stabilize completely the glassy structure, while ZrO_2 proved to be an effective glass stabilizer.
- Addition of CeO_2 to the host matrix did lead to formation of crystallites, embedded in the glassy network. With addition of ZrO_2 , however, the glass network could be stabilized.
- From RMC simulation of the neutron diffraction data we have obtained the partial atomic pair correlation functions for these multi-component glasses.
It was established that the short-range structure of the CeO_2 doped samples preserves the basic network configuration of the matrix glasses, making them suitable for radioactive waste material storage.

References

1. Inman, J.M. , Houde-Walter, S.N, McIntyre, B.L., Liao, Z. M., Parker, R.S. & Simmons, V., 1996, *Journal of Non-Crystalline Solids* **194**, 85.
2. Donald, I.W., Metcalf, B.L. & Taylor, R.N.j., 1997, *Journal of Material and Science* **32**, 5851.
3. Li, H., Vienna, J.D., Hrma, P., Scchweiger, M.J., Smith, D. & Gong, M., 1996, *Ceramic Transactions*, **72**, 399.
4. Orlhac, X., Fillet.C. & Phalippon , J. 1998, *Scientific Basis for Nuclear Waste Manag.*, **556**, 263.
5. Swenson, J., Börjesson, L. & Howells, W.S., 1995, *Physical Review B* **52**, 9310.
6. Sváb, E., Deák, F. & Mészáros, Gy., 1996, *Mater. Sci. Forum* **228-231**, 247.
7. Temleitner, L., Mészáros, Gy., Pusztai, L. & Sváb, E., 2004, *Physica B*, **350**, 865.
8. Kőszegi, L. 2001, *Journal on Neutron Research* **9**, 381.
9. Sváb, E., Mészáros, Gy., Konczos, G., Ishmaev, S.N., Isakov, S.I. & Chernyshov, A.A., 1988, *J. Non-Cryst. Solids* **104**, 291.
10. McGreevy, R.L. & Pusztai, L. 1988, *Molec. Simul.* **1**, 359.

Acknowledgements. The authors are grateful to Dr. L. Pusztai for helpful consultations. This study was supported by the Hungarian Research Grant OTKA T-42495 and by the EC HPRI-RII3-CT-2003-505925.

Z. Kristallogr. Suppl. **23** (2006) 467-472

Neutron diffraction studies of temperature induced phase transitions in Rb_2KFeF_6 elpasolite

S. G. Vasilovsky[1], V. V. Sikolenko[1,4,*], A. I. Beskrovny[1], A. V. Belushkin[1], I. N. Flerov[2], A. Tressaud[3], A. M. Balagurov[1]

[1]Joint Institute for Nuclear Research, Dubna, Russia
[2] Kirensky Institute of Physics, Krasnoyarsk, Russia
[3] Institut de Chimie de la Matière Condensée de Bordeaux, Pessac, France
[4] Hahn-Meitner-Institut, Berlin, Germany
[*]Contact author; e-mail: Sikolenko@hmi.de

Keywords: neutron diffraction, elpasolites, Rietveld analysis

Abstract. A neutron diffraction study of temperature induced phase transition in Rb_2KFeF_6 elpasolite has been performed. At room temperature the structure is cubic with space group Fm3m. At T = 170 K a structural phase transition takes place. Space group and atom coordinates in this phase has been defined. The crystal structure is good refined by orthorhombic space group Pmnn. Possible models are discussed.

Introduction

Rb_2KFeF_6 fluoride belongs to compounds family with general chemical formula A_2BMF_6 (A, B – monovalent cations, M – trivalent cation). The space group of their cubic prototype is *Fm3m* (Z = 4). In this system two kinds of non-equivalent octahedral groups (BF_6 and MF_6) alternate along the three four-fold axes. The region of cubic lattice stability depends on tolerance factor [1]:

$$t = \frac{\sqrt{2}\left(r_{A^+} + r_{F^-}\right)}{2r_{F^-} + r_{B^+} + r_{M^{3+}}}$$

where r_A, r_B, r_M and r_M are ion radii of A, B, F and M. t = 1 for ideal perovskite-type structure. BO_2 plane is under squeezed stresses and AO plane is under stretched stresses at the $t < 1$. Usually it leads to mutual turns of BO_6 octahedrons [2].
Fm3m symmetry is usually observed in the wide temperature region at the $0.88 < t < 1.0$. Distortion of the octahedral group takes place at the $t < 0.88$. This fact leads to crystal symmetry reduction.

Temperature dependence of phase transitions in crystals with high M^{3+} radius have been recently studied [3]. At the M = Sc, In, Lu the consecution of two transitions Fm3m → I4/m → P21/n has been observed.

The structure of crystals with low M^{3+} (M = Cr, Ga, Fe) radius is still poorly known. These compounds usually demonstrate ferroelastic phase transition which corresponds considerable high changing in entropy ΔS.

We studied structure of the Rb_2KFeF_6 (t = 0.885; ΔS/R = 1.88) at the wide temperature region.

Experimental

Rb_2KFeF_6 was prepared by solid-phase sintering with stoichiometric quantities of RbF + KF + FeF_3 mixture at the 700 ◦C in the Institute of Solid State Chemistry of Bordeaux. Neutron diffraction experiments have been performed at the High Resolution Fourrier Diffractometer HRFD and DN-2 diffractometer at the IBR-2 pulsed reactor in Frank Laboratory of Neutron Physics (Dubna) [4]. HRFD is a reverse time-of-flight diffractometer with a high resolution Δd/d ~ 2.10-3 in interplanar spacing region 0.5 < d < 4 Å. Scattering angle is fixed at the 2Θ = 152◦. DN-2 is a multipurpose time-of-flight diffractometer with average resolution Δd/d ~ 2 % and high flux up to 107 n/cm2s2. The data were analyzed by the Rietveld method using MRIA program [5].

Results

Figure 1 shows neutron diffraction pattern and the result of Rietveld refinement at the room temperature. Rb_2KFeF_6 has a cubic structure (space group Fm3m) with a = 8.865 Å. We used several models for refining of atoms positions. The result is presented in table 1.

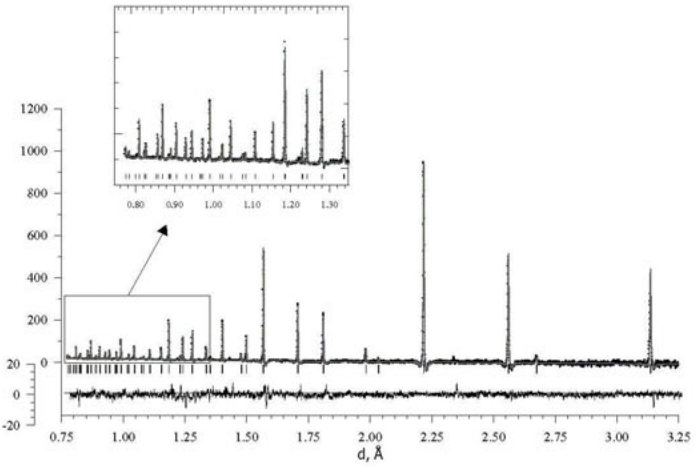

Figure.1. Neutron diffraction pattern and the result of Rietveld refinement of Rb_2KFeF_6 at T = 290 K. The peak at d = 2.34 Å is 111 peak from Al container.

In the first model (column a) we fixed atoms in the particular positions: Rb – 8c, Fe – 4a, K – 4b, F – 24e. In this assumption we obtain very high thermal factors and quite high value of χ^2.

Table 1. Rietveld refinement data at the T = 290 K. a – all atoms fixed in particular positions; b – F in 24e, Rb displaced in [100] direction, c – Rb in 8c, F displaced in [110] direction (96k); d, e, f – F displaced in [110], Rb in [100],[110], [111] correspondingly.

		a	b	c	d	e	f
Rb	x	1/4	0.275(1)	1/4	0.272(1)	0.2656(4)	0.260(1)
	y	1/4	1/4	1/4	1/4	0.2656(4)	0.260(1)
	z	1/4	1/4	1/4	1/4	1/4	0.260(1)
	B, Å^2	2.06(4)	0.74(7)	1.85(4)	0.85(3)	0.97(5)	1.19(5)
	ΔRb, Å	0	0.221(2)	0	0.195(2)	0.196(2)	0.154(2)
K	B, Å^2	4.1(2)	1.19(6)	1.18(9)	1.15(7)	1.14(5)	1.2(1)
Fe	B, Å^2	1.01(3)	0.66(4)	0.62(3)	0.64(4)	0.61.4	0.62(3)
F	x	0.218(1)	0.2163(2)	0.2164(2)	0.2164(2)	0.2164(2)	0.2163(2)
	y	0	0	0.0204(3)	0.0197(4)	0.0198(4)	0.0204(3)
	z	0	0	0.0204(3)	0.0197(4)	0.0198(4)	0.0204(3)
	B, Å^2	4.5(1)	B_{11}=0.97(2) B_{22}=4.45(1) B_{33}=4.45(1)	B_{11}=0.89(1) B_{22}=1.69(1) B_{33}=1.69(1)	B_{11}=0.89(1) B_{22}=1.72(1) B_{33}=1.72(1)	B_{11}=0.89(1) B_{22}=1.70(1) B_{33}=1.70(1)	B_{11}=0.89(1) B_{22}=1.65(1) B_{33}=1.65(1)
	ΔF, Å	0	0	0.154(3)	0.154(3)	0.154(3)	0.154(3)
χ^2		5	2.2	2.4	2.2	2.2	2.2
R_w, %		8.2	5.8	5.9	5.8	5.8	5.8

The t-factor value for Rb_2KFeF_6 is equal to 0.87. This value is lower than theoretically predicted boundary of cubic lattice stability [1]. According to group-theory analysis [6] distortions of initial Fm3m structure caused by octahedron or/and polar atoms displacements are possible. Data of [7] suppose the possibility of 4 positions of fluorine atoms in cubic phase (96k position). Therefore we performed refinements with fluorine atoms in 96k position and Rb – in 8c position (column c of the table 1), Rb is displaced along [100] direction(column d of the table 2), Rb is displaced along [100] direction (column e of the table 2), Rb is displaced along [111] direction (column f of the table 1). The difference in refinement quality is very low and there is impossible to choose the only model based only on neutron diffraction data.

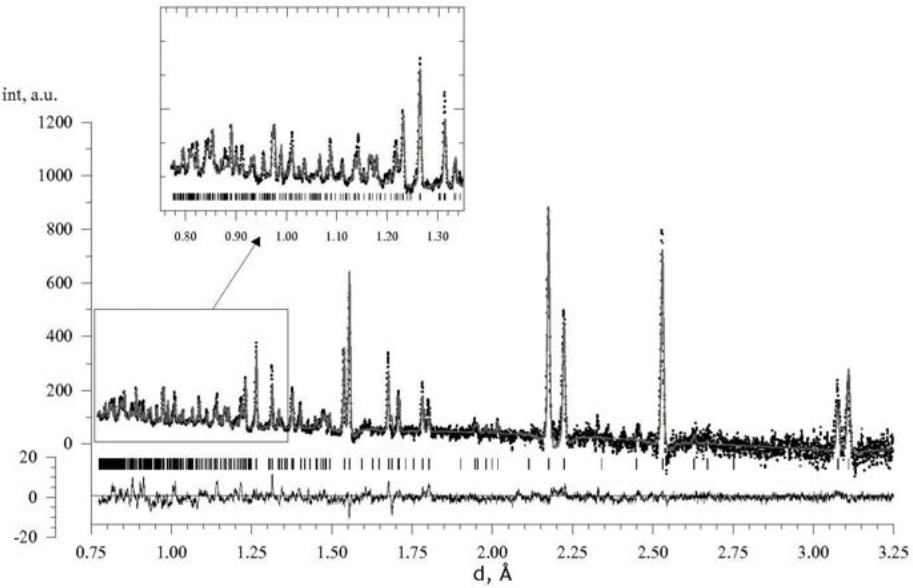

Figure 2. Neutron diffraction pattern and the result of Rietveld refinement of Rb_2KFeF_6 at T = 10 K.

Figure 2 shows neutron diffraction pattern and the result of Rietveld refinement at the temperature T = 10K, which is much lower than the temperature of structural phase transition (T ~ 170 K [3]). The crystal structure precisely described in the frame of Pmnn space group with the a = 6.1567(3) Å, b = 6.1508(3) Å, c = 8.8942(3) Å., $\chi^2 \sim 2.34$. Detail information is shown in the table 2. This result is corresponds with possible variants of phase transitions predicted in [8].

Table 2. Rietveld refinement data at the T = 10 K.

atom	position	x	y	z	B_{iso}, Å^2
Rb	4*f*	0	0.5	0.2644(1)	0.76(2)
K	2*b*	0	0	0.5	0.3(1)
Fe	2*a*	0	0	0	0.4(1)
F	4*e*	0	0	0.2155(2)	0.7(1)
F	4*g*	0.2319(2)	0.2079(2)	0	0.6(1)
F	4*g*	0.7681(2)	0.2079(2)	0	0.6(1)

Discussion

Phase transitions in elpasolites family depend on two main factors: electron structure of M^{3+} cation and value of the tolerant factor t. Determinating factor for non-Jahn-Teller cations like Fe^{3+} is a tolerant factor.[2, 3]. It is equal 0.87 in the case of Rb_2KFeF_6. This value is lower than the theoretical boundary of crystal lattice stability. This fact allows us to suppose that fluorine atoms are disorder in 4 equivalent positions (96k) in the initial cubic phase at room temperature. Strong anisotropy of thermal vibrations of fluorine atoms confirms this assumption. Rb is also displaced from the 8c position in the cubic phase, but we cannot precisely define a direction of displacement from the our data (see columns d, e, f in the table 1). From the other side all atoms are ordered in the low-temperature phase. According to our data, the turn of octahedrons around of an fourth order axis on 2.8 degree takes place. FeF_6 octahedrons turn counter-clockwise and KF_6 octahedrons turn clockwise.

Conclusions

We have performed neutron diffraction study of the Rb_2KFeF_6 crystal structure at the 10 and 290 K. At the room temperature the structure can be described in the frame of Fm3M space group. Disordered in 4 equivalent positions fluorine atoms are responsible for lattice instability which leads to structural phase transition at T = 170 K. According to our data we can conclude that phase transition connects mainly with a superposition of two mechanisms: ordering of fluorine atoms and displacement of rubidium.

Acknowledgements.
This work has been supported by the INTAS grant 1997-10177.

References

1. Shannon, R.D. Revised effective ionic radii and systematic studies of interatomis distances in halides and chalcogenides. 1976,*Acta Cryst.* **A32**, 751-767.

2. Alexandrov, K.S. and Beznosikov, V.B., 1999, *Perovskite-type crystals*. Nauka publishers.
3. Flerov, I.N, Gorev, M.V. Entropy and phase transition mechanism in elpasiolites 2001, *Solid State Physics* **43**, 124-131.
4. Aksenov, V.L.; Balagurov, A.M.; Simkin, V.G.; Bulkin, A.P.; Kudryashev, V.A.; Trounov, V.A.; Antson, O.; Hiismaki, P.; Tiita, A.: Performance of the high resolution Fourier diffractometer at the IBR-2 pulsed reactor. 1996, *J. Neutron Research*, **5**, 181-200.
5. Zlokazov, V.B.and Chernyshev, V.V.: MRIA – aprogram for a full profile analysis of powder multiphase neutron diffraction time-of-flight (direct and Fourier) spectra. 1992, *J.Appl.Cryst*. **25**, 447-451.
6. Alexandrov, K.S and Misyul, S.V.: Phase transitions associated with rotational distartion of the structure in crystals related to perovskite. 1981, *Soviet physics - Crystallography* **26** , 612-618.
7. Massa, W.; Dance, J.M.; Darriet, j.: Properties od the dimeric iron fluoride. 1986, *Rev.Chim.Mineral*. **23** , 508-514.
8. Flerov, I.N.; Gorev, M.V.; Grannec, J,; Tressaud, A.: Role of metal fluoride octahedral in the mechanism of phase transitions in A_2BMF_6 elpasolites. 2002, *J.of Fluor. Chem* **116** , 9-14.

IV.4.2 *Determination of Crystal Structure*

Z. Kristallogr. Suppl. **23** (2006) 475-480

Cation distribution in $Li_2M(II)Sn_3O_8$, M(II) = Mg, Co, Fe

T. Trendafilova[1,*], D. Kovacheva[1], K. Petrov[1], A. Hewat[2]

[1]Institute of General and Inorganic Chemistry, Bulgarian Academy of Sciences, Acad. G. Bonchev street, bl.11, 1113 Sofia, Bulgaria
[2]Institute Laue-Langevin, Grenoble, BP 156, F-38042 Grenoble Cedex 9, France
[*]Contact author; e-mail: tatianka@abv.bg

Keywords: cation ordering, double-hexagonal phases, superstructure, neutron and X-ray diffraction

Abstract. New complex oxides with the general formula $Li_2M(II)Sn_3O_8$ (M = Mg, Co, Fe) have been synthesized and studied by powder neutron and X-ray diffraction. They crystallize in the orthorhombic system, space group $Cmc2_1$, Z = 12. The structure consists of a hexagonal close packed array of oxygen layers stacked along <c> direction in a sequence (ABCB) in which cations occupy 1/8 of the tetrahedral and 1/2 of the octahedral interstices. The cation distribution of these phases can be regarded as an intermediate between that of the disordered $LiFeSnO_4$ (space group $P6_3mc$) and the completely ordered $Li_2MnSn_3O_8$ (space group $Cmc2_1$). The factors that play a role for the cation distribution are discussed.

Introduction

Lithium containing complex metal oxides are currently of much interest because of their attractive physical properties, such as electronic and ionic transport, reversible lithium intercalation, electrochemical sensing etc. Many of these oxides crystallize in different structure types like perovskite, sodium chloride, spinel etc. Choisnet and colleagues in 1978 [1] discovered a new structure type. It can be described as a double-hexagonal (DH) array of four oxygen layers, stacked along the <c> direction in a sequence ABAC. Cations occupy the octahedral and the tetrahedral lattice sites of the space group $P6_3mc$. This structure is tolerant with respect to isomorphic cationic substitutions. It is stable at temperatures below 800 – 1100 °C. At higher temperatures (1200 – 1300 °C) it transforms reversibly to ramsdellite [2, 4, 5] or spinel type [3, 6] structure.
The DH phases synthesized earlier exhibit mixed occupancies of the octahedral lattice sites as a rule. In some of them individual atoms occupy the tetrahedral cation sites [1, 3]. Mixed occupancy (Li, Fe) of the tetrahedral site was observed for $LiFeSnO_4$ [2, 4], while $Li_2Fe_3SbO_8$ exhibits mixed occupancies of the tetrahedral and the octahedral lattice sites [3]. In a previous work [7] we communicated two new compounds belonging to the DH structure type, exhibiting complete cation ordering.

In the present paper we report the synthesis and structural characterization of three new compounds - $Li_2MgSn_3O_8$, $Li_2CoSn_3O_8$ and $Li_2FeSn_3O_8$ with partial cation ordering. The cation distributions of these phases seem to be intermediate between those of the disordered $LiFeSnO_4$ (space group $P6_3mc$) and the completely ordered $Li_2MnSn_3O_8$ (space group $Cmc2_1$).

Experimental

The starting reagents used in the synthesis were Li_2CO_3, SnO_2, $Fe(COO)_2.2H_2O$, $CoCO_3$ and MgO. The compounds were obtained by mixing and grinding stoichiometric amounts of the starting compounds. The samples with composition $Li_2FeSn_3O_8$ and $Li_2CoSn_3O_8$ were heated in an atmosphere of flowing argon at 900 °C for 3h and at 950 °C for 3h respectively. The $Li_2MgSn_3O_8$ sample was heated in air for 3h at 1000 °C.

The XRD data for structure refinements were collected on a Bruker D-8 diffractometer equipped with a bent graphite diffracted-beam monochromator, using Cu-K_α radiation, from 5 to 140 °2θ with a constant step of 0.02° in 2θ and 6 s. counting time per step. For neutron diffraction experiments, fine powdered samples were placed in a 12 mm vanadium can. Powder patterns were collected at room temperature with a constant wavelength of 1.594 Å over the range 5 –160 °2θ, with a step 0.05 ° in 2θ, on the high-resolution neutron powder diffractometer D2B at the Institute Laue-Langevin in Grenoble, France.

The FULLPROF program suite [8] was used for the multi-pattern structural refinements. The pseudo-Voigt function defined within seven full widths at half maximum (FWHM) was used for approximation of the diffraction profiles. The refined instrumental and structural parameters were: zero shifts, scale factors, background parameters, lattice parameters, line profile parameters, atomic positional parameters, individual isotropic displacement parameters and cation site occupancies. The scattering lengths used for the refinement of the neutron diffraction data were: (Li) –0.190, (Sn) 0.6225, (O) 0.5803, (Mg) 0.373, (Co) 0.568 and (Fe) 0.945 10^{-12} cm.

Results and discussion

XRD and ND patterns were used to obtain the crystal structure data of the three new phases i.e. a multi-pattern refinement was performed. The fitted XRD and neutron diffraction patterns of $Li_2CoSn_3O_8$ are shown in figure 1. Lattice symmetry and cell parameters are given in table 1. Detailed structure information will be submitted to the ICSD.

Table 1. Cell parameters and c/a ratio for the three new compounds.

S.G. $Cmc2_1$	a[Å]	B [Å]	c [Å]	c/a	Z
$Li_2CoSn_3O_8$	18.2717(7)	10.9951(4)	9.8446(1)	1.616	12
$Li_2MgSn_3O_8$	18.2594(3)	10.5496(2)	9.8353(1)	1.615	12
$Li_2FeSn_3O_8$	18.3004(9)	10.5641(6)	9.8544(1)	1.616	12

The structure of these phases represents a double-hexagonal (DH) array of four oxygen layers, stacked along the <c> direction in a sequence ABAC. Cations occupy 1/2 of the octahedral and 1/8 of the tetrahedral lattice sites, forming two different cation layers: one, contain-

ing three cations with octahedral coordination Kagomé layer - [Oc_3], and another with two cations in tetrahedral and one in octahedral coordination - [T_2Oc]. The polyhedral representation of the structure can be seen in figure 2. Octahedra occupied by Sn(1), Sn(2) and Sn(3) form six-member isolated rings, linked together by six octahedra with mixed occupancies. The electrostatic repulsion between the tin cations, occupying two adjacent edge-sharing octahedra leads to larger Sn – Sn distances within the [Oc_3] layer, causes elongation of the unit cell parameters *a* and *b*. This affects the observed c/a ratio which is lower than the ideal value. The Kagomé layer has two types of holes, one surrounded by six SnO_6 octahedra and the other by three $(Li^+/M^{2+})O_6$ and three SnO_6 octahedra. The octahedral holes in the [Oc_3] Kagomé layer are blocked by Sn^{4+} occupied octahedra and (Li^+/M^{2+}) occupied tetrahedra, while the Li^+ occupied tetahedra link groups of three octahedra, (two occupied by Sn^{4+} and one – by (Li^+/M^{2+})).

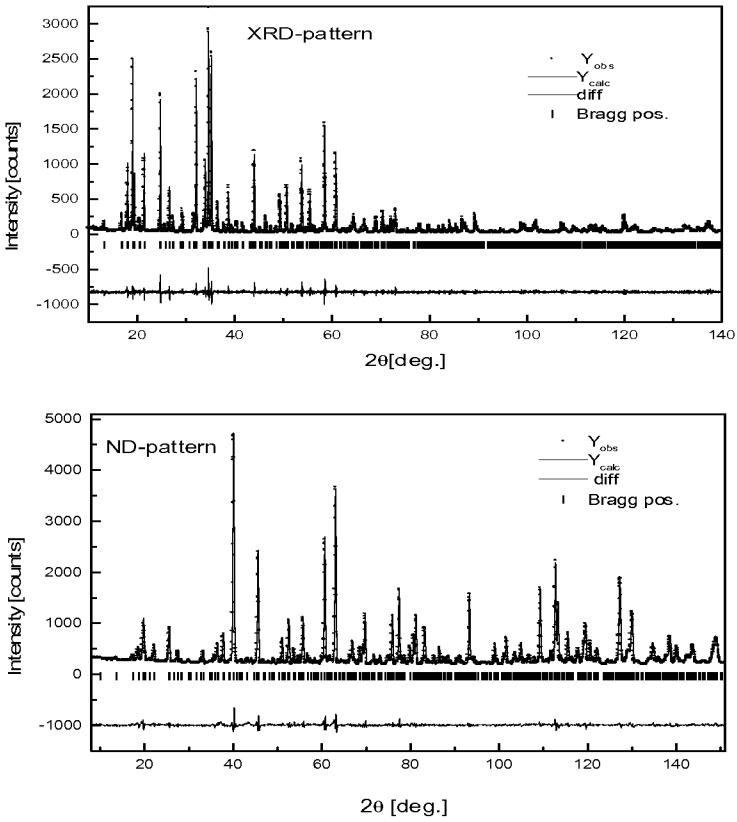

Figure 1. Common fit of XRD and neutron diffraction patterns for $Li_2CoSn_3O_8$.

The factors that determine the cation distribution in the DH-type structure were not discussed until now. From our point of view they have to be similar to the factors governing the cation distribution in the spinel structure, since the relationship between the two structure types is very close. Fortunately, for the spinel structure, many theoretical considerations and calculations have been made in order to identify and evaluate the factors that control cation distribution [9-14]. According to [12] the cation distribution in a crystal depends on the minimum of the free energy A = E - TS, there T is the absolute temperature, S is the entropy and E is the internal energy. The last term includes the electrostatic, the elastic, the electron bonding and the exchange contribution.

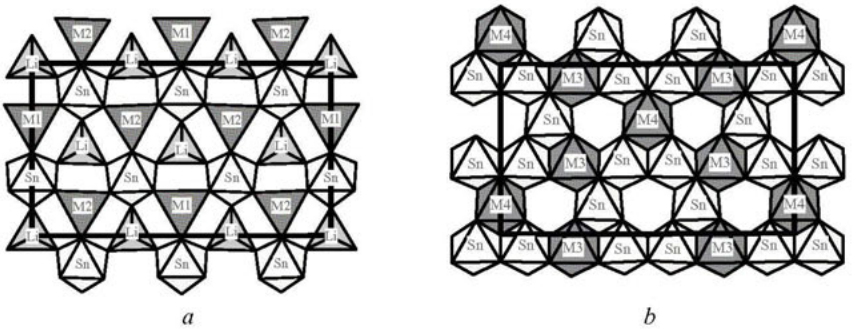

Figure 2. Projection of the structure of $Li_2MSn_3O_8$ (M=Mg, Co, Fe) along the c-axis. (a) [T_2Oc] layer and (b) [Oc_3] layer. Polyhedra denoted with M are mix-occupied by lithium and divalent metal ions.

The main factor that determines the distribution of cations comes from the electrostatic contribution. From this point of view, the mutual repulsive electrostatic force between high-valence cations occupying two adjacent edge-sharing octahedra is relatively high and leads to the lattice instability.

The second factor is geometrical or ion size factor. From this aspect the mixed occupation of one interstice by ions with different ionic radii would introduce high local distortions. The greater the size differences the higher the energy of the local strains and mixed occupancy will become unfavourable.

The factor usually called "site preference" is a complex one and accounts for the different character of chemical bonding and the crystal field effect related to the electron configuration (especially for the 3d-metal ions). The ionic character of the bonding corresponds to a higher coordination number thus ions with higher oxidation state will occupy more easily an octahedral site. For ions with predominant covalent or partially covalent type bonding the tetrahedral coordination is favourable.

The balance between the above-mentioned factors may be influenced by the phase composition and the synthesis conditions. The difference between DH and spinel type structures

originates from the difference in the oxygen layers sequence. This affects cation interactions between two adjacent layers. The DH structure is more compact then the spinel one, which has been shown by comparison of the molar volume of compounds crystallizing in both structure types [6]. We suppose that in the case of compact structure, the geometrical factor should play a dominant role in the cation distribution. Having these considerations in mind the explanation of the observed cation distribution in the DH phases seems to be reasonable.

In addition we have to mention the stoichiometry factor, i.e. the proportion of the different cations in the formula unit. For example, the composition $Li_{1.6}Zn_{1.6}Sn_{2.8}O_8$ [1] does not allow full cation ordering between two tetrahedral and two octahedral sites in the structure. Ordering occurs only in the [T_2Oc] layer, while [Oc_3] layer remains with statistical occupancy. The opposite case is realized with the composition $Li_2MnSn_3O_8$ [7], where cation ordering occurs not only in the [T_2Oc] layer (4 tetrahedral and 2 octahedral sites), but also in the [Oc_3] layer (5 octahedral sites). If the electrostatic factor was dominant, the cation disordering within the Oc_3 layer would minimize the repulsion and would stabilize the DH-structure. The observed two-dimensional ordering in the [Oc_3] layer for $Li_2ZnSn_3O_8$ and $Li_2MnSn_3O_8$ indicates that for both compositions the geometrical factor prevails over the electrostatic one. In this particular case, the difference between the octahedral ionic radii of Sn^{4+} (0.69) and Li^+ (0.76) [15] seems to be dominant and leads to the expulsion of Li^+ from the mixed sites into the linking sites of the Kagomé layers. Moreover, the site preference of Zn^{2+} and Mn^{2+} for tetrahedral coordination is in accordance with the higher degree of covalence for the bonds formed by the two ions [12, 14]. Thus a full cation ordering in the DH structure takes place. The site preference factor seems to be the most reasonable for explaining the cation distribution in the compounds $Li_2MSn_3O_8$ (M=Mg, Co, Fe). In the three compounds a mixed occupancy by lithium and the divalent metal ions occurs at two of the tetrahedral sites of the [T_2Oc] layer while the rest two sites remain occupied only by lithium. Mixed occupancy occurs also in the [Oc_3] layer, where octahedral positions linking six-member rings are occupied by mixed lithium and divalent metal ions. Considerations exposed in [14, 16] may be applied to the cation distribution observed in the compounds $Li_2MSn_3O_8$ (M=Mg, Co, Fe). The site preference of the Mg^{2+}, Fe^{2+} and Co^{2+} to the octahedral coordination before the tetrahedral is very weak and these ions compete with lithium ions for the octahedral sites. As a result the mixed occupancy of some tetrahedral and octahedral positions was observed. On the other hand the electrostatic factor seems to play more important role for the tetrahedral site occupation. As it was mentioned above, there are two different tetrahedral interstices. One of them connects groups of three octahedra, (two occupied by Sn^{4+} and one – by (Li^+/M^{2+})) and the presence of lithium ions in this tetrahedron decreases the electrostatic repulsion between two layers. The other tetrahedron is placed at one side of the empty octahedral position in the Kagomé layer and it may be occupied by ions with higher oxidation state.

Conclusions

New complex oxides with general formula $Li_2M(II)Sn_3O_8$ (M = Mg, Co, Fe) have been synthesized. The crystal structures were obtained from the simultaneous refinements of both X-ray and neutron powder diffraction data. The cation distribution of these phases can be regarded as an intermediate between those of the disordered $Li_{1.6}Zn_{1.6}Sn_{2.8}O_8$ and $LiFeSnO_4$

(space group $P6_3mc$) and the completely ordered $Li_2MnSn_3O_8$ (space group $Cmc2_1$). The factors that determine the cation distribution in the DH-type structure are: the stoichiometry, the electrostatic, the geometrical and the site preference factor. The balance between these factors may be influenced by the phase composition and the synthesis conditions. We suppose that in the case of compact structure, the geometrical factor should play a dominant role in the cation distribution. The site preference of Mg^{2+}, Fe^{2+} and Co^{2+} for the octahedral coordination rather than the tetrahedral is very weak and results in mixed occupancy of some tetrahedral and octahedral positions of the DH-structure.

References

1. Choisnet J. , Raveau B., 1979, *Mat.Res. Bull.* **14**, 1381.
2. Choisnet J., Hervieu M., Raveau B., Tarte P., 1981, *J. Solid State. Chem.*, **40**, 344.
3. Tarte P., Cahay R., Preudhomme J., Hervieu M., Choisnet J., Raveau B., 1982, *J. Solid State Chem.* **44**, 282.
4. Lacorre Rh., Hervieu M., Pannetier J., Choisnet J., Raveau B., 1983, *J. Solid State Chem.* **50**, 196.
5. Lacorre Rh., Hervieu M., Choisnet J.,. Raveau B, 1984, *J. Solid State Chem.* **51**, 44.
6. Choisnet J., Hervieu M., Raveau B., Tarte P., 1982, *J. Solid State. Chem.*, **45**, 280.
7. Kovacheva D., Trendafilova T., Petrov K., Hewat A., 2002, *J. Solid State Chem.* **169**, 44.
8. Rodriges-Carvajal J., 1993, *Physica B,* **192**, 55.
9. McClure D., 1957, *J. Phys. Chem. Solids,* **3,** 311.
10. Dunitz J., Orgel L., 1957, *J. Phys. Chem. Solids,* **3,** 20.
11. Dunitz J., Orgel L., 1957, *J. Phys. Chem. Solids,* **3,** 318.
12. Goodenough J., Loeb A., 1955, *Physical Review,* **98**, 391.
13. O`Neill H., Navrotski A., 1983, *Am. Miner.* **68**, 181.
14. Cormak A., Lewis G., Parker S., Catlow C., 1988, *J. Phys. Chem. Solids,* **49,** 53.
15. Shannon R., 1976, *Acta Crystallogr,* **A 32,** 751.
16. Grimes R., Anderson A., Heuer A., 1989, *J. Am. Chem. Soc,* **111**, 1.

Acknowledgements. Financial support from the Institute Laue-Langevin and from the Organizing Committee of EPDIC-9 is gratefully acknowledged.

Z. Kristallogr. Suppl. **23** (2006) 481-486

Crystal structure of the monoclinic $Ba_2MgSi_2O_7$ persistent luminescence material

T. Aitasalo[1,2], J. Hölsä[1], T. Laamanen[1], M. Lastusaari[1*], L. Lehto[1], J. Niittykoski[1,2], F. Pellé[3]

[1]University of Turku, Department of Chemistry, FI-20014 Turku, Finland
[2]Graduate School of Materials Research, Turku, Finland
[3]CNRS, UMR 7574, ENSCP, Chimie de la Matière Condensée de Paris, 11, r. P. et M. Curie, F-75231 Paris cedex 05, France
[*]Contact author; e-mail: miklas@utu.fi

Keywords: disilicate, crystal structure, powder diffraction, persistent luminescence

Abstract. Previously unknown structure of $Ba_2MgSi_2O_7$ persistent luminescence material was observed to be monoclinic with the space group *C2/c* (No. 15), $Z = 4$, $a = 8.41275(1)$, $b = 10.71005(1)$, $c = 8.43871(1)$ Å and $\beta = 110.71(1)^\circ$ based on X-ray powder diffraction data. The structure is composed of discrete $[Si_2O_7]^{6-}$ units connected by tetrahedrally coordinated Mg atoms to form sheets in the ac plane. Layers of eight-coordinated Ba atoms run parallel to the $Mg(Si_2O_7)$ sheets perpendicular to the unit cell *b* axis.

Introduction

Silicates with rigid and stable crystal structures are well known for their use as luminescent materials [1]. Persistent luminescence, *i.e.* afterglow, has usually been considered undesired for a phosphor material, but applications in *e.g.* exit signage have aroused a need for materials with long and intense afterglow. Modern persistent luminescence materials like $MAl_2O_4:Eu^{2+}$ (M = Ca, Sr) function by storing energy from both sun and lamp irradiation and then, due to thermal stimulation, gradually releasing the energy as visible light in the dark [2]. For $Ba_2MgSi_2O_7:Eu^{2+}$, Tm^{3+} an afterglow of over 6 hours has been observed [3].
Mixed alkaline earth/transition metal disilicates $M_2M'Si_2O_7$ (M = Ca, Sr and Ba; M' = Be, Mg, Fe, Co, Cu, and Zn) contain discrete $[Si_2O_7]^{6-}$ units formed by two corner-sharing SiO_4 tetrahedra. The most common crystal structure is of the tetragonal Åkermanite type with the space group $P\bar{4}2_1m$ (No. 113), $Z = 2$ [4-7]. Only $Ba_2CoSi_2O_7$ [8], $Ba_2ZnSi_2O_7$ [9] and $Ba_2CuSi_2O_7$ [10] possess a monoclinic structure with the space group *C2/c* (No. 15), $Z = 4$. Both structures have been reported for $Ba_2CoSi_2O_7$ [8,11]. $Ba_2MgSi_2O_7$, on the other hand, may crystallize in the Åkermanite type structure [12] or an unknown one for which only an experimental diffraction pattern has been reported [13]. The $Ba_2MgSi_2O_7:Eu^{2+}$, Tm^{3+} showing persistent luminescence [3] has this unknown crystal structure.

In this work, the unknown crystal structure of $Ba_2MgSi_2O_7$ was analyzed based on powder diffraction data and compared to the tetragonal one by bond valence calculations.

Experimental

Polycrystalline $Ba_2MgSi_2O_7$ was prepared by a solid state reaction between stoichiometric amounts of $BaCO_3$ (Merck, Pro Analysi), $Mg(NO_3)_2$ (Merck, Pro Analysi) and fumed SiO_2 (Sigma, 99.8 %) using firing for 1 h at 700 °C followed by annealing for 5 h at 1250 °C in a reducing N_2 + 12 % H_2 gas sphere. The sample was not doped with the luminescent Eu^{2+} ion. The X-ray powder diffraction pattern was measured at room temperature with a Huber 670 image plate (2θ range: 4-100°) Guinier camera using monochromatic copper $K_{\alpha 1}$ radiation (λ = 1.5406 Å). The dataset was summed from six 1/2 hour measurements. Preferred orientation was minimized by oscillating the sample horizontally.

The structure determination was carried out by using the following programs: XFit [14] (peak search), Crysfire [15] (indexing), Chekcell [16] (space group search), EXPO [17] (structure solution by direct methods), Fox [18] (structure solution by direct space methods) and FullProf2k [19] (refinement).

The bond valence calculations were carried out by using equation (1) [20], where s_{ij} is the bond valence, R_{ij} the experimental bond length, R_0 the characteristic length [21], and B an empirical parameter with a universal value of 0.37 [22]. The global instability index (GII) values compare the calculated bond valences and the formal valence (V_i) for all the species (N) in the asymmetric unit (equation 2) [23].

$$s_{ij} = exp[(R_0 - R_{ij})/B]. \quad (1)$$

$$GII = \sqrt{\sum_{i=1}^{N} [\sum_{j} (s_{ij} - V_i)^2 / N]} \; . \quad (2)$$

Structure Determination

The diffraction pattern was confirmed to be that of the unknown structure [13] and then indexed. The best observed/calculated reflections ratio of 22/55 was obtained with a monoclinic cell (a = 8.448, b = 10.726, c = 8.425 Å and β = 110.8°) and space groups Cc (No. 9) and $C2/c$ (No 15). This cell and the space groups indicated a similarity to the typical monoclinic $M_2M'Si_2O_7$ structure. Curiously, the pattern in ref. [13] did not yield this unit cell.

Parallel tempering with Fox [18] in the more symmetric $C2/c$ space group clearly proved the structural similarity to the $M_2M'Si_2O_7$ structure, whereas direct methods failed to produce the oxygen positions. Subsequently, the structure refinement was started in the $C2/c$ space group with the atomic positions of $Ba_2CoSi_2O_7$ [8] and a good agreement (R_{wp} = 7.89 and R_B = 4.75 %) between the observed and calculated patterns was obtained (Figure 1). Moreover, the unit cell (Table 1) and atomic positions (Table 2) yielded bond distances and angles (Table 3) that were in good agreement with those of $Ba_2CoSi_2O_7$ [8] and the Åkermanite type $Ba_2MgSi_2O_7$ [12]. Refinement was not attempted in the Cc space group, which has only general atomic positions, since even in $C2/c$, the lighter atoms very easily assumed positions with unphysical interatomic distances. In the final structural data (Table 2), some of the isotropic temperature factors are still not entirely realistic.

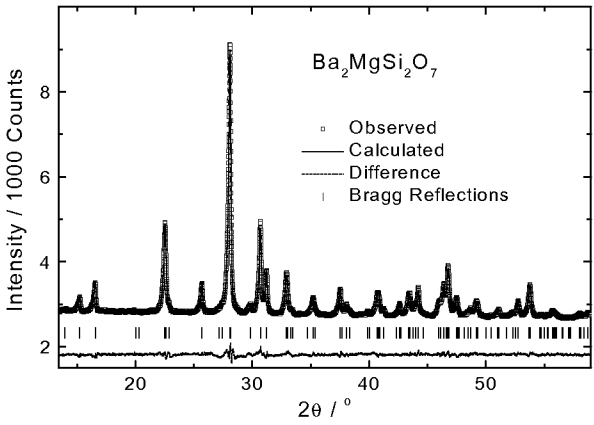

Figure 1. X-ray Rietveld plot of the monoclinic $Ba_2MgSi_2O_7$.

Table 1. Crystallographic data for the monoclinic and tetragonal [12] forms of $Ba_2MgSi_2O_7$.*

Space group	*C2/c* (No. 15)	$P\bar{4}2_1m$ (No. 113)
Z	4	2
a / Å	8.41275(1)	8.2036(4)
b / Å	10.71005(1)	
c / Å	8.43871(1)	5.4058(4)
β / °	110.71(1)	
V / Å^3	711.2	363.8
V:*Z* / Å^3	177.8	181.9
R_{wp} / % (background subtracted)	7.89	
R_B / %	4.75	
R_w / %		2.4
GII. / v.u.	0.11	0.16

*Single crystal data.

Table 2. Atomic positions and isotropic temperature factors for monoclinic $Ba_2MgSi_2O_7$.

Atom	Wyckoff symb.	Symmetry	*x*	*y*	*z*	*B* / Å^2
Ba	8f	C_1	0.2739(1)	0.45661(6)	0.0263(1)	0.96(2)
Mg	4e	C_2	0	0.2592(6)	1/4	0.49(9)
Si	8f	C_1	0.8892(8)	0.2825(3)	-0.1341(7)	1.56(9)
O1	4e	C_2	0	0.3345(7)	-1/4	2.07(27)
O2	8f	C_1	0.6992(10)	0.3432(7)	-0.2359(9)	0.03(25)
O3	8f	C_1	0.9727(11)	0.3528(8)	0.0428(10)	0.54(26)
O4	8f	C_1	0.8909(11)	0.1334(4)	-0.1317(10)	0.45(14)

Table 3. Bond distances and angles for $Ba_2MgSi_2O_7$ and $Ba_2CoSi_2O_7$.

Distances / Å and Angles / °	$Ba_2MgSi_2O_7$ *C2/c*	$Ba_2CoSi_2O_7$* [8] *C2/c*	$Ba_2MgSi_2O_7$* [12] $P\bar{4}2_1m$
Ba-O1	2.942(3)	2.947(3)	
Ba-O2	2.815(8)	2.828(4)	
Ba-O2	2.737(8)	2.732(4)	
Ba-O3	2.815(8)	2.818(4)	
Ba-O3	2.821(9)	2.836(4)	
Ba-O4	2.694(7)	2.693(4)	
Ba-O4	2.811(8)	2.814(4)	
Ba-O4	2.867(8)	2.864(4)	
<Ba-O>	2.813	2.817	2.793
M-O2 x2	1.971(9)	1.978(4)	1.966(4) x4
M-O3 x2	1.958(9)	1.963(4)	
<M-O>	1.965	1.971	1.966
Si-O1	1.667(6)	1.668(3)	1.665(3)
Si-O2	1.657(9)	1.628(4)	1.637(4) x2
Si-O3	1.596(10)	1.624(4)	1.600(6)
Si-O4	1.598(6)	1.611(5)	
<Si-O>	1.630	1.633	1.635
O2-M-O2	112.4(6)	112.9(3)	121.5(2) x2
O2-M-O3 x2	113.8(3)	114.3(2)	103.8(1) x4
O2-M-O3 x2	99.6(3)	99.1(2)	
O3-M-O3	118.4(6)	117.9(3)	
<O-M-O>	109.6	109.6	109.7
O1-Si-O2	101.6(4)	103.3(2)	103.6(2) x2
O1-Si-O3	103.8(4)	103.5(2)	
O1-Si-O4	109.7(5)	109.2(3)	109.7(3)
O2-Si-O3	109.0(5)	108.3(2)	108.1(3)
O2-Si-O4	113.7(5)	115.2(2)	115.4(2) x2
O3-Si-O4	117.4(5)	115.9(2)	
<O-Si-O>	109.2	109.2	109.3
Si-O1-Si	141.0(6)	142.2(43)	144.3(5)

*Single crystal data.

Structural Details

The structure is built up of alternating Ba and $Mg(Si_2O_7)$ layers perpendicular to the unit cell *b* axis. The discrete $[Si_2O_7]^{6-}$ units, with O1 as the linking oxygen for the two distorted eclipsed SiO_4 tetrahedra, are connected in the *ac* plane by Mg atoms coordinated tetrahedrally

to oxygens. The barium atoms are sandwiched between a triangle and a pentagon of oxygens nearly parallel to one another resulting in an eight-coordination.

The variation of the observed Si-O bond lengths is slightly larger than in $Ba_2CoSi_2O_7$ but in good agreement with the tetragonal type (Table 3). Also, the Si-O-Si angle falls between the range (139.4-144.3°) reported for the Åkermanite type $M_2MgSi_2O_7$ [12]. The Si-O bond to the bridging oxygen, however, is not as clearly the longest one as one would expect, but this is probably due to the fact that the data in this work was obtained from powder rather than single crystals. The observed bond lengths and angles in the distorted MgO_4 tetrahedron are in good agreement with those in the other $M_2M'Si_2O_7$ with similar M' ionic radii, *i.e.* in the Cu [5, 10], Co [4, 8], Zn [4, 9], and Mg [4, 12] compounds.

Both structural types of $Ba_2MgSi_2O_7$ are layered and they contain the isolated $[Si_2O_7]^{6-}$ units. The most striking difference is the orientation of the disilicate anions. If the structures are viewed as projections on the *ab* (tetragonal) and *ac* planes (monoclinic) (Figure 2), the next disilicate unit along the monoclinic -101 direction is obtained from the previous one by a translation followed by a reflection on the *ac* plane, whereas along the tetragonal 110 direction a 90° rotation on the *ab* plane is required, as well. Thus, the monoclinic structure is not merely a distorted tetragonal one, but a result of a rather drastic rearrangement of the $Mg(Si_2O_7)$ layer. Another structural difference is the distorted tetragonal antiprismatic coordination (4+4) for Ba in the tetragonal type in contrast to the 3+5 one in the monoclinic form.

It seems that the ratio of the ionic radii of the M and M' cations largely determines the type of structure that is formed for $M_2M'Si_2O_7$. The Åkermanite type is preferred with a ratio below *ca.* 2.3. The one exception is $Ca_2BeSi_2O_7$ [4] with the ratio of 4.1, which probably possesses the looser tetragonal structure because the small Be^{2+} ions would make the monoclinic type $Be(Si_2O_7)$ layer too tight and thus bring the Ca^{2+} ions too close together.

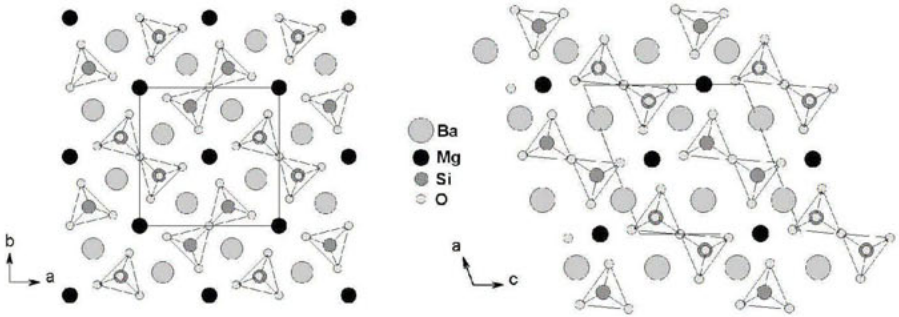

Figure 2. Comparison of the atomic arrangements in the tetragonal (left) and monoclinic (right) forms of $Ba_2MgSi_2O_7$.

The bond valence calculations revealed no discrepancies in either of the structure types of $Ba_2MgSi_2O_7$ and the *GII* values of both forms (Table 1) stay well below the 0.2 v.u. considered as the limit above which a crystal structure becomes unstable facing a possible collapse [23]. The lower *GII* value for the monoclinic form for both $Ba_2MgSi_2O_7$ and $Ba_2CoSi_2O_7$ (GII_{Mon} = 0.12 and GII_{Tetr} = 0.21) may be an indication of a preference for this structure in agreement with the fact that the monoclinic form can be prepared by a solid state reaction [8], while the Åkermanite type requires a melt or a flux [11, 12].

References

1. Shionoya, S. & Yen, W.M. (Eds.), 1999, *Phosphor Handbook* (Boca Raton FL: CRC Press).
2. Aitasalo, T., Hölsä, J., Krupa, J.-C., Lastusaari, M. & Niittykoski, J., 2003, in *Physics of Laser Crystals*, Nato Science Series II: Mathematics, Physics and Chemistry, Vol. 126, edited by J.-C. Krupa & N.A. Kulagin (Dordrecht: Kluwer), pp. 35-50.
3. Aitasalo, T., Hölsä, J., Laamanen, T., Lastusaari, M., Lehto, L., Niittykoski, J. & Pellé, F., 2005, *Ceram.-Silikáty*, **49**, 13.
4. Kimata, M., 1983, *Z. Kristallogr.*, **163**, 295.
5. Tovar, M., Dinnebier, R.E. & Etsel, W., 1998, *Mater. Sci. Forum*, **278-281**, 750.
6. Kusaka, K., Hagiya, K., Ohmasa, M., Okano, Y., Mukai, M., Iishi, K. & Haga, N., 2001, *Phys. Chem. Miner.*, **28**, 150.
7. FIND IT v. 1.3.1, 2003, *FIZ/NIST Inorganic Crystal Structure Database*, Database December 2003, (Fachinformationszentrum Karlsruhe).
8. Adams, R.D., Layland, R., Payen, C. & Datta, T., 1996, *Inorg. Chem.*, **35**, 3492.
9. Kaiser, J.W. & Jeitschko, W., 2002, *Z. Kristallogr. - New Cryst. Struct.*, **217**, 25.
10. Malinovskii, Y.A., 1984, *Sov. Phys. Dokl.*, **29**, 706.
11. El Bali, B. & Zavalij, P.Y., 2003, *Acta Crystallogr.*, **E59**, i59.
12. Shimizu, M., Kimata, M. & Iida, I., 1995, *N. Jb. Miner. Mh.*, H1, 39.
13. Klaesens, H.A., Hoekstra, A.H. & Cox, P.M., 1957, *J. Electrochem. Soc.*, **104**, 93.
14. Coelho, A.A. & Cheary, R.W., 1997, *X-ray Line Profile Fitting Program, XFIT*, School of Physical Sciences, University of Technology, Sydney, Broadway, New South Wales, Australia.
15. Shirley, R., 2000, *The CRYSFIRE System for Automatic Powder Indexing: User's Manual* (Guilford: Lattice Press).
16. Laugier, J. & Bochu, B., 2002, *CHEKCELL, Powder Indexing Helper Tool for Unit Cell and Spacegroup Assignment*, LMGP, ENSP Grenoble (INPG), Domaine Universitaire, BP 46, F-38402 Saint Martin d'Hères, France.
17. Altomare, A., Burla, M.C., Camalli, M., Carrozzini, B., Cascarano, G.L., Giacovazzo, C., Guagliardi, A., Moliterni, A.G.G., Polidori, G. & Rizzi, R., 1999, *J. Appl. Cryst.*, **32**, 339.
18. Favre-Nicolin, V. & Cerny, R., 2002, *J. Appl. Cryst.*, **35**, 734.
19. Rodriguez-Carvajal, J., 2002, *FullProf.2k (Version February 2002)*, Laboratoire Leon Brillouin (CEA-CNRS), Gif-sur-Yvette, France, unpublished.
20. Zachariasen, W.H., 1978, *J. Less-Common Met.*, **62**, 1.
21. Brese, N.E. & O'Keeffe, M., 1991, *Acta Crystallogr.*, **B47**, 192.
22. Brown, I.D. & Altermatt, D., 1985, *Acta Crystallogr.*, **B41**, 244.
23. Salinas-Sanchez, A., Garcia-Muñoz, J.L., Rodriguez-Carvajal, J., Sáez-Puche, R. & Martinez, J.L., 1992, *J. Solid State Chem.*, **100**, 201.

Z. Kristallogr. Suppl. **23** (2006) 487-492

Cation distributions in fully hydrated Sr- and Rb- bicationic zeolites: an X-ray anomalous powder diffraction study

H. Palancher[1,2], C. Pichon[1*], J. L. Hodeau[2], J. F. Bérar[2,3], J. Lynch[1], B. Rebours[1] and J. Rodriguez-Carvajal[4]

[1]Institut Français du Pétrole, BP3 69390 Vernaison, France
[2]Laboratoire de Cristallographie, CNRS BP166X 38042 Grenoble, France
[3]French CRG D2AM, ESRF, BP220 38043 Grenoble, France
[4]Laboratoire Léon Brillouin, CEA/CNRS, CEA-Saclay, 91191 Gif/Yvette, France
[*]Contact author; e-mail: christophe.pichon@ifp.fr

Keywords: X-ray anomalous powder diffraction, zeolite X, cation distribution, full hydration.

Abstract. X-ray anomalous powder diffraction studies on bicationic X zeolites at high water loading has shown preference for occupation by Sr^{2+} cations of sites I', II and the disordered positions in the supercage (site *) whatever the other cation (Ca^{2+}, Rb^{+}). Rb^{+} occupies preferentially site II, then site* if enough of these cations are present. Ca^{2+} shows strong preference for site I' and site * in SrCaX and RbCaX. In all samples studied, site II' is mainly populated by water molecules.

Introduction

Industrial background

Adsorption properties of molecular sieves such as X, Y zeolites are widely used in industrial processes (in particular for separation and purification of hydrocarbon isomers). Adsorption selectivity of these materials depends strongly on the type, the number and the location of cations in the structure where they compensate the negative charge of the framework. Knowledge of cation distribution on each site is of great interest in the search for better molecular sieves which could be based on bicationic zeolites. However, for this type of solid, very few studies are reported in literature and most have been performed at a high dehydration level [1, 2, 3, 4].

In this paper, we describe, using X-ray anomalous powder diffraction, the evolution of Sr^{2+} and Rb^{+} distributions at high hydration level with the amount and nature of other elements present.

Limits of conventional XRD for cation distribution study in bicationic zeolites

In faujasite structures [5], cations occupy known sites (cf. figure 1-a). Commonly used for cation distribution determination in molecular sieves, conventional XRD (X-ray diffraction) is limited when characterising bicationic zeolites: two different cations can be located in nearby atomic positions.

In dehydrated samples, the precise position of each cation is driven by its ionic radius since cations are bonded with framework oxygen atoms. For example, in SrRbX, Sr^{2+} and Rb^{+} cation positions can be differentiated in the electron density map (derived from the inversed Fourier transform of the structure factors calculated from the integrated peak intensities), because the large difference of atomic radii of the two elements (r_{Sr2+} = 1.18 Å and r_{Rb+} = 1.52 Å) leads to slightly different site positions (figure 1-d). However, when trying to determine Sr^{2+} and Ca^{2+} cation location in SrCaX (r_{Ca2+} = 1.00 Å), the electron densities due to Ca^{2+} and Sr^{2+} overlap (figure 1-e): electron density on site II exhibits the same shape as that measured on the monocationic SrX (figure 1-c).

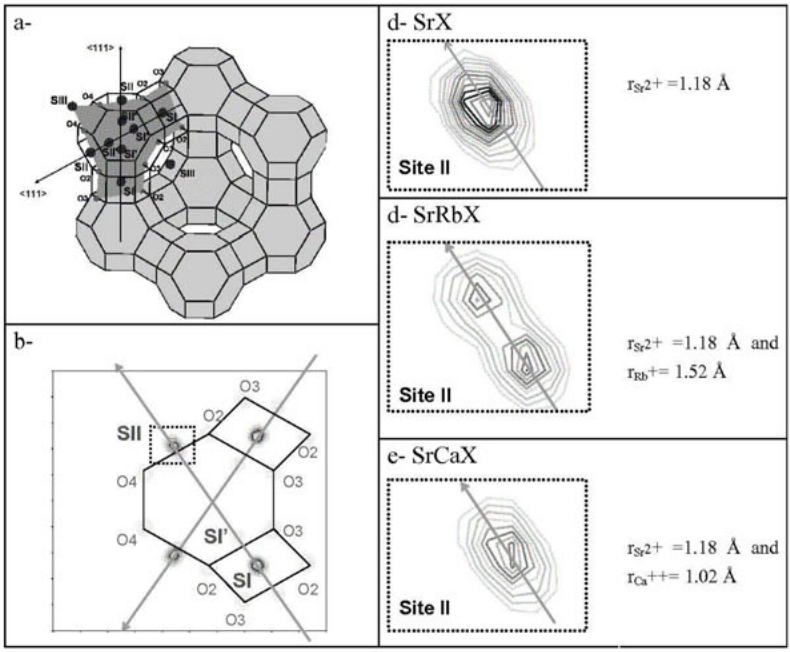

Figure 1. Study of population of cation site II on electron density maps in the plane P (represented in fig. a- and b-) in three dehydrated samples SrX (c-), SrRbX (d-) and SrCaX (e-).

This kind of problem (overlap of electron densities due to different species) may also be encountered in hydrated monocationic samples since water molecules can be adsorbed near cation sites [1, 2]. In addition, since other water molecules can form hydrogen bonds with cations, chemical bond lengths between these cations and oxygen framework atoms may

exceed the sum of ionic radii [6]. Taking into account that no clear information about this increase is available in literature, the interpretation of electron density map derived from a single powder pattern is particularly difficult.
Additional information is therefore needed to distinguish these species. Accurate investigation of Rb^{+} and Sr^{2+} distributions in water saturated samples ($r_{O^{2-}}$ = 1.40 Å and $r_{Rb^{+}}$ = 1.52 Å) requires the chemical contrast enhancement given by the use of anomalous X-ray diffraction. This phenomenon leads to variations with energy of the atomic scattering factor of an element under an X-ray beam of energy close to one of its absorption edges. The wide range of applications of this technique has been reviewed recently [7].

Experimental section

Sample preparation
In a first step, SrX and CaX zeolites were prepared by aqueous ion exchange from a NaX sample at 353 K [8] (two ion exchange steps were required for CaX). SrRbX, SrCaX and RbCaX bicationic samples, not previously reported in literature to our knowledge, were prepared using the same procedure starting from:

- SrX for SrRbX, SrCaX,
- CaX for RbCaX.

Starting from the same NaX powder, two successive aqueous ion exchange steps were performed to obtain RbNaX. It was not possible for our sample to achieve full ion exchange as reported in [9]. After each ion exchange step, the samples were activated at 573 K under nitrogen flow before slow re-hydration whilst decreasing the temperature to 293 K.
Elementary and thermogravimetric analyses coupled with an XRD study of dehydrated samples give the unit cell content as:

- $Sr_{39}Na_4Si_{108}Al_{84}O_{384}$, 257 H_20 (for SrX),
- $Sr_{32}Rb_{17}Na_4Si_{108}Al_{84}O_{384}$, 211 H_20 (for SrRbX),
- $Sr_{24}Ca_{18}Na_1Si_{108}Al_{84}O_{384}$, 250 H_20 (for SrCaX),
- $Rb_{19}Ca_{31}Na_4Si_{108}Al_{84}O_{384}$, 200 H_20 (for RbCaX),
- $Rb_{44}Na_{37}Si_{108}Al_{84}O_{384}$, 195 H_20 (for RbNaX).

Note that electro-neutrality of these structures is obtained.
SrX, SrCaX, SrRbX, RbCaX, RbNaX samples have been characterised at high hydration level at 293 K using X-ray diffraction.

X-ray anomalous diffraction data collection
Diffraction patterns (see for ex. figure 2) have been collected over a wide angular range (up to at least $\sin\theta/\lambda$=0.57 $Å^{-1}$) on the synchrotron radiation beamline BM2 at the ESRF.
For anomalous diffraction studies, measurements were performed at the Rb K absorption edge, at 15192 eV (about 10 eV below the absorption edge (E_K(Rb)-10 eV)) and at 14800 eV (approximately E_K(Rb)-400 eV) and, for the Sr K absorption edge, at 16096 eV (E_K(Sr)-10 eV) and at 15192 eV (E_K(Sr)-900 eV). The SrRbX sample was characterised at both Sr and Rb absorption edges.

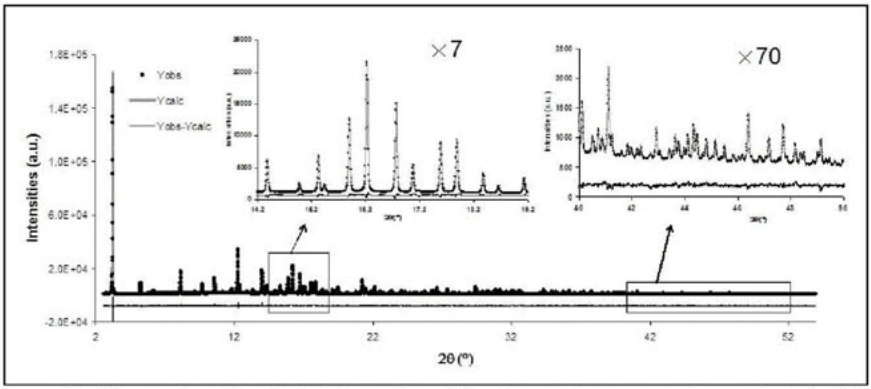

Figure 2. Measured and calculated powder diffraction pattern on water saturated CaSrX (E=15192 eV) at 293 K.

X-ray anomalous diffraction data treatment

A methodology for anomalous powder diffraction data analysis has been established including simultaneous refinement of all diffraction patterns using FullProf software package [10]. Its effectiveness has been validated by the determination Sr^{2+} and Rb^{+} cation distributions in hydrated [11] and dehydrated [12] SrRbX ($Z_{Rb}+ = Z_{Sr}2+ =35$ e.u. and $b_{Rb} \approx b_{Sr} \approx 0.7.10^{-12}$ cm^{-1} with Z: number of electrons (which determines the scattering factor for X-rays) and b: scattering length for neutrons). The efficiency of this technique in probing sites located on the (111) axis (sites I, I', II', II) is far better than when analysing the sites in the supercage, out of this axis (sites labelled site*), which are characterised by a high Debye-Waller factor and often high symmetry (96 or 192 equivalent positions in unit cell). Therefore, the amount of cations occupying the latter sites is deduced from the difference between the total number of cations (from chemical analysis) and the sum of cations located on sites I, I', II', II by Rietveld refinement.

XRD data refinement was performed in Fd-3m space group. For each data collection energy, final agreement factors are low (i.e. all calculated R_{Bragg} range from to 2.5 to 3.8 %). The numbers of water molecules determined by thermogravimetric and XRD studies are in close agreement: respectively 257 c.f. 286 H_20 for SrX, 250 c.f. 284 for SrCaX, 211 c.f. 260 for SrRbX, 200 c.f. 254 for RbCaX and 195 c.f. 230 for RbNaX.

Effect of substitution on cation distribution

Distributions of extra-framework species are reported in table 1 and 2. Their complexity must be underlined: some water molecules have been located on each cation site. On site II', they are the only species present (except in SrX where residual Sr^{2+} cations have been also located on this site).

Table 1. Cations and water molecules distributions in hexagonal prisms and sodalite cage (sites I, I' and II') in highly hydrated SrX, SrCaX, SrRbX, RbCaX, RbNaX.at 293 K.

	Site I					Site I'					Site II'	
	Sr^{2+}	Ca^{2+}	Rb^{+}	Na^{+}	H_20	Sr^{2+}	Ca^{2+}	Rb^{+}	Na^{+}	H_20	Sr^{2+}	H_20
SrX	0	---	---	0	11.1	12.7	---	---	4£	4	1	27.3
SrCaX	0	0.9	---	0	7.0	8.1	12.2	---	0	0	0	28.8
SrRbX	0	0	1.2	0	4.0	17.0	---	0	0	0	0	32.0
RbCaX	---	0	0	0	0	---	23	0	4£	0	---	32.0
RbNaX	---	---	0	7.5	0	---	---	0	19.1	0	---	31.4

£ Occupancies fixed by chemical analysis.

Table 2. Cations and water molecules distributions in the supercage (site II and site) in highly hydrated SrX, SrCaX, SrRbX, RbCaX, RbNaX.at 293 K.*

	Site II					Site*				
	Sr^{2+}	Ca^{2+}	Rb^{+}	Na^{+}	H_20	Sr^{2+}	Ca^{2+}	Rb^{+}	Na^{+}	H_20
SrX	11.5	---	---	0	13.6	14.5	---	---	0	230
SrCaX	6.6	0	---	0	11.4	9.9	4.9	---	0	237
SrRbX	5.7	---	16.1	0	6.5	8.6	---	0	4£	217
RbCaX	---	0	19.1	0	0	---	7.5	0	0	222
RbNaX	---	---	24.0	7.0	7.5	---	---	19.0	9.2	191

£ Occupancies fixed by chemical analysis.

Sr^{2+} cation distributions

Our cation distributions in $Sr_{39,5}Na_4X$ are close to those obtained previously on $Sr_{42}X$ [13] (12.7 c.f. 11.1 on site I' and 11.5 c.f. 15.0 on site II) except for site I which is clearly not occupied by Sr^{2+} cations in our study (2.1 Sr^{2+} cations were found on site I in the earlier study). Moreover residual presence of Sr^{2+} in site II' can be noticed in SrX. In the three Sr containing solids analysed here, Sr^{2+} is mainly located in site I', II and in the supercage in a complex arrangement with water molecules. In SrRbX, the presence of 16 Rb^{+} cations per unit cell in site II compels Sr^{2+} to move from the supercage (the fraction of Sr cations in site II falls from 0.29 to 0.18 and that of site* from 0.37 to 0.27) to site I'. Introduction of Ca^{2+} cations, which strongly prefer site I' and site* (Ca^{2+} cations do not occupy site II in CaRbX and CaSrX), does not modify the Sr^{2+} cations distributions (i.e. only the total per unit cell, not the proportion on each site, is affected). No evidence of occupation of site I by Sr^{2+} has been found at this high hydration level.

Rb^{+} cation distributions

In $Rb_{44}Na_{37}X$, no presence of Rb^{+} cations in the sodalite cage or hexagonal prism is suggested by this anomalous diffraction study, in contrast with previous results [1]. Differences in the Rb^{+} exchange rate or in the hydration level may explain this observation. However, in both cases no additional cations may be added on sites I and I' (the proximity between sites I and I' implies constraints on the populations [1]). In the solids studied here, Rb^{+} cations

prefer site II. At high exchange rates (RbNaX) site* is occupied by Rb^+ cations, their presence in sodalite cage or in hexagonal prism (noticed only in SrRbX) remaining very limited due to their large size.

Conclusion

Cation distributions in bicationic X zeolites exchanged with alkaline (Rb^+) and alkaline-earth (Ca^{2+}, Sr^{2+}) cations have been investigated because of their possible use as molecular sieves, in the separation process of (meta- and para-) xylene isomers (after KBaY, BaX zeolite is nowadays used at an industrial scale). Interest of anomalous diffraction studies in bicationic zeolites at high water loading has been demonstrated. In these adsorption conditions, preference of Sr^{2+} cations for sites I', II and sites* has been established (in SrX, SrRbX and SrCaX) whilst Rb^+ cations occupy mainly site II and then site* if Rb^+ quantity is sufficient.
At this stage, accurate characterisation of bicationic zeolites under dynamic adsorption conditions by anomalous X-ray diffraction is possible on the basis of this experience of highly loaded samples and of the development of a dedicated reaction cell [14].

References

1. Shepevlev, Yu.F., Butikova, I.K. & Smolin, Yu.I., 1991, *Zeolites* **11**, 287.
2. Norby, P., Poshni, F.I., Gualtieri, A.F., Hanson, J.C. & Grey, C.P., 1998, *J. Phys. Chem.* B, **102**, 839.
3. Kirschhock, C.E.A., Hunger, B., Martens, J. & Jacobs, P.A., 2000, *J. Phys. Chem.* B, **104**, 439.
4. Wilkinson, A.P., Cheetham, A.K., Tang, S.C. & Reppart, J., 1992, *Chem. Commun.*, 1485.
5. Detailed description of faujasite framework and building schemes can respectively be found in the web atlas (http://topaz.ethz.ch/IZA-SC/StdAtlas.htm) and at the web address (http://www.iza-structure.org/databases/ModelBuilding/EMT.pdf).
6. Olson, D.H., 1970, *J. Phys. Chem.*, **74**, 2758.
7. Hodeau, J.L., Favre-Nicolin, V., Bos, S., Renevier, H., Lorenzo, E. & Berar, J.F., 2001, *Chem. Rev.*, **101**, 1843.
8. Sherry, H.S., 1968, *J. Phys. Chem.*, **72**, 4086.
9. Sherry, H.S., 1966, *J. Phys. Chem.*, **70**, 1159.
10. Rodriguez-Carvajal, J., 2002, FullProf version 2.10 LLB, CEA/Saclay, France, http://www-llb.cea.fr/fullweb/poudres.htm.
11. Palancher, H., Hodeau, J.L., Pichon, C., J. Lynch, Berar, J.F., Rebours, B. & Rodriguez-Carvajal, J., 2005, *Angew. Chem. Int. Ed.*, **44**, 1725-1729.
12. Hodeau, J.L., Nassif, V., *et al.*, 2003, *ECM-21 Durban* (South Africa).
13. Olson, D.H. & Sherry, H.S., 1968, *J. Phys. Chem.*, **72**, 4095.
14. Palancher, H., Pichon, C., Hodeau, J.L., Lynch, J., Rebours, B., Berar, J.F., Prevot, S., Conan, G. & Bouchard, C., 2005, *J. Appl. Crystallogr.*, **38**, 270.

Z. Kristallogr. Suppl. **23** (2006) 493-498

Model of structure disorder of illite: preliminary results

S. Ferrari[1,*], A. F. Gualtieri[1], G. H. Grathoff[2], M. Leoni[3]

[1]University of Modena and Reggio Emilia, Department of Earth Sciences, Via S.Eufemia, 19, 41100, Modena, Italy
[2]Portland State University, Department of Geology PO Box 751 Portland, OR 97207-0751, USA
[3]University of Trento, Department of Materials Engineering and Industrial Technologies, Via Mesiano, 77, 38050, Trento, Italy
[*]Contact author; e-mail: ferrari.simone@unimore.it

Keywords: illite, powder diffraction, structure disorder, pattern simulations

Abstract. This paper presents preliminary results of the structure model of a pure illite sample from Hungary. The clay sample mined in the Tokaj region (Northern Hungary) is composed of predominating illite and minor smectite and quartz. Enrichment by sedimentation in water solvent of the illite fraction led to a nearly pure sample which was fully characterized using conventional microscopic and chemical analyses. Although, illite is a well known clay mineral used for many industrial applications (its crystallinity index is used to establish the degree of illitization in oil source rocks linked to oil generation) a structure model has never been refined to date. This is due to the fact that pure samples to be used for structure characterization are a rarity in nature and because the structure is affected by extensive planar disorder. Thus, the structural characterization of this sample is of great importance for the understanding of the structure of illite in general. The planar disorder prevents a simple structure refinement using the Rietveld method and different algorithms must be used. Here, we present the results of structure simulations of powder patterns using NEWMOD, WILDFIRE and DIFFaX, which reveal the structure features and structure model of disorder. They are a good starting point for the combined structure/microstructure refinement which will be attempted using DIFFaX$^+$.

Introduction

The term illite [1] refers to an aluminum-potassium mica-like, non-expanding, dioctahedral mineral, present in the clay fraction (<4 μm). Illite crystallizes in the monoclinic system, and its structure is very similar to that of 2:1 mica where two tetrahedral sheets sandwich an octahedral sheet to build up a TOT sequence [2]. In nature, illite shows several polytypes; the same polytypes present in muscovite (1M, $2M_1$, $2M_2$, 3T), and the polytype $1M_d$ (turbostratic), completely disordered, have been recognized. An approximate formula for illite is: $K_{0.88}Al_2(Si_{3.12}Al_{0.88})O_{10}(OH)_2$ [3-6].

The most important method to study disordered structures is the simulation of powder patterns. Many codes that perform simple simulations of defective layered structures appeared in literature. NEWMOD [7] can be considered as one of the ancestors, followed by many other programs, such as WILDFIRE [8,9]. Perhaps the most straightforward definition of a defective stack is that proposed by Treacy et al. [10] in recursive terms. The outcome of the work of Treacy et al. is DIFFaX (Diffracted Intensity from Faulted Xtals).
The strategy of action used in this project accomplishes: (i) full chemical, mineralogical and physical characterization of the sample; (ii) preliminary qualitative and semi-quantitative investigation of the structure model and structure disorder via simulations using NEWMOD, WILDFIRE and DIFFaX; (iii) final quantitative characterization of the structure model and structure disorder via combined structure/microstructure refinement attempted using DIFFaX$^+$ [11]. DIFFaX$^+$ has been proposed to overcome some of the limitations of DIFFaX, allowing all instrumental, structural and microstructural parameters to be refined using the available diffraction data. In this work, the results of the first two steps for the study of illite from Northern Hungary are presented.

Experimental method

The illite sample was collected in the Hungarian mine in the Tokaj mountains near Sátoraljaújhely, in the North-East of Hungary. The X-ray powder diffraction (XRPD) qualitative analysis using a Philips PW1729 Diffractometer evidenced only illite and quartz. The sample was hand-ground in an agate mortar, and a few grams of powder put in a sedimentation tube for 70 h with water solvent to separate the fraction <1.5 μm. XRPD on that separated fraction confirmed the presence of illite only. A the measurement with a very good counting statistics was then collected to be used for the pattern simulations (from 3 to 130 °2θ, step of 0.02 °2θ, 35 s/step, 40 kV and 30 mA, slits of 1/4°, 0.2 mm, 1/4°). The sample was side-loaded on an aluminum holder to minimize the effect of preferred orientation. On the separated fraction, the chemical content has been determined by XRF with an X-ray Spectrometer Philips PW1480. Images at microscopic scale were collected using a Jeol JEM 2010 TEM. SEM and FTIR data were also collected but will not be shown here.
The study of structural model and disorder was first attempted simply by a structure refinement using GSAS [12]. Since the fit was clearly unsatisfactory, simulation of the observed pattern were performed using the suites NEWMOD, WILDFIRE and DIFFaX. WILDFIRE can simulate several powder patterns of the different polytypes in illitic material mixtures. Disorder is a function of the number of rotations between the 2:1 sheets, of the cis/trans-vacant sites ratio in the octahedral sheet and of the percentage of expandable layers [13]. The possible rotations are 60°, 120°, 180°, 240° and 300°. Besides these characteristics, WILDFIRE can also take under consideration the number of cells, preferred orientation, the mean defect-free distance along *c* direction, and the K and Fe content in the unit cell. NEWMOD, allows the simulation of the basal peaks series in several sheet silicates, such as clay minerals.

Results and discussion

The sample purity of the separated clay fraction, after the 70 h long (particles with average grain size < 1.5 μm) was confirmed by the powder pattern shown in figure 1. Analysing the *d* values, we concluded that most of the sample is composed of polytype 1M, since reflections at 3.66 and 3.08 Å (1M reflections) are much larger than the ones at 3.89 and 2.89 Å ($2M_1$ reflections). We can also notice a "bell-shaped" background in the range 22-32 °2θ: this is due to the content of n60° stacking faults in illite structures, as suggested by Drits et al. [14]. The chemical composition (wt%) of the illite sample (SiO_2 50.2%, TiO_2 0.08%, Al_2O_3 30.39%, Fe_2O_3 0.33%, MgO 3.45%, MnO 0.01%, CaO 0.24%, Na_2O 0.17%, K_2O 7.03%, P_2O_5 0.07%, H_2O 8.04%) led us to conclude that the chemical content matches that of other illites described in the literature: Kaube illite [1] and Imt-1 from the Source Clay Repository. The TEM image of the illite particles shows that they are lath-shaped (figure 2). Some broken platy crystals, indicating that the original shape was very similar to a pseudo-hexagonal one, are also observed.

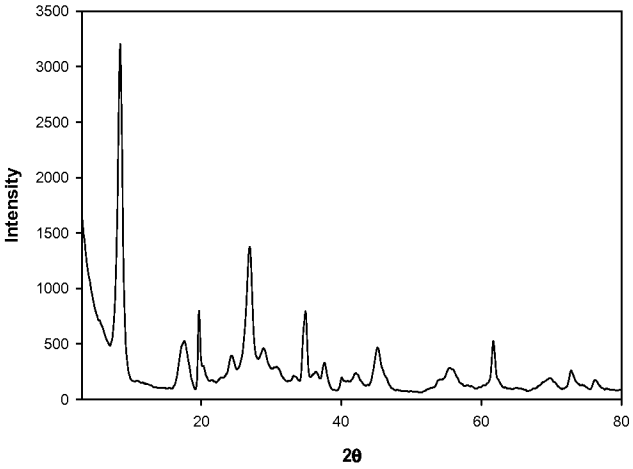

Figure 1. Zoom of the powder pattern of the Hungarian illite in the range 3-80 °2θ.

Early attempts to refine the structure of this illite with the Rietveld method using GSAS failed, a confirmation of the limits of the Rietveld method with structures affected by extensive planar disorder. The agreement factors of the best refinement were unsatisfactory (W_{Rp} = 48% and $R(F^2)$ = 59%).

A systematic study was performed using WILDFIRE. As an example, figure 3 shows two selected simulations compared to the observed pattern in the range 16-44 °2θ (the maximum angular range the software can deal with). Simulation S1 shows correct peak positions although the fit of the intensities is very poor. For this simulation, only trans-vacant positions and shifts without rotation (P_0) equal to 65% were considered. Simulation S2 shows that the

problem of the intensities has been reduced by correcting for the preferred orientation of the basal reflections with the Dollase model S2 is the best obtained result.

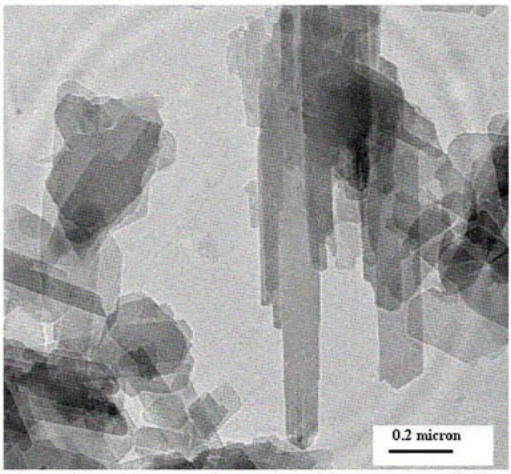

Figure 2. TEM image of particles of the investigated illite.

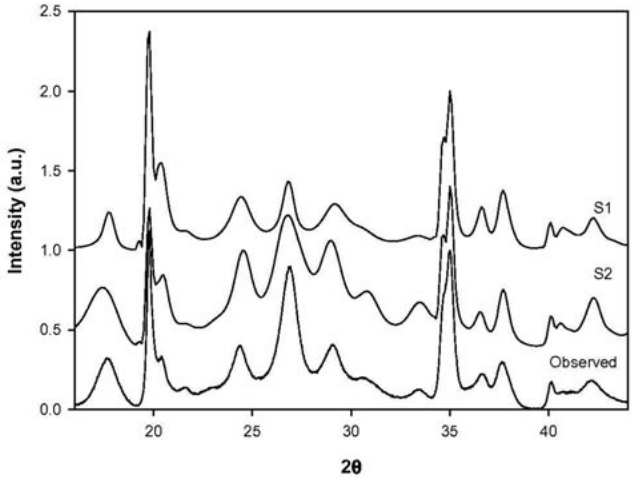

Figure 3. Simulations of the Hungarian illite XRD with WILDFIRE.

The use of the software with NEWMOD allows us to determine the presence of 10% of expandable layers, very common in natural illites. The best simulation has been made under these conditions: 10% of expandability, 75% of Dollase factor, 30% of cis-vacant layers,

75% of P_0. Thus, the predominant polytype of the Hungarian illite is 1M, since pure 1M is characterized only by shifts without any type of rotation. The presence of both cis- and trans-vacant layers can also be confirmed by the DTG analysis, in fact the two types of layers show different dehydroxylation temperatures [15]: 670 °C for the earlier and 550 °C for the latter; respectively. Since both peaks are present and the area of the trans-vacant is larger than the other, we confirm that both types are present in our sample and trans-vacant layers are more abundant than cis-vacant.

The other code used for the simulations is DIFFaX. The models we used were based on three types layers: 1) ideal orthonormalized layer, 2) ideal layer 60° rotated, 3) ideal layer 120° rotated. The combination of different probabilities of existence of the layers, together with the variation of parameters such as the occupancy of the K site, the thermal parameters, the number of layers along *c* direction and the dimension of the particles in the plane *a-b*, allows us to draw a series of simulations. The probability of existence of the layers is calculated from the probability matrix. For example, in a model with three layers with a 3 x 3 matrix corresponding to $\alpha_{11} = 20$, $\alpha_{12} = 40$, $\alpha_{13} = 40$, $\alpha_{21} = 40$, $\alpha_{22} = 20$, $\alpha_{23} = 40$, $\alpha_{31} = 40$, $\alpha_{32} = 40$, and $\alpha_{33} = 20$, the probability of existence of each layer is 33%.The best result we obtained is shown in figure 4 (the simulation is named S, compared to the observed XRD pattern).

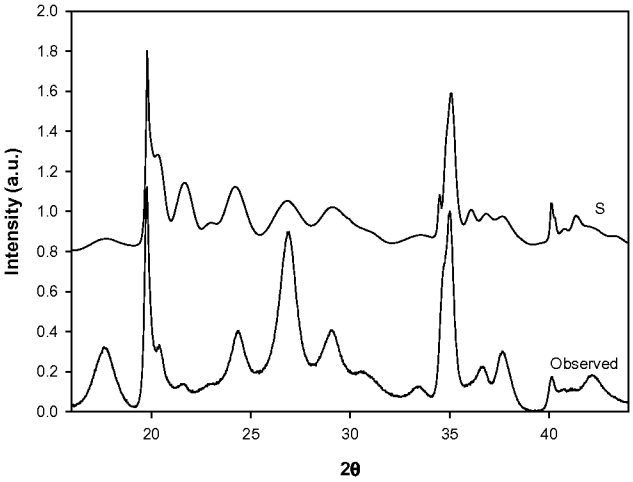

Figure 4. Simulations of the Hungarian illite XRD with DIFFaX.

The peak positions are correct but the misfit with the observed intensities is evident. This is due to a limitation of DIFFaX which has no correction factor for preferred orientation. The conditions used for the simulation S are: 40% layer 1, 35% layer 2, 25% layer 3, 0.8 K atoms per $O_{10}(OH)_2$, 5 cells along *c* and an average dimension of the particles in the *a-b* plane of 300 nm.

Concluding remarks

In this study, we accomplished the chemical, mineralogical and physical characterization of an illite sample from the Tokaj region (Northern Hungary) with the preliminary modelling of the structure using several codes. The sample is a nearly pure illite, being Ca and Na interlayer cations in a little fraction (10%) of smectite layers. The predominant polytype is 1M, suggested by simulations and XRD observations. Both cis- and trans-vacant layers are present: their relative percentage (0.3:0.7) is determined by simulations and confirmed on the basis of thermal analyses. The so obtained results are a good starting point for the refinement with DIFFaX$^+$, where many parameters such as atomic positions, atomic population, preferred orientation, thermal parameters, and microstructure and disorder parameters can be simultaneously refined.

References

1. Środoń, J. & Eberl, D.D., 1984, *Mineralogical Society of America Reviews in Mineralogy*, **13**, 495.
2. Brigatti, M.F. & Guggenheim, S., 2002, *Mineralogical Society of America Reviews in Mineralogy*, **46**, 1.
3. Rosenberg, P.E., 2002, *Am. Miner.*, **87**, 103.
4. Yates, D.M. & Rosenberg, P.E., 1996, *Geoch. et Cosmo. Acta*, **60**, 1873.
5. Yates, D.M. & Rosenberg, P.E., 1997, *Geoch. et Cosmo. Acta*, **61**, 3135.
6. Inoue, A., Kohyama, N, Kitagawa, R. & Watanabe, T., 1987, *Clay Clay Miner.*, **35**, 111.
7. Reynolds, R.C., 1985, *NEWMOD.* Available from R.C. Reynolds, 9 Book Rd., Hanover, NH 03755, USA.
8. Reynolds, R.C., 1993, *Computer applications to X-ray powder diffraction analysis of clay minerals* (R.C. Reynolds, Jr. and J.R. Walker, Eds.), vol. 5, pp. 43–78. Clay Minerals Society, Boulder, Colorado.
9. Reynolds, R.C., 1994, *WILDFIRE:* R.C. Reynolds, Hanover, New Hampshire.
10. Treacy, M.M.J., Newsam, J.M. & Deem, M.W., 1991, *Proc. R. Soc. London Ser. A*, **433**, 499.
11. Leoni, M., Gualtieri, A.F. & Roveri, N., 2004, *J. Appl. Cryst.*, **37**, 166.
12. Larson, A.C. & Von Dreele, R.B., 1994, *Los Alamos National Laboratory Report LAUR 86-748.*
13. Grathoff, G.H. & Moore, D.M., 1996, *Clay Clay Miner.*, **44**, 835.
14. Drits, V.A., Plançon, A., Sakharov, B.A., Besson, G., Tsipursky, S.I. & Tchoubar, C., 1984, *Clay Miner.*, **19**, 541.
15. Cuadros, J & Altaner, S.P., 1998, *Eur. J. Miner.*, **10**, 111.

Z. Kristallogr. Suppl. **23** (2006) 499-504

XRD study of the stacking mode of the nacrite/alkali halides complexes

S. Naamen*, H. Ben Rhaïem, M. S. Karmous, A. Ben Haj Amara

Laboratoire de Physique des Matériaux, Faculté des Sciences de Bizerte, Tunisia
* Contact author; e-mail: naasonia@yahoo.fr

Keywords: nacrite, 8.4Å hydrated nacrite, Cesium chloride; potassium Bromide, potassium chloride, XRD

Abstract. Homogenous nacrite/CsCl, KCl and KBr complexes have been successfully prepared by immersing an homogeneous 8.4 Å hydrated nacrite in CsCl, KCl or KBr saturated solutions. These three complexes have been studied using X-ray diffraction (XRD). The X-ray diffraction analysis was based on the comparison between experimental and calculated XRD patterns. The XRD patterns showed basal spacings equal to 7.2 Å, 10.0 Å, 10.4 Å and 10.5 Å respectively for the non-treated nacrite, the nacrite/KCl, nacrite/KBr and nacrite/CsCl complexes. This result indicated the intercalation of the hydrated salts between the nacrite layers. The determination of the structural parameters was achieved using a direct method involving a monodimensional electron density projection. This method allows the determination of the number and the positions of the intercalated entities. The best reliability factors obtained for these complexes nacrite/alkali halides are less than 7 %. For the nacrite/CsCl and nacrite/KBr complexes, the cations are located near the oxygen atom plane. The anions are situated above the hydroxyl groups and the H_2O molecules in the middle of the interlamellar space. For the nacrite/KCl complex, the cation, the anion and one H_2O molecule are located near the hydroxyl groups and another water molecule is situated under the oxygen atom plane of the second layer.

Introduction

It is well known that the alkali halides can be intercalated within the kaolinite layers [1, 2, 3, 4, 5]. The intercalation is obtained: **1-** By mechanochemical methods in the presence of trace amount of water containing the salt. This method caused the destruction of the kaolinite structure and the formation of amorphous material [6]. In fact the XRD diffractogram of the CsCl complex obtained by mechanochemical synthesis [4, 5, 7] did not show any feature indicating intercalation; although the 7.2Å peak disappeared after the kaolinite had been ground with the Caesium salt and no other peak appeared in the diffractogram. **2-** Using an intermediate agent such as hydrazine, dimethylsulfoxide (DMSO) or ammonium acetate. The intercalation was obtained: **(a)** By immersing these complexes in alkali halide solutions [1, 5, 8, 3]. Using this method KI, CsI, KBr cannot be intercalated. **(b)** By grounding the alkali

halides with kaolinite in air or in presence of water and heating the mixing at varied temperature [2, 4]. Using this method the authors have intercalated all alkali halides [8].
The hydrated salts penetrate within the interlayer space of the kaolin layers and thus expand the basal spacing from 7.2 Å to 10-14.4 Å. Yariv *et al.*, [3] suggested that the hydrated CsCl/kaolinite complex does not show long-range periodicity. After heat treatment at 250 °C and dehydration, an ordered stacking of parallel layers was obtained. KBr- and KCl-Kaolinite complexes were synthesized by heating discs of the DMSO-kaolinite intermediate [3, 8] at temperature > 200 °C. The d_{001} values of the KBr, CsCl and KCl complexes were respectively 10.4 Å 10.5 and 10 Å [3]. Their diffractograms showed an integral series of *00l* reflections, indicating well-ordered stacking of layers. In all previous studies, concerning the intecalation of kaolinite with alkali halides was studies, XRD measurements were only used to identify the formed complexes.
Using IR spectroscopy Michaelian *et al.*, [4] suggested, for a kaolinite/CsCl complex, a structure in which a water molecule is coordinated to the Cs^+ cation donates one proton to an inner surface oxygen and another proton to the halide, while accepting a proton from an inner surface hydroxyl groups. This structure suggested that the cation Cs^+, the anion Cl^- and the water molecule are located at the same z-coordinate along the normal to the (a, b) plane of the layers wthin the interlamellar space. In spite of all publications, the exact structure of the kaolinite/alkali halides complexes has not been defined clearly because the use of X-ray diffraction was limited to a qualitative analyses.
In the present paper we describe a method of nacrite intercalation with CsCl, KCl or KBr salts. We can note that the selected salts were characterized by a high atomic diffusion factor for X-rays and can be located accurately in the interlamellar space of nacrite. The homogeneous 8.4 Å hydrated nacrite was used as an intermediate agent of the intercalation of CsCl, KCl or KBr hydrated salt within the interlamellar space. The complexes were investigated by means of XRD. XRD was used to analyze quantitatively the *00l* reflections of the CsCl, KCl and KBr/nacrite complexes. The method is based on the comparison between experimental and calculated electron density in order to determine the number and the position of the water molecules, (Cs^+, K^+) and (Cl^-, Br^-) ions along the normal to the (*a*, *b*) plane.

Experimental

The complexes were prepared from a Tunisian nacrite [9]. Hydrated nacrite was obtained by the method described by Ben Haj Amara *et al.*, [10] as follows: 2 g of clay were ground with 3.5 g of KAc and kept in 20 ml of a saturated KAc solution for several days until the intercalation was completed. The resulting KAc complex was washed with water and air-dried in order to obtain the 8.4 Å hydrated nacrite. The nacrite/CsCl, KBr or KCl complexes were synthesized by immersing the 8.4 Å hydrated nacrite in saturated solutions of CsCl, KCl or KBr.

X-ray diffraction patterns of oriented powder were obtained, by reflection, with a diffractometer Bruker D8-advance equipped with a vertical goniometer and using Cu-Kα_1 radiation. The intensities were measured every 0.02° (2θ) as the number of counts registered in a period of 100s in order to obtain the maximum of intensity.

Methods

The electron density ρ (Z) was obtained using a monodimensional inverse Fourier transform along the normal to the layer [11].

$$\rho(z) = \frac{8}{V_c} \sum_{l=0}^{N} \left| F_{00l} \right| \cos\left(\frac{2\pi Z}{d_{002}} l - \alpha_{00l} \right)$$

The method is based on the comparison between the experimental and calculated patterns.

F_{00l} represents the structural factor for the *00l* reflection and takes into account the structural formula of the mineral, the number of water molecules, Cl^-, Br^-, K^+ and Cs^+ ions per unit-cell and their Z coordinates (Å) along the perpendicular to the layer; α_{00l} corresponds to the calculated structure factor phase.

The validity of the method is evaluated by the reliability factor:

$$R = \frac{\Sigma \left\| F_{cal} \right| - \left| F_{obs} \right\|}{\Sigma \left| F_{obs} \right|}$$

F_{obs} and F_{cal} are the structure factors of the observed and calculated *00l* reflections respectively.

The analysis of the basal reflection intensities allowed the determination of the structural characteristics of the complexes. The Z coordinates of the nacrite used in this work were taken from the Zheng *et al.*, [12] refinement. The origin is placed on the sheet of surface oxygen atoms of the unit-cell.

Results and discussion

Qualitative analysis

XRD patterns of the nacrite complexes show a series of ten *00l* reflections for the nacrite/CsCl, nacrite/KCl and nacrite/KBr complexes (figure 1a, 1b and 1c). The examination of the *00l* reflection profiles shows a single basal spacing of 10.5Å, 10.4Å and 10Å respectively for the nacrite/CsCl, the nacrite/KBr and the nacrite/KCl complexes. These results indicate that these complexes are homogenous phases. There are no anomalies concerning the width at half-maximum intensities (FWHM) for all *00l* reflections.

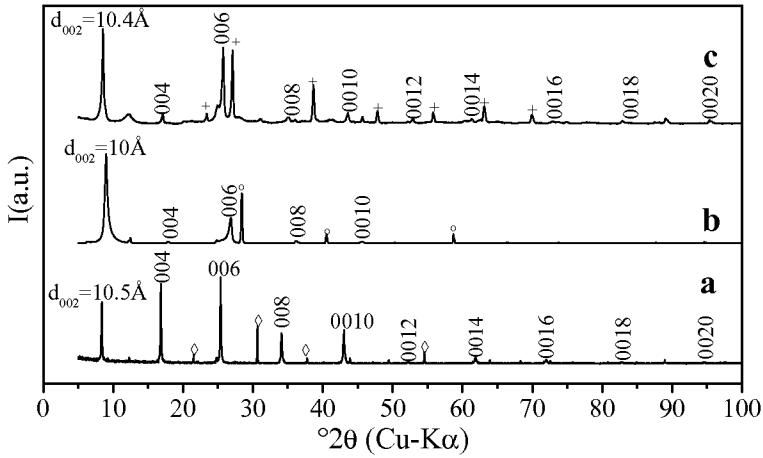

Figure 1. Experimental XRD patterns obtained by reflection for the nacrite/CsCl (a), nacrite/KCl b) and nacrite/KBr (c) complexes.

Quantitative analysis

The best reliability factors were obtained using the structural parameters reported in the table 1.

Table 1. Numbers and positions of the intercalated entities in the interlamellar space per half-unit cell.

The nacrite/CsCl complex (R = 6.9%)	**The nacrite/KBr complex (R = 3.85%)**	**The nacrite/KCl complex (R= 4.3%)**
1 Cs^+ at $Z(Cs^+) = 8.28 \pm 0.1$Å	0.55 K^+ at $Z(K^+) = 8.45 \pm 0.1$ Å	0.6 K^+ at $Z(K^+) = 6.74 \pm 0.1$Å
1 Cl^- at $Z(Cl^-) = 6.47 \pm 0.1$Å	0.55 Br^- at $Z(Br^-) = 6.9 \pm 0.1$Å	0.6 Cl^- at $Z(Cl^-) = 6.47 \pm 0.1$Å
1 H_2O at $Z(H_2O) = 7.33 \pm 0.1$Å	$Z_1(H_2O) = 7.05 \pm 0.1$Å $Z_2(H_2O) = 7.5 \pm 0.1$Å	$Z_1(H_2O) = 7.64 \pm 0.1$Å $Z_2(H_2O) = 9.13 \pm 0.1$Å

The examination of these results shows that the anion is linked to the hydroxyl groups of the nacrite layers and the cation is located near the oxygen atom plane of layers.
The Z value obtained for Cs^+, K^+ and Cl^-, Br^- in the nazcrite/CsCl and nacrite/KBr suggest:

- ✓ An interaction between the Cs^+ or K^+ cations and the basal oxygens.
- ✓ An interaction between Cl^- and Br^- anions and the surface hydroxyls
- ✓ An interaction between the water molecules, situated in the middle of the interlamellar space, the (Cs^+, Cl^-) and (K^+, Br^-) ions.

In the case of the nacrite/KCl complex, one H_2O molecule situated at 9.13Å can interact with the surface oxygen's. The Cl^- and K ions are situated respectively from the surface hydroxyls and approximately at the same cote.

The best agreements between experimental and calculated profiles of the electron densities for these complexes are given in figure 2.

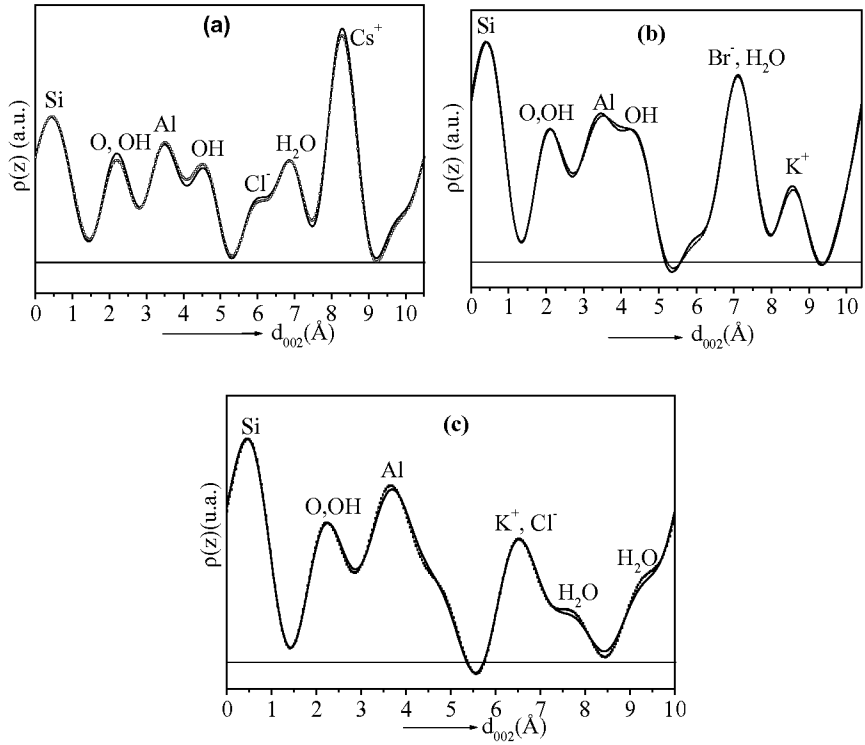

Figure 2. Agreement between calculated (—) and experimental (...) electron densities for the nacrite/CsCl (a), nacrite/KBr (b) and nacrite/KCl (c) complexes.

Conclusion

The present study shows that nacrite intercalation with aqueous solutions of CsCl, KCl or KBr is possible. The obtained complexes are stables and homogenous. Using the concept describing the stacking mode layers, based on the comparison between experimental and calculated XRD patterns allows determining the structural characteristics of nacrite/CsCl, nacrite/KCl and nacrite/KBr complexes. The changes observed in their stacking mode can be correlated to the variation of the intercalated cations. Thus, the cation plays an important role in the intercalation process.

References

1. Weiss, A., Thielepape, W., and Orth, H, 1966, *Proc. Int. Clay Conf., Jerusalem.* 277-293.
2. Yariv, S., 1975, *Powder Technology*, **12**, 131-138.
3. Yariv, S., Lapides, I., Nasser, A., Lahav, N., Brodsky, & Michaelian, K.H, 2000, *Clays and clay minerals,* **48**, No. 1, 10-18.
4. Michaelian, K.H., Yariv, S., Nasser, A., 1991a, *Can. J. Chem.* **69**, 749-754.
5. Michaelian, K.H., Friesen, W.I., Yariv, S., Nasser, A., 1991b, *Can. J. Chem.* **69**, 1786-1790.
6. Michaelian, K.H., 1990, Infrared Phys. **30**, 181.
7. Yariv, S, 1986, *Int. J. Tropic. Agric.*, **IV**, 310-322.
8. Lapides, I., Lahav, N., Michaelian, K.H., Yariv, S., 1997, *J. Thermal Anal.* **49**, 1423-1432.
9. Ben Haj amara A., Ben Brahim J., Besson G & Pons C H., 1995, *Clay Minerals*. **30**, 295-306.
10. Ben Haj Amara, A., 1997, *Clay Minerals*. **32**, 285-292.
11. Ben Haj Amara A, Ben Brahim J., Plançon A & Ben Rhaiem H., 1998, *J. Appl. Cryst.* **31**, 654-662.
12. Zheng H. & Bailey S. W, 1994, *Clays and clay minerals.* **42**, 46-52.

Z. Kristallogr. Suppl. **23** (2006) 505-510

Crystal structure determination and Rietveld refinement of rosasite and mcguinnessite

N. Perchiazzi[1]

[1]Department of Earth Sciences, Università di Pisa. Via S.Maria 53, I-56126, Pisa, Italy
*Contact author; e-mail: natale@dst.unipi.it

Keywords: rosasite, mcguinnessite, structure determination, Rietveld refinement

Abstract. The crystal structure of rosasite, $(Cu, Zn)_2(CO_3)(OH)_2$, and mcguinnessite, $(Mg,Cu)_2(CO_3)(OH)_2$ have been determined from powder data. The two minerals are isostructural, with space group $P2_1/a$ and cell constants a=12.8976(3), b=9.3705(1), c=3.1623(1) Å, β=110.262(3)°, V =358.54(2) Å^3, for rosasite and a=12.9181(4), b=9.3923(2), c=3.1622(1) Å, β=111.233(3)° , V =357.63(2) Å^3 for mcguinnessite.
The crystal structure refinements were lead up to R_p =7.51%, wR_p=10.39% for rosasite and R_p =5.12%, wR_p=6.22% for mcguinnessite. In both the two structures, the Cu coordination octahedron is distorted towards an elongated tetragonal bipyramid, whereas the Zn (in rosasite) and Mg (in mcguinnessite) coordination octahedra display an almost regular shape, their distortion being due to a partial occupancy of Cu. The carbonate group was refined as a rigid body, with a regular triangular geometry. Metal coordination octahedra polymerize through edge sharing to form octahedral "columns" and "ribbons", running along [001] and responsible for the acicular habit of these minerals. The structural relationships between rosasite and malachite are discussed.

Introduction

Rosasite, $(Cu, Zn)_2(CO_3)(OH)_2$ is a fairly common mineral, which belongs, together with the rare mineral mcguinnessite $(Mg,Cu)_2(CO_3)(OH)_2$ to the malachite-rosasite group, with general formula $Me^{2+}(CO_3)(OH)_2$ also including glaukosphaerite (Me^{2+}=Cu,Ni), kolwezite (Cu,Co), malachite (Cu), nullaginite (Ni), pokrovskite (Mg). Apart from malachite and rosasite, complete single crystal studies are missing for the other phases, mainly because of their microcrystalline fibrous habit, and their symmetry and cell parameters were mainly deduced from powder pattern indexing, resulting in a fair degree of uncertainty on their crystallography.
As pointed out in [1] for the rosasite series, the "principal unknown in these minerals is the value of $c\sin\beta$", whereas the $hk0$ reflections in these powder patterns are remarkably similar. In [1], a value of c=3.2±0.3 A was measured through single-crystal photographs of rosasite

fibres from Widgiemooltha, Australia, moreover observing the a^*b^* net is dimensionally similar to malachite, with $h00$ and $0k0{=}2n$ as in malachite. Mcguinnessite, $(Mg,Cu)_2(CO_3)(OH)_2$ was firstly described in [2], through a detailed set of physical, optical and chemical data. Given the very fine grain and the fibrous habit of mcguinnesite, a single crystal study of the mineral could not be performed, its x-ray powder pattern being indexed on the basis of a malachite-like cell and space group. Anyway, in [2] the conflicting presence of some reflections, forbidden by the space group of malachite is pointed out.

A complete single-crystal study of rosasite from Tsumeb, Namibia, was presented in [3], reporting it is monoclinic, $P2_1/a$ with a = 12.873, b = 9.354, c = 3.156 Å, β = 110.36°. A detailed X-ray powder pattern is also reported, together with new electron microprobe data pointing to the chemical formula $(Cu_{1.18}Zn_{0.82})(CO_3)(OH)_2$. In the same work it is moreover stated that "A crystal structure determination is presently being undertaken by J.T. Szymansky, CANMET".

The results of this last study, the crystal structure being refined up to R=11%, were briefly reported in an abstract [4]. These authors highlighted the strict similarity between the crystal structures of malachite and rosasite, but unfortunately details of the rosasite structure such as atomic coordinates and bond distances were not given.

Apart from malachite [5], no other structural determinations are available for the minerals of the malachite group. We therefore undertook the crystal structure determination of rosasite and of mcguinnessite, with the aim of clarifying the structural relationships between the various phases of the malachite group. A comprehensive Rietveld structural study of the malachite-rosasite group phases is presently in progress in our laboratory.

Experimental

A sample of rosasite from Ojuela mine, Durango, Mexico (Natural History Museum of Pisa University catalog number #17092) and a sample of mcguinnessite from the type locality of Red Mountain, Arizona, USA, were used in the present study. Both rosasite and mcguinnessite were present in the above samples as spheroidal aggregates of extremely thin fibrous crystals. The material was carefully hand picked under the binocular microscope to avoid contamination from unwanted phases, and gently hand milled in an agate mortar under acetone, to fill with the resulting powder a 0.5 mm Lindemann capillary.

Powder diffraction data for both phases were collected with primary Ge(111) monochromated Cu$K_{\alpha 1}$ radiation on a D8 Bruker Vario diffractometer equipped with a PSD detector, working in rotary capillary geometry, so to use a low, carefully selected, amount of material, as well as to reduce the strong preferred orientation due to the [001] fibrous habit of rosasite and mcguinnessite. For both rosasite and mcguinnessite, two datasets were collected, 11-50° and 50-100° 2θ, with step size 0.0156° 2θ and counting times 24s (16s mcguinnessite) and 48s (32s mcguinnessite).

Structure solution and Rietveld refinement

For the structural study of rosasite we assumed the space group $P2_1/a$, and initially the cell constants given in [3]. Refined cell parameters were a = 12.8976(3), b = 9.3705(1),

c = 3.1623(1) Å, β = 110.262(3)°, V = 358.54(2) Å^3, for rosasite and a = 12.9181(4), b = 9.3923(2), c = 3.1622(1) Å, β = 111.233(3)° , V = 357.63(2) Å^3 for mcguinnessite.

The crystal structure of rosasite was solved through the EXPO [6] program, which allowed us to identify the position of the two metals and of two oxygen atoms. This uncomplete model was used as a starting one for the subsequent Rietveld refinement, which was performed through the GSAS/EXPGUI suite of programs [7,8].

The missing oxygens and the carbon atom were located examining the Fourier difference maps, the displacement parameters and the distances and angles listing. The two hydroxyl groups were clearly identified through a bond valence balance and are henceforth denoted as O4 and O5. Zn was assumed to be in the more regular metal coordination polyhedron, and the occupancy of this site was fixed to the value $Zn_{0.8}Cu_{0.2}$, indicated by the microprobe data [3].

Both the malachite-like and the rosasite-like starting models were tested in the structure solution of mcguinnessite. Any effort to refine its crystal structure in a malachite-like model failed, whereas fairly promising results were obtained using a rosasite-like structure, assumed in the subsequent Rietveld refinement.

In mcguinnessite, a mixed occupancy of Mg and Cu was assumed for both the two independent octahedral sites, as indicated by the scrutiny of the displacement factors, assuming, as indicated by the microprobe data [2], a Mg/Cu ratio~1.12. The refined occupancies were Cu1 = 0.79Cu + 0.21Mg, and Mg2 = 0.85Mg + 0.15Cu.

In the early stages of both the two refinements, constraints on the Me-O bonds were introduced, initially with high statistical weights, which were progressively reduced in the course of the refinement, finally removing all the constraints. The carbonate group was refined as a rigid body, imposing a C-O distance of 1.284 Å [9]. Isotropic displacement parameters were refined for all the atoms. The Rietveld refinement finally converged to R_{wp} = 10.39% R_p = 7.51% for rosasite and R_{wp} = 4.45% R_p = 6.22% for mcguinnessite.

Structure description

The final refined atomic coordinates, and isotropic displacement parameters for the two structures are reported in Table 1, whereas selected interatomic distances and angles are presented in Table 2. Partial occupancies were refined for the site Zn2 = 0.8Zn + 0.2Cu in rosasite, and for Cu1 = 0.79Cu + 0.21Mg, Mg2 = 0.85Mg + 0.15Cu in mcguinnessite. The geometry of the coordination polyhedra of the two independent metals allows a clear distinction between the positioning of Cu^{2+} and of Zn^{2+}/Mg^{2+}cations. As shown in Table 2, the Cu octahedron, due to the Jahn-Teller effect, is strongly distorted towards an elongated bipyramidal coordination both in rosasite and in mcguinnessite. Two oxygens and two hydroxyls, with Cu-O distances clustering close to 2 Å, are arranged in a nearly planar square coordination, with two additional longer bonds to complete its sixfold coordination. As expected, the polyhedron hosting Zn in rosasite and Mg in mcguinnessite is a more regular one, the former polyhedron being slightly larger than the latter. Zn-O distances range from 2.01 to 2.26 Å in rosasite and Mg-O distances are in the range 2.00-2.22 Å for mcguinnessite, with mean values <Zn-O> 2.13 Å and <Mg-O> 2.12 Å. The distortion from a regular shape can be attributed to the partial occupancy by Cu in these sites.

Table 1. Final refined coordinates and isotropic displacement parameters ($Å^2$) for rosasite and mcguinnessite.Me2 is the Zn-Mg site in rosasite and mcguinnessite respectively.

	Rosasite				Mcguinnessite			
	x	*y*	*z*	U_{iso}	*x*	*y*	*z*	U_{iso}
Cu1	0.2103(2)	0.0007(3)	0.449(1)	0.0129(5)	0.2117(2)	-0.0043(4)	0.446(1)	0.0147(4)
Me2	0.3945(2)	0.2302(2)	0.1730(9)	0.0163(5)	0.3920(2)	0.2283(3)	0.179(1)	0.0196(8)
C	0.1414	0.2745	0.6654	0.011(5)	0.1374	0.2705	0.6614	0.083(5)
O1	0.1353(1)	0.1420(3)	0.760(3)	0.009(3)	0.1311(1)	0.1360(1)	0.724(2)	0.042(2)
O2	0.2312(1)	0.3433(3)	0.863(1)	0.014(3)	0.2289(1)	0.3361(2)	0.8708(8)	0.027(2)
O3	0.0520(1)	0.3447(3)	0.471(2)	0.017(3)	0.0477(1)	0.3431(1)	0.490(2)	0.033(2)
O4	0.3543(7)	0.0946(9)	0.648(4)	0.012(3)	0.3518(5)	0.0907(7)	0.614(3)	0.033(2)
O5	0.4187(9)	0.385(1)	-0.256(6)	0.049(4)	0.4235(4)	0.3769(6)	-0.257(2)	0.012(2)

Table 2. Bond distances (Å) and angles (°) in the coordination polyhedra of rosasite and mcguinnessite. Symmetry transformations used to generate equivalent atoms i = ½-x, y-½, -z ; ii = ½-x, y-½, 1-z ; iii= x, y, z-1 ; iv= ½-x, y-½, 2-z ; v= x+½; ½-y ; z ;vi= x, y, z+1 ; vii = x+½; ½-y; z-1.

Rosasite						Mcguinnessite					
Cu1	-O5^{i}	1.89(1)	Zn2	-O4^{iii}	2.01(1)	Cu1	-O4	1.909(7)	Mg2	-O3^{v}	2.007(3)
	-O4	1.952(9)		-O3^{v}	2.046(3)		-O5^{i}	1.977(6)		-O4^{iii}	2.087(9)
	-O2^{ii}	2.057(5)		-O5	2.07(1)		-O1	2.076(6)		-O5	2.104(8)
	-O1	2.078(8)		-O4	2.16(1)		-O2^{ii}	2.084(4)		-O4	2.110(9)
	mean	**1.995**		-O2^{iii}	2.256(3)		mean	**2.011**		-O5^{vi}	2.183(8)
	-O1^{iii}	2.443(7)		-O5^{vi}	2.251(1)		-O1^{iii}	2.499(6)		-O2^{iii}	2.220(4)
	-O2^{iv}	2.519(3)		mean	**2.134**		-O2^{iv}	2.524(3)		mean	**2.119**
O1-CU1-O4 96.0(3)						O1-CU1-O4 98.6(3)					
O1-CU1-O5^{i} 91.3(5)						O1-CU1-O5^{i} 87.4(2)					
O2^{ii}-CU1-O4 90.8(3)						O2^{ii} -CU1-O4 90.1(3)					
O2^{ii}-CU1-O5^{i} 81.7(4)						O2^{ii}-Cu1-O5^{i} 83.9(2)					

An hydrogen bonding scheme was derived for both the two structures by looking at those distances shorter than 3.1 Å, between oxygen atoms not belonging to the same polyhedron. The two OH^- groups, O4 and O5, engage as acceptors the oxygen atoms O3 and O1 respectively, with O4···03 of 2.721(9) and 2.742(7) Å (rosasite and mcguinnessite, respectively) and O5···O1 of 2.80(1) and 2.706(7) Å (rosasite, mcguinnessite). The bond valence balance, computed according to [10,11], is satisfactory for both minerals, with deviations less than 15% from the ideal anion sums, thus confirming the soundness of these crystal-chemical models.

In the following description of the polyhedral connections, we shall refer to rosasite only, given its isostructurality with mcguinnessite. Both the Zn and the Cu octahedra connect by edge-sharing to form Cu-based and Zn-based octahedral "columns", and two columns large "ribbons" (Figure 1), running along [001], and responsible for the acicular habit of the mineral.

As alreay pointed out in [4] there is a close resemblance between the crystal structures of rosasite (mcguinnessite) and of malachite, when seen projected along *c* (Figure 1).

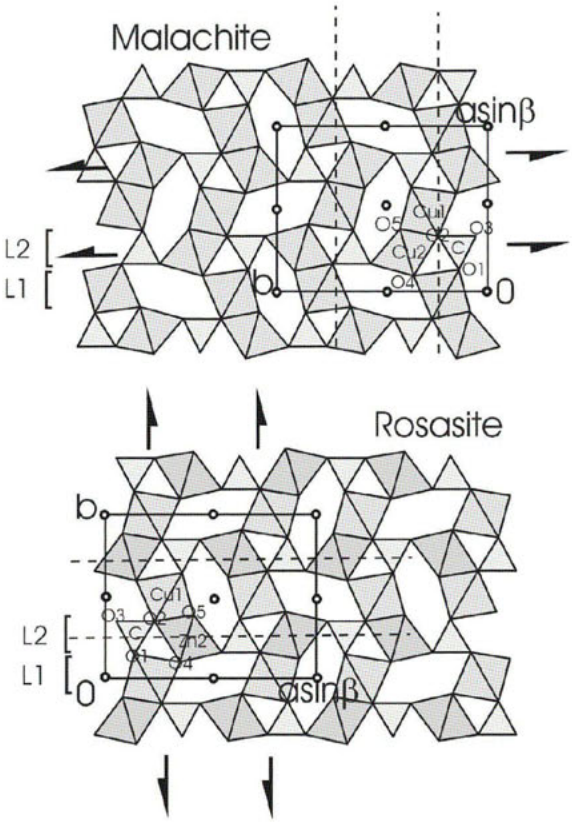

Figure 1. The close relationships between the crystal structures of rosasite and malachite, when seen along [001]. In both the two structures the same two kind of layers, denoted as L1 and L2, regularly alternate along the ≈ 9.5 Å axis.

One can identify, in both the two structures, two kinds of "layers", regularly stacked along the ≈ 9.5 Å axis, and with thickness ≈ ¼ of the stacking periodicity. Referring to rosasite, a first layer (L1) is made up by Cu polyhedra only, and is placed nearly centered at $y \approx 0$, the Cu polyhedra inside this layer being related by the inversion centers. A second layer (L2), hosting Zn and C polyhedra, is placed centered at ¼*b*, with the polyhedra of the layer related by the *a* glide present at $y = ¼$. Comparing the structure of rosasite (mcguinnessite) and of malachite in terms of the above "layers" one can remark that in both the two minerals the Cu-only (L1) layer hosts the more distorted metal polyhedron, whereas the L2 layer is made up by carbonate groups and by the more regular metal coordination polyhedron. Although the two structures are quite similar in [001] projection, the different orientation of the space group symmetry operators respect to the layers, leads anyway to the distinct crystal structures of these two phases.

Conclusions

The crystal structure of rosasite and mcguinnessite have been determined and refined from powder data. The two minerals are isostructural, crystallizing in the space group $P2_1/a$. Their structure host Cu in distorted octahedra, whereas almost regular octahedra are formed by Zn in rosasite and by Mg in mcguinnessite. Both the hydrogen bonding scheme and the valence balance confirm the reliability of the presented structural models. A comparison between the structures of rosasite and of malachite shows their close resemblance in [001] projection. These two structures are described in terms of layers, stacked along the ≈9.5 Å axis, remarking how the different orientation of the space group operators respect to these layers leads anyway to the different structures of malachite and rosasite.

References

1. Jambor, J., 1976, *Can. Mineral.*, **14**, 574.
2. Erd, R.C., Cesbron, F.P., Goff, F.E., Clark, J.R., (1981), *Mineral. Rec.*, **12**, 143.
3. Roberts, A. C., Jambor, J. L., Grice, J. D., (1986), *Powd. Diff.*, **1**, 56.
4. Szimansky, J.T., Le Page, Y., (1986), Program with Abstracts – Geol. Ass. Canada, Mineral. Ass. Canada, **11**, 133.
5. Zigan, F., Joswig, W., Schuster, H.D., Mason, S.A., (1977), *Zeit. Krist.*, **145**, 412.
6. Altomare, A., Burla, M.C., Cavalli, M., Carrozzini, B., Cascarano, G.L., Giacovazzo, C., Gagliardi, A., Molitemi, G. G., Polidori, G., & Rizzi, R., (1999), *J. Appl. Cryst.*, **32**, 339.
7. Larson, A.C., Von Dreele, R.B,. (2000), Los Alamos National Laboratory Report LAUR 86.
8. Toby, B.H., (2001, *J. Appl. Cryst.*, **34**, 210.
9. Zemann, J., (1981), *Fortschr. Mineral.* **59**, 95.
10. Brese, N.E., O'Keeffe, M., (1991), *Acta Cryst.*, **B47**, 192.
11. Ferraris, G., Ivaldi, G., (1988), *Acta Cryst.*, **B44**, 341.

Acknowledgements
S. Merlino is thanked for his helpful suggestions.

Z. Kristallogr. Suppl. **23** (2006) 511-516

Rietveld analysis of polytypic $Zn_{1-x}Mg_xSe$ and $Zn_{1-x-y}Mg_xBe_ySe$ solid solutions

R. Minikayev[1], W. Paszkowicz[1,*], F. Firszt[2], H. Męczyńska[2] and A. Marasek[2]

[1]Institute of Physics PAS, Al. Lotników 32/46, 02-668 Warsaw, Poland
[2]Institute of Physics, N. Copernicus University, ul. Grudziądzka 5, 87-100 Toruń, Poland
[*]Contact author; e-mail: paszk@ifpan.edu.pl

Keywords: polytype, structure, hexagonality, Rietveld refinement, quantitative analysis

Abstract. Rietveld method is used for structure refinement of Bridgman-grown $Zn_{1-x}Mg_xSe$ (x = 0.17), and $Zn_{1-x-y}Mg_xBe_ySe$ (x = 0.12, y = 0.04) crystals built from 3*C* (sphalerite), 8*H*, and 4*H* polytypes. Contributions of these polytypes, their lattice parameters and atomic positions were determined. The lattice parameters of the main (weight fraction 70%) 8*H* phase in $Zn_{0.83}Mg_{0.17}Se$ are a = 4.0325(3) Å and c = 26.358(4) Å. Structural data for 8*H* and 4*H* components of both crystals, are, to the best of the authors' knowledge, the first ones reported for ZnSe-based polytypes except from common 3*C* (sphalerite) and 2*H* (wurtzite) phases.

Introduction

Polytypes (polymorphs representing various stacking orders of equivalent planes, cf. Refs [1, 2] occur for those tetrahedrally bonded semiconducting compounds, for which the formation energies of wurtzite (2*H*, with *...AB|AB...* stacking) and sphalerite (3*C*, with *...ABC|ABC...* stacking) polymorphs do not differ much. For semiconducting solid solutions, the polytypes can be observed close to the transition point between the wurtzite and sphalerite phases, and their formation may be influenced by the thermal history of the crystal.

$Zn_{1-x}Mg_xSe$ and other ZnSe-based solid solutions are components of heterostructures which are of interest in optoelectronic technologies for construction of blue-green lasers and UV-visible photodetectors. The occurrence of crystal defects leads to structure degradation of Mg-containing films. Studies of polytypism in such crystals and thin layers/multilayers may lead to a better understanding of phase relationships and defect nature.

A combined X-ray/high-resolution electron microscopy (HRTEM)/luminescence study [3] has permitted for systematising the conditions at which the higher polytypes (4*H* and 8*H* with stackings *...ABAC|ABAC...* and *...ABCABACB|ABCABACB...*, respectively) form in Bridgman-grown bulk $Zn_{1-x}Mg_xSe$ crystals. Namely, they occur in as-grown crystals in the vicinity of the transition point, $x \cong 0.18$. The polytype sequence along each unannealed crystal of composition close to x = 0.18, is 3*C*→8*H*→4*H*→2*H* (ordered with the value of *hexagonality parameter*, η, and simultaneously with Mg content, both gradually increasing from the tip to the end of the crystal) [3]. The parameter η is defined as a fraction of hexago-

nal stacking in the mixture of hexagonal and cubic stackings: a layer *B* in a close packed system is assumed to adopt a 'hexagonal stacking', when the atoms of adjacent layers are at the same positions (*ABA*), and a 'cubic stacking', when these positions are not equivalent, (*ABC*). Pure *ABC* and *ABA* stackings represent the cubic sphalerite (η=0) and hexagonal wurtzite (η=1) structures, respectively. Results for the crystals studied in Ref. [3] show that in the vicinity of $x \cong 0.18$, the stacking-fault density is high in the constituent phases. Annealing of the crystal causes a very strong reduction of the 4*H* and 8*H* presence and reduces the stacking fault density. The mentioned tendency of higher polytypes to disappear on annealing is in agreement with opinion that polytypes are metastable phases rather than true equilibrium phases (see, e.g., Ref. [4]). A further modification of II-VI compounds by incorporation of Be atoms into the cationic sites causes a reduction of unit-cell size accompanied by an increase of the bandgap value as well as by improvement of resistance against defect propagation in layers being components of optoelectronic devices [5]. In this work, X-ray diffraction is used to investigate the structure of $Zn_{1-x}Mg_xSe$ and $Zn_{1-x-y}Mg_xBe_ySe$ crystals.

Experiment and refinement conditions

The studied crystals were grown at N. Copernicus University by a high-pressure variant of the Bridgman method. Details of the growth process can be found in Refs [3,6,7]. Circular, ~1.5 mm thick plates cut perpendicularly to the axis were studied. The Mg and Be content was determined by electron microprobe and chemical analysis. Powder diffraction measurements were performed for finely ground crystals, using a laboratory Bragg-Brentano diffractometer (PhilipsX'Pert MPD, $CuK\alpha_1$ radiation) equipped with a Johansson monochromator and a semiconductor strip detector.

Starting models of the polytype-structures (cf. table 1) with space group $P6_3mc$ for 8*H*, 4*H* and 2*H* phases and $F\bar{4}3m$ for sphalerite phase were based on literature data [1,9]. In the hexagonal ones, the value of the *u* parameter describes the relative length of the cation-anion bond aligned along the [001] direction (for details see, *e.g.*, Ref. [10]). The (small) ε indicated at the *z* position of Se atoms is thus a measure of the bond distortion ($\varepsilon = 0$ for undistorted bond). Selection of the structure of the 8*H* polytype from among three possible ones was based on the HRTEM observations (see Ref. [3]) of the *ABCABACB* stacking for the same crystal plate. A Rietveld-refinement program, Fullprof.2k (v. 2.70) [8], was used for structural analysis. Pearson VII profile-shape function was assumed. The following parameters were refined: scale factor, lattice parameters, *u* values, isotropic atomic displacements, peak shape/asymmetry parameters, systematic line-shift and one preferred-orientation parameter according to the March-Dollase model. Parameters describing the peak shape for minority 2*H* and 4*H* phases in sample S2 models were assumed to be the same as for 8*H* phase. The background was assumed to be a 5^{th} order polynomial.

Results and discussion

Polytype identification in mixtures by using positions of powder-diffraction peaks is not straightforward due to typically severe overlap. For a mixture, the positions of overlapping lines are almost identical, but their relative intensities differ. Therefore, verification of different structural models should be performed taking the intensities into account. Rietveld analysis has been helpful in studies of SiC and GaN polytypic mixtures. The only example of Rietveld analysis for polytypic mixtures of II-VI pseudobinaries found in literature is a study

of thin Cd(Te,S) nanocrystalline layers aimed for identification of polytype phases in a difficult case of very small crystallites [11]; the cited study involved mainly the 3*C* and 2*H* polytypes.

Table 1. Applied models of the polytype structures: atomic positions, space groups and hexagonality, η.

Polytype	Atom	*x*	*y*	*z*	Space group	*η*
3*C*	Zn1	0.000	0.000	0.000	$F\bar{4}3m$	0
	Se1	0.25	0.25	0.25		
8*H*	Zn1	0.000	0.000	0.000	$P6_3mc$	0.25
	Zn2	1/3	2/3	0.125		
	Zn3	1/3	2/3	0.375		
	Zn4	1/3	2/3	0.75		
	Se1	0.000	0.000	$z_{Zn1}+(3/32+\varepsilon)$ ($\equiv u_{8H}$)		
	Se2	1/3	2/3	$z_{Zn2}+(3/32+\varepsilon)$		
	Se3	1/3	2/3	$z_{Zn3}+(3/32+\varepsilon)$		
	Se4	1/3	2/3	$z_{Zn4}+(3/32+\varepsilon)$		
4*H*	Zn1	0.000	0.000	0.000		0.5
	Zn2	1/3	2/3	0.25		
	Se1	0.000	0.000	$z_{Zn1}+(3/16+\varepsilon)$ ($\equiv u_{4H}$)		
	Se2	1/3	2/3	$z_{Zn2}+(3/16+\varepsilon)$		
2*H*	Zn1	1/3	2/3	0.000		1
	Se1	1/3	2/3	$z_{Zn1}+(3/8+\varepsilon)$ ($\equiv u_{2H}$)		

Figures 1 and 2 illustrate the Rietveld refinement results for the studied as-grown $Zn_{1-x}Mg_xSe$ and $Zn_{1-x-y}Mg_xBe_ySe$ crystals. The results of phase analysis and Rietveld refinement procedure are included in table 2. The indicated errors are the standard deviations given by the program multiplied by the *SCOR* parameter [12] in order to represent both, the statistical and the model-dependent errors.

For the $Zn_{1-x}Mg_xSe$ crystal (sample S2), preliminary identification based on X-ray peak positions has yielded the 8*H* phase [3]. Three other ordered polytypes (3*C*, 4*H* and 2*H*) found for the same sample in Ref. [3] by HRTEM were included in the models. Three starting models were considered: 3*C*+8*H*+2*H*, 3*C*+8*H*+4*H* and 3*C*+8*H*+4*H*+2*H*; two of them are included in table 2). The model 2, characterised by the lowest R_{wp} factor, was selected. All refinements involving the 2*H* phase yielded a (small) contribution of this phase, comparable with its error. Therefore, it was concluded that the amount of 2*H* phase is marginal in this sample, and this phase was not included in the final calculations. Figure 3 illustrates the Rietveld-refinement based pattern decomposition into constituent-phase patterns according to model 2. According to this model, the weight fractions of 3*C*, 8*H* and 4*H* phases are, respectively, 23(4)%, 70(9)% and 7(3)%. The lattice parameters of the main 8*H* phase in sample S2 are a = 4.0325(3) Å and c = 26.358(4) Å which compare well with those determined using the least-squares method in Ref. [3], a = 4.0314(2) Å and c = 26.353(2) Å. Both, a and c, values are slightly larger than the previous ones. This is attributed to i) largely improved statistics of the diffraction data permitting the weak and high-angle reflections to contribute

to structural information. ii) avoiding the influence of secondary 3*C* and 4*H* phases on the result. The calculated positional parameter is u_{8H}=0.0948(2) being relatively high (the ideal value is 0.09375). The crystallographic data obtained for the 4*H* polytype (a = 4.0321(7) Å and c = 13.184(3) Å) should be treated as tentative, because they are derived from a model where it is a minority phase displaying no characteristic reflections (all are hidden under 8*H* reflections). Refinements for $Zn_{1-x-y}Mg_xBe_ySe$ (sample S6) permitted for confirmation of the presence of 3*C*, 8*H* and 4*H* phases in the studied part of the crystal. The polytypism for this sample is observed at a Mg content being lower ($x \cong 0.12$) than the above-mentioned transition point for $Zn_{1-x}Mg_xSe$ system ($x \cong 0.18$), in agreement with expectations based on the reduction of average ionicity resulting from incorporation of Be atoms into cationic sites. A reduction of the unit-cell dimension is due to small Be atom size. To the best of our knowledge the structural data for the phases contributing to both samples studied are the first ones concerning ZnSe-based polytypes other than 3*C* and 2*H*.

To identify the polytypes such as 3*C*, 8*H*, 4*H* and 2*H* observed in some II-VI solid solutions, modelling of full diffraction profile is a valuable tool. However, in real situations when the major components exhibit high defect density and some minor components are not easily

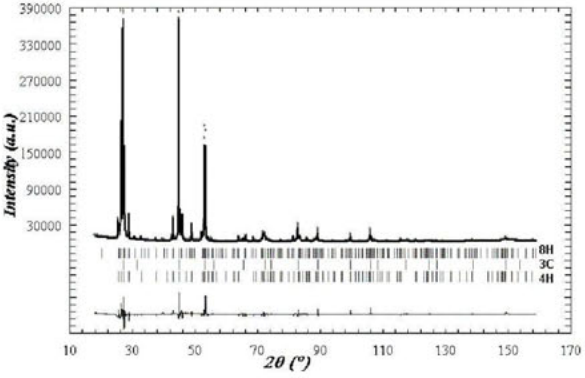

Figure 1. Rietveld refinement for the powder diffraction data of the studied $Zn_{1-x}Mg_xSe$ sample S2, x = 0.17 (model 2).

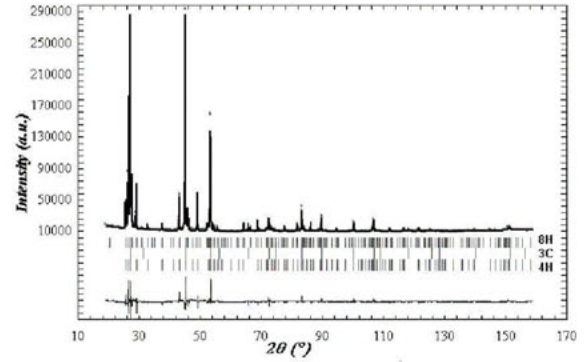

Figure 2. Rietveld refinement for the powder diffraction data of the studied $Zn_{1-x-y}Mg_xBe_ySe$ sample S6, x = 0.12, y = 0.04.

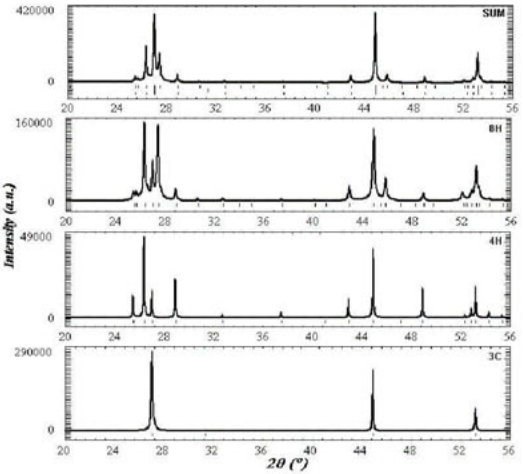

Figure 3. Rietveld-refinement based decomposition of powder pattern of the three-phase polytypic mixture $Zn_{0.83}Mg_{0.17}Se$ (sample S2, upper panel) into 3C, 8H and 4H phases according to model 2. The figure displays the component patterns in three lower panes and the sum of the calculated patterns in the upper panel. The numerical intensities reflect the contribution of the component patterns to the mixture pattern. The background component is not included.

identified, one cannot expect a high accuracy of refinement. Indeed, the runs of difference curves show that the agreement between experiment and calculation is not ideal. This is attributed to the joint effect of minor contribution of other polytypes (including the disordered polytype observed in Ref. [3] for sample S2) and presence of stacking faults.

In summary, in the present paper, it is demonstrated that problems of polytype identification and quantitative analysis for ZnSe-based polytype mixtures are solvable by Rietveld refinement of proper structural models. The refinement was performed for $Zn_{1-x}Mg_xSe$ and $Zn_{1-x-y}Mg_xBe_ySe$ crystals containing 3*C*, 8*H*, and 4*H* polytypes and the structural properties of component phases were determined for each of these two samples. Contributions of these phases is calculated to be 23(4)%, 70(9)%, 7(3)%, respectively, in the first crystal and 27(6)%, 44(8)%, 29(7)% in the second one. The applied method gives better identification results than that based on peak positions, because for polytypic mixtures severe overlap makes that peaks of minority phases are invisible. Consideration of peak intensities through the Rietveld analysis is helpful in 'hidden'-polytype identification, with natural limitations due to the poor quality inherent to the polytypic crystals, manifesting itself in the presence of stacking faults and minor amounts of other polytypes.

References

1 Verma, A.R. & Krishna, P., 1966, *Polymorphism and Polytypism in Crystals*, John Wiley & Sons, New York.

2 Krishna, P., (ed.), 1983, *Crystal Growth and Characterization of Polytype Structures*, Pergamon Press, Oxford.

3 Paszkowicz, W., Dłużewski, P., Spolnik, Z.M., Firszt, F. & Męczyńska, H., 1999, *J. Alloys Compds*, **286**, 224.

4 Limpijumnong, S., Lambrecht, W.R.L., 1998, *Phys. Rev. B*, **57**, 12017.

5 Guha, S. & Petruzello, J., 1997, in: *II-VI Blue/Green Light Emitters: Device Physics and Epitaxial Growth* (*Semiconductors and Semimetals*, vol. 44), ed.: R.L. Gunshor & A.V. Nurmikko, Academic Press, San Diego, p. 271.

6 Malinski, M., Bychto, L., Firszt, F., Szatkowski, J. & Zakrzewski, J., 2001, *Analyt. Sci, Sp. Iss.*, **17**, S133.

7 Firszt, F., Łęgowski, S., Męczyńska, H., Szatkowski, J., Banasiak, A., Paszkowicz, W., Falke, U., Schultze, S. & Hietschold, M., 2000, *J. Cryst. Growth*, **214/215**, 880.

8 Rodriguez-Carvajal, J., 2001, *Newslett. IUCr Commission Powd. Diffr.*, **26**, 12.

9 Ramsdell, L.S. & Kohn, J.A., 1952, *Acta Crystallogr.*, **5**, 215.

10 Schulz, H. & Thiemann, K.H., 1977, *Solid State Commun.*, **23**, 815.

11 Tagliente, M.A., Penza M., Gusso M. & Quirini A., 1999, *Thin Solid Films*, **353**, 1-2, 129.

12 Bérar, J.-F. & Lelann, P., 1991, *J. Appl. Crystallogr.*, **24**, 1-5.

Table 2. Results of Rietveld refinement for $Zn_{1-x}Mg_xSe$ (sample S2) and $Zn_{1-x-y}Mg_xBe_ySe$ (sample S6) crystals. f stands for the weight fraction of the given phase as derived from the refinement. The refined values of lattice parameters, reduced axial ratio c/na, and u are less certain, for minority polytypes, (written in italics) due to severe overlap of the main reflections.

Sample	Compo -sition	Phase *f* [%]	*a* [Å], *c* [Å]	*c/na*	*u*	R_B [%]	R_F [%]	R_{WP} [%]
sample S2 (A394/V) *model 1*	x=0.17	3*C* 30(7)	5.7039(4)	---	---	3.42	3.99	18.8
		8*H* 68(9)	4.0322(2), 26.358(2)	0.8171(8)	u_{8H}= 0.0940(2)	8.80	7.66	
		2*H* 2(1)	*4.0319(7), 6.591(3)*	*0.8174(8)*	u_{2H}= *0.3750*	13.50	10.50	
sample S2 (A394/V) *model 2*	x=0.17	3*C* 23(4)	5.7046(4)	---	---	3.60	3.52	18.6
		8*H* 70(9)	4.0325(3) 26.358(4)	0.8170(9)	u_{8H}= 0.0948(2)	9.62	7.41	
		4*H* 7(3)	*4.0321(7) 13.184(3)*	*0.8174(9)*	u_{4H}= *0.1877(2)*	9.80	6.83	
sample S6 (A452-XVIII)	x=0.12, y=0.04	3*C* 27(6)	5.6773(7)	---	---	4.49	4.51	21.1
		8*H* 44(8)	4.014(1), 26.24(1)	0.817(4)	u_{8H}= 0.0953(2)	11.90	9.09	
		4*H* 29(7)	4.0139(7), 13.130(3)	0.818(1)	u_{4H}= 0.1891(2)	8.01	6.84	

Acknowledgements. This work was supported in part through the European Commission program G1MA-CT-2002-4017 (Centre of Excellence CEPHEUS) and by the Committee for Scientific Research (Poland) under grant No: 1 P03B 092 27.

Z. Kristallogr. Suppl. **23** (2006) 517-522

A proposition for the structure of ammonium hydrogen (acid) urate from uroliths

P. Friedel[1,*], J. Bergmann[2], R. Kleeberg[3], G. Schubert[4]

[1] Leibniz-Institute of Polymer Research Dresden, Hohe Str.6, D-01069 Dresden,
[2] Ludwig-Renn-Allee 14, D-01217 Dresden,
[3] Freiberg University of Mining and Technology, Inst. of Mineralogy, Brennhausgasse 14, D-09599 Freiberg,
[4] Charité Berlin, Friedrichshain Hospital, Laboratory of Uroliths, Landsberger Allee 49, D-10249 Berlin
*Contact author: E-mail: friedel@ipfdd.de

Keywords: natural urolith; XPD; indexing; crystallite size distribution; force field constrained Rietveld refinement

Abstract. From naturally formed ammonium hydrogen urate, a common compound in uroliths, X-ray powder diffraction measurements, indexing and force-field-constrained Rietveld refinement including anisotropic characterization of peak width broadening were performed using the BGMN[tm] program. The ammonium hydrogen (acid) urate crystallizes in a triclinic unit cell with $a = 0.3650\,(3)$, $b = 1.0215\,(4)$, $c = 1.0597\,(5)\,nm$, $\alpha = 113.9\,(1)$, $\beta = 91.1(1)$ and $\gamma = 92.3(1)^{\circ}$. The symmetry was determined as $P\overline{1}$ (Space group No. 2). The agreement factor R_{wp} could be obtained to 7.43%. Inside the unit cell an additional ammonia molecule was placed with a probability of $p_{NH_3} = 0.34$. This reduced occupancy and the anisotropic peak width hint to structural gradient related to the varying conditions of formation.

Introduction

The natural formation of ammonium hydrogen (acid) urate, a common type of uroliths inside the urinary tracts, is a well known problem in medicine. The crystal structure of this compound is still unknown, although a proposal for the cell symmetry was given by Tettenhorst [1] and the structures of similar compounds are known (Dubler [2], Frincu [3]). The difficulties in determining the mean crystal structure of this substance are caused by the lack of single crystals and by the badly resolved and varying diffraction patterns of the natural material. Some of this problems could be overcome by application of techniques and refinement models similar to that of poorly crystalline polymers [4].

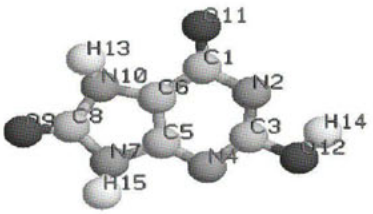

Figure 1: Structure of the most stable hydrogen (acid) urate ion.

Experimental

The chemical composition of two parts of a relatively well crystallized human urolith was characterized by elemental analysis and found to be close to the theoretical values of ammonium hydrogen (acid) urate, $C_5H_7N_5O_3$: C, 32.1/32.2 wt% (calc. 32.44 wt%); N, 36.2/36.7 wt% (calc. 37.83 wt%);. The experimental density of 1.772 $g\,cm^{-3}$ was taken from Tettenhorst [1]. X-ray powder measurements were performed using Cu Kα radiation with an HZG 4/A-2 X-ray diffractometer (Seifert-FPM GmbH, Freiberg i.Sa., Germany). Reflection and transmission measurements were carried out in the angular range 2θ = 5-125° with $\Delta 2\theta = 0.02°$ and t =20 s, for texture evaluation. Powder diffraction patterns were obtained on naturally formed urolithic powder. The measurements were carried out with a Soller collimator (0.5/25) and a primary horizontal-beam divergence of 0.2 ° in order to achieve optimum resolution.

Procedure for development of the structure proposal

By means of the software package BGMN[tm] , based on a newly developed Rietveld algorithm [6, 7], the index calculation, the crystal packing and a refinement of the atomic coordinates within the unit cell were accomplished. The Rietveld refinement was supported by force field constraints as described in [4].

We used the program package part INDEX searching for unit cell parameters and found that a triclinic symmetry (see Tab. 1) satisfies the raw diffraction data better than a monoclinic one (see Tettenhorst [1]).

For a first confirming of this proposed cell, a cell constrained pattern fitting (LeBail-method) was performed. Some misfits of the profile shape of several lines indicate anisotropic line broadening. This could be related to structural gradients, resulting from the rapidly changing formation conditions inside the urinary tract. The introduction of an anisotropic parameter G as a symmetrical tensor of rank 4, describing the line broadening according to anisotropic micro strains, similar to Stephens [12], improved the fitting to an agreement factor (R_{wp} = 4.54 %) for the triclinic model. The same line broadening model was used in the final Rietveld refinement.

For getting the starting geometry and bonding informations it was the fastest and easiest way to perform quantum mechanical *ab initio* calculations by using the software

GAMESS [5] with basis set STO-6G for the ions (hydrogen (acid) urate, ammonium) and molecules (2,6,8-Trihydroxy purine and ammonia). Basing on this geometric information, the hard or soft constraints of the coordinates have been set in the final Rietveld refinement.

2,6,8-Trihydroxy purine is a two basic acid because of the π-ring-system-stabilization effect ($pK_{S,1} = 5.496$ [8], and $pK_{S,2} = 10.3$ [9]), and only the hydrogen (acid) urate can be expected to satisfy the physiological conditions inside the urinary tract. The starting geometry of this molecule, calculated as described above, can be seen in Figure 1.

Rietveld refinement parameter In order to determine the orientation of the molecules and ions within the unit cell, the starting position of the hydrogen (acid) urate ion, of the NH_4^+ ion and of one NH_3 molecule with variable probability between 0 and 1 was set in a similar manner like described in [4]. This means, for every molecule one set of twist angles ρ_x, ρ_y and ρ_z and one shift vector $SP(x, y, z)$ was defined corresponding to the cartesian axis. For each molecule, the twist angle and the shift vector were chosen as parameters. Furthermore, a deviation of the planar urate structure must be assumed, so six internal torsional parameters for variation during the fitting process were defined. Additionally, an anisotropic line broadening parameter set as a symmetrical tensor of rank 4 was chosen as described above. The force-field-constrained Rietveld structure refinement is a combined minimization of both the conventional Rietveld and the force field part [4]. The force field energy contains two parts, the bonding and the non bonding

$$Q_{FF} = Q_{bd} + Q_{nbd}, \tag{0.1}$$

defining a force field as described by van Gunsteren [10] and Weiner [11], using the parameters for van der Waals type and hydrogen-bridging interactions as described in [4].

Results and discussion

During the final refinement 263 peaks were fitted (Figure 2(a)) and an agreement factor R_{wp} of 4.54 % was reached. The resulting lattice angles (see Table 1) of β with 91.1 ° and γ of 92.3 ° (triclinic) are closed to the results of Tettenhorst [1] with double cell volume, so that this larger cell probably could be used as an alternative one.

More parameters are listed in Table 1, and the fractional coordinates are given in Table 2.

Table 1: Calculated lattice and orientational parameters of the hydrogen (acid) urate ion, the NH_4 ion and the NH_3 molecule.

Tricl.	$a\,(nm)$	0.3650(3)
lattice	$b\,(nm)$	1.0215(4)
	$c\,(nm)$	1.0597(5)
	$\alpha\,(^{\circ})$	113.9(1)
	$\beta\,(^{\circ})$	91.1(1)
	$\gamma\,(^{\circ})$	92.3(1)
	$V\,(nm^3)$	0.361(5)
	$\rho_X\,(\frac{g}{cm^{-3}})$	1.758
	Z	2
hydrogen	urate	
Shift	$x\,(nm)$	0.189 (2)
	$y\,(nm)$	−0.402(1)
	$z\,(nm)$	0.284(1)

hydrogen	urate	
Twist	$\rho_{z,HU}\,(^{\circ})$	28.7(71)
	$\rho_{y,HU}\,(^{\circ})$	68.2(23)
	$\rho_{x,HU}\,(^{\circ})$	−21.0(77)
NH_4^+		
Shift	$x\,(nm)$	0.408(3)
	$y\,(nm)$	−0.144(2)
	$z\,(nm)$	−0.163(2)
NH_3		
Shift	$x\,(nm)$	0.151(6)
	$y\,(nm)$	0.155(4)
	$z\,(nm)$	0.049(4)
Prob.	p_{NH_3}	0.34(2)

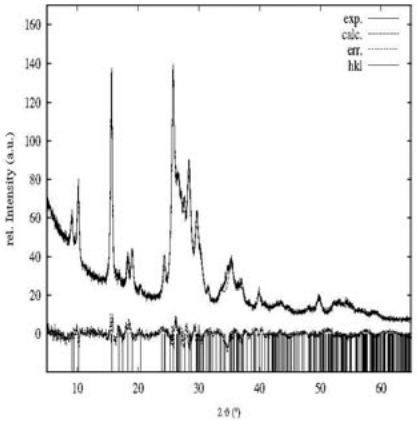

(a) Rietveld fit of the powder diffraction pattern.

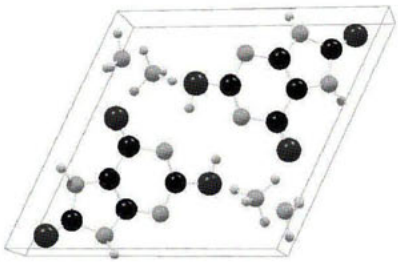

(b) The view inside the unit cell.

Figure 2: Proposal for the crystalline structure of the natural uroliths.

It can be seen that we have taken into account the presence of an additional ammonia molecule with reduced probability inside the unit cell. There are different reasons for this assumption. Because of the unit cell volume found to be $V = 0.361\,nm^3$ a Z value of 2 had to be assumed. Packing the mass of two ammonium hydrogen (acid)

Table 2: Fractional atom coordinates x, y and z of the hydrogen (acid) urate ion, the NH_4^+ ion and the NH_3 molecule including their probabilities p.

	x	y	z
hydr. urate			
C1	0.3987	-0.4446	0.2503
N2	0.5359	-0.4306	0.3833
C3	0.6804	-0.3032	0.4691
N4	0.7011	-0.1702	0.4663
C5	0.5678	-0.1862	0.3386
C6	0.4680	-0.3093	0.2289
N7	0.4193	-0.0696	0.3156
C8	0.2394	-0.1256	0.1819
O9	0.0999	-0.0574	0.1234
N10	0.2778	-0.2773	0.1291
O11	0.2545	-0.5587	0.1647
O12	0.8474	-0.3040	0.5887
H13	0.0666	-0.3385	0.0645
H14	0.8116	-0.4059	0.5728
H15	0.3102	0.0132	0.3943
NH_4^+			
N01	1.0846	-0.2117	-0.1680
H02	1.0908	-0.2887	-0.1272
H03	1.1999	-0.2512	-0.2646
H04	1.2338	-0.1193	-0.1023
H05	0.8140	-0.1877	-0.1780
NH_3			
N20	0.4426	0.1765	0.0630
H22	0.6599	0.1980	0.0128
H23	0.3744	0.0694	0.0073
H25	0.2292	0.2281	0.0419

p
0.34
0.34
0.34
0.34

urate into our unit cell the density would be $1.70\,g\,cm^{-3}$. Experimentally density values of natural uroliths are not given by the literature, because they are not pure substances in general. So we used the measured density of the material synthesized by Tettenhorst which was determined to $1.772\,g\,cm^{-3}$. Consequently, a density of $1.70\,g\,cm^{-3}$ would be too small, and packing only two ammonium hydrogen (acid) urate ion pairs into the unit cell would not fill it. An additional argument for this assumption of this additional NH_3 in the structure is the observation of Tettenhorst [1] that the synthesis of well crystallized material was supported by excess of NH_3 , with respect to the stoichiometric ammonium hydrogen urate.

The reduced occupancy of NH_3 could also mean that there are domains with and without such a molecule. This could be related to the anisotropic line broadening mentioned above. Corresponding calculations have been shown hints that there is probably a lattice tensor deviation mostly in x direction.

Conclusions and outlook

We can present a proposal for the mean crystal structure of ammonium hydrogen (acid) urate from natural formed uroliths. Under physiological conditions inside the urinary tract of frequently changing temperatures and concentrations of uric acid and ammonia one have to expect an urolith with crystallite size distribution and micro strains different from that of a regular single crystal. This frequently changing conditions enforce also a changing "offer" of ammonia and uric acid depending on the protein metabolism. In this way the formation of crystallites with structural gradient is probable.

In the light of this knowledge it seems to be necessary to increase the efforts to investigate also the peak broadening and its reasons, which has to be based on a set of different natural and (for comparison) artificial samples. The presence of ammonia and ammonium, working together with hydrogen acid urate as a pH buffering system, may give some informations about the pH conditions inside the urinary tract and could be used potentially for medical indications.
Further studies, based on a set of natural and synthetic samples, should be done for a verification of this hypothesis.

References

[1] R. T. Tettenhorst, R. E. Gerkin *Powder Diffraction* **14**, 305 (1999)

[2] E. Dubler, G. B. Jameson, Z. Kopajtic *Journal of Inorganic Biochemistry* **26**, 1 (1986)

[3] M. C. Frincu, C. E. Fogarty, J. A. Swift *Langmuir* **20**, 6524 (2004)

[4] P. Friedel, J. Tobisch, D. Jehnichen, T. Taut, M. Rillich, C. Kunert, F. Böhme *J. Appl. Cryst.* **31**, 874 (1998)

[5] M. Schmidt, K. Baldridge, J. Boatz, J. Jensen, S. Koseki, M. Gordon, K. Nguyen, T. Windus, S. Elbert *Quantum Chemistry Program Exchange Bull.* **10**, 52 (1990)

[6] J. Bergmann, T. Taut *Rietveld Analysis Program BGMN* Seifert-FPM GmbH Freiberg/Sa Am St. Niclas Schacht 13, 09599 Freiberg/Sa, Germany (1999)

[7] J. Bergmann, P. Friedel, R. Kleeberg *CPD News Letters* **8**, 5 (1998)

[8] B. Finlayson, A. Smith *J. Chem. Eng. Data* **19**, 94 (1974)

[9] F. Bergmann, S. Dikstein *J. Am. Chem. Soc.* **77**, 691 (1955)

[10] W. F. Van Gunsteren, H. J. C. Berendsen *Angew. Chem.* **102**, 1020 (1990)

[11] S. J. Weiner, P. A. Kollman, D. Case, U. C. Singh, C. Ghio, G. Alagona *J. Amer. Chem. Soc.* **106**, 765 (1984)

[12] P. W. Stephens *J. Appl. Cryst.* **32**, 281 (1999)

Acknowledgments

The authors are indebted to the colleagues of the computer center of the Dresden University of Technology, Germany for the access to the computing power and different software packages.

Z. Kristallogr. Suppl. **23** (2006) 523-528

X-ray powder diffraction data of synthetic ß- Tricalcium Phosphate

M. Ermrich[1*], F. Peters[2]

[1]Röntgenlabor Dr. Ermrich, Am Kandelborn 7, D - 64354 Reinheim, Germany
[2]Curasan AG, In der Schildwacht 13, D - 65933 Frankfurt/Main, Germany
[*]Contact author: roentgenlabor-dr.ermrich@t-online.de

Keywords: X- Ray powder diffraction, ß- TCP, biomineral, bioceramic

Abstract. Synthetic Tricalcium Phosphate (ß- TCP), with the lowest as possible Mg- content which is necessary for the structure stabilization, was investigated by powder diffraction. Using the well-known structure the rhombohedral cell parameters were refined to (space group R-3c, 167) $Ca_3(PO_4)_2$: a = b = 10.4183(5) Å, c = 37.3464(23) Å, γ = 120°, V = 3510.52(47) Å^3; Z = 21, D_x = 3.081 g/cm^3. These values represent the lowest lattice parameters as possible.

Introduction

The Whitlockite mineral and its crystallographic data (PDF #9-169, [1]) are generally in use to identify the ß- TCP phase in practice. But, the lattice parameters change with different Mg- contents [2]. At the latest now, beginning with the synthesis of ß- TCP e.g. as biomaterial it leads to an unsatisfactory assignment. Finally the synthesis of pure ß- TCP succeeded. For that, only a very low amount of < 0,5 wt.% Mg is necessary to stabilize the structure as already given by the raw materials.

Synthesis

Calcium hydrogen phosphate (extra pure) and Calcium carbonate (analytical grade) from Merck was used for the synthesis of the pure phase ß- tricalcium phosphate. The substances were mixed together in a planetary ball mill in an amount to reach a molar calcium to phosphorous ratio of 1.5.
The mixture was then compacted in an hydraulic press to achieve a good contact of the particles and sintered at 1100°C for 48 hours. Dry air was conducted through the oven to remove water and carbon dioxide from the sample while sintering.

Experimental

X-ray powder diffraction data were measured at room temperature with a STOE STADIP θ/θ- diffractometer using Cu- Kα- radiation. The measurement was carried out in an angle

region of 5° to 140° with a counting time of 10s per 0,02° step. For the calculation the region up to 90 °(2θ) was used. Experimental details of recording powder patterns are summarised in table 1.

Table 1. Experimental conditions

Instrument	STOE STADIP θ/θ- Diffractometer
Radiation	Cu- Kα, λ = 1,5418 Å
Parameters	U = 42kV, I = 40mA
Monochromator	reflected beam, plane Graphite
Detector	Scintillation counter
Slits	0,7mm, 0,3mm, 2x8mm
Sampel holder	reflection type, rotating
Range/ 2θ	5° - 140°
Step size / 2θ	0,02°
Counting time per step	10s
Specimen particle size	d50 = 10µm
Instrumental profile breadth	< 0,1° at 30° (2θ)
Temperature	22°C

Results

The X-ray powder data for $Ca_3(PO_4)_2$ are represented in tables 2 and 3, respectively. The X-ray diffraction pattern is shown in figure 1. Unit cell refinement was performed by the STOE program WINX^{POW} [3]. The initial cell parameters were obtained by the PDF data #9-169. The volume V and the density ρ are 0,3% ... 0,5% smaller / higher compared to the PDF- #9-169 and both to [4] and [5], [6] respectively. This agrees with the investigations in [2]; cell parameters decrease continuously with the addition of Mg^{2+} with the respective ionic radii of Ca^{2+} and Mg^{2+}.

Conclusions

Synthetic ß- TCP, $Ca_3(PO_4)_2$, has been stabilized with the lowest as possible Mg- content and then characterized. The unit cell parameters have been refined using the Rietveld refinement procedure. These parameters should be used for the assignment of ß- TCP with priority for those materials, which are synthetically produced in contrast with the natural mineral Whitlockite. They represent the lowest as possible parameters.
The data replace the PDF card #9-169 in set 55 of the ICDD with the card No. #55-898.

References

1. PDF #9-169 of the ICDD, data based on Grant-in-Aid (1957), de Wolff, P., Technisch Physische Dienst, Delft, The Netherlands

2. Farmery, R., Richard, N. and Boch, Ph. (1994). „Preparation of α- and ß- Tricalcium Phosphate Ceramics, with and without Magnesium Addition." *Ceramics International* **20**, pp. 327-336
3. WINX^{POW} Version 1.06(1999). (C) STOE & CIE GmbH Darmstadt/Germany
4. Dickens, B., Schroeder, L.W. and Brown, W.E. (1974). „Crystallographic studies of the role of Mg as a stabilizing impurity in ß-$Ca_3(PO_4)_2$. I. The crystal structure of pure ß- $Ca_3(PO_4)_2$", *J. of Solid State Chem.* **10**, pp. 232-248.
5. Elliott, J.C. (1994). "Structure and Chemistry of The Apatites and Other Calcium Orthophosphates", *Studies in Inorganic Chemistry* **18**, ELSEVIER SCIENCE B.V. Amsterdam, p. 37.
6. Yashima, M., Sakai, A., Kamiyama, T., Hoshikawa, A. (2003). "Crystal structure analysis of beta-tricalcium phosphate $Ca_3(PO_4)_2$ by neutron powder diffraction", *J. of Solid State Chem.*, Vol. 175, Issue 2, pp. 272-277

Table 2. Comparison of unit cell parameters of Whitlockite (PDF #9-169 and [4], [5], [6]) and synthetic ß- TCP (Mg- content < 0,5wt. %)

Sample $Ca_3(PO_4)_2$	Space group	Unit cell parameters (Å), Volume (Å^3)	Density ρ (g/cm^3)
Whitlockite,	R-3c (167)	a = 10.429	3.072
PDF #9-169		c = 37.38	
		V = 3,520.91	
[4], [5] ß-TCa,MgP	R-3c (167)	a = 10.439(1)	3.067
		c = 37.375(6)	
		V = 3,527.20	
[6] neutron diffraction	R-3c (167)	a = 10.4352(2)	3.067
		c = 37.4029(5)	
		V = 3,527.26	
Synthetic ß- TCP	R-3c (167)	a = 10.4183(5)	3.081
		c = 37.3464(23)	
		V = 3,510.52(47)	

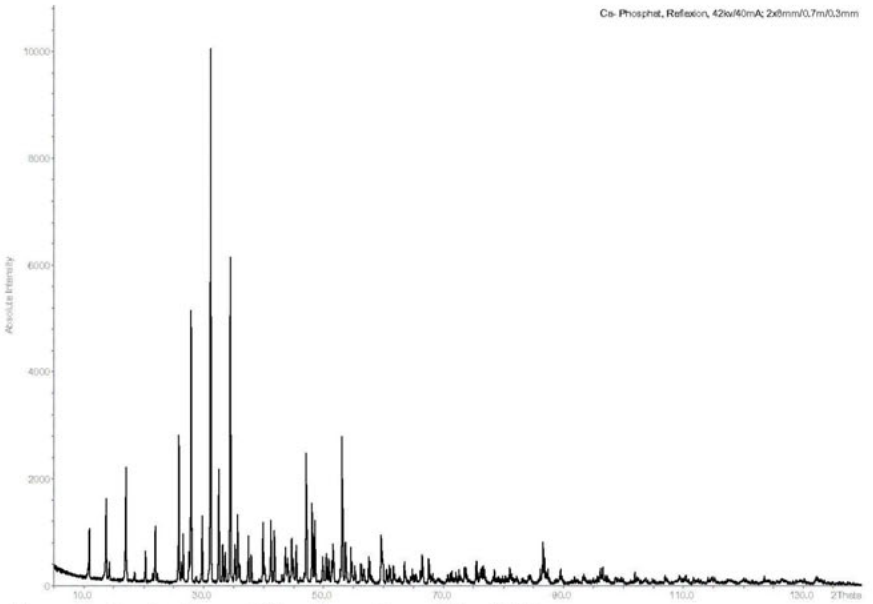

Figure 1. Powder X-ray diffraction pattern of $Ca_3(PO_4)_2$.

Table 3. Powder diffraction data for $Ca_3(PO_4)_2$ [Figure of merit F(138) = 49.9]

N	2Th(obs)	H	K	L	2Th(calc)	obs-calc	Int.	d(obs)	d(calc)
1	10.879	0	1	2	10.882	-.0033	9.0	8.1263	8.1239
2	13.653	1	0	4	13.637	.0160	16.4	6.4805	6.4881
3	14.246	0	0	6	14.218	.0288	2.7	6.2119	6.2244
4	17.032	1	1	0	17.008	.0241	21.8	5.2018	5.2091
5	18.471	1	1	3	18.448	.0223	1.8	4.7997	4.8054
6	20.247	2	0	2	20.235	.0124	5.2	4.3824	4.3851
7	21.405	0	1	8	21.414	-.0086	1.3	4.1478	4.1462
8	21.876	0	2	4	21.863	.0127	10.5	4.0596	4.0619
9	22.252	1	1	6	22.236	.0160	1.7	3.9919	3.9948
10	25.782	1	0	10	25.798	-.0152	26.2	3.4527	3.4507
11	26.222	2	1	1	26.220	.0022	3.4	3.3958	3.3961
12	26.546	1	2	2	26.549	-.0035	8.8	3.3551	3.3547
13	27.472	1	1	9	27.458	.0142	4.7	3.2440	3.2457
14	27.827	2	1	4	27.829	-.0027	53.2	3.2035	3.2032
15	28.649	0	0	12	28.660	-.0114	1.1	3.1134	3.1122
16	28.764	1	2	5	28.755	.0093	.9	3.1012	3.1022
17	29.676	3	0	0	29.681	-.0048	12.2	3.0080	3.0075
18	31.052	0	2	10	31.063	-.0111	100.0	2.8778	2.8768

19	32.479	1	2	8	32.488	-.0091	22.0	2.7545	2.7537
20	33.045	0	3	6	33.053	-.0080	7.4	2.7086	2.7080
21	33.504	1	1	12	33.515	-.0111	6.1	2.6726	2.6717
22	34.398	2	2	0	34.405	-.0067	64.8	2.6051	2.6046
23	35.042	0	1	14	35.049	-.0073	4.3	2.5587	2.5581
24	35.180	2	2	3	35.174	.0058	7.0	2.5490	2.5494
25	35.617	2	1	10	35.623	-.0053	13.4	2.5186	2.5183
26	35.941	1	3	1	35.940	.0012	3.7	2.4967	2.4968
27	37.173	1	3	4	37.167	.0058	2.1	2.4167	2.4171
28	37.384	2	2	6	37.398	-.0142	8.1	2.4036	2.4027
29	37.883	3	1	5	37.888	-.0045	5.7	2.3730	2.3728
30	39.197	2	0	14	39.202	-.0053	.6	2.2965	2.2962
31	39.850	1	0	16	39.861	-.0105	11.7	2.2603	2.2598
32	40.117	1	1	15	40.108	.0085	3.5	2.2459	2.2464
33	40.862	3	1	8	40.884	-.0223	1.5	2.2067	2.2055
34	41.142	4	0	4	41.137	.0050	13.4	2.1923	2.1925
35	41.722	3	0	12	41.731	-.0088	11.3	2.1631	2.1627
36	43.008	1	2	14	43.014	-.0063	1.6	2.1014	2.1011
37	43.499	1	3	10	43.498	.0013	5.0	2.0788	2.0789
38	43.594	0	0	18	43.587	.0069	5.5	2.0745	2.0748
39	43.770	3	2	1	43.766	.0038	2.5	2.0666	2.0667
40	43.977	2	3	2	43.977	-.0003	5.0	2.0573	2.0573
41	44.575	0	4	8	44.578	-.0029	9.6	2.0311	2.0310
42	44.816	3	2	4	44.813	.0027	4.5	2.0207	2.0208
43	44.975	3	1	11	44.965	.0095	1.0	2.0140	2.0144
44	45.366	2	2	12	45.369	-.0028	8.4	1.9975	1.9974
45	46.069	4	1	0	46.063	.0058	.6	1.9686	1.9689
46	46.680	4	1	3	46.669	.0102	2.3	1.9443	1.9447
47	47.022	3	2	7	47.053	-.0305	30.2	1.9309	1.9298
48	48.042	2	3	8	48.044	-.0013	18.0	1.8923	1.8922
49	48.449	4	1	6	48.453	-.0041	14.6	1.8773	1.8772
50	49.820	0	1	20	49.828	-.0082	5.4	1.8289	1.8286
51	49.943	3	1	14	49.930	.0127	1.0	1.8246	1.8251
52	50.360	3	2	10	50.362	-.0020	6.8	1.8105	1.8104
53	50.784	5	0	2	50.791	-.0072	5.1	1.7964	1.7961
54	51.322	1	4	9	51.322	.0005	5.2	1.7788	1.7788
55	51.543	0	5	4	51.542	.0004	8.8	1.7717	1.7717
56	52.685	3	3	0	52.671	.0141	2.7	1.7359	1.7364
57	53.019	2	0	20	53.033	-.0146	34.3	1.7258	1.7254
58	53.616	3	0	18	53.621	-.0048	9.3	1.7080	1.7078
59	53.789	2	4	1	53.774	.0146	1.3	1.7029	1.7033
60	54.470	5	0	8	54.472	-.0024	7.8	1.6832	1.6831
61	54.673	2	4	4	54.676	-.0026	2.1	1.6774	1.6773
62	54.989	1	0	22	54.997	-.0087	.5	1.6685	1.6683
63	55.157	4	1	12	55.156	.0004	3.6	1.6639	1.6639

64	56.168	2	3	14	56.203	-.0347	3.2	1.6363	1.6353
65	56.606	0	5	10	56.601	.0054	2.9	1.6246	1.6248
66	56.694	2	2	18	56.675	.0191	2.1	1.6223	1.6228
67	56.825	5	1	1	56.823	.0019	.5	1.6189	1.6190
68	57.489	3	3	9	57.488	.0015	5.7	1.6018	1.6018
69	57.689	5	1	4	57.692	-.0032	3.0	1.5967	1.5966
70	57.999	0	2	22	58.003	-.0039	1.4	1.5889	1.5888
71	59.558	2	4	10	59.554	.0043	9.0	1.5510	1.5511
72	59.655	3	2	16	59.655	-.0006	7.4	1.5487	1.5487
73	60.416	1	5	8	60.421	-.0046	3.2	1.5310	1.5309
74	60.899	2	1	22	60.912	-.0134	4.1	1.5200	1.5197
75	61.064	3	3	12	61.061	.0031	1.3	1.5163	1.5163
76	61.623	6	0	0	61.628	-.0051	3.7	1.5039	1.5037
77	61.958	3	1	20	61.956	.0022	.7	1.4965	1.4966
78	62.403	5	1	10	62.419	-.0158	.9	1.4869	1.4866
79	62.634	4	3	1	62.628	.0056	1.2	1.4820	1.4821
80	63.448	4	3	4	63.448	-.0003	5.1	1.4649	1.4649
81	63.913	3	4	5	63.938	-.0249	.5	1.4554	1.4549
82	64.441	5	2	0	64.440	.0011	1.5	1.4447	1.4448
83	64.752	0	4	20	64.760	-.0076	3.1	1.4385	1.4384
84	65.268	4	3	7	65.233	.0352	2.1	1.4284	1.4291
85	65.434	3	2	19	65.426	.0079	.7	1.4252	1.4253
86	66.032	3	4	8	66.036	-.0040	2.9	1.4137	1.4136
87	66.368	5	2	6	66.370	-.0022	6.8	1.4074	1.4073
88	67.497	2	3	20	67.500	-.0032	5.3	1.3866	1.3865
89	67.939	4	3	10	67.943	-.0038	1.4	1.3786	1.3785
90	68.138	1	6	1	68.143	-.0048	1.3	1.3751	1.3750
91	68.748	5	2	9	68.744	.0044	.6	1.3643	1.3644
92	69.037	3	4	11	69.043	-.0059	1.1	1.3593	1.3592
93	69.385	6	1	5	69.398	-.0130	.5	1.3534	1.3531
94	70.409	1	1	27	70.367	.0424	.8	1.3362	1.3369
95	70.674	3	3	18	70.687	-.0135	1.8	1.3318	1.3316
96	71.153	1	2	26	71.169	-.0159	2.5	1.3240	1.3238
97	71.416	6	1	8	71.416	-.0004	2.2	1.3198	1.3198
98	71.853	3	2	22	71.868	-.0153	.9	1.3128	1.3126
99	71.991	5	2	12	72.005	-.0139	2.1	1.3107	1.3104
100	72.520	4	4	0	72.527	-.0066	3.0	1.3024	1.3023
101	72.903	3	4	14	72.911	-.0085	.9	1.2965	1.2964
102	73.452	3	5	1	73.451	.0007	3.2	1.2882	1.2882
103	73.602	5	3	2	73.604	-.0023	3.1	1.2859	1.2859
104	74.016	0	2	28	74.060	-.0439	.5	1.2797	1.2791
105	74.182	2	3	23	74.162	.0198	.5	1.2773	1.2776
106	75.425	4	2	20	75.435	-.0103	5.1	1.2593	1.2591

Z. Kristallogr. Suppl. **23** (2006) 529-534

Distribution of sodium cations and chemisorbed methyl groups in the structure of NaX and NaLSX zeolite catalysts by powder neutron diffraction and ^{13}C NMR.

S. Vratislav[1,*], M. Dlouhá[1], V. Bosáček[2]

[1]Czech Technical University, Faculty of Nuclear Sciences and Physical Engineering, Department of Solid State engineering, 115 19 Prague 1, Czech Republic
[2]Heyrovský Institute of Physical Chemistry, 182 23 Prague 8, Czech Republic
[*]Contact author: e-mail: Stanislav.Vratislav@fjfi.cvut.cz.

Keywords: neutron diffraction, structure analysis, zeolitic catalysts

Abstract. Powder samples of NaX and NaLSX faujasite (Si/Al = 1) in dehydrated state and with adsorbed methyliodide were investigated by neutron diffraction and ^{13}C MAS NMR. The distribution of Na+ cations and chemisorbed methylium ions in the zeolite framework structure (faujasite type) was estimated using the GSAS package and difference Fourier maps. Surface methoxy groups were located mostly at O_1 and O_4 lattice oxygen. The changes in populations of cationic sites after chemisorption were detected.

Introduction

Research activities in the structure investigation of zeolites are stimulated by their potential practical use in chemical technology. Zeolites exhibit a regular structure which can be easily modified. These are important candidates for different types of catalysts and many laboratories try therefore to „tailor" zeolitic catalysts of the requested properties. Nature of acid or basic sites and the distribution of sodium cations and chemisorbed methyl groups in the zeolitic lattice belong to the most important problems of surface chemistry. Theoretical investigations [1] demonstrated that chemical properties of protons are controlled by actual basicity of the lattice oxygen atoms and by the character of bonds where protons are attached. It is well known that chemisorbed carbenium ions on zeolites and other alumosilicates are bonded to basic lattice oxygen atoms, forming thus surface alkoxy species [1]. Experimental support was obtained also from the results of diffraction methods, where namely neutron diffraction provided direct evidence on the location of protons in faujasites with various H+/Na+ ratio [2]. Preparation of the surface alkoxy species is based usually on the reaction of alkohols with surface OH groups or on the reaction of methyliodide with zeolitic cations or acid protons. Methylium ions, evolved in the reaction of adsorbed methyliodide with reactive free

sodium cations (or acid protons), create the bridging form of surface methoxy compounds which are detected by ^{13}C MAS NMR with typical chemical shift of their signal [2,3].The chemical shift of bridging methoxy carbon is very sensitive to the electronegativity of the lattice oxygen atom. It is evident that chemisorbed methylium ions (cations) take part in the charge compensation of the skeleton negative charge and that they substitute the removed plus charges of zeolitic cations (or acid protons in OH) producing e.g. sodium iodide clusters in extra-lattice positions or water molecules as in the case of the reaction of methanol with OH groups.

The aim of our study was to estimate the regular distribution of cations and the location of chemisorbed species CH_3^+ in the lattice and to elucidate the role and participation of various lattice oxygen types in chemisorption of methyl cations. We have shown in the previous studies [4] that methyl groups are located on NaX at new positions associated with oxygen atoms O_1 or O_4.

Experimental

Well-developed crystals of NaY, NaX and NaLSX with a high content of sodium cations and with a low content of defects and decationation were used in this study.

Table 1. Details of experimental data collection and Rietveld refinement[a]

sample	T /K/	space group	R_p	R_{wp}	χ^2	λ /A°/	a /nm/
NaX	7	Fd3	0.0583	0.0476	2.075	1.3621	2.5032(5)
NaX ^{CD3}	7	Fd3	0.0597	0.0486	2.062	1.3621	2.5049(6)
NaLSX	294	Fd3	0.0576	0.0443	2.035	1.3621	2.5081(3)
NaLSX $_{CD3}$	294	Fd3	0.0571	0.0473	2.054	1.3621	2.4981(4)
NaLSX $_{CD3}$	7	Fd3	0.0569	0.0459	2.037	1.3621	2.4936(4)
NaY ^{CD3}	7	Fd3m	0.0591	0.0515	2.083	1.3621	2.4851(6)

Remarks: [a]Rietveld refinement was used to minimize $\Sigma w_i (I_{o,i} - I_{c,i})^2$ where $I_{o,i}$ and $I_{c,i}$ are the observed and calculated powder diffraction intensities for the ith point, respectively. Weights w_i are $1 / I_{o,i}$. Weighted and unweighted profile R factors are defined as $R_{wp} = \{[\Sigma w_i (I_{o,i} - I_{c,i})^2] / [\Sigma w_i (I_{o,i})^2]\}^{1/2}$ and $R_p = \Sigma |I_{o,i} - I_{c,i}| / \Sigma I_{o,i}$. The structure R factor is defined as $R_F = [\Sigma(F_o - F_c)^2] / [\Sigma(F_o)^2]$. The expected R factor (the statistically best possible value for R_{wp}) is defined as $R_e = [(N - P)] / (\Sigma w_i I_{o,i}^2)]^{1/2}$ where N is the number of observed powder diffraction data points and P is the number of refined parameters. χ^2 was calculated from $(R_{wp} / R_e)^2$. λ – wavelenghts of monochromatic neutron beam.

Preparation of samples for neutron diffraction and NMR experiments was carried out as follows: a sample of zeolite was dehydrated under vacuum of 10^{-5} mbar in a glass vessel at 400 °C for 10 hours. Powdered zeolite was then transferred under vacuum into a thin-glass cylindric vessel (diameter of 12 mm, height of 35 mm) and sealed off for the diffraction

experiment. Another portion of the same sample was sealed off under vacuum in a tube for the MAS NMR measurement as described earlier [3]. The mentioned methyl iodide was enriched before the ^{13}C NMR measurement with a small amount of $^{13}CH_3I$ (99% ^{13}C - fy.Aldrich), in order to increase the ^{13}C content in the adsorbate and to facilitate the detection of chemisorbed species. Chemisorption of methyl iodide was carried out in a special all glass-device where the dehydrated and evacuated sample was exposed to a known amount of methyl iodide vapour.

^{13}C MAS NMR spectra were measured on a BRUKER DSX200 spectrometer equipped with magic angle spinning probehead at 50,32 MHz with proton decoupling using pulse programs for Hahn echo and for cross polarisation (details see in [3]). A rotor spinning frequency of 4.5 – 5 kHz was applied.

For diffraction experiments samples were loaded either with CH_3I or with CD_3I (99%D, fy. Aldrich). Neutron powder diffraction patterns were collected at temperatures of 298 and 7 K on the KSN-2 diffractometer, which is placed at the LVR-15 research reactor in Řež near Prague [4]. This device was equipped with close-circuit liquid helium cryostat - type CP-62-ST/5 (Cryophysics SA). The wavelength of 0.1362 nm was used and the resolution $\delta d/d$ = 0.00075 was achieved. The complete structural parameters were determined by Rietveld analysis of powder neutron diffraction data using the GSAS software package [5] including difference Fourier maps. Some experimental parameters of the neutron diffractometer KSN-2 and characteristic features of the refinement processing are given in table 1.

Results and discussion

Structural parameters obtained from our powder neutron diffraction measurements of an initial dehydrated NaX and NaLSX samples[4, 5, 6] at room temperature are in agreement with results of the previous studies [7, 8]. The diffraction patterns (collected at 7 K or 294 K) of chemisorbed samples were used to determine the complete set of structural parameters. Difference Fourier maps revealed the positions of chemisorbed methyl groups and the distribution of cations after chemisorption. The complete sets of structural parameters of our chemisorbed samples were published in [4, 6] for NaX and in [7] for NaLSX. Parameters of NaLSX were refined in both recently discussed space groups [8] i.e. in the Fd3 space group and in the Fddd (orthorhombic) group but without any significant difference. Zeolite LSX (low silica X) has a Si/Al ratio of 1 and represents the highest number of charge-compensating cations of all faujasites.

Cations distribution.

Our experimental data allow to compare the changes in the occupation of positions of the lattice atoms in original evacuated NaX and in the same sample after chemisorption of methyl iodide. We observed serious changes in the distribution of the lattice elements after chemisorption of methylium ions. These changes were detected not only with occupation factors of cationic sites but sometimes also in coordinates of Na^+ cations where a splitting (at 7 K) of the position SI' into two sites Na2 and Na3, which are separated at helium temperature but merged at room temperature, was revealed.

Table 2. Occupation factors P of cationic sites indDehydrated faujasites NaX and NaLSX

Zeolite	NaX					NaLSX				
Cation site	SI	SI´	SII	SIII'(1,2)	SIII'(3)	SI	SI´	SII	SIII'(1,2)	SIII'(3)
Type	16c	32e	32e	96g	96g	16c	32e	32e	96g	96g
P	3	29	31	21	9	0	25	32	34	8

Table 3. NaX with chemisorbed CH_3I (Final fractional coordinates[a] and standard deviations[b]).

Atom	site	P	x	y	z	U_{iso} / $\overset{0}{A}^2$/
T1	96g	1.00	-0.05420(8)	0.1261(10)	0.0351(8)	0.008(5)
T2	96g	1.00	-0.05589(8)	0.0362(8)	0.1242(10)	0.009(6)
O1	96g	1.00	-0.1103(3)	0.0006(3)	0.10620(3)	0.017(4)
O2	96g	1.00	-0.0012(3)	-0.0031(3)	0.1419(3)	0.015(5)
O3	96g	1.00	-0.03567(3)	0.0748(3)	0.0706(3)	0.018(6)
O4	96g	1.00	-0.0698(3)	0.0718(3)	0.1807(3)	0.019(5)
Na1	16c	-	0.00000	0.00000	0.00000	-
Na2	32e	0.91(8)	0.0487(7)	0.0487(7)	0.0488(7)	0.035(7)
Na3	32e	-	0.0583	0.0583	0.0583	-
Na4	32e	1.01(3)	0.2306(2)	0.2306(2)	0.2306(2)	0.003(2)
Na5	96g	-	0.421	0.323	0.160	-
Na6	96g	-	0.435	0.278	0.167	-
Na6´	96g	-	0.467	0.314	0.155	-
Na7[c]	96g	0.28(3)	-0.209(3)	0.295(3)	0.088(3)	0.042(8)
M1[d]	96g	0.12(3)	-0.133(5)	0.193(5)	0.106(4)	0.067(9)
M2[d]	96g	0.12(3)	-0.133(5)	0.106(4)	0.193(4)	0.059(8)
I[e]	96g	0.26(3)	-0.217(5)	0.193(4)	0.193(4)	0.041(7)

[a] Origin at $\bar{3}$ of Fd3; a_o= 24.898(4) $\overset{0}{A}$. [b] Values in parentheses are the estimated standard deviations of the last digit. [c] Position not detected in the original evacuated NaX crystals [d] M1 and M2 positions of the supposed chemisorbed methyl groups. [e] Position assigned to iodine in created NaI clusters.

Cations are distributed over six possible sites as proposed by Olson [9] in the frame of the Fd3 space group. In recent publications [9,10,11] the distribution of Na cation in faujasites was also tested by high resolution ^{23}Na MAS NMR. The NMR results altogether confirm the results from diffraction methods. It is clear that also our neutron diffraction results, presented in the table 2, are well in line (considering various composition of materials and experimental deviations) with the observed cation distribution in all NaX and NaLSX samples published in literature. Cations in SII positions are represented after chemisorption only with the fully occupied Na4 site (32 per unit cell).

Location of chemisorbed groups.

Nuclear densities M1 and M2 assigned to chemisorbed methyl groups were determined by means of difference Fourier maps. Nuclear density contours at the O4 oxygen denoted M1 and M2 are remarkable. Their estimated distances from the oxygen atoms are given in table 4. Let us turn our attention to the observed fact that the M1-O1 (or M1-O4) and M2-O1 (or M2-O4) given in table 3 are spread in the interval from 0.15 to 0.17 nm. It has been shown that in NaLSX the position M1 as well as M2 assigned to the CH_3-group (or CD_3-group) exhibit a shorter distance to O4 than to O1, although in NaX structure the situation is inverse. It is assumed that this effect is associated with the amount of particles in supercages. Also an experiment with argon, which was subsequently adsorbed after preparation of the surface methyl groups and which filled the supercages and restrict the movement of $-CH_3$, has shown a weak decrease in $M_i - O_j$ (i = 1,2; j = 1,4) distances. Comparing this distance with the published C-O bond length for bridging methoxy group, e.g. in dimethyl-aluminium methoxide trimer (d = 0.1436 nm) [12] or in trinuclear methoxy-bridged Ti-Mg complexes (d = 0.1417 nm) [13] exhibited by compact nonporous crystals, it is clear that the distances observed by us in microporous crystals are larger than the C-O bond length estimated in nonporous crystals. To discuss this problem, it would be necessary to take into consideration at least two factors: (1) rotation and precession mobility of the C-O bond of anchored methyl group, and (2) interactions of methyl hydrogens (or D atoms) with other species in their vicinity, e.g. with other lattice oxygen atoms [6]. Nevertheless, the O-C distance lengthening may be also associated with the interaction of the considered chemisorbed CH_3 (or CD_3) group with other species. Further lengthening of the bonds may be possible only through strong intermolecular interactions [14,15] or under the influence of force field gradients in the zeolitic supercavities.

Table 4. Selected distances of chemisorbed methyl groups from lattice oxygen O1 and O4.

zeolitic catalyst	T /K/	CH_3I^* 1mol/u.c	M1-O1 /nm/	M1-O4 /nm/	M2-O1/nm/	M2-O4 /nm/
NaX (+Ar)	7	14.6	0.1663(4)	0.1670(4)	0.1556(5)	0.1572(5)
NaX	7	15.3	0.1653(5)	0.1764(4)	0.1661(5)	0.1789(4)
NaLSX	7	26.4	0.1573(6)	0.1535(5)	0.1712(6)	0.1572(5)
NaLSX	298	24.8	0.1627(6)	0.1530(5)	0.1656(6)	0.1548(5)

Remarks: *Adsorbed molecules per unit cell M1, M2 – chemisorbed methyl groups

Concluding remarks

From our results, the following conclusions can be drawn:
- Chemisorption of methylium ions at nucleophilic lattice oxygen sites has a remarkable effect on the distribution of cations in the lattice. It demonstrates that long-range forces and variations of electrostatic field gradients significantly change the cations distribution.
- Methylium ions are located in X faujasite at O4 and O1 lattice oxygen atoms only in α-supercavity. Although the location at two different sites corresponds well with two observed ^{13}C MAS NMR signals at 54 and 58 ppm of surface bridging methoxyls.

References

1. Mortier, W.J., Sauer, J., Lercher J. A., Noller, H.,1984, *J. Phys. Chem.* **88**, pp. 905-10
2. Jirák, Z., Vratislav, S., Bosáček, V.1980, *J. Phys. Chem. Solids* **41**, pp. 1098-95
3. Bosáček V., *J. Phys. Chem.,* 1993, **97**, 10732.
4. Vratislav, S., Dlouhá, M., Bosáček, V., 2000, *Physica B*, **276-278**, pp. 29-31
5. Von Dreele R. B. and Larson A. C., LANSCE Newsletter No. 4, Winter 1988, Los Alamos
6. Vratislav, S., Dlouhá, M., Bosáček, V., 2002, *Applied Physics A*, **74**, pp.1320-21.
7. Vratislav S., Dlouhá M., Bosáček V., 3rd European Conference on Neutron Scattering, Communication **B54**, Montpellier 2003, France, *Physica B* in print
8. Czjzek M., Jobic H., Fitch A.N., Vogt T., *J. Phys. Chem.* 1992, **96**, 1535.
9. Olson D. H., *Zeolites* 1995, **15**, 439.
10. Plevert J., Di Renzo F., Fajula F., Chiary G., *J. Phys. Chem. B,* 1997, **101**, 10340
11. Baehtz C., Fuess H., Phys. Chem. Chem. Phys., 2002, **4, 4543-4548**
12. Chisholm M.H., Clark D.L., Hampden-Smith M.J., Hoffman D.H., *Angew. Chem, Int. Ed. Engl.* 1989**, 28**, 432.
13. Gyepes R., Hiller J., Thewalt U., Polášek M., Šindelář P., Mach K., *J. Organomet.Chem.* 1996, **516**, 177.
14. Chuvilkin N.D., Korsunov V.A., Kazansky V.B., Kinet. Katal. (in Russian) 1986, **27**, 1323.
15. Blaszkowski S.R., van Santen R.A., J. Phys. Chem. 1995, **99**, 11728.

Acknowledgements. This research has been supported by GA ČR grant No. 202/03/0981 and by MŠMT grant No. MSM6840770021.

IV.4.3 *Determination of Magnetic Structure, Magnetic Materials*

Z. Kristallogr. Suppl. **23** (2006) 537-542

Structural and magnetic study of magnetoelectric perovskite Sr_2CoMoO_6

S. A. Ivanov[1*], S.-G. Eriksson[2], R. Tellgren[3], H. Rundlöf[3], M. Tssegai[3]

[1]Karpov' Institute of Physical Chemistry, Moscow, Russia
[2]Department of Inorganic Chemistry, University of Gothenburg, Sweden
[3] Institute of Chemistry, Uppsala University, Uppsala, Sweden
[*]Contact author; e-mail: ivan@cc.nifhi.ac.ru

Keywords: neutron diffraction, perovskite , crystal structure, magnetic structure

Abstract. A study of the crystal and magnetic structure of the double perovskite Sr_2CoMoO_6 has been carried out on a polycrystalline sample using neutron diffraction (NPD) data between 10-700K. An analysis of NPD patterns at 295K has shown that this compound crystallizes in the tetragonal space group I4/m with a = 5.5616(1) and c = 7.9470(2) Å and has a 1:1 ordered arrangement of the B-sites. This compound undergoes a I4/m→Fm$\bar{3}$m improper ferroelectric phase transition near 563 K. A low-temperature antiferomagnetic ordering (below T_N = 37 K) has been followed from a sequence of low-temperature NPD data sets. The magnetic structure is defined by the propagation vector $\vec{k}$ = (1/2,0,1/2). Alongside the obtained experimental results on magnetic and electric properties some aspects of magnetoelectricity in this perovskite is also discussed.

Introduction

Magnetoelectric materials simultaneously manifesting both ferroelectric and ferromagnetic properties have been an interesting subject of study not only for their possible application in electronic devices but also from the viewpoint of material science [1]. At present time the number of candidate materials is strongly limited and the effects are typically too small to be useful in applications [2]. It is very important to understand under which thermodynamic conditions and chemical environment the coexistence of magnetic and ferroelectric orderings can take place. It has been shown [2] that ferroelectricity and magnetism are rarely found in the same compound. Much experimental work still needs to be done in order to reach a clear understanding of this coexistence and create such compositions. Sr_2CoMoO_6 belong to the class of perovskite compounds, which simultaneously can exhibit the long- range ordering of electrical and magnetic dipoles [3-5]. This double perovskite was first prepared and studied by Galasso [3]. Later it was reported to be an antiferromagnetic with T_N = 34K [4-7] and an improper ferroelectric with T_C = 563K [8]. The crystal structure at room temperature has been reported several times [3-8] but there are some differences in the structural details re-

ported by different authors and still many points remaining unclear. X-ray diffraction was the main technique used in these studies to elucidate the structure of Sr_2CoMoO_6. NPD techniques are much more sensitive than X-ray methods for structural studies of magnetoelectric oxides with strong cubic pseudosymmetry. We have therefore undertaken NPD studies on this compound. The main purpose of this study was to resolve the discrepancy in the literature on Sr_2CoMoO_6 and to determine the temperature evolution of the nuclear and magnetic structures.

Experimental

According to the procedure described in [8] a high quality ceramic Sr_2CoMoO_6 sample was prepared by mixing appropriate amounts of oxides or carbonates and grinding in ethanol. The mixtures were then sintered in air at 1523 K for 24 hours, pressed into pellets and fired at 1623K for 10 hours with one intermediate grinding. The samples were characterized by X-ray powder diffraction (XRD diffractometer URD-63, Cu K_α -radiation) for phase identification and to check phase purity. The prepared sample was pure single phase. Electron probe microanalysis shows that the studied sample has close to the expected cation ratio which was estimated as $Sr_{2.01(2)}Co_{0.98(2)}Mo_{1.01(2)}O_6$. Magnetic measurements were consistent with antiferromagnetic ordering with $T_N = 36$ K in full agreement with the results in references [5,7]. Medium- resolution NPD data were collected at the Swedish Research reactor R2 at Studsvik with the Huber two-circle diffractometer equipped with an array of 35 ^{3}He detectors. The wavelength was 1.470(1) Å. Diffractograms were registered at temperatures 10, 100, 200, 300 and 700 K. Absorption effects were corrected for in the Rietveld refinements using the experimentally determined value $\mu R = 0.0645 cm^{-1}$. The step-scan covered a 2θ- range 4.00° to 139.92° with a step-length 0.08°. The diffraction data were refined by the Rietveld method using the FULLPROF software [9]. Each structural model was refined to convergence and the best result was chosen on the basis of agreement factors and stability of the refinement. Magnetic susceptibilities were measured with a Quantum Design SQUID magnetometer at an applied field of 10 Oe in the temperature range 5- 400 K. Zero field cooled measurements (ZFC) were performed by cooling the samples to 10 K, applying the field, and measuring the magnetisation as the samples were heated. A detailed procedure of the dielectric and electrical measurements has been described elsewhere [8].

Results

According to the X-ray analysis, the sample was perfectly phase pure. XRD patterns at 300 K could be indexed on the basis of a I- centered tetragonal cell with lattice parameters a = 5.5616(1) and c = 7.9470(2) Å. This indexing is only in slight disagreement with the cell parameters reported in [7], while the indexing performed in [6,8] is completely different from the cell parameters found in this research. Inspection of the NPD pattern at 700 K provided some evidence for several low intensity superstructure reflections suggesting a doubling of the perovskite unit cell because of the ordering between Co and Mo cations at the B sites (see Figure 1). Owing to the existence of these weak peaks in this pattern possible models based on disordered B-cation distributions were rejected from future consideration for the

high temperature phase. The high temperature NPD data were refined in space group $Fm\bar{3}m$ with a = 7.9388(2)Å (see Table 1). Refinements of the site occupancy factors of the cations and oxygen atoms did not reveal significant changes from full occupancy.

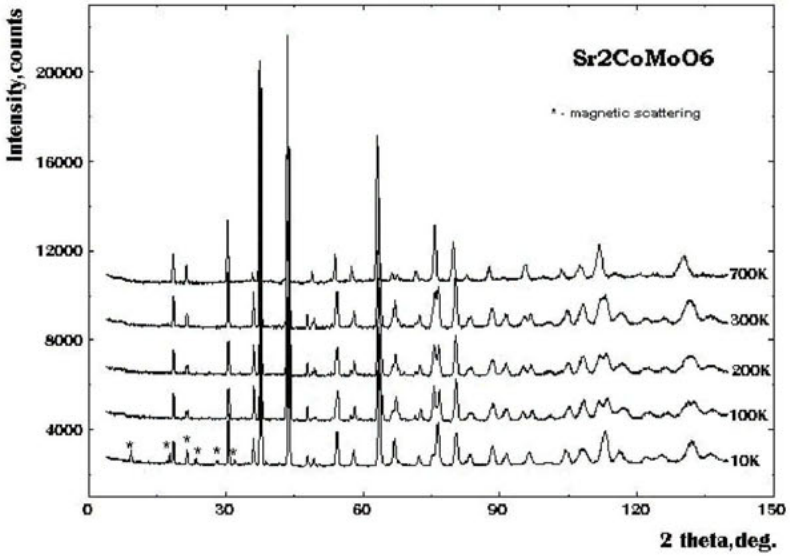

Figure 1. Temperature evolution of NPD patterns for Sr_2CoMoO_6 .

However, the same structural model could not account for the NPD data obtained at 300 K. It was found that Sr_2CoMoO_6 has a tetragonally distorted perovskite-type structure at all the temperatures indicated. It was shown that space group I4/m provided the best fit to our powder pattern. The final Fourier difference synthesis calculation showed no significant maxima. Table 2 lists the main interatomic distances. The average Co-O bond length is very similar to that found in other oxides containing Co^{+2} [10] and close to the Co^{2+}-O bond length calculated from Shannon´s ionic radii [11] for a 6 coordinated high spin state. The Co-O-Mo superexchange pathways are almost linear (the Co-O-Mo angle is about 166.7° at 10K). MoO_6 octahedra are larger and slightly elongated compared to regular CoO_6 octahedra. In order to get some insight into the cation distribution, we carried out bond-valence sum calculations according to Brown´s model [12] which gives a relationship between the formal valence of a bond and the corresponding bond lengths. From individual cation-anion distances the valences of the cations were calculated. The Co cations exhibit the valences +2.20(1), which slightly differ from the expected Co^{+2} valence in this compound. In compensation, the va-

lence of the Mo cation is somewhat lower than +6 (5.64(2)). From these results we can conclude that the Co cations formally show a +2 valence.

Table 1. The nuclear and magnetic structure of Sr_2CoMoO_6 at different temperature.

T = 700 K, space group $Fm\bar{3}m$, a = 7.9388(2) Å, V = 500.3 Å^3
R_p = 3.58, R_{wp} = 4.75, R_B = 5.21, χ^2 = 1.92

Atom	Position	x	y	z	B,Å^2
Sr	(8c)	1/4	1/4	1/4	1.66(2)
Co	(4a)	0	0	0	0.34(1)
Mo	(4b)	1/2	1/2	1/2	0.40(1)
O	(24e)	0.2596(3)	0	0	1.84(2)

T = 295 K, space group I4/m, a = 5.5616(1) Å, c = 7.9470(2) Å, V = 245.8 Å^3
R_p = 3.54, R_{wp} = 4.71, R_B = 4.59, χ^2 =1.91

Sr	(4d)	0	1/2	1/4	0.79(3)
Co	(2a)	0	0	0	0.12(2)
Mo	(2b)	0	0	1/2	0.17(2)
O1	(8h)	0.2890(5)	0.2282(5)	0	0.73(4)
O2	(4e)	0	0	0.2583(6)	1.04(4)

T = 100K, space group I4/m, a = 5.5469(1) Å, c = 7.9674(2) Å, V = 245.1 Å^3
R_p = 3.32, R_{wp} = 4.71, R_B = 4.19, χ^2 = 2.05

Sr	(4d)	0	1/2	1/4	0.29(3)
Co	(2a)	0	0	0	0.08(2)
Mo	(2b)	0	0	1/2	0.10(2)
O1	(8h)	0.2934(5)	0.2234(5)	0	0.47(3)
O2	(4e)	0	0	0.2594(6)	0.58(3)

T = 10K, space group I4/m, a = 5.5761(1) Å, c = 7.8809(2) Å, V = 245.0 Å^3
R_p = 3.25, R_{wp} = 4.70, R_B = 4.04, χ^2 = 1.88, R_{MAG} = 6.8, Magnetic moment: μ_{Co} =2.42(5)μB

Sr	(4d)	0	1/2	1/4	0.25(3)
Co	(2a)	0	0	0	0.07(2)
Mo	(2b)	0	0	1/2	0.09(2)
O1	(8h)	0.2897(5)	0.2299(5)	0	0.33(3)
O2	(4e)	0	0	0.2572(1)	0.48(3)

Following [13], the phase transition with the I4/m→Fm$\bar{3}$m symmetry change is connected with a tilting of BO_6-octahedra about the c axis (corresponding to a so called $a^0\ a^0\ c^-$ tilt system). The improper ferroelectric phase transition was observed previously in Sr_2CoMoO_6 near 563K [4,8]. If one takes into account the values of the polyhedra distortions, the ferroic properties of Sr_2CoMoO_6 may be connected with the Sr sublattice. It was found that the distortion of the SrO_{12} polyhedra was significantly larger ($24.2x10^{-4}$) then for the Co and Mo ones ($0.01x10^{-4}$ and $0.03x10^{-4}$, respectively).

Table 2. Selected interatomic distances (Å) for Sr_2CoMoO_6 at the different temperatures.

Bond	700K	295K	100K	10K
		2.633(5)x4	2.611(3)x4	2.631(3)x4
Sr-O(Å)	2.808(1)x12	2.782(4)x4	2.771(3)x4	2.789(3)x4
		2.969(5)x4	2.995(4)x4	2.955(4)x4
Co-O(Å)	2.061(6)x6	2.048(5)x4	2.046(4)x4	2.059(3)x4
		2.053(5)x2	2.067(4)x2	2.031(3)x2
Mo-O(Å)	1.908(6)x6	1.914(6)x4	1.915(5)x4	1.911(4)x4
		1.921(6)x2	1.917(5)x2	1.909(4)x2

At 10 K (below T_N) NPD data have been found to contain considerable amount of magnetic contributions and new peaks appear on positions forbidden for the main reflections in s.g. I4/m (see Figure 1). In order to verify that the observed extra intensities indeed were magnetic to its origin X-ray diffraction measurements were carried out for comparison. These new reflections correspond to magnetic satellites defined by the propagation vector $\vec{k}$ = (1/2,0,1/2). The NPD pattern at 10 K was refined for a two phase model namely the nuclear phase (space group I4/m) and the magnetic phase (space group P1) simultaneously. An antiferromagnetic structure was modelled with magnetic moments at the Co positions. The best fit was obtained for a model with magnetic moments aligned along the [101] direction. The refinement of the magnetic moment at T = 10 K resulted in average values of $\mu = 2.42(5)\ \mu_B$. Similar magnetic moment values of Co^{2+} have been observed in other perovskites [10]. The magnetic arrangement can be described as a stacking of ferromagnetic layers of Co moments which located perpendicular to the body diagonal and coupled antiferromagnetically to adjacent Co layers.

It is interesting to note that other perovskites like Sr_2MMoO_6 (M^{2+} = Mn, Fe, Ni, Cr) and Sr_2CoBO_6 (B^{6+} = W, Te, Re, U) also show the magnetic properties [14,15]. It is important to understand the possible influence of the B-site cations on T_N remembering that it is strongly related with the value of the B^{2+}-O-B^{6+} angle and with lattice distortions. It should be emphasized that T_N increase with a decrease of size of the different B-site cations for both of the above mentioned Mo- and Co- perovskite series. At the same time the influence of A-site cations on T_N still remain to be solved because the available data is very restricted.

Concluding remarks

The phase-pure perovskite Sr_2CoMoO_6 was synthesised and structurally characterised applying the Rietveld analysis of NPD data at different temperatures. This compound shows one structural phase transition I4/m → Fm $\bar{3}$ m as a result of an antiphase octahedral tilting (about 7°) along the c axis. The Co and Mo octahedra are fully ordered. The precise metal-oxygen distances derived from NPD data made it possible to calculate the valences of the cations and the distortion of their polyhedra. These results suggest an electronic configuration as Co^{2+} - Mo^{6+}. The proposed antiferromagnetic structure (below T_N) can be modelled with magnetic moments at the Co positions (μ=2.42μ_B at 10 K) aligned along the [101] direction. Structural and magnetic features of magnetoelectric Sr_2CoMoO_6 are considered and compared with those of other quaternary complex perovskite oxides.

References

1. Venevtsev, Yu.N., Gagulin, V.V., 1994, *Ferroelectrics*, **162**, 23.
2. Hill, N.A., 2002, *Ann.Rev.Mater.*, **32**, 1.
3. Galasso, F., 1960, *J.Phys.Chem.*, **64**, 165.
4. Kupriyanov, M.F.,Fesenko, E.G. 1962, *Sov.Phys.Crystallog.*, **7**, 358.
5. Blasse, G., 1965, *Bull.Soc.Chim.Fr.*, 1212.
6. Morimoto, Y.,Xu, Sh., Machida, A., Akimoto, T., Nishibori, E., Takata, M., Sakata, M. 2000, *Phys.Rev.B.*, **61**, R7827.
7. Viola,M.C., Martinez-Lope,M.J., Alonso,J.A., Velasco,P., Martinez,J.L., Pedregosa, J.C., Carbonio, R.E., Fernandez-Diaz, M.T. 2002, *Chem.Mater.*, **14**, 812.
8. Gagulin, V.V., Korchagina, S.K., Ivanova, V.V. 2003, *Inorg.Mater.*, **39**, 625.
9. Rodriguez-Carvajal, J. 1993, *J.Phys.*, **192**, 55.
10. Martinez-Lope, M.J., Alonso, J.A.,Casais M.T., Fernandez-Diaz, M.T. 2002, *Eur.J.Inorg.Chem.*,2463.
11. Shannon, R.D. 1976, *Acta Crystallog.,Sect.A* **32**, 751.
12. Brese, N.E., O'Keefe, M. 1991, *Acta Crystallog.,Sect.B* **47**, 192.
13. Glazer, A.M. 1972, *Acta Crystallog.,Sect.B* **28**, 3384.
14. Itoh, M., Ohta, I., Inaguma, Y. 1996, *Mater. Sci. and Engin.*, **B41**, 55.
15. Venevtsev, Yu.N., Politova, E.D., Ivanov, S.A. 1985, Ferro- and Antiferroelectrics of Barium Titanate Family (Chemistry, Moscow) p.256.

Acknowledgements. The financial support for this research from the Swedish Strategic Foundation (SSF), within the frames of the program "Complex oxides for advanced applications", and Russian Foundation for Basic Research, is gratefully acknowledged.

Z. Kristallogr. Suppl. **23** (2006) 543-548

Crystal structure and magnetism of $Pr[Fe(CN)_6]\cdot 4D_2O$

V. Kavečanský[1,2,*], M. Mihalik[1], S. Maťaš[1,2], Z. Mitróová[1], M. Lukáčová[1, 2]

[1]Institute of Experimental Physics, Slovak Academy of Sciences, 47 Watson Str., SK-04353 Košice, Slovakia
[2]Hahn-Meitner Institute, Neutron Scattering Center, Glienicker Str. 100, D – 14109 Berlin, Germany
*Contact author; e-mail: viktor.kavecansky@saske.sk

Keywords neutron diffraction and scattering, rare-earth ferricyanides, magnetic properties

Abstract. We present an analysis of neutron diffraction patterns taken from the powder $Pr[Fe(CN)_6]\cdot 4D_2O$ at room temperature and in the temperature range from 1.6 to 40 K. Deuterium atoms were localized by direct space method based on a Monte Carlo simulation process (Fox) and the structure was refined by Rietveld method. Application of detailed crystallographic analysis can be very helpful for understanding of magnetic behaviour.
Although the study of magnetic properties of $Pr[Fe(CN)_6]\cdot 4H_2O$ by NMR spectroscopy, magnetization, DC and AC susceptibility measurements has indicated magnetic correlations, at low temperatures, no significant difference between low and high temperature powder neutron patterns has been detected. Neutron diffraction experiment revealed that the compound does not order magnetically down to 1.6 K.

Introduction

The design of materials exhibiting new physical properties represents a current area of solid state physics research. In the field of molecular magnetism among main challenges belong reaching high values of such parameters as transition temperatures, coercive fields and magnetization. Knowledge of crystal and magnetic structures can significantly contribute to solve the problem.
Rare-earth ferricyanides $Re[Fe(CN)_6]\cdot nH_2O$ (n = 4,5), as a member of Prussian blue family, represent the type of materials that can be used for this purpose. Their physical properties have been extensively studied for a few decades [1-9]. Depending on chemical composition and preparation conditions they form tetrahydrate and pentahydrate complexes. In 1976 the crystal structure of such materials was classified by Hulliger et al. as orthorhombic (nearly pseudo-hexagonal) and hexagonal, respectively [1]. The problem of crystal structure of the complexes was later discussed by Mullica et al. (1989-1996) [2-4], Yukawa et al.(1996) [5], Wang et al. (1999) [6] and Langer et al. (2004) [7].

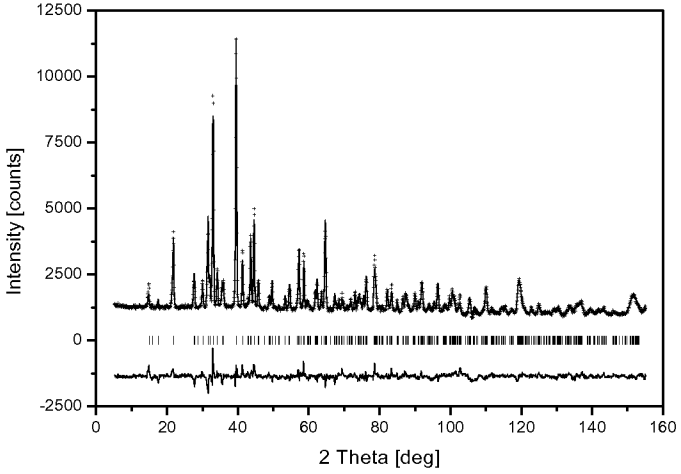

Figure 1. Rietveld refinement plot for $Pr[Fe(CN)_6] \cdot 4D_2O$.

The hexagonal structure ($P6_3/m$) of $La[Fe(CN)_6]\cdot 5H_2O$ was worked out by Bailey et al. [8] and later confirmed by Wang et al. [6]. However, the structure contains a water molecule with C_{2v} symmetry localized on a three-fold axis. The arrangement, which is rather unusual, represents possible conflict between molecular and crystal symmetry.

Crystal structure of tetrahydrate complexes has been described as orthorhombic (*Cmcm*) where no such possible conflict occurs [9]. However, the data often indicate pseudohexagonal symmetry. Detailed analyse of $Pr[Fe(CN)_6]\cdot 4H_2O$ revealed that the single crystal was twinned with three components [7].

The crystal structure of $Sm[Fe(CN)_6]\cdot 4H_2O$ was determined by Kietaibl and Petter [9] by single crystal X-ray diffraction analysis. The structure consists of FeC_6 octahedra located along screw axis. Sm atom is coordinated by six N atoms lying at the apices of a trigonal prism. The polyhedron is completed by two coordinated water molecules (O1). The next two water molecules (O2) occupy holes in the structure above and below the trigonal prism faces and are obviously less strongly bonded [1].

Magnetic properties of the rare-earth ferricyanides (magnetic susceptibility $\chi(T)$ (T = 4 – 300 K) and magnetization M(H) (at 1.3 K and up to 120 kOe) along with predicted types of magnetic ordering for various rare-earth ions were reported by Hulliger et al. [1]. However, up to now there is no published information concerning the magnetic structure of such type of materials.

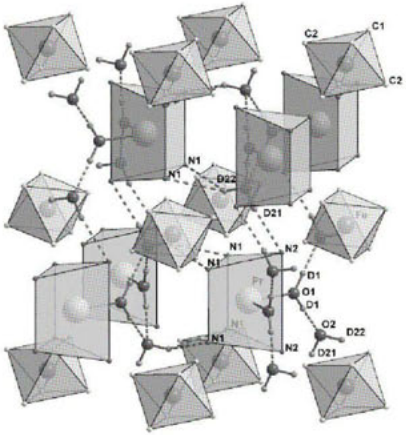

Figure 2. Schematic view of the crystal structure emphasizing the octahedral coordination of FeC_6 and trigonal prismatic coordination of PrN_6. Hydrogen bonded chains O1—D1····O2, O2—D21····N2 and O2—D22····N1 are pictured.

Experimental

The crystal structure of powder sample was characterized by X-ray diffraction and next studied by neutron diffraction methods. However, neutron diffraction experiments require substitution of hydrogen by deuterium atoms. As, in contrast with X-ray diffraction experiments, contribution of the deuterium atoms to the neutron scattering intensity is significant, their positions in the unit cell must be determined.

The deuterium atoms were directly implemented during the preparation process into the compound instead of hydrogen. The $Pr[Fe(CN)_6]\cdot 4D_2O$ salt was synthesized in similar manner as described for the $Re[Fe(CN)_6]\cdot 4D_2O$ [10] by mixing of saturated D_2O solution of $K_3[Fe(CN)_6]$ with D_2O solution of rare earth ions Pr^{3+}. The resulting precipitate was filtered, washed with the deuterium oxide and ethanol and dried above KOH.

The neutron diffraction experiments were carried out at the BER II reactor in HMI in Berlin. The powder sample has been investigated at room temperature at E9 instrument (λ = 1.7972 Å) covering an angular range from 6° to 156° 2θ. The possible magnetic ordering was investigated at E6 instrument (λ = 2.45 Å) in the temperature range 1.6 – 40 K.

Diffraction pattern was indexed by McMaille [11], program based on Monte Carlo simulation. Localization of deuterium atoms was performed by the direct-space method using reverse Monte-Carlo approach (Fox [12]). For the structure simulation building units (FeC_6 octahedra, D_2O water molecules and other atoms that were taken as isolated) were used.

After deuterium positions in $Pr[Fe(CN)_6]\cdot 4D_2O$ were localized, the complete crystal structure was refined using Rietveld method (Fullprof, GSAS) [13-14].
DC magnetization and AC susceptibility of a powder sample were measured by SQUID magnetometer in the temperature range from 5 K to 200 K and magnetic fields up to 5 T.

Results

Indexing procedure has confirmed the orthorhombic symmetry of the phase $Pr[Fe(CN)_6]\cdot 4D_2O$. The structureless (profile matching) fit gave refined values of lattice parameters a = 7.4968(2) Å, b = 12.9582(4) Å, c = 13.8253(4) Å, $\alpha = \beta = \gamma = 90°$. In accordance with the single crystal analysis of $Pr[Fe(CN)_6]\cdot 4D_2O$ [7] the *Cmcm* space group was suggested. The final fit of the structure including localized deuterium atoms ($R_{wp} = 5.69$, reduced $\chi^2 = 4.64$) is shown in figure 1. All atoms were refined isotropically, deuterium atoms with a common atomic displacement parameter. The refined structure was validated by Platon [15].

Table 1. Refined values of positional and isotropic displacement parameters (Ueq = 1/3 of the trace of the orthogonalized U Tensor).

Atom	x	y	z	U_{eq}[Å^2]
Pr	0	0.1743(7)	0.25	0.0085(9)
Fe	0	0.5	0.5	0.0058(5)
C1	0.1811(9)	0.4505(6)	0.5876(5)	0.0108(6)
C2	0	0.3643(6)	0.4423(8)	0.0128(5)
N1	0.2050(7)	0.0720(5)	0.3629(4)	0.0142(4)
N2	0	0.2865(5)	0.4037(5)	0.0156(7)
O1	0.2634(15)	0.2838(11)	0.25	0.0255(5)
D1	0.3327(12)	0.3033(10)	0.3046(6)	0.046(10)
O2	0.5	0.3350(6)	0.4023(6)	0.0211(8)
D21	0.5	0.3063(17)	0.4636(9)	0.046(10)
D22	0.5	0.4063(6)	0.4139(9)	0.046(10)

Refined structural parameters are listed in table 1, some selected bond distances and bond angles in table 2. The schematic view of the crystal structure is shown in figure 2 [16]. The crystal structure was found to be analogous to the structure formerly described [1]. The uncoordinated water molecule (O2) is bonded to O1 and to three N atoms through hydrogen bonds (O1–D1···O2, O2–D21···N2 and to two N1 atoms by symmetrically bifurcated O2–D22···N1 bond).
Zero-field-cooled (ZFC) and field-cooled (FC) magnetization curves investigated at magnetic fields H = 10, 50 and 100 Oe are shown in figure 3(a). In all cases there is a considerable irreversibility between the ZFC and FC branch of the DC magnetisation. Below $T \approx$ 20 K the magnetisation starts to increase. The ZFC curves deviate from the FC magnetisation below T_f = 14.5 K, which is independent on applied magnetic field, and show a broad maximum at about T = 12K. The occurrence of the cusp in $M(T)$ dependence is typical for the small particle system. The maximum in the ZFC magnetisation curve at $T = T_M$ marks the

transition from the stable (Stoner-Wohlfarth) single domain particles at lower temperatures (below the blocking temperature T_B) to the superparamagnetic ones.

Table 2. Selected bond distances (in [Å], left) and bond angles (in [deg]). Indexes c, h, j and n denote symmetry operators -x, y, ½-z; x, y, ½-z; ½+x, ½-y,1-z; and ½-x, ½+y, z, respectively.

Pr	–	O1	2.432(13)	N1_c	–	Pr	–	O1	79.3(3)
Pr	–	N1	2.560(7)	O1	–	Pr	–	O1_c	108.6(6)
Pr	–	N2	2.575(8)	N1_c	–	Pr	–	N2_c	77.8(2)
Fe	–	C1	1.929(7)	N1	–	Pr	–	N2_c	142.7(1)
Fe	–	C2	1.931(8)	C1	–	Fe	–	N2	88.4(2)
O1	–	O2	2.822(6)	C2	–	Fe	–	N2	1.3(1)
O2	–	D1	1.888(9)	Pr	–	O1	–	O2	46.1(3)
O1	–	D1	0.951(11)	Pr	–	O1	–	N1	52.1(3)
O2	–	D21	0.926(16)	D1_h	–	O1	–	D1	105.1(1)
O2	–	D22	0.938(11)	D21	–	O2	–	D22	103.8(2)
N2_j	–	D21	2.194(3)	O2	–	D21	–	N2_j	170.4(5)
N1_n	–	D22	2.733(5)	O2	–	D22	–	N1_n	136.8(8)

The low temperature increasing of $M(T)$ can be due to presence of superparamagnetic clusters in the powder sample, because the size distribution of powder particles is very broad (from 4 μm to 30 μm) and, therefore, obviously the smallest particles are already paramagnetic, respectively superparamagnetic down to the lowest temperatures. AC susceptibility measurements shown in figure 3(a) indicate a broad maximum at about T=12 K. This maximum can be associated with the blocking temperature or can indicate the transition to a magnetic ordered state.

Although the results of NMR spectroscopy, magnetization, DC [17, 18] and AC susceptibility measurements (a maximum in zero-field-cooling magnetization curves, $\chi'(T)$, $\chi''(T)$ at about T = 12 K) indicate magnetic correlations in the system at low temperatures pointing to a magnetic phase transition at about T = 12 K, no significant difference between low and high temperature powder neutron diffraction patterns has been detected. Neutron diffraction

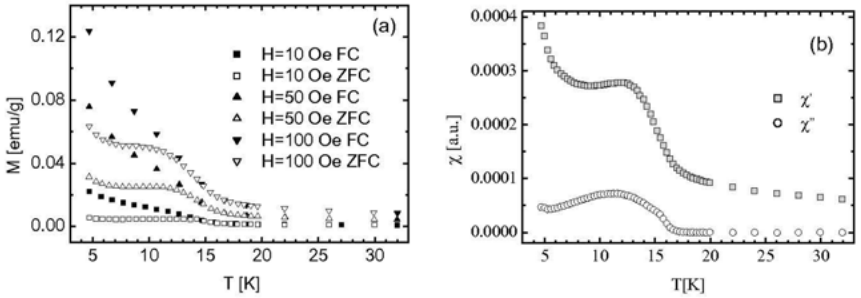

Figure 3. The temperature dependencies of magnetization and AC susceptibility show maxima in ZFC (a) and $\chi'(T)$ and $\chi''(T)$ (b) curves, which can indicate magnetic phase transition.

experiment revealed that the compound does not order magnetically down to 1.6 K, which is consistent with magnetic ordering temperature $T_N < 1$ K suggested in [1].
Recently, heat capacity measurements [19] revealed that $Pr[Fe(CN)_6]\cdot 4H_2O$ undergoes a magnetic phase transition at $T_c = 1.3$ K.

References

1. Hulliger, F., Landolt, M., & Vetsch, H., 1976, *J. of Solid State Chem.***18**, 283.
2. Mullica, D.F., Perkins, H.O., Sappenfield, E.L., Leschnitzer, D., 1989, *Acta Cryst. C*, **45,** 330.
3. Mullica, D.F., Sappenfield, E.L., 1989, *J. Solid State Chem.* **82**, 168.
4. Mullica, D.F., Hayward, P.K., Sappenfield, E.L., 1996, *Acta Cryst. C*, **52**, 61.
5. Yukawa, Y., Igarashi, S., Kawaura, T., Miyamoto, H., 1996, *Inorg. Chem.*, **35**, 7399.
6. Wang, X., Yukawa, Y., Masuda, Y., 1999, *J. of Alloys and Comp.* **290**, 85.
7. Langer, V., Smrčok, Ľ., Masuda, Y., 2004, *Acta Cryst C* **60**, i104.
8. Bailey, W.E., Williams, R.J., Milligan, W.O., 1973, *Acta Cryst. B*, **29,** 1365.
9. Kietaibl, H., Petter, W., 1974, *Helv. Phys. Acta*, **47**, 425.
10. Mitróoová, Z., Zentko, A., Trpčevská, J., Lukáčová, M., Csach, K., Bokor, M., 2003, *Rare earth Ferricyanides*, *Solid State Phenomena*, **90-91**, 85.
11. Le Bail, A., 2003, *Monte Carlo indexing with McMaille*, Structure Solution from Powder Diffraction Data, (Stará Lesná, Slovakia), p 11.
12. Favre-Nicolin, V., Černý, R., 2002, *J. Appl. Cryst.* **35**, 734.
13. Rodriguez-Carvajal, J., 1990, "*FULLPROF: A Program for Rietveld Refinement and Pattern Matching Analysis*", Abstracts of the Satellite Meeting on Powder Diffraction of the XV Congress of the IUCr, Toulouse, France, p127.
14. Larson, A.C., Von Dreele, R.B., 2000, "*General Structure Analysis System (GSAS)*", Los Alamos National Laboratory Report LAUR 86-748.
15. Spek, A.L., 2003, *J. Appl. Cryst.*, **36**, 7 – 13.
16. Brandenburg, K., Putz, H., 2005, *Diamond Ver.3.0*, Crystal Impact, Bonn, Germany
17. Zentko, A., Bokor, M., Lukáčová, M., Maryško, M., Mihalik, M., Mitróová, Z., Zentková, M., 2003, *phys. stat. sol. A*, **196** (1), 340.
18. Zentková, M., Zentko, A., Žežula, I., 1998, *Acta physica slovaca*, **48,** 837-840.
19. Mitróova, Z., Mihalik, Marián, Zentko, A., Lukáčová, M., Mihalik, Matúš, Vejpravová, J., Kiss, L. F., 2004, *Czech. J. Phys.*, **54,** Suppl. D, D559.

Acknowledgements. The work was supported by EU and BENSC-HMI Berlin (Projects PHY-01-1203/02 and PHY-01-1216/02), by VEGA No. 2/4050/04 and APVT-20-009902. Magnetization and AC susceptibility measurement were performed by M. Maryško from Institute of Physics, Prague.

IV.4.4 *Microstructure, Phase Analysis*

Z. Kristallogr. Suppl. 23 (2006) 551-556

Microstructure of crystalline phases in electrotechnical porcelains

J. M. Amigó[1], F. J. Serrano[1], M. A. Kojdecki[2,*], J. Bastida[1], V. Esteve[3], M. M. Reventós[1]

[1]Departament de Geologia, Universitat de València, 46100 Burjassot, Spain
[2]Instytut Matematyki i Kryptologii, Wojskowa Akademia Techniczna, 00-908 Warszawa, Poland
[3]Departament de Química Inorgànica i Orgànica, Universitat Jaume I, 12080 Castelló, Spain
*Contact author; e-mail: M.Kojdecki@imbo.wat.edu.pl

Keywords: X-ray powder diffraction, crystalline microstructure, electrotechnical porcelains, alumina porcelains, silica porcelains

Abstract. The crystalline microstructure of industrial samples of silica and alumina porcelains was determined through analysing their X-ray diffraction patterns. A statistical model describing polycrystalline materials was applied for characterising the microstructure with parameters found by modelling and simulating the diffraction patterns and comparing them to the measured ones to achieve the best approximation. Correlations of the microstructure parameters with the mineral compositions of the investigated materials were found.

Introduction

A comparative study of silica and alumina porcelain insulators [1, 2] was performed in the previous work [3] on commercial samples obtained at 1300 ºC with the same time of firing, by considering their mineral and chemical compositions which were related with their thermal and mechanical properties. The study was carried out on mullite, corundum and quartz, which are the principal crystalline phases which together with glass phase form porcelains of both types as composite materials. In this work that study is updated by characterising their crystalline microstructure by applying a recently developed method [4, 5, 6]. The samples (of seven distinct mineral compositions), finely crushed, were split using a rotatory splitter and ground in an agate mortar and pestle, then dried and pressed into standard tablets. The powder diffraction patterns were recorded at room temperature with a diffractometer (Bruker D5000) in step-scanning mode, using CuK_α radiation and a secondary graphite monochromator. The diffraction patterns of the samples were recorded over the range $5 \div 90$ of diffraction angle with 0,02° step. The instrumental line profiles were recorded from the standard reference material LaB_6 (SRM 660a) over the range $20 \div 131$.

Model of polycrystalline material

A sample of a polycrystalline solid or a crystalline powder is considered as a set of crystallites (i.e. domains scattering X-rays coherently) of the same *shape*, randomly oriented in space. The sizes of crystallites are characterised by the *volume-weighted crystallite size distribution* [4-7], which may be interpreted as a density of probability of finding a crystallite of assumed shape and size, taken with a weight proportional to its volume, in an analysed sample. The size of a crystallite is any of its linear dimensions, while the shape is described by the ratios of its characteristic dimensions (like edge lengths of a prism). Each of the crystallites is assumed to have the perfect lattice but with the parameters varying from each other i.e. the crystalline lattice strain is assumed to be second-order strain, homogeneous and isotropic inside each crystallite. The variation of the lattice parameters of the crystallites, with respect to the reference lattice parameters obtained upon averaging over all crystallites, is characterised by the *second-order crystalline lattice strain distribution* [4-7], which may be interpreted as a density of probability of finding a crystallite with assumed interplanar distances, taken with a weight proportional to its volume, in an analysed sample. Other possible distortions of the crystallites (like stacking faults and point defects inside) are neglected.

Computations and results

The pure line profiles were computed through regularised deconvolution [8]. The strongest line profiles (five to nine) from each crystalline phase were selected for further analysis. In the computations the crystallites were modelled as spheres, cylinders or rectangular prisms (in orthorhombic mullite) or hexagonal prisms (in hexagonal corundum and quartz). The minimal error of fitting the pure line profiles, calculated from experimental data, by those simulated in accordance with the determined microstructure characteristics, was a criterion for selecting the prevalent crystallite shape (R in tables 2, 3 and 4, calculated as R_{wp}).

Averaged characteristics of all samples

The averaged microstructure characteristics, calculated for the three principal phases according to the size distributions and the strain distributions, are shown in table 1. The volume-weighted mean crystallite is characterised by the standardised size Z equal to cube root of its volume; E is the mean-absolute second-order strain; S is the flexural strength [3] and C is the weight content of each mineral phase and glass in a sample [3]. The samples labelled S1, S2, S3 and S4 are alumina porcelains, the samples S5, S6 and S7 are silica porcelains.

Table 1. Averaged characteristics of three crystalline phases in all samples.

Sample	Strength	Glass	Corundum			Quartz			Mullite		
	S [MPa]	C [%]	C [%]	Z [Å]	E	C [%]	Z [Å]	E	C [%]	Z [Å]	E
S1	125	51.1	33.2	945	0.00038	12.1	1502	0.00074	3.3	587	0.00045
S2	131	50.7	34.2	1065	0.00039	10.8	907	0.00042	4.0	682	0.00057
S3	144	51.1	35.3	1161	0.00035	8.5	648	0.00049	5.0	584	0.00061
S4	147	50.9	34.9	917	0.00034	8.4	1345	0.00039	5.8	666	0.00054
S5	103	62.7	8.8	881	0.00039	23.0	689	0.00060	5.4	656	0.00045
S6	98	61.2	8.9	1132	0.00036	23.8	779	0.00051	5.9	611	0.00044
S7	99	63.6	8.5	1221	0.00036	22.6	712	0.00059	5.1	938	0.00066

Microstructure of corundum

A sphere was found as the most probable prevalent shape of crystallites in corundum (hexagonal, a = 47588 Å, c = 12.992 Å). The resulting volume-weighted crystallite size distributions were bimodal. By decomposing each size distribution into two logarithmic-normal components (with $R_{wp} \approx 5$ %) and attributing each component to a hypothetical crystallite fraction, the mean standardised crystallite size (*Z1*, *Z2*, *Z*), the ratio of standard deviation to mean size (*T1*, *T2*) and the weight content (*C1*, *C2*) of each fraction were calculated.

Table 2. Averaged characteristics of corundum in all samples.

Sample	Corundum - total				First fraction			Second fraction		
	C [%]	*Z* [Å]	*E*	*R* [%]	*C1* [%]	*Z1* [Å]	*T1*	*C2* [%]	*Z2* [Å]	*T2*
S1	33.2	1021	0.00038	12.9	51	877	0.94	49	1210	0.44
S2	34.2	1131	0.00039	16.1	39	925	1.07	61	1300	0.47
S3	35.3	1223	0.00035	14.2	15	475	0.40	85	1357	0.50
S4	34.9	1002	0.00034	18.6	49	922	1.06	51	1155	0.45
S5	8.8	981	0.00039	12.9	82	933	1.10	18	1443	0.40
S6	8.9	1193	0.00036	13.5	46	952	1.23	54	1468	0.40
S7	8.5	1371	0.00036	16.1	87	1425	0.93	13	1695	0.31

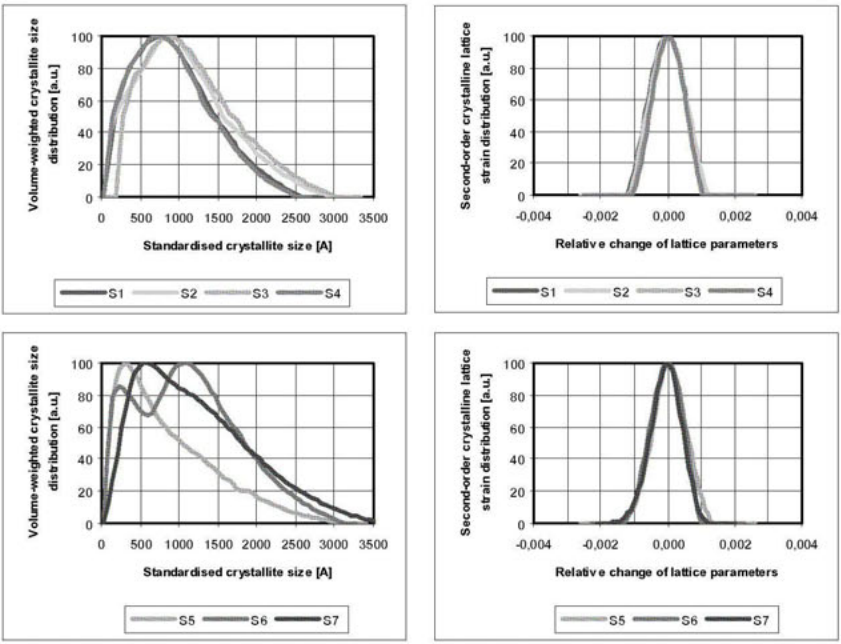

Figure 1 a ,b, c ,d. Volume-weighted standardised crystallite size distributions and second-order crystalline lattice strain distributions of corundum in porcelains (all normalised to the same maximum).

Microstructure of quartz

A hexagonal prism (of base diagonal D, height L along [001] and aspect ratio G = L/D) was found as the most probable prevalent shape of crystallites in quartz (hexagonal, a = 4.913 Å, c = 5.405 Å). The resulting volume-weighted crystallite size distributions were monomodal or bimodal logarithmic-normal ones ($R_{wp} \approx 5$ %). The mean volume-weighted standardised crystallite size ($Z1$, $Z2$, Z), the ratio of standard deviation to mean size ($T1$, $T2$) and the weight content ($C1$, $C2$) of each fraction were calculated as for corundum.

Table 3. Averaged characteristics of quartz in all samples.

Sample	Quartz - total					First fraction			Second fraction		
	C [%]	G	Z [Å]	E	R [%]	$C1$ [%]	$Z1$ [Å]	$T1$	$C2$ [%]	$Z2$ [Å]	$T2$
S1	12.1	2.62	1579	0.00074	14.0	69	1436	0.64	31	1933	0.38
S2	10.8	0.93	931	0.00042	14.7	62	690	0.56	38	1327	0.45
S3	8.5	0.62	682	0.00049	21.2	100	682	0.69	0	-	-
S4	8.4	0.41	1281	0.00039	32.2	100	1281	0.63	0	-	-
S5	23.0	0.98	825	0.00060	12.1	100	825	0.58	0	-	-
S6	23.8	1.11	886	0.00051	15.1	100	886	0.81	0	-	-
S7	22.6	0.62	737	0.00059	12.5	57	615	0.95	43	933	0.57

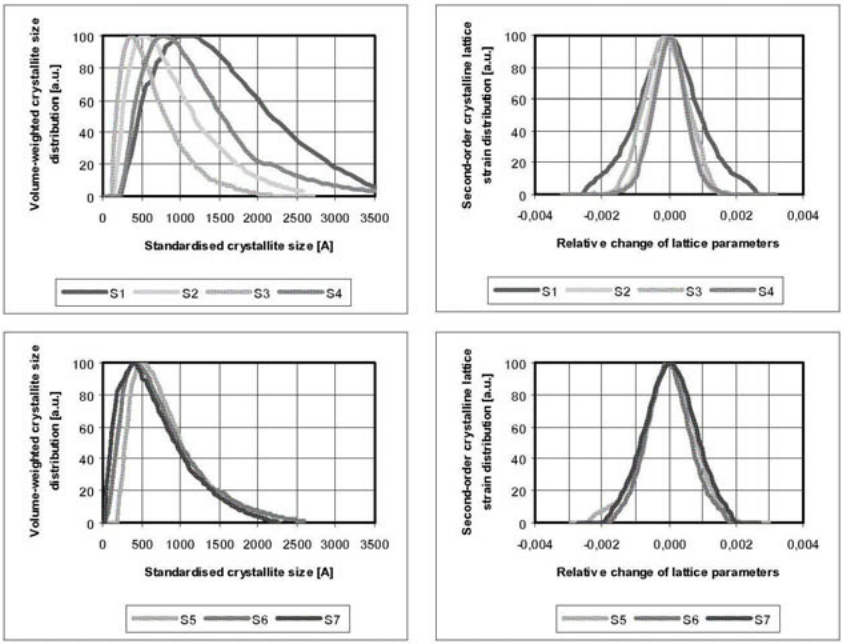

Figure 2 a,b,c,d. Volume-weighted standardised crystallite size distributions and second-order crystalline lattice strain distributions of quartz in porcelains (all normalised to the same maximum).

Microstructure of mullite

A parallelepiped (of edges *A*, *B*, *L* in directions [100], [010], [001] and aspect ratios $F = B/A$ and $G = L/A$) was found as the most probable prevalent shape of crystallites in mullite (orhorhombic, $a = 7.5456$ Å, $b = 7.6898$ Å, $c = 2.8842$ Å). The resulting volume-weighted crystallite size distributions were bimodal logarithmic-normal ones ($R_{wp} \approx 7$ %). The mean volume-weighted standardised crystallite size (*Z1*, *Z2*, *Z*) and the other parameters (*T1*, *T2*), (*C1*, *C2*) of each fraction were calculated as for corundum.

Table 4. Averaged characteristics of mullite in all samples.

Sample	Mullite - total						First fraction			Second fraction		
	C [%]	*F*	*G*	*Z* [Å]	*E*	*R* [%]	*C1* [%]	*Z1* [Å]	*T1*	*C2* [%]	*Z2* [Å]	*T2*
S1	3.3	1.21	1.33	637	0.00045	12.9	29	335	0.73	71	767	0.57
S2	4.0	1.13	1.21	726	0.00057	16.1	60	514	0.93	40	1067	0.33
S3	5.0	1.15	1.33	642	0.00061	14.2	49	616	1.03	51	716	0.37
S4	5.8	1.28	2.27	755	0.00054	18.6	67	744	1.13	33	910	0.43
S5	5.4	1.21	1.32	742	0.00045	12.9	72	739	1.06	28	921	0.34
S6	5.9	0.96	1.62	680	0.00044	13.5	72	640	0.99	28	880	0.39
S7	5.1	0.90	1.65	1027	0.00066	16.1	41	979	1.08	59	1120	0.52

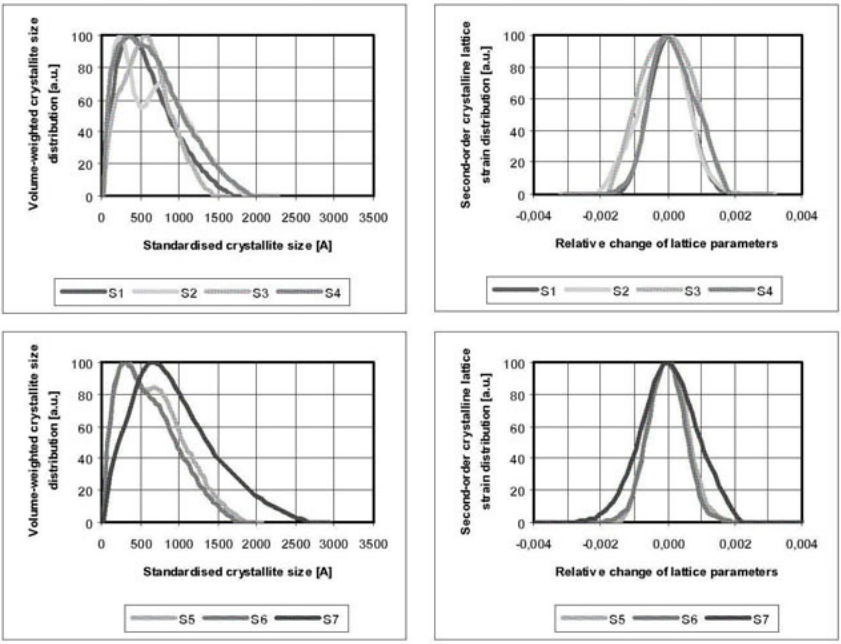

Figure 3 a,b,c,d. Volume-weighted standardised crystallite size distributions and second-order crystalline lattice strain distributions of mullite in porcelains (all normalised to the same maximum).

Conclusion

The model of polycrystal and the method for determining its parameters after X-ray diffraction pattern, used here for characterising the crystalline phases in electrotechnical porcelains, enable obtaining the quantitative characterisation of the crystalline microstructure.
In this silica-alumina binary system of the three principal mineral phases (corundum, quartz and mullite, primary or secondary), complemented with glass, mainly the mineral composition, being a result of raw material formula and thermal treatment, influences both microscopic and macroscopic properties. The bimodality of size distributions is probably a result of formation of secondary mullite with other phases involved. Some correlations are visible:

- The aspect ratio of quartz crystallites correlates with the quartz content.
- In the S4 porcelain the highest flexural strength correlates with the most elongated crystallites of mullite and the most flattened crystallites of quartz.
- The aspect ratio of the size distribution (i.e. the ratio of standard deviation to mean size) oscillates about 1.0 (in corundum and mullite) or 0.6 (in quartz) for the first fraction of crystallites and about 0.4 for the second fraction (in all three phases).
- The mean standardised crystallite size of each fraction in each phase correlates with the content of the phase in a porcelain, especially in alumina porcelains.

These results characterise the crystalline microstructure of the investigated crystalline phases in a consistent and clear way, better than those obtained by simplified methods [9].

References

1. Liebermann, J., 2000, *Cfi-Ceram. Forum Int.*, **77** (6), pp. 17-23.
2. Liebermann, J., 2000, *Am. Ceram. Soc. Bull.*, **79** (5), pp. 55-58.
3. Amigó, J.M., Clausell, J.V., Esteve, V., Delgado, J.M., Reventós, M.M., Ochando, L.E., Debaerdemaeker, T., Martí F., 2004, *J. Eur. Ceram. Soc.*, **24**, pp. 75-81.
4. Kojdecki, M.A., Mielcarek, W., 2000, *Mat. Sci. Forum*, **321-324**, pp. 1040-1045.
5. Kojdecki, M.A., Bastida, J., Serrano, F.J., Clausell, J.V., 2001, *Mat. Sci. Forum*, **378-381**, pp. 747-752.
6. Kojdecki, M.A., 2004, *Mat. Sci. Forum*, **443-444**, pp. 107-110.
7. Wilson, A.J.C., 1963, *The Mathematical Theory of X-ray Powder Diffractometry*, , (Eindhoven: Philips Technical Library).
8. Kojdecki, M.A., 2001, *Mat. Sci. Forum*, **378-381**, pp. 12-17.
9. Amigó, J. M., Serrano, F. J., Kojdecki, M. A., Bastida, J., Esteve, V., Reventós, M. M., Martí, F., 2005, *J. Eur. Ceram. Soc.*, 1479-1486.

Acknowledgements. The financial support from the Spanish Ministry of Education, Culture and Sport for the stay of M.A.K. in the University of Valencia (D.G.U. No SB2001-0088) is gratefully acknowledged. This research is supported by the Generalitat Valenciana projects: No GV01-527 and Grupos 04/27. The samples of the investigated materials were provided by Francisco Martí, Laboratorio Central, Nalda S.A. (Almassera, Valencia, Spain).

Z. Kristallogr. Suppl. 23 (2006) 557-562

Micro(nano)structure of the glacial state in triphenyl phosphite (TPP)

P. Derollez[1,*], A. Hédoux[1], Y. Guinet[1], J. Lefebvre[1], M. Descamps[1], O. Hernandez[2]

[1]Laboratoire de Dynamique et Structure des Matériaux Moléculaires, UMR CNRS 8024, Université de Lille 1, 59655 Villeneuve d'Ascq Cedex, France
[2]Laboratoire de Chimie du Solide et Inorganique Moléculaire, UMR CNRS 6511, Institut de Chimie de Rennes, Université de Rennes 1, 35042 Rennes Cedex, France
[*]Contact author; e-mail: Patrick.Derollez@univ-lille1.fr

Keywords: triphenyl phosphite, powder synchrotron X-ray diffraction data, Rietveld refinements, microstructural analysis.

Abstract. The structure and microstructure of the glacial state in triphenyl phosphite (TPP, $P(OC_6H_5)_3$) transformed at 222 K have been determined from powder synchrotron X-ray diffraction data through Rietveld and Le Bail refinements. It is shown that the glacial state is composed of crystallites of the stable crystal phase coexisting with non-transformed supercooled liquid. The apparent size of the crystallites – depending on the ageing temperature at which the glacial state is isothermally formed – is found to be equal to 329.2(2) Å at 222 K. A simulated diffraction pattern shows that at temperatures lower than 220 K, the more amorphous-like shape is due to the coexistence of non-transformed supercooled liquid and to a size effect of the crystallites of the stable phase.

Introduction

The phenomenon of polyamorphism is of a great interest in the field of the first-order transition between two amorphous phases ('polyamorphic transition'). The evidence at low temperature and atmospheric pressure of an apparently amorphous phase in triphenyl phosphite (TPP, $P(OC_6H_5)_3$) [1], distinct from the glass, the supercooled liquid and the normal liquid (and so named glacial phase) was initially considered as an original manifestation of polyamorphism.

The description and the understanding of this polymorphism situation are hotly debated from controversial interpretations [1-19] about the nature of the glacial state (GS). Our previous experimental studies [12-18] converge into the description of the GS as composed of nano- to micro-domains of the crystalline state embedded in the matrix of non-transformed supercooled liquid. In this context, we report a structural and microstructural study of the GS formed at 222 K, from powder synchrotron X-ray diffraction data, that gives in particular the first structural refinement of this state. From the microstructural parameters at 222 K, a diffraction pattern of the nanostructured state is simulated and is compared with an experimental pattern of the GS at 216 K.

Experimental

Collection of the powder X-ray diffraction pattern of crystal and glacial TPP were carried out on the high resolution powder diffraction BM16 beamline at the European Synchrotron Radiation Facility (ESRF, Grenoble, France). The monochromatic wavelength was fixed at 0.850871 Å. The details of the experimental setup are reported in [18]. A careful determination of the instrumental resolution function allows us to treat the microstructural effects in crystalline and glacial TPP sample through a whole-powder-pattern profile refinement.
The GS was formed by maintaining isothermally the sample at 222 K (above the calorimetric glass transition T_g = 201.8 K) after quenching the melt down to 190 K and heating ($\dot{T} = 6\,K/min$) up to 222 K. The use of the ESRF-synchrotron source has also given the opportunity to measure and analyze the diffraction pattern of the supercooled liquid at the annealing temperature (216 K) as well as the time dependence of the diffraction pattern during the isothermal transformation.
From laboratory X-ray diffraction experiments [13], it was observed that the shape of the diffraction pattern of the GS was drastically dependent upon the ageing temperature (T_a). For $T_a \geq 222$ K, intense broad Bragg peaks are superimposed to the diffuse halo of the non-transformed supercooled liquid. On the other hand, the GS's formed at lower temperatures display a more amorphous-like shape, probably due to the huge broadening of the Bragg peaks.

Powder synchrotron X-ray diffraction studies

Rietveld refinements

The diffraction pattern of the crystal and the glacial state prepared at 222 K are shown in figure 1. Obviously, a qualitative analysis of the pattern of the glacial state evidences broadened Bragg peaks of the crystal coexisting with a halo characteristic of an amorphous contribution. To determine the nature of the non-crystalline contribution and to characterize the crystal structure corresponding to the Bragg peaks, Rietveld refinements were performed by using the JANA2000 software [21]. The structure of the glacial state is very similar to the one of the crystal state, in terms of cell parameters, space group and structural model [18].
The background was modelled using 36 parameters orthogonal cosine Fourier series. To avoid strong correlations between the structural, profile and background parameters, the phenyl groups were considered as rigid-bodies. Thus, each of them was characterized by three translational and three rotational molecular degrees of freedom. The major point to be noted is that the Bragg peaks of the GS are all indexed within the symmetry (space group *R*-3) and unit-cell of the crystal phase. Furthermore, the good agreement between the calculated and observed patterns of the GS reveals that this state must be considered as composed of broadened Bragg peaks of the crystal superimposed to a huge amorphous-like background. The molecular conformation in the GS is close to the approximate C_s symmetry found in the crystal [17].
In figure 2, the refined background is compared with the structure factor of the metastable liquid at the beginning of the isothermal aging necessary for the formation of the GS. The background of the diffraction pattern of the GS is clearly similar to the shape of the structure factor of the supercooled liquid. Thus, the background of the GS pattern corresponds mainly

to the diffusion from non-transformed supercooled liquid, neglecting the contribution from the capillary and from the thermal diffuse scattering. It can be noticed a slight shift between the background and S(Q) of the liquid which could be inherent to a pressure effect from crystallites on the remaining liquid embedded in the crystalline matrix.

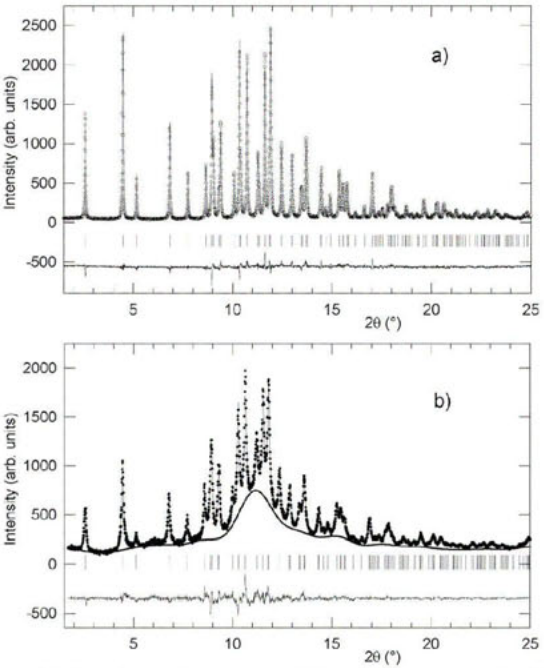

Figure 1 a) Final Rietveld plot of crystalline TPP at 110 K. b) Final Rietveld of the glacial state prepared at 222 K (the refined background is represented by the thick line). The powder patterns measured up to 45°2θ have been truncated at 25°2θ to give a clear comparison.

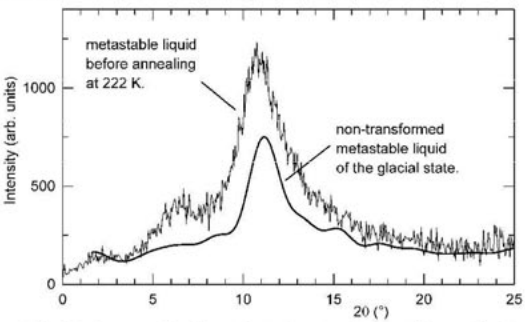

Figure 2. Comparison of the background of the glacial state deduced from the Rietveld refinement (see figure 1b) with the diffraction pattern of the liquid at the beginning of the isothermal ageing at 222 K.

Le Bail whole-powder-pattern profile refinements

The diffraction patterns of both the crystal and glacial phases were analyzed using the Le Bail method [20] included in FullProf [22, 23], taking into account the instrumental resolution function. In the refinements, the crystallites are supposed to be spherical. The final values of the cell parameters, the apparent size of crystallites and the maximum strain in the samples are reported in table 1.

Table 1. Cell parameters and. microstructural features in the crystal at 110 K and in the glacial state at 222 K, from the Le Bail profile-fitting refinements.

	crystal at 110 K	glacial state at 222 K
a (Å)	37.7632(3)	38.0317(20)
c (Å)	5.7279(1)	5.7852(4)
Apparent size (Å)	927(4)	329.2(2)
Maximum strain (%)	0.164(1)	0.152(1)

The cell parameters of the crystal phase at 110 K are slightly lower than those of the GS at 222 K, probably due to the thermal expansion [17, 18].The maximum strains (~ 0.16 %) as well as the individual isotropic strain parameters are similar in both phases, with a common value indicating that the main contribution to the microstructure is a size effect in both cases. On the other hand, the size parameters show strong differences, so that the apparent size of crystallites in the crystal phase (927(4) Å) is near three times higher than the size of the crystallized domains in the GS (329(1) Å). This latter value is in very good agreement with the size of 312(3) Å given in [13]. The introduction of supplementary profile parameters (anisotropic microstructural effects) does not increase significantly the quality of the Le Bail refinements, indicating that the assumption of spherical crystallites is relevant. In this 222 K GS, crystallites can be considered as micro-domains, whereas the amorphous-like shape of the diffraction pattern of GS formed below 222 K suggests in this case the presence of nanocrystals [13].

Simulation of the nanostructured glacial state

The polyamorphism in TPP is associated with the amorphous-like shape of low-frequency Raman spectra and diffraction patterns of the glacial state formed in the low-temperature range [210 K, 220 K]. The diffraction pattern of TPP annealed at 216 K is shown in figure 3. The glacial state formed at this temperature is really amorphous-like shaped, and the interpretation of these data is a clue for the structural description of the apparently amorphous glacial state. Since the nano-structured state does not allow refinements as in the previous micro-structured state, the diffraction pattern has been simulated. The parameters which determine the size of the crystallites have been chosen to explain the huge broadening of the Bragg peaks. In a first stage, the simulated diffraction pattern has been calculated from the structural parameters of the glacial state at 222 K, the diffraction pattern of the liquid and suitable micro-structural size parameters giving a size of crystallites of 50 Å. In a second stage, the weighted diffraction pattern of the supercooled liquid was added to the simulated diffraction pattern of nanocrystals corresponding to contribution of the non-transformed liquid (about 40-50% at 216 K [15]). The pattern of the simulated glacial state is shown in figure 3.

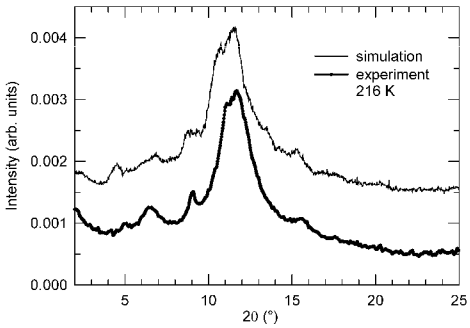

Figure 3. Comparison of the simulated and experimental (216 K) patterns.

Taking into account the hypotheses used in the calculated diffraction pattern of nanocrystals (isotropic size effect, no size distribution) a good agreement with the experimental diagram is obviously observed. A more detailed inspection of the simulated diffraction pattern indicates that the structural features emerging during the glaciation are present:

(i) the structuration of the main peak and the emergence of broad features on the high-2θ side of the main peak

(ii) the enhancement of the small-angle intensity

(iii) and the observation of the peak near 2θ = 9°, corresponding to Q = 1.1 $Å^{-1}$. However this peak appears more broadened than in the experimental diffraction pattern. This discrepancy between experimental and simulated data can be assigned to two main approximations (isotropic size and one single size for nanocrystals) used to calculate the diffraction pattern of the glacial state.

From two different structural analyses of the crystal [5,17], the long-range order can be described as an hexagonal packing of one-dimensional infinite rods formed by molecules aligned parallel to the *c*-axis of the hexagonal unit cell. From the combination of Raman and diffraction studies [17], it was determined that the cohesion in one infinite rod is due to the existence of two different C-H…O hydrogen bonds. This description can be recognized in nanocrystals through the structural features respectively labeled (ii) and (iii). The broadening of the peak near 2θ = 9° indicates that the formation of infinite rod along the c-direction in a medium range-order is observed in the amorphous-like glacial state, and can be related to a slight anisotropic size of nanocrystals.

Conclusion

The structural and microstructural description of glacial TPP appears as a fundamental step towards the understanding of the origin of this intriguing state. A Rietveld refinement from synchrotron X-ray diffraction data confirms that the GS is composed of microcrystallites of the stable crystal phase coexisting with non-transformed supercooled liquid. The microstructural analysis of the GS transformed at 222 K indicates through a relevant whole-powder-pattern profile refinement that a size-effect is the major contribution to the broadening of the Bragg peaks. In this context, it is reasonable to consider that the origin of the polyamorphism, i.e. the amorphous line shape of the diffraction pattern of the GS, is connected to a size effect of crystallites of the stable phase rather than topological defects as suggested by

Kivelson and coworkers [1-4, 11]. It is an original example of microstructural analysis in a molecular system which provides important information about the origin of a phase transformation.

References

1. Cohen, I., Ha, A., Zhao, X., Lee, M., Fischer, T., Strouse, M.J. & Kivelson, D.,1996, *J. Phys. Chem.*, **100**, 8518.
2. Alba-Simionesco, C. & Tarjus, G., 2000, *Europhys. Lett.*, **52**, 297.
3. Kivelson, D. & Tarjus, G., 2002, *J. Non-Crystalline Solids*, **307-310**, 630.
4. Tarjus, G., Alba-Simionesco, C., Grousson, M., Viot, P. & Kivelson, D., 2003, *J. Phys.: Condens. Matter*, **15**, S1077.
5. Senker, J. & Lüdecke, J., 2001, *Z. Naturforsch.*, **56b**, 1089.
6. Senker, J. & Rössler, E., 2001, *Chem. Geol.*, **174**, 143.
7. Senker, J. & Rössler, E., 2002, *J. Phys. Chem. B*, **106**, 7592.
8. Dvinskikh, S., Benini, G., Senker, J., Vogel, M., Wiedersich, J., Kudlik, A. & Rössler, E., 1999, *J. Phys. Chem.*, **103**, 1727.
9. Mizukami, M., Kobashi, K., Hanaya, M. & Oguni, M., 1999, *J. Phys. Chem.*, **103,** 4078.
10. Johari, G. & Ferrari, C., 1997, *J. Phys. Chem.*, **101**, 10191.
11. Demirjian, B., Dosseh, G., Chauty, A., Ferrer, M.-L., Morineau, D., Lawrence, C., Takeda, K., Kivelson, D. & Brown, S., 2001, *J. Phys. Chem. B* ,**105**, 2107.
12. Hédoux, A., Guinet, Y. & Descamps, M., 1998, *Phys. Rev. B*, **58**, 31.
13. Hédoux, A., Hernandez, O., Lefebvre, J., Guinet, Y. & Descamps, M., 1999, *Phys. Rev. B*, **60**, 9390.
14. Hédoux, A., Derollez, P., Guinet, Y., Dianoux, A.J. & Descamps, M., 2001, *Phys. Rev. B*, **63**, 144202.
15. Hédoux, A., Guinet, Y. & Descamps, M., 2001, *J. Raman Spectrosc.*, **32**, 677.
16. Hédoux, A., Dore, J., Guinet, Y., Bellissent-Funel, M.C., Prévost, D., Descamps, M. & Grandjean, D., 2002, *Phys. Chem. Chem. Phys.*, **4,** 5644.
17. Hernandez, O., Hédoux, A., Lefebvre, J., Guinet, Y., Descamps, M., Papoular, R. & Masson, O., 2002, *J. Appl. Cryst.*, **35**, 212.
18. Derollez, P., Hernandez, O., Hédoux, A., Guinet, Y., Masson, O., Lefebvre, J. & Descamps, M., 2004, *J. Molecular Structure*, **694**, 131.
19. Tanaka, H., Kurita, R. & Mataki, H., 2004, *Phys. Rev. Letters*, **92**, 25701.
20. Le Bail, A., Duroy, H. & Fourquet, J.L., 1988, *Mat. Res. Bull.*, **23**, 447.
21. Petříček, V. & Dušek, M. (2000). *Jana2000. The crystallographic computing system. Institute of Physics*, Praha, Czech Republic.
22. Rodriguez-Carvajal, J., *FullProf 2000*, version July 2001, LLB, CEA/Saclay, France.
23. Roisnel, T. & and Rodriguez-Carvajal, J., 2001, *Mater. Sci. Forum*, **378-381**, 118.

Z. Kristallogr. Suppl. 23 (2006) 563-568

Correlation between texture and tabletting properties of some pharmaceutical tablets

M. Koivisto[1,3,*], E. Suihko[2], V.-P. Lehto[1]

[1]Department of Physics, University of Turku, FI-20014 Finland
[2]Department of Pharmaceutics, University of Kuopio, P.O.Box 1627, FI-70211, Finland
[3]Graduate School of Materials Research, Turku, Finland
[*]Contact author; e-mail: mikjuko@utu.fi

Keywords: texture, tabletting, compaction behaviour

Abstract. A compaction simulator and a hydraulic press were used to compact single-component tablets from six different pharmaceuticals. These pharmaceuticals had different compaction behaviour and the correlation between the tabletting properties and the preferred orientation were studied. Most of the studied materials were texturized in compression and the degree of the texture appeared to be dependent on the compaction behaviour of the material. The plastic and brittle materials had clear texture but the elastic sample was not texturized. The compaction pressure had no effect on the orientation of the crystals but the pole figures were smoothed slightly when the pressure was increased. It is suggested that the texture of pharmaceuticals may affect e.g. the dissolution properties of the tablets and based on the present study the texture analysis will offer a potential new research tool for pharmaceutical physicists to study tablets.

Introduction

Pharmaceutical tablets are usually made by compressing crystalline powder. The result is a polycrystalline object whose properties may depend on the orientation of the crystallites [1]. However, the effects of tablet texture are not widely studied. Still, it is uncertain whether the texturization is a problem in practice or not [2]. It has been suggested that for e.g. dissolution speed, breaking strength and hardness may depend on the preferred orientation of the crystallites of tablets [3].

The purpose of the present study was to clarify the possibilities of the modern X-ray texture goniometry on the field of pharmaceutical materials analysis. Four pharmaceutical excipients and two drugs were used as model substances. The compacting properties of the materials were different varying from elastic to brittle. The results of the texture measurements were linked to the tabletting properties such as yield pressure, breaking strength and particle size and shape.

Materials and methods

Tabletting

Flat-faced tablets with a diameter 8 mm were compacted with a tablet simulator (PuuMan Oy) from α-lactose monohydrate (lactose), mannitol, sodium chloride and ibuprofen powders. The used compaction profile was a triangle with a punch speed 60 mm/s. The used compression pressures were 99 MPa, 298 MPa and 497 MPa. Dicalsium phosphate (dihydrate) and acetylsalicylic acid (aspirin) tablets were compacted with a hydraulic press using compression pressures 74 MPa, 370 MPa and 739 MPa. A 13 mm flat-faced tablet mould was used and the compaction time was 60 s. In order to examine the effect of particle size to the formation of texture three different particle size fractions of aspirin were used. The tablet moulds were lubricated with magnesium stearate prior to compression of each tablet.

Characterization of samples

The lactose, mannitol, sodium chloride and ibuprofen powders and tablets were characterized visually using a Cambridge S200 scanning electron microscope SEM. The radial breaking strength of the tablets compacted with the simulator were measured with a CT5 Universal tester. The simulator data were used to perform a Heckel analysis, which gives the yield pressure of the materials [4].

Texture measurements

Ni-filtered Cu-radiation was used for X-ray texture measurements, which were performed with a Philips X'Pert Pro MPD equipped with a ATC-3 texture goniometer. The pole figures of the chosen crystallographic planes were recorded as follows: Duration of one φ-circle (rotation) was 360 s and the intensity value was recorded at 5 degree (5 s) intervals. A ψ-axis (tilt) was measured from 0 to 70 degrees, interval 5 degrees. The primary radiation was focused with 2 mm axial and 1 mm equatorial divergence collimator cups. A 0.18 degree parallel plate collimator and 0.04 Rad Soller slit were used in the diffracted beam path.

Results and discussion

The measured yield pressure of the α-lactose monohydrate was 175 MPa. This means that the compaction behaviour of lactose is combination of brittle and ductile. According to the SEM analysis the lactose particles fragmented in compression. The radial breaking strengths of the tablets were 0.3 MPa, 1.4 MPa and 2.4 MPa corresponding to the compression pressures 99 MPa, 298 MPa and 497 MPa, respectively. The increase in the breaking strength as a function of the compaction pressure means that tablets compacted with higher pressure were denser.

Also the lactose powder sample was texturized slightly but the texturization of lactose was stronger in the tablets. Moreover, the preferred orientation increased as a function of compaction pressure. The selected pole figures of lactose tablet compacted with 99 MPa pressure are shown in figure 1. It can be seen that the crystal planes (011) and (110) are oriented parallel to the tablet surface. Knowing the geometry of the unit cell of lactose [5] the shape of the other pole figures can be explained.

According to Fukuoka [6] the preferred orientation of crystallites in tablets occurs by cleavage along the crystal planes having small interaction energy. Taken into account the structure

of the α-lactose monohydrate [7] the preferentially oriented crystals planes (011) and (110) might be the cleavage planes of lactose. (To confirm this, also the atomic bond strengths should be known.) Therefore, the texturization of lactose might be mainly caused by the fragmentation and the subsequent arrangement of particles in compression.

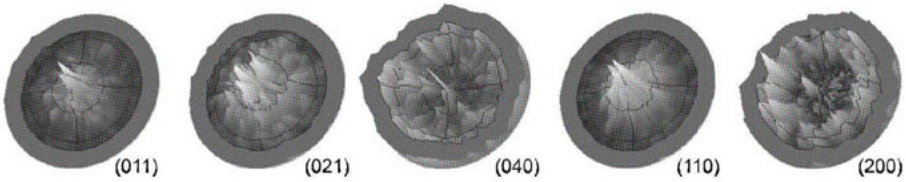

Figure 1. Pole figures of lactose tablet (compaction pressure 99 MPa).

The compaction behaviour of δ-mannitol is brittle (yield pressure 204 MPa) and it is very similar substance to lactose. However, the mannitol tablets had higher radial breaking strength (0.7 MPa, 2.5 MPa and 3.7 MPa) than lactose tablets. Even the mannitol powder is texturized and the preferred orientation of crystals did not increase much after the tablet was made. The reason for this kind of behaviour could be the elongated particles of mannitol, which was confirmed with SEM.

In the figure 2, it can be seen that the crystal plane (020) of mannitol is oriented parallel to the tablet surface. The texturization of the plane (020) has been clarified in our previous study [2]. The reason for the slightly different results between the previous and the present study is the difference in the x-ray optics and in dissimilar mannitol powder.

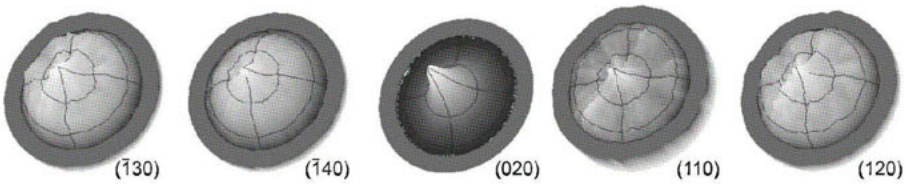

Figure 2. Pole figures of mannitol tablet (compaction pressure 99 MPa).

Sodium chloride is mainly plastic because its yield pressure is 130 MPa. The sodium chloride particles had cubic appearance and the tablets were quite hard the radial breaking strengths being 0.7 MPa, 2.7 MPa and 3.8 MPa. The crystal plane (200) is strongly oriented parallel to the tablet surface (figure 3). The pole figures of the other measured crystal planes can be explained with the geometry of the sodium chloride unit cell.

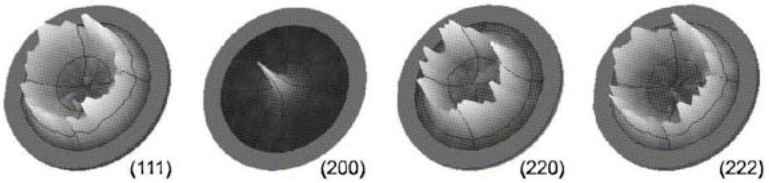

Figure 3. Pole figures of sodium chloride tablet (compaction pressure 99 MPa).

The compaction of ibuprofen is difficult because ibuprofen is elastic material having yield pressure of 42 MPa. The tabletting of ibuprofen was interfered with e.g. cap forming. The radial breaking strengths of ibuprofen tablets were 1.4 MPa, 1.7 MPa and 1.2 MPa.
All the measured pole figures of ibuprofen did not indicate any significant texture (figure 4). The reason for this might be, besides elasticity, the wide particle size and shape distributions of ibuprofen, which was observed with SEM.

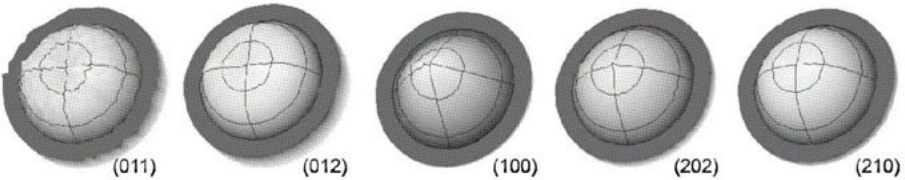

Figure 4. Pole figures of ibuprofen tablet (compaction pressure 99 MPa).

The dicalsium phosphate dihydrate powder is slightly texturized and the preferred orientation is stronger in compressed tablets. However, the compression pressure did not affect clearly on the degree of preferred orientation. The yield pressure of dicalsium phosphate is 431 MPa [4], which means that its compaction behaviour is totally brittle. As seen in figure 5, the crystal plane (020) of dicalsium phosphate are oriented preferentially parallel to the tablet surface. Presumably, the dicalsium phosphate particles tend to fracture along (020) axis inducing the texturization.
The shape of the pole figures of the planes $(\bar{1}21)$ and (121) could be explained by the geometry of the dicalsium phosphate unit cell [5]. However, the theoretical angle between the planes (020) and $(\bar{1}12)$ is 78° but the intensity maximum of the pole figure of $(\bar{1}12)$ plane is at the ψ-angle 35°. This might mean that also the $(\bar{1}12)$ plane is oriented preferentially or that the reference data is incorrect.

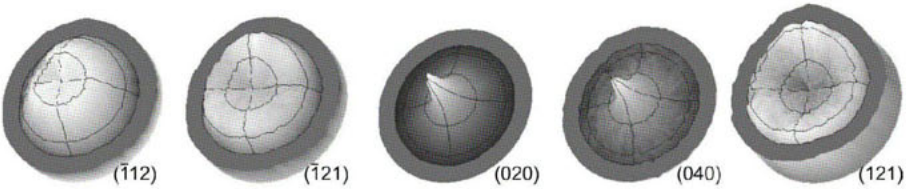

Figure 5. Pole figures of dicalsium phosphate tablet (compaction pressure 74 MPa).

The compaction behaviour of aspirin is plastic and very similar to sodium chloride. The yield pressure of aspirin is 73 MPa [4]. The aspirin powder is not texturized but texturization occurs when the tablet is compressed. The direction of preferred orientation remains when the compaction pressure increases. However, the pole figures got smoother as a function of compression pressure. This means that besides plastic deformation aspirin particles will also fracture at higher pressures.
It can be seen (figure 6) that the crystal planes (002), (100) and (202) have oriented parallel to the tablet surface. The geometry of the aspirin unit cell explains the shape of the pole fig-

ures of the planes (211) and (310). The result is in agreement with the result by Nakai et al. [8] who concluded that the (100) plane of aspirin is the plane, which orients preferentially.

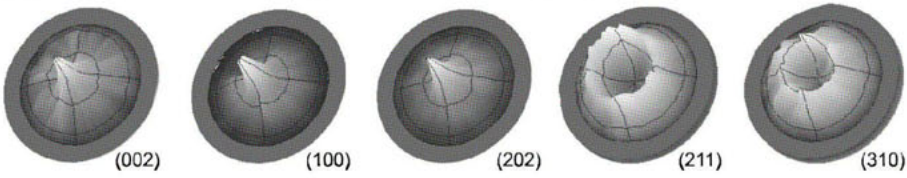

Figure 6. Pole figures of aspirin tablet (compaction pressure 74 MPa).

The increase in the compaction pressure did not change the direction of texture of the studied samples. The pole figures of the (111) plane of sodium chloride samples compacted with different pressures are presented in figure 7. The powder specimen does not indicate any texture but all of the sodium chloride tablets are texturized. The pole figures of the tablets compacted at higher pressures are more smoother, which might mean that the higher compaction pressure is the smaller particles become. In other words, the particles of sodium chloride will fracture at higher pressures and the x-rays diffract more uniformly from smaller crystallites resulting smoother pole figures. The similar behaviour was observed also in the case of aspirin. Nevertheless, the compaction pressure did not notably affect the shape of the pole figures of samples having more brittle compaction behaviour.

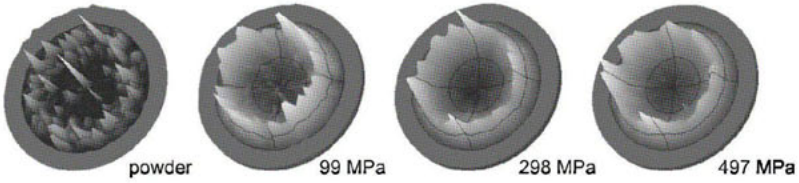

Figure 7. The effect of compaction pressure on the pole figures of (111) plane of sodium chloride tablets.

Generally, decreasing the particle size of the sample can decrease the degree of preferred orientation. In figure 8 the pole figures of three different aspirin tablets having different particle size are presented. The pole figures of (211) plane of the aspirin tablets made from bigger particles are rougher than the pole figure of the tablet having smaller particles. The explanation is obvious because the diffraction occurs less uniformly from bigger crystallites and particles.

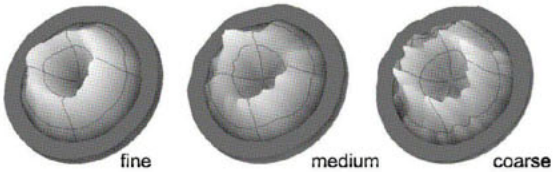

Figure 8. The effect of particle size of the aspirin powder on the pole figures of (211) plane of aspirin tablets (compaction pressure 370 MPa).

Conclusions

The tabletting and texturization behaviour of the studied materials have been collected in the table 1. Based on this study the texturization of the pharmaceutical needs nonelastic material. When it comes to the advantages and disadvantages of the texturization of the pharmaceutical tablets one needs to be very careful when making conclusions based on this study. According to the present results the more the crystallites in the tablets are preferentially oriented the harder the tablets are. Nevertheless, hard tablets could have poorer dissolution properties. As a conclusion, the modification of texture by modifying the tablet formulation could also modify the therapeutic effects of tablets. Moreover, the texture analysis seems to offer a potential non-destructive research method for the pharmaceutical materials research.

Table 1. The tabletting behaviour of investigated materials vs. texturization.

Substance	Yield pressure [MPa]	Tabletting behaviour	Textures?	Primary plane of texturization
Lactose	175[1]	brittle/plastic	yes	(011) & (110)
Mannitol	204[1]	brittle/plastic	yes	(020)
Sodium chloride	130[1]	plastic	strongly	(200)
Ibuprofen	42[1]	elastic	no	-
Dicalsium phosphate	431[2]	brittle	yes	(020)
Aspirin	73[2]	plastic	strongly	(100)

[1] Measured

[2] Literature value [4]

References

1. Cullity, B.D., 1978, *Elements of X-ray Diffraction, 2ed.* (USA: Addison-Wesley).
2. Koivisto, M., Virjonen, T., Heikkilä, T. & Lehto, V.-P., 2004, *J. Pharm. Biopharm. Anal.*, **36**, 559.
3. Kourula, J., Laine, E. & Paronen, P., 1985, *Farmaseuttinen Aikakauskirja-DOSIS*, **1**, 18.
4. Alderborn, G. & Nyström, C, 1996, *Pharmaceutical Powder Compaction Theory* (New York: Marcel Dekker).
5. International Centre for Diffraction Data (ICDD), 1996, *Powder Diffraction File PDF-2 Database, sets 1-46.*
6. Fukuoka, E., Makita, M. & Yamamura, S., 1993, *Chem. Pharm. Bull.*, **41**, 1284.
7. Allen, F.H., 2002, *Acta Crystallogr.*, **B58**, 380.
8. Nakai, Y., Fukuoka, E. & Nakagawa, H., 1978, *Yakugaku Zasshi*, **98**, 23.

Acknowledgements. The authors wish to thank Markku Heinonen, University of Turku for the SEM pictures.

Z. Kristallogr. Suppl. **23** (2006) 569-574

Incrustation of precious stones in dental apatite

L. Bucio[1,*], I. A. Belío-Reyes[2], J. A. Rodríguez[3], M. N. Orta[1], J. Arenas-Alatorre[1], C. Magaña[1] and R. Velázquez[4]

[1]Instituto de Física, UNAM. Apdo. Postal 20-364, 01000 Mexico D.F., Mexico
[2]Facultad de Odontología, Universidad Autónoma de Sinaloa Campus Culiacán, Blvd.. de las Américas y Universitarios, 80010 Culiacán, Sinaloa, Mexico
[3]Facultad de Odontología, Universidad de Guadalajara, Sierra Morena 950, Guadalajara, Jalisco, Mexico
[4]Centro de Física Aplicada y Tecnología Avanzada, UNAM Campus Juriquilla, 76000 Querétaro, Mexico
[*]Contact author; e-mail: bucio@fisica.unam.mx

Keywords: copal, crystallinity, dental incrustations, precious stones, powder diffraction.

Abstract. There is evidence that in ancient cultures in Mexico copal was probably used for gluing precious stones in teeth cavities and for dental restorations as well. We have investigated potential applications of this material in modern dentistry. In this work we report the presence of preferred orientation of the apatite crystallites in the visible tooth surface and a possible monoclinic symmetry of a crystalline phase in copal from X-ray powder diffraction analysis. Scanning Electron Microscopy shows adhesion of copal to dental tissue by penetrating the dentin tubules in the tooth tissue. Then, copal can be considered seriously as an adhesive to use in dentistry today.

Introduction

From the X to VI centuries B.C., the incrustations of precious stones in dental apatite were commonly practiced in ancient Mexico. According to several authors [1-3] pyrite, hematite, jadeite and turquoise were typically used for this purpose. The technique probably consisted in creating a cavity on the tooth surface (of anterior teeth) by mean of a drill-like tool and perhaps also using powdered quartz with water as an abrasive. The stone was then fixed by using an adhesive like *copal* [2] or calcium phosphate-based cement [3]. With regard to this, Swedish scientist S. Linné cited by Fastlicht [1, 4] pointed out the following: "It is no concern of mine to judge if this is praiseworthy but I have heard prominent specialists express their surprise when observing that this cement has kept its purpose after 1,500 years, while today despite of our advanced technology, this not even last the life of a patient." There are also evidences reporting tooth modifications for therapeutic purposes [5]. In such studies amber coloured spots were observed in the dental crowns, perhaps due to the use of a *copal-based* resin. At present, dental inlays (silver-based alloys) can last almost 8 years, and de-

spite that one do not obtain a real adherence between these inlays and the dental tissue; alloys inlays are frequently used today because of their cheapness and relatively long presence in the mouth. On the contrary, in the case of ceramic inlays (i.e. metal free porcelain) an interface between tooth and the inlay is created using phosphoric acid, adhesives or a so-called dual cement. Both surfaces are joined together creating an UV-polymerized thin hybrid layer (polymethyl-methacrylate). Ceramic metal free inlays have an approximate service life of 10 years [6] and have the advantage of be very aesthetic and cosmetic; but they are not sufficient resistant to rupture and are very expensive.

In this work, we deal with the crystallinity and adhesive properties of copal as an interesting material for potential applications in modern dentistry, and for understanding the scientific studies reported about the dental incrustations practiced in ancient Mexico. To do this, samples of recently-extracted teeth have been prepared with incrustations of turquoise by using *copal* mixed with powdered apatite as an adhesive. This sample preparation procedure is supported by the work reported by Fastlicht and Pompa y Padilla [1, 2] where the presence of powdered apatite has been detected by X-ray diffraction experiments. In the same work *copal* is considered very seriously as the adhesive [1]. The second supporting fact is noted in an amazing book by F. Martínez Cortés entitled *Sticky-Materials, Gums and Resins in Prehispanic Mexico* [3]. Apparently *copal* was the basis of the sticky-materials employed to elaborate several wonderful pieces such as the granite mask discovered in Malinaltepec, Guerrero, Mexico, which appear decorated with small fragments of glued turquoise platelet-like stones. In the literature, *copal* is regarded as an amorphous material; to our knowledge this is the first time that information about the crystallinity of *copal* is reported.

Some features concerning to *copal* is its composition, which consist of a complex mixture of water insoluble organic compounds, which are mostly diterpenoids with predominantly labdane skeletons with minor fractions of mono and sesquiterpenoids [11]. An important fraction of the constituent terpenes is polymerized, resulting in a hard resin. Ozic acid, $C_{19}H_{29}COOH$, contributes especially to the formation of a highly cross-linked polymer. Then, the crystallinity in copal perhaps can be achieved taking into account the possibilities of packing labdane-like molecules.

Origin of Samples and Characterization

10 samples of teeth (incisive extracted for periodontal disease) were selected at random from a bank available at the research laboratory of the Dentistry Faculty at the Universidad Autónoma de Sinaloa, Sinaloa State, Mexico. After the extraction, the samples were washed and stored in bidistilled water. With respect to *copal* and *amber*, two specimens of the first were obtained from markets located in Texcoco, Mexico State and Tepoztlán, Morelos State, Mexico; *amber* was obtained from Simojovel, Chiapas, Mexico. The samples of *copal* were apparently extracted from *Bursera Jorullensi*, the typical copal tree which exists in the mentioned localities. The precious stones used in this study were turquoises from a jeweller in Mexico City.

X-Ray Powder Diffraction (XRD) Measurements

Three samples of teeth were used to obtain XRD patterns from the visible surface of teeth when smiling (dental enamel). Each piece was fixed in such a way that the plane of the sample was in coincidence with the diffraction plane. The XRD patterns were recorded at 300 K

on a Bruker D8 Advance Diffractometer (Cu Kα, λ = 1.5418 Å) with a secondary graphite monochromator, scintillation detector, fixed scatter and divergence slits (1°) and operated at 40 kV and 30 mA. The 2θ range was from 5 to 60° employing step/scan mode with Δ2θ = 0.05° and Δt = 2 s. The same conditions were applied to *copal*, *amber* and the samples labelled as "turquoise" (previously powdered) in order to check them as crystalline turquoise, $CuAl_6(PO_4)_4(OH)_8\ 4H_2O$ (PDF file 6-214, ICSD 21062). For the XRD analysis of *copal* and *amber*, the samples were powdered in an agate mortar. In all cases a XRD pattern typically from an amorphous phase were obtained, except for the case of copal obtained from Texcoco. In this particular case, the sample showed clearly Bragg reflections corresponding to a one or more crystalline phases (figure 1). For a better result, the sample was prepared cutting small pieces of copal for a partial powdering process in such a way to avoid an excessive pressure and preserve crystallinity. The sample was then selected for new detailed analysis by XRD. The conditions for this run were the same that those previously described, setting 35 kV, 30 mA, 2θ from 5 to 50°, Δ2θ = 0.02° and Δt = 10 s. Mica powder (NIST 675) was used as external standard to calibrate the zero-shift of the goniometer.

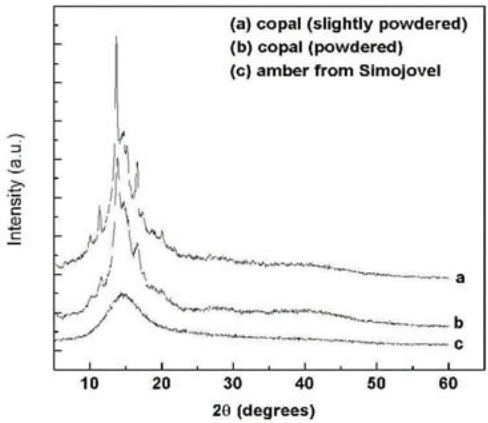

Figure 1. XRD patterns of (a) slightly powdered copal from Texcoco; (b) powdered copal from Texcoco, and (c) amber from Simojovel.

Dental Incrustations of Turquoise

Round cavities (about 1mm depth) were made in the middle of each incisive by using a low-speed air turbine. Turquoise was cut in such a way that fits exactly on the tooth cavity. Teeth were edged during 10 s with phosphoric acid (37%) and then washed. *Copal* and powdered apatite were mixed together by heating them. At the time of putting the incrustation, *copal* was heated again to glue the stone into the cavity.

Low Vacuum Scanning Electron Microscopy (LVSEM)

For the observation of samples, each piece was cut parallel to the main tooth axis with an automatic Jean Wirtz cutter. The surface exposed was then polished and cleaned with compressed air. For the LVSEM images, the equipment used was a JEOL LV-6000.

Results

The visible surfaces of teeth when smiling show a preferred orientation of apatite crystals such that the *c*-axis of the hexagonal unit cell of apatite crystals is normal to the tooth surface (figure 2). Therefore, copal or whatever material chosen for cementation, is in contact with the textured apatite crystallites (if the cavity does not reach the dentin).

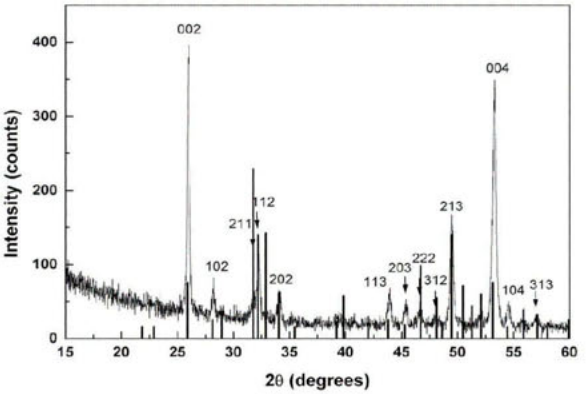

Figure 2. XRD data obtained from the surface of an incisor tooth. The Bragg peaks of hydroxyapatite (PDF file 9-432) are represented as vertical bars. Notice the effect of the preferred orientation of apatite crystals by the strong intensity of the 002 and 004 Bragg reflections.

In the XRD pattern of *copal* from Texcoco, we could not identify the Bragg peaks with some of the crystalline phases reported in the JCPDS files. Although the Bragg peaks can be considered as coming from more than one crystalline phase, we assumed the presence of one single phase. With this assumption, we could index the powder diffraction pattern in the monoclinic system by mean of the program DICVOL91 [7] with the first 20 well-resolved peak diffraction positions. The cell parameters found were $a \approx 24.59$ Å, $b \approx 13.56$ Å, $c \approx 6.76$ Å, $\beta \approx 106.3°$, $V \approx 2164.4$ Å^3, $M_{20}' = 31.5$ [8]. The full profile was fitted by mean of FULL-PROF program [9] without prior knowledge of a structural model (figure 3). With the good starting cell and profile parameters we obtained the data listed in table 1. A pseudo-Voigt function modified by Thompson, Cox & Hastings [10] was chosen to generate the line shape for the diffraction peaks. In the final run the following parameters were fitted in the space group P2/*m* (no. 10): zero point, background (first refined by using linear interpolation between a set background points with refinable heights, after that, the background was fixed), unit cell dimensions, half-width, pseudo-Voigt parameters for the peak shape and global thermal isotropic factors. A total number of 9 independent parameters were refined in the final cycle. Lanthanum hexaboride, LaB_6 (NIST 660A), and Mica powder (NIST 675) were used to obtain the instrumental resolution function (IRS) included in the full profile fitting.

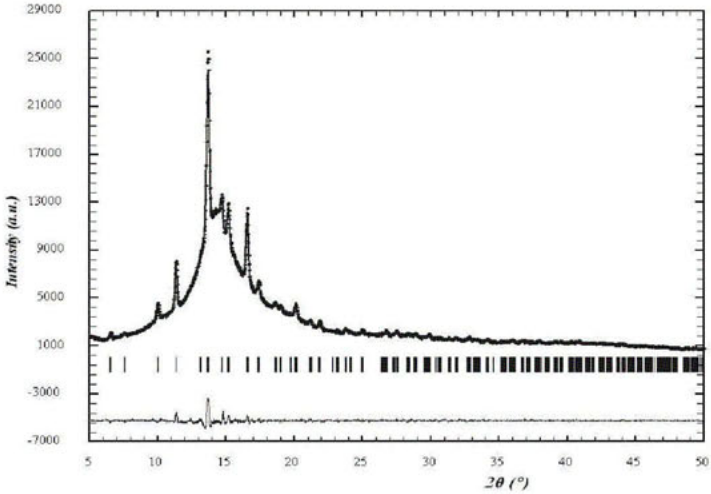

Figure 3. Full profile fitting of copal. The experimental data is represented as cross symbols, the calculated profile is the continuous line, the difference appears on the bottom line, and the Bragg reflections are represented as vertical marks. Notice the presence of amorphous content.

Table 1. Crystallographic data for a possible single crystalline phase present in copal from Texcoco after a full profile fitting of the XRD pattern using the space group P2/m.

Cell parameters		Reliability Factors (%)	
a = 24.358(3) Å	B = 106.373(7)°	R_{wp}	2.69
b = 13.500(1) Å	V = 2126.3(4) Å^3	χ^2	2.08
c = 6.7398(6) Å		R_{Bragg}	1.26

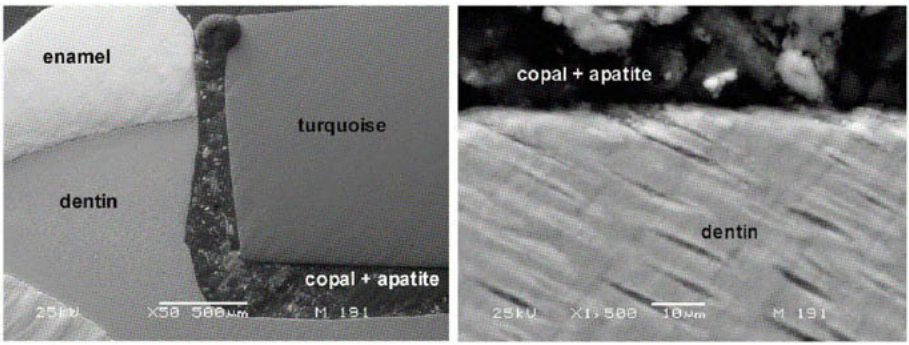

Figure 4. Left: Interfaces between enamel, dentin, copal and turquoise. Right: Copal coming into dentin tubules.

The images obtained by LVSEM (figure 4), show certain adhesion between dental tissue-copal and copal-turquoise, in the first case by penetrating the dentin tubules. There are rounded shapes in the copal-apatite microstructure, similar to those that can be seen in the glue of Malinalco turquoise mask. Apparently, copal is capable to get into dentin tubules gluing the stone creating an hybrid layer similar to other resins developed for their use in dentistry today, such as light cure resins. Using fire for a few seconds directly on the stone and copal, a very thin layer can be obtained, and also those rounded shapes in *copal* because it is no common to observe them if a heating process is not applied.

Concluding remarks

Enamel in the visible tooth surface presents high degree of preferred orientation of the apatite crystallites. *Copal* as a raw material presents a certain degree of crystallinity which disappears or diminishes when copal is powdered or slightly heated above room temperature; if the crystalline fraction were one crystalline phase, it would apparently belongs to the monoclinic system. Copal-apatite composite could be considered seriously as a dental adhesive. The use of copal in ancient Mexico seems to be well justified in the light of our results.

References

1. Fastlicht, S., La Odontología en el México Prehispánico., 1971, *Rev. Asoc. Dental Mexicana y del Colegio de Cirujanos Dentistas*, Mexico City, pp. 39-59.
2. Pompa y Padilla, J. A., 1995, *Arqueología Mexicana* **3**, 62.
3. Martínez Cortes, F., 1974, *Pegamentos, Gomas y Resinas en el México Prehispánico.* SEP-Setentas No. **124**, Mexico City, pp. 134-136.
4. Linné, S., 1948, *Ethnos*, Stockholm, 3-4.
5. Andrade, E., Pineda, J.C., Zavala, E.P., Murillo, G., Chavez, R., Lazcurain, R., Espinosa, M., Villanueva, O., 1998, *Nucl. Ins. Meth. Phys. Res.* B**136-138**, 908.
6. West Man International Dental Lab Pvt. Ltd. 153, Nangloi Sayyed, New Delhi - 110 041, India.
7. Boultif, A. and Louer, D., 1991, *J. Appl. Cryst.* **24**, 987.
8. A. Altomare, C. Giacovazzo, A. Guagliardi, A.G.G. Moliterni, R. Rizzi and P.E. Werner, 2000, *J. Appl. Cryst.* **33**, 1180.
9. Rodríguez-Carvajal J., 1990, Fullprof: A program for Rietveld refinement and pattern matching analysis. Abstracts of the Satellite Meeting on Powder Diffraction of the XV Congress of the IUCr, p. 127.
10. Thompson, P., Cox, D.E. and Hastings, J.B. , 1987, *J. Appl. Cryst.* **20**, 79.
11. Vandenabeele, P., Grimaldi, D.M., Edwards, H.G.M. and Moens, L., 2003, *Spect. Acta* A **59**, 2221.

Acknowledgements. A. Osornio, M. Aguilar Franco, M. E. Villafuerte and Laboratorio Central de Microscopia, IFUNAM; Projects DGAPA-UNAM, PAPIIT IN-101003, CECYT-Sinaloa State and CONACYT.

Z. Kristallogr. Suppl. **23** (2006) 575-580

Microstructural analysis of ZnO from different aqueous synthesis routes

G. Vanhoyland[1], D. Mondelaers[1], H. Van den Rul[2], J. D'Haen[2], L.C. Van Poucke[1] and J. Mullens[1,*]

[1]Laboratory of Inorganic and Physical Chemistry, University Hasselt, Agoralaan, Building D, 3590 Diepenbeek (Belgium)
[2]IMEC VZW, division IMOMEC, Wetenschapspark 1, 3590 Diepenbeek (Belgium)
[*]Contact author; e-mail: jules.mullens@uhasselt.be

Keywords: microstructure, ZnO, nanocrystalline, powder diffraction

Abstract. In this study a microstructural analysis of powder diffraction data was carried out for ZnO that has been obtained by means of 1) controlled double-jet precipitation and 2) a solution-gel route. A particular feature of these routes is the use of water as solvent. In both cases nanocrystalline ZnO was obtained, but with a different microstructure.

symbols

f	pure-specimen (physically) broadened profile
FWHM	Full Width at Half Maximum
g	instrumentally broadened profile
G	Gaussian component
h	observed broadened profile
L	Lorentzian component
β	integral breadth (= peak area/max. peak intensity)
ε	apparent crystallite size (volume-weighted for integral breadth methods, area-weighted for Fourier methods)
ϕ	angle between the normal to the plane (hkl) and the cylinder axis
φ	Voigt parameter (= FWHM/β)
*	data in reciprocal space units

Introduction

Nanocrystalline materials have attracted much interest over the last years due to their specific properties and the continuous pushing towards miniaturisation in technological applications. As an example of the former, nanocrystalline ZnO shows a blue shift in the absorption spectrum as compared to the bulk microcrystalline equivalent [1]. At the origin of the difference in properties is the much higher ratio 'sample surface'-to-'sample volume' for nanocrystalline compounds, which means that surface effects become more important and could even domi-

nate bulk properties. Moreover, due to this higher ratio nanocrystalline material shows a much higher reactivity in solid state reactions, which is important e.g. in catalysis, but also for the decomposition of precursors in order to obtain functional oxides. With respect to the latter, it is well known from the literature [2, 3] that the morphology of the crystallites in the final oxides depends on the way they are synthesized. Among other factors such as the temperature and duration of the applied heat treatment, also the nature of the precursor material is of major importance. This is clearly illustrated in case of ZnO for which Louër et al. pioneered the microstructural characterization by means of powder diffraction already 2 decades ago [4 and 7, ex-hydroxide-nitrate ZnO]. In subsequent articles the microstructure of ZnO obtained from several precursors was studied: ex-oxalate ZnO [5], ex-acetate ZnO [2], ex-hydroxide-carbonate ZnO [2, 6]. In all cases it was established that the ZnO crystallites had the form of hexagonal prisms with the main axis parallel to the c-axis of the unit cell. For the microstructural characterization this shape was approximated by a cylinder in order to relate apparent crystallite sizes to actual physical crystallite dimensions. Depending on the sample, the microstructural characterization was done either by Fourier methods (for ex-hydroxide-nitrate ZnO in [4] and ex-acetate ZnO) or the integral breadth method based on the Voigt approximation (for ex-hydroxide-nitrate ZnO in [7], ex-oxalate ZnO and both ex-hydroxide-carbonate ZnO). For more details on these methods see [7 and references therein].

From these microstructural analyses, it was established that ex-hydroxide-nitrate ZnO and ex-hydroxide-carbonate ZnO from ref. [6] contained no structural mistakes. The ex-hydroxide-nitrate ZnO is even an example of pure size-broadening, whereas in the ex-hydroxide-carbonate from [6] both size and strain broadening are present. For the other three ZnO additional broadening due to structural imperfections (stacking faults more in particular) was found. As a result, the β_f values could be divided into three different groups according to their Miller indices:

Group 1: *hk0* or $h - k = 3n$; Group 2: $h - k = 3n \pm 1$, *l* odd; Group 3: $h - k = 3n \pm 1$, *l* even

Furthermore, $\beta_{f1} < \beta_{f2} < \beta_{f3}$. However, group 1 reflections are not affected by these mistakes and were used to determine the crystallite size and in case of ex-hydroxide-carbonate ZnO from [6] also the strain. Ex-oxalate ZnO and ex-hydroxide-carbonate ZnO from [2] were strain-free.

For all compounds, the actual (physically meaningful) dimensions of the crystallites were calculated from the apparent sizes, ε_F (Fourier method, area-weighted) or ε_β (integral breadth method, volume-weighted). In case of a cylindrical shape with diameter D and height H, the following relations hold for ε_β [5] [$q = H (\tan\phi)/D$ and $\Phi = \tan^{-1}(D/H)$]:

$$\varepsilon_\beta = \frac{D}{\pi} \csc\phi \left[8/3 + 2q \cos^{-1} q - (1/2q) \sin^{-1} q - 5/2 \left(1 - q^2\right)^{1/2} + 1/3 \left(1 - q^2\right)^{3/2} \right] \qquad (1)$$

for $0 \le \phi \le \Phi$

$$\varepsilon_\beta = D \csc\phi \left[8/3\pi - 1/4q \right] \qquad \text{for } \Phi \le \phi \le \pi/2 \qquad (2)$$

In the present study the ideas introduced by Louër et al. have been applied to characterize the microstructure of ZnO that was obtained from two different synthesis routes: 1) controlled double jet precipitation (CDJP) and 2) a solution-gel method. A common characteristic to both synthesis routes is the use of water as solvent. Compared to the solution-gel synthesis, the thermal budget of the CDJP route is much lower since no additional thermal decomposition is required to form the oxide. The microstructural characterization of both compounds was carried out using the integral breadth method following the procedure described in [8]. In case both size and strain effects were present (as evidenced from the W-H plot) it was assumed that β_{iL}^* accounts for size, whereas β_{iG}^* represents the strain.

Experimental

The CDJP-ZnO was synthesized as described in [9] using $ZnCl_2$ and NaOH in a 1:2 molar ratio. The synthesis was carried out at 70 °C. Under these conditions pure ZnO is formed. The precipitate was filtered, washed thoroughly with deionised water by decantation and dried at 60 °C before characterization.

The ex-sol ZnO was synthesized by means of an aqueous solution-gel route, as described in [10]. The precursor gel was dried at 60 °C for 24 h and subsequently thermally decomposed at 500 °C for 6 hours.

X-ray diffraction measurements were carried out on a Siemens D5000 diffractometer equipped with a Ge(111) primary monochromator (Cu-$K_{\alpha 1}$, 1.54056Å). The step sizes varied between 0.025°(2θ) and 0.1°(2θ) depending on the FWHM of the diffraction peak. The counting times varied between 60 s and 250 s per step, depending on the peak intensity. The Instrumental Resolution Function (IRF) was determined using SRM660a from NIST. The squares of the $FWHM_g$ and β_g were fitted by the quadratic in $\tan\theta$ (Cagliotti function) in order to find the values for β_g and φ_g at the positions of the ZnO diffraction peaks through interpolation. The pattern decomposition was carried out by means of the software program Profile (from Socabim and supplied by Siemens) using the pseudo-Voigt function. It was not necessary to use the split versions. Care was taken to fit the peaks far in the tails. Therefore clusters of peaks had to be fitted. E.g. for both samples the cluster of (100), (002) and (101) was fitted (R_P = 2.6% and 2.7%).

Results and discussion

From figure 1, in which the FWHM is compared with the Instrumental Resolution Function (IRF), it is obvious that for both compounds diffraction peaks are broadened. Moreover, the data show a pronounced scatter which indicates that the sample broadening is anisotropic or (hkl) dependent.

For ex-sol ZnO the (102) and (200) had a super-Lorentzian shape (which means the Voigt parameter is below the Lorentzian limit of 0.6366 [11]). These reflections were consequently neglected in further calculations because the Voigt function is not able to describe this behaviour adequately. The Williamson-Hall (W-H) plot, in which a large spread of the data points can be seen, is shown in figure 2. However, when grouping the reflections according to their Miller indices (see Introduction), all (hkl)'s belonging to group 1 fall approximately on a straight line. Since this line has a non-zero slope, both size and strain effects are present.

Reflections of groups 2 and 3 show much more scatter and are additionally affected by stacking faults. In this respect, the situation is similar to ex-acetate ZnO [2]. Since ex-sol ZnO originates from an acetate-citrate precursor, this may be an inherent feature to this type of precursors. The group 1 reflections are unaffected by the stacking faults and can therefore be used to calculate the diameter (D) and the height (H) of the cylindrical crystallites via a least squares fitting of equations (1) and (2). The actual dimensions of the cylinder are then D = 34.8(6) nm and H = 28.5(5) nm. It should be mentioned that this result is somewhat biased since the size-strain separation is based on the L and G components of single lines.

CDJP-ZnO shows a different behaviour. None of the diffraction peaks had a super-Lorentzian shape. In the W-H plot (figure 3) data points for particular reflections with different orders [e.g. (100) and (200); (101) and (202); (002) and (004)] fall approximately on straight lines with zero slope meaning that strain effects are negligible. Furthermore, the intercept for the (00l) reflections is less than for the (hk0), which suggests that the crystallite morphology on average approximates a cylinder with its axis collinear to the c-axis of the hexagonal unit cell. This behaviour is similar to ex-hydroxide-nitrate ZnO [4, 7]. Using the cylindrical model, a least-squares fit of equations (1) and (2) results in D = 15.9(6) nm and H = 15.1(5) nm for the average cylinder.

Table 1. ex-sol ZnO, group 1 reflections.

(hkl)	β_h (°(2θ))	ϕ_h	β_g (°(2θ))	β_f (°(2θ))	ϕ_f	ε_β (Å)
(100)	0.3848	0.685	0.0829	0.3508	0.677	297
(002)	0.3917	0.676	0.0835	0.3558	0.667	285
(110)	0.4536	0.693	0.0903	0.4124	0.692	291
(112)	0.5103	0.694	0.0953	0.4640	0.696	279
(114)	0.7208	0.675	0.1183	0.6446	0.680	241

Table 2. CDJP-ZnO.

(hkl)	β_h (°(2θ))	ϕ_h	β_g (°(2θ))	β_f (°(2θ))	ϕ_f	ε_β (Å)
(100)	0.7273	0.735	0.0829	0.7041	0.737	130
(002)	0.6526	0.735	0.0835	0.6277	0.737	147
(101)	0.7282	0.735	0.0839	0.7034	0.738	132
(102)	0.7505	0.734	0.0871	0.7215	0.738	134
(110)	0.7936	0.735	0.0903	0.7608	0.739	132
(103)	0.7795	0.735	0.0929	0.7434	0.740	139
(200)	0.8708	0.732	0.0945	0.8330	0.737	127
(112)	0.8461	0.735	0.0953	0.8074	0.741	132
(201)	0.8432	0.734	0.0959	0.8037	0.740	133
(004)	0.7648	0.728	0.0978	0.7220	0.734	152
(202)	0.8938	0.732	0.1004	0.8491	0.738	133
(104)	0.8450	0.728	0.1033	0.7961	0.735	146

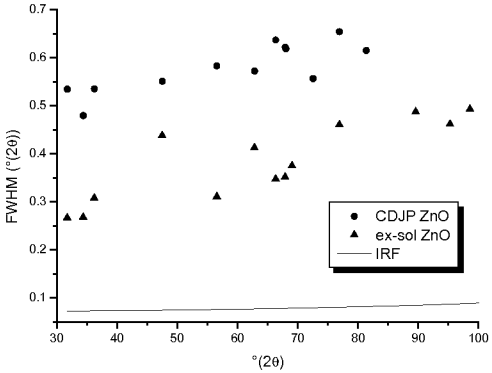

Figure 1. FWHM of ex-sol ZnO and CDJP ZnO, compared with the Instrumental Resolution Function.

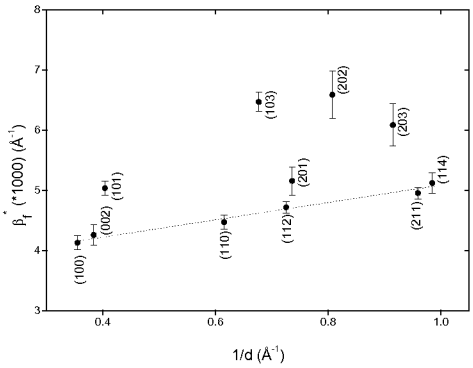

Figure 2. W-H plot of ex-sol ZnO (the line through group 1 reflections serves only as a guide to the eye).

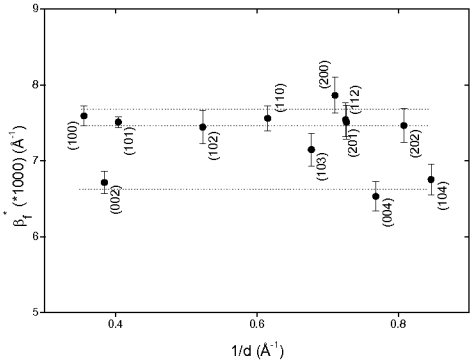

Figure 3. W-H plot of CDJP-ZnO (the lines serve only as a guide to the eye).

Concluding remarks

This study has demonstrated the capability of both aqueous synthesis routes to produce nanocrystalline ZnO. Moreover, a different microstructure for both types of ZnO was observed. In ex-sol ZnO both size and strain effects account for the peak broadening. Additionally, particular (hkl)'s are affected by stacking faults. The crystallites are hexagonal prisms, as commonly found for ZnO. This shape was approximated by a cylindrical model with D = 34.8(6) nm and H = 28.5(5) nm. For CDJP-ZnO also a cylindrical model was selected although D (= 15.9(6) nm) and H (= 15.1(5) nm) are not much different. This sample contained no structural mistakes and strain was found to be negligible.

References

1. Bahnemann, D.W., Kormann, C. and Hoffmann, M.R., 1987, *J. Phys. Chem.*, **91**, 3789.
2. Audebrand, N., Auffrédic, J.-P. and Louër, D., 1998, *Chem. Mater.*, **10**, 2450.
3. Audebrand, N., Auffrédic, J.-P. and Louër, D., 2000, *Chem. Mater.*, **12**, 1791.
4. Louër, D., Auffrédic, J.-P., Langford, J.I., Ciosmak, D. and Niepce, J.C., 1983, *J. Appl. Cryst.*, **16**, 183
5. Langford, J.I., Boultif, A., Auffrédic, J.-P. and Louër, D., 1993, *J. Appl. Cryst.*, **26**, 22.
6. Sigoli, F.A., Paiva-Santos, C.O., Jafelicci, M. and Davolos, R., 2001, *Powder Diff.*, **16(3)**, 153.
7. Louër, D., 1999, IUCr Monograph 10 "*Defect and Microstructure Analysis by Diffraction*", Editors Snyder, R.L, Fiala, J. and Bunge, H.J., Oxford University Press, 686.
8. Langford, J.I., Delhez, R., de Keijser, Th.H. and Mittemeijer, E.J., 1988, *Aust. J. Phys.*, **41**, 173.
9. Van den Rul, H., Mondelaers, D., Vanhoyland, G., Mullens, J. and Van Poucke, L.C., 2003, *Ceramic Eng. Sci. Proc.*, **24(3)**, 93.
10. Mondelaers, D., Vanhoyland, G., Van den Rul, H., D'Haen, J., Van Bael, M.K., Mullens, J. and Van Poucke, L.C., 2002, *MRS Bulletin*, **37(5)**, 901.
11. Wertheim, G.K., Butler, M.A., West, K.W. and Buchanan, D.N.F., 1974, *Rev. Sci. Instrum.*, 11, 1369.

Acknowledgements.
G.V. is a postdoctoral fellow of the Fund for Scientific Research – Flanders (Belgium) (FWO-Vlaanderen).

Z. Kristallogr. Suppl. 23 (2006) 581-586

The effect of Al and Gd doping on the structure, microstructure and thermal expansion of gallium nitride (GaN)

Z. K. Heiba, Sameh Ahmed, Ali Abo-Shama and Karimat El-Sayed*

Physics Department, Faculty of Science, Ain- Shams University, Cairo, Egypt
*Contact author; e-mail: elkarimat@yahoo.com

Keywords: powder diffraction, GaN, two-step method, size/strain analysis

Abstract. The changes in the crystal structure, microstructure and thermal expansion occurred upon doping GaN with Al or Gd have been investigated by X-ray diffraction technique. The results showed that Al as well as Gd atoms are accommodated interstitially but in different interstitial positions in the GaN lattice. Anisotropic crystallite size and microstrain are found for the three samples - pure, Al and Gd doped GaN. Also anisotropic thermal expansion is found for the different temperatures ranges (-193, -100, 25, 100, 200). The changes obtained in crystallite size, microstrain and lattice thermal expansion were correlated with the structural changes produced by doping.

Introduction

Gallium Nitride (GaN) is being used in optoelectronic devices in the range from green to ultraviolet, blue laser is one of the most important achievements done with GaN [1], moreover GaN–based electronic has attractive material properties, such as a band gap of 3.39 eV, a break down field of nearly 5×10^6 v/cm, a drift velocity of 2.7×10^6 cm/s and it can be used also at high temperature [2, 3]. Doping materials improve the quality of the electronic and optoelectronic materials. Accordingly, the aim of the present work is to dope GaN with two different elements alternatively, and to see the effect of these dopants atoms on the structural, microstructural and thermal expansion of the studied samples.

Experimental

The general formula "GaN:Ax" is used for doping GaN, where Ax is the required molecular weight of the dopant elements (Al or Gd). Pure GaN (Aldrich 99.9%), Al (Aldrich 99.99 %) and Gd (Aldrich ++99.9%) were used as starting materials. The fractional dopant mass with respect to one gram molecular weight in case of Al is $GaN:Al_{0.15}$, and in case of Gd is $GaNGd_{0.05}$, respectively. The GaN and the dopant materials were mixed together in an agate mortar and then introduced into silica tube sealed under vacuum of 10^{-5} bar, after that left in

a tube furnace at 600 C° for a month. The tubes were oscillated periodically inside the furnace by a motor to insure the homogeneity of the resulting powder.
Powder X-ray diffraction patterns were recorded at different temperatures (-193, -100, 25, 100, 200 °C) using a Philips X'pert MPD diffractometer with Bragg-Brentano para-focusing geometry and graphite monochromated Cu-Kα radiation. The samples were loaded to the holder by back loading to avoid preferred orientation.

Results and Discussion

Structural analysis

Figure 1 shows the diffraction patterns obtained for the Al-doped GaN as a mixture before heating and after thermal heating. The changes in the peak profile shapes and broadening indicating the structural and microstructural changes produced by doping can be observed. The disappearance of Al lines and presence of traces of Al oxide due to some oxygen remaining in the evacuated tubes can also be clearly seen.

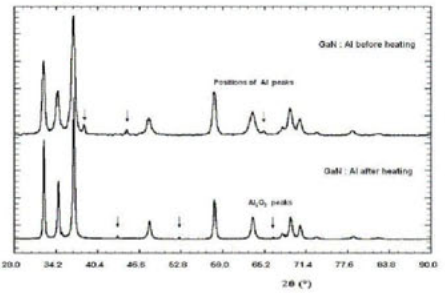

Figure 1. Diffraction patterns of GaN:Al before and after heating.

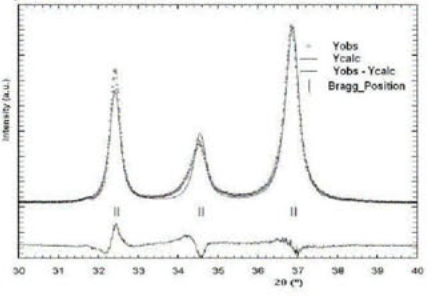

Figure 2. Part of the profile fitting resulting from Rietveld refinement showing the order dependence of broadening.

GaN has the wurtzite structure (built from two hexagonal structure sublattices) with c/a = 1.633 and $P6_3mc$ space group [4]. The Rietveld method (FULLPROF) [5] was tried in order to refine the GaN structure, but unfortunately a big discrepancy between the observed and calculated intensities was present for the peaks *100* and *002*. This was due to the presence of anisotropy in peak broadening and peak asymmetry as shown in figure 2. The presence of anisotropy and asymmetry is due mainly to the native defects in the layers stacked perpendicular to the *c*-axis. To overcome the problem of anisotropy and asymmetry the two-step method [6] was used, step 1 for profile fitting and step 2 for structural and microstructural analysis using the program POWLS 80 [7, 8]. The profile fitting showed high anisotropy of X-ray line broadening, this can especially be seen on the (100) reflection. Similar anisotropy is present in the integral breadth β and the shape factor φ. Table 1 shows the unit cell parameters obtained from the refinements for the pure, Al- and Gd-doped GaN. Table 2 shows the different structural parameters and the reliability R_B-factors for the three different samples, table 3 gives the bond length and angles. Both dopant atoms Al and Gd are found to take the position 2*a*; {(00*z*), (00*z*+1/2)} of the space group $P6_3mc$ but with different *z* coor-

dinates; for Al; z is 0.4237 and for Gd; z is 0.274. Figures 3 and 4 show the positions of Al and Gd atoms in the unit cell of GaN.

Table 1. Refined lattice parameters and corresponding volume.

	a (Å)	c (Å)	V (Å^3)
Pure GaN	3.1831(4)	5.1883(5)	45.5257(4)
GaN :$Al_{0.15}$	3.1945(5)	5.1983(7)	45.9407(2)
GaN:$Gd_{0.05}$	3.1946(8)	5.2035(8)	45.9900(4)

Table 2. Refined structural parameters obtained from program POWLS.

			Fractional atomic coordinates			Relative occ.	R_B-Value
			x	y	Z		
Pure GaN	Ga1	2b	⅓	⅔	0.0	1.0	0.044
	Ga2	2b	⅔	⅓	0.5	1.0	
	N	2b	⅓	⅔	0.3783 (62)	2.0	
Al-doped GaN	Ga1	2b	⅓	⅔	0.0	1.0	0.046
	Ga2	2b	⅔	⅓	0.5	1.0	
	N	2b	⅓	⅔	0.3763 (55)	2.0	
	Al	2a	0.0	0.0	0.4237 (524)	0.1442 (214)	
Gd-doped GaN	Ga1	2b	⅓	⅔	0.0	1.0	0.024
	Ga2	2b	⅔	⅓	0.5	1.0	
	N	2b	⅓	⅔	0.3789 (34)	2.0	
	Gd	2a	0.0	0.0	0.2774 (637)	0.0104 (20)	

Table 3. Bond lengths and angles.

	Bond length (Å)		Bond angle (°)	
Pure	Ga1-N1	1.963	Ga1-N1-Ga2	108.961
GaN	Ga2-N1	1.943	N1-Ga1-N2	109.975
Al-doped	Ga1-N1	1.967	Ga1-N1-Ga2	108.932
GaN	Ga2-N1	1.950	N1-Ga1-N2	108.933
Gd-doped	Ga1-N1	1.968	Ga1-N1-Ga2	108.949
GaN	Ga2-N1	1.950	N1-Ga1-N2	108.950

Crystallite sizes-strain analysis

The experimentally observed broadening of the line profile was corrected for instrumental broadening by using the Stokes deconvolution method [9]. LaB_6 sample was used as the sample characterizing the instrumental broadening. The apparent size of crystallites and microstrain were calculated by using the Warren-Averbach Fourier method [10] for single and multiple line analysis. The convolution of the size-broadened and the strain broadened profile in reciprocal space correspond to the product of their Fourier transform in real space. Accordingly the cosine coefficient $A(n,L)$ of the Fourier series is:

$$A(n,L) = A^S(n) \cdot A^D(n,L). \quad (1)$$

Where $A^S(n)$ contains only size information and it is order independent and $A^D(n, L)$ contains only strains order-dependent. L is a correlation distance perpendicular to the diffracting plane. If more than one order of reflection is available, separate information on $A^S(n)$ and $A^D(n,L)$ can be extracted for small value of L by applying:

$$\ln A(n,L) = \ln A^S(n) + \ln A^D(n,L) = \ln A^S(n) + \frac{2\pi^2 L^2 < e^2(L) >}{d^2}, \quad (2)$$

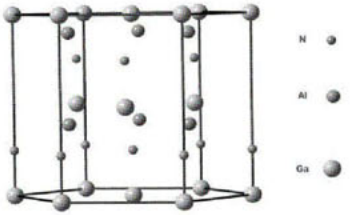

Figure 3. Interstitial positions of Al.

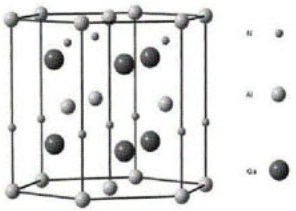

Figure 4. Interstitial positions of Gd.

Table 4. Crystallite size and microstrain for pure GaN.

hkl	Single line			Multiple line			
	$<\varepsilon>_V$ (Å)	$<\varepsilon>_A$ (Å)		hkl	$<\varepsilon>_A$ (Å)		$\tilde{e}$ %
		dist^n	slope		distn	slope	
100	262	138	157	100/200	163	172	0.150
002	113	73	77	002/004	82	86	0.172
101	156	96	101	101/202	112	119	0.187
102	104	68	73				
110	207	126	134				
103	91	62	67				
200	165	106	112				
112	120	79	83				
201	146	95	100				
004	103	70	74				
202	122	76	80				
104	153	82	85				

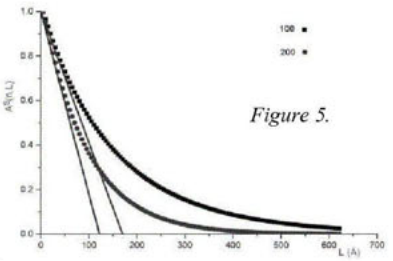

Figure 5.

where $<e^2(L)>$ is the mean square strain, d is the interplanar spacing of the diffracting plane. Strain can be obtained from a plot of ln $A(n,L)$ versus $1/d^2$ for multiple order of reflection *hkl* and $A^S(n,L)$ from the intercepts. By drawing $A_S(n,L)$ against L one can obtain the average area crystallite size $<\varepsilon>A$, figures 5-7, since $[dAS(L)/dL]L \rightarrow 0$ gives mean approximate size $<\varepsilon>A$. The average volume crystallite size $<\varepsilon>V$ was also extracted applying the integral breadth method [11]. The crystallite size $<\varepsilon>A$ obtained from single and multiple line analysis, the average microstrain $\tilde{e}$ from multiple lines and $<\varepsilon>V$ from integral breadth are all

given in tables 4-6 for the pure, Al- and Gd-doped GaN, respectively. Figure 8 shows the crystallite size distributions obtained from the multiple lines analysis of these three samples.

Table 5. Crystallite size and microstrain for GaN: $Al_{0.15}$.

hkl	Single line			Multiple line			
	$\langle\varepsilon\rangle_V$ (Å)	$\langle\varepsilon\rangle_A$ (Å)		hkl	$\langle\varepsilon\rangle_A$ (Å)		$\tilde{e}$ %
		distn	slope		distn	slope	
100	364	218	279	100/200	163	172	0.161
002	263	142	160	002/004	86	86	0.239
101	240	136	150	101/202	119	119	0.145
102	154	97	102				
110	342	182	198				
103	132	86	91				
200	186	118	125				
112	180	115	121				
201	200	127	135				
004	194	123	131				
202	124	82	87				
104	118	75	80				

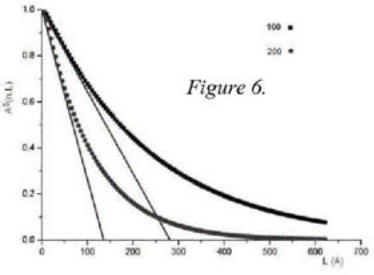

Figure 6.

Table 6. Crystallite size and microstrain for GaN:$Gd^{0.05}$

hkl	Single line			Multiple line			
	$\langle\varepsilon\rangle_V$ (Å)	$\langle\varepsilon\rangle_A$ (Å)		hkl	$\langle\varepsilon\rangle_A$ (Å)		$\tilde{e}$ %
		distn	slope		distn	slope	
100	542	211	221	100/200	249	264	0.180
002	172	82	84	002/004	76	79	0.201
101	215	116	120	101/202	128	134	0.165
102	86	60	63				
110	232	140	153				
103	101	67	72				
200	156	98	104				
112	150	94	100				
201	170	108	114				
004	151	96	101				
202	132	80	83				
104	178	115	122				

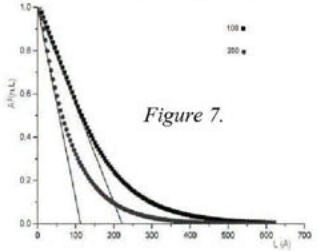

Figure 7.

From the results obtained for crystallite size and strain for single and multiple reflections, it can be found that the crystallite size is anisotropic. The crystallite size along the *a*-axis direction is nearly twice that of the *c*-axis direction for pure GaN. For the Al-doped GaN there are a detectable increase in the crystallite size in both directions (*a*, *c*) compared with the pure GaN but the ratios between the crystallite size in *a*-axis with respect to that of *c*-axis is still twice as in pure GaN. For the Gd doped GaN the anisotropy in the crystallites size were large. The microstrain analysis showed that the lattice microstrain is slightly larger in the

c- axis than in the *a*-axis direction. This is mainly due to the special position taken by Al and Gd atoms along the *c*-axis which cause this strain.

Thermal expansion

The rate of change of $\Delta a/a$ and $\Delta c/c$ with respect to temperatures (-193, -100, 25, 100, 200 °C) for pure and Al-doped GaN are shown in figure 9 for the *a*-axis and figure 10 for the *c*-axis. From these results it follows that no phase change takes place by changing the temperature in the examined temperature range (-193 to 200 °C), moreover the rate of change of the lattice parameter a for the pure and Al doped GaN is maximum in the temperature range (-100 to 100 °C). The rate of change of lattice parameter *c* for pure GaN behaves differently from that of Al-doped GaN. This is mainly due to microstrains induced by the insertion of the Al atoms into the GaN lattice. Figure 11 shows the behaviour of the change in the unit cell volume of both pure and Al-doped GaN. In general, the changes in the lattice parameters with temperature are very small. The average thermal expansion is 2.5×10^{-6} K^{-1}.

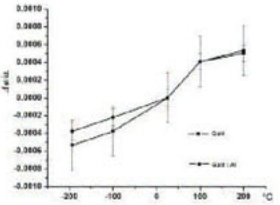

Figure 9. Relative change of lattice parameter a.

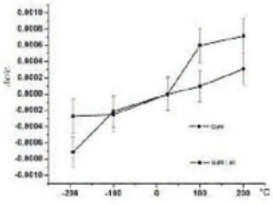

Figure 10. Relative change of lattice parameter c.

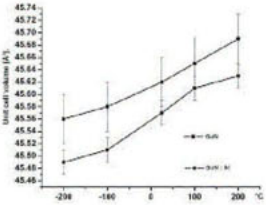

Figure 11. Relative change of unit cell volume.

References

1. Pankove, I.J., and Moustakas, T.D., 1998, *Gallium Nitride (GaN)I*, Academic Press.
2. Morkoc, H., Strite, S., Gao, G.B., Lin, M.E., Sverdlor, B., and Burns, M., 1994, *J. Appl. Phys.*, **76**, 1363.
3. Chow, T.P., and Tyagi, R., 1994, *IEEE Trans.Electron Devices*, **41**, 1481.
4. Juza, R., Hahn, H.Z., 1938, *Anorg. Chem.*, **239**, 282.
5. Rodriguez-Carvajal, J., *FULLPROF Manual, Laboratoire Leon Brillouin (CEA-CNRS) CEA/Saclay*, 91191, 2001 Gif Sur Yvette CEDEX, France.
6. Will, G., Frazer, B.C. and Cox, D.E., 1965, *Acta Crystallogr.*, **19**, 854.
7. Will, G., 1989, Z. *Kristalogr.* , **188**, 169.
8. Will, G., Jansen, E. and Schafer, W., *POWLS80. Program for calculating and refining powder diffraction data., 1982; Report Jul-1867 KFA, Julich, FRG.*
9. Stokes, A. R., 1948, *Proc. Phys. Soc. London*, **61**, 382.
10. Warren, B. E. and Averbach , B. L., 1950, *J. Appl. Phys.*, **21**, 595.
11. Delhez, R., de Keijser, Th. H., Mittemiejer, E. J., 1982, *Fresenius. Z. Anal. Chem.*, **312**, 1.

Z. Kristallogr. Suppl. **23** (2006) 587-592

Quantitative phase analysis of ordinary Portland cements using synchrotron radiation powder diffraction

A. G. De la Torre, A. Cabeza, E. R. Losilla, M. A. G. Aranda*

Departamento Química Inorgánica, Universidad de Málaga, 29071 Málaga, Spain
*Contact author; e-mail: g_aranda@uma.es

Keywords: synchrotron radiation, QPA, Rietveld method, amorphous content.

Abstract. High-resolution synchrotron X-ray powder diffraction data have been analysed using the Rietveld methodology to obtain the mineralogical composition of four commercial and NIST RM-8488 Portland clinkers. Alite phase coexistence has been observed in four patterns. White Portland clinkers show a single alite or a very small amount of a second alite phase with smaller unit cell volume likely due to a higher magnesium content. Grey Portland clinkers show a much more pronounced alite phase coexistence. This effect is not so pronounced or even negligible when low resolution data, i.e. laboratory X-ray powder diffraction data are used. Moreover, the full mineralogical composition (including the non-diffracting content) has been determined from the overestimation of the added standard, α-Al_2O_3, in the Rietveld analyses. White clinkers contain ~15 wt% of non-diffracting content while this fraction is much smaller in grey clinkers, ~7 wt%.

Introduction

Final performances of industrial materials such as Ordinary Portland Cements (OPC) depend -among others- on their mineralogical composition. Rietveld analysis [1] of X-ray powder diffraction data is the most powerful and available technique for direct Quantitative Phase Analysis (QPA). This is a standardless methodology, but the crystal structures of all phases must be known as the process consists in the comparison of the measured and calculated patterns. Recently, this methodology has been applied to complex materials such as grey and white Portland clinkers and cements of different chemical and phase composition [2-8] using Laboratory X-ray Powder Diffraction (LXRPD) including the quantification of the non-diffracting contents [9,10]. These materials contain at least four phases: alite (C_3S or Ca_3SiO_5), belite (C_2S or Ca_2SiO_4), aluminate (C_3A or $Ca_3Al_2O_6$) and ferrite (C_4AF or $Ca_4Al_2Fe_2O_{10}$). The methodology is also being adapted to carry out on-line mineralogical analyses in cement factories to be used in quality control [11,12]. However, LXRPD data may contain systematic errors such as strong preferred orientation, optical aberrations which

change with 2θ, microabsorption and strong peak overlapping of the different phases. Furthermore, the small mean penetration depth (~ 25 μm for CuK_α) in reflection geometry may lead to poor particle statistics especially if the sample is not rotated.
Hence, it is desirable to validate QPA obtained by LXRPD with an analytical technique that minimises these drawbacks, e.g. High-Resolution Synchrotron X-ray Powder Diffraction (HRSXRPD). Rotating capillary geometry (transmission) often reduces preferred orientation very effectively. High energy X-rays minimise microabsorption and improve particle statistics considerably since a very large amount of sample is tested in wide capillaries. High resolution data minimise the overlapping and parallel synchrotron X-rays geometry, with an analyser crystal, does not show optical aberrations. Specifically, we have previously reported HRSXRPD data to achieve good QPA of commercial OPC [13] and to show that accurate Rietveld QPA can be obtained for cements [14]. Other authors have also used synchrotron radiation [9,15,16,17] and neutron diffraction [15,18] for the QPA of cements.
Here, we report QPA of commercial grey and white OPC and NIST RM-8488 clinker by using HRSXRPD, which includes the quantification of the non-diffracting content.
A comparative powder diffraction study of a clinker at different resolutions is also shown.

Experimental

Samples
Four commercial clinkers, selected from four factories, have been analysed using HRSXRPD. These clinkers were labelled W1, W2, G1 and G2, (W stands for white Portland clinker and G stands for grey Portland clinker). NIST RM-8488 reference clinker was also analysed. All samples were mixed with a known amount of α-Al_2O_3 standard, see table 1.

X-ray data collection
HRSXRPD patterns were collected on the ID31 powder diffractometer of ESRF, European Synchrotron Radiation Facility, (Grenoble, France) using a short and penetrating wavelength λ=0.40027 Å (30.97 keV) selected with a double-crystal Si (111) monochromator and calibrated with NIST SRM 640c silicon powder (a = 5.43094 Å). The Debye-Scherrer configuration was used with the samples loaded in wide borosilicate glass capillaries, diameter of 2 mm, and rotated during data collection. The overall measuring time was ≈100 min to have very good counting statistics over the wide angular range 2.5-30° (in 2θ) (9.15-0.77 Å). The data from the multi-analyser Si(111) stage were normalised and summed up to 0.003° step size. Powder data for one sample, G1, were collected with a slightly different wavelength, λ = 0.42970 Å. The samples were ground to very fine powders and the wide capillaries used ensure that the specimens are representative.
Two additional patterns for G2 sample were collected in reflection geometry: i) using a PANalytical CubiX PRO diffractometer operated with strictly monochromatic $CuK\alpha_1$ radiation λ = 1.540598 Å [Ge (111)] and an X'Celerator detector, and ii) using a Siemens D5000 diffractometer with $CuK\alpha_{1,2}$ radiation (λ = 1.542 Å) with a secondary curved graphite monochromator. The flat samples were rotated during data collection.

X-ray data analysis

Rietveld methodology was applied to analyse powder patterns by means of the GSAS suite of programs [19]. References of the crystal structure descriptions for cement phases were reported in reference [14] including that of the corundum standard. The refined overall parameters were: background coefficients, unit cell parameters, zero-shift error, peak shape parameters (pseudo-Voigt function) and mass fractions of the phases. The anisotropic peak shape parameter (STEC in GSAS program) was refined when necessary. The HRSXRPD patterns did not show preferred orientation for alite but the two LXRPD patterns showed preferred orientation (flat samples) that was corrected using the spherical-harmonic algorithm in GSAS with order = 6. The texture indices converged to values close to 2.5 (a value of 1 represents an ideal random powder whereas ∞ stands for a single crystal).

Results and discussion

Phase coexistence of alite

Alite is the polymorph of Ca_3SiO_5 present in OPC which is usually monoclinic [20, 21]. This phase is stabilised at room temperature by the presence of foreign ions in the structure. Figure 1 displays a selected region of all the clinker HRSXRPD patterns with alite phase coexistence highlighted by asterisks. W1 did not show alite phase coexistence, see figure 1. Conversely, W2, G1, G2 and RM 8488 displayed this coexistence. Two alite phases computed with the same structural description [20] but with different unit cell volumes were introduced to carry out the refinements/quantifications. Rietveld results for all samples are given in table 1.

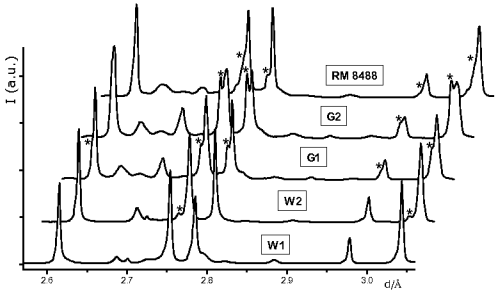

Figure 1. Selected region of HRSXRPD raw clinker patterns. Asterisk highlights alite coexistence in several clinkers.

Alite MIII (monoclinic) is stabilised mainly by the substitution of Ca^{2+} by Mg^{2+}. White Portland clinkers contain very small amounts of Mg^{2+} (both clinkers contain 0.60 wt% expressed as MgO and measured by X-Ray Fluorescence). Consequently, the unit cell volume of C_3S of these samples are larger, see table 1. Furthermore, alite phase coexistence, if present, is very small (W2 clinker contains 2.0(1) wt% of the C_3S phase with the smallest unit cell volume). Grey clinkers (G1 and G2) have higher contents of Mg^{2+} (1.62 and 1.24 wt%, respectively), and they display overall smaller unit cell volumes, see table 1. The amount of the alite phase with the smallest volume (119.9 $Å^3$ per unit formula) is higher in the grey than in the white clinkers, see table 1. Additionally, they contain a small amount of free MgO as periclase. RM-8488 clinker also shows two alites with different unit cell

volumes in the pattern without periclase (0.98 wt% of magnesium expressed as MgO). These results indicate that both alite phases may contain magnesium cations. However, the Mg^{2+}-content in the sub-phase with the smallest unit cell volume should be higher. The superstructures of these two coexisting alites could be different but the same structural description was used in the analyses since there are no alternative structures available. More synthetic and high-resolution structural work is needed to properly understand and describe the structural role of impurities (Mg^{2+}, Al^{3+}, etc.) in alite(s).

Table 1. Rietveld quantitative SXRPD results for the clinkers. The weighed amounts of α-Al_2O_3, the derived non-diffracting content. The unit cell volumes (V/Z) for the C_3S sub-phases are also given.

Phases /wt%	W1	W2	G1	G2	RM-8488	RM-8488[#]
$C_3S(1)$	51.7(1)	55.3(1)	32.1(2)	23.8(2)	35.6(2)	
$C_3S(2)$	-	2.0(1)	16.7(2)	26.6(2)	11.5(3)	
C_3S_total	-	57.3(1)	48.8(3)	50.4(3)	46.3(4)	48.5
C_2S	19.7(2)	8.5(2)	10.9(2)	8.3(1)	10.7(2)	13.8
C_3A	2.4(1)	6.0(1)	6.3(1)	6.7(1)	2.6(1)_2.5(1)*	3.2
C_4AF	-	-	10.6(1)	9.3(1)	11.8(1)	9.1
$NaK_3(SO_4)_2$	-	-	1.5(1)	1.5(1)	-	
K_2SO_4	-	0.6(1)	-	-	-	
MgO	-	-	0.37(4)	0.43(3)	-	
Al_2O_3	26.2(1)	27.6(1)	21.55(7)	23.40(7)	25.3(1)	
Al_2O_3(weighed)	21.99	24.34	20.33	21.79	23.75	
Amorphous	20.6(5)	15.6(5)	8.8(4)	7.1(4)	8.0(5)	
V $C_3S(1)$ / Å^3	120.91	120.87	120.42	120.43	120.68	
V $C_3S(2)$ / Å^3	-	119.90	119.94	119.93	120.13	
R_{WP}/%	13.8	15.7	9.1	9.3	9.3	

* RM-8488 contains two polymorphs of C_3A, cubic (2.6 %) and orthorhombic (2.5 %).

[#] The phase values for RM-8488 are those given in the 1441 technical note of NIST but recalculated to contain a 25.3 wt% of an extra crystalline phase for the sake of comparison.

Clinker quantitative phase analysis using different radiations/resolutions

Rietveld QPA results given in table 1 indicate that alite phase coexistence is very pronounced in grey clinkers which contain high amounts of magnesium. This is the first direct evidence of alite phase coexistence in commercial OPC which became possible due to the extremely high resolution of the ID31 synchrotron powder diffraction data. As a consequence, we have studied the influence of the alite phase coexistence in the Rietveld analysis of LXRPD data taken at different resolutions. Thus, G2 clinker was also analysed using CuKα_1 and CuK$\alpha_{1,2}$ radiation, hereafter LXR_1PD and $LXR_{1,2}PD$ data, respectively. A full comparison of HRSXRPD analytical results and the mineralogical contents obtained by LXR_1PD and $LXR_{1,2}PD$ data is shown in table 2. In figure 2, a selected region of (a) HRSXRPD, (b) LXR_1PD and (c) $LXR_{1,2}PD$ Rietveld plots for G2 clinker is shown. It must be noted that laboratory data taken with CuK$\alpha_{1,2}$ radiation do not show any signs of phase coexistence and the Rietveld analyses yielded good agreement indices when the alite phase is described by a single structural model.

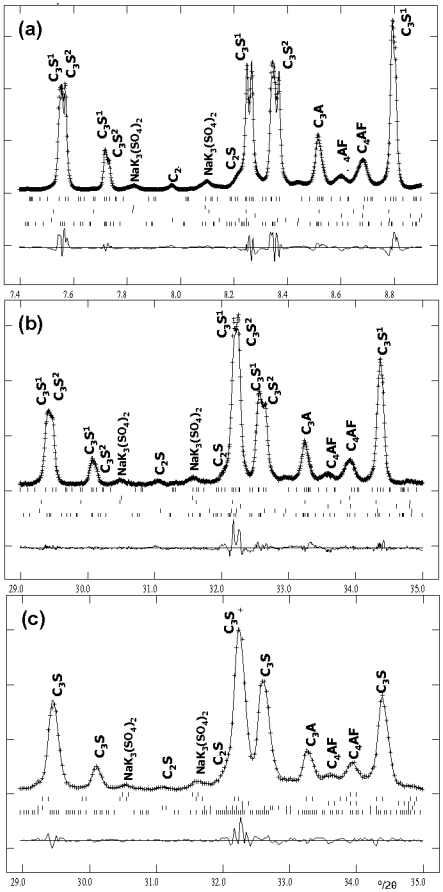

However, when strictly monochromatic radiation is used, some signs of phase coexistence (splitting of several peaks) are evident in the patterns and need to be taken into account in the Rietveld analysis. These split peaks could not be described by using a single phase alite with lower symmetry.

Non-diffracting content analysis

All clinkers were mixed with Al_2O_3 in order to indirectly obtain the amorphous contents [22]. The derived non-diffracting content of each clinker is given in table 1. To achieve accuracy in results, sufficient crystallite orientation statistics must be ensured. HRSXRPD is much better providing that than LXRPD since a larger sample volume is analysed [14]. The present study indicates that the average non-diffracting/amorphous content of white Portland clinkers is remarkably higher than that of grey Portland clinkers. These results are in agreement with the manufacturing processes and other reports [9,13]. The amount of liquid phase in grey OPC kilns is large and the particles are relatively well crystallised (low non-diffracting contents). However, the amount of liquid phase in white OPC kilns is smaller and, thus, particles contain more defects which leads to an increase of the non-diffracting content.

Figure 2. Selected region of (a) HRSXRPD, (b) LXR$_1$PD and (c) LXR$_{1,2}$PD Rietveld plots of G2 clinker with peaks from each phase labelled. C_3S^1 and C_3S^2 stand for the two alites.

Table 2. Rietveld QPA of G2 clinker using different radiations and different types of diffraction geometry.

Phases /wt%	SXRPD	LXR$_1$PD	LXR$_{1,2}$PD
$C_3S(1)$	31.1(1)	27.6(1)	69.3(2)
$C_3S(2)$	34.7(2)	39.3(1)	-
C_3S_overall	65.8(2)	66.9(1)	69.3(2)
C_2S	10.7(2)	10.9(2)	10.8(5)
C_3A	8.8(1)	7.5(1)	7.4(2)
C_4AF	12.1(1)	12.4(2)	10.9(2)
$NaK_3(SO_4)_2$	2.0(1)	2.3(1)	1.6(1)
MgO	0.6(2)	-	-
R_{WP}/%	9.3	9.7	11.3

References

1. Rietveld, H.M., 1969, *J. Appl. Crystallogr.*, **2**, 65.
2. Walenta, G. & Fullmann, T., 2004, *Powder Diffr.* **19,** 40.
3. Pritula, O., Smrcok, E., Ivan, J. & Izdinsky, K., 2004, *Ceramics-Silikaty*, **48,** 34.
4. Fullmann, T. & Walenta, G., 2003, *ZKG International*, **56**, 45.
5. Schmidt, R. & Feldman, T., 2003, *World Cement*, **April,** 64.
6. Lundgaard, N. & Jons, E.S., 2003, *World Cement*, **April**, 59.
7. Courtial, M., de Noirfontaine, M.-N., Dunstetter, F., Gasecki, G. & Signes-Frehel, M. 2003, *Powder Diffr.*, **18,** 7.
8. Pritula, O., Smrcok, L. & Baumgartner, B. 2003, *Powder Diffr.*, **18,** 16.
9. Suherman, P.M., Riessen, A.V., Oconnor, B., Li, D., Bolton, D. & Fairhurst, H., 2002, *Powder Diffr.*, **17**, 178.
10. Whitfield, P.S. & Mitchell, L.D., 2003, *J. Mater. Science*, **38**, 4415.
11. Scarlett, N.V.Y. & Madsen, I.C., 2001, *Powder Diffr.*, **16,** 71.
12. Enders, M., 2003, *ZKG International*, **56**, 54.
13. De la Torre, A.G., Cabeza, A., Calvente, A., Bruque, S. & Aranda, M.A.G., 2001, *Anal. Chem.*, **73**, 151.
14. De la Torre, A.G. & Aranda, M.A.G., 2003, *J. Appl. Crystallogr.*, **36**, 1169.
15. Peterson, V., Hunter, B., Ray, A. & Aldridge, L.P., 2002, *Appl. Phys. A*, **74,** S1409.
16. Emanuelson, A., Landa-Canovas A.R. & Hansen, S. 2003, *Cem. Concr. Res.* **33,** 1623.
17. Peterson, V., Hunter, B. & Ray, A. 2004, *J. Am. Ceram. Soc.*, **87,** 1625.
18. Peterson, V., Hunter, B. & Ray, A. 2002, *Proceedings of the Australian Institute of Physics 15th Biennial Congress*, Sydney, page 1.
19. Larson, A.C. & Von Dreele, R.B., 1994, "General Structural Analysis System", Los Alamos National Lab. Rep. No. LA-UR-86-748.
20. De la Torre, A.G., Bruque, S., Campo, J. & Aranda, M.A.G., 2002, *Cem. Concr. Res.* **32,** 1347.
21. de Norfontaine, M.N., Dunstetter, F., Courtial, M., Gasecki, G. & Signes-Frehel, M. 2003, *Z. Kristallogr.* **218**, 8.
22. De la Torre, A.G., Bruque, S. & Aranda, M.A.G., 2001, J. Appl. Crystallogr. **34**, 196.

Acknowledgements. We thank ESRF for providing synchrotron X-ray beam time on ID31.

IV.5 Organic Materials

Z. Kristallogr. Suppl. **23** (2006) 595-600

Ab initio structure determination of two anhydrous forms of α-lactose by powder X-ray diffraction

C. Platteau, J. Lefebvre, S. Hemon*, F. Affouard, J. F. Willart and P. Derollez

Laboratoire de Dynamique et Structure des Matériaux Moléculaires (UMR CNRS 8024), Bâtiment P5, Université des Sciences et Technologies de Lille, 59655 Villeneuve d'Ascq Cédex, France.
*Contact author: Stephanie.Hemon@univ-lille1.fr

Keywords: powder diffraction, structure determination, anhydrous α-lactose

Abstract. Powder X-ray diffraction patterns of the stable anhydrous form of α–lactose and of a mixture of α-lactose monohydrate with hygroscopic anhydrous α–lactose were recorded at room temperature. The starting structural models were found by a Monte-Carlo simulated annealing method. The final structures were obtained through Rietveld refinements with soft restraints on interatomic bond lengths and bond angles and crystalline energy minimisation to locate the H atoms of the hydroxyl groups. The stable form of α–lactose is triclinic with space group P1, Z = Z'= 2, a = 7.6522 (2), b = 19.8637 (5), c = 4.9877 (1) Å, α = 92.028 (1), β = 106.261 (1), γ = 97.153 (1) °, V = 720.18 (3) Å3. For hygroscopic anhydrous α–lactose, the symmetry is monoclinic, space group P21, Z = 2, Z' = 1, a = 7.7795 (3), b = 19.6931 (7), c = 4.9064 (1) Å, β = 103.691 (2)°, V = 730.32 (4) Å3.

Introduction

Lactose (4-O-β-D-galactopyranosyl-D-glucopyranose, $C_{12}H_{22}O_{11}$), is a 'mixed' disaccharide containing a galactose and a glucose unit linked through a β–1,4 linkage. It exhibits two anomers (α–lactose and β–lactose) which differ in the configuration of the terminal hydroxyl group of the glucose unit. For the α–anomer, three crystalline forms have been characterised [1] : the α–lactose monohydrate (hereafter named αL-H_2O), the hygroscopic anhydrous α–lactose (αL_H) and the stable anhydrous α–lactose (αL_S). The β–anomer has only one crystalline form (βL); mixed compounds α-β-lactose have also been identified with different stoechiometries (α/βL) [2], [3]. The crystalline structures of the αL-H_2O form [4], [5], [6] and βL form [7] were solved from single crystal samples with an automatic X-ray diffractometer.
The aim of this article is to give the crystallographic structure of two anhydrous forms of α-lactose by powder X-ray diffraction: the αL_H and αL_S forms. The reason why we used powder data is given for each phase in the next parts.

Experimentation

We have followed the same procedure for the two phases:
1) The data were collected on the laboratory diffractometer equipped with an INEL curved sensitive detector CPS120. A bent quartz monochromator allows selection of the $K_{\alpha 1}$ wavelength of a Cu X-ray tube (λ = 1.54056 Å). The powder was introduced in a Lindemann glass capillary (diameter = 0.7mm), mounted on the axis of the diffractometer. It was rotated during the experiment in order to reduce the effect of possible preferential orientations.
2) The profiles of *n* reflections were individually refined with the program WINPLOTR [8] in order to obtain their exact 2θ positions. We used then the program TREOR [9] to find the unit cell and to index the reflections. A part of the X-ray diffraction pattern was refined with the cell found by TREOR and using the "profile matching" option [10] of the program FullProf [11], in order to determine the space group.
3) Lattice and profile parameters, zero point and interpolated background calculated with the previous refinements were introduced in the program F.O.X. [12] in order to get a starting structural model. A molecule of α-lactose, with C and O atoms only, is built with bond lengths, bond angles and torsion angles calculated from the atomic coordinates of Fries *et al.* [4]. This molecule is introduced randomly in the cell. The "parallel tempering" algorithm of this program was used.
4) The final structure was obtained through Rietveld refinements with soft restraints on interatomic bond lengths and bond angles (program Fullprof [11]) and crystalline energy minimisation to locate the H atoms of the hydroxyl groups: calculations are performed using the DL_POLY molecular modelling package [13] on a system of N = 80 (4 x 2 x 5 crystalline cells) lactose molecules using periodic boundary conditions. Each molecule is described by its 45 atoms which interact through the Ha force field [14] developed for carbohydrates. Electrostatic interactions are handled by the Ewald method. We work in the NVE statistical ensemble where the number of atoms (N), the volume (V) and the energy (E) are fixed. A cut-off radius of 10 Å is used. In order to determine positions of the hydroxyl H atoms, energy minimisation calculations (T = 0) are realised from the structure obtained experimentally. C–O–H angles are initially chosen to be 180°. No dihedral interaction is applied to the hydroxyl H. During minimisation, only H atoms of the hydroxyl groups are allowed to move in order to maintain the experimental structure as much as possible.

Results

The hygroscopic anhydrous phase of α–lactose

α-lactose monohydrate annealed at 135 °C allowed to get *a mixture of this compound with hygroscopic anhydrous α–lactose*. A powder X-ray diffraction pattern of this mixture was recorded at room temperature. To determine the lattice parameters of the phases, the profiles of the 58 reflections with a 2θ angle lower than 40° were refined with the program Winplotr. Among the 58, 44 reflections were attributed to the αL-H_2O form but 14 of them ranging from 9 to 33° do not belong, unambiguously, to the αL-H_2O phase. Having isolated the αL_H phase, we could continue the procedure as described. We have found a monoclinic symmetry, a space group $P2_1$ with 2 molecules per cell (Z' = 1), and the following lattice parameters: a = 7.7795 (3), b = 19.6931 (7), c = 4.9064 (1) Å, β = 103.691 (2)°, V = 730.32 (4) $Å^3$. The final Rietveld plot is given on figure 1 (*Rp*=0.0657, *Rwp*=0.0733, *Rexp*=0.0222,

χ^2 = 10.9). The calculated specific percentage of αL_H phase contained in the powder is 83 (1) %. The projection of the unit cell is given on figure 3a.

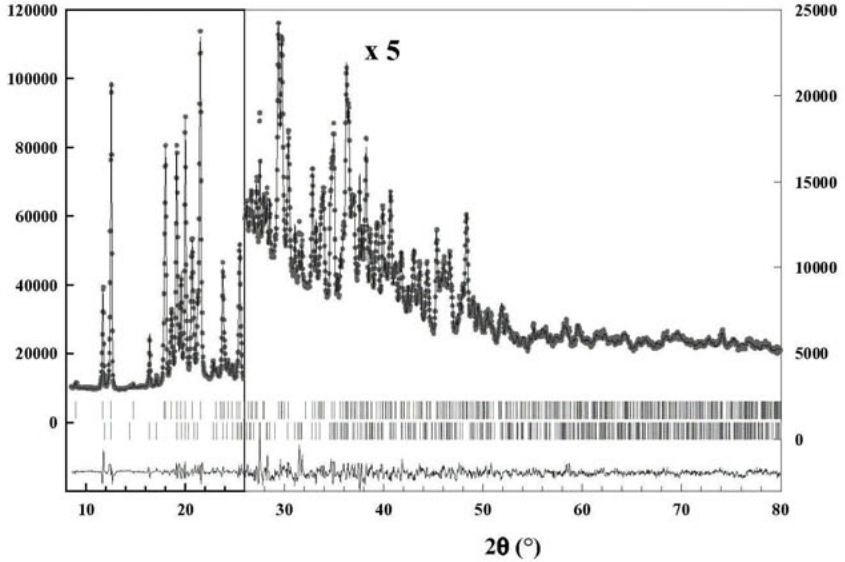

Figure 1. Final Rietveld plot of the hygroscopic phase of α-lactose. Observed data points are indicated by dots, the best-fit profile (upper trace) and the difference pattern (lower trace) are solid lines. The vertical bars correspond to the position of Bragg peaks: upper bars for αL_H, lower bars for αL-H_2O.

The stable anhydrous phase of α–lactose.

The stable anhydrous α–lactose (αL_S) form, not commercially available, can be obtained from αL-H_2O either by heating at about 140°C or by dehydration in an hygroscopic solvent such as methanol [15], which we have used. To get single crystals to perform X-ray experiments with an automatic diffractometer, the αL_S powder must be dissolved in a solvent and, then, crystals grow either by temperature lowering or by evaporation. In solution, the molecule of lactose can undergo hydration to form αL-H_2O or mutarotation to form βL. For this reason, the structure of the αL_S form was solved *ab initio* from powder X-ray pattern using the Rietveld method. We have found a triclinic symmetry, a space group P1 with 2 molecules per cell, and the following lattice parameters: a = 7.6522 (2), b = 19.8637 (5), c = 4.9877 (1) Å, α = 92.028 (1)°, β = 106.261 (1)°, γ = 97.153 (1)°, V = 720.18 (4) Å^3. The final Rietveld plot is given on figure 2. (*Rp*=0.0555, *Rwp*=0.0624, *Rexp*=0.0159, χ^2=15.5). The projection along c* of the unit cell is given on figure 3b.

The reduced atomic coordinates, the bond lengths, the bond angles and the torsion angles for the two phases are given elsewhere [16, 17].

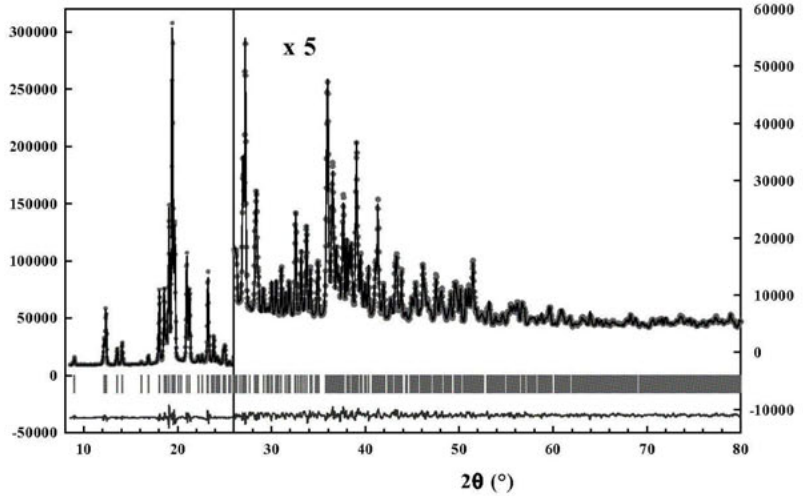

Figure 2. Final Rietveld plot of the stable anhydrous phase of α–lactose. Observed data points are indicated by dots, the best fit profile (upper trace) and the difference pattern (lower trace) are solid lines. The vertical bars correspond to the position of Bragg peaks.

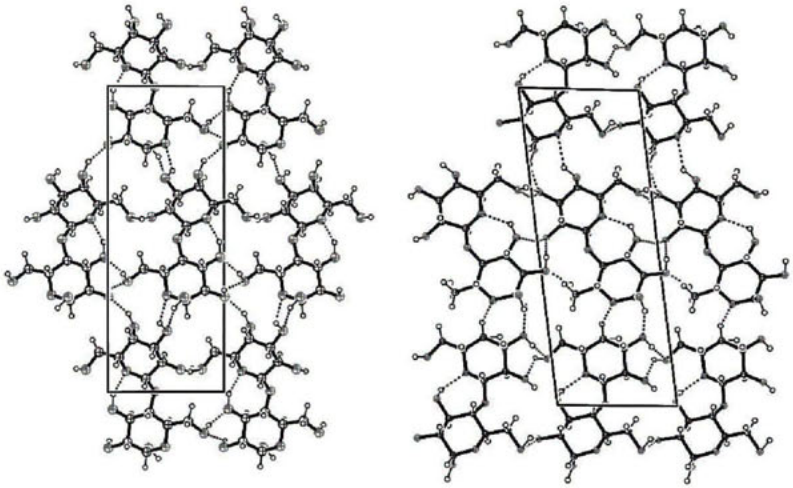

Figure 3. (a) Projection of the unit cell of the hygroscopic α-lactose along c. Dashed lines correspond to H bonds. (b) Projection along c* of the unit cell of the stable anhydrous form of α-lactose. Dashed lines correspond to H bonds.*

Discussion

Despite the different crystalline systems, very similar unit cells are observed between the αL_S form and the other two polymorphs of α–lactose. Only very small differences between the lattice parameters of the two anhydrous forms are seen : the relative changes are as follow : 1.7 % for *a*, -0.9 % for *b* and -1.63 % for *c*. The changes of the α and β angles equal 2.0 and 2.6°, respectively. The change in the γ angle is larger (7.2°) leading to a small 1.4% contraction of the cell volume of the αL_S form with respect to the αL_H one. For the three polymorphic forms of α–lactose, molecules are oriented with their long axis approximately along the ***b*** direction. For αL_S, molecules 1 (see figure 2b) of the cell lie in (***a***, ***c***) planes with the reduced coordinates of their mass centre at about $y \cong 0.5$; they correspond to the molecules generated by the twofold screw axis of the αL_H form. Molecules 2 are also in (***a***, ***c***) planes and their mass centre is at $y \cong 0.0$ and they correspond to the molecules of asymmetric unit of the αL_H form.

The crystalline cohesion of the two forms is achieved by networks of O–H···O hydrogen bonds different to those of the monohydrate phase. The detailed description of the hydrogen bonds networks of the two anhydrous forms of α–lactose and their comparison with those of the monohydrate form is made elsewhere [16, 17].

References

1. Garnier S., 2001, Thesis, University of Rouen, (France).
2. Burshill J.H., Wright W.B., Fuller H.F. & Bell AV., 1965, *J. Sci. Food Agric.* **16**, 62.
3. Lerk C.F., Andreae A.C., Boer A.H. de, Hoog P. de, Kussendrager K. & Leverink J. Van, 1984, *J. Pharm. Sci.* **73**, 856.
4. Fries D.C., Rao S.T. & Sundaralingam M., 1971, *Acta Cryst.* **B27**, 994.
5. Beevers C.A. & Hansen H.N., 1971, *Acta Cryst.* **B27**, 1323.
6. Noordik J.H., Beurskens P.T., Bennema P., Visser R.A. & Gould R.O., 1984, *Z. Kristallogr.* **168**, 59.
7. Hirotsu K. & Shimada A., 1974, *Bull. Chem. Soc. Japan* **47**, 1872.
8. Roisnel T. & Rodriguez-Carvajal J., 2002, *Mater. Sci. Forum* **378-381**, 118.
9. Werner P. E., Eriksson L. & Westdahl M., 1985, *J. Appl. Cryst.* **18**, 367.
10. Le Bail A., Duroy H. & Fourquet J. L., 1988, *Mater. Res. Bull.* **23**, 447.
11. Rodriguez-Carvajal J., 2001, *FullProf, version 1.9c*, LLB, CEA/Saclay, France.
12. Favre-Nicolin V. & Cerny R., 2002, *J. Appl. Cryst.* **35**, 734.
13. Smith W. & Forester T.R., 1996, *J. Molec. Graphics* **14**, 136.

14. Ha S. N., Giammona A., Field M. & Brady J. W., 1988, *Carbohydrate Res.* **180**, 207.
15. Kreveld A. van, 1969, *Neth. Milk Dairy J.* **23**, 258.
16. Platteau C., Lefebvre J., Affouard F. & Derollez P., 2004, *Acta Cryst. B* **60**, 453.
17. Platteau C., Lefebvre J., Affouard F., Willart J.F., Derollez P. & Mallet F., 2005, *Acta Cryst. B* **61**, to be published.

Acknowledgements
This work is supported by the INTERREG IIIA Contract of the European Commission, Project n° 50 : "Therapeutic materials", (FEDER).

Z. Kristallogr. Suppl. **23** (2006) 601-606

Structure determination of 1-pentanol ($C_5H_{12}O$) at 183 K

M. Ramírez-Cardona[1,*], J. C. Escamilla-Casas[1], M. A. Cuevas-Diarte[2], I. Barajas-Rosales[3]

[1]Centro de Investigaciones en Ciencias de la Tierra, U.A.E.H. Carr. Pachuca-Tulancingo, km. 4.5. C.P. 42076. Pachuca, Hidalgo. México
[2]Departament de Cristal.lografia. Universitat de Barcelona. Martí i Franquès s/n. 08028. Barcelona. Catalunya. España
[3]Centro de Investigaciones Químicas, U.A.E.H. Carr. Pachuca-Tulancingo, km. 4.5. C.P. 42076. Pachuca, Hidalgo. México
[*]Contact author; e-mail: mariusr@uaeh.reduaeh.mx

Keywords: 1-pentanol, Patterson Search method, hydrogen bond

Abstract. Powder X-ray diffraction pattern of the crystalline phase of 1-pentanol was recorded with a sensitive curved detector (CPS120) at 183 K. The structure has been solved with the Patterson Search [1] method. The resulting structure was refined by rigid-body Rietveld analysis. The cell is monoclinic, space group $P2_1/c$, Z = 4 and with the following parameters: a = 15.592(9) Å, b = 4.349(1) Å, c = 9.157(1) Å, β = 104.7(7) °, V = 600.6(3) Å^3. The structure contains one molecule in the asymmetric unit with the O−H bond in gauche conformation with respect to the alkyl skeleton. Packing is defined by OH···OH hydrogen bonds that link the 1-pentanol molecules along the b axis as zigzag chains.

Introduction

Normal alkanols are among the simplest substituted hydrocarbons (a single −OH group replaces a hydrogen atom at one end of the aliphatic chain) and they constitute a family of fundamental amphiphilic substances [2]. The hydroxyl group in the molecule plays an important role, by comprising varied hydrogen bonds, in the preservation of the layered structure of the crystal. Furthermore, the conformational behaviour is an important factor that determines the geometry of the OH···OH hydrogen bond. In this matter, vibrational spectroscopic investigations revealed that in solid state, alcohol molecules adopt three conformations for the bond axes of CH_2-CH_2-O-H: Tt, Tg and Gt (T or t represents trans, and G or g represents gauche [3]). X-ray diffraction studies in compounds of this family are scarce. However, some crystal structures of long chain n-alcohols have been determined by single X-ray diffraction: 1-eicosanol ($C_{20}H_{42}O$, [4]), 1-octadecanol ($C_{18}H_{38}O$, [5]), 1-heptadecanol ($C_{17}H_{36}O$, [5b]) and 1-hexadecanol ($C_{16}H_{34}O$, [6]). The importance of this work resides in that it determines the structure of a normal alcohol ($C_nH_{2n+2}O$) with small number of carbon atoms (n=5) of the polymethylene chain. The structure of 1-pentanol*

(hereafter C5*) has not been determined before. The hydrogen bonding of C5 was compared with that of larger members and of 1-butanol ($C_4H_{10}O$ [3]). In this research, the determination of the structure was achieved by using powder X-ray diffraction technique. Since the glassy form is frequently encountered in C5, it is difficult to obtain single crystals. Diffraction data have to be collected at low temperature due to crystalline C5 melts at 194.7 ± 0.9 K. In order to avoid the glassy phase and to obtain a fully crystallized powder, the initial liquid sample was quenched at 140 K and then slowly heated up to 183 K. DSC's (Differential Scanning Calorimetry) analyses (100-200 K) of a crystalline sample did not show any solid-solid transition.

A Patterson search method [1] was applied in the resolution of the C5 structure. This method consists on properly positioning a model (hydrogen atoms are not included) into the unit-cell by means of rotation and translation functions. The goal is to obtain the best coincidence between calculated and experimental Patterson functions. Subsequently, the structure was refined by Rietveld analysis taking into account different conformations of the OH group.

Structure solution

Experimental

The liquid sample of 1-pentanol is commercially available (FLUKA, >99% purity). A powder X-ray diffraction pattern was collected at 183 K on a horizontally mounted diffractometer (Debye-Scherrer geometry, transmission mode). A bent quartz monochromator enables the selection of the $K\alpha_1$ wavelength of a Cu X-ray tube (λ = 1.54056 Å). The apparatus was equipped with an INEL CPS120 curved position-sensitive detector that consists of 4096 channels and the angular step was ~ 0.03 °(2θ). To convert the channels to 2θ degrees, an external standard (a mixture of NAC ($Na_2Ca_2Al_{12}F_4$) and silver behenate - $CH_3(CH_2)_{20}COOAg$ - [7]) was measured in the same diffractometer. The liquid was introduced at room temperature in a sealed Lindemann glass capillary (diameter = 0.5 mm) and was rotated around the θ axis during the experiment to ensure proper averaging of crystallites. The pattern was collected over 20 h. A liquid-nitrogen cryostat (INEL CRY950, 80-460 K) enabled access to low temperatures with temperature fluctuations within 0.5 K, and was used for the *in situ* crystallization according to the following procedure. The liquid 1-pentanol was quenched at 140 K. After the temperature stabilization, the sample was heated up to 183 K at a rate of 2 $K \cdot min^{-1}$. It was kept at this temperature for approximately 2 h in order to achieve full crystallization of the powder.

The powder diffraction data was indexed with the DICVOL91 program [8]. The program found a monoclinic cell with the following lattice parameters and figures of merit: a = 15.577, b = 4.344 Å, c = 9.151 Å, β = 104.8°, V = 598.8 $Å^3$, M(33) = 21.8, F(33) = 40.9. The space group compatible with the systematic absences and with the crystal density was $P2_1/c$. The refinement of profile parameters and the intensity extraction were performed on the C5 pattern (7°-60° 2θ) with the "Profile Matching" option [9] of the FULLPROF program [10]. The background was determined with a linear interpolation between 91 points regularly distributed from 7° to 60° 2θ. With the refinement of profile parameters the R_{wp} converged at 0.077, with a = 15.592(9) Å, b = 4.349(1) Å, c = 9.157(1) Å, β = 104.7(7) °, and V = 600.6(3) $Å^3$.

Asymmetric unit

To solve the structure by *Patterson Search* methods, it is necessary to know the approximate molecular geometry of the possible conformers. Taking into account the number of molecules within the asymmetric unit (Z' = 1) and the conformational information reported in [4, 13] four types of conformers were considered to solve the structure:

Tt: All-trans conformer, C-C, C-O and O-H bonds have trans conformation. Figure 1(i).

Tg: All the C-C bonds of the polymethylene chain, as well as the C-O bond, show trans conformation. The O-H bond has a gauche conformation with respect to the skeleton. Figure 1(ii).

Tt'/Tg': The hydrocarbon skeleton adopts all-trans conformation. This isomer has C-C-C-O torsion angle in trans form. The hydroxyl hydrogen atom is on a disordered site with an occupancy factor of 0.5. t' and g' represents this disorder (O-H bond adopts trans and gauche conformations, respectively). This conformer corresponds to that encountered in the γ phase of 1-eicosanol [4]. Figure 1(iii).

Gt: This isomer has all C-C-C-C torsion angles in trans form and the C-C-C-O torsion angle in gauche form. It agrees with one of the conformers of the asymmetric unit of the β phase (Z' = 2) in long chain n-alkanols [11]. The O-H bond has trans conformation with respect to the polymethylene chain. Figure 1(iv).

Patterson search† (P.S†)

The structure was solved by *Patterson Search* methods using the coordinates of two conformers of 1-butanol ($C_4H_{10}O$ [3]) to build the search model. Hydrogen atoms have not been included in the models. A Patterson search was applied for each conformer with ROTSEARCH program [12]. The first conformer consists of a C-C-C-C-C-O chain with an all-trans conformation (conformer Tt, Tg, or Tt'/Tg', without hydrogen atoms). This molecular model can be denominated as T in accordance to the above-mentioned nomenclature. The second molecular fragment was a C-C bonds chain with an all-trans conformation, and the C-O bond in gauche conformation: conformer Gt without hydrogen atoms. Thus, it can be denominated as G. No soft constraints on bond lengths and angles were allowed in the search. The best solution occurred when the T model was used.

Structure refinement

Consequently, the molecular fragment T (positioned and oriented into the unit-cell by the Patterson search method) should be completed by adding the H atoms. Thus, three Rietveld refinements were performed using Tt, Tg and Tt'/Tg' structural models. The atomic coordinates, including the hydrogen atoms, were used as starting point for every Rietveld refinement with FULLPROF in the 7° − 60° 2θ range. Since the full molecular model for several conformations for C5 was available, the rigid-body refinement was preferred. Likewise, the TLS formalism [13] was considered.

The parameters refined by Rietveld method were: the overall scale factor, the parameters of the center of the asymmetric unit and its orientation, the asymmetry parameter, the translational mean square displacements and librational components, and two peak shape parameters (X_{ST} and Y_{SZ} of TCH-pseudovoigt peak function [14]). The results of the refinements are resumed in Table 1. No differences in the Rietveld plot were observed

between the three refinements, due to the weak influence of H atoms in the X-ray diffraction. This procedure caused the R_{wp} to converge at 0.043, 0.051 and 0.055 for Tg, Tt and Tt'/Tg' structures, respectively. The soft constraint on H···O distance introduced in the refinements caused these changes to the R_{wp}. The final fractional atomic coordinates for Tg structure and the plot of its Rietveld refinement are shown in table 2 and figure 2, respectively. The atom numbering is provided in figure 3.

Results and discussion

The crystal structure is illustrated in figure 4 as the projection of the unit cell along [010] and [100]. Only the structure of C5 from Tg conformer preserves the archetypal-layered structure of the normal alcohols (figure 4). However, the molecules are not positioned in a parallel arrangement within the layer, contrasting with β and γ phases occurring in long chain compounds. Cohesion between molecules of different layers is achieved by O — H···O hydrogen bonds; this bonds are shown in Figure 4 in the *bc* plane. Table 3 summarized the structural characteristics of the hydrogen bonds of C5 and other n-alkanols. Each hydrogen bond is associated with a specific conformer. The Tg conformer implies an special O — H···O geometry (O1···O(i) 2.681(1) Å and O1—H···O(i) 102.8(9) º [(i) –x, -1/2+y, ½-z]) that it is not encountered in other compound of the family.

Conclusions

The crystal structure of 1-pentanol was determined by powder X-ray diffraction, using a P.S. method. Although the P.S. procedure final results showed that the quality of the X-ray powder pattern is high enough, it is not possible to elucidate the OH-group conformation. Although the atomic arrangement of refined structures (from Tt, Tg and Tt'/Tg' conformers) could not be distinguished visually, the reliability factors validated all the results. An alternative to the methods that only consider the intensities extracted from X-ray pattern is to perform a potential energy minimization procedure; in this manner, it facilitates to choose the correct conformer. In a future work, the results of the simultaneous optimization of lattice energy and R_B will be presented for the C5 case. Likewise, the neutron diffraction would be an appropriate method for locating the hydrogen atoms.

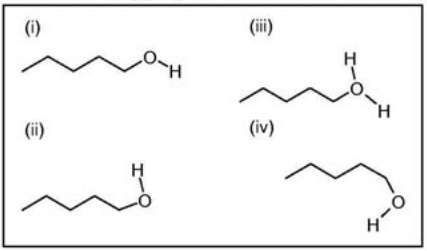

Figure 1. Conformations of C5. (i) Tt; (ii) Tg; (iii) Tt'/Tg'; (iv) Gt.

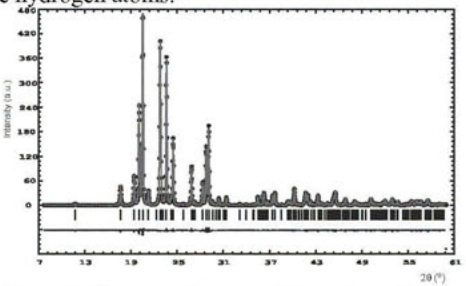

Figure 2. Rietveld refinement of the pattern of C5 (Tg conformation) at 183 K.

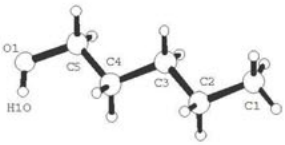

Figure 3. C5 molecule, showing the atom numbering.

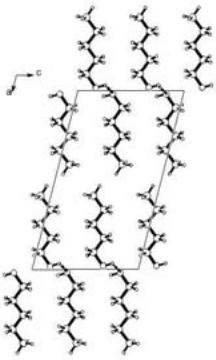

a)

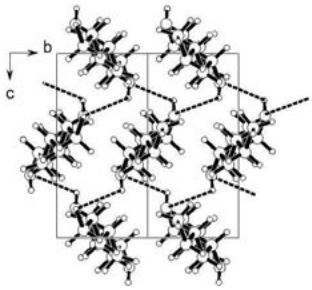

b)

Figure 4. C5, a) Structure in [010] projection. b) Layered structure, in [100] view. Dashed lines are hydrogen bonding in infinite chain along b axis.

Table 1. Details of the rigid-body Rietveld refinements from X-ray powder data of 1-pentanol (Tg isomer in the asymmetric unit).

Range of 2θ (°)	7–60
Space group, Z	$P2_1/c$, 4
Unit-cell dimensions (Å,°)	a = 15.592(9), b = 4.349(1), c = 9.157(1) Å, β = 104.7(7) °
Volume (Å^3)	600.6(3)
Temperature (K)	183
Scale factor	1.47
Peak shape parameters	U = 0.036(1)°, V = -0.059(1)°, W = 0.040(2)° , X_{ST} = 0.00006(2)° , Y_{SZ} = 0.003(5)°
Asymmetry parameter	0.075(3)
TLS factors	T_{11} = 0.027, T_{22} = 0.063, T_{33} = 0.037, L_{33} = 0.0005
Center of the rigid body $\sigma(X_o)$, $\sigma(Y_o)$, $\sigma(Z_o)$	0.003, 0.006, 0.002
$\sigma(\phi)$, $\sigma(\psi)$, $\sigma(\varphi)$	0.02°, 0.10°, 0.15°
Residuals	R_p = 0.039, R_{wp} = 0.043, R_B = 0.081, $R_{exp.}$ = 0.021

Table 2. Fractional atomic coordinates for C5 (C, O and hydroxyl H atoms).

	x	*y*	*z*
C1	0.4128 (5)	-0.155 (1)	0.5974 (3)
C2	0.3341 (5)	-0.062 (1)	0.4657 (3)
C3	0.2547 (5)	0.030 (1)	0.5279 (3)
C4	0.1759 (5)	0.121 (1)	0.3961 (3)
C5	0.0967 (5)	0.214 (1)	0.4583 (3)
O1	0.0205 (5)	0.303 (1)	0.3376 (3)
H1O	0.0336 (5)	0.294 (1)	0.2565 (3)

Table 3. Hydrogen bonding characteristics of some n-alkanols.

Compound	Z'	Conformer/s in a.u.	D-H···A	H···A (Å)	D···A (Å)	D-H···A (°)	Ref.
$C_5H_{12}O$	1	Tg	O-H1O···O(i)	2.376(1)	2.681(1)	102.8(2)	This work
$C_4H_{10}O$	2	Tt, Tg	O1-H1O···O(ii),O2-H2O···O(ii)	2.196(2)	2.827(2)	120.3(3)	[15]
$C_{14}H_{30}O$ (γ)	1	Tt'/Tg'	O-H1O···O(iii),O-H1O'···O(iv)	1.945(4)	2.591(4)	121.7(6)	[15]
				2.306(4)	3.154(4)	138.9(6)	
$C_{17}H_{36}O$ (β)	2	Tt, Gt	O1-H1O···O(v),O2-H2O···O(vi)	1.838(1)	2.751(1)	151.2(5)	[5b]
				2.089(1)	2.711(1)	115.2(5)	

Symmetry codes: (i) –x, -½+y, ½-z; (ii) -x,-1-y,1-z; (iii) –x, 2-y, 1-z; (iv) –x, y, 3/2-z; (v) x,y,z; (vi) 1-x, ½+y, ½-z.

References

1. Rius, J. & Miravitlles, C., 1988, *J. Appl. Cryst.* **21**, 224-227.
2. a) Kertes, A.S. & King, C.J., 1987, *Chem. Rev.* **87**, 687-710.; b) Small, D.M., 1986, *Handbook of Lipid Research*, Vol. 4, pp. 233-241. New York: Plenum Press.; c) Tanford, C., 1980, *The Hydrofobic Effect: Formation of Micelles and Biological Membranes*, 2nd ed.; New York: Wiley.
3. Ohno, K., Yoshida, H., Watanabe, H., Fujita, T. & Matsura, H., 1994, *J. Phys. Chem.* **98**, 6924-6930.
4. Michaud, F., Ventolà, L., Calvet, M.T., Cuevas-Diarte, M.A., Solans, X. & Font-Bardía, M., 2000, *Acta Cryst. C*, **56**, 219-221.
5. a) Fujimoto, K., Yamamoto, T. & Hara, T., 1985, *Rep. Prog. Polym. Phys. Jpn.* **28**, 163-166. b) Seto, T., 1962, *Mem. Coll. Sci. XXXA* **1**, Art. 9.
6. Abrahamsson, S., Larsson, G. & von Sydow, E., 1960, *Acta Cryst.* **13**, 770-774.
7. Blanton, T.N., Huang, T.C., Toraya, H., Hubbard, C.R., Robie, S.B., Louër, D., Göbel, H.E., Will, G., Gilles, R. & Raftery, T., 1995, *Powd. Diffr.* **10**, 2, 91-95.
8. Boutlif, A. & Louër, D., 1991, *J. Appl. Cryst.* **24**, 987-993.
9. Le Bail, A., Duroy, H. & Fourquet, J.L., 1988, *Mater. Res. Bull.* **23**, 447-452.
10. Rodríguez-Carvajal, J., 1998, *Fullprof*, version 3.5d, LLB, CEA/Saclay, France.
11. Ventolà L., Ramírez, M., Calvet, T., Solans, X. & Cuevas-Diarte, M.A., 2002, *Chem. Mater.* **14**, 508-517.
12. Rius, J. & Miravitlles, C., 1987, *J. Appl. Cryst.* **20**, 261-264.
13. Schomaker, V. & Trueblood, K. N., 1968, *Acta Cryst. B,* **24**, 63-78.
14. Thompson, P., Cox, D.E., & Hastings, J.B., 1987, *J. Appl. Cryst.* **20**, 79-83.
15. Ramírez-Cardona, M., 2002. PhD Thesis. Universitat de Barcelona.

Acknowledgements. Authors are grateful to Dr. Jordi Rius for his assistance in the use of the Patterson search method.

Z. Kristallogr. Suppl. **23** (2006) 607-612

Crystallographic texture changes of wood due to air parameter variations

J. T. Bonarski[1,*], W. Olek[2]

[1]Institute of Metallurgy and Materials Science, Polish Academy of Sciences, ul. Reymonta 25, 30-059 Kraków, Poland
[2]Faculty of Wood Technology, Agricultural University of Poznań, ul. Wojska Polskiego 38/42, 60-637 Poznań, Poland
[*]Contact author; e-mail: nmbonars@imim-pan.krakow.pl

Keywords: crystallographic texture, low lattice symmetry, microfibril angle

Abstract. Wood being a natural biopolymer reveals a distinct preferred orientation of its crystalline part, i.e. cellulose. The traditional methods characterizing the spatial organization of the structural component of wood are usually limited to the microfibril angle determination only. It was recognized that the angle is an insufficient parameter describing the complexity of the submicroscopic structure. Therefore, it can not be used to evaluate the wood structure changes caused by the natural variation of air parameters. The Orientation Distribution Function (ODF) was used to quantify the changes of the crystallographic structure. The results from water sorption experiments were used as the input data in analysis of the crystallographic texture of the cellulose. The results obtained by ODF confirmed the usefulness of the concept and the application of the advanced texture analysis to the description of the influence of air parameters on the wood structure.

Introduction

The in-service wood products are in contact with moist air of variable temperature and relative humidity. The consequence of the contact is the permanent hygroscopic disequilibrium leading to cycling changes of wood moisture content. Water from the moist air is transported into wood and bound at the so-called active sorption sites, which are primary present in the amorphous part of cellulose [1-4]. The remaining part of wood cellulose forms crystallographically ordered regions of the very limited ability to bound water. The cyclic changes of the moisture content of wood are accompanied by the phenomenon of sorption hysteresis, which decreases in successive sorption cycles. An explanation of the hysteresis was proposed by Chudinov [5]. He stated that a probable reason for the phenomenon may be a difference of cellulose organization during the adsorption and desorption processes. Siau [3] suggested that the hysteresis may be explained by the phenomenon of linking active sorption sites. However, the hypotheses related to the hysteresis have still not been verified experimentally. The crystallographic organization of wood cellulose is traditionally described by the mean microfibril angle, which is defined as the angle between the longitudinal direction of cellulose microfibrils and the longitudinal direction of wood cells. However, the angle does not reflect changes of the structure of the ordered regions induced by air parameter variations. It

has already been shown that the application of the texture function provides much more valuable information when compared to the concept of the mean microfibril angle [6]. The objective of this paper is to apply the texture function to quantify changes in the crystallographic structure of wood cellulose as induced by cycling changes of parameters of moist air.

Material and methods

Material

The investigations were performed for mature normal birch wood (*Betula pendula* Roth.). The material was firstly equilibrated to the moisture content of ca. 10%. From it the samples were cut in the shape of rectangular prisms. The thickness of samples corresponded to the radial anatomical direction and was equal to ca. 6 mm. The radial plane of samples was subjected to X-ray examination.

Sorption experiment

The cycling desorption and adsorption of bound water in wood was performed using the desiccator method. Phosphorus pentoxide was used in the first desiccator to obtain air relative humidity close to 0% and therefore to dry wood samples to the moisture content of almost 0%. The second desiccator contained distilled water and therefore, the air kept in the desiccator was almost saturated. It let to obtain wood moisture content close to the Fiber Saturation Point (here ca. 28%). Each desorption and adsorption cycle lasted three days. The temperature inside the experimental set-up containing the desiccators was controlled at the constant level of 26°C. The number of the full desorption and adsorption cycles performed in the experiments was equal to 52.

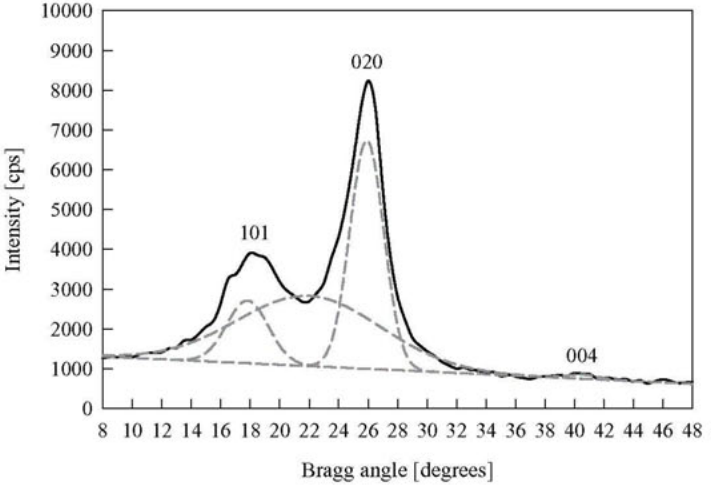

Figure 1. X-ray diffraction pattern with separated profiles of cellulose reflections and amorphous "halo". Fitting procedure performed with DAMfit software package [7].

Texture experiment

The typical X-ray diffraction pattern obtained for cellulose is shown in figure 1. A relatively high background, visible for the range of the Bragg angle ranging from 10° to 35°, can be attributed to the non-crystalline or amorphous portion of the cellulose. The pattern was used to select reflections (here 101, 020 and 004) for which the pole figures $P_{(hkl)}(\alpha, \beta)$ of the following planes (101), (010) and (001), respectively were registered by means of the X-ray diffraction technique. The Schulz back-reflection technique [8] for the following ranges $\alpha = 0°...75°$ and $\beta = 0°...360°$ with steps $\Delta\alpha = 5°$ and $\Delta\beta = 5°$ was applied, respectively. Measurements were performed with a Philips X'Pert system equipped with the texture goniometer ATC-3. The filtered X-ray radiation CoKα (λ = 0.179026 nm) was used. The set of the obtained experimental (incomplete) pole figures $P_{(hkl)}(\alpha, \beta)$, i.e. (101), (010) and (001) for the crystalline part of the cellulose is presented in figure 2. In order to calculate the texture function (here the ODF) as well as to obtain the complete pole figures (i.e. for the range of the polar angle α ranging from 0° to 90° - figure 2) the ADC method was used [9]. The numerical analysis was performed with the use of the software package Lab-Tex [10].

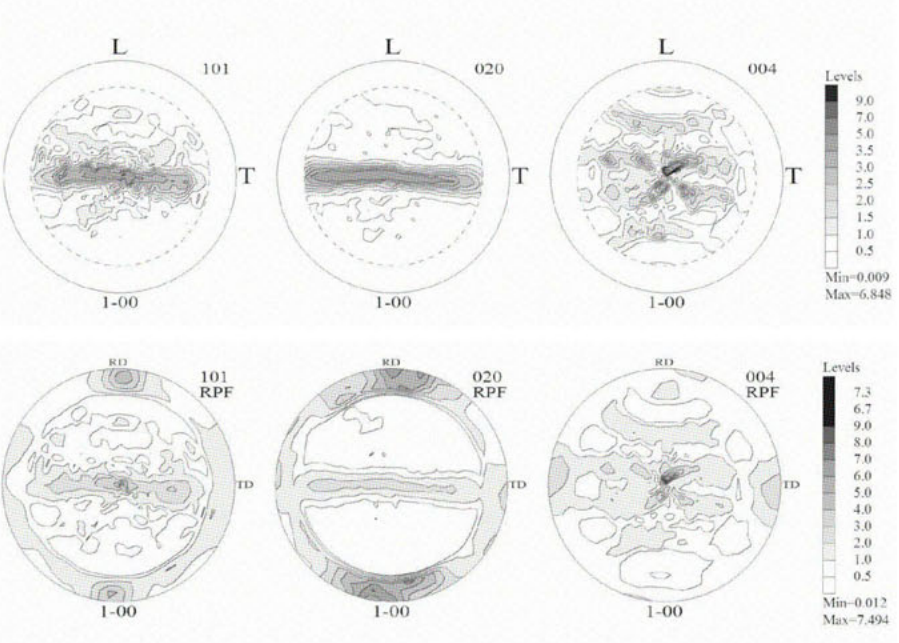

Figure 2. Experimental (top) and complete pole figures (bottom) at the initial stage of the sorption experiment. L – longitudinal anatomical direction, T – tangential anatomical direction, RD - and TD - correspond to the L and T direction, respectively. RPF – recalculated (complete) pole figure, 1-00 – symbol of the sample (initial stage of sorption).

Results

The quantitative texture analysis has been performed for the same wood sample, but for two different stages of the sorption test: *initial stage* (coded as *1-00*) and *after 52-th cycle* (coded as *1-50*). The Orientation Distribution Function (ODF) for the both stages of sorption has been calculated on the basis of the selected pole figures of crystallographic phase of wood, here the native cellulose. The ODF allowed to calculate the inverse pole figures of the longitudinal direction (L) which are helpful for the interpretation of the spatial arrangement of the cellulose. Both the inverse pole figures and the selected part of the ODF are presented in figures 3 and 4 respectively. The texture of cellulose in both sorption stages (i.e. *1-00* and *1-50*) is distinctly different. The observed differences concern the character of the spatial distribution of ordered areas of cellulose in the longitudinal direction. In the *initial* stage of sorption the orientation of the ordered areas is much more regularly distributed around the anatomical direction *L* as compared to the *1-50* state. After the 52-th cycle of sorption, some ordering of the texture was observed in the form of the increasing density of the (110) poles (figure 3). The differences in the texture can be described in details by the ODF which enables to identify the adequate texture components as well as to determine its quantitative changes. The observed additional ordering of the spatial arrangement of the cellulose is not accompanied by changes in the degree of crystallinity, defined as the ratio of the ordered regions of cellulose giving diffraction effects to the total registered signal of X-ray scattering. The degree of crystallinity in the both analyzed sorption states was similar and equal to $77 \pm 1.5\%$. Thus the degree of crystallinity is much less sensitive to the cycling sorption than the crystallographic texture.

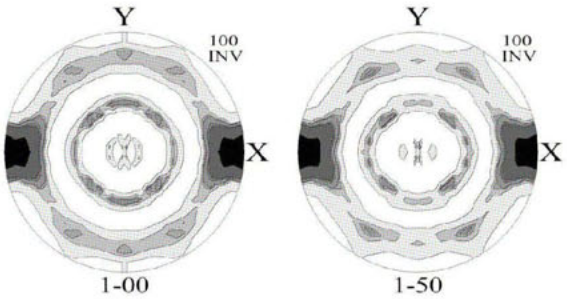

Figure 3. Inverse pole figures for the longitudinal direction (L) of the investigated birch wood sample. X, Y and Z are the axes of the crystalline lattice of cellulose. Maximum value equal to 6.3 [generated by the software package LaboTex (LaboSoft, 2003)].

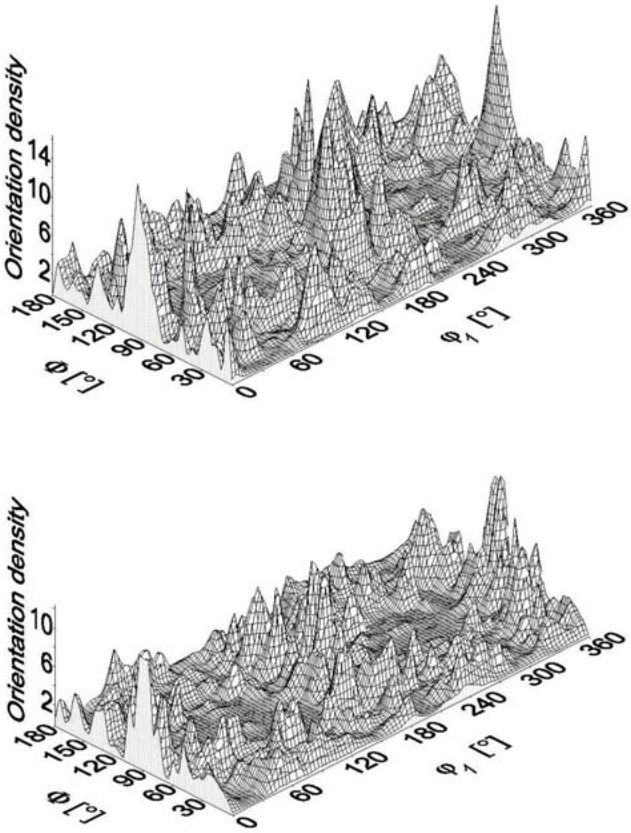

Figure 4. ODF for a selected constant φ_2 value (φ_2 = 90°) of the Euler orientation space (φ_1, Φ, φ_2) of wood cellulose at the initial stage (top) and at the 52-th cycle of sorption (bottom) [generated by the software package LaboTex (LaboSoft 2003)].

Concluding remarks

The spatial arrangement of cellulose of the examined wood, changes during subsequent cycles of water sorption. The rearrangement is manifested by an increase in order in the crystalline part as observed in the texture changes. They are the result of rotations of the cellulose ordered regions around the longitudinal axis of microfibrils. The crystallographic texture can be recognized as the indicator of dimensional stability which influences mechanical properties wood when applied as a construction material.

References

1. Kollmann, F.F.P. & Côté, W.A., 1968, *Principles of wood science and technology. I Solid wood* (Berlin: Springer-Verlag).
2. Siau, J.F., 1984, *Transport processes in wood* (Berlin: Springer-Verlag).
3. Siau, J.F., 1995, *Wood: influence of moisture on physical properties* (Virginia Tech, Blacksburg).
4. Skaar, C., 1988, *Wood-water relations* (Berlin: Springer-Verlag).
5. Chudinov, B.S., 1984, *Voda v drevesine*. (Novosibirsk: Nauka).
6. Bonarski, J., Olek, W. & Pawlik, K., 1996, *Textures of natural polymers - wood*. Proceedings of the 11th International Conference on Textures of Materials ICOTOM-11, September 16-20, 1996, X'ian, China, pp. 1215-1220.
7. Bonarski J., *Computer programs*, (not published works).
8. Schulz, L.G., 1949, *J. Appl. Phys.*, **20**, 1030-1033.
9. Pawlik, K., 1986, *physica status solidi (b)*, **134**, 477-483.
10. LaboSoft, 2003, *LaboTex v. 2.1.016 – the texture analysis software package*. Labo Soft s.c.

Acknowledgements. The work was financially supported by the State Committee for Scientific Research as the 3 P06L 047 22 research grant.

Z. Kristallogr. Suppl. **23** (2006) 613-618

Poly(ethylene glycol) interactions with proteins

J. Hašek

Institute of Macromolecular Chemistry, Academy of Sciences of the Czech Republic
Heyrovského nám.2, 162 06 Praha 6
*Contact author; E-mail: hasek@imc.cas.cz

Keywords: poly(ethylene glycol), PEO, PEG, POE, protein-polymer interaction

Abstract. Main drawback of crystallographic methods in study of polymer materials is a virtual impossibility to grow single crystals. This paper shows how to overcome this obstacle by dissolving polymers in large solvent cavities of protein crystals. The simple trick of placing the polymer molecule into the regular scaffold of protein crystal allows an experimental determination of polymer segments bound at the protein surface with reliability and accuracy of standard protein crystal crystallography. The performance of this method is demonstrated by the case of poly(ethylene glycol) – the compound frequently used as a component of many pharmaceutical and cosmetic preparations. The paper also describes typical interactions between the polymer and biological materials.

Introduction

Interaction of polymers with biological macromolecules is an important topic because of the many applications of polymers in pharmaceutics, surgery, agriculture, etc. Polymers used for medical treatment are extensively tested to ensure they have no adverse long-term effects on organisms, health or environment. To understand the many different statistical correlations that are unavoidably observed in the tests of biological processes it is necessary to understand the basic principles of adhesion between polymer and biological molecules in atomic resolution. In spite of the fact that intermolecular interactions are theoretically and experimentally studied by many indirect methods, X-ray crystallography plays here a prominent distinct role because it provides direct observation of polymer complexes as a whole ensemble with all the details of their structure including changes due to pH and buffer composition. It shows the inner mobility of macromolecules, instability in molecular assemblies and also the mobility of solvent molecules surrounding the macromolecules.
Poly(ethylene glycol) PEG [synonyma poly(oxy ethylene) POE or poly(ethylene oxide PEO] is one of the most frequently used precipitating agents in protein crystallization for its very specific interactions with proteins. Polymer molecules adsorbed at the protein surface support crystallization by blocking undesirable interactions between proteins, by covering undesirable hydrophobic surface or by direct interactions in the inter- and intraprotein clefts. This paper shows some empirical rules, which generally govern adhesion of poly(ethylene glycol)

at the surface of protein molecules, derived from direct experimental observation by X-ray diffraction.

Diffraction experiment

X-ray diffraction is not a very effective tool for observation of bulk polymer material in solid state or in solution where an immense number of different conformations and intermolecular interactions are expected. A different situation appears when one is interested in interaction of polymers with biomacromolecules. Protein crystals contain large solvent cavities (30-70 % of total volume). Solvent contents in these cavities change to preserve equilibrium with the buffer in which the measurement is performed. Thus, we can observe molecular fragments of any dissolved component which adsorbs selectively on the protein surface. Crystals of large proteins easily incorporate large polymer molecules (up to several hundreds of monomer units) from buffer.

Diffraction methods, determining the time- and space-averaged electron density, are sensitive to any type (static or dynamic) of molecular disorder. Thus, only the parts of polymer molecules selectively adsorbed on the protein surface, and thus fixed in the regular scaffold of the protein crystal are visualized by standard X-ray diffraction. Refined atomic displacement parameters are low at sites of strong interaction between polymer and protein, but rapidly increase with increasing distance from the sites of adhesion. Solvent and all dissolved parts of the polymer molecules in cavities are not visible in electron density maps.

The process of intermolecular adhesion is competitive and therefore the adhesion of the polymer of interest can be controlled by composition of mother liquor soaked in the crystal. Polymers or other additives either co-crystallize with the protein (in most cases) or are soaked in the crystals of interest already prepared in advance using some technique allowing sufficient time for diffusion of the components and stabilization of the system.

Interactions between poly(ethylene glycol) and bio-molecules

A variety of molecular weight fractions of poly(ethylene glycol) is used in literature and in commercially available crystallization screens (e.g. ethylene glycol, PEG400, PEG550, PEG1000, PEG1500, PEG2000, PEG3000, PEG4000, PEG6000, PEG8000, PEG10000, PEG20000). We observed many interactions of PEG with proteins studied in our laboratory where we paid special attention to localization of ligands adhered to protein surface. Clearly, a much larger number of interactions of PEG is found in literature.

Inclusion of PEG fragment in the structure model and its refinement lowers R factor and make the maps of electron density more clear, however, does not significantly change the positions of protein atoms. Therefore, special care should be taken when retrieving data from PDB [1] to analyse the PEG interactions. As a rule, PEG is not considered to be the aim of the research and thus, it happens in some cases that the responsible author does not interpret the electron density of the polymer at all, or places in the respective position a chain of atoms just to satisfy electron density without any special care of its chemical relevance. So, a simple retrieval of relevant coordinates from PDB [1] need not give a rigorous and realistic image in all cases. However, it is relatively easy to recalculate the electron density in the place of interest and to perform a more careful analysis at the respective site. At present, the PDB deposits raw experimental data for almost all new diffraction measurements and thus a more

careful retro-analysis of polymer interactions is possible in the most cases published in the last decade.

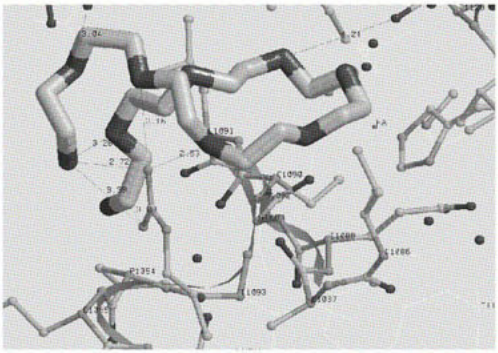

Figure 1. Large loop of PEG molecule at the protein surface is formed mainly due to interaction with positively charged ends of arginine [3] (PDB code 1ICJ).

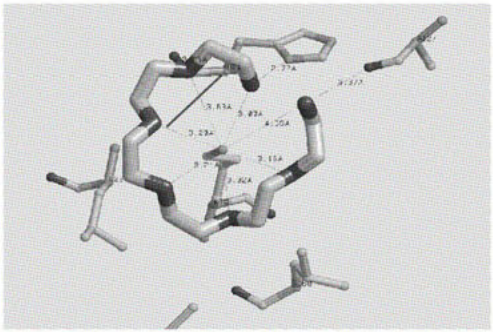

Figure 2. PEG molecule anchored between His and Lys surrounds the $NH3^{+}$ ion at the end of Lys and leaves protein with the seventh PEG monomer unit already dissolved in solution [4] (PDB code 1O57).

An inspection of the Protein Data Bank [1] revealed 283 PEG - protein surface interactions. Five typical examples of these interactions are shown in figures 1-5 (RASMOL /2/). The first figure shows a long loop of PEG chain formed by interaction with arginine at the surface of the protein (peptide deformylase from *Escherichia coli* (resolution 1.9 Å, PDB code 1ICJ).

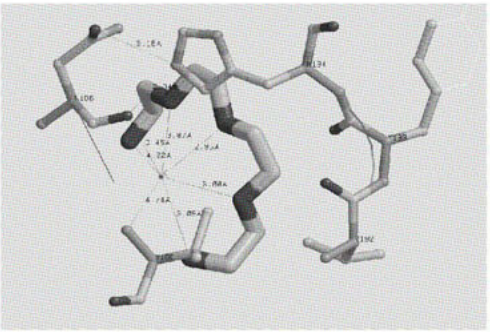

Figure 3. Hydrophobic outer part of the loop of the PEG molecule formed by encapsulation of K^+ ion covers a large area of the hydrophobic surface of protein glyceraldehyde 3-phosphate dehydrogenase [5] (PDB code 1OBF). Five ether oxygens are fixed at the protein surface. The remaining part of the PEG molecule is solvated in the intermolecular cavity.

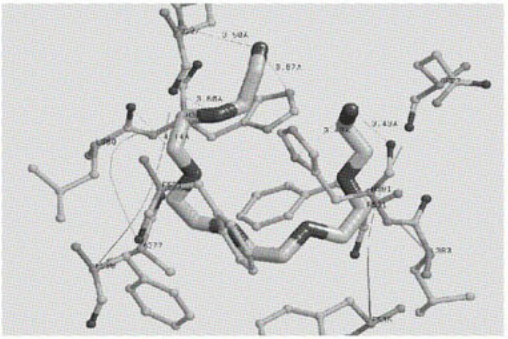

Figure 4. Six monomer units of PEG molecule form a loop inserted in the phenylalanine rich part of a protein by embedding the Na^+ ion from solution. The input and output sites of the loop are fixed to the protein by His and Ser contacts [6] (PDB code 1J07). Six PEG monomer units are bound to protein, the rest is solvated in intermolecular cavities.

Very characteristic and stabile patterns of PEG, i.e. ring of 6-7 monomer units similar to 18-crown-6 complexes [7], are formed around the positively charged residues at the protein surface. Figure 2 shows six PEG monomers wrapping the end of a lysin side chain. Seven consecutive ether oxygens coordinate to the NH_3^+ group (purine operon repressor from *Bacillus subtilis* (resolution 2.2 Å, PDB code 1O57).

Surprisingly, a similar local reorganization of PEG can lead to hydrophobic adhesion of PEG to protein. Figure 3 shows six PEG monomers rolled around the K^+ cation extracted from buffer. The outer hydrophobic shell of this pseudo-crown ether ring fits the hydrophobic cleft on the surface of glyceraldehyde 3-phosphate dehydrogenase from *Alcaligenes xylosoxidans* (resolution 1.7 Å, PDB code 1OBF).

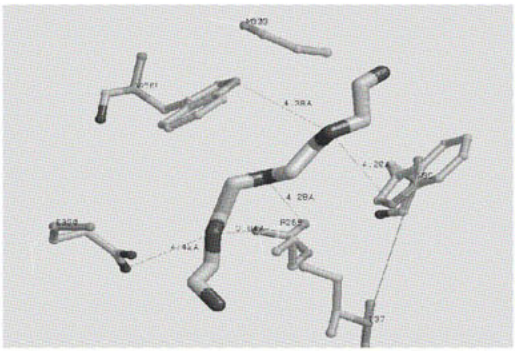

Figure 5. Extended conformation of PEG in a cleft at the protein surface. Four monomers of PEG are firmly inserted in the cleft between glutamic acid, arginine and two tryptophane residues at the surface of the protein ([7] (PDB code 1ESC).

Conclusion

Protein crystallography provides an effective tool for direct experimental observation of interactions between polymers and biological material. Crystals of large proteins swollen with 40-70 % of solvent can readily incorporate sufficient amounts of soluble polymers. The active interfaces between polymer and protein are usually shown with high precision while the parts of polymer chains without contacts to protein surface remain dynamically disordered (dissolved) inside the intermolecular cavities filled with buffer and contribute thus only to the background in electron density maps.

It is observed, that poly(ethylene glycol) molecules tend to encapsulate and multiply coordinate the positively charged lysine, arginine and histidine residues (Figs 1-2). PEG molecules also tend to form linear binding patterns in clefts of the protein surface where the predominant contacts are hydrogen bonds to aminoacid side chains acting as hydrogen donors and hydrogen bonds to the main-chain NH groups (Fig.5). A very specific type of interaction is

the coordination embedding of the cation trapped from solution, forming prevailingly hydrophobic contacts of the complex cation outer envelope with the protein surface (Fig.3-4).
Thus, the typical modes of the poly(ethylene glycol) interaction with the protein surface can be categorized into four groups:

- multiple coordination contacts to positively charged lysine, arginine and histidine residues
- hydrogen bonds to side chains of amino acid residues,
- hydrogen bonds to the main chain NH groups,
- coordination embedding of the cation from solution and forming hydrophobic contacts of the outer envelope of complex cation with prevailingly hydrophobic areas at the protein surface.

The poly(ethylene glycol) molecule is very flexible, possessing a variety of interactions to proteins. Its flexibility in fitting the protein surface including a propensity to leak into the intra and intermolecular clefts and its ability to modify temporarily the respective parts of protein surface make it a universal agent for protein crystallization.

References

1. Berman, H. M., Westbrook, J., Fen, Gilliland Z., G., Bhat,T. N., Weissig H., Shindyalov, I. N. & Bourne P. E., 2000, *Nucleic Acids Res.*, **28**, 235.
2. Sayle, R. and Milner-White James, 1995, *Trends Biochem. Sci.*, **20** (9), 374.
3. Becker A, Schlichting I, Kabsch W, Schultz S, Wagner AF, 1998, *J. Biol. Chem.*, **273**, 11413-11416.
4. Sinha SC, Krahn J, Shin BS, Tomchick DR, Zalkin H, Smith JL, 2003, *J. Bacteriol.*, **185**, 4087-4098.
5. Antonyuk SV, Eady RR, Strange RW, Hasnain SS, 2003, *Acta Crystallogr. Sect.D: Biol. Crystallogr.*, **59,** 835-842.
6. Bourne Y, Taylor P, Radic Z, Marchot P., 2003, *EMBO J.*, **22**(1), 1-12.
7. Wei Y, Schottel JL, Derewenda U, Swenson L, Patkar S, Derewenda ZS, 1995, *Nat. Struct. Biol.,* **2**, 218-223.

Acknowledgement. This research was supported by projects GACR 204/02/0843 and MSMT 1K05008.

Author Index

Volume I: pp. 1–260
Volume II: pp. 261–618